UNIVERSITÉ DU LUXEMBOURG

PhD-FSTC-2019-12
The Faculty of Sciences, Technology and Communication

DISSERTATION

Presented on 26/02/2019 in Luxembourg

to obtain the degree of

DOCTEUR DE L'UNIVERSITÉ DU LUXEMBOURG

EN SCIENCES DE L'INGÉNIEUR

by

Thomas Harzheim
Born on 27 May 1986 in Eschweiler (Germany)

MIXED FREQUENCY SINGLE RECEIVER ARCHITECTURES AND CALIBRATION PROCEDURES FOR LINEAR AND NON-LINEAR VECTOR NETWORK ANALYSIS

Dissertation Defence Committee

Prof. Dr.-Ing. Klaus Solbach, Dissertation Supervisor
Professor, University of Duisburg-Essen

Prof. Dr.-Ing. Holger Heuermann
Professor, FH Aachen – University of Applied Sciences

Prof. Dr.-Ing. Holger Voos
Professor, Université du Luxembourg

Prof. Dr.-Ing. Jean-Régis Hadji-Minaglou, Chairman
Professor, Université du Luxembourg

Prof. Dr.-Ing. Ulrich Sorger
Professor, Université du Luxembourg

Declaration

This dissertation is the result of my own work and includes nothing, which is the outcome of work done in collaboration except were specifically indicated in the text. It has not been previously submitted, in part or whole, to any university or institution for any degree, diploma, or other qualification.

Signed: Thomas Harzheim

Date: 23 January 2019

Thomas HARZHEIM

Faculty of Science, Technology and Communication (FSTC)
University of Luxembourg

Institute for Microwave and Plasma Technology (IMP)
FH Aachen - University of Applied Sciences, Germany

Abstract

In this thesis several new advancements in the field of linear and non-linear vector network analysis are presented. Three distinct but interconnected topics are addressed in this work:

First the concept and feasibility of the single receiver vector network analyzer (VNA) architecture and the implications for existing error models are analyzed, starting with the one-port reflectometer, through two-port unidirectional 5-term, bidirectional 10-term and finally 7-term error models.

New VNA error models, which are able to capture the effects of the leaky RF receiver input wave selector switch, are derived, along with new calibration and correction procedures for this architecture. Modifications to the existing test-set architectures are introduced to reduce the effects of the leaky RF receiver input wave selector switch and shorten the required measurement time in this VNA architecture.

A purpose built 275 MHz to 6000 MHz single receiver VNA system based upon commercial of-the-shelf components is presented and analyzed. Measurements carried out with this VNA system are used in conjunction with numerical test-set and VNA simulations to verify the efficacy of the new calibration and correction methods as well as different VNA test-set architectures according to EURAMET[1] standards and procedures.

The second main topic of this thesis is the introduction of phase repeatable synthesizers as a new calibration and correction phase reference standard for non-linear VNA measurements. Due to the high output power capability of this new phase reference standard, new non-linear test-set and measurement scenarios such as the full non-linear two port characterization of high power solid-state amplifiers become possible, which were out of reach before due to low system signal-to-noise ratios provided by comb-generator based sources in this setup.

The third and final topic of this thesis integrates the contents and achievements of the two previous topics to prove and verify the feasibility of VNA based harmonic, i.e. non-linear, transponder based stepped-FMCW radar systems operating directly in the frequency domain. A new stepped-FMCW theory based on mixed-frequency S-parameters is presented in conjunction with a phase-slope based ranging procedure which avoids time-domain transformation.

A complete system-analysis and modeling of the harmonic radar system including the passive transponder tag is provided. Numerous high-resolution measurements are presented and analyzed to verify the validity and accuracy of the non-linear harmonic radar equation, to evaluate illumination and harmonic return signal polarization based propagation effects in a multi-path indoor measurement scenario and to demonstrate the performance of the harmonic radar system in severe clutter situations.

[1] European Association of National Metrology Institutes.

Contents

1 Preface

Today the vector network analyzer (VNA) by itself has become an essential tool in the RF and microwave industry. The VNA, which was originally a fairly specialized instrument intended for laboratory and research and development use, has since grown out this niche and is widely employed in the microwave industry for characterization and quality control of devices directly at the production lines.

It has become a common-place procedure for manufactures of passive and active components in the microwave industry to ship only 100 % known good parts, more often than not tested by VNA in an automated test equipment (ATE) setup. This strict quality control has become a necessity due to the high level of integration, small form factor requirements and comparatively low margins present in consumer goods and the throughout the whole supply chain. These factors combined lead to the situation that if a faulty component is assembled onto a printed circuit board (PCB), the whole assembly is written off after unit testing, as rework or repair is more often than not deemed economically unfeasible.

The VNA as an instrument by itself can be described as an integrated stimulus / response measurement device, which is able to measure electromagnetic wave quantities by their magnitude and respective phase of a device under test (DUT) in response to a stimulus wave and apply mathematical corrections to the measurements. Nowadays, a VNA instrument generally contains all the necessary components to generate the stimulus, normally by the means of phase locked loops (PLL) and/or direct digital synthesis (DDS) synthesizers, directional couplers to separate waves by their direction of travel into incident and reflected waves, and the required vector receivers to convert the physical properties of the waves into a numerical representation, in a compact package. Unfortunately, this high level of integration cannot suit every measurement setup and most instruments are only build for the most common denominator of all measurement tasks: The small signal[2] scattering (S-)parameter measurement.

Besides the microwave front-end components already mentioned, a multitude of other components are needed to form a usable VNA, as precision data acquisition and processing, reference frequency generation and stabilization, triggering, data storage and means of input/output facilities are all equally important for building a usable instrument and equally complex in their implementation.

In contrast to classical fully integrated instruments which combine all aforementioned components in the same enclosure for use as as integrated laboratory measurement instrument, the current generation of VNAs is also available in the form of so-called

[2]Small signal in this context means, that the power of the incident stimulus at the measurement ports is such, that the DUT only exhibits linear response characteristics. Therefore for practical reasons the output power of most VNAs maxes out at 10 to 13 dBm and only internal couplers can be used.

headless devices for use with an additional PC for data display, storage, user interface and computation. These headless VNAs are especially suited for embedded integration into an ATE setup and because of their reduced size, cost and power requirements can even open up new applications for the VNA concept.

An interesting embedded application for the classical VNA is the remote sensing of physical properties via the interaction of matter with electromagnetic waves. One notable example for employing a VNA for non-traditional measurement tasks are the contact less moisture sensors, for example made by Indutech [63], which are able to measure the moisture of bulk goods on conveyors by measuring the complex transfer function of the good placed in-between two antennas and fitting the result to a phase and attenuation shift model to determine the water content. A further noteworthy non-standard application is the use of a two-port VNA with two orthogonal polarized wide-band antennas for the contactless sensing of a multitude of wheel parameters of an automobile, as presented in [55]. In both sensing applications the VNA excels because of its low instantaneous occupied bandwidth and high dynamic range and accuracy, despite only using only micro watts of transmit power to comply with regulatory standards.

Historically VNAs have only been viewed as an instrument for measuring linear time invariant (LTI) system properties, as S-parameters, the most often measured variable by a VNA, are linear by nature. Standard S-parameters describe the relation of incident and reflected waves and their respective nodes by a set of linear equations and therefore can only model linear network behavior. A mathematical definition of the LTI notion and S-parameters can be found in [54] and a more in-depth analysis in [27] and [98].

Unfortunately, real components and especially active RF components seldom behave in a true linear and time invariant manner, especially on the scale of the vast orders of power magnitudes involved in mobile communication, which easily span 12 to 15 orders of magnitude between transmitted and received signal power, with less and less of the precious resource of frequency spectrum available for new applications. Even small imperfections in passive components or non-linear effects in active components, that were only designed with approximate linear models available, lead to signal degradation due to interference, thus lowering the available spectral capacity.

Furthermore, the demand for exactly characterized non-linear behavior is on the rise, because only non-linear amplifier models allow a repeatable design and production of highly efficient switching mode Class-E/F power amplifiers, while cutting down on total development time and required prototyping reiteration cycles.

Out of this need two fairly different measurement instruments were developed over the past years: The large signal network analyzer (LSNA) and the non-linear network analyzer (NVNA)[87]. Although named quite similarly, both concepts realize the measurement of non-linear S-parameters quite differently — while the LSNA uses a wide-band, time domain capture based approach to acquire all harmonic responses to one or multiple stimulus signals at once due to a harmonic mixer front-end and a high bandwidth base-band ADC, the NVNA as an extension of a classical narrow-band VNA captures the harmonic and non-linear response components one after another with a narrow-band receiver. Due to the large analogue bandwidth required the LSNA concept is generally limited in dynamic range by its noise figure and is therefore more suited to large signal

amplifier designs. The NVNA on the other hand lacks in time resolution, but offers the possibility to analyze quasi-static non-linear responses with a superior dynamic range of over 150 dB with large signal stimulation.

The work presented in this thesis will concentrate on the advancement of the VNA and NVNA concepts towards a more practical and integrable approach by presenting the theory, verification, measurements and application of a modular VNA concept to allow the realm of non-linear vector measurements to leave the laboratory setting and propagate to a wider range of applications and lower entry costs into this class of measurements.

Furthermore an interesting new application for simple non-linear VNAs as the core element of a new frequency domain high dynamic range non-linear harmonic radar system for the cooperative detection and ranging of passive and active non-linear will be presented in this work.

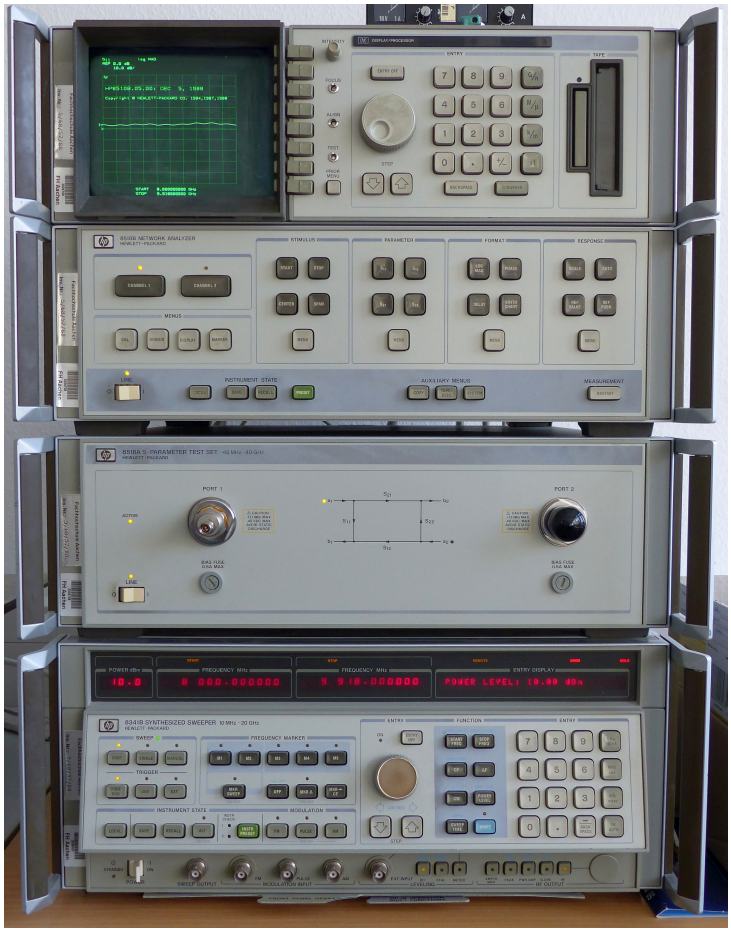

Figure 1.1: Picture of the venerable HP 8510B four-receiver VNA system, including a 8516A two-port 40 GHz bidirectional S-parameter test-set and a 8341B 20 GHz stimulus synthesizer generator, which laid the foundation for modern VNA systems, error models and calibration procedures.

2 The Switched Receiver VNA - Properties, Correction Schemes and Optimization Methods

2.1 An Introduction to Vector Network Analyzer Architectures and Error Models

In order to classify the new VNA architecture presented in chapters 2.3.2 to 2.3.7 in this work into the right context, it is necessary to recapitulate on the prevalent architectures and types of VNAs in general. Therefore, it is necessary to identify common building blocks that can be identified in all the different approaches to the same measurement problem.

The general architecture of the classical VNA microwave front-end, as shown in [27, 49, 60, 122, 143], can be generally broken down in to three main parts or building blocks:

- One or multiple stimulus generators, consisting of a synthesized RF source locked to a common reference and an output power level control mechanism, abbreviated as transmitter or TX in the following,
- One or multiple vector receivers that can measure an RF signal by magnitude and phase, consisting of a down converting mixer fed by a common RF source or fitted with its own synthesizer, analog filters and signal conditioning, amplifiers and an analog to digital converter (ADC), abbreviated as receiver or RX in the following,
- The so called test-set, compromising one or multiple directional couplers and/or switches which control the flow of RF signals from the generators to the DUT and to the receivers and also allows to separate the incident and reflected waves from each other and/or differentiate different frequency ranges.

The simplest VNA design with full error correction offers only one, so called, port that represents the physical interface of the instrument to the DUT. In the context of signal flow graph analysis, this port is comparable to the definition of the node from the network theory.

When only one port or node is available, the only wave ratio than can be derived from its interface on behalf of the energy budget is the complex reflection factor, or coefficient, S_{11}. This ratio describes the proportionality between the reflected power wave b_1 and the incident power wave a_1 at the location of the node, yielding $S_{11} = \frac{b_1}{a_1}$. The position

of this distinct node used to describe the S-parameter is called the (calibration) reference plane. As only this one reflection parameter can be measured, a VNA using this topology is called a reflectometer, which is also the basic building block of multi-port network analyzers.

Without loss of generality the incident source wave a_S generated in the TX is assumed to be unknown and therefore needs to be measured. For that reason, a reflectometer configuration needs at least one TX, two RX and at least one bi-directional coupler (or two normal directional couplers mounted back-to-back) in order to measure the incident and reflected waves a_1 and b_1 independently. The a_i receiver is generally called reference channel or receiver, and the b_i receiver is called the measurement channel.

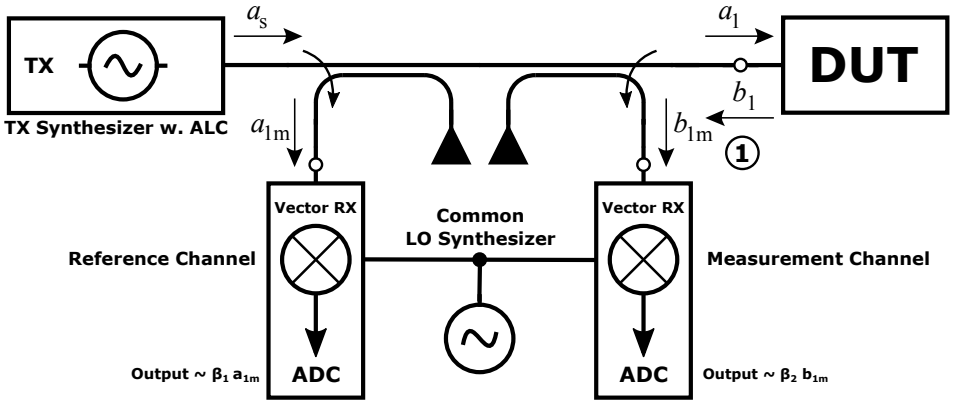

Figure 2.1: Schematic of the one-port reflectometer VNA.

This configuration is shown in Fig. 2.1 and is found in a multitude of headless and hand-held devices on the market like the Anritsu [20] MS46121A head-less VNA, the Anritsu Site Master series and Copper Mountain [141] R-series USB reflectometers and is especially useful for a quick performance evaluation of inherently one-port devices like antennas[3].

The reflectometer is the basic building block upon which most VNA architectures are based. Multi-port instruments can be built by combining the data of multiple reflectometers, as long as their local oscillator signals (LO) are shared between all vector receivers[4].

It is important to note that in Fig. 2.1 two new wave quantities are introduced: a_{1m} and b_{1m}, which describe the measured waves at the receivers and that are proportional to the a_1 and b_1 waves at the port interface — but not equivalent to the waves of the DUT at the reference plane. This results from the fact that no RF components are perfect, as the TX source shows finite return loss, also called source match in this arrangement, the

[3] An antenna is generally simplified as a passive reciprocal one-port device, as their air interface representing the second port or node can not be measured reliably without the help of anechoic chambers or antenna ranges to generate a total power balance, at least in a field or volume production test.

[4] This statement will be explained and qualified later, when the new VNA architecture is presented.

directional couplers employed only have finite directivity, return and insertion loss and spatial extent will introduce extra phase shift to the measured waves. Additionally, the receivers used in the VNA are non-ideal, as they also show an associated conversion loss, finite input return loss and further imperfections caused by the data acquisition process.

In contrast to scalar spectrum analyzers, VNAs can measure complex wave quantities in their magnitude and phase, resulting in a full description of the phasor. It is this unique measurement capability that enables the VNA to be fully error corrected by a mathematical error model of the system, which allows for an improvement in measurement accuracy and dynamic range by several orders of magnitude in comparison to scalar systems built from the same basic test-set components.

In order to describe the imperfections of the VNA instrument and its systematic errors, two different schools of thought exist to generate and correct the linear and time invariant (LTI) descriptions of the system in a so-called error model:

- Signal flow diagrams, as used in [27, 48, 119], which are almost exclusively used to describe one and two port VNA architectures with minor cross-talk, because the associated diagrams and their derived transfer functions quickly gain size and complexity, but offer an intuitively accessible description of the model, and

- Error networks or error adapters, as used in most of the modern error corrections schemes like GSOLT [51], all 7-term and 15-term procedures presented in [30, 49, 143], and most multi-port correction schemes published since the 1990s. Their main drawback is their strict LTI definition of the complete system, which requires additional correction methods outside of the original error model to capture and correct instrument state dependent effects. All VNA imperfections are abstracted into a corresponding abstract error network matrix parameter, resulting from the linear superposition of the underlying effects in comparison to an ideal VNA.

Despite their different approaches to model the systematic errors present in a VNA, both types of error models describe the same underlying instrument, although using a different methodology. When non-LTI effects, such as varying source and load match of the port depending on its TX/RX state, are ignored, these models can be used interchangeably and can be transformed into the corresponding other form with various methods (see [27, 80]).

This property can easily be seen in Fig. 2.2, where both the signal flow and the error-box network representations of the reflectometer 3-term error model are shown side by side. In order to emphasize the similarities, the signal flow diagram is shown with the corresponding error network coefficients added. For this basic one-port VNA model, the coefficients can be described as follows:

- e_{00} and E_{DF}: Directivity error, forward, which models the finite directivity of the directional couplers in the test-set, normalized to a_1,

- e_{11} and E_{SF}: Source match error, forward, that captures the error introduced by the finite return loss of the test-set and absorbs the superposition of various other matching related errors,

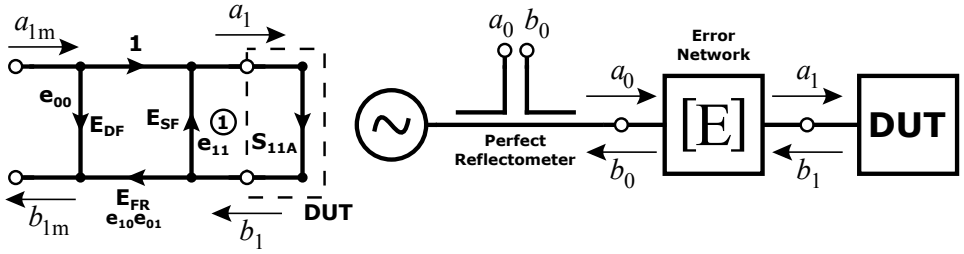

Figure 2.2: Signal flow diagram and equivalent error-box representation of the 3-term reflectometer model with error network coefficients added in the signal flow chart.

- $e_{10}e_{01}$ and E_{FR}: Tracking error, forward/reverse, that describes the error caused by the insertion loss in both the forward and reverse wave direction of the test-set.

By applying Mason's gain rule for solving signal flow graphs for their transfer function ([99]), the actual S_{11A} of the DUT at the reference plane on port 1 can be determined from the measurable ratio $S_{11M} = \frac{b_{1m}}{a_{1m}}$ by rearranging the results to

$$S_{11A} = \frac{S_{11M} - E_{DF}}{E_{FR} + E_{SF} \cdot (S_{11M} - E_{DF})} \,. \tag{2.1}$$

Since the relation between S_{11A} and S_{11M} is now known, calibration standards with a fully or partially known input reflection coefficient Γ, with the type of standard depending on the actual calibration and correction algorithm, can be connected to the respective port to determine the coefficients from in-situ measurement results of S_{11M}. As one unknown coefficient generally corresponds to one term in the linear equation system of the model, and three unknowns are present in Eq. (2.1), the measurements of three devices with known S_{11A} must be performed to determine the coefficients. This procedure of capturing the VNA error model coefficients is commonly called calibration, which often leads to the confusion of this procedure with the periodic metrological calibration of other measurements devices ([27]).

In case of a coaxial reflectometer calibration using in the 3-term error model, the most common coaxial calibration standards are a known open ($\Gamma = +1 \cdot e^{-j2\beta l}$, including the coefficients for Taylor-Series approximation of the fringe capacity), a known short ($\Gamma = -1 \cdot e^{-j2\beta l}$) and a load or match ($\Gamma = 0$), although other standards such as multiple offset shorts are also be used in band-limited wave-guide measurements ([27]).

The measurement of the match standard directly yields the E_{DF} component, as S_{11A} is defined to be zero and determines the reference impedance of the calibration. E_{FR} and E_{SF} can then be determined by the measurement of the open and the short calibration standard.

Fig. 2.2 shows that, the 3-term error model must be in fact considered a 4-term model, as there are four paths between nodes with their corresponding coefficients present in the error network.

However, as standard S-parameters are only expressing dimensionless ratios, it is entirely possible to choose one of the coefficients to be equal to one and therefore normalize all other coefficients to this value, reducing the number of terms for solving these values, and therefore the number of required calibration standards and measurements, by one ([119]).

In stricter mathematical terms, this linear dependency can easily be deduced from Eq. (2.1), as E_F and E_R are only present as a product. Therefore, the forward (E_F) and reverse tracking (E_R) errors caused by the insertion loss and other properties of the test-set are abstracted into the unified $E_{FR} = E_F\,E_R$ or ($e_{10}e_{01}$) coefficient.

An important consequence of this normalization is that even after successful determination of the E_{DF}, E_{SF} and E_{FR} values, the physical reflectometer is only calibrated relative to itself, or more specifically, to the TX generator, receiver and physical reflectometer combination the coefficients were determined with. In the inversion of this argument this also means, that while these three coefficients contain the properties of the reflectometers, such as directivity and isolation, as a subset, they are not representative for its original performance and a mere system level abstraction of the interaction of all test-set components.

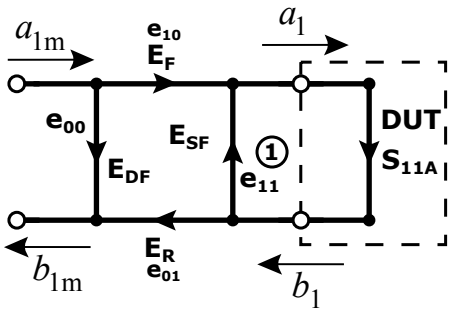

Figure 2.3: Signal flow diagram of the fully known 4-term reflectometer with separated E_F/e_{10} and E_R/e_{01} coefficients.

A recent addition to the reflectometer concept is the fully determined 4-term reflectometer, as shown in Fig. 2.3. This error model has two main advantages for both linear and non-linear network analysis, which are presented in [53]:

- Error correction of a multiport complete reflectometer VNAs without any through corrections required during calibration, coining the name "'without-thru"' for this procedure, and
- Enabling frequency converting non-linear VNA measurements by magnitude a phase in calibrated manner.

The need for a fully characterized, or absolutely calibrated, reflectometer in order to perform corrected frequency converting non-linear measurements is obvious when the following is considered:

The frequency or signal components, which are generated in the DUT, are related to the phase and magnitude of the stimulus provided by the VNA at the reference plane. The forward stimulus applied by the VNA is only affected by the E_F and E_D term at one frequency (compared to the a_{1m} measurement), whereby the measured non-linear reflection response on one more different frequencies is affected by the E_R (and E_S) term as a non-linear function of a_1 and therefore a_{1m}, E_D and E_F. Therefore the normalization applied for the 3-term model of Fig. 2.2 with the combined E_{FR} factor is not valid anymore.

In order to completely generate all four error coefficients of the "'without-thru"' model in Fig. 2.3, two additional active calibration standards must be used as well:

- A power meter which is used to accurately measure the incident power $|a_1|$ at the DUT reference / connector plane, and
- A known pre-characterized phase reference (transfer) standard, also known as harmonic phase reference (HPR).

The HPR provides an external stimulus signal, which is completely known in magnitude and phase, in order to separate the E_{FR} factor from the 3-term calibration into the E_R and E_F component at the frequencies of interest. Currently the standard method to generate harmonic reference signals utilizes the phase locked 10 MHz output of standard VNAs and the transfer function of highly non-linear components such as step recovery diodes (SRD) or non-linear transmission lines (NLTL) to generate a so called frequency comb. This comb output contains harmonic copies of the original reference signal and can be used for this purpose if properly pre-characterized. A wealth of information about the calibration of the HPR itself can be found in [150].

Another use for the HPR besides providing a reference calibration stimulus is the phase correction of the VNA synthesizers in non-linear VNA instrumentation, as outlined in [53, 108, 143].

It is important to stress again at this point, that the so called calibration of a VNA and the metrological periodic calibrations performed upon other measurement instruments have little in common. When a normal measurement device is calibrated, its measurements are compared to more accurate instruments using metrological reference standards in order to determine and correct for the measurement error of this instrument in the limits set by its resolution and dynamic range. This is only done in fairly coarse intervals.

A VNA on the other hand uses known calibration standards, which are known in their characteristics with a higher accuracy and dynamic range or resolution than the instrument hardware itself is capable to measure uncalibrated, and using them to determine the terms in the error model and correct for these errors by post-processing. For an accurate measurement, this self calibration of the VNA has to be repeated for even minor changes in environmental conditions through drift in the electronics and test-set or measurement device settings. An extensive discussion of factors that demand a re-calibration of a VNA, besides a change in device settings, is found in [27].

In total, there are numerous calibration and error correction procedures available for different VNA architectures, each using their own sub-sets of known or only partially

known calibration standards and often with special applications in mind, which are impossible to completely list in this context. The reference sections and contents of [27, 48, 49, 119, 122, 125, 143] provide a broad overview over this area of VNA metrology.

An aspect that drives the architecture of VNA concepts is the total bill of material (BOM) costs of the completed instrument, as synthesizers for the TX generators and vector receivers are fairly complex and therefore expensive sub assemblies. Historically for the first step towards multi-port VNAs, the two-port instrument, three different systematic and architectural concepts were followed that greatly influenced the development of error correction mechanisms:

- The four-receiver two-port VNA, also called a double reflectometer VNA,
- The unidirectional two-port VNA, which only allows measurement in one stimulus direction, and
- The three-receiver two-port VNA, as an extension of the unidirectional VNA for two-port stimulus.

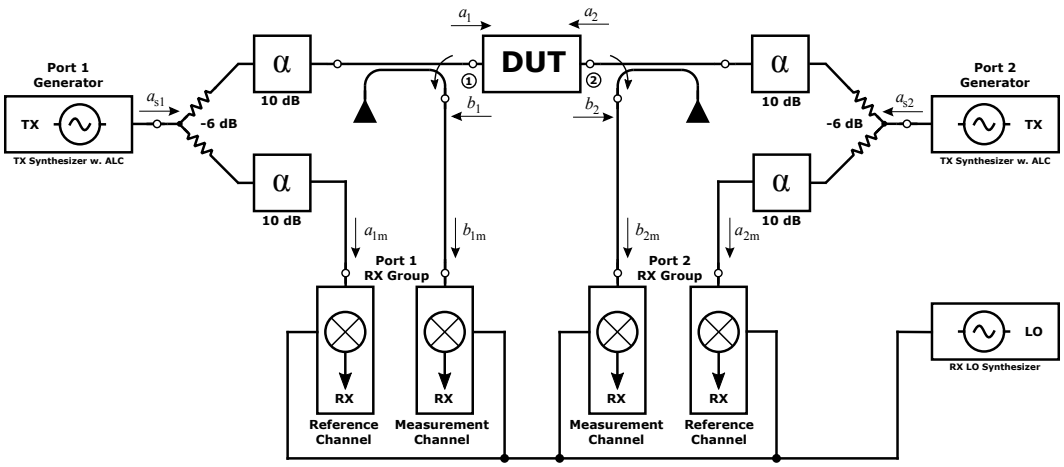

Figure 2.4: Schematic of a four-receiver double reflectometer VNA, with resistive 2R couplers as directional elements for the a-waves / reference channels and resistive padding for increased isolation and hardware source and load match at the measurement ports.

The architecture of the four-receiver VNA depicted in Fig. 2.4 is fairly simple to explain, as it basically just doubles the one-port reflectometer and therefore employs four receivers and two TX stimulus generators. It is able to measure all four S-parameters of a two-port network and all four associated wave quantities independent from the current stimulus direction and offers the greatest amount of error correction flexibility, accuracy and measurement quality. This architecture is now predominant for VNAs meant for laboratory and complex ATE use. The four-receiver VNA offers the highest dynamic range and accuracy of all architectures by providing complete error correction

and allowing for self calibration procedures using partially known standards, at the cost of part count and complexity. All modern 7-, 12- and 15-term error model based calibration procedures can be applied to the two-port four-receiver VNA, which allows for various forms of error correction capabilities tailored to the application and measurement task at hand.

In practice, two different four-receiver VNA test-set architectures exist: In the most flexible configuration, each VNA port is equipped with its own dedicated stimulus synthesizer that can be controlled individually in output frequency and amplitude. As this is a comparatively expensive solution to the stimulus generation problem, such test-sets are only found in non-linear measurement capable VNA and are required for multi-frequency measurements such as mixer characterization. The simpler solution to this problem uses a repeatable absorptive semiconductor switch to route the signal of a sole stimulus generator to the driven port, while the other reflectometer interface is terminated in a load.

Well known examples of this concept are the ZVA, ZVB and ZNB series from Rohde & Schwarz [110], the Anritsu VectorStar series [20] and the PNA series from Keysight Technologies[5] [142].

From a historical standpoint, the HP 8510 is of special note for this concept, as many error correction mechanisms and metrological concepts for this architecture were developed on this popular platform [27].

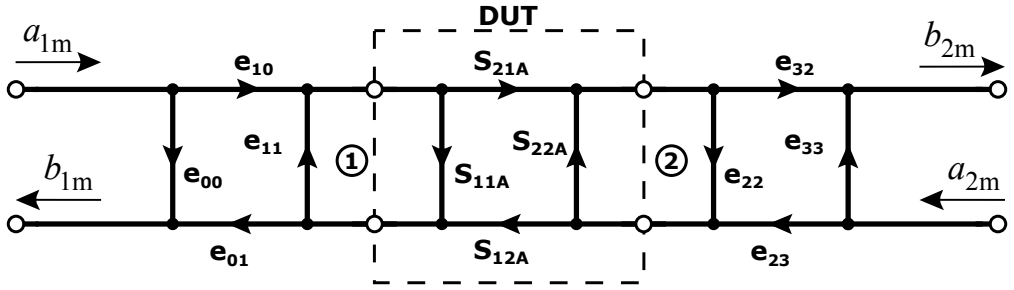

Figure 2.5: Signal flow diagram of the 7-/8-term error model for the full reflectometer two-port VNA with 4 receivers

The very nature of the full reflectometer signal flow graph depicted in Fig. 2.5 lends itself to an error-box network analysis using a system of linear matrix equations, as three distinct concatenated two-port networks can be identified. These are:

- The two-port error network T_X of the first reflectometer on port 1,
- The two-port network of the DUT and
- The two-port error network T_Y of the second reflectometer on port 2.

[5] Keysight Technologies is the successor of Agilent's electronic measurement equipment division, which in turn was the successor of the Hewlett Packard's (HP) electronic measuring equipment, medical devices and scientific instrumentation business.

As S-parameters matrices are generally not directly cascadable, these networks must be described with concatenable parameters that honor the individual load and source match interactions of the networks to calculate the response of the complete chain, as measured by a fictive ideal VNA. The most common way to describe a chain of parameters are T-parameters that can be calculated from the S-parameters through a linear transformation and vice versa ([54]). Another solution mostly found in American publications and literature is the representation in the form of ABCD-matrices, which converts power waves to current and voltage components (see [27, 54] for a definition). Unfortunately there is no general consent of both the definition of the T-parameters and the naming convention of the error-box networks, so for this thesis the following definition

$$\begin{bmatrix} b_1 \\ a_1 \end{bmatrix} = \begin{bmatrix} T_{11} & T_{12} \\ T_{21} & T_{22} \end{bmatrix} \begin{bmatrix} a_2 \\ b_2 \end{bmatrix} \tag{2.2}$$

is used. By using the a and b wave quantities, S-parameters and T-parameters can be converted to each other, using the relation[6]

$$\begin{bmatrix} T_{11} & T_{12} \\ T_{21} & T_{22} \end{bmatrix} = \frac{1}{S_{21}} \cdot \begin{bmatrix} -\Delta S & S_{11} \\ -S_{22} & 1 \end{bmatrix} \text{ , with } \Delta S = S_{11}S_{22} - S_{21}S_{12} \tag{2.3}$$

and for converting from T- to S-parameters with

$$\begin{bmatrix} S_{11} & S_{12} \\ S_{21} & S_{22} \end{bmatrix} = \frac{1}{T_{22}} \cdot \begin{bmatrix} T_{12} & \Delta T \\ 1 & -T_{21} \end{bmatrix} \text{ , with } \Delta T = T_{11}T_{22} - T_{21}T_{12}\,. \tag{2.4}$$

Due to the cascading properties of the T-parameters, the error model of Fig. 2.5 can be conveniently described as a system of linear equations in the form of

$$T_M = T_X \cdot T_A \cdot T_Y\,. \tag{2.5}$$

When the parameters of the error-box networks T_X and T_Y are known through calibration, the error correction can be performed by rearranging Eq. (2.5) to solve for the actual T-Parameters of the DUT T_A, yielding

$$T_A = T_X^{-1} \cdot T_M \cdot T_Y^{-1}\,, \tag{2.6}$$

which then can be converted back to the corrected two port S-parameters of the DUT by applying Eq. (2.4).

[6] A problem of this conversion is the inherently numerically unstable $\frac{1}{S_{21}}$ term in finite resolution computing of values. There are other methods of concatenation available that mitigate this problem, but are beyond the scope of this work.

When analyzing the system of linear equations obtained from Fig. 2.5 for the standard relational S-parameter case, it can once again be found that all 8 error terms present in the 2x2 error matrices T_X and T_Y can only be determined to a common factor, which can be eliminated by normalization ([49]). Therefore, only 7 independent error terms need to be determined, for which a multitude of procedures using different quantities of fully or partially known calibration standards are available.

In practice, the most common way to determine the error coefficients of the 7-term model is a direct logical extension of the 3-term procedure, by using a match, short, open calibration of the two reflectometer ports in the model and determining the forward and reverse tracking terms by measuring a (partially) known reciprocal thru connection, which is generally abbreviated as SOLT for a fully determined or flush thru and UOSM[7] ([31, 154]) for a only partially determined or unknown reciprocal thru calibration standard.

While one drawback of these procedures is the fairly high number of individual connections and therefore operator time required for performing a calibration, the most important issue of the SOLT/UOSM procedures is caused by the weak[8] match standard used to define the system directivity and reference impedance, which results in decreased performance of the procedure for sub-cm wavelengths. Despite these problems, SOLT/UOSM allows for one- and multi-port calibration procedures over a vast frequency range without ambiguities using the same basic set of standards and thus enables universal calibration kits to be produced requiring only four standards per connector gender and type.

In addition to SOLT/UOSM there are much more advanced and versatile procedures such as the thru-reflect-line (TRL) and line-line-reflect (LLR) families of calibration algorithms available for the 7-term error model. These procedures generally remove all one-port calibration standards except for the well-defined reflect and employ fully or partially known two-port transmission line based standards to determine the other coefficients. Depending on the exact implementation of the algorithm, different requirements arise for the amount of known properties of the calibration standards and their respective allowed definition uncertainty. As the transmission line impedance Z_L, especially in air dielectric lines, is defined only by mechanical dimensions which can be reliably produced with and easily measured down to sub $10\,\mu m$ tolerances, they offer an elegant way to define the electrical RF reference impedance in an easily traceable metrological route to national mechanical standards and allow the omission of the weakly defined match or resistive impedance standard. Unfortunately this precision comes at a price, as the transmission line impedance Z_L is only effective for electrical lengths of $\beta l \neq 180° \equiv \lambda/2$, which results in an area of lower correction performance centered around these points. Also, air dielectric coaxial transmission lines usually need a lot of time, care and effort to

[7] Unknown, Open, Short, Match, also widely known as Unknown-Thru calibration.

[8] Weak in this context means, that generally match standards only offer return loss figures lower than 40 dB when compared with an ideal system impedance termination, while the system dynamic range is usually much higher. Also they are fairly weakly defined standards in the metrological chain, as they inhibit parasitic properties driven by the skin effect which are hard to model consistently. As the match defines the reference impedance and S-parameters are generally referenced to $Z_0 = 50\,\Omega$, the increasing imaginary impedance over frequency of the resistive element results in measurement errors.

assemble for each individual calibration connection, making these procedures impractical for frequent coaxial use.

Contrary to the coaxial use case, these procedures are commonly used for measurement of planar circuits, transmission lines and IC dies using an automated probing system, due to the lower number of necessary connections during calibration and the excellent and repeatable manufacturability of transmission lines and short circuits on planar substrates and wafers in co-planar wave guide (CPW)[9] transmission line technology. Both TLR and LLR derived procedures have found their niche in the automatic test equipment world, while seldom being used outside metrological measurements otherwise. A good overview of many TLR, LLR and more generalized Txx and Lxx algorithms can be found in [49].

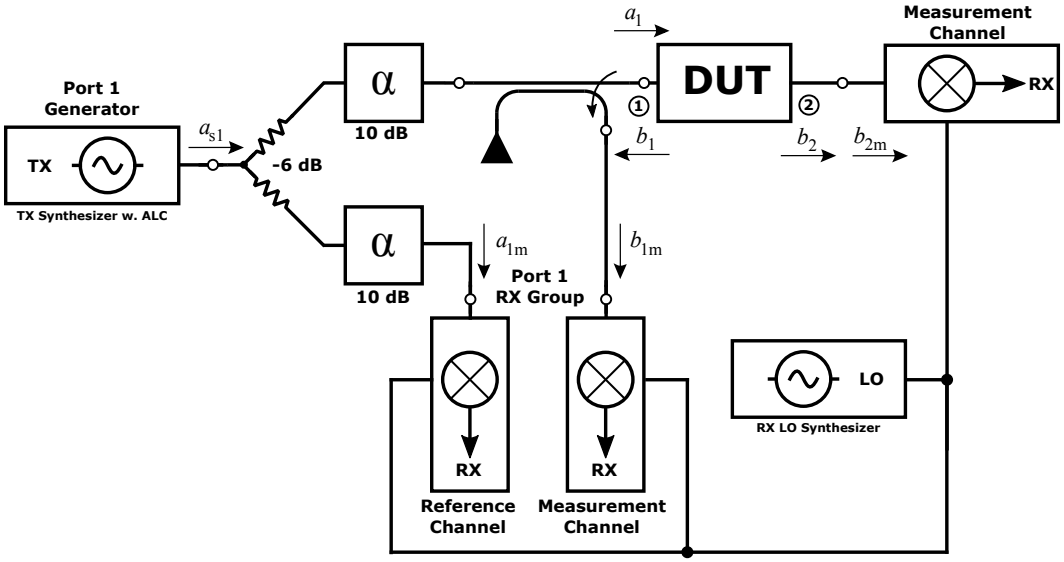

Figure 2.6: Schematic of an unidirectional incomplete reflectometer VNA, with a resistive 2R coupler as the directional element for the a-wave / reference channel and resistive padding for increased isolation and hardware source match at the measurement ports.

The two-port unidirectional VNA, which is also called transmission/reflection analyzer to denote the reduced architecture, is only able to measure the input return loss S_{11} and the forward transmission coefficient S_{21} of the DUT by using a complete reflectometer for the first port and only one receiver for the second port, therefore totaling one TX generator and three vector receivers.

This poses some special problems for the error correction of S_{21}, as the interaction between the return loss on port 2 of the DUT and the corresponding load match of the RX on port 2 can not be characterized. Contrary to the usual mathematical error correction approach of the VNA, the influence of this effect can only be mitigated by providing resistive padding and therefore good return loss at this port. Nevertheless,

[9] Also sometimes called ground-signal-ground or GSG.

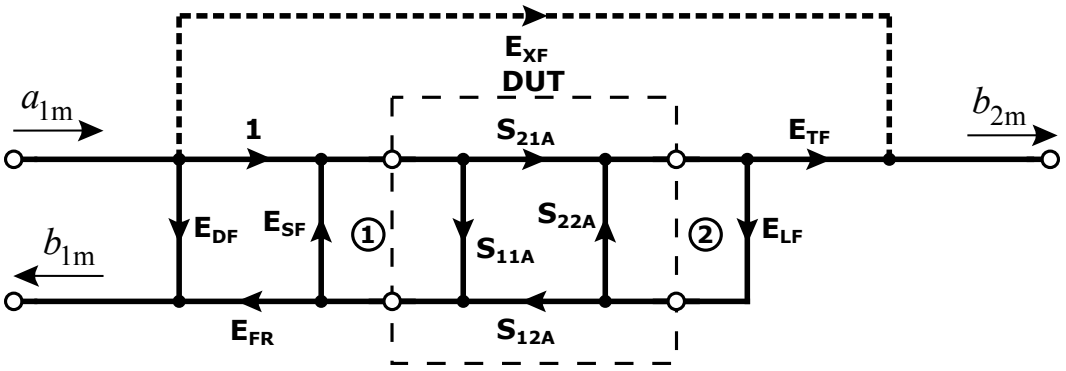

Figure 2.7: Signal flow diagram of the unidirectional 5-term error model for the incomplete reflectometer two-port VNA with three receivers.

very accurate measurements can be achieved with this setup under certain circumstances, mainly depending on the properties of the test-set and the DUT, as presented in [27]. The measurement of S_{11} and S_{21} is sufficient for most ATE setups and is often used for the production test of amplifiers.

The reverse S-parameters S_{22} and S_{12} can only be measured by reversing the connections of the DUT itself, making this a good example of taking advantage of the LTI properties of the S-parameter definition in order to reduce measurement system complexity. Unfortunately the repeatability of RF connectors or rather their connection and the often non-LTI nature of DUTs hinders this procedure, as presented in [54]. Even precision coaxial N connectors only exhibit repeatability in the order of -80 dB in their reflection and transmission properties. As VNAs nowadays offer dynamic ranges in excess of 120 dB, this figure can not be neglected for precision measurements.

Well known examples of the unidirectional architecture are the Anritsu MS4622 Scorpion [20] (without the auto-reversal option), the Rohde & Schwarz ZND [110] and the DG8SAQ VNWA 3 [129], the latter being popular in the amateur radio community. A good summary and analysis of calibration and error correction procedures that are possible when using this architecture is presented in [48].

The signal flow diagram for the two-port unidirectional architecture shown in Fig. 2.7 is a direct extension of the reflectometer error model, with an additional receiver for the transmitted wave component b_2 added, which allows $S_{21m} = \frac{b_{2m}}{a_{1m}}$ to be measured.

In comparison to the reflectometer error model shown in Fig. 2.2, the following new error coefficients are added for the transmission measurement:

- E_{TF}, describing the forward tracking error losses to b_{2m} in the test-set,
- E_{LF}, which captures the finite return loss of the second port of the instrument and is called forward load match, and finally
- E_{XF}, capturing cross-talk between the a_{1m} and b_{2m} waves, but is usually omitted in the correction math and models.

When analyzing the diagram of this architecture, it becomes clear that the reflectometer Eq. (2.1) for obtaining S_{11A} from the measured test-set waves is still valid for this VNA architecture, as the error introduced by the $S_{22A}\,E_{LF}$ loop can usually not be accounted for, simply because S_{22A} and S_{12A} cannot be measured by the instrument test-set.

For the measurement of unknown devices port 2 of the VNA is therefore assumed to be perfectly matched[10], which allows S_{21A} to be approximated by

$$S_{21A} = \frac{S_{21m} - E_{XF}}{E_{TF} \cdot (1 + \frac{S_{11m} - E_{DF}}{E_{FR}} \cdot E_{SF})} \;, \text{ with } \; E_{LF} \stackrel{!}{=} 0. \tag{2.7}$$

In order to find the two new remaining coefficients E_{TF} and E_{XF} in expression Eq. (2.7), new calibration measurements and two-port standards must be used:

- Two ideal match standards connected to both ports for measuring E_{XF} and
- A partially or fully known thru for determining E_{TF}, depending on the actual device implementation.

The E_{XF} cross-talk path shown here is directly equivalent to the match-match S_{21m} measurement, as all four DUT S-parameters for this compound isolation standard are defined to be zero. Usually this factor and its correspond calibration step is omitted, as this form of correction for leaky probing and test-set isolation issues usually does more harm than good for measurements obtained with normal VNAs ([27]).

A discussion of the impact of the actual thru standard model implementation can be found in [27], as this can have varying effects on the position of the measurement reference plane, depending on the type and gender of the RF-connectors used.

The only time when E_{LF} can be measured and used for correction in the 5-term model is during the calibration with a thru model that is known to be reciprocal with $S_{21A} = S_{12A} = e^{-\beta l}$ and symmetric with $S_{11A} = S_{22A} = 0$ and therefore transparent to the load match. This is usually only possible with a flush thru standard using either a genderless coaxial APC-7 connector system or a direct thru connection using the matching opposite gender connector for the second test-set port. In this case, E_{LF} can be measured accurately with the fully calibrated reflectometer part of the model and improve the measurement of the standard and position of the reference plane, although this is not often implemented.

An analysis of common manufacturer specific implementations of this error model used for the unidirectional incomplete reflectometer VNA is also found in [48].

The three-receiver VNA concept consist of two vector receivers for measuring the b_1 and b_2 waves via their associated directional couplers on the ports, while only using one generator TX assembly with an accompanying reference channel vector receiver and directional coupler. This TX/RX combination is then switched via an absorptive SPDT

[10] This assumption directly leads to the practical application tip of adding a well-matched attenuator to port 2 when requiring precise transmission measurements of reflective DUTs, hereby trading dynamic range for the reduction of $S_{22A} \cdot E_{LF}$ induced S_{21} ripple and S_{11} measurement uncertainty.

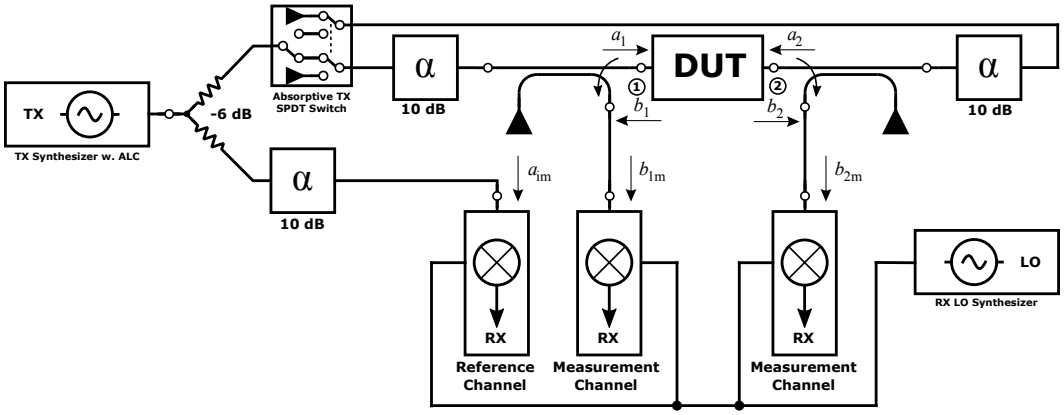

Figure 2.8: Schematic of a three-receiver incomplete reflectometer VNA, with a resistive 2-R coupler as the directional element for the a-wave / reference channel and resistive padding for increased isolation and hardware source and load match at the measurement ports.

switch that terminates the inactive port into a matched 50 Ω load, creating two distinct stimulus paths for a_1 and a_2, therefore creating a dual unidirectional architecture[11].

As only one reference coupler and receiver channel is present behind the stimulus selector switch, this approach is very different from the use of a stimulus switch in the double reflectometer configuration. In direct comparison this also includes its correction and measurement abilities, as only three of the four wave quantities of the DUT can be measured for a given stimulus direction.

The introduction of the stimulus selector switch allows for the measurement (and correction) of all four DUT S-parameters without manual reversal and re-connection, but complicates the error model as there are two distinct instrument states. Similar to the manual reversal procedure, this approach is only possible due to the inherent time invariant nature of the S-parameters, as only one stimulus path can be measured at a given time.

These two distinct time invariant (TI) states of the stimulus reversal switch, and therefore states of the VNA test-set, mandate a two-part description of the error model, which in itself, can only be applied to a time invariant state by definition. Therefore the bi-directional 10-term error model, which excludes the isolation terms mentioned earlier, is constructed from the stateful superposition of two stimulus direction dependent 5-term unidirectional VNA error models, which is easily visible from the corresponding signal flow diagram shown in Fig. 2.9.

The stimulus selector switch is assumed to be repeatable in its two distinct states in the 10-term error model, and is allowed to show differences in insertion loss and return-loss depending upon the stimulus direction, but is assumed to have an isolation higher or equal than the dynamic range of the receivers.

[11] This is obvious in originally unidirectional VNAs like the Anritsu MS4622A, which can be upgraded to a full two-port VNA with an "'auto reversal switch"' option.

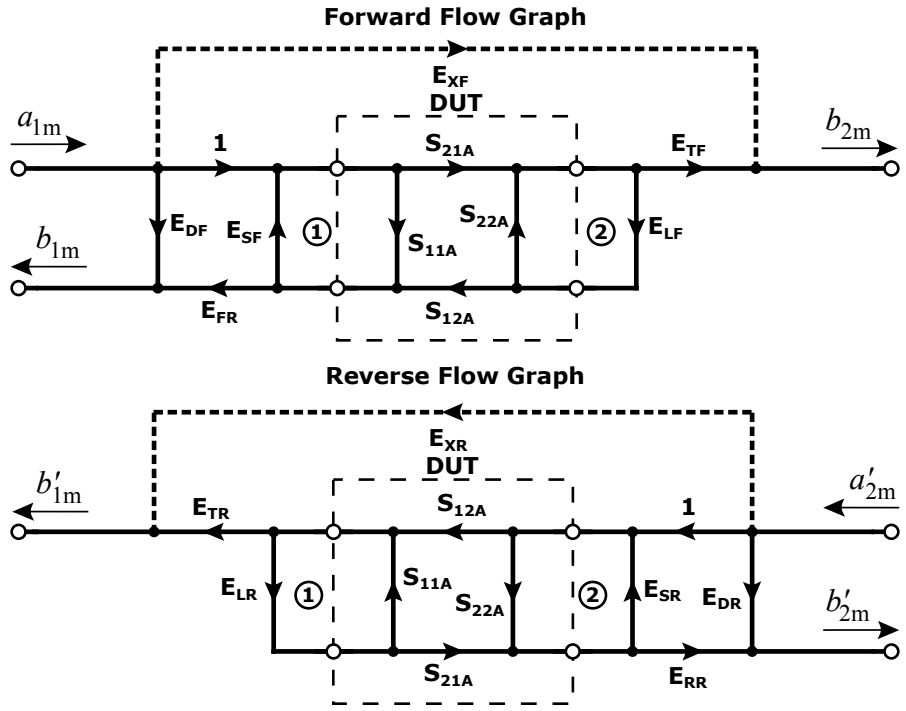

Figure 2.9: Signal flow diagram of the 10-/12-term error model of the incomplete reflectometer two-port VNA with three receivers, isolation cross-talk paths shown as dashed lines.

By applying the rules of signal flow graph analysis, the signal flow diagram of the 10-/12-term model yields the expressions

$$S_{11m} = \frac{b_{1m}}{a_{1m}} = E_{DF} + \frac{E_{FR} \cdot (S_{11A} + \frac{S_{21A} \cdot E_{LF} \cdot S_{12A})}{1 - S_{22A} E_{LF}}}{1 - E_{SF} \cdot (S_{11A} + \frac{S_{21A} \cdot E_{LF} \cdot S_{S12A}}{1 - S_{22A} \cdot E_{LF}})}, \tag{2.8}$$

$$S_{21m} = \frac{b_{2m}}{a_{1m}} = E_{XF} + \frac{S_{21A} \cdot E_{TF}}{(1 - S_{11A} \cdot E_{SF}) \cdot (1 - S_{22A} \cdot E_{LF}) - E_{SF} \cdot S_{21A} \cdot S_{12A} \cdot E_{LF}}, \tag{2.9}$$

for the forward stimulus measuring position (S_{11m}, S_{21m}) of the generator/receiver switch and the expressions

$$S_{22m} = \frac{b'_{1m}}{a'_{2m}} = E_{DR} + \frac{E_{RR} \cdot (S_{22A} + \frac{S_{21A} E_{LR} S_{12A})}{1 - S_{11A} E_{LR}}}{1 - E_{SR} \cdot (S_{22A} + \frac{S_{21A} \cdot E_{LR} \cdot S_{S12A}}{1 - S_{11A} \cdot E_{LR}})}, \tag{2.10}$$

$$S_{12m} = \frac{b'_{2m}}{a'_{2m}} = E_{XR} + \frac{S_{12A} \cdot E_{TR}}{(1 - S_{11A} \cdot E_{LR}) \cdot (1 - S_{22A} \cdot E_{SR}) - E_{SR} \cdot S_{21A} \cdot S_{12A} \cdot E_{LR}}, \tag{2.11}$$

for the reverse stimulus measuring position (S_{22m}, S_{12m}), which is found in [27]. In order to keep the complete equations more readable, it is helpful to introduce immediate

solutions for the S-parameters in the form of

$$S_{11N} = \frac{S_{11m} - E_{DF}}{E_{FR}}, \tag{2.12}$$

$$S_{21N} = \frac{S_{21m} - E_{XF}}{E_{TF}}, \tag{2.13}$$

$$S_{12N} = \frac{S_{12m} - E_{XR}}{E_{TR}}, \tag{2.14}$$

$$S_{22N} = \frac{S_{22m} - E_{DR}}{E_{RR}}, \tag{2.15}$$

as so called normalized S-parameters, which are already corrected for their direct cross-talk at their nodes (S_{xx} for directivity and load match, S_{xy} and S_{yx} for tracking and isolation). When these normalized intermediate solutions are used, the following expressions for the actual S-parameters can be found as

$$S_{11A} = \frac{S_{11N} \cdot (1 + S_{22N} \cdot E_{SR}) - E_{LF} \cdot S_{21N} \cdot S_{12N}}{(1 + S_{11N} \cdot E_{SF})(1 + S_{22N} \cdot E_{SR}) - E_{LF} \cdot E_{LR} \cdot S_{21N} \cdot S_{12N}}, \tag{2.16}$$

$$S_{21A} = \frac{S_{21N} \cdot (1 + S_{22N} \cdot (E_{SR} - E_{LF}))}{(1 + S_{11N} \cdot E_{SF})(1 + S_{22N} \cdot E_{SR}) - E_{LF} \cdot E_{LR} \cdot S_{21N} \cdot S_{12N}}, \tag{2.17}$$

$$S_{12A} = \frac{S_{12N} \cdot (1 + S_{11N} \cdot (E_{SF} - E_{LR}))}{(1 + S_{11N} \cdot E_{SF})(1 + S_{22N} \cdot E_{SR}) - E_{LF} \cdot E_{LR} \cdot S_{21N} \cdot S_{12N}}, \tag{2.18}$$

$$S_{22A} = \frac{S_{22N} \cdot (1 + S_{11N} \cdot E_{SF}) - E_{LR} \cdot S_{21N} \cdot S_{12N}}{(1 + S_{11N} \cdot E_{SF})(1 + S_{22N} \cdot E_{SR}) - E_{LF} \cdot E_{LR} \cdot S_{21N} \cdot S_{12N}}. \tag{2.19}$$

Contrary to the original formulation of the 7-term error model, the 10-term error model has a distinct advantage in handling the problems associated with real VNA hardware. As the model provides different source- and load-match coefficients depending upon the stimulus direction, this model is much less susceptible to measurement errors caused to port-state dependent impedance changes encountered in both three-receiver and four-receiver test-set architectures. While the source of this effect can easily be identified in the stimulus reversal switch used in two-port VNAs with only one stimulus synthesizer, this effect is even present in VNAs equipped with stimulus generators for each reflectometer port due to the slight changes in impedance caused by the synthesizer on/off state.

As the 7-term, strictly LTI based, error-box network model originally did not account for this effect, stimulus direction honoring methods such as the switch (or impedance state) correction algorithms shown in [49] or the calibration procedure agnostic formulation of the so-called switch terms presented in [80], were developed to correct this error in the 7-term error model.

Additionally, the switch-terms extension of the 7-term error model also allowed a formal proof for the equivalence of both error models ([80]). This on the one hand allows converting 7-term error models including their switch-terms to a 10-term error model, but more importantly allows using 7-term error models for correction on non-model compliant three-receiver VNA architectures via two-tier calibration on the other

hand ([27]), i.e. combining a SOLT 10-term calibration for obtaining the switch terms with a subsequent 7-term TRL calibration for enhanced precision using air-dielectric transmission-line standards on a three-receiver VNA ([68]).

In practice, most four-receiver VNA architectures are run in three-receiver mode during the actual measurement of the DUT to increase the overall measurement speed in a virtual three-receiver configuration. The fourth receiver is only used if explicitly required by the calibration and correction scheme selected by the operator ([27]).

An advancement upon the 10-term two-port error model for multi-port VNAs with n-ports and $(n+1)$-receivers, based upon the extension of the error network description for incomplete reflectometer architectures known as GSOLT, can be found in [51]. Another interesting expansion of the original concept to create, calibrate and error correct a multi-port VNA from a two-port four-receiver VNA using $(n/2+n)$ virtual receivers by using a switching matrix can be found in [32].

Well known examples for the three-receiver two-port VNA architecture are the HP 8573 series and the Rohde & Schwarz ZVRE and ZVC series. An in depth explanation of the three-receiver concept using a signal flow analysis can be found in [27], while [122, 49] analyze the problem using the error-box network model.

In order to distinguish unidirectional and three-receiver two-port VNAs from their reflectometer based two-port counterparts, they are also sometimes labeled as incomplete reflectometer VNA architectures in the literature ([32, 48]).

Figure 2.10: Picture of a PC-based SDR-Kits DG8SAQ 1 kHz to 1.3 GHz two-port unidirectional three-receiver VNA.

2.2 Theoretical Description, Calibration and Error Correction of the Switched Receiver Concepts

2.2.1 Motivation for the Single Receiver VNA Architecture

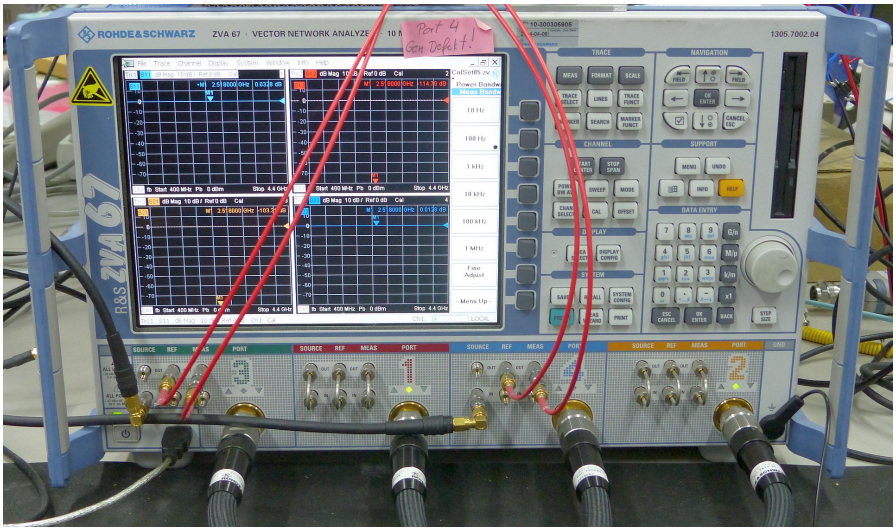

Figure 2.11: Rohde & Schwarz ZVA67 four-port, 8 receiver full reflectometer 10 MHz - 67 GHz VNA with arbitrary frequency measurement, multi- and differential-stimulus capability and an installed direct generator/receiver access option.

From the previous introduction to basic VNA architectures it can be easily argued, that the design, production and testing of multi-port VNAs in a full reflectometer configuration is a time and money consuming process due to the sheer number of sub-assemblies and components involved.

In order to discuss and understand the various viable methods of complexity and cost reduction employed in mid- and lower-tier VNAs, it is at first necessary to look at all the different assemblies required to build a modern, arbitrary frequency measurement and multi-stimulus operation capable, n-reflectometer VNA .

The bill of materials (BOM) for constructing a contemporary full featured heterodyne VNA, like a Rohde & Schwarz ZVA (see Fig. 2.11) or a Keysight PNA-X, can be coarsely grouped into the following coarse sub-assembly categories:

1. An embedded computer system managing the user interface, communication interfaces (like Ethernet, USB/Serial, or GPIB), the data collection, calibration procedures and data visualization,

2. A display, keyboard and/or touchscreen interface for a bench-top stand-alone VNA instrument,

3. A precision reference clock (usually 10 MHz) distribution and conditioning assembly

which provides an isolated divided or multiplied representation of the clock to the RF/IF assemblies,

4. An enclosure to provide shielding, mechanical rigidity, mounting points for all sub-assemblies and a central power supply to all assemblies,

5. Internal coaxial microwave cables for connecting the assemblies and high quality metrology grade connectors for the external user accessible test-set ports,

6. Directional couplers, bridges or power splitters ([136]) for sampling the incident and reflected waves of the test-set ports,

7. RF/IF assemblies for each port, containing:
   - One stimulus synthesizer[12] with automatic level control,
   - RF isolation amplifiers for both receiver inputs,
   - Pre-selectors or optional step-attenuators for one or both wave receivers,
   - Two sampling-, passive diode switching or active Gilbert cell based high linearity down-converting mixers for both the a- and b-channel,
   - One local oscillator (LO) synthesizer for the a/b-wave down-converters,
   - IF lowpass or bandpass filtering,
   - Configurable IF amplifiers,
   - And one or more high resolution analog to digital (sampling) converters (ADC) with their associated sampling clock generators, data capture and pre-processing units per receiver channel.

When analyzing this BOM it is obvious, that the assemblies in points 1 to 4 are necessary and regardless of the number of measurement ports, while the amount of sub-assemblies of points 5 to 7 scales linearly with the number of RF interfaces. Of all these assemblies, the RF/IF assembly, containing the receiver front-end, filtering and data acquisition systems, is by far the most involved and complex sub-unit.

In remote controlled production test environments and for lower-end VNAs, the display and a keyboard interface on the device itself are nowadays usually omitted. The assemblies 5 and 6 need to be physically present to connect n-ports of a DUT to n-ports and form the physical test-set, so no further topological complexity and cost reduction methods can be employed[13].

However, depending on the intended application, measurement tasks and target price, it is possible to exploit certain redundancies in the per port RF/IF assembly to reduce cost and space requirements.

In the mid-range VNA segment, these assembly redundancies with their resulting feature reductions are:

[12] Also often called the port generator.

[13] Except for implementing receive-only ports in unidirectional stimulus VNA designs, which are usually internally terminated into an attenuator.

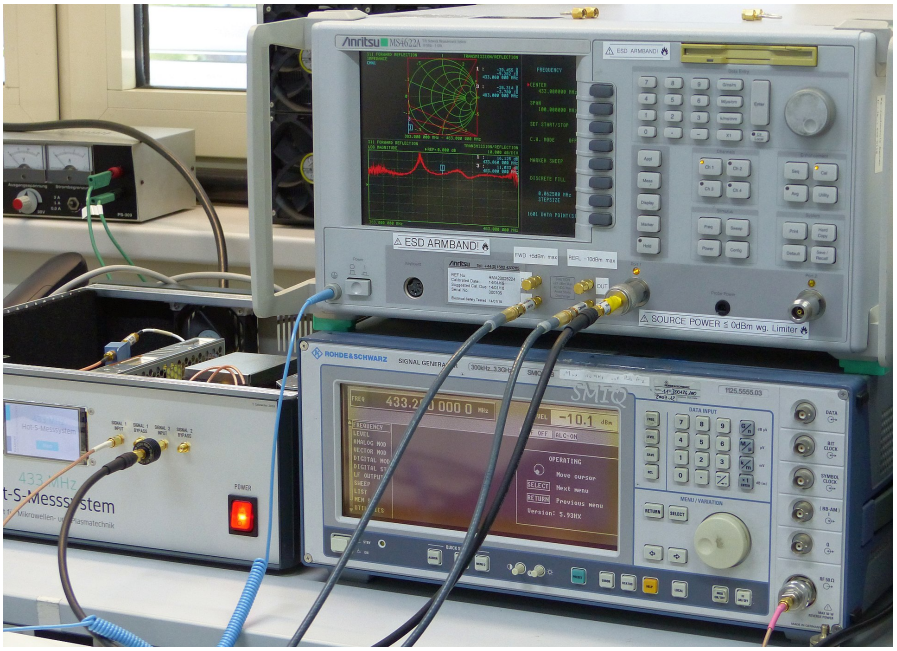

Figure 2.12: Anritsu MS4622 Scorpion, semi-switched receiver, unidirectional two-port 10 MHz - 3 GHz VNA, modified by the author for direct generator and receiver access and used in a 433 MHz 1 kW Hot-S_{11} atmospheric UHF plasma characterization setup.

- Centralized generation and distribution of the low jitter ADC sampling clock signal.
- One shared LO synthesizer for all down-converters, which prevents simultaneous frequency converting transmission measurements. This introduces a RF cross-talk path between the receiver channels, which limits the usable dynamic range of the instrument considerably.
- Reduced resolution for a-wave receiver channel ADCs, as the dynamic range of the a-wave is generally orders of magnitude lower than the b-wave when using a standard test-set. This however limits the a-receiver's flexibility in the direct receiver access role.
- Stimulus synthesizers which are shared between two or more ports by employing a highly repeatable and isolating absorptive electronic switch[14] while still retaining full reflectometers with 2 receivers each for the 7-term model. This removes multi-tone stimulus measurement capabilities such as scalar mixer measurements and especially automatic intermodulation measurements from VNAs which are then only left with one stimulus source.

[14]This is also often called an auto-reversing module.

From this list it is possible to identify one persistent trend emerging for reducing cost and system complexity: A reduction in the total amount of synthesizers. In the lower end of the VNA spectrum, generally aimed at the price sensitive production test and educational markets, some even more restricting additional cost-saving measures are employed:

- A three-receiver hardware architecture with one shared a-wave coupler for all stimulated ports, which omits direct 7-/15-term calibration capability without an additional two-tier SOLT-calibration for capture of the switching terms.
- A unidirectional 5-term architecture, which only allows for S_{11} and S_{21} measurements[15] by omitting the generator switch and reflectometer on the second port.
- Shared and switched IF-paths after the down-converter, which limits measurement speed by sequential data capture and isolation[16] between waves.
- Semi-switched front-end receiver designs, which only have one a- and one b-wave receiver channel and therefore heavily cut down on all RF/IF assembly costs. All a- and b-waves of the test-set are then multiplexed with highly isolating and repeatable electronic switches in the right combination for the specific S-parameter to be measured. A well-known example for this concept is the Anritsu MS462XX Scorpion series.

In recent years, an even more radical approach to reduce the total cost and complexity of a VNA was presented in 2010 by Schramm et al. ([128]) and 2011 by Isaksson and Zenteno ([65]) in the scientific literature: The switched or single receiver VNA.

This concept, originally presented in the context of synthetic instrumentation[17], reduces the number all down-converters, LOs, IF-paths and ADCs to all but one single RF/IF assembly. The wave selection for the single wave-receiver is handled by an absorbing electronic front-end switch with high repeatability and isolation between wave channels, which multiplexes the required amount of synthetic a- and b-wave input channels from the test-set to the sole receiver.

[15] More receiver-only ports are generally imaginable, but not common.

[16] This is generally of lesser concern today, as electronic IF switches provide orders of magnitude more isolation than microwave switches.

[17] Synthetic instruments are build from flexible remote controlled general purpose laboratory instrument blocks such as ADC/DAC cards, switch matrices, synthesizers, multi-meters, etc., with its behavior as a combined instrument defined by software.

2.2.2 General Description of the Switched Receiver VNA

The motivation for building a single switched receiver VNA stems from a simple basic question rooted in observing the serialized structure of analog ADC front-ends commonly integrated into systems on a chip (SoC) devices or microcontrollers:

When it is possible in a multiple analog input channel sampling scenario to substitute multiple parallel slow ADCs with one fast ADC, an analog input multiplexer and input scanning logic for signals time invariant on the timescale of the scanned sequential sampling process, why is the same cost and complexity saving measure not applied to VNA receiver front-ends, as the very definition of the S-parameters includes the linearity and time invariance of DUT's behavior as a prerequisite?

While this naive question seems quite simple and straight-forward at first, the following sections in this chapter will present, cover and analyze the intricacies and challenges introduced by consequently following along this paradigm and its implications for VNA error models, calibration, error correction procedures and the actual hardware implementation.

In order to follow the original posing of the question, the equivalent components between the concepts in the quasi-DC and RF domain must be identified first:

- The RF input wave selector switch, consisting of an absorptive semiconductor single pole (1 output), n-throw (n selectable inputs), PIN diode switch for high switching speed and repeatability (see [54]) as an RF-equivalent of the analog input multiplexer,
- The VNA receiver itself, as a complex frequency domain measurement device equivalent to the time domain measurements performed by the ADC, and
- A sequencer controlling and coordinating all necessary device configurations of the VNA system, such as gain settings, sampling frequency settings of the stimulus and LO synthesizers, data acquisition and storage, with the position of the RF input wave selector switch.

While the identification and assertion of equivalent sub-units and components is pretty straightforward and easily done, the properties of the real components at RF and microwave frequencies available for building such a single receiver VNA system, combined with the high dynamic range in excess of 80 to 100 dB expected from a modern VNA, makes finding a definitive answer to this question a daunting, and at the same time scientifically interesting, task.

As an introduction to the overall topic, it is helpful to visualize the modified measurement procedure of the single switched receiver VNA in contrast to a normal full-receiver VNA and analyze the direct consequences of the serialized frequency domain sampling procedure.

A graphical depiction of the measurement process for a four-receiver double reflectometer VNA capturing a standard frequency sweep, i.e. acquiring or measuring the complex wave quantities a_1, b_1, a_2 and b_2 emanating from the test-set, and consequently

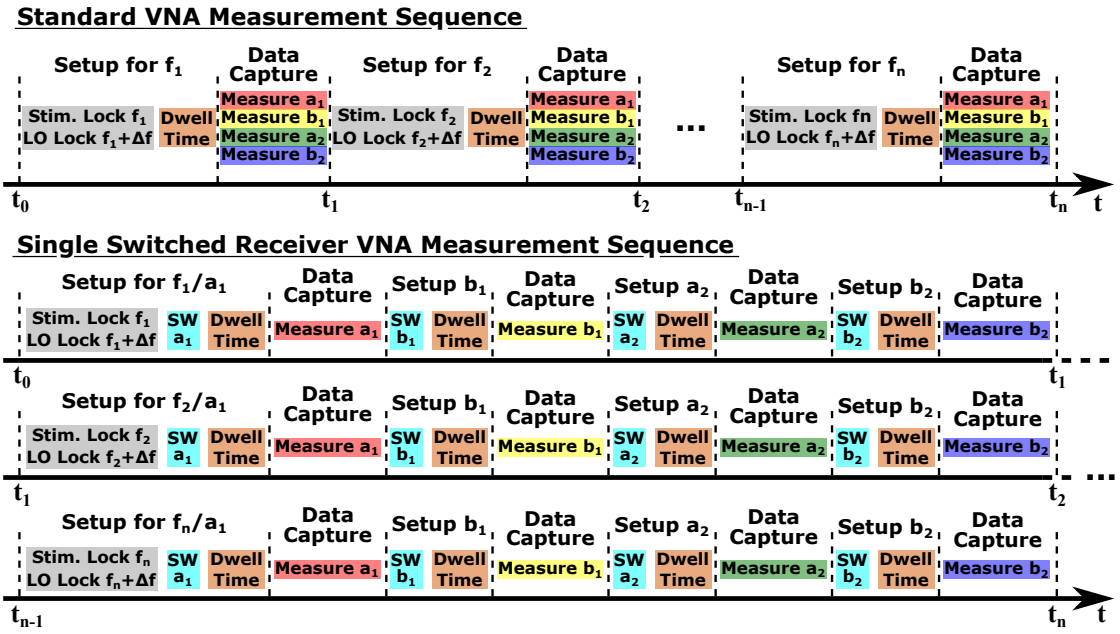

Figure 2.13: Graphical depiction of the measurement sequence for normal full receiver VNAs and the single switched receiver VNA concept. Individual measurement time contributions not to scale.

related to the stimulus response of the DUT, at multiple strictly defined n sampling points f_1, f_2, ..., f_n in the frequency domain, and the equivalent serialized switched single receiver measurement procedure, is shown in Fig. 2.13.

The measurement procedure of the normal full receiver VNA follows a simple scheme: First the necessary frequencies for the stimulus and local oscillator synthesizers are set and frequency lock is obtained. The dwell-time, which in first order mainly depends upon the selected IF filter bandwidth, is allowed to pass after synthesizer lock to allow all system responses to settle and obtain a momentary TI state for the sampling point of interest.

After the dwell-time has passed, the data sampling, acquisition and conversion is performed simultaneously for all complex wave quantities using four parallel receivers. Generally this is also performed in a fully synchronous sampling process, where all sampling clocks for the ADCs and LO-signals for the mixers are derived and distributed from one central source for linear, only S-parameter measurement capable, VNAs, to relax the stability requirements imposed upon the stimulus and LO-signal synthesizers ([27]). When the sampling process is finished, the process starts again for the next frequency in the sweep frequency list until the sweep is complete.

In contrast, the serialized single switched receiver sampling procedure shown in the bottom of Fig. 2.13 is more complex and time-consuming, as expected from the similarly complex scanning ADC example of the original question. The sequential sampling process of the four wave quantities starts in the very same way as in the normal VNA procedure by

obtaining frequency lock for the stimulus and LO-signal generators for the measurement frequency of interest. Next, the appropriate test-set signal source of interest, which is the wave quantity a_1 in this case, must be selected by the sequencer using the receiver input wave selection switch[18].

The dwell-time is then allowed to pass to allow all components to settle to a steady state and the data sampling, acquisition and conversion is performed for the single wave quantity. When the data acquisition of the first wave quantity is complete, the sequencer advances the RF input wave selector switch position to the next wave quantity b_1, which requires an additional passing of the dwell-time to allow components to settle to a steady state before a measurement of the wave quantity is performed. This process is repeated until all the required wave quantities are measured for the specific frequency sampling point. This cycle is repeated with new pairs of stimulus and LO-synthesizer frequencies until the data capture for all sampling points defined in the sweep list is complete.

When comparing this procedural outline with the original statement made at the beginning of this section, there is one important point in the assumption that is easily skipped, but in essence conveys one of the most troublesome points when applying the concept of a single switched receiver or converter to signals at microwave or RF frequencies — the time invariance of the signals time on the timescale of the scanned sequential sampling process.

If the DUT is assumed to be LTI in its behavior, the crucial point for obeying the time invariance of the signals is easily identified from Fig. 2.13 as the stimulus and LO-signals used in the VNA system. Both independently synthesized signals are essential for measuring the DUT response and must be assumed to be constant, and therefore time invariant, in their amplitude and phase behavior during the whole switch scanning procedure to yield results comparable to the original parallel sampling approach.

This demand stems from the very definition of the S-parameters, which in their raw and non-error corrected form are defined directly from the ratios of the measured test-set wave quantities and therefore inherit the LTI definition of the S-parameters for their raw wave quantity ratios.

When looking at the timescales involved in the measurement process in direct comparison between the classical parallel and the sequential single switched receiver approach, regardless of other system imperfections such as finite switch isolation, it can be easily argued from Fig. 2.13, that the stability requirements imposed upon both synthesizers and the ADC sampling clock must be higher than in the classical approach for the same measurement error bounds due to the serialization, and therefore time stretching, of the original process.

This prolonged coherence time is not only proportional to the number of serialized measurement channels and pure acquisition time, but also includes the dwell-time required to reach a new steady state for each individual switch position. As VNAs generally use

[18] In reality, this first selection can already occur during synthesizer lock to save time, but due to the short time required to change the input on a semiconductor RF switch, the quasi non-existent contact bounce exhibited by these switches and therefore time to reach a quasi TI state, this delay is generally orders of magnitude shorter than the other contributors and only featured here explicitly for reasons of clarity.

narrow-band IF filters to reach sufficiently low levels of system noise-floor and therefore high dynamic range and sensitivity combined with high precision and resolution data converters, the settling time required to reach a sufficient and repeatable steady state can easily exceed the time necessary for capturing the required number of ADC samples.

This observation may lead to the fallacy that S-parameters defined from adjacently scanned wave quantities may show lower amounts of stimulus and LO-signal drift related measurement error. While this assumption is true for the raw wave ratios them-self, this is negated by the fact that error corrected S-parameters are generally interdependent upon all measured raw S-parameter ratios, as will be shown in the later in chapters 2.2.4 to 2.2.9 of this work.

When looking back at the sequence shown for the single receiver, it is important to note that the order of steps shown, i.e. obtaining synthesizer lock before scanning all wave input channels and changing frequencies, is not chosen arbitrarily, but is deeply rooted in the repeatability of RF signal generators and especially PLL based synthesizers in frequency hopping or sweeping applications.

When PLL-based synthesizers are analyzed for their compliance to the TI signal magnitude and phase criterion, it is important to differentiate between different TI levels that can be achieved by this synthesizers in coherent applications. The different levels achievable by a PLL or DDS based frequency synthesizer are:

- Amplitude stability,
- Amplitude repeatability,
- Phase stability, and
- Phase repeatability.

Stability in this context is defined as a stable, momentary, state achieved in a specific frequency sampling point during a frequency sweep, that is held for the duration of one full receiver wave selector switch scan and receiver measurement operation to obtain all wave quantities of interest.

This is the most basic TI state requirement for single receiver VNAs to obtain the comparable results to a classical VNA architecture and allows LTI based error models to be used for this architecture.

While the phase stability of a PLL based synthesizer is ensured by the phase control loop action performed by the PLL in frequency and phase lock when a full four quadrant phase-frequency detector (PFD) is used and is easily verified during operation by monitoring the output of the analog or digital lock-detect circuits generally integrated into a PLL, the amplitude stability is not part of the control action performed by the PLL and must be ensured by other means.

In practice, different techniques are used to achieve amplitude stability for the output signals of a PLL, depending on the actual application for the signal. In VNA stimulus synthesizers an automatic level control (ALC) circuit, consisting of a power detector, a directional coupler and a voltage variable amplifier or attenuator are used in a control loop to stabilize the output amplitude by comparing a temperature stabilized set-point voltage

with the output of the power detector to ensure a constant output voltage ([27]). An added benefit of the ALC, besides ensuring amplitude stability, is that this stabilization method also allows the generation of various output amplitudes over a large dynamic range.

In case of the LO-synthesizers in a (super-)heterodyne vector receiver this involved ALC setup is generally not necessary, as the balanced active and passive mixers used in this architecture only require a fixed but stable LO drive signal amplitude to ensure LTI behavior of the mixer. Therefore it is common to use limiting amplifiers to provide stable mixer operation. These limiting amplifiers are essentially very high gain amplifiers designed to clip the output signal at a certain repeatable amplitude level. As balanced mixers are essentially operated as switches driven into hard saturation by the LO signal anyway, the almost square wave shaped and clipped output signal of the limiting amplifier results in the same operating and conversion performance of the mixer as observed for a sinusoidal drive signal of the same power.

In order to define both amplitude and phase repeatability in the context of VNA measurements it is important to remember, that VNAs are usually used in a list based stepped frequency mode. Phase and amplitude repeatability in this context means, that the same stable steady state is reached for each of both parameters for a distinct frequency when other frequencies were locked in the meantime, therefore the amplitude and phase can be considered constant for a specific frequency sampling point and therefore time invariant regardless of the frequency locking history of the synthesizer.

While synthesizer amplitude repeatability is comparably easy to achieve by careful design and selection of the ALC circuit or limiting amplifier, true phase repeatability is usually not achievable by synthesizers commonly used in VNAs[19].

As surprising as this may seem at first glance, a repeatable synthesizer output phase is generally not necessary for the measurement of linear S-parameters, as any arbitrary stable phase offset present in the measured wave quantities introduced by the synthesizers is eliminated by the wave ratio definition and calculation of the S-parameters. The cause of this problem is deeply rooted in the architecture of the Fractional-N and DDS arbitrary frequency synthesis techniques used for small minimum frequency step-sizes and their locking speed optimized implementations found in VNAs ([143]).

The inclusion of a non-repeatable output phase offset of the VNA synthesizers in combination with the tolerance of the S-parameters calculation for stable, but arbitrary, phase offsets is the reason for the structure of the single receiver measurement process shown before in Fig. 2.13, where all wave quantities are measured during one phase stable lock-cycle of the synthesizers.

If this pattern was to be changed, for example by measuring all a_1 wave quantities for each frequency sampling point exclusively and then repeating this sequence again each of the individual wave quantities over frequency, no usable phase information could be obtained from the measurement results due to varying phase offsets for the same

[19] A semi-exception to this statement is the defined coherence and true differential mode implemented in modern R&S ZVA variants, which allows a configurable repeatable phase offset between internal stimulus synthesizers, but not in respect to the system reference clock.

frequency sampling points caused by the re-locking of the PLL.

Upcoming Research Work

The cause of the non-repeatable output phase and a possible solution for achieving phase repeatability for Fractional-N synthesizers will be discussed in-depth in the description of the developed VNA synthesizer hardware and the introduction of the synthesizer phase reference standard in chapters 2.3.3, 3.1 and 3.3 this work.

Several new advancements in VNA test-set topologies and measurement techniques, resulting from the deployment of phase repeatable synthesizers for linear and non-linear VNA measurement procedures in single and multi-receiver VNA architectures, will be presented in the course of this work in chapters 2.2.11, 2.3.3, 3.3 and 4.3 and discussed in detail with regard to the specific application.

Although the consequences and differences of TI stability and repeatability are important concepts to keep in mind for the rest of this thesis, it is helpful to assume TI repeatability for all signals, or ideal frequency synthesis, for the following discussion of single switched receiver VNA error models.

In the following sections, extensions to and modifications of VNA error models, calibration and error correction procedures as well as test-set topologies for the single switched receiver VNA architectures switch will be derived and analyzed from standard full and incomplete reflectometer VNA architectures. The focus of this new VNA error models is the mitigation of the cross-talk induced effects of real, and therefore leaky, RF switches in the receiver input wave selector switch application.

Furthermore, a new method of deriving the signal flow diagrams of the switched single receiver VNA will be presented, which honors the individual and discrete TI states of the test-set introduced by the discrete, switch position dependent, TI states of the RF receiver input wave selector switch.

While this bottom-up procedure of selectively analyzing the individual TI states of the test-set may to generate the complete composite VNA error model may seem trivial at first, it is in stark contrast to approaches to the same problem presented by Schramm et al. ([128]), and Isaksson and Zenteno ([65]), where only a strict top-down approach based solely upon the complex 7- and 15-term error model, was performed.

This bottom-up approach, not followed by the other publications, also includes the systematic construction and derivation of the more complex multi-port error models from the basic building block of VNAs: The (switched) one-port reflectometer VNA.

2.2.3 Analysis of the Switched Receiver Reflectometer

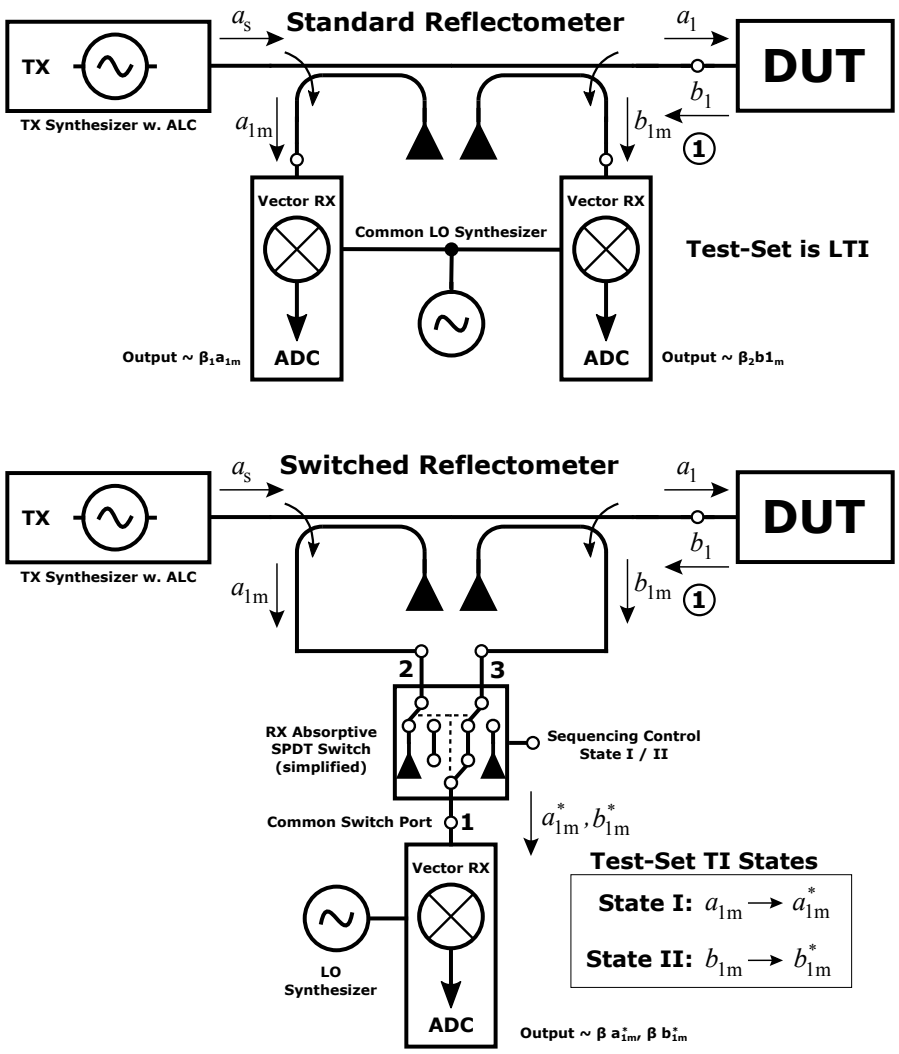

Figure 2.14: Schematic of the standard VNA reflectometer and its corresponding switched receiver VNA reflectometer equivalent including the two distinct TI states of the test-set.

The basic building block of all switched receiver VNA designs, the switched reflectometer, contains a single pole double throw (SPDT) absorptive PIN-diode switch for the receiver input wave selector function. This SPDT switch multiplexes the test-set waves a_{1m} and b_{1m} from their directional couplers sequentially to the single receiver and can be described as a passive linear three-port device with a distinct set of S-parameters for each TI state of the switch, and therefore the test-set, with the corresponding position indicated from now on by a roman numeral in the superscript i of the parameters.

The superscript 0 is used here to denote the special case of general isolation, which is

implemented in some integrated PIN-diode switches. This refers to a state where all switch ports, including the common port, are internally connected to their associated termination resistors with no intended thru connection. This is sometimes erroneously referred to as the off-state of the switch. While this state is not strictly useful in the reflectometer configuration, it is necessary to introduce it here for other single receiver VNA topologies. The subscript of the following transmission S-parameters follows standard convention,

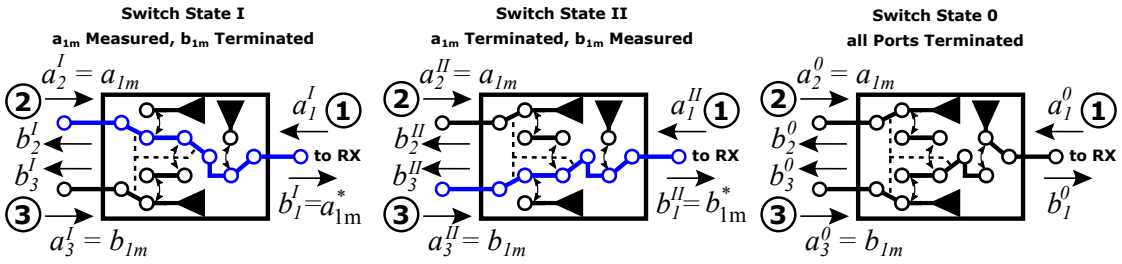

Figure 2.15: Schematic of the three TI states of the switched reflectometer wave selector switch, including internal switch positions for absorptive behavior.

with $\mathrm{IL}^i_{x,y}$ and $\mathrm{IL}^i_{y,x}$ denoting the insertion loss of the intended connection path, while $\mathrm{Iso}^i_{x,y}$ and $\mathrm{Iso}^i_{y,x}$ describes the isolation values between ports in switch state i. The port reflection factors $S^i_{x,x}$ are denoted as RL^i_x. Therefore it is possible to write

$$[S^{\mathrm{I}}] = \begin{bmatrix} \mathrm{RL}^{\mathrm{I}}_1 & \mathrm{IL}_{1,2} & \mathrm{Iso}^{\mathrm{I}}_{1,3} \\ \mathrm{IL}_{2,1} & \mathrm{RL}^{\mathrm{I}}_2 & \mathrm{Iso}^{\mathrm{I}}_{2,3} \\ \mathrm{Iso}^{\mathrm{I}}_{3,1} & \mathrm{Iso}^{\mathrm{I}}_{3,2} & \mathrm{RL}^{\mathrm{I}}_3 \end{bmatrix}, \qquad \begin{pmatrix} a^*_{1m} \\ b^{\mathrm{I}}_2 \\ b^{\mathrm{I}}_3 \end{pmatrix} = [S^{\mathrm{I}}] \cdot \begin{pmatrix} a^{\mathrm{I}}_1 \\ a^{\mathrm{I}}_2 \\ a^{\mathrm{I}}_3 \end{pmatrix}, \tag{2.20}$$

$$[S^{\mathrm{II}}] = \begin{bmatrix} \mathrm{RL}^{\mathrm{II}}_1 & \mathrm{Iso}^{\mathrm{II}}_{1,2} & \mathrm{IL}_{1,3} \\ \mathrm{Iso}^{\mathrm{II}}_{2,1} & \mathrm{RL}^{\mathrm{II}}_2 & \mathrm{Iso}^{\mathrm{II}}_{2,3} \\ \mathrm{IL}_{3,1} & \mathrm{Iso}^{\mathrm{II}}_{3,2} & \mathrm{RL}^{\mathrm{II}}_3 \end{bmatrix}, \qquad \begin{pmatrix} b^*_{1m} \\ b^{\mathrm{II}}_2 \\ b^{\mathrm{II}}_3 \end{pmatrix} = [S^{\mathrm{II}}] \cdot \begin{pmatrix} a^{\mathrm{II}}_1 \\ a^{\mathrm{II}}_2 \\ a^{\mathrm{II}}_3 \end{pmatrix}, \tag{2.21}$$

$$[S^0] = \begin{bmatrix} \mathrm{RL}^0_1 & \mathrm{Iso}^0_{1,2} & \mathrm{Iso}^0_{1,3} \\ \mathrm{Iso}^0_{2,1} & \mathrm{RL}^0_2 & \mathrm{Iso}^0_{2,3} \\ \mathrm{Iso}^0_{3,1} & \mathrm{Iso}^0_{3,2} & \mathrm{RL}^0_3 \end{bmatrix}, \qquad \begin{pmatrix} b^0_1 \\ b^0_2 \\ b^0_3 \end{pmatrix} = [S^0] \cdot \begin{pmatrix} a^0_1 \\ a^0_2 \\ a^0_3 \end{pmatrix}, \tag{2.22}$$

to describe the three states of the SPDT wave selection switch with S-parameters. A schematic, which shows the position of the internal switches of an absorptive switch for the different states and the mapping of the waves to the ports and test-set, is shown in Fig. 2.15.

As a simplification of the problem it is fair to assume, that the isolation terms between the switch ports themselves and the common port as well as the insertion loss terms are reciprocal for each of the switch's TI states, as linear passive behavior is assumed, yielding $\mathrm{IL}^i_{x,y} = \mathrm{IL}^i_{y,x}$ and $\mathrm{Iso}^i_{x,y} = \mathrm{Iso}^i_{y,x}$.

In order to simplify the description of the various switch states further, it is, without loss of generality, possible to borrow from the communication engineering principle of carrier-to-interference (C/I) and normalize all transmission terms in each TI state to the associated IL^i of the position to simplify and stream-line the analysis of the leaky switch.

Although this operation breaks the strictly passive description of the switch, it transforms the S-parameters $[S^{\mathrm{i}}]$ into an accurate representation of the cross-talk situation $[S^{\mathrm{i}*}]$ at the common receiver port of the switch for wave ratio measurements with the single receiver.

The cross-talk between the ports can further be separated into cross-talk originating from the test-set ports to the common receiver port, denoted C_x^i, and cross-talk X_x^i between test-set connections. The additional isolation state $[S^0]$ is omitted from here on for reasons of clarity. With this, it is possible to rewrite the cross-talk oriented description $[S^{\mathrm{i}*}]$ of the switch states to

$$[S^{\mathrm{I}*}] = \begin{bmatrix} \mathrm{RL}_1^{\mathrm{I}} & 1 & C_3^{\mathrm{I}} \\ 1 & \mathrm{RL}_2^{\mathrm{I}} & X_3^{\mathrm{I}} \\ C_3^{\mathrm{I}} & X_3^{\mathrm{I}} & \mathrm{RL}_3^{\mathrm{I}} \end{bmatrix}, \qquad \begin{pmatrix} a_{1m}^* \\ b_2^{\mathrm{I}} \\ b_3^{\mathrm{I}} \end{pmatrix} = [S^{\mathrm{I}*}] \begin{pmatrix} a_1^{\mathrm{I}} \\ a_2^{\mathrm{I}} \\ a_3^{\mathrm{I}} \end{pmatrix}, \tag{2.23}$$

$$[S^{\mathrm{II}*}] = \begin{bmatrix} \mathrm{RL}_1^{\mathrm{II}} & C_2^{\mathrm{II}} & 1 \\ C_2^{\mathrm{II}} & \mathrm{RL}_2^{\mathrm{II}} & X_2^{\mathrm{II}} \\ 1 & X_2^{\mathrm{II}} & \mathrm{RL}_3^{\mathrm{II}} \end{bmatrix}, \qquad \begin{pmatrix} b_{1m}^* \\ b_2^{\mathrm{II}} \\ b_3^{\mathrm{II}} \end{pmatrix} = [S^{\mathrm{II}*}] \begin{pmatrix} a_1^{\mathrm{II}} \\ a_2^{\mathrm{II}} \\ a_3^{\mathrm{II}} \end{pmatrix}, \tag{2.24}$$

$$\text{by using } C_x^i, X_x^i = \frac{\mathrm{Iso}_{x,y}^i}{\mathrm{IL}^i} \text{ and } \frac{\mathrm{IL}^i}{\mathrm{IL}^i} = 1\,.$$

In order to proceed with the analysis, a practical approach which includes the properties of the physical test-set must be followed to further simplify the switch cross-talk description. The situation described with Eq. (2.24) is shown graphically in Fig. 2.16 for the X_2^{II} bidirectional cross-talk term between ports 2 and 3 in state II of the switch for illustration and further discussion.

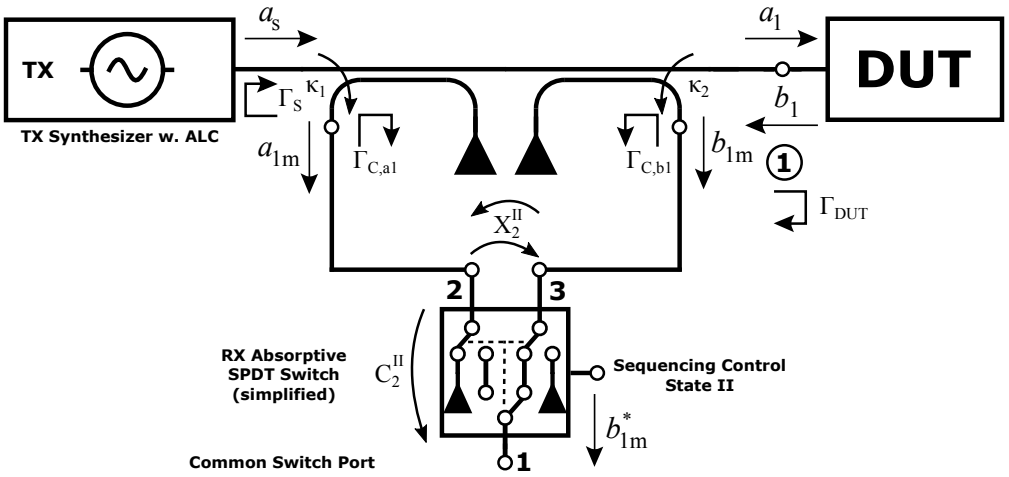

Figure 2.16: Schematic of the switched reflectometer in state II, b_{1m}^* for inter-test-set cross-talk analysis of X_2^{II}.

In the following it is possible to expect, that the isolation $|X_2^{\mathrm{II}}| \approx |C_2^{\mathrm{II}}|$, which is a valid assumption for most semiconductor switches. Without loss of generality, the wave

selection switch is also assumed to be well-matched and therefore $S_{ii} \approx 0$. In the b^*_{1m} measurement position, the interference present at the receiver is caused by the a_{1m} wave of the test-set and is the result of the superposition of three test-set component dependent paths, as shown in Fig. 2.16:

- The dominating direct cross-talk $a_{1m} \cdot C_2^{\mathrm{II}}$ from port 2 to the common receiver at port 1 via the SPDT switch,
- The smaller $a_{1m} \cdot X_2^{\mathrm{II}} \cdot \Gamma_{C,b1}$ inter-test-set cross-talk loop that directly influences the b^*_{1m} measurement, and
- Finally the $a_{1m} \cdot X_2^{\mathrm{II}} \cdot \Gamma_{C,b1} \cdot X_2^{\mathrm{II}} \cdot \Gamma_{C,a1} \ll a_{1m}$ loop that returns to the analysis' starting point.

At this point it is important to remember the concept of superposition and abstraction used in the origin of the 3-term model E_S source match term, which can be also applied here. As we are only interested in the quantification of the total interference originating from the a_{1m} wave, we can superpose the minor, but still important paths, with the dominant path into one common factor C_2^{II} and define all $X_2^{\mathrm{II}} = 0$.

While this factor does not cover all the physical relations and paths of the hardware model, similar to the abstract source-match coefficient E_S, it gives an accurate representation of the effects seen by the single receiver behind the switch. This superposition even holds up if the input ports of the switch have finite return loss, therefore we can set all $RL_x^i = 0$ for further analysis.

In addition to the aforementioned paths, a DUT dependent cross-talk path $a_{1m} \cdot X_2^{\mathrm{II}} \cdot \kappa_2 \cdot \Gamma_{\mathrm{DUT}} \cdot \kappa_2$ can be identified in Fig. 2.16. This path can easily be neglected, if the condition $|\kappa_2|^2 \ll |X_2^{\mathrm{II}}|$ is obeyed for the construction of the test-set[20].

The same thought experiment and analysis as carried out for b^*_{1m} can be conducted for the a^*_{1m} position of the switch. This analysis gives similar results, except for the last path, which depends upon more stable generator return loss Γ_S instead of the DUT. Analogous to the other switch-state, this path can be neglected under the condition $|\kappa_1|^2 \ll |X_3^{\mathrm{I}}|$. With this knowledge, it is possible to rewrite Eq. (2.23) and Eq. (2.24) to the more convenient form of

$$\begin{pmatrix} a^*_{1m} \\ b_2^{\mathrm{I}} \\ b_3^{\mathrm{I}} \end{pmatrix} = [S^{\mathrm{I}*}] \begin{pmatrix} a_1^{\mathrm{I}} \\ a_2^{\mathrm{I}} \\ a_3^{\mathrm{I}} \end{pmatrix}, \text{ with } [S^{\mathrm{I}*}] = \begin{bmatrix} 0 & 1 & C_3^{\mathrm{I}} \\ 1 & 0 & 0 \\ C_3^{\mathrm{I}} & 0 & 0 \end{bmatrix}, \text{ and} \tag{2.25}$$

$$\begin{pmatrix} b^*_{1m} \\ b_2^{\mathrm{II}} \\ b_3^{\mathrm{II}} \end{pmatrix} = [S^{\mathrm{II}*}] \begin{pmatrix} a_1^{\mathrm{II}} \\ a_2^{\mathrm{II}} \\ a_3^{\mathrm{II}} \end{pmatrix}, \text{ with } [S^{\mathrm{II}*}] = \begin{bmatrix} 0 & C_2^{\mathrm{II}} & 1 \\ C_2^{\mathrm{II}} & 0 & 0 \\ 1 & 0 & 0 \end{bmatrix}, \tag{2.26}$$

[20] It will be shown later, that this constraint does not hold up, as its influence will be absorbed into E_D by superposition.

from which the final switched receiver measured waves

$$a^*_{1m} = 1 \cdot a_{1m} + C^{\mathrm{I}}_3 \cdot b_{1m}\,, \text{ and} \tag{2.27}$$

$$b^*_{1m} = C^{\mathrm{II}}_2 \cdot a_{1m} + 1 \cdot b_{1m} \tag{2.28}$$

can be extracted. With this description of the receiver waves, a two part stateful signal flow graph for the switched receiver reflectometer can be constructed from an augmented standard 3-term flow graph with an additional cross-talk path per state. This flow graph is constructed by combining the graphs corresponding to Eq. (2.27) and Eq. (2.28) with the 3-term reflectometer graph in a process shown in Fig. 2.17.

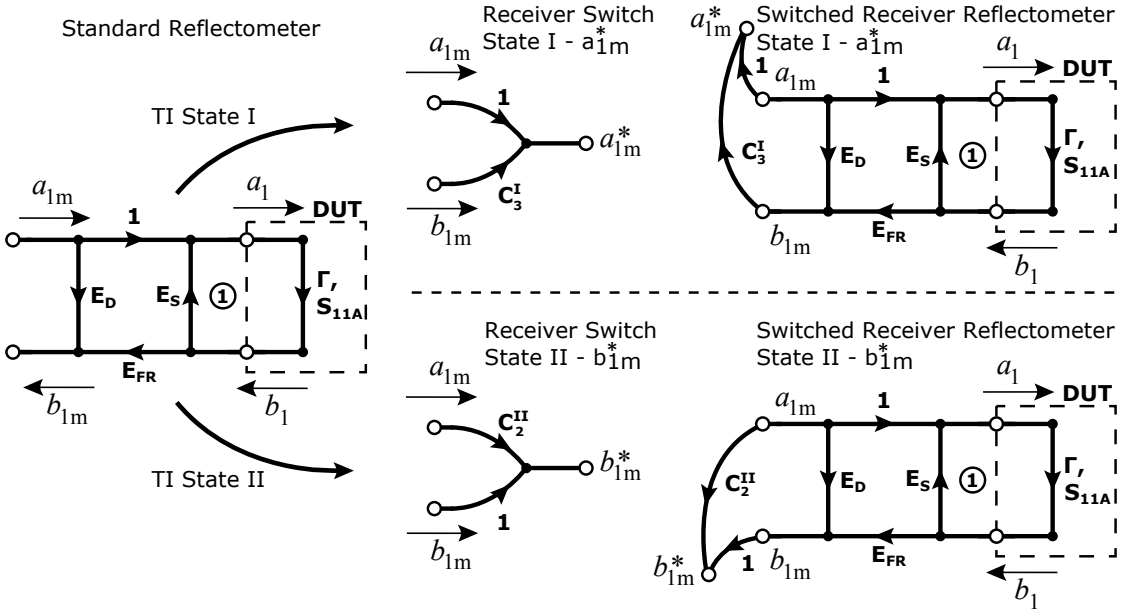

Figure 2.17: Construction of the stateful reflectometer signal flow graph from the 3-term and switch cross-talk signal flow graphs.

When analyzing the first switch state I for a^*_{1m}, with a_{1m} as the source and b_{1m} as the sink of the signal in the graph, we find that the standard reflectometer equation

$$S_{11m} = \frac{b_{1m}}{a_{1m}} = E_D + \frac{1 \cdot \Gamma\, E_{FR}}{1 - E_S\, \Gamma} \tag{2.29}$$

still holds true, with S_{11m} as the measurable S_{11}, and Γ as the real reflection coefficient of the DUT. However, these wave quantities are not directly measurable in the switched reflectometer, as we can only determine their cross-talk influenced version a^*_{1m} and b^*_{1m}, and therefore, only

$$S^*_{11m} = \frac{b^*_{1m}}{a^*_{1m}} \neq S_{11m} = \frac{b_{1m}}{a_{1m}} \tag{2.30}$$

can be measured by the receiver. This can be resolved by first solving Eq. (2.29) for b_{1m} and inserting the expression into Eq. (2.27), yielding

$$a^*_{1m} = a_{1m} \cdot \left[1 + C_3^{\mathrm{I}} \cdot (E_D + \frac{1 \cdot \Gamma\, E_{FR}}{1 - E_S\, \Gamma})\right] \tag{2.31}$$

for state I, a^*_{1m}, of the receiver switch. For solving the second state of the flow graph we can conveniently use the graph node reduction rule, resulting in a modified directivity term

$$E'_D = E_D + C_2^{\mathrm{II}}\,, \tag{2.32}$$

because the node b_{1m} can be removed due to the connecting path coefficient being equal to 1 when analyzing for b^*_{1m} as the signal sink. E_D and C_2^{II} are now connecting to the same nodes in parallel and by applying this simplification, we find

$$\frac{b^*_{1m}}{a_{1m}} = E'_D + \frac{1 \cdot \Gamma\, E_{FR}}{1 - E_S\, \Gamma} \tag{2.33}$$

as the solution for the signal graph of state II in Fig. 2.17 for measuring b^*_{1m} with the vector receiver.

When Eq. (2.31), which describes state I, is solved for a_{1m} and inserted into Eq. (2.33), which describes state II, this results in the final expression

$$\underbrace{\frac{b^*_{1m}}{a^*_{1m}}}_{=S^*_{11m}} \cdot \left[1 + C_3^{\mathrm{I}} \cdot (E_D + \frac{1 \cdot \Gamma\, E_{FR}}{1 - E_S\, \Gamma})\right] = E'_D + \frac{1 \cdot \Gamma\, E_{FR}}{1 - E_S\, \Gamma} \tag{2.34}$$

$$\Leftrightarrow S^*_{11m} = (E'_D + \frac{1 \cdot \Gamma\, E_{FR}}{1 - E_S\, \Gamma}) \cdot \left[1 + C_3^{\mathrm{I}} \cdot (E_D + \frac{1 \cdot \Gamma\, E_{FR}}{1 - E_S\, \Gamma})\right]^{-1} \tag{2.35}$$

for the measurable switched reflectometer return loss S^*_{11m}. This equation combines both TI states of the test-set and the switch into one unified expression for the measurable return loss S^*_{11m}. The Eq. (2.35) can now be rearranged and factorized similarly to the well-known 3-term reflectometer calibration equation

$$S_{11m} = S_{11m}\, \Gamma E_S + \Gamma\, \Delta E + E_D\,, \text{ with} \tag{2.36}$$

$$\Delta E = E_{FR} - E_S\, E_D\,, \text{ which yields} \tag{2.37}$$

$$S^*_{11m} = S^*_{11m}\, \Gamma \cdot \underbrace{\frac{E_S + C_3^{\mathrm{I}}\, E_S\, E_D - C_3^{\mathrm{I}}\, E_{FR}}{1 + C_3^{\mathrm{I}}\, E_D}}_{=E^*_S} + \Gamma \cdot \underbrace{\frac{E_{FR} - E'_D\, E_S}{1 + C_3^{\mathrm{I}}\, E_D}}_{=\Delta E^*} + \underbrace{\frac{E'_D}{1 + C_3^{\mathrm{I}}\, E_D}}_{=E^*_D}\,, \tag{2.38}$$

$$\Leftrightarrow S^*_{11m} = S^*_{11m}\, \Gamma \cdot E^*_S + \Gamma \cdot \Delta E^* + E^*_D \tag{2.39}$$

for the switched reflectometer. By comparing the standard reflectometer equation and the result of the switched reflectometer analysis we can draw several important conclusions:

- The number of unknown coefficients does not change for the switched reflectometer model, therefore
- There are still 3 unknown coefficients, which can be solved in a linear system with 3 known Γ_i calibration standards and 3 corresponding $S_{11m,i}$ measurements.
- Most effects of direct switch leakage are absorbed due to superposition into the existing E_S and E_D coefficients of the 3-term model.
- The hardware directivity of the switched reflectometer test-set will be slightly lower than the normal test-set due to $E'_D = E_D + C_2^{\mathrm{II}}$.

However, there is an unknown factor $(1 + C_3^{\mathrm{I}}\, E_D)^{-1}$ common to all coefficients in the classical 3-term formulation of Eq. (2.38). To analyze the residual errors caused by the two distinct TI states of the test-set during S^*_{11m} measurements, it is necessary to rearrange Eq. (2.38) and factor out $\alpha = 1 + C_3^{\mathrm{I}}\, E_D$, which results in

$$S^*_{11m} = \alpha^{-1} \cdot (S^*_{11m}\, \Gamma \cdot E''_S + \Gamma \cdot \Delta E'' + E''_D)\,. \tag{2.40}$$

For the correction case, which is Eq. (2.36) and Eq. (2.40) rearranged to solve for an unknown $\Gamma = S_{11}^{\mathrm{DUT}}$ with otherwise fully known coefficients, it is assumed, that the corrected values are not equal, therefore $\Gamma^* \neq \Gamma$, and the 3-term coefficients and the measured return loss to be approximately equal. So using

$$\Gamma^* = \frac{\alpha\, S^*_{11m} - E''_D}{S''_{11m}\, E''_S + \Delta E''}\,, \text{ and} \tag{2.41}$$

$$\Gamma = \frac{S_{11m} - E_D}{S_{11m}\, E_S + \Delta E}\,, \text{ using } E''_S \approx E_S\,,\ \Delta E'' \approx \Delta E\,,\ E''_D \approx E_D\,, \text{ this results in} \tag{2.42}$$

$$\Delta\Gamma = \Gamma^* - \Gamma = \frac{\alpha\, S^*_{11m} - E''_D}{S^*_{11m}\, E''_S + \Delta E''} - \frac{S_{11m} - E_D}{S_{11m}\, E_S + \Delta E} \tag{2.43}$$

$$\Delta\Gamma \approx \alpha\, S^*_{11m} - S_{11m} \overset{S^*_{11m} \approx S_{11m}}{\longrightarrow} \Delta\Gamma \approx C_3^{\mathrm{I}}\, E_D \tag{2.44}$$

from which it is possible to deduce, that a residual dynamic composite correction error, caused by the static $C_3^{\mathrm{I}} \cdot E_D$ part and the measured return loss of the DUT, exists. This is based upon the state dependent cross-talk to the measurement of the reference wave a^*_{1m}.

The reference cross-talk coefficient α could be determined in-situ with the help of a fully known mismatch standard, but fortunately this error, while metrological relevant, generally does not cause any major measurement errors and dynamic range reduction in practice, as the magnitude of the error is proportional to the input return loss of the DUT and easily below the source match, noise, and resolution performance of the VNA system.

Therefore, it is fair to assume $\alpha = 1$ for most practical intents and purposes and re-use the standard 3-term reflectometer calibration and correction algorithms Eq. (2.1) based upon the open, match and short standards ([27, 49, 60, 119, 122, 143]) without any change and determine the error coefficients E_D, E_S and E_{FR} by using Eq. (2.36) to build and solve the linear system

$$\begin{bmatrix} E_D \\ E_{FR} - E_D \cdot E_S \\ E_S \end{bmatrix} = \begin{bmatrix} 1 & \Gamma_{\text{Open}} & \Gamma_{\text{Open}} \cdot S_{11m,\,\text{Open}} \\ 1 & \Gamma_{\text{Short}} & \Gamma_{\text{Short}} \cdot S_{11m,\,\text{Short}} \\ 1 & \Gamma_{\text{Match}} & \Gamma_{\text{Match}} \cdot S_{11m,\,\text{Match}} \end{bmatrix}^{-1} \cdot \begin{bmatrix} S_{11m,\,\text{Open}} \\ S_{11m,\,\text{Short}} \\ S_{11m,\,\text{Match}} \end{bmatrix} . \tag{2.45}$$

2.2.4 Analysis of the Switched Receiver Unidirectional SOLT VNA

Considering the promising results of the reflectometer analysis, it is the next logical step to extend the stateful signal flow graph model of the switched reflectometer to the unidirectional 'Enhanced Response' or 'One Path - Two Ports' 5-term VNA model by adding one additional switched receiver input to the wave selector switch in a SP3T configuration.

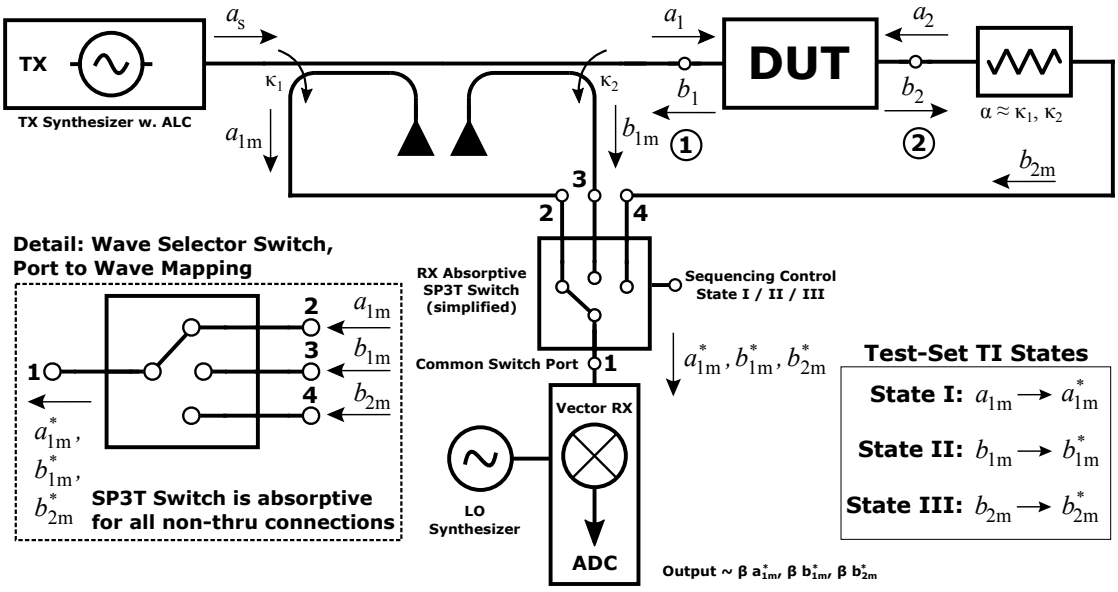

Figure 2.18: Schematic of the unidirectional two-port switched receiver VNA.

This third input is used for multiplexing the b_2 wave, which is transmitted through the DUT to a second, receive-only, port of the two-port VNA as shown in Fig. 2.18. This modification allows for normalized transmission measurements and adds a third state and three additional cross-talk paths to the signal flow graph, as shown in Fig. 2.19.

Similar to the procedure and argumentation presented in the reflectometer analysis it

can be found that

$$\begin{pmatrix} a_{1m}^{*} \\ b_{2}^{\mathrm{I}} \\ b_{3}^{\mathrm{I}} \\ b_{4}^{\mathrm{I}} \end{pmatrix} = [S^{\mathrm{I}*}] \begin{pmatrix} a_{1}^{\mathrm{I}} \\ a_{2}^{\mathrm{I}} \\ a_{3}^{\mathrm{I}} \\ a_{4}^{\mathrm{I}} \end{pmatrix}, \text{ with } [S^{\mathrm{I}*}] = \begin{bmatrix} 0 & 1 & C_{3}^{\mathrm{I}} & C_{4}^{\mathrm{I}} \\ 1 & 0 & 0 & 0 \\ C_{3}^{\mathrm{I}} & 0 & 0 & 0 \\ C_{4}^{\mathrm{I}} & 0 & 0 & 0 \end{bmatrix}, \tag{2.46}$$

$$\begin{pmatrix} b_{1m}^{*} \\ b_{2}^{\mathrm{II}} \\ b_{3}^{\mathrm{II}} \\ b_{4}^{\mathrm{II}} \end{pmatrix} = [S^{\mathrm{II}*}] \begin{pmatrix} a_{1}^{\mathrm{II}} \\ a_{2}^{\mathrm{II}} \\ a_{3}^{\mathrm{II}} \\ a_{4}^{\mathrm{II}} \end{pmatrix}, \text{ with } [S^{\mathrm{II}*}] = \begin{bmatrix} 0 & C_{2}^{\mathrm{II}} & 1 & C_{4}^{\mathrm{II}} \\ C_{2}^{\mathrm{II}} & 0 & 0 & 0 \\ 1 & 0 & 0 & 0 \\ C_{4}^{\mathrm{II}} & 0 & 0 & 0 \end{bmatrix}, \tag{2.47}$$

$$\begin{pmatrix} b_{2m}^{*} \\ b_{2}^{\mathrm{III}} \\ b_{3}^{\mathrm{III}} \\ b_{4}^{\mathrm{III}} \end{pmatrix} = [S^{\mathrm{III}*}] \begin{pmatrix} a_{1}^{\mathrm{III}} \\ a_{2}^{\mathrm{III}} \\ a_{3}^{\mathrm{III}} \\ a_{4}^{\mathrm{III}} \end{pmatrix}, \text{ with } [S^{\mathrm{III}*}] = \begin{bmatrix} 0 & C_{2}^{\mathrm{III}} & C_{3}^{\mathrm{III}} & 1 \\ C_{2}^{\mathrm{III}} & 0 & 0 & 0 \\ C_{3}^{\mathrm{III}} & 0 & 0 & 0 \\ 1 & 0 & 0 & 0 \end{bmatrix}, \tag{2.48}$$

for the wave quantities and S-parameters of the four port, SP3T, receiver wave selector switch, which can be broken down to three distinct TI states.

Analogous to the procedure used for the reflectometer, it is possible to extract the following, insertion loss normalized, cross-talk equations

$$a_{1m}^{*} = 1 \cdot a_{1m} + C_{3}^{\mathrm{I}} \cdot b_{1m} + C_{4}^{\mathrm{I}} \cdot b_{2m}\,, \tag{2.49}$$

$$b_{1m}^{*} = C_{2}^{\mathrm{II}} \cdot a_{1m} + 1 \cdot b_{1m} + C_{4}^{\mathrm{II}} \cdot b_{2m}\,, \text{ and} \tag{2.50}$$

$$b_{2m}^{*} = C_{2}^{\mathrm{III}} \cdot a_{1m} + C_{3}^{\mathrm{III}} \cdot b_{1m} + 1 \cdot b_{2m}\,, \tag{2.51}$$

for the measurement waves seen by the unidirectional single receiver from Eq. (2.46) to (2.47).

From the results shown in Eq. (2.49) and (2.50) we can see, that all original cross-talk paths of the switched single receiver reflectometer are still present in the switched unidirectional VNA configuration and all considerations made for this architecture are still valid for an isolating ($S_{21A} = S_{12A} = 0, b_{2m} = 0$) DUT regarding the S_{11} measurement, because no signal reaches the b_{2m} node in the flow graph.

The unidirectional single receiver VNA configuration presents a multitude of new cross-talk paths, which can be identified as:

- The cross-talk C_{4}^{I} from the b_{2m} wave upon the a_{1m}^{*} reference measurement in Eq. (2.49), depending on the DUT,
- The cross-talk C_{4}^{II} from the b_{2m} wave upon the b_{1m}^{*} reflection tracking measurement in Eq. (2.50), as a function of the DUT,
- The quasi-static cross-talk C_{2}^{III} from the a_{1m} reference wave to the b_{2m}^{*} wave measurement, which can be assumed to be constant, if the a-wave coupler is assumed to be perfect and the output signal of the stimulus generators is time invariant. C_{2}^{III} considerably lowers the usable dynamic range and accuracy for the transmission measurement, independent from the return loss of the DUT.

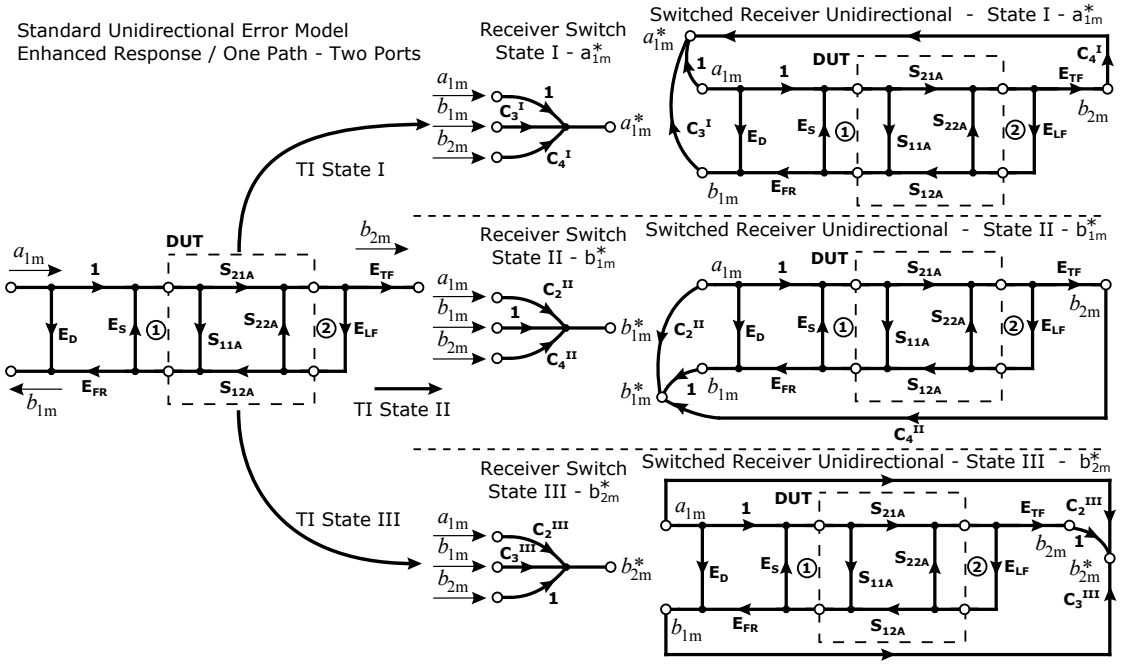

Figure 2.19: Construction of the stateful signal flow graph of the unidirectional switched receiver VNA.

- The DUT return-loss, or S_{11m} based, C_3^{III} cross-talk upon the b_{2m}^* wave measurement, which worsens the signal-to-interference situation for transmission measurements of reflective DUT even more.

In order to analyze the impact and possibility of error models based correction for this cross-talk paths, it is necessary to look back at the implications obtained from the reflectometer analysis first. From Eq. (2.49) we can see, that a DUT transmission dependent cross-talk originating from b_{2m} interferes with the a_{1m}^* measurement. From the previous discussion of the reflectometer it is already known, that cross-talk upon the reference wave will show up as a common error in all measurements taken by the system. Furthermore, it is known, that the cross-talk coefficient C_3^{I} associated with b_{1m} can not be determined in a normal in-situ calibration, as it only occurs in linear combinations in Eq. (2.38). Unfortunately, this also means that there is no simple way to determine the C_4^{I} cross-talk in-situ, because without any prior knowledge about C_3^{I}, it is not possible to differentiate between the different cross-talk paths for port 1.

While it would be possible to use a separate calibrated and phase locked signal source as a stimulus for port 2 while disabling the internal generator at port 1 to determine C_4^{I} from the measurement result, this approach is far from practicable in reality due to the costs and logistics involved in introducing a calibrated signal source. Additionally, this procedure would only work, if $C_4^{\mathrm{I}} \gg C_3^{\mathrm{I}}$ is satisfied and therefore allows the b_{1m} cross-talk to be neglected. While the diagnosis that this error is non-correctable is unsatisfactory,

a topological solution based on the TI state properties of the switched receiver test-set that reduces the effect of this cross-talk path will be presented later on.

In the case of unidirectional VNA measurements, this error is generally acceptable for non-metrological measurements. For moderate switch isolation values $C_4^{\mathrm{I}} \leq -40\,\mathrm{dB}$ and with an attenuator present at the second receive-only port that is matched in its value to the coupling factor of the directional couplers used in the reflectometer, the resulting error will be below the source match threshold. This assumption is especially valid, when the basic measurement uncertainties introduced by the non-correctable $S_{22A} \cdot E_L$ interaction loop and the not fully determined thru standard[21] used for the 5-term calibration procedure in the non-insertable[22] thru case are taken into account ([27]).

In case of the transmission based cross-talk from the b_{2m} wave to the b_{1m}^* measurement, the argument can, for most VNA applications except metrology, be closed in almost the same way. As the most commonly used calibration for the 5-term model is based around the assumed perfect match standard[23], the reflection tracking errors for passive DUTs, introduced by the C_4^{II} cross-talk, are generally below the source match achievable by this calibration method, if the test-set is well-balanced and $C_4^{\mathrm{I}} \leq -40\,\mathrm{dB}$ is assumed.

When an active DUT is measured in this configuration, the cross-talk also becomes negligible, because of the attenuator with an attenuation value corresponding to the expected gain of the DUT that should be inserted between the DUTs output and port 2 of the VNA in the unidirectional topology. This attenuation is absorbed into the transmission tracking term during the calibration measurement of the thru standard. Besides reducing the magnitude of the cross-talk, this procedure is generally considered good practice anyway when measuring active devices, even with standard, non-switched VNAs, as it improves the non-correctable $S_{22A} \cdot E_L$ interaction loop in the 5-term model, protects the vector receiver and test-set from damage due to excessive input power and makes sure that the b_{2m} transmission wave measurement is performed in the linear region of the VNA receiver ([27, 60, 143]).

When the same isolation of 40 dB is assumed for C_2^{III} and C_3^{III}, which are both present in the b_{2m}^* measurement in Eq. (2.51), the resulting achievable usable dynamic range for the transmission measurement $S_{21m}^* = b_{2m}^*/a_{1m}^*$ is quite incapacitating, even for a low-cost VNA that is built down to a price.

Fortunately, both of these factors can easily be determined in-situ during calibration with normal SOLT calibration kit standards and can be corrected during measurement of the actual DUT, as will be shown in the next section.

[21] Thru standards produced for SOLT calibration are generally only specified for their transmission losses and reciprocal electrical length. While E_{LF} is generally determined during 5-term calibration and used for the correction of E_{TF}, this is only accurate for a zero-length flush thru.

[22] Non-insertable in this case means, that both VNA reference plane ports are of the same connector gender, therefore no zero-length or direct connection can be made for the thru measurement.

[23] For calibration purposes the match is assumed to have a broadband input reflection coefficient of $\Gamma_M = 0$ (except sliding loads), however in reality return loss specifications of $\geq 28\,\mathrm{dB}$ from DC to 18 GHz and resistance bounds of $50\,\Omega \pm 0.25\,\Omega$ are common (Rosenberger RPC-N(f) 05K150-010).

2.2.5 (5+2)-Term Calibration and Correction

When taking a closer look at the construction of the stateful signal flow graph of the unidirectional switched receiver VNA shown in Fig. 2.19, it can be seen, that the cross-talk paths C_2^{III} and C_3^{III}, which interfere with the usable dynamic range of the transmission measurement, are located in one single state of the switch, which is only active during S_{21m} measurements and perfectly matches this stateful representation of the system.

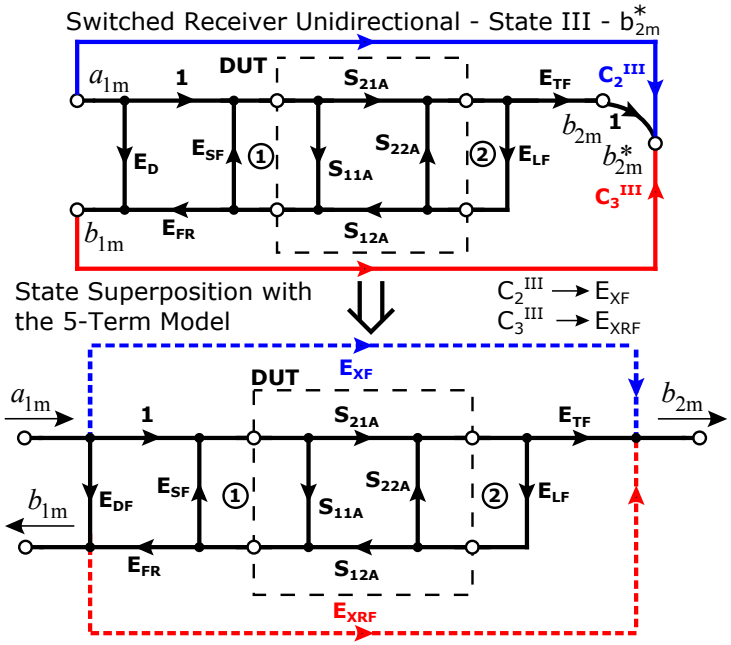

Figure 2.20: Construction of the (5+2)-term error model by superposing state III of the unidirectional switched receiver signal flow graph with the 5-term model.

As an outcome of the switched reflectometer analysis it is known, that the cross-talk path associated with the switched reflectometer can be mostly ignored for all practical intents and purposes. Therefore it is possible use the graph of state III in Fig. 2.19 to construct an accurate extension of the 5-term error correction and calibration model by superposing the original 5-term model with the switch state based signal flow graph. This process is shown visually in Fig. 2.20. In construction of this model, a node reduction is performed with b_{2m}^* becoming the original b_{2m} of the 5-term model and add C_2^{III} and C_3^{III} as additional cross-talk associated paths into the new model.

These new paths directly interfere with the measured b_{2m} result after the modification by the E_{TF} forward transmission tracking term true to the original switch state-based model. These new coefficients are renamed in accordance with the original SOLT coefficient naming style as

- $E_{XF}(C_2^{\mathrm{III}})$, as the (reference) cross-talk, forward, originating from a_{1m}, and
- $E_{XRF}(C_3^{\mathrm{III}})$, as the cross-talk, reflection, forward, originating from b_{1m} - or when

normalized to a_{1m}, which is the case in the $S_{21m} = b_{2m}/a_{1m}$ measurement, becomes referenced to $S_{11m} = b_{1m}/a_{1m}$.

This new error model is tailored to the specific systematic errors present in the unidirectional switched receiver VNA test-set and will be called the *(5+2)-term model* to avoid confusion with the well-established 7-term model that serves a completely different purpose.

In order to characterize these paths and determine appropriate calibration standards, it is helpful to remember the effects of the E_{XF} and E_{XRF} cross-talk: Without any correction, the switched receiver VNA will measure an erroneous S_{21m} transmission, even if a perfectly isolating DUT (or none at all) is inserted at the reference planes of port 1 and 2.

With this in mind it is obvious, that two port isolation standards, i.e. obeying $S_{12A} = S_{21A} \stackrel{!}{=} 0$, are needed to capture E_{XF} and E_{XRF}. With this assumption, a new signal flow graph describing the capture of the error coefficients can be constructed, which is shown in Fig. 2.21.

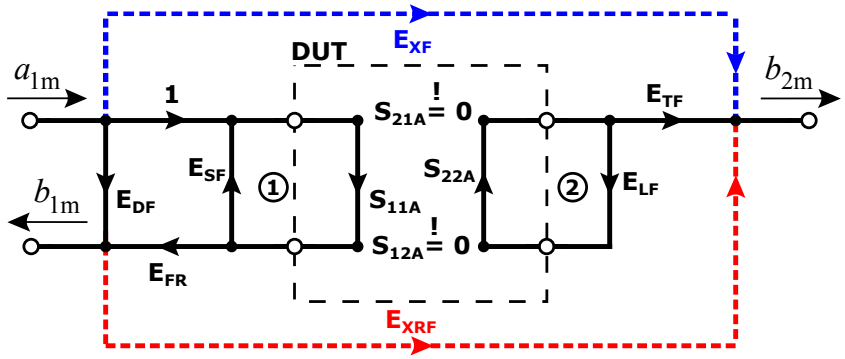

Figure 2.21: Signal flow graph for the (5+2)-term error model in case of a two port isolation standard.

When choosing a suitable two port isolation standard it is important to remember, that a two port isolation standard can be constructed out of two known one-port calibration standards from a standard calibration kit, as only two known input reflection factors $\Gamma_1 = S_{11A}$ and $\Gamma_2 = S_{22A}$ are needed and as long as the standards are assumed to be perfectly isolated and non-radiating [49].

The one-port standards available in a generic SOLT calibration kit are generally one characterized short, one characterized open and one load or match standard that can be used for this purpose. An additional match standard of the same gender is also often found in older calibration kits for performing the so called SOLT isolation measurement.

While the SOLT isolation measurement (in the 6- or 12-term error model) shares some resemblance to the procedure presented here, its error model and algorithms are very different. This correction has fallen out of favor for normal VNAs, as there are almost no use-cases where the inclusion of the isolation term is beneficial for the measurement result [27] and 15-term calibration procedures available on modern four-receiver VNAs

outperform these extend SOLT-procedures in every aspect (see [17, 38, 50, 56, 57, 49, 118] as an overview).

With the contents of the calibration kit and the simplifications chosen to get to the error model in Fig. 2.21, it is necessary to use one match of the calibration kit to terminate the receive-only port 2. While no stimulus is present at this port in the error model in Fig. 2.21, there will be some residual unintended reverse stimulus caused by leakage of the receiver wave selection switch present at this port that must be terminated for accurate measurement results (see schematic of the unidirectional switched receiver VNA in Fig. 2.18).

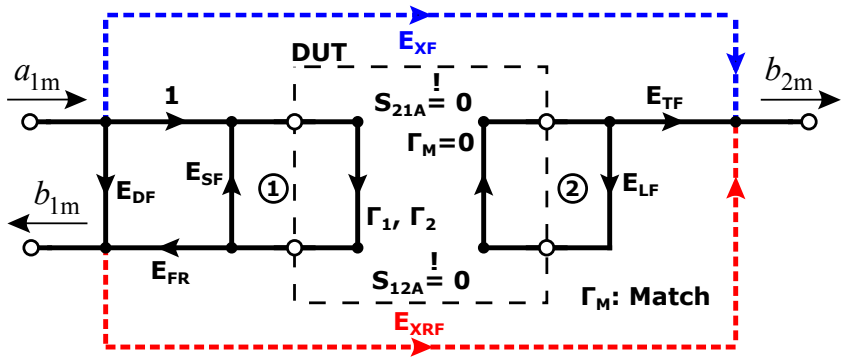

Figure 2.22: Signal flow graph for the measurement of the two-port isolation standards Γ_1/match and Γ_2/match in the (5+2)-term calibration procedure.

With these considerations in mind, it is possible to reformulate the calibration acquisition signal flow graph in Fig. 2.21 to the final version in Fig. 2.22 and obtain

$$S_{21m} = \frac{b_{2m}}{a_{1m}} = E_{XF} + E_{XRF} \cdot (E_{DF} + \frac{\Gamma\, E_{FR}}{1 - \Gamma\, E_{SF}}) \tag{2.52}$$

by signal flow graph analysis as the main equation for the acquisition of the E_{XF} and E_{XRF} coefficients by S_{21m} measurement. As one can see from Eq. (2.52), there is one equation for two unknowns and therefore is the need to construct the linear system

$$S_{21m,\,\Gamma_1} = E_{XF} + E_{XRF} \cdot (E_{DF} + \frac{\Gamma_1\, E_{FR}}{1 - \Gamma_1\, E_{SF}})\text{, and} \tag{2.53}$$

$$S_{21m,\,\Gamma_2} = E_{XF} + E_{XRF} \cdot (E_{DF} + \frac{\Gamma_2\, E_{FR}}{1 - \Gamma_2\, E_{SF}}) \tag{2.54}$$

with two linearly independent known terminations Γ_1 (e.g. the short standard) and Γ_2 (e.g. the open standard) on port 1 to solve for the two unknown switch cross-talk coefficients, yielding the two additional terms in the (5+2)-term error model.

When an independent 3-term calibration of the reflectometer, using Eq. (2.45) and yielding the E_D, E_{FR} and E_S coefficients, is performed beforehand, Eq. (2.53) and (2.54) can be solved for E_{XRF} using the transmission measurements $S_{21m,\,\Gamma_1}$ and $S_{21m,\,\Gamma_2}$ of

the isolation standards (Γ_1 + Match) and (Γ_2 + Match), which results in

$$E_{XRF} = \frac{(S_{21m,\,\Gamma_2} - S_{21m,\,\Gamma_1})(\Gamma_1\, E_{SF} - 1)(\Gamma_2\, E_{SF} - 1)}{(\Gamma_2 - \Gamma_1) \cdot E_{FR}}\,. \tag{2.55}$$

Now either Eq. (2.53) or (2.54) can be solved for the remaining coefficient E_{XF}, as E_{XRF} is known, leading to

$$E_{XF} = S_{21m,\,\Gamma_1} - E_{XRF} \cdot (E_{DF} + \frac{\Gamma_1\, E_{FR}}{1 - \Gamma_1\, E_{SF}})\,, \text{ or} \tag{2.56}$$

$$E_{XF} = S_{21m,\,\Gamma_2} - E_{XRF} \cdot (E_{DF} + \frac{\Gamma_2\, E_{FR}}{1 - \Gamma_2\, E_{SF}})\,. \tag{2.57}$$

If a SOLT calibration kit with an included additional match is available, it is possible to use this second match as one of the linear independent standards with $\Gamma_2 = 0$, resulting in the much more compact form

$$E_{XRF} = -1 \cdot \frac{(S_{21m,\,\mathrm{SM}} - S_{21m,\,\mathrm{MM}})(\Gamma_S\, E_{SF} - 1)}{\Gamma_S\, E_{SF}}\,, \text{ and} \tag{2.58}$$

$$E_{XF} = S_{21m,\,\mathrm{MM}} - E_{DF} \cdot E_{XRF}\,, \tag{2.59}$$

for Eq. (2.55) and Eq. (2.57), with $S_{21m,\,\mathrm{SM}}$ denoting the transmission measurement result of the short-match and $S_{21m,\,\mathrm{MM}}$ as the measurement corresponding match-match calibration measurement, at the cost of a reduced signal-to-noise-ratio (SNR) for the resulting coefficients E_{XF} and E_{XRF} due to lower power injection in the E_{XRF} path in Fig. 2.22.

In case of the two remaining transmission error coefficients, E_{LF} (load match, forward) and E_{TF} (transmission tracking, forward), E_{LF} can be determined equivalent to the classical 5-term error model as

$$E_{LF} = \frac{S_{11m} - E_{DF} - S_{11A} \cdot [(E_{DF} - S_{11m}) \cdot E_{SF} - E_{FR})]}{S_{12A}\, S_{21A} \cdot [(S_{11m} - E_{DF}) \cdot E_{SF} + E_{FR}] + S_{22A} \cdot \nu}\,, \text{ with} \tag{2.60}$$

$$\nu = [S_{11m} - E_{DF} + S_{11A} \cdot (E_{SF} \cdot (E_{DF} - S_{11m}) - E_{FR})]\,,$$

for a fully known thru standard (reflection and transmission) or, as generally the case,

$$E_{LF} = \frac{S_{11m} - E_{DF}}{S_{12A}\, S_{21A} \cdot ((S_{11m} - E_{DF}) \cdot E_{SF} + E_{FR})}\,, \tag{2.61}$$

if only the transmission S-parameters (electrical length and loss) are known. No modification of Eq. (2.60) and (2.61) for the switch cross-talk is necessary, because only a reflectometer measurement into the thru connection is performed.

The calculation of the E_{TF} tracking term must take the E_{XF} and E_{XRF} receiver switch cross-talk into account. This can be accomplished by solving the signal flow graph in Fig. 2.20 for E_{TF}, which results in

$$E_{TF} = \frac{S_{21m} \cdot (E_{LF}\, E_{SF}\, S_{11A}\, S_{22A} - E_{LF}\, S_{22A} - E_{LF}\, E_{SF}\, S_{12A}\, S_{21A} - E_{SF}\, S_{11A} + 1)}{S_{21A} - E_{XF} - S_{11m}\, E_{XRF}}\,, \tag{2.62}$$

for a fully known thru standard, or

$$E_{TF} = \frac{S_{21m} \cdot (1 - E_{LF}\, S_{22A} - E_{LF}\, E_{SF}\, S_{12A}\, S_{21A})}{S_{21A} - E_{XF} - S_{11m}\, E_{XRF}}\,, \tag{2.63}$$

if only the transmission S-parameters of the thru standard are known.

At this point it is important to highlight one fundamental difference between the E_{XF} and E_{XRF} error coefficients: If the port generator output impedance is assumed to be constant for different output power settings, all reflectometer and transmission error coefficients stay constant. Therefore, the calibration obtained with a different output power setting is still valid, because all coefficients are determined via wave relations of the test-set. While this is also true for the E_{XRF} coefficient, as its cross-talk depends on S_{11m} and therefore a relative, absolute power independent, measurement, this property does not apply to E_{XF} coefficient and is therefore stimulus generator output power dependent. E_{XF} can be described as a complex power leakage coefficient.

In order to obtain the error corrected $S_{11,\mathrm{DUT}}$ and $S_{21,\mathrm{DUT}}$ of an unknown DUT, with all error coefficients of the model known, it must be stressed again, that in the unidirectional case E_{LF} is only calculated and used for the correction of the E_{TF} thru calibration measurement. As no information about $S_{22,\mathrm{DUT}}$ can be obtained in a unidirectional system, it must be assumed that the forward load match is perfect, therefore $E_{LF} \stackrel{!}{=} 0$ and especially $S_{22,\mathrm{DUT}} \cdot E_{LF} = 0$, which reduces the equation obtained from signal graph flow analysis of Fig. 2.20 to the normal reflectometer error correction equation

$$S_{11,\mathrm{DUT}} = \frac{S_{11m} - E_{DF}}{E_{FR} + E_{SF} \cdot (S_{11m} - E_{DF})}\,, \tag{2.64}$$

which is consistent with the standard 5-term procedure. While some implementations of the 5-term procedure assume reciprocity and symmetry of the DUT to mitigate this shortcoming, the results are generally worse than just assuming the load match to be perfect [27]. If the same analysis is carried out for $S_{21,\mathrm{DUT}}$ in Fig. 2.20, the result is

$$S_{21,\mathrm{DUT}} = \frac{S_{21m} - E_{XF} - E_{XRF} \cdot S_{11m}}{E_{TF} \cdot (1 + E_{SF} \cdot \frac{S_{11m} - E_{DF}}{E_{FR}})}\,, \tag{2.65}$$

for the error corrected transmission S-parameter of the DUT. This result is consistent with the original 5-term error model with an added cross-talk error correction of the leaky single receiver wave selector switch.

2.2.6 Analysis of the Switched Receiver Bidirectional SOLT VNA

While the modified unidirectional *One Path — Two Port* or *Enhanced Response* (5+2)-term measurement is sufficient for some applications, most passive and low power active devices are nowadays characterized in their full two port parameters. For this measurement the simplest commonly used calibration and correction procedure is the Short-Open-Load-Thru (SOLT) algorithm, which is in essence a two state[24] unidirectional calibration.

[24]The number of TI states is determined by the number of measurement ports. While the original formulation of SOLT only allows for two ports, multi-port extensions of the procedure, such as GSOLT ([51]) exist, with a corresponding higher number of superimposed TI states.

No.	SOLT 5-term	SOLT (5+2)-term V1	SOLT (5+2)-term V2
1	(O) [P1]	(O) [P1]	(O-M) [P1-P2]+(O) MSO [P1]
2	(S) [P1]	(S-M) [P1-P2]+(S) MSO [P1]	(S-M) [P1-P2]+(S) MSO [P1]
3	(M) [P1]	(M-M) [P1-P2]+(M) MSO [P1]	(M) [P1]
4	Thru [P1-P2]	Thru [P1-P2]	Thru [P1-P2]
Total #	5 Con.	7 Connections	7 Connections

Table 2.1: Comparison of calibration standard measurements for SOLT and (5+2)-term, O: Open, S: Short, M: Match, Con.: Total number of required calibration standard connections

These two states are then superimposed to generate the full two port results. A few different two- or multi-port test-set architectures exist that allow for SOLT measurements:

- The three-receiver test-set, consisting of a single stimulus generator source followed by the sole reference wave coupler. After this coupler, a switch which is assumed to be perfectly isolating and highly repeatable, but is allowed to have finite return loss is placed to switch the stimulus to the required test-set port. This stimulus switch is followed by a b_i-wave coupler for each port. This is sometimes called an incomplete reflectometer test-set, but is more commonly referred to as the three-receiver, 10-term SOLT architecture ([27, 49, 143]).

- The four-receiver test-set, which is built around a single stimulus source directly follow by the highly repeatable stimulus switch. Each test-set port contains a complete reflectometer capturing the a_i- and b_i-waves at the test-set ports. The stimulus switch is allowed to be leaky and to show finite return loss, if 7-term calibration methods with switch terms corrections are used ([49, 80, 143]). If this architecture is used in combination with the 10-term model, the switch must be assumed to be perfectly isolating, just as in the original three-receiver architecture.

- The alternate four-receiver test-set, which omits the stimulus switch altogether by employing a dedicated stimulus generator synthesizer for each port of the test-set and hereby increasing the isolation between stimulus directions and switch repeatability issues considerably. Therefore, this is the test-set architecture that most likely achieves the requirement for perfect stimulus isolation in SOLT and is generally treated as a special sub-case of the four-receiver architecture.

While the test-set architecture may not seem to be relevant for the switched receiver at first, it is important to realize that the number of possible cross-talk paths introduced by the leaky receiver wave selector switch is proportional to its number of inputs, therefore the three- and four-receiver test-sets need a slightly different analysis path for the single receiver architecture.

With the results of the previous sections on unidirectional measurements in the switched receiver architecture in mind, the schematic of a switched three-receiver 10-term VNA can directly be constructed by applying the above mentioned general structure, resulting in the schematic shown in Fig. 2.23. With the additional forward and reverse stimulus

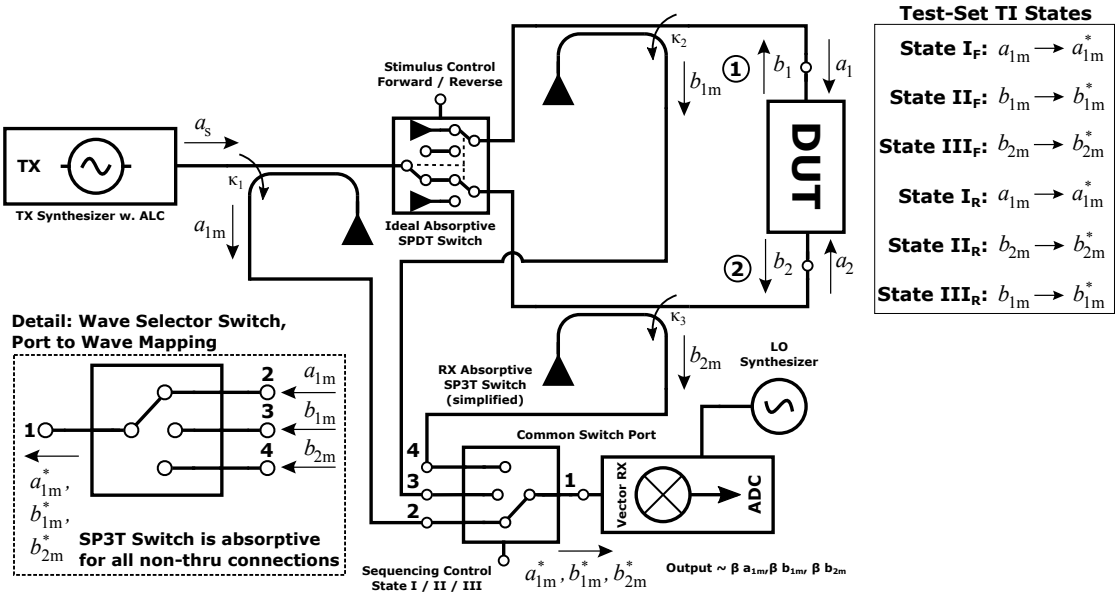

Figure 2.23: Schematic of the 3 virtual receiver, two-port switched receiver VNA, with ideal stimulus reversal switch.

states and the receiver wave to port mapping in mind, the corresponding stateful signal flow chart of the switched three-receiver 10-term VNA can easily be deduced from the original two state 10-term model as shown in Fig. 2.24.

By comparing the signal flow charts of the unidirectional 5-term and the three-receiver 10-term model it can be seen, that the principal description of the receiver wave selector switch cross-talk does not change. The receiver input wave selector switch and its corresponding wave quantities can therefore once again be described by

$$\begin{pmatrix} a^*_{1m} \\ b^{\mathrm{I}}_2 \\ b^{\mathrm{I}}_3 \\ b^{\mathrm{I}}_4 \end{pmatrix} = [S^{\mathrm{I}*}] \begin{pmatrix} a^{\mathrm{I}}_1 \\ a^{\mathrm{I}}_2 \\ a^{\mathrm{I}}_3 \\ a^{\mathrm{I}}_4 \end{pmatrix}, \text{ with } [S^{\mathrm{I}*}] = \begin{bmatrix} 0 & 1 & C^{\mathrm{I}}_3 & C^{\mathrm{I}}_4 \\ 1 & 0 & 0 & 0 \\ C^{\mathrm{I}}_3 & 0 & 0 & 0 \\ C^{\mathrm{I}}_4 & 0 & 0 & 0 \end{bmatrix}, \tag{2.66}$$

$$\begin{pmatrix} b^*_{1m} \\ b^{\mathrm{II}}_2 \\ b^{\mathrm{II}}_3 \\ b^{\mathrm{II}}_4 \end{pmatrix} = [S^{\mathrm{II}*}] \begin{pmatrix} a^{\mathrm{II}}_1 \\ a^{\mathrm{II}}_2 \\ a^{\mathrm{II}}_3 \\ a^{\mathrm{II}}_4 \end{pmatrix}, \text{ with } [S^{\mathrm{II}*}] = \begin{bmatrix} 0 & C^{\mathrm{II}}_2 & 1 & C^{\mathrm{II}}_4 \\ C^{\mathrm{II}}_2 & 0 & 0 & 0 \\ 1 & 0 & 0 & 0 \\ C^{\mathrm{II}}_4 & 0 & 0 & 0 \end{bmatrix}, \tag{2.67}$$

$$\begin{pmatrix} b^*_{2m} \\ b^{\mathrm{III}}_2 \\ b^{\mathrm{III}}_3 \\ b^{\mathrm{III}}_4 \end{pmatrix} = [S^{\mathrm{III}*}] \begin{pmatrix} a^{\mathrm{III}}_1 \\ a^{\mathrm{III}}_2 \\ a^{\mathrm{III}}_3 \\ a^{\mathrm{III}}_4 \end{pmatrix}, \text{ with } [S^{\mathrm{III}*}] = \begin{bmatrix} 0 & C^{\mathrm{III}}_2 & C^{\mathrm{III}}_3 & 1 \\ C^{\mathrm{III}}_2 & 0 & 0 & 0 \\ C^{\mathrm{III}}_3 & 0 & 0 & 0 \\ 1 & 0 & 0 & 0 \end{bmatrix}. \tag{2.68}$$

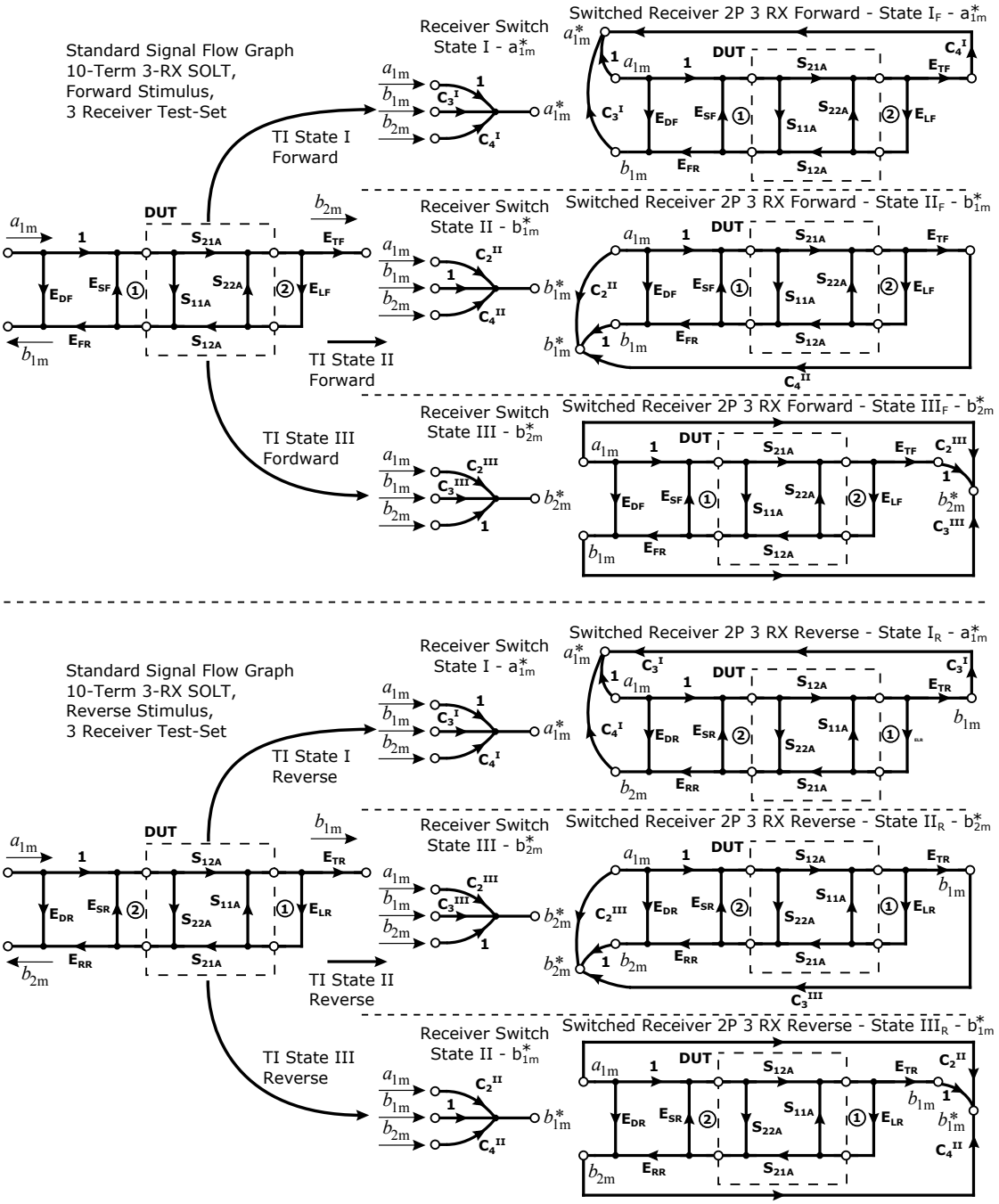

Figure 2.24: Construction of the stateful signal flow graph of the two-port SOLT 10-Term, switched 3 receiver VNA.

The measured switched test-set waves can be extracted analogous to the unidirectional case, but additionally honoring the stimulus state by

$$a^*_{1m,F} = 1 \cdot a_{1m} + C^{\mathrm{I}}_3 \cdot b_{1m} + C^{\mathrm{I}}_4 \cdot b_{2m}\,, \tag{2.69}$$

$$b^*_{1m,F} = C^{\mathrm{II}}_2 \cdot a_{1m} + 1 \cdot b_{1m} + C^{\mathrm{II}}_4 \cdot b_{2m}\,, \tag{2.70}$$

$$b^*_{2m,F} = C^{\mathrm{III}}_2 \cdot a_{1m} + C^{\mathrm{III}}_3 \cdot b_{1m} + 1 \cdot b_{2m}\,, \tag{2.71}$$

$$a^*_{1m,R} = 1 \cdot a_{1m} + C^{\mathrm{I}}_3 \cdot b_{1m} + C^{\mathrm{I}}_4 \cdot b_{2m}\,, \tag{2.72}$$

$$b^*_{1m,R} = C^{\mathrm{II}}_2 \cdot a_{1m} + 1 \cdot b_{1m} + C^{\mathrm{II}}_4 \cdot b_{2m}\,, \text{ and} \tag{2.73}$$

$$b^*_{2m,R} = C^{\mathrm{III}}_2 \cdot a_{1m} + C^{\mathrm{III}}_3 \cdot b_{1m} + 1 \cdot b_{2m}\,, \tag{2.74}$$

and defining the cross-talk influenced S-parameters measured through the leaky receiver wave selector switch as

$$S_{11m} = \frac{b^*_{1m,F}}{a^*_{1m,F}}\,,\; S_{21m} = \frac{b^*_{2m,F}}{a^*_{1m,F}}\,,\; S_{12m} = \frac{b^*_{1m,R}}{a^*_{1m,R}}\,,\; S_{22m} = \frac{b^*_{2m,R}}{a^*_{1m,R}}\,. \tag{2.75}$$

When these results are compared with the analysis of the unidirectional test-set it can be seen, that few has changed in comparison to the unidirectional case and the same considerations and limitations as outlined in the previous section apply.

However, when the cross-talk coefficients are combined with state of the stimulus switch, it is obvious that the b-wave cross-talk associated coefficients in Eq. (2.70), (2.71), (2.73) and (2.74) change their role depending on the stimulus direction. While this may seem like a possibility to determine the otherwise unresolvable reflectometer cross-talk coefficients from the corresponding and determinable transmission cross-talk terms in the other stimulus direction, it is important to realize, that these coefficients are representing the superposition of a multitude of cross-talk paths embedded in the test-set. Therefore, these two cases must be treated separately and the internal reflectometer cross-talk can only be treated via absorption in the normal 3-term model.

When using the SOLT calibration and correction on a switched four-receiver test-set architecture, the situation however changes quite considerably. This is caused by the additional port needed for the receiver wave selector switch due to the additional directional coupler present in the test-set, which can be seen in the corresponding schematic shown in Fig. 2.25. Based on this schematic, the stateful signal flow graph representation of the test-set is modified to incorporate the additional cross-talk path caused by the corresponding unused reference wave, a_{2m} in the forward and a_{1m} in the reverse stimulus direction, and the additional switch state for the second reference coupler measuring a^*_{2m}. This switched four-receiver SOLT signal flow graph is shown in Fig. 2.26.

Similar to the approaches taken before, it is possible to formulate the wave quantities using the cross-talk normalized S-parameters of the switch as

$$\begin{pmatrix} a^*_{1m} \\ b^{\mathrm{I}}_2 \\ b^{\mathrm{I}}_3 \\ b^{\mathrm{I}}_4 \\ b^{\mathrm{I}}_5 \end{pmatrix} = [S^{\mathrm{I}^*}] \begin{pmatrix} a^{\mathrm{I}}_1 \\ a^{\mathrm{I}}_2 \\ a^{\mathrm{I}}_3 \\ a^{\mathrm{I}}_4 \\ a^{\mathrm{I}}_5 \end{pmatrix} \text{ , with } [S^{\mathrm{I}^*}] = \begin{bmatrix} 0 & 1 & C^{\mathrm{I}}_3 & C^{\mathrm{I}}_4 & C^{\mathrm{I}}_5 \\ 1 & 0 & 0 & 0 & 0 \\ C^{\mathrm{I}}_3 & 0 & 0 & 0 & 0 \\ C^{\mathrm{I}}_4 & 0 & 0 & 0 & 0 \\ C^{\mathrm{I}}_5 & 0 & 0 & 0 & 0 \end{bmatrix}, \tag{2.76}$$

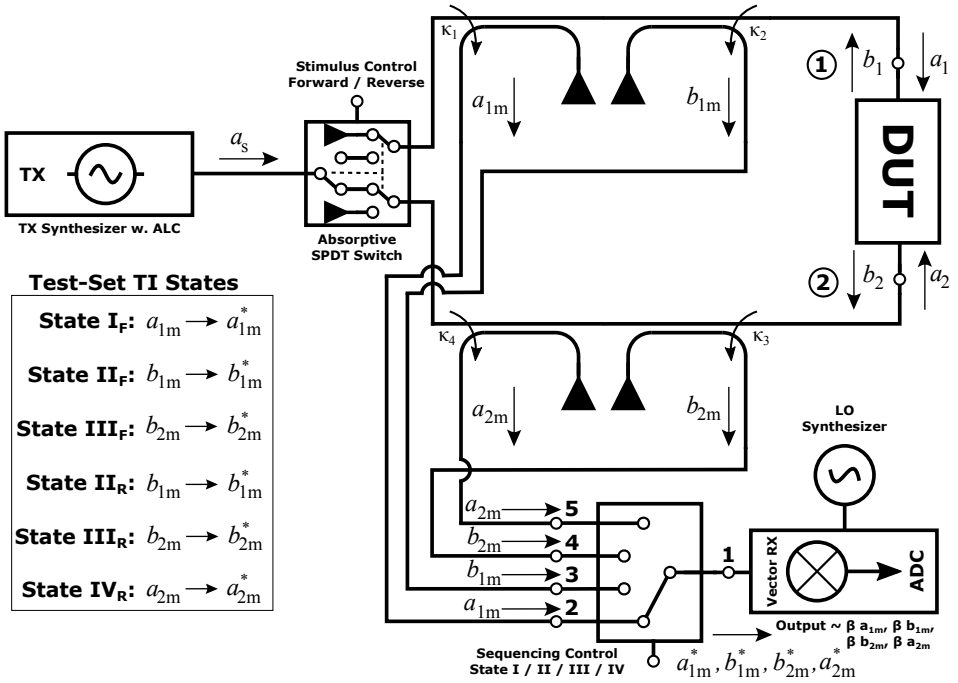

Figure 2.25: Schematic of the 4 virtual receiver, two-port switched receiver VNA, with ideal stimulus reversal switch and SOLT states.

$$\begin{pmatrix} b_{1m}^{*} \\ b_2^{\mathrm{II}} \\ b_3^{\mathrm{II}} \\ b_4^{\mathrm{II}} \\ b_5^{\mathrm{II}} \end{pmatrix} = [S^{\mathrm{II}*}] \begin{pmatrix} a_1^{\mathrm{II}} \\ a_2^{\mathrm{II}} \\ a_3^{\mathrm{II}} \\ a_4^{\mathrm{II}} \\ a_5^{\mathrm{II}} \end{pmatrix} \text{ , with } [S^{\mathrm{II}*}] = \begin{bmatrix} 0 & C_2^{\mathrm{II}} & 1 & C_4^{\mathrm{II}} & C_5^{\mathrm{II}} \\ C_2^{\mathrm{II}} & 0 & 0 & 0 & 0 \\ 1 & 0 & 0 & 0 & 0 \\ C_4^{\mathrm{II}} & 0 & 0 & 0 & 0 \\ C_5^{\mathrm{II}} & 0 & 0 & 0 & 0 \end{bmatrix}, \tag{2.77}$$

$$\begin{pmatrix} b_{2m}^{*} \\ b_2^{\mathrm{III}} \\ b_3^{\mathrm{III}} \\ b_4^{\mathrm{III}} \\ b_5^{\mathrm{III}} \end{pmatrix} = [S^{\mathrm{III}*}] \begin{pmatrix} a_1^{\mathrm{III}} \\ a_2^{\mathrm{III}} \\ a_3^{\mathrm{III}} \\ a_4^{\mathrm{III}} \\ a_5^{\mathrm{III}} \end{pmatrix} \text{ , with } [S^{\mathrm{III}*}] = \begin{bmatrix} 0 & C_2^{\mathrm{III}} & C_3^{\mathrm{III}} & 1 & C_5^{\mathrm{III}} \\ C_2^{\mathrm{III}} & 0 & 0 & 0 & 0 \\ C_3^{\mathrm{III}} & 0 & 0 & 0 & 0 \\ 1 & 0 & 0 & 0 & 0 \\ C_5^{\mathrm{III}} & 0 & 0 & 0 & 0 \end{bmatrix}, \tag{2.78}$$

$$\begin{pmatrix} a_{2m}^{*} \\ b_2^{\mathrm{IV}} \\ b_3^{\mathrm{IV}} \\ b_4^{\mathrm{IV}} \\ b_5^{\mathrm{IV}} \end{pmatrix} = [S^{\mathrm{IV}*}] \begin{pmatrix} a_1^{\mathrm{IV}} \\ a_2^{\mathrm{IV}} \\ a_3^{\mathrm{IV}} \\ a_4^{\mathrm{IV}} \\ a_5^{\mathrm{IV}} \end{pmatrix} \text{ , with } [S^{\mathrm{IV}*}] = \begin{bmatrix} 0 & C_2^{\mathrm{IV}} & C_3^{\mathrm{IV}} & C_4^{\mathrm{IV}} & 1 \\ C_2^{\mathrm{IV}} & 0 & 0 & 0 & 0 \\ C_3^{\mathrm{IV}} & 0 & 0 & 0 & 0 \\ C_4^{\mathrm{IV}} & 0 & 0 & 0 & 0 \\ 1 & 0 & 0 & 0 & 0 \end{bmatrix}, \tag{2.79}$$

for the four discrete TI states of the 5 port, SP4T, receiver wave selector switch, which

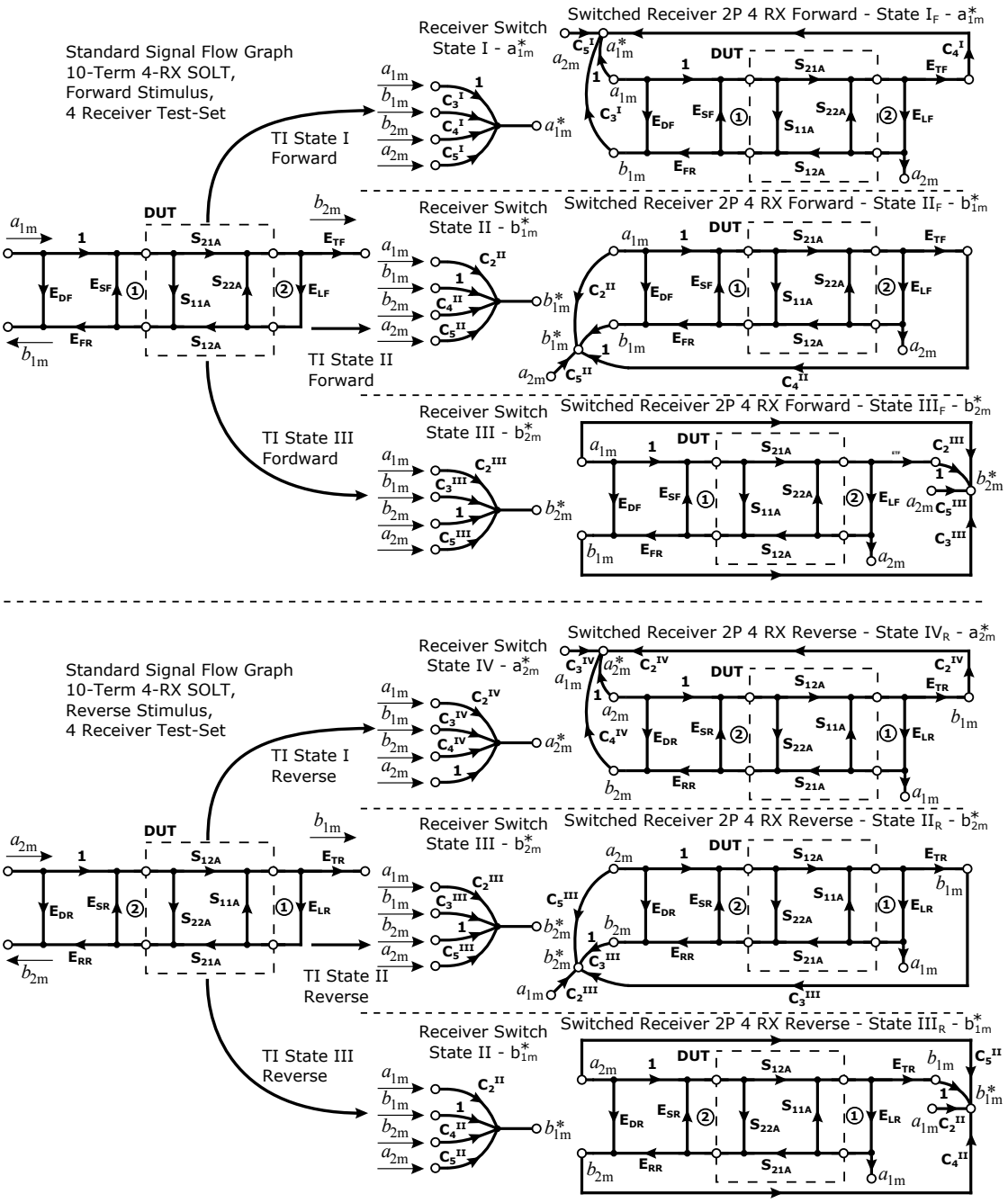

Figure 2.26: Construction of the stateful signal flow graph of the two-port SOLT 10-Term, switched four-receiver VNA.

results in the cross-talk normalized expressions

$$a^*_{1m,F} = 1 \cdot a_{1m} + C^{\mathrm{I}}_3 \cdot b_{1m} + C^{\mathrm{I}}_4 \cdot b_{2m} + C^{\mathrm{I}}_5 \cdot a_{2m}\,, \tag{2.80}$$

$$b^*_{1m,F} = C^{\mathrm{II}}_2 \cdot a_{1m} + 1 \cdot b_{1m} + C^{\mathrm{II}}_4 \cdot b_{2m} + C^{\mathrm{II}}_5 \cdot a_{2m}\,, \tag{2.81}$$

$$b^*_{2m,F} = C^{\mathrm{III}}_2 \cdot a_{1m} + C^{\mathrm{III}}_3 \cdot b_{1m} + 1 \cdot b_{2m} + C^{\mathrm{II}}_5 \cdot a_{2m}\,, \tag{2.82}$$

$$a^*_{2m,R} = C^{\mathrm{IV}}_2 \cdot a_{1m} + C^{\mathrm{IV}}_3 \cdot b_{1m} + C^{\mathrm{IV}}_4 \cdot b_{2m} + 1 \cdot a_{2m}\,, \tag{2.83}$$

$$b^*_{1m,R} = C^{\mathrm{II}}_2 \cdot a_{1m} + 1 \cdot b_{1m} + C^{\mathrm{II}}_4 \cdot b_{2m} + C^{\mathrm{II}}_5 \cdot a_{2m}\,, \text{ and} \tag{2.84}$$

$$b^*_{2m,R} = C^{\mathrm{III}}_2 \cdot a_{1m} + C^{\mathrm{III}}_3 \cdot b_{1m} + 1 \cdot b_{2m} + C^{\mathrm{III}}_5 \cdot a_{2m}\,, \tag{2.85}$$

for the measured test-set waves seen by the sole VNA vector receiver through the leaky wave selector switch, which allows to formulate the definition of the measured S-parameters as

$$S_{11m} = \frac{b^*_{1m,F}}{a^*_{1m,F}}\,,\; S_{21m} = \frac{b^*_{2m,F}}{a^*_{1m,F}}\,,\; S_{12m} = \frac{b^*_{1m,R}}{a^*_{2m,R}}\,,\; S_{22m} = \frac{b^*_{2m,R}}{a^*_{2m,R}}\,. \tag{2.86}$$

Compared to the switched three-receiver 10-term realization, it is obvious that the additional fourth switched receiver input channel generates new cross-talk paths for each wave measurement. This cross-talk, originating from a_{2m} in the forward and a_{1m} in the reverse stimulus direction state, is not captured in the direct application of the 10-term model to this approach, as these waves are usually not measured and omitted in the corresponding state of the error model.

If these cross-talk paths are analyzed further, it can be deduced from Fig. 2.25 and Fig. 2.26, that these paths are fed via the $S_{21A} \cdot E_{LF}$ and $S_{12A} \cdot E_{LR}$ routes thru the signal flow graph. In order to simplify the discussion, it is valid to assume that all test-set internal coaxial cables are well-matched and therefore the E_{LF} and E_{LR} coefficients are mainly based upon the return loss of the stimulus selector switch termination in its absorbing state.

This internal $50\,\Omega$ termination Γ_{SW} is usually of sufficiently high return loss, so it is possible to omit this additional interference caused by this path when compared to the other cross-talk coefficients. This is true except for high gain active DUTs with $|S_{21A}| \vee |S_{12A}| \gtrapprox \Gamma_{SW}$ measured in a low power stimulus region, which are usually better characterized in the forward, or gain direction, by a 5-term test-set anyway ([27]).

Nevertheless, the return-loss of the stimulus selector switch termination and the coaxial interconnects represent an important optimization and design consideration point when designing a switched receiver test-set with four receivers in mind, which is somewhat contrary to the normal 10-term viewpoint on this switch. However, an improved Γ_{SW} can usually be achieved easily by adding well-matched attenuators in series with one or more stimulus switch outputs, albeit at the cost of total stimulus power at the DUT reference plane for the corresponding port.

Therefore, the situation in the 10-term model is fairly similar to the 5-term case with an additional state for the mirrored stimulus direction added. The main cross-talk paths of practical concern are still caused by the quasi-static reference cross-talk C^{III}_2 in the

forward and C_5^{II} in the reverse stimulus state and the $S_{11m} \cdot C_3^{\mathrm{III}}$ dependent forward stimulus and $S_{22m} \cdot C_4^{\mathrm{II}}$ dependent backward stimulus path for the transmission wave receivers. This directly results in four additional coefficients that need to be determined during calibration.

2.2.7 (10+4)-Term Calibration and Correction

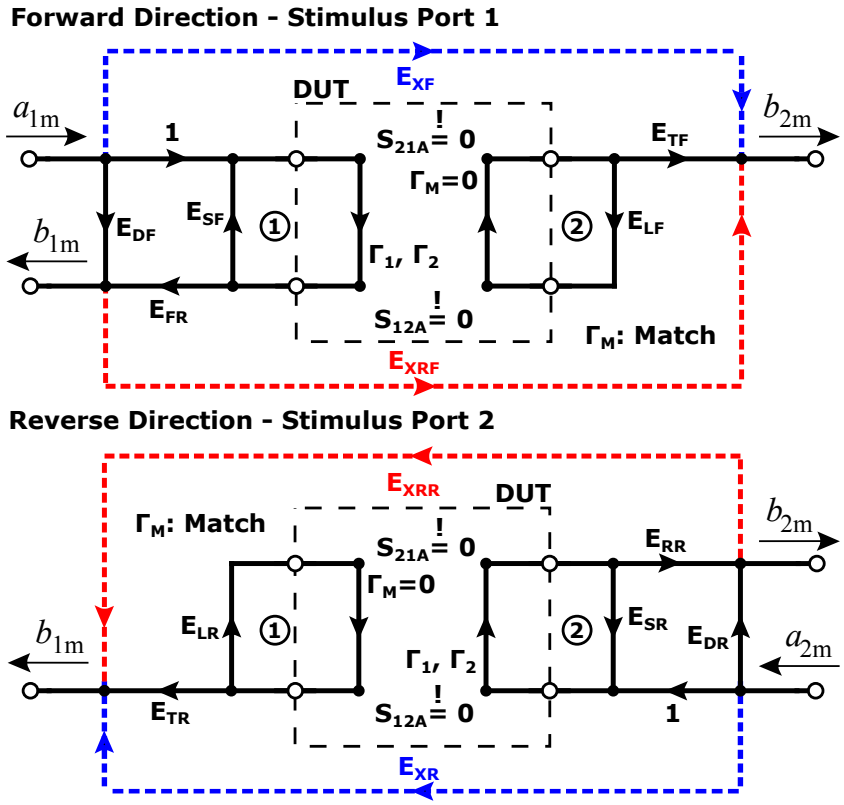

Figure 2.27: Bidirectional signal flow graph for the measurement of the two-port isolation standards Γ_1/match and Γ_2/match in the (10+4)-term calibration procedure.

In the previous section on the analysis of the combination of the single switched receiver with the 10-term model it was determined, that the results of the 5-term analysis and therefore the (5+2)-term calibration and correction method can be re-used to improve upon the measurement capabilities of the switched receiver 10-term architecture. Therefore, it is immediately obvious that the same calibration standards and procedures used for the unidirectional (5+2)-term calibration can also be applied here in the bidirectional case with an added state for reverse stimulus.

In addition to the two forward cross-talk coefficients E_{XF} and E_{XRF}, two corresponding new reverse stimulus representations of the cross-talk, which will be called E_{XR} (cross-talk, reverse) and E_{XRR} (cross-talk, reflection, reverse) in accordance with the common SOLT naming nomenclature, must be added to the model. Furthermore, the fact that

both states of the 10-term model consist of two superimposed 5-term models, one for each stimulus direction, can be directly used to create the (10+4)-term bidirectional version shown in Fig. 2.27 from the (5+2)-term signal flow graph for cross-talk calibration presented in Fig. 2.22.

In accordance with the (5+2)-term error model, it can be directly deduced that

$$S_{21m} = \frac{b_{2m}}{a_{1m}} = E_{XF} + E_{XRF} \cdot (E_{DF} + \frac{\Gamma\, E_{FR}}{1 - \Gamma\, E_{SF}}) \text{, and} \tag{2.87}$$

$$S_{12m} = \frac{b_{2m}}{a_{1m}} = E_{XR} + E_{XRR} \cdot (E_{DR} + \frac{\Gamma\, E_{RR}}{1 - \Gamma\, E_{SR}}) \text{,} \tag{2.88}$$

as the expression for the measured transmissions of the isolation standards during calibration. Since both (5+2)-term halves of the (10+4)-term model are independent of each other, it is necessary to formulate two linear systems consisting of two measurements each to solve for the cross-talk coefficients. Also, it is known from the derivation of (5+2)-term error model that the non driven port, which is port 2 in the forward and port 1 in the backward stimulus direction, needs to be terminated with a match standard and two additional known reflection standards must be connected to each of the driven ports, resulting in four measurements in total.

In the general case, with two fully known reflection standards Γ_1 and Γ_2, analysis shows that

$$E_{XRF} = \frac{(S_{21m,\,\Gamma_2} - S_{21m,\,\Gamma_1})(\Gamma_1\, E_{SF} - 1)(\Gamma_2\, E_{SF} - 1)}{(\Gamma_2 - \Gamma_1) \cdot E_{FR}} \tag{2.89}$$

$$E_{XF} = S_{21m,\,\Gamma_1} - E_{XRF} \cdot (E_{DF} + \frac{\Gamma_1\, E_{FR}}{1 - \Gamma_1\, E_{SF}}) \text{, or} \tag{2.90}$$

$$E_{XF} = S_{21m,\,\Gamma_2} - E_{XRF} \cdot (E_{DF} + \frac{\Gamma_2\, E_{FR}}{1 - \Gamma_2\, E_{SF}}) \text{,} \tag{2.91}$$

for the forward direction, which is identical to the (5+2)-term model. When the reverse stimulus direction is analyzed in the same manner, the expressions

$$E_{XRR} = \frac{(S_{12m,\,\Gamma_2} - S_{12m,\,\Gamma_1})(\Gamma_1\, E_{SR} - 1)(\Gamma_2\, E_{SR} - 1)}{(\Gamma_2 - \Gamma_1) \cdot E_{RR}} \tag{2.92}$$

$$E_{XR} = S_{12m,\,\Gamma_1} - E_{XRR} \cdot (E_{DR} + \frac{\Gamma_1\, E_{RR}}{1 - \Gamma_1\, E_{SR}}) \text{, or} \tag{2.93}$$

$$E_{XR} = S_{12m,\,\Gamma_2} - E_{XRR} \cdot (E_{DR} + \frac{\Gamma_2\, E_{RR}}{1 - \Gamma_2\, E_{SR}}) \text{,} \tag{2.94}$$

are found for the two additional reverse stimulus coefficients.

The E_{DF}, E_{FR} and E_{SF} reflectometer coefficients are determined via an independent 3-term MSO calibration of port 1, while the E_{DR}, E_{RR} and E_{SR} reflectometer coefficients are determined by an independent 3-term MSO calibration of port 2.

Analogous to the (5+2)-term calibration procedure it is also possible to choose $\Gamma_2 = 0$ if a second match standard is available in the calibration kit, which simplifies Eq. (2.89)

to (2.94) to the much more compact form

$$E_{XRF} = -1 \cdot \frac{(S_{21m,\,\mathrm{SM}} - S_{21m,\,\mathrm{MM}})(\Gamma_S\, E_{SF} - 1)}{\Gamma_S\, E_{SF}}\,, \tag{2.95}$$

$$E_{XRR} = -1 \cdot \frac{(S_{12m,\,\mathrm{MS}} - S_{12m,\,\mathrm{MM}})(\Gamma_S\, E_{SR} - 1)}{\Gamma_S\, E_{SR}}\,, \tag{2.96}$$

$$E_{XF} = S_{21m,\,\mathrm{MM}} - E_{DF} \cdot E_{XRF}\,, \tag{2.97}$$

$$E_{XR} = S_{12m,\,\mathrm{MM}} - E_{DR} \cdot E_{XRR}\,, \tag{2.98}$$

if the known short standard of the kit is used for Γ_1, with $S_{ijm,\,\mathrm{SM}}$ denoting the transmission measurement results of the short-match and $S_{ijm,\,\mathrm{MM}}$ for the match-match calibration standard measurements. Again, the same reduction in data quality, as mentioned in the (5+2)-term error model derivation, still applies for the (10+4)-term model when using the match-match standard due to the SNR reduction in the E_{XRF} and E_{XRR} paths. Nevertheless, due to the match-match isolation standard being symmetric, fewer connections when compared to the general case must be made for calibration, which can be of importance in some applications.

The remaining transmission tracking coefficients E_{TF} and E_{TR}, as well as the load match coefficients E_{LF} and E_{LR}, can be determined in the same manner as presented in the (5+2)-term procedure. The load match coefficients can be obtained by

$$E_{LF} = \frac{S_{11m} - E_{DF} - S_{11A} \cdot [(E_{DF} - S_{11m}) \cdot E_{SF} - E_{FR})]}{S_{12A}\, S_{21A} \cdot [(S_{11m} - E_{DF}) \cdot E_{SF} + E_{FR}] + S_{22A} \cdot \nu_F}\,, \text{ with} \tag{2.99}$$

$$\nu_F = [S_{11m} - E_{DF} + S_{11A} \cdot (E_{SF} \cdot (E_{DF} - S_{11m}) - E_{FR})]\,, \text{ and}$$

$$E_{LR} = \frac{S_{22m} - E_{DR} - S_{22A} \cdot [(E_{DR} - S_{22m}) \cdot E_{SR} - E_{RR})]}{S_{12A}\, S_{21A} \cdot [(S_{22m} - E_{DR}) \cdot E_{SR} + E_{RR}] + S_{11A} \cdot \nu_R}\,, \text{ with} \tag{2.100}$$

$$\nu_R = [S_{22m} - E_{DR} + S_{22A} \cdot (E_{SR} \cdot (E_{DR} - S_{22m}) - E_{RR})]\,.$$

for a fully known thru standard (reflection and transmission) or, as generally the case,

$$E_{LF} = \frac{S_{11m} - E_{DF}}{S_{12A}\, S_{21A} \cdot ((S_{11m} - E_{DF}) \cdot E_{SF} + E_{FR})}\,, \text{ and} \tag{2.101}$$

$$E_{LR} = \frac{S_{22m} - E_{DR}}{S_{12A}\, S_{21A} \cdot ((S_{22m} - E_{DR}) \cdot E_{SR} + E_{RR})}\,, \tag{2.102}$$

for a thru were only the transmission parameters are defined in terms of electrical length and loss. Finally, both transmission tracking parameters E_{TF} and E_{TR} can be determined by

$$E_{TF} = \frac{S_{21m} \cdot (E_{LF}\, E_{SF}\, S_{11A}\, S_{22A} - E_{LF}\, S_{22A} - E_{LF}\, E_{SF}\, S_{12A}\, S_{21A} - E_{SF}\, S_{11A} + 1)}{S_{21A} - E_{XF} - S_{11m}\, E_{XRF}}\,, \tag{2.103}$$

$$E_{TR} = \frac{S_{12m} \cdot (E_{LR}\, E_{SR}\, S_{11A}\, S_{22A} - E_{LR}\, S_{11A} - E_{LR}\, E_{SR}\, S_{12A}\, S_{21A} - E_{SR}\, S_{22A} + 1)}{S_{12A} - E_{XR} - S_{22m}\, E_{XRR}}\,, \tag{2.104}$$

for a fully known thru standard, or

$$E_{TF} = \frac{S_{21m} \cdot (1 - E_{LF}\, S_{22A} - E_{LF}\, E_{SF}\, S_{12A}\, S_{21A})}{S_{21A} - E_{XF} - S_{11m}\, E_{XRF}}\,, \text{ and} \tag{2.105}$$

$$E_{TR} = \frac{S_{12m} \cdot (1 - E_{LR}\, S_{11A} - E_{LR}\, E_{SR}\, S_{12A}\, S_{21A})}{S_{12A} - E_{XR} - S_{22m}\, E_{XRR}}\,, \tag{2.106}$$

for a thru, were only the transmission properties S_{21A} and S_{12A} are defined.

To obtain the corrected full two-port S-parameters from a DUT measurement, it is useful for reasons of clarity to use the normalized form of the basic 10-term SOLT correction algorithm, as presented in [27] and the introduction 2.1 of this chapter.

In this form the correction process is divided into two distinct steps which helps to de-clutter the fairly long closed form solution of the SOLT signal flow graph. First any leakage associated with the measured parameter is subtracted from the raw measurement. This especially includes the E_{XF} and E_{XR} reference cross-talk and the E_{XRF} and E_{XRR} reflection tracking cross-talk paths in the (10+4)-term error model. The results are then normalized to the corresponding reflection or transmission tracking coefficient, which results in the normalized S-parameter expressions

$$S_{11N} = \frac{S_{11m} - E_{DF}}{E_{FR}}\,, \qquad S_{22N} = \frac{S_{22m} - E_{DR}}{E_{RR}}\,, \tag{2.107}$$
$$S_{21N} = \frac{S_{21m} - E_{XF} - E_{XRF} \cdot S_{11m}}{E_{TF}}\,, \qquad S_{12N} = \frac{S_{12m} - E_{XR} - E_{XRR} \cdot S_{22m}}{E_{TR}}\,,$$

for the (10+4)-term procedure. The normalized and leakage corrected normalized S-parameters are then corrected for the various mismatch loops present in the signal flow graph, which results in the final error corrected S-parameters of the DUT

$$S_{11,\mathrm{DUT}} = \frac{S_{11N} \cdot (1 + S_{22N}\, E_{SR}) - E_{LF}\, S_{21N}\, S_{12N}}{(1 + S_{11N}\, E_{SF})(1 + S_{22N}\, E_{SR}) - E_{LF}\, E_{LR}\, S_{21N}\, S_{12N}}\,, \tag{2.108}$$

$$S_{22,\mathrm{DUT}} = \frac{S_{22N} \cdot (1 + S_{11N}\, E_{SF}) - E_{LR}\, S_{21N}\, S_{12N}}{(1 + S_{11N}\, E_{SF})(1 + S_{22N}\, E_{SR}) - E_{LF}\, E_{LR}\, S_{21N}\, S_{12N}}\,, \tag{2.109}$$

$$S_{21,\mathrm{DUT}} = \frac{S_{21N} \cdot [1 + S_{22N} \cdot (E_{SR} - E_{LF})]}{(1 + S_{11N}\, E_{SF})(1 + S_{22N}\, E_{SR}) - E_{LF}\, E_{LR}\, S_{21N}\, S_{12N}}\,, \tag{2.110}$$

$$S_{12,\mathrm{DUT}} = \frac{S_{12N} \cdot [1 + S_{11N} \cdot (E_{SF} - E_{LR})]}{(1 + S_{11N}\, E_{SF})(1 + S_{22N}\, E_{SR}) - E_{LF}\, E_{LR}\, S_{21N}\, S_{12N}}\,. \tag{2.111}$$

A comparison in the required number of calibration connections and standards between the established 10-term SOLT calibration and both variants of the (10+4)-term procedure presented here is shown in Table 2.2.

No.	SOLT 10-term	SOLT (10+4)-term V1	SOLT (10+4)-term V2
1	(O) [P1]	(O) [P1]	(O-M) [P1-P2]+(O) MSO [P1]
2	(S) [P1]	(S-M) [P1-P2]+(S) MSO [P1]	(S-M) [P1-P2]+(S) MSO [P1]
3	(M) [P1]	(M-M) [P1-P2]+(M) MSO [P1],[P2]	(M) [P1]
4	(O) [P2]	(O) [P2]	(M-O) [P1-P2]+(O) MSO [P2]
5	(S) [P2]	(M-S) [P1-P2]+(S) MSO [P2]	(M-S) [P1-P2]+(S) MSO [P2]
6	(M) [P2]	N/A	(M) [P2]
7	Thru [P1-P2]	Thru [P1-P2]	Thru [P1-P2]
Total #	8 Con.	10 Connections	12 Connections

Table 2.2: Comparison of calibration standard measurements for SOLT and (10+4)-term, O: Open, S: Short, M: Match, Con.: Total number of required calibration standard connections.

2.2.8 Analysis of the Switched Receiver 7-Term Four-Receiver VNA using the Unknown Thru Procedure

The SOLT calibration has proven its value over the years, however it is not without drawbacks. Generally speaking, there are many accepted limitations of the procedure due to its requirement to either use a flush thru or a known thru standard for transmission calibration:

- In a measurement setup where cable phase stability over movement is of concern, the known thru standard has to be of approximately the same length as the connector distance of the DUT, which is usually not feasible,
- For connectors on a DUT which are not positioned in a straight line, e.g. on a 90° offset, no calibrated off the shelf thru standards of the same shape are generally available,
- DUT measurements on ports with different connector types or genders are similarly problematic, requiring a defined thru with the same connectors, and
- Some SOLT implementations or the calibration standards themselves do not take the loss of the thru connection into account, which results in a minor but noticeable offset in the corrected data, especially at higher microwave frequencies.

Due to these inherent limitations of SOLT, the 'unknown-thru' or 'unknown-open-short-match' (UOSM) calibration method, originally presented in [31] with further error and uncertainty analysis shown in [154], is nowadays the quasi-standard for two-port calibrations on modern four-receiver VNAs. Contrary to SOLT, the UOSM procedure only requires a thru standard with reciprocal physical transmission behavior ($S_{21,\mathrm{Thru}} = S_{12,\mathrm{Thru}}$), an approximate knowledge of the thru's electrical length to about $\pm 90°$ and sufficiently low insertion loss to obtain a good SNR. The UOSM signal flow graph and 7-term error-box network definition used from here on is shown in Fig. 2.28.

The so called 'switch-terms correction', presented in [49] and [80] in different implementations, is generally used as a stateful extension to the bare 7-term LTI model

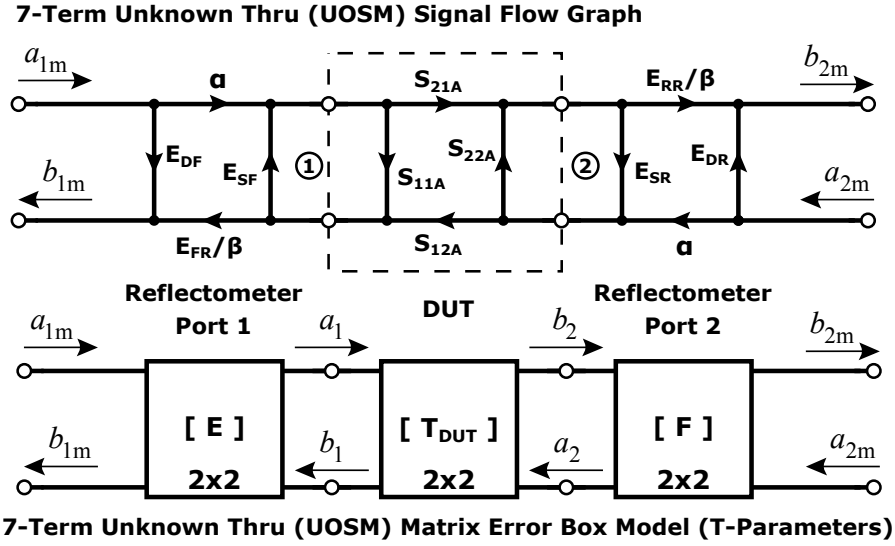

Figure 2.28: Signal flow graph and error-box network model of the 7-term 'unknown-thru' (UOSM) procedure with the nomenclature used in this work.

underlying the UOSM procedure. This additional raw error correction is applied to the measured S-parameters that are used for calibration and correction in the UOSM to improve calibration accuracy. This switch-term extension captures the effect, that the impedance of a given VNA port is not time invariant due to its changing role: If the stimulus selector switch is used to direct the generator synthesizer to a VNA port it will present a different input reflection coefficient to the calibration reference plane than in its absorbing state when the stimulus direction is reversed. This time variance of the test-set is not present in the bare 7-term model and needs to be accounted for.

The switch-terms are generally considered very stable and must only be measured once for a given calibration setup ([27, 49, 80, 143]), although a per measurement correction can also be used at the cost of increased measurement time.

Although three-receiver VNA architectures generally do not directly support 7-term methods, a workaround ([68, 138]) exists to use UOSM (or most other 7-term calibration procedures such as the various Txx and Lxx self calibration procedures [30, 49], et al.) on these architectures. This procedure is necessary, because the reference coupler is located behind the stimulus switch when seen from the DUT reference plane and therefore topologically does not allow for the necessary direct wave measurements to take place. Fortunately, the acquisition of the switch-terms can alternatively be accomplished by a so called *two-tier calibration* ([68]), which first uses a full SOLT calibration to determine the full 10-term model to obtain the time-invariant switch-terms ([27, 68]). This is then followed by a modified 7-term calibration routine that only uses three instead of four receivers that are augmented by the first tier switch-terms for calibration and correction on the originally non-compliant architecture. Nevertheless, the aforementioned limitations of SOLT still apply, if only for the determination of switch-terms themselves. Due to its

reliance upon SOLT, this procedure is especially challenging for non-coaxial calibration standards and DUTs, since SOLT calibration standards are either not available or do not produce suitable and accurate calibration results.

The UOSM calibration method is also later used as the reference for comparing the numerical simulation and measurement results of a reference four-receiver system with the results obtained with the various switched receiver VNA calibration and error correction methods presented in chapters 2.4.5, 2.4.6, 2.5.5 and 2.5.6 in this work and therefore a complete derivation is given here. This will be followed by an analysis of UOSM for the switched receiver VNA in a four-receiver test-set configuration as shown in Fig. 2.25.

Like the SOLT algorithm, the UOSM procedure is initially based on the individual 3-term MSO calibration of the two individual reflectometers representing the test-set interface, yielding the coefficient matrices $[E]$ for the first and $[F]$ for the second port (for reference see Fig. 2.28).

As the 7-term calibration algorithms are generally using linear matrix algebra for closed form solutions, it is at first necessary to define the raw two port S-parameter measurement data matrix $[S_m]$, using the relations of the raw measurement waves a_i and b_i in the forward and reverse stimulus direction, as

$$[S_m] = \begin{bmatrix} S_{11m} & S_{12m} \\ S_{21m} & S_{22m} \end{bmatrix} = \begin{bmatrix} \frac{b_{1m,F}}{a_{1m,F}} & \frac{b_{1m,R}}{a_{2m,R}} \\ \frac{b_{2m,F}}{a_{1m,F}} & \frac{b_{2m,R}}{a_{2m,R}} \end{bmatrix} . \tag{2.112}$$

In order to apply the switch-term correction ([80, 154]) on a four-receiver VNA, it is necessary to define the switch-term correction matrix $[C_{sw}]$, which contains the raw a-wave reference receiver measurement results of an unspecified, low insertion loss, and reciprocal, thru connection to determine the switch-induced impedance changes of the ports as

$$[C_{sw}] = \begin{bmatrix} 1 & \frac{a_{1m,R}}{a_{2m,R}}\big|_{\text{Thru}} \\ \frac{a_{2m,F}}{a_{1m,F}}\big|_{\text{Thru}} & 1 \end{bmatrix} . \tag{2.113}$$

When the switch-term correction matrix $[C_{sw}]$ is known, the corrected S-parameters measurement values $[S_{mc}]$ can then be calculated by simply evaluating

$$[S_{mc}] = [S_m] \cdot [C_{sw}]^{-1} . \tag{2.114}$$

With the prerequisites for general 7-term procedures determined, the $[E]$ and $[F]$ S-parameter matrices must be re-arranged to

$$[E] = \begin{bmatrix} E_{DF} & E_{FR}/\beta \\ 1 \cdot \alpha & E_{SF} \end{bmatrix} , [F] = \begin{bmatrix} E_{SR} & 1 \cdot \alpha \\ E_{RR}/\beta & E_{DR} \end{bmatrix} , \tag{2.115}$$

to comply with the signal flow chart and the T-parameter matrices convention of Fig. 2.28, and the error-box network model. An additional degree of freedom is added to the tracking parameter coefficients in the form of the β and α factors to account for the modification of the 3-term parameters by the transmission tracking calibration later on.

Since S-parameters can not be directly concatenated, all S-parameter error-boxes must be transformed into their corresponding T-parameter representation. This is performed, exemplary for the DUT, by

$$[T_{\mathrm{DUT}}] = \begin{bmatrix} \frac{-\Delta S}{S_{21,\mathrm{DUT}}} & \frac{S_{11,\mathrm{DUT}}}{S_{21,\mathrm{DUT}}} \\ \frac{-S_{22,\mathrm{DUT}}}{S_{21,\mathrm{DUT}}} & \frac{1}{S_{21,\mathrm{DUT}}} \end{bmatrix}, \; \Delta S = S_{11,\mathrm{DUT}} \cdot S_{22,\mathrm{DUT}} - S_{21,\mathrm{DUT}} \cdot S_{12,\mathrm{DUT}}, \quad (2.116)$$

which results in

$$[T_E] = \frac{\beta}{\alpha} \cdot \begin{bmatrix} -\Delta E & E_{DF} \\ -E_{SF} & 1 \end{bmatrix}, \qquad [T_F] = \frac{\beta}{\alpha} \cdot \frac{1}{E_{RR}} \cdot \begin{bmatrix} -\Delta F & E_{SR} \\ -E_{DR} & 1 \end{bmatrix}, \quad (2.117)$$
$$\Delta E = E_{DF} \cdot E_{SF} - E_{FR}, \qquad \Delta F = E_{SR} \cdot E_{DR} - E_{RR},$$

for the corresponding T-parameters for the two-port error-box network matrices $[E]$ and $[F]$. A description for the measured switch-term corrected T-parameters $[T_{mc}]$, which are the combined result of the measurable behavior of system, consisting of the error-box networks $[T_E]$ and $[T_F]$ and the wanted two port properties of the DUT $[T_{\mathrm{DUT}}]$, can be determined in the form of

$$[T_{mc}] = [T_E] \cdot [T_{\mathrm{DUT}}] \cdot [T_B], \text{ with } [T_E] \text{ and } [T_F] \text{ inserted} \quad (2.118)$$
$$[T_{mc}] = \underbrace{\frac{\beta}{\alpha}\frac{1}{E_{RR}}}_{=k_i} \cdot \underbrace{\begin{bmatrix} -\Delta E & E_{DF} \\ -E_{SF} & 1 \end{bmatrix}}_{=[T'_E]} \cdot [T_{\mathrm{DUT}}] \cdot \underbrace{\begin{bmatrix} -\Delta F & E_{SR} \\ -E_{DR} & 1 \end{bmatrix}}_{=[T'_F]}, \text{ or}$$
$$[T_{mc}] = k_i \cdot [T'_E] \cdot [T_{\mathrm{DUT}}] \cdot [T'_F]. \quad (2.119)$$

As the used thru standard is defined to be reciprocal, i.e. $S_{21,\mathrm{Thru}} = S_{12,\mathrm{Thru}}$, the determinant of the T-parameter representation of the standard $|[T_{\mathrm{Thru}}]| = 1$. By exploiting this constraint, it is possible to solve Eq. (2.118) for k_i in its determinants and factorize the result in the same way as shown in Eq. (2.119), yielding

$$|[T_{mc}]| = |[T_E]| \cdot |[T_{\mathrm{Thru}}]| \cdot |[T_F]| \;\Leftrightarrow\; |[T_{mc}]| = k_i^2 \cdot |[T'_E]| \cdot |[T'_F]|, \quad (2.120)$$

using the determinants of the matrices

$$|[T_{mc}]| = \frac{S_{12mc}}{S_{21mc}}, \;\; |[E']| = E_{FR}, \;\; |[F']| = E_{RR}, \;\; |[T_{\mathrm{Thru}}]| = 1, \quad (2.121)$$

resulting in

$$k_i^2 = \frac{|[T_{mc}]|}{|[E']| \cdot |[F']|} \Leftrightarrow k_i^2 = \frac{S_{12mc}}{S_{21mc} \cdot E_{FR} \cdot E_{RR}}, \text{ which yields} \quad (2.122)$$
$$k_i = \pm \sqrt{\frac{S_{12mc}}{S_{21mc} \cdot E_{FR} \cdot E_{RR}}}, \quad (2.123)$$

as the sign ambiguous square root solution k_i for the 7-term tracking coefficient modifier k. To solve this sign ambiguity, the approximate knowledge of the thru's length is

taken into account. While there are more efficient and universal ways available to solve the square root sign ambiguity ([138]), the procedure outlined in the original publication [31] will be followed here. Using the positive solution of k_i as an initial guess, an estimated measurement result $[X] = [T_{\mathrm{DUT}}]$ using the switch-term corrected 'unknown-thru' measurement $[T_{mc}]$ can be calculated by rearranging Eq. (2.118) to

$$[X] = [T_E]^{-1} \cdot [T_{mc}] \cdot [T_F]^{-1} \,, \tag{2.124}$$

and extracting the estimated transmission S-parameter S'_{21A} from the T-parameter representation $[X]$, yielding

$$S'_{21A} = k_i/[X_{22}] \text{ and } S''_{21A} = -k_i/[X_{22}] \,. \tag{2.125}$$

The argument of the estimated thru measurement results S'_{21A} and S''_{21A} can now be used to decide upon the sign of the square root by calculating their argument difference $\angle\Delta S_{21}$ between each of the estimates and the transfer function $S_{21,Thru} = e^{-j\beta\cdot l}$ of the approximately known length $\beta \cdot l$ of the thru defined upon the interval $[-\pi, +\pi]$ by calculating

$$\angle\Delta S'_{21} = \angle(S'_{21A}) - \angle(S_{21,Thru}) \,(\mathrm{mod}\,\pi) \,, \tag{2.126}$$
$$\angle\Delta S''_{21} = \angle(S''_{21A}) - \angle(S_{21,Thru}) \,(\mathrm{mod}\,\pi) \,, \tag{2.127}$$

and choosing the sign for k which results in the smallest absolute angular difference between both estimates and the thru-model, or formally

$$k = \begin{cases} +k_i & , \, |\angle\Delta S'_{21}| \leq |\angle\Delta S''_{21}| \\ -k_i & , \, \text{else} \end{cases} \,. \tag{2.128}$$

With the sign ambiguity of k resolved, the fully corrected S-parameters of the DUT can be determined in their T-parameter form by calculating

$$[T_{\mathrm{DUT}}] = \frac{1}{k} \cdot [T_E]^{-1} \cdot [T_{mc}] \cdot [T_F]^{-1} \,, \tag{2.129}$$

and subsequently converting $[T_{\mathrm{DUT}}]$ to its S-parameter $[S_{\mathrm{DUT}}]$ representation by calculating

$$[S_{\mathrm{DUT}}] = \begin{bmatrix} \frac{T_{11,\mathrm{DUT}}}{T_{22,\mathrm{DUT}}} & \frac{\Delta T_{DUT}}{T_{22,\mathrm{DUT}}} \\ \frac{1}{T_{22,\mathrm{DUT}}} & \frac{-T_{21,\mathrm{DUT}}}{T_{22,\mathrm{DUT}}} \end{bmatrix} \text{, using} \tag{2.130}$$
$$\Delta T_{DUT} = T_{11,\mathrm{DUT}} \cdot T_{22,\mathrm{DUT}} - T_{21,\mathrm{DUT}} \cdot T_{12,\mathrm{DUT}} \,.$$

When the UOSM calibration is used in conjunction with a switched receiver VNA in a four-receiver test-set configuration, a similar situation to the four-receiver SOLT analysis arises, albeit without distinct states that cover the state of the stimulus selector switch. This is caused by the LTI definition of the error-boxes used for calibration and error correction and is covered separately by the switch-terms. The resulting four distinct

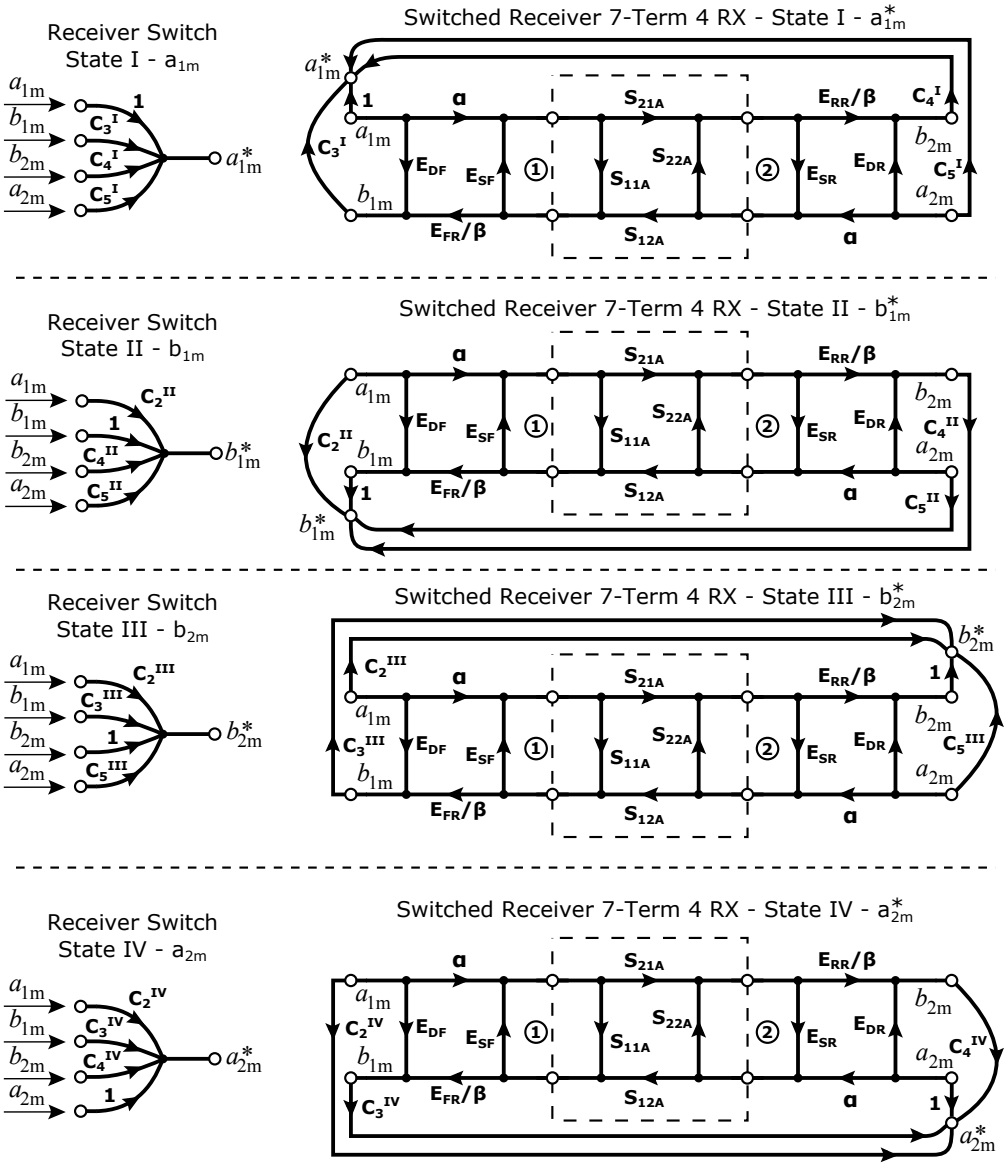

Figure 2.29: Construction of the stateful signal flow graph of the 7-term model for the switched receiver VNA with a four-receiver test-set.

states corresponding to the four required receiver wave selector switch positions are shown in Fig. 2.29. The same cross-talk normalized S-parameters for the switch as in the four-receiver SOLT case apply, therefore Eq. (2.76) to (2.79) covering the TI states of the switch also apply here, which directly leads to

$$a^*_{1m,F} = 1 \cdot a_{1m} + C_3^{\mathrm{I}} \cdot b_{1m} + C_4^{\mathrm{I}} \cdot b_{2m} + C_5^{\mathrm{I}} \cdot a_{2m}\,, \tag{2.131}$$
$$b^*_{1m,F} = C_2^{\mathrm{II}} \cdot a_{1m} + 1 \cdot a_{1m} + C_4^{\mathrm{II}} \cdot b_{2m} + C_5^{\mathrm{II}} \cdot a_{2m}\,, \tag{2.132}$$
$$b^*_{2m,F} = C_2^{\mathrm{III}} \cdot a_{1m} + C_3^{\mathrm{III}} \cdot b_{1m} + 1 \cdot b_{2m} + C_5^{\mathrm{II}} \cdot a_{2m}\,, \tag{2.133}$$
$$a^*_{2m,F} = C_2^{\mathrm{IV}} \cdot a_{1m} + C_3^{\mathrm{IV}} \cdot b_{1m} + C_4^{\mathrm{IV}} \cdot b_{2m} + 1 \cdot a_{2m}\,, \tag{2.134}$$
$$a^*_{1m,R} = 1 \cdot a_{1m} + C_3^{\mathrm{I}} \cdot b_{1m} + C_4^{\mathrm{I}} \cdot b_{2m} + C_5^{\mathrm{I}} \cdot a_{2m}\,, \tag{2.135}$$
$$b^*_{1m,R} = C_2^{\mathrm{II}} \cdot a_{1m} + 1 \cdot b_{1m} + C_4^{\mathrm{II}} \cdot b_{2m} + C_5^{\mathrm{II}} \cdot a_{2m}\,, \tag{2.136}$$
$$b^*_{2m,R} = C_2^{\mathrm{III}} \cdot a_{1m} + C_3^{\mathrm{III}} \cdot b_{1m} + 1 \cdot b_{2m} + C_5^{\mathrm{III}} \cdot a_{2m}\,, \tag{2.137}$$
$$a^*_{2m,R} = C_2^{\mathrm{IV}} \cdot a_{1m} + C_3^{\mathrm{IV}} \cdot b_{1m} + C_4^{\mathrm{IV}} \cdot b_{2m} + 1 \cdot a_{2m}\,, \tag{2.138}$$

for the measured test-set waves seen by the single receiver behind the leaky wave selector switch, which can be more neatly rewritten as

$$\begin{pmatrix} a^*_{1m,i} \\ b^*_{1m,i} \\ b^*_{2m,i} \\ a^*_{2m,i} \end{pmatrix} = \begin{bmatrix} 1 & C_3^{\mathrm{I}} & C_4^{\mathrm{I}} & C_5^{\mathrm{I}} \\ C_2^{\mathrm{II}} & 1 & C_4^{\mathrm{II}} & C_5^{\mathrm{II}} \\ C_2^{\mathrm{III}} & C_3^{\mathrm{III}} & 1 & C_5^{\mathrm{III}} \\ C_2^{\mathrm{IV}} & C_3^{\mathrm{IV}} & C_4^{\mathrm{IV}} & 1 \end{bmatrix} \cdot \begin{pmatrix} a_{1m} \\ b_{1m} \\ b_{2m} \\ a_{2m} \end{pmatrix}\,. \tag{2.139}$$

The same limitations, as outlined in the four-receiver SOLT sections 2.2.6 and 2.2.7 before, apply to UOSM-corrected measurements when no further switch correction is applied, as essentially the same calibration procedure starting with two independent MSO reflectometer calibrations is used and only a more universal method for obtaining the transmission tracking coefficients is employed. However, the UOSM corrected results are expected to show higher amounts of measurement error than the results obtained with the 10-term model due to the strict LTI adherence of the 7-term error-box network based definition. This effect is caused by the susceptibility of the 7-term model to slight violations of the underlying model assumptions in direct comparison with the 10-term model under the same circumstances (see [49]). Unfortunately, this effect is stimulated by a switched receiver VNA, as the receiver input wave selector switch causes four discrete TI-states of the test-set, which are not captured by the error-box network model in any way.

It is interesting to note, that in contrast to the usage of SOLT with the four-receiver test-set switched receiver VNA, the C_5^{I} and C_3^{IV} cross-talk coefficients will be corrected by the switch-terms corrections by superposition of the effects (see measured waves in Eq. (2.113)), as leakage of the stimulus selector switch and the receiver input wave selector switch are indistinguishable from each other for calibration of these coefficients.

Furthermore, this finding also allows to use the switch-terms correction ([80]) as a method to correct for this residual cross-talk paths C_5^{I} and C_3^{IV} in the four-receiver

test-set case for the (10+4)-term correction. It is important to understand, that the switch-terms correction resides outside of the 7-term error model and the correction is performed on the raw S-parameter measurements (see Eq. (2.114)) before any further error correction is performed (see Eq. (2.113)). Therefore, it can also be applied to the (10+4)-term four-receiver test-set case in the same way and resolve the issue of finite switch absorption return loss presented there. This duality is especially evident when comparing the definition of the raw S-parameter measurements from the measurable waves for the four-receiver SOLT case in Eq. (2.86) and the 7-term UOSM case in Eq. (2.112), which are identical.

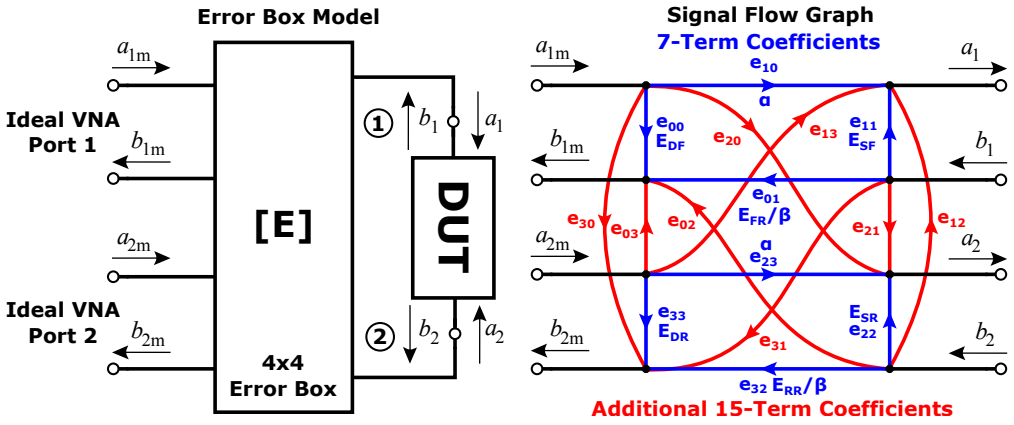

Figure 2.30: Error-box network / adapter model and corresponding signal flow graph of the 15-term error model.

When the results obtained with this TI state based bottom-up approach, which started from the reflectometer and consists at this point of the normal 7-term error model plus 12 additional insertion loss normalized cross-talk coefficients in Eq. (2.139) and Fig. 2.29 for the receiver wave selector switch, is compared with the 15-term model (see Fig. 2.30) top-down LTI approach to switched single receiver VNA error correction presented by Schramm et al. ([126, 127, 125]), the results obtained by the quite different approaches mostly agree. While the 8 additional 15-term cross-talk paths in the signal flow graph in Fig. 2.30 are not in the right topological position, this is not an issue and is caused by the abstract nature of the 15-term error-box network approach which only looks at the total superposition of all effects.

What is of concern however, is that the 15-term model is short of 4 error coefficients internal to each reflectometer which are present in the state based description of the error model in Eq. (2.139). A further analysis shows, that the constraints presented in the reflectometer analysis in chapter 2.2.3 of this work must be added to the 15-term approach presented by Schramm et al., as the effects of the uncorrected switch state dependent reflection cross-talk upon the a-wave reference measurement and state dependent modulation of the directivity term still exist, although full error correction is assumed by the publication.

Therefore, the LTI criterion of the reflectometer as the basic building block of a VNA

and its error models is violated and with implications differing by varying degrees based upon receiver switch isolation and test-set directivity from the assumptions made for the underlying 3-term calibration, or one of the port error-box networks $[E]$ and $[F]$ without the tracking terms. This is a residual, non-correctable error inherent to both approaches, which must be considered in the test-set design — even when the 15-term correction is used in conjunction with the switched single receiver VNA architecture.

2.2.9 Transmission Cross-Talk Extension of the 7-Term UOSM Procedure for Switched Receiver VNAs (xUOSM)

While the full 15-term correction MOS-16 presented by Schramm et al. ([127]) is available as an extension of the 7-term model for a usable correction of the receiver switch leakage, its application can sometimes be difficult in practice due to the more complex calibration and number of standards involved. For most measurement tasks, especially in production tests, the minute decrease in return loss measurement dynamic range present in the (10+4)-term correction when compared to the 15-term correction is generally acceptable, if the cross-talk for the transmission parameter measurements can still be corrected for full dynamic range.

When the (10+4)-term model switch cross-talk coefficients E_{XF}, E_{XRF}, E_{XR} and E_{XRR} for correcting the S_{21} and S_{12} measurements, are to be used with the 7-term four-receiver test-set error model that allows UOSM calibration without a ted+ious two tier calibration, two fundamentally different procedures are possible.

The direct approach to span a bridge between those different formulations of VNA error models would be to perform all the raw measurements outlined in the (10+4)-term calibration with an unknown thru instead of a defined thru. Both MSO reflectometer calibrations and the thru with switch-terms correction measurements are then evaluated with UOSM to a complete non-cross-talk-corrected 7-term model. By using the additional switch-terms correction, this 7-term model can be transformed to its equivalent 10-term three-receiver test-set representation using the conversion algorithms found in [27, 80] to fill the basic 10-term core of the (10+4)-term error model. As the basic SOLT part of the model is now known, the four remaining cross-talk coefficients can be calculated from the raw calibration standard measurement data by using Eq. (2.89) to Eq. (2.98), completing the model.

While this approach might seem straight forward at first, there is one major drawback involved in this procedure: The measurement of the unknown thru is not corrected for the transmission tracking cross-talk introduced by the receiver wave selector switch. This leads to additional errors in the calibration and subsequently error corrected measurement data. As these errors depend on the insertion and return loss characteristics of the thru standard, this negates the motivation for choosing UOSM instead of SOLT in the first place.

For the second possible procedure the definition of the E_{XF}, E_{XRF}, E_{XR} and E_{XRR} error coefficients from the extension of the SOLT models must be revisited. When a closer look is taken at the bidirectional signal flow graph shown in Fig. 2.27 it can be seen, that the cross-talk terms solely depend on their associated reflectometer. Furthermore,

the reflection tracking cross-talk caused by E_{XRF} and E_{XRR} is only proportional to the related measured raw return loss S_{iim} of the associated reflectometer and is therefore independent of the rest of the signal flow chart during DUT measurement and error correction. Also, knowledge about the coefficients of the associated reflectometers is only necessary during calibration, which is important as the tracking parameters will be modified by the subsequent UOSM calibration.

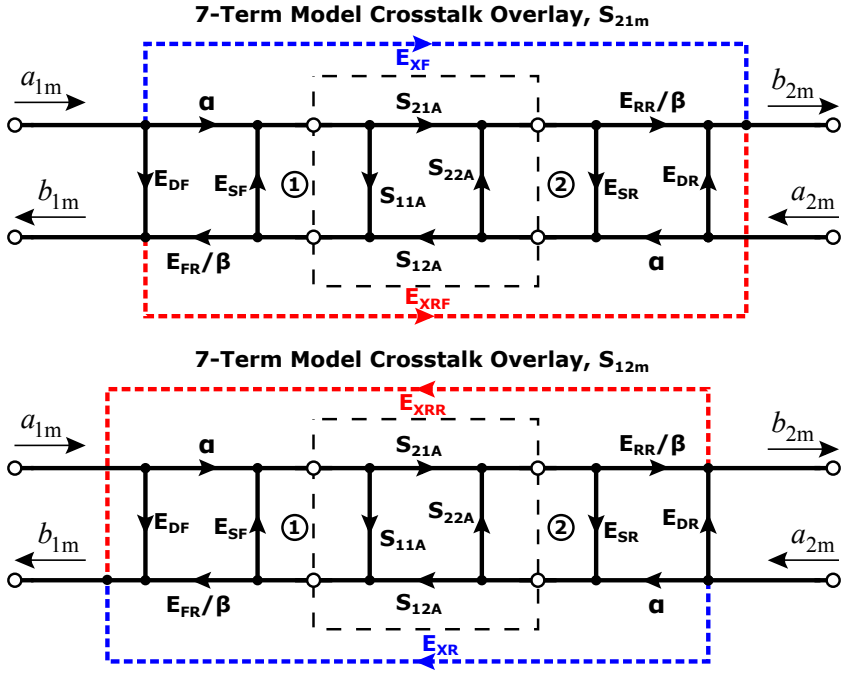

Figure 2.31: 7-Term xUOSM signal flow graph with stimulus direction dependent cross-talk correction.

With this in mind, it is possible to exploit the dual reflectometer calibration performed as an initial step for UOSM outside of the 7-term error model by using Eq. (2.89) to (2.98) with the unmodified 3-term MSO parameters of port 1 in [E] and 2 in [F], together with the measurement of two linear independent two-port isolation standards to establish E_{XF}, E_{XRF}, E_{XR} and E_{XRR} in exactly the same manner as outlined in the (10+4)-term procedure.

When the cross-talk coefficients are known, the measured raw transmission S-parameters S_{21m} and S_{12m} can be corrected for the cross-talk using the signal flow graph in Fig. 2.31, yielding the cross-talk corrected raw S-parameters S_{21mxc} and S_{12mxc} by applying

$$S_{21mxc} = S_{21m} - E_{XF} - S_{11m} \cdot E_{XRF}\,, \text{ and} \tag{2.140}$$

$$S_{12mxc} = S_{12m} - E_{XR} - S_{22m} \cdot E_{XRR}\,. \tag{2.141}$$

Using this result, the raw S-parameter matrix $[S_m]$ in Eq. (2.112) used for the switch-term

correction in the 7-term model can be redefined as

$$[S_{mxc}] = \begin{bmatrix} S_{11m} & S_{12mxc} \\ S_{21mxc} & S_{22m} \end{bmatrix}, \tag{2.142}$$

or, with Eq. (2.140) and (2.141) inserted and only raw wave quantities used, as

$$[S_{mxc}] = \begin{bmatrix} \frac{b_{1m,F}}{a_{1m,F}} & \frac{b_{1m,R}}{a_{2m,R}} - E_{XR} - \frac{b_{2m,R}}{a_{2m,R}} \cdot E_{XRR} \\ \frac{b_{2m,F}}{a_{1m,F}} - E_{XF} - \frac{b_{1m,F}}{a_{1m,F}} \cdot E_{XRF} & \frac{b_{2m,R}}{a_{2m,R}} \end{bmatrix}, \tag{2.143}$$

which can then finally be corrected for the effects of the switch-terms by applying

$$[S_{mc}] = [S_{mxc}] \cdot [C_{sw}]^{-1}. \tag{2.144}$$

Using this intermediate step allows the correction of the transmission measurements without altering the UOSM calibration procedure itself, which is consistent with the results presented in [80] for the usually pointless 7-term isolation correction inherited from the SOLT model.

This cross-talk correction is not limited to 7-term UOSM alone and could also be applied to other calibration and error correction procedures of the Txx and Lxx family ([49]), if a two-tier calibration approach with a preceding isolation calibration using the two known isolation standards in a 3-term MSO calibration is feasible.

As this correction is applied to the raw S-parameters alone, it is also possible to scale and apply this correction to multi-port measurement problems in a straight forward way by performing the isolation standard measurements for each port and extending Eq. (2.143) in the same form as in Eq. (2.140) and (2.141) for the additional transmission measurements.

2.2.10 Direct Wave-Based Switch Cross-Talk Correction

In addition to the partial in-situ switch cross-talk calibration and correction procedures presented before, which are extension of existing VNA error models for the cross-talk path introduced by the switch, there exists another possible option when the compact form of the linear system that describes the effects of all insertion loss normalized switch cross-talk coefficients for the four-receiver case in Eq. (2.139) is revisited.

If all cross-talk coefficients in Eq. (2.139) are known, it would be possible to calculate the original, non-cross-talk influenced, test-set waves from the wave quantities measured by the single receiver through the leaky wave selector switch by solving the linear system for these values in the form of

$$\begin{pmatrix} a_{1m} \\ b_{1m} \\ b_{2m} \\ a_{2m} \end{pmatrix} = \begin{bmatrix} 1 & C_3^{\mathrm{I}} & C_4^{\mathrm{I}} & C_5^{\mathrm{I}} \\ C_2^{\mathrm{II}} & 1 & C_4^{\mathrm{II}} & C_5^{\mathrm{II}} \\ C_2^{\mathrm{III}} & C_3^{\mathrm{III}} & 1 & C_5^{\mathrm{III}} \\ C_2^{\mathrm{IV}} & C_3^{\mathrm{IV}} & C_4^{\mathrm{IV}} & 1 \end{bmatrix}^{-1} \cdot \begin{pmatrix} a_{1m}^* \\ b_{1m}^* \\ b_{2m}^* \\ a_{2m}^* \end{pmatrix}. \tag{2.145}$$

In theory, this switch cross-talk coefficients could be determined with high accuracy by a separate multi-port VNA S-parameter measurement. However, the required 5 (or more) port VNA is far from standard, additional external sequencing for the switch is obligatory and the procedure itself is only possible if the common output port of the receiver wave selector switch is accessible for measurements at all. An alternative to external characterization is to use a phase and amplitude repeatable stimulus synthesizer, in combination with the vector receiver of the system to perform a self calibration due to the normalized nature of the coefficients.

While this procedure, whether it is performed by an external VNA or by the system itself, is not practical for every measurement setup due to the strict requirement to break up the test-set, the procedure could be performed as a high frequency resolution factory calibration that can be used as a data set for interpolation between the calibration sampling points. This procedure is possible due to the stability of the properties of electronics switches and by following the same argumentation as the factory pre-calibration of the switch-terms ([80]) performed by some VNA manufacturers for three-receiver VNAs.

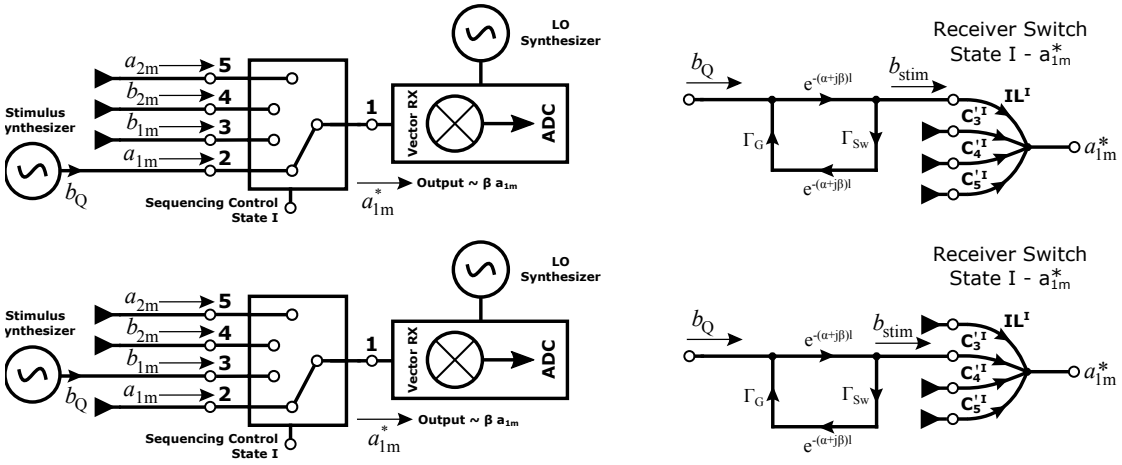

Figure 2.32: Schematic and signal flow graph for two connection states of the same switch position for the direct wave-based switch cross-talk correction.

The basic first steps of the in-system switch cross-talk coefficient measurement is shown in Fig. 2.32. The stimulus synthesizer is connected to the first wave port (a_{1m}) of the switch, while all other ports of the switch are terminated in 50 Ω terminations.

The phase repeatable output signal b_Q of the synthesizer can be described as

$$b_Q = U_0 \cdot e^{-j\omega+\phi_0}\,, \tag{2.146}$$

with the amplitude U_0 and the arbitrary, but repeatable, phase offset ϕ_0. For the sake of completeness, it is also necessary to consider the input return loss Γ_G of the generator, the return loss Γ_{Sw} of the switch and the electrical length and attenuation $e^{-(\alpha+j\beta)l}$ of the cable used for the connection in the signal flow graph. When the return loss of the different switch inputs is assumed to be well-matched and sufficiently similar between

ports, it is possible to ignore the associated loop in the signal flow chart for the ratio measurements, as will be shown for the phase offset introduced by the argument of the cable transfer function as an example. At the switch input reference plane, it is therefore possible to describe the stimulus signal b_{stim} as

$$b_{\text{stim}} = b_Q \cdot e^{-(\alpha+j\beta)\cdot l} = U_0 \cdot e^{-j\omega+\phi_0} \cdot e^{-(\alpha+j\beta)\cdot l} = U_0 \cdot e^{-j\omega+\Phi}\,. \tag{2.147}$$

When the first TI state of the switch is active, therefore a_{1m} and in turn the signal of the stimulus synthesizer is selected for measurement by the receiver, the measurement wave $a^*_{1m,1}$ seen by the receiver can be described as

$$a^*_{1m,1} = \beta \cdot (b_{\text{stim}} \cdot IL^{\text{I}} + 0 \cdot C_3'^{\text{I}} + 0 \cdot C_4'^{\text{I}} + 0 \cdot C_5'^{\text{I}}) = \beta \cdot IL^{\text{I}} \cdot U_0 \cdot e^{-j\omega+\Phi}\,, \tag{2.148}$$

with $i = 1$ denoting the port the stimulus signal is applied to. A schematic and the corresponding signal flow graph is shown in the top of Fig. 2.32. When the stimulus signal is then applied to the second port b_{1m} of the switch, while terminating the a_{1m} input and leaving the switch in the same TI state as before, the first non-normalized cross-talk coefficient $C_3'^{\text{I}}$ can be acquired by measuring

$$a^*_{1m,2} = \beta \cdot (0 \cdot IL^{\text{I}} + b_{\text{stim}} \cdot C_3'^{\text{I}} + 0 \cdot C_4'^{\text{I}} + 0 \cdot C_5'^{\text{I}}) = \beta C_3'^{\text{I}} \cdot U_0 \cdot e^{-j\omega+\Phi}\,. \tag{2.149}$$

By normalizing this measurement to the results of the insertion loss path measurement from Eq. (2.148), the insertion loss normalized cross-talk coefficient C_3^{I} can be obtained in the form required for the correction by Eq. (2.145) by evaluating the expression

$$\frac{a^*_{1m,2}}{a^*_{1m,1}} = \frac{C_3'^{\text{I}} \cdot U_0 \cdot e^{-j\omega+\Phi}}{IL^{\text{I}} \cdot U_0 \cdot e^{-j\omega+\Phi}} = \frac{C_3'^{\text{I}}}{IL^{\text{I}}} = C_3^{\text{I}}\,. \tag{2.150}$$

When this procedure is performed for all possible permutations of stimulus port and switch TI state, all the coefficients needed for the direct wave based correction shown in Eq. (2.145) can be determined. The required combinations of switch states and stimulus ports for obtaining all coefficients is shown in table 2.3.

Stimulus	Position I	Position II	Position III	Position IV
Port 2 (a_{1m})	IL^{I}	$C_2'^{\text{II}}$	$C_2'^{\text{III}}$	$C_2'^{\text{IV}}$
Port 3 (b_{1m})	$C_3'^{\text{I}}$	IL^{II}	$C_3'^{\text{III}}$	$C_3'^{\text{IV}}$
Port 4 (b_{2m})	$C_4'^{\text{I}}$	$C_4'^{\text{II}}$	IL^{III}	$C_4'^{\text{IV}}$
Port 5 (a_{2m})	$C_5'^{\text{I}}$	$C_5'^{\text{II}}$	$C_5'^{\text{III}}$	IL^{IV}

Table 2.3: Receiver wave switch measurements for direct wave correction

When all the individual results are acquired, the correction matrix $[C]$ can easily be

derived from the measurement results $m(i)$ by performing the normalization according to

$$[C] = \begin{bmatrix} 1 & \frac{m(C_3'^{\mathrm{I}})}{m(IL^{\mathrm{I}})} & \frac{m(C_4'^{\mathrm{I}})}{m(IL^{\mathrm{I}})} & \frac{m(C_5'^{\mathrm{I}})}{m(IL^{\mathrm{I}})} \\ \frac{m(C_2'^{\mathrm{II}})}{m(IL^{\mathrm{II}})} & 1 & \frac{m(C_4'^{\mathrm{II}})}{m(IL^{\mathrm{II}})} & \frac{m(C_5'^{\mathrm{II}})}{m(IL^{\mathrm{II}})} \\ \frac{m(C_2'^{\mathrm{III}})}{m(IL^{\mathrm{III}})} & \frac{m(C_3'^{\mathrm{III}})}{m(IL^{\mathrm{III}})} & 1 & \frac{m(C_5'^{\mathrm{III}})}{m(IL^{\mathrm{III}})} \\ \frac{m(C_2'^{\mathrm{IV}})}{m(IL^{\mathrm{IV}})} & \frac{m(C_3'^{\mathrm{IV}})}{m(IL^{\mathrm{IV}})} & \frac{m(C_4'^{\mathrm{IV}})}{m(IL^{\mathrm{IV}})} & 1 \end{bmatrix} = \begin{bmatrix} 1 & C_3^{\mathrm{I}} & C_4^{\mathrm{I}} & C_5^{\mathrm{I}} \\ C_2^{\mathrm{II}} & 1 & C_4^{\mathrm{II}} & C_5^{\mathrm{II}} \\ C_2^{\mathrm{III}} & C_3^{\mathrm{III}} & 1 & C_5^{\mathrm{III}} \\ C_2^{\mathrm{IV}} & C_3^{\mathrm{IV}} & C_4^{\mathrm{IV}} & 1 \end{bmatrix} . \quad (2.151)$$

This procedure may seem simple and straight forward at first, but it is important to remember the simplifications and remarks in constructing the model this correction is based on. The coefficients obtained by this procedure can only capture the direct cross-talk path from one switched wave input to another, neglecting many other cross-talk paths through the switch and especially the test-set, which was not in any way included in this simple procedure. These paths are therefore not captured, considered and corrected for, and is in contrast to the in-situ calibration procedure presented before, where most of these effects will be captured and corrected by the superposition property of the TI paths in the error model.

In consequence, the direct wave based correction is only expected to produce any positive results when it is used in conjunction with an ideal test-set as an mathematical model and thought experiment. Due to the finite isolation present in real directional couplers and the corresponding inter-path interaction, as outlined in the reflectometer discussion, this correction method is not expected to produce sufficient correction results when it is used with a VNA real test-set for both numerical simulations and real VNA hardware measurements.

Nevertheless, this purely hypothetical method is still included here, as it aids the overall understanding of the underlying phenomena and allows for a convenient measurement procedure to characterize the cross-talk paths of the receiver input wave selector switch in-situ by the VNA system itself, which will be used later on in the system description.

2.2.11 The Switched Reference Extension of the Switched Receiver Concept

While all previously presented correction methods focused on the mathematical correction of the switch leakage, a new VNA test-set topology is presented here to mitigate some effects introduced by the leaky wave selector switch.

When looking back at the definition of the multiple discrete TI states of the switched single receiver VNA test-set and assume the DUT to be LTI and especially invariant to a change in stimulus signal, it is possible to replace the reference a-wave coupler in the test-set with a SPDT switch. This switch selects, whether the stimulus is applied to the DUT or the reference wave input of the receiver input wave selector switch. A schematic of this modified test-set is shown for the simple reflectometer case in Fig. 2.33.

In order to obtain the same signal amplitude for the a-wave at the receiver input compared to the traditional test-set, an attenuator must be inserted into the reference wave position path between the two switches. This attenuator should have an attenuation

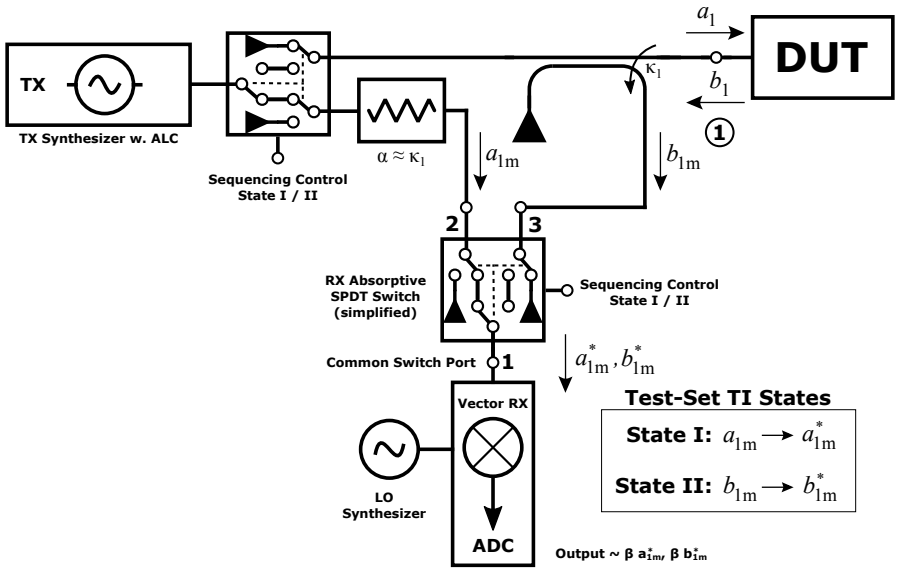

Figure 2.33: Schematic of the switched reference switched single receiver reflectometer.

approximately equal to the coupling factor of the direction coupler used before, if the insertion loss of the stimulus selector switch can be considered negligible.

While this architectural change in the test-set topology introduces a new source for repeatability issues by the addition of another switch in the signal path, this can be nowadays be considered a minor issue due to the excellent repeatability of semiconductor switches. Furthermore, the over all improvements expected by this simple addition to the switched single receiver concept are expected to easily outweigh this effect.

By inserting the reference wave switch into the reflectometer, two main points of concern discussed in the analysis of the switched reflectometer are mitigated by this modification, assuming a sufficiently high switch isolation:

- There is no cross-talk present for the reference a-wave measurement, which would normally show up as a normalization present in all the coefficients of the error model, resulting in closer adherence of the hardware to the original error model. As the stimulus signal is removed, or heavily attenuated, from passing to the rest of the test-set, other sources of interference are removed.

- The state dependent modulation of the E_D directivity term in the second TI state of the test-set is effectively suppressed, because of the increased isolation provided by the topology. While this is not of concern for the reflectometer itself, it is important for the 7- or 15-term error model, which assumes a strict LTI test-set.

- Additionally, the a-wave measurement is now far more isolated from feedback effects of DUT input return loss, easily surpassing the isolation provided by a directional coupler. When the stimulus synthesizer of the VNA is assumed to be phase and amplitude repeatable, this strict isolation of the a-wave measurement

allows to reduce the amount of a-wave measurements in subsequent sweeps. As TI behavior is assumed, the a-wave must only be re-measured on time scales where the inherent drift of the system and/or the synthesizers are of concern for the required measurement accuracy. For the sequential measurement procedure of the single receiver VNA, this leads to a significant speed-up of the measurement speed, and effectively converging to the speed of a normal dual receiver reflectometer architecture for longer timescales.

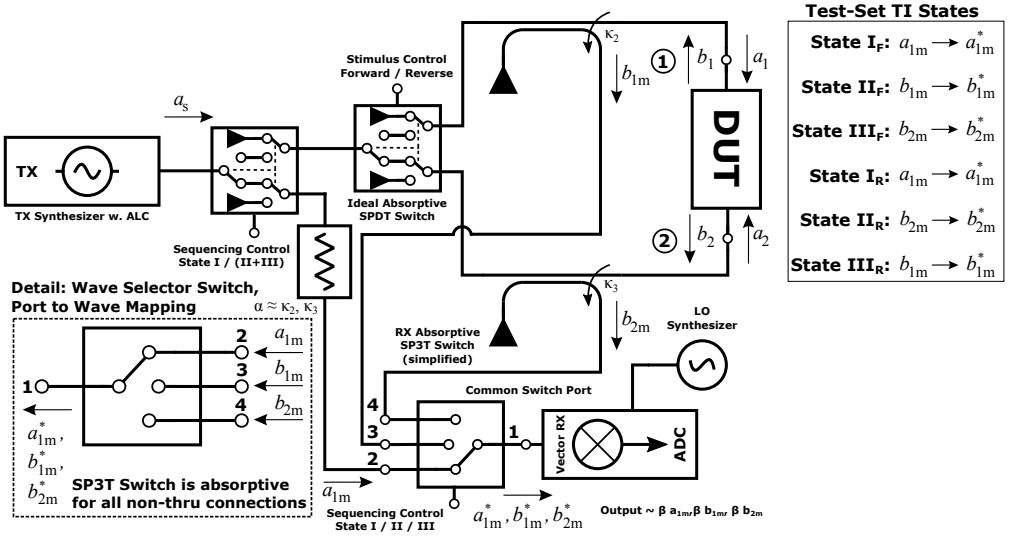

Figure 2.34: Schematic of the switched reference, switched single receiver, three-receiver test-set, SOLT VNA.

When the concept of the reference wave switch is applied to the three-receiver SOLT test-set architecture, its benefits are immediately obvious. As the reference channel is now well isolated at the receiver wave selector switch, the E_{XF} and E_{XR} paths can be omitted except for very demanding measurements from the cross-talk correction calibration in the (5+2) and (10+4)-term procedure, hereby reducing the number of required isolation standard measurements per port from two to one.

Furthermore, this test-set modification restores the source power independence of the original SOLT error model, because both remaining E_{XRF} and E_{XRR} cross-talk paths only depend on wave ratios, rather than the absolute wave quantities used by E_{XF} and E_{XR}. As the E_{XRF} and E_{XRR} paths can easily be assumed to be the source of the strongest interference in the three-receiver test-set, the overall usable dynamic range for transmission measurements is vastly increased by this measure.

While the possible measurement time reduction for subsequent sweeps is not as dramatic as in the reflectometer case when repeatable signals are used, the acquisition time of the single receiver VNA only approximately doubles for the unidirectional measurement case when compared to a fully equipped VNA, when synthesizer lock times and the ratio of ADC acquisition time to IF filter step-response settling times are ignored.

A further reduction in measurement time is possible for three-receiver bidirectional two-port measurements, as the a-wave has to be measured only once for both stimulus directions due to the high isolation of the switch. In total, this converges to a difference in measurement speed of just a factor of two, in contrast to a factor of three in the normal switched single receiver configuration, when a full-receiver VNA is used as the reference.

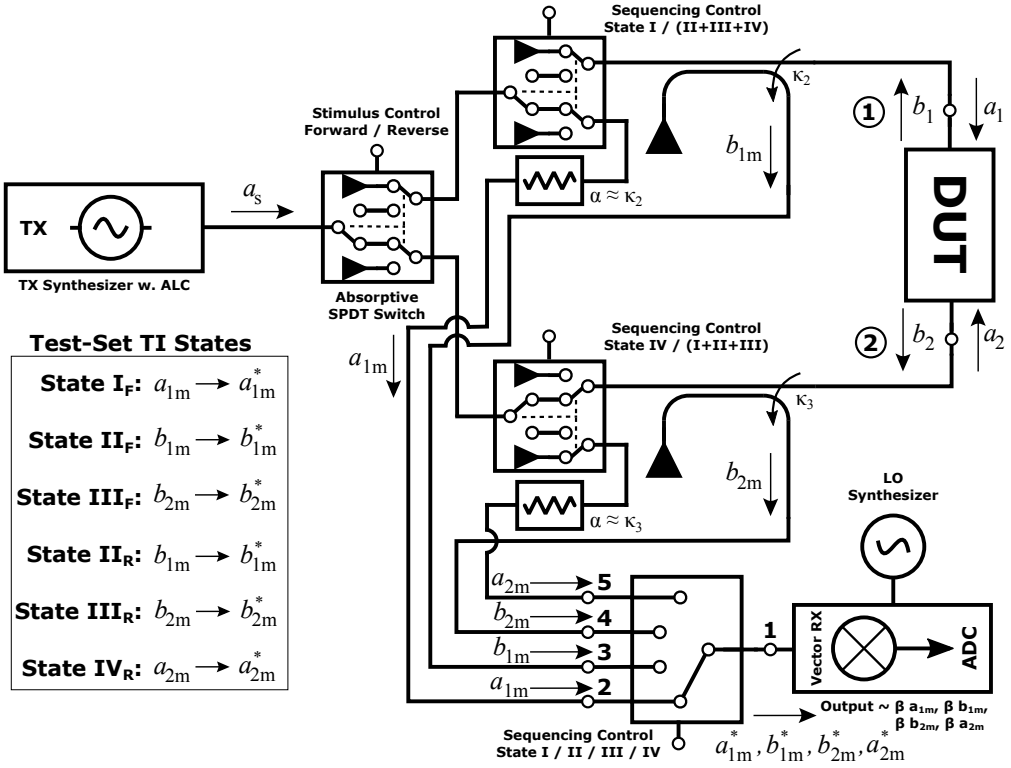

Figure 2.35: Schematic of the switched reference, switched single receiver, four-receiver test-set VNA. Switch configuration shown for the forward stimulus measurement of a_{2m}.

Despite the positive consequences of the modification for reflectometer and three-receiver test-set architectures, there is one important drawback associated with the reference wave switch in four-receiver test-set architectures, as shown in Fig. 2.35. While applying SOLT models to this architecture is met with no issues, this new topology does not allow for 7-term or 15-term error models to be directly applied due to one simple problem: The direct switch terms measurement ([80]) is not possible in this architecture. When looking at the switch terms correction matrix in Eq. (2.113), it can be directly noticed, that the calibration measurement requires the acquisition of a_{2m} for a thru connection under forward stimulus, or a_{1m} under reverse stimulus, respectively. When looking at the forward stimulus measurement of a_{2m} shown in Fig. 2.35, it is immediately obvious that no useful information can be extracted by this measurement due to the stimulus switch. While some signal will be measurable due to the finite isolation of the

Type	Reflectometer	Unidir. 3 RX	Bidir. 3 RX	4 RX w/o Sw. Terms
Full Receiver Config.	1	1	2	2
Semi-Switched w. Ref.	1	2	4	4
Single Switched RX	2	3	6	8
Swi. RX TI Swi. Ref	1	2	4	N/A

Table 2.4: Comparison of relative data acquisition speed (a.u.) between different VNA receiver architectures, processing time, synthesizer lock-time and IF filter step-response settling times not taken into account.

reference wave switch in this state, no useful information for the switch-terms correction can be extracted whatsoever. Furthermore, the change in return loss that invalidates the LTI nature of the 7-term model for this configuration is the internal termination of the reference wave selector switch itself — and not the stimulus selector switch as in the original formulation of the problem ([49, 80]).

As a consequence, the four-receiver test-set with reference wave switches effectively degrades to a three-receiver test-set topology, despite the fact that four measurement receivers are available. While this may seem to be a major drawback at first, the good stability of the switch-terms can be used to determine them either during production or by a user performed SOLT calibration instead ([27, 68]) and save them for later use with a slightly modified 7-term procedure ([68]). Even with this minor drawback, the elimination of the most dominant cross-talk path caused by the reference test-set signals and the isolation of the reference a_i-waves from test-set dependent cross-talk still prevail.

2.2.12 Summary

In the previous sections 2.2.3 to 2.2.11 new VNA architectures, error models, calibration procedures, and error correction methods, based upon well proven and accepted procedures for standard VNAs, were developed and derived, starting from the basic switched reflectometer structure by stateful analysis of the signal flow graphs.

It was proven, that the switched single receiver reflectometer can be corrected using the unmodified 3-term model, as all the additional error coefficients introduced by the switch are absorbed into the existing model when certain, easily fulfilled, conditions are met during construction.

An extension to the 5-term error error for increasing the dynamic range of unidirectional S_{11}/S_{21} measurements in the switched single receiver architecture was derived from the superposition of the switch and test-set error models. A calibration procedure based upon the common SOLT calibration standards was conceived for this model to determine the additional error coefficients introduced by the (5+2)-term model.

Based upon the development process of the (5+2)-term model, the inherent relationship between the 5-term unidirectional and the 10-term bidirectional SOLT error models were used to extend the (5+2)-term model for bidirectional measurements of two port DUTs, resulting in the extended (10+4)-term model for increasing the dynamic range of single switched receiver two-port measurements.

The findings obtained by this step and the localization of the cross-talk coefficients outside of the original error model, akin to the original formulation of the 7-term model Switch Terms, then allowed the extension of the 7-term error model to account for this cross-talk. This was demonstrated by modifying the common UOSM 7-term calibration procedure to the switch cross-talk correcting xUOSM procedure.

Finally, the concept of the switched reference wave topology to reduce the high-powered reference wave cross-talk by modification of the test-set, and a novel concept for accelerating single receiver VNA measurements based upon this technique, was introduced.

After the following description of the developed single receiver VNA hardware, a numerical performance verification of the new calibration procedures in comparison with the unaltered original algorithms will be presented for different test-set configuration to confirm the theoretical findings of this section, followed by the presentation and discussion of the actual measurement results obtained by the real single receiver VNA hardware.

2.3 The Switched Single Receiver VNA Hardware Concept

2.3.1 The Necessity of Custom VNA Hardware

The switched single receiver VNA and its appropriate error models and correction schemes are unfortunately caught in a dilemma regarding the scientific method and causality: Ideally all measurements comparing a normal reflectometer, or otherwise accepted VNA architecture, and the switched single receiver architecture and its enhanced error models, should be carried out using the same test-set, stimulus synthesizer(s) and receiver(s). The only new variable should be the addition of the receiver input wave selector switch in order to reduce the number of variables and sources of error to a point, where all additional and new effects can be attributed to the switch alone.

Unfortunately, this procedure can not be successfully carried out due to the lack of low-level programming possibilities of VNAs known to the author and was also not carried out successfully in other works. This is due to the fact, that the non phase repeatable stimulus and LO synthesizers used in VNAs are generally re-locked between subsequent measurements or trigger events, regardless of sweep or CW single point mode, and thus violate the stimulus and conversion TI criterion necessary for the successful wave scanning operation of the receiver wave selector switch between subsequent measurements.

The reason for this behavior is simple: Normal full and semi-switched receiver VNAs just do not need to care for this criterion, as the corresponding stimulus reference a-wave is always captured at the same time as the b-wave using the same LO signal during the same TI lock state of both sources. As S-parameters are ratiometric values, this cancels out any phase repeatability errors introduced by fractional-N stimulus or LO synthesizers ([53]).

While this issue could be resolved by a low-level programming access to the sequencing and flow control present in a normal VNA, this is generally not possible with the command and control options exposed to the user over remote control interfaces and its documented SCPI[25] or VISA[26] command set. Re-configuring the low level sequencing performed in the VNA is certainly possible for VNA manufacturers them self, but no information is publicly available and access to proprietary information is understandably coupled with extensive non-disclosure agreements.

Therefore, previous publications covering this subject either turned to the method of synthetic instrumentation based on the VXI module standard by National Instruments and using a signal generator, a down-converter and ADC modules for this system ([125]) or used a stand-alone vector signal generator combined with a vector signal analyzer for this purpose ([65]), and compared their results with measurements obtained by a normal reference VNA system.

While both of these approaches to the problem offer a high degree of flexibility for testing and evaluating the switched single receiver VNA concept, they only offer solutions based upon of more black boxes of finer granularity and subsequent compromises resulting from the capabilities and features of the involved instruments. Contrary to the methods

[25] Standard Command for Programmable Instruments
[26] Virtual Instrument Software Architecture

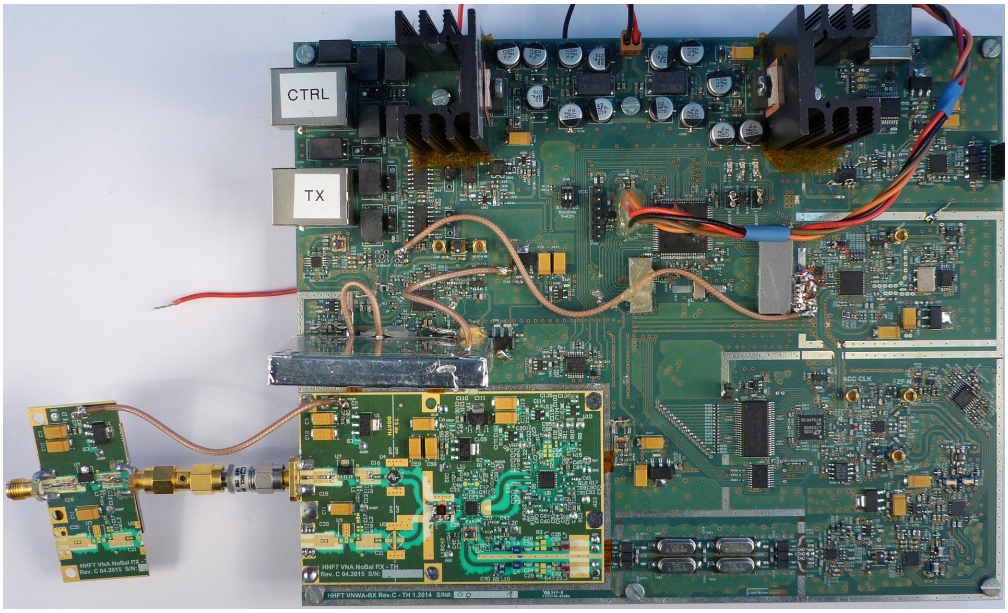

Figure 2.36: 1.5 - 3.0 GHz vector receiver prototype developed by the author for non-contact spoil moisture measurements in the DRAGON EU research project (FP7-Enviroment, Number 308389, [93]) and modified for higher dynamic range and accuracy for the initial switched receiver VNA measurements.

used in these works, a custom VNA system tailored to the specific challenges present in the single receiver architecture will be used for verification in this thesis. While the primary function of this hardware will be to verify the theoretical error correction concepts presented in chapters 2.2.3 to 2.2.11 of this work, it also serves to verify the fundamental promises of and motivations for the single receiver VNA architecture: Reductions in total cost, size and complexity - up to a point, that a usable switched single receiver VNA system, capable of performing mixed frequency measurements and showing performance figures comparable to normal commercial VNAs can be designed and built from scratch by a single individual from common commercial-off-the-shelf components.

Additionally, this approach to the hardware used in the demonstrations serves to demonstrate the rapid speed of development present in the microwave semiconductor market and harness the market's new development to introduce new concepts such as fully integrated, phase repeatable, wide-band synthesizers and their associated benefits into the conservative realm of vector network analysis and present new applications based upon these developments.

The hardware used in this thesis is based upon a previous, far less capable, vector microwave measurement system, that was developed for non-contact spoil moisture measurements on conveyor belts in tunnel boring machines during the EU research project DRAGON[27] ([93]) for the error correction of an X-ray fluorescence material

[27]Research funding category FP7-Environment, funding number 308389.

analysis instrument. This predecessor system was developed as a discrete standalone embedded system for transmission phase and absorption measurements in the 2.45 GHz ISM band. A prototype of the receiver used in this system, which was later vastly enhanced and modified for initial system concept evaluation of the switched receiver VNA system used here, is shown in Fig. 2.36.

2.3.2 A General Hardware Architecture Overview

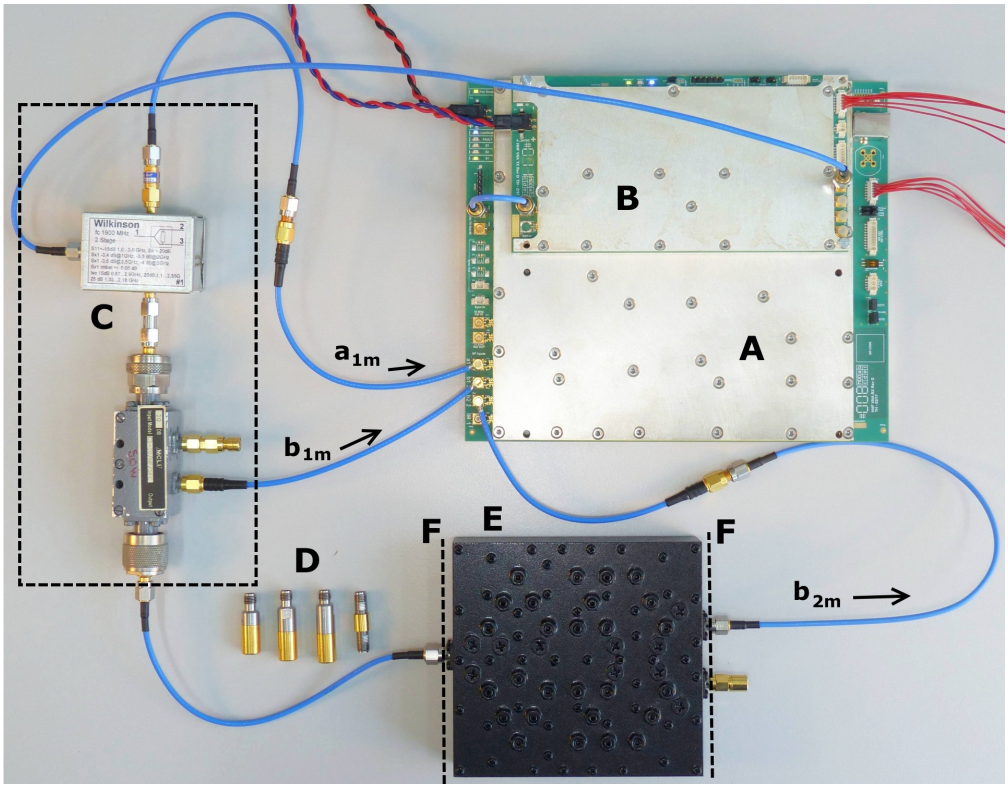

Figure 2.37: Exemplary switched single receiver VNA system, unidirectional SOLT three-receiver test-set. Annotations: A - receiver module with integrated receiver wave selector switch, B - stimulus synthesizer module, C - reflectometer, consisting of a Wilkinson power divider for the a-wave and a transmission line coupler for the b-wave, D - Rosenberger RPC-3.50 MSO and thru calibration standards, E - device under test (DUT), F - calibration reference planes for port 1 and 2.

The VNA hardware used in, and developed for, this work can be broken down into three main modules or PCB assemblies:

- The switched single receiver VNA main assembly, or RX module, which also includes the receiver input wave selector switch,

- The normal stimulus synthesizer assembly, or TX module, which includes the reference wave switch, and
- The harmonic phase reference module (HPR), which will be presented separately later in chapter 3.3.

No special additional test-set components like directional couplers or resistive bridges were developed for the measurements, except for the semiconductor microwave switches integrated into the receiver and stimulus synthesizer module. Instead, the test-set of a commercial VNA is used for the measurements with the switched receiver VNA system to obtain a higher degree of comparability between the different architectures and error models. If one was to build a complete VNA system from the modules presented here, the incentive to develop custom test-set components is nowadays very low, as complete 50 MHz to 6 GHz directional resistive bridge assemblies, including the DUT facing RF connector, can be obtained for less than $300 ([86]).

The switched single receiver VNA system is designed as a compact embedded headless system with no internal data visualization or storage capabilities in mind, as can be seen from the exemplary VNA system shown in Fig. 2.37. All time critical operations, embedded command and control as well as simple data format transformation procedures are handled by the module system itself, while all processing time intensive floating-point operations such as the complex valued calibration and error correction calculations, data visualizations and data storage operations are offloaded to an external PC, or a single board computer for embedded applications.

All assemblies are fitted with silver plated milled aluminum clam shell enclosures including EMI gaskets at the interface between the enclosure and case. An example for this construction method is shown in Fig. 2.38. All RF feedthroughs penetrating the walls of the enclosures were simulated and optimized using the corresponding transmission line model of the PCB in Ansys HFSS[28] for minimum impact on the transmission line return loss and maximum isolation between adjacent chambers. The enclosures fulfill many important tasks in the overall system concept:

- Providing RF shielding and separation between different sections on the assemblies,
- Shielding and isolation between the comparatively high power RF section of the TX module and the sensitive receiver section of the RX module,
- Working as a heat sink by including milled posts and thermal conductive pads on the lower half of the clam shell enclosure,
- Providing mechanical rigidity against flexing of the PCBs to protect the delicate surface mount components, and
- Providing mounting points for attaching the modules to each other, yielding a compact footprint of the system.

[28] High Frequency Structure Simulator, a fully integrated, 3D electromagnetic field simulator software suite using frequency domain finite element analysis.

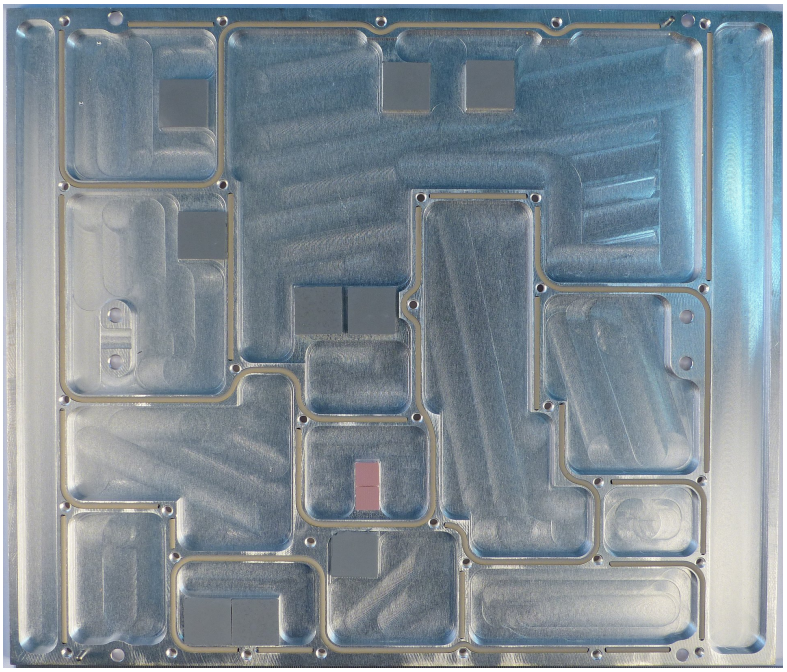

Figure 2.38: Bottom clam shell enclosure of the switched single receiver main assembly, exemplary for the construction method applied to the modules. Light gray: EMI gaskets, rectangular dark gray and pink: Thermally conductive silicone pads on milled post for heat transfer from heat sinks integral to the PCB to the case and mounting.

The communication between the different modules is handled by a differential full-duplex RS-422 bus system, running at 2 MBaud and using a custom binary protocol optimized for speed, which allows one RX module to control up to 30 other modules like stimulus synthesizers, harmonic phase references and further extensions such as low-noise amplifiers or switch matrices for different embedded applications. The embedded software running on the microcontrollers of each module is designed to be as autonomous as possible to reduce the time reserved for communication between the modules and therefore in turn reducing the time necessary for completing a measurement task, as even minor delays can quickly add up in a sweeping measurement system that samples many points per sweep.

The single switched receiver, or RX, module acts as the communication hub of the VNA system and provides a command, control and data interface, either via a serial UART emulation over USB 2.0 with a baudrate of 3 MBaud or a full duplex RS-422 data link running at different user selectable baudrates, supplemented by additional opto-isolated measurement trigger and status lines for embedded applications. A variant of the common ASCII, or text based, SCPI-99 protocol ([144]) is used for command, control and data transfer over these interfaces. The command interpretation is handled by a parser integral to the state machine controlling the RX module and the VNA system as a whole. The

subset of SCPI commands used by the system is similar to the implementation used by other VNA manufacturers and therefore simplifies the integration of the modules into various software environments, such as MATLAB / Simulink, LabVIEW or Python scikit-rf.

The collection of housekeeping data, self-test results and error checking and handling for on-board peripherals and the various other modules present on the communication bus is performed by the RX module in a centralized manner by a background task, while each individual module in the system additionally signalizes errors that occurred in their local realm with a local LED error indicator to simplify the debugging process.

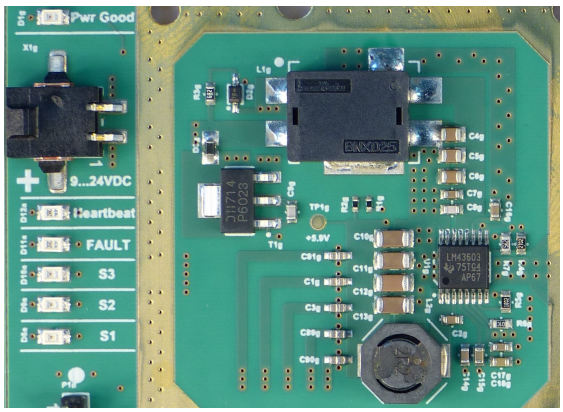

Figure 2.39: Detail of the low EMI switch mode down converter voltage regulator and input filter and protection design used in all VNA modules.

All modules are designed to run from a 9...24 V DC supply and are protected against input voltage transients and reverse polarity DC connection by an active p-channel MOSFET input polarity protection circuit, followed by extensive wide-band electromagnetic interference (EMI) filtering to improve both the isolation between the modules an the susceptibility to external interference sources, such as noisy switch mode power supplies (SMPS) and their conducted emissions.

The input voltage is then converted to a heavily filtered intermediate voltage rail by a non-isolated high efficiency switch mode power supply, which was optimized for the lowest possible spectral impact on the IF-, sampling and reference frequencies used throughout the system. While spread-spectrum modulation of the switching frequency was considered, testing revealed that the SMPS controller used had such a low correlation in its spectral emissions for the frequencies used in the system, that no further improvement could be observed for the system noise-floor when a pseudo random noise FSK modulation of the intended switching frequency was performed using the external switching frequency synchronization capabilities of the SMPS IC.

The SMPS then converts the input voltage to an intermediate voltage rail that is used as the input to low noise linear low drop regulators (LDO) for creating the final voltage rails. These LDOs were chosen for their amount of additional spectral noise energy and its distribution, as well as their power supply rejection ratio at the switching frequency

of the on-board SMPS.

All external connections that are exposed on connectors on the outsides of the modules when the clam shell cases are attached, are protected by polymer-based low capacitance ESD suppressors for protection against 30 kV ESD events for the human body model. These ESD suppressors are also used in the exposed RF paths which are terminated onto SMP connectors to protect the ESD Class 1 susceptible components used throughout the various RF paths. These RF components can be severely damaged by a non-noticeable static discharge of less than 2000 V in the human body model. Usually, only narrow band microwave applications can be protected in that way due to the junction capacitance of the common protection diodes which in turn needs other reactive components to regain an acceptable input return loss. However, new developments in polymer based suppressors offer an extremely low capacitance of 40 fF and therefore allow the omission of the additional bandwidth limiting matching network and enabling wide-band operation.

The PCBs of all modules are manufactured in a multi-layer mixed substrate process. A fairly thick FR-4 core provides mechanical stability and rigidity, while the outer layers are manufactured using a 254 um thick Isola I-Tera MT low-loss microwave laminate, which provides a stable dielectric constant over frequency and shows only a fraction of the dielectric losses associated with FR-4 substrates in the lower microwave regions and is also compatible with FR-4 in a mixed layer stack due to matched thermal expansion coefficients.

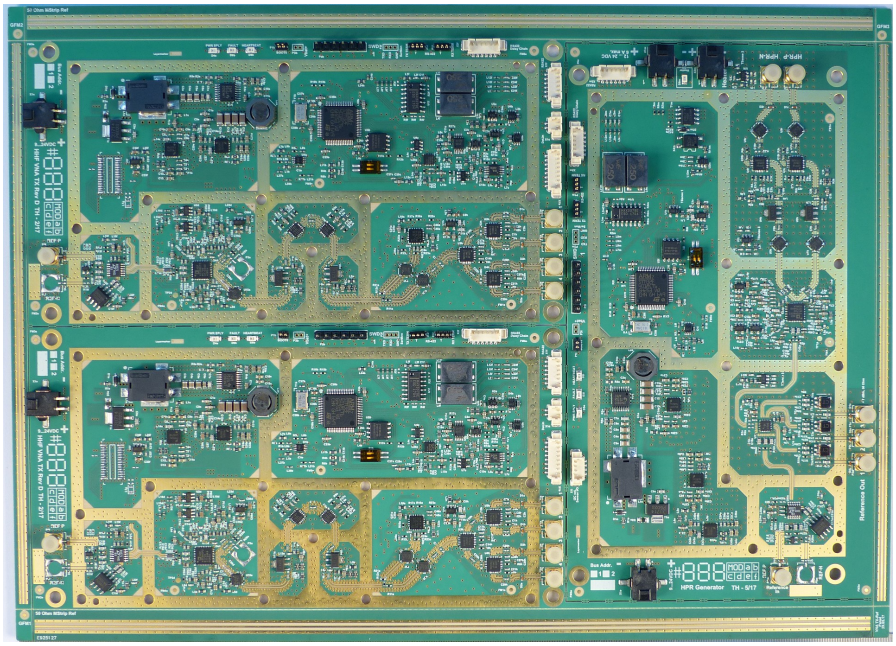

Figure 2.40: Two stimulus synthesizer PCBs and one harmonic phase reference PCB still combined in their panel after the pick and place procedure and reflow soldering. Breakaway tabs with microstrip and coplanar transmission lines with ground added for safe machine handling and impedance control.

Transmission lines in the microwave RF section of the boards are designed as coplanar transmission lines with ground (CPWG) to minimize coupling between lines, lower inductance to ground for components mounted in a shunt configuration and to provide an improved return loss for all the microwave ICs in the RF paths due to matched line to pad widths. The microwave ICs used are mostly packaged in quad-flad-packages (QFP) with a maximum pad width of 0.3 mm and signal pins in a ground-signal-ground configuration matched to the CPWG transmission lines. The IF- and the LVPELC[29] based clock-tree signals are mostly laid out in 100 Ω differential edge-coupled microstrip technology to improve isolation and common mode suppression in all cases were differential in- and outputs are feasible.

All modules were first build as hand soldered prototypes to check for layout errors and test each of the sub-assemblies present on the modules on their own, while the measurement results presented later-on were obtained on system that was build in a low volume production run by a contract manufacturer. This was done in order to improve the overall reliability of the system and the repeatability of the measurements, since most IC packages and passive component sizes used on the assemblies do not allow for long term reliable hand soldering to be performed and must be soldered using re-flow soldering techniques combined with a strictly controlled temperature curve for quality control.

The following description of the VNA hardware starts by providing a first look at the synthesizers used in both the receiver for generating the LO-signal supplied to the front-end mixer as well as the stimulus synthesizer module due to their direct impact on, and importance for, the measurements taken with a single switched receiver VNA due to the TI requirements associated with both signal sources. A general overview over the construction and properties of both the stimulus synthesizer and the receiver module including its front-end and IF section will be given afterwards. Finally, a short discussion of the system clock properties, its derived signals, subsequent distribution and the implications arising from the clock tree for the acquisition of the sampled RF measurement signal will be given.

2.3.3 An Introduction to the Synthesizers Used for the VNA

As outlined in the initial description of the concept, the design and properties of the synthesizers used throughout the VNA system are extremely critical due to the strict TI requirements necessary for high quality measurement results. For the measurement of complex signals, it is necessary to keep both components of a complex phasor, the vector magnitude and its phase, stable during a measurement for both the stimulus synthesizers and the LO synthesizer.

Stabilization of the signal magnitude is usually achieved by employing an automatic level control (ALC) loop, which will be described later on in the description of the stimulus synthesizer module, and its function is in principle agnostic about the source

[29] Low-voltage positive-referenced emitter coupled logic, a current driven high speed logic family, which is nowadays especially used for low jitter clock signals in a differential logic configuration.

and generation method of the signal. The stability of the phase component is however mainly determined by the signal generation method.

Nowadays, two main methods for generating frequency and phase stable signals are used: The direct digital synthesis (DDS) method and phase locked loop (PLL) based synthesizers. Both methods share the same basic property, that an extremely stable reference signal of a lower frequency is used to generate a derived signal of higher frequency, which ideally shares the frequency and phase stability characteristics of the lower frequency reference signal proportional to the multiplication factor.

Due to the good availability of high-Q crystal based oscillators such as TCXOs[30] and OCXOs[31], with drift and temperature coefficients in the sub PPM range and excellent phase wander and phase noise characteristics[32]. Both signal generation methods can create stable signals in the microwave frequency range that are suitable to the purpose of this application.

The main difference between those two methods lies in the creation realm of the output signal: The DDS method uses a direct digital generation of the signal by a numerical controlled oscillator (NCO), which is then converted by a digital-to-analog converter (DAC) followed by a lowpass reconstruction filter to its analog representation, while the PLL directly creates the output signal by using a voltage controlled oscillator (VCO) in the analog domain by using a integrating feedback loop closed by a low jitter microwave frequency divider and a phase frequency detector (PFD) with additional digital circuits and counters.

Direct digital synthesis of the waveform is usually more frequency agile in sweeped sampling operation due to its fast output settling time, offers a more granular control over the output frequency, has better close-in phase noise performance than a PLL and allows for arbitrary waveform outputs that can also be controlled in amplitude ([139]). However, there is one important and limiting feature present in the DDS method: As DACs are used for signal generation, the signal reconstruction must adhere to the Nyquist-Shannon sampling theorem and therefore needs a minimum DAC sample-rate, which is at least the double of the highest generated output frequency.

While it is technically possible to use special high speed microwave capable DACs in a combined DDS circuit as the signal source for the VNA, the price-performance characteristics of such DACs and especially fully integrated DDS circuits do not scale well for such a stripped down low-cost system concept in direct comparison with the recent developments in the fully integrated PLL synthesizer market. In this light it is also important to realize, that the support circuitry and PCB technology and space required for microwave capable DDS and DAC ICs is also generally more complex and expensive.

In order to counter this drawback, direct combinations of DDS and PLL synthesizers, in which the DDS generates a low frequency, scaled representation, of the output signal

[30] Temperature compensated crystal oscillator (TCXO).

[31] Ovenized or temperature controlled crystal oscillator (OCXO).

[32] Phase noise and phase wander essentially describe the same basic process of phase variation, however on a different frequency scale. While phase wander covers the low frequency phase deviation and drift component down to DC, the phase noise component covers the higher frequency components of phase deviation, therefore close-in and far-out phase noise are common synonyms.

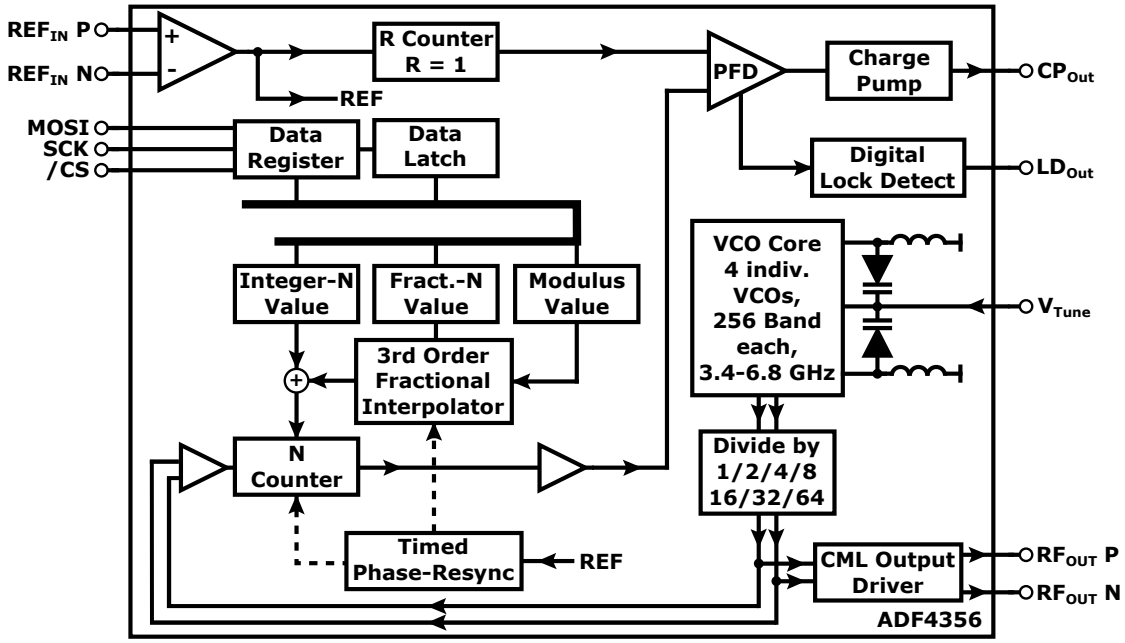

Figure 2.41: Simplified schematic block diagram of the ADF4356 fully integrated wide-band synthesizer IC. Redrawn to show only the parts relevant to this work. The complete original block diagram can be found in [23].

which is in turn used as the reference signal for an Integer-N PLL synthesizer to multiply it up to the intended output frequency, are used in some high end VNAs as stimulus and LO synthesizers to combine the best properties of both technologies. Nevertheless, this approach to VNA signal generation also inherits the combined implementation complexity of both procedures and was therefore discarded for the system presented here.

Fortunately new developments in fully integrated synthesizers, which integrate a Integer- and Fractional-N PLL core, high speed low jitter output dividers, one or more integrated VCOs and additional configurable support circuitry in one compact IC package, alleviate some drawbacks present in classic PLL-based synthesizer designs. While the frequency settling time for a PLL-synthesizer is still a magnitude slower than the settling time of a DDS-based generator, higher maximum PFD frequencies and lower minimum RF pre-scaler values introduced by the latest synthesizer generations led to a serious decrease in time to frequency lock, or lock-time. While this is not an important figure for CW measurement operation, the lock-time is one of the main contributors to the frequency sweep measurement time in a VNA. Furthermore, the introduction of very deep (or high resolution) modulus and fractional counter registers for sub-Hz output frequency resolution, combined with the added possibility of phase control in Fractional-N mode, considerably closes the feature gap between both technologies, while still retaining the comparatively easy VCO[33] based signal generation in the microwave frequency range.

[33](Analog) voltage controlled oscillator

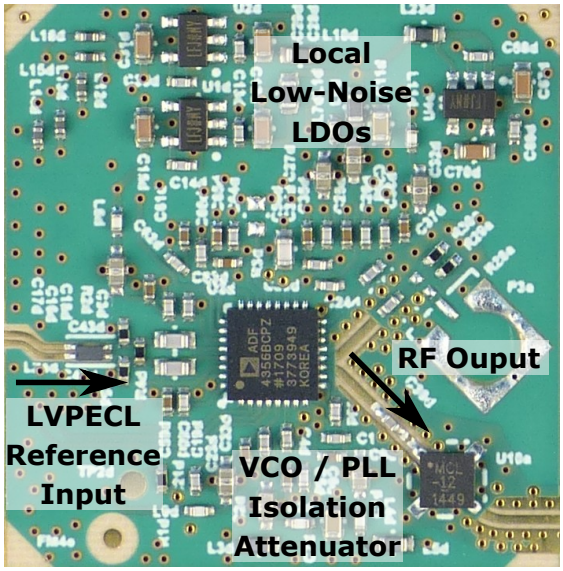

Figure 2.42: Annotated detail picture of ADF4356 wideband synthesizer IC section as used on the stimulus synthesizer PCB. Not shown are the two selectable loop filters on the other side of the PCB.

In this work, the fully integrated synthesizer ADF4356 ([23]) made by Analog Devices ([7]) is used in the final iteration of the hardware and is therefore used for all measurements presented in this work. A simplified block diagram of this IC, reduced to only the configuration and features used throughout this work, is shown in Fig. 2.41, while the full block diagram can be found its datasheet ([23]). The IC itself incorporates all the necessary components, except the reference frequency source, the external loop filter and the optional automatic level control, to build a capable synthesizer in an extremely compact footprint. The ADF4356 can generate signals in a fundamental output frequency range of 3.4 to 6.8 GHz, which can be divided down to a minimum frequency of 53.125 MHz by internal low jitter, high speed, dividers. To enhance the TI repeatability, these dividers can be fully integrated into the PLL feedback loop by multiplexers to cancel out their variations in propagation delay between divider settings and over temperature. The IC supports at total Fractional-N resolution, or depth, of 52-bit by combining one fixed and one configurable modulus divider with the accompanying two fractional counters to control the third-order fractional interpolator which in turn controls the modulation of the N-counter values to achieve fractional multiples of the reference frequency signal. This results in a theoretical output frequency resolution in the μHz-range, depending on the actual PFD frequency.

A picture of the compact, single ended output, implementation used on the stimulus synthesizer PCB is shown in Fig. 2.42.

In order to achieve a good phase noise performance and to cancel out process variations in the manufacturing of passive components on the IC, the VCO section integrates 4 different VCOs, which in turn include 256 switchable overlapping sub-bands to cover

the whole 3.4 GHz to 6.8 GHz base frequency range. Each VCO sub-band only covers a frequency range of 3 to 5 MHz, which results in a low tuning voltage sensitivity K_V and increases noise immunity and phase noise performance substantially when compared to a sole external VCO covering a bandwidth of 3.4 GHz in a classical PLL synthesizer setup.

This band splitting of the VCOs results in one important drawback for the repeatability of the output signal: In normal operation, the exact choice of VCO, its band, and its bias settings, are determined by an auto calibration routine inside the IC each time any of the output frequency determining registers, like the N- or fractional register, is updated. The outcome of the auto calibration routine depends on various environmental parameters like the die temperature and supply voltages. The inbuilt routine tries to determine a set of parameters that will result in an optimum performance in a given situation and is described as probabilistic in its outcome in the datasheet due to the influence of noise in the decision-making process ([23]).

What seems to be more like a nuisance at first due the general increase in lock times has important consequences for the amplitude and phase behavior of the synthesizer: As no ALC is integrated into the synthesizer itself, the amplitude of the output signal is unique to each VCO and its related sub-settings. At first glance it may seem that the phase of the output signal is not influenced by the selection of a different VCO and settings for the same frequency as the phase is controlled by the feedback loop of the PLL. The residual phase error achieved by the control loop is mainly determined by the loop gain for proportional control action ([90]). The gain of the closed control loop is in turn proportional and unique to the tuning sensitivity K_V of the chosen VCO, which therefore results in unique residual phase errors for each of the different VCOs and their settings. This automatic tuning process makes TI repeatability of the output signal very hard to achieve, even for Integer-N operation of the synthesizer under environmentally controlled conditions.

Contrary to various other synthesizers evaluated during different prototyping stages and revisions of the hardware, such as the ADF4351 and the MAX2870 fully integrated synthesizers, manual control over this calibration process with manual read- and write-back of the settings is possible for the ADF4356 family by following the procedure outlined in [6]. This special mode of the synthesizer both decreases the lock time by avoiding repeated tuning of the VCOs and restores the TI repeatability by writing the settings from a previous VCO calibration of the frequency point manually back into the PLL registers for each frequency to be locked. The other synthesizers nevertheless achieved TI stability and are still useful for switched receiver VNA linear S-parameter measurements. However, more advanced techniques, such as the measurement speed increase by sparse switched reference a-wave measurements or other applications presented later on, require TI repeatable stimulus and LO synthesizers.

The ADF4356 furthermore includes a configurable phase resync timer that is clocked by the reference clock signal ([45]). This timer allows the synthesizer to achieve a repeatable output phase even for Fractional-N output frequencies and in turn TI repeatability. Usually Fractional-N synthesizers do not allow for a repeatable output phase, as the $\Sigma\Delta$-third-order fractional interpolator used to modulate between the N and N+1 N-counter values required to achieve a fractional output frequency is continuously clocked by the

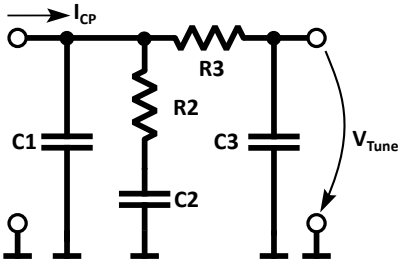

f_{PFD}	500 kHz	10 MHz
C1	82 pF	330 pF
R2	47 kΩ	3.3 kΩ
C2	560 pF	3 nF
R3	22 kΩ	8.2 kΩ
C3	33 pF	18 pF

Figure 2.43: PLL loop filter topology and component values for reference frequencies of $f_{PFD} = 500\,\text{kHz}$ and $f_{PFD} = 10\,\text{MHz}$ for a charge pump current of $I_{CP} = 0.9\,\text{mA}$ used throughout all synthesizers in the VNA.

reference clock signal without an inbuilt reset circuit.

While the N-counter is synchronously reset when a new N-value is latched into the registers, the internal counters of the ΣΔ-interpolator are not, which results in a quasi-random discrete output phase each time a frequency is locked. These random phase offsets are spaced by $\Delta\Phi = 360°/\,\text{MOD}$ degrees, with MOD being the modulus counter value configured in the PLL's registers. This problem is avoided by the phase resync timer.

When a programmable number of PFD or reference clock cycles after the latching of the new register values has passed, which is usually chosen in a way that a non repeatable phase lock has already been achieved by the synthesizer, the internal counters of the ΣΔ-interpolator are reset synchronously to the next falling or rising edge transition of the reference clock signal ([22]). This results in a repeatable output phase of the synthesizer and does not interfere with the Fractional-N locking process, although at the cost of a slightly prolonged lock-time for the frequency of interest.

The loop filters used in the embedded ADF4356 synthesizers were initially synthesized and simulated with the ADIsimPLL tool provided by Analog Devices for their PLL ICs. By testing these loop filters in the hardware, it was found by experimentation that the synthesis tool did not honor the effective change in K_V caused by switching the output dividers into the feedback loop and only a single mean K_V over frequency value was used for the synthesis and analysis of the filters. In actual operation, this resulted in an unstable frequency locking behavior of the PLL due to feedback control loop instability at certain output frequencies and erratic behavior of the output signal, even when the initial output frequency lock could be successfully achieved.

In order to design a set of custom loop filters, the typical K_V over frequency graph covering the 3.4 to 6.8 GHz base frequency range was digitized from the datasheet ([23]) and curve fitted in MATLAB. The effective reduction in K_V for each divider-in-the-loop step, shown in Fig. 2.44, was then calculated from this data and used in conjunction with the third-order passive lowpass loop filter synthesis procedure outlined in [90]. These filters were designed for PFD frequencies of 500 kHz and 10 MHz and target loop filter bandwidths of 15 kHz and 25 kHz for a fixed charge-pump current of $I_{CP} = 0.9\,\text{mA}$.

After obtaining the initial optimization component values for these two filter designs,

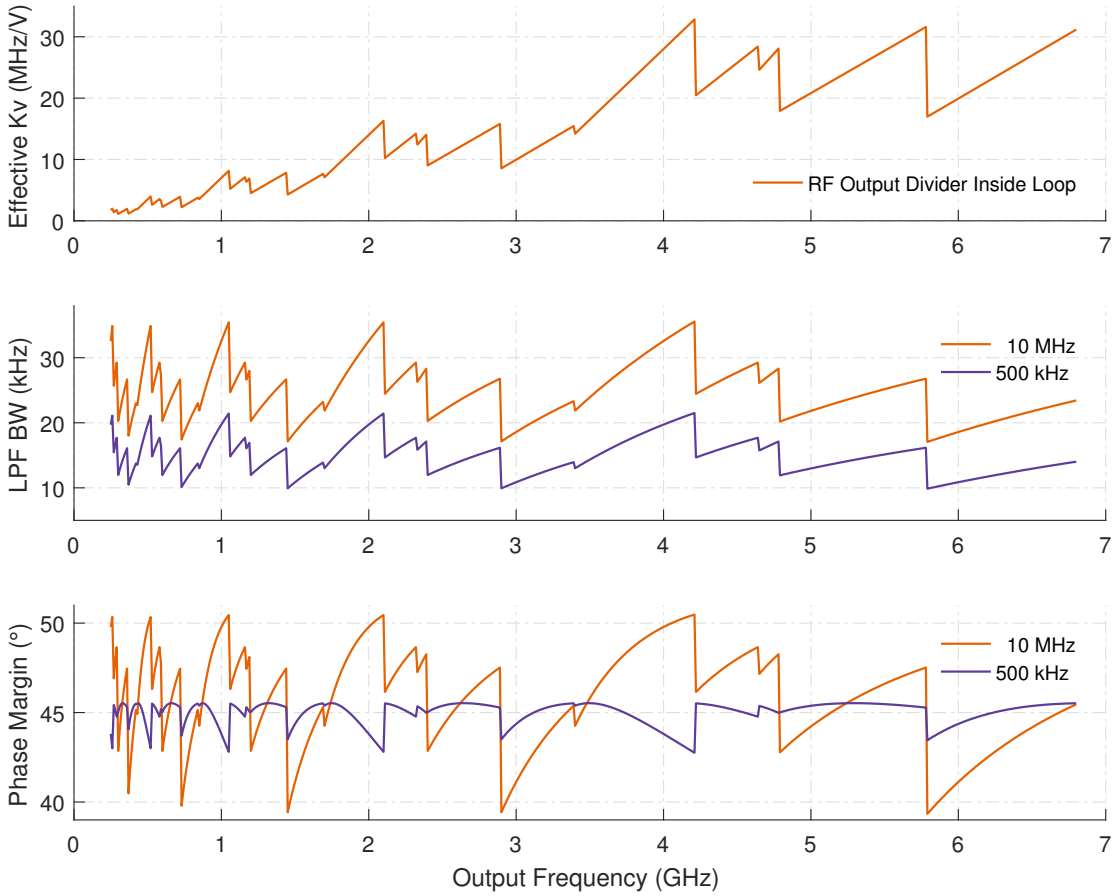

Figure 2.44: VCO tuning sensitivity, PLL loop filter bandwidth and phase margin of the control loop for $f_{PFD} = 500\,\text{kHz}$ and $f_{PFD} = 10\,\text{MHz}$ as a function of synthesizer output frequency for a charge pump current of $I_{CP} = 0.9\,\text{mA}$.

a numerical simulation of the loop filter bandwidth and control loop phase margin was carried out by combining the procedures explained in [90] with the data extracted from the K_V over frequency graph, which was extended in frequency range by calculating the influence of the output divider, to check for effective bandwidth of the control loop and the loop phase margin over frequency.

An iterative procedure of adjusting and re-checking the loop stability was used to obtain the final component values shown in Fig. 2.43. The corresponding final loop filter bandwidths and phase margins over frequency simulation results for the final iteration of both filters are shown in Fig. 2.44.

In the final design, the loop filter designed for a PFD frequency of 10 MHz is the primary choice due to its faster locking time, higher bandwidth and therefore better close-in phase noise performance, when a suitable stable reference is used. The second filter designed for a PFD frequency of 500 kHz is intended as a secondary backup for

situations, when Integer-N PLL operation of the system is strictly required. This is not possible when running the PLLs with a PFD frequency of 10 MHz due to the IF frequency of 8 MHz used in the vector receiver of the system. Therefore, either the active stimulus or the LO synthesizer in the receiver down-converter must be using Fractional-N mode to achieve mixing to this frequency in 10 MHz PFD mode.

In the actual hardware, both loop filters are selectable by software command, while the physical switching between those filters is accomplished by two low leakage, low $R_{DS,\mathrm{ON}}$ silicon analog MUX switches between the charge-pump output and the VCO tuning voltage input of the IC.

Extensive testing by an automated script, which tries to synthesize random output frequencies in the whole output frequency range and checks the lock detect status provided by the ADF4356 in conjunction with automated spectrum analyzer measurements, was carried out to ensure reliable operation of both PLL loop filter designs.

In order to characterize the spectral performance and TI properties of the synthesizers for the numerical system simulation in MATLAB presented later on, phase noise measurements were carried out with a Rohde & Schwarz FSU67 spectrum analyzer with installed phase noise measurement option for randomly chosen frequencies over the whole frequency range intended for VNA operation. For these tests, a stimulus synthesizer assembly was used. The automatic level control of the stimulus generator was disabled in software and the output was configured for maximum output power. The 10 MHz reference frequency for the stimulus generator module was provided by the OCXO integrated into the FSU67 via its external reference output.

Both Integer-N and Fractional-N mode output frequencies were chosen and close-in phase noise measurements for frequency offsets from 10 Hz to 10 kHz, as well as far-out phase noise measurements for frequency offsets from 10 Hz to 10 MHz from the carrier, were performed. The obtained single-sided power spectral density (PSD) over carrier offset-frequency plots are shown in Fig. 2.45 to Fig. 2.48.

In order to use these results for the time domain based numerical VNA system simulations, the time domain RMS jitter of the output signal must be calculated from the frequency domain measurement results.

For calculating the RMS jitter of the output signal, the total power of the phase noise over the frequency range of interest must be calculated by integration. In the VNA application here, this bandwidth covers the frequency range of 10 Hz to 2 kHz due to the IF bandwidth of the receiver. The integrated noise power can be calculated from the close-in phase noise measurements either by piece-wise integration of larger linear sections of the plot or by numerical integration of the results ([111]). If the total integrated power of the phase noise N_{PHN} present in the frequency range of interest is known and converted back into a dBc value relative to the measured carrier power, an approximation of the RMS phase jitter ϕ_{RMS} in radians ([71]) can easily be determined by

$$\phi_{\mathrm{RMS}} \approx \sqrt{2 \cdot 10^{N_{PHN}/10}}\,, \tag{2.152}$$

or by using the known frequency f_0 of the carrier to the corresponding RMS time domain

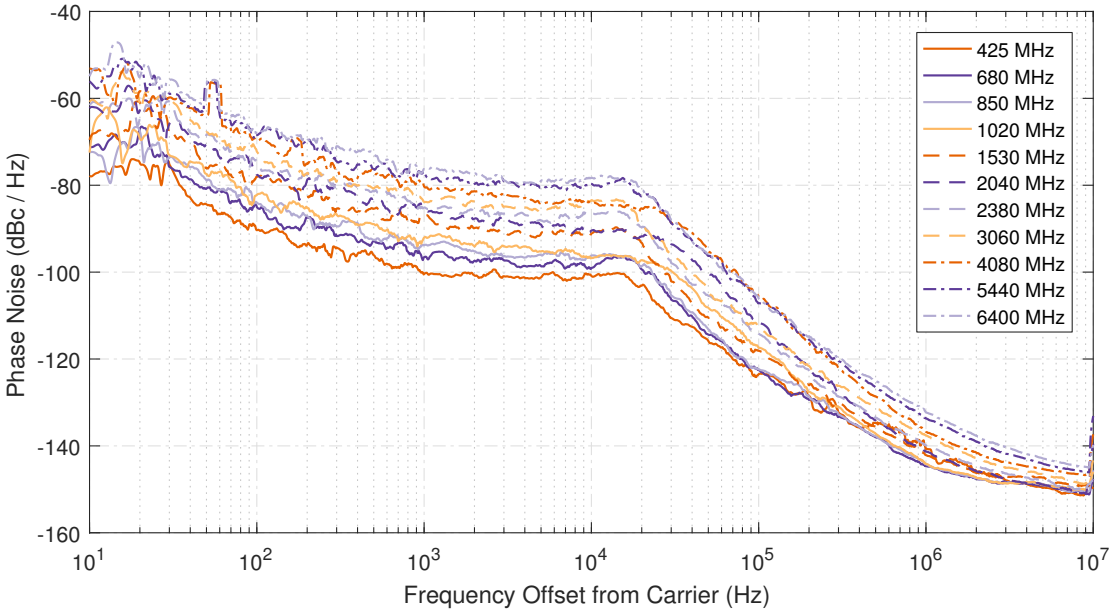

Figure 2.45: Measurement results of the wideband far-out phase noise power spectral density of the VNA synthesizers for Integer-N and Fractional-N frequencies at $f_{PFD} = 10\,\text{MHz}$.

jitter $t_{j,\text{RMS}}$ by calculating

$$t_{j,\text{RMS}} \approx \frac{\sqrt{2 \cdot 10^{N_{PHN}/10}}}{2\,\pi\,f_0}\ . \tag{2.153}$$

The results obtained for the angular phase and the RMS time domain jitter from the close-in PSD spectrum measurents of the synthesizer are shown in Fig. 2.49. The characteristics of these results are consistent with the behavior expected from inserting an ultra low jitter, or ideal, divider into the path of the signal: The measured angular jitter increases linearly with frequency, while the time domain jitter stays almost constant throughout all measured frequencies, thus verifying the performance expected from the integrated divider concept.

From the results shown in Fig. 2.49, it is also possible to determine the mean RMS time domain jitter of the synthesizers for the numerical VNA system simulation as $t_{j,\text{RMS}} = 0.548\,\text{ps}$, with a confidence of 95 % and an error margin of $\pm 0.008\,\text{ps}$.

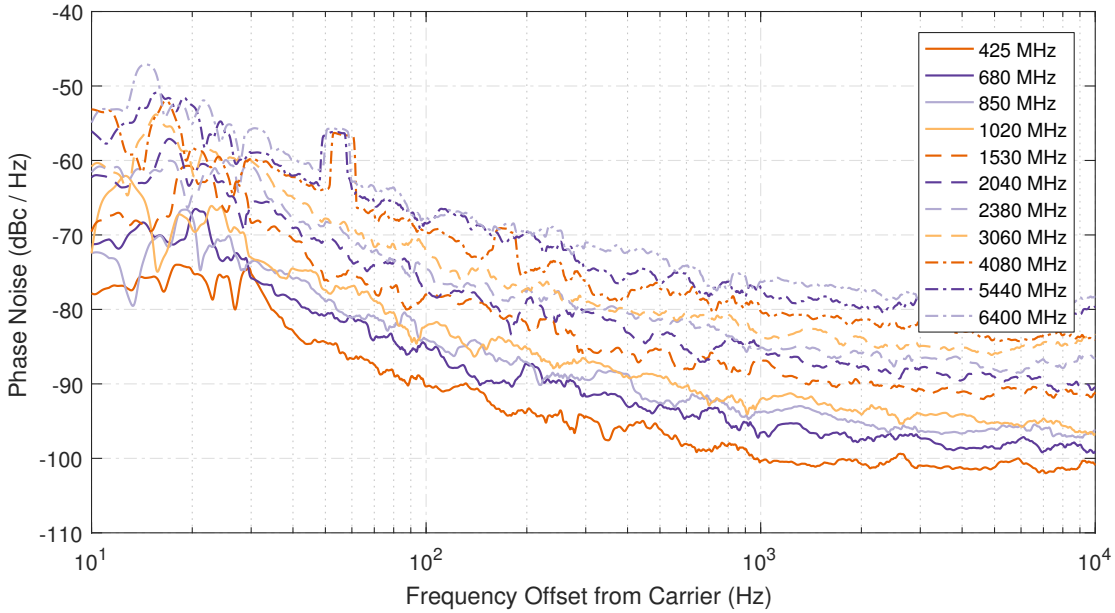

Figure 2.46: Measurement results of the wideband close-in phase noise power spectral density of the VNA synthesizers for Integer-N and Fractional-N frequencies at $f_{PFD} = 10\,\text{MHz}$.

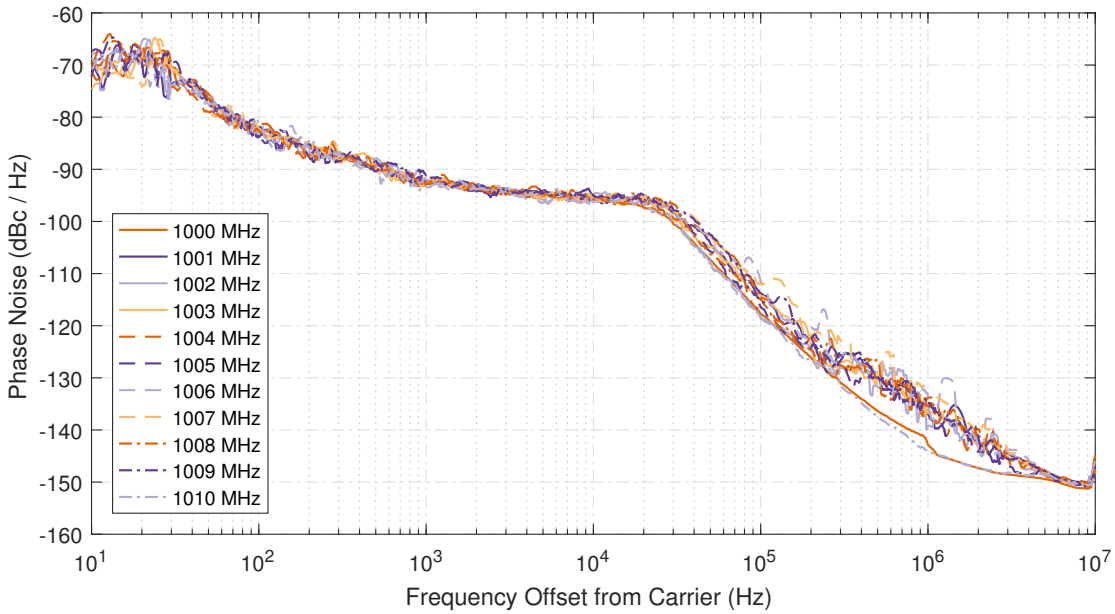

Figure 2.47: Measurement results of the narrowband far-out phase noise power spectral density of the VNA synthesizers for Integer-N and Fractional-N frequencies at $f_{PFD} = 10\,\text{MHz}$.

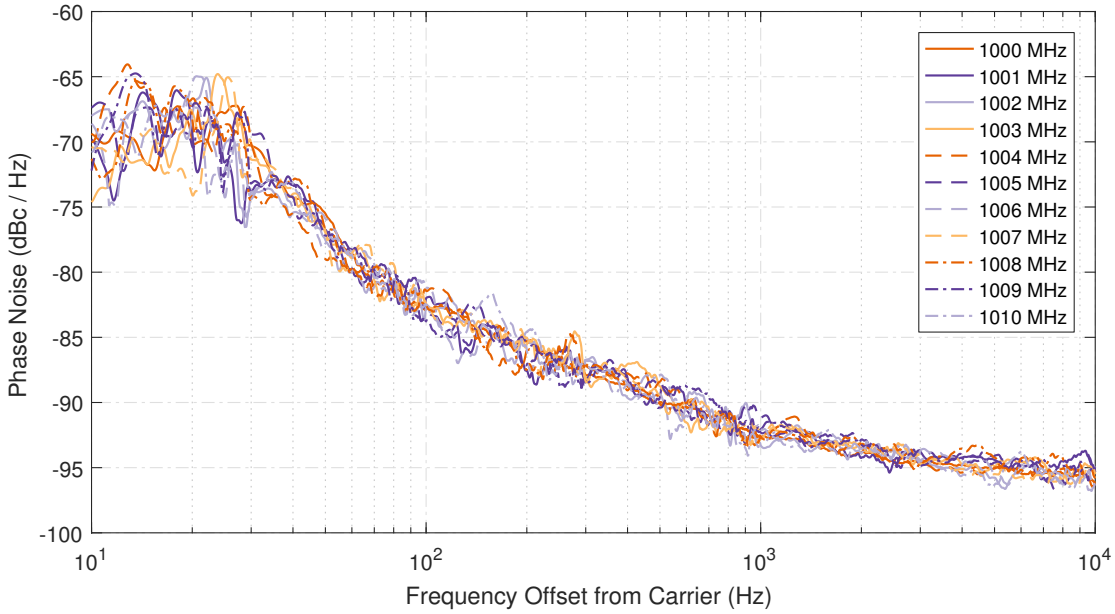

Figure 2.48: Measurement results of the narrowband close-in phase noise power spectral density of the VNA synthesizers for Integer-N and Fractional-N frequencies at $f_{PFD} = 10\,\text{MHz}$.

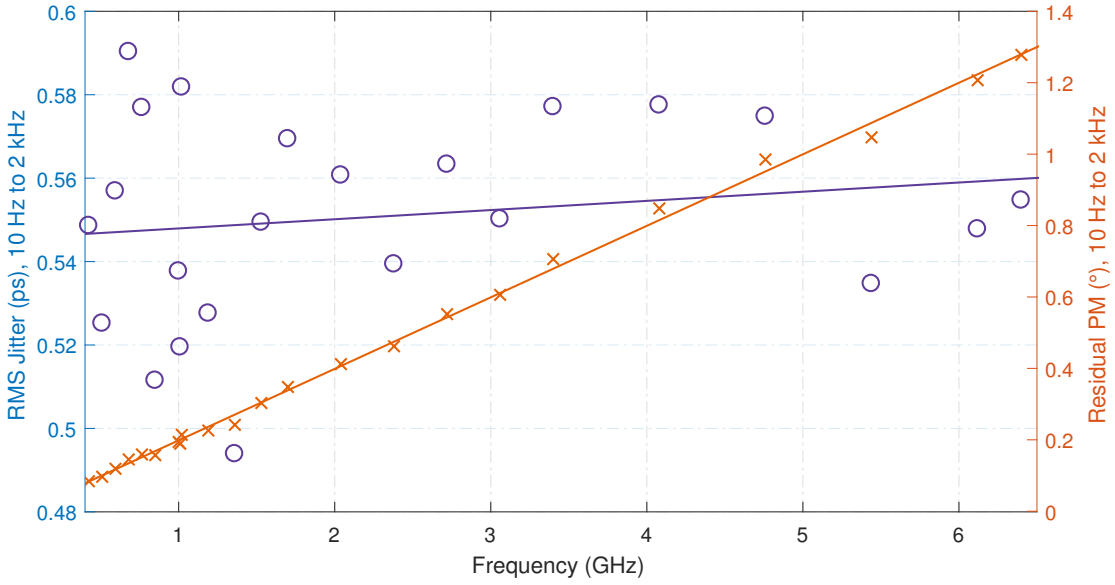

Figure 2.49: Residual phase modulation and time domain RMS jitter of the synthesizers integrated from 10 Hz to 2 kHz offset from the carrier at $f_{PFD} = 10\,\text{MHz}$.

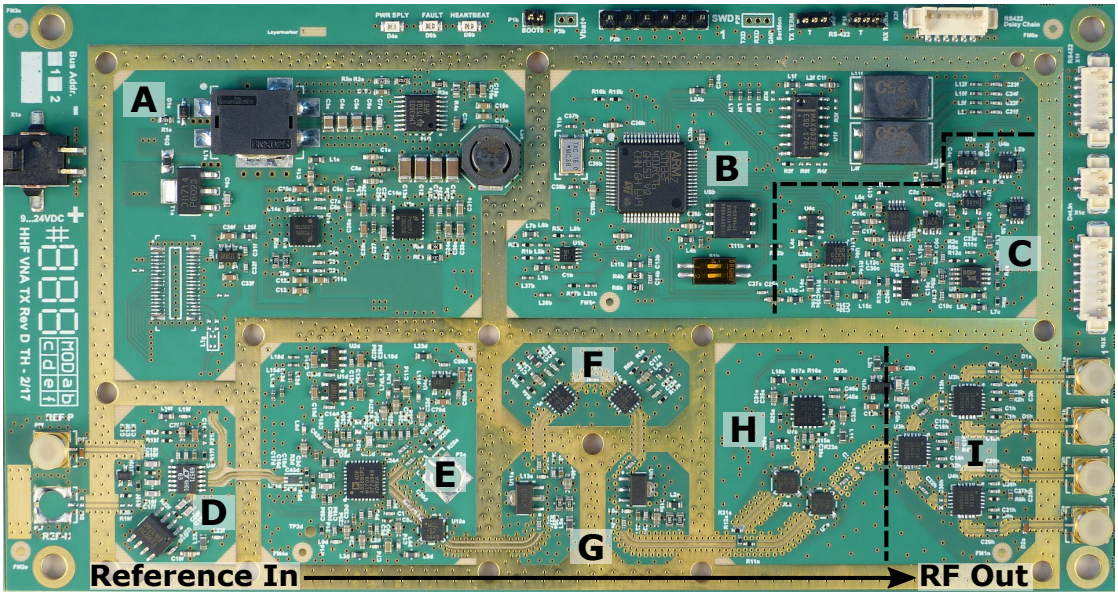

Figure 2.50: Annotated picture of the top-side of the stimulus synthesizer module. Annotations: A - power supply, B - microcontroller, RS-422 transceiver and common mode chokes, C - ADC/DAC, voltage reference and analog signal conditioning for the level control loop, D - reference input limiting amplifier with presence detection, E - RF synthesizer, F - voltage variable attenuators, G - MMIC gain blocks, H - logarithmic detector, I - PIN-diode output switches.

2.3.4 The Stimulus Synthesizer Module

In the switched single receiver VNA concept, the stimulus synthesizer module is developed as a test-bed for all other synthesizers. It is the first subsystem in the design to be completed and is used develop the required techniques to achieve TI repeatability of the synthesizers. In order to accelerate the overall development process, the module was designed to be as autonomous from the receiver module as possible to allow testing and characterization of the synthesizer, the automatic level control loop and firmware unconstrained by the progress of the much more challenging development and testing of the receiver.

An annotated picture, including highlighting of the different functional sections of the stimulus synthesizer module, is shown in Fig. 2.50, while a functional block diagram of the assembly is shown in Fig. 2.51.

The following performance figures were realized for the VNA stimulus generator module prototype:

- An output frequency range of 275...6800 MHz, smallest step-size, or resolution, 100 Hz due to communication protocol limitations in the firmware.
- Two software selectable PLL loopfilters for different synthesizer reference frequencies,

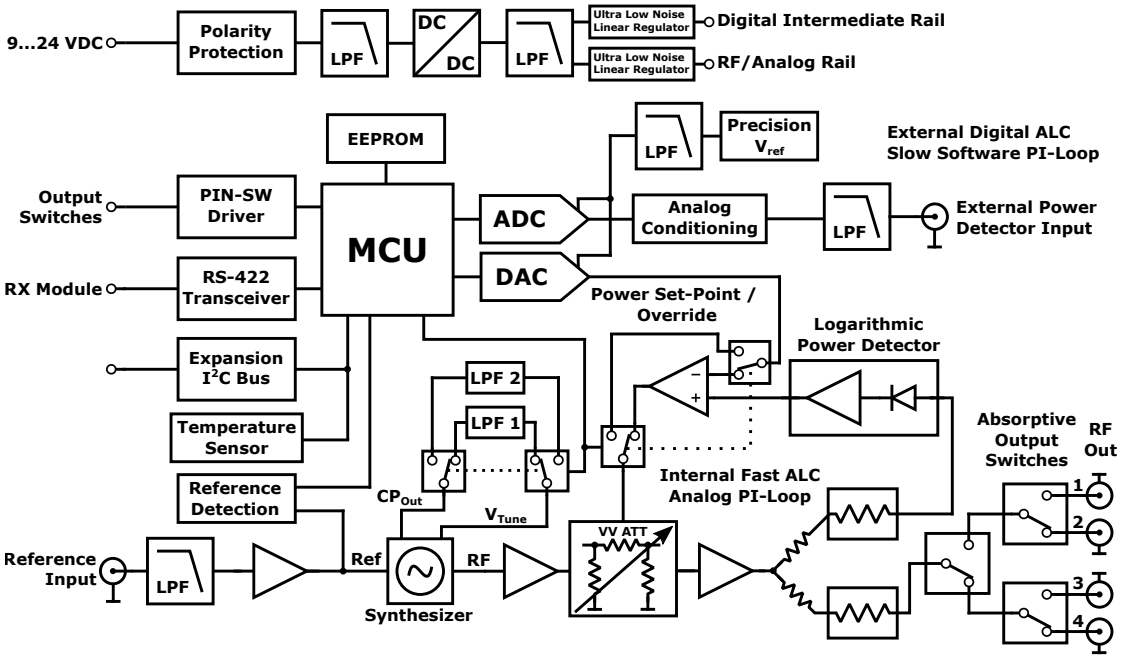

Figure 2.51: Block diagram of the stimulus synthesizer module.

currently supported 10 MHz (default) and 500 kHz as a backup.

- A leveled RF-output power range of -55...+5 dBm with 0.1 dB resolution, slightly more power is available in manual ALC override at lower frequencies.
- Support for output power calibration based upon a two point linear interpolation including data storage. The calibration is performed with 1 MHz sampling point distance over the whole output frequency range.
- An integrated high-speed analog PI-controlled automatic level control loop with a loop bandwidth of 1 MHz, and an additional software-based PI-control loop for integrating with external power detectors and amplifiers for Hot-S11 and passive intermodulation measurements.
- An internal SP4T PIN-diode switch for the output signal, which can either be used as the stimulus selector switch in less demanding applications and/or as the reference wave switch.
- Various internal self-test and diagnostics, such as multiple PCB temperatures, PLL lock status, reference frequency signal presence detection and a watchdog timer.
- A full-duplex RS-422 interface for communicating with a PC for test and characterization or the receiver module over the 2 MBaud instrument bus.

- A selectable device address for applications requiring multiple stimulus synthesizers, such as a dual generator four-receiver test-set, passive intermodulation measurements or Hot-S11 measurements. Up to 15 stimulus synthesizers modules can share one bus with the single receiver assembly.

The power supply of the assembly (see Fig. 2.50.A) re-uses general switch mode power supply concept used throughout all assemblies of the VNA system. The power consumption of the module is approximately only 6 W in full operation. The SMPS is followed by special ultra low noise linear low drop-out regulators (LDO) built for sensitive RF applications. Heat sinking for this section is provided by the aluminum clam shell case, hereby following the general system concept outlined earlier.

The ARM Cortex-M3F microcontroller (see Fig. 2.50.B) in the system runs a compact state machine written in C with a CPU core clock of 72 MHz. This state machine

- Handles all the communication via external interfaces using an ESD- and failure-hardened RS-422 transceiver,
- Controls the PLL-synthesizer and the auxiliary electronics such as the temperature sensors,
- Collects telemetry and status information of the assembly from various ICs for the BITE[34] function of the system,
- Provides sequencing and timing for the PLL-IC for manual VCO calibration,
- Integrates the software-based external ALC loop for providing leveled output power in combination with external power amplifiers and accompanying power detectors, and
- Performs the calculation of interpolated intermediate output power control set-points for the internal ALC loop using the calibration data stored in the on-board EEPROM.

The communication over the RS-422 interface is performed using a custom variable length binary datagram protocol, with the specific intend of minimizing transmission time and parsing effort for faster response times. Up to 31 sub-assemblies can be addressed on the daisy-chained RS-422 bus, with the receiver module acting as the bus-master, which asserts tasks to the other clients on the bus.

Each task/datagram is acknowledged for both reception and execution to allow for easy debugging in the system. Additionally, every acknowledgment sent by the modules includes the most important status information, such as PLL lock state and reference frequency signal presence in case of the stimulus synthesizer, coded into quick-status bit fields, which helps to reduce communication and response time for often needed status checks. Time intensive polling of information is only used infrequently for non-time critical tasks, which frees up resources in the receiver module considerably. The protocol

[34] Built-in test equipment

state machine additionally includes a simple form of congestion control to signalize the bus-master that the maximum command queue depth has been reached and the task at hand has to be re-scheduled at a later time. The bus-address and the baud-rate of the communication interface can be set via a pair of DIP-switches on the PCB to allow for a quick reconfiguration of the stimulus generator in an experimental setup.

The internal ALC loop calibration is performed by a custom calibration script written in Python, which controls both the stimulus synthesizer module over a RS-422 converter and a Rohde & Schwarz FSV7 signal analyzer via SCPI over Ethernet as the power measurement device. The output power is calibrated at two points in the dB-linear output voltage slope region of the power detector circuit using an intelligent bisection search method implemented in the python script.

This script enormously reduces the required calibration time by exploiting the continuity of the DAC set-points for a given output power between adjacent frequency sampling points and provides an educated guess for the bisection algorithm. When this simple addition is used, the number of bisection steps is reduced from 11 ± 2 to 3 ± 1 for a termination criterion of $\Delta P = 0.05\,\mathrm{dB}$ when using a 1 MHz step-size for the calibration grid. The power is measured by the FSV7 in zero span mode using frequency tracking via the calibration script. A sweep-time of 10 ms is used for the zero-span amplitude measurement and a variance analysis is carried out by the calibration script to check for instabilities in the analog ALC loop at various power levels and frequencies during the calibration, which simplifies the testing on new assemblies.

The analog signal conditioning, ADC and DAC section of the stimulus synthesizer (see Fig. 2.50.C) contains all the components necessary to provide control and feedback for both ALC loops implemented in the assembly. A precision 16-bit DAC, fed by a low-noise, active low-pass filtered and temperature insensitive reference voltage is used for the set-point control of the analog high-speed ALC loop. Various analog multiplexers under control of the state machine are inserted in key locations of the loop to ensure a fail-safe, low-power start-up of the loop for use with external power amplifiers and to allow a manual breaking of the closed analog control loop to allow for direct DAC-control of the voltage variable attenuator used as the actuator. A precision medium-speed 16-bit ADC is used to capture an active low-pass filtered external diode detector input signal to provide feedback for the software PI-control loop implemented in the state machine.

The reference frequency input limiting amplifier and the reference presence detection circuit (see Fig. 2.50.D) form the beginning of the RF signal path of the stimulus generator. The limiting amplifier allows the module to accept a wide range of power levels and signal forms for the PLL reference signal. Even low slew-rate signals can be used without significant degradation of jitter performance in the LVPECL output signal waveform. The analog bandwidth of the limiting amplifier can be controlled via the command interface to optimize the reference signal jitter for a given frequency and signal waveform. The reference frequency signal presence detection is performed on the output side of a LVPECL to CMOS buffer, which feeds an AC coupled and lowpass filtered version of the reference clock to a peak detector circuit. The DC output voltage of the detector is then sampled by an ADC and used by the controller to determine and report the reference signal status. As the diode detection is performed upon an isolated and buffered

representation of the reference signal, no adverse effects are expected to degrade the sensitive reference frequency signal presented to the synthesizer.

The synthesizer section of the stimulus synthesizer module (see Fig. 2.50.E) follows the guidelines given in introduction to the general synthesizer in chapter 2.3.3 of this work. The only difference in this implementation of the ADF4356 based synthesizer is the single ended output network in comparison with the differential output network used in the receiver. While the single ended output reduces the available output power by 3 dB, it avoids necessary baluns which would limit the usable output bandwidth for interfacing with the single ended components in the RF signal path. The resulting power loss is easily recovered in the following gain section. The implementation of the switchable loop filter is not shown in Fig. 2.50.E, as it is placed on the backside of the PCB. On the differential reference clock input side a common mode filter is used to reduce coupled interference from the clock input to improve the jitter performance of the synthesizer and to increase the attenuation for RF leakage towards the clock input. A surface mounted attenuator is used between the RF output of the synthesizer and the gain stage to stabilize the return loss seen by the PLL/VCO output over frequency to avoid frequency pulling effects on the VCO ([54]), which are more pronounced in this configuration due to the asymmetric termination of the differential PLL output.

The voltage variable attenuator (VVATT) section (see Fig. 2.50.F) provides the control action for the automatic level control loop. Two voltage variable attenuators are connected in series for a total amplitude dynamic range of 55 dB over the whole frequency range and 60 dB for frequencies below 5 GHz. The VVATTs were selected for their dB-linear control voltage slope, which matches the voltage slope characteristics of the detector and the error amplifier used to close the loop. This choice helps to stabilize the high bandwidth analog ALC loop, as the gain of the loop transfer function stays constant over all output amplitudes. Besides the direct integration into the ALC loop, the loop can be broken by multiplexers and direct control authority from the controller via the DAC can be applied to the VVATTs for diagnostic purposes and special use cases.

The MMIC gain section (see Fig. 2.50.G) is wrapped around the VVATTs in the signal path. Two ultra wideband MMIC 16 dB gain blocks with a flat gain characteristic over frequency and temperature are used for insertion loss compensation of the padding attenuator at the synthesizer output, the insertion loss of the VVATTs and following stages, while still providing a solid gain overhead to boost the output signal power at the interface connectors up to +13 dBm in un-leveled mode for lower output frequencies. Besides their obvious signal gain function, the gain blocks provide isolation for the synthesizer IC against the varying return loss over attenuation setting of the VVATTs and isolate the synthesizer against any return loss seen at the output of the stimulus synthesizer module, which greatly enhances the repeatability characteristics of the output signal.

The output signal logarithmic detector section (see Fig. 2.50.H) contains the amplitude detector as the core feedback element and the error amplifier for closing the amplitude control loop. The output signal of the synthesizer is coupled to the high-dynamic range logarithmic detector via an unequal split wideband resistive divider. While this solution is not optimal for the insertion loss presented to the output signal, it allows for a simple

directional coupling of the forward wave component over the whole frequency range of the synthesizer ([54]). The isolation of this coupler, and therefore the detector signal, against return loss changes at the output is improved by an attenuator at its output towards the DUT interface. The temperature compensated high video bandwidth logarithmic amplifier detector covers a dynamic range of approximately 60 dB and contains the integrator and the error amplifier necessary for the PI level control loop. While the detector and error amplifier is capable of much higher bandwidths, the total bandwidth of the ALC loop must be limited to 1 MHz for loop stability due to comparatively slow response of the two VVATTs. Additionally, there are digital logic safeguards in place, that inhibit any RF output of the system when the controller and its software state machine are not completely initialized by opening the control loop and forcing the VVATTs to maximum attenuation as a safe default. This seems like a minor detail at first, but this feature is extremely important in large-signal VNA applications, such as Hot-S11 and passive intermodulation measurements (PIM) which both make extensive use of power amplifiers, to prevent damage to the equipment, the DUT, and prevent injury of the operator. Should the state machine on the controller cease to execute properly, the watch dog timer of the system will reset the controller and put the synthesizer back into its default safe state of operation.

The last stage in the RF signal flow of the stimulus synthesizer is the integrated SP4T output wave selector switch (see Fig. 2.50.I). This switch allows a flexible configuration of a VNA system depending on the application at hand. While it can be used as the stimulus selector switch for non-demanding applications due to its isolation performance, it is mainly intended as an integrated a-wave selector switch for the switched reference architecture. Additionally, this output multiplexer provides an easy and convenient way to connect different test-sets, especially for high power, band-limited, stimulus applications for individual frequency bands such as Hot-S11 and PIM, to a single stimulus synthesizer without any additional external components and control interfaces.

2.3.5 The Switched Receiver Module

The receiver module (see Fig. 2.52), as the core of the VNA system used in this work, is of much more complex than the stimulus synthesizer module presented before. Therefore, its description is split into three distinct parts:

First a short overview over the system concept, its general characteristics and a look into its procedures is given. This is followed up by a separate discussion of the RF front-end, the receiver input wave selector switch and the IF amplifier chain. Finally, an overview over the clock generation, distribution and the sampling process, including the signal processing applied to the measurements, is presented due to their importance for the following numerical simulation of the synthetic VNA system.

By using the top-level block diagram of the VNA receiver and the annotated picture of the top side of the assembly, the following functional groups that make up the receiver assembly can be identified:

- The switch mode power supply, followed by low noise low dropout post regulators (Fig. 2.52.A).

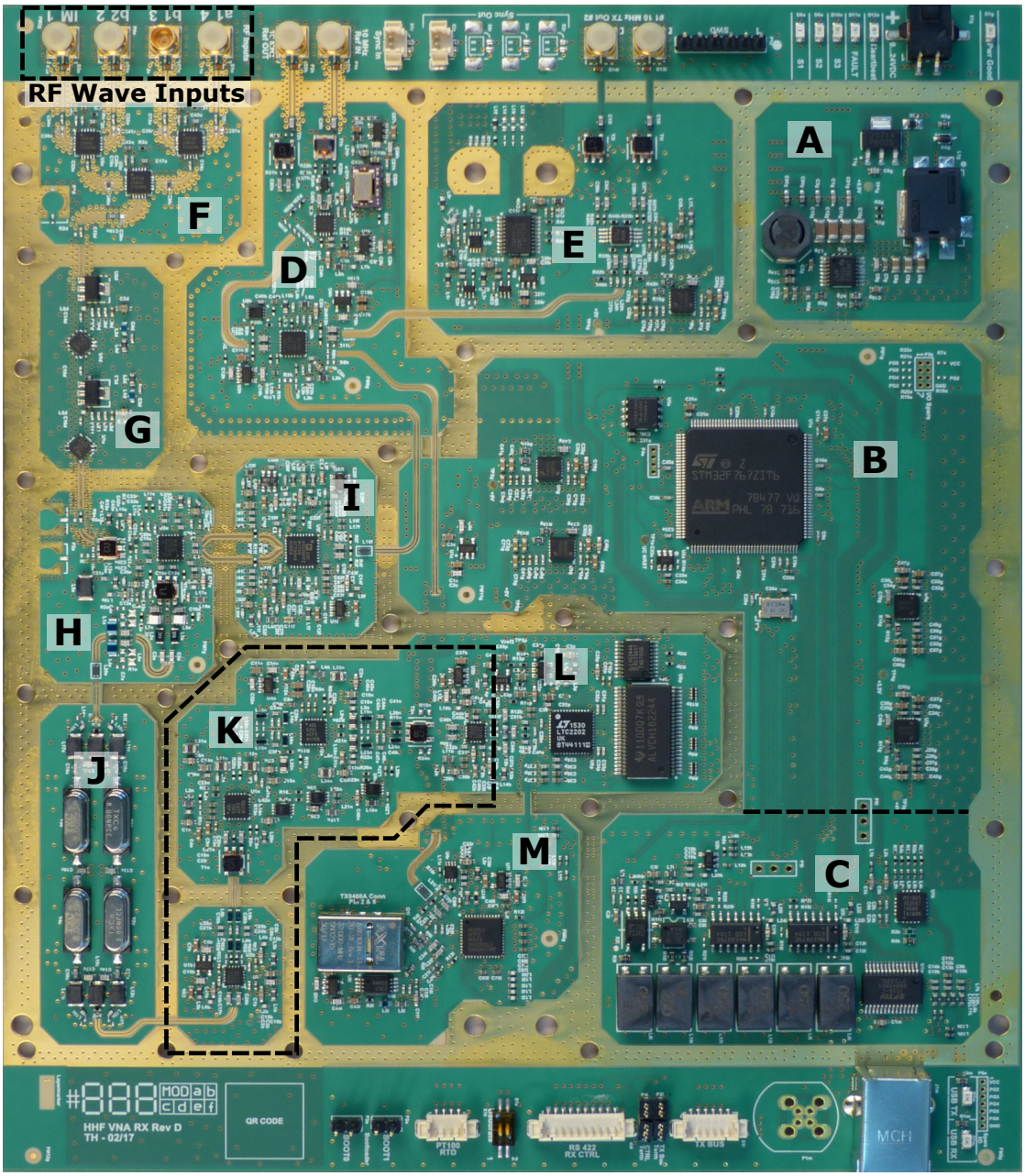

Figure 2.52: Annotated picture of the top-side of the receiver module. Annotations: A - power supply, B - ARM Cortex-M7F MCU, C - digital bus transceivers, D - system clock generation and distribution, E - reference filter & amplifier, synchronization circuits, F - receiver wave input selector SP4T switch, G - LNAs and isolation attenuators, H - active down-converting mixer, I - LO synthesizer, J - differential IF crystal filter, K - variable gain IF-amplifiers, L - sampling ADC and driver amplifier, M - TCVCXO sampling PLL.

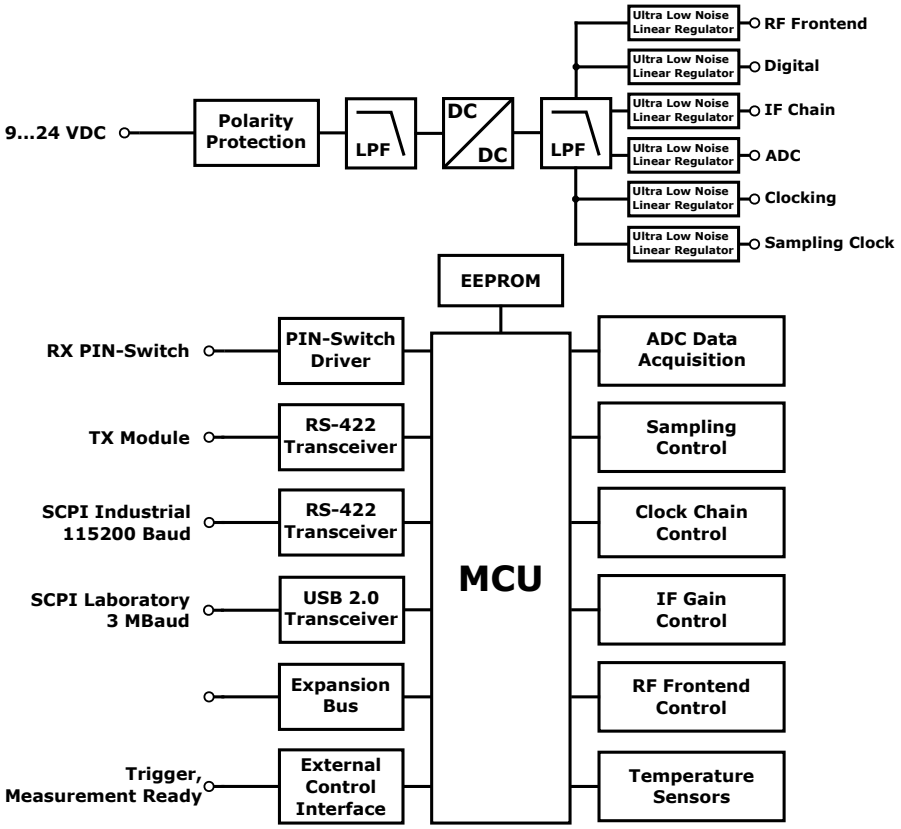

Figure 2.53: Top-level controller centric schematic diagram of the receiver assembly.

- The ARM Cortex-M7F microcontroller, which handles all of the data acquisition, communication, configuration and calculations performed by the system (Fig. 2.52.B).
- The various bus transceivers and optocouplers for communication with a PC over USB or a PLC over RS-422 and the local system bus which connects all assemblies over RS-422 (Fig. 2.52.C).
- The central system reference clock generation, source selection and distribution section, which is also the start of the system clock chain (Fig. 2.52.D).
- The synchronization multiplexing, distribution and external reference filter and amplification section, which is important to establish phase coherency in the system (Fig. 2.52.E).
- The integrated absorbing receiver wave input selector switch, as the defining feature of a switched single receiver VNA (Fig. 2.52.F).
- The isolation and low noise amplifier RF front-end gain section (Fig. 2.52.G).

- The differential active Gilbert cell high IP3 down-converting mixer including an IF pre-filter and wide-band IF termination (Fig. 2.52.H).
- The LO-synthesizer, which provides the differential repeatable LO drive signal for the down-converting mixer (Fig. 2.52.I).
- The differential IF narrow-band 8 MHz crystal ladder bandpass filter with a bandwidth of 2.2 kHz (Fig. 2.52.J).
- The differential IF gain section, consisting of two fixed gain and two variable gain amplifiers (VGA) (Fig. 2.52.K)
- The 16-bit coherent sampling semi-flash ADC running at 8 MSPS and its precision voltage reference (Fig. 2.52.L).
- The 8 MHz quadrature sampling PLL TCVCXO synthesizer, which provides a stable, coherent and ultra-low jitter sampling clock for the ADC including four configurable quadrature phase offsets (Fig. 2.52.K).

The power supply used in the receiver board is identical to the one in the stimulus synthesizer module and will be skipped here. The power consumption of the whole receiver assembly is approximately 10 to 12 W, depending on the input voltage and current state of operation.

The ARM Cortext-M7F based microcontroller on the receiver board is the central control, data acquisition and communication hub instance of the whole VNA system. The controller contains 2048 kB of embedded flash program memory and 512 kB of SRAM for data storage, integrates an IEEE-754 compliant double precision floating-point unit and an extended DSP command set, various SPI, I^2C and USART communication interfaces and numerous timers and counters. The CPU runs multiple nested state machines at a core clock of 168 MHz for command and control, measurement sequencing and data capture, telemetry data acquisition, data processing and calculation as well as a SCPI99 text command parser for remote control.

All time critical data transmissions from and to external interfaces is handled via direct memory access (DMA) transfers without CPU intervention, while important status pins are asserted interrupt functions for event capture to free up the single CPU core of the microcontroller. At the time of writing, the whole control program consists of more than 25 k lines of C code and implements over 200 different SCPI99 commands in three fundamentally different modes of device operation: Linear vector network analysis, PIM measurements and a mixed frequency harmonic vector measurement mode.

No hardware abstraction API or common interface driver libraries from the manufacturer could be used for the firmware of the CPU due to strict processing time requirements and compiler optimization issues. Instead, lean custom device drivers for the peripherals internal to the controller as well as the ICs on the PCB were written using the basic ARM CMSIS register mnemonics and abstraction libraries, which were optimized by hand from the compiler assembly code for time critical pieces of the software such as the IF data acquisition and sweep control routines.

Status data is collected regularly from all peripheral ICs and subsystems of the system and condensed into different status reports, which are either displayed on the status LEDs of the system or available over the SCPI command interface. Various self-test and status information routines where implemented to help with the debugging of the whole VNA ecosystem.

During the actual measurements, the 16 MByte/s sampling data stream from the 16-bit 8 MSPS ADC is processed and compressed into a IEEE-754 double precision phasor value as soon as possible, in order to make the best use of the fairly limited amount on embedded SRAM available on the microcontroller. Nevertheless, this limits the maximum amount of sampling points per sweep to 401 points, as enough residual RAM must be kept available for the SCPI parser and various status information flags and state machine values. Because of this limitation, no raw I/Q data is available over the communications interfaces in its current state. A detailed explanation and the implications of the repeatable non-realtime I/Q-sampling performed by the receiver will be discussed later on.

These serious limitations could be avoided in a commercial product by adding additional discrete SRAM or SDRAM to the external memory controller interface of the microcontroller. However this was explicitly avoided here for the demonstration of the scientific viability of the concept due to IC package restrictions.

The 144-pin LQFP package version of the controller used here is just barely able to cover all necessary serial and parallel I/O required by the system. If an external RAM bank was to be added, a 216-pin variant of the processor in a TFBGA package using a 0.8 mm pitch would be needed to bear the necessary spare continuous I/O banks required for the external address- and data-lines for the memory bus. Unfortunately, routing a fan-out of a BGA package of this pin density is simply not compatible with the design restrictions imposed by the 4 layer mixed RF and FR-4 PCB manufacturing process used for this work. Switching to a higher layer count of the board, while technically feasible in full-scale production, was quickly discarded due to the exponential increase of the manufacturing costs associated with special layer stack RF prototype PCBs in small quantities and the diminishing scientific return obtained from sweeps with sampling point counts of more than 401 points.

Trigger and measurement status indication is provided over the SCPI command and control interfaces as well as two dedicated opto-isolated status lines for trigger initiation and measurement status indication, and augmented by status LEDs on the PCB. While a single sweep mode after trigger initiation is the default setting, as it is standard with SCPI instrumentation due to synchronization, various other trigger modes such as continuous trigger, timer based repeating trigger and automatic re-triggering after error recovery are implemented.

The measurement results are normally sent as ASCII text via SCPI in the usual SCPI challenge-response procedure and are provided in real- and imaginary part, linear magnitude and phase as well as dB-scaled magnitude and phase representation. For time-critical applications an autonomous hexadecimal coded binary streaming mode is configurable to send the raw double precision floating point sampling phasor data during the PLL lock and dwell-time pauses for the consecutive sampling points. While

this violates the standard implementation rules for SCPI, this results in a considerable improvement in measurement speed.

For the configuration of the measurement setup all standard commands for number of points, start, stop, center and span frequencies are implemented to fill the stimulus frequency table in either a linear or logarithmic fashion. As an alternative, each stimulus frequency point can be edited manually after the auto-fill procedure or all measurement frequency points can be set manually altogether. Furthermore, the stimulus power can be set individually for each frequency sampling point, which in combination with the total flexibility in the stimulus frequency table, allows for very complex measurement scenarios to be performed in one single sweep of the VNA. Two different additional sweep tables are available in the two-tone PIM / Hot-S11 mode to allow for freely configurable two-tone stimuli frequencies and individual power settings as well as the actual receiver measurement frequency.

The central state machine of the receiver also performs the VCO calibration initiation and central data collection required for the phase repeatable operation of the ADF4356 synthesizers for all frequency points and all synthesizers throughout the system. This includes, if configured, the harmonic frequencies for the receiver or other sweep plans for the second stimulus synthesizer.

For the normal linear VNA mode, several sub-modes with varying degrees of data capture autonomy are programmed for different test-set configurations, which are mainly implemented for PLC control of the VNA. These special modes were not used for the measurement presented throughout this work to avoid additional sources of error. Instead, a full scan of all four virtual wave receiver channels was always performed for a measurement, regardless of the actual number of connected test-set waves. While this procedure does not reflect realistic measurement times, it ensures the consistency of the data delivered by such a complex embedded prototype system.

2.3.6 The Receiver RF Front-End and IF Section

While the receiver components mentioned before are essential for the operation of VNA system, they are not the performance relevant components of a high dynamic range vector receiver system, which is even in this day and age of software defined radios and instrumentation mostly defined by the hardware characteristics of the RF and IF subsystems.

The vector receiver of this system was designed as a direct conversion, double sideband (DSB), high IF frequency receiver. No image or mirror rejection of the unwanted sideband is performed. A schematic block diagram of the RF and IF signal path components is shown in Fig. 2.54.

While the use of DSB conversion may seem to be an unconventional choice for a frequency domain RF measurement device at first, and would certainly not be tolerable for a spectrum analyzer front-end, this architecture is a popular choice for VNAs. A VNA is generally designed and expected to measure only the response to its own known stimuli signals and can therefore apply priori knowledge about the expected response of the DUT. As the frequency of the response can be assumed to be precisely known, no frequency

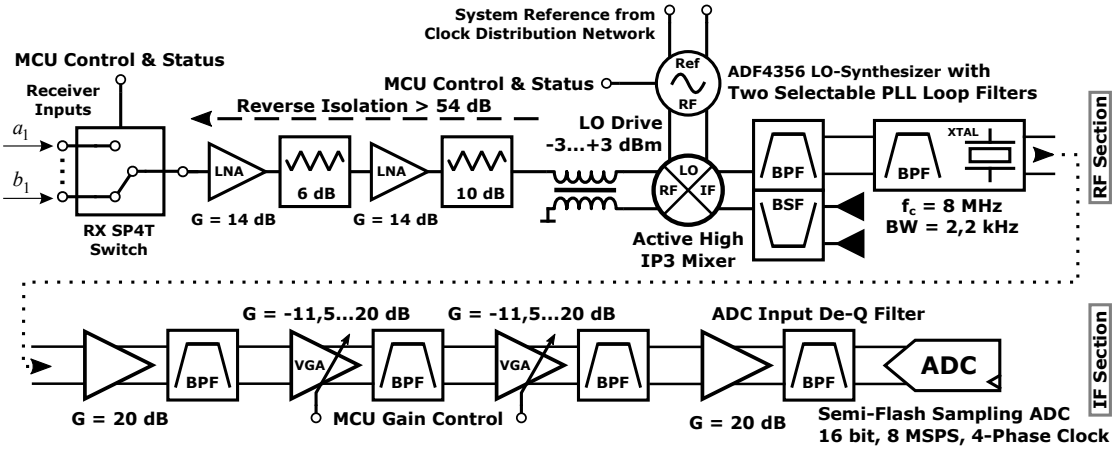

Figure 2.54: Schematic block diagram of the wide-band RF and 8 MHz IF path of the switched VNA receiver

ambiguity problems arise. This even holds true for non-linear measurements of devices, as the underlying model function, which for example follows a square or cubic transfer function, allows solving for this uncertainty and provides hints for careful frequency and LO-side planning.

The double side-band down-conversion requires fewer frequency converting components, such as mixers, compared to dual or triple conversion (superheterodyne) concepts, which is generally favorable for the overall system spurious signal and linearity performance. This is especially true for the third order intercept point of the system that is important for PIM measurements. Additionally, this DSB down-conversion front-end reduces the amount of system complexity and BOM cost due to fewer synthesizers or fixed frequency low phase noise oscillators and high quality filters in the system. While an I/Q image rejection mixer based front-end could be used instead if the simple DSB conversion used here, it is hard to achieve multi-octave bandwidths in this architecture due to the limited bandwidths of the necessary phase shifters and couplers ([53]).

In contrast to a normal VNA receiver, which would begin its RF signal chain with an amplifier to provide both gain for the input signal and isolation for the LO-leakage of the mixer, the first item in the RF signal chain shown in Fig. 2.54 is the defining component of the overall single receiver VNA concept: The receiver input wave selector switch.

Following the theoretical analysis of the concept, this switch needs to:

- Be well-matched on all ports, especially for the isolation states of the inputs,
- Show good return and low insertion loss for the selected path,
- Be repeatable in the transmission characteristics of the switch states so the state dependent TI criterion is fulfilled, and
- Provide sufficient isolation between the input wave ports.

While selecting a suitable integrated RF switch IC to multiplex between two wave inputs is a fairly straight forward task, selecting a single IC capable of handling three or more inputs involves far more design choices and possible realization issues due to the physical proximity of the additional ports and the required matching circuits. At the time of writing, absorbing SP2T switches, which must include additional internal switches to either connect the RF input to the common output port or an internal 50 Ω (or 75 Ω for CATV) termination, have caught up to the internally much simpler reflective SP2T switches in terms of insertion loss and isolation performance in the lower microwave frequency ranges below 8 GHz.

This is unfortunately not true for semiconductor switches with a higher count of inputs, where the much simpler reflecting design of the RF switch still shows considerable better performance characteristics than its absorbing counterpart, if they are available at all. Nevertheless, even the reflecting SP3T or SP4T semiconductor switches generally perform worse in terms of isolation between inputs when compared with their SP2T counterparts. While this effect can be somewhat influenced by the internal semiconductor design of the switch, it ultimately comes down to the finite isolation of the input and output transmission lines themselves, which have to be brought in close proximity to each other to connect with the PCB land pattern of the SMD package of the switch. While amount of achievable isolation can be influenced to a certain degree by the choice of transmission line technology and the routing of the signals, they ultimately have to connect to the same IC die.

Therefore, the input wave selector switch is generally built in a cascaded multi-stage fashion to achieve the intended performance specifications. Cascading multiple switches can considerably increase the isolation between the wave inputs, but each additional stage in turn lowers the repeatability of individual transmission paths, which presents an interesting optimization problem. A comprehensive analysis of receiver input wave selector switch performance metrics and its required design trade-offs can be found in [125]. If the amount of cascaded switch stages for a SP4T topology is limited to a maximum of two subsequent switches, two distinct topologies using different types of switches are possible: The first option is a H- or star-topology, as presented in [125], that uses individual SP2T switches for each wave input port to connect or isolate them to or from a central SP4T switch, which in turn connects to the single receiver. Absorption is provided by the SP2T switches, while the central SP4T switch can be reflective for increased isolation. Therefore, four SP2T switches and one SP4T switch are needed.

In this work, an Y- or tree-topology is used, which only uses absorbing RF switches and the conclusions about the influences of the cross-talk paths obtained by the switched reflectometer analysis to reduce the number of individual switches down to only three absorptive SP2T switch ICs. A graphical explanation of the different topologies, including a picture of the actual realization on the receiver assembly, is shown in Fig. 2.55.

The cross-talk coefficients of this Y-topology receiver input wave selector, which were obtained from the direct wave based calibration and correction procedure, are shown in Fig. 2.56. It is difficult to compare the results presented here with the isolation performance of the H-topology shown in [125], as this implementation was measured without an appropriate RF shielding enclosure and therefore is lacking much of the

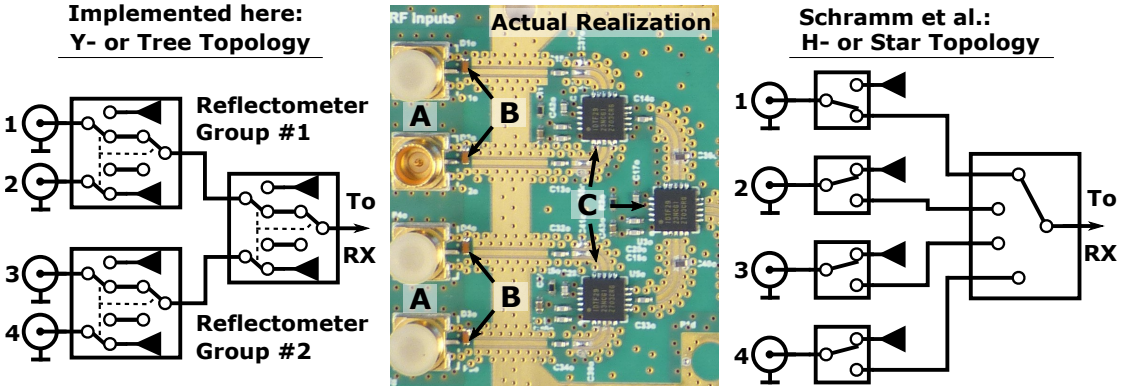

Figure 2.55: Front-end receiver wave selector switch topologies. Left: Schematic of the Y-switch topology used for the receiver wave selector input switch. Center: Picture of the actual implementation on the receiver PCB. Right: Schematic of the H-switch topology used by Schramm et al. ([125]). Annotations: A - SMP RF input connectors, B - RF polymer ESD surge protectors, C - IDT F2923 absorptive constant impedance SPDT switch IC.

transmission line coupling and stray field effects influencing the isolation performance, as most of the energy is radiated into free-space and not loosely coupled into the cavity formed by an EMI enclosure. While omitting the enclosure offers a nice increase in isolation and measured return loss on paper, this method is a far cry from usable for real world measurement applications.

The reduction in part count for the Y-topology however comes at a price: While the symmetrical H- or star-topology realizes almost identical isolation figures between each of the wave input ports, when all switches and especially their individual isolation values are assumed equal, the Y- or tree-topology will always show an asymmetrical distribution of the isolation for a given port. This may seem like a serious disadvantage at first, but when the conclusions of the switched single receiver reflectometer discussion are taken into account, it can be reasoned that the a_1 and b_1 waves of a stimulus applying reflectometer have far more relaxed isolation requirements than the high dynamic range a_2 (for switch-terms measurement) and b_2 waves of the receiving reflectometer, and vice versa.

This observation makes it possible to define reflectometer wave port groups in the input switch layout, which are allowed to have a lower isolation between their associated waves, compared to the rest of the test-set, and can therefore share a common switch IC, as shown by the reflectometer groups 1 and 2 in Fig. 2.55. The second switch stage then selects and isolates these reflectometer groups from each other, which allows a much more scalable realization in terms of both PCB space and BOM cost in the case of a higher port count VNA variant. The isolation in a local reflectometer port group can be considerably enhanced by the use of the switched reference wave technique presented earlier.

Nevertheless, careful planning must be made when using the Y- or tree-topology with

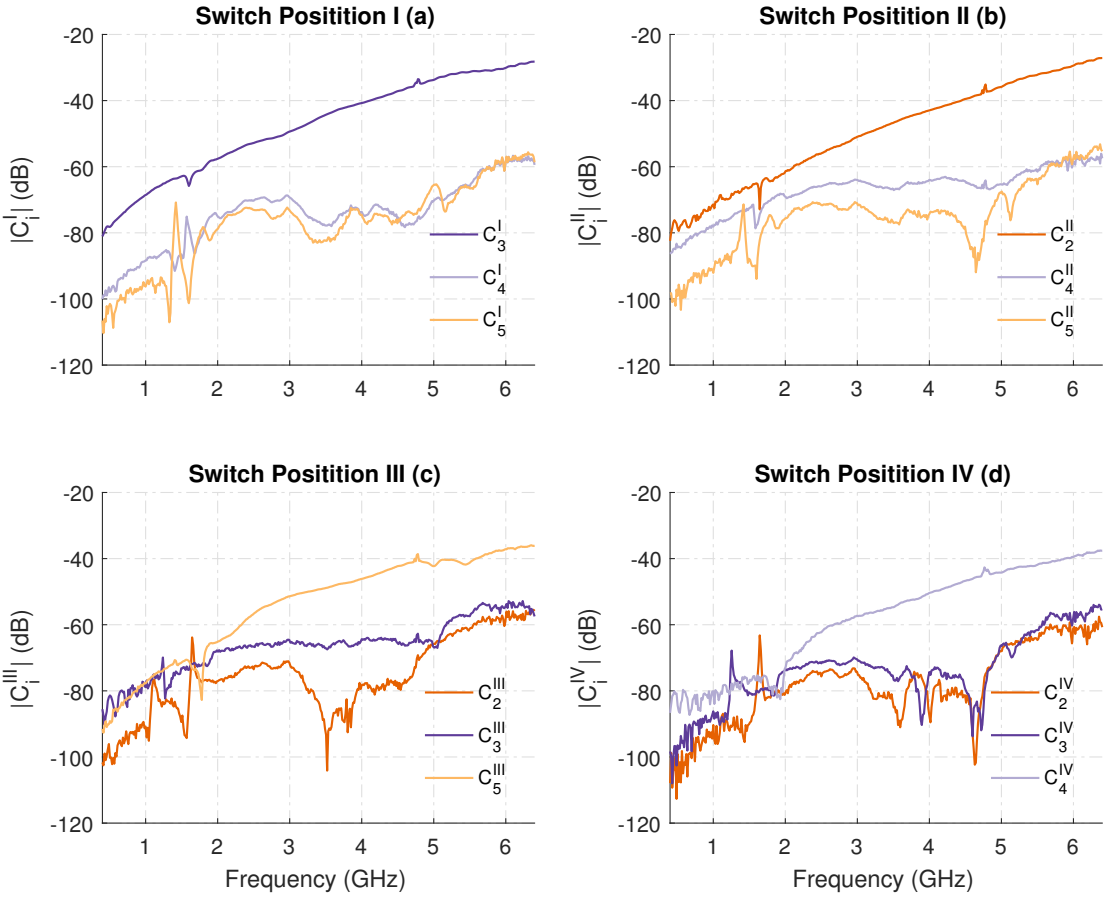

Figure 2.56: Measured magnitude of the cross-talk coefficients of the front-end receiver input wave selector switch with clam shell enclosure installed over the frequency range 400 MHz to 6400 MHz using the direct wave based calibration method presented in chapter 2.2.10.

incomplete reflectometer test-sets, such as the three-receiver test-architecture, in dual side stimulus operation. While (5+2)-term measurements in forward stimulus will just work fine in this case, as the strict wave assignments to a specific reflectometer group are still obeyed, this is not the case during reverse stimulus with (10+4)-term measurements under the same circumstances.

In this situation, the sole a-wave of the three-receiver test-set shares its SP2T switch with the transmitted b_1 wave of the DUT in the Y-topology and not its corresponding b_2 wave for reverse stimulus, therefore leading to a greatly reduced dynamic range under these circumstances. While some influence of the cross-talk can be reduced by the (10+4)-term calibration and correction, especially when combined with the switched reference technique, its still advisable to use the H-topology for the three-receiver test-set architectures.

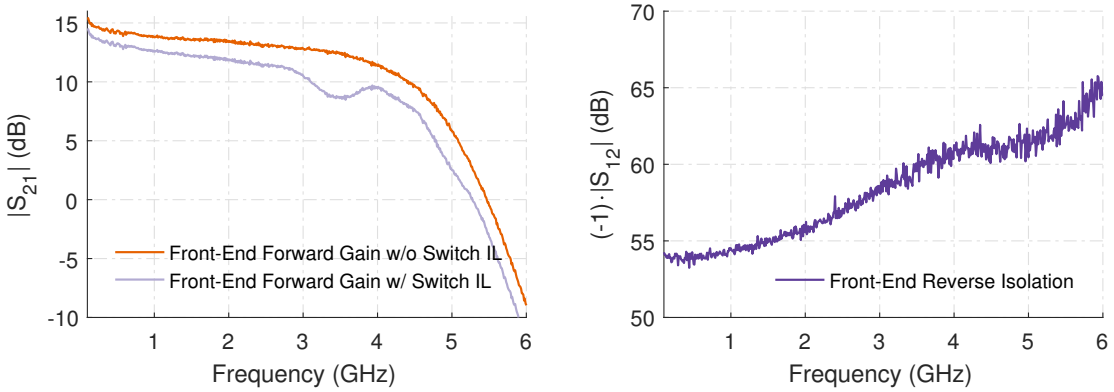

Figure 2.57: Simulated receiver front-end gain and reverse isolation at the RF input of the down-converting mixer.

The IDT F2923 SPDT switches used for the hardware realization of the concept also have an important additional internal sequencing feature that lends itself towards their use in a single receiver VNA input wave selector switch: Their multiple internal SPDT switches are synchronized in such a way, that the change in return loss seen at a port during state transition is minimized and therefore unintentional source- or load-pulling to an active DUT, the front-end amplifiers of the receiver or external low noise amplifiers in the test-set signal path, are avoided. This would usually be the case with other absorbing semiconductor switches, as they follow the break-before-make convention and present an open circuit on the ports during the state transition phase, which can lead to adverse effects when conditionally stable active devices are either used in the signal path or are measured as a DUT.

The receiver wave input selector switch is followed by a combined low-noise amplifier (LNA) and isolation stage (see Fig. 2.54 for reference), which was carefully optimized for the contrary design goals of a low noise figure over a multi-octave bandwidth, a constant gain curve over frequency, high linearity and good input return loss, while still keeping the total power consumption at bay and providing sufficient isolation against LO-signal leakage into the test-set. The combination of these design goals was met by cascading two special purpose 14 dB gain MMIC LNAs, with a noise figure of 1.6 to 2.6 dB in the frequency range of 500 to 4000 MHz, with an additional 6 dB attenuator added after the first amplifier and a 10 dB attenuator after the second amplifier. This combination stood out as a local optimum in isolation and total noise figure in iterating over Friis's formula ([54, 99]) for different possible combinations of amplifiers and attenuators for this task. The front-end performance figures for this topology is shown in Table 2.5, which includes all components of the input path up to the mixer input balun, while the gain and isolation is shown over a larger frequency range in Fig. 2.57. Even at the isolation minimum of 54 dB provided by this stage, the total-receiver LO-signal leakage is reduced to less than -90 dBm over the whole frequency range, referenced to the switch input.

The frequency conversion from the RF to the 8 MHz IF frequency is performed by an

f (MHz)	**500**	**900**	**1900**	**2700**	**3500**	**4000**
Gain (dB)	13.3	13	11.9	11	10.2	10.1
IP1dB (dBm)	-2.1	-2.1	-1.7	-1.8	-1.2	-2.6
OP1dB (dBm)	10.2	9.9	9.2	8.2	8.0	6.5
IIP3 (dBm)	17	16.9	17.9	14.6	12.4	8.3
OIP3 (dBm)	30.3	29.9	29.8	25.6	22.6	18.4
NF (dB)	3.2	3.4	3.9	4.4	5.9	5.5

Table 2.5: Front-end RF signal chain performance figures. Calculated from the RF input wave selector switch up to the mixer input.

active, highly linear, double balanced and fully differential mixer core, which includes both limiting amplifiers for the LO drive signal and an integrated first IF amplifier to compensate for the conversion losses of the mixing process and to provide higher IF to RF isolation. While an automatic bias adjustment that adjusts the current depending on the input signal amplitude is possible for the active mixer core as a power saving measure, this feature is disabled and the bias is manually set to the highest permissible current to ensure a constant linear and repeatable transfer function, regardless of the applied input power. The conversion of the single ended RF input signal to the differential signal required for the mixer is performed by a special, device matched, transmission line balun to maximize the usable bandwidth and minimize the return and conversion loss over the whole input frequency range of the mixer. The return loss presented to the isolation amplifier stage was furthermore manually optimized for the specific implementation on the PCB layout with additional tuning capacitors on the differential output side to enhance its return loss performance above 3 GHz. Due to the limiting LO amplifiers in the mixer and the differential output of the synthesizer, no additional level control circuitry or balun is needed on the LO-drive side of the circuit. The limiting amplifiers allow for a LO drive level of 0 dBm $\pm$ 10 dB without any significant change in mixer conversion performance, which would be impossible to accomplish by using a passive double balanced diode ring mixer alone, and therefore significantly reduce the BOM cost and space requirements for a high bandwidth LO drive signal.

The mixer was additionally chosen for its silicon-germanium (SiGe) semiconductor manufacturing process, as SiGe exhibits a much lower 1/f or flicker noise corner frequency than silicon and especially gallium-arsenide based semiconductors and allows the 8 MHz IF frequency to be in the constant thermal Gaussian noise section of the output power spectral density spectrum, therefore lowering the effective noise power contribution in the IF filter pass band considerably ([123]).

Similarly, the design of a system with a fairly high IF frequency of 8 MHz without further down-conversion for sampling was also determined by the amount of flicker and $1/f^2$ Brownian noise added to the signal by the IF amplifier stages and in the ADC analog front-end, the $1/f$ and $1/f^2$ noise present in the supply voltage rails and the good availability of repeatable precision AT-cut fundamental mode crystals with low initial tolerance and temperature coefficients for this specific frequency.

f (MHz)	**500**	**900**	**1900**	**2700**	**3500**	**4000**
Conv. Gain (dB)	13.2	12.8	11.2	10.0	9.9	9.5
IP1dB (dBm)	-4.4	-4.2	-3.4	-3.1	-2.7	-3.7
OP1dB (dBm)	7.8	7.5	6.8	6.0	6.2	4.8
IIP3 (dBm)	14.3	13.1	14.4	11.9	11.4	7.1
OIP3 (dBm)	27.5	25.8	25.6	22.0	21.3	16.6
NF (dB)	6.7	6.7	6.6	7.0	7.5	7.3
NF+SSB (dB)	9.7	9.7	9.6	10	10.5	10.3

Table 2.6: Front-end RF to IF signal chain conversion performance figures. Calculated from the RF input wave selector switch to the IF output of the mixer before the impedance conversion triplexer filter. NF+SSB describes the effective total noise figure of the DSB mixing process with 3 dB added for the noise power of the additional unwanted sideband.

The 200 Ω differential IF output of the mixer is terminated in an impedance converting triplexer network that provides a narrow-band differential impedance conversion from 200 Ω to the 100 Ω impedance used for the 8 MHz IF signal and a matched broadband termination otherwise. This choice improves the wide-band performance of the mixer considerably by avoiding the re-mixing, or upconversion, of out of band IF signals reflected from the IF filter with the LO signal in the mixer and provides a first, fairly broad, pre-filtering of the 8 MHz IF signal.

Any residual common mode signal is attenuated by a common mode choke before reaching the main differential 8 MHz crystal-based IF filter.

The differential 2.2 kHz wide crystal filter is critical for the VNA selectivity and a low system noise figure and was designed from scratch by characterizing suitable 8 MHz low tolerance AT-cut fundamental mode crystals and fitting their equivalent circuit diagram as a starting point for the classic Dishal crystal ladder filter synthesis procedure ([24, 25]), which resulted in a single ended initial design of the filter. This single ended filter was then converted to its differential implementation by applying the circuit mirroring conversion method ([54]) and subsequently optimized in Keysight ADS ([142]) for the following key aspects:

- A flat differential pass-band response around the center frequency,
- A low differential pass-band insertion loss for lower system noise figure,
- High differential and common mode stop-band attenuation up to the upper frequency limit of the mixer's IF output of 600 MHz and especially the analog bandwidth of the sample and hold circuit in the ADC of 380 MHz,
- Good differential stop-band attenuation up to the maximum LO and RF frequency of the receiver to attenuate RF-IF and LO-IF leakage, and
- A steep filter pass-band skirts to match the effective noise bandwidth with the usable signal bandwidth of the filter.

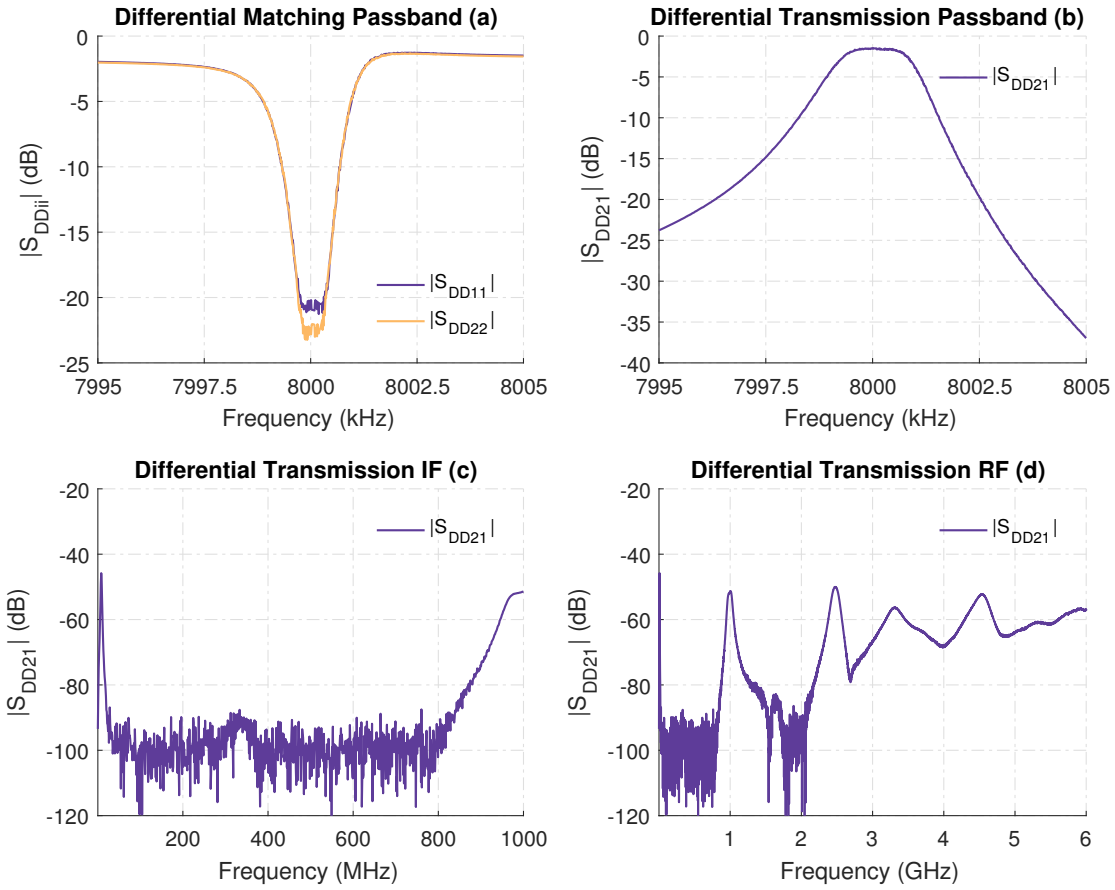

Figure 2.58: Measured differential narrow- and wide-band selectivity performance of the crystal-based 2.2 kHz wide filter for the 8 MHz IF frequency.

The measured performance characteristics of the final iteration of the filter are shown in Fig. 2.58. A differential pass-band insertion loss of 1.6 dB was achieved for a filter bandwidth of 2.2 kHz centered around the 8 MHz IF frequency.

Using estimated insertion loss of approximately 1 dB for the impedance conversion network at the IF output of the mixer, a mean noise figure of $F = 10$ dB can be estimated for the down-converted 2.2 kHz (33.4 dBHz) section of RF signal spectrum after the IF filter.

The IF filter is followed by a variable gain amplifier stage, which has a software selectable gain of $G_{IF} = 17 \ldots 80$ dB, adjustable in 0.5 dB increments via the SCPI command interface. This amounts to a total system gain, from the switch input to the analog to digital converter, of $G_{sys} \approx= 27 \ldots 90$ dB. The IF amplifier chain consists of four cascaded amplifiers in total and begins with a fixed 20 dB differential high linearity IF amplifier to minimize the impact of the variable gain amplifiers (VGA) upon the overall noise figure of the receiver. The following two amplifiers realize the variable gain of the IF chain with a configurable gain setting of $G_{var} = -11.5 \ldots 20$ dB each. The IF

chain is then completed by the low impedance output ADC driver amplifier.

An analog control voltage interface for the VGAs was explicitly ruled out at this point in the IF chain due to the high chance of interference coupling into the control lines, which would result in an unintended AM-modulation of the received signal.

Each of the amplifier stages is coupled by LC-bandpass filters centered around the IF frequency to reduce the influence of amplification of the wide band IF amplifier noise on the narrow band IF signal.

The ADC front-end filter is designed as a low impedance, low-Q filter to attenuate the step response of the filter to the rapidly changing ADC input impedance caused by the switching action of the sample and hold circuit and the sampling capacitor in the ADC.

Later testing revealed, that the quality factor of the noise reduction filters in the implementation of the hardware used to perform the measurements presented in this work was unfortunately not high enough, which resulted in an elevated noise figure on the measurements for gain setting above $G_{IF} \approx 40\,\mathrm{dB}$ due to amplification of 1/f and thermal noise. This effect manifests itself as a 1 MHz wide noise skirt around the IF signal, originating from the IF amplifier chain and consistent with the measured bandwidth of the LC-filters. While this can be corrected for in digital post-processing of the signal by applying digital filters, this also increases the number of samples required for the same S/N considerably and will be corrected in a later revision by replacing all but the low-Q ADC front-end LC-filter with 20 kHz wide ceramic resonator filters tuned to the IF center frequency. A reduction in integrated noise power of 17 dB for the highest VGA gain setting is expected by this measure, increasing the system sensitivity and the number of required samples for the same SNR considerably.

2.3.7 Clock Generation, Distribution, IF Sampling and Signal Processing

In order to describe the sampling process used in the vector receiver, it is at first necessary to look at the clock generation and distribution chain as a whole, due to their interwoven nature in the overall system design and the compromises that must have been accepted to keep the amount of digital signal processing on the Cortex-M7F core at a minimum. A base frequency of 10 MHz is used for the clock chain to facilitate compatibility with existing measurement equipment and the good availability of precision low-jitter and low phase noise crystal oscillators for this frequency required for stand-alone use of the system. Furthermore, this specific base frequency allows external high stability reference source such as OCXOs, GPS disciplined oscillators or rubidium frequency standards to be used with the system, as these sources are generally fitted with 10 MHz outputs. An overview of the clock chain components internal to the receiver is shown in Fig. 2.59. The clock chain was designed with the following features in mind:

- Sub-picosecond additive RMS jitter performance for the reference signal supplied to both the microwave synthesizers and the ADC sampling synthesizer, which is of paramount importance for the overall system phase measurement accuracy and the achievable dynamic range of the ADC conversion process.
- Flexible configuration of the reference clock frequency supplied to each microwave

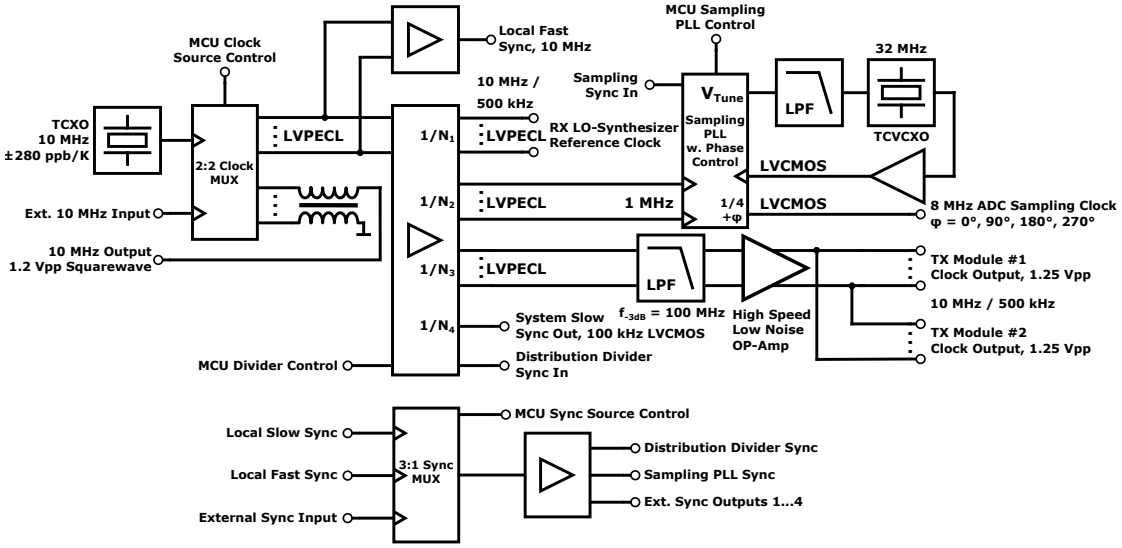

Figure 2.59: Schematic block diagram of the receiver clock and synchronization chain.

synthesizer during Integer-N operation to allow for trade-offs between lock-time and frequency spacing.

- System-wide coherency of the divided clock signals to ensure phase repeatability of all signals synthesized from any representation of the reference clock by implementing a low-speed master sync clock. This synchronization pulse can also be used to coherently sync multiple receiver boards to form a classic multi-receiver VNA.

- Easy external access to an unaltered representation of the internal 10 MHz reference signal combined with an easy switch-over to an external 10 MHz signal source to facilitate integration with other measurement equipment in a combined measurement setup for system integration and debugging.

All measurements presented throughout this work were carried out using the internal 10 MHz TCXO featuring an initial frequency tolerance of ±1 ppm, a temperature coefficient of ±280 ppb and a nominal integrated jitter of $t_{\mathrm{XO}} = 500\,\mathrm{fs}$. In the clock chain, this LVCMOS output TCXO is followed by a logic standard converting 2:2 clock multiplexer with an additive RMS jitter of approximately $t_{\mathrm{MUX}} = 100\,\mathrm{fs}$. This multiplexer converts the interference susceptible single ended LVCMOS reference signal to a robust differential LVPECL clock and provides a single ended high slew-rate representation of the LVPECL reference clock on an external connector for other measurement devices. Alternatively, an external reference frequency signal can be selected as the signal source to be fed into the rest of the clock chain by software control. This external clock signal is limited in amplitude via low 1/f noise Schottky diodes and balanced using a balun to allow low slew-rate sinusoidal reference frequency sources to be used with the clock signal logic buffer without impairing the jitter performance of the signal (not shown for clarity in Fig. 2.59).

The core of the clock distribution chain is a low jitter 1:4 LVPECL distribution buffer with integrated, software configurable $n_i = 1 \ldots 1024$ integer output dividers, adding a typical additive RMS clock jitter of $t_{\mathrm{Div}} = 100\,\mathrm{fs}$ depending on the division factor, for LVPECL in- and output signals. In normal operation, this buffer supplies the both the internal LO-synthesizer and the external stimulus synthesizers with their respective coherent 10 MHz or 500 kHz reference frequency and the sampling PLL synthesizer with a coherent 1 MHz reference signal.

In order to achieve clock domain coherence[35] between the divided output signals, an external synchronization pulse must be applied to reset all output divider counters simultaneously, synchronizing them to the same level transition of the reference input clock. While this may seem akin to the phase re-sync procedure implemented in the ADF4356 itself, its implementation is manually achieved by a flip-flop based circuit that is triggered by the controller and releases the synchronization signal on the rising edge transition of the synchronization strobe signal throughout the whole system. When this synchronization signal is distributed to other receiver assemblies connected to the same 10 MHz source, coherent measurements between multiple receivers can be achieved.

To bootstrap the main divider of the system itself, the synchronization signal is derived from the 10 MHz reference input itself (Local Fast Sync in Fig. 2.59) during power-up. After the initial configuration of the divider, this task is handed over to a coherent 100 kHz signal (System Slow Sync in Fig. 2.59), generated by the main buffer via the synchronization multiplexer. This slower coherent synchronization signal is then subsequently used to synchronize the sampling PLL synthesizer with its lower reference frequency of 1 MHz and can be distributed more easily to other receiver boards due to better EMI properties of the signal.

The representations of the reference clock signal which are distributed to the one or two external stimulus amplifiers are handled in quite a different way than the rest of the LVPECL reference clock signals. Due to the high slew rate of the square wave LVPECL clocks, which therefore contain an extremely high amount of power in the odd numbered harmonics, combined with the high sensitivity of the receiver, the risk of interference by these externally routed signals upon the RF measurements is fairly high.

In order to mitigate this source of coherent interference, this branch of the clock tree is filtered by a differential 100 MHz low-pass filter with an integrated LVPECL conformal termination and then amplified via a low noise high speed differential operational amplifier to 2.5 Vpp amplitude to avoid the additional jitter which would be introduced by another re-constructive 1:2 LVPECL clock buffer. A differential passive resistive -6 dB splitter is used to generate two differential 1.25 Vpp clock signals, which are in turn converted to a single ended output via a balun for transmission via a coaxial cable to the stimulus synthesizer (splitter and baluns not shown for clarity in Fig. 2.59). The low jitter input comparator ($t_C = 45\,\mathrm{fs}$) in the stimulus synthesizer regenerates the LVPECL clock signal from this slew-rate limited form of the reference clock for the synthesizer IC ($t_{\mathrm{Syn}} = 95\,\mathrm{fs}$).

[35] Clock coherence in this context is defined as a repeatable, simultaneous, equal edge transition start of all clock outputs, which results in a periodic simultaneous zero transition of the outputs, even when the signals have a different frequency.

When the probability spectrum density function of the additive RMS jitter is assumed to follow a random Gaussian normal distribution and each contribution to the total observed jitter can be modeled as statistically independent and uncorrelated, it is possible to apply the central limit theorem to estimate the total jitter from the start of the clock chain to the stimulus synthesizer output signal ([132]) using

$$t_{j,RF}(\text{RMS}) = \sqrt{\sum_{i=1}^{n} t_i^2(RMS)} = \sqrt{t_{\text{XO}}^2 + t_{\text{MUX}}^2 + t_{\text{Div}}^2 + t_C^2 + t_{\text{Syn}}^2} \approx 530\,\text{fs}\,, \quad (2.154)$$

which is in very close accordance with the already presented measured mean output jitter of the stimulus synthesizer of $t_{j,RMS} = 548\,\text{fs}$, which was calculated from the results of the RF output signal phase noise measurements presented in chapter 2.3.3 of this work.

A similar estimation can be made for the influence of the jitter upon signals sampled by the ADC, although the situation is far more complex for a sufficient description for the sum of all effects ([72, 159]).

In a high-speed sampling ADC system, the main influences upon the converted results can be identified as:

- The noise power N present in the analog bandwidth $f_{-3\,\text{dB}}$ of the sample and hold (S&H) circuit in the analog front-end of the converter ([159]),
- The inherent noise floor of the ADC due to analog amplifiers, 1/f noise and digital cross-talk interference ([159]),
- The quantization noise introduced by the finite resolution of the ADC due to its inherent 1/2 least-significant-bit (LSB) conversion uncertainty ([72]),
- The amount of differential non-linearity (DNL) present in the real quantization transfer function of the ADC ([72]),
- The amount of integral non-linearity (INL) present in the real quantization transfer function if multi-tone stimuli are applied ([72]), and
- The amount of jitter and its phase noise distribution present in the sampling clock signal driving the S&H circuit ([15, 16, 74, 131]).

The noise power seen by the S&H circuit of the ADC can be strongly influenced by the design of the IF and driver circuitry in the receiver. As the noise bandwidth of the down-converted RF signal in this design is filtered by the crystal based IF filter, the resulting 10 dB of front-end noise figure in 2.2 kHz bandwidth is almost negligible compared to the Johnson-Nyquist noise present in the 380 MHz full power bandwidth of the S&H circuit contained in the ADC ($\Delta F_{BW} = 52.3\,\text{dBHz}$). Following this reasoning, the noise shaping filters between the IF amplifier stages are used to limit the amplified total noise power reaching the ADC analog front-end.

It is also misleading to think of the un-aliased analog bandwidth $f_s/2$, with f_s being the sample rate of the ADC as governed by the Nyquist-Shannon sampling theorem, to be

relevant for the noise power of the converted signal. While full information reconstruction of band-limited signals is only possible in the Nyquist-Shannon bandwidth of the system, the conservation of energy does still apply for aliased signals above the Nyquist-Shannon limit. All the noise power seen by the S&H circuit, multiplied by its sampling rate dependent transfer function, is therefore aliased back into the base-band output of the ADC in the digital domain.

The inherent noise floor of the ADC, as the name implies, can only be marginally lowered by external means and is mostly influenced by the design and choice of the converter itself. What can be influenced however is the amount of digital cross-talk interference reaching the analog front-end of the ADC. This cross-talk can be minimized by the following standard mixed signal PCB layout guides, which where also used to create the PCB layout of the ADC section of the PCB:

- Individual ground planes for the digital and analog parts of the ADC circuit with a single star ground point,
- Individual power supply rails with their own filter and regulation circuits to increase the power supply rejection ratio,
- Physical separation of susceptible analog voltages (input, reference voltage, common mode offset voltage for pseudo differential ADCs, analog supply rail) and fast switching digital gates,
- Minimal capacitive loading of the internal digital bus drivers of the ADC to minimize the amount of current drawn during the transition moment of the internal push-pull logic output stage and therefore minimize H-field coupling on the ADC die and adjacent traces. This can be accomplished by using a low input capacity bus driver on a separate voltage rail to directly terminate the logic outputs right at the physical perimeter of the ADC to minimize the trace capacitance. This can be enhanced by low value series resistors, if permitted by signal integrity constraints, to limit the peak current by lowering the signal slew rate due to the RC time constant of the circuit. And
- Finally, a digital scrambling or randomizing scheme, if offered by the ADC, can be used to spread the spectral energy of the output signal over a wide bandwidth.

In this specific case, the randomization is accomplished by XORing all ADC data output bits with the bit of the highest entropy, which is the LSB of the converted data. This operation is easily reversed in the controller software running on the Cortex-M7F after data capture due to the symmetry of the XOR operation by performing a bit wise XOR operation on all ADC data bits again using the value of the LSB, which yields the unscrambled data.

The differential non-linearity (DNL) and integral non-linearity (INL) errors are dynamic properties of the ADC used for the conversion and are both caused by deviations from the theoretical linear transfer function of the ADC when converting from the continuous analog domain to the discrete and quantized digital domain. In a linear ADC, the

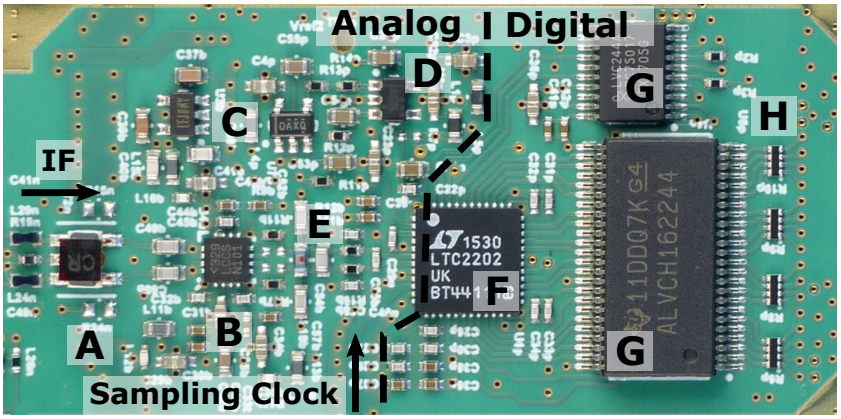

Figure 2.60: Annotated implementation detail picture of the IF amplifier chain tail end, the ADC and support circuitry. Annotations: A - differential IF impedance transformer, B - differential low impedance ADC driver amplifier with offset input, C - low noise active low pass filter for the ADC reference voltage, D - analog domain low noise LDO, E - low-Q ADC input bandpass filter, F - pseudo-differential semi-flash 16 bit sampling ADC, G - digital bus drivers, H - series termination for the digital outputs, dashes - ground plane split.

quantization steps are defined to be equidistant over the whole range of conversion, which yields a discrete linear transfer function. In reality, this is unfortunately not the case with (semi[36]-)flash architecture high speed ADCs due to the sheer number of precision comparators and resistive divider steps[37] needed to obtain the conversion result. Even minor differences in resistance values and comparator offset voltages can result in a fairly large deviation from the linear transfer function when compared with the voltage resolution of the LSB. In practice, this is either corrected by laser trimming of the analog components during manufacturing in full flash architectures or by digital look-up tables written during production test for the pipelined semi-flash architecture ([72]). Despite all efforts taken during manufacturing of precision high-speed ADCs, some residual deviations in the transfer function, in the form of DNL and INL, remain. The main difference between DNL and INL lies in their specific scope: While the DNL is a statistical mean, which is determined by looking at all the minor differences from the equidistant ideal steps of the linear transfer function and is often segmented into values for different segments of the full scale ADC drive, the INL describes a maximum deviation, or the integral of several DNL step up to that point, from the linear transfer function. A graphical explanation for the INL and DNL figures is given in Fig. 2.61.

[36] Semi-flash ADC architectures are a hybrid between successive approximation and flash ADCs, where the 1-bit comparison of the successive approximation process is replaced with higher resolution flash ADCs and DACs with all conversion steps unrolled and pipelined, yielding a much faster and time deterministic conversion result with a delay corresponding to the pipeline length or depth.

[37] 65535 comparators with an equivalent number of resistive reference voltage divider steps are needed for a 16 bit full flash architecture ADC.

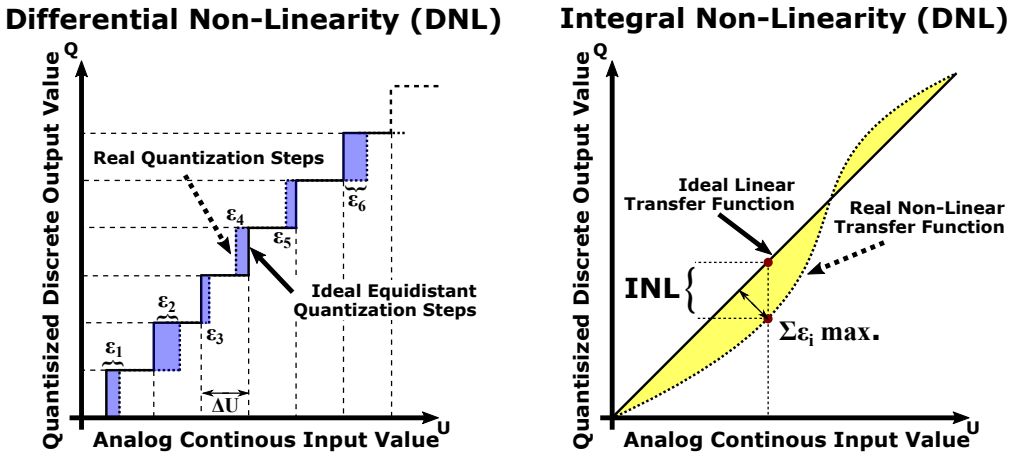

Figure 2.61: Graphical explanation of differential non-linearity (DNL) and integral non-linearity (INL) in an ADC transfer function.

The impact of DNL and INL upon the converted signal is however quite different: As the DNL consist of randomly distributed, minor[38], uncorrelated and therefore statistical independent variations in the converted signal, its effects are, in accordance with the central limit theorem, treated as additive Gaussian white noise (AWGN), similar to the quantization noise induced by the 1/2 LSB uncertainty. The effects of the INL however are, besides the obvious measurement errors, closely related to the transfer function linearity of amplifiers and determine the IP2 and IP3 of the ADC under multi-tone excitation, which is often compressed into the SINAD[39] figure of merit. In the single CW tone, narrow-band IF application here, the INL is only relevant as a measure of total measurement linearity of the ADC.

In order to explain the effect of sampling jitter, which consist of the combination of sampling clock jitter and the inherent aperture jitter of the S&H circuit, it is helpful to use the graphical explanation given in Fig. 2.62. When a constant sinusoidal input signal is present and a subsequent signal processing is used which yields a complex quantized value, an ideal sampling process performing the sampling at t_s would yield one sample of the constant output signal vector. When a stochastic variation Δt is added to the coherent sampling time t_s, this variation is equivalent to the vector addition of a random error vector δ to the original signal. This error vector influences both the magnitude and the phase of the conversion result and inherits the statistical properties and power spectrum density function of the original sampling jitter. If the sampling clock jitter has AWGN properties, this additional error vector can simply be treated again as an additional source of white noise. For a full scale 0 dBFS sinusoidal ADC input signal of the frequency f_{sig}, the RMS jitter t_j induced signal-to-noise ratio (SNR) can be estimated

[38] Also known as "no missing codes" in ADC datasheets, which means that the deviation ϵ of the instantaneous step-size is never larger than a regular conversion step, and therefore no output values are skipped in a continuous input voltage sweep.

[39] Signal-to-interference ratio including noise and distortion.

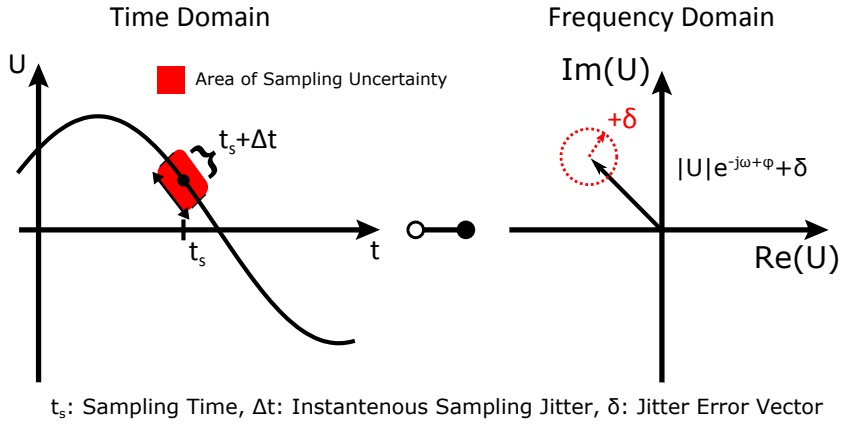

Figure 2.62: Graphical explanation of the error vector introduced by stochastic jitter processes. Only one sampling point shown for clarity.

according to [72] for an ideal ADC using

$$\mathrm{SNR}_{\,0\,\mathrm{dBFS}} = 20 \cdot log_{10} \frac{1}{2\pi \cdot f_{sig} \cdot t_j} \,. \tag{2.155}$$

By analyzing the SNR results of Eq. (2.155) shown in Fig. 2.63 for different jitter values and signal frequencies it can easily be seen, that a sub-picosecond total RMS jitter of the sampling aperture, which includes the sampling clock jitter and the internal S&H aperture jitter, is absolutely necessary to avoid jitter SNR degradation for a 16 bit converter sampling a signal at a frequency of 8 MHz, when a realistic ADC SNR of 80 to 85 dB for a 16 bit converter is used as the decision threshold.

The total SNR for an ADC with N bits resolution, sampling a full scale 0 dBFS sinusoidal input signal of the frequency f_{sig} with a combined RMS sampling jitter t_j, an average DNL ϵ and an effective input noise voltage U_N(RMS) can be calculated according to [72] as

$$\mathrm{SNR}_{\,0\,\mathrm{dBFS}} = -20 \cdot log_{10} \Bigg[\underbrace{(2\pi f_{sig} \cdot t_j)^2}_{\text{S\&H jitter}} + \underbrace{\frac{2}{3}\left(\frac{1+\epsilon}{2^N}\right)^2}_{\text{Quantization and DNL}} + \underbrace{\left(\frac{2\sqrt{2}U_N}{2^N}\right)^2}_{\text{Effective Input Noise}} \Bigg]^{0.5} , \tag{2.156}$$

which simplifies to the well-known, ADC bit count dependent, SNR equation

$$\mathrm{SNR} = 6.02 \cdot N + 1.76\,\mathrm{dB}\,, \tag{2.157}$$

for an ideal ADC with no input noise, no DNL and an ideal S&H process with N bits of quantization resolution. By rearranging Eq. (2.157) for the number of bits, it is possible to quantify the effective number of bits (ENOB) of an ideal ADC for a given SNR, which is usually the overall performance figure given in ADC datasheets instead of the

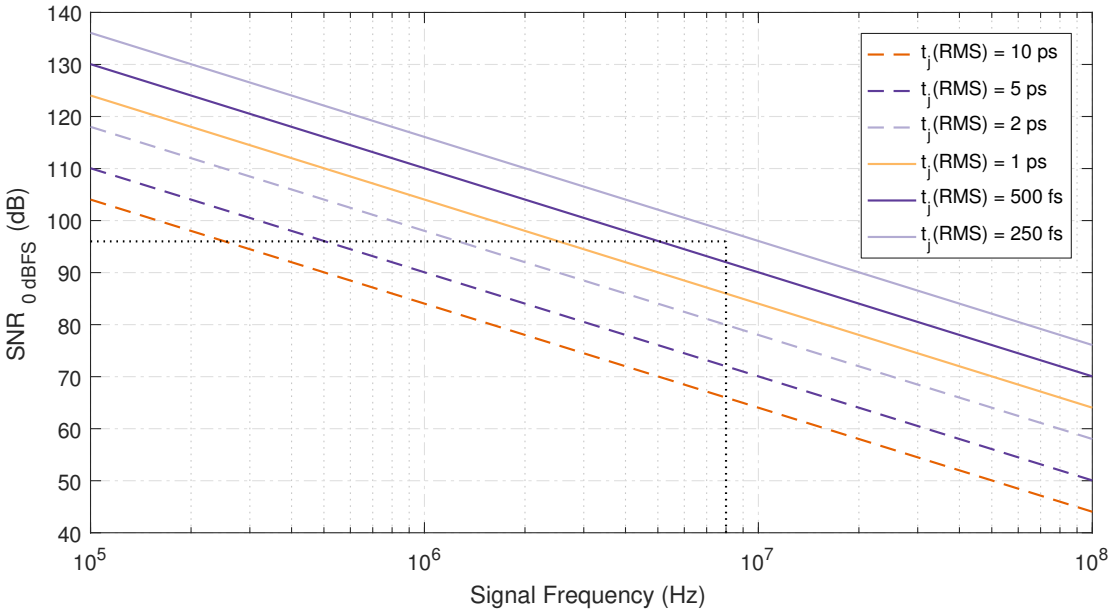

Figure 2.63: Signal-to-Noise ratio (SNR) for different RMS sampling jitter values over frequency for an otherwise ideal ADC. Reference lines added for a SNR of 96 dB (ideal 16 bit ADC) and the IF frequency of 8 MHz.

values required to directly calculate the SNR using Eq. (2.156). For the LTC2202 16 bit ADC used in the hardware prototype, the available SNR using an ideal sampling clock to control the internal S&H circuit with its own aperture jitter of $t_j(\mathrm{RMS}) = 200\,\mathrm{fs}$ is 81.6 dB, which results in an ENOB of 13.26 bit for the IF frequency range of the receiver.

The acquisition of the magnitude and phase components of the IF signal is performed by a modified I/Q sampling process in order to reduce the digital signal processing workload for the sole microcontroller. To understand the acquisition of the complex valued data by the ADC and the generation procedure of the coherent sampling clock, it is beneficial to omit the modifications made to the sampling process at first and just assume the classical form of I/Q sampling. In normal I/Q sampling of a narrow-band fixed frequency IF signal, the easiest form of phasor sampling is performed by a sampling clock that is exactly four times the signal frequency, therefore $f_s = 4 \cdot f_{IF}$ ([124]).

In order to get a repeatable measurement result from of the IF signal, the sampling clock must additionally be repeatably phase locked to the same reference frequency source as all other synthesizers that are involved in the generation of the IF signal. This requirement is in stark contrast to the implementation of a sampling clock generation in a classical VNA with individual receivers for each measurement channel, where the frequency lock alone is sufficient, as long as all ADCs are supplied by the same sampling clock source. This is possible for the measurement of linear S-parameters, because the wave measurements are always referenced to other waves measured by the same clock source, therefore only the relative phase difference needs to be repeatable - and not the

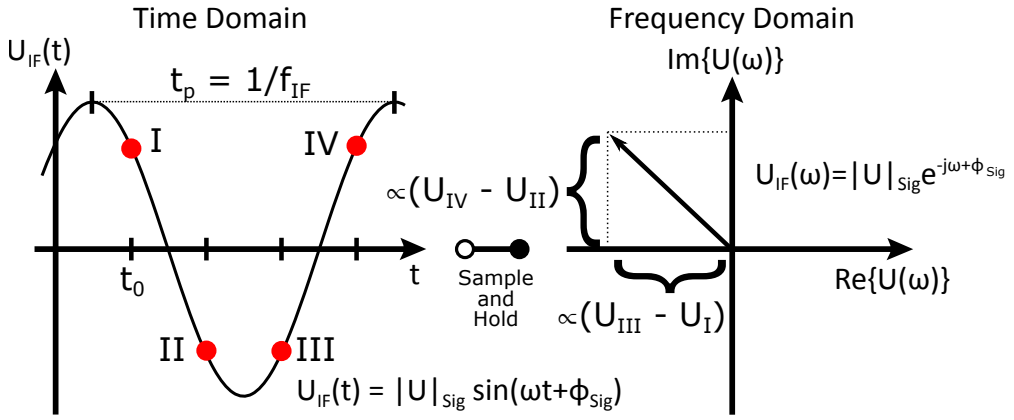

Figure 2.64: Graphical explanation of the vector data conversion process by using the sample and hold circuit to perform the Hilbert transformation from the time- into the complex frequency domain.

absolute phase referenced to the system reference clock ([54]).

For the system topology used in this work, a phase locked sampling clock of $f_s = 4 \cdot 8\,\text{MHz} = 32\,\text{MHz}$ would be required for a repeatable placement of the four sampling points I to IV with regard to the IF signal, as shown in Fig. 2.64. As the sampling clock is exactly four times the signal frequency, the distance between adjacent sampling points is exactly $360°/4 = 90°$ with regard to the IF signal. In this original implementation of the I/Q-sampling process, the Nyquist-Shannon sampling criterion with regard to the IF frequency is fulfilled and all samples are completely enclosed in the baseband bandwidth of 16 MHz, resulting in a rotating phasor $y(t) = A \cdot \sin(2\pi f_{\text{D,IF}}\, t + \phi_0)$ with $f_{\text{D,IF}} = 8\,\text{MHz}$ in the baseband output[40].

The information contained in the magnitude and angle of the rotating phasor can be extracted from the baseband output by applying a Fast-Fourier-Transformation (FFT) with an appropriately sized number of bins ([79]), or more computationally efficient with the Goertzel algorithm ([37]), as the frequency of the phasor is already precisely known. This process is called digital down conversion (DDC). However, none of these procedures are within the computational reach of the onboard RAM resources available on the microcontroller used to capture the ADC output data.

Instead, the more computationally efficient I/Q-sampling process uses a different approach: When each one of the consecutive sampling points I to IV is considered to be an individual measurement series, therefore only one fourth of the real sampling frequency is effectively used per individual sampling point, the situation changes considerably for the separated samples. The Nyquist-Shannon frequency limit for baseband sampling is now at $f_{\text{IF}}/2$ due to $f_s = f_{\text{IF}}$, which results in an aliasing and bandpass undersampling of the individual sampling point right down to $f = 0\,\text{Hz}$ or DC. When the IF signal and

[40] To be formally correct with the nomenclature of time discrete signal processing, this expression must be rewritten in relative terms of baseband angular frequency to sampling time, i.e. $\sin(\frac{2\pi}{N}k)$, which was omitted in this description for the sake of clarity.

the sampling clock are phase locked and TI stable, this results in constant consecutive samples for each of the sampling points I to IV of the signal. No further multiplication with a numerical controlled oscillator or other signal processing is necessary to remove the rotation of the phasor information at the IF frequency, as the sampling process itself removes the IF carrier frequency.

To reconstruct the vector components from the individual sampling points, it is helpful to remember that basic trigonometric functions can be used to describe a sinusoidal time domain signal y(t) in its in-phase I and quadrature Q components form as

$$y(t) = A \cdot \sin(\omega t + \phi_0) = \underbrace{A \cdot \cos\phi_0}_{=I} \cdot \sin(\omega t) + \underbrace{A \cdot \sin\phi_0}_{=Q} \cdot \cos(\omega t) \tag{2.158}$$
$$y(t) = I \cdot \sin(\omega t) + Q \cdot \cos(\omega t)\,.$$

This representation of the signal can then be combined with properties of the position of the sampling point in respect to the original IF signal. As the sampling points are now at DC due to the bandpass undersampling process and the samples $y(i)$ taken of the signal are exactly spaced $\pi/2 = 90°$ apart, it is possible to simply assign the samples to the I/Q components in the form

$$y(\mathrm{I}_0) = Q\,,\ \ y(\mathrm{II}_{\pi/2}) = I\,,\ \ y(\mathrm{III}_{\pi}) = -Q\,,\ \ y(\mathrm{IV}_{3\pi/2}) = -I\,,\ \ \text{or} \tag{2.159}$$
$$y(\mathrm{I}_0) = I\,,\ \ y(\mathrm{II}_{\pi/2}) = -Q\,,\ \ y(\mathrm{III}_{\pi}) = -I\,,\ \ y(\mathrm{IV}_{3\pi/2}) = Q\,, \tag{2.160}$$

depending upon the arbitrary decision, which component is detected first, by following the trajectory of the phasor ([54, 124]).

The magnitude and phase information A and ϕ_0 of the phasor can now be calculated from the measurements ([54]) using

$$A = \frac{1}{2} \cdot \sqrt{[y(\mathrm{I}_0) - y(\mathrm{III}_{\pi})]^2 + [y(\mathrm{II}_{\pi/2}) - y(\mathrm{IV}_{3\pi/2})]^2}\ ,\ \ \text{and} \tag{2.161}$$
$$\phi_0 = \arctan\left[\frac{y(\mathrm{I}_0) - y(\mathrm{III}_{\pi})}{y(\mathrm{II}_{\pi/2}) - y(\mathrm{IV}_{3\pi/2})}\right]\,. \tag{2.162}$$

The simplicity of this procedure is unfortunately not without drawbacks, as any DC offset (or offset to the virtual ground in case of a pseudo-differential ADC) or any alignment errors of the sampling points results in a periodic envelope ripple with the frequency of f_{IF} in the converted results ([124]). Furthermore, all even harmonics of the signal created by the IF amplifier chain or the front-end mixer are also alias down to DC due to the undersampling used for the frequency transformation and the relations of the frequencies ([124]), which results in non-correctable interference to the measurement signal.

These drawbacks of the sampling process are mitigated in this design by choosing a pseudo-differential ADC which includes a matched offset voltage generator in combination with an ADC driver with DC offset voltage injection capability. This limits the maximum DC offset referenced to virtual ground potential to about ±2 mV, which is only 0.16 % of the ADC's full scale voltage of ±1.25 V. In order to avoid harmonic aliasing, the

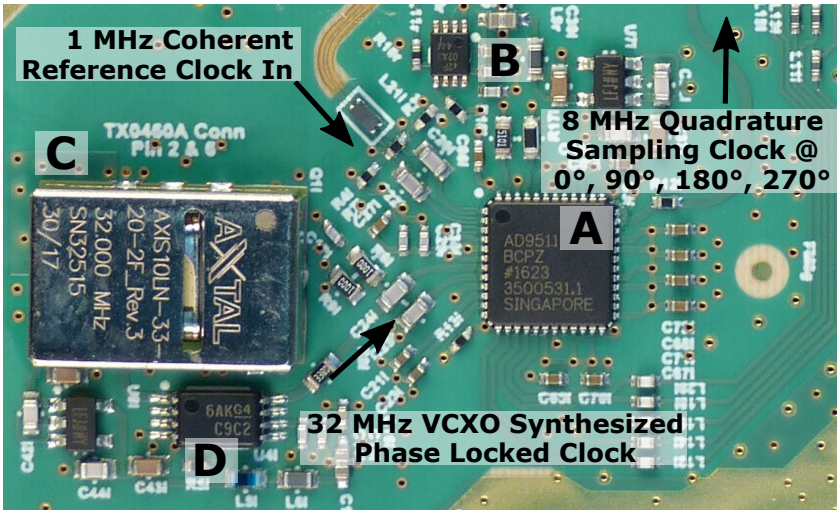

Figure 2.65: Annotated picture of the sampling clock PLL synthesizer implementation. Annotations: A - sampling PLL IC, B - external manual phase re-sync circuit, C - 32 MHz VCXO, D - VCXO clock buffer.

amplifiers used in the IF chain where chosen for their linearity and IP2 performance. Additional attenuation of the harmonic components is provided by the noise shaping filters used between the individual amplifier stages.

In the actual realization of the I/Q-sampling process used in the VNA receiver, a modification to the procedure is made to lower the effective datarate of the ADC. When all signals are assumed to be TI stable and only the wanted IF-signal is present at the input of the ADC, the actual sampling frequency of the ADC becomes irrelevant, as long as the 90° spaced samples can be precisely taken. Furthermore, it is not relevant when and in which order the signal samples are taken, as long as the angular spacing is preserved and the analog bandwidth of the S&H circuit of the ADC is high enough. Based upon this observation, the sampling frequency is lowered to $f_s = 8\,\text{MHz}$ and the actual selection of the sampling point index I to IV of the original procedure is performed by shifting the phase of the sampling clock in 90° increments.

The phase shifting is performed by the PLL clock synthesizer IC, which allows for precise synchronous divider shift offsets depending on the programmed divisor, i.e. a division factor of 4 allows for $360°/4 = 90°$ spaced steps. Contrary to the often used configurable analog delay line approach, the use of configurable synchronous divider tabs in the synthesizer IC avoids the degradation of the phase noise performance usually associated with this procedure. To allow for a division factor of four and therefore also four equally spaced sampling points for a 8 MHz signal, a 32 MHz low phase noise phase locked first stage sampling clock is synthesized using a voltage controlled crystal oscillator (VCXO), which is locked to a 1 MHz reference clock for integer multiplier, and used to clock the low jitter phase shifting divider in the PLL IC (see Fig. 2.65 for reference).

Sampling clock coherency is established in a similar way to the main clock divider

circuit by using a edge triggered flip-flop, armed by the microcontroller, to reset the output divider synchronous to the coherent system-wide synchronization pulse signal. This re-synchronization is necessary for each change in output phase and introduces some additional overhead, which intrudes an additional sampling delay of approximately 15 us, when the communication time of the controller for reconfiguring the PLL dividers is included. To reduce the overall measurement time and to allow the controller to store the sample data via DMA[41] transfers, each sampling point is sampled to its final sampling depth count before the sampling phase is advanced. While this increases the TI stability requirements upon all components involved considerably, testing showed no adverse effects for the limited sampling point depths possible with the system.

The RMS jitter of the sampling clock is estimated similarly to the RF synthesizer output jitter with one major difference: As the sampling PLL's output loop filter is designed to have a very low bandwidth of only 250 Hz to comply with the narrow tuning bandwidth of the 32 MHz TCVCXO, the sampling clock jitter is dominated by the phase noise properties of the components internal to the synthesis loop and the jitter associated with the rest of the clock chain can mostly be ignored. Therefore, the sampling RMS jitter can therefore be estimated to as

$$t_{j,s}(\mathrm{RMS}) = \sqrt{t^2_{\mathrm{j,VCXO}} + t^2_{\mathrm{j,Buffer}} + t^2_{\mathrm{j,SynthDiv}} + t^2_{\mathrm{j,S\&H}}} \tag{2.163}$$

$$t_{j,s}(\mathrm{RMS}) = \sqrt{(525\,\mathrm{fs})^2 + (100\,\mathrm{fs})^2 + (275\,\mathrm{fs})^2 + (200\,\mathrm{fs})^2} \approx 633\,\mathrm{fs}\,,$$

which results in a theoretical aperture jitter SNR of 90 dB for the sampling of the 8 MHz IF frequency using Eq. (2.155).

Another welcomed effect of the reduced clock speed is that the ADC data rate drops from 64 Mbyte/s to 16 Mbyte/s and the ADC sample rate from 32 MSPS to 8 MSPS. Both reductions allow enormous cost savings in the design, as the lower data rate allows the microcontroller to handle the ADC data interface on its own via direct-memory-access (DMA) transfers without a FPGA, therefore reducing BOM cost PCB space and layer count. The lower sampling rate also allows to choose an ADC with lower maximum sampling rate specifications, with the added benefit of generally better ENOB performance of these ADCs. While a slower conversion rate also results in a longer measurement time, the additional time required to acquire the four sampling points to their required sampling depth in sequence instead of the direct interleaved measurement at $4 \cdot f_{\mathrm{IF}}$ is only noticeable for very high sampling depths in a sweeping VNA measurement due to synthesizer lock and filter dwell-times.

As the lock time of the synthesizers in this system is about 1 ms per frequency point alone and the 2.2 kHz wide crystal filter, if modeled as an RC equivalent, needs an additional filter step response settling dwell-time of

$$t_{\mathrm{Dwell}} = 11.09 \cdot RC = 11.09 \cdot (2.2\,\mathrm{kHz})^{-1} = 5.041\,\mathrm{ms} \tag{2.164}$$

to settle down to 16 bits corresponding to 99.99847 % of the full step response (see [159] for more time constants and calculation) per point after lock, it is immediately obvious,

[41] Direct Memory Access, autonomous data transfers performed by a separate configurable DMA controller controller core without CPU intervention to a specified RAM address.

that the impact of sampling the data at only 8 MSPS compared to 32 MSPS is marginal for the total measurement time of a sweep.

The coherent I/Q sampling procedure also simplifies the digital post-processing of the samples considerably: When consecutive samples are assumed to be repeatable and time invariant, the noise processes involved converge towards an AWGN normal Gaussian distribution and the least significant bits of the ADC's output are sensitive enough to cover the noise floor, coherent oversampling and averaging of the sampling points can be used to both increase the effective number of bits, the dynamic range of the ADC, provide a matched auto-correlation filter against non-correlated interference, reduce the influence of trigger jitter and realizes a digital low-pass filter to reduce the effective noise bandwidth of the samples ([79, 112, 113, 133]).

The following prerequisites must be fulfilled by the sampling system to allow for a successful enhancement of the effective ADC resolution by oversampling the signal ([133]):

- The spectral spectral density function of the noise process must be normal distributed Gaussian white noise (AWGN).
- The noise level must be sufficiently high and the ADC must have the sufficient resolution n and sensitivity to allow a random change of at least 1 LSB or $\Delta = U_{\text{fullscale}}/2^n$ by the noise alone.
- The IF signal must be representable as a random variable possessing equal probability of being converted to with one of two adjacent LSB codes.

While there is some correlation present in the noise of the system that is confined within the loop bandwidth of the synthesizers ([114]), this portion of noise bandwidth is negligible compared to the white thermal noise present in the ADC S&H bandwidth and therefore oversampling can still be applied here.

The oversampling is performed by a phase accurate sample accumulation and decimation process, i.e. all subsequent samples of a specific sampling point are added and decimated to a specified higher resolution. This process amplifies stationary signals while non-coherent, and therefore non-stationary, signals are attenuated.

In order to increase the resolution of the measurement results by n bits of additional resolution, corresponding to a process gain SNR increase of

$$\text{GSNR}_{\text{OVS}} = n \cdot 6.02\,dB \tag{2.165}$$

as of Eq. (2.157), $N = 4^n$ coherent samples must be captured, summed, and decimated, or averaged for the DC case here, by a factor of $Div = 2^n$ to yield the improved result (derivation in appendix of [133]). The decimation is performed by Div and not by N because of the integer representation of a fractional value relative to the ADC's reference voltage. It is however important to note, that a division of the sample sum by Div and not by N does not change the overall coherent averaging factor due to the increased range of values - the effective process averaging factor is still N.

The operation and effect of this procedure can be visualized as performing an operation that performs a linear interpolation between subsequent changes of the conversion result's

Added Resolution	Total ENOB	Number of Samples	Decimation Factor	$GSNR_{OVS}$	ADC SNR
0 bit	13.3 bit	1	1	0 dB	81.6 dB
1 bit	14.3 bit	4	2	6 dB	87.6 dB
2 bit	15.3 bit	16	4	12 dB	93.6 dB*
3 bit	16.3 bit	64	8	18 dB	99.6 dB*
4 bit	17.3 bit	256	16	24 dB	105.6 dB*
5 bit	18.3 bit	1024	32	30 dB	111.6 dB*

Table 2.7: SNR impact of different coherent oversampling factors for the sampling system. Asterisks denote values above calculated sampling clock RMS S&H jitter ADC SNR threshold of 90 dB under the assumption of Nyquist sampling.

LSB towards its statistical mean, which is determined by the original continuous analog input signal. The noise created by the stochastic variation of the LSB between adjacent quantization results can be modeled as a non-correlated AWGN process with a variance proportional to the LSB's voltage resolution and a mean of zero. As the interpolation is performed towards the coherent mean of all samples, all non-coherent signal components, including the LSB noise and other non-correlated interference, is heavily attenuated by the oversampling process.

The corresponding equivalent filter function and an in-depth signal theoretical discussion of this special case of coherent oversampling of low-frequency or DC signals can be found in [112, 113].

The division of a value by a divisor which itself is a power of 2 can be very efficiently calculated in binary integer arithmetic by performing a right bit-shift by n and usually takes only one CPU cycle to complete (excluding register load and store commands), regardless of n, when a modern barrel-shifter is implemented in the CPU core. As the data transfer from the ADC into the RAM of the controller is handled by DMA, the calculation of the oversampled result can be performed in parallel by the controller while the data of the next sampling point is being captured. The acquired raw ADC data is stored in two interleaved buffers that can fit the required sampling depth plus the pipeline depth of the ADC. One buffer is used for DMA capture, while the other is read out by the CPU to perform the oversampling decimation and vice versa.

In addition to the oversampling procedure, coherent averaging for the sampled data is implemented in floating point arithmetic. As the averaging is performed upon complex valued and stationary I/Q samples generated by a coherent sampling process, the averaging performed during oversampling and the additional coherent averaging procedure both provide the same SNR increase, or process gain, of

$$\mathrm{GSNR}_{\mathrm{coh}}(dB) = 20 \cdot \log_{10}(\sqrt{N}) = 10 \cdot \log_{10}(N)\,, \tag{2.166}$$

for an average performed over N samples (derivation in [79]), instead of the non-coherent (video) averaging process gain of

$$\mathrm{GSNR}_{\mathrm{Video}}(dB) = 10 \cdot \log_{10}(\sqrt{N}) \tag{2.167}$$

achievable by scalar RF measuring devices. The process gain achieved by the coherent averaging is therefore identical to the oversampling process gain presented before. While

it may seem unnecessary to implement a separate averaging method in the first place, this splitting of the signal processing was necessary due to RAM constraints on the microcontroller. As the data taken during the oversampling portion of the sample cycle are transferred via DMA, no online summing of results can be performed. Furthermore, the ADC data needs to be descrambled[42] prior to accumulation. Both of these requirements demand that enough consecutive RAM is available to store all the required samples before any processing can be performed, which is a scarce resource when only internal SRAM is available, and therefore sets a hard limit on the maximum number of samples that can be acquired for one sampling point. The post-capture coherent averaging on the other hand only needs four variables per sampling point: One accumulator of sufficient size that can handle the sum of all values without overflow and the count of the averaging measurements performed for each of the I and Q components of the phasor. However, these savings in SRAM come at a price, as the sampling process for coherent averaging takes significantly longer than for equivalent oversampling of the signal due to higher number of 90° sampling phase shifts required in this sequential implementation of the I/Q-sampling process.

In its current state, the receiver hardware supports a maximum oversampling factor of $N = 1024$. When more post-processing of the sample data is required, coherent averaging must be used additionally.

In order to verify the performance and capabilities of the oversampling and averaging procedures on the hardware, verification measurements using different combinations of oversampling, averaging factors and IF gain are carried out in a pseudo spectrum analyzer measurement measuring the received power over frequency. A continuous 1 GHz stimulus signal generated by a SRS SG384 DDS/PLL synthesizer, linked and locked to the 10 MHz reference frequency output of the receiver, was used at the stimulus source and connected to one of the receiver input wave selector switch inputs.

A frequency sweep from 982 to 1002 MHz with a step-size of 62.5 kHz (321 measurement points) was configured on the receiver while keeping the SRS384 output frequency constant. The sweep was performed for signal generator output powers of -25.2 dBm and -55.2 dBm, which resulted in measured ADC signal magnitude levels of $P(f = 1\,\text{GHz}) = -3.1\,\text{dBFS}$ and $P(f = 1\,\text{GHz}) = -2.2\,\text{dBFS}$ for IF VGA gain settings of $G_{\text{VGA}} = -10\,\text{dBm}$ and $G_{\text{VGA}} = 20\,\text{dBm}$ respectively.

The input power present at the VNA receiver input after cable losses was measured by a Rohde & Schwarz NRP-Z55 thermal power head for the higher and a Rohde & Schwarz FSU67 in zero span for the lower output power, which resulted in $-26.0\,\text{dBm}$ and $-56.0\,\text{dBm}$ of input power at the VNA reference plane.

The sweeps were performed for all implemented 4^N, $N = 1 \ldots 5$ oversampling values and averaging factors of $\text{AVG} = 10^n$, $n = 0 \ldots 5$.

When the results of these measurements, which are shown in Fig. 2.66 to 2.71, are analyzed some important conclusions can be drawn:

[42] XORing all bits of the conversion results with the value of the LSB. Used to artificially widen the spectrum of the EMI generated by the parallel digital data bus and in turn lowering the spectral power of the EMI in the IF passband.

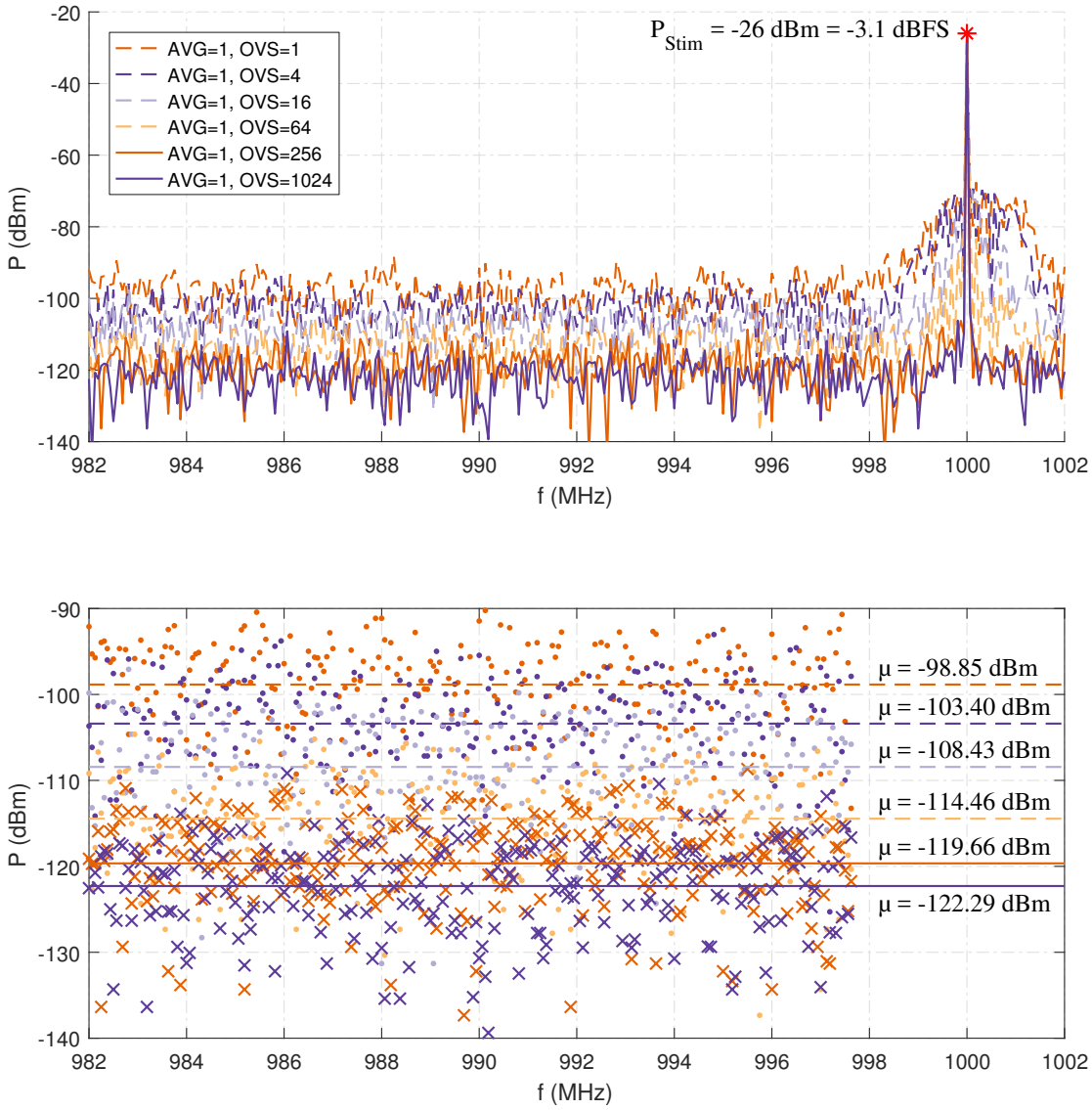

Figure 2.66: Measurement results of the input power referred system noise-floor for different oversampling factors for the frequency range of 982 to 1002 MHz with a step-size of 62.5 kHz, including a reference carrier of -26 dBm, equivalent to -3.1 dBFS using a total IF VGA gain of G=-10 dB, at 1000 MHz. Reference signal generated by SRS SG384 coupled to the 10 MHz output of the VNA receiver. Second graph shows a detail of the thermal noise-floor dominated area from 982 to 998 MHz, with lines added for the corresponding mean noise power μ.

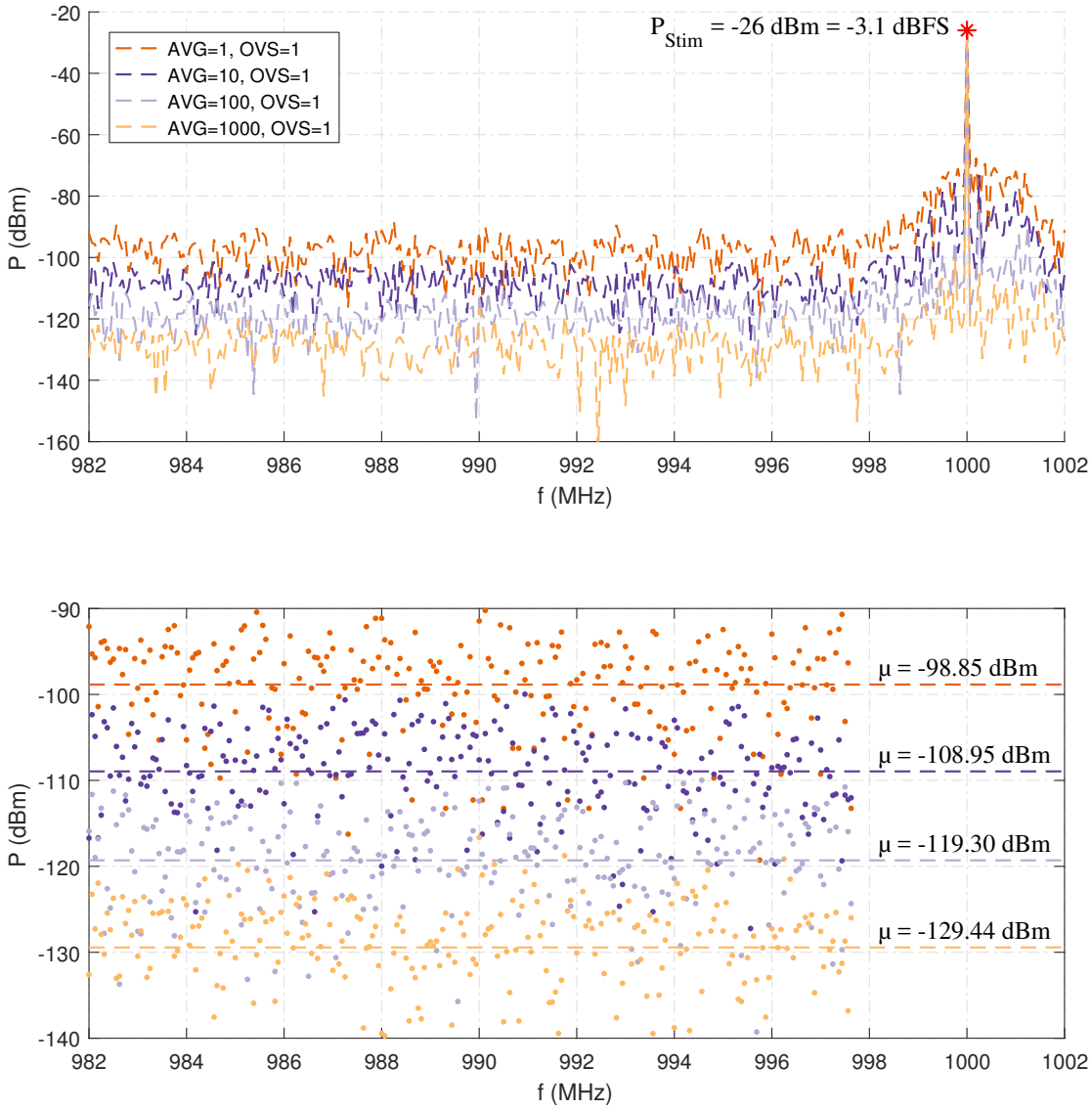

Figure 2.67: Measurement results of the input power referred system noise-floor for different averaging factors for the frequency range of 982 to 1002 MHz with a step-size of 62.5 kHz, including a reference carrier of -26 dBm, equivalent to -3.1 dBFS using a total IF VGA gain of G=-10 dB, at 1000 MHz. Reference signal generated by SRS SG384 coupled to the 10 MHz output of the VNA receiver. Second graph shows a detail of the thermal noise-floor dominated area from 982 to 998 MHz, with lines added for the corresponding mean noise power μ.

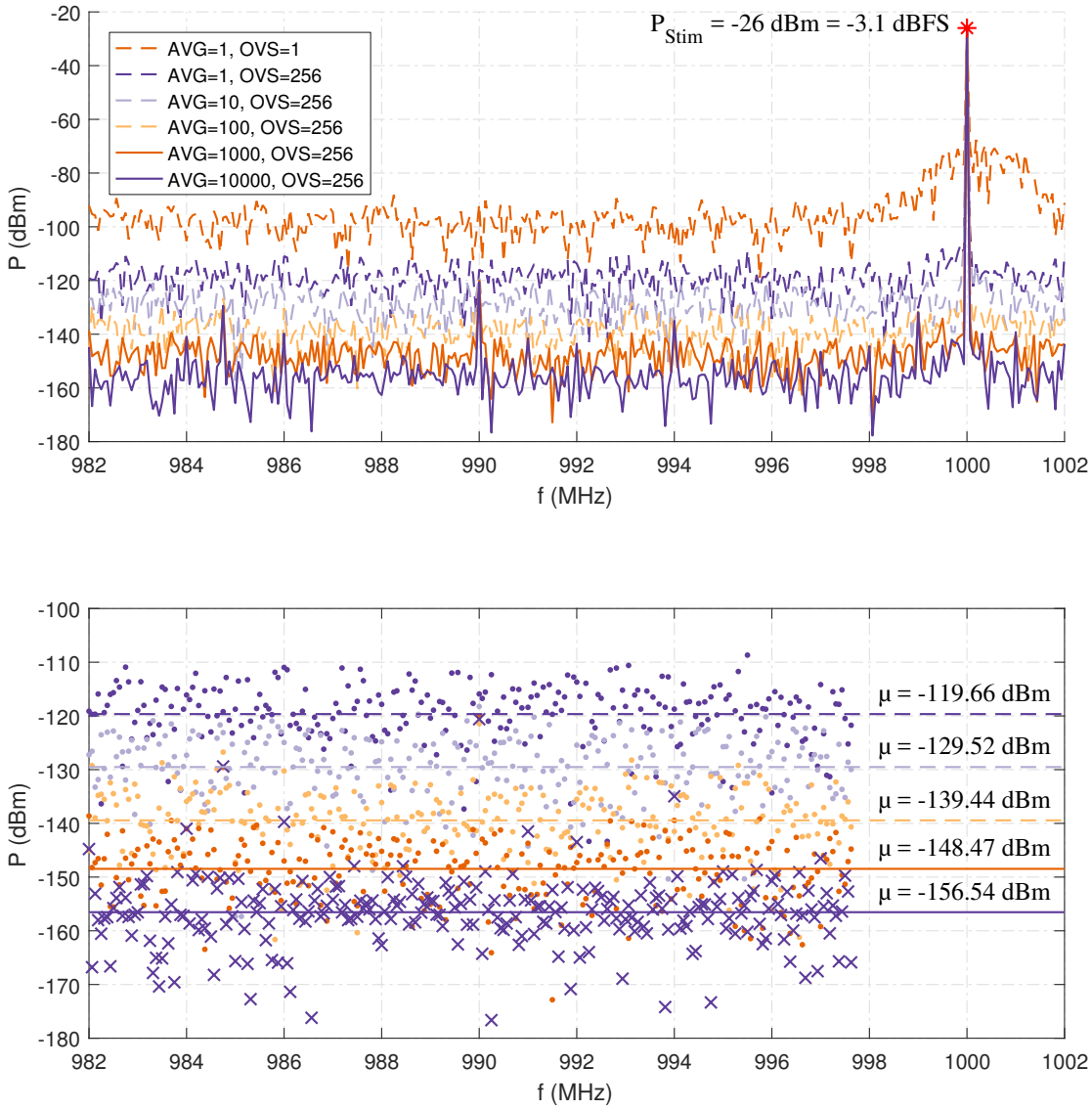

Figure 2.68: Measurement results of the input power referred system noise-floor for different averaging factors and a oversampling factor OVS = 256 for the frequency range of 982 to 1002 MHz with a step-size of 62.5 kHz, including a reference carrier of -26 dBm, equivalent to -3.1 dBFS using a total IF VGA gain of G=-10 dB, at 1000 MHz. Reference signal generated by SRS SG384 coupled to the 10 MHz output of the VNA receiver. Second graph shows a detail of the thermal noise-floor dominated area from 982 to 998 MHz, with lines added for the corresponding mean noise power μ.

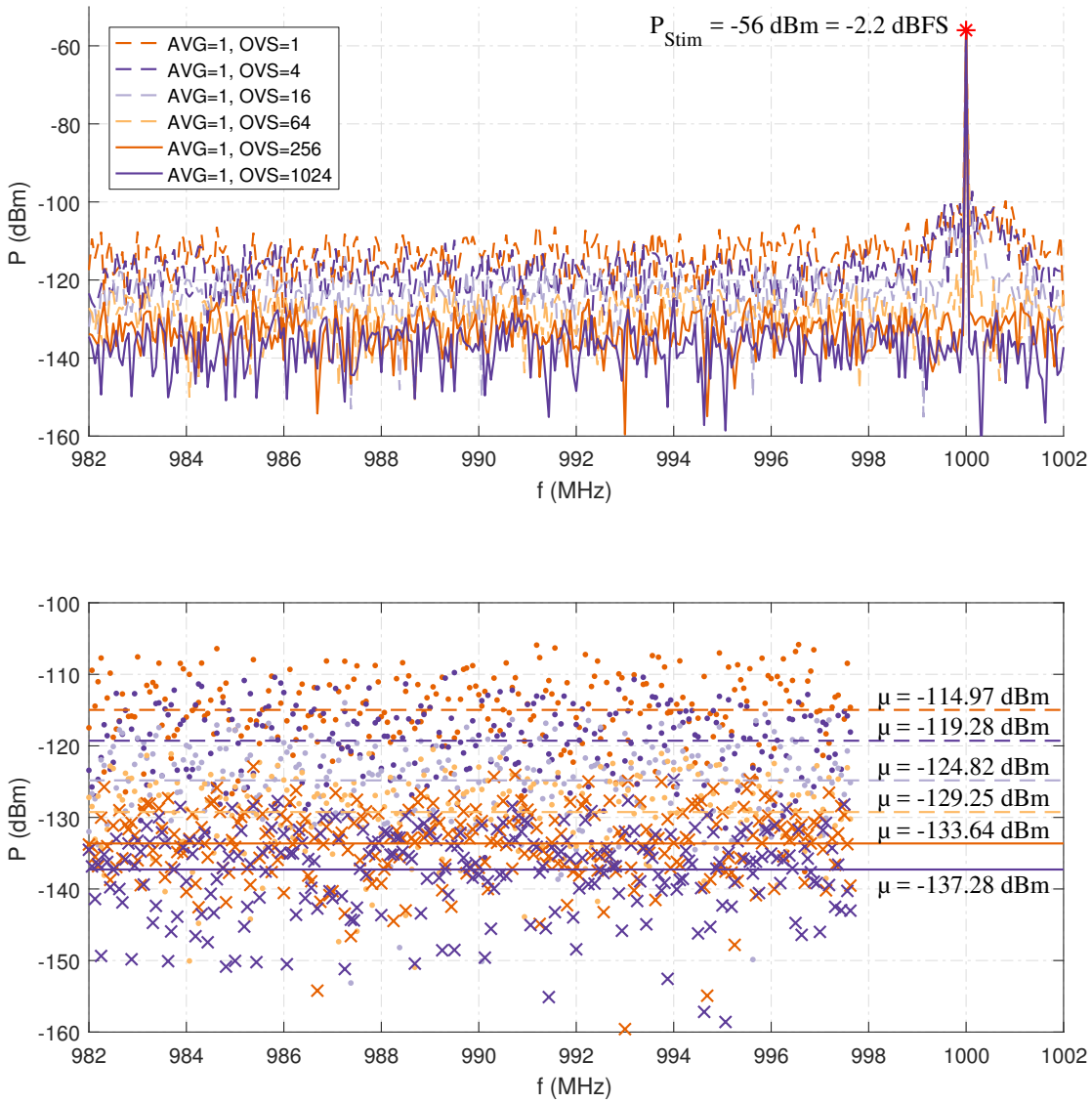

Figure 2.69: Measurement results of the input power referred system noise-floor for different oversampling factors with no averaging for the frequency range of 982 to 1002 MHz with a step-size of 62.5 kHz, including a reference carrier of -56 dBm, equivalent to -2.2 dBFS using a total IF VGA gain of G=20 dB, at 1000 MHz. Reference signal generated by SRS SG384 coupled to the 10 MHz output of the VNA receiver. Second graph shows a detail of the thermal noise-floor dominated area from 982 to 998 MHz, with lines added for the corresponding mean noise power μ.

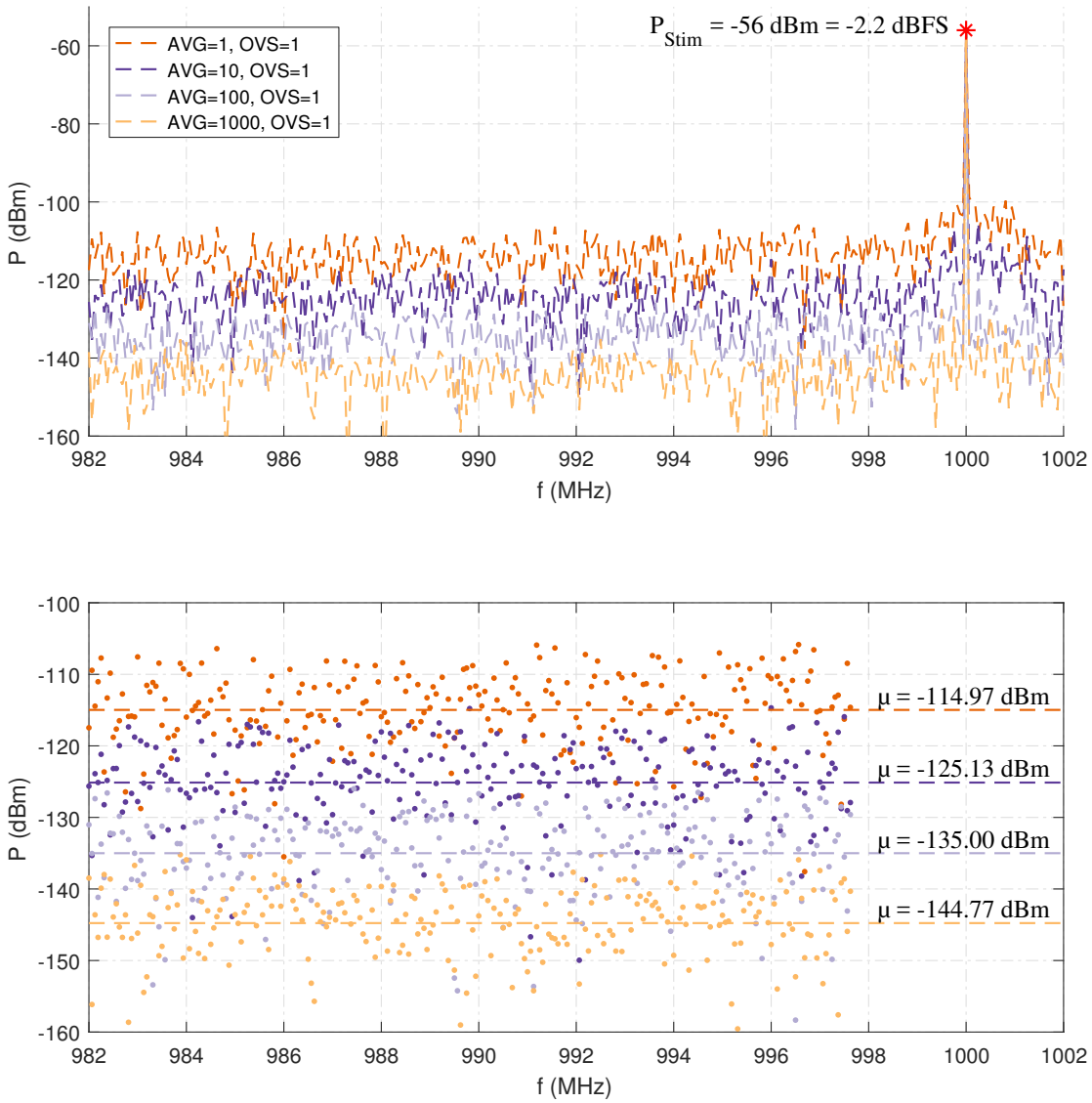

Figure 2.70: Measurement results of the input power referred system noise-floor for different averaging factors with no oversampling for the frequency range of 982 to 1002 MHz with a step-size of 62.5 kHz, including a reference carrier of -56 dBm, equivalent to -2.2 dBFS using a total IF VGA gain of G=20 dB, at 1000 MHz. Reference signal generated by SRS SG384 coupled to the 10 MHz output of the VNA receiver. Second graph shows a detail of the thermal noise-floor dominated area from 982 to 998 MHz, with lines added for the corresponding mean noise power μ.

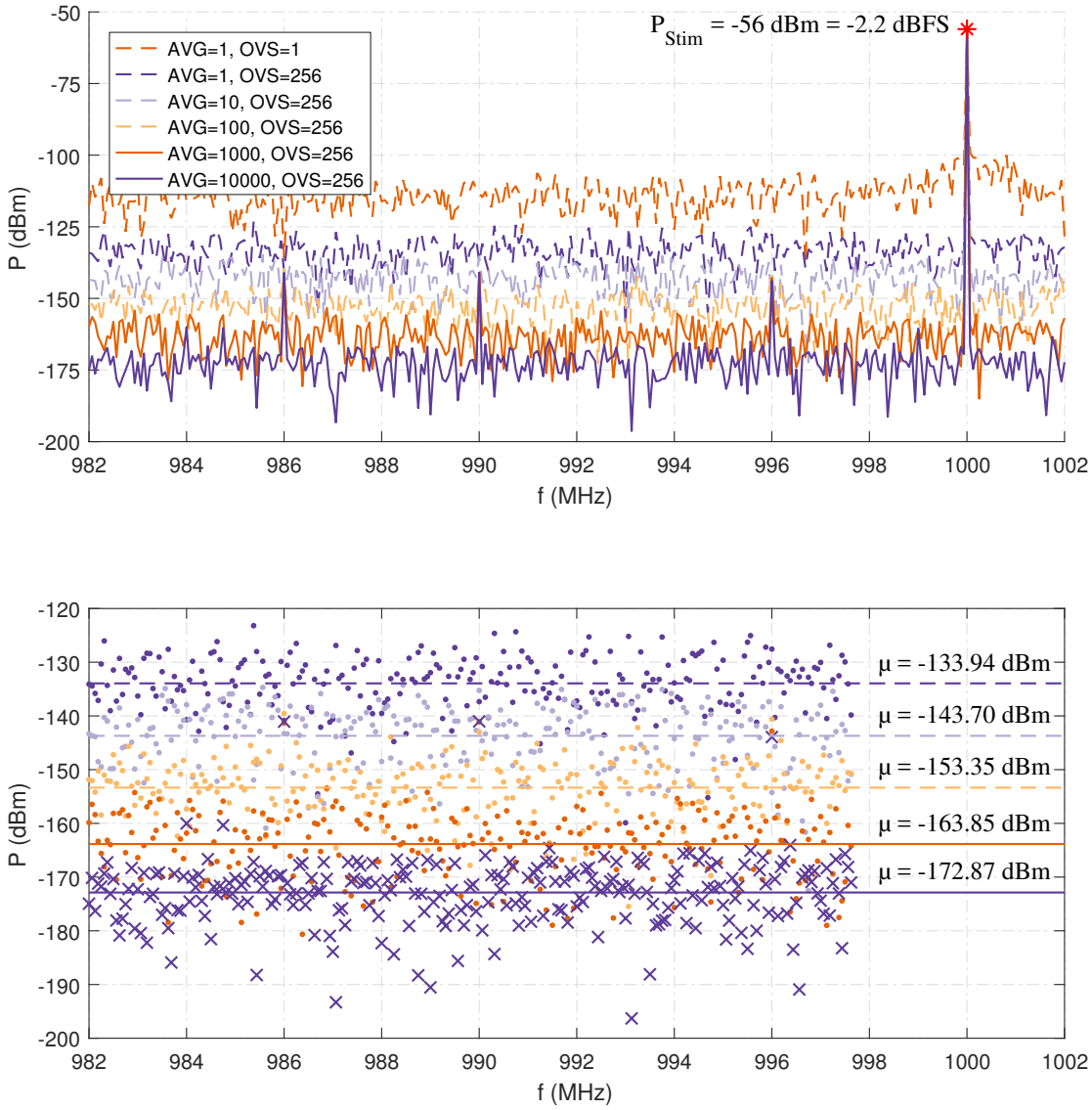

Figure 2.71: Measurement results of the input power referred system noise-floor for different averaging factors and a oversampling factor OVS = 256 for the frequency range of 982 to 1002 MHz with a step-size of 62.5 kHz, including a reference carrier of -56 dBm, equivalent to -2.2 dBFS using a total IF VGA gain of G=20 dB, at 1000 MHz. Reference signal generated by SRS SG384 coupled to the 10 MHz output of the VNA receiver. Second graph shows a detail of the noise-floor dominated area from 982 to 998 MHz, with lines added for the corresponding noise power mean μ.

- The oversampling and averaging procedures perform as expected, although the SNR process gain achieved via averaging is slightly more effective.
- The expected process gain of 6 dB per additional oversampling step is not achieved in all cases and is more often than not only measured to be 4 dB (see Fig. 2.66 and 2.69), which is most likely due to the sequential measurement of the under-sampled sampling points I to IV, which in turn increases the TI stability requirements of the IF signal and the sampling clock for higher oversampling factors. It can also be seen, that the oversampling performs better for higher IF gain settings which produce more broadband noise due to the aforementioned lack of narrow-band noise shaping filters and therefore adheres more closely to the prerequisites for the oversampling process.
- The $10 \cdot \log(N)$ process gain expected from the coherent averaging technique is accurately reproduced in the measurements. This is especially visible in the measurements shown in Fig. 2.67 and 2.70. A tenfold increase in the number of averaged samples results in a 10 dB lower mean noise power.
- When comparing the measurements taken at different IF gain settings it can be clearly seen, that the ADC input noise is dominated by the IF chains own noise figure. This is especially evident when comparing the baseline mean noise power between measurements where no averaging or oversampling is applied. The measured noise power, which should be primarily dominated by the quantization noise of the ADC in these cases, is only reduced by 15 dB for an increase in VGA gain of 30 dB. This effect will be mitigated in later revisions of the receiver hardware by employing narrow-band noise shaping filters in between the IF amplifier stages.
- The dynamic range of the 13.2 bit (ENOB) ADC can be extended to approximately 133 dB by combining both techniques, as evident in the 10000 times averaged and 256x oversampled measurement shown in Fig. 2.68, at the cost of prolonged measurement time.
- The auto-correlation filter properties of the procedures can be nicely seen in the phase noise skirt of the reference carrier tone produced by the SG384. Although the phase noise is almost 40 dB higher in power than the noise floor of the system, the phase noise skirt is often even more attenuated that the inherent system noise floor for an increase in averaging or oversampling factor.
- When the configurable IF gain is used to shift the dynamic range of the ADC, an input referred mean noise floor of -172.9 dBm can be achieved by the VNA receiver, as demonstrated by the measurement shown in Fig. 2.71. Furthermore, it can be seen that some internal coherent sources of interference present at 986 MHz, 990 MHz and 996 MHz in Fig. 2.68 and 2.70 are not attenuated, but recovered from below the starting noise floor and gain SNR with every increase in oversampling or averaging factor.

Most importantly, the different averaging and oversampling factors do not have any significant influence on the absolute value of the reference carrier signal and therefore do not alter the measurement result of coherent signals.

The following magnitude deviations for the reference carrier power between the different settings for the oversampling and averaging factors were observed:

- Below 0.005 dB for the -56 dBm (Fig. 2.70) and 0.0025 dB for the -26 dBm (Fig. 2.67) test-case when only averaging was applied,
- Less than 0.022 dB for the -56 dBm (Fig. 2.69) and 0.03 dB for the -26 dBm (Fig. 2.66) test-case when only oversampling was applied, and
- Less than 0.01 dB for both the -56 dBm (Fig. 2.70) and the -26 dBm (Fig. 2.68) test-case when both methods were applied simultaneously.

In conclusion the demonstrated dynamic range, repeatability and noise performance of the receiver is sufficient to resolve the switch cross-talk coefficients of the (5+2)-term, (10+4)-term and 7-term xUOSM cross-talk correction methods presented earlier in this work throughout chapters 2.2.5 to 2.2.9 with an adequate SNR.

This high sensitivity demonstrated by the prototype system also allows the simpler dual-match calibration standard based variants of these aforementioned procedures to be used for calibration. However, care must be taken to match the test-set and the input power levels presented to the VNA receiver to its lower maximum input power limit for linear measurements by additional attenuation or lower stimulus generator output power when compared with a normal VNA receiver.

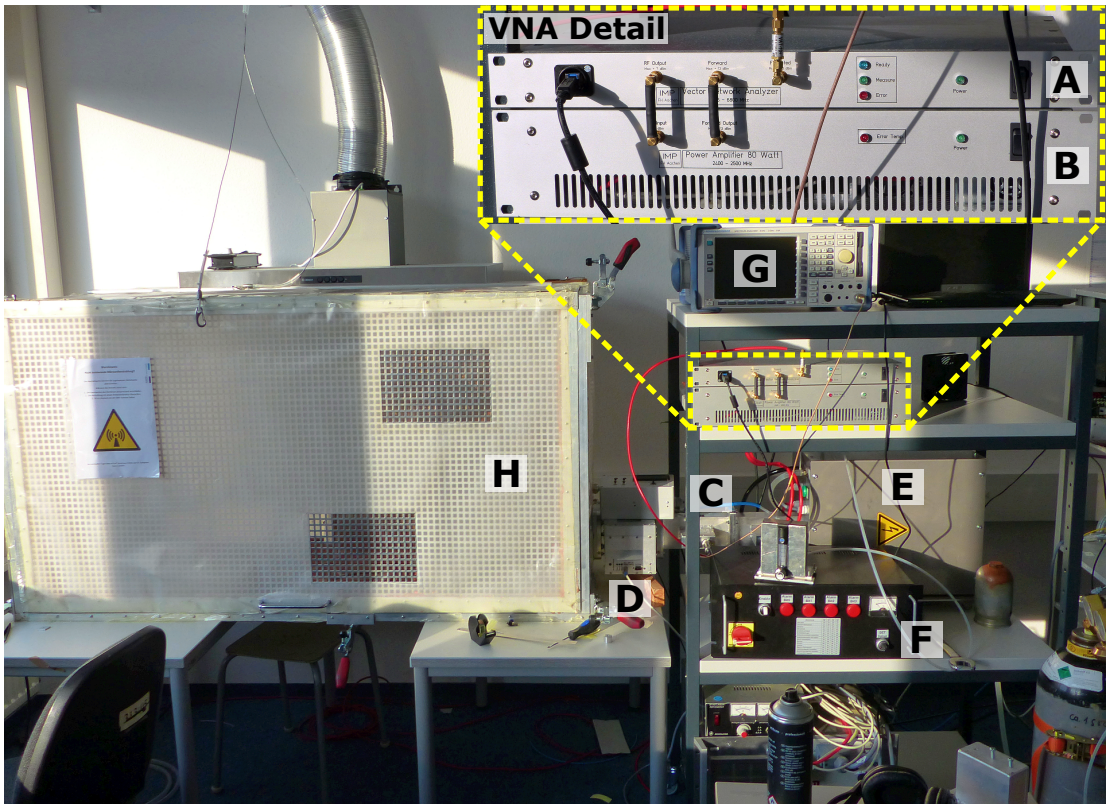

Figure 2.72: Picture of a 6 kW magnetron based 2.45 GHz ISM-band Hot-S_{11} plasma characterization setup using the modular VNA system presented in this work. Annotations: A - single receiver VNA, B - 80 W stimulus signal power amplifier, C - S-band waveguide directional couplers, D - motorized three-stub S-band waveguide tuner, E - 6 kW CW 2.45 GHz magnetron source, F - magnetron PSU and control unit, G - R&S FSP3 monitoring spectrum analyzer, H - EMI shielded experiment chamber with forced air ventilation.

2.4 Numerical Simulation and Comparison of the Concepts

2.4.1 Description of the Simulation Environment and Work Flow

In order to develop, test and evaluate the performance of the different single receiver VNA test-set topologies including the error and cross-talk correction methods presented earlier without the added uncertainty of a completely new VNA hardware design and to allow for tests with easily changeable switch and performance settings, a custom synthetic single receiver simulation environment and work-flow was developed for this thesis.

The numerical synthetic single receiver VNA simulation used in the following sections can be split into the following individual parts and tasks:

- Replication and S-parameter simulation of the test-set, including the receiver wave selector input switch, and the DUT for each individual state of the test-set in Keysight Advanced Design System (ADS).
- Numerical simulation of the receiver I/Q data acquisition process, performed by a model of the receiver sampling process in MATLAB, which uses the performance figures of the receiver outlined in chapter 2.3.7 of this work to generate synthetic measurement results comparable to the actual hardware.
- Calculation of the synthetic complex test-set wave data by a numerical I/Q sampling model using the transmission paths of the S-parameter files generated by ADS.
- Performing the calibration and correction on the synthesized test-set wave data using the various error correction methods presented earlier, which were also implemented in MATLAB.

The generation of the test-set S-parameters, including the DUT itself, is modeled after the stateful flow-graph diagrams introduced in the theoretical analysis of the single switched receiver architecture.

For each state of the receiver input wave selector and the stimulus switch (or direction), one dedicated state is captured in the test-set simulation in ADS. The definition of discrete test-set states furthermore allows to perform a form of multi-port-two-port reduction by assigning the active ports of the corresponding state a $50\,\Omega$ measurement port, for which the S-parameters will be simulated and captured, while inactive ports are terminated with an ideal $50\,\Omega$ termination resistor and therefore reduce the number of measurement ports necessary for the simulation. This is exemplary shown for the reflectometer reference implementation in Fig. 2.73.

The overall aim of the S-parameter simulation in Keysight ADS is to generate a numerical representation of the test-set signal path from the source to the sink of the signal - which is essentially equivalent to the forward transmission S-parameters S_{21}, S_{43}, etc., for a given state of generator and receiver switch selection state combination. This implicitly includes all cross-talk and mismatch effects present in the test-set, which are captured by their super-positioned influence on the active path. All possible ports are modeled with finite fixed return loss through mathematical two-port S-parameter

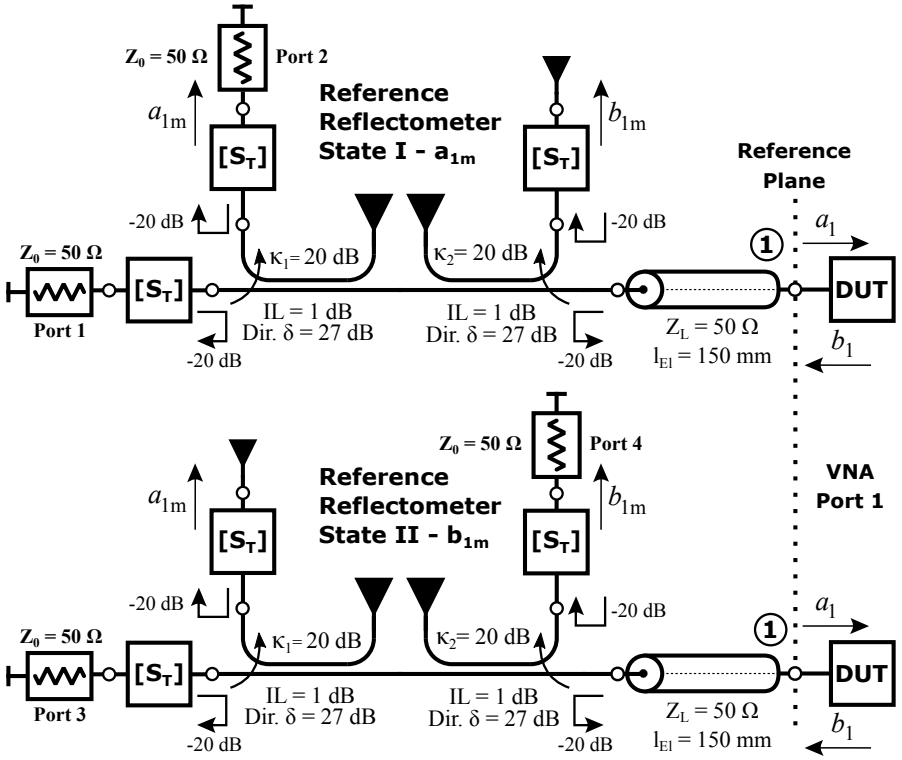

Figure 2.73: Schematic of the full two-receiver reference reflectometer implemented in Keysight ADS.

description boxes that are fixed between the states, therefore the benefits of ideal terminations in simulation environments do not apply at any time.

Synthesized reference test-sets are built for a standard synthetic reference VNA with two receivers in case of the one-port reflectometer and four receivers for the double reflectometer used for two-port measurements. For the switched single receiver, both the straight forward replacement of the individual receivers by a receiver input wave selector switch and the switched reference wave method were implemented. The switched receiver architectures simulated include the one-port reflectometer, the unidirectional virtual three-receiver test-set and the virtual four-receiver test-set, in order to verify the performance of all correction methods against the standard VNA reference implementation. Only SPDT switches are used in the simulations and the Y- or tree-configuration is used for the receiver input wave selector switch, as discussed earlier in the hardware section in chapter 2.3.6.

The performance of the receiver input wave selector switch is varied for the various architectures to investigate the influence of different amounts of cross-talk upon the correction efficacy of the algorithms, which is hard to perform in a switch-state respecting manner in reality, as the classical 15-term correction check method of inserting a constant low insertion loss cross-talk path by connecting an attenuator using two tee sections

across the test-set ports ([57, 49]) fails in terms of TI switch state assertion, due to its absolute time invariance, which is not the case with a multi-state leaky receiver wave selector switch.

The simulation and synthesis of wave data is performed for the following switch isolation cases:

- A good quality semiconductor PIN-diode based switch with 46 dB of isolation,
- An average semiconductor PIN-diode based switch with 30 dB of isolation,
- A very low isolation switch with 20 dB of isolation, which is used only for the one-port reflectometer test case, and
- A switch modeled by S-parameters provided by the manufacturer of the PIN-diode switch used in the hardware implementation (IDT F2923).

All the synthetic switches are defined to have constant parameters over the frequency range. This includes a constant return loss of RL = 20 dB on all of their ports, including the absorption state for the inactive port, and an insertion loss of IL = 1 dB for the active path.

The directional couplers used in the simulated test-sets are modeled after the parameters of the common L3 Narda-Miteq 3003-20, one octave 2-4 GHz 27 dB directional coupler, which was used in the early evaluation stages of the hardware. In contrast to the real coupler, the simulated synthetic coupler is again modeled to be frequency independent in its characteristics.

The numerical simulation of the different VNA topologies in Keysight ADS is carried out in the frequency range of 400 MHz to 6400 MHz using 401 equidistant frequency sampling points, which results in a frequency step-size of 15 MHz in the output S-parameters files.

The synthetic calibration standards used for the simulated wave data generation are modeled after the Rosenberger RPC-N female calibration standards taken from a 05CK100-150 RPC-N calibration kit (Fig. 2.74), which is also used for calibration for the verification of the algorithms using the real VNA hardware.

Due to the polynomial frequency dependent capacitance model necessary for modeling the fringe capacitance of the open calibration standard ([27]), its S_{11} parameter is pre-calculated in MATLAB for the frequency range and step-size necessary for the simulation, saved in a touchstone ([28]) S1P file, and used as a black box S1P element in Keysight ADS. While not strictly necessary otherwise, this procedure is also used to integrate the S_{11} model of the short and the two-port model of the thru standard into the ADS simulation. The match or load standard is modeled as an ideal 50 Ω termination, while the return loss of the thru is also assumed to be ideal, i.e. $S_{11} = S_{22} = 0$, as no further data besides length and loss factor is specified.

Each virtual connection of a DUT or calibration standard is captured in its own S-parameter file that contains all wave transmission path of all states of the model. This results in 4-port S4P touchstone files for the reflectometer analysis and 16-port S16P touchstone files for all of the two port test-sets.

Figure 2.74: Rosenberger 05CK100-150 RPC-N SOLT 18 GHz calibration kit, including isolation match standards and sliding loads for both connector genders.

The numerical simulation of the I/Q sampling receiver, which was carried out using MATLAB, tries to replicate the sampling procedure implemented on the receiver as truthfully as possible. In order to perform the simulation, the transmission path S-parameters (see Fig 2.73) corresponding to the synthetic test-set waves a_i and b_i are extracted and converted to their magnitude and phase representation which is then used as the argument for the numerical sampling simulation.

The I/Q sampling simulation covers the following effects:

- The finite data resolution, saturation, and overflow effects caused by the integer math on the controller,
- Analog clipping of the values or digital overflow due to input saturation of the ADC,
- All jitter related noise effects by applying the central limit theorem and using a unified total RMS jitter figure,
- The quantization noise present in an ideal 16 bit ADC,
- The noise-floor or ENOB of the ADC itself, and
- The oversampling and coherent averaging routines.

All noise effects are modeled as AWGN processes by using normal distributed, pseudo-random numbers, scaled to the appropriate values.

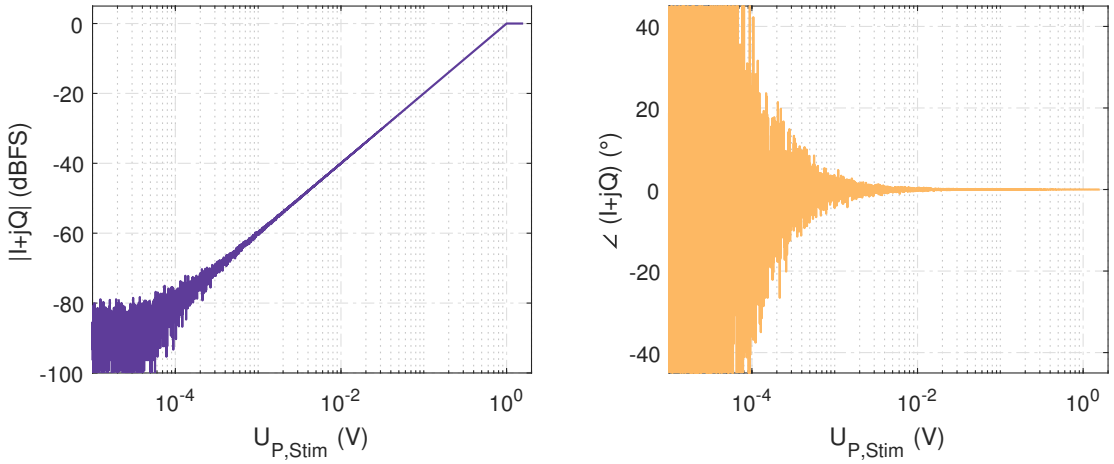

Figure 2.75: Response of the simulated I/Q sampling receiver 16-bit ADC to an IF stimulus signal $y(t) = U_P \cdot \sin(2\pi \cdot 8\,\text{MHz} \cdot t + \Phi_0)$ peak voltage sweep. $0\,\text{dBFS} \equiv 833.5\,\text{mV}_p \equiv 1.667\,\text{V}_{pp}$, $\Phi_0 = 0°$ and a combined sampling aperture RMS jitter of $t_j(\text{RMS}) = 1000\,\text{fs}$.

The fundamental equation used to generate the analog sampling points is based upon the model of an ideal S/H circuit with additive jitter using

$$y(t_s) = S_{2,1}^{\text{Path}} \cdot G \cdot \sin(2\pi \cdot f_{\text{IF}}(t_0 + t_j) - \angle(S_{2,1}^{\text{Path}}) + \Delta\Phi_s)\,, \tag{2.168}$$

with $t_0 = 0$ due to repeatable coherence, G as the virtual gain of the sampling system and $\Delta\Phi_s = \{0, \pi/2, \pi, 3\pi/2\}$ as the phase advance corresponding to the sampling point. The gain G is needed to match the virtual transmission paths of the ADS simulation to the simulated input voltage dynamic range of 1.667 V or ±833.5 mV of the ADC and corresponds to the overall gain of the real VNA receiver. Due to the simulated insertion loss of the components and the coupling factor of the directional couplers used in the simulation (see Fig: 2.73), a simulated IF conversion gain of $G = 15\,\text{dB}$ is used throughout the simulation for a simulated input power back-off of approximately 6 dB to 0 dBFS.

In order to generate the synthesized data, the following procedure is followed for each of the virtual sampling and phase advance points I to IV:

1. A new random, normal distributed, additive jitter time offset t_j with the mean $t_j(\text{RMS})$ is generated.
2. Eq. (2.168) is evaluated using the random jitter component t_j, the corresponding complex S_{21} of the active wave path and the current phase advance $\Delta\Phi_s$ of the sampling point, yielding a simulated sampled analog voltage.
3. The random AWGN noise floor, as defined by the ADC ENOB, is added to the analog voltage sample.
4. The analog voltage sample is clipped to $U_{\text{max}}, U_{\text{min}} = \pm 833.5\,\text{mV}$.

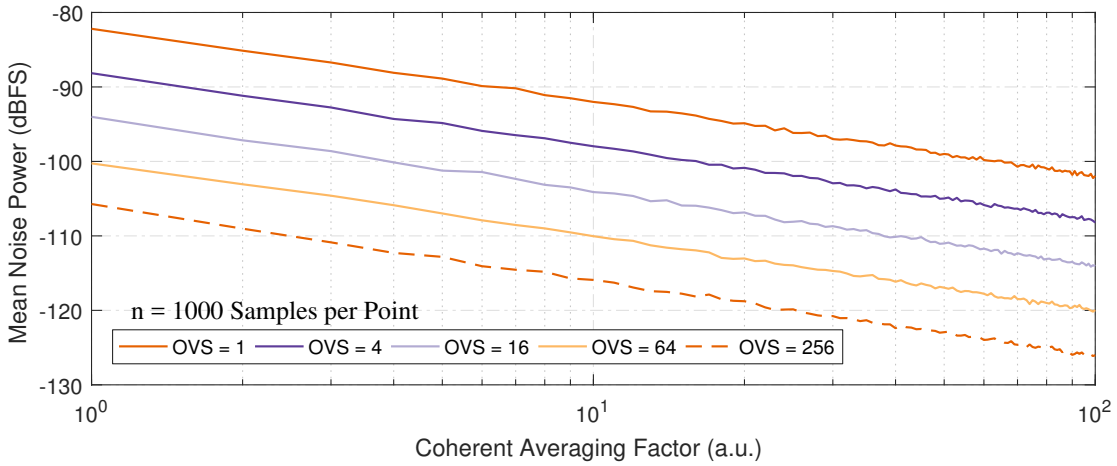

Figure 2.76: Simulated effect of different oversampling and averaging factors on the mean noise power of the numerical 16-bit I/Q sampling receiver, sample size n = 1000 simulation results per mean noise power calculation.

5. The sample is converted and quantized to a digital integer based representation of the analog voltage by rounding $y_D(t_s) = (y(t_s) + U_{\max})/(U_{\max} - U_{\min}) * 2^{16} - 1$ to the nearest integer.

6. The result is clipped to the digital integer value range.

7. Steps 1 to 6 are repeated 4^N times as required for the oversampling factor N and the results are summed in one of four 32 bit accumulators for each sampling point.

8. The oversampling accumulators are scaled back by 2^N.

9. The sampling phase $\Delta\Phi_s$ is advanced and steps 1 to 8 are performed again until all four sampling points are captured

10. Steps 1 to 9 are repeated as required for the coherent averaging factor and the complex I/Q result is calculated and accumulated in double precision floating point values for the I and Q part.

11. The back-scaling of the averaging accumulator is performed, which yields the final complex I/Q phasor in its double precision floating point representation.

The result of a simulated analog input voltage sweep evaluated by the numerical ADC simulation is shown in Fig. 2.75, while the effect of different oversampling and coherent averaging factors upon the resulting I/Q noise-floor without any input signal is shown in Fig. 2.76. For all the following simulation results, a total RMS jitter of $t_j(\mathrm{RMS}) = 1000\,\mathrm{fs}$ is used. This is based upon the RMS sum of the sampling clock jitter, the stimulus and

the LO synthesizer, calculated as

$$t_j(\text{RMS}) = \sqrt{t_{\text{j,s}}^2 + t_{\text{j,Syn}}^2 + t_{\text{j,Syn}}^2)}\,, \tag{2.169}$$
$$t_j(\text{RMS}) = \sqrt{(633\,\text{fs})^2 + (530\,\text{fs})^2 + (530\,\text{fs})^2} = 981\,\text{fs} \approx 1000\,\text{ns}.$$

The simulation of the sampled test-set waves is iterated over all sampling points and wave paths of the test-set in the S-parameter data. The resulting synthetic test-set wave data is saved in the same format as the real measurement results, which allows a transparent use of measured and simulated data with the same calibration and correction algorithms, which increases the confidence in the measurement results obtained with the VNA hardware considerably.

All numerical VNA simulation results presented in this chapter are generated with a simulated $t_j(\text{RMS}) = 1000\,\text{ns}$, an oversampling factor of 3 corresponding to 64 samples, and an additional coherent averaging performed over 10 I/Q samples to simulate the results of a practical compromise between measurement speed and dynamic range sought out by a user of a real VNA system.

2.4.2 Selection of Appropriate Synthesized Devices Under Test

In order to asses the performance of the calibration and correction routines, measurements of a multitude of synthetic verification standards are simulated in ADS and used to synthesize the appropriate test-test wave data with the ADC simulation. These verification measurements can be coarsely divided into three classes:

- One-port reflectometer verification and performance estimation standards,
- Standard two-port verification and performance estimation standards, and
- Additional complex two-port verification and performance estimation standards built from multiple basic verification standards, which are especially tailored to the specific transmission cross-talk issues present in switched single receiver VNAs.

In the simulated single port reflectometer measurements, the following DUTs are replicated in ADS:

- The MSO 3-term calibration standards, with a perfect match (or load) of exactly $Z_0 = 50\,\Omega$, a short with an electrical $Z_L = 50\,\Omega$ transmission line length of 15.10 mm, modeled after the short standard found in the RPC-N calibration kit used for the hardware measurements, and an open standard with an electrical $Z_L = 50\,\Omega$ transmission line length of 12.32 mm using the polynomial C coefficients of the open, serial #02364, found in the Rosenberger RPC-N calibration kit,
- Ideal, mathematical defined, return-loss one-port standards for a return loss of $RL = \{6\,\text{dB}, 10\,\text{dB}, 20\,\text{dB}, \text{and } 40\,\text{dB}\}$, as a stand-in for reference attenuator one-port measurements to estimate the return loss measurement accuracy after 3-term correction,

- Simulated loss-less airline measurements for transmission line impedances of $Z_L = 50\,\Omega$ and $Z_L = 25\,\Omega$ using line lengths of $l = 150\,\text{mm}$ and $l = 300\,\text{mm}$, terminated with the calibration load or short to directly measure the residual systematic errors of the calibration ([27, 52, 157]) in the form of residual directivity and source match of the reflectometer, and
- A dynamic DUT showing both reflection and good return loss alternating over the frequency range of interest, by combining the a $Z_L = 50\,\Omega$ airline terminated by the calibration short with the calibration match using a tee junction, which uses the $\lambda/2$ and $\lambda/4$ transformation of the shorted high-Q airline stub to synthesize both high and low SNR data in the same sweep for the b_1 test-set wave which will be discussed in more detail in the following paragraphs.

The ideal return loss standards are additionally combined with a simulated $Z_L = 50\,\Omega$ $l = 150\,\text{mm}$ loss-less airline in order to cover most of the smith chart plane, simulating a S_{11} measurement for reflection passive DUTs ([157]). The 6 dB and 10 dB terminations also double as mismatch verification standards to check for receiver linearity (see [157]).

The residual directivity measurement, as carried out by the $50\,\Omega$ airline in combination with the calibration match measurement, is very sensitive to the accuracy of the directivity coefficient E_D ([27, 157]). While this measurement is usually carried out to check for defects of a (sliding-)load standard or swapped standards during normal VNA calibration, it is important for comparing the single receiver VNA architecture performance with the normal VNA topology due to the modification of the 3-term error coefficients including E_D by the receiver input wave selector switch cross-talk coefficients, which is not captured in the model.

The ripple test ([52]), performed by the $50\,\Omega$ airline in combination with the calibration short measurement, is sensitive to errors in all error coefficients (([157]) and allows to define error boundaries in the both magnitude and phase ([52]) for measurement results of other DUTs presenting comparable receiver SNR. This verification measurement is furthermore important for not only verifying and comparing the basic accuracy of the switched receiver reflectometer architectures with the standard reflectometer, but also for the correction of the influence of the DUT reflection (or b_{1m}) dependent cross-talk upon the reference wave measurement a^*_{1m} in combination with the mismatch standards.

For the uni- and bi-directional two port measurements the number of simulated one-port verification standards is thinned out and only includes the ripple and residual directivity tests using $50\,\Omega$ and $25\,\Omega$ 150 mm loss-less airlines to confirm and evaluate the accuracy of the reflectometer calibration in the multi-port context and demonstrate the DUT reflection dependent transmission cross-talk with a verification standard that is linear independent of the calibration standards.

In addition to the MSO 3-term standard connections to each driven port, a thru connection and measurement is performed, which is modeled to be loss-less, perfectly matched, and with an electrical length of $l_{\text{thru}} = 46.10\,\text{mm}$ equivalent to the female thru in the Rosenberger RPC-N calibration kit.

In order to account for the (5+2)-Term, (10+4)-Term and the 7-Term model extensions,

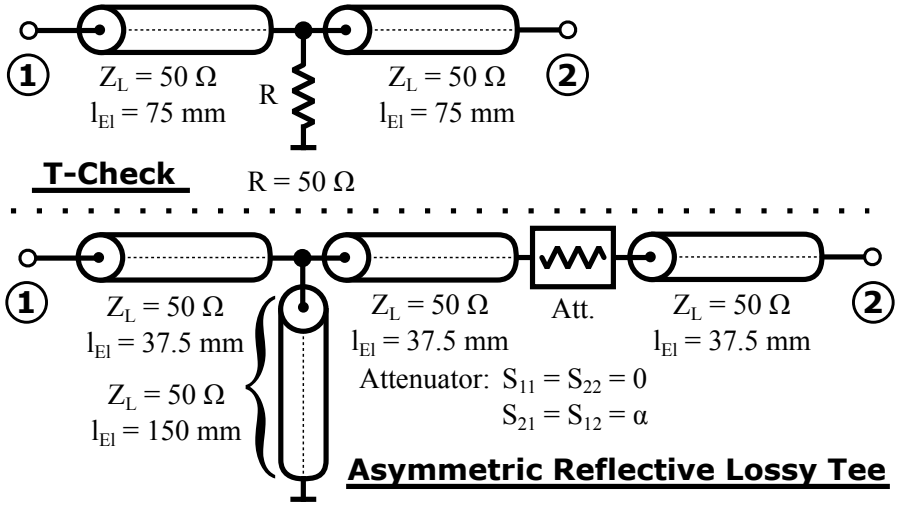

Figure 2.77: Additional simulated two port compound verification standards. Left: Ideal T-Check. Right: New asymmetric reflective lossy tee (ARLT).

additional isolation standard measurements are performed, consisting of additional match-match, short-match and match-short measurements to account for the simpler form of receiver switch cross-talk coefficient determination when two match standards are available, as demonstrated in Eq. (2.58) and (2.59) for the (5+2)-Term procedure and Eq. (2.95) to (2.98) for the (10+4)-Term procedure.

In accordance with the recommendations of EURAMET[43], the following two-port verification devices are used in the numerical simulation ([157]):

- A simulated $Z_L = 50\,\Omega$, $l = 150\,\text{mm}$ loss-less airline,
- A simulated $Z_L = 25\,\Omega$, $l = 150\,\text{mm}$ loss-less airline, also called a Beatty line in the two-port verification device context ([12]),
- A simulated T-Check device (see Fig. 2.77, [94]), that provides a quantitative figure of merit (FOM) to compare the two port measurement accuracy between the different topologies, calibration, and error correction procedures ([157]), and
- Asymmetric reflective lossy tees (ARLT, see Fig. 2.77), which are introduced here as a new tracking verification device and is especially tailored to the cross-talk issues present in single switched receiver VNAs as an enhanced replacement for the classical reference attenuator measurements in the traditional VNA metrology ([157]).

The $50\,\Omega$ airline is used as a phase and impedance reference standard and is sensitive to minor variation in almost all error coefficients ([157]). In the synthesized and simulated measurement case here, this standard is especially useful, as the assumptions $|S_{11}| =$

[43]EURAMET - European Association of National Metrology Institutes.

$|S_{22}| = 0$ and $|S_{21}| = |S_{12}| = 1$ are not mere approximations and therefore allow a precise comparison of the accuracy of load match coefficients between different topologies and algorithms.

The 25 Ω airline, or Beatty line, shares the same properties at the $n \cdot \lambda/2$ frequency points but also doubles as a mismatch standard especially at $n \cdot \lambda/4$, which is again interesting for comparing the switches single receiver measurements with a classical architecture due to the reflexion — transmission cross-talk and allows checking for the reflexion and transmission tracking accuracy at the same time. A 25 Ω transmission line will convert the 50 Ω load match impedance to exactly 12.5 Ω at $n \cdot \lambda/4$ and the resulting $|S_{11}| = -4.44\,\text{dB}$ and $|S_{21}| = -1.94\,\text{dB}$ at this points can be precisely calculated.

The T-Check is integrated mainly as an easy way to compare the results with a simple and accepted FOM that is especially sensitive to reciprocity violations in the error coefficients, but also allows for a simple qualitative check of the measurement accuracy. By using the error corrected measurements of all four S-parameters, the T-Check parameter c_T is calculated as ([94])

$$c_T = \frac{|S_{11} \cdot S_{21}^* + S_{12} S_{22}^*|}{\sqrt{(1 - |S_{11}|^2 - |S_{12}|^2)(1 - |S_{21}|^2 - |S_{22}|^2)}}\,, \tag{2.170}$$

with the asterisk denoting the complex conjugate in this case. This combined form of the T-Check can separated into a more granular forward $c_{T,F}$ and reverse $c_{T,R}$ T-Check parameter ([94]) in the form of

$$c_{T,F} = \frac{S_{11} S_{21}^* + S_{21} S_{11}^*}{1 - |S_{11}|^2 - |S_{21}|^2}\,, \tag{2.171}$$

$$c_{T,R} = \frac{S_{22} S_{12}^* + S_{12} S_{22}^*}{1 - |S_{22}|^2 - |S_{12}|^2}\,. \tag{2.172}$$

The dimensionless T-Check parameter c_T should be exactly equal to 1 for a perfect, error corrected, measurement system when a loss-less ideal tee and an ideal $R = 50\,\Omega$ termination is used. In reality, a result of $C_T = 1 \pm 0.1$ is generally accepted to be adequate for non-metrological measurements ([94, 157]) when a purpose made T-Check device using loss-reduced construction methods, a very accurate 50 Ω termination and a mechanically extremely short field line aligned match is used. Even greater variance is considered acceptable, when the T-Check device is build from a discrete tee junction and a match standard of the appropriate gender.

The new asymmetric reflective lossy tee (ARLT) verification standard (see Fig. 2.77 for a schematic and Fig. 2.78 for a picture of the components) was developed especially for this work and the verification of the cross-talk correction performance of the calibration and correction algorithms. The ARLT standard can be constructed from standard calibration and verification kit contents, with the addition of a tee junction of the appropriate connector standard and gender. This new standard combines the properties associated with 25 Ω Beatty line standard with the transmission tracking and return loss verification abilities of the reference attenuators normally used in the VNA verification context.

From the simulated S-parameters of the standard shown in Fig. 2.79 for an ideal loss-less ARLT with 40 dB of attenuation it can easily be seen, that the standard combines many

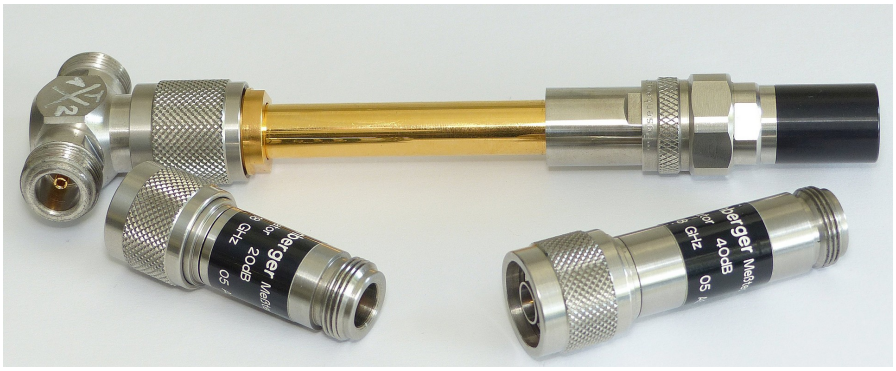

Figure 2.78: Rosenberger calibration and verification kit devices with an additional 3x(f)-N-connector tee used to assemble the asymmetric reflective lossy tee verification standard.

desirable properties tailored to the cross-talk issues introduced by the leaky receiver input wave selector switch of the single receiver VNA design:

- The return loss presented to port 1 continuously alternates over frequency between a highly reflective and well matched state due to $n \cdot \lambda/2$ and $n \cdot \lambda/4$ transformation by the shorted airline stub, which both stimulates the switch cross-talk paths, and allows checking for the dynamic range of the return loss measurement with a linear independent device.

- The return loss present on port 2 can be assumed to be almost constant and well-matched for higher attenuation values, which allows the cross-talk effects in the transmission measurements to be solely attributed to signal emanating from port 1. The return loss present at port 2 also doubles as a precisely determined frequency dependent mismatch standard for lower attenuation values.

- The device is reciprocal, i.e. $S_{21} = S_{12}$, which allows to directly assess the effect of the cross-talk on the transmission path by the corresponding excitation direction due to the orthogonal return loss behavior present at the two ports. For reference attenuator values $\alpha \geq 20\,\mathrm{dB}$, presenting a $|S_{22}| \leq -40\,\mathrm{dB}$, it is fair to assume that S_{12} will not be affected by the receiver wave input selector switch cross-talk and be representative for the transmission tracking performance, while S_{21} will show the hardware performance of the switch and the efficacy of the subsequent mathematical correction performed by the error model.

- The base level of insertion loss present in the S_{21} and S_{12} measurements can be precisely controlled by the reference attenuator and can easily be adapted to the requirements of different scenarios. Due to the high additional insertion loss present at the $n \cdot \lambda/2$ frequency points of the shorted airline stub, this measurement is perfectly suited to assess the overall transmission measurement dynamic range

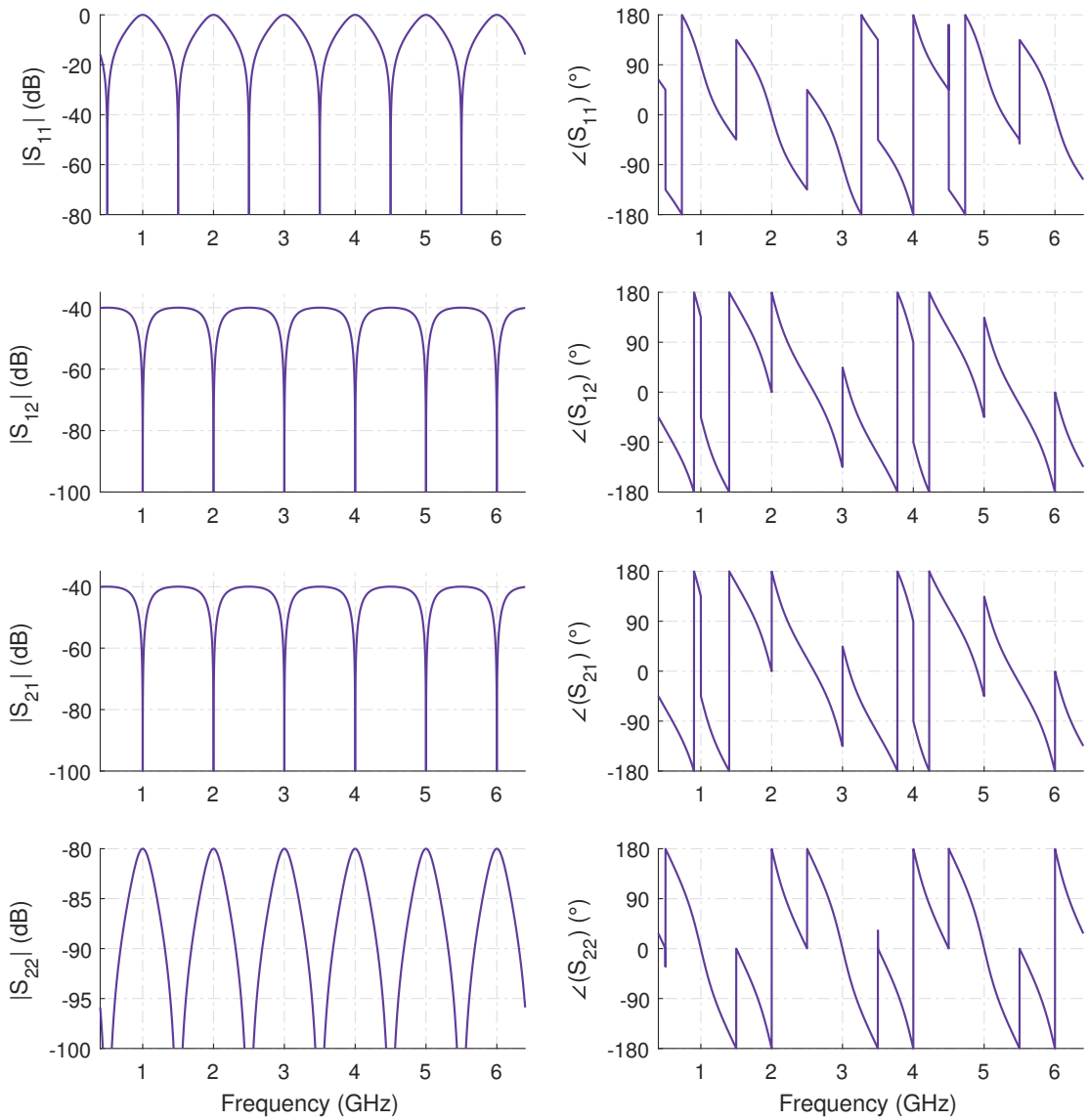

Figure 2.79: S-parameters of an asymmetric reflective lossy tee (see Fig. 2.77 for schematic) with 40 dB of attenuation and an electrical length of the 50 Ω shorted airline stub of 150 mm. Ideal simulated two port data.

capability of a VNA, its accuracy in low SNR conditions and the effectiveness of the different calibration and correction algorithms.

Beside the useful S-parameter magnitude properties of the ARLT, the phase information is also extremely effective in assessing even minor differences between architectures and correction algorithms due to the multitude of resonator based phase jumps present on both the reflection and the transmission parameters. This property leads to an electrically long unwrapped phase in a small overall package to test the tracking performance and the high slew rate of the phase jumps makes it easy to highlight even minor differences in measurement and error correction performance.

2.4.3 Numerical Reflectometer Results

The numerical reflectometer simulations are especially designed to test and verify the assumption made in the switched single receiver reflectometer discussion, that all cross-talk path introduced by the input wave selector switch will be absorbed into and successfully corrected by the existing 3-term model of the reflectometer.

Three different variants of test-sets were included in the simulation:

- A standard two receiver reflectometer with no input wave selector switch, as shown in Fig. 2.73,
- A switched single receiver reflectometer, as shown in Fig. 2.80, and
- A switched single receiver reflectometer with only one directional coupler for the b_1 wave implementing the switched reference wave technique, which is shown in Fig. 2.81.

All switched single receiver test-set simulations are performed using the three different switch models that are also used for further analysis as well as an additional fourth ultra low isolation test case proving only 20 dB of switch isolation to stress the assumptions made about the switched reflectometer error correction.

All synthetic switch cases are simulated to show the same isolation between the common output and the selectable wave inputs as well as between the wave inputs themselves, i.e. $C_i = X_i$ when using the notation of the reflectometer discussion, which is generally the case to within a few dB when using semiconductor PIN-diode switches.

The return loss of the switches is assumed to be constant on all ports using a return loss of $RL = 20\,\text{dB}$.

In contrast to these idealized constant performance figures, the IDT F2923 switch is simulated using the three-port S-parameters provided and measured by the manufacturer for its different states ([64]) to cover a realistic frequency dependent behavior.

The switch used for the switched reference wave topology (see Fig. 2.81) always shares its S-parameters with the receiver input wave selector switch used in the simulation.

In order to distinguish between the two different switched receiver test-set topologies evaluated in the simulations, the abbreviation *SRX* is used for the single receiver topology

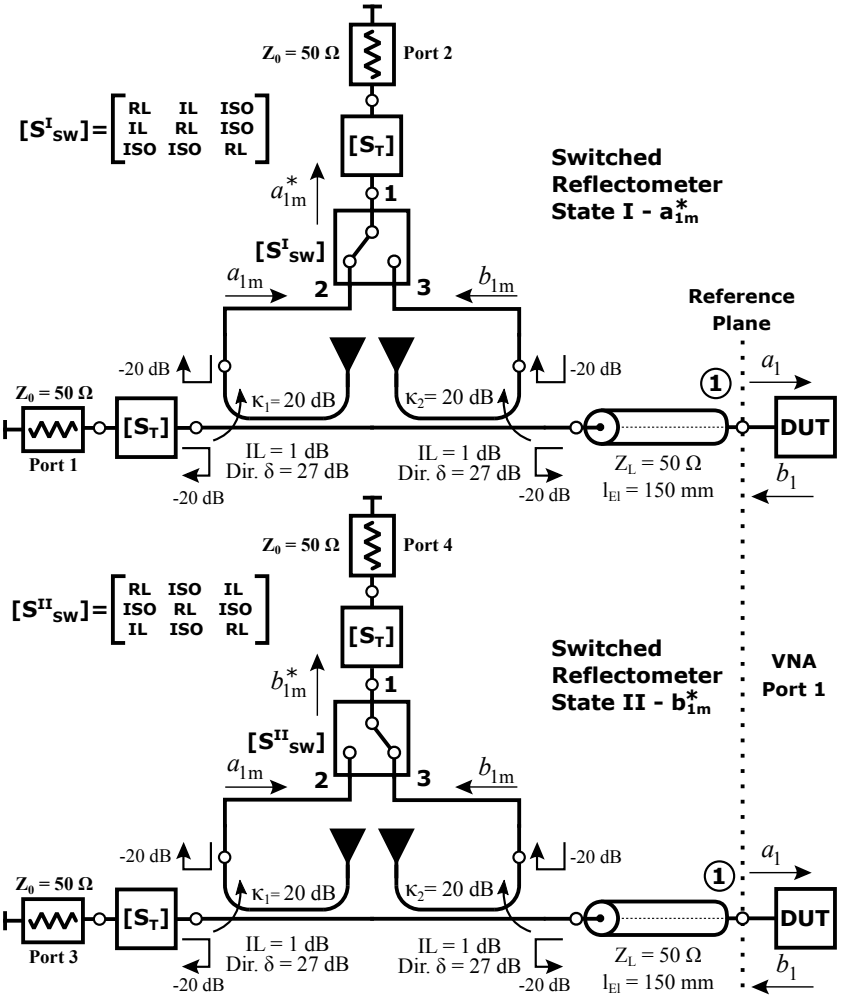

Figure 2.80: Schematic of the switched single receiver reflectometer test-set simulation implemented in Keysight ADS.

using a full set of directional couplers, while the abbreviation *SWR* is used for the switched reference implementation.

A simulated standard 3-term MSO calibration, according to Eq. (2.45), was performed with each of the test-set variants using the simulated equivalents of the Rosenberger RPC-N SOLT calibration standards.

The reflectometer error model coefficients E_D, E_{FR} and E_S that were obtained by this procedure in the different test-set topologies are shown in Fig. 2.82.

The error coefficients of the switched receiver reflectometer, shown in the left column of Fig. 2.82.A, verify the assumptions made during the coefficient comparison performed in theoretical analysis between the transfer function of the switched reflectometer obtained by stateful analysis and the classical reflectometer equation, as shown in Eq. (2.38). This is especially evident in the modification of the E_D reflectometer directivity coefficient

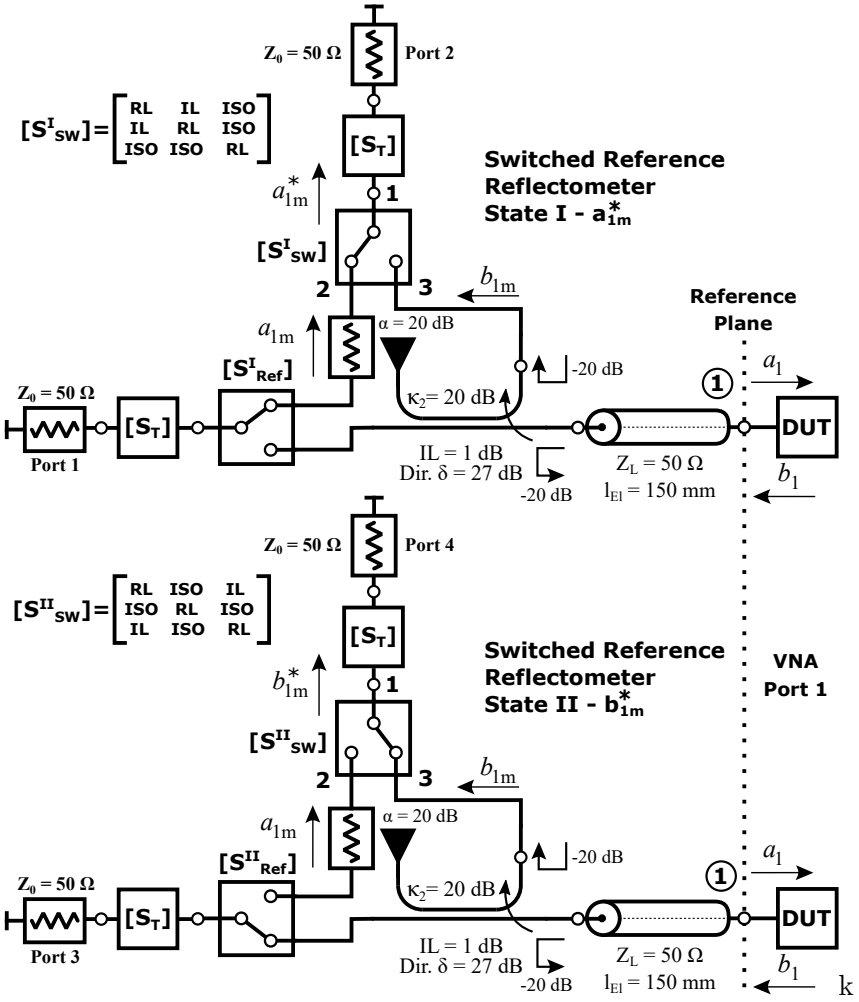

Figure 2.81: Schematic of the switched reference single receiver reflectometer test-set simulation implemented in Keysight ADS.

by the C_3^{I} and C_3^{II} switch cross-talk coefficients, which results in a proportional increase of the coefficient's value, and therefore decrease in actual test-set directivity, for lower switch isolations, which can be deduced from Eq. (2.38) by

$$E_D^* = \frac{E_D'}{1 + C_3^{\mathrm{I}}\, E_D} = \frac{E_D + C_2^{\mathrm{II}}}{1 + C_3^{\mathrm{I}}\, E_D}\,, \tag{2.173}$$

when compared with the values of E_D obtained using the same test-set in the reference two receiver configuration.

The same effect can also be observed for the value of the source match coefficient E_S in the measurements using synthetic switches, while the simulated E_S results for the real IDT F2923 switch IC are heavily influenced by the real return loss of the switch, in combination with the other test-set cross-talk and reflection paths, and therefore show

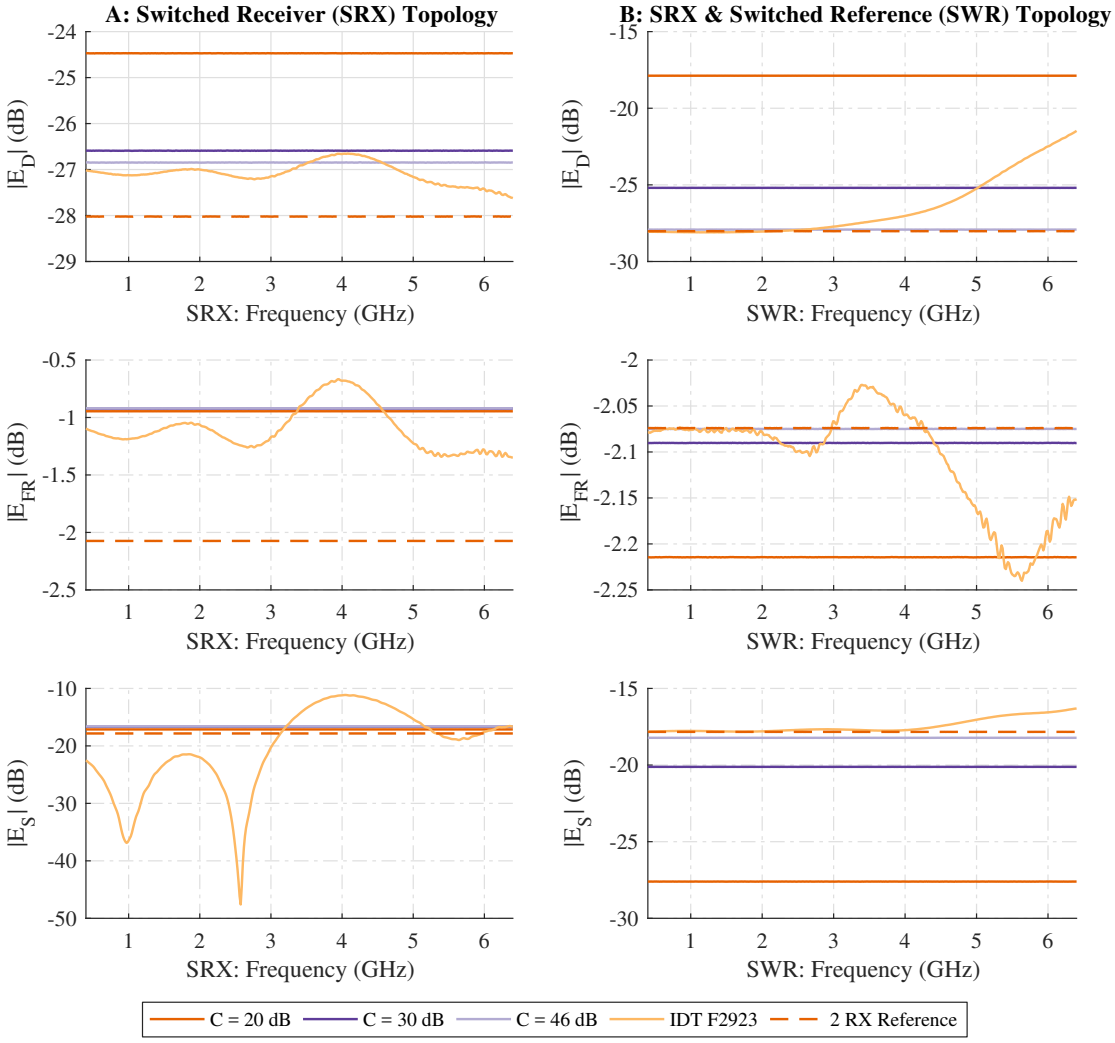

Figure 2.82: Reflectometer 3-term error model coefficients determined by MSO calibration for the simulated switched single receiver test-set topology (A - left column) and with additional reference wave switch (B - right column).

far greater variance in their values.

The error coefficients of the switched reference topology, shown in Fig. 2.82.B, replicate the results of the single switched receiver topology with the added effect, that the increase in overall isolation provided by the reference wave selector switch is equivalent to an increase in directivity of the reference a-wave directional coupler present in the classical test-set approach. This is especially evident in the E_D results, which show a far greater sensitivity to the switch isolation when compared with the classical two coupler reflectometer topology.

As a side note it is interesting to see, that an inverted effect of the switch isolation

upon the E_{FR} and E_S magnitude values exists in this topology for this specific test-set. This effect is caused by a different phase based superposition of the many cross-talk paths into the final abstract error coefficients and is no indication of a different error correction performance by the 3-term error model in this test-set topology.

A simulated direct residual directivity measurement ([27, 157]) was performed next in order to assess the reflectometer correction performance. For this test, two ideal 50 Ω 150 mm and 300 mm long loss-less transmission lines, terminated by a perfect 50 Ω resistor, were used. The results of this simulation are shown in Fig. 2.83 with an additional analysis of the statistical mean of the measurement data shown in Table 2.8.

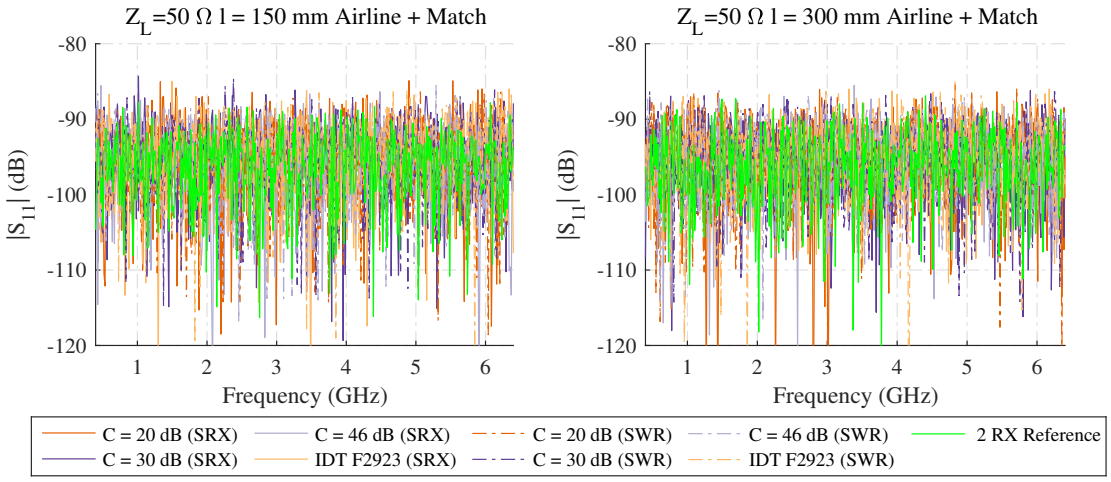

Figure 2.83: Numerical error corrected 3-term model results for the simulated measurement of the direct source match test with $Z_L = 50\,\Omega$, $l = 150\,\text{mm}$, and $l = 300\,\text{mm}$ airlines and the calibration match for different switch isolation coefficients C_i and in the switched single receiver architecture (SRX) and switched single receiver with switched reference architecture (SWR).

Line & Architecture	$C = 20\,\text{dB}$	$C = 30\,\text{dB}$	$C = 40\,\text{dB}$	IDT F2923
$l = 150\,\text{mm}$, (SRX), $\mu(\lvert S_{11}\rvert)$	-95.48 dB	-95.47 dB	-96.29 dB	-95.67 dB
$l = 300\,\text{mm}$, (SRX), $\mu(\lvert S_{11}\rvert)$	-96.24 dB	-95.92 dB	-95.83 dB	-95.49 dB
$l = 150\,\text{mm}$, (SWR), $\mu(\lvert S_{11}\rvert)$	-96.24 dB	-95.77 dB	-96.43 dB	-95.29 dB
$l = 300\,\text{mm}$, (SWR), $\mu(\lvert S_{11}\rvert)$	-95.67 dB	-95.68 dB	-96.15 dB	-95.28 dB

Table 2.8: Statistical mean for the simulated direct source match measurement shown in Fig. 2.83. Reference values for the two receiver reflectometer: $\mu(\lvert S_{11}\rvert, l = 150\,\text{mm}) = -96.75\text{dB}$ and $\mu(\lvert S_{11}\rvert, l = 300\,\text{mm}) = -96.63\text{dB}$.

From the direct residual directivity measurements shown in Fig. 2.83 it can be seen, that no difference in reflectometer correction performance between the reference two-receiver topology, the switched single receiver and the switched single receiver with switched reference wave exists in the 3-term error correction model. All variances shown are purely

caused by the simulated noise floor of the system and the measurement results for the ideal return loss object shown only the reflectometer system noise floor in all instances. This observation is backed up by the analysis of the statistical means over frequency shown in Table 2.8.

While this analysis alone is sufficient for the standard non-coupled reflectometer, another independent verification of the measurement performance is needed for the switched reflectometer architectures due to the DUT dependent cross-talk on both the reference a_{1m} and the b_{1m} outbound from the DUT.

This linear independent analysis of the reflectometer performance is performed by the ripple test, which in this cases uses the same two ideal 150 mm and 300 mm long loss-less 50 Ω transmission lines, but this time terminated by the calibration short model. This test, as outlined in [52, 157] allows to indirectly calculate the residual directivity of a reflectometer by performing an analysis of the $\lambda/4$ ripple envelope present in this measurement. This analysis effectively compares the difference between the reflectometer calibration reference impedance and the characteristic impedance of the transmission line used for the ripple test, which are both, in this controlled synthetic environment, precisely defined as $Z_L = 50\,\Omega$. Both the direct residual directivity measurement and the ripple test provide a precise measure of the measurement accuracy obtainable by the reflectometer, although on vastly different ends of the smith chart plane.

From the results of the ripple test measurements shown for all reflectometer topologies in Fig. 2.84 it can be seen, that the results of the ripple tests are practically identical for all architectures and no distinct ripple envelope above the inherent quantization noise floor of the simulated ADC can be identified for any of the tested topologies. When comparing the estimated noisy ripple envelope to the values shown in the ripple test tables presented in [52], it can be concluded that the source match (or residual directivity for that matter) is at least -70 dB, corresponding to an peak to peak ripple envelope value of 0.005 dB, which is consistent with the results obtained by the residual directivity measurement using an ideal match.

Therefore, no differences in correction performance arise for the switched reflectometer architectures even for strongly reflective DUTs, despite the reflection dependent cross-talk paths in the reflectometer introduced by the receiver input wave selector switch when the unmodified 3-term error model and correction algorithm is used.

Both of these numerical tests completely verify the assumptions made in the theoretical discussion of the switched single receiver reflectometer. Additional verification objects in the form of VSWR standards from the catalog shown in [157] were simulated and synthesized to check for any possible linearity issues introduced by the new reflectometer topologies. The results of this numerical VSWR standard measurements for return loss standards of $|S_{11}| = -6\,\text{dB}$, $|S_{11}| = -10\,\text{dB}$, $|S_{11}| = -20\,\text{dB}$, and $|S_{11}| = -40\,\text{dB}$, connected by an ideal 150 mm 50 Ω transmission line to the calibration reference plane to cover at least one whole rotation in the smith chart plane by the VSWR standard, are shown in Fig. 2.85.

Just as before, the only differences observable in the results are due to different levels of simulated stochastic noise present in the synthesized wave measurements and therefore the error corrected data. All topologies yield the same results in terms of measurement

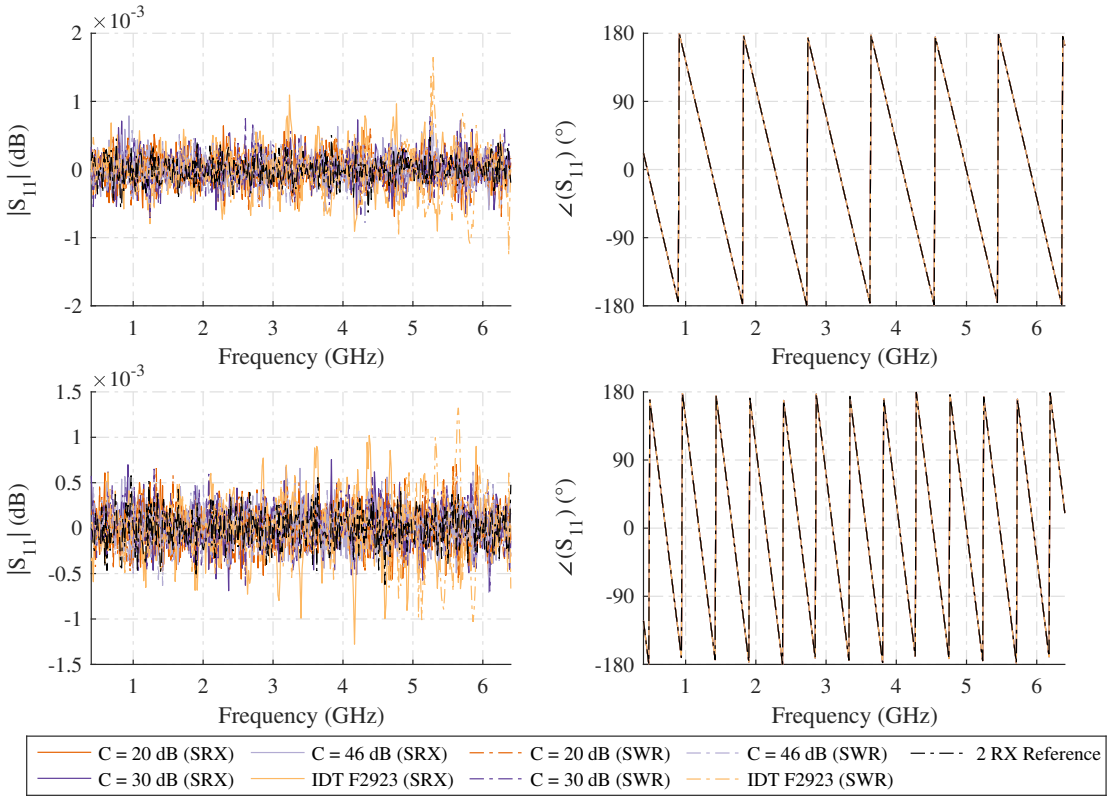

Figure 2.84: Numerical error corrected 3-term model results for the simulated measurement of the ripple test with $Z_L = 50\,\Omega$, $l = 150\,\text{mm}$ (top row), and $l = 300\,\text{mm}$ (bottom row) airlines for different switch isolation coefficients C_i and in the switched single receiver architecture (SRX) and switched single receiver with switched reference architecture (SWR).

accuracy throughout the whole plane of the smith chart.

To further verify the results of the previous synthetic verification measurements, additional test-set simulations and data syntheses were carried out for a $Z_L = 25\,\Omega$ Beatty line terminated by the calibration match and an airline based shorted tee structure, as described in the introduction of this section (2.4.2).

The results of the synthetic Beatty line measurements are shown in Fig. 2.86, which further reassure error correction performance of the 3-term error and correction model on the switched reflectometer architecture.

The same result is found for the highly dynamic measurement of the shorted airline tee structure shown in Fig 2.87. No statistically significant measurable differences in both magnitude and phase of the verification standard can be found between all of the reflectometer architectures in their S_{11} measurement abilities.

Based upon the presented verification data it can therefore be asserted, that a switched receiver reflectometer can be successfully corrected using the existing 3-term error model

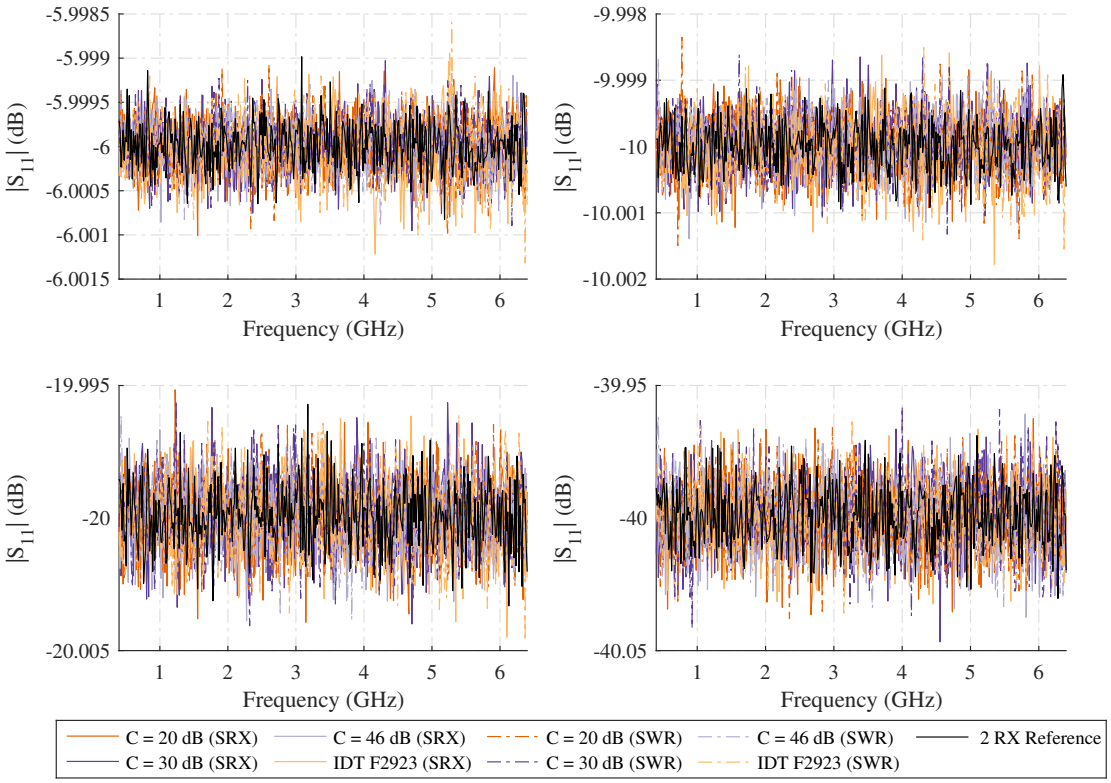

Figure 2.85: Numerical error corrected 3-term model results for the simulated measurement of the return loss standards for different switch isolation coefficients C_i and in the switched single receiver architecture (SRX) and switched single receiver with switched reference architecture (SWR).

and correction models. In practice, the measurement inaccuracies arise due to a non-TI synthesizer stimulus and LO signal, the repeatability of the receiver input wave selector switch and, if used, the repeatability of the reference wave selector switch.

2.4.4 Numerical Unidirectional SOLT Results

In order to test the general measurement ability of the switched receiver architecture in a simple two-port unidirectional VNA test-set, the stateful test-set simulation models for the unidirectional two-port switched receiver VNA shown in Fig. 2.88, the unidirectional two-port switched receiver VNA with added reference wave switch shown in Fig. 2.90 and a four-receiver double reflectometer reference VNA test-set shown in Fig. 2.90 were constructed and simulated in its corresponding TI states using Keysight ADS. These simulations were performed to assess the effects of the cross-talk introduced by the receiver input wave selector switch upon the measurement results, and to test the assumption made for the (5+2)-term error model, correction algorithms and its S_{21} measurement correction efficacy when compared with the 5-term standard error model.

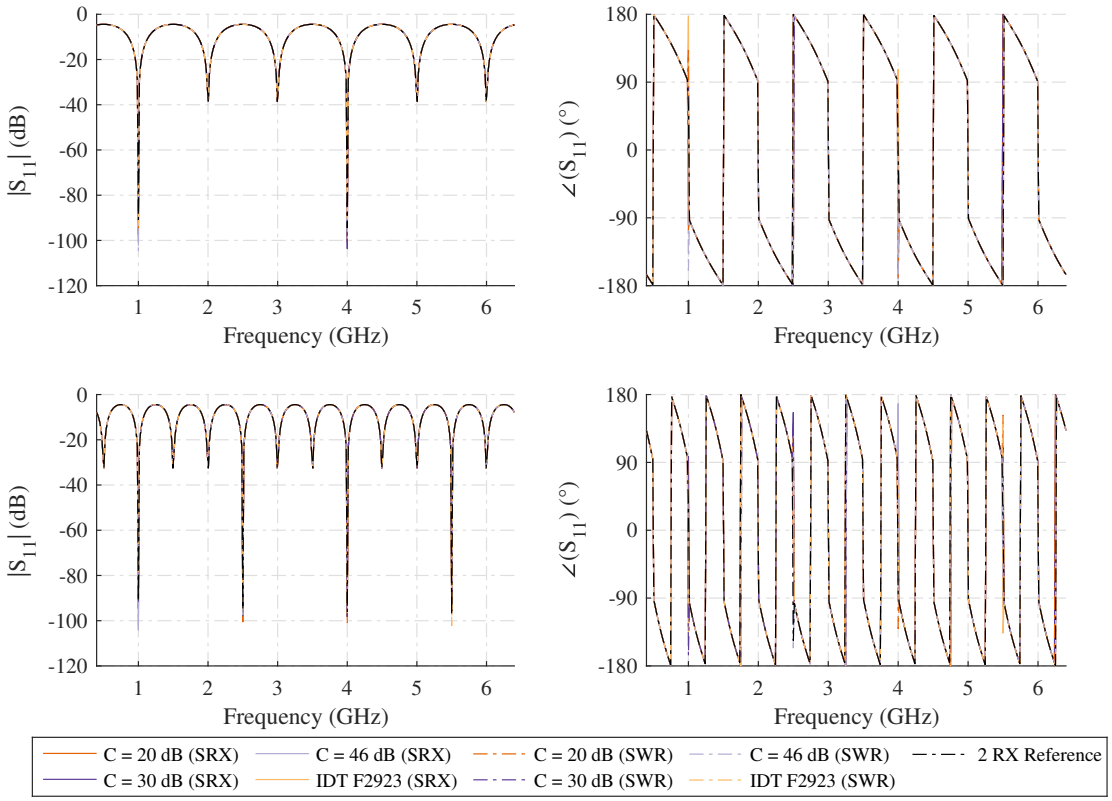

Figure 2.86: Numerical error corrected 3-term model results for the simulated measurement of the Beatty line test with $Z_L = 25\,\Omega$, $l = 150\,\text{mm}$ (top row), and $l = 300\,\text{mm}$ (bottom row) airlines terminated by the calibration match for different switch isolation coefficients C_i and in the switched single receiver architecture (SRX) and switched single receiver with switched reference architecture (SWR).

The four-receiver double reflectometer reference VNA test-set implementation shown in Fig. 2.90 is also re-used as the reference in further analysis of the other two-port receiver input wave selector switch cross-talk correction methods. For reasons of clarity, only the forward stimulus direction, and therefore only four receiver states, are shown in Fig 2.90. In the reverse stimulus direction the same configuration is used, while the termination present for the reflectometer of the second port in Fig 2.90 is swapped with the reference S-parameter termination shown for the reflectometer of the first port. The S-parameter numbering is iterated in the same way as shown in the figure, which resulting in a 16-port S-parameter representation for all of the possible test-set states.

It is important to note at this point, that most of the following figures are optimized for a screen based edition of this work where zooming into the vector graphics used in the figures is feasible. It is possible that some important details in the data and detail content of the schematics are lost in a printed edition of this work, which is unfortunately

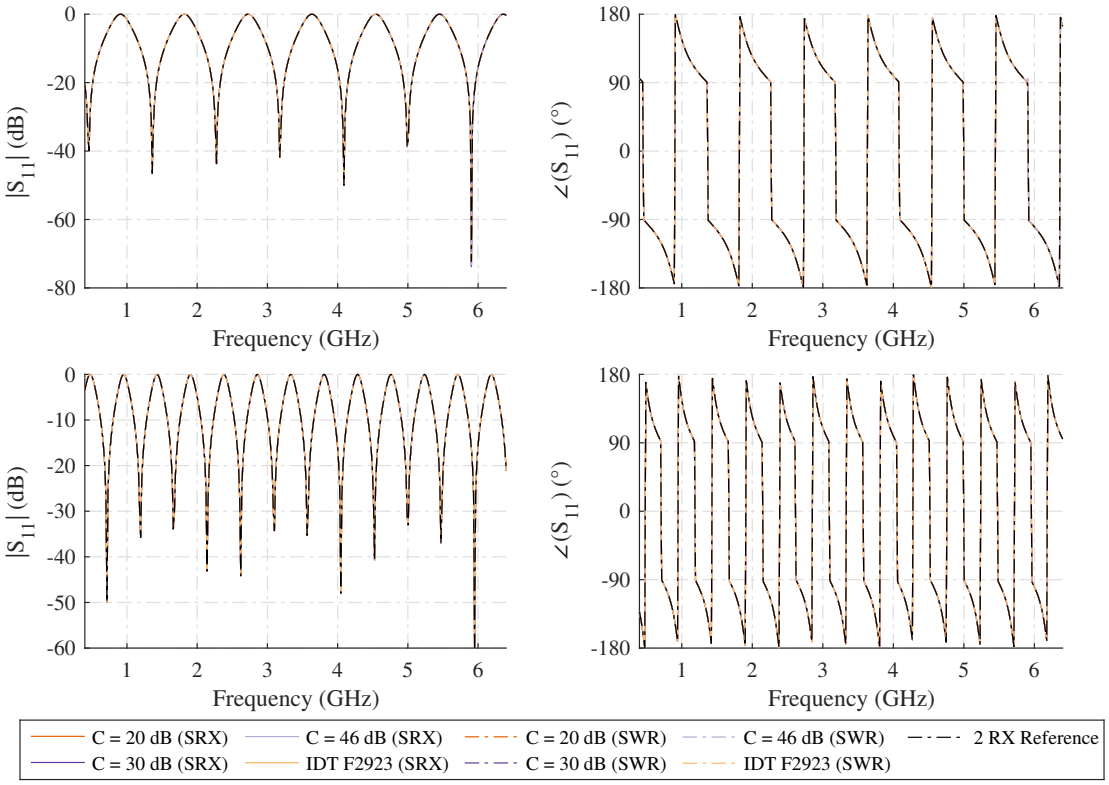

Figure 2.87: Numerical error corrected 3-term model results for the simulated measurement of the tee, terminated by the calibration and $Z_L = 50\,\Omega$, $l = 150\,\text{mm}$ (top row), and $l = 300\,\text{mm}$ (bottom row) airlines and the calibration short for different switch isolation coefficients C_i and in the switched single receiver architecture (SRX) and switched single receiver with switched reference architecture (SWR).

hard to avoid due to the huge dynamic range of the data, even when using a logarithmic scale for the magnitude data.

While delta plots between the results of the different architectures and calibration and correction algorithms are certainly an option in a general case, they fail to adequately visualize data that is heavily influenced by noise, which is almost always the case with the correction of the high dynamic range transmission measurements the algorithms presented in this work in chapters 2.2.3 to 2.2.9 aim for.

The unidirectional test-sets for the switched receiver architectures specifically use a directional coupler as the termination of the b_{2m} wave originating from the DUT, and not an attenuator with a value corresponding to the coupling factor, in order to keep a more direct comparability between the full double reflectometer reference implementation and the reduced switched receiver test-sets.

The simulation of the switched receiver architecture is performed on a distinct set

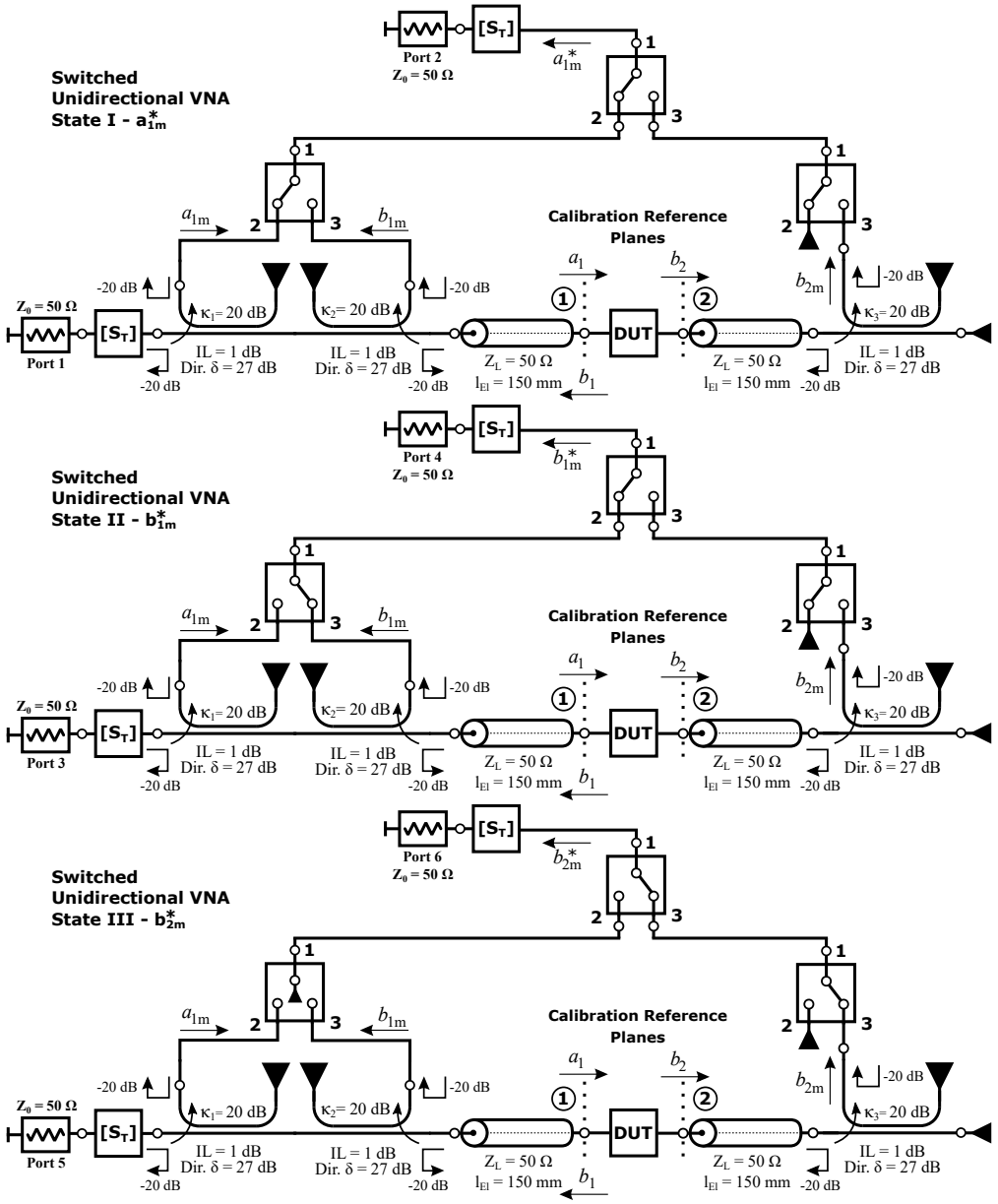

Figure 2.88: Schematic of the switched receiver unidirectional VNA test-set simulation implemented in Keysight ADS.

of reduced test-sets to capture the unique interference situation in terms of the input receiver wave selector switch. This is important to assess the performance, as every additional RF connection from the switch to the test-set, even when not used in the capture of measurement data, opens a multitude of new interference paths, which is not the case in the four-receiver double reflectometer reference implementation.

While this may sound like an arbitrary simplification of the evaluation of the architecture

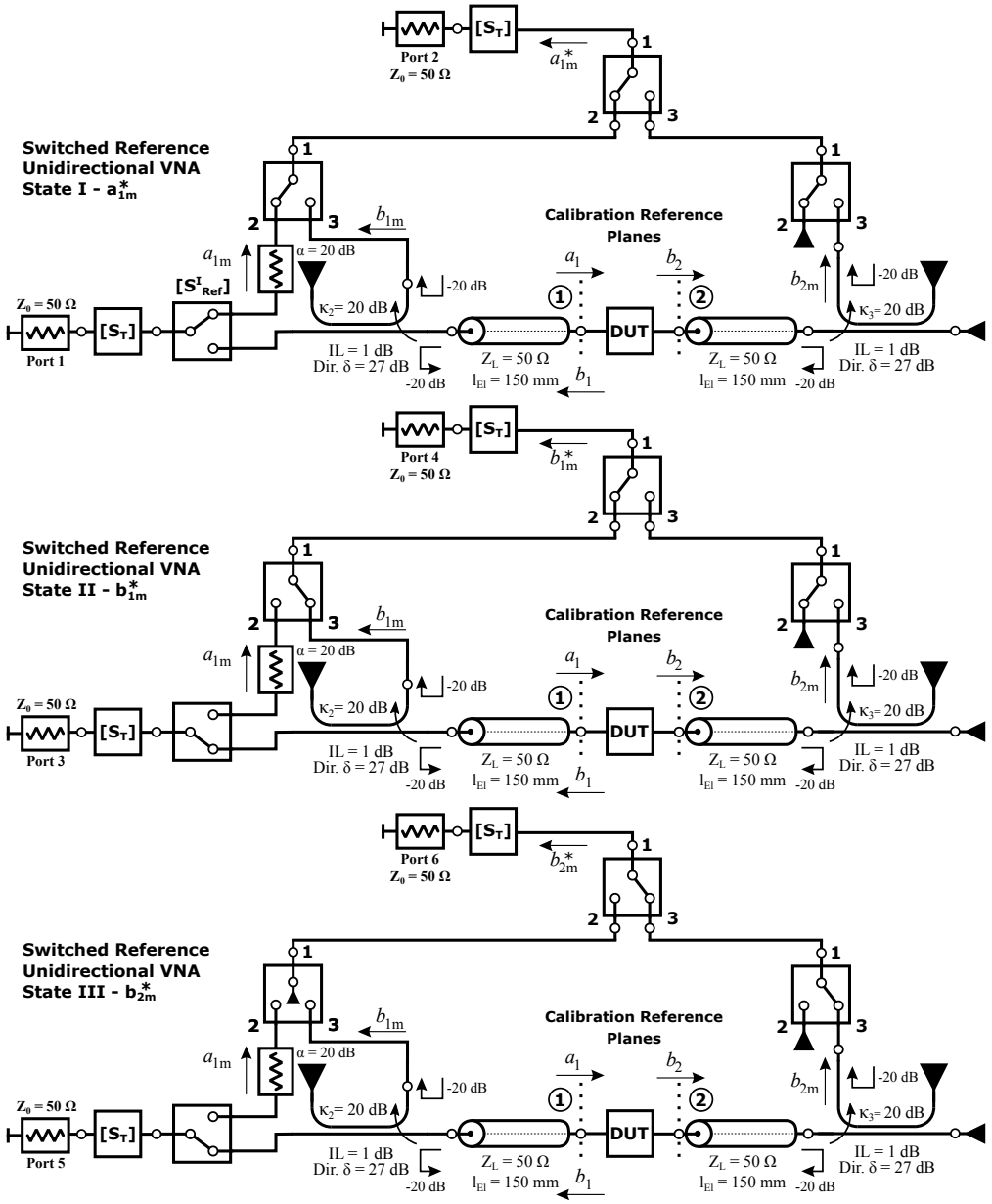

Figure 2.89: Schematic of the switched receiver unidirectional VNA with switched reference test-set simulation implemented in Keysight ADS.

at first, it is important to note, that the motivation of the introduction of the new architecture is to allow for simpler special purpose VNAs, and not to present a replacement for general purpose laboratory VNAs. Following this reasoning it can be expected, that the physical test-set matches the error model used for calibration and correction.

In order to present a fair reference platform for the unidirectional switched receiver

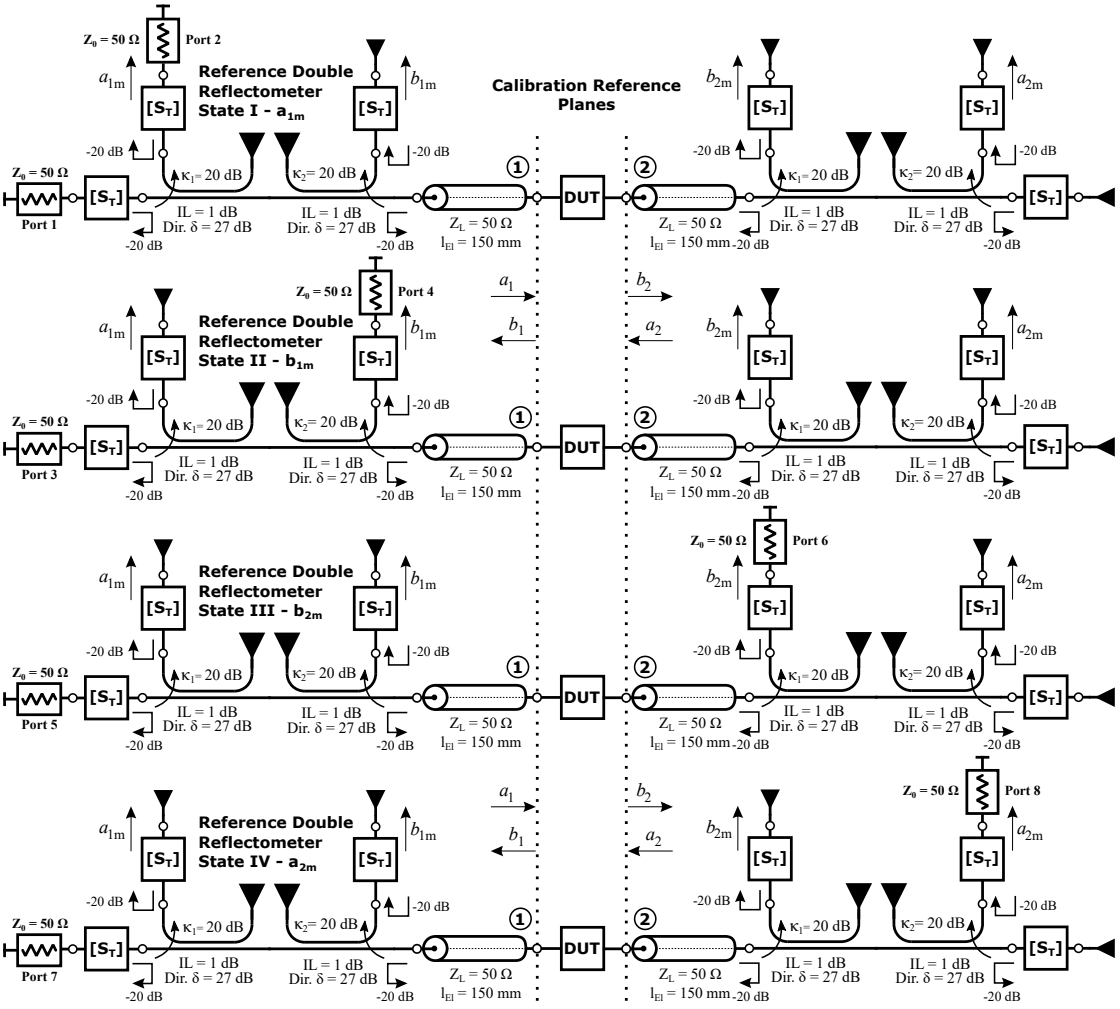

Figure 2.90: Schematic of the reference four-receiver double reflectometer VNA test-set simulation implemented in Keysight ADS. Only one stimulus direction shown for reasons of clarity.

VNA architectures, the four-receiver reference VNA is only calibrated with the 5-term procedure in these cases, which results in the same impairments caused by the non-correctable $S_{22} \cdot E_{LF}$ et al. loops in the signal flow diagram of the error model. This effect can easily be seen in comparison between the 5-Term model error corrected synthetic data of a shorted 150 mm loss-less 50 Ω transmission line stub tee and its corresponding UOSM corrected data for the synthetic four-receiver double reflectometer test-set architecture (see Fig. 2.90) in Fig. 2.91.

As outlined in the introduction of this section (see 2.4.1), the non-realistic ultra low isolation switch case of $C = 20\,\text{dB}$ is omitted for the two-port test-set analysis to reduce the amount of data and its visualization to a sensible level.

A calibration in both the 5-term and the (5+2)-term error model is performed for each

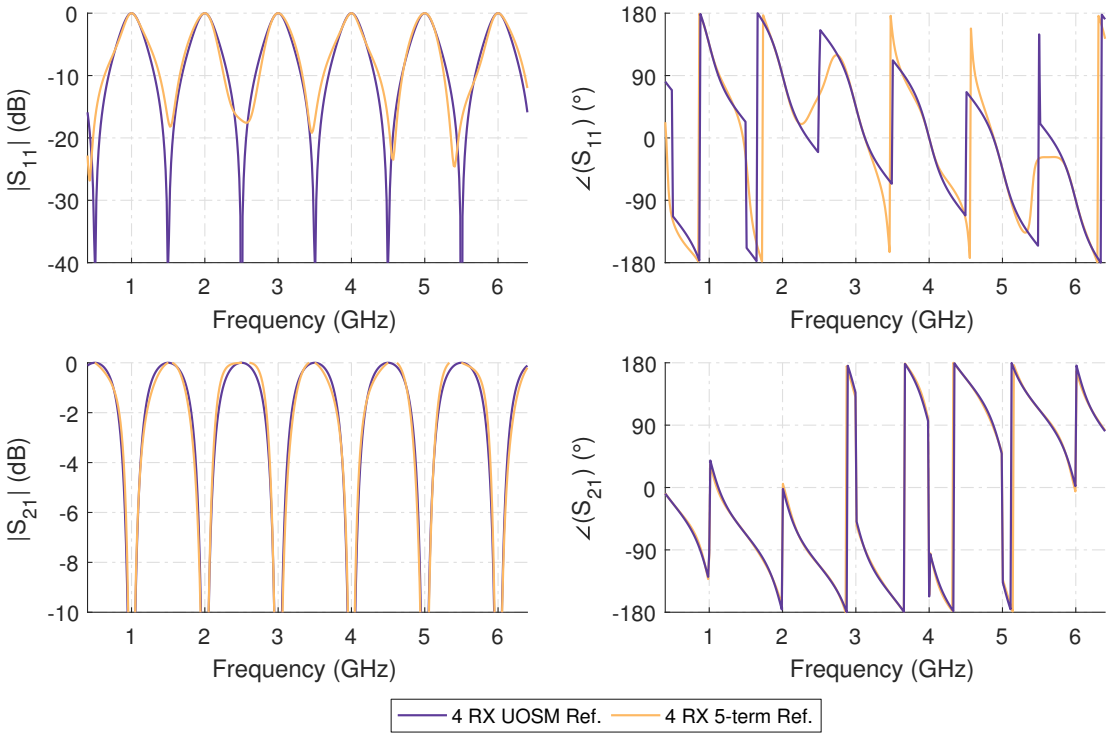

Figure 2.91: Differences in the correction performance of mismatched DUTs between the 5-Term error model and full two port error model correction shown for a shorted 150 mm 50 Ω loss-less airline stub tee using the synthetic reference double reflectometer test-set.

of the two switched single receiver test-set architectures to compare and show the efficacy of the transmission switch cross-talk correction.

The cross-talk coefficient capture of (5+2)-term calibration is performed in its simple variant using the Match-Match and Short-Match calibration isolation standards, as outlined in Eq. (2.58) and (2.59), instead of the Short-Match and Open-Match isolation standard variant of Eq. (2.55) and (2.57), due to the ease of implementation and the availability of a perfect simulated match standard.

No statistically significant difference between the 3-term reflectometer error coefficients obtained in these architectures could be determined when compared to the results already presented for the reflectometer in Fig. 2.82. This is to be expected from the test-set configuration, as virtually no leakage can reach the transmission reception side of the unidirectional test-set, which could otherwise cause interference by reflection of the non-terminated second port. Due to the use of a second isolation switch for the b_2 wave component, as shown in Fig. 2.89 and 2.88, this cross-talk is quickly attenuated below the noise floor of the system, even for the $C = 30\,\mathrm{dB}$ low-isolation switch case.

The resulting transmission tracking error coefficients of the numerical 5-term calibration procedures are shown in Fig. 2.92 for the SRX and SWR topologies. In this plots it

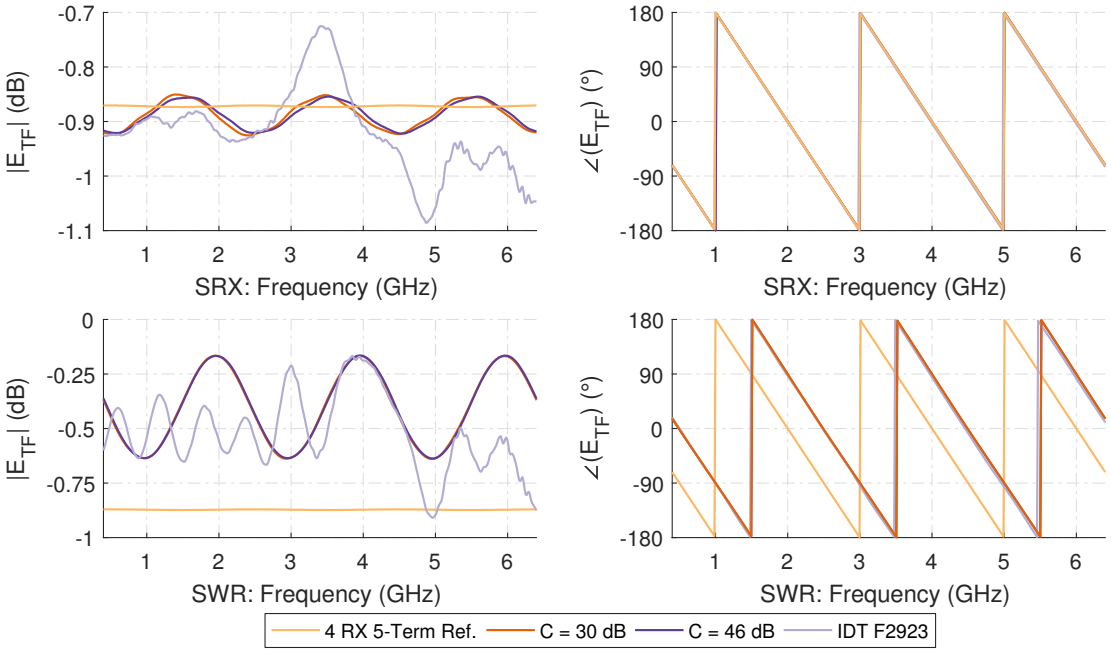

Figure 2.92: Numerical results of the E_{TF} forward tracking error coefficient data of the 5-term calibration procedure for the switched single receiver (SRX) and switched single receiver with reference wave switch (SWR) architectures.

is easy to identify an isolation dependent ripple in the switched topology E_{TF} values in comparison to the values of E_{TF} obtained for the same test-set configuration in the reference four-receiver double reflectometer setup.

This is to be expected for an additive interfering signal with different phase relations over the frequency range. Nevertheless, this effect does not seriously degrade the tracking performance in the unidirectional test-set configuration, as the tracking error introduced by the missing E_{LF} compensation in the final error corrected DUT data is usually far more pronounced and relevant. This ripple can be compensated for a fully known or flush thru standard by the E_{TF} coefficient, as outlined in the theoretical discussion of the (5+2)-term procedure.

The results of the cross-talk calibration steps for the E_{XF} and E_{XRF} coefficients in the (5+2)-term procedure are shown in Fig. 2.93. When the magnitude of the two coefficients for the switched receiver topology in the left column of Fig. 2.93 is compared with the Y- or tree-structure of the receiver input wave selector switch, and its wave mapping for the simulated test-set shown in Fig. 2.88, it is obvious, that the measured synthesized coefficients thoroughly track the isolation of two switches in series corrected by their insertion for the corresponding active state and their additional return loss interaction loops. These results perfectly match the assumptions made in modeling these parameters in the theoretical discussion in the first place.

Exactly the same can be said for the E_{XF} and E_{XRF} coefficients determined by the

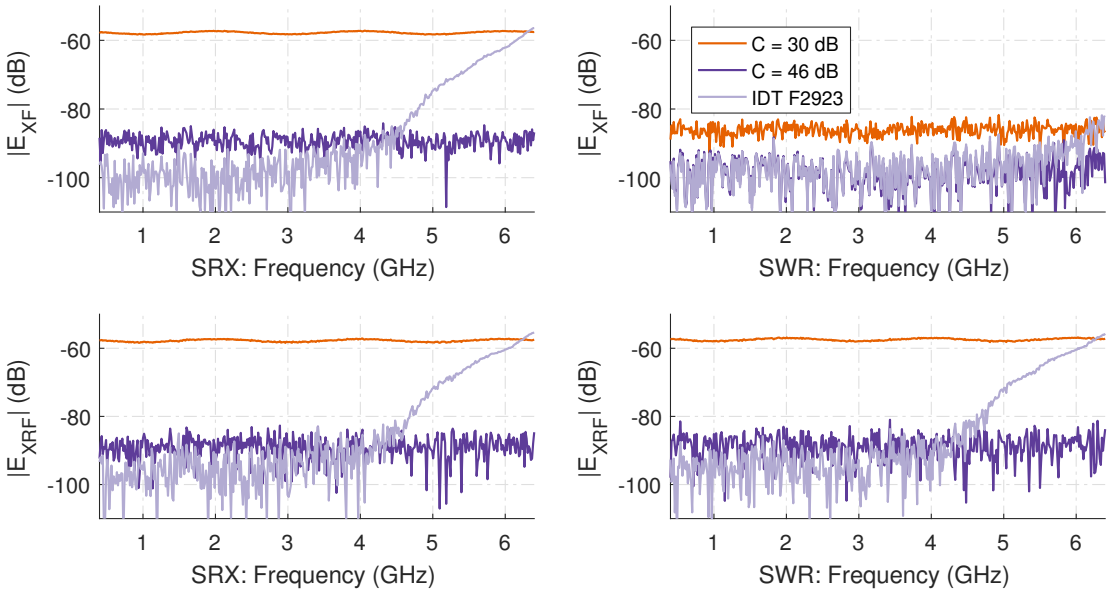

Figure 2.93: Numerical results of the $|E_{XF}|$ and $|E_{XRF}|$ (5+2)-Term calibration cross-talk coefficients for the switched single receiver (SRX, left column) and switched single receiver with reference wave switch (SWR, right column) architectures.

calibration process for the switched reference architecture shown in the right column of Fig. 2.93. The constant cross-talk upon the b_2 wave measurement by the reference wave a_{1m} channel is reduced by one additional switch isolation, which can easily be seen when comparing the level of E_{XF} between the left and right column of the figure.

Additionally it can be seen, that the two error coefficients are captured with varying S/N ratios due to the limited dynamic range of the simulated VNA receiver. This outcome is especially useful for testing the correction performance and accuracy of the corrected transmission S-parameters in the presence of a very noisy correction factor. As the error model these parameters are based upon is derived from the stateful concept of SOLT and exist outside of the normal error model, no significant alteration of the error corrected data is expected for a very small, noise dominated error model coefficients when the isolation exceeds the dynamic range of the measurement system.

This is in stark contrast with the effects observed for the noise sensitive 15-term error correction model applied to the receiver input wave selector switch cross-talk in [125], where an additional post-processing step is needed to analyze the error coefficients for their mean-to-variance ratio in their calibration data and discard coefficients below a certain SNR threshold to avoid the corruption of the corrected DUT S-parameters when the isolation of the switch is in the vicinity of the dynamic range of the system.

When the reflectometer ripple test is performed using a 150 mm loss-less 50 Ω transmission line with the synthesized switched single receiver and switched single receiver with reference wave switch test-sets, it is possible to validate the assumptions made in the

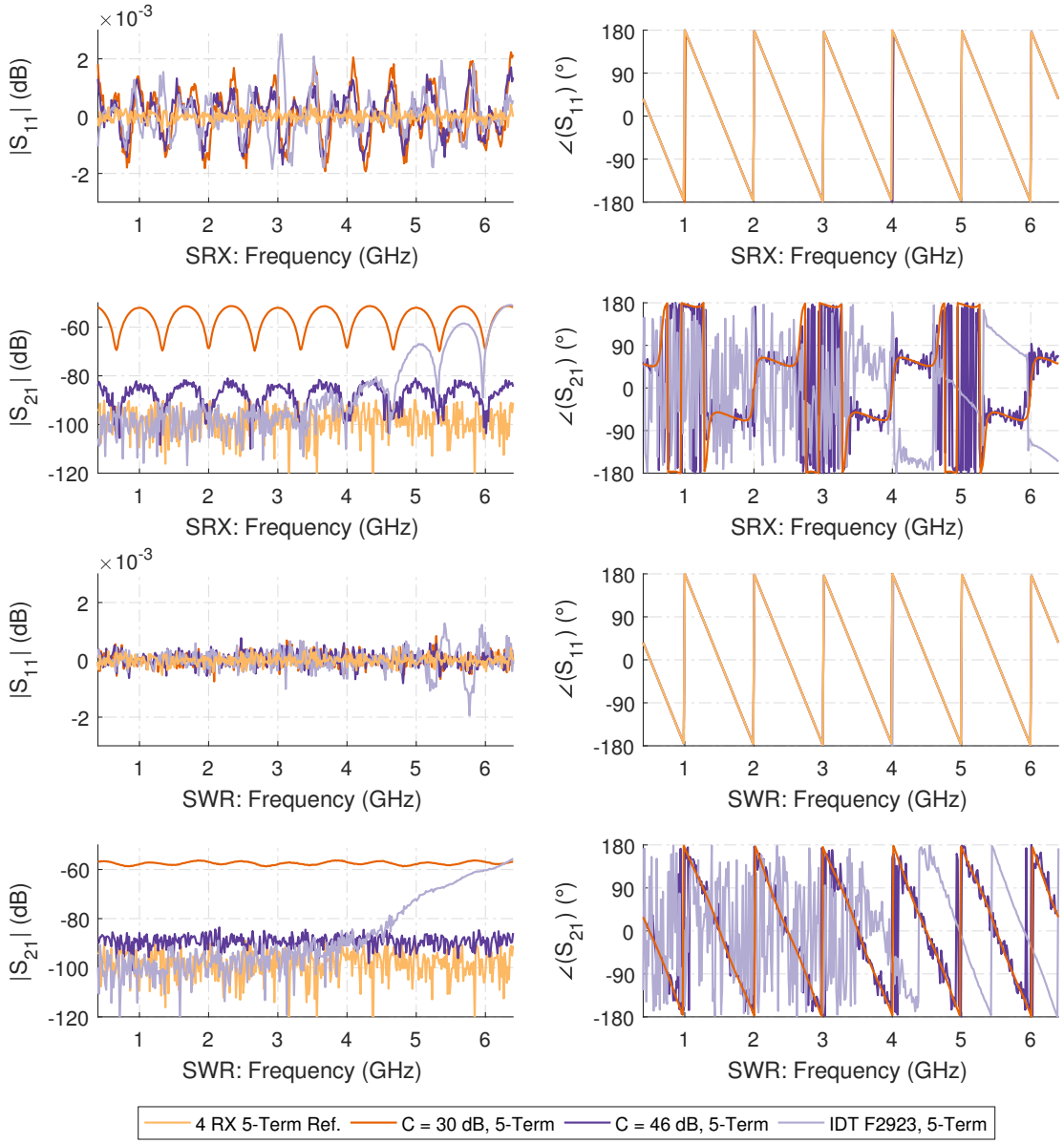

Figure 2.94: Numerical 5-term error corrected results of the ripple test measurement using a 150 mm loss-less 50 Ω transmission line terminated by the calibration short for the single switched receiver (SRX) and single switched receiver with reference wave switch (SWR) test-set architectures.

introduction of the (5+2)-term correction procedure and the introduction of the reference switch concept when only the classical 5-term unidirectional correction method is applied by comparing the apparent transmission. The 5-term error corrected data of the ripple test is shown in Fig. 2.94.

When the results obtained for the unidirectional test-set S_{11} ripple envelope are compared with the numerical simulation results of both switched receiver reflectometer architectures in Fig. 2.84, it can be seen, that no significant change in the reflectometer source match performance is observed by the addition of the additional receiver channel. This is in accordance with the observation of quasi-identical reflectometer error coefficients. Nevertheless, the switched reference wave test-set architecture performs slightly better than the switched single receiver in the ripple test in terms of the ripple envelope magnitude due to a lower overall cross-talk interference upon the receiver. The scale of this benefit is however only barely relevant for practical return loss measurements and only interesting on metrological scales.

The measured imaginary S_{21} transmissions of the isolating ripple test standard in Fig. 2.84 perfectly demonstrate the transmission measurement dynamic range limiting effects due to cross-talk in both single receiver test-set architectures, which are the motivation for the introduction of the (5+2)-term correction procedure in the first place.

The S_{21} measurement performed in the SWR topology clearly shows the additive interference of both the a_{1m} reference wave channel and the DUT dependent b_{1m} wave upon the b_{2m} measurement. This results in a vast reduction of the usable dynamic range of this parameter which, when referenced to the undisturbed receiver noise-floor, is equal to a reduction of 50 dB for the $C = 30\,\mathrm{dB}$ test-set case.

The S_{21} measurement performed in the SRX topology on the other hand clearly shows the advantage offered by the substitution of the reference wave coupler in the reflectometer by a SPDT switch. Compared to the simulated SRX measurements, the influence of the reference wave cross-talk is greatly reduced and only the DUT dependent cross-talk shows up in the S_{21} measurement, which is almost identical with the E_{XRF} coefficient for both topologies shown in Fig. 2.93.

While the cross-talk reduction seen in the S_{21} data may not seem to be significant at first, it is important to remember that due to the strong reduction of the quasi-static a_{1m} cross-talk, which corresponds to E_{XF} in the (5+2)-term model, by the SWR method, only the DUT dependent cross-talk, corresponding to E_{XRF}, remains. Therefore, the dynamic range of the transmission measurement is restored for well-matched DUTs by this new test-set topology modification.

Nevertheless, the well-matched DUT case represents only a small subset of the usual measurement tasks, which usually include S_{21} measurements of highly reflective isolating DUTs. A prime example for this case is the measurement of SAW/BAW or cavity filter stop-band attenuation, which is emulated in the synthetic measurements by error correction of the ripple test using the (5+2)-term error model which is shown in Fig. 2.95.

Since the loss-less transmission line terminated by a short, as used for the synthetic ripple test, represents the worst-case for passive DUTs for all phase angles, it can be deduced from the S_{21} noise floor shown in Fig. 2.95, that a dynamic range increase, and therefore receiver input wave cross-talk reduction, of at least 30 to 35 dB is possible by using the (5+2)-term error model and correction for the given single receiver test-sets and ADC characteristics, independent of the presence of the reference wave switch.

From the synthetic measurement data of the 5- and (5+2)-term error corrected mea-

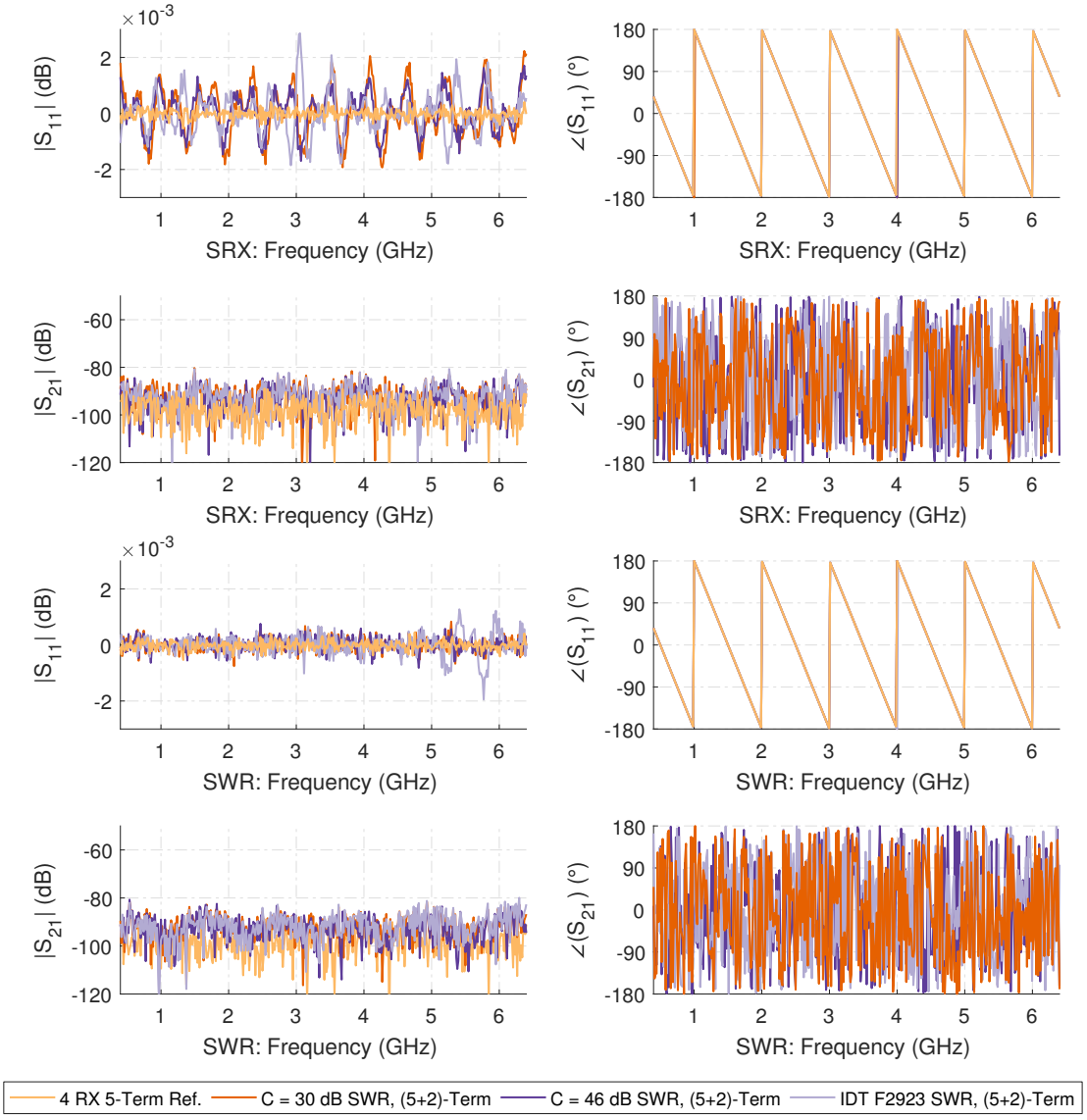

Figure 2.95: Numerical (5+2)-term error corrected results of the ripple test measurement using a 150 mm loss-less 50 Ω transmission line terminated by the calibration short for the single switched receiver (SRX) and single switched receiver with reference wave switch (SWR) test-set architectures.

surement of an ideal 50 Ω 150 mm loss-less transmission line thru connection shown in Fig. 2.96 it can be seen, that both the observed interference caused ripple present in the E_{TF} tracking error terms of the single receiver test-set architectures, as well as the additional error introduced by the (5+2)-term, are extremely minor and only matter in a metrological context.

In practice, the maximum peak to peak ripple of 0.03 dB present in the $C = 30$ dB

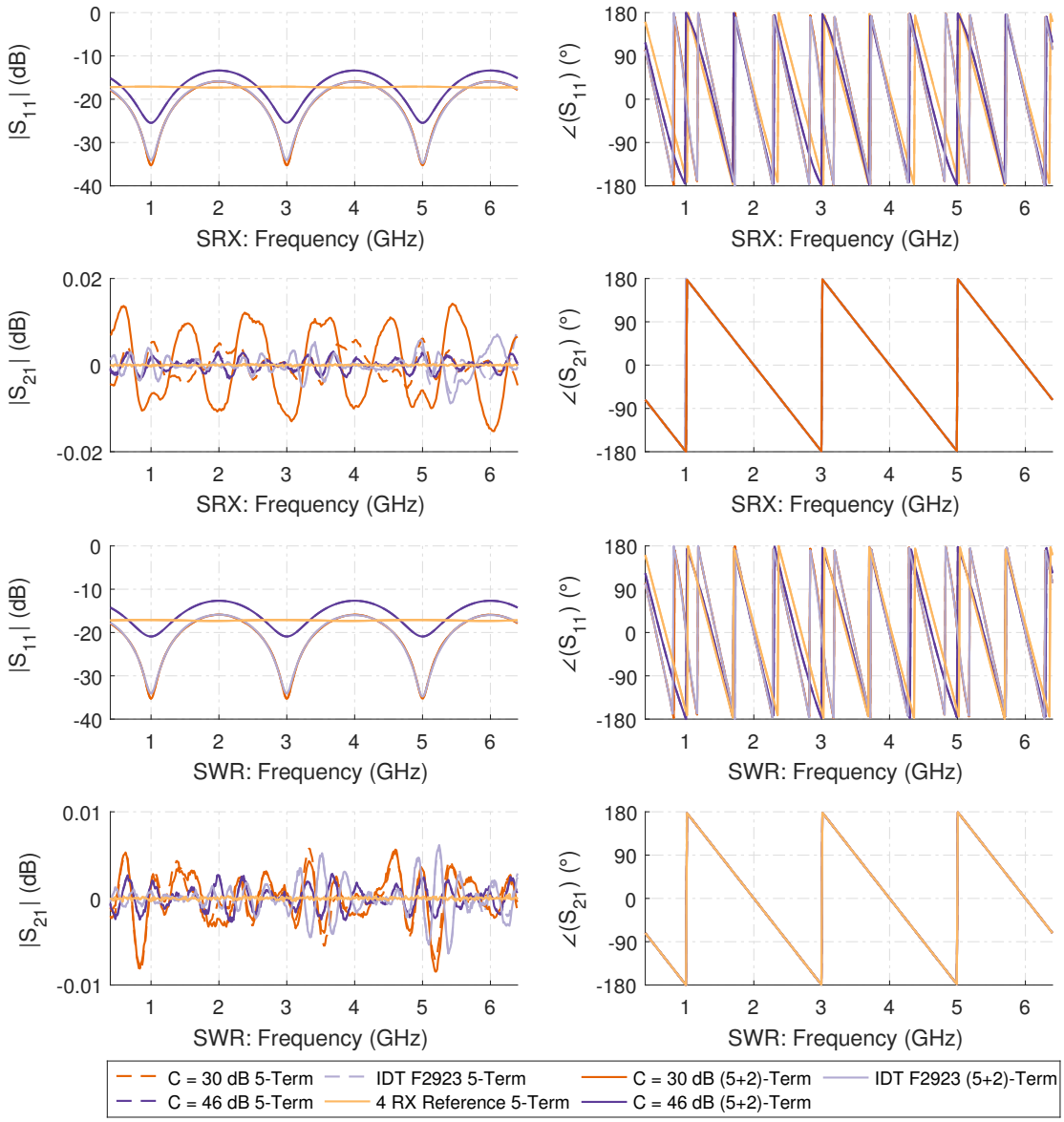

Figure 2.96: Numerical 5- and (5+2)-term error corrected results of a 150 mm loss-less 50 Ω transmission line thru connection for the single switched receiver (SRX) and single switched receiver with reference wave switch (SWR) test-set architectures.

(5+2)-term error corrected measurement in the SRX test-set is easily surpassed by the uncertainty introduced by the missing $E_{LF} \cdot S_{22}$ correction for non-ideal DUTs and can be reduced to 0.01 dB in the SWR test-set configuration. This error is expected to be well below the repeatability limits of the semiconductor PIN-diode switches.

Some part of the S_{21} ripple seen in Fig. 2.96 is also caused by the different return

loss figures presented to the coupled outputs of the directional couplers in the synthetic test-set. While the wave termination of a receiver is assumed to be fairly perfect, i.e. $RL = 40\,\text{dB}$, to simplify the interactions in the simulated test-sets, the synthetic wave switches present a more realistic broadband return loss of $RL = 20\,\text{dB}$ on both the terminated and active input port to the couplers.

This effect caused by the hardware load match can be seen nicely in the S_{11} measurement of the ideal loss-less $50\,\Omega$ transmission line in Fig. 2.96. This also correlates with the observation, that the least isolating synthetic switch with $C = 30\,\text{dB}$ shows the best return loss results in this measurement, because less energy is reflected back to the stimulus reflectometer due to isolation losses associated with this paths.

Additional synthetic measurement and correction results of the $Z_L = 25\,\Omega$ Beatty line can be found in appendix A of this work, as this measurement is strongly dependent on the E_{LF} and E_{LR} correction performance of an algorithm. This correction can not be performed in the unidirectional measurement case, which therefore limits the significance of this verification standard for the 5- and (5+2)-term model analysis.

In order to evaluate the cross-talk effects of the receiver input wave selector switch upon the tracking performance and dynamic range of the S_{21} measurement further, synthetic asymmetric reflective lossy tee measurements were performed for attenuations of $\alpha = 0\,\text{dB}$, $\alpha = 20\,\text{dB}$, $\alpha = 40\,\text{dB}$, and $\alpha = 80\,\text{dB}$ to cover the whole dynamic range of the simulated receiver. The S_{21} measurement results of these simulations for the $C = 30\,\text{dB}$ test-set, which is the most susceptible of the selection to cross-talk, is shown in Fig. 2.97 with the correction performed in both the 5- and (5+2)-term error model and for the SWR and SRX test-set configuration.

The complete synthetic unidirectional ARLT measurement results for all test-sets, attenuation values and switch models, including the corresponding S_{11} measurements and phase component information for both parameters, can be found in appendix A of this work.

In the ARLT S_{21} measurement shown in Fig. 2.97 it can be clearly seen, that for the 5-term correction case the substitution of the reference coupler by the reference wave switch provides a modest average dynamic range improvement of 5 to 6 dB when compared with the SRX topology alone, when a switch isolation of only 30 dB is present. Nevertheless, tracking errors start to appear in the results of the 5-term error correction for both architectures above 20 dB of ARLT attenuation, while the receiver input wave selector switch cross-talk prohibits any accurate measurements in the 80 dB ARLT attenuation case altogether.

The (5+2)-term corrected data in Fig. 2.97 shows an impressive increase in tracking performance and dynamic range, even for the 80 dB ARLT attenuation case. Tracking errors are non-existent in both test-set topologies for the 40 dB ARLT attenuation case and the data truthfully follows the four-receiver reference 5-term data in the 80 dB attenuation case right down to the system noise-floor at a slightly elevated trace noise level. An increase of up to 45 dB of usable S_{21} dynamic range can be observed by the cross-talk correction performed by the (5+2)-term model.

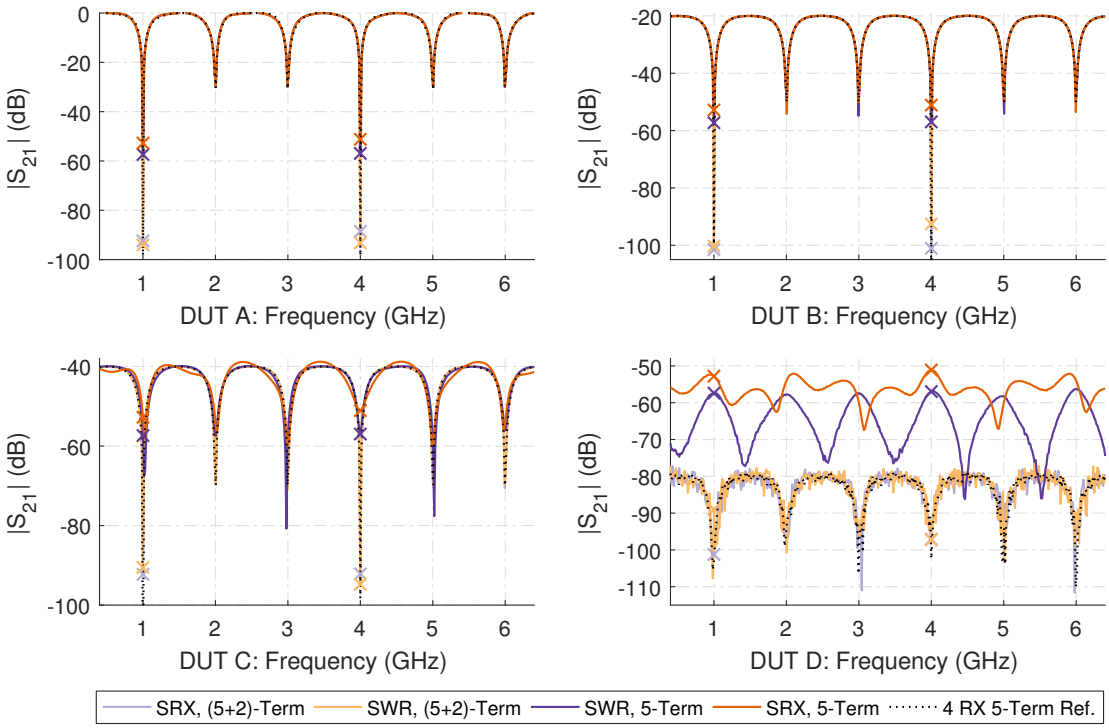

Figure 2.97: Numerical S_{21} measurement results for the $C = 30\,\text{dB}$ switch test-set of the asymmetric reflective lossy tee (ARLT) in various configurations, corrected by 5- and (5+2)-term error model and for the single switched receiver (SRX) and single switched receiver with reference wave switch (SWR) test-set architectures. DUT A - ARLT 0 dB attenuation, DUT B - ARLT 20 dB attenuation, DUT C - ARLT 40 dB attenuation, and DUT D - ARLT 80 dB attenuation.

2.4.5 Numerical Bidirectional SOLT Results

Now that the efficacy of the (5+2)-term error model cross-talk correction is demonstrated for the unidirectional VNA test-set case, the simulation of the unidirectional virtual three switched receiver test-sets is extended by an additional a_2 switch position and corresponding coupler to form a full double reflectometer configuration. The schematic of this new stateful test-set configuration is shown for the single switched receiver topology in Fig. 2.98 and for the single switched receiver topology with switched reference wave in Fig. 2.99. As already demonstrated for the schematic of the four-receiver reference double reflectometer, only the forward stimulus direction is depicted in these figures for reasons of clarity. For the reverse stimulus situation the termination of the reflectometer is interchanged with a port termination and the port numbers increased in the same manner as already described for the reference double reflectometer.

The incomplete three-receiver double reflectometer test-set variant, which uses one

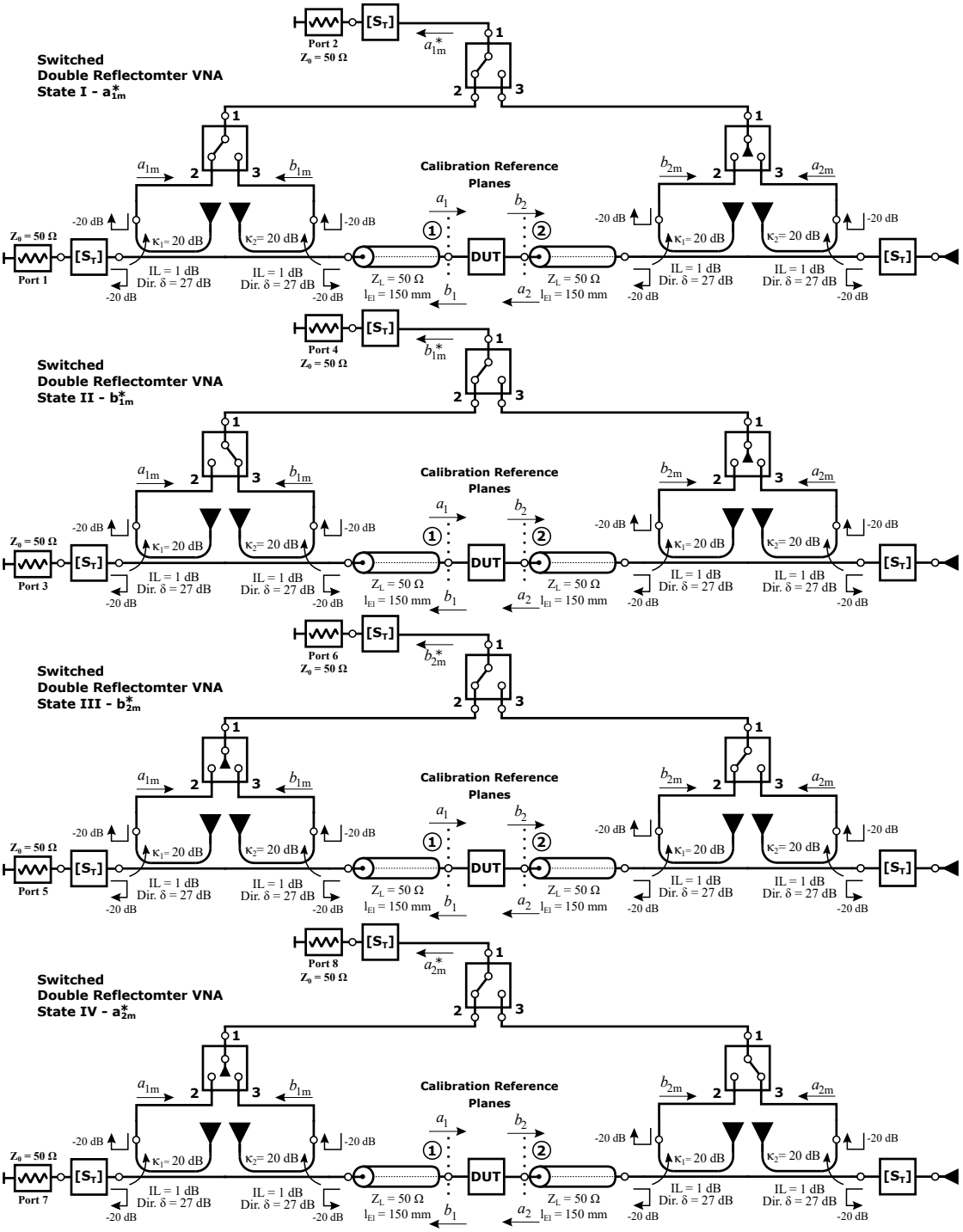

Figure 2.98: Schematic of the switched receiver double reflectometer VNA test-set simulation implemented in Keysight ADS. Only one stimulus direction shown for reasons of clarity.

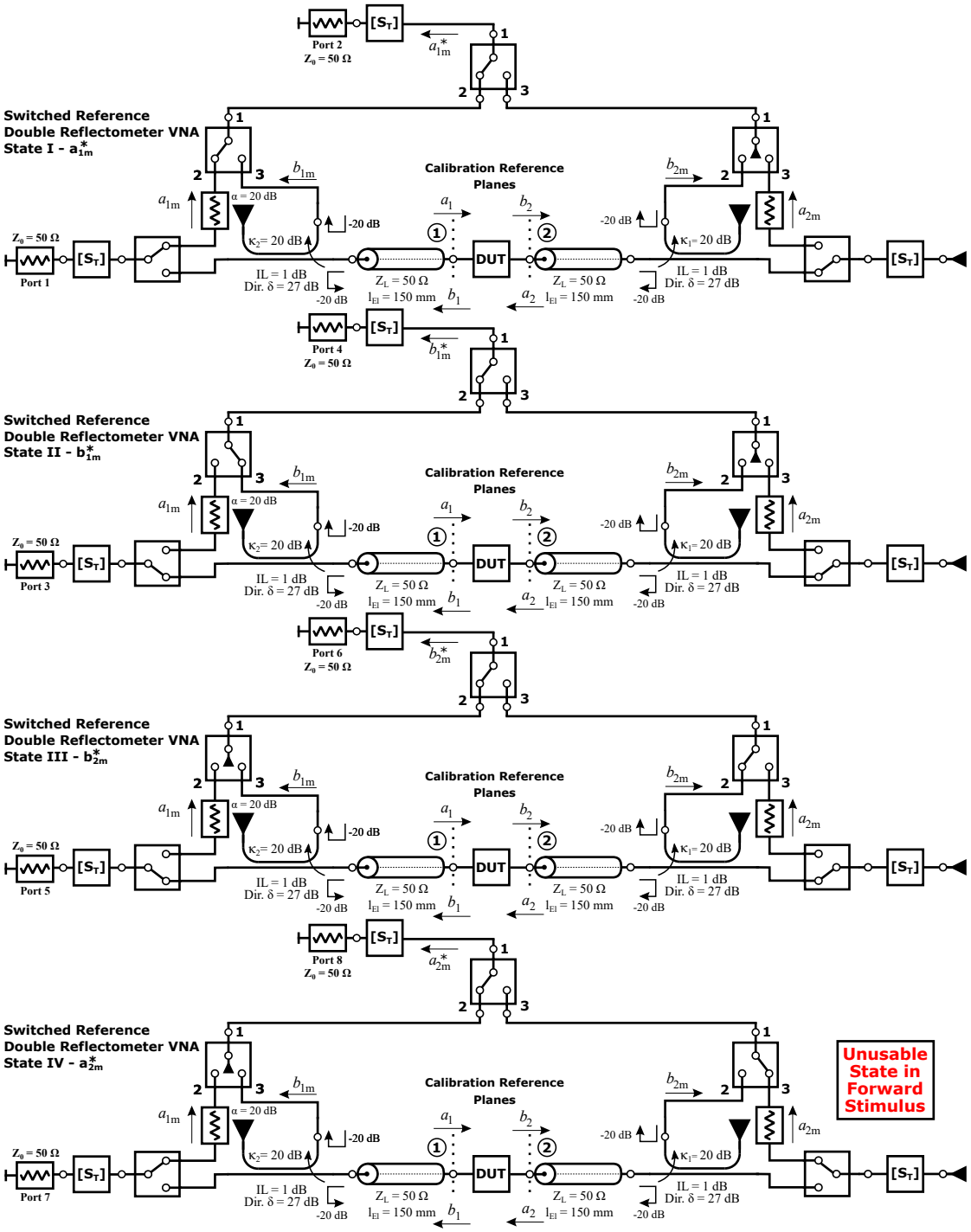

Figure 2.99: Schematic of the switched receiver double reflectometer VNA with switched reference test-set simulation implemented in Keysight ADS. Only one stimulus direction shown for reasons of clarity.

common reference wave coupler before the stimulus reversal switch as shown in Fig. 2.23, was specifically not implemented for the synthetic SOLT measurements due to the lack of direct comparability of the results with the 7-term xUOSM cross-talk correction, which strictly requires a four-receiver test-set for direct one tier calibration.

Due to the properties of the switched reference wave concept shown in Fig. 2.99, this direct comparison is only possible for the full double reflectometer architecture present in the SRX concept. In the SWR topology, only three out of the four possible states per stimulus direction generate sensible, DUT dependent, results. In states IV - $a^*_{2\mathrm{m}}$ in the forward and I - $a^*_{1\mathrm{m}}$ in the reverse stimulus direction no direct path exists between the waves of the DUT and the corresponding receiver channel due to the DUT facing isolation of the reference wave switch.

This property effectively degenerates the four-receiver double reflectometer SWR test-set to an equivalent three-receiver test-set, despite the presence of four receiver channels. This effectively prevents the successful direct in-situ determination of the switch terms. While this is not relevant for calibration and error correction in the SOLT 10- and (10+4)-term models, the 7-term based UOSM and xUOSM calibration and error correction methods can only be used on the SWR test-set topology by applying a two-tier calibration procedure based upon the extracted the switch terms from a subsequent complete SOLT calibration, which will be explained in the following section 2.4.6.

The calibration for the 10- and (10+4)-term error model is performed in the same way as in the unidirectional VNA test-set case, with an added reflectometer 3-term calibration for the second port. The cross-talk coefficient calibration in the (10+4)-term error mode is performed with the same choice of Match-Match, Short-Match and Match-Short isolation standards, as described in Eq. (2.95) to (2.98) and the description of the (5+2)-term simulation.

Just like in the unidirectional VNA test-set simulation, no differences in the forward reflectometer error model coefficients E_{DF}, E_{FR} and E_{SF}, as well as the reverse reflectometer error model coefficients E_{DF}, E_{FR} and E_{SF}, can be observed compared to the single reflectometer test-set case, which is due to the isolation between the ports present during the individual 3-term calibration of both reflectometers and the absolute symmetry of both synthetic test-sets shown in Fig. 2.98 and 2.99.

As the architecture is now capable of two sided return loss measurements, the load match coefficients E_{LF} and E_{LR} can now be determined during the thru calibration of the SOLT procedure. The results obtained by the SOLT calibration for the load match coefficients and tracking coefficients E_{TF} and E_{TR} is shown in Fig. 2.100 for all architectures.

While the tracking terms shown in Fig. 2.100 are essentially identical with the results obtained for the 5-term calibration in the unidirectional architecture, it can be easily seen that the load match terms for both sides in the SRX test-set are very similar to a phase de-embedded version of the results obtained for the return loss measurement in the $50\,\Omega$ 150 mm loss-less ideal transmission line through measurement in the unidirectional architecture shown in Fig. 2.96, as expected from the signal flow and error model mirroring principle the SOLT model is based upon.

However, in case of the SWR test-set the load match terms for both sides are very

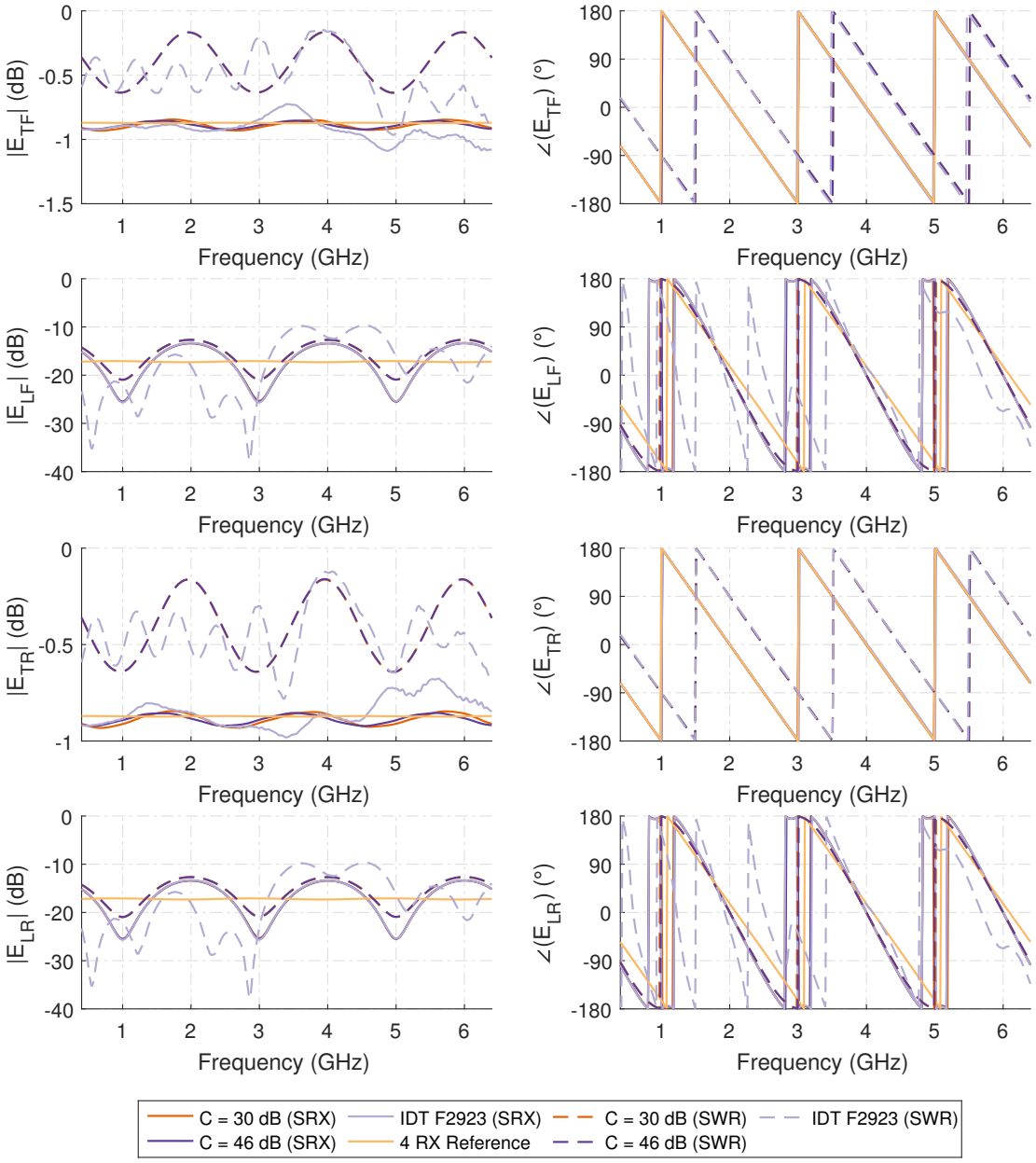

Figure 2.100: Numerical results for the forward and reverse tracking (E_{TF}, E_{TR}) and load match (E_{LF}, E_{LR}) error coefficient data of the 10-term calibration procedure for the switched single receiver (SRX) and switched single receiver with reference wave switch (SWR) architectures using the double reflectometer test-sets.

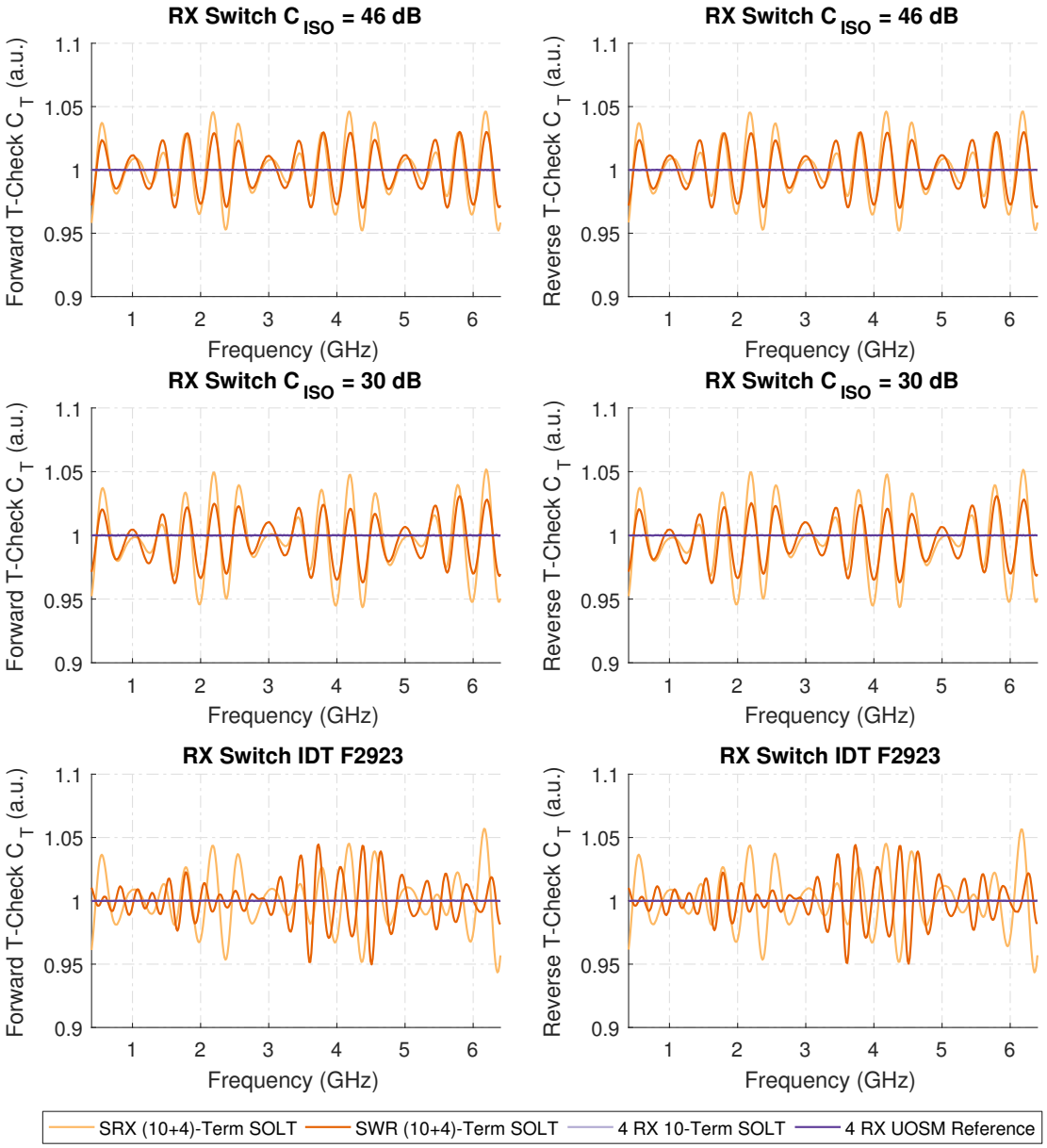

Figure 2.101: Numerical results for the T-Check measurements using the (10+4)-term correction model for all synthetic switches and for the switched single receiver (SRX) and switched single receiver with reference wave switch (SWR) architectures using the double reflectometer test-sets.

different from the unidirectional measurement of the ideal loss-less 50 Ω through connection. This effect can be explained by comparing the unidirectional SWR test-set in Fig. 2.89 with its double reflectometer counterpart in Fig. 2.99. While the coupler of the opposing reflectometer side is terminated in Fig. 2.89 by an nearly ideal termination, the reflectometers of the four-receiver architecture in Fig. 2.99 are terminated by the isolation state of the reference wave switch. This hardware load match of the isolating state is therefore an important design parameter for SWR based single receiver VNA systems. While this may be not instantaneously obvious due to the error correction of the load match applied by the error models, this is relevant to the measurement of the properties of active devices to avoid non-linear memory load-pull effects which in turn could alter the measured linear S-parameters of the device in its operating point.

Due to the synthetic symmetric nature of the test-sets, the results for the forward and reverse receiver input wave selector switch coefficients are identical to the results already presented for the unidirectional test-set forward correction case in the previous section 2.4.4 and bear no new insights. For the sake of completeness, the magnitude of these coefficients for the switched four receiver test-sets is shown in Fig. A.21 in appendix A of this work.

Now that a full two port error correction of the hardware imperfections is possible, it is feasible to perform a T-Check upon the error corrected synthetic test-set architectures. The results of the T-Check measurements for the (10+4)-term corrected test-set topologies in its evaluated C_T FOM, seperated into the forward and reverse stimulus direction results, is shown in Fig. 2.101, while the results of the 10-term corrected measurements is shown in Fig. A.22 in the appendix due to almost identical results.

From the (10+4)-term T-Check results we can see, that while the observable maximum deviations of $\Delta C_T = \pm 0.05$ are still within the acceptable bounds of $\Delta C_T = \pm 0.1$ ([94, 157]), the SOLT error model does not cover all the errors and non-idealities present in a switched single receiver test-set. This becomes especially evident when the results of the SRX and SWR test-sets are compared with the 10-term or 7-term UOSM corrected T-Check data for the four-receiver reference implementation, which produces a near ideal result for this FOM using the synthetic calibration standards and an ideal T-Check device.

When the difference in C_T deviation between the two synthetic switched with different isolation, but equal and constant return loss, is analyzed further, it can be seen that only minor differences exist between the data for the $C = 30\,\mathrm{dB}$ and $C = 46\,\mathrm{dB}$ test-sets in both the SRX and SWR configuration. The results obtained by thee T-Check for the IDT F2923 based test-set, the switch termination return loss data shown in the E_{LF} and E_{LR} plot for the SWR test-set configuration in Fig. 2.100, and the isolation of the IDT F2923 switch shown in Fig. 2.93 can be combined to deliver a clue to the source of this effect. When $|E_{LF}|$ is correlated with the pattern of the C_T it is possible to conclude, that the deviation from the ideal T-Check result depends upon the ΔRL of the switch between its isolating state and the return loss seen through the insertion loss path of the switch into the receiver, when the path is active.

This switch state dependent modulation of the return loss between 40 dB and 20 dB is not overly severe in the synthetic switch test-sets, but it is clearly a violation of the

underlying LTI assumption of the error model, that leads to a degradation in correction performance which can easily be seen in the T-Check results, and needs to be accounted for in the measurements performed on the real VNA hardware by resistive padding of the measurement wave output ports.

This violation of the underlying error model can also be seen, when the results of the loss-less ideal 50 Ω 150 mm transmission line thru connection are compared between the unidirectional test-set in Fig. 2.96 and bidirectional test-set in Fig. 2.102. The full measurement results can be found in the appendix. While the S_{21} transmission measurement ripple for the normalized unidirectional measurement is only relevant on a metrological scale, the ripple present for the same DUT in the fully two port error correct bidirectional measurement is severe and quite unexpected.

When these findings are combined with the results of the loss-less 25 Ω bidirectional Beatty line measurements in Fig. 2.102, which also confirms the transmission tracking errors, and the ripple position and frequency present in the T-Check results in Fig. 2.101, with the observational knowledge that the S_{11} and S_{22} measurements are far more robust due to absorption of the switch cross-talk effects into the 3-term error model, it can be concluded that the errors seen in this verification measurement are most likely due to the modulation of the E_{LF} and E_{LR} error terms as a function of the switch position.

The assumption is furthermore supported by the fact, that the measurement results acquired with the unidirectional test-sets where the forward load match is assumed to be perfect, i.e. $E_{LF} = 0$, do not show this effect. Additionally, it can be deduced from the very two-state structure of the SOLT error model, which already captures the stimulus direction dependent changes in return loss in the model by the two forward and reverse load match terms, that the relevant impedance change is caused by a change in switch return loss between the transmission and reflectometer measurement states of the test-set.

These return loss changes are not captured by the SOLT based error model and thus violate the underlying LTI assumption, leading to the serious tracking errors for low insertion-loss DUTs shown in Fig. 2.102.

The synthetic results for the 10-term SOLT corrected ripple test using the SRX and SWR double reflectometer test-set is almost identical as in the unidirectional test-set case, which again was to be expected. The numerical results for theses synthetic measurements are found in the appendix. Despite this minor setback it can be seen, that the receiver input wave selector switch cross-talk correction provided by the (10+4)-term error model performs extremely well for both the forward and the reverse stimulus magnitude of the transmission isolation measurements provided by the bidirectional ripple-test shown in Fig. 2.103. An increase in usable dynamic transmission measurement range of up to 45 dB can be observed for the $C = 30$ dB low isolation switched test-set. The complete synthetic measurement results, including phase data, are again found in appendix A of this work.

Just as in the unidirectional ripple-test case, the SWR architecture provides a much lower amount of interference based trace noise for the reflection measurements in the bidirectional configuration, resulting in a near perfect synthetic $|S_{11}|$ ripple envelope. Both architectures show a calibrated bidirectional reflectometer source match in excess of 70 dB for isolating DUTs.

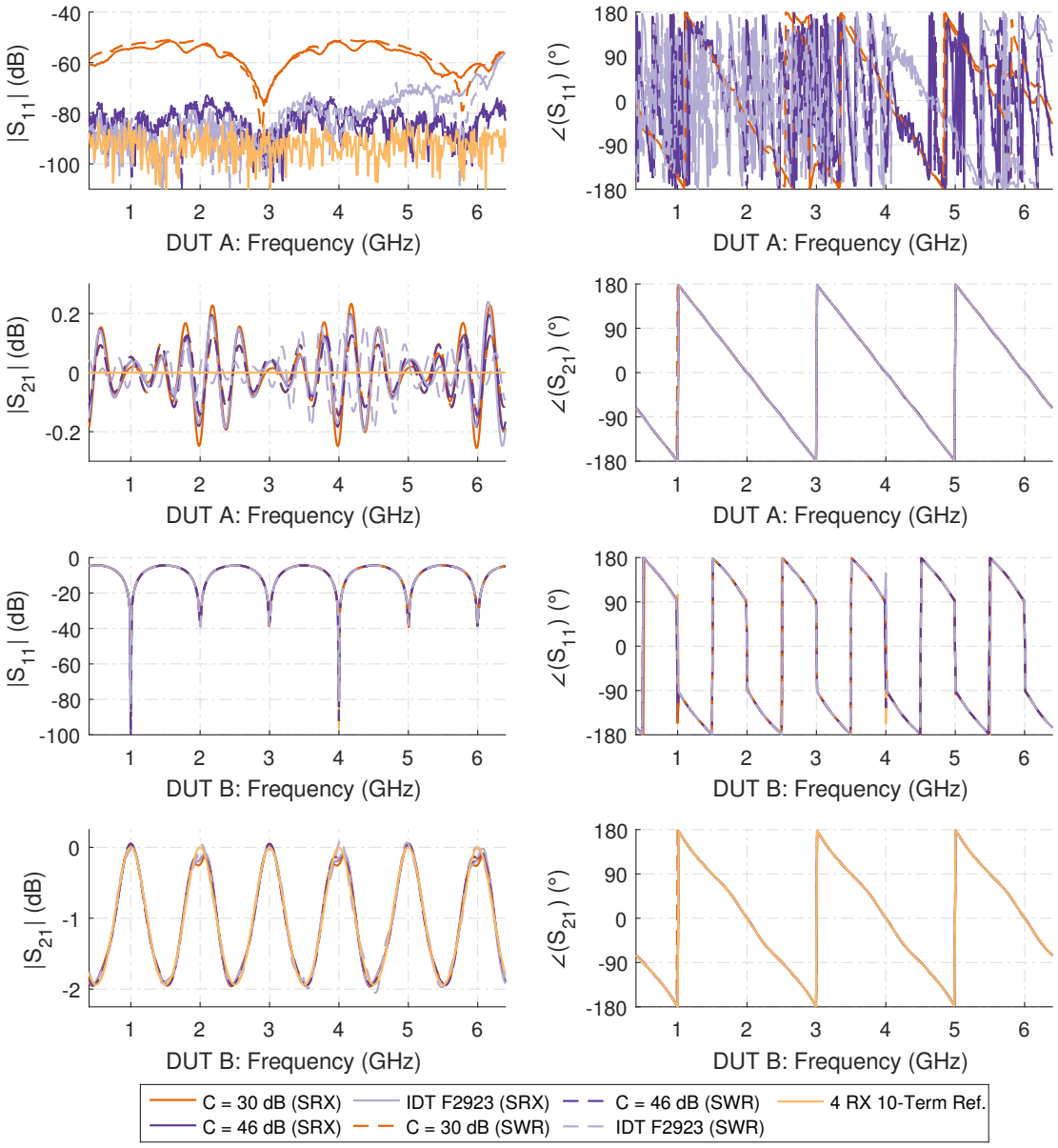

Figure 2.102: Numerical (10+4)-term error corrected synthetic measurement results of a loss-less 50 Ω 150 mm ideal transmission line (DUT A) and a loss-less ideal 25 Ω 150 mm transmission line (DUT B) for all synthetic switches and for the switched single receiver (SRX) and switched single receiver with reference wave switch (SWR) architectures using the double reflectometer test-sets.

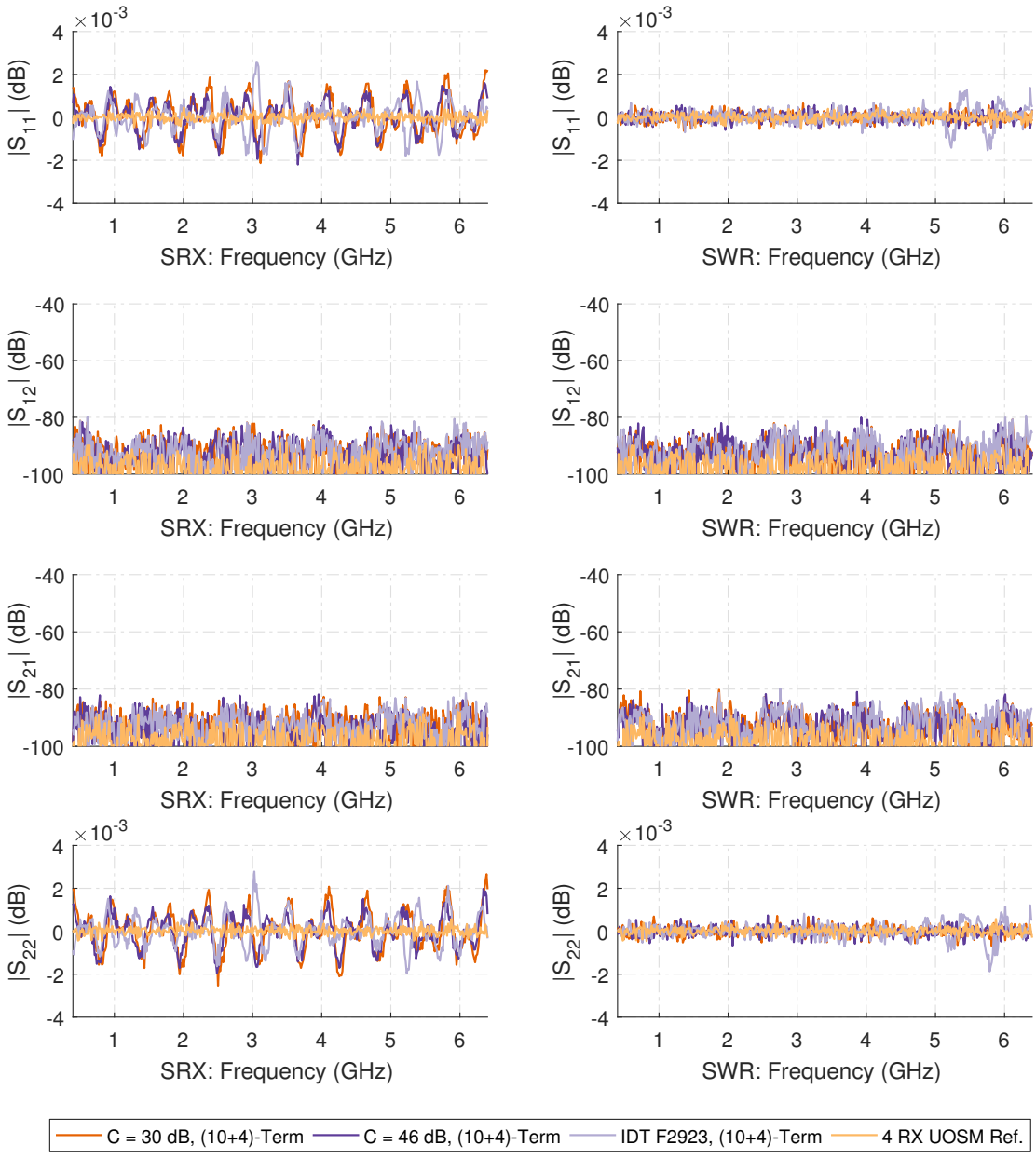

Figure 2.103: Numerical (10+4) error model corrected measurement results of the ripple test measurement using two 150 mm loss-less 50 Ω transmission lines terminated by the calibration shorts on both ports for all synthetic switches and for the switched single receiver (SRX) and switched single receiver with reference wave switch (SWR) architectures using the double reflectometer test-sets.

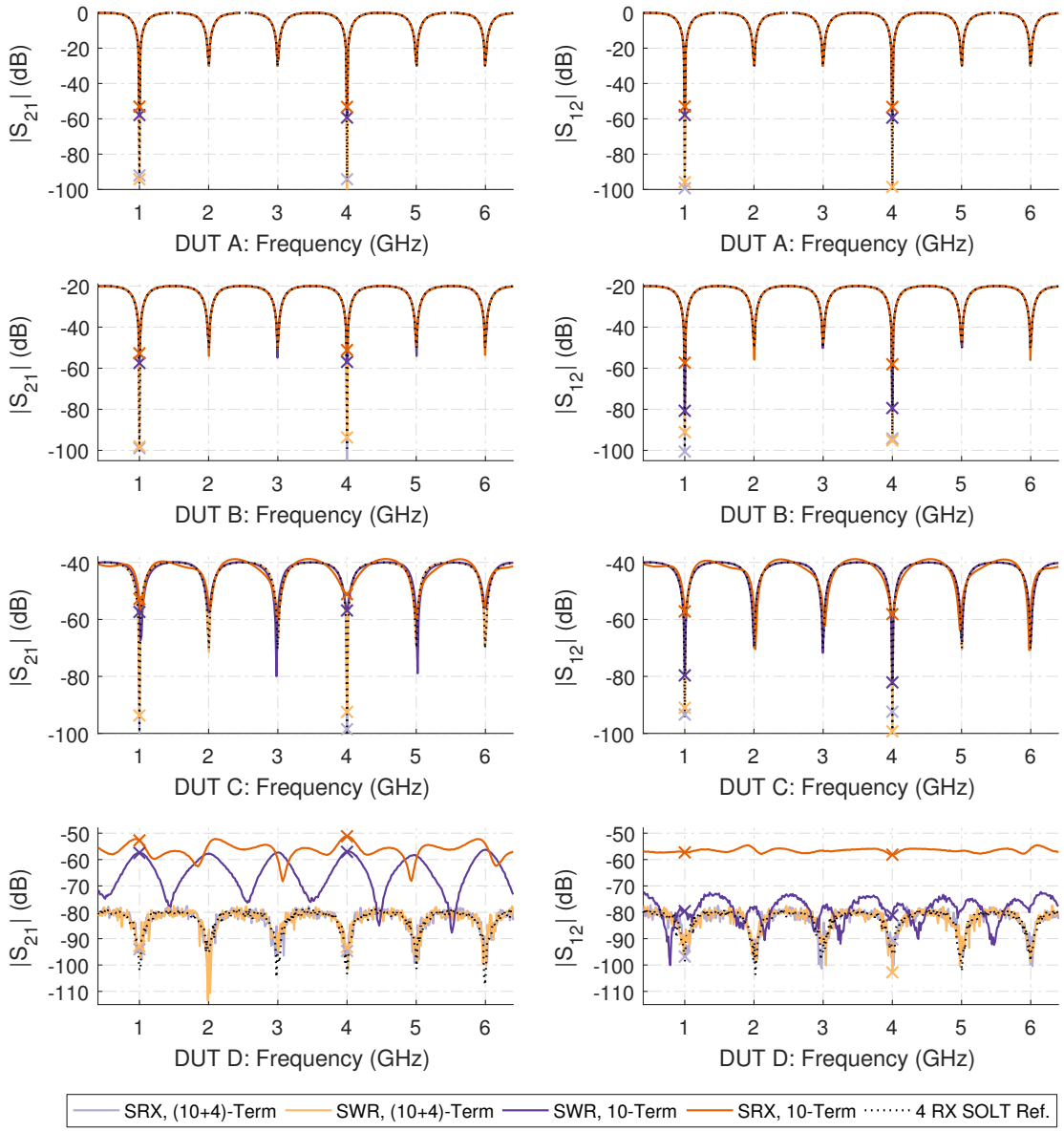

Figure 2.104: Numerical $|S_{21}|$ and $|S_{12}|$ measurement results for the $C = 30\,\text{dB}$ switch test-set of the asymmetric reflective lossy tee (ARLT) in various configurations, corrected by the 10- and (10+4)-term error model and for the single switched receiver (SRX) and single switched receiver with reference wave switch (SWR) test-set architectures. DUT A - ARLT 0 dB attenuation, DUT B - ARLT 20 dB attenuation, DUT C - ARLT 40 dB attenuation, and DUT D - ARLT 80 dB attenuation.

The results of the synthetic bidirectional 10- and (10+4)-term error corrected asymmetric reflective lossy tee are shown in aggregated form in Fig. 2.104 with only $|S_{21}|$ and $|S_{12}|$ for an isolation of $C = 30\,\mathrm{dB}$ shown, while the complete measurement results containing all synthetic switches and all S-parameters by magnitude and phase can be found in the appendix.

The obtained $|S_{21}|$ plots, shown in Fig. 2.104 for both architectures, are almost identical with the results obtained with the unidirectional test-set and its corresponding error correction, except for a reduction in tracking errors for the 0 dB attenuation case due the E_{LF} and E_{LR} correction in the 10- and (10+4)-term model.

Besides the obvious, it is interesting to see the progression of the gradually better matched second port of the DUT, and therefore lower cross-talk inflicted by the b_{2m} cross-talk, upon the S_{12} measurement in the 10-term corrected results in both SRX and SWR test-set topologies. While the SRX topology barely gains any ground by increasing the return loss due to its nearly constant a_{2m} cross-talk, the SWR topology shows a substantially $S_{22,\,\mathrm{DUT}}$ dependent increase in usable S_{12} dynamic range due to the heavy attenuation of the a_{2m} cross-talk path by the reference wave switch.

The S_{12} measurements in the SWR test-set architecture also show, that the (10+4)-term error correction method is fairly impervious to both noisy input values and noisy error correction coefficients. When these measurements are compared with the ones obtained in the SRX architecture and the high attenuation measurements of $|S_{21}|$ in both architectures, it can be clearly seen, that no additional trace noise associated with this correction and architecture method, despite depending on a noisy E_{XR} coefficient attenuated by the reference switch and a noisy S_{22m} value needed for the E_{XRR} correction.

This observation distinctly shows the robustness of this SOLT derived receiver input wave selector switch cross-talk correction method when compared with the noise sensitive 15-term error correction model applied to the same problem in [125], which needs additional measures in the form of variance checking and nullifying of the cross-talk coefficients to avoid measurement quality degradation.

2.4.6 Numerical 7-Term UOSM and xUOSM Results and Conclusion

For the final synthetic verification carried out with the switched single receiver test-sets, the 7-term error model combined with the UOSM and xUOSM calibration procedures, both bidirectional double reflectometer test-sets in the SRX topology (Fig. 2.98) and the SWR topology (Fig. 2.99) are reused. Additionally, the 7-term model with UOSM calibration is now also applied to the synthetic reference measurements performed by the four-receiver double reflectometer reference test-set introduced in Fig. 2.90.

Due to the inherent stimulus direction dependent degeneration of the four-receiver SWR test-set to only three usable receivers (see discussion in the previous section 2.4.5 and Fig. 2.99 for reference), two fairly different test-set dependent implementations of the UOSM and xUOSM calibration, the 7-term model error correction, and especially the switch-terms correction are needed.

The four-receiver SRX test-set, analogous to the four-receiver reference implementation, uses a straight forward approach for the determination of the error model coefficients.

At first, both reflectometers are individually calibrated in the 3-term model with their respective synthetic MSO calibration standard measurements, using Eq. (2.45). With these calibrated reflectometers, the receiver input wave selector switch cross-talk coefficients are determined by applying Eq. (2.95) through (2.98) to the synthetic measurements of the Match-Match, Short-Match and Match-Short isolation standards.

The switch terms coefficients Γ_F and Γ_R are then determined by evaluating the measurement of the synthetic thru connection with Eq. (2.113), and stored for further correction of the measurement data. As a final step, the unknown-thru calibration procedure, described in Eq. (2.115) through Eq. (2.128), is applied to the thru measurement data using an electrical length model of the thru to assemble the complete 7-term error-box coefficient matrix. The 7-term corrected measurement of the DUT can now be calculated by applying Eq. (2.130).

In contrast, the SWR test-set requires a quite different approach for a successful 7-term calibration, caused by the missing DUT dependent a_{2m} measurement under forward and the missing a_{1m} measurement under reverse stimulus. This unfortunate result of the test-set topology prohibits a direct determination of the switch term coefficients and an alternative two-tier calibration approach must be used instead.

In order to perform the two-tier calibration, the reflectometers are individually calibrated in the 3-term model using Eq. (2.45) with the synthetic MSO measurements of both ports. The receiver input wave selector switch cross-talk coefficients can also be determined in the usual way by applying Eq. (2.95) to (2.98) to the synthetic measurement results of the aforementioned isolation standards.

While everything up to this point is just like the procedure applied to the reference and the SRX test-set, the switch terms coefficients Γ_F and Γ_R must now be determined using the two-tier 7-term procedure for three-receiver VNAs, described for TRL in [27, 68] or explicitly for UOSM in [138].

In following the two-tier approach, the bidirectional measurement of a fully known, or flush thru, is needed in combination with the reflectometer calibration to build and calculate a complete 10-term SOLT error model first. Using this complete 10-term description, which includes the individual load and source match coefficients based upon the stimulus directions, it is now possible to calculate Γ_F and Γ_R, while the rest of the error model coefficients are discarded. This completes the first tier of the calibration.

As the switch terms coefficients are now known, the S-parameter measurement of the approximately known reciprocal thru, which only requires three-receivers per stimulus direction, can now be used with Eq. (2.115) to Eq. (2.128), together with the approximately known electrical length of the thru, and the two 3-term error-box networks of the reflectometers, to assemble the full 7-term error-box network model matrix, completing the second tier of the calibration procedure.

Due to the commonality of standards between 7-term UOSM and 10-term SOLT calibration and the application of a (well) known thru standard, no additional connections and measurements of other calibration standards are fortunately necessary to perform these two complete nested calibrations in a row. Just a different additional processing of the calibration measurements is needed to perform the transition from the three-receiver test-set to its virtual, 7-term model conform, four-receiver representation.

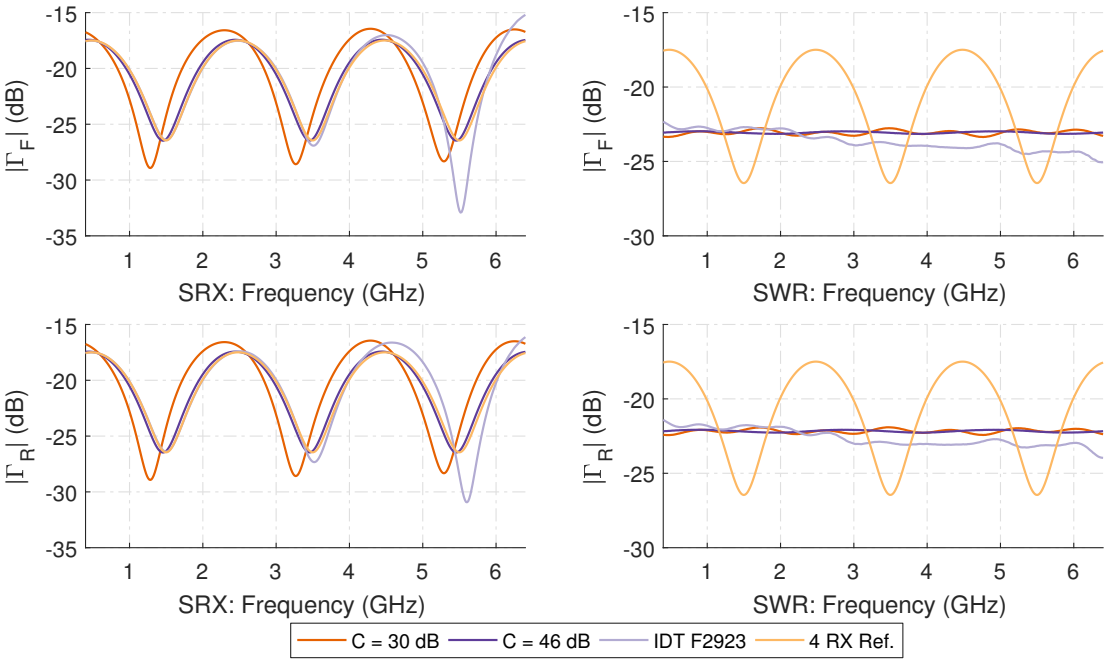

Figure 2.105: Numerical results for the Γ_F and Γ_R switching terms coefficients obtained for the switched single receiver (SRX) architecture via the direct thru measurement method and the switched single receiver with reference wave switch (SWR) architecture by applying a two-tier SOLT/7-term calibration using the double reflectometer test-sets.

The quite unexpected results of the T-Check measurements for the switched single receiver SRX and SWR architectures and the four-receiver reference test-set are shown in Fig. 2.106 for the UOSM corrected measurement, where no receiver input wave selector switch cross-talk correction is applied, while Fig. 2.107 shows the 7-term xUOSM transmission cross-talk corrected C_T results, for all the three investigated test-set switch isolations.

After the mediocre results of performing the synthetic T-Check with the (10+4)-term SOLT correction (Fig. 2.101), the improvement of ΔC_T by a factor of 5 for the SRX test-set topology, and the even better results for SWR architecture demonstrated by the $C = 46\,\mathrm{dB}$ case, and the real S-parameters of the IDT F2923 switch, which are both almost indistinguishable from the C_T values of the reference four-receiver test-set, are quite a surprise. The far better results of the SWR over SRX architecture are most likely the result of higher isolation for the a_i reference measurement against the other state dependent sources of interference in the SWR test-set.

The results obtained with the quite dynamic switched reference wave single receiver test-set are especially surprising, foremost due to the two-tier calibration process, but especially when the assumed robustness of the SOLT 10-term model and the susceptibility of the 7-term model to even minor model violations on normal VNA architectures are

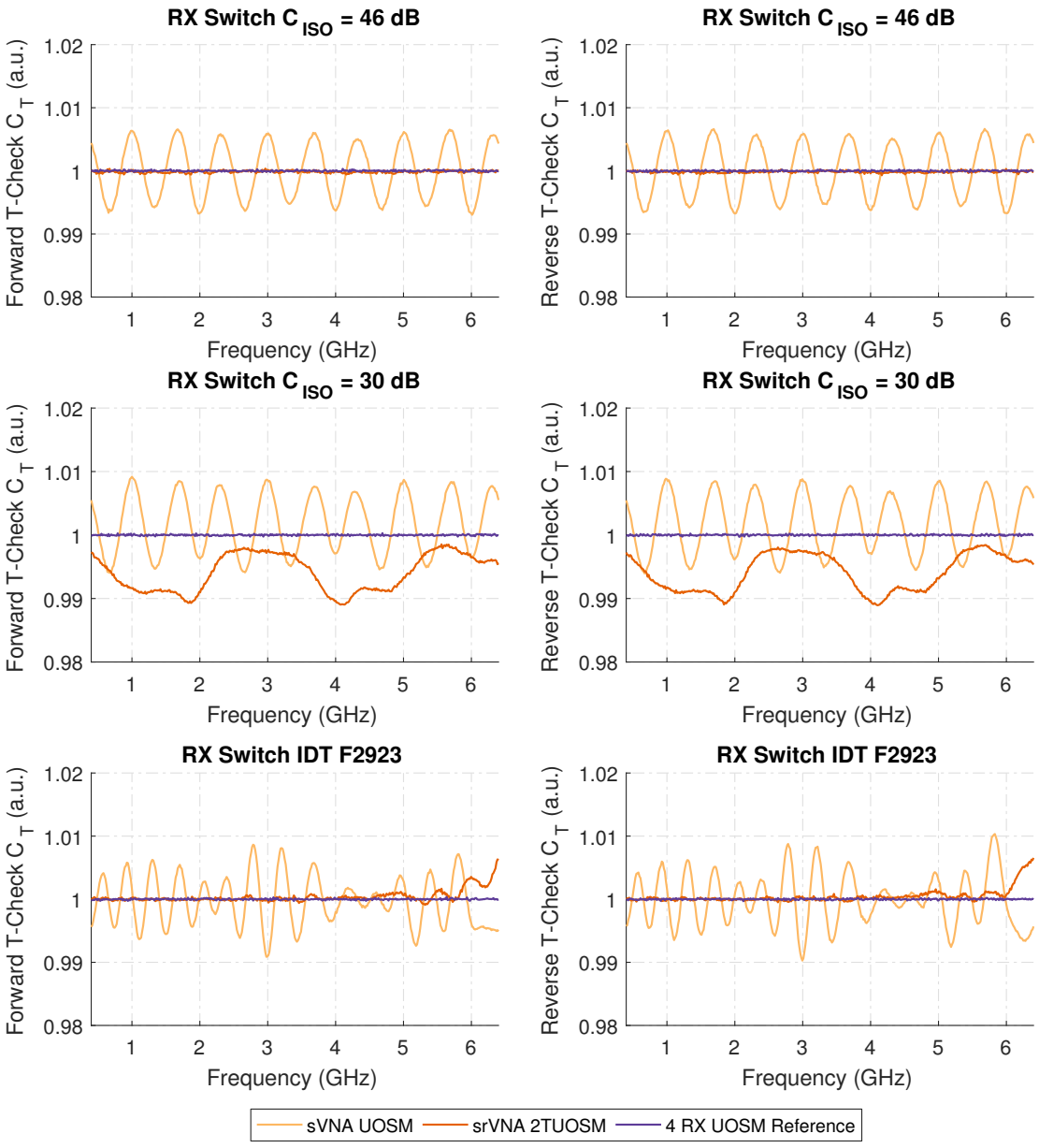

Figure 2.106: Numerical results for the T-Check measurements using the 7-term UOSM correction model for all synthetic switches and for the switched single receiver (SRX) and switched single receiver with reference wave switch (SWR) architectures using the double reflectometer test-sets.

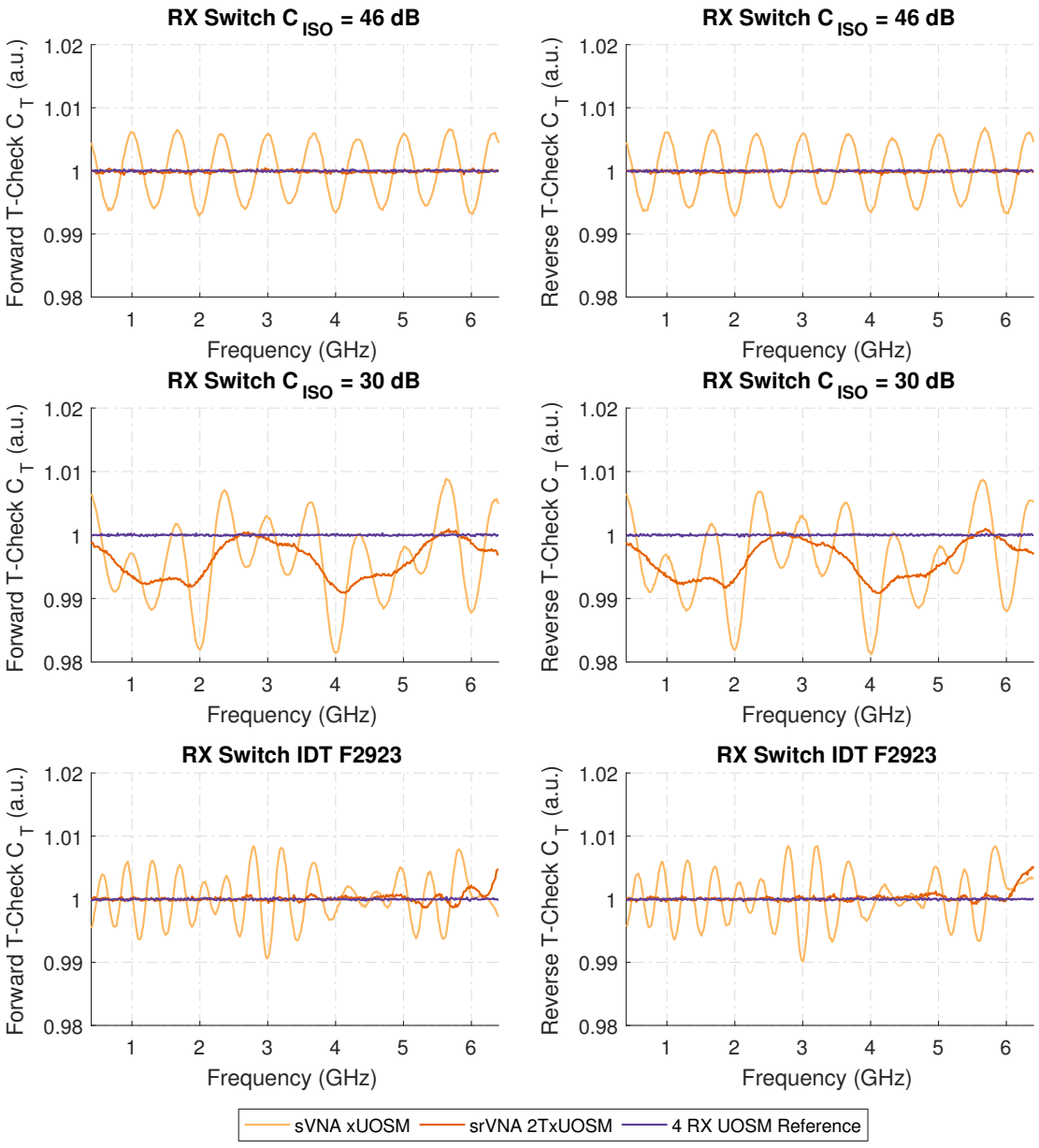

Figure 2.107: Numerical results for the T-Check measurements using the 7-term xUOSM correction model for all synthetic switches and for the switched single receiver (SRX) and switched single receiver with reference wave switch (SWR) architectures using the double reflectometer test-sets.

taken into account ([49]), while quite the opposite result is the case here.

The very positive outcome of the T-Check measurements are furthermore supported by the error corrected results of the loss-less ideal 50 Ω 150 mm transmission line thru connection and the loss-less ideal 25 Ω 150 mm transmission line or (Beatty line) thru connection, both shown in Fig. 2.108. The results of these verification measurements are close to ideal for the SRX test-set architecture for both the S_{11} and the S_{21} parameters, while the SWR test-set topology still performs an order of magnitude better than the results demonstrated for this architecture in the 10- and (10+4)-term measurements. The full two-port S-parameter measurement results for these measurements can be found in appendix A of this work.

The results for the bidirectional ripple test measurements, shown for the non-cross-talk corrected UOSM 7-term model in Fig. 2.109, and for the xUOSM 7-term cross-talk corrected error model in Fig. 2.110, carried out with the same ideal loss-less 150 mm 50 Ω transmission lines and the calibration short simultaneously on both ports as in the SOLT case, further attest the potential and error correction performance of the xUOSM - SWR test-set combination in both the reflection tracking accuracy and transmission dynamic range improvement by the receiver input wave selector switch cross-talk correction applied outside of the 7-term error model. The full measurement results presenting all S-parameters obtained by the ripple test are again found in appendix A of this work.

The advantage of a smaller peak-to-peak $|S_{11}|$ ripple envelope value found for the SWR architecture in the unidirectional and bidirectional test-sets still persists for the 7-term error corrected ripple test measurement. Overall, the S_{11} ripple envelope source match performance is comparable to the other test-set and error correction variants shown, reaching values in excess of 70 dB theoretical source match performance.

When the dynamic range improvement due to the cross-talk correction is compared between the non-corrected measurement shown in Fig. 2.109 and the results for the cross-talk corrected xUOSM measurements in Fig. 2.110, it is apparent, that approximately the same amount of dynamic range reconstruction is achieved with the 7-term error model and its extension, as shown in the unidirectional (7+2)-term (Fig. 2.94) and the bidirectional (10+4)-term (Fig. 2.103) ripple test isolation measurements.

From the beginning, the 7-term based correction methods were expected to perform approximately 10 to 15 dB worse than SOLT based methods in this regard, due to the susceptibility of this model to the aforementioned minor model violations, which can show up as a reduction in total dynamic range even for perfectly isolated four-receiver VNAs, caused for example by minor connector torque errors during calibration. That the combination of the switch-terms and the receiver input wave selector switch cross-talk correction perform so well in the 7-term model on the switched receiver architecture was not anticipated.

This observation is further confirmed by the synthetic measurement results of the asymmetric reflective loss tee shown for the $C = 30$ dB test-set configuration in Fig. 2.111, while the full results of the verification measurements can be found in the appendix. From the data shown in this figure it can be noticed, that the tracking performance for the highly reflective 0 dB attenuation case is extremely improved by applying the 7-term UOSM correction to the switched receiver architectures, which results in far better tracking

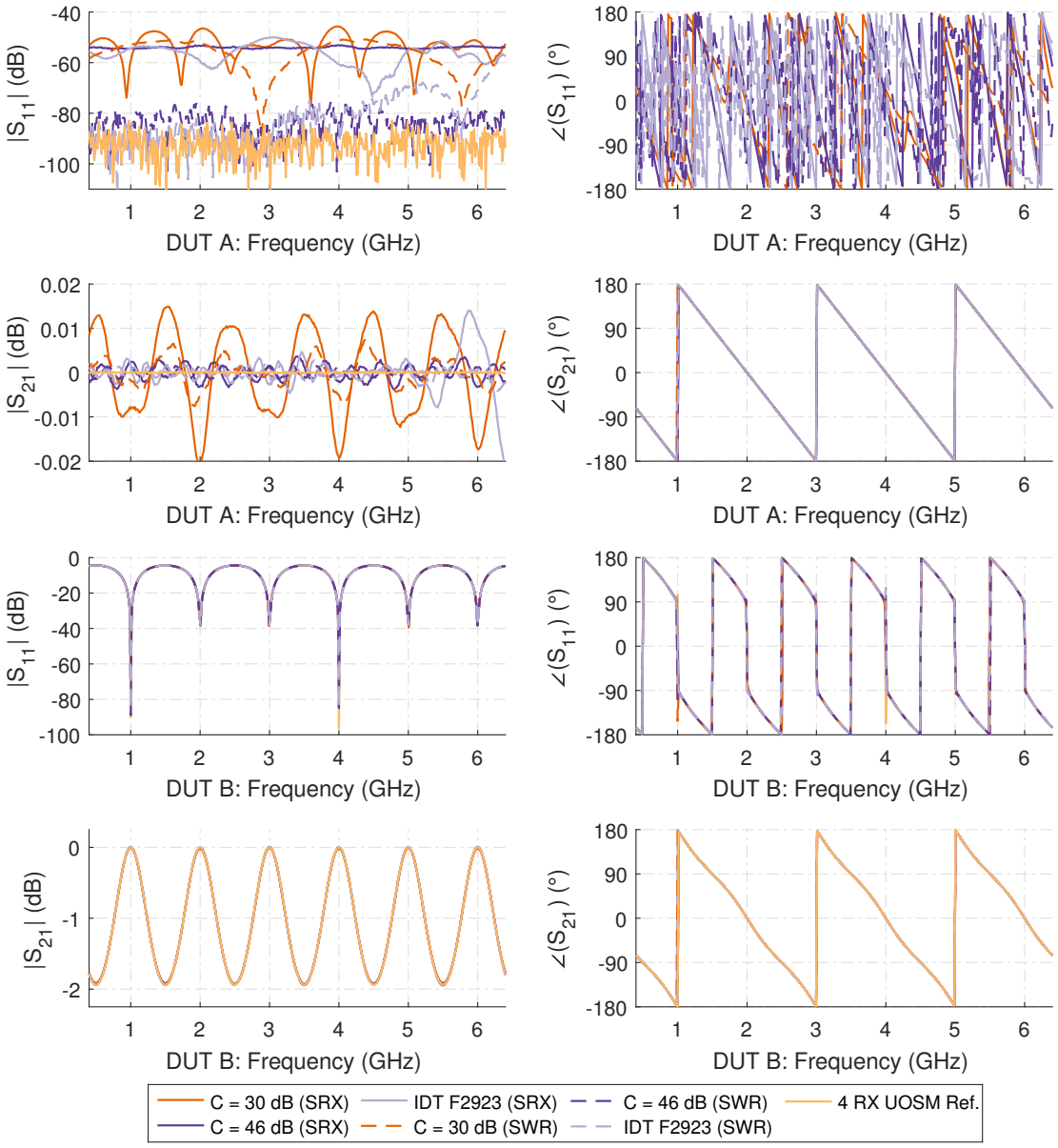

Figure 2.108: Numerical 7-term xUOSM error corrected synthetic measurement results of a loss-less 50 Ω 150 mm ideal transmission line (DUT A) and a loss-less ideal 25 Ω 150 mm transmission line (DUT B) for all synthetic switches and for the switched single receiver (SRX) and switched single receiver with reference wave switch (SWR) architectures using the double reflectometer test-sets.

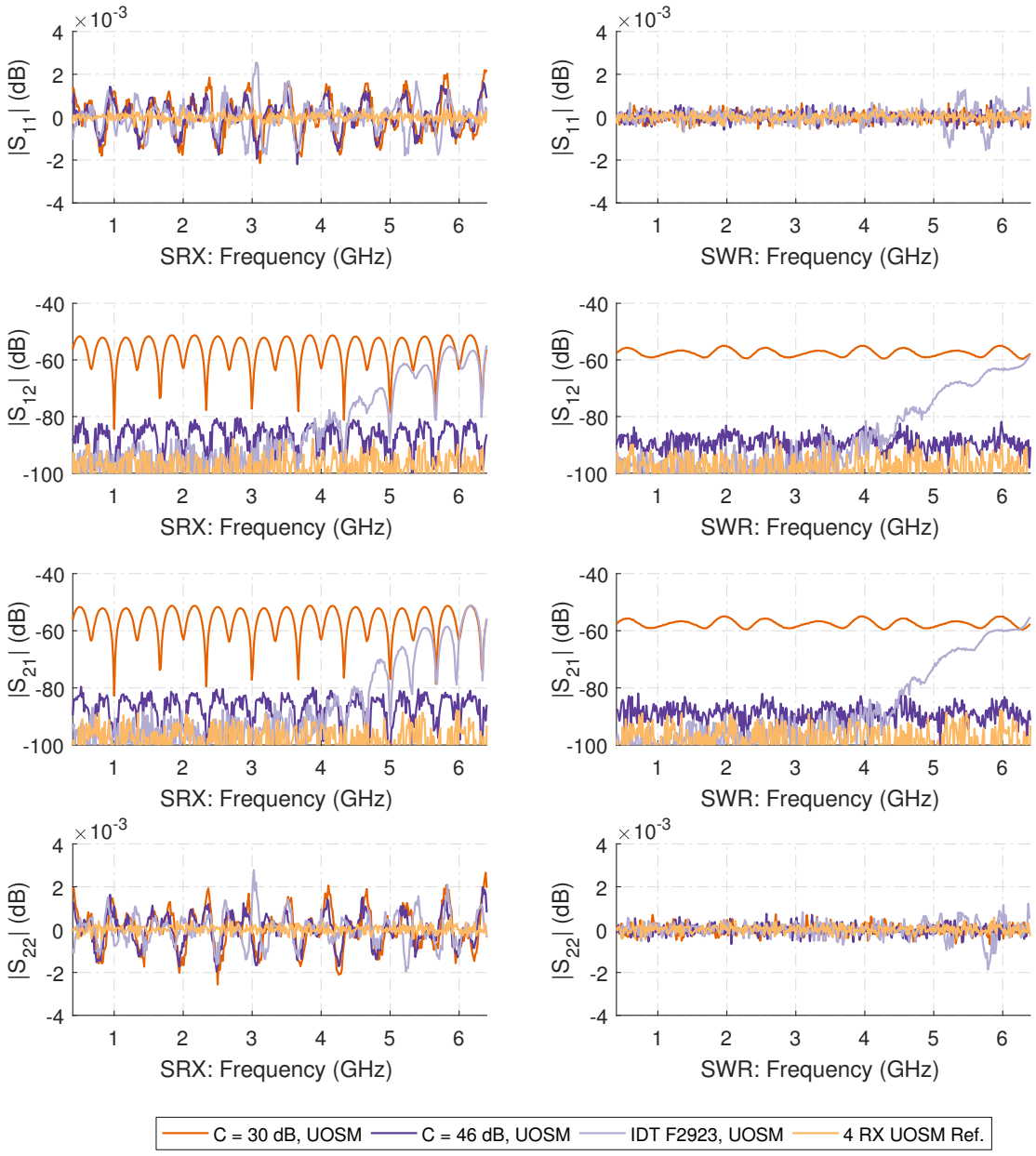

Figure 2.109: Numerical 7-term error model UOSM corrected measurement results of the ripple test measurement using two 150 mm loss-less 50 Ω transmission lines terminated by the calibration shorts on both ports for all synthetic switches and for the switched single receiver (SRX) and switched single receiver with reference wave switch (SWR) architectures using the double reflectometer test-sets.

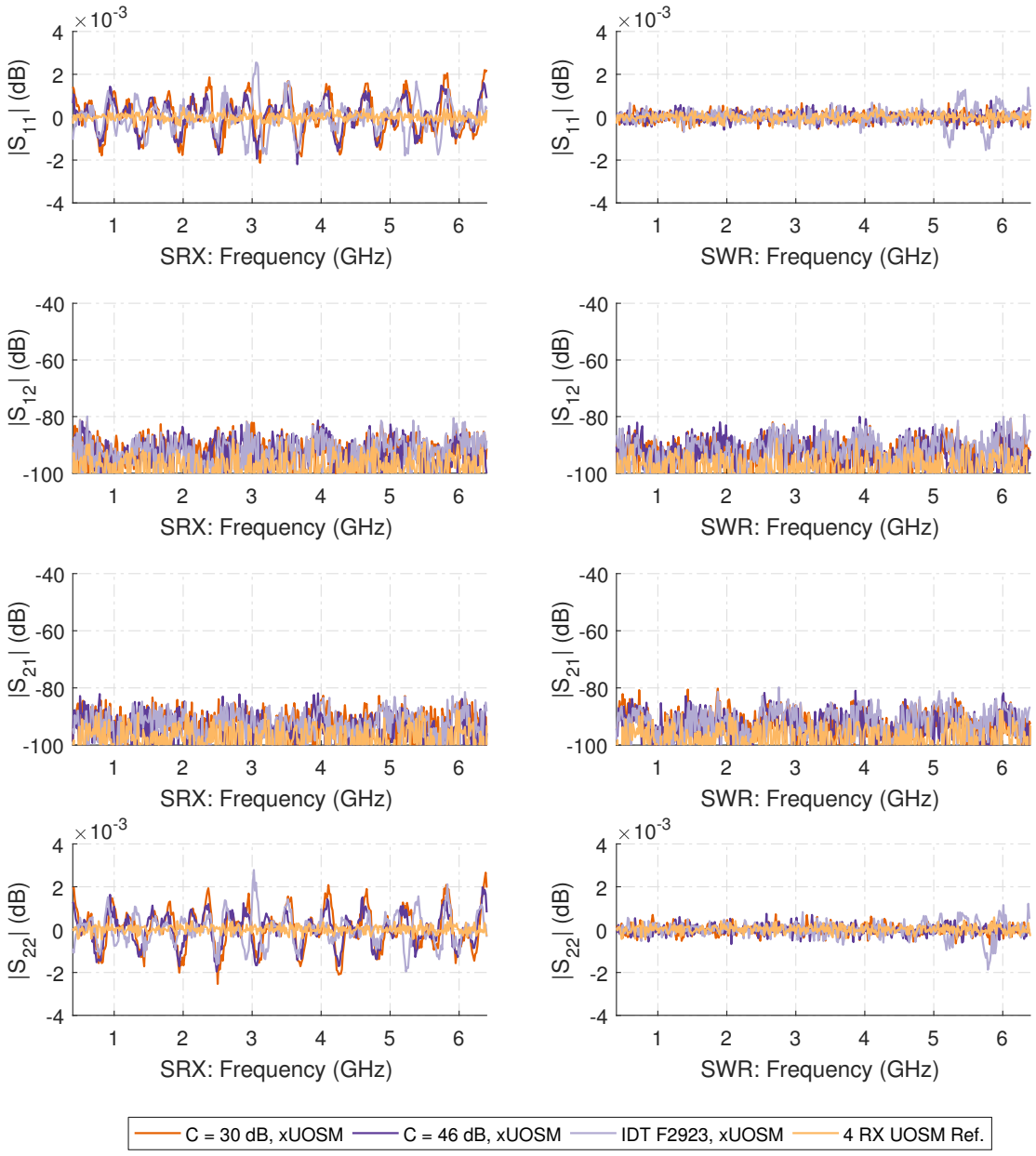

Figure 2.110: Numerical 7-term error model xUOSM corrected measurement results of the ripple test measurement using two 150 mm loss-less 50 Ω transmission lines terminated by the calibration shorts on both ports for all synthetic switches and for the switched single receiver (SRX) and switched single receiver with reference wave switch (SWR) architectures using the double reflectometer test-sets.

performance compared to the 10-term SOLT model on the same architecture. This additionally confirms the findings already made with the Beatty line thru measurements, shown in Fig. 2.108, and the T-Check FOMs shown in Fig. 2.106 and Fig. 2.107. The forward and reverse transmission measurement xUOSM cross-talk correction works as well as in the (10+4)-term SOLT corrected measurements and allows even the $C = 30\,\mathrm{dB}$ test-set to perform transmission measurements to within 5 to 10 dB of the receiver noise floor with good transmission tracking performance, even for the 80 dB attenuation case in both measurement stimulus directions. A slightly elevated trace noise level is observed in direct comparison to the reference test-set.

While no explanation in closed form exists at this point for the better error correction performance seen with the 7-term UOSM error model when compared with the 10-term error SOLT model on the switched receiver test-test architectures, the most likely cause for this effect is the absorption of some receiver input wave selector switch return loss variations into the Γ_F and Γ_R switch-terms coefficients.

While these coefficients were originally envisioned to allow for different load and source matches of the port depending on the stimulus direction ([80]), and therefore emulate parts of the 10-term SOLT model which are not part of the original LTI 7-term concept, the switch terms correction apparently also corrects some effects, like the aforementioned load match modulation, which are not captured in any way by the 10-term SOLT approach.

This effect can also be observed when the results for the switch-terms coefficients shown in Fig. 2.105 are revisited. There, distinct differences can be seen between the results of the $C = 30\,\mathrm{dB}$ and $C = 46\,\mathrm{dB}$ test-sets, which both share the same synthetic constant return loss, that can not be readily explained with the classical intended usage and formulation of the switch term correction method in [80], and therefore provide a hint to the absorption of other effects into the switch-terms coefficients by superposition.

From the synthetic numerical results for different test-set configurations, error models and correction methods it can be concluded, that the switched receiver architecture can reach a performance similar to the reference full receiver configuration of the corresponding test-set topology, when appropriate correction methods and error model extensions are used.

It was shown, that the synthetic switched reflectometer topology can be fully error corrected with the existing 3-term error model without any further extension to the well-established existing algorithm.

The unidirectional switched receiver topology can also be successfully corrected to perform almost as well as a classical 5-term three-receiver VNA with its inherent measurement uncertainties, when the (5+2)-term extension to the classical 5-term error model is used, which in turn verified the efficacy of this new extension to the classical SOLT error model.

It turned out as quite a surprise, that after the promising results of the (5+2)-term correction, the analogous bidirectional double reflectometer (10+4)-term error model and correction on the one hand excelled in its original design intention, namely the correction of the receiver input wave selector switch cross-talk in both stimulus direction, but showed various transmission measurement tracking errors caused by the modulation of the load match coefficients which were not expected in this severity for the synthetic test-sets.

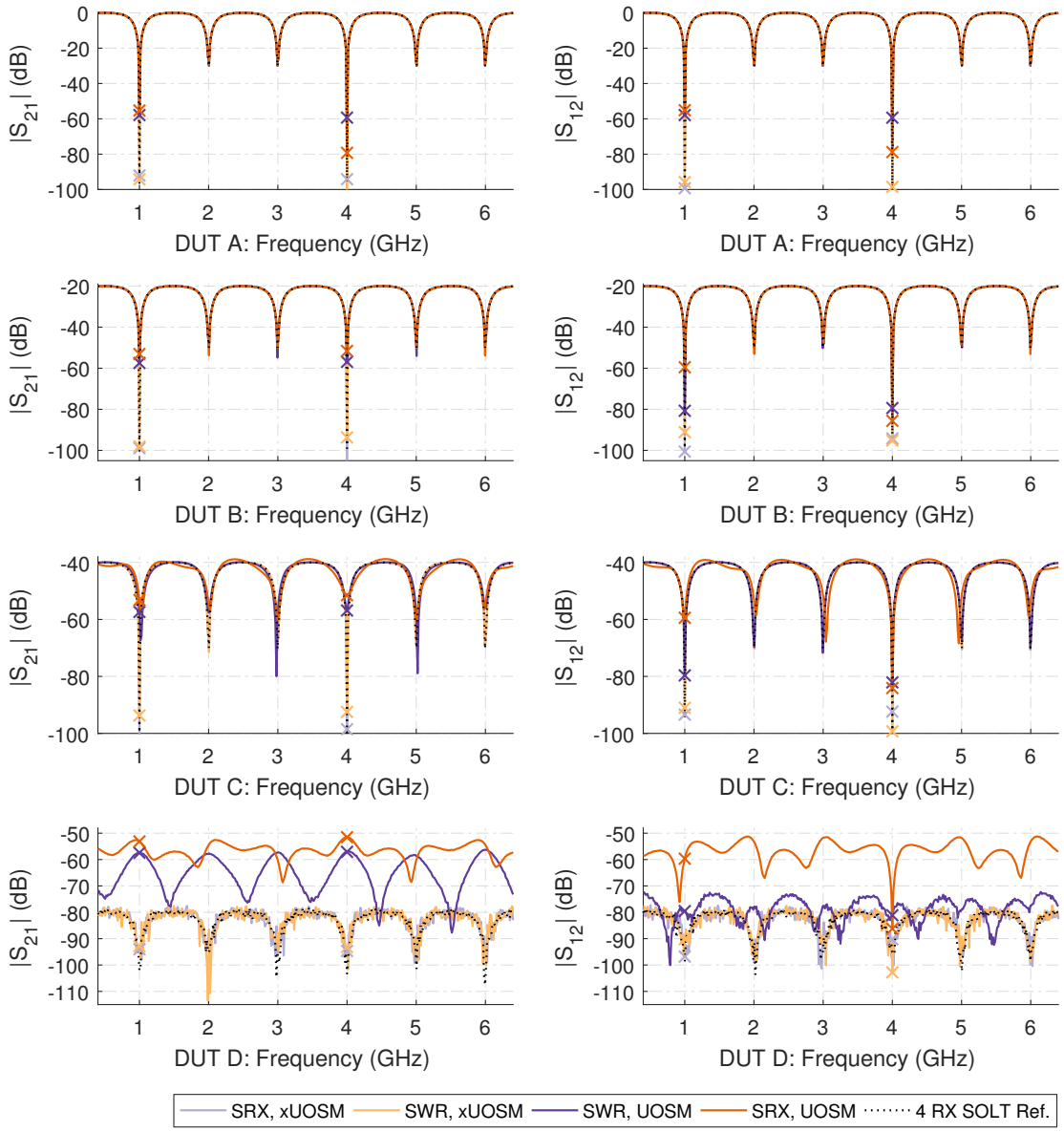

Figure 2.111: Numerical $|S_{21}|$ and $|S_{12}|$ measurement results for the $C = 30\,\text{dB}$ switch test-set of the asymmetric reflective lossy tee (ARLT) in various configurations, corrected by the 7-term UOSM and xUOSM error model and for the single switched receiver (SRX) and single switched receiver with reference wave switch (SWR) test-set architectures. DUT A - ARLT 0 dB attenuation, DUT B - ARLT 20 dB attenuation, DUT C - ARLT 40 dB attenuation, and DUT D - ARLT 80 dB attenuation.

Nevertheless, the efficacy of the four-error error coefficients capturing the effects of the receiver wave selector switch crosstalk in the (10+4)-term error model was demonstrated.

This unfortunate result when the basic 10- or (10+4)-term error model was applied was however more than compensated for by the excellent and very promising results of the 7-term UOSM, and especially xUOSM, procedures with the added switching-terms correction in both direct and two-tier variants. In combination, these methods provided nearly identical measurement results when compared the synthetic four-receiver reference VNA, even under adverse SNR conditions.

Nevertheless, further research is needed to pinpoint the exact source for these phenomena and the exact cause for the correction ability of the switch-terms correction for these effects.

In regard to test-set architectures, the viability of the new switched reference test-set (SWR) topology and its positive influence upon the signal to interference ratio was demonstrated for all multi-port single switched receiver test-set implementation. A clear improvement in the quality of the measurement results was shown for almost all verification test cases for the SWR test-set when compared with the classical SRX approach of [125] by replacing the reference wave coupler of the reflectometer with a semiconductor switch.

Finally, the synthetic measurements also provided the numerical verification of the custom implementation of the various calibration and error correction methods as a precursor to the validation measurements performed on the real VNA hardware.

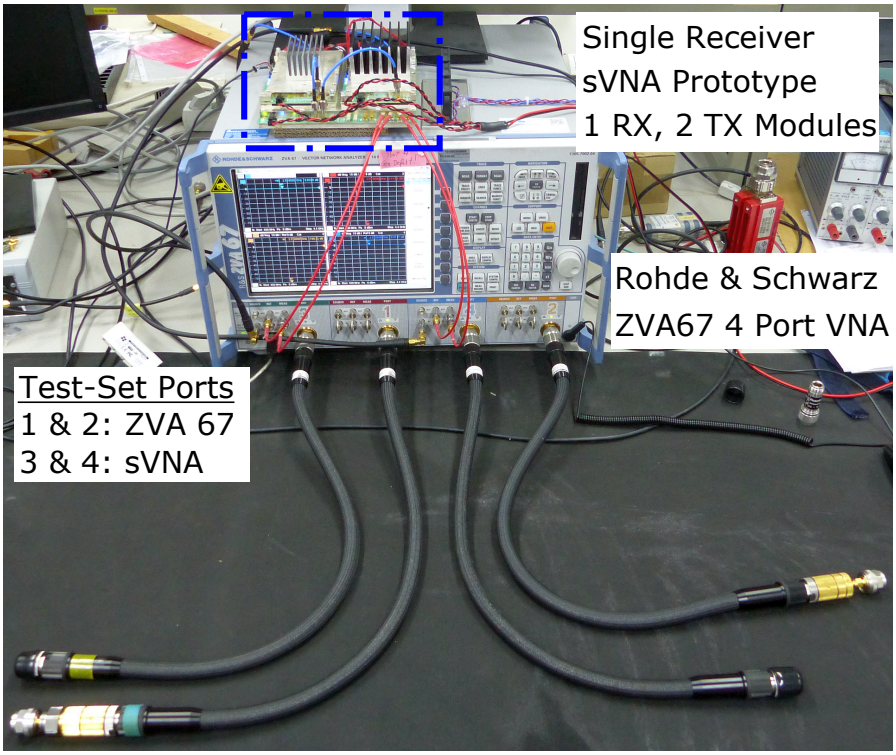

Figure 2.112: Picture of the VNA hardware evaluation setup based around the sVNA protoype and the Rohde & Schwarz ZVA67 VNA and test-set.

2.5 Measurement Results and Comparison of the Concepts

2.5.1 General Description of the Measurement Setup

In order to verify the findings of the numerical synthetics analysis of the error models and their correction algorithms, an experimental setup centering around the single switched receiver VNA prototype presented earlier and a four port ZVA67 from Rohde & Schwarz as the reference device and test-set donor for the single receiver VNA is used, which can be seen in an overview picture of the setup shown in Fig. 2.112. The single receiver VNA prototype will be abbreviated sVNA for the SRX test-set configuration and srVNA for the SWR test-set configuration presented earlier from here on, to clearly distinguish the numerical synthetic test-sets and results from the measurements performed on the real VNA hardware.

The only part of the test-set contained in the receiver and the stimulus synthesizer modules are the silicon PIN diode switches, therefore additional directional couplers and appropriate physical rigid and repeatable coaxial connector terminations are needed to complete the measurement setup for the sVNA and srVNA experiments.

While resistive bridge couplers, including test-port coaxial connectors for frequencies up to 6 GHz, are readily available nowadays from the usual microwave suppliers, the addition

Figure 2.113: Detail picture of the ZVA67 test-set connections and configuration used for the measurements. Port 1 and 2 are connected to the internal stimulus synthesizers and receivers of the ZVA67, while Port 3 and 4 are connected to the single receiver VNA prototype in a four-receiver SRX configuration.

of more unknown factors besides the changed test-set architecture and a completely new stimulus synthesizer and receiver system does not help to increase the direct comparability of the measurement results between different VNAs and architectures.

Luckily, the four port ZVA67 used as the reference VNA for the measurements is fitted with the optional direct receiver, transmitter and test-set access option, where all RF connections to the test-set can either be used in their original intended function by leaving the original coaxial jumper links in place, or by removing the jumper links, allows for new or additional test-set connections used in applications like Hot-S_{11}, large signal or intermodulation measurements.

As the methods presented in chapters 2.2.3 to 2.2.9 of this work are limited to double reflectometer two-port measurements and a four port VNA with direct test-set access is available, this allowed the utilization of the internal double reflectometers of port 3 and 4 of the ZVA67 to complete the single receiver VNA measurement system, while retaining the ability to use ports 1 and 2 of ZVA67 for the reference measurements. An exemplary case of the modified test-set connections is shown in Fig. 2.113.

By using the two unused internal double reflectometers of the ZVA67, a higher degree of direct data comparability when comparing the measurement results between the ZVA67 and the single receiver VNA architectures is achieved, as it is fair to assume that all the couplers used in the internal test-set of the ZVA67 show similar performance figures. This therefore allows the deduction, that any differences seen in the verification measurement results are either caused by the single receiver test-set architecture itself, or the properties of the newly developed stimulus synthesizers and the vector receiver.

In order to enhance the comparability between the two very different VNAs even further, 1.85 mm (or PC-1.85), ruggedized, 650 mm, 70 GHz, armoured, phase stable VNA test-cables (R&S ZV-Z96, made by Gore) are used for all the four test-set ports, including those connected to the single receiver VNA. To physically convert the 1.85 mm to a more suitable N-connector, ruggedized HP PC-2.4 (mateable with ruggedized PC-1.85)

Figure 2.114: Picture of the Rosenberger RPC-N (f) 18 GHz SOLT/MSO-T calibration standards used for all calibration measurements. Standards are a subset of the standards included in a Rosenberger 05CK100-150 SOLT RPC-N calibration kit.

to 3.5 mm test-port adapters are used as an intermediate step. Finally, Rosenberger precision SMA to RPC-N(m) adapters are used to convert the 3.5 mm to the N-connector standard where all necessary verification devices are available to the author.

The internal calibration of the ZVA67, and the calibration of the single receiver VNA using the custom calibration routines verified in the numerical analysis, is carried out with the same set of Rosenberger 18 GHz RPC-N(f) SOLT calibration standards, taken from a Rosenberger 05CK100-150 RPC-N SOLT calibration kit, as shown in Fig. 2.114. Before the verification measurements, these standards were checked for their mechanical integrity and conformity to its original manufacturer specifications by measuring the position of the center conductor reference planes with the supplied precision gauge kit, after thorough cleaning with isopropanol alcohol and drying with oil free compressed air. All standards were found to be within the specified mechanical tolerances.

All reference measurements of the verification standards performed with the ZVA67 are carried out using a very basic device configuration, which mimics the settings chosen for a usual measurement task. The one-port verification measurements are error corrected by the proprietary MSO 3-term implementation of the ZVA67, while all two port verification device measurements are error corrected by the proprietary implementation of the full double reflectometer unknown-thru (UOSM) 7-term calibration procedure.

All verification device measurements conducted with the ZVA67 are performed using the following settings:

- A Frequency range of 400 MHz to 4400 MHz using 401 linear spaced frequency sampling points, resulting in step-size of $\Delta f = 10$ MHz between samples,
- An IF bandwidth setting of 100 Hz, with no additional averaging applied, and
- A source power setting of 0 dBm, referenced to the device test-set port outputs.

In order to facilitate the mechanical repeatability of the connections and the comparability of the results, torque wrenches set for the appropriate nominal torque for the RPC-N and SMA connectors are used throughout all the measurements.

As the proprietary online correction algorithms implemented on the ZVA67 are used, S1P and S2P touchstone files are exported directly from the ZVA67 after each measurement is performed for later evaluation.

For the single receiver VNA measurements a different procedure is used: All raw wave measurement data is captured first and the error correction resulting in S-parameters is performed offline in MATLAB afterwards. Furthermore, a full switch scan over all four wave inputs is always performed for each stimulus direction of the single receiver VNA measurements, even if only two or three wave quantities are needed for the error correction. While this may seem counter-productive at first, this choice was deliberately made to avoid possible errors and minor differences in the firmware implementation, so that always the same output routine and state machine paths are taken for the measurements in each of the different test-set configurations.

The data obtained with the single receiver VNA hardware is saved via a MATLAB routine in the same format and implementation as already used in the numerical analysis for verification of the test-sets and the correction and calibration algorithms. This helps to avoid implementation errors and allows to quickly check the correction algorithm for errors by supplying known synthetic data to discern between hardware or firmware errors and the actual implementation of the algorithm itself.

The verification device measurements are conducted with the single receiver VNA hardware using the same basic frequency settings as in the ZVA67 measurement of the verification devices, i.e. a frequency range of 400 MHz to 4400 MHz using 401 linear spaced frequency sampling points.

An oversampling factor of 1024x and a coherent averaging factor of 10x, coupled with a dwell-time of 4 ms per sampling point, is used for the measurements in combination with the fixed 2.2 kHz IF filter, which results in an equivalent Nyquist-sampling noise bandwidth of approximately 390 Hz.

Using these settings, the single receiver VNA prototype takes about 18 seconds to complete one full scan of the four receiver input wave selector switch positions including data transfer. In total 1604 measurements are performed per stimulus direction and frequency sweep. Of these 18 seconds, around 6.5 seconds are needed for the accumulated IF filter step response dwell-times alone.

A source power of +4 dBm, referenced to the stimulus synthesizer output, is used for all single receiver VNA measurements. Due to resistive padding and test-set and cable losses, this is reduced to approximately -10 dBm at the calibration reference plane, compared to -1 dBm due to connector and cable losses for the ZVA67 measurements. As only passive devices are used for the verification measurement purposes of this work, the impairment of the lower DUT stimulus power is compensated to a degree in the test-set parametrization by placing the resulting single receiver input power closer to the input referred compression power of the ADC, contrary to the design of the ZVA67 which allows for approximately 10 dB of reflection and transmission gain to be measured linearly in the aforementioned configuration.

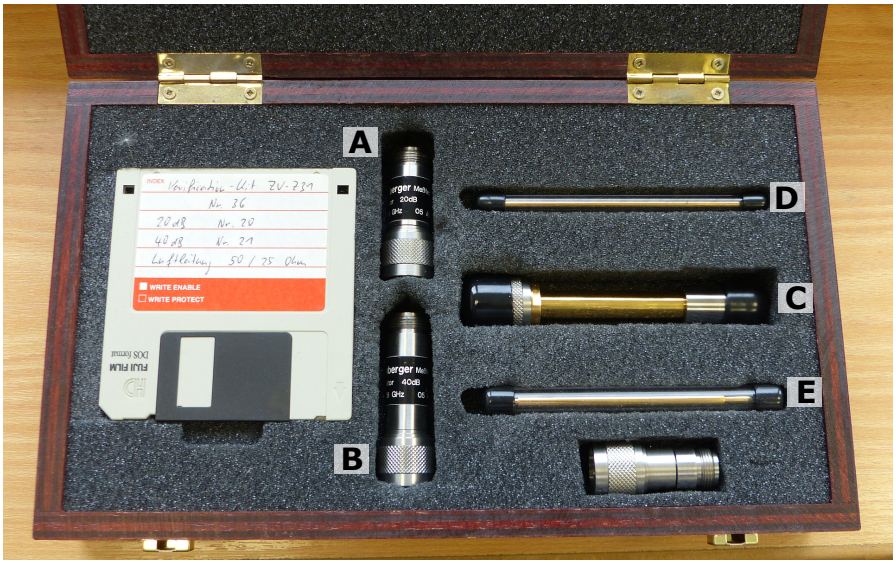

Figure 2.115: Picture of the Rohde & Schwarz ZV-Z31 18 GHz RPC-N verification kit and its contents which is used for the measurements. Annotations: A - 20 dB reference attenuator (m)-(f), B - 40 dB reference attenuator (m)-(f), C - 150 mm RPC-N (m)-(f) airline outer conductor assembly, D - $Z_L = 50\,\Omega$ RPC-N (m)-(f) airline inner conductor, E - $Z_L = 25\,\Omega$ RPC-N (m)-(f) airline inner conductor.

The different insertion loss values of the individual test-sets are compensated by adjusting the variable IF gain of the receiver. Appropriate receiver ADC power measurement results for all wave quantities of the match, short and thru terminations, along with the settings of the variable gain IF amplifiers, will be presented for each of the single receiver test-set configurations.

Both the ZVA67 and the single receiver VNA are allowed to warm-up to thermal equilibrium for one hour prior to the start of the measurements. After the warm-up period, all related measurements, including the measurements of the calibration standards, are conducted in one consecutive run to minimize the temperature drift of the test-set, the stimulus synthesizers and receivers of both devices.

2.5.2 Selection of Appropriate Devices Under Test

Similar to the verification devices used in the numerical synthetic analysis of the switched single receiver concepts, the selection of appropriate verification devices for the real measurements follows the EUMETCAL recommended VNA verification standard list and VNA verification guidelines ([157]). Unfortunately, not all the listed verification measurement devices are available in metrological quality to the author and are therefore substituted by other appropriate devices in combination with the measurement of the same devices performed using the ZVA67 for direct comparison.

Figure 2.116: Rosenberger RPC-N 18 GHz (m)-(m) armoured 600 mm VNA test cables used as a stand-in for longer airline measurements.

Where appropriate, precision metrology devices contained in the Rohde & Schwarz ZV-Z31 18 GHz RPC-N verification kit shown in Fig. 2.115 are used — either as stand-alone verification DUTs or in combination with other devices to form a new composite verification standard. The kit contains the outer conductor of a RPC-N (m)-(f) 150 mm airline with two precision inner conductors for a Z_L of $Z_L = 25\,\Omega$ and $Z_L = 50\,\Omega$ (for detail picture in disassembled state see right side of Fig. 2.120).

Unfortunately a beaded precision airline, as recommended by EUMETCAL, was not available to the author and therefore extra precautions, as outlined in [157], are taken during assembly of the airline to retain a comparable level of mechanical repeatability between measurements and connections.

As a replacement for verification measurements requiring mechanically and electrically longer airlines, a Rosenberger 600 mm RPC-N (m)-(m) armoured VNA test-cable with a manufacturer calibration certificate and known good specifications, which especially includes a good and constant transmission line impedance which is close to $Z_L = 50\,\Omega$, is used as a replacement for a 300 mm, or longer, airline. While this test-cable is not in any way as electrically or mechanically accurate as the airlines used otherwise, its ruggedness and insensitivity of its characteristics to mechanical movement still allow for its use as a comparative transfer standard between the different VNAs and test-set architectures.

The ZV-Z31 verification kit also contains two high precision, calibrated, 18 GHz reference attenuators in RPC-N for 20 dB and 40 dB of attenuation (see Fig. 2.117). As all the verification standards contained in the ZV-Z31 kit are of the RPC-N (m)-(f) variety, the (f)-(f) RPC-N calibration thru of the Rosenberger 05CK100-150 calibration

Figure 2.117: Picture of the Rosenberger RPC-N 18 GHz 20 dB and 40 dB high precision, calibrated, 18 GHz reference attenuators used as verification devices.

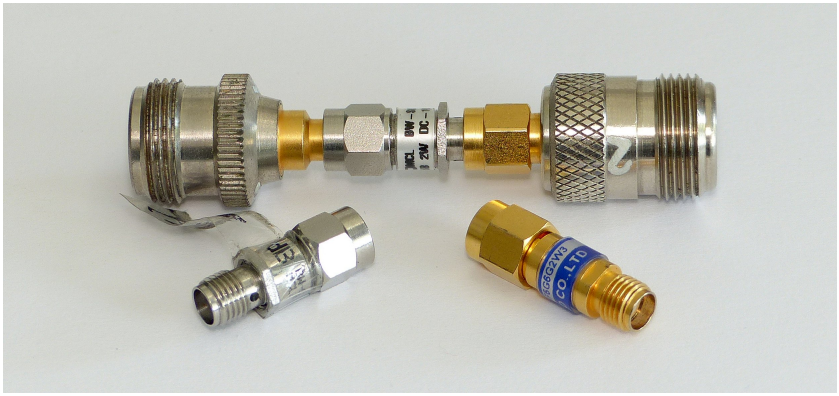

Figure 2.118: Picture of the SMA (m)-(f) 3 dB, 6 dB and 10 dB attenuators with their corresponding N(f)-SMA(m)/(f) adapters.

kit is used to provide a (f)-(f) interface at the reference planes in the case of direct thru connections between two ports.

The two calibrated RPC-N precision reference attenuators are augmented by a set of standard laboratory grade 3 dB, 6 dB and 10 dB SMA (m)-(f) attenuators with corresponding RPC-N(f)-SMA(m)/(f) adapters. While this is far from an ideal choice, these attenuators are still able to provide valid comparative results between the ZVA67 and the switched receiver VNA measurements. The whole assortment of adapters and attenuators used in conjunction is shown in Fig. 2.118.

In accordance with [94], the T-Check device is assembled from discrete components using a Rosenberger 53K301-K00N5 3x RPC-N(f) tee junction and the RPC-N(m) match from the 05CK100-150 calibration kit. While this approach does not exactly observe all the theoretical requirements of an ideal T-Check device, it is still suitable for usage up to the lower GHz range and especially for comparative measurements using the same

Figure 2.119: Picture of the T-Check verification standard substitution, consisting of a Rosenberger 53K301-K00N5 3x RPC-N(f) tee junction and one RPC-N(m) match from the 05CK100-150 SOLT calibration kit.

T-Check device ([94]). A picture of the assembled T-Check standard can be seen in Fig. 2.119.

The asymmetric reflective lossy tee standard, which was introduced in the discussion of the synthetic verification standards, is constructed similar to the T-Check device. A 3x RPC-N(f) tee junction is used in conjunction with the assembled ZV-Z31 150 mm $Z_L = 50\,\Omega$ airline and the RPC-N(f) short standard to form the base of the reflective tee. The 20 dB, 40 dB and finally both precision reference attenuators of the ZV-Z31 kit combined, resulting in 60 dB of attenuation, are subsequently added into the reflective tee for increasing transmission loss of the verification standard, which is shown in Fig. 2.119.

In order to evaluate the performance of the switched single reflectometer with or without the use of the switched reference wave technique, the following one-port device measurements beside the MSO calibration are conducted:

- Re-measurement of the match standard directly after the calibration measurement without reconnection to estimate the S_{11} measurement noise-floor.
- Ripple tests with $Z_L = 50\,\Omega$ and $Z_L = 25\,\Omega$ 150 mm airlines terminated by the RPC-N(f) calibration short, as well as an additional ripple test carried out with the Rosenberger 600 mm test-cable.
- Measurements of the 3 dB, 6 dB, 10 dB and 20 dB attenuators terminated by a short to verify the reflection tracking ability, as a replacement for mismatch standards.
- And finally measurements of the $Z_L = 50\,\Omega$ and $Z_L = 25\,\Omega$ 150 mm airlines terminated by the RPC-N(f) calibration match, to perform a direct residual directivity measurement under other cross-talk conditions than the reflection ripple test as well as to perform a reflection tracking measurement.
- Additional measurements using match terminated tees with a shorted $Z_L = 50\,\Omega$

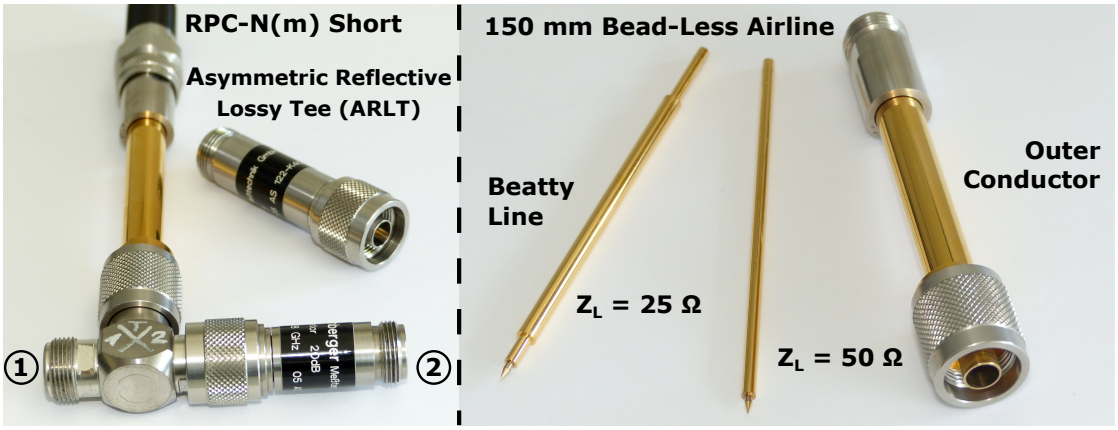

Figure 2.120: Composite picture of the asymmetric reflective lossy tee (ARLT) verification standard with port reference information (left), assembled from other verification standards, and a detail picture of the 150 mm bead-less airline with its $Z_L = 25\,\Omega$ and $Z_L = 50\,\Omega$ inner conductors disassembled (right).

150 mm airline and the Rosenberger VNA test-cable are also carried out as supplementary measurements, which are found in the appendix.

The two port verification standards that are used to evaluate and compare the architectures are also oriented after the standards already used during the numerical verification phase of the architectures. The following measurements are conducted:

- Ripple tests with $Z_L = 50\,\Omega$ and $Z_L = 25\,\Omega$ 150 mm airlines terminated by the RPC-N(f) calibration short, as well as an additional ripple test carried out with the Rosenberger 600 mm test-cable on the stimulus driven ports to evaluate both the reflectometer performance under high b_i interference as well as the receiver input wave transmission cross-talk correction efficacy.
- Direct residual directivity measurements using the $Z_L = 50\,\Omega$ 150 mm airline and the calibration match to evaluate the reflectometer source match under low b_i interference.
- Low loss through connections using the $Z_L = 50\,\Omega$ 150 mm airline and an additional measurement using the $Z_L = 25\,\Omega$ Beatty airline, with the calibration thru as an adapter, to evaluate the transmission tracking and load match correction performance.
- Transmission tracking linearity, dynamic range and cross-talk correction efficacy measurements using the 3 dB, 6 dB and 10 dB SMA attenuators with their adapters as well as the 20 dB, 40 dB and (20+40) dB precision reference attenuators with the calibration thru as a (f)-(f) adapter.
- Measurement of the asymmetric reflective lossy tee in conjunction with 0 dB, 20 dB, 40 dB and (20+40) dB of attenuation to compare the reflection and transmission

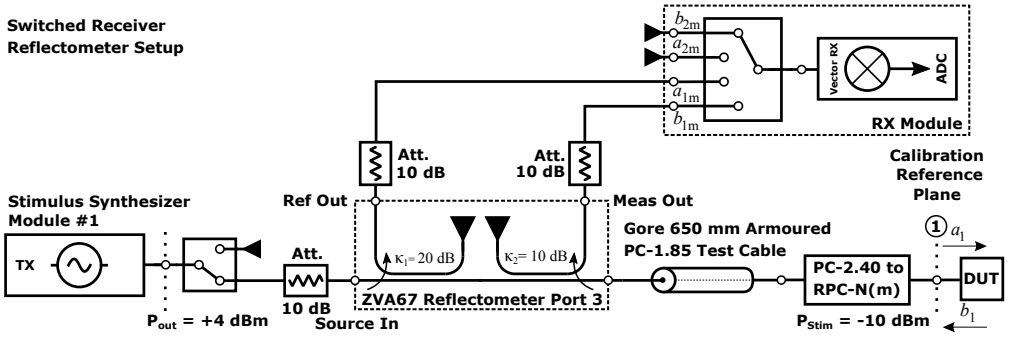

Figure 2.121: Schematic of the switched receiver reflectometer (sVNA) verification measurement setup.

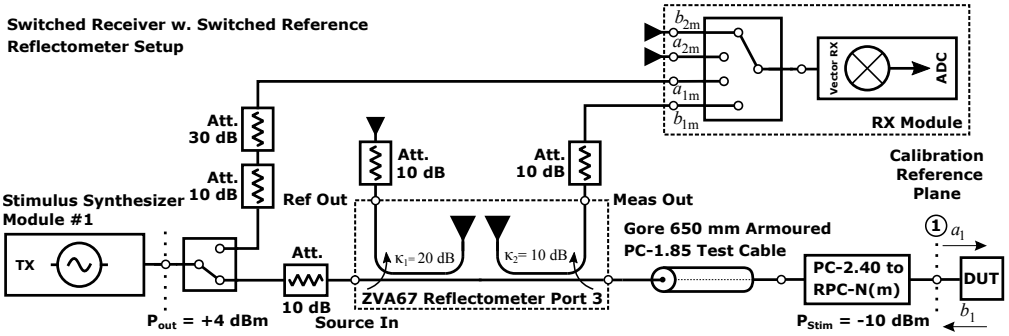

Figure 2.122: Schematic of the switched receiver switched reference reflectometer (srVNA) verification measurement setup.

tracking, dynamic range and cross-talk correction ability in one combined measurement.

2.5.3 Reflectometer Measurements

The verification measurement of the switched single receiver (sVNA) and switched single receiver with reference wave switch (srVNA) start with the most basic VNA topology: The one-port reflectometer. The configuration of the test-set that is used for the measurement in the sVNA architecture are shown in Fig. 2.121, while the configuration that uses the reference wave switch contained in the stimulus synthesizer module is shown in Fig. 2.122.

In the switched single receiver with reference wave switch test-set topology, the combined coupling factor of 20 dB, the added 10 dB of resistive padding at the generator input of the test-set and the 10 dB of padding added at the reference wave output, are emulated by adding an adding an additional 30 dB and 10 dB attenuator in series into the switched reference wave signal path, resulting in comparable reference wave amplitudes, and therefore receiver gain settings, for both topologies.

The 10 dB attenuators shown in both Fig. 2.121 and Fig. 2.122 at the generator input and the coupled wave outputs of the ZVA67 test-set were added after initial tests and

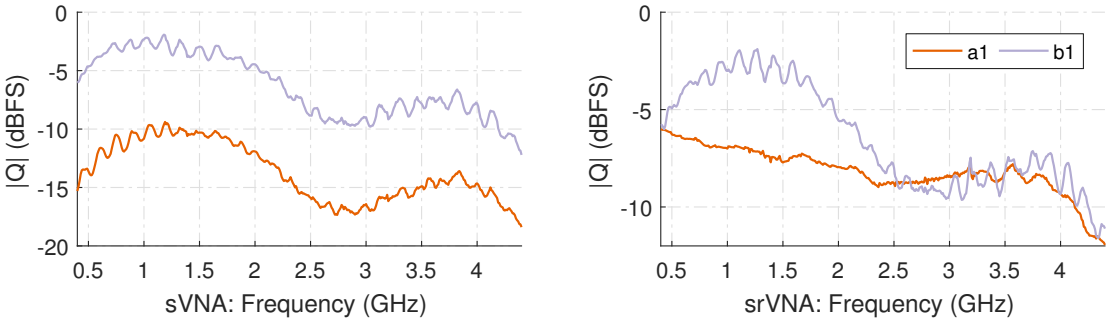

Figure 2.123: Raw ADC wave magnitudes measurements for both the sVNA and srVNA reflectometer test-sets when terminated by the calibration short. Total combined IF VGA setting $G_{\text{var}} = -5\,\text{dB}$.

S-parameter measurements, where an unexpected and very pronounced dependence of coupling factor and its forward and reverse direction directivity and isolation upon the actual VNA hardware return loss was observed for both wave outputs. It is unclear which specific wide-band directional coupler architecture is used in the ZVA67, but this effect makes it necessary to add additional resistive padding to the ports to stabilize the return loss seen by wave outputs of the test-set.

In order to check whether this effect is persistent and caused by the single receiver VNA hardware itself, additional test were carried out before the measurements using an improvised test-set consisting of Narda 3003 20 dB directional couplers for the b_i waves and resistive 6 dB 2R splitters for the a_i waves.

None of the effects observed with the ZVA67 test-set could be reproduced. Due to the limited bandwidth of the improvised test-set in relation to the length of available verification airlines, the decision was made to proceed with the verification measurements using the ZVA67 test-set with added resistive padding as shown in Fig. 2.121 and Fig. 2.122. Before the start of the measurements, the dynamic range of the receiver, as a function of the stimulus synthesizer output power, the test-set insertion loss and wave coupling factors and the IF VGA gain setting, are checked by analyzing the raw measurement wave data for the residual dynamic range before compression occurs. In case of the reflectometer, the a_1 wave should ideally be independent of the input reflection factor of the DUT, while the b_1 wave will reach its maximum amplitude for passive devices when a short is used as the termination of the calibration reference plane, when maximum power transfer effects due to impedance conversion and therefore better matching are ignored.

The results of this measurement, carried out with the RPC-N (f) calibration short at the reference plane for an IF amplifier gain setting of $G_{var} = -5\,\text{dB}$ and an approximate absolute receiver input power of -34 dBm for the b_1 wave, is shown in Fig. 2.123 for the sVNA and the srVNA verification setups.

After the confirmation of proper settings and signal levels, a normal 3-term MSO calibration is carried out on both the sVNA and the srVNA test-set architecture. The error coefficients for the 3-term error model obtained by this reflectometer calibration

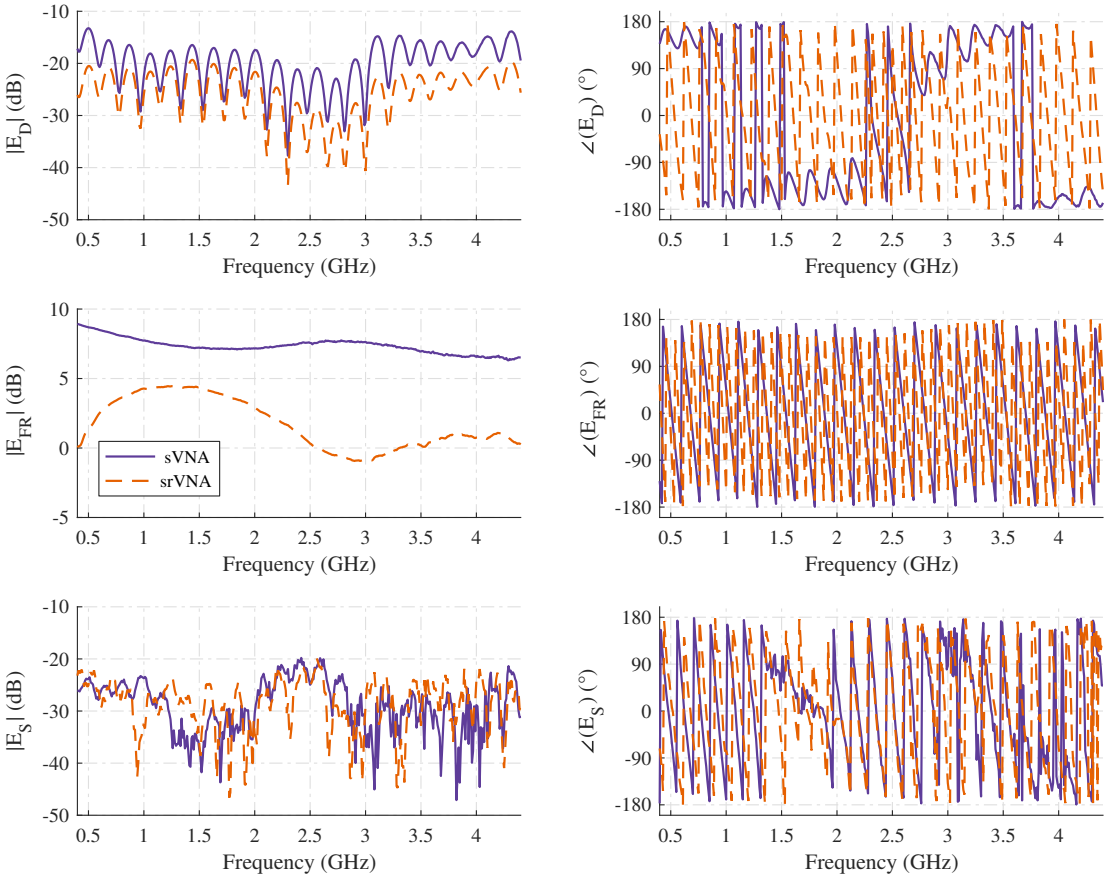

Figure 2.124: Error coefficient values for the MSO 3-term calibration performed with the single receiver VNA hardware setup, for both the sVNA and the srVNA test-set architecture.

are shown in Fig. 2.124. Reference 3-term error model coefficient values for the 3-term procedure implemented on the ZVA67 could not be readily obtained, due to the use of its internal proprietary implementation of the algorithm.

From the results shown for $|E_D|$ in Fig. 2.124 it can be seen, that the couplers of the ZVA67 test-set are operated somewhat outside of their optimum frequency range, which is to be expected for such a high frequency device. The ripple seen in the $|E_D|$ coefficient values is not caused by the input and output return loss of the single receiver VNA or its connecting coaxial cables, but was also observed by measuring the S-parameters of the same internal coupler using the other ports of the ZVA67 beforehand. The positive dB values shown for the magnitude of the $|E_{FR}|$ reflection tracking coefficient, which is usually shown to be $|E_{FR}| \leq 0\,\mathrm{dB}$ in the literature, are caused by the amplitude differences originating from the dissimilar coupling factors used in the ZVA67 reflectometer. This total path loss difference between the a_1 and the b_1 wave results in a reflection tracking offset when the same receiver and gain settings are used to capture both wave quantities.

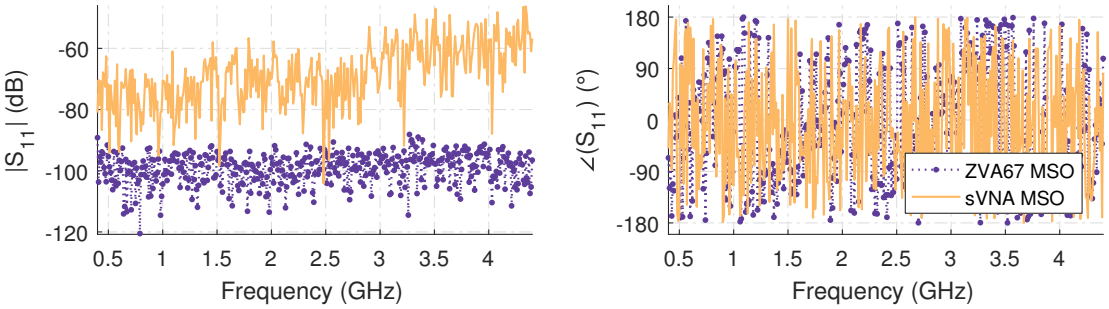

Figure 2.125: Measurement results of the match calibration standard with the sVNA setup, corrected with the 3-term error model after a re-measurement directly after the calibration measurement for estimating the S_{11} dynamic range.

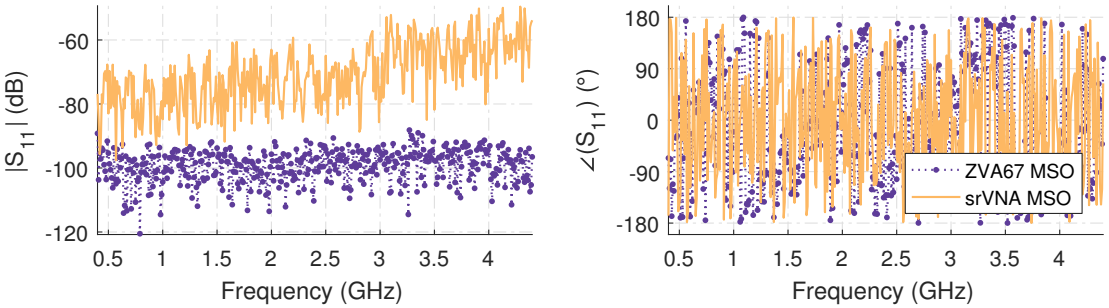

Figure 2.126: Measurement results of the match calibration standard with the srVNA setup, corrected with the 3-term error model after a re-measurement directly after the calibration measurement for estimating the S_{11} dynamic range.

This can also be seen nicely in the raw ADC wave data magnitude shown for the termination of the reference plane with the calibration short in Fig. 2.123.

The calibration is carried out in the order Open-Short-Match to facilitate a direct re-measurement of the match calibration standard without the uncertainties introduced by a mechanical re-connection of the standard to estimate the dynamic range of the error corrected S_{11} measurement. The results of this immediate re-measurement are shown in Fig. 2.125 for the sVNA test-set and in Fig. 2.126 for the srVNA in comparison with the same measurement carried out on the ZVA67.

When these results for the S_{11} dynamic range are compared with the numerical simulations carried out beforehand, a difference of 25 to 40 dB between the simulation and the measured results can be found for this measurement. These discrepancies are most likely caused by the following effects of the switched receiver system, which were not included in the numerical simulations:

- The frequency dependent increase of the insertion loss in the test-set and an increase in conversion loss in the receiver front-end,

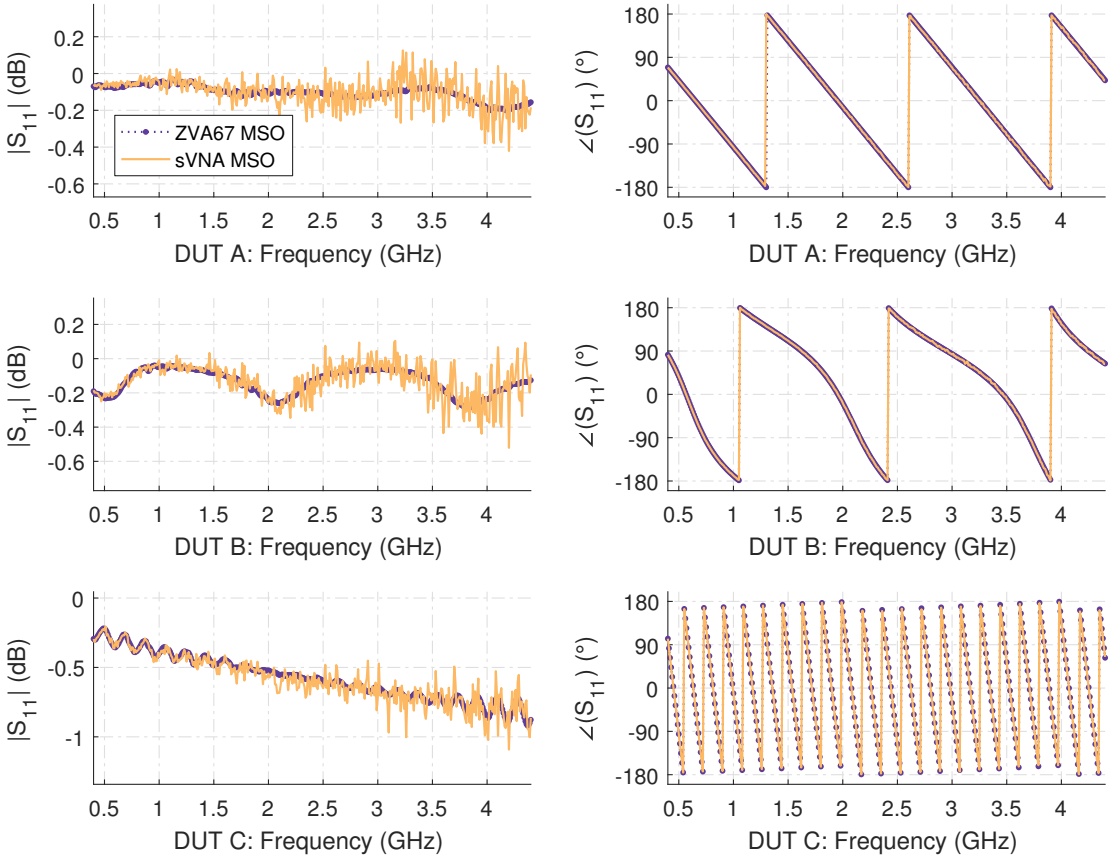

Figure 2.127: Measurement results for the ripple test peformed with various transmission lines and corrected with the 3-term model with the sVNA setup. DUT A: 150 mm $Z_L = 50\,\Omega$ bead-less airline terminated with the calibration short. DUT B: 150 mm $Z_L = 25\,\Omega$ bead-less airline terminated with the calibration short. DUT C: 600 mm $Z_L = 50\,\Omega$ Rosenberger RPC-N VNA test-cable terminated with the calibration short.

- The slow drift (or wander) of the stimulus and LO synthesizer signal between receiver input wave selector switch positions, which leads to the violation of the basic TI assumption made for the switched single receiver concept,
- The limited repeatability of the semiconductor wave selection switches leading to additional stochastic TI model violations, and
- The highly elevated noise floor in the IF section due to insufficient narrow-band noise shaping filtering between stages.

When a closer look is taken at the results shown in Fig. 2.125 and Fig. 2.126 it can be noticed, that the average value of the noise floor almost linearly increases with frequency, which strongly hints to the insertion loss / conversion loss hypothesis. This thesis is

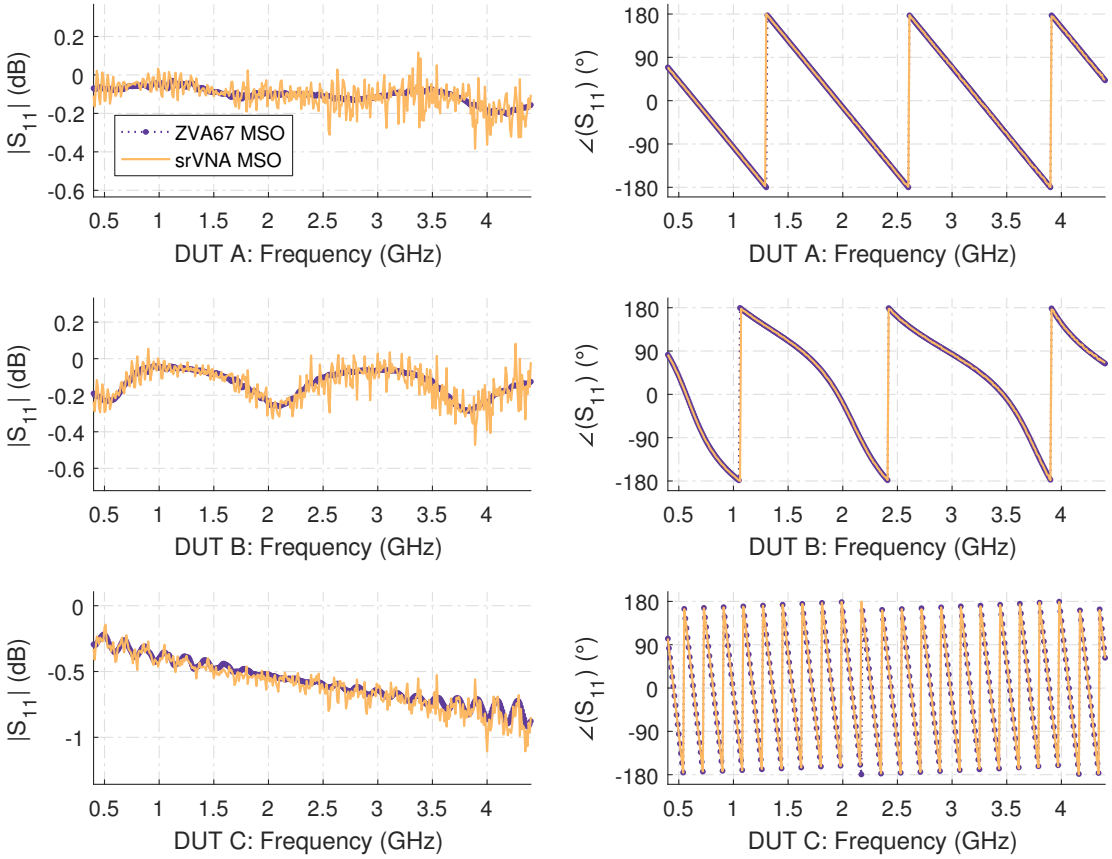

Figure 2.128: Measurement results for the ripple test peformed with various transmission lines and corrected with the 3-term model with the srVNA setup. DUT A: 150 mm $Z_L = 50\,\Omega$ bead-less airline terminated with the calibration short. DUT B: 150 mm $Z_L = 25\,\Omega$ bead-less airline terminated with the calibration short. DUT C: 600 mm $Z_L = 50\,\Omega$ Rosenberger RPC-N VNA test-cable terminated with the calibration short.

supported by the raw wave magnitude measurements in Fig. 2.123, and can be possibly accredited to the wander of the stimulus and LO synthesizer signal between switch positions as the main cause for this effect.

Switch repeatability issues would lead to a much increased S_{11} noise-floor in the srVNA test-set measurement due to the added reference wave switch, while an elevated noise floor in the IF chain would show up as a frequency independent change in broadband noise-floor in these measurements.

This results may seem somewhat negative at first, but it is important to realize that the demonstrated S_{11} dynamic range in both test-set architectures is far better than normally required for non-metrological return loss measurements.

After the calibration of the reflectometers, the ripple test measurements using the

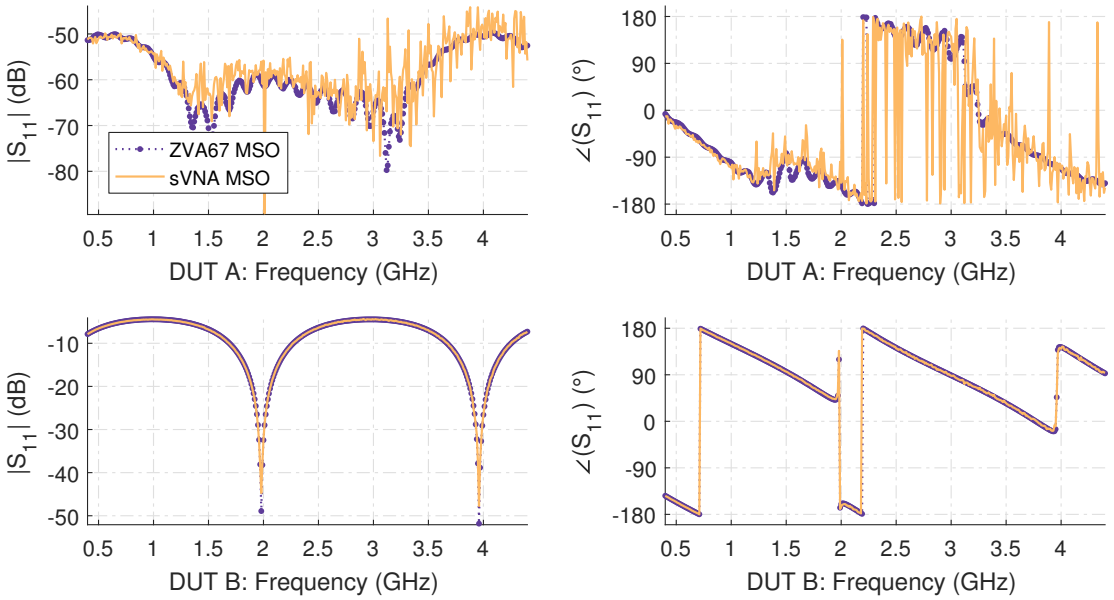

Figure 2.129: Measurement results for the bead-less airlines terminated by the calibration match and corrected with the 3-term model with the sVNA setup. DUT A: Direct residual directivity measurement using a 150 mm $Z_L = 50\,\Omega$ bead-less airline terminated with the calibration match. DUT B: 150 mm $Z_L = 25\,\Omega$ bead-less airline terminated with the calibration match.

150 mm $Z_L = 50\,\Omega$ bead-less airline, the 150 mm $Z_L = 25\,\Omega$ bead-less airline and the 600 mm $Z_L = 50\,\Omega$ Rosenberger RPC-N VNA test-cable, all terminated by the calibration short, are carried out on both single receiver VNA test-set architectures. The 3-term error model corrected results for these measurements are shown for the sVNA test-set in Fig. 2.127 and for the srVNA topology in Fig. 2.128.

In these measurement results an interesting effect can be observed for all ripple test measurements that was not present in any way in the numerical analysis of the single receiver VNA systems: A high frequency ripple or noise, superimposed upon the return loss magnitude measurement results of the ripple test DUTs, which will be discussed at the end of this section.

If this high frequency ripple is ignored for a moment and the average envelope values obtained in the ripple test are used as a reference, it is possible to estimate that a comparable overall source match performance in regard to the ZVA67 is obtained in both switched receiver architectures, when the reduced dynamic range of the S_{11} measurements is taken into account. Using the average values, a conservative peak-to-peak ripple envelope of approximately 0.1 dB can be estimated, which is equivalent to a good reflectometer source match of 45 dB in a high b_1 wave crosstalk interference scenario.

This estimation is confirmed by results of the direct residual directivity measurements performed with the 150 mm $Z_L = 50\,\Omega$ bead-less airline, terminated by the calibration match, shown for the sVNA architecture in Fig. 2.129 and for the sVNA test-set in

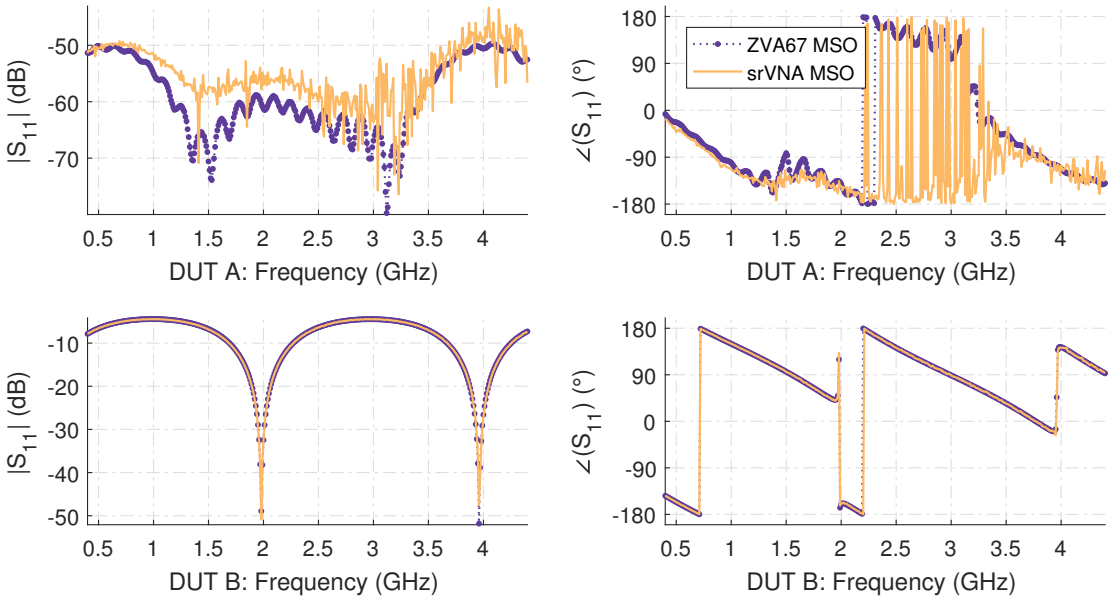

Figure 2.130: Measurement results for the bead-less airlines terminated by the calibration match and corrected with the 3-term model with the srVNA setup. DUT A: Direct residual directivity measurement using a 150 mm $Z_L = 50\,\Omega$ bead-less airline terminated with the calibration match. DUT B: 150 mm $Z_L = 25\,\Omega$ bead-less airline terminated with the calibration match.

Fig. 2.130, which are performed after the initial ripple test measurements.

The direct measurements of the source match show a residual directivity of better than 45 dB for both topologies and confirm the estimated results of the ripple test, but are obtained in a very different interference scenario for the single receiver VNA. Both single receiver VNA architectures performed similarly to the ZVA67, but at an admittedly higher trace noise level due to lower signal-to-noise ratio, as determined by the calibration match dynamic range measurements. The measurement of the 150 mm $Z_L = 25\,\Omega$ bead-less airline terminated by the calibration match is performed right after the residual directivity measurement. The results of these measurements are also shown in Fig. 2.129 and Fig. 2.130, which attest both architectures a good reflection tracking performance. This is confirmed by the final reflectometer measurements of the various shorted attenuators used as a one-port mismatch device. The results of these final verification measurements are shown in Fig. 2.131 for the sVNA and in Fig. 2.132 for the srVNA architecture. Although some small systematic variations of the reflection tracking results can be seen in these results, they are well within the repeatability bounds for the chosen mismatch standards.

All the conducted reflectometer measurements show a new kind of high frequency ripple superimposed upon the measurement results, which is more easily noticed in the magnitude of the S_{11} parameter results for the ripple test.

When the measurement results shown for both architectures and ripple test DUTs of

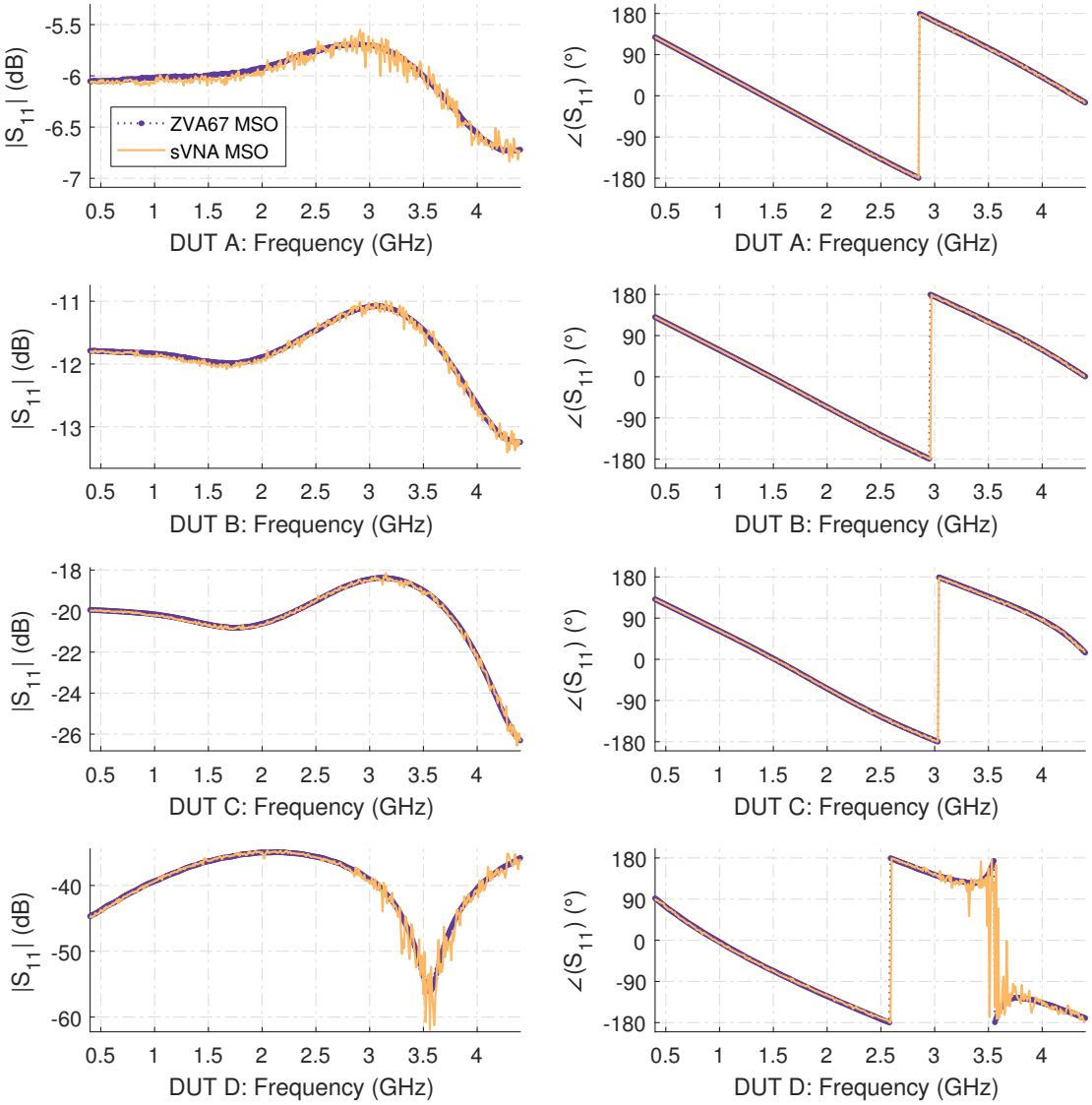

Figure 2.131: Measurement results for various SMA attenuators including a N(m)-SMA(f) adapter corrected with the 3-term model with the sVNA setup. DUT A: 3 dB attenuator. DUT B: 6 dB attenuator. DUT C: 10 dB attenuator. DUT D: 20 dB attenuator.

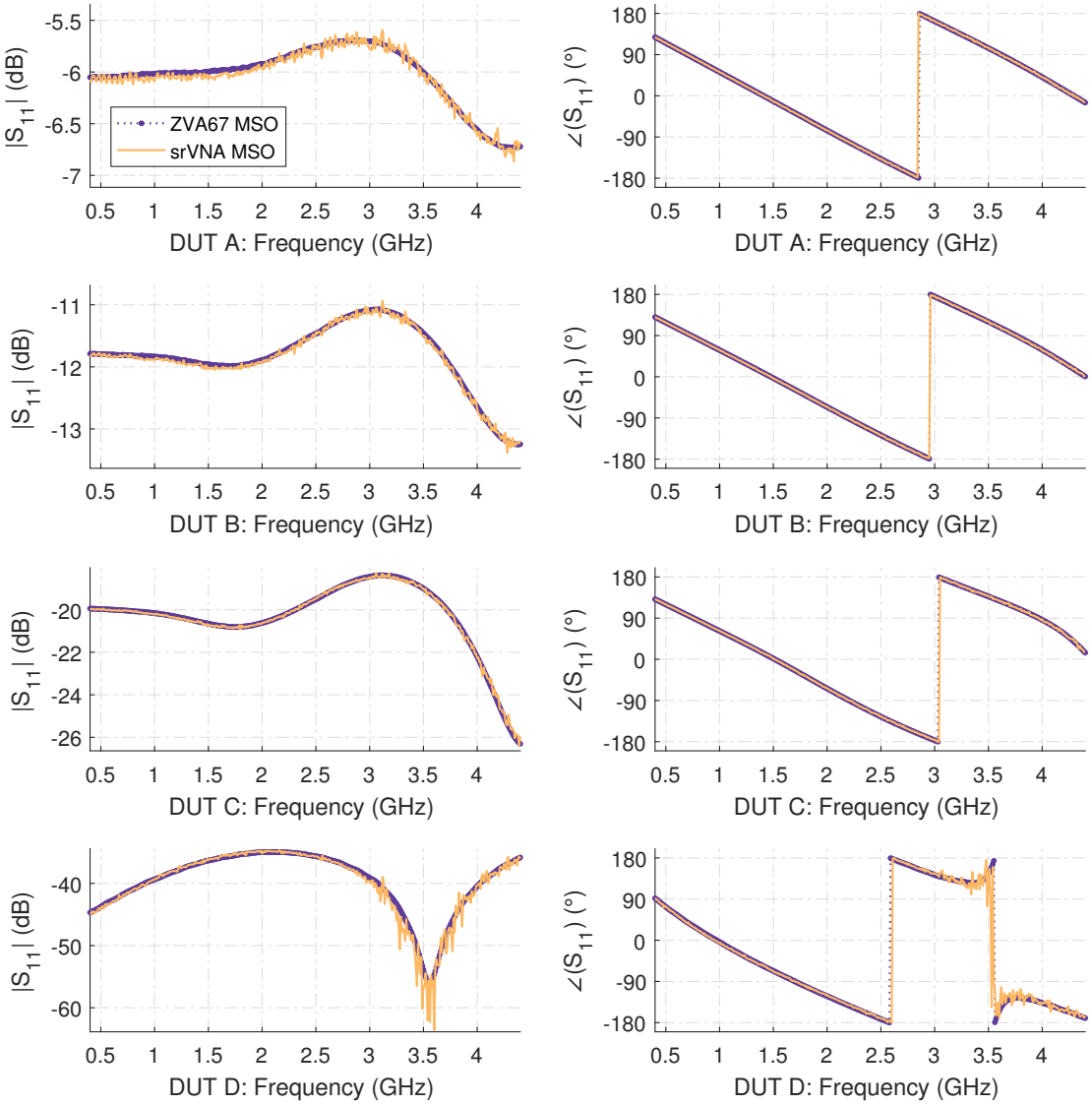

Figure 2.132: Measurement results for various SMA attenuators including a N(m)-SMA(f) adapter corrected with the 3-term model with the srVNA setup. DUT A: 3 dB attenuator. DUT B: 6 dB attenuator. DUT C: 10 dB attenuator. DUT D: 20 dB attenuator.

varying electrical length and impedance are combined with the reference measurements of the same devices performed with the ZVA67, it can be argued, that this effect is not correlated in any way with the effects the original ripple test intends to show, but is caused by the switched single receiver VNA system or its interaction with the ZVA67 test-set alone.

Before adding the additional resistive padding to the in- and outputs of the ZVA67 port test-set, this high frequency ripple or noise effect was even more pronounced, which leaves a non model compliant interaction of the couplers as the most plausible cause. This is also supported by the observation, that the high frequency ripple is slightly more pronounced in the ripple tests performed in the srVNA architecture.

The effective change in coupler parameters is caused by the varying return loss presented by the receiver input wave selector switch and the reference wave switch, which in turn results in a change in coupler termination. This effect was not considered in the theoretical discussion of the switched reflectometer and is not corrected for in the error model and therefore leads to this non-correctable errors, which are attenuated by the resistive padding added to the coupler ports.

What is however unclear at this point is the observation, that this effect did not occur in the numerical simulation and analysis performed beforehand, which on the other hand certainly speaks strongly against this hypothesis and hints at other, yet unknown, causes for this observation which warrants further research in this subject.

When the list of system properties not captured by the original simulation, but present in the real measurement, is revisited, the most likely candidate beside the repeatability of the electronic switches is the TI behavior of the synthesizers during the receiver input wave selector switch scanning operation.

When this drift is modeled as an interference scenario, the ripple test error vector results of [52] can be used to estimate, that a combined stimulus synthesizer and LO synthesizer phase drift induced error of approximately $\pm 0.3°$ between switch states is enough to account for the $\pm 0.1\,\mathrm{dB}$ of high frequency ripple seen in the measurement results. When the synthesizer phase noise and time domain jitter measurement results presented earlier and the frequency characteristics of this effect are taken into account, this explanation is at least as likely as the change of impedance to be the dominating root cause of this effect.

Nevertheless, more research and experiments are necessary beyond the scope of this work to analyze the origins of this effect.

2.5.4 Unidirectional SOLT Measurements

After the completion of the switched single receiver reflectometer measurements, the test-sets of both the sVNA and the srVNA topology are modified to account for the additional, DUT transmitted, b_2 wave receiver channel required for unidirectional S-parameter measurement in the 5-term and new (5+2)-term error model.

Tough not strictly required, Port 4 of the ZVA67 is used as the mechanical and electrical termination of the PC-1.85 VNA test-cable, but with no signal connection to any of the inbuilt couplers. Instead, a 20 dB attenuator is used at the generator port of the test-set

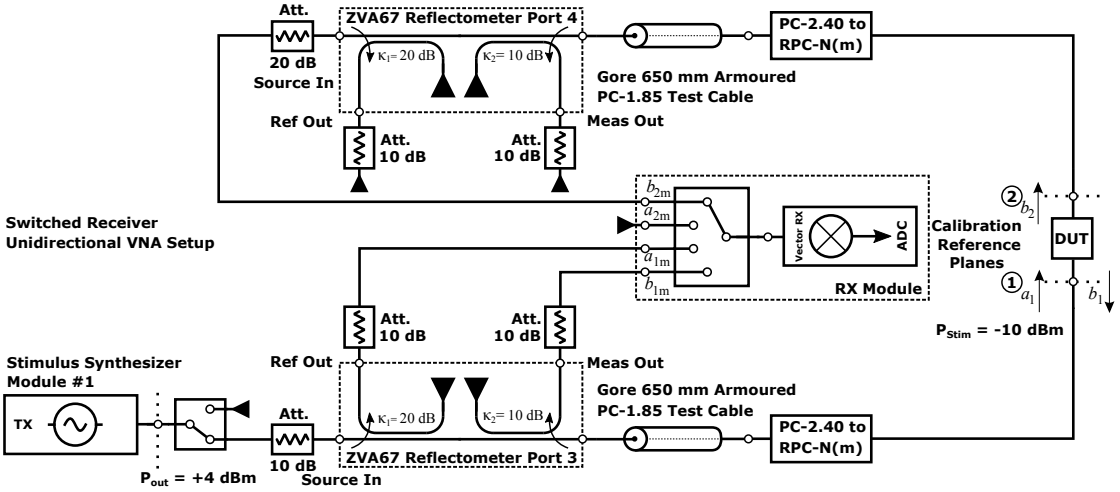

Figure 2.133: Schematic of the switched receiver unidirectional VNA verification measurement setup.

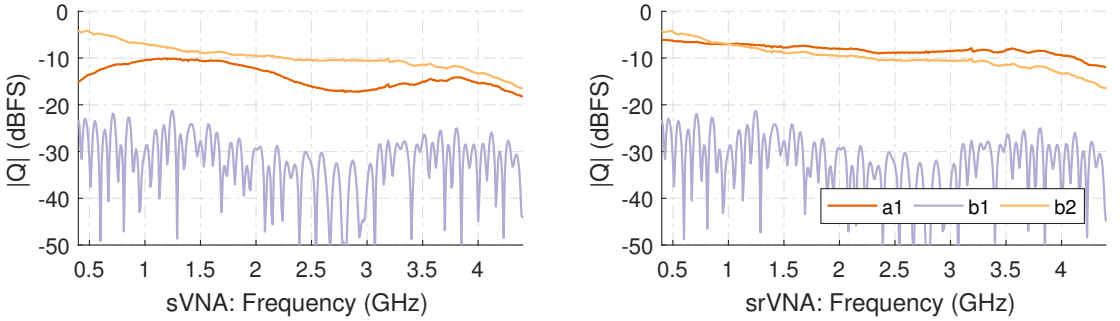

Figure 2.134: Raw ADC wave magnitudes measurements for both the sVNA and srVNA unidirectional test-sets for the RPC-N calibration thru connection. Total combined IF VGA setting $G_{\mathrm{var}} = -5\,\mathrm{dB}$.

for termination and attenuation of the b_2 wave which is routed to the b_{2m} input of the receiver module, as shown in Fig. 2.133 for the sVNA and in Fig. 2.135 for the srVNA test-set architecture.

With these necessary modifications done, a signal linearity and ADC dynamic range check is performed using the RPC-N calibration thru standard. The raw ADC magnitude value results of the thru connection for all relevant wave quantities of both test-set configurations are shown in Fig. 2.134, which confirms the right wave amplitude levels for linear measurements of passive DUTs.

The same components and overall IF VGA settings are used for the reflectometer part of this unidirectional test-set, which results in the same test-set wave magnitudes for the short termination as already shown in Fig. 2.123 before, which are therefore not reproduced here again.

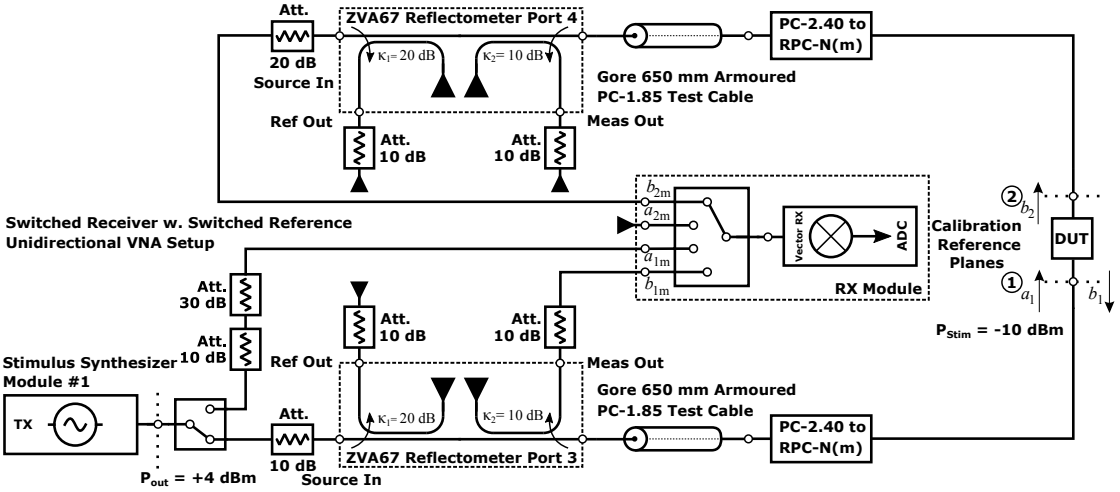

Figure 2.135: Schematic of the switched receiver unidirectional VNA with switched reference verification measurement setup.

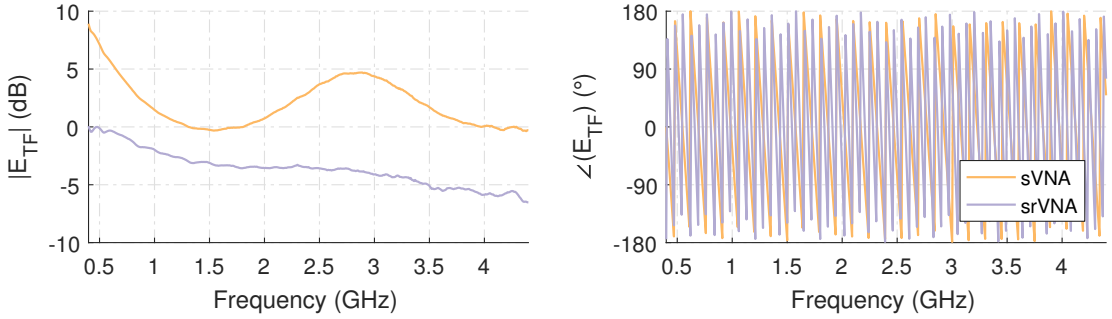

Figure 2.136: Measurement results for the forward tracking error coefficient E_{TF} obtained via the 5-term calibration performed on the sVNA and srVNA unidirectional test-set setups.

After checking for linearity and compression on all test-set waves, a 5- and (5+2)-term calibration using the Short-Match and Match-Match isolation standards, just as in the synthetic VNA verification, is performed on both test-set architectures. As expected from the simulation, the reflectometer 3-term error coefficients of the 5- and (5+2)-term error model match the coefficient values already shown before in Fig. 2.124 and are therefore not reproduced here again.

The results for the E_{TF} forward tracking coefficient of both test-set topologies is shown in Fig. 2.136, while the load match E_{LF} coefficient values are omitted, as they can only be used for the forward thru-normalization calibration measurement in the 5- and (5+2)-term calibration and error model.

The results for the two receiver input wave selector switch cross-talk coefficients E_{XF} and E_{XRF}, obtained via the (5+2)-term calibration procedure, are shown in Fig. 2.137.

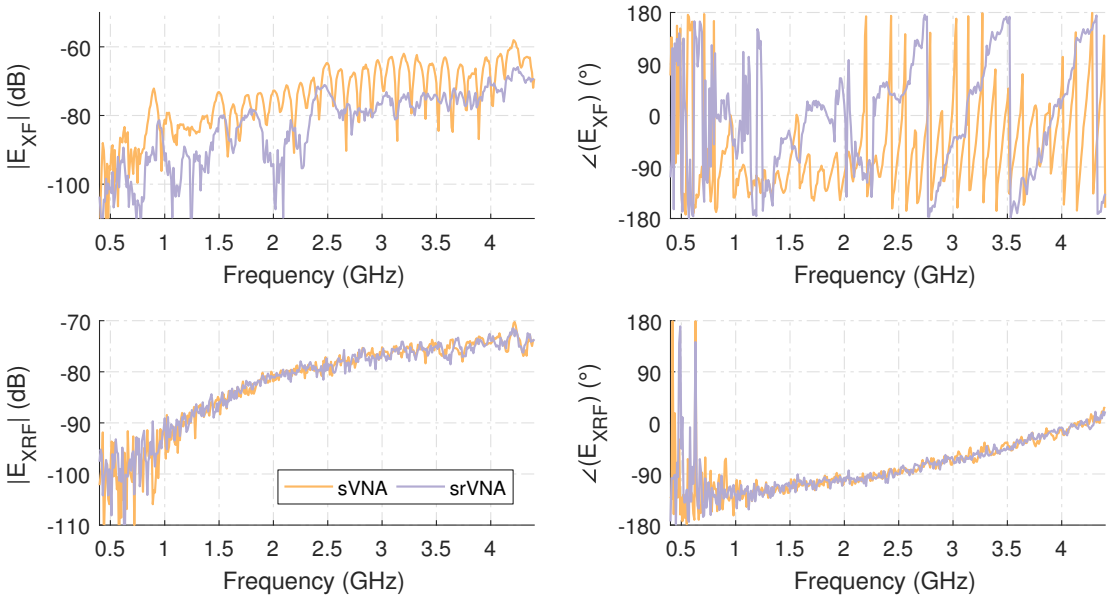

Figure 2.137: Measured (5+2)-term receiver input wave selector switch cross-talk coefficients obtained from the calibration procedure for both the sVNA and srVNA unidirectional test-sets.

Both coefficients are within the expected range and show plausible results in direct comparison with the test-set modified coefficient values of Fig. 2.137 and the pure switch cross-talk coefficients for the receiver hardware shown earlier in Fig. 2.56 during the discussion of the VNA receiver hardware module.

It is however interesting to see in Fig. 2.137, that the advantage in cross-talk suppression shown for the srVNA architecture, which includes the reference wave switch, demonstrated in the synthetic analysis of both architectures does not the same efficacy in the real physical implementation of the method.

While there is certainly an advantage of 15 to 20 dB visible in the $|E_{XF}|$ data, there are seemingly other cross-talk paths, such as direct cross-talk between the stacked modules, there as well, which reduce the efficacy of this method in the srVNA setup under test.

Next, a subset of the reflectometer verification measurements is performed using the unidirectional sVNA and srVNA topologies. The measurement results of these one-port isolating measurements can be found in appendix B of this work in order to streamline the two-port measurements shown hereafter, as they essentially performed exactly the same as reflectometer verification measurements for both architectures performed and discussed before.

Nevertheless, just as in the synthetic case, the apparent S_{21} measurement data acquired during the ripple and direct residual directivity tests allows a quick evaluation of the (5+2)-term cross-talk correction efficacy in comparison with the non-corrected 5-term results. The results of the ripple test and direct residual directivity measurements, reduced to the results of apparent transmission for reasons of clarity, are shown in

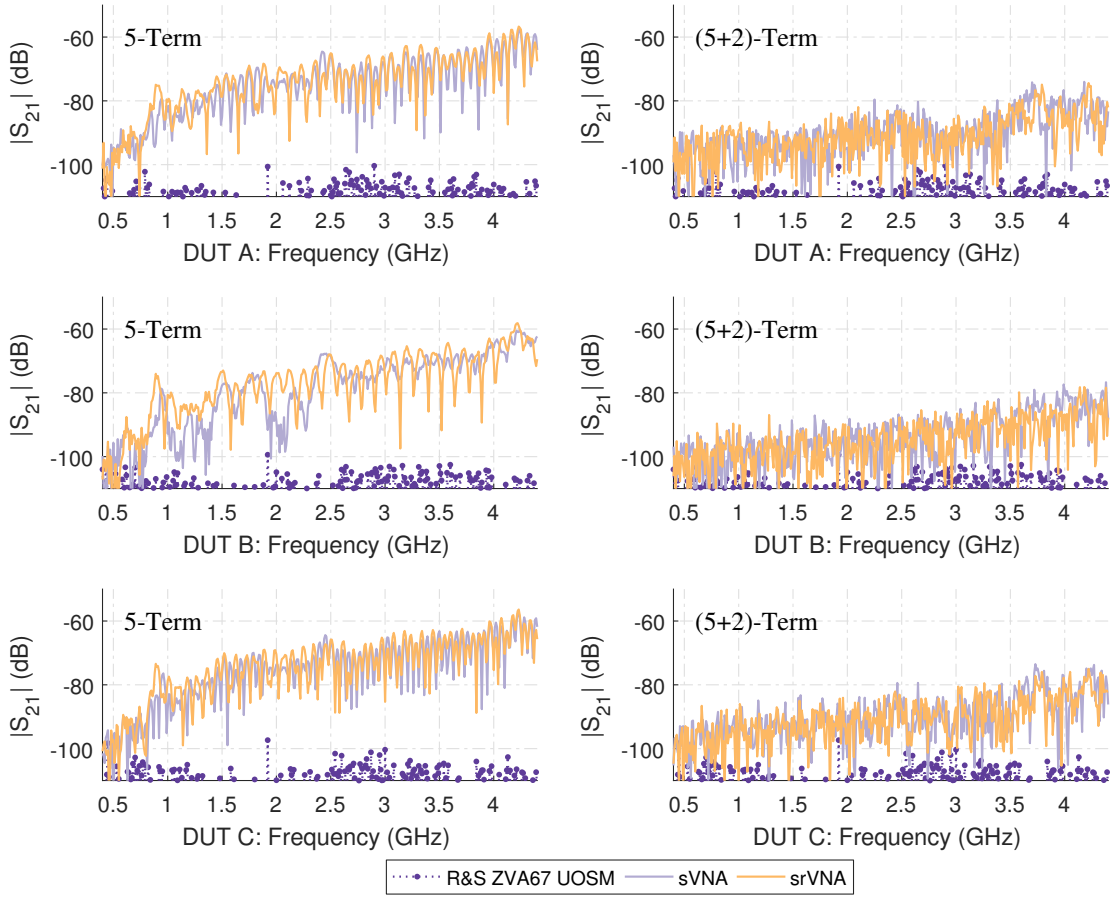

Figure 2.138: Measured S_{21} isolation figures obtained during the ripple test and direct residual directivity measurements, corrected by the 5-term and (5+2)-term procedure for both the sVNA and srVNA unidirectional test-set setup. DUT A: 150 mm $Z_L = 50\,\Omega$ bead-less airline terminated by the calibration short. DUT B: 150 mm $Z_L = 50\,\Omega$ bead-less airline terminated by the calibration match. DUT C: Rosenberger 600 mm RPC-N VNA test-cable terminated by the calibration short.

Fig. 2.138, while the full measurement results can be seen in compressed form in Fig. B.3 and Fig. B.4 in the appendix.

From the isolation improvements obviously visible between the 5-term model error corrected measurements in the left column of Fig. 2.138 and the (5+2)-term error corrected measurements shown in the right column of the same figure, it can be clearly observed and verified, that the (5+2)-term error correction holds up to the observation made in the synthetic analysis and verification of the correction method and also performs an increase in isolation almost right down to the noise-floor of the VNA receiver under real world measurement conditions covering the extreme points and trajectories on the complex smith chart plane.

Furthermore, no distinct advantage for any of the two unidirectional single receiver test-set architectures can be identified in the results shown in Fig. 2.138. The minor exception is a marginal isolation benefit provided by the srVNA topology in the non cross-talk correct 5-term S_{21} isolation measurement results seen in the residual directivity measurements, which is in accordance with the E_{XF} and E_{XRF} cross-talk coefficient calibration results shown in Fig. 2.137 for both test-set architectures.

After the reflectometer measurements, the first verification measurements for the transmission measurement performance using the unidirectional single receiver architectures are conducted. For these measurements, a thru connection using the 150 mm bead-less RPC-N (f)-(m) airline, together with the $Z_L = 50\,\Omega$ and $Z_L = 25\,\Omega$ center conductors, is performed for each of the architectures. Additionally, the Rosenberger RPC-N (f)-(f) calibration thru is used to mate the airline to the connector standard of the reference plane at the second port.

The results for these transmission verification measurement are shown in Fig. 2.139 for both architectures using the 5-term error correction model and in Fig. 2.140 for the same measurements but corrected by (5+2)-term error model.

When looking at the results presented in both figures, a familiar pattern already known from the synthetic unidirectional verification simulations can be identified: Due to the missing E_{LF} compensation, the return loss measurement is limited by the hardware load match of the system, which is easily observed in the discrepancies present between the UOSM full two-port error corrected S_{11} measurement of the $Z_L = 50\,\Omega$ airline and the identical results presented for both unidirectional architectures. Furthermore, the familiar effect of the missing load match correction in the superimposed S_{21} ripple present in the $Z_L = 25\,\Omega$ thru measurement is evident for both error models and topologies.

Besides these two effects, which are an inherent drawback of the error correction model and only partly an effect of the single receiver architecture, excellent transmission tracking performance of the single receiver VNA within the connection and assembly repeatability bound of a bead-less airline is demonstrated, but with the same characteristic high frequency ripple, as discussed in the reflectometer measurement section 2.5.3, also present here.

Interestingly, this ripple shows almost the same characteristics as the one observed and analyzed in the reflectometer section 2.5.3. This observation, combined with the fact that always the same switch scan routine is performed over the four receiver wave inputs of the switch, regardless of the actual number of used inputs for the test-set configuration,

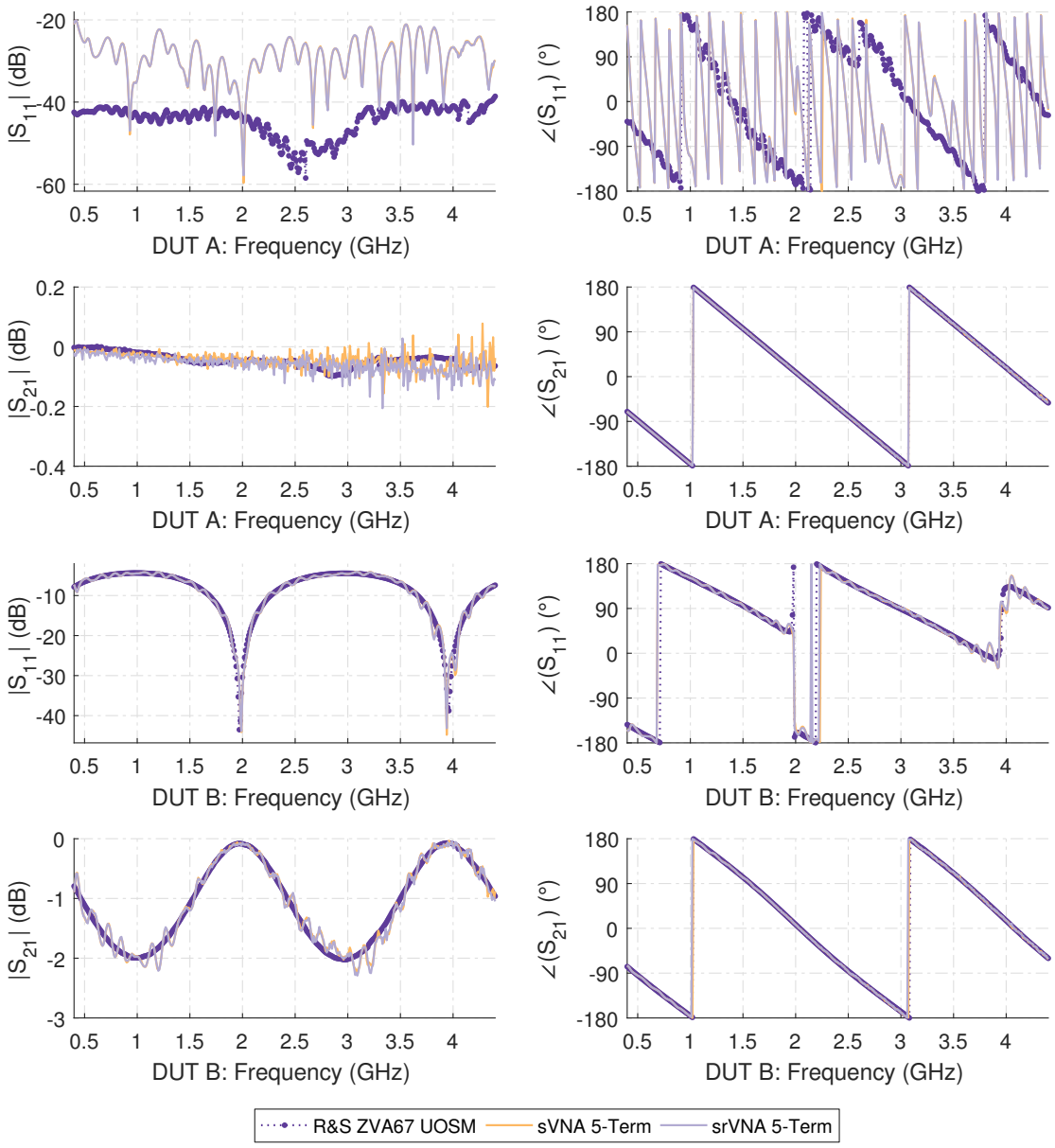

Figure 2.139: Measurement results of the $Z_L = 50\,\Omega$ and $Z_L = 25\,\Omega$ 150 mm airline thru connections, corrected by the 5-term error model for both the sVNA and srVNA unidirectional test-set setups. DUT A: 150 mm $Z_L = 50\,\Omega$ bead-less airline thru with additional Rosenberger (f)-(f) calibration thru. DUT B: 150 mm $Z_L = 25\,\Omega$ bead-less airline thru with additional Rosenberger (f)-(f) calibration thru.

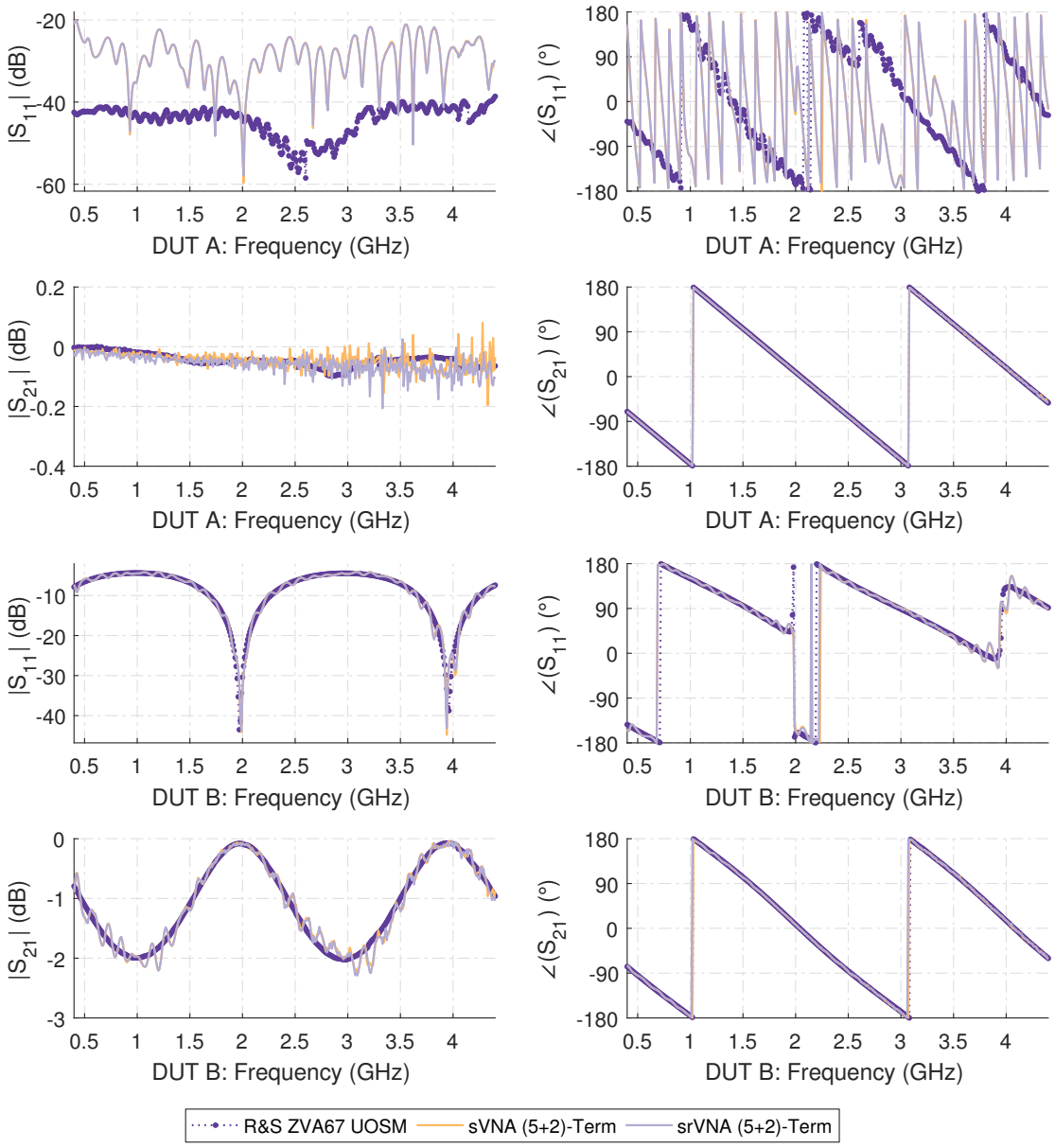

Figure 2.140: Measurement results of the $Z_L = 50\,\Omega$ and $Z_L = 25\,\Omega$ 150 mm airline thru connections, corrected by the (5+2)-term error model for both the sVNA and srVNA unidirectional test-set setups. DUT A: 150 mm $Z_L = 50\,\Omega$ bead-less airline thru with additional Rosenberger (f)-(f) calibration thru. DUT B: 150 mm $Z_L = 25\,\Omega$ bead-less airline thru with additional Rosenberger (f)-(f) calibration thru.

provides observable evidence for the synthesizer TI violation hypothesis as the main source of the effect, while switch repeatability as an additional source can not be fully ruled out in-situ either.

No additional trace noise can be observed in the (5+2)-term error corrected measurements of the well matched $Z_L = 50\,\Omega$ low-loss airline thru connection and the $\lambda/2$ frequency points of the $Z_L = 25\,\Omega$ airline thru connection, despite of the low S_{11m} SNR present for the E_{XRF} correction, which is a first practical demonstration of the high robustness of this procedure and therefore confirms the simulation results.

In order to evaluate the linear transmission tracking performance of the single receiver VNA, measurements of the 3 dB, 6 dB and 10 dB SMA attenuators with their corresponding RPC-N to SMA adapters are performed next. These measurements, including the 20 dB Rosenberger RPC-N reference attenuator measurement, are within the expected bound of the system and show the nominal expected results.

While the reflection tracking is hindered as expected by the missing E_{LF} correction of the 5-term model for lower attenuation values, the transmission measurements in both the 5- and the (5+2)-term error models and both test-set setups are within the repeatability boundaries of the mechanical connectors. Even under the different SNR situation present in the attenuator measurements well above the interference noise floor, no elevated transmission measurement trace noise besides the high frequency trace noise discussed earlier could be observed for the (5+2)-term corrected data in direct comparison with the 5-term corrected results.

The results of the 3 dB and 6 dB measurements are shown for the 5-term error correction in Fig. B.5, while the (5+2)-term corrected data is shown in Fig. B.6 in the appendix. Similarly, the 10 dB and 20 dB measurement for the 5-term corrected data is shown in Fig. B.7 and for the (5+2)-term corrected data in Fig. B.8 as well.

The results of the unidirectional attenuator measurements however start to diverge considerably for the 40 dB, the 20 dB, and 40 dB attenuator combination, as the resulting b_2 originating from the DUT approaches the interference limited noise floor of the receiver. This can easily be identified in the S_{21} measurement results presented in Fig. 2.141 for the 5-term corrected measurement data. It can be clearly observed, that even under the good return loss presented to the stimulus port by the attenuators, and therefore low $|S_{11m} \cdot E_{XRF}|$ cross-talk magnitude, the nearly constant cross-talk originating from the reference wave via $|a_1 \cdot E_{XF}|$ starts to degrade the S_{21} measurement performance considerably.

By comparing the interference ripple envelopes seen in the S_{21} magnitude measurements between the 40 dB attenuator measurement corrected by the 5-term error model and the (5+2)-term error corrected results of the combined 20 dB and 40 dB attenuators presented in Fig. 2.142, it can be directly estimated that the (5+2)-term error correction provides a decrease of approximately 20 dB in interference based S_{21} noise floor, which is in accordance with the earlier observations made during the isolation measurements of the reflectometer verification standards in Fig. 2.138.

Finally, the asymmetric reflective lossy tee measurements are performed to conduct a more realistic test of the (5+2)-term error correction performance in a direct comparison with the 5-term corrected results of the same DUT. For this test, the asymmetric reflective

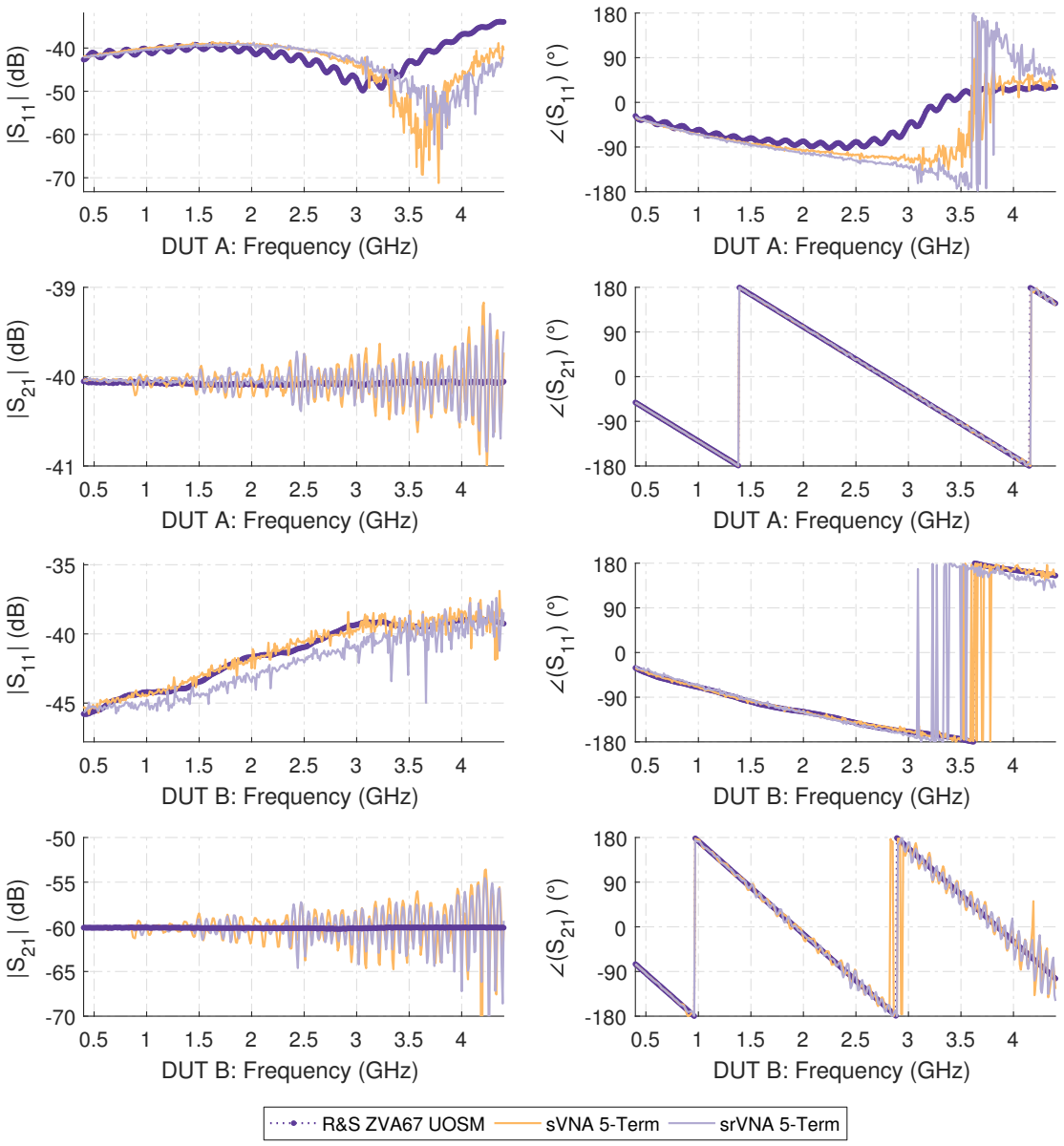

Figure 2.141: Measurement results of the 40 dB attenuator and the combination of the 20 dB and 40 dB reference attenuators used as a thru connection for the 5-term error correction measured in both the sVNA and srVNA architectures. DUT A: 40 dB Rosenberger reference attenuator and Rosenberger (f)-(f) calibration thru. DUT B: 20 dB and 40 dB Rosenberger reference attenuators and Rosenberger (f)-(f) calibration thru.

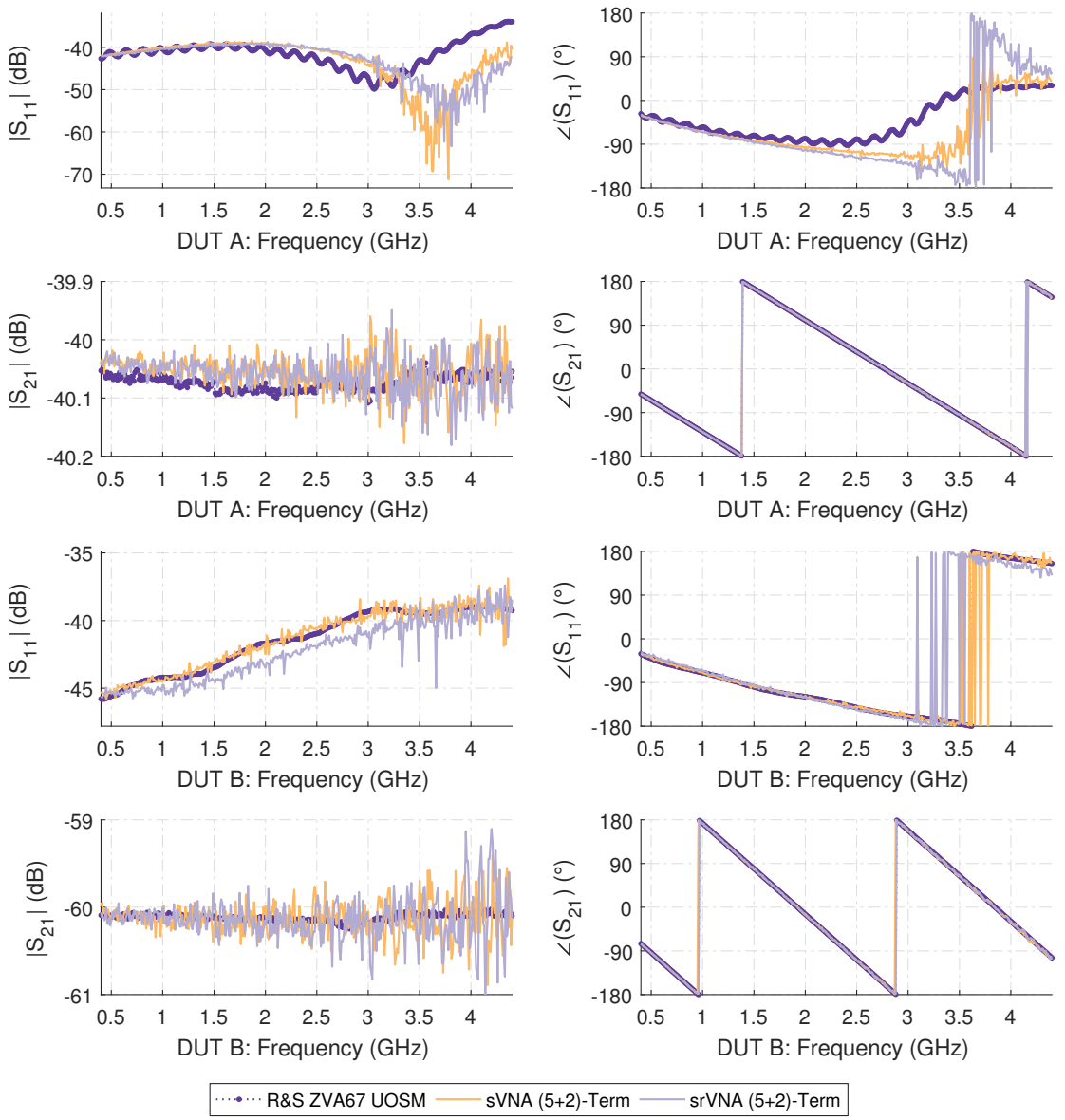

Figure 2.142: Measurement results of the 40 dB attenuator and the combination of the 20 dB and 40 dB reference attenuators used as a thru connection for the (5+2)-term error correction measured in both the sVNA and srVNA architectures. DUT A: 40 dB Rosenberger reference attenuator and Rosenberger (f)-(f) calibration thru. DUT B: 20 dB and 40 dB Rosenberger reference attenuators and Rosenberger (f)-(f) calibration thru.

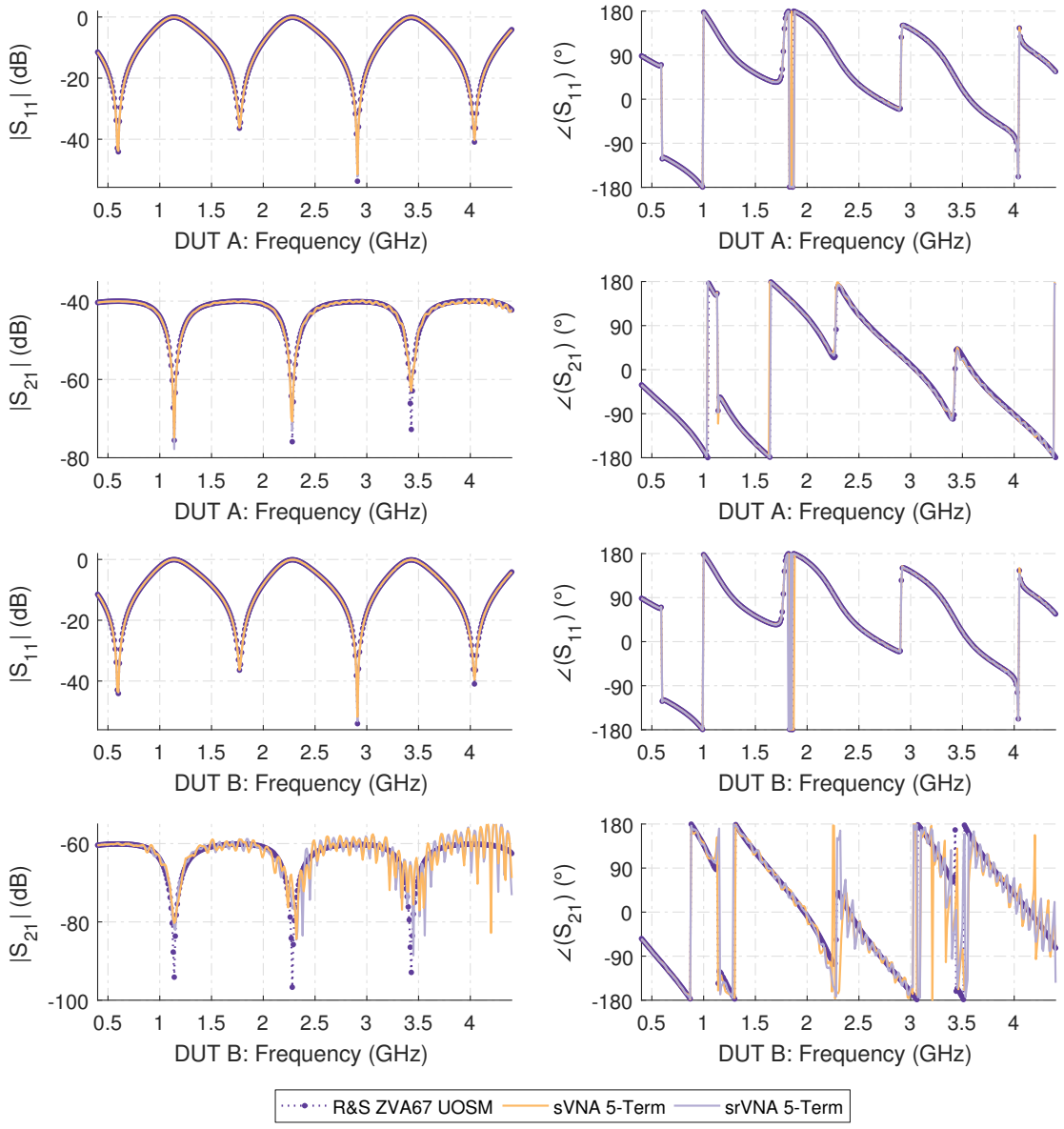

Figure 2.143: Measurement results of the asymmetric reflective lossy tee (ARLT) with different attenuation values, corrected by the 5-term error model for both the sVNA and srVNA unidirectional test-set setups. DUT A: ARLT with 40 dB of attenuation. DUT B: ARLT with 60 dB of attenuation.

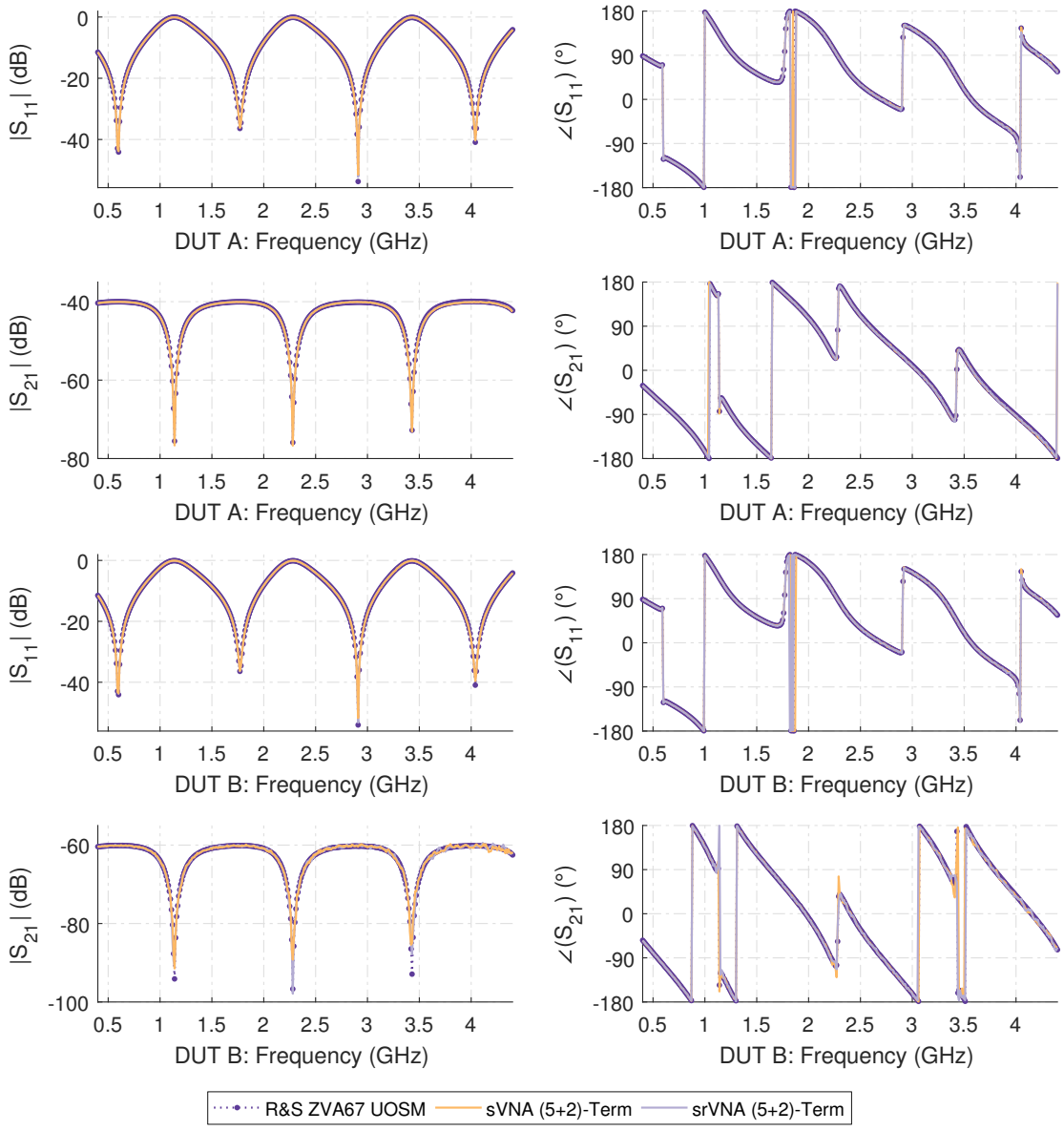

Figure 2.144: Measurement results of the asymmetric reflective lossy tee (ARLT) with different attenuation values, corrected by the (5+2)-term error model for both the sVNA and srVNA unidirectional test-set setups. DUT A: ARLT with 40 dB of attenuation. DUT B: ARLT with 60 dB of attenuation.

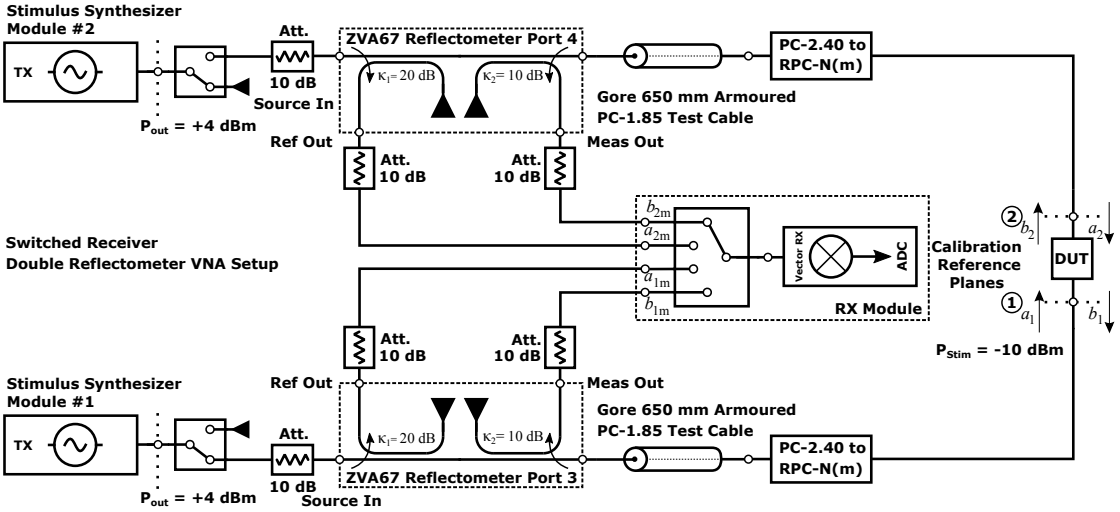

Figure 2.145: Schematic of the switched receiver double reflectometer VNA verification measurement setup.

lossy tee is assembled as shown in the introduction of this chapter (2.5.2) in Fig. 2.120, and subsequently re-measured with increasing values of attenuation provided by the 20 dB and 40 dB Rosenberger precision reference attenuators.

The measurement of the ARLT with no additional attenuation and the results for the 20 dB ARLT measurement are found in appendix B of this work (5-term error model in Fig. B.9 and (5+2)-term in Fig. B.10), as they just verify the transmission and reflection tracking ability of the unidirectional single receiver VNA setup, which is already well-established at this point.

The ARLT measurements using the 40 dB reference attenuator, and the combination of both 20 dB and 40 dB reference attenuators, is shown for the 5-term error model corrected data in Fig. 2.143 and for the (5+2)-term error model corrected data in Fig. 2.144. These verfication measurements represent a very different situation in terms of the cross-talk processes in comparison to the attenuators measurements alone, which were dominated solely by the E_{XF} cross-talk.

Here, due to the extremely reflective, frequency periodic, nature of the DUT, the influence of the E_{XRF} cross-talk varies considerably over frequency. Nevertheless, it can be directly observed from the results shown in Fig. 2.144, that the (5+2)-term error model performs just as well as before, with the reduction of interference based transmission noise-floor visible in both the overall interference ripple deviation from the reference measurement, as well as the overall dynamic range of the S_{21} measurement, regardless of the $|S_{11}|$ of the DUT.

2.5.5 Bidirectional SOLT Measurements

After the completion of the unidirectional single receiver VNA verification measurements, the test-set configuration is changed for the last time to the full double reflectometer

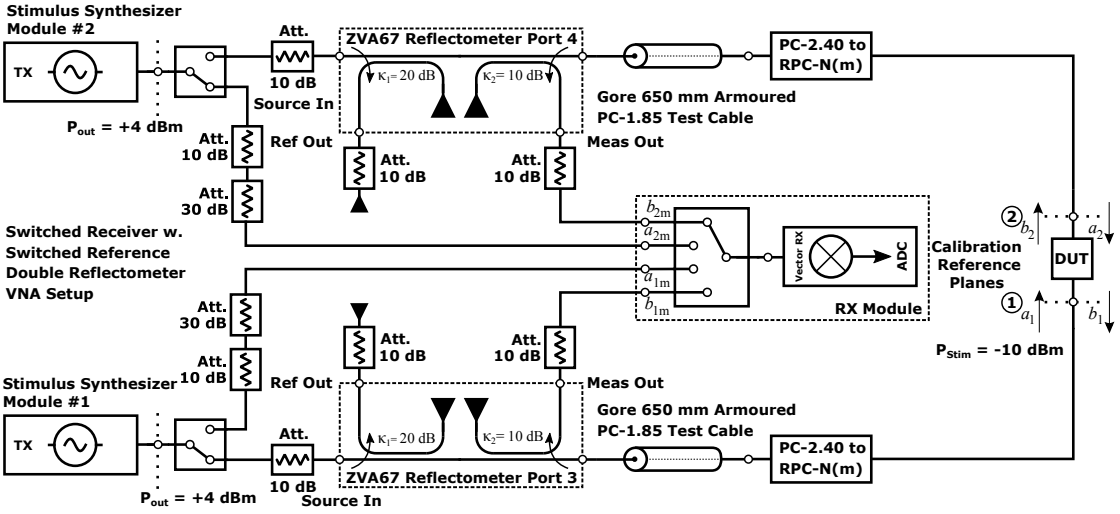

Figure 2.146: Schematic of the switched receiver double reflectometer with switched reference VNA verification measurement setup.

configuration shown in Fig. 2.145 for the sVNA and in Fig. 2.146 for the srVNA topology. Resistive padding is added in the same way for the second port, as already presented and discussed in the reflectometer and unidirectional VNA measurement setups.

In addition to the use of both directional couplers of the second ZVA67 test-set, an additional stimulus synthesizer module is used for the second port of the single receiver VNA setups. This decision was explicitly made to avoid the introduction of further leakage paths and non-TI behavior of the test-set when a stimulus reversal switch is used instead of a second separate stimulus synthesizer module.

Due to the second stimulus direction necessary for the double reflectometer, and one complete scan of the receiver input wave selector switch is performed per stimulus direction, this therefore doubles the amount of measurements and the total measurement time to approximately 35 seconds for the 8 wave input quantities, using the aforementioned settings, which results in a total number of 3208 measurement points acquired per bidirectional sweep. This in turn stretches the TI assumption of the synthesizers even further than in the measurement shown before.

The same test-set configuration and captured raw measurement data is used for both the following 10- and (10+4)-term SOLT based error correction, as well as the 7-term UOSM and xUOSM bases error correction methods presented later on.

Before the measurement of the calibration standards, a dynamic range check of both reflectometers, using the same procedure as outlined in the reflectometer measurement section 2.5.3, and a transmission measurement dynamic range check, as outlined in the unidirectional measurement section 2.5.4, are performed with virtually identical results to the raw ADC values presented before, which are therefore omitted for reasons of clarity.

After the linearity check, a standard MSO calibration is performed for each reflectometer with the addition of the bidirectional measurement of the thru standard to calculate

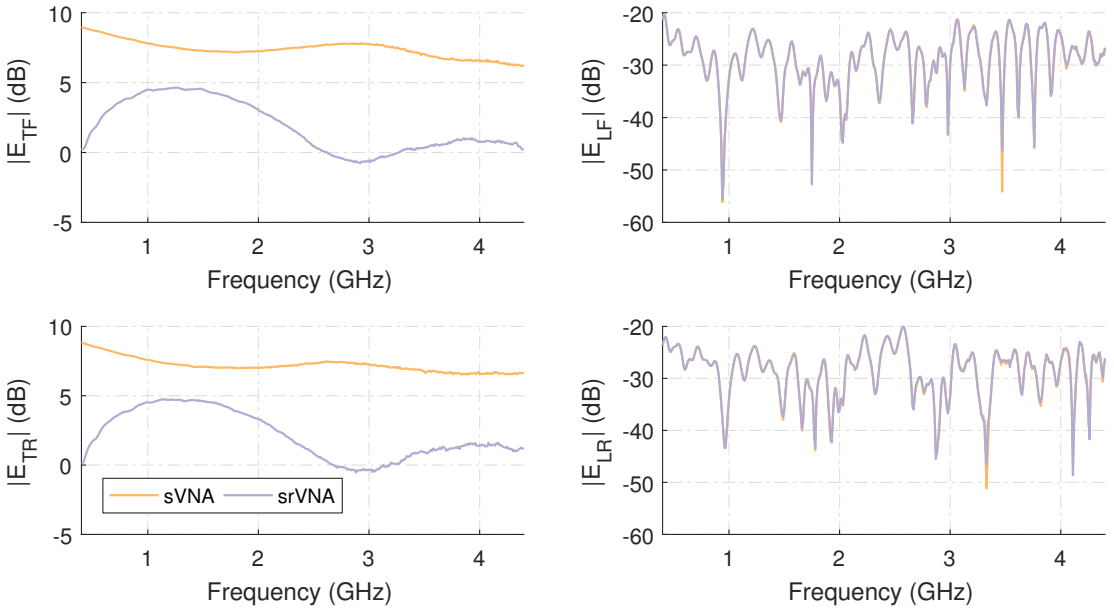

Figure 2.147: Measurement results for the tracking and source match error coefficients obtained via the 10-term calibration performed on the sVNA and srVNA double reflectometer test-sets.

the standard 10-term error model coefficients. For the (10+4)-term model cross-talk calibration measurements, the same Short-Match, Match-Short and Match-Match combination of isolation standards, as used before in the numerical verification of the procedure, are measured to calculate the additional 4 coefficients of the (10+4)-term model.

The 3-term reflectometer coefficients for both ports contained in the 10-term model are found to be almost identical and without any noteworthy observable differences between the two ports and the 3-term coefficients shown before and are therefore omitted here.

The tracking and load match coefficient magnitudes of the 10-term error model are shown for both stimulus directions in Fig. 2.147. While the E_{TF} and E_{TR} transmission tracking coefficients obtained via the SOLT calibration procedure are both similar and comparable to the results obtained in the unidirectional setup for both architectures, the load match coefficients E_{LF} and E_{LR} shown in Fig. 2.147 can now be determined in the double reflectometer setup and are used for a full two port return loss correction of low insertion loss DUTs.

The receiver input wave selector switch cross-talk coefficients obtained by the (10+4)-term calibration procedure are shown in Fig. 2.148. While some differences can be observed between the forward and reverse stimulus cross-talk coefficients, these test-set based cross-talk coefficients are in complete accordance with the slightly asymmetric switch isolation measured between the individual switch inputs and presented earlier in Fig. 2.56.

Interestingly, a distinct difference between the reference wave cross-talk coefficient

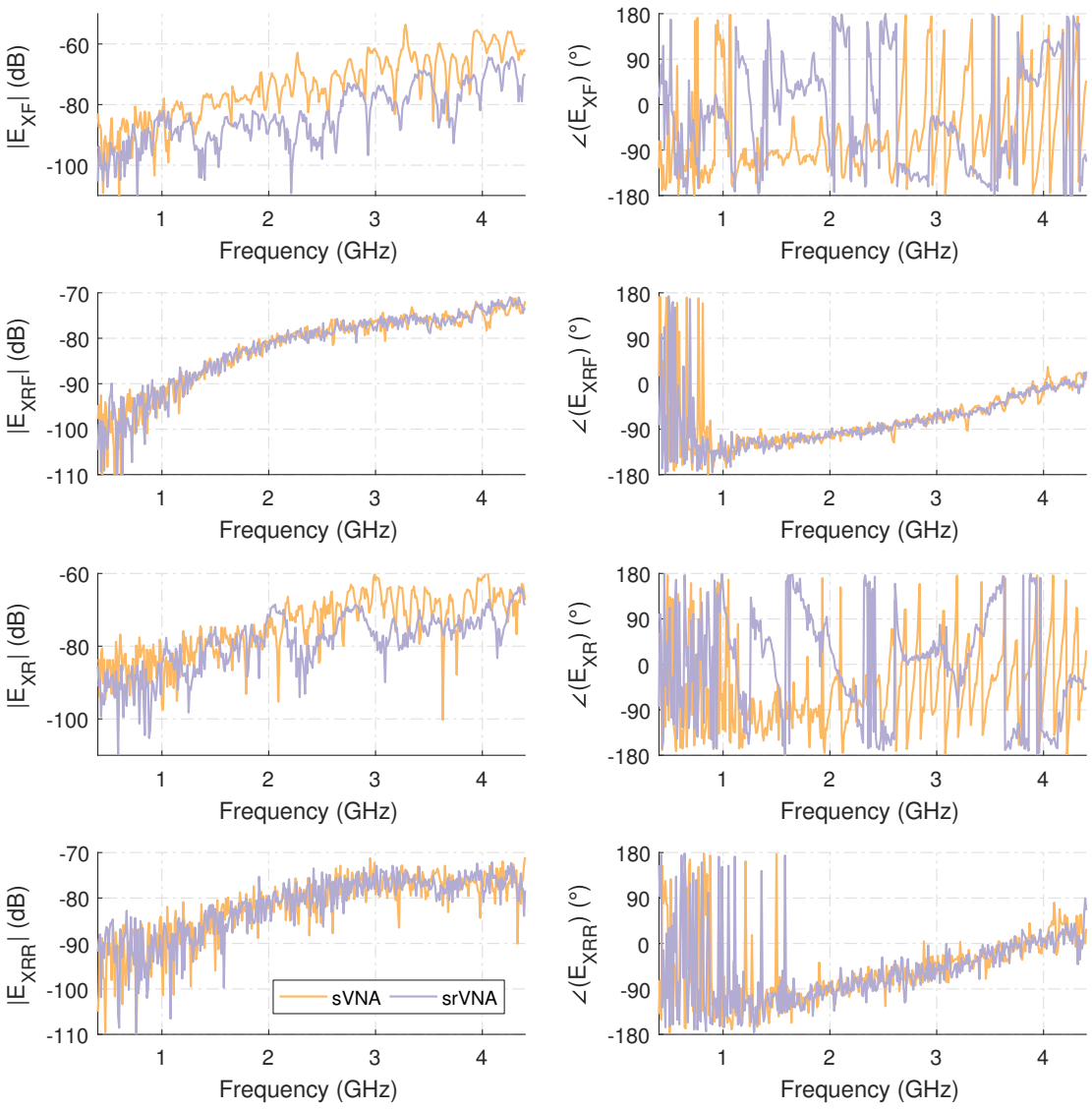

Figure 2.148: Measured (10+4)-term receiver input wave selector switch cross-talk coefficients obtained from the calibration procedure for both the sVNA and srVNA double reflectometer test-sets.

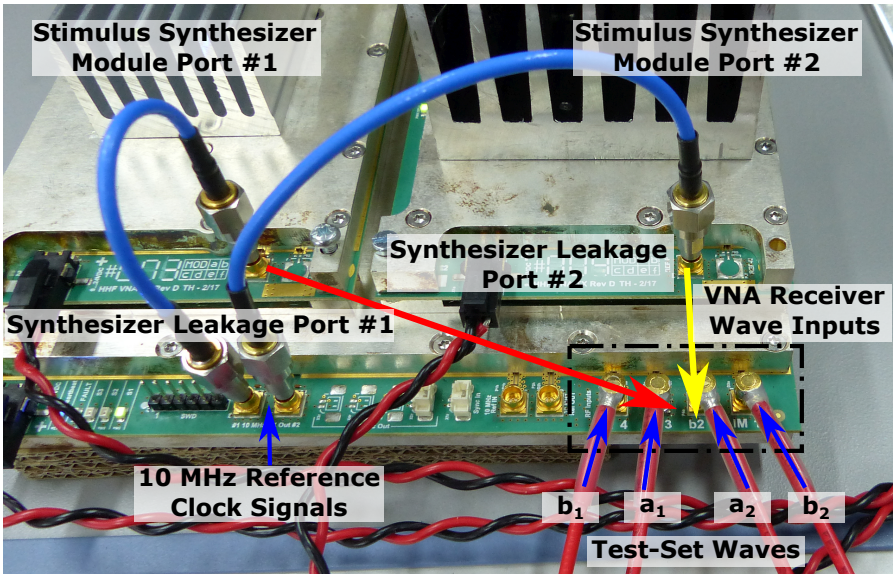

Figure 2.149: Annotated detail picture of the single switched receiver double reflectometer measurement setup highlighting the different physical separation between the stimulus synthesizer modules and the receiver switch wave inputs, shown for the sVNA configuration.

E_{XF} in the forward and E_{XR} in the reverse direction can be observed for both topologies in Fig. 2.148.

The source and main cause of this effect can be determined by looking at the annotated detail picture of the single switched receiver module assembly shown in Fig. 2.149. The 10 MHz reference inputs of the stimulus synthesizer modules are connected to the ADF4356 synthesizer via a low jitter sine to LVPECL clock converter, as outlined in the description of the VNA hardware modules in chapter 2.3.4, and therefore represent a preferred way of interference caused by insufficient air gap isolation.

While the reference clock input of the stimulus synthesizer associated with port 1 of the measurement setup is located some distance away from the receiver wave inputs, which especially includes the b_2 wave input active during the S_{21} measurement, the 10 MHz input of the stimulus synthesizer associated with the second port is directly above and adjacent to the wave inputs of the receiver.

This proximity reduces the isolation considerably, which manifests itself in higher cross-talk coefficient magnitudes for the reverse stimulus direction visible in the data shown in Fig. 2.148, and a reduced correction performance by the receiver input wave selector switch cross-talk correction methods. This is caused by the variable, non-TI, electromagnetic radiated field coupling process, which depends upon the immediate surroundings of the measurement setup and is obviously not constant due to the manipulation of DUTs by the operator in close vicinity.

This observation, in combination with the direct coupling of the wave inputs on the

receiver PCB, also serves as an explanation for the missing efficacy of the switched reference method observed in the cross-talk coefficient data, as this cross-talk path circumvents the original receiver switch cross-talk paths, including the reference wave switch, completely. This effect was unfortunately only discovered during later data analysis and is therefore present as a persistent error and offset in all the double reflectometer data sets. This effect could be resolved in a later hardware revision by adding extensive lowpass filtering to the 10 MHz inputs of the generators shown in Fig. 2.149 and therefore attenuating the discussed cross-talk path.

After this short excursion and the measurements of the calibration standards, one-port verification measurements are performed using both reflectometer ports. Just as it was observed in the unidirectional single receiver VNA measurements, no noteworthy effects beyond the ones already mentioned in the discussion of the reflectometer measurements could be observed in the error corrected results for both architectures. The results of these measurements are found in appendix B of this work.

As demonstrated with the unidirectional test-set measurements, the measured apparent transmission of the ripple test and residual directivity measurements, which use perfectly isolating standards per definition, can be used as a simple way to validate the efficacy of the (10+4)-term error model in comparison with the standard 10-term SOLT correction. This is shown in Fig. 2.150. From the isolation measurements seen in the figure it can be clearly observed, that the receiver input switch cross-talk correction also performs for the bidirectional double reflectometer measurements shown in Fig. 2.150 with the same efficacy as demonstrated for the forward stimulus $|S_{21}|$ in case of the unidirectional test-set measurements.

Nevertheless, the results of the aforementioned isolation deficiency caused by the second stimulus synthesizer can be clearly seen in the isolation measurements of both the 10-term corrected data, as well as the switch cross-talk corrected (10+4)-term error model results, of the reverse stimulus $|S_{12}|$-parameters. Due to the TI violations introduced by the radiation coupling, the efficacy of the cross-talk correction is reduced by up to 15 dB for the $|S_{12}|$ measurements, in direct comparison with the corrected $|S_{21}|$ data.

The full results of the ripple and direct source match measurements for both stimulus directions can be found for the 10-term error model corrected data in Fig. B.11, and for the (10+4)-term corrected data in Fig. B.12, in appendix B of this work.

After the one-port verification measurements, a T-Check measurement using the T-Check device assembled from a RPC-N 3x(f) tee junction and the male calibration match standard, as shown in Fig. 2.119 earlier, is performed. The resulting forward and reverse T-Check C_T FOMs are shown in Fig. 2.151.

Due to the non-ideal nature of the T-Check standard used here, the results are more of a comparative nature between the T-Check values obtained with the ZVA67, and the results obtained with both switched single receiver VNA topologies, instead of the absolute results obtained with the ideal T-Check device used in the synthetic numerical analysis of the architectures.

Rather surprisingly, the results obtained for the forward and reverse C_T values in both the 10- and (10+4)-term corrected measurement results do not show the distinct ripple deviation when compared with the four-receiver UOSM corrected reference results which

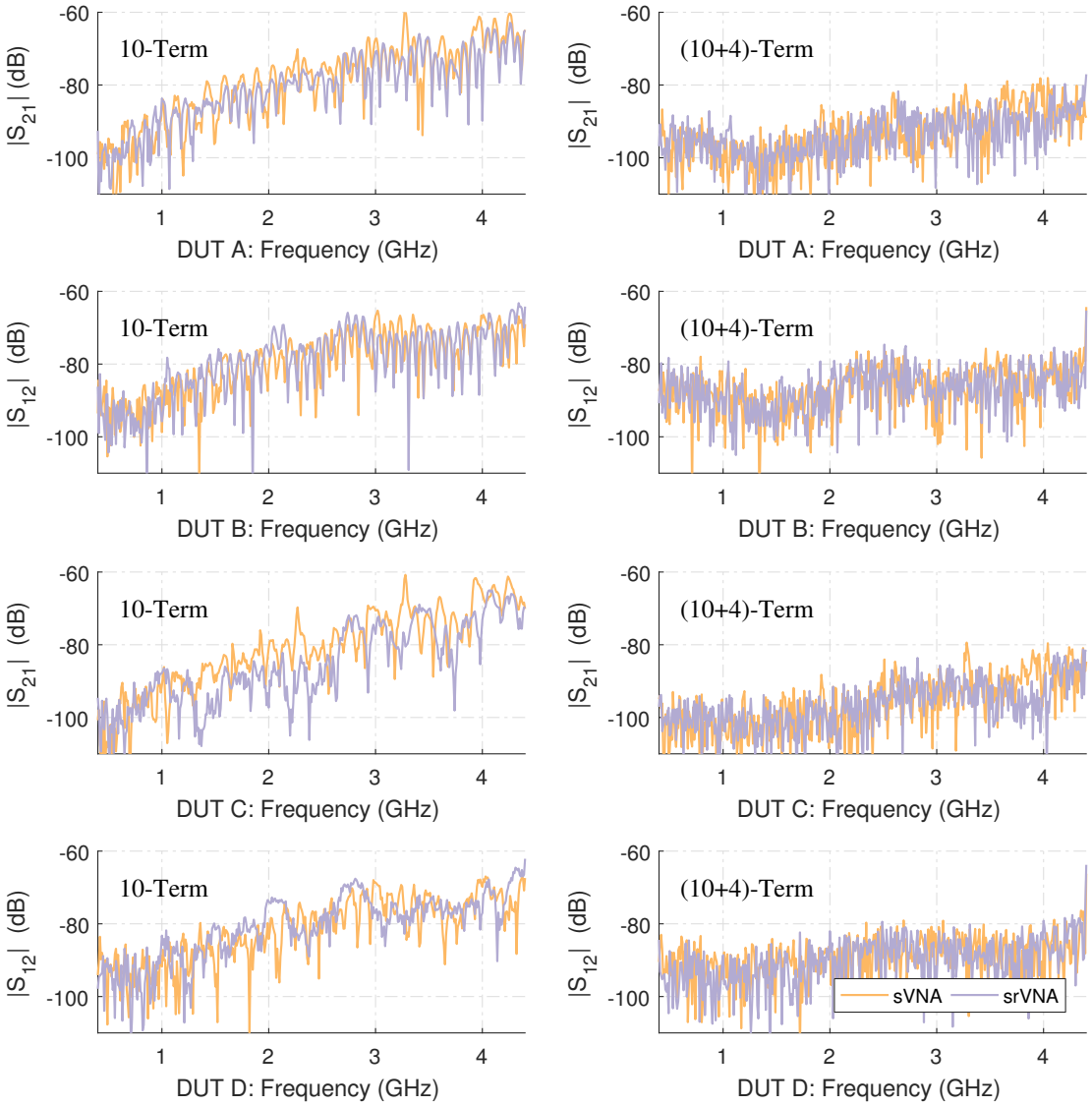

Figure 2.150: Measured S_{21} and S_{12} isolation figures obtained during the ripple test and direct residual directivity measurements, corrected by the 10-term and the (10+4)-term procedure for both the sVNA and the srVNA double reflectometer test-sets. DUT A: Port 1, 150 mm $Z_L = 50\,\Omega$ bead-less airline terminated by the calibration short. DUT B: Port 2, 150 mm $Z_L = 50\,\Omega$ bead-less airline terminated by the calibration short. DUT C: Port 1, 150 mm $Z_L = 50\,\Omega$ bead-less airline terminated by the calibration match. DUT D: Port 2, 150 mm $Z_L = 50\,\Omega$ bead-less airline terminated by the calibration match.

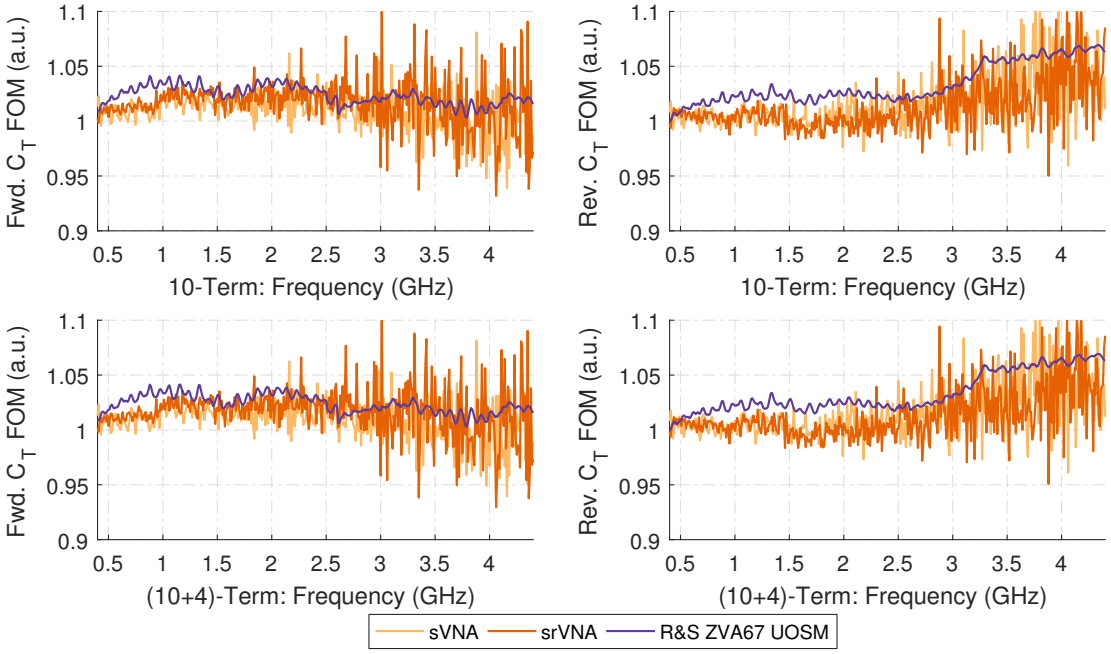

Figure 2.151: Measurements results of the T-Check verification standard, corrected by the 10-term and the (10+4)-term procedure for both the sVNA and srVNA double reflectometer test-sets.

was observed in the numerical analysis of the test-sets. Instead, both error models achieve results close to the reference measurement carried out with the ZVA67, independent of the single receiver test-set topology. Unfortunately, the measurements performed above 3 GHz are dominated by the aforementioned trace noise phenomenon on both the sVNA and srVNA architectures, but still perform within the generally accepted deviation boundary of $\Delta C_T = \pm 0.1$ (a.u.) ([157]) of this verification test, when the ZVA67 measurement is used as the reference for this comparison.

Next, the bidirectional measurements of the direct 150 mm RPC-N airline thru connections using the bead-less $Z_L = 50\,\Omega$ and the $Z_L = 25\,\Omega$ center conductors are performed, including the calibration thru standard as a (f)-(f) adapter in the same manner as described in the unidirectional single receiver VNA verification measurements.

From the results shown in Fig. 2.152 for the 10-term and in Fig. 2.153 for the (10+4)-term corrected measurement data it can be observed, that the bidirectional transmission tracking performance of both single receiver VNA test-sets is well within acceptable levels for practical measurements and the main source of measurement error is still the ± 0.1 dB high frequency trace noise present in all measurements.

No further discernible trace noise is added to both transmission measurements by the (10+4)-term correction in direct comparison with the 10-term corrected results, despite using S_{11} and S_{22} measurement data close to the system noise floor, which can easily be seen by the noisy phase argument of both S-parameters.

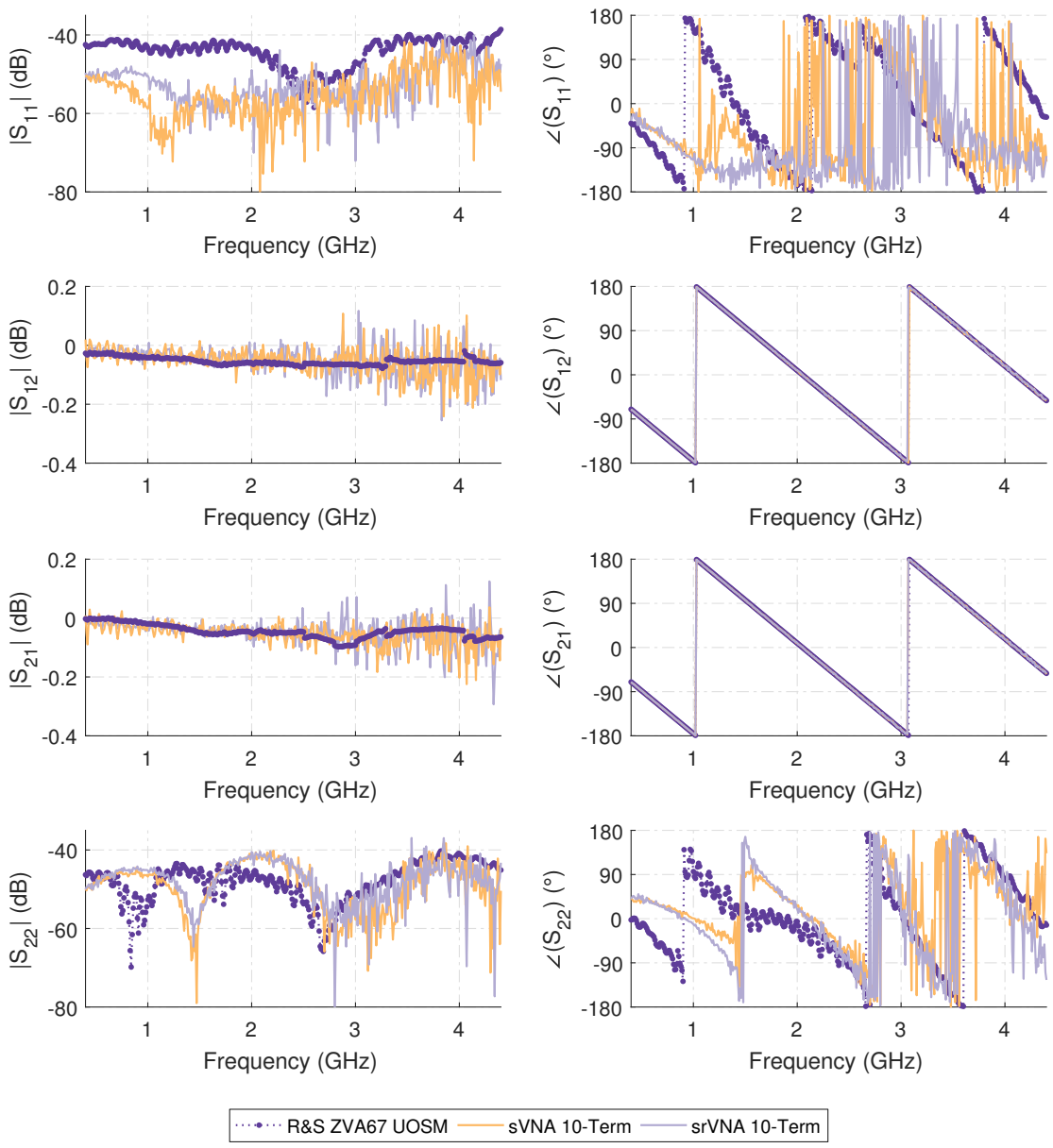

Figure 2.152: Measurement results of the 150 mm $Z_L = 50\,\Omega$ bead-less airline thru connection with the additional Rosenberger RPC-N (f)-(f) calibration thru corrected by the 10-term procedure for both the sVNA and the srVNA double reflectometer test-sets.

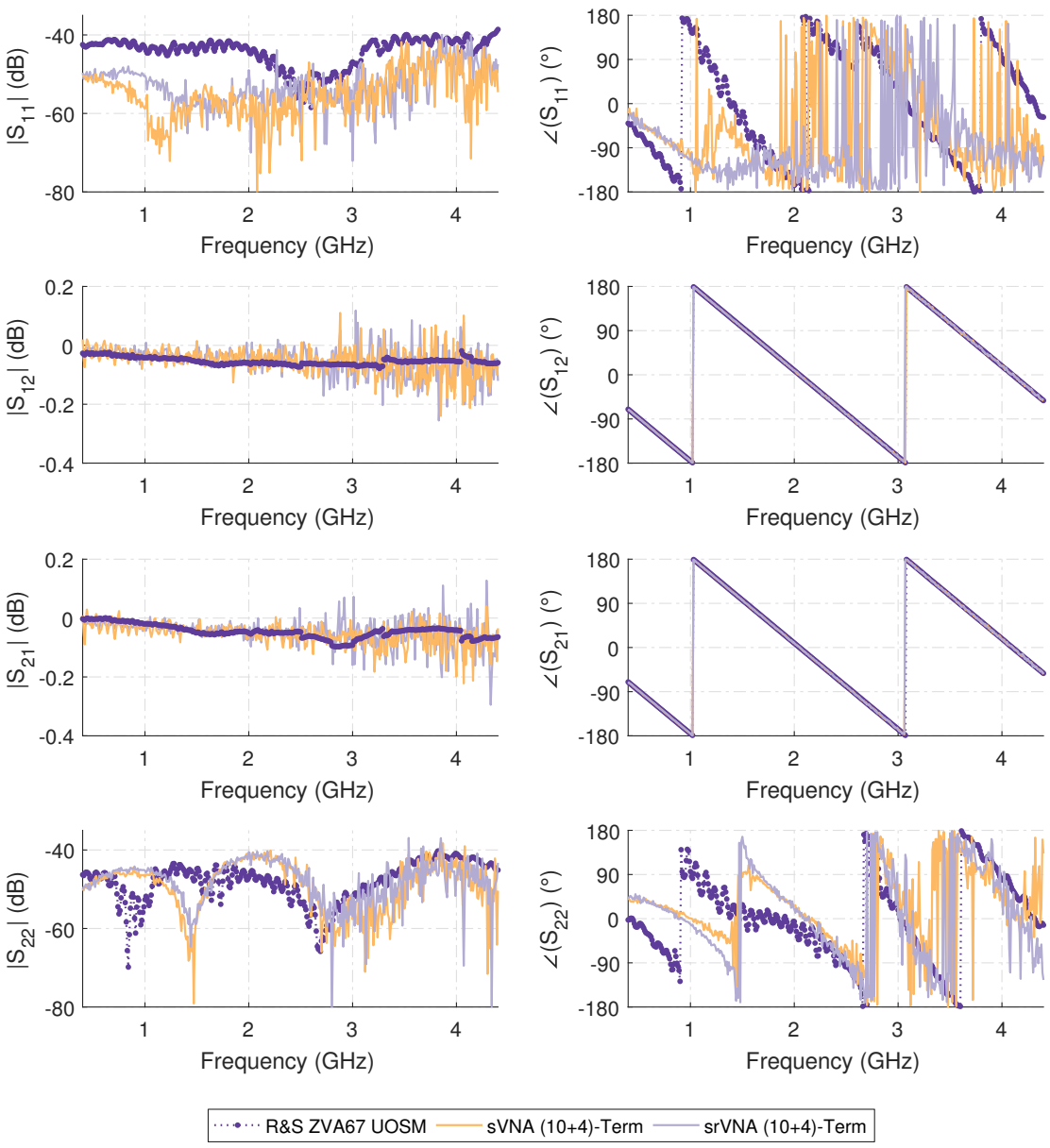

Figure 2.153: Measurement results of the 150 mm $Z_L = 50\,\Omega$ bead-less airline thru connection with the additional Rosenberger RPC-N (f)-(f) calibration thru corrected by the (10+4)-term procedure for both the sVNA and the srVNA double reflectometer test-sets.

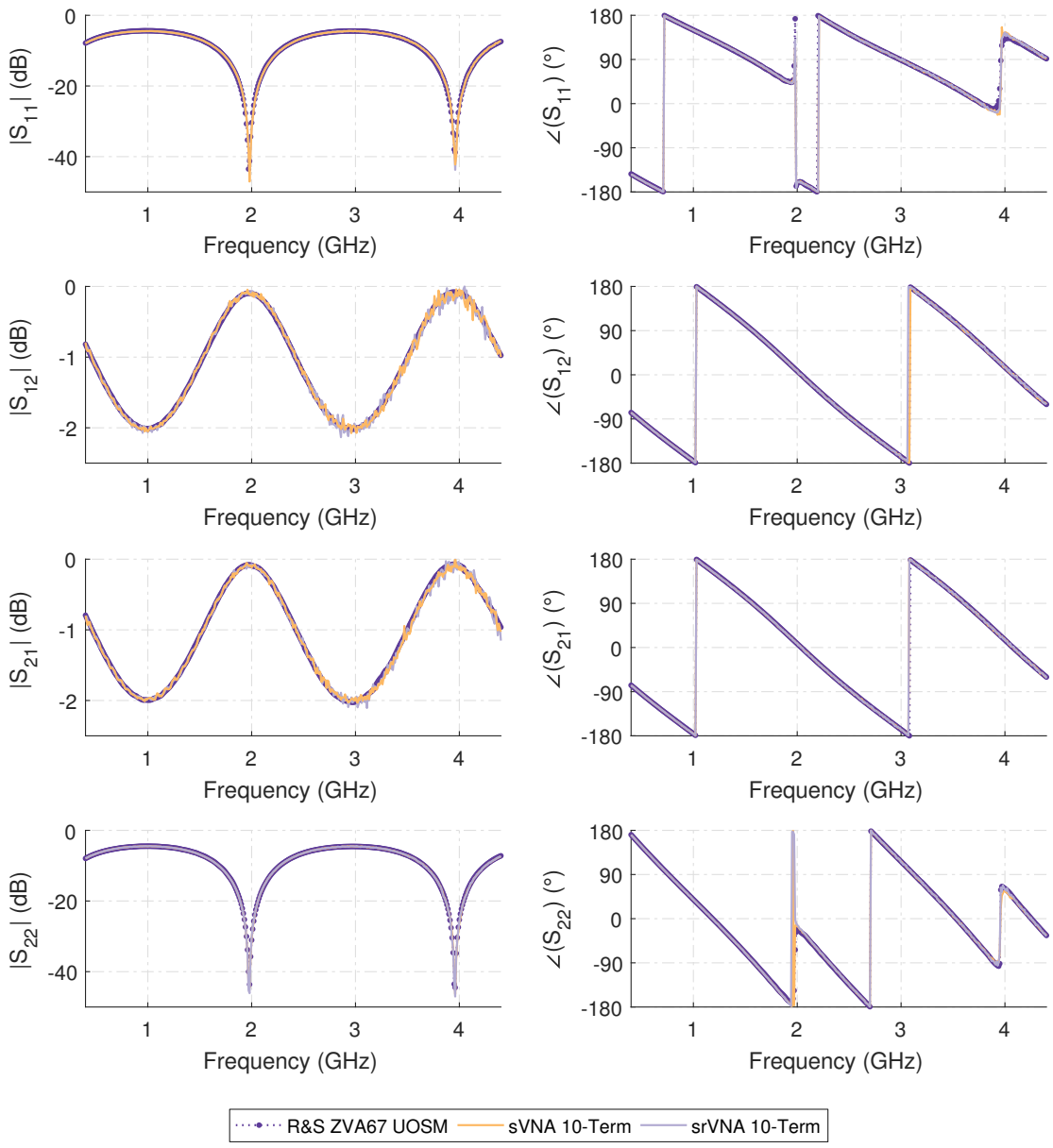

Figure 2.154: Measurement results of the 150 mm $Z_L = 25\,\Omega$ bead-less airline thru connection with the additional Rosenberger RPC-N (f)-(f) calibration thru corrected by the 10-term procedure for both the sVNA and the srVNA double reflectometer test-sets.

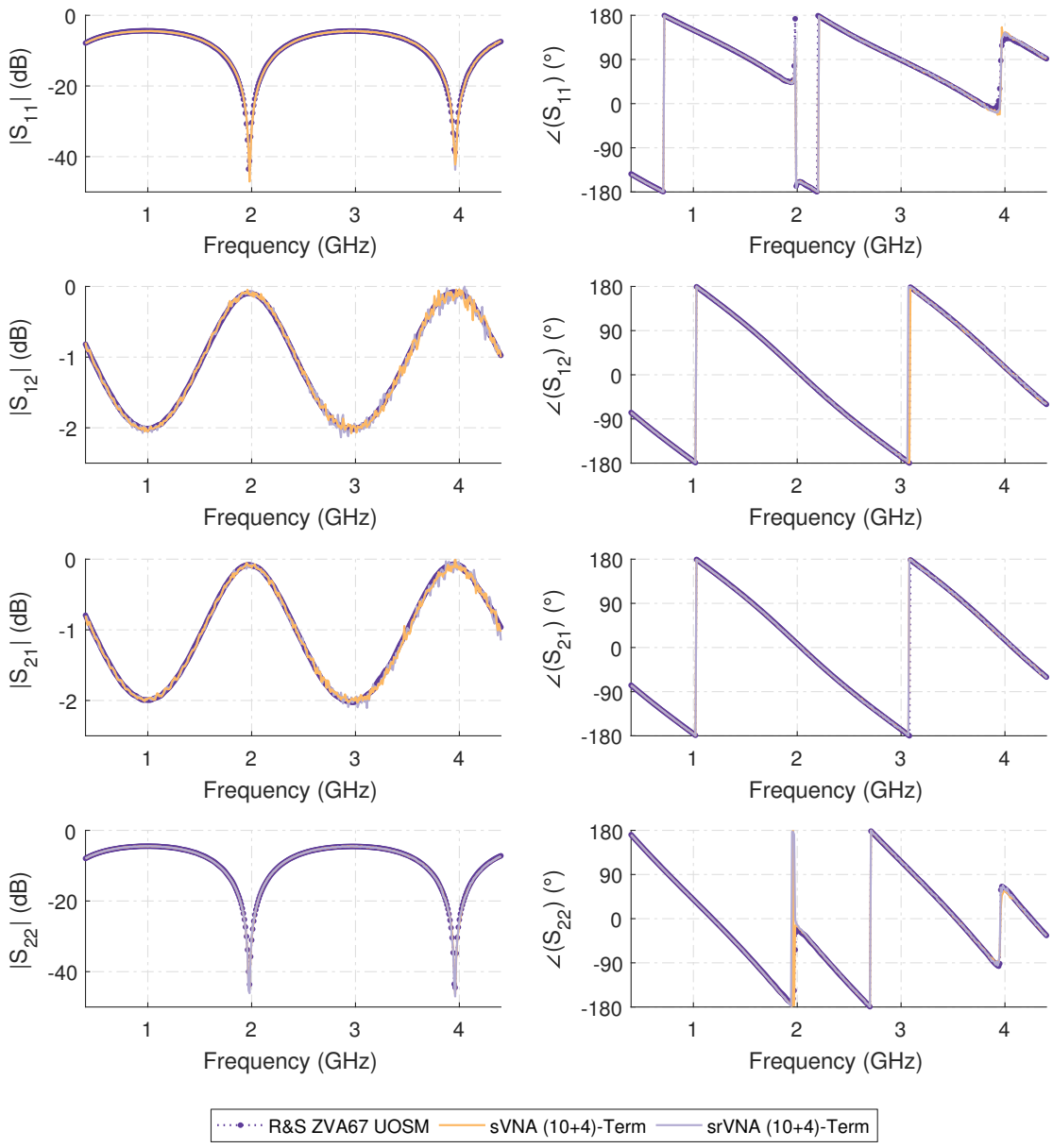

Figure 2.155: Measurement results of the 150 mm $Z_L = 25\,\Omega$ bead-less airline thru connection with the additional Rosenberger RPC-N (f)-(f) calibration thru corrected by the (10+4)-term procedure for both the sVNA and the srVNA double reflectometer test-sets.

Furthermore this measurement reveals, that the deficiencies in the load match correction performance that were observed in the $|S_{11}|$ and $|S_{22}|$ data of numerical analysis of the same measurement are only relevant on a metrological error scale for the test-set configuration used here, as the mechanical repeatability error of the bead-less airline far surpasses the difference in return loss seen between the sVNA, srVNA and ZVA67 measurements in both stimulus directions.

While this may seem to contradict the results of the synthetic analysis at first, the most plausible explanation for this difference in correction behavior can be seen by comparing the source match coefficients E_{SF} and E_{SR}, as well as the load match coefficients E_{LF} and E_{LR}, obtained during calibration between the synthetic analysis and the measurements carried out on the real test-sets. Due to the added resistive padding of the reflectometer interfaces, the source and load match coefficient results obtained with the hardware measurements show a much better uncorrected test-set hardware return loss than the values assumed for their synthetic counterparts. This observation coincides with the discussion of the single receiver VNA load match correction performance of the UOSM with switching terms procedure in the analysis of the synthetic, UOSM corrected, verification measurement results.

The observation of good correction performance in the basic SOLT error model with the single receiver architecture measurements is also supported by the results of the $Z_L = 25\,\Omega$ 150 mm airline thru connection, shown for the 10-term error corrected data in Fig. 2.154, and in Fig. 2.155 for the (10+4)-term error corrected results.

No discernible reflection tracking errors beyond the mechanical repeatability of the bead-less airline are discernible for both single receiver test-set topologies in the S_{11} and S_{22} error corrected data. The same statement is true for the S_{21} and S_{12} transmission measurements, which showed severe systematic tracking errors of up to 0.25 dB in the numerical synthetic version of this measurement. In the measurement results obtained by both single receiver VNA topologies, none of these effects can be observed.

Right after the airline measurement, the transmission tracking linearity tests, using the various SMA attenuators and their precision reference RPC-N counterparts, are conducted in the same way as described in the unidirectional test-set measurement case. No noteworthy effects besides the high frequency trace noise already described are observed in the measurement results for both SOLT error correction methods and test-set topologies in comparison with the ZVA67 reference measurements. The measurement results for these verification DUTs can be found in the appendix, starting with Fig. B.13 for the SMA attenuators, and ending with Fig. B.18 for the bidirectional measurement of the 40 dB reference attenuator.

The measurement results of the Rosenberger 20 dB and 40 dB RPC-N reference attenuator combination, with the added Rosenberger RPC-N (f)-(f) calibration thru standard as an adapter, is shown for the 10-term correction in Fig. 2.156, while the (10+4)-term error corrected measurement data is shown in Fig. 2.157.

Just as demonstrated by the (5+2)-term measurements, this measurement is the ideal realistic test case for the (10+4)-term error model to verify the correction ability of this method under noisy inputs signal conditions due to the very good return loss of the attenuator combination at both calibration reference planes, resulting in a S_{11m} and

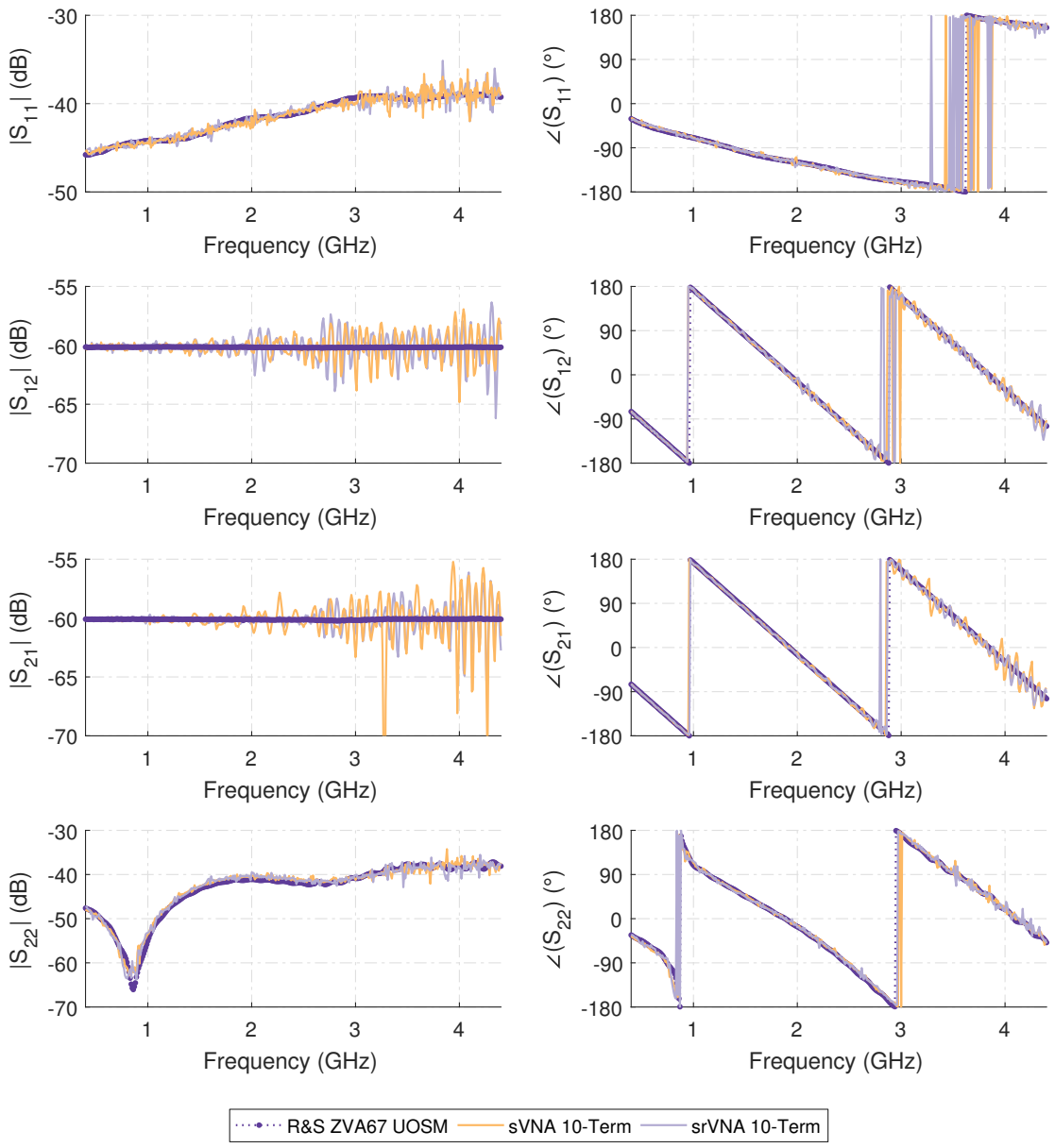

Figure 2.156: Measurement results of the combined 20 dB and 40 dB reference attenuators with the additional Rosenberger RPC-N (f)-(f) calibration thru corrected by the 10-term procedure for both the sVNA and the srVNA double reflectometer test-sets.

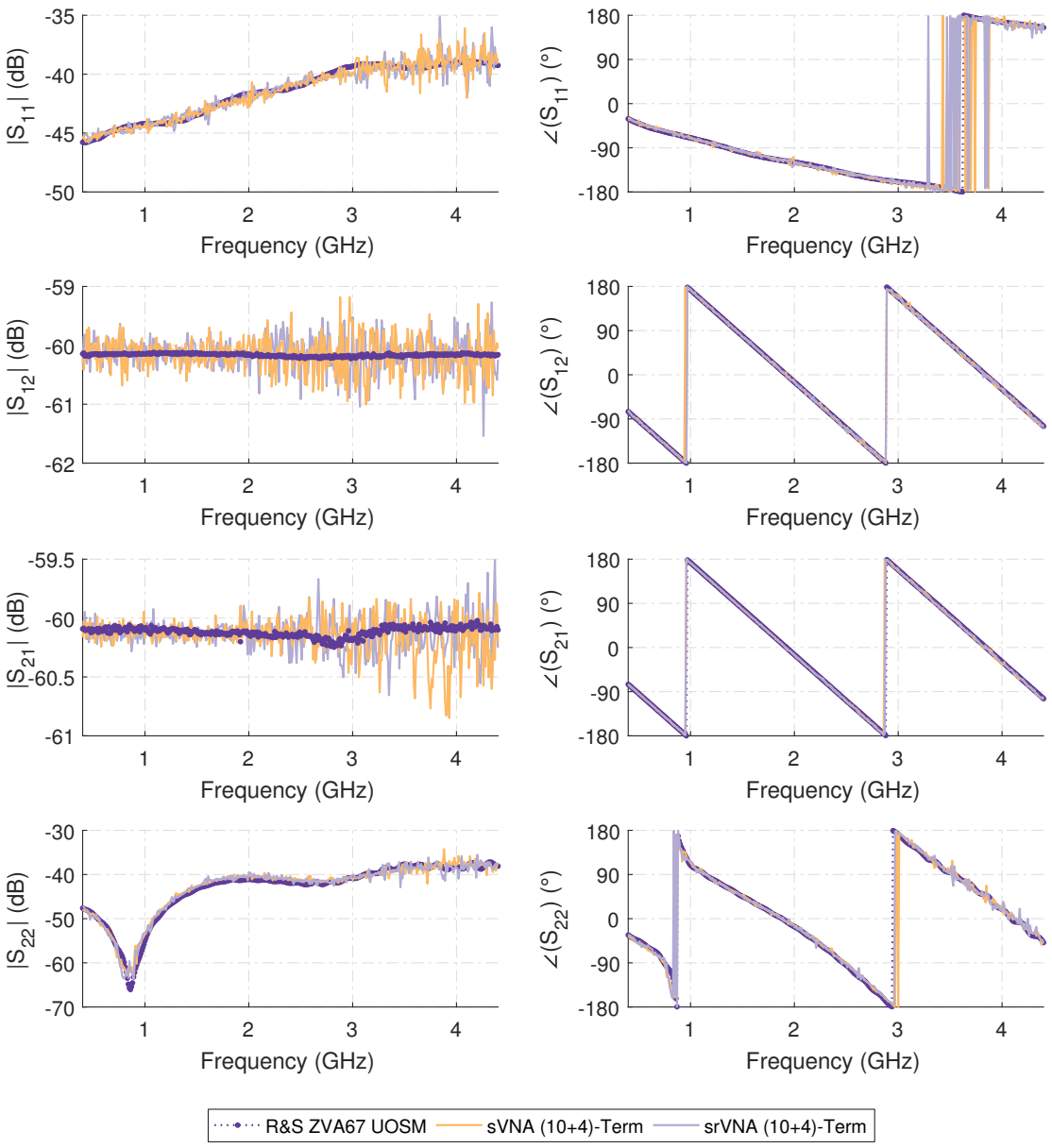

Figure 2.157: Measurement results of the combined 20 dB and 40 dB reference attenuators with the additional Rosenberger RPC-N (f)-(f) calibration thru corrected by the (10+4)-term procedure for both the sVNA and the srVNA double reflectometer test-sets.

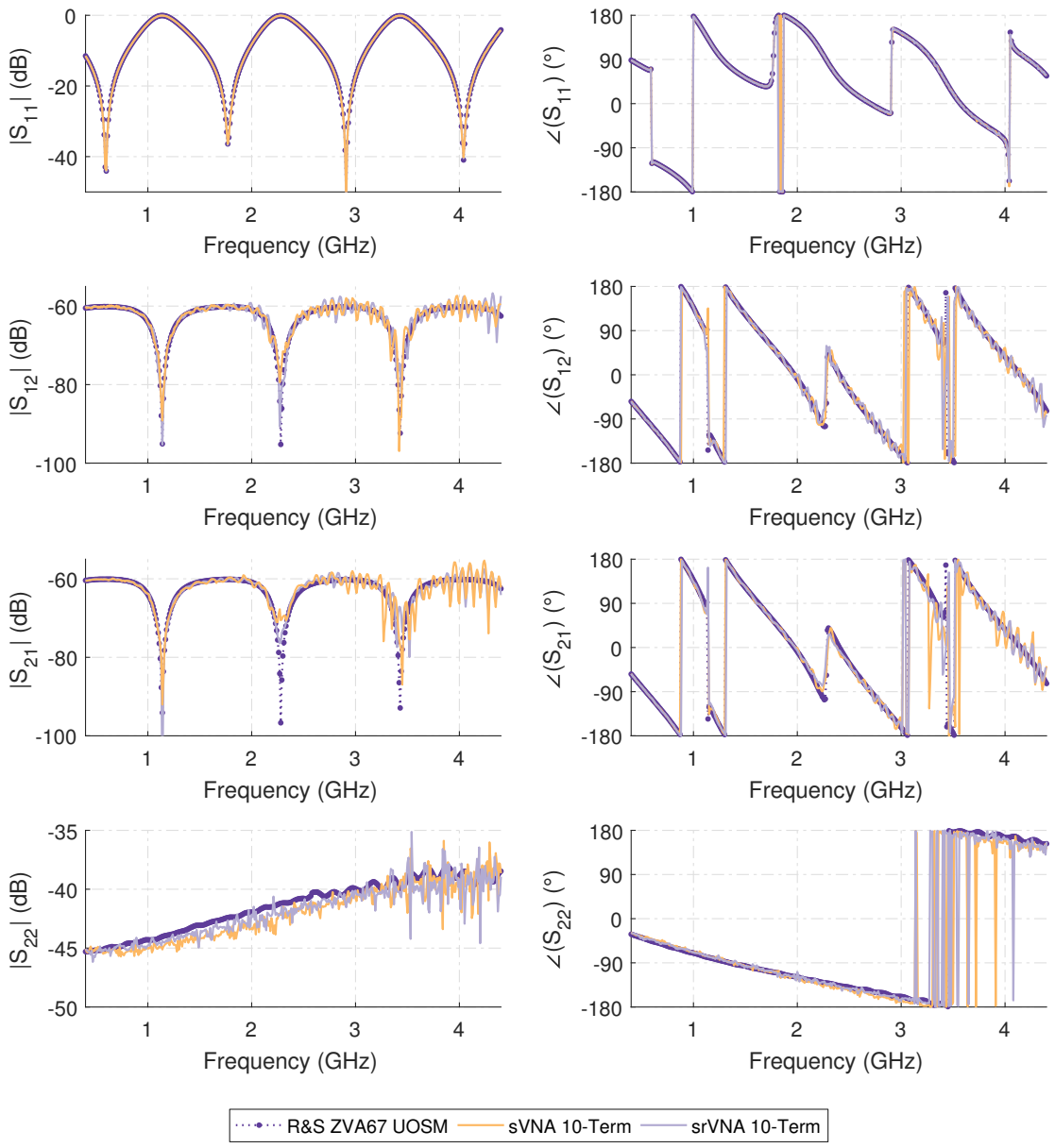

Figure 2.158: Measurement results of the asymmetric reflective lossy tee using the combined 20 dB and 40 dB reference attenuators with the additional Rosenberger RPC-N (f)-(f) calibration thru corrected by the 10-term procedure for both the sVNA and the srVNA double reflectometer test-sets.

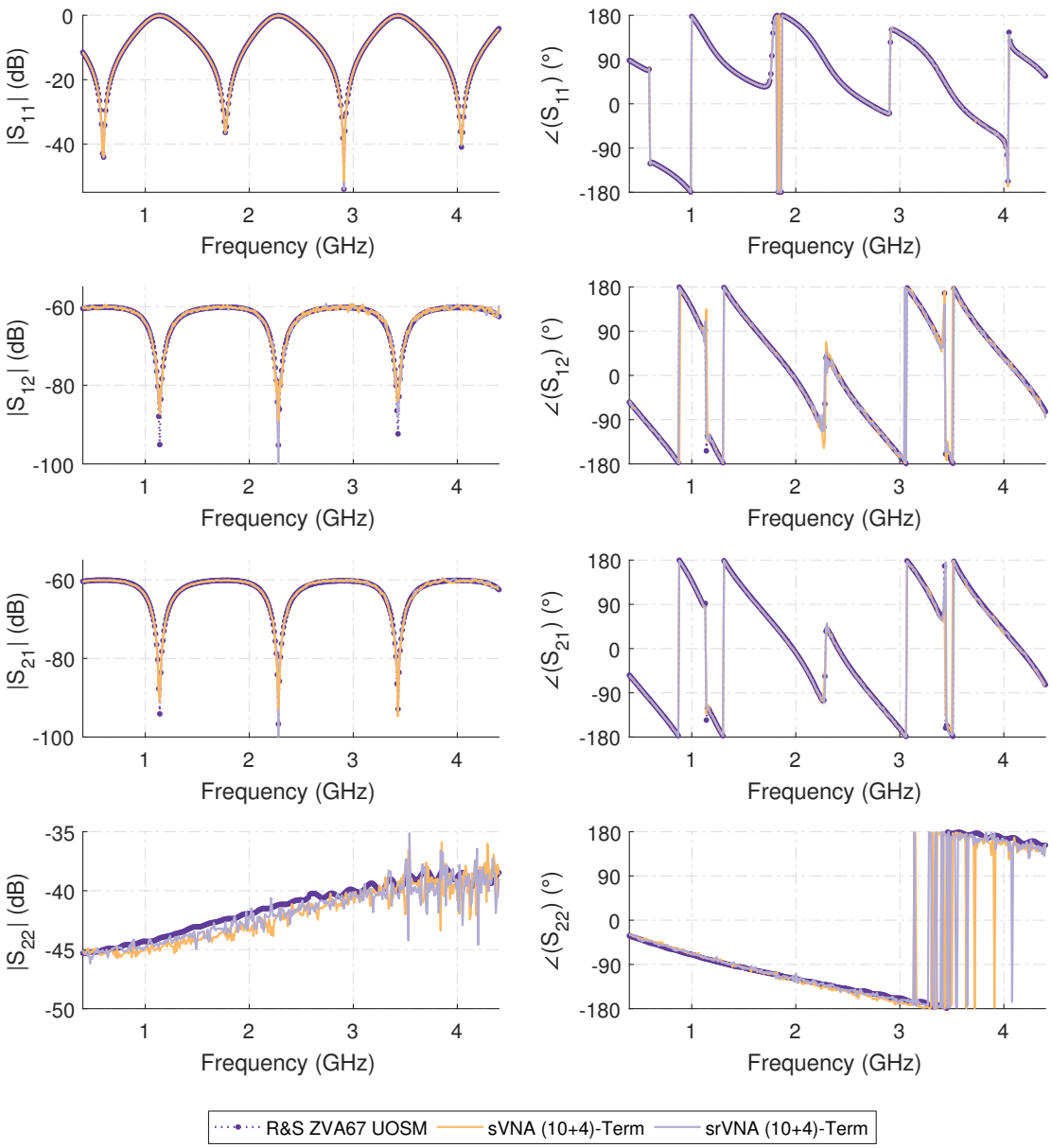

Figure 2.159: Measurement results of the asymmetric reflective lossy tee using the combined 20 dB and 40 dB reference attenuators with the additional Rosenberger RPC-N (f)-(f) calibration thru corrected by the (10+4)-term procedure for both the sVNA and the srVNA double reflectometer test-sets.

S_{22m} with low SNR.

Nevertheless, a dramatic improvement in measurement accuracy is demonstrated by the correction performed by the (10+4)-term error model, shown in Fig. 2.157, in direct comparison of the S_{21} and S_{12} measurement with the non cross-talk corrected measurement using the same raw measurement data in Fig. 2.156.

Unfortunately, the effect of the insufficient isolation between the second stimulus generator and the receiver for the S_{12} measurement can also be identified again. While some reduction in cross-talk interference is visible in the $|S_{12}|$ data, only a fraction of the correction performance demonstrated for the forward stimulus direction is achieved.

Finally, the measurements of the asymmetric reflective lossy tee, using the Rosenberger RPC-N 3x(f) tee, the 150 mm $Z_L = 50\,\Omega$ airline, the calibration short and the various combinations of the Rosenberger RPC-N precision reference attenuators, are performed to evaluate both the reflection and transmission tracking performance for the case of no additional and 20 dB of attenuation, as well as the (10+4)-term correction performance using the 40 dB and the 20 dB and 40 dB attenuator combination under high reflection conditions for the stimulus applied to the first port.

The measurement results of these DUTs for the no attenuation, 20 dB of attenuation and 40 dB of attenuation test-cases showed no noteworthy deviations in comparison with the ZVA67 reference measurements in both reflection and transmission tracking capabilities and can be found, starting with the ARLT measurement with no attenuation and corrected using the 10-term error model in Fig. B.19, and ending with the ARLT measurement using the 40 dB Rosenberger RPC-N precision attenuator corrected by the (10+4)-term error model in Fig. B.24, in appendix B of this work.

By comparing the measurement results of the ARLT using the combination of the 20 dB and 40 dB RPC-N reference attenuators, shown for the 10-term error model corrected data in Fig. 2.158, and for the (10+4)-term error model corrected data in Fig. 2.159, it can be observed, that the SOLT version of the receiver input wave selector switch cross-talk correction does not fail here either and enables measurements in both test-set architectures, which are extremely close to the results obtained on the ZVA67 reference platform.

All in all the double reflectometer measurements conducted with the sVNA and srVNA test-set architectures performed much better in conjunction with the 10-term and (10+4)-term error models than it was anticipated from the synthetic analysis of these test-sets and algorithms, which is much likely caused by the resistive padding in form of the 10 dB attenuators added to the test-set connections. This measure provides a much better hardware source and load match than the test-set topologies examined in the synthetic analysis of the error correction models.

In hindsight it is somewhat unfortunate, that the cross-talk path originating from the 10 MHz reference frequency clock signal connection was not discovered earlier on and was only found post initial data analysis. While the correction ability of the transmission measurements originating from the second stimulus synthesizer were severely impeded by this non-TI cross-talk, this also raises the question if a correction performance similar to the results of the numerical system analysis could have been demonstrated using the sVNA and especially the srVNA test platforms.

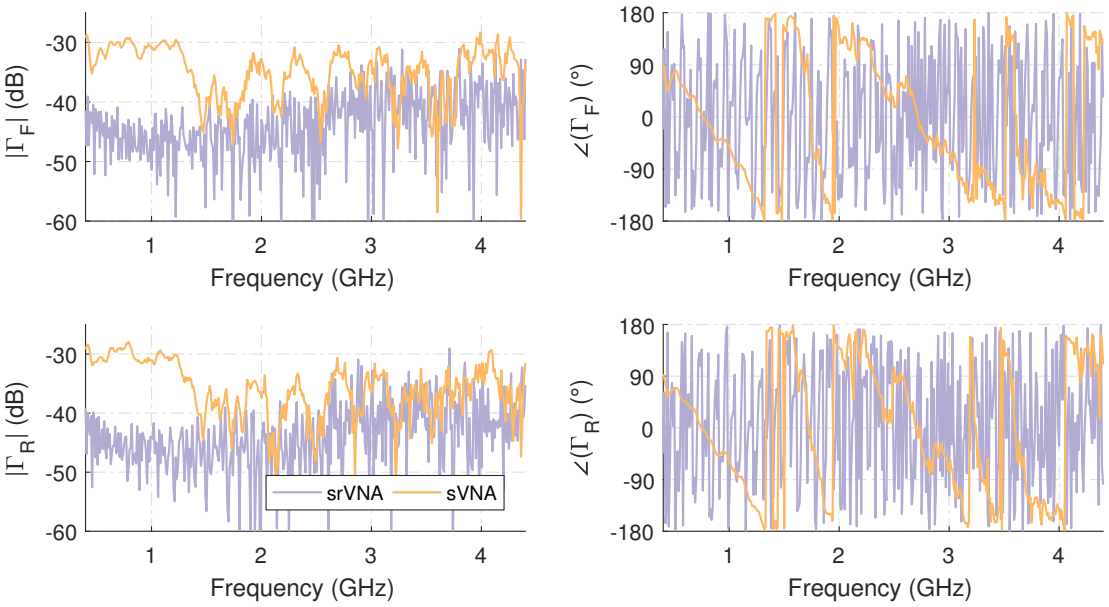

Figure 2.160: Calibration results for the switch terms correction coefficients Γ_F and Γ_R, obtained for the 7-term UOSM model via the direct method and for the xUOSM calibration procedures via two-tier SOLT calibration for both sVNA and srVNA test-set architectures.

Nevertheless, this phenomenon provides an interesting insight into the various problems and intricacies that are encountered when building a viable high dynamic range vector network analyzer system.

2.5.6 7-Term UOSM and xUOSM Measurement Results and Conclusion

The final verification measurements using the 7-term error model unknown-thru (UOSM) and receiver switch cross-talk corrected unknown-thru (xUOSM) calibration procedures are by strict definition not new measurements at all, but re-use the raw measurement data already captured during the SOLT 10- and (10+4)-term calibration DUT measurements, although with a different underlying error model and correction algebra, as laid out in the theoretical discussion of the procedures and the analysis of the synthetic measurement data. These measurement results now use the same basic error correction scheme that was used as the preferred calibration and error correction method to capture the verification DUT reference measurement with the Rohde & Schwarz ZVA67 VNA, using its own proprietary inbuilt implementation of the algorithm.

This allows for a direct head-to-head comparison of their correction accuracy and presents an interesting opportunity to re-evaluate the correction efficacy of the receiver input switch cross-talk correction, which is analogous to the well-known switch terms correction also performed outside of the core 7-term error model, in a different context.

The switch terms correction coefficients Γ_F and Γ_R, which capture the change in input

reflection coefficient presented to the DUT reference plane depending upon the stimulus state, are shown in Fig. 2.160. As outlined in the analysis of the synthetic measurements carried out with the simulated test-sets and the theoretical description of the procedure, the Γ_F and Γ_R values for the sVNA four-receiver double-reflectometer architecture are directly determined from the stimulus direction dependent raw a_1 and a_2 wave quotients obtained from the measurement results of the thru calibration standard and saved for further correction.

This direct switch terms calibration measurement is not possible using the srVNA test-set topology, as only three out of four virtual switched receivers are able to measure DUT dependent wave quantities per stimulus direction due to the reference wave switched used as a replacement for the a_1 and a_2 wave couplers to enhance isolation. Instead, the switching terms coefficients are calculated from the 10-term error model coefficient data obtained via the previous SOLT 10-term calibration of the srVNA test-set topology.

Despite the excessive resistive padding used for both the sVNA and srVNA test-sets, the same pattern already found in the numerical analysis of the test-set can be observed here, as the switch terms correction coefficients for the srVNA test-set architecture attest a more stable hardware return loss characteristic between the change of stimulus direction role for each measurement port than is observed with the more classical sVNA four-receiver architecture.

The rest of the 7-term UOSM and xUOSM calibration procedure is carried out as normal by re-using the measurement data of the 10-term and (10+4)-term calibration data to obtain both the full 7-term error model correction coefficients, as well as the receiver wave input switch cross-talk correction coefficients.

The first measurements to be re-evaluated using the 7-term error model and the UOSM and xUOSM calibration and correction are the reflectometer ripple test and the residual directivity measurements, including the measured isolation of the one-port verification standards covering most of the smith chart complex impedance plane. The results of the S_{21} and S_{22} isolation measurements is shown in Fig. 2.161, while the full results including the comparatively uneventful S_{11} and S_{22} reflectometer results are found in Fig. B.25 and Fig. B.26 in appendix B of this work.

When the results of the non-cross-talk corrected UOSM 7-term and the cross-talk corrected xUOSM 7-term error model isolation figures are compared with the results shown in Fig. 2.150 earlier for the 10- and (10+4)-term corrected same raw data set, two important observations can be made:

First and foremost it can easily be seen, that the non cross-talk corrected sVNA test-set topology performs much worse using the 7-term model in terms of S_{21} and S_{12} dynamic range in direct comparison to both the srVNA architecture, using the same 7-term UOSM error correction, as well as both architectures using the same basic 10-term SOLT correction of the same dataset in Fig. 2.150. This results in a distinct advantage of the srVNA topology for 7-term UOSM measurement, despite the aforementioned efficacy reduction due to the stimulus generator cross-talk. The obvious dynamic range impairment of up to 20 dB demonstrated for the sVNA test-set topology using the 7-term error model error correction is a well-known phenomenon for classical full receiver VNAs, which is caused by minor model violations by the test-set hardware ([49]).

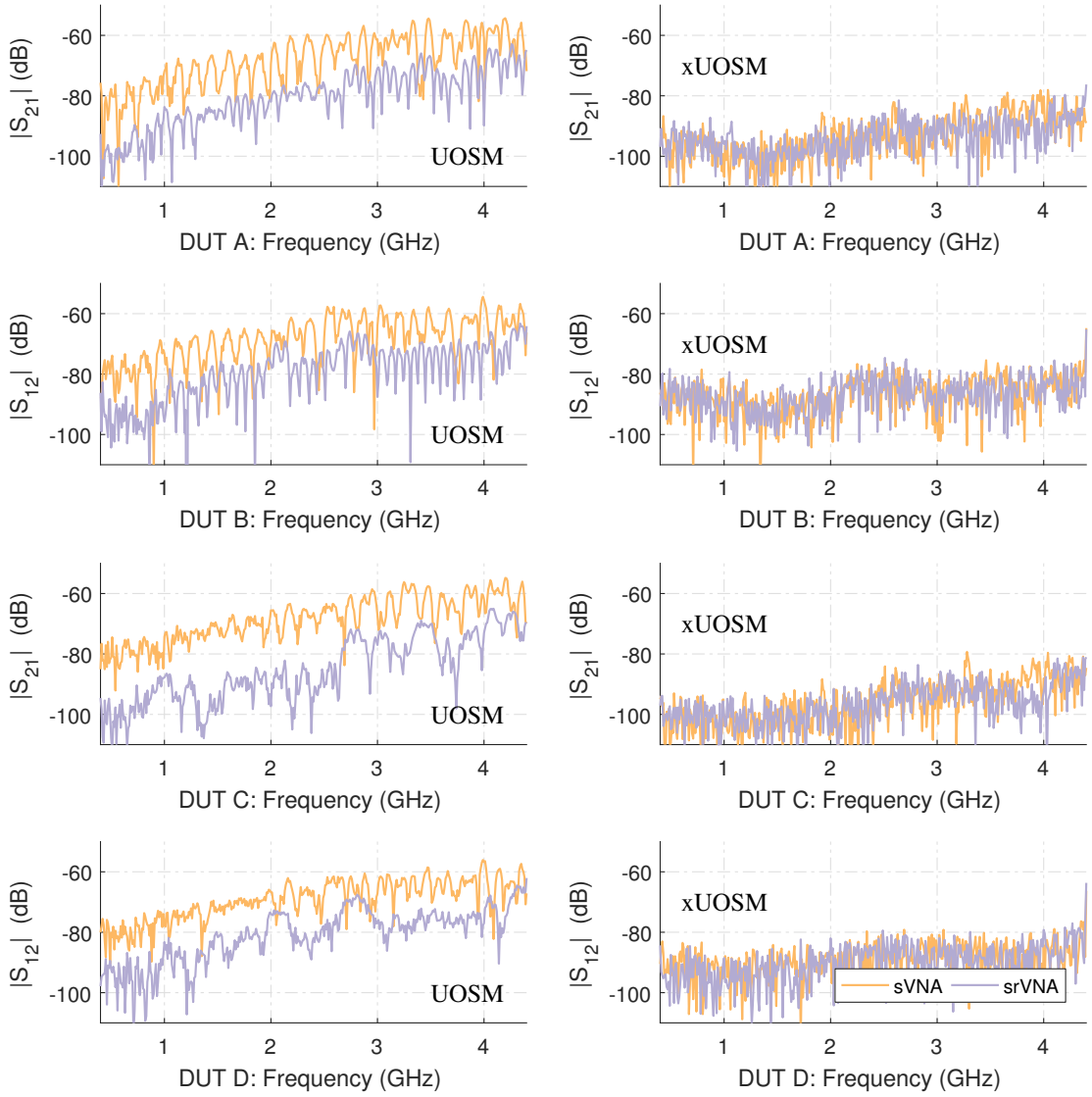

Figure 2.161: Measured S_{21} and S_{12} isolation figures obtained during the ripple test and direct residual directivity measurements, corrected by the UOSM 7-term and the 7-term xUOSM procedure for both the sVNA and the srVNA double reflectometer test-sets. DUT A: Port 1, 150 mm $Z_L = 50\,\Omega$ bead-less airline terminated by the calibration short. DUT B: Port 2, 150 mm $Z_L = 50\,\Omega$ bead-less airline terminated by the calibration short. DUT C: Port 1, 150 mm $Z_L = 50\,\Omega$ bead-less airline terminated by the calibration match. DUT D: Port 2, 150 mm $Z_L = 50\,\Omega$ bead-less airline terminated by the calibration match.

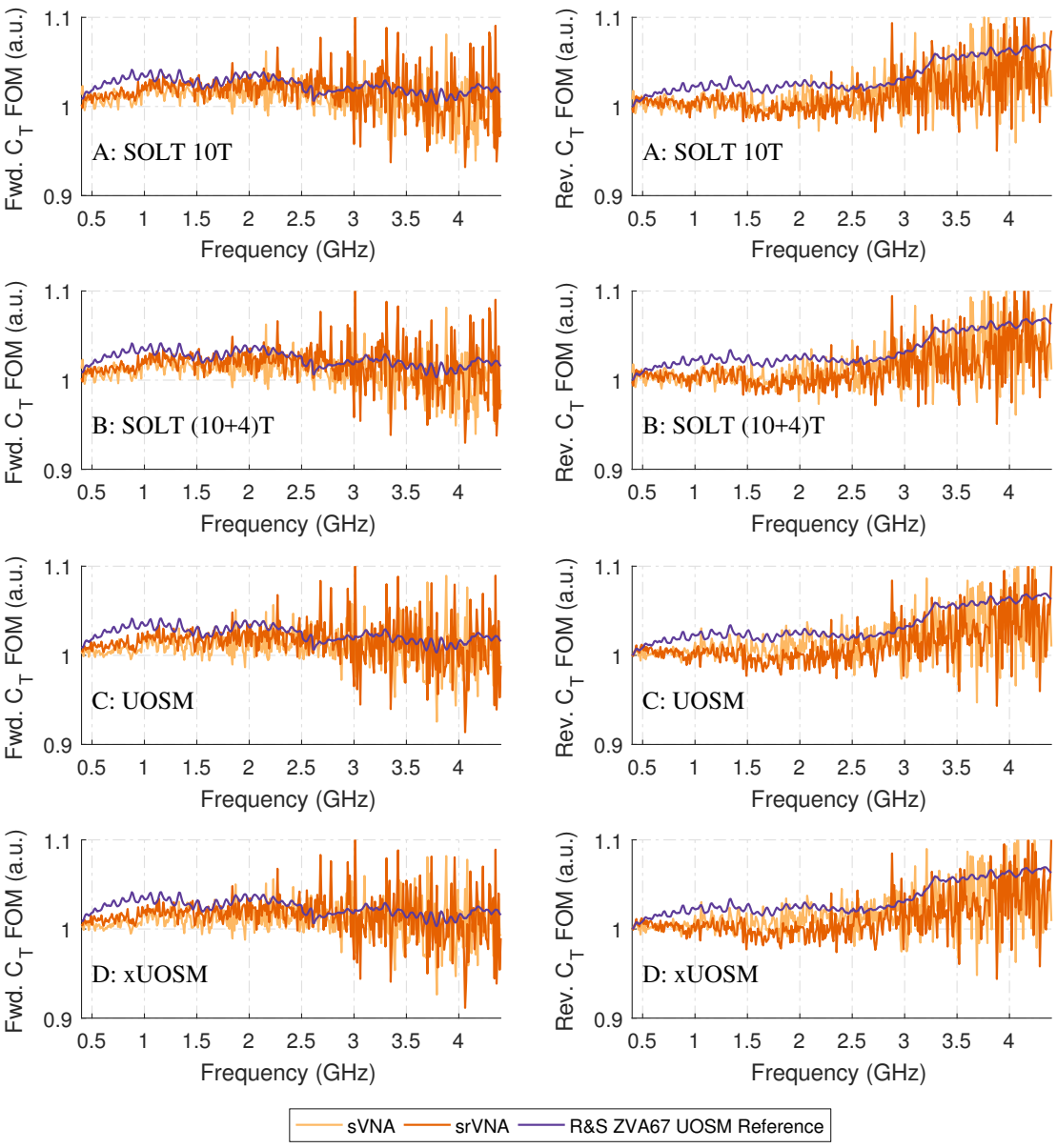

Figure 2.162: Measurements results of the T-Check verification standard, corrected by the 10-term, the (10+4)-term, UOSM 7-term and xUOSM 7-term procedure for both the sVNA and srVNA double reflectometer test-sets.

The second important observation that can be made from the isolation measurements shown in Fig. 2.150 is, that the isolation gap between both single receiver test-set architectures in the 7-term error model is closed by the xUOSM 7-term extension. Using this new method results in almost exactly the same performance as demonstrated the (10+4)-term corrected results before, even for the sVNA test-set setup.

It can be assumed, that the 7-term model violations, and the accompanying dynamic range reduction for transmission measurements seen in the sVNA topology, are most likely caused by the state dependent cross-talk originating from the a_{1m} and a_{2m} reference waves upon the b_{2m} and b_{1m} measurements, which is heavily attenuated in the srVNA architecture, and corrected for by the xUOSM extension.

The first two-port measurement that is re-evaluated using the 7-term error model is the measurement of the T-Check standard. The results are shown as a comparison between all bidirectional error models and correction schemes in Fig. 2.161. While a distinct advantage can be observed for the 7-term based UOSM and xUOSM calibration methods in the C_T coefficient results in the analysis of the synthetic test-set measurement data, there is hardly any noticeable difference between the deviations shown for all the correction schemes in Fig. 2.161 present. The only minor visible difference is the slightly better performance of the srVNA architecture in the results obtained in the 7-term model reverse direction, when the original ΔC_T distance to the ideal result of $C_T = 1$ is considered as the reference. As the T-Check device used for this test is however assembled from discrete components, and therefore far from the ideal assumption of the three port model the T-Check device itself is based upon, these results alone remain inconclusive and no statistically significant differences between error models and correction methods, in contrast to the results of the numerical analysis, can be observed.

Exactly the same conclusions can be drawn for the results of the 7-term UOSM corrected bidirectional thru measurements of the $Z_L = 50\,\Omega$ 150 mm airline including the RPC-N calibration thru as an adapter, shown for the UOSM corrected data in Fig. 2.163 and for the xUOSM corrected data in Fig. 2.164, as well as the $Z_L = 25\,\Omega$ 150 mm airline measurement using the same adapter shown in Fig. 2.165 for the UOSM correction and in Fig. 2.166 for the xUOSM corrected measurement data. No noticeable deviation can be observed in all of these measurements for the S_{21} and S_{12} results of both DUTs.

The only exceptions to this fairly broad conclusion are the noticeable differences in the noise-floor for the S_{11} and S_{22} measurements carried out using the sVNA architecture in comparison to the srVNA topology, which are fairly distinct in the results shown in Fig. 2.163 and Fig. 2.164. This elevated S_{11} and S_{22} noise floor, while not immediately obvious, is also caused by the aforementioned and analyzed violation of the basic 7-term error model in the sVNA test-set. This phenomenon is a direct result of the to S-parameter interdependence created by the S- to T-parameter conversion, the matrix inversion calculation, and the subsequent T- to S-parameter conversion necessary for the 7-term error model calibration and correction process.

Next, all transmission linearity verification measurements of the various attenuators are also re-evaluated using the 7-term UOSM and xUOSM error and correction model. The results for the 3 dB, 6 dB, 10 dB, 20 dB and 40 dB attenuator thru connections can be found in appendix B of this work, starting with Fig. B.27 for the combined results

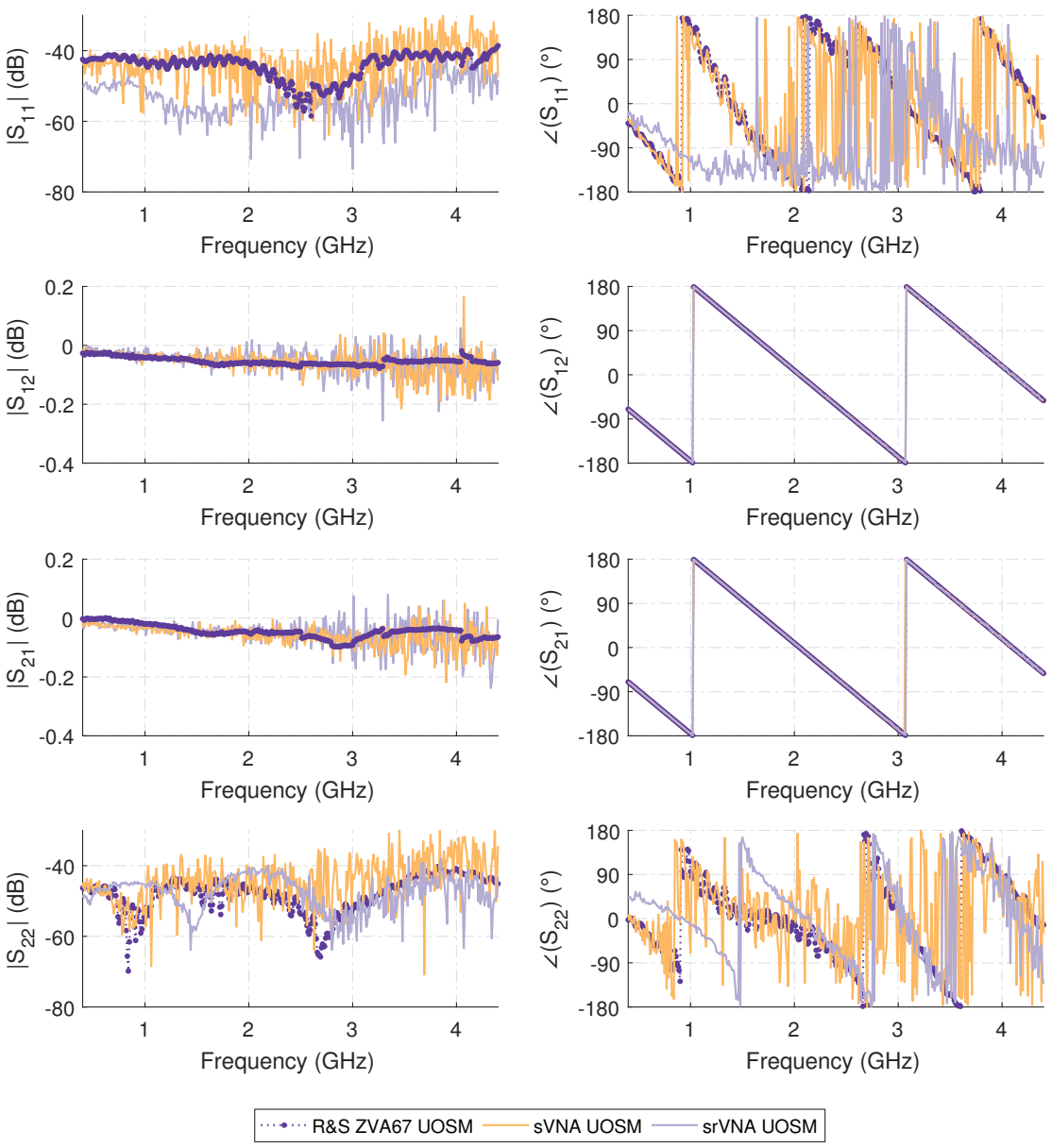

Figure 2.163: Measurement results of the 150 mm $Z_L = 50\,\Omega$ bead-less airline thru connection with the additional Rosenberger RPC-N (f)-(f) calibration thru corrected by the UOSM 7-term procedure for both the sVNA and the srVNA double reflectometer test-sets.

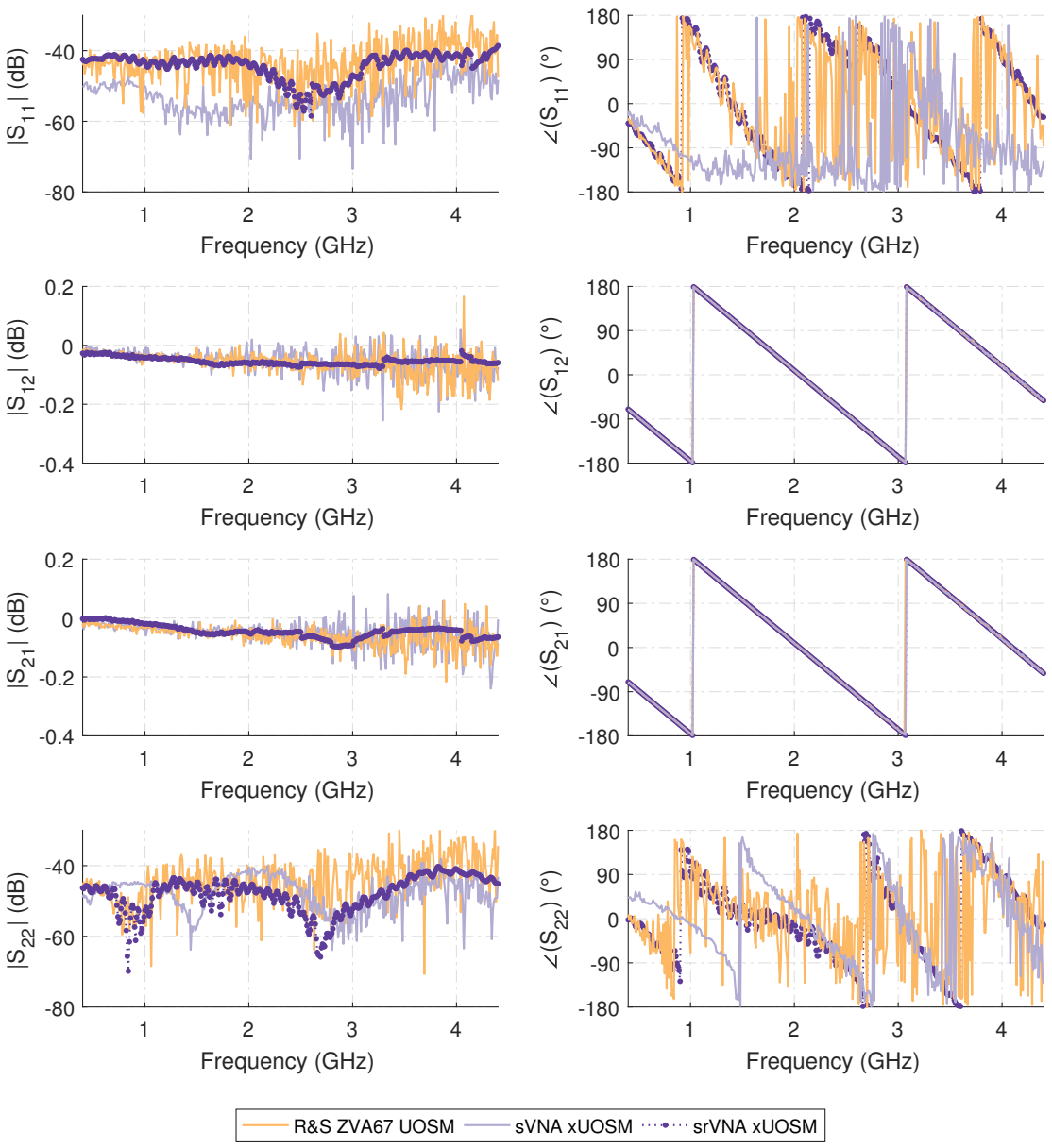

Figure 2.164: Measurement results of the 150 mm $Z_L = 50\,\Omega$ bead-less airline thru connection with the additional Rosenberger RPC-N (f)-(f) calibration thru corrected by the xUOSM 7-term procedure for both the sVNA and the srVNA double reflectometer test-sets.

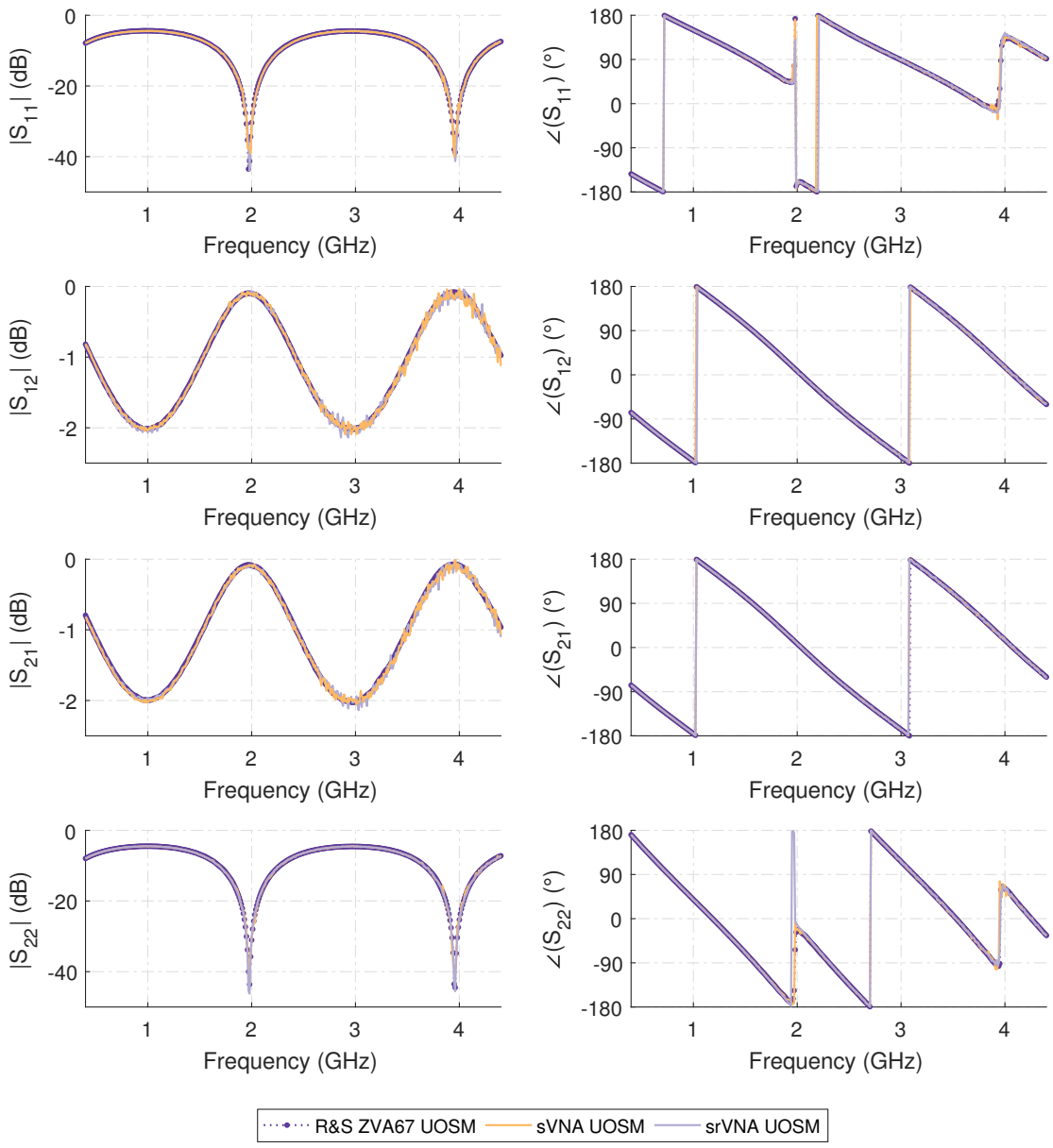

Figure 2.165: Measurement results of the 150 mm $Z_L = 25\,\Omega$ bead-less airline thru connection with the additional Rosenberger RPC-N (f)-(f) calibration thru corrected by the UOSM 7-term procedure for both the sVNA and the srVNA double reflectometer test-sets.

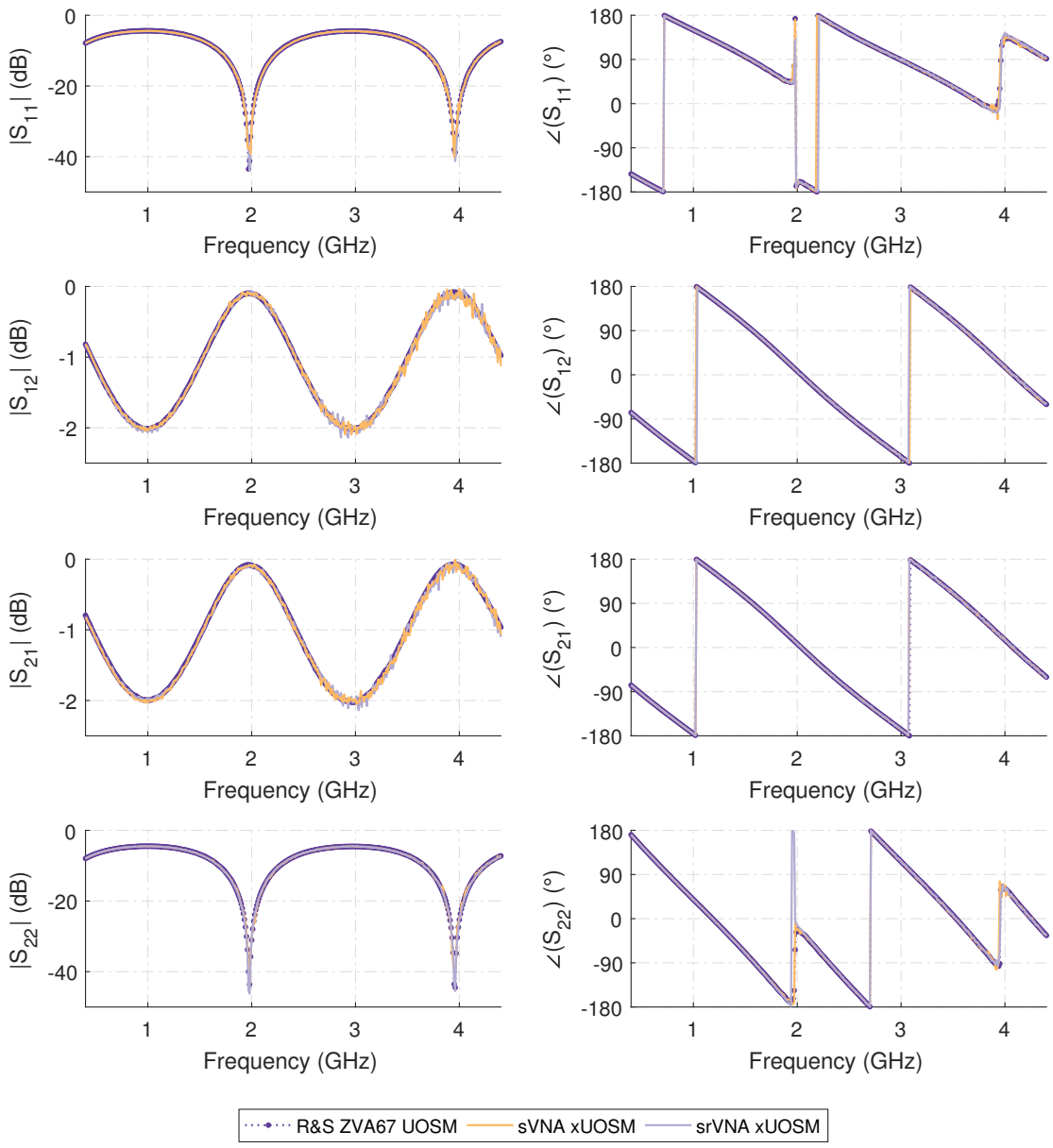

Figure 2.166: Measurement results of the 150 mm $Z_L = 25\,\Omega$ bead-less airline thru connection with the additional Rosenberger RPC-N (f)-(f) calibration thru corrected by the xUOSM 7-term procedure for both the sVNA and the srVNA double reflectometer test-sets.

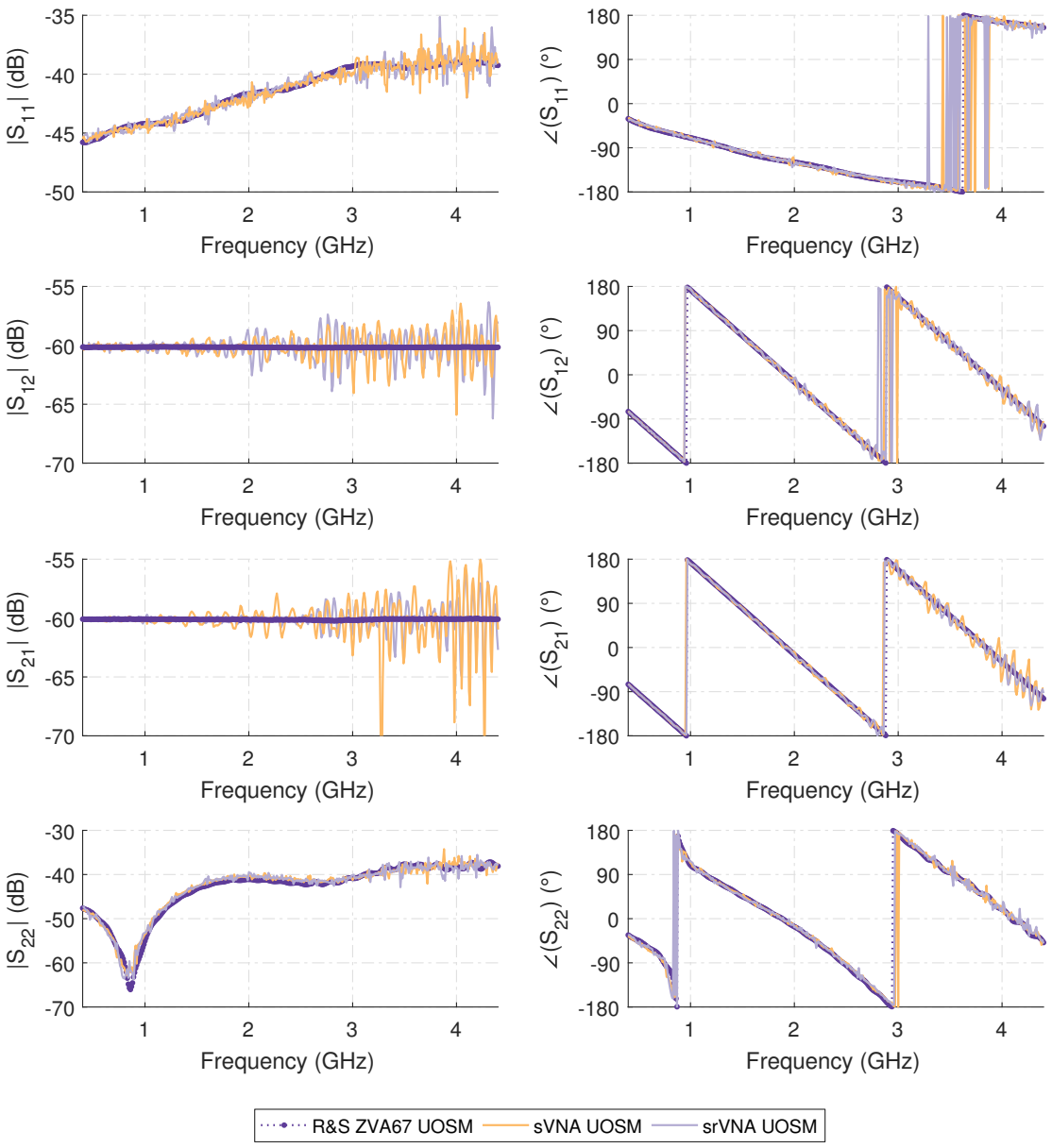

Figure 2.167: Measurement results of the combined 20 dB and 40 dB reference attenuators with the additional Rosenberger RPC-N (f)-(f) calibration thru corrected by the UOSM 7-term procedure for both the sVNA and the srVNA double reflectometer test-sets.

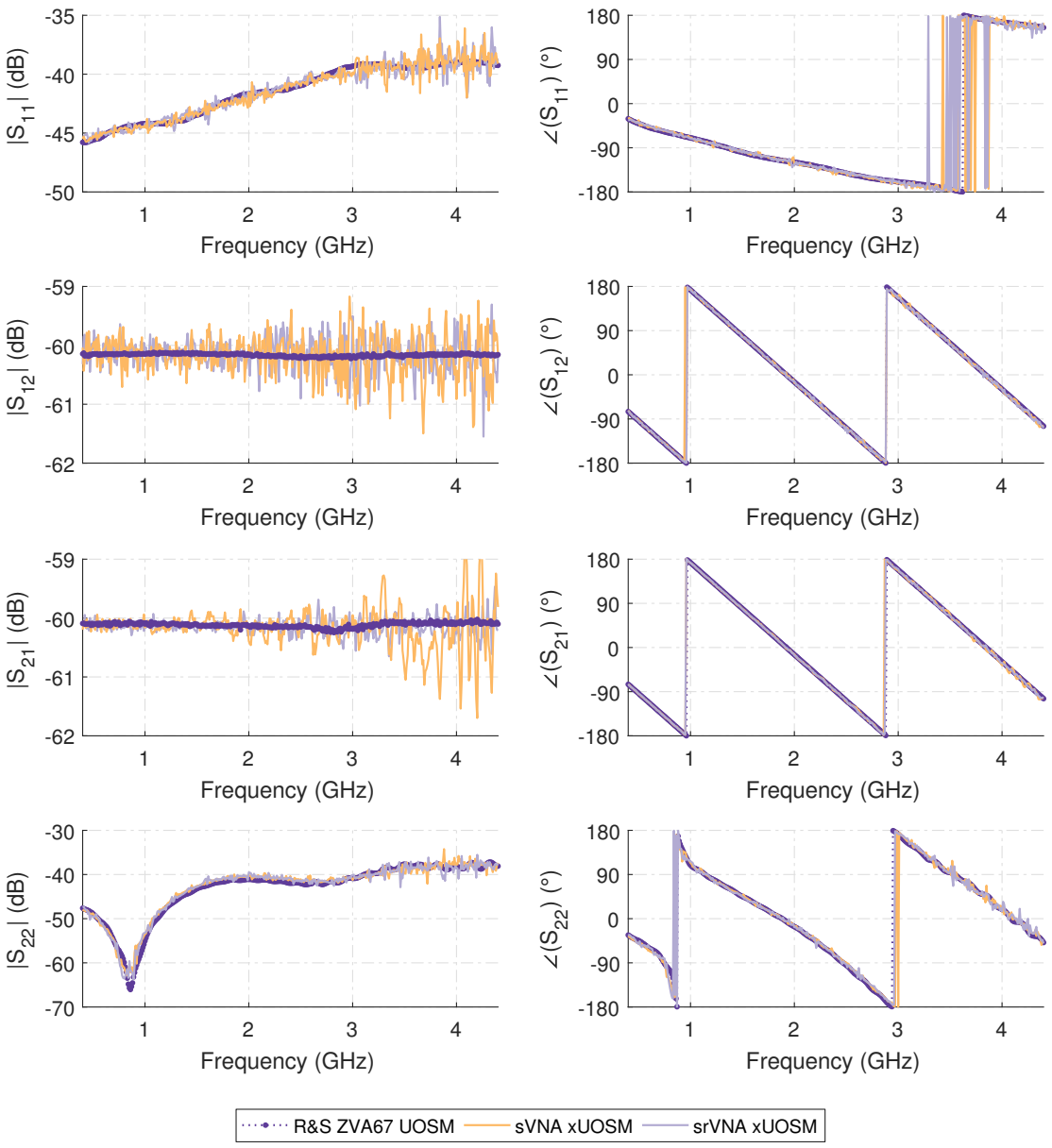

Figure 2.168: Measurement results of the combined 20 dB and 40 dB reference attenuators with the additional Rosenberger RPC-N (f)-(f) calibration thru corrected by the xUOSM 7-term procedure for both the sVNA and the srVNA double reflectometer test-sets.

of the SMA attenuators using the UOSM 7-term correction, and ending with Fig. B.38, showing the xUOSM 7-term corrected results of the 40 dB RPC-N reference attenuator measurement.

In contrast to the nominal results of the lower attenuation value thru connections, the re-evaluated measurement results of the combined 20 dB and 40 dB RPC-N reference attenuators, shown for the UOSM 7-term corrected data in Fig. 2.167, and for the xUOSM corrected results in Fig. 2.168, allows the observation of an interesting difference in measurement performance between the two single receiver test-set architectures.

In the non cross-talk corrected 7-term UOSM error model results shown in Fig. 2.167, the already well-known pattern of elevated transmission measurement noise floor for the sVNA architecture can be observed in contrast to the results obtained with the srVNA topology. What is however more interesting to see, is the reflection tracking performance seen for both architectures in the $|S_{22}|$ measurement of the well-matched, high attenuation, DUT.

The reflection magnitude tracking shown in this $|S_{22}|$ measurement is well below the reflection measurement noise-floor observed in the 7-term $Z_L = 50\,\Omega$ 150 mm airline thru connection measurements and is consistent with the results obtained using the 10-term error model. While this effect is also observable in the $50\,\Omega$ airline thru connection results corrected by the 10-term model, it is far more pronounced for the sVNA 7-term error corrected results.

As no new measurements were performed for the UOSM and xUOSM corrected measurements and therefore no additional uncertainty is introduced by the mechanical repeatability of the standards and connectors and only a re-evaluation of the data in a different error model is performed, this leads to the conclusion, that the 7-term error model is far more susceptible to the cross-talk originating from the transmission wave quantities b_2 or b_1, depending on the stimulus direction, upon the reflectometer wave measurement quantities than the 10-term error model.

This conclusion is especially valid for the naive four-receiver sVNA implementation and put into perspective by the introduction of the reference wave switch test-set extension in the srVNA test-set topology, which reduces this effect considerably.

Furthermore, the effects of the increased cross-talk correction performance in the srVNA architecture using the 7-term model can be clearly observed in the xUOSM corrected results of the 20 dB and 40 dB RPC-N reference attenuator combination shown in Fig. 2.168.

While the results for the cross-talk corrected isolation measurements of the ripple test and residual directivity measurements, shown earlier in Fig. 2.161, seemed to be pretty much on par for both single switched receiver architectures, easily visible $|S_{21}|$ and $|S_{12}|$ error correction performance differences, clearly in favor of the srVNA topology, can be observed in this measurement.

The clear advantage for the srVNA topology for 7-term model based error correction is even more obvious in the results obtained by the re-evaluation of the bidirectional ARLT measurements, which are shown for the ARLT DUT using 60 dB of attenuation in Fig. 2.169 for the UOSM 7-term corrected data, while the 7-term xUOSM results are shown in Fig. 2.170.

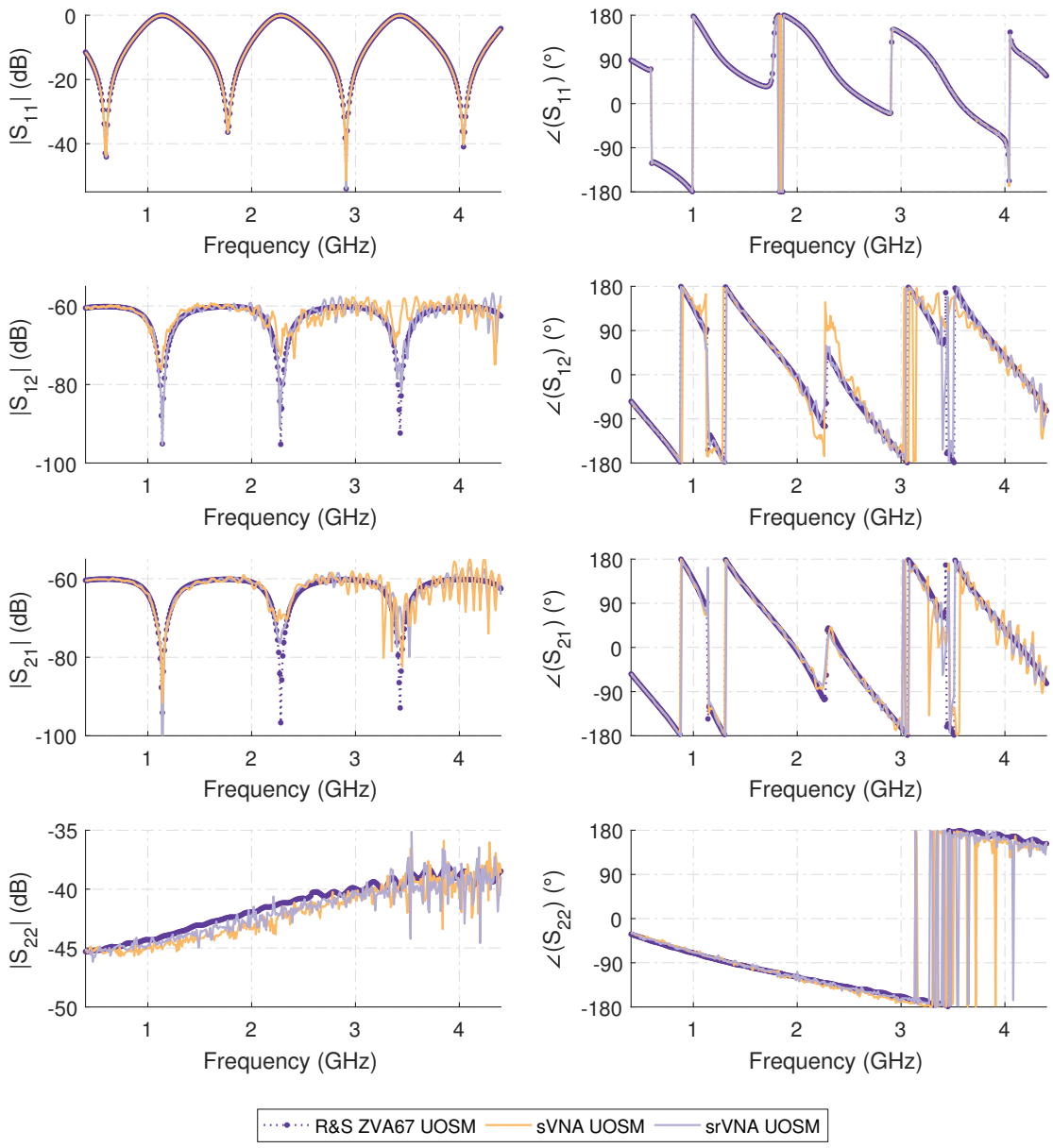

Figure 2.169: Measurement results of the asymmetric reflective lossy tee using the combined 20 dB and 40 dB reference attenuators with the additional Rosenberger RPC-N (f)-(f) calibration thru corrected by the UOSM 7-term procedure for both the sVNA and the srVNA double reflectometer test-sets.

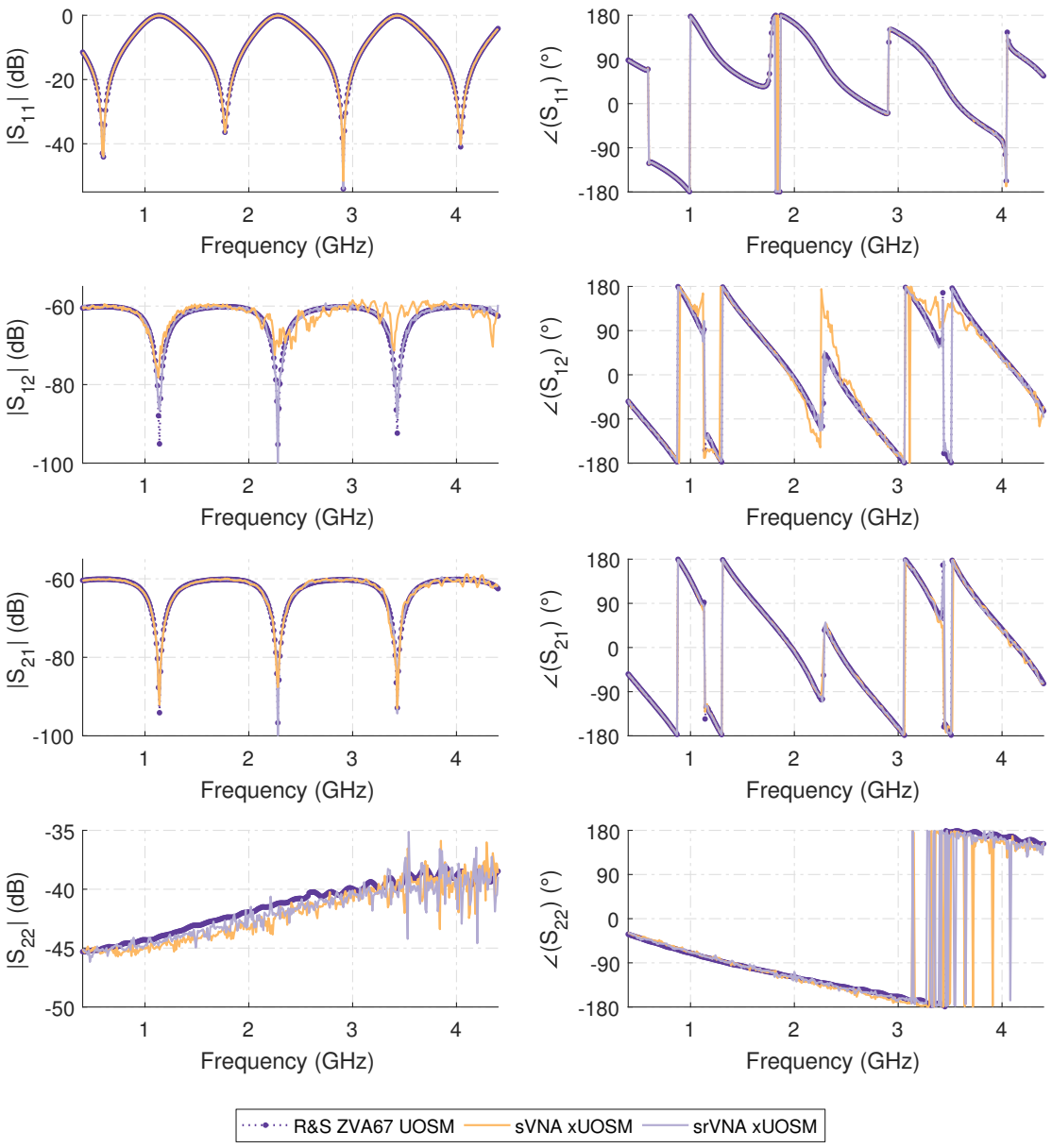

Figure 2.170: Measurement results of the asymmetric reflective lossy tee using the combined 20 dB and 40 dB reference attenuators with the additional Rosenberger RPC-N (f)-(f) calibration thru corrected by the xUOSM 7-term procedure for both the sVNA and the srVNA double reflectometer test-sets.

The additional ARLT measurements results, covering the 0 dB to 40 dB ARLT measurements, can be found in appendix B of this work, starting with Fig. B.33 for the 0 dB ARLT measurement using the 7-term UOSM error model to Fig. B.38, showing the 7-term xUOSM corrected results for the ARLT DUT using the 40 dB RPC-N reference attenuator.

By revisiting the ARLT measurements using 60 dB of attenuation, the distinct advantage in S_{21} and S_{12} dynamic range provided by the new srVNA topology in comparison with the sVNA test-set architecture can be easily observed. While the S_{21} and S_{12} tracking performance for the xUOSM corrected srVNA is excellent in the data shown for both parameters, severe signal to interference problems are obvious in the data acquired on the sVNA platform. While the sVNA S_{21} measurement, which is corrected using high SNR S_{11} data, can be successfully cross-talk corrected by using the xUOSM procedure, the S_{12} measurement, which uses the low SNR S_{22} data, fails to perform as well as the forward correction in xUOSM by a wide margin.

This observation made for the sVNA topology is heavily contrasted by the results obtained with the srVNA test-set architecture, which achieves comparatively close tracking of the S_{12} reference data shown in Fig. 2.170, even under these very adverse conditions.

Everything considered it can be concluded, that the srVNA architecture provides a better dynamic range an more accurate results than the sVNA test-set topology when the 7-term error model is applied as the error correction method.

While the two-tier calibration approach, which uses a SOLT calibration using the calibration standards shared with UOSM to solely acquire the switch terms and which is strictly necessary for the srVNA topology, may seem cumbersome at first. However it is important to realize, that the switch term correction coefficients are considered to be extremely stable and are often even supplied as a factory calibration with the device by the manufacturer for the latest generation of three-receiver two port VNAs ([142]).

No constant user re-calibration of these coefficients is necessary and the SOLT calibration required to obtain Γ_F and Γ_R must only be repeated when the frequency sampling points are changed and complex interpolation between frequency domain samples is not an option.

Therefore, the srVNA architecture is not limited to the UOSM procedure alone, but can use the whole family of Txx and Lxx 7-term calibration procedures (see [49]) to obtain the necessary coefficients of the model, especially for non-coaxial two port measurements.

Due to their similar formulation outside of the basic 7-term error model and the well proven long-term properties of semiconductor switches used as the foundation for the switch terms, the same coefficient stability assumptions should apply for the receiver input wave selector cross-talk correction method for the 7-term model presented in chapter 2.2.9 of this work, which also allows performing cross-talk corrected measurements using the Txx and Lxx calibration procedures, increasing transmission dynamic range and error model conformity.

Furthermore, the general formulation of the receiver input switch cross-talk calibration procedure, based upon two known reflection coefficients and the postulated isolation of the calibration standard, also allows for combinations of LLR or TRL calibration standards to be used for obtaining these coefficients, instead of the Match-Match Short-Match

combination used here. This could prove especially useful for planar measurements or higher measurement frequencies, where the fabrication of an adequate match standard is hard to achieve.

In combination, these two properties could prove extremely useful for further research, as the properties of correction the relevant receiver input switch cross-talk and the basis error correction are completely decoupled from each other, in stark contrast to the 15-term approach to the problem presented in [125].

In practice, a re-calibration of the basic 7-term error model can be performed without re-calibrating the switch cross-talk correction coefficients, which therefore uses a fewer number of calibration standards, measurements and operator time.

2.5.7 Switched Reference a-Wave Speed-Up Results

At this point, the competitive measurement capabilities of a single receiver vector network analyzer system in comparison with a classic full receiver VNA system are well-established. Due to the new correction methods and the switched reference wave test-set topology presented in chapter 2.2.11 of this work, the inherent dynamic range and accuracy impairments of this system simplification technique are reduced to a point which is comparable with mid-range off the shelf network analyzers.

There is however one important drawback still present which has not been addressed up until now: The measurement speed.

As outlined in the very introduction to the single receiver VNA concept, the description of the switch, and to further extent in [125], the basic operation performed by the sole receiver is the sequential scanning of all the required receiver input wave selector switch channels.

When this is compared with a classic full receiver architecture, where all receivers are generally sampled simultaneously, a simple catchphrase for the single receiver VNA could be formulated as: Trading cost for (measurement) time. When its assumed, that the PLL locking times are negligible and the data acquisition times between architectures are equal, the measurement speed penalty of a switched single receiver VNA architecture is proportional to the number of its virtual receivers, e.g. a virtual three-receiver SOLT architecture will only achieve 1/3 of the measurement speed of a normal fully equipped three-receiver SOLT VNA.

When the switched reference wave test-set technique was introduced in the theoretical section in chapter 2.2.11 of this work, the possibility of a faster single receiver VNA measurement by combining this test-set topology variant with TI repeatable synthesizers was mentioned as a side note as well.

The basic principle, which is exploited in this mode of operation, is the extremely high state dependent effective directivity offered by a decent high isolation semiconductor PIN-diode switch. In comparison, the effective directivity of the reference wave switch is at least one order of magnitude higher than the directivity offered by good transmission line couplers and more than two orders of magnitude better than the directivity offered by the resistive 2R-splitter commonly used in this application.

This high effective directivity of the a_i reference coupler, which is generally not necessary

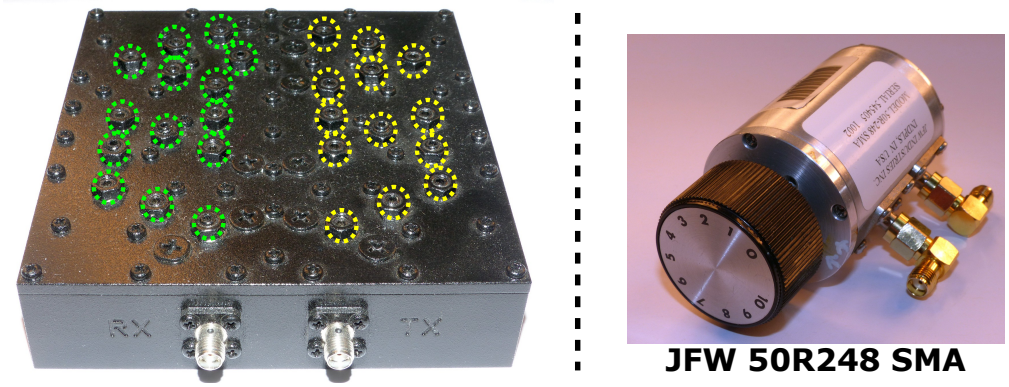

Figure 2.171: Left: WiMAX/IEEE-802.16 RX/TX cavity duplex filter and combiner for the 3.5 GHz band, tuning screws for adjusting individual cavity frequency responses and coupling factors highlighted. Right: 0 dB to 10 dB rotary step attenuator used as a repeatable DUT for the a-wave speed-up measurements.

at all in a classical VNA test-set setup, results in one important approximation: If the directivity of the reference wave coupler is higher than the effective source match of the calibrated system, no difference in a_i can be measured for time variant DUTs regardless of the change in input reflection coefficient, or b_1, presented by the DUT to the measurement port.

Therefore, the measurement results of a_i waves using the switched reference technique can be considered time invariant and constant, when TI repeatable stimulus, LO synthesizer and sampling clock signals are used throughout the VNA system.

In practice, this conclusion results in a significant speed-up of the single receiver VNA measurements, as only directly DUT dependent the b_i waves must be measured in consecutive sweeps, while the a_i waves must be only measured, considered from a realistic standpoint, on a drift correction basis. If an ideal system that shows no temperature dependent or other drift effects is assumed, applying this technique increases the measurement speed of the srVNA topology to 50 % of the full receiver hardware configuration.

To verify these assumptions, the measurement setup using the three-receiver 5-term srVNA configuration, shown earlier in Fig. 2.135, is used again to simulate the tuning procedure of a variable DUT, which is common in production environments for applications such as the manual or automatic adjustment of coupled resonator filters or microwave cavity filters to customer specifications. An example of a microwave cavity duplex filter, which is adjusted to specification using tuning screws under VNA supervision, is shown in Fig. 2.171.

While it would be tempting to use a real world example DUT for these test, the screw tuning procedure of the filter shown in Fig. 2.171 is not very repeatable for manual operation. Instead, a variable 10 dB step attenuator offering 1 dB step resolution is used as an alternative, more repeatable, DUT.

An analysis of the repeatability of the step attenuator, although not strictly necessary

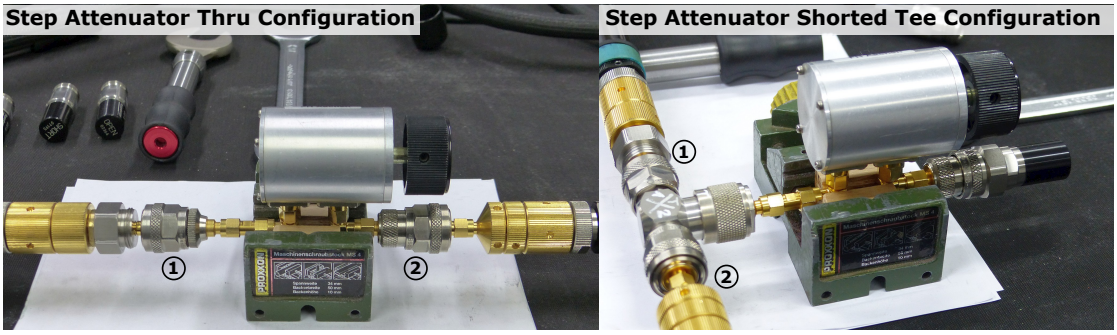

Figure 2.172: Picture of the two DUT configurations used for the step attenuator in the unidirectional srVNA a-wave speed-up technique measurements.

for the analysis of the a-wave speed-up procedure presented later, carried out using the ZVA67 VNA, can be found in appendix B of this work, spanning from Fig. B.43 to Fig. B.46.

In order to simulate DUTs with different S_{11} parameters, and therefore different a-wave interference properties, the repeated unidirectional measurements of the step-attenuator using various attenuation settings are carried out in two DUT configurations: The basic two port thru connection of the attenuator, which simulates the tuning process of a matched DUT, and a reflective shorted tee configuration, where the step attenuator is used as the variable element in a shorted transmission line stub. Both measurement configurations are shown, including the added mechanical support for increasing repeatability, in Fig. 2.172.

Before the measurement of both configuration are started, the srVNA system is allowed to reach thermal equilibrium judged by the values of the various internal temperature sensors in the stimulus synthesizer assembly, as well as the switched receiver module, to enhance the TI repeatability of both synthesizers. The equilibrium is considered achieved, when no variation of more than $\pm 0.2\,K$ over a time span of 60 seconds is observed for any of the internal temperature sensors. No active or passive temperature stabilization, such as a PID controlled thermostat heater, a temperature controlled cooling fan, or thermal insulating material or wrapping, is used.

The srVNA system is configured using the same configuration settings as presented and verified in the unidirectional single receiver VNA verification measurement section 2.5.4 and a (5+2)-term calibration (see chapter 2.2.5) is performed before the start of the measurement. A full switch scan over four inputs is performed for each measurement, therefore no real measurement time and data reduction is performed on the raw DUT data.

The synthesizers of the VNA system are used and configured in TI repeatable mode. Due to the frequency configuration, covering 400 MHz to 4400 MHz with 401 points, and a PFD frequency of 10 MHz, the stimulus synthesizer is running in pure Integer-N mode, while the LO synthesizer in the receiver must use its Fractional-N synthesis mode, combined with the phase re-sync procedure, due to the required ±8 MHz frequency offset

necessary for direct conversion to the IF frequency.

The measurements of the tee and the thru configurations are carried out using the following DUT tuning pattern: The attenuator is rotated to its initial 0 dB position and the first measurement is performed. The attenuator setting is then advanced by 1 dB and another measurement is started. This process is repeated until the 10 dB setting is reached, resulting in 11 measurements for all the different attenuation settings.

Then the attenuator is switched back all the way to its initial 0 dB reference position setting and the process is repeated for an additional 4 cycles, yielding a total of 55 measurements, which are completed in 21 minutes for the thru measurements performed first, and 22 minutes for the tee measurements performed subsequently. Therefore, one complete tuning cycle, covering 0 dB to 10 dB, is completed in approximately 4.5 minutes.

The raw measurement results are post-processed and error corrected using the (5+2)-term error model in three different ways:

- Each raw $S_{11,m} = b_1/a_1$ and $S_{21,m} = b_2/a_1$ parameter of the DUT is calculated using its related concurrent a_1 wave measurement, as usual. These S-parameters are used as the reference.

- A first step of post-processing measurement time reduction is performed by generating a set of raw $S_{11,m}$ and $S_{21,m}$, which is only referenced upon the first a_1 measurement of a cycle, i.e. the a_1 measurement of the 0 dB attenuator position. The (5+2)-term error model corrected results of these S-parameters are additionally indexed Ri for referenced intermediate.

- Finally, a third set of $S_{11,m}$ and $S_{21,m}$ parameters is calculated, using only the very first a_1 measurement of the initial 0 dB attenuator measurement for all 54 subsequent measurements, spanning 5 complete tuning cycles. The (5+2)-term error model corrected results of these S-parameters carry the index $R0$.

The results of these different post-processing steps is shown in the following figures using delta plots. These highlight the differences resulting between the concurrently a_1 referenced and error corrected S-parameter results and the measurement results of the S-parameters referenced to either the first a_1 measurement of the cycle or the very first a_1 measurement performed in the whole series.

The full S-parameters for the a-wave speed-up technique post-processing, and the concurrently referenced measurement results, can be found for both the thru and the tee DUT configuration in Fig. B.47 to Fig. B.54 in appendix B of this work.

In the intermediately referenced measurement for the well-matched thru DUT configuration, shown in Fig. 2.173 and Fig. 2.174 for different and time sequential step attenuator settings, it can be observed, that the procedure perfectly works on short time spans, in this case approximately 4.5 minutes, for the last measurement performed on the 10 dB setting of the attenuator. The differences observed in both amplitude and phase follow precisely the pattern expected for a minute drift of the stimulus and LO signals in the time domain, resulting in small amplitude and phase differences, increasing proportionally with the measurement and therefore stimulus and LO signal frequency. The demonstrated

accuracy of the results is sufficient for all but the most demanding measurement tasks and completely acceptable for production test use.

These first results alone already confirm the viability and efficacy of using TI repeatable synthesizers in a single receiver VNA system.

Even if these results seem somewhat unimpressive at first glance, it is important to realize, that these results are not repeatable by performing this measurement with a normal VNA system using TI stable synthesizers for signal generation.

TI repeatable signal generation is not only sufficient, but required to repeat the results, regardless of the reference wave switch concept.

The results obtained for the well-matched thru DUT are confirmed by the intermediately referenced measurement results for the reflective tee DUT configuration, shown in Fig. 2.175 and Fig. 2.176. These measurements support the assumptions made about the high effective directivity achieved by the isolation provided by the reference switch concept, as all the measurements, which are progressively better matched with increasing attenuation settings of the step attenuator, are referenced to the a_1 measurement performed in the highly reflective 0 dB attenuation state of the shorted stub tee configuration and therefore the maximum interference state.

While some glimpse of DUT dependency can be observed in the results, manifesting itself in a ripple envelope pattern of the same frequency characteristic as the S_{11} magnitude of the shorted tee in its 0 dB setting, this effect is highly attenuated by the switch isolation and could not be repeated using a directional coupler instead of the reference wave switch in the test-set.

The deviation observed in the measurement results that use only the very first measurement of the a_1 wave for the whole subsequent 54 measurements over a time span of 21 min, shown for the thru DUT configuration in Fig. 2.177 and Fig. 2.178, is also pretty remarkable, considering the fact that no active stabilization measures other than allowing the VNA assembly to warm up to thermal equilibrium were performed.

While some deterioration in performance is visible in comparison with the intermediate referenced results, the demonstrated repeatability is quite surprising and allows for a significant acceleration in measurement speed, when the effective duty cycle $D \leq 1\%$ for the a_1 wave measurement over the whole measurement time is considered.

The results obtained for the deviation of the initially referenced S-parameter data using reflective tee DUT configuration, shown in Fig. 2.179 and Fig. 2.180, follow the same reasoning. While the deviation observed here is by far the worst of all data-sets, it still remarkable that this level of repeatability could be achieved. The resulting measurement data is still usable in a general measurement context, although with the phase deviation exceeding 10° in the extreme, the drift approaches a regime that is relevant and noticeable in some automatic measurement and production test scenarios.

All in all, a new method of single receiver measurement time reduction by using a high isolation switch instead of a coupler for the reference wave and the successful application of the synthesizer TI repeatability in the developed single receiver VNA hardware was demonstrated for the classical network analysis. The remaining chapters of this work will focus new applications based upon and enabled by the TI repeatability characteristics of the synthesizers demonstrated here for the a-wave speed-up technique.

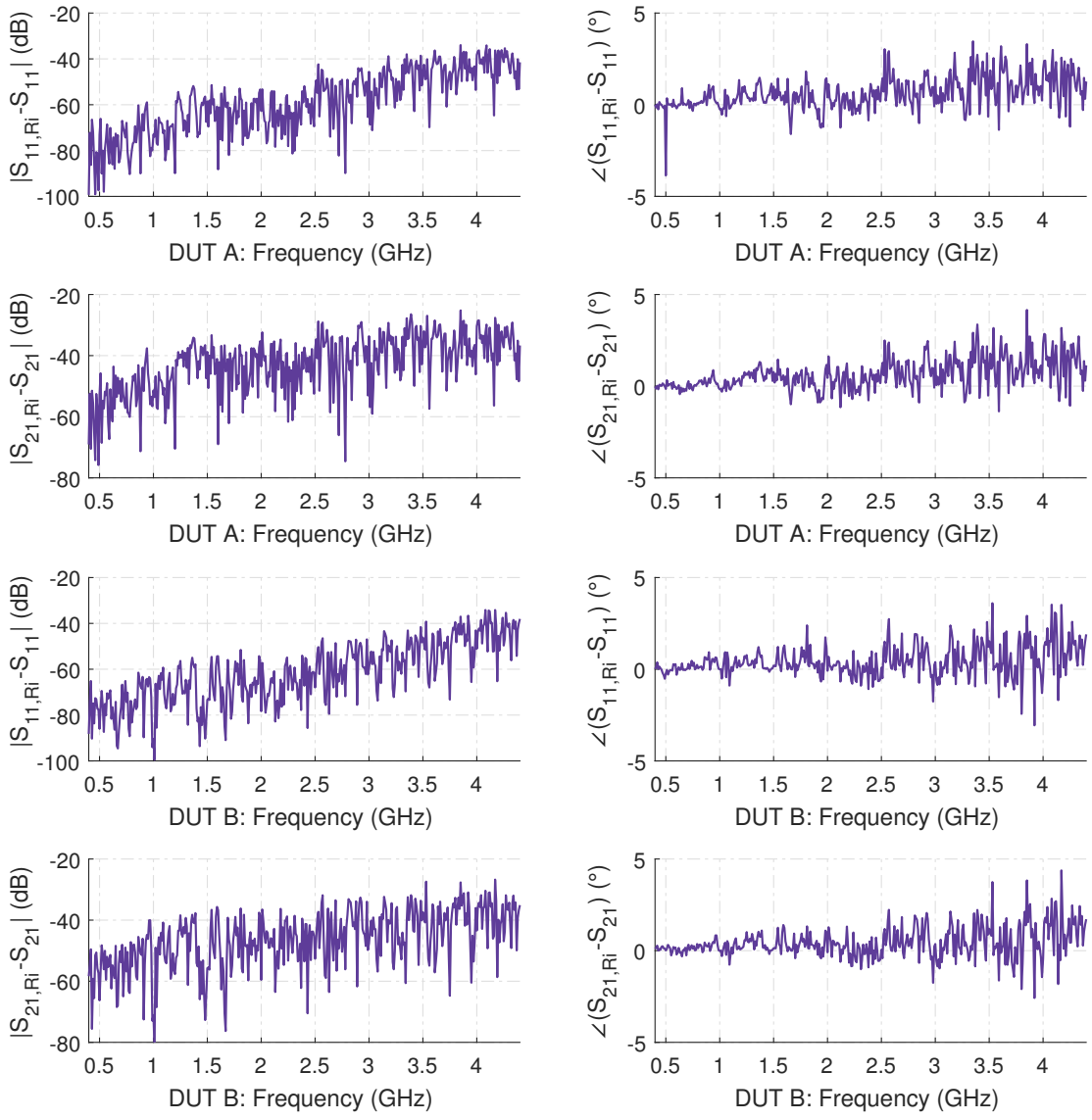

Figure 2.173: Differences in S-parameter results for the a-wave speed-up thru measurement DUT compared to concurrent a_1 measurement, referenced to first a_1 measurement of the cycle. DUT A - step attenuator 1 dB setting, DUT B - step attenuator 3 dB setting.

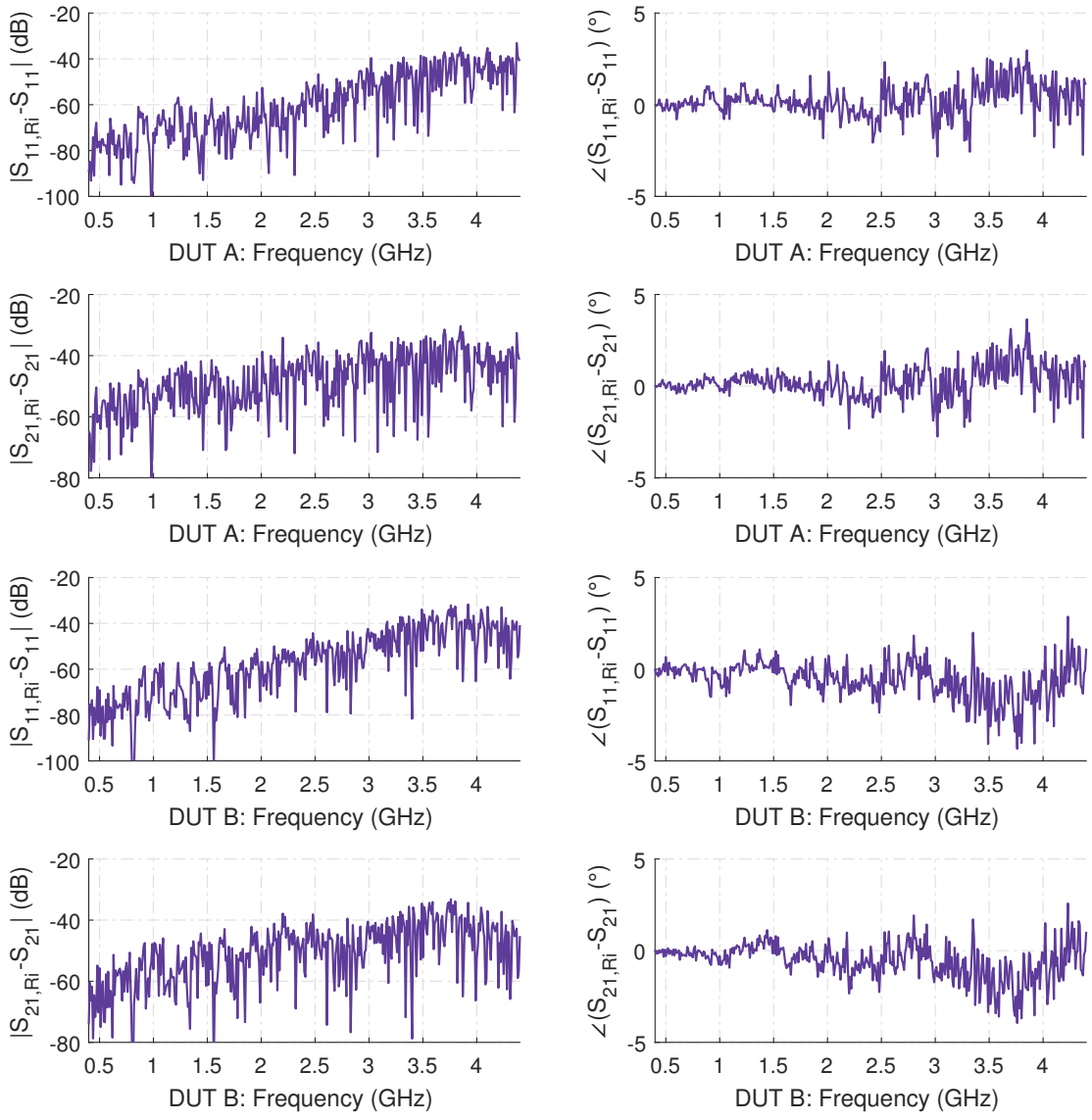

Figure 2.174: Differences in S-parameter results for the a-wave speed-up thru measurement DUT compared to concurrent a_1 measurement, referenced to first a_1 measurement of the cycle. DUT A - step attenuator 6 dB setting, DUT B - step attenuator 10 dB setting.

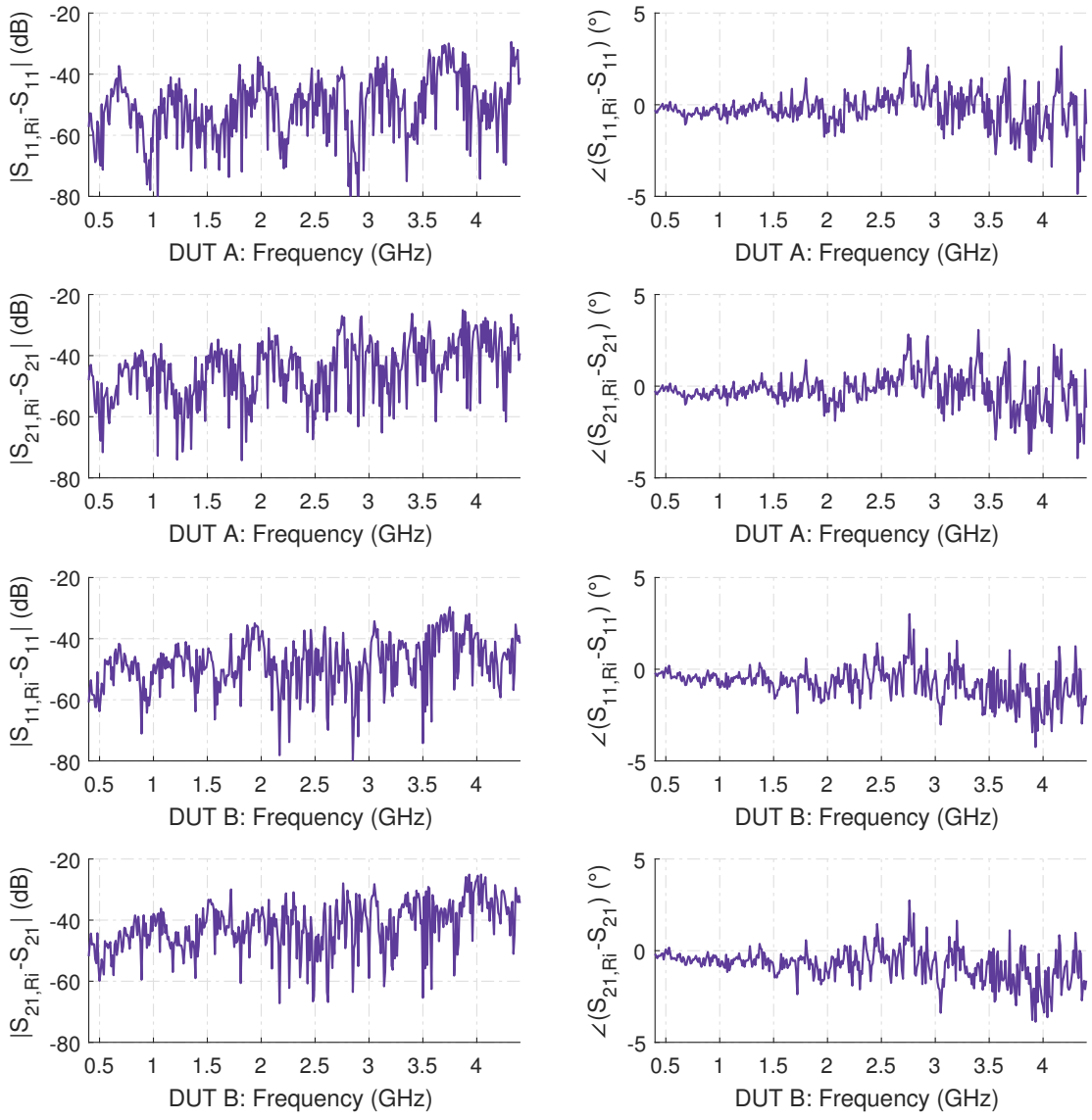

Figure 2.175: Differences in S-parameter results for the a-wave speed-up tee measurement DUT compared to concurrent a_1 measurement, referenced to first a_1 measurement of the cycle. DUT A - step attenuator 1 dB setting, DUT B - step attenuator 3 dB setting.

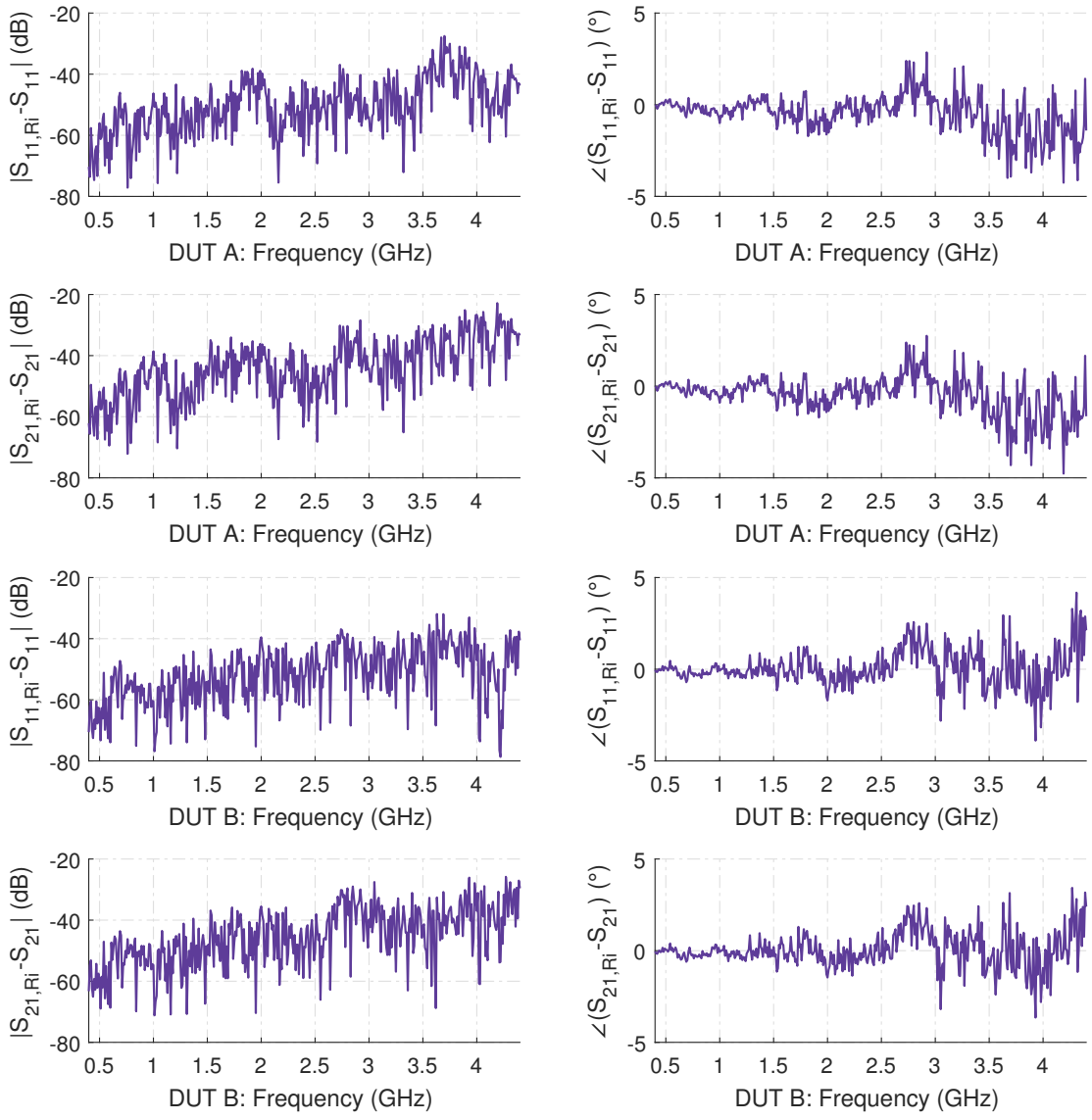

Figure 2.176: Differences in S-parameter results for the a-wave speed-up tee measurement DUT compared to concurrent a_1 measurement, referenced to first a_1 measurement of the cycle. DUT A - step attenuator 6 dB setting, DUT B - step attenuator 10 dB setting.

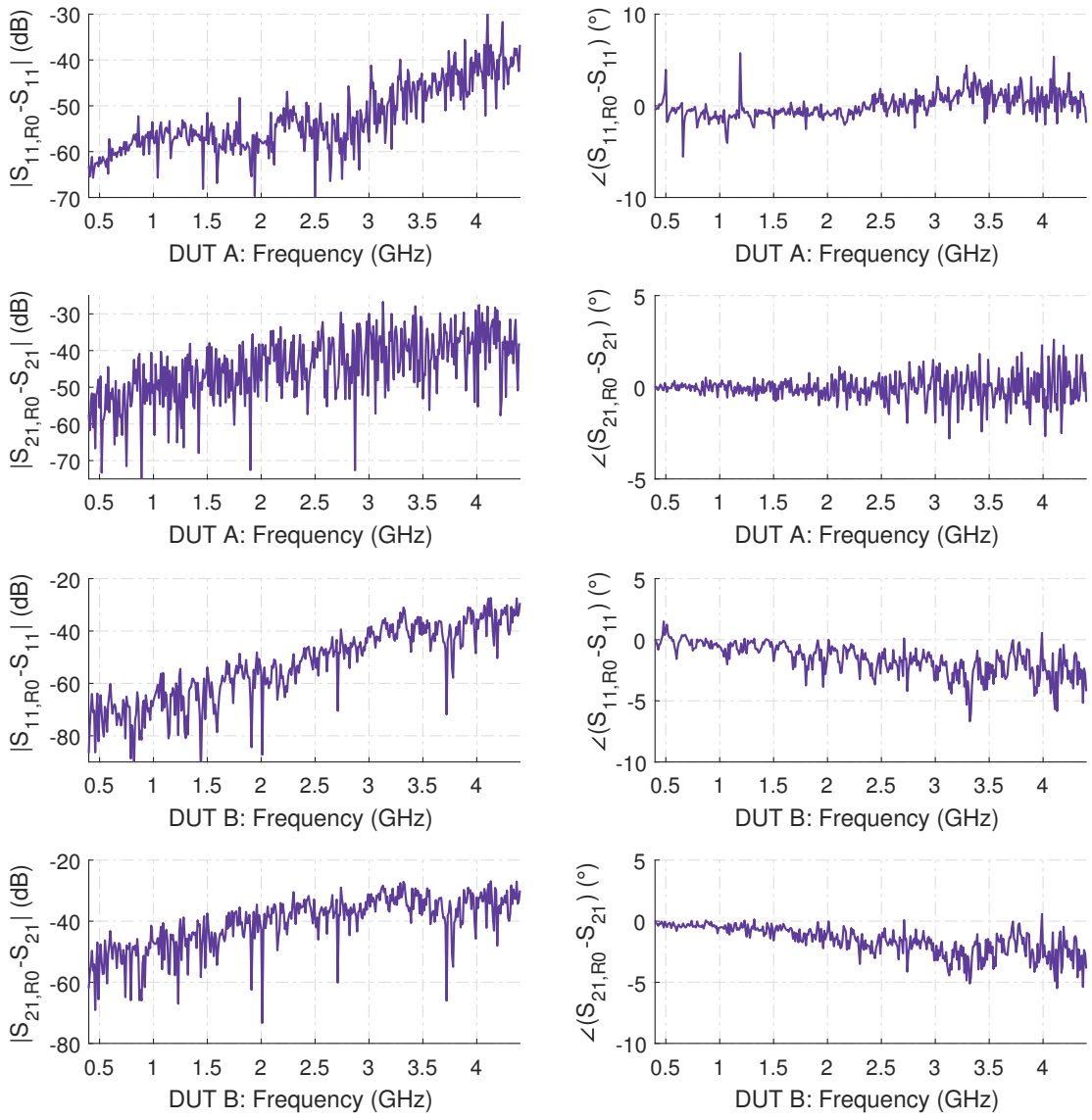

Figure 2.177: Differences in S-parameter results for the a-wave speed-up thru measurement DUT compared to concurrent a_1 measurement of the 5th and last tuning cycle, referenced to very first a_1 measurement. DUT A - step attenuator 0 dB setting, DUT B - step attenuator 3 dB setting.

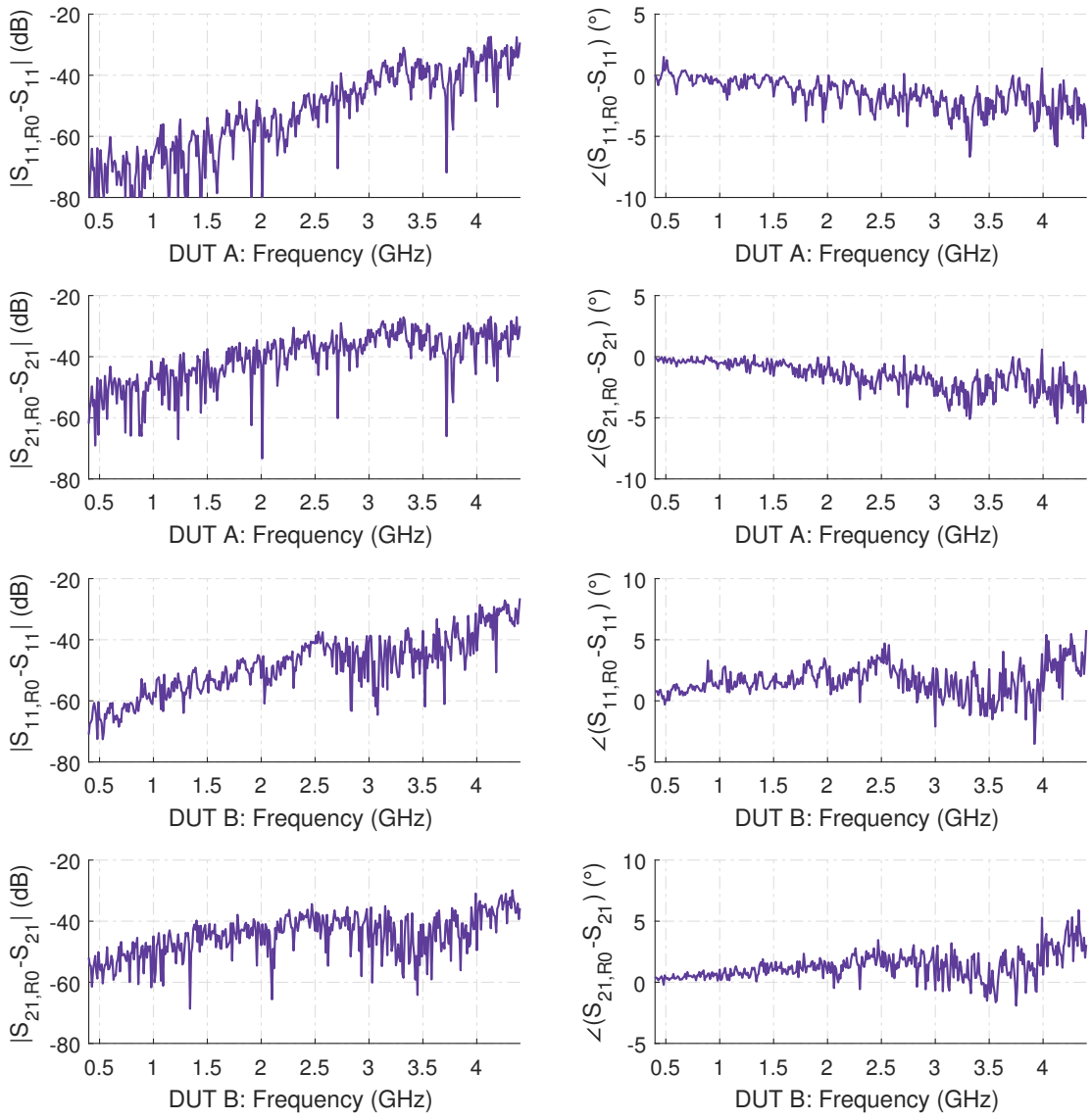

Figure 2.178: Differences in S-parameter results for the a-wave speed-up thru measurement DUT compared to concurrent a_1 measurement of the 5th and last tuning cycle, referenced to very first a_1 measurement. DUT A - step attenuator 6 dB setting, DUT B - step attenuator 10 dB setting.

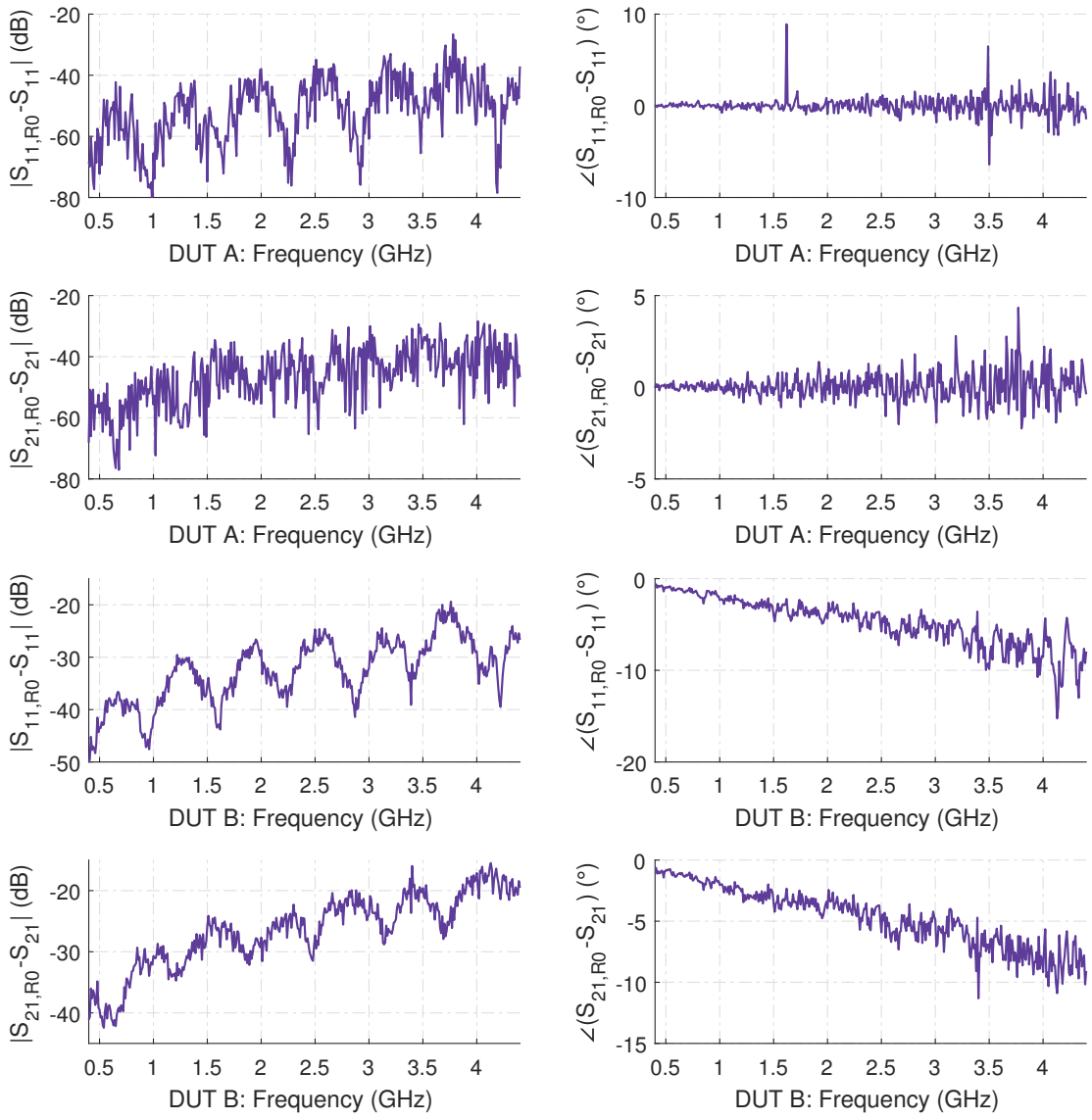

Figure 2.179: Differences in S-parameter results for the a-wave speed-up tee measurement DUT compared to concurrent a_1 measurement of the 5th and last tuning cycle, referenced to very first a_1 measurement. DUT A - step attenuator 0 dB setting, DUT B - step attenuator 3 dB setting.

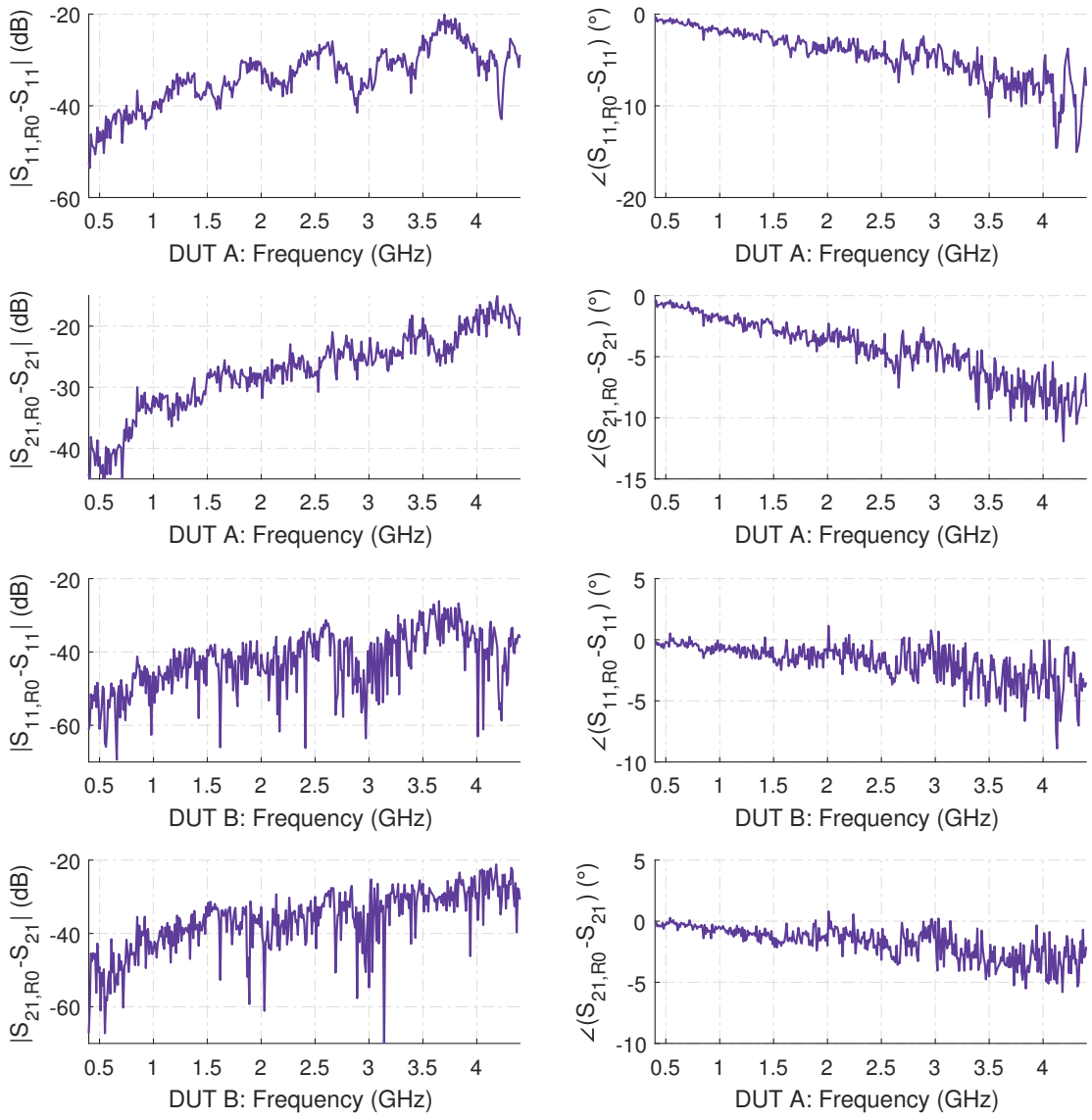

Figure 2.180: Differences in S-parameter results for the a-wave speed-up tee measurement DUT compared to concurrent a_1 measurement of the 5th and last tuning cycle, referenced to very first a_1 measurement. DUT A - step attenuator 6 dB setting, DUT B - step attenuator 10 dB setting.

3 TI Repeatable Synthesizers - A New Calibration Standard for NVNA Measurements

3.1 Introduction to NVNA Measurements

Up to this point in this work, only standard S-parameter measurements that are per definition only valid for measurements performed in the linear region of a DUT under small signal excitation were discussed and measured. While S-parameters are commonly used to describe the piece-wise linear transfer properties of active two- or multi-port DUTs such as MMIC amplifiers, they are only valid for one specific operating point of the device and only for small signal stimulus. In the case of amplifier circuits, the classical S-parameters can only describe a small, very specific, subset of the device's behavior. In practice, this generally results in a multitude of S-parameters files that are necessary for the description of an active device, which are captured under different operating point and stimulus drive conditions.

Another common non-linear device behavior, which is not covered in any way by the linear definition of the S-parameters, is the conversion of energy from one frequency to one or multiple other frequencies, which are generally harmonically related for a one-tone stimulus and mixing products for two-tone stimuli. This behavior is commonly found in frequency multipliers, mixers, and efficient amplifier designs beyond class B operation, such as highly efficient, switching amplifiers in class E/F configuration using tuned harmonic termination. When designing such devices, the classical S-parameters are practically of no use at all, as they can only provide a description of the energy balance at the DUT's terminals for signals which are of the same frequency as the applied stimulus signal of the VNA.

In order to describe and measure non-linear device behavior similar to the convenient S-parameters, two different problems have to be solved: On the one hand, a new description method of the terminal behavior of a DUT must be used instead of the linear S-parameters that is ideally able to describe and model all of its non-linear behavior. On the other hand, the VNA measurement system itself must be changed and modified to allow these measurements to be performed and work around the properties and limitations of the VNA hardware. Additionally, the existing error models have to be adopted to this new modus operandi, as they are also only based upon linear S-parameters and therefore can only capture and correct linear effects in the VNA error model for the same frequency as the stimulus signal.

At the time of writing, the de-facto industry standard and solution to all of these prob-

lems are the X-parameters extensively used by, and proprietary to, Keysight Technologies. While the name itself only suggest a non-linear replacement for the S-parameters alone, they are in fact a complete and closed ecosystem, starting with their very definition and description, the non linear VNA measurement equipment including their calibration and error models in the PNA-X line of VNAs, as well as the accompanying simulation and modeling software Keysight ADS.

The X-parameters are based upon the frequency domain polyharmonic distortion black-box modeling principle, introduced by Verspecht and Root in [116] and further explained in [152], and can be understood as a large signal, single and two-tone stimulus, non-linear extension to the S-parameters to capture non-linear behavior and the return loss and transmission characteristics of the DUT for the large signal stimulus and its harmonics. This non-linear device model can be used to simulate and capture non-linear effects such as harmonic generation, AM-PM conversion, non-linear gain characteristics, capacitance modulations effects resulting in signal voltage dependent behavior and non-linear effects caused by various long-term memory effects in the active components ([151]). The complete X-parameter description shares strong similarities with non-linear frequency domain harmonic balance simulations.

Due to the complexity of the polyharmonic distortion model and the underlying derivation of the Volterra series approximation of non-linear device behavior, no in depth explanation for the X-parameters will be given here and instead referred to [108, 115] for a complete derivation of the parameters and additional background information about non-linear active device behavior, including semiconductor memory effects.

Nevertheless, a short explanation for the X-parameter properties relevant to the required use of phase reference and calibration standards will be given, based upon the abstract presented in [4], following the nomenclature used by Agilent / Keysight for the wave parameters.

The relations between incident waves A_{ij} of dissimilar frequency and the resulting output waves B_{ij} of different frequency, at the terminals of a multi-port device, can be described using the X-parameters by

$$\begin{aligned} B_{ef} = X^F_{ef}(\mathrm{DC}, |A_{11}|) \cdot P^f + \sum_{g,h} X^S_{ef,gh}(\mathrm{DC}, |A_{11}|) \cdot P^{f-h} \cdot A_{gh} \\ + \sum_{g,h} X^T_{ef,gh}(\mathrm{DC}, |A_{11}|) \cdot P^{f+h} \cdot A^*_{gh} \ , \end{aligned} \tag{3.1}$$

where the subscripts e and g denote the port or terminal numbers of the multi-port DUT and subscripts f and h are used for the corresponding harmonic number of the spectral component. Besides the daring notation, it is easy to identify the DC operating point of the device and the amplitude of the incident, or stimulus, large signal component $|A_{11}|$, which by nomenclature is the power of the fundamental frequency ($f = 1$), measured at the fundamental frequency ($h = 1$), as the argument of all parameters. While the amplitude dependency of the three different X-parameters X^F, X^S, and X^T is quite visible, the phase information of the stimulus signal is somewhat hidden in the description, as it is conveyed by normalizing the phase information of all parameters to the A_{11} stimulus argument using $P = e^{j\varphi(A_{11})}$, which is important for the actual implementation of the

measurement as the response of the DUT is measured at all harmonics of interest relative to the phase of the stimulus signal.

Of the three X-parameters, only the X_F parameter describing the direct multi-spectral response of the DUT to the large signal stimulus tone A_{11} is intuitive. The X^S parameter is based upon the linear perturbation modeling approach, which captures the measured disturbance of the DUT's large signal operating point set by A_{11} to an additional small signal stimulus tone, while the other parameter X^T describes additional spectral responses of the device to model the phase of the output waves independent of the incident waves, but relative to the phase of the A_{11} large signal tone.

From a non-linear VNA system engineering point of view, the VNA test-set must integrate a mixed hybrid between a large-signal S_{11} measurement system and a Hot-S_{11} test-set to generate the necessary stimuli for all X-parameters at each port. While the large stimulus incident power is often only required at one port, an additional tone (in X-parameter nomenclature also called an extraction tone) of sufficient amplitude is necessary with or without additional simultaneous large signal stimulus present at the other ports.

While the X-parameters provide a very powerful and comprehensive way for describing the non-linear behavior of devices, their direct interpretation in regard to the measurement device topology required to capture the parameters is not intuitive at all. To understand the difficulties introduced by mixed frequency measurement on the VNA platform, it is far more useful to turn to the mixed frequency, or frequency translating, S-parameters introduced in [53], which are contained as a subset in the X-parameters for devices that are not operated in compression and do not show any memory effects. A complete set of conversion rules between X- and S-, T-, Z- and Y-parameters can be found in [29]. In contrast to the X-parameters, the mixed frequency parameter allow an approach to non-linear measurements more akin to the classical S-parameters.

In order to introduce the mixed frequency (MF) S-parameters and the accompanying measurement tasks performed by the non-linear VNA (NVNA), it is practical to introduce the parameter definition by looking at a simple real world example. If the task of characterizing a MMIC gain block in linear bias for its fundamental frequency (in the following denoted by I) S-parameters and the vector component of its second harmonic (denoted II) output and input reflection components as a function of the stimulus fundamental a_1^I in a unidirectional VNA configuration is considered, its mixed frequency parameters for the fundamental frequency can be described at the two terminals of the device by

$$b_1^I = S_{11}^{I,I} \cdot a_1^I + S_{12}^{I,I} \cdot a_2^I \,, \text{ and} \tag{3.2}$$

$$b_2^I = S_{21}^{I,I} \cdot a_1^I + S_{22}^{I,I} \cdot a_2^I \,, \tag{3.3}$$

which is identical to the standard S-parameter description, with the added (I, I) superscript denoting the target and source frequency as the fundamental frequency component, similar to the port notation used for the S-parameters. This can be simplified for the unidirectional measurements case, under the assumption of perfect VNA load match at

the second port, to

$$b_1^I = S_{11}^{I,I} \cdot a_1^I \,, \text{ and} \tag{3.4}$$

$$b_2^I = S_{21}^{I,I} \cdot a_1^I \,. \tag{3.5}$$

In order to describe the harmonic transmission and reflection response of the DUT to the fundamental frequency stimulus a_1^I, additional MF S-parameters following the same notation can simply be added by using

$$b_1^{II} = S_{11}^{II,I} \cdot a_1^I \,, \text{ and} \tag{3.6}$$

$$b_2^{II} = S_{21}^{II,I} \cdot a_1^I \,, \tag{3.7}$$

to define the frequency converting behavior of the DUT at its terminals, with $S_{11}^{II,I}$ denoting the complex reflection transfer parameter capturing the conversion from energy at the fundamental to the second harmonic and $S_{21}^{II,I}$ describing the complex transmission parameter in the same way, when also a perfect VNA load match for the second harmonic at a perfect single tone stimulus signal is assumed, which would otherwise introduce additional terms similar to the normal S-parameters for the linear behavior at the second harmonic into Eq. (3.6) and Eq. (3.7), i.e. $S_{11}^{II,II}$ and $S_{21}^{II,II}$.

While the mathematical description of the MF S-parameters is fairly straight forward, their measurement, even in this simple example, faces various challenges:

- The LO and the stimulus synthesizer of a VNA are generally not TI phase repeatable with respect to each other, therefore introducing an unknown phase error into the measurements necessary for Eq. (3.6) and Eq. (3.7) due to required receiver LO frequency change,
- The absolute magnitude or power of the a_1^I wave is not known at the calibration reference plane, and
- The 3-term error model of the reflectometer is normalized upon either the forward or the reverse tracking parameter due to linear dependencies in the model.

All of these points are addressed for normal VNAs by the Without-Thru calibration procedure, presented in [53], by modifying the 3-term reflectometer error model, which only includes the normalized forward and reverse reflectometer tracking coefficient $E_{RF} = E_R \cdot E_F$, to include an additional fourth coefficient and allows the separation of the E_{RF} coefficient into E_R and E_F. This separation is accomplished by using a calibrated amplitude and phase reference signal in combination with a power meter as two additional calibration standards to resolve both the linear dependencies in the reflectometer error model and the phase uncertainty introduced by the non TI repeatable LO and stimulus synthesizers.

While the concept of the quasi random LO and stimulus phase error $\Delta\phi$, introduced by Fractional-N frequency synthesis used in the synthesizers, may seem counter-intuitive

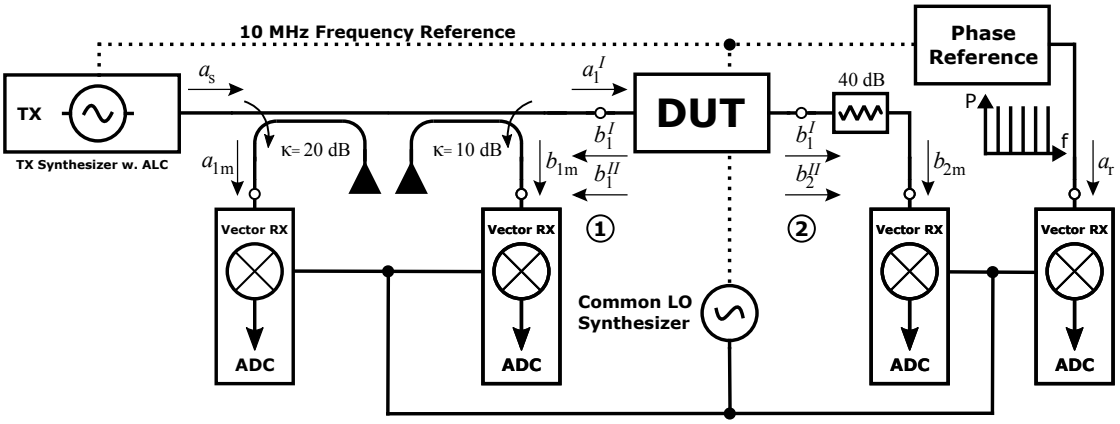

Figure 3.1: Schematic of an unidirectional mixed frequency non-linear VNA test-set setup using an online phase reference for LO and stimulus synthesizer phase error correction.

at first, it is easy to see from the expanded form of the single tone, or frequency, $S_{21}^{I,I}$ measurement

$$S_{21}^{I,I} = \frac{b_2^I}{a_1^I} = \frac{|b_2^I| \cdot e^{j\angle b_2^I} \cdot e^{j\Delta\phi^I}}{|a_1^I| \cdot e^{j\angle a_1^I} \cdot e^{j\Delta\phi^I}} = \frac{|b_2^I| \cdot e^{j\angle b_2^I}}{|a_1^I| \cdot e^{j\angle a_1^I}}\,, \tag{3.8}$$

that the phase error or offset $\Delta\phi^I$ just cancels out. If the LO frequency is now changed to the second harmonic in order to measure b_1^{II} or b_2^{II}, a new quasi random phase offset $\Delta\phi^{II} \neq \Delta\phi^I$ appears, which prohibits direct referencing of the measured waves when only TI stable synthesizers are used.

In order to prevent this phase error when measuring signals using the VNA receivers on frequencies independent of the stimulus frequency[44], two possible solutions exist for this architectural problem: The mathematically and equipment wise elegant solution of using only TI repeatable synthesizers for the stimulus and LO signals, as presented and used in the previous chapter of this work, or the addition of an external calibrated phase reference, connected to the 10 MHz frequency reference output of the VNA, with known and repeatable amplitudes and phases for its reference signal tones.

In addition to the phase reference standard, an otherwise unused vector receiver, connected to the same LO frequency source as the receivers used for the mixed frequency measurements, is necessary. This setup is shown in Fig. 3.1 for an unidirectional NVNA test-set setup, using a comb generator based phase reference standard connected to the 10 MHz reference signal, and a normal four-receiver double reflectometer VNA with direct receiver access to form the complete NVNA test-set.

When the measured wave quantities are then referenced upon the phase of the measured wave a_r, originating from the reference source with the same frequency as the measured

[44] This mode of operation is also often called arbitrary (receiver) frequency mode in the documentation of commercial VNAs.

wave quantity, the random phase offset error is canceled out again as shown in Eq. (3.8) and the wave quantities can be re-written as

$$a'_{1m} = \frac{a_{1m}}{a_r} \cdot |a_r|\,, b'_{1m} = \frac{b_{1m}}{a_r} \cdot |a_r|\,, \text{ and } b'_{2m} = \frac{b_{2m}}{a_r} \cdot |a_r|\,, \tag{3.9}$$

for the phase corrected, referenced, and measured test-set waves of arbitrary frequency which are now made TI repeatable. Nevertheless, several issues of this phase correction concept can be directly identified from Eq. (3.9): The accuracy of all measurements is now directly coupled to the TI characteristics of the phase reference, the TI properties of all components in the signal path, and the characteristics of the receiver in the VNA itself. This is especially true, when the propagation of errors due to the normalization of each wave quantity using the measured signal a_r is considered.

Therefore, it is important to provide a phase reference signal that is conditioned for the best SNR and measurement performance of the receiver without front-end overloading and compression to achieve a similar noise performance compared to normal S-parameter measurements in the phase referenced data. While this may seem a trivial task at first, it is important to realize that the phase reference sources in common use today are generally using a multi-tone frequency comb output signal which is especially troublesome in this regard. Due to the high peak envelope power and corresponding crest factor present in the frequency comb signal form, it is easy to overload the receiver front-end which in turn is limited by its multi-frequency IP2 performance. Unfortunately these IP2 products generated locally in the receiver are also harmonics of its respective fundamental frequency and therefore fall right upon other higher frequency phase reference comb components and diminish the signal to interference ratio, and in turn the overall measurement accuracy, of the reference signal rather quickly.

Now that the TI repeatability of the measured test-set wave components is established, the classical 3-term MSO model must be modified to allow for error corrected measurements of signals not originating from the stimulus synthesizer and its linear dependent model E_{RF} loop component, which is accomplished by the 4-term reflectometer error model for the Without-Thru calibration procedure shown in Fig. 3.2.

By analyzing the 4-term reflectometer signal flow diagram shown in Fig. 3.2 and using the phase normalized wave definition of Eq. (3.9), the wave relations can therefore be written as

$$\begin{pmatrix} a_1 \\ b'_{1m} \end{pmatrix} = \begin{bmatrix} E_F & E_S \\ E_D & E_R \end{bmatrix} \cdot \begin{pmatrix} a'_{1m} \\ b_1 \end{pmatrix}. \tag{3.10}$$

When trying to find a solution for Eq. (3.10) by connecting known reflection standards $r_x = S_{11A}$ to the reference plane, similar to the solution of the classical 3-term model, the resulting expression

$$m_x = E_D + \frac{E_F \cdot E_R \cdot r_x}{1 - E_S \cdot r_x} \;\Leftrightarrow\; m_x = E_D + \frac{E_{RF} \cdot r_x}{1 - E_S \cdot r_x}\,, \tag{3.11}$$

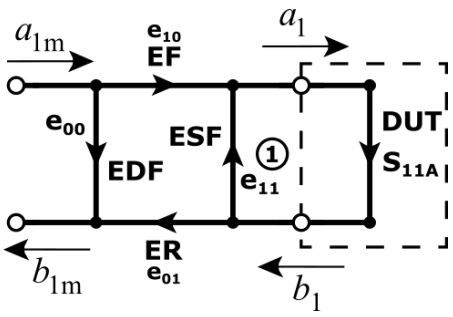

Figure 3.2: Signal flow diagram of the fully known 4-term reflectometer model with separated E_F/e_{10} and E_R/e_{01} coefficients for the Without-Thru mixed frequency calibration procedure.

clearly shows the linear dependence of the $E_F \cdot E_R = E_{RF}$ coefficients, which can not be separated in-situ without additional information outside of the reflectometer itself. Therefore the two additional calibration standards, the phase reference and the power meter, can now be used to separate both coefficients and gain individual E_F and E_R coefficient values for all frequencies of interest. The E_S and E_D coefficients of the error model are determined by the classic MSO calibration.

When a power meter is connected to the calibration reference plane, very accurate results for the magnitude $|a_1|$ of the DUT stimulus wave a_1 can be obtained by this instrument, which must be additionally corrected for the return loss Γ_P of the power meter (see [27]) to perform a source power calibration of the NVNA.

The power measured by the power head at the reference plane is calculated by

$$P_m = |a_1|^2 \cdot (1 - |\Gamma_P|^2)\,, \tag{3.12}$$

which can be rewritten by using the path for a_1 in the 4-term signal flow diagram (Fig. 3.2) and the first line of Eq. (3.10) as

$$\frac{P_m}{1 - |\Gamma_P|^2} = |E_F \cdot a'_{1m} + E_S \cdot b_1|^2\,. \tag{3.13}$$

By using the second equation in Eq. (3.10), this equation can be rewritten to get an expression for the magnitude of E_R in the form of

$$|E_R|^2 = |E_S \cdot (b'_{1m} - \Delta E \cdot a'_{1m})|^2 \cdot \frac{1 - |\Gamma_P|^2}{P_m}\,, \text{ with } \Delta E = E_S \cdot E_D - E_{RF}\,. \tag{3.14}$$

In order to get the phase argument required for determining E_R, a second output of the phase reference is now used to stimulate the reflectometer port with a wave a_r of known amplitude and phase, while the stimulus synthesizer of reflectometer is switched of. With the known, or previously 3-term measured, input reflection coefficient Γ_r of the phase reference, this results in

$$a_1 = \frac{b_1 - a_r}{\Gamma_r}\,, \tag{3.15}$$

for the wave a_1 at the calibration reference plane. Using the first line of Eq. (3.10) again to eliminate a_1, resulting in the expression

$$\frac{b_1 - a_r}{\Gamma_r} = |E_F \cdot a'_{1m} + E_S \cdot b_1|^2 \,, \tag{3.16}$$

which can be re-arranged for b_1, and combined with the second line of Eq. (3.10) to eliminate the last reference plane wave, resulting in

$$\angle E_R = \angle\left[\frac{1}{a_r}(b'_{1m} - b'_{1m}E_S\Gamma_r - E_D a'_{1m} + \Delta E\, a'_{1m}\Gamma_r)\right], \tag{3.17}$$

for the missing phase argument of E_R. Since E_R is now fully determined in its magnitude and phase, E_F can be simply calculated from its linear combination E_{RF} obtained via the 3-term MSO calibration in the form of

$$E_F = \frac{E_{RF}}{E_R} \,, \tag{3.18}$$

which completes the determination of all error coefficients in the 4-term error model. This process has to be determined for all frequencies of interest, including all of the required harmonics for the non-linear measurements.

The determination of the forward tracking term E_{TF}, which is necessary to augment the reflectometer model for unidirectional two-port measurements, can now be accomplished by performing the usual known or flush-thru calibration as in the standard unidirectional 5-term error model at all frequencies of interest.

3.2 Comb Generator Phase Reference Standards

Now that one of the basic calibration procedures for non-linear VNA measurements is introduced, one of the two required additional standards for non-linear measurement will be discussed in detail: The harmonic phase reference (HPR) calibration standard.

During the initial development of non-linear S-parameter measurement devices, which especially also includes the sampling oscilloscope and sampling mixer based large-signal network analyzers (LSNA, see [87] for reference), various methods were tried to establish a measurement standard that would allow for calibrated frequency converting measurements. This includes the development of various measurement instruments and topologies to allow for the capture of magnitude and phase information at arbitrary frequencies of interest, combined with an even greater number of different scalar and vector calibration procedures. A very good comparison between the different architectures and calibration options of this early period of non-linear measurement systems can be found in [150].

Most of the first non-linear measurement systems used a golden-diode or golden-device approach, where the approximately square-law non-linear transfer function characteristics of a specially selected and characterized diode under large signal excitation by the system itself are used, such as the early concept presented in [78]. Nevertheless, this approach was quickly dropped due to the lack of traceable calibration for the golden-devices combined

with the lack of repeatability between process batches inherent to the semiconductor manufacturing process.

Shortly afterwards, an approach based upon the characterization of a frequency comb generator using a sampling oscilloscope with traceable calibration and complex frequency response error correction was presented in [150] and its accompanying publications, which laid the foundation of non-linear network analysis using LSNAs and NVNAs as known today.

Most microwave frequency comb generators are built using the hyper abrupt switching characteristics of step-recovery diodes (SRD), or the non-linear, pulse compressing, transfer function of the varactor diode based non-linear transmission lines (NLTL), although other comb generators based upon high-speed ECL and LVPECL logic gates also exist for output frequencies below 10 GHz, as shown in [53].

In commercial products the NLTL based comb generators have completely superseded SRD based comb generators due to their performance advantages and GaAs manufacturing process compatibility with integrated MMIC components which allows a tight integration and therefore higher performance due to missing bond wire series inductance, which results in significant better performance than their SRD counterparts built from discrete components ([39]). The combination of a GaAs NLTL, low jitter dividers and wideband MMIC amplifiers integrated onto one single die also forms the basis for the U9391 series of comb phase references used in and together with the Keysight PNA-X series of commercial X-parameter capable NVNAs ([142]).

Nevertheless, SRD based comb generators are still actively researched today for harmonic phase reference applications due to their better accessibility when compared to fully integrated NLTL comb generators and will be used in the following discussion of phase reference standards, because of previous experience of the author with this comb references (see [47]) to explain their workings, and especially their shortcomings, in comparison with the new proposed phase reference standard presented afterwards.

As stated by the name, SRD based comb generators use the name giving type of microwave diode to generate an output pulse train with a repetition rate corresponding to the inverse of the input drive frequency f_D. Due to the extremely fast rise time of the output pulses, these can be approximately modeled as a chain of continuous dirac impulses in the time domain with a distance of $t_P = 1/f_D$, which in turn as stated by the Fourier transformation of a dirac pulse train in the time domain, results in a equidistant frequency comb in the frequency domain with $\Delta f = f_D$.

Step-recovery diodes are, as the name implies, characterized by their extremely fast transition from the reverse conducting state into an isolating high impedance state while under reverse bias which brought up their second common name snap-off diode in older microwave literature. For high frequency large signal stimulus every semiconductor diode shows the so called reverse recovery effect, caused by the lifetime and availability of minority charge carriers in the pn-junction region, which leads to a finite and ideally short reverse conduction time of the diode until these minority charge carriers have been either removed by drift, or by charge carrier recombination, from the junction region ([70]).

While this effect is generally very undesirable for diodes in normal switching, and

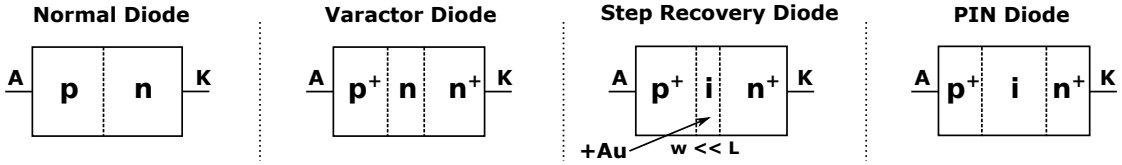

Figure 3.3: Silicon doping profiles of different common microwave diode types.

especially RF rectification applications in switch-mode power supplies, as it causes increased losses and lower system efficiency, the reverse recovery time in SRDs is artificially prolonged compared to other types of diodes by a special semiconductor doping profile as shown in Fig. 3.3 ([70]). By introducing an non-doped or intrinsic region between two highly doped p^+ and n^- regions, a lot of additional minority charge carriers are available for sustaining diode conduction under reverse bias, just as it is the case with PIN-diodes which also harness this effect for RF large signal insensitivity above a threshold frequency ([54]).

In contrast to PIN-diodes, which are built using a fairly long intrinsic doping region in the lateral direction, the doping geometry of SRDs is modified by keeping the intrinsic region very short[45], while also enlarging the contact area of the doping regions. This layer construction allows them to be still controllable via a large signal RF stimulus by reducing the minority charge carrier diffusion distance in contrast to the similar doped PIN-diodes, which require a DC current signal for control ([70]).

The effect of the hyperabrupt p^+in^- doping profile is furthermore enhanced with additional gold doping or electron beam irradiation of the intrinsic region to enhance the transient performance of the diode when changing from reverse conduction to its high impedance state, which is the main cause for the bad compatibility of SRD with other manufacturing processes besides the low transit frequency of silicon for MMIC circuits ([36]). The time required for the diode to change from reverse recovery conduction to its high impedance off state is also called the transition time t_T, which can be shorter than 50 ps for high-speed SRDs.

The time the diode is still conducting under reverse bias conditions is mainly determined by two factors: The minority charge carrier lifetime τ, which is a design parameter of the doping profile of the diode itself, and the time integral of the forward current applied during the forward-biased conduction state of the diode. Both the τ of the diode and the applied forward current have to be chosen for the fundamental frequency drive signal f_D to achieve maximum harmonic output power in a comb generator circuit. The charge Q_F, which is stored in the diode junction in the form of minority charge carries, can be approximated by $Q_F = I_F \cdot \tau$ and can therefore be influenced by the amount of large-signal stimulus current and an additional DC bias. This charge Q_F has to be removed from the junction during reverse bias to switch the SRD to its high impedance state. The removal of minority charge carriers is usually assumed to be performed at

[45] Short in this semiconductor context means shorter than the mean diffusion length L of minority charge carriers.

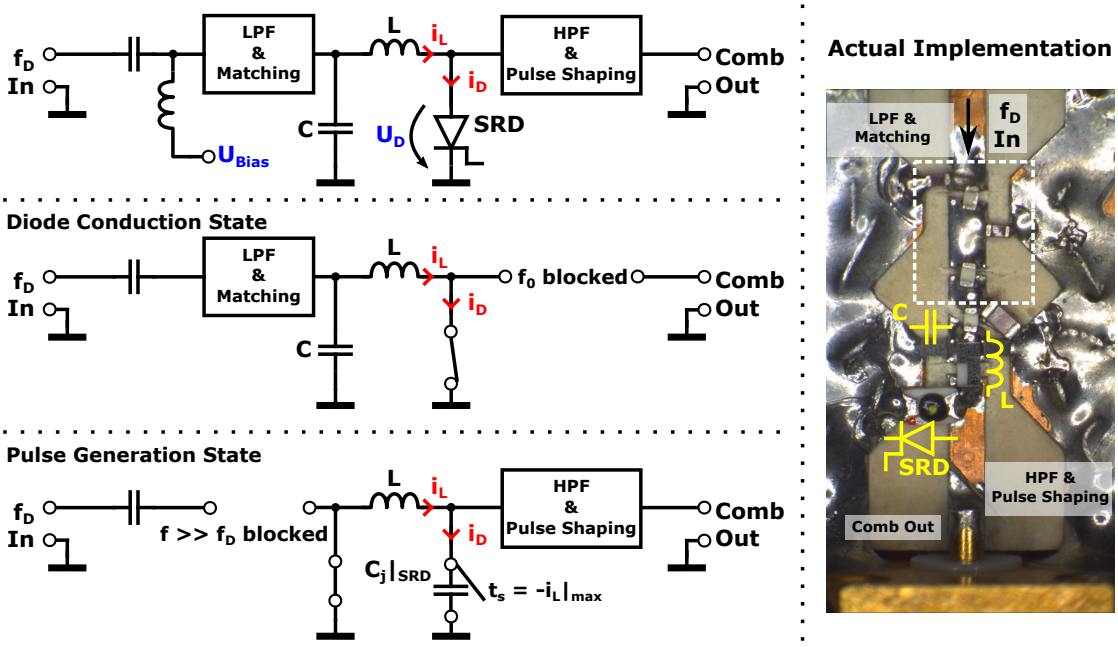

Figure 3.4: Left: Schematic of a basic SRD based comb generator including the two distinct states of the SRD. Right: Annotated picture of an actual SRD based comb generator implementation using a microstrip gap to implement the output HPF and pulse shaping network.

a constant rate by charge carrier recombination in combination with passive resistive biasing placed in a DC-return bypass path, but can be influenced to a certain degree, when an active external bias is applied to the diode ([47]).

With this information, the design of the comb generator itself is fairly straight forward and is shown in Fig. 3.4 without the power amplifier for the fundamental stimulus signal at f_D. In the phase reference application, this amplifier is usually required to boost the usually low power stimulus or reference signal to a power and amplitude level that can forward bias the SRD for a sufficiently long time at the required current to achieve optimum switch-off performance. Additional design guidelines, a more in depth analysis of the operation and a collection of empirical optimization guidelines for SRD comb generators can be found in [33, 43, 58, 59, 88].

Reflective low- and highpass filters, placed at the low frequency f_D drive input and the high frequency pulse output of the comb generator, are used to isolate the output from the high power fundamental frequency drive signal[46] and to isolate the drive network from the high frequency pulse to improve the conversion efficiency of the generator.

Due to the large signal switching action performed by the SRD, the comb generator circuits shown in Fig. 3.4 can be redrawn and separated into two distinct states, which also highlight the distinct functions of the two additional critical components of the comb

[46] A drive power of 17 dBm to 33 dBm at the fundamental frequency is common for SRD comb generators.

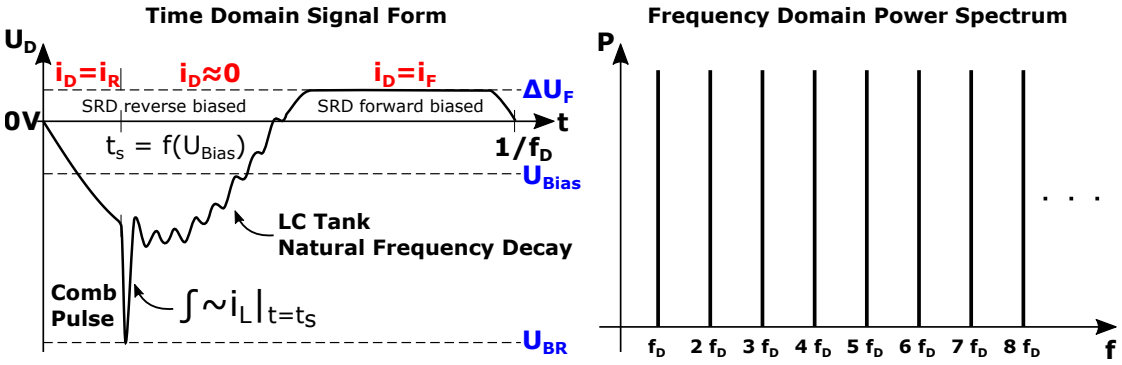

Figure 3.5: Time domain diode voltage over one cycle of the input signal of the step-recovery diode and frequency domain output power spectrum of the comb generator.

generator, the so called working inductor L and the shunt capacity C, in the circuit. While the SRD is forward biased and only the fundamental frequency is present, the highpass pulse shaping network blocks the fundamental frequency drive signal from reaching the generator output. The capacitor C and the working inductor L help to improve the return loss seen by the drive generator in addition to the impedance matching provided by the lowpass input network.

When reverse bias is applied to the diode, it is still conducting while the minority charge carriers are depleted at a constant rate, which is determined by the parameters of the diode and the DC bias network. When all charge carriers are removed from the junction area, the SRD abruptly changes into its high impedance state, as shown in the lower schematic diagram in Fig. 3.4. The exact time the switching operation occurs is determined by the amount of charge deposited into the diode in its forward conduction state by I_f, the minority charge carrier lifetime τ and the DC biasing. For the highest possible comb output power, the moment of the SRD conduction state change must coincide with the peak of the current i_L through the working inductor in the reverse bias cycle, because all the energy available to the output pulse itself is stored in the magnetic field of the working inductor L.

As shown in the diode voltage graphed over one cycle of the fundamental drive signal in Fig. 3.5, the abrupt change in current flow in combination with the energy stored in the magnetic field of the working inductor L generates the high voltage comb output pulse via the counter-electromotive force of the collapsing magnetic field up to the reverse break-down voltage U_{BR} of the SRD. The capacitor C, which is ideally a short circuit at $f \gg f_D$, provides the current return path for this pulse.

The time domain shape of this pulse, and therefore the amount and distribution of harmonic content in the frequency domain, is determined by the Q factor of the working inductor and its amount of energy stored in the magnetic field, the junction capacity of the SRD in its off-state and its reverse breakdown voltage U_{BR}, the associated highpass and pulse shaping output filter network of the comb generator, and unfortunately the return loss characteristics of the output load itself. An exemplary measurement of the

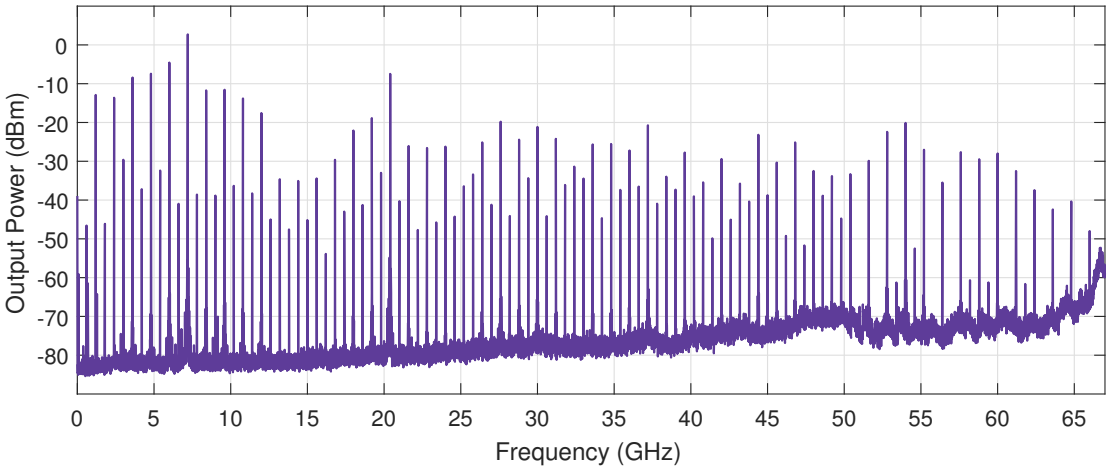

Figure 3.6: Measured exemplary output power spectrum of the step-recovery diode based comb generator for microwave drive frequencies shown in Fig. 3.4, using a fundamental input frequency $f_D = 1200\,\text{MHz}$ and a drive power of 27 dBm. Main comb frequency distance $\Delta f = f_D = 1200\,\text{MHz}$, additional shifted comb components caused by the generation of subharmonics due to capacitance modulation of the SRD at $f_{\text{offset}} = f_D/2 = 600\,\text{MHz}$ to the main comb ([47]).

output power spectrum of a comb generator, built for drive signal frequencies from 600 MHz to 1.5 GHz (photo on the right side of Fig. 3.4), is shown in Fig. 3.6 for a drive power of 27 dBm at $f_D = 1200\,\text{MHz}$ and a corresponding frequency comb spacing of $\Delta f = f_D = 1200\,\text{MHz}$.

In order to generate the harmonic reference frequencies in a non-linear measurement instrument, and therefore also setting the measurement frequency grid position and spacing, two fundamentally different comb generator drive solutions are possible depending on the system architecture of the NVNA measurement system and the measurement task at hand:

- If only one stimulus generator, and therefore one stimulus tone, is used, it is possible to directly drive the comb generator with the fundamental frequency stimulus sweep signal by tapping and amplifying the signal of the stimulus synthesizer. The frequency grid position and distance is therefore directly coupled to the stimulus generator sweep settings of the VNA and the frequency spacing is only limited by the capabilities of the VNA itself. The SRD comb generator shown before belongs to this class of harmonic phase references.

- When multi-tone stimulus signals are required, each stimulus synthesizer generally follows its own sweep pattern, and no or few overlapping frequency harmonic grid points exist. Therefore, a low frequency signal, usually the 10 MHz reference clock or divided representations thereof, is used to drive a low input frequency comb generator that independently generates reference points over the measurement

frequency range of interest. Non-linear frequency converting measurements can only be performed on the grid established by the harmonic phase reference.

While the first, stimulus synthesizer coupled, method is sometimes still used in the large-signal unidirectional non-linear load-pull characterization of power transistors, where the large signal stimulus is often supplied by a separate synthesizer and power amplifier, and the VNA is only used for the sweeping small signal extraction stimulus, the multi-tone multi-stimulus approach required for the measurement and extraction of X-parameters is nowadays considered to be the standard. Therefore, the latter method of using a spectral dense low fundamental drive frequency approach to create the reference frequency points, as used by the Keysight U9391 NLTL comb generators in combination with the PNA-X, is considered to be the gold standard for multi-tone non-linear measurements.

Furthermore, comb generators designed for direct stimulus generator drive are limited in their input frequency bandwidth to approximately one octave by design. This is due to the required lowpass and SRD impedance matching network at the input and the cut-off frequency and large signal stimulus drive signal isolation required for the output highpass filter network.

Generating the frequency comb with a low frequency reference signal, and therefore creating a dense grid of reference frequency points, is however met with one serious problem: As all of the power available to the harmonics has to be contained in the time integral of the comb generator voltage pulse waveform, the power P_k available to a specific harmonic $k \in \mathbb{N}_{>0}$ is limited [41].

When the pulse shape is assumed to be rectangular with a pulse width of $t_p = \Delta$ with a peak voltage of V_P for simpler analysis, an upper limit for the power P_k of an individual comb harmonic can be found by

$$P_k = \frac{V_p^2 f_D^2}{50\,\Omega}\Big(\int\limits_{-\Delta/2}^{\Delta/2} cos(2\pi k f_D t)\,\mathrm{d}t\Big)^2 \leq \frac{(V_p f_D \Delta)^2}{50\,\Omega}\ , \tag{3.19}$$

which yields a limit of $P_k \leq -75\,\mathrm{dBm}$ per harmonic for typical values of $V_p = 400\,\mathrm{mV}$, $t_p = 10\,\mathrm{ps}$ and a comb spacing of $\Delta f = f_D = 10\,\mathrm{MHz}$.

Furthermore, it can be deduced from the approximation in Eq. (3.19), that an n_C times denser comb frequency spacing results in a corresponding power loss α_C of

$$\alpha_c(dB) = 20 \cdot log_{10}(n_c) \tag{3.20}$$

per harmonic tone in the output signal ([107]).

The minimum input power requirement on the LSNA / NVNA receiver side is mainly determined by its thermal noise floor depending on the noise figure and filter bandwidth as well as the dynamic range of the instrument. While an output power of -75 dBm per tone is usually sufficient for the phase reference standard directly connected to a NVNA receiver for the LO phase correction, this low output power level leaves only marginal headroom for the insertion and coupler losses present in a NVNA test-set during the non-linear reflectometer calibration.

As a practical example, a modern ZVA24 VNA from Rohde & Schwarz without direct receiver access exhibits an input referred noise floor of $N_0 \approx -115\,\mathrm{dBm}$ in 10 Hz IF filter bandwidth [109], which includes the test-set insertion and coupler losses. For a modest IF bandwidth of 1 kHz this results in an SNR margin of 30 dB, yielding a phase error of $\pm 2°$ by noise alone. If the comb spacing is decreased from 10 MHz to 500 kHz for the same HPR, the power per harmonic tone must drop by $\alpha_c = 26\,\mathrm{dB}$. In order to keep the same SNR as before, the IF bandwidth must be reduced by the same amount, which is often not feasible due to increased measurement times. In this example an acceptable SNR of 24 dB is reached again at an IF bandwidth of 10 Hz with a corresponding error of $\pm 3.6°$, although at the cost of a 100 times slower measurement.

This situation is somewhat remedied by using the direct receiver access for the phase reference used for the LO compensation, as these figures are improved by 10 to 20 dB by omitting the coupler losses of the test-set. Nevertheless, the HPR signal has to be measured during every sweep for every frequency point of interest resulting in even longer sweep times. NVNA instruments with a coherent and TI repeatable LO frequency synthesis similar to the method presented in [5] by using the defined coherence mode of the ZVA67 and the VNA system presented in chapters 2.3.2 to 2.3.7 of this work do not suffer this penalty, as they only need to measure the HPR once for every frequency point or on a drift correction basis.

While this figures based upon the internal small signal test-set of the VNA are still acceptable for calibration with lower IF filter bandwidths, the situation changes considerably when a multi-tone bi-directional large signal test-set is used. The exemplary large-signal high-gain power amplifier test-set shown in Fig. 3.1, which is loosely based upon the S-Band 250 W LDMOS amplifier X-parameter and load-pull device characterization test-set presented in the case study [92], helps to visualize this calibration SNR problem.

If the first port of the setup shown in Fig. 3.7 is assumed to be consistent with the integrated test-set calculation of the ZVA24 presented before, the problem is directly apparent when the same phase reference calibration is performed for the large-signal part of the test-set present on the second port. Due to the 40 dB higher coupling factors of the large signal reflectometer couplers, the receiver SNR is also decreased by the at least same amount.

Even a comb spacing of 10 MHz combined with an IF filter bandwidth of 10 Hz results in a practically unusable SNR of only 10 dB for the receivers of the second port, as the noise induced phase error increases to $\pm 17.54°$, which is consistent with the conclusion of the case study in [92] conducted by Agilent/Keysight themselves. It is safe to say, that a denser comb spacing in this setup is practically completely out of reach by using the low fundamental frequency comb generator method without affecting the dynamic range of the receivers for large signal vector measurements.

Over time, different solutions to this dilemma of finer harmonic phase reference (HPR) frequency spacing versus per harmonic power P_k were published. They either aim to increase the generator pulse duration while keeping the peak voltage fixed, such as [41], utilize the equipment and post processing intensive method of multi-sine excitation with arbitrary waveform or vector signal generators in a LSNA [155] or NVNA setup, as

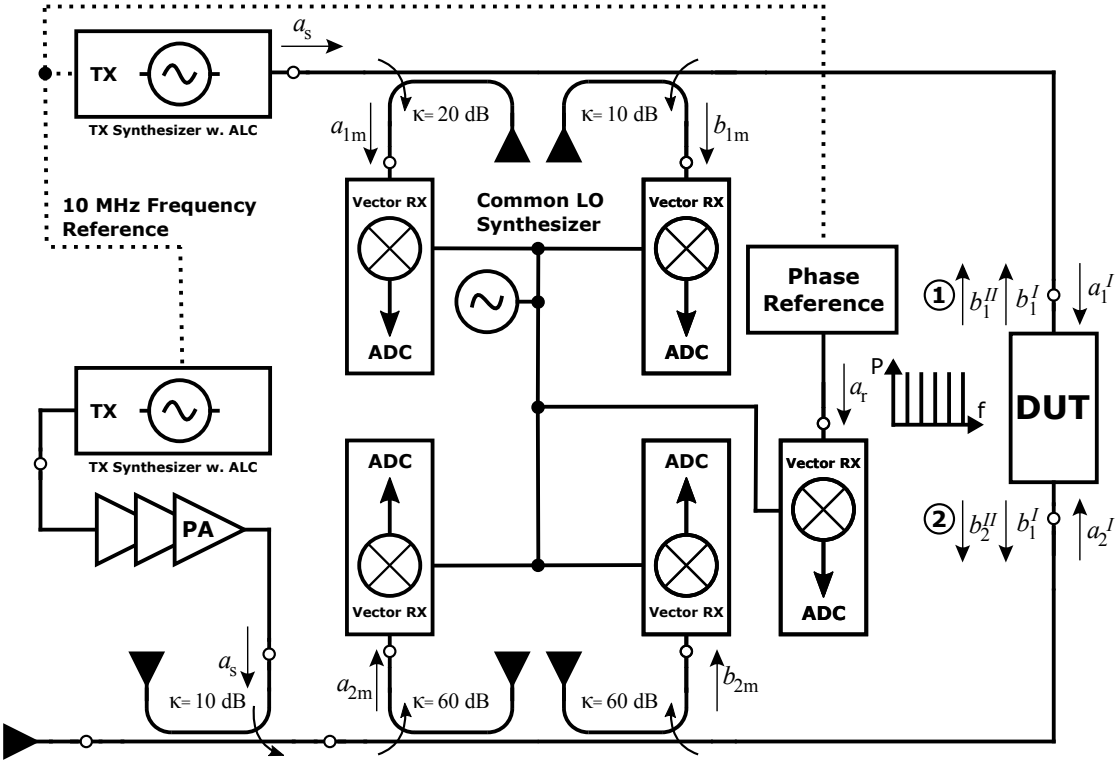

Figure 3.7: Schematic of a high power NVNA test-set for bi-directional large signal, active high gain device characterization.

presented in [62, 106, 107, 158], while others simply aim to maximize the total HPR output power [39, 47].

3.3 The Proposed New Synthesized Phase Standard

In the following section a new approach to the HPR output power and comb density problem based upon TI repeatable synthesizers is presented. This new harmonic phase reference standard uses the fully integrated ADF4356 [23] synthesizer IC from Analog Devices, which was already introduced in the hardware description of the single receiver VNA system in chapter 2.3.3 of this work, although in a different context. The harmonic output frequency range of 54 MHz to 6.8 GHz is covered by the approach without the need for multiple switched external VCOs or dividers.

Contrary to its application in the synthesizers of a normal single receiver VNA system, which only required TI stability, additional measures must be followed to achieve true TI repeatability of the synthesizer in the HPR to allow the calibration of the standard and later usage of the phase reference standard in combination with the obtained calibration coefficients. Therefore a full list of basic conditions to achieve a phase repeatable state with any capable integrated wide band synthesizer is provided in addition to the

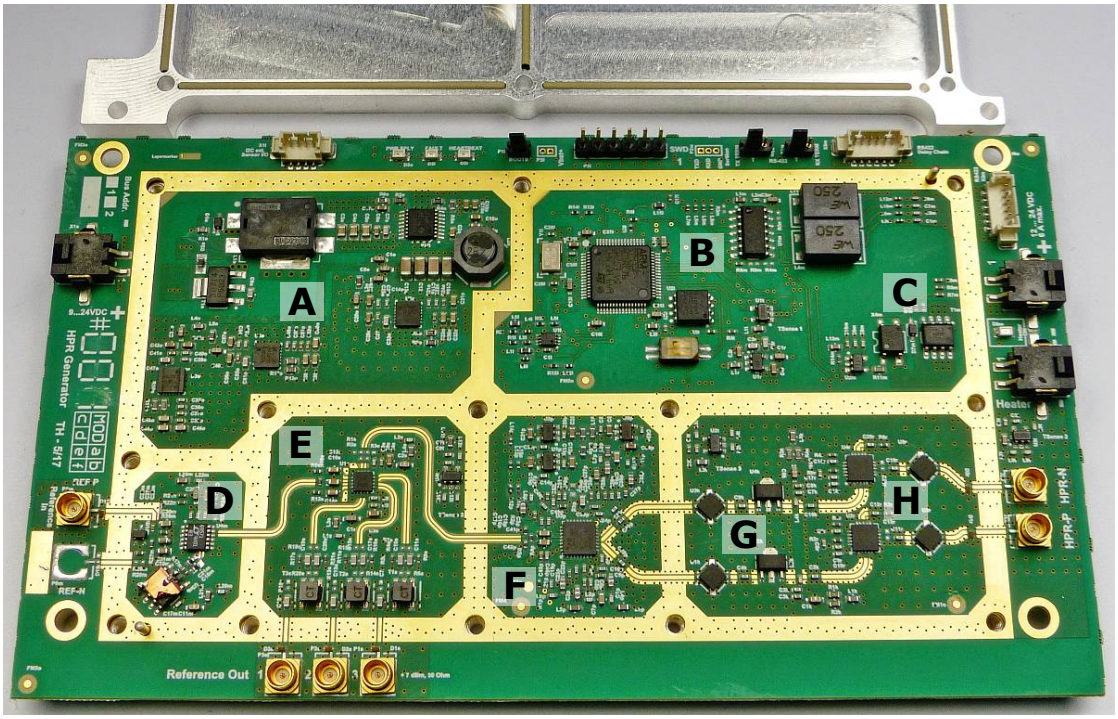

Figure 3.8: Picture of the synthesized phase reference prototype. Annotations: A - DC/DC converter and linear regulators, B - microcontroller and RS-422 transceiver, C - isolated thermostat heater control, D - reference input with limiter, squarer and reference detection, E - clock buffer with trigger outputs, F - ADF4356 PLL synthesizer, G - resistive padding and isolation amplifiers, H - output switches for two differential reference signal outputs.

description already provided in the section 2.3.3 of this work.

The proposed synthesized phase reference (SPR) standard, based upon the modified VNA stimulus generator module, as shown in Fig. 3.8, uses only few resources of the associated VNA and is independent of the single receiver VNA hardware presented before. Only a 10 MHz reference frequency connection and one VNA receiver channel, or full reflectometer port, is needed for LO correction. In contrast to comb generators, no additional external or internal generator is needed for the reference stimulus drive signal, therefore even the ubiquitous two-port VNA with no direct generator or receiver access can be employed for a non-linear reflection measurement test-set.

In order to achieve a repeatable output phase while frequency hopping with a PLL, it is necessary at first to take a look at the innards of the specific PLL synthesizer implementation. A detailed description of the PLL synthesizer used for the HPR can be found in [23] and to a lesser but more compact extent in the VNA hardware description in chapter 2.3.3 of this work.

Since a modern dual mode Fractional-N and Integer-N PLL core integrates a multitude of counters, dividers, modulators and feedback options, it is necessary to identify a

possible mode of operation that enables the intended repeatable phase output.

In general the following four conditions must be fulfilled by the synthesizer configuration and design to achieve a TI repeatable output phase:

i. The phase frequency detector (PFD) must be able to cover all four phase quadrants.

ii. The PLL loop filter must be at least of second order characteristic or higher.

iii. All internal frequency determining counters that are not synchronously reset to the same edge transition of the reference clock signal during frequency update must be avoided, bypassed or set to one.

iv. All RF output dividers present in the synthesizer must be completely enclosed by the PLL feedback loop.

While (i) is standard feature in modern PLLs and (ii) can easily be achieved in the design process, fulfilling conditions (iii) and (iv) take considerably more effort depending on the synthesizer implementation at hand.

When applying these rules to the synthesizer used here, conditions (i), (ii) and (iv) can be achieved regardless of the operation mode by design and register configuration.

Condition (iii) however can only be satisfied in true Integer-N mode, where a synchronous reset of the counter is performed on N value load. While a timer controlled synchronous reset of the fractional mode registers, called phase re-sync, is available in this specific IC, a repeatable output phase can only be achieved during one power-on state in this mode.

After power cycling the IC, a different output phase is generated that is unfortunately only repeatable for this specific cycle alone, which is likely caused by the asynchronous loading of the registers compared to the supplied reference clock and the associated internal counter resets of the IC itself.

Also the reference divider of the PLL must be bypassed, which enforces $f_{PFD} = f_D$. This reduces the options to an Integer-N only mode. Using the expression $f_{out} = N \cdot f_{PFD}$, with $N \in \mathbb{N}_{>0}$, this results in

$$b_{0,S}(k,t) = b_k \cdot sin(2\pi N_k f_D t + \phi_k) \tag{3.21}$$

for all possible time discrete output waves $b_{0,S}(k,t)$ of the synthesized reference, with k being the picket index, b_k as the corresponding amplitude and ϕ_k its related phase.

When this result is compared with the formally same description of a comb generator output signal it can be found, that this is exactly the same description as for a specific picket in a HPR frequency comb outbound wave $b_{0,C}$ with

$$b_{0,C}(t) = \sum^{k} b_k \cdot sin(2\pi N_k f_D t + \phi_k)\,. \tag{3.22}$$

As already mentioned in the VNA hardware description in chapter 2.3.3 of this work, the ADF4356 achieves its high bandwidth with a multitude of switchable inductors and capacitors used by four internal VCOs and frequency dependent bias settings for the

oscillators. This allows the VCO to have a nearly flat tuning response over the whole base bandwidth of 3.4 to 6.8 GHz and a low phase noise despite its low tuning voltage range. Exemplary phase noise measurement results and an estimation of its time domain jitter can also be found at the end of chapter 2.3.3 of this work.

The optimal settings for L, C, VCO core and bias depend on environmental factors and production variances and are usually determined by an inbuilt autonomous calibration routine each time a new frequency is locked. Unfortunately this procedure is not completely deterministic and different outcomes result in phase offsets for reasons unknown to the authors. Therefore an additional condition must be satisfied for this kind of VCO implementation:

v. When fully integrated synthesizers are used, it must be ensured that only one specific combination of L, C, VCO core and bias is used for a given frequency picket.

In the case here, condition (v) can be accomplished by a procedure available found in [6], which allows to perform a VCO calibration sweep of all pickets of interest and determine the VCO settings. These values can then be employed later to enforce repeatable VCO behavior.

An ideal PLL / VCO based synthesizer that fulfills all the aforementioned conditions should theoretically show a fairly flat output phase spectrum like SRD or NLTL based HPRs. Due to the multiple VCO cores, different bias settings and other measures employed in an fully integrated synthesizer ICs, this only holds true on a very small fraction of the overall output bandwidth. However since the phase is repeatable, the phase value ϕ_k and amplitude b_k of a frequency picket can be determined by using a sampling oscilloscope as a transfer standard for characterization.

A multitude of setups based on sampling oscilloscope measurements with varying grades of accuracy, time base, jitter and frequency response correction methods, equipment requirements and traceability to national standards are available for this task, which were originally designed for characterizing classic comb generator based HPRs.

Notable highly accurate procedures and setups, which are beyond the scope of this work and are often situated in the measurement realm of national standard laboratories like NIST or the PTB, are presented in [19, 40, 42, 67, 69, 105, 150].

It is important to note, that the SPR approach is not well suited for the wideband instantaneous capture nature of the LSNA concept [87]. This concept requires a multi-tone reference, whereas a PLL / VCO based system can only provide a single reference tone (with its minor harmonics) at a given time. Nevertheless, an LSNA could still be calibrated using the synthesizer HPR, although only by modifying the existing calibration procedures and algorithms.

A NVNA in contrast measures in a frequency and time discrete manner. If the frequency output of a single tone reference is coordinated with the measurement frequency of the instrument by the instrument control software or an accompanying computer used for measurement automation, no differences in data capture and processing arise.

This enables this concept to concentrate all of its output power on a single frequency point and avoids the implicit SNR impairment of the wideband comb reference for denser output tone spacing for adverse test-set conditions.

3.4 The Experimental Setup

3.4.1 The Synthesized Phase Reference (SPR)

In order to validate this thesis a prototype of the synthesized phase reference (SPR) was designed and built by modifying the VNA stimulus generator module. The result of this process is shown in Fig. 3.8. The design of the SPR shares many elements, including the synthesizer itself, with the stimulus generator module, which fortunately allowed reusing most of the controller software, parts of the PCB layout and the milled enclosures. The main modifications performed to the original stimulus generator are:

- Modification to the reference frequency input clock distribution chain to include buffered, high slew rate, low-jitter, 50 Ω reference frequency outputs mainly for triggering the sampling oscilloscope during calibration, but also to centralize the clock distribution and skew for different modules,
- The addition of a second output generator by using the second, phase inverted, output of the differential synthesizer IC output stage to allow one SPR module to be used as both the phase calibration and phase correction source,
- Removal of the automatic level control circuitry to enhance phase repeatability due to fewer MMICs in the signal path,
- Higher reverse isolation for isolation amplifier assemblies,
- Removal of the integrated SP4T wave selector switch,
- Additional temperature sensors placed at critical points in the clock distribution tree, and
- The addition of a processor controller isolated high power heater control output for PI controlled temperature stabilization of the assembly.

The SPRs clock chain starts with a low jitter reference input squarer and limiter stage, which converts the drive signal f_D to a high slew rate, low voltage positive emitter coupled logic (LVPECL) clock signal, just as in the VNA stimulus generator module.

This representation of f_D is then buffered by a 1:4 LVPECL buffer. One output is used to feed the PLL reference input while the remaining outputs are locally terminated and converted to a single ended 50 Ω clock using a balun. These outputs provide a high slew rate, low jitter, square wave version of f_D. For the edge sensitive trigger of a sampling oscilloscope, this f_D square wave signal and the pulse train of classical HPR comb pulse, with its repetition frequency f_D, results in equal triggering conditions and sampling start

points. Due to this property and provisions generally accepted HPR characterization setups for the comb based references can be reused even at low f_D frequencies with corresponding low sinusoidal slew rates for characterizing the SPR.

The SPR prototype module is fitted with the same software controlled dual loop-filter configuration as presented in the general description of the VNA synthesizers in chapter 2.3.3 of this work. The same component values are re-used from the stimulus and LO-synthesizer design for both loop filters, which are designed for PLL PFD frequencies of 10 MHz and 500 kHz.

To fulfill rule (v) from the previous section, a sweep of N for both PFD frequencies is performed beforehand and the corresponding VCO settings are saved (see [6]) to a look up table in the EEPROM of the SPR for future reference.

During early testing of the modules it was observed, that the VCO settings, the clock propagation delays and output skews of the clock ICs are sensitive to temperature changes, which was anticipated from the beginning by including the temperature control ability. Therefore the assembly is thermostated to a weighted average temperature of $45\,°C$ by a software control loop PWM switching a resistive heater through an isolated power MOSFET for all of the measurements presented here. The resistive heater is fed from a separate power supply to avoid supply modulation and is fixed to the aluminum enclosure of the SPR.

Temperature data for the PI software control loop is provided by four temperature sensors on the PCB and the weighted average of the measurement results is used as the input for the PI control loop. Thermal blankets in the form of bubble-wrap sheets and Styrofoam blocks are used to reduce the thermal losses of the heated assembly thus lowering the power requirements and accelerating the warm-up time.

Both differential RF outputs of the synthesizer are isolated from external VSWR feedback by an improved isolation amplifier stage. An absorptive SPDT PIN-diode switch is inserted into the output to switch between the SPR signal and a reflection termination on the PCB instead of the SP4T reference wave switch section on the stimulus generator PCB. If the SPR is connected to a calibrated full reflectometer port, the switchable short can be used by the VNA to measure the electrical length of the connecting cable to correct the phase calibration data for the additional electrical offset length introduced by the cable.

3.4.2 The Characterization Setup

A schematic overview of the characterization setup is shown in Fig. 3.9 and the corresponding composite photo of the measurement setup is shown in Fig. 3.10. The clock chain is fed using the 10 MHz TCXO with a TK of 300 ppb/K from a single receiver VNA module which is also used to interface the SPR module to the control PC. An extensive description of the receiver module clock chain can be found in the corresponding section of the single receiver VNA hardware description.

The 10 MHz reference clock signal is split by an LVPECL buffer in the VNA receiver module into two clock paths: One is used to lock the oscilloscopes mainframe horizontal time base to the 10 MHz reference frequency, while the other is used to drive a low jitter

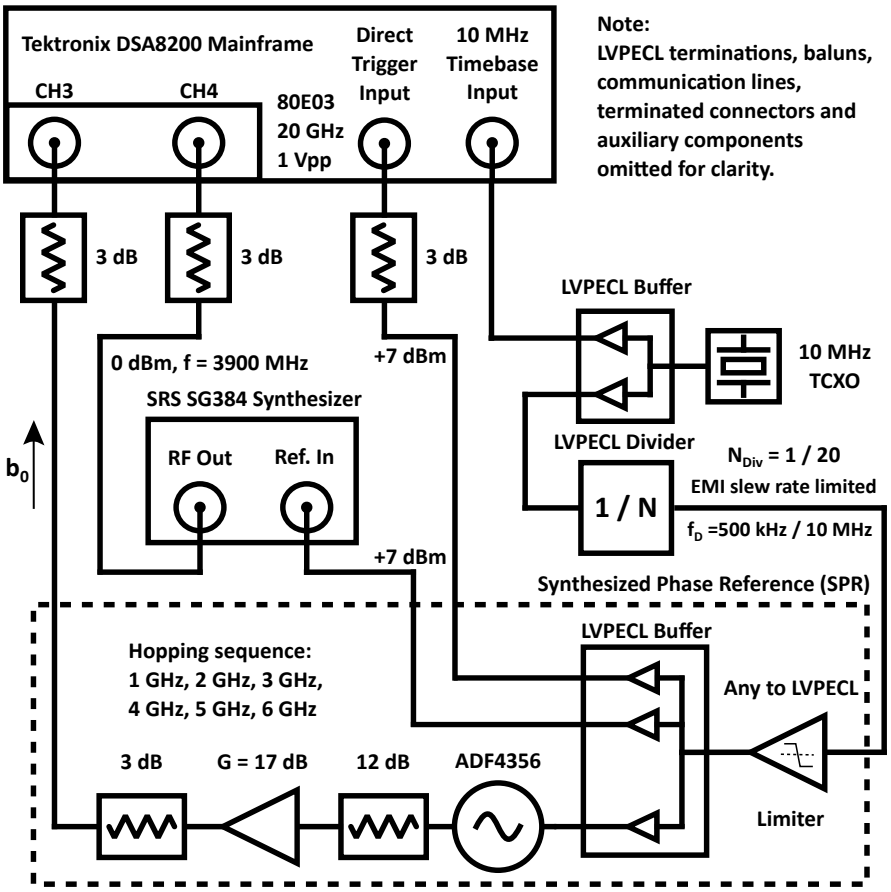

Figure 3.9: Block diagram of the characterization setup. Second output of the synthesized phase reference omitted for clarity.

LVPECL configurable divide by N buffer. This buffer generates the configurable drive frequency $f_D = 10\,\mathrm{MHz}/N$ for the SPR. Both originally differential LVPECL signals are converted to single ended $50\,\Omega$ signals by baluns for off-board routing.

One of the buffered high slew rate f_D outputs provided by the SPR is used to trigger the sampling oscilloscope. A second f_D output is used as the reference for a Stanford Research Systems (SRS) SG384 synthesizer. One of the SPRs outputs and the output of the SG384 is then connected to a dual channel 80E03 20 GHz sampling module in the oscilloscope mainframe. 3 dB attenuators are added to both sampler inputs and the mainframes trigger input to improve the input return loss and reduce the effect of sampler bounce. These attenuators are later de-embedded from the data in post-processing. All longer coaxial cable runs were taped down to avoid any phase change by unintentional cable movement.

A 4-channel thermocouple probe was added to measure the DSA8200 air intake, outlet, ambient and the air temperature in the direct vicinity of the SPR assembly to monitor the environmental parameters of the measurement setup. Internal temperature data

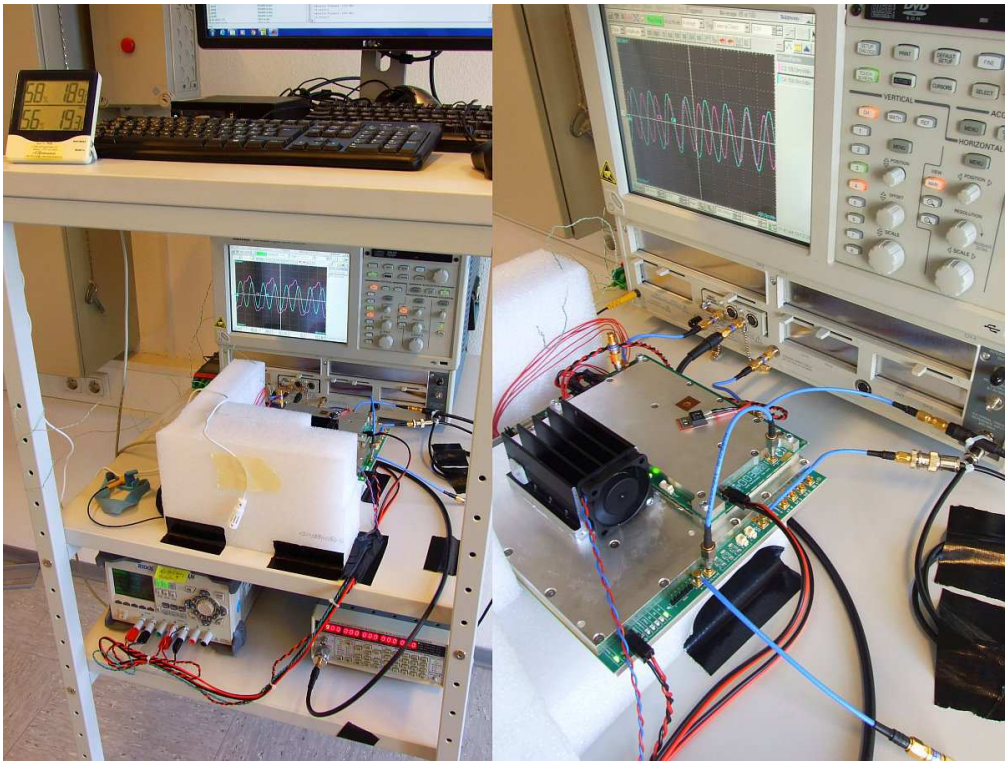

Figure 3.10: Composite photo of the characterization setup. Left: Overview showing the Tektronix DSA8200 sampling oscilloscope, the power supply, the Stanford Research SG384 synthesizer, most of the interconnects and the synthesized phase reference mounted on top of a research VNA module providing the drive frequency and communication. The bottom of the modules is thermally insulated to assist the PI temperature control. Right: Detailed view of the connections made for the characterization setup.

of sampling oscilloscope is acquired for both the mainframe and the sampling head. Additional temperature data is gathered from four sensors on the SPR and one sensor in the VNA module that provides the SPRs drive signal. All measurements were performed in an air conditioned room with a median temperature of $19\,^{\circ}\mathrm{C} \pm 1\,\mathrm{K}$.

3.4.3 Data Acquisition and Processing

The data acquisition by the sampling oscilloscope is performed under control of a MATLAB script via VISA. The horizontal timebase is locked to the 10 MHz VNA reference clock and set to a record length of 4000 points at 50 ns trigger offset for a total epoch length of 2 ns with 100 averages. Averaging is performed under the assumption, that the probability density function of the trigger jitter is symmetric. This results in a low pass filtering of amplitude and no alteration of the phase [137]. Waveforms of the SPR are captured in a 1 to 6 GHz hopping pattern with step size of 1 GHz, mimicking

its intended NVNA operation. 500 measurements per picket were performed from a cold start followed by another 500 measurements in steady state. The total measurement time was 10 to 12 h for 1000 hopping patterns. After completion, the SPR was powered off and allowed to cool down over night while the other instruments were left running. Data was captured for drive frequencies of 500 kHz and 10 MHz over the course of three days each.

Amplitude and phase recovery of the $b_0(f)$ values from the scope data is performed by least-squares sine function approximation including a dc offset. The initial guess consists of the Fourier coefficients of a symmetric square wave of the appropriate frequency, as the output stage of the synthesizer IC consist of a modified current mode logic driver [23]. Curve fitting is performed up to the 9th harmonic for each picket to minimize the residual error function and improve fitting accuracy. All mentioned temperatures were logged after the completion of each hopping pattern for later analysis.

3.4.4 Experimental Issues

The SRS SG384 was initially included in the setup to perform the NIST jitter and timebase correction (TBC) outlined in [42] using an additional sampling head and a 90° hybrid coupler. However its short term jitter performance is not on par with the SPR. Since the authors did not want to introduce another unknown into the setup by using a second SPR as a waveform source for the TBC algorithm, averaging of samples was used instead. The SG384 was left in the experiment with constant frequency and power output as a sanity check for the acquired data due to the long times of unattended operation involved.

During the review process of the associated paper ([46]), it also became clear, as explained by one of the reviewers, that the Tektronix DSA8200 mainframe is unfortunately not capable of performing the TBC algorithms at all, which is due to its internal sampling pulse generation. In the DSA8200, the sampling pulses generated for the different sampler module slots are only coherent for one drop-in sampling module slot. As the TBC algorithms requires a quadrature data capture of the reference signal, and therefore uses two sampler channels for capturing the in-phase 0° and quadrature 90° component generated by an external 90° hybrid, an additional third sampling pulse coherent channel is needed to capture the SPR output waveform. Only two port sampler modules are available for the DSA8200, so using the TBC algorithm and measurement setup in combination with this sampling scope is impossible.

Also the behavior of the horizontal timebase of the DSA8200 was found to be erratic, as the amount of waveform timebase distortion after averaging seemed to be correlated with the trigger offset position. The chosen trigger offset of 50 ns was determined experimentally for minimal observable waveform distortion in the epoch. An extended analysis and explanation for this distortion effect can be found in [149].

3.5 Characterization Results and Conclusion

The lock times of the SPR were found to be faster than 1 ms for $f_D = 10$ MHz and 3 ms for $f_D = 500$ kHz. These times are important to note, as they represent an additional

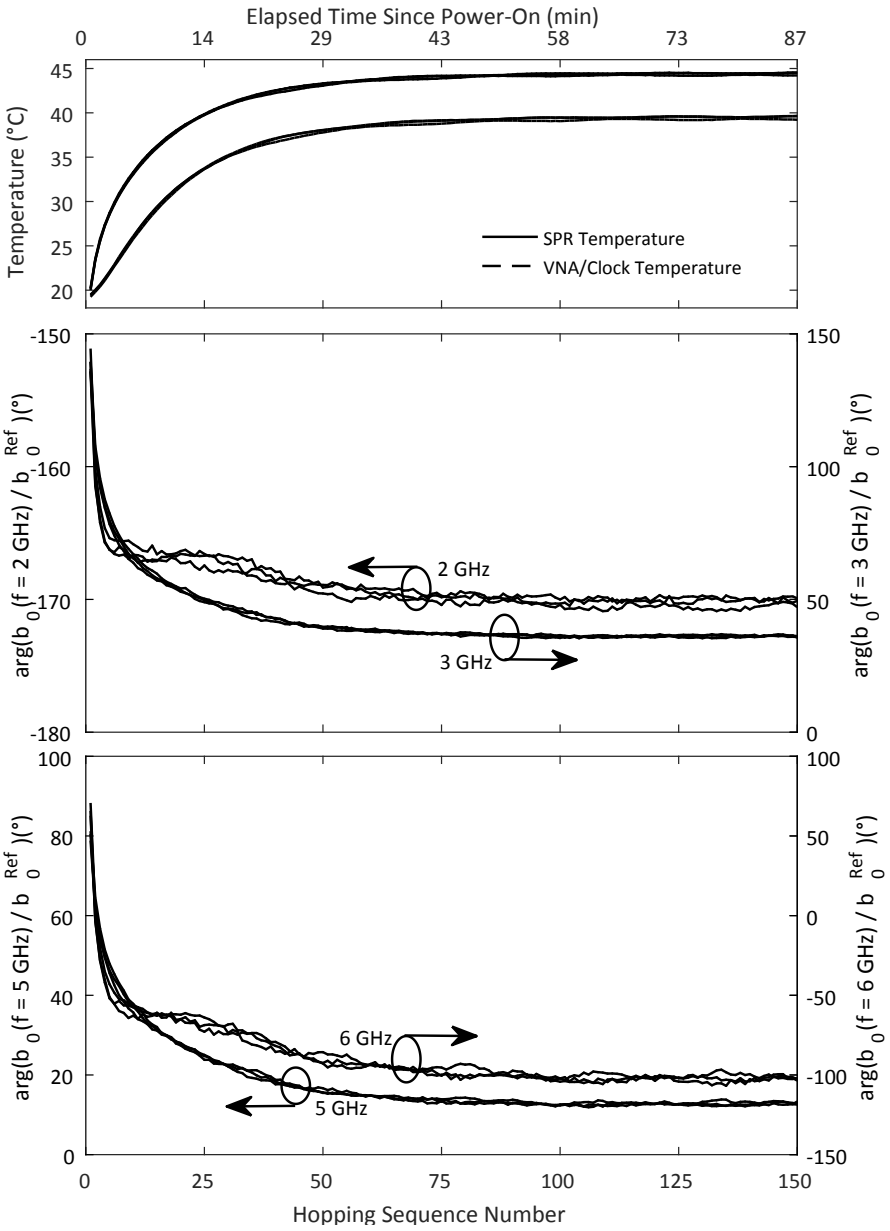

Figure 3.11: Measured phase reference start-up phase behaviors of the outbound waves $b_0(\mathrm{f})$ referenced to $b_0^{Ref}(\mathrm{f} = 1\,\mathrm{GHz})$ and instrumentation temperatures for 150 hopping sequences in three separate sessions, drive frequency $f_D = 10\,\mathrm{MHz}$. Phase repeatability was achieved and steady state reached after a warm-up period of 60 minutes.

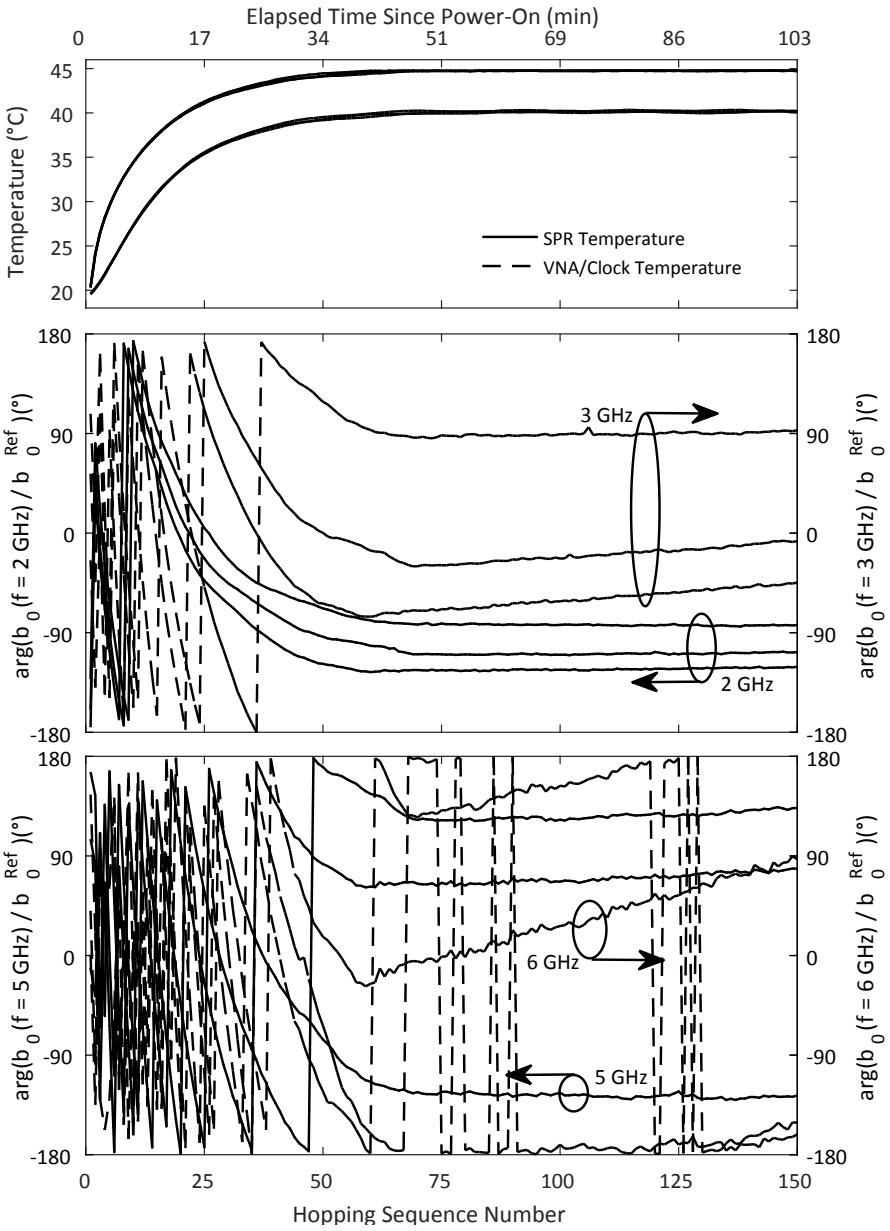

Figure 3.12: Measured phase reference start-up phase behaviors of the outbound waves b_0(f) referenced to the phase of b_0^{Ref}(f = 1 GHz) and instrumentation temperatures for 150 hopping sequences in three separate sessions, drive frequency $f_D = 500\,\text{kHz}$. Phase repeatability was not achieved for this frequency.

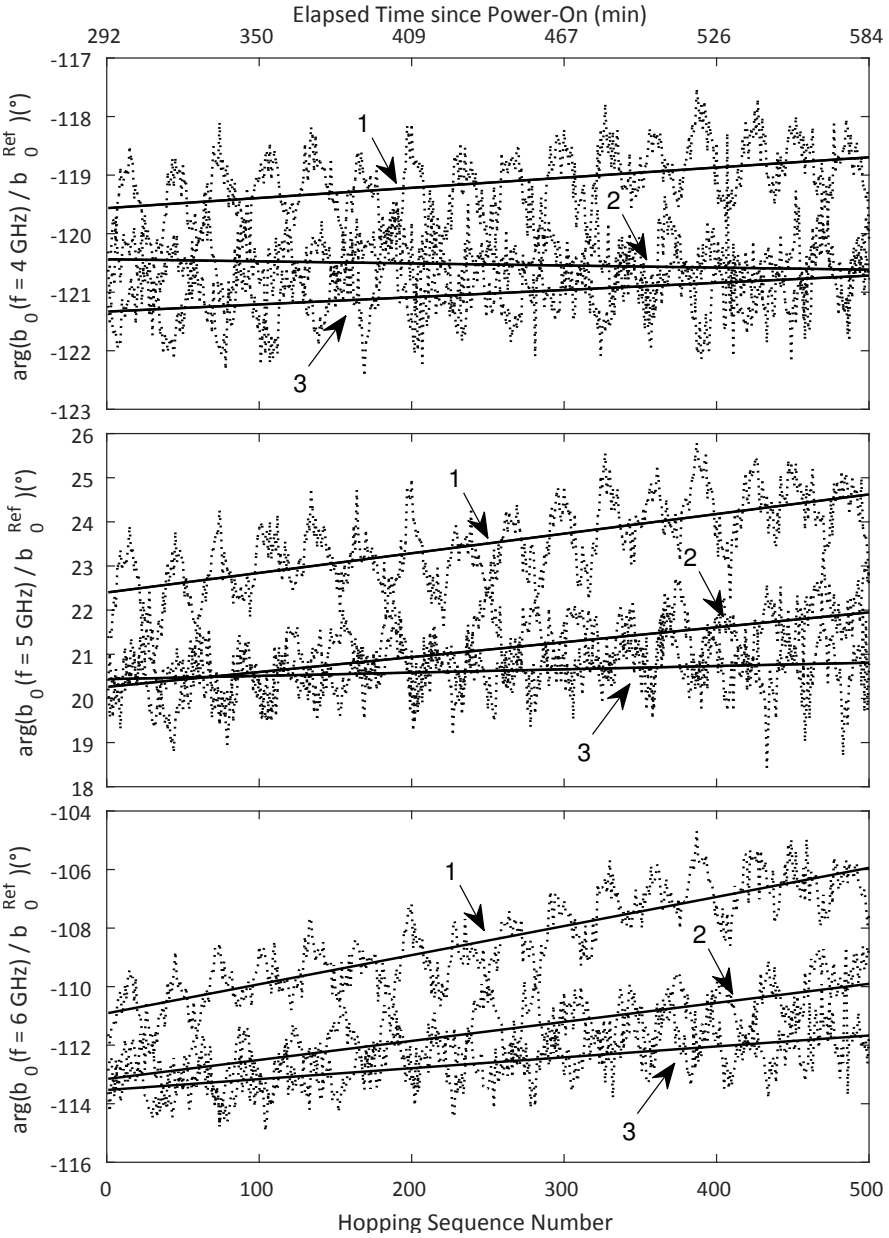

Figure 3.13: Measured phase reference outbound waves $b_0(\mathrm{f})$ referenced to the phase of $b_0(\mathrm{f} = 1\,\mathrm{GHz})$ for 500 hopping sequences captured in three separate sessions after 500 warm-up hopping sequences, $f_D = 10\,\mathrm{MHz}$, dotted lines show raw data and solid lines linear fit trend, number indicates day of measurement. The ripple shown correlates to the $\pm 1\,\mathrm{K}$ ambient temperature change caused by the air conditioning hysteresis.

$f(b_0)$(GHz)	1	2	3	4	5	6
$\mu(\lvert b_0\rvert)$(dBm), 10 MHz,n = 1..500	5.26	4.54	3.20	1.73	0.00	1.25
$\mu(\lvert b_0\rvert)$(dBm), 10 MHz,n = 501..1000	5.28	4.56	3.22	1.75	-0.01	1.27
$S(\lvert b_0\rvert)$(dB), 10 MHz,n = 501..1000	0.01	0.01	0.01	0.01	0.01	0.01
$\mu(\lvert b_0\rvert)$(dBm), 500 kHz,n = 1..500	5.25	4.54	3.10	1.65	-0.12	1.07
$\mu(\lvert b_0\rvert)$(dBm), 500 kHz,n = 501..1000	5.26	4.56	3.12	1.67	-0.12	1.09
$S(\lvert b_0\rvert)$(dB), 500 kHz,n = 501..1000	0.01	0.01	0.01	0.01	0.01	0.01

Table 3.1: Measured mean amplitudes and amplitude standard deviations of the synthesized phase reference prototype

dwell-time required on top of the NVNA IF filter settling time which is not required for comb based references, thus slowing down the overall measurement speed.

The start-up phase and temperature behavior of the SPR for $f_D = 10\,\text{MHz}$ is shown in Fig. 3.11. The data consists of 3 measurement runs, separated by an overnight cool down period. All phase values shown are referenced to the synthesized 1 GHz picket which is used as a virtual fundamental frequency of the hopping sequence.

From the results shown in Fig. 3.11 it can be seen, that the prototype requires about an hour to reach a stable temperature and phase equilibrium. Phase repeatability was achieved for all hopping frequencies between hopping sequences, power cycles and cool-down periods over the course of 3 days, as can be seen by the almost congruent phase plots.

In case of the measurements presented in Fig. 3.12 it can be seen, that phase repeatability was only achieved for the specific run and not between power cycles on different days. Furthermore the $f_D = 500\,\text{kHz}$ measurements show a strong drift tendency not present in the $f_D = 10\,\text{MHz}$ measurements. This negative result is attributed to the synthesizers lower reference frequency input limit of 10 MHz [23] and is consistent with the results one would expect with a slight drift of the input stages switching threshold.

Another possible source of this drift is a slight change in propagation delay over time and temperature of the LVPECL clock divider (see Fig. 3.9) in the receiver module. Unfortunately no temperature dependent propagation delay characteristics are available for this part and the cause of this effect could not be determined with this setup.

This presents many interesting opportunities for further research and experiments with other and better characterized components. It is important to note that delays in the SPR clock chain path directly correlate to a proportional delay of the output signal. A phase drift of 10° for a $b_0(\text{f} = 6\,\text{GHz})$ output signal requires only a change of 4.63 ps in the time domain. For a drive frequency of 500 kHz, this is equivalent to a drift of only 2.31 ppb of the signal period.

Furthermore, measurement artifacts in the form of trigger drift in the DSA8200 and time base distortion effects can also not be ruled out from the data acquired in this process. As the observed repeatability is already one order of magnitude below the trigger uncertainty in the DSA8200 data sheet and no NIST TBC correction could be applied due to the construction of the sampler mainframe, this leaves a lot of room for re-running this experiment with a better characterized and TBC correctable sampling oscilloscope

from another manufacturer.

The observed amplitude repeatability was excellent for both modes. Mean amplitude values and their observed standard variations are shown in Table 3.1. The difference between the acquired measurement data and the fitted function in the time domain was generally observed to be below 5 % deviation, with the majority of it being located in the inherently noisy zero crossing region of the signal waveform.

An output power comparison between the SPR presented in this work and different common comb based phase references is given in Tables 3.2 and 3.3. Likewise SNR values for the ZVA example used in the introduction are given for two different frequencies using a fixed VNA IF bandwidth of 100 kHz.

	P at 1 GHz	P at 6 GHz	$\Delta f = f_D$	f_{min}	f_{max}
This Work	5.2 dBm	1.1 dBm	0.5 or 10 MHz	54 MHz	6.8 GHz
[39]	-44 dBm	-44 dBm	320 MHz	320 MHz	50 GHz
[47]	-12 dBm	-8 dBm	1200 MHz	1200 MHz	67 GHz
[155]	-40.5 dBm	N/A	20 MHz	20 MHz	4 GHz
Keysight U9391C	-58 dBm	-58 dBm	10 MHz	10 MHz	26.5 GHz
MACOM MLPNC-7100S1	-6 dBm	-28 dBm	75 MHz	75 MHz	6 GHz

Table 3.2: Comparison of the output power achieved by the SPR prototype with other common harmonic phase references

	SNR 1 GHz ZVA[109], internal, $BW_{IF} = 100$ kHz	SNR 6 GHz ZVA[109], internal, $BW_{IF} = 100$ kHz	SNR 1 GHz ZVA[109], NVNA Fig. 3.7 Port 2, $BW_{IF} = 100$ Hz	SNR 6 GHz ZVA[109], NVNA Fig. 3.7 Port 2, $BW_{IF} = 100$ Hz
This Work	65 dB	66 dB	55 dB	56 dB
[39]	16 dB	24 dB	6 dB	14 dB
[47]	48 dB	57 dB	38 dB	47 dB
[155]	19.5 dB	N/A	9.5 dB	N/A
Keysight U9391C	2 dB	7 dB	-8 dB	-3 dB
MACOM MLPNC-7100S1	54 dB	37 dB	44 dB	27 dB

Table 3.3: Comparison of the output power achieved by the SPR prototype with other common harmonic phase references

The long term drift behavior of the harmonic output phases relative to the synthesized 1 GHz fundamental for the successful $f_D = 10$ MHz measurements is shown in Fig. 3.13. It can be seen, that the temperature modulation of the b_0 phase most probably occurs in propagation delay domain in the clock chain before the synthesizer, as the effect scales with the output frequency. This indicates leverage points for further improvement of the SPR concept, since this part of the setup was re-used from a different design and not initially optimized in this regard.

Additionally, the clock divider in the VNA receiver assembly was only passively temperature stabilized due to physical contact with the thermostated SPR (see Fig. 3.10).

The drift sources could be separated and determined by further experiments by a thorough systematic drift analysis as carried out in [69]. For the synthesized harmonics of the 1 GHz output signal shown in Fig. 3.13, residual relative average phase drifts of 0.089 °/ h at 4 GHz, 0.29 °/ h at 5 GHz and 0.69 °/ h at 6 GHz relative to the synthesized and measured 1 GHz fundamental phase were observed in the linear fit trend. An initial steady-state relative phase repeatability better than 2° compared to the average phase value was achieved for all frequencies.

The ripple present in the measurement data shown in Fig. 3.13 was found to be strongly correlated with the ambient temperature change of the room induced by the ±1 K hysteresis of the air conditioning equipment and not a systematic residual phase error of the synthesizer. Further temperature tests and isolation of the source of the effect could unfortunately not be carried out due to lack of a regulated temperature chamber.

It is however also possible, that the observed temperature modulation of the output phase and some of the drift shown in the data can be accredited to a temperature dependent change of the actual horizontal time base, or epoch, start controlled by the trigger circuitry of the DSA8200 sampling oscilloscope mainframe. No temperature coefficient data for the repeatability of the trigger circuit is available in the DSA8200 data sheet. While the sampler heads and modules themselves also use an active temperature regulation in form of a heater, it is unclear if this is also true for the trigger circuit in the mainframe. Therefore, it would be wise to re-run these experiments in a more controlled temperature environment and with a better characterized sampling scope in order to separate the source of the observed drift effects.

In conclusion it can be said, that the SPR concept is a viable augmentation of the non-linear network analysis toolkit, especially for high-insertion loss test-set situations encountered in power amplifier characterization measurements. The demonstrated SNR is outstanding when compared with other phase reference options and even more remarkable, when the 10 MHz virtual comb frequency spacing is considered. Nevertheless further research and development must be performed on the concept of the SPR, especially in the realm of the overall characterization setup, as the real possibility exists, that most of the measured effects are caused by measurement equipment and not the SPR alone.

4 Cooperative Localization of Non-Linear Backscatter Tags by Stepped Frequency CW Harmonic Radar

4.1 An Introduction to Harmonic Radar

In this final chapter an interesting off-label application for the TI repeatable VNA modules is described: The cooperative localization of non-linear backscatter tags by stepped frequency CW harmonic radar.

Harmonic or non-linear radar is characterized, in contrast to normal radar, that its transmit and receiver frequencies are not in the same band, and generally an integer multiple of each other and could therefore be called a frequency division multiplex radar system in communication technology terms or a mono-static two frequency system in radar terminology ([104]).

In practice, the received frequency is generally higher than the interrogating transmit frequency, e.g. $f_{\mathrm{RX}} = 2 \cdot f_{\mathrm{TX}}$, which is governed by the non-linear transfer characteristics used to build such a system. This is in contrast to intermodulation based non-linear radar systems, which are also known in literature ([120, 153]), and are sometimes erroneously described as (multitone-) harmonic radar ([82]).

The frequency doubling, or multiplication, of the interrogator transmit signal is achieved via the transfer characteristics of a non-linear device in a so-called tag, which needs to be attached to the object the radar system should detect, range, and track. Therefore, this radar system falls into the category of cooperative localization techniques ([18]), or secondary radars, akin to transponder based radar systems ([104]), e.g. Mode-S or ADS-B used in air traffic control.

This is in contrast to the operating mode of primary radars, which solely rely upon the passive reflection of their signals from their target for ranging and detection and can therefore detect and range targets in a non-cooperative manner. The primary raison d'être of a harmonic radar system is the reliable localization of tags in extreme and dynamic clutter environments. In recent times, the strict definition of cooperative localization has loosened up a bit, as advances in signal processing and solid state microwave amplifiers the harmonic detection of electronic devices in general ([8, 82]), and not only of tags intentionally designed for the task.

In order to further define such a system, the non-linear backscatter tags used for harmonic radar generally require little to no own power supply and most often only rely on the transmitted interrogator signal from the radar system as their sole or primary power source, similar to short range passive RFID tags operating at 137 kHz or 13.56 MHz.

In term of their features and implementations, harmonic radar systems and concepts use widely different approaches to obtain the ranging function integral to the radar acronym. Almost every standard radar wave- and / or pulse-form has also been applied to the harmonic radar concept to obtain range information, while some simple scalar CW harmonic radar systems just provide detection capabilities combined with only a vague estimated range information by providing a received signal strength indicator (RSSI) to the user.

The operating frequency of harmonic radar systems is mainly driven by the external constraints placed on the tag design due to the opposing requirements of efficient antennas, as mandated by the conversion losses of the passive frequency doubling process, and the size and degree of cooperativity shown by the tagged object ([83, 104]). While most publications focus on the UHF and lower microwave frequency range below 12 GHz for their interrogator and return signals, operating mostly in the coordinated L-, S-, C- and X-band radar frequency allocations for the high power interrogator signal ([83]), harmonic radar systems with interrogator frequencies of 38.5 GHz and tag return frequencies of 77 GHz for tracking very small insects on very short distances are reported in literature ([140]). Despite the vastly different operating frequency ranges, Schottky diodes are almost universally used for implementing the passive frequency doubler function on the tag ([104]).

Harmonic radar itself is hardly a new concept, with the earliest publications on this subject dating back to 1976 ([44, 83]). The main commercial application of harmonic radar is the localization of tagged skiers and hikers that become buried after the descent of an avalanche during a subsequent search and rescue operation, as pioneered by the widely used RECCO Rescue System ([1]). This system operates with either a hand-held or a helicopter based interrogator, transmitting at 917 MHz, receiving at 1834 MHz, and uses a passive diode based frequency doubler tag integrated into the sporting equipment. The RECCO harmonic radar system is likely to be based on a scalar harmonic CW system and only provides an indication tone to the user that is proportional to the RSSI as a ranging information. Official, publicly available, documentation of the exact operation principle of this widely fielded harmonic radar system, besides marketing figures, is however scarce.

In the scientific research context, numerous harmonic radar systems have been built for various clutter limited applications over the years (see ([83]) for extensive list), including such diverse applications as:

- Biological behavioral research by tracking the movements of (very) small animals such as bees and frogs in their natural habitat ([10, 61, 73, 77, 84, 85, 146, 147, 148]),
- Presence detection of electronic equipment containing PN-junctions in counter surveillance operations ([8]),
- Remote sensing of environmental parameters, especially temperature ([2, 76]),
- Presence detection of pedestrians as a cooperative driver assistance system ([120]), and

- Measuring the vital signs of patients by remotely measuring their chest displacement ([135]).

Similar to the overall variety of applications, a multitude of basic radar operation principles are used for the actual harmonic ranging of the tag, which can be relatively broadly divided into magnetron and (coherent) solid-state based time domain (doppler-)pulse radar systems in contrast to solid-state frequency modulated continuous wave (FMCW) derived radars operating in the frequency domain.

Regardless of the actual overall system design concept and the radar ranging principle used, all non-linear radar systems face the same basic issue: Diminishing maximum detection and ranging ranges compared to normal radar systems, due to much higher overall path losses caused by inefficient frequency doubling process in, and limited antenna gain of, the tag ([34, 83, 104]).

In order to analyze this important system limitation of the harmonic radar system, it is helpful to use the non-linear extension of the radar equation for the signal seen by the interrogator receiving antenna to analyze the link budget of the system. By following the complete derivation, development and verification of the non-linear radar equation given in [34], along with the basic propagation and effect modeling in [75], the amount of the 2nd harmonic return signal power $P_{R,2}$ at the receiving antenna feed point of the interrogator can be calculated as

$$P_{RX,2} = \frac{G_{RX,2}\,\lambda_2^2 \cdot (P_{TX} \cdot G_{TX})^2 \cdot \sigma_2}{(4\pi)^4 \cdot R^6}\,, \tag{4.1}$$

using the non-linear pseudo harmonic radar cross section (RCS) σ_2 of the tag for illumination at the fundamental frequency and a return signal on the 2nd harmonic calculated as

$$\sigma_2 = d_2 \cdot G_{TXT,2} \cdot \left[\frac{G_{RXT}\lambda_1^2}{4\pi}\right]^2, \tag{4.2}$$

with $G_{RX,2}$ representing the isotropic gain of the interrogator receiver antenna for the 2nd harmonic, G_{TX} for the isotropic gain of the interrogator fundamental frequency illumination antenna, G_{RXT} for the isotropic gain of the illumination signal reception antenna of the tag, and G_{TXT} for the isotropic gain of the harmonic re-transmission antenna of the tag. Furthermore, λ_1 and λ_2 denote the wavelengths of the illumination and harmonic return signals, while R denotes the slant range between the interrogator and the tag. Finally, P_{TX} denotes the input power at the interrogator's illumination signal transmit antenna feed point, while d_2 covers the conversion losses of the passive diode doubler in the harmonic radar tag. An overview of all of these key system parameters is shown in Fig. 4.1.

The received power P_{RXT} seen by the frequency doubler in the tag can be calculated as usual by combining the normal one way path loss formula to calculate the illumination field strength at the slant range R and the effective antenna area of the fundamental

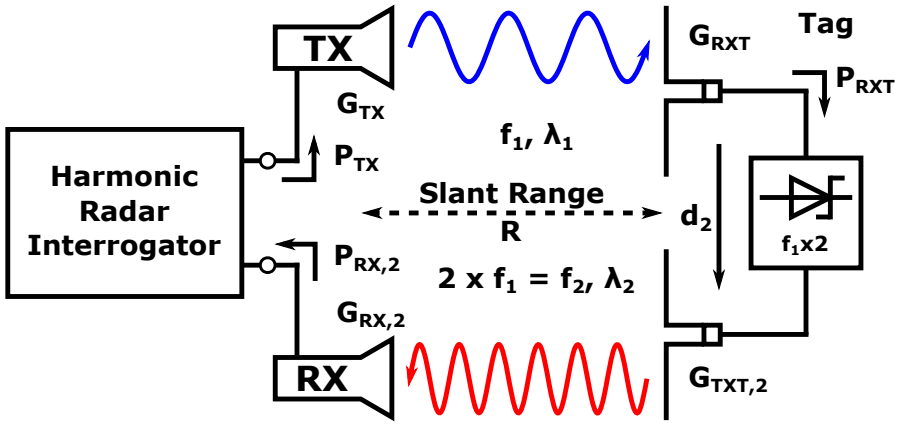

Figure 4.1: Simple schematic diagram of a harmonic radar system using a Schottky diode frequency doubler in the tag.

frequency receiving antenna of the tag in the form of

$$P_{RXT} = \underbrace{\frac{P_{TX} \cdot G_{TX}}{4\pi \cdot R^2}}_{\substack{\text{Illumination Power} \\ \text{Density @ R}}} \cdot \underbrace{\frac{G_{RXT} \cdot \lambda_1^2}{4\pi}}_{\substack{\text{Effective Antenna} \\ \text{Area of the Tag @ } f_1}} = \frac{P_{TX}\, G_{TX}\, G_{RXT}\, \lambda_1^2}{(4\pi\, R)^2} \,. \tag{4.3}$$

While it is not immediately obvious from the description of the non-linear radar equation shown in Eq. (4.1), and somewhat hidden in the original derivation given in [34], there exists a square-law dependency between the harmonic output power P_{TXT} and the fundamental input power P_{RXT} of the non-linear doubler circuit. In this form of the non-linear radar equation Eq. (4.1), this non-linear transfer function of the tag is modeled by the memory-less power-series model for non-linear device behavior. For the general case of N-harmonics relative to a fundamental frequency $n = 1$ and time domain E-field signals, this series approximation can be written as ([83])

$$E_{TXT}(t) = \sum_{n=1}^{N} A_n E_{RXT}^n(t) \,, \tag{4.4}$$

where A_n is a complex valued coefficient describing the transfer characteristics from the fundamental illumination signal to the corresponding harmonic n. Without the loss of generality, this can be re-written into a scalar representation modeling the power transfer characteristics from the illumination fundamental to the sum of harmonics generated by the non-linear process as

$$\sum P_{TXT,n} = \sum_{n=1}^{N} d_n P_{RXT}^n \,, \tag{4.5}$$

which simplifies to

$$P_{TXT,2} = d_2 \cdot P_{RXT}^2 \,, \tag{4.6}$$

for the power of the second harmonic emanating from the frequency doubler, as a function of the received power P_{RXT}, with d_2 used as a scalar scaling factor to describe the conversion gain of the non-linear conversion process ([34]). This description of the doubler's non-linear behavior is fairly simple, when compared with the Volterra-Series description used for the X-parameters presented before. While a Volterra-Series description would also be able to model non-linear memory effects caused by charge storage in the active elements of the tag, this simple power series model still holds up for the modeling accuracy required for harmonic radar ([83]).

Overall, this non-linear power square-law transfer function leads to the situation, that the received power by the interrogator at the second harmonic of the fundamental illumination signal is proportional to

$$P_{RX,2} \propto \frac{P_{TX}^2}{R^6} \text{ , compared to } P_{RX} \propto \frac{P_{TX}}{R^4} \tag{4.7}$$

for a normal fundamental frequency primary radar system ([34]).

To complicate the description of the non-linear harmonic radar equation even further, the doubler conversion gain factor d_2 is not constant at all as mentioned in the original publications, but is effectively a function of the actual input power P_{RXT} to the tag. This consequence is caused by two different effects of the non-linear element: The change in differential device resistance as a function of the applied power, as well as output power saturation, or compression, of the harmonic output signal.

Due to the huge dynamic ranges involved in harmonic radar, the relatively small conversion gain deviation caused by the varying return loss of the non-linear element at the fundamental input and harmonic output frequencies is usually neglected from a system design point of view.

Nevertheless, this is an important factor in the general design and optimization of the frequency doubler in the harmonic radar tag itself ([9, 103, 134]) in the form of a best-fit compromise for the expected dynamic range of the received illumination signal at the tag, which is either achieved by a special antenna design, or external distributed or discrete matching components ([104]), to achieve the square-law power characteristic of an ideal second harmonic passive diode doubler.

Another effect that is not covered by the constant conversion gain assumption is the effect of compression in the harmonic output signal of the frequency doubler, which again, depends on the exact matching of the doubler to the antennas itself, analogous to the load-pull effects present in RF amplifiers. In contrast to normal radar, this leads to the interesting effect, that the effective RCS σ_2 of a non-linear harmonic radar tag can decrease over decreasing slant range or increased transmitter power, when the harmonic output power compression point of the doubler is exceeded.

Therefore, a lower distance boundary exists for the validity of Eq. (4.1), which is mainly determined by the harmonic compression characteristics of the doubler and its received input power P_{RXT}. This lower distance boundary was to the authors knowledge not mentioned in the relevant literature and can easily be visualized by analyzing the results of Eq. (4.1) calculated for a practical example.

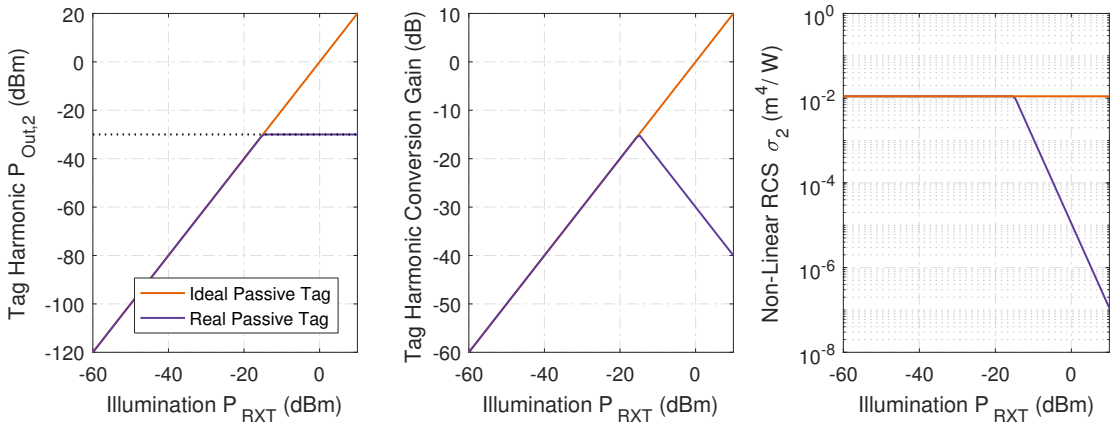

Figure 4.2: Second harmonic output power $P_{\mathrm{Out},2}$, harmonic conversion gain and non-linear radar cross section σ_2 characteristics as a function of the power of the received fundamental illumination signal P_{RXT} for both an ideal doubler and a real doubler with an harmonic intercept point of 0 dBm and a harmonic compression level of $P_{\mathrm{Out},2} = -30$ dBm at -15 dBm fundamental input power.

For this example, the following key system parameters are used, which are also identical with the parameters of the measurement system presented later on:

- An interrogator with a transmit antenna gain of $G_{TX} = 10$ dBi and a second harmonic reception antenna gain of $G_{RX,2} = 17$ dBi,
- A fundamental illumination signal center frequency of $f_1 = 2.925$ GHz in the maritime radar S-band frequency allocation, coupled with the second harmonic reception frequency of $f_2 = 2 \cdot f_1 = 5.85$ GHz in the 5.8 GHz ISM-band allocation,
- A variable illumination signal interrogator output power of $P_{TX} = 10 \ldots 30$ dBm, referenced to the illumination signal antenna feed-point,
- A tag with a reception antenna gain of $G_{TXR} = 5$ dBi for the illumination signal and a transmit antenna gain of $G_{TXT} = 4$ dBi for the re-transmission of the second harmonic generated by
- A passive Schottky diode based doubler, with a harmonic output power intercept point of 0 dBm, and a harmonic compression output power of $P_{\mathrm{Out},2} = -30$ dBm at $P_{RXT} = -15$ dBm.

The results of the evaluation of the non-linear radar Eq. (4.1), using the aforementioned system parameters and the characteristics of the passive Schottky diode based doubler shown in Fig. 4.2, are presented in Fig. 4.3 for three interrogator output powers in 10 dB increments from 10 dBm to 30 dBm of antenna feed point input power, resulting in a illumination signal EIRP of 20 dBm to 40 dBm, calculated for an ideal and a harmonic output power limited tag.

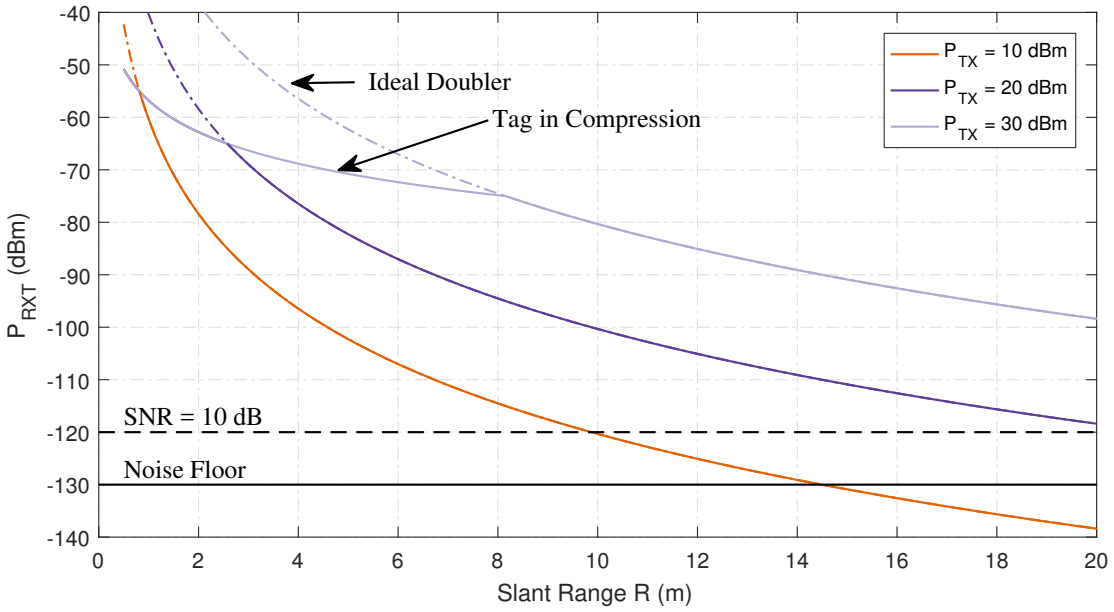

Figure 4.3: Synthetic harmonic received signal strength P_{RXT} over slant range for interrogator output powers of 10 dBm, 20 dBm and 30 dBm.

Using the 10 m slant range mark as a reference, the $(P_{TX})^2$ dependence of the harmonic return signal is easily observable, as a 10 dB increase in illumination power results in a 20 dB increase in return signal power.

Furthermore, the effect of the tag output power compression is easily visible in the slope of the received signal strength. When the passive doubler in the tag is in compression, which is the case with received fundamental input powers exceeding -15 dBm (see Fig. 4.2), resulting in a constant harmonic output power of -30 dBm, the slope of the received signal power changes to a R^{-2} proportionality instead of the R^{-6} proportionality caused by the passive doubler operating in its square law power transfer region at further distances.

The noise floor line drawn into Fig. 4.3, at a received harmonic power of -130 dBm, is oriented after the performance figures of most sensitive S-band / C-band harmonic radar interrogator system presented and published in [8].

By looking at the expected synthetic received harmonic signal strength in comparison with the transmitted power, it can be easily seen, that the construction of a working harmonic radar interrogator system is by no means an easy feat and requires a good mechanical and electrical system design to allow dynamic ranges in excess of 140 dB.

When the non-linear radar equation is analyzed for key system parameters which are important to the overall system performance, several key parameters can be identified which need their own respective trade-off discussion. It is important to realize from Eq. (4.1), that the performance figures of the components carrying the fundamental frequency illumination signal are all included in the square-law dependence of the received signal power, while all components working with the harmonic return signal

only show a linear influence.

Therefore, the components can be grouped from a system design point of view as:

- The interrogator fundamental output power P_{TX}, the fundamental frequency interrogator transmit antenna gain G_{TX}, and the fundamental frequency tag receive antenna gain G_{RXT}, whose performance figures affect the received harmonic signal power squared, and
- The interrogator receiver sensitivity and noise floor, the harmonic frequency interrogator receive antenna gain $G_{RX,2}$, and the harmonic frequency tag transmit antenna gain $G_{TXT,2}$, whose performance figure only contributes linearly to the received signal strength.

While it may be tempting, by judging from this list, to achieve a higher maximum range of the interrogator and the harmonic radar system by just applying a higher illumination signal output power due to the P_{TX}^2/R^6 proportionality, this approach is limited in its efficacy by two fundamental properties of the overall system and microwave components:

- Due to the non-linear behavior of RF power amplifiers, a (linear) power amplifier will eventually generate the second harmonic of the fundamental driving signal itself, depending on the level difference between its output power and output second order intercept point (OIP2, [21]). These emissions can easily overpower the harmonic tag return signal at longer ranges due to reflections from clutter and their $\propto R^{-4}$ normal radar return characteristic compared to $\propto R^{-6}$ for the tag return.
- Furthermore, the receiver front-end itself can also generate the second harmonic in response to the fundamental illumination signal, when sufficiently high levels of the illumination signal can reach the amplifiers and/or mixers due to their own IIP2/OIP2 transfer function characteristics, either through leakage, or an $\propto R^{-4}$ fundamental frequency radar return in front of the interrogator.

Both of these effects are extremely problematic, as the frequency doubling of the illumination signal is only expected to be generated by the non-linear properties of the harmonic radar tag itself and not any other components in the signal chain. Both of these effects therefore lead to serious decline in overall system dynamic range, and in turn maximum range reduction, due to the extremely low power return signal of the tag at farther distances.

For a non-optimized harmonic radar system design, the $P_{RX,2,\mathrm{Tag}}/P_{RX,2,\mathrm{Sys}}$ or C^{II}/I^{II} ratio is generally more relevant as a system performance limiting factor, rather than the receiver noise-floor of the interrogator with no input signals present.

In a practical system design, this issue can be resolved by applying the following methods throughout all system components:

- Excessive bandpass filtering of the signal paths, both for the fundamental transmit illumination signal to avoid harmonic frequency radiation from the interrogator transmit antenna, and the received harmonic return signal to avoid fundamental

frequency overloading of the receiver front-end. This is method is especially effective, when absorptive instead of reflective filter topologies are used to reduce radiated emissions from cables, connectors and enclosures. Additionally, this explicitly includes the deployment of narrow-band antennas for the interrogator to avoid direct feed-through between the transmit and receive antennas and the corresponding high-power / low-power RF domains.

- Performing output power back-off in the system design by leaving generous headroom to the compression power of the individual active components. While this measure reduces the system's power efficiency considerably, this in turn also lowers the amount of unintentional harmonic generation due to a higher IIP2/OIP2 signal distance and the square law proportionality of the associated second harmonic generation ([21]).

- Active, closed-loop, linearization of the power amplifiers, by applying input signal pre-distortion to cancel out the harmonics at the amplifier output ([35]), which is only possible for the fundamental frequency interrogator signal PA.

In practice, only a careful trade-off between the desired output power, total power and thermal budget, filter insertion losses and noise figure, R&D funding and time, as well as space requirements, all strictly oriented after the intended application, must be made to resolve this points successfully.

This careful, application driven, conclusion is also valid for all the antennas involved in the complete harmonic radar system and the well-known fundamental property of antennas, governed by the conservation of energy, that from the three basic antenna properties of gain / radiation characteristic, physical size, and bandwidth, only two can be optimized in conjunction, while the third antenna property will always be the product of a trade-off depending on the other two properties ([104]).

On the interrogator side, the antenna configuration can vary from high-gain, narrow pencil beam antennas, supported by a one or two axes azimuth/elevation positioner pedestal enabling azimuth or volumetric scans, to simple fixed medium gain horn antennas, as governed by the intended application and prior knowledge about the estimated position of the harmonic radar tag. Reported antenna gains for both the transmit and receive antennas vary widely from 5 dBi up to 43 dBi, in both linearly and circular polarized configurations([83]).

In case of the fundamental frequency reception and harmonic transmission antennas of the tag, the variance in antenna implementations is similarly high, as the design of the tag, including its antennas, is mainly determined by the cooperativeness and size of the tagged object and the frequencies used for the harmonic radar system. This usually leads to the deployment of nearly omnidirectional or even approximately isotropic low gain antennas due to an unknown orientation of the tag to the interrogator, requiring an appropriate compensation for the link budget in the selection of the interrogator antennas. The tag antenna designs are also mainly determined by the application itself, ranging from simple wire loops and dipoles ([9, 10, 84, 85, 134, 135]), to (flexible) planar PCB antennas ([73, 77, 101, 103, 140]), flexible paper backed antennas ([95, 97]) to patch

antennas ([76]), depending on the required level of conformity and a priori knowledge in the application. A good overview of different tag antenna designs can be found in [104].

Despite the vast amount of different antenna implementations for the harmonic radar tag, there is one distinct feature, inherent to the implementation of the doubler, that divides the basic design of the tags: One group of tags uses dedicated matching and filter networks for optimizing the return loss of the antennas and the input and output impedance of the Schottky diode doubler for minimal conversion loss with a common inter-system impedance, usually 50 Ω between functional units, at the cost of size and complexity, while the other group of tag designs uses the antenna design itself by modifying their complex feed-point impedance for optimal power conversion between frequencies, which generally results in more compact tag designs ([104]).

Due to the difficult system characterization of fully integrated antenna matched tags, only few performance figures are published for fully integrated tag designs ([104]). Additionally, this design decision effectively denies the separate optimization of the Schottky diode doubler for minimal conversion loss, because access with conventional RF measurement equipment such as signal generators, spectrum analyzers or VNAs is close to impossible and therefore, only iterative optimization of the tag itself coupled with numerical simulations of the doubler and the antennas is possible.

Where either size, weight or surface conformity is not a primary concern, almost all published tag designs therefore resort to the discrete matching network approach, which allows to decouple the design decisions and trade-offs from another and therefore accelerate the development time and possibly the tag performance compared to the fully integrated tag approach.

The last performance figure affecting the overall performance of the system is the sensitivity and noise-floor of the receiver. This system parameter, contrary to all previous metrics, is heavily influenced by the requirements of the actual harmonic radar ranging procedure and illumination waveform due to differing bandwidth requirements and signal processing gains achievable with different radar procedures and topologies. Therefore, it is better in this context to use the input power referred minimum-detectable/discernible-signal (MDS) metric, which describes the minimum input power that is required to generate a signal, that is clearly distinguishable from the system noise floor by automatic (detectable) or operator (discernible) means after all signal post-processing steps, the so called process gain, are applied.

When only a harmonic tag presence detection and no direct ranging is required, single frequency CW signals can be used to great effect, as demonstrated by the success of the commercial RECCO Rescue System. As the instantaneous bandwidths of both the fundamental illumination and the harmonic return signal are essentially zero, high-Q low bandwidth bandpass filtering can be used to lower the noise power seen by the receiver. The ranging however is now only possible by the extremely inaccurate RSSI figure.

The most popular harmonic ranging procedure and waveform by far is the pulse radar technique ([83]), were only short duration RF pulses from 10 ns to 50 μs in length, corresponding to signal bandwidths of 20 kHz to 100 MHz, are sent by the interrogator and the time of flight (TOF) of the return signal is measured to determine the slant range R to the tag. The popularity of the harmonic pulse radar technique can be explained by

three simple facts:

First and foremost, comparatively cheap, high peak power, RF pulse magnetron sources, which are able to generate up to 200 kW of peak pulse power, are available as COTS components for all common radar frequency bands.

Additionally, just like in traditional pulse (Doppler) radar, the overloading of the receiver front-end, and therefore local second harmonic generation in the interrogator, is of lesser concern, when a blind or dead-zone, which results in a minimal detection distance, can be accepted for the radar system due to the short duration of the pulse itself and the TOF of the return signal. Allowing a radar dead-zone and a therefore a minimal detection distance greatly simplifies the interrogator receiver design, as long as the input RF power time integral can be kept below the destruction threshold of the components.

Finally, the pulse radar concept itself is well-known among radar researchers and engineers and knowledge in classical radar design and signal post-processing can quickly be applied to its frequency converting non-linear counterpart.

Nevertheless, the harmonic pulse radar concept itself has one important drawback: Due to the high bandwidth required for the short pulses, the receiver MDS level is generally higher than in all other radar concepts, as the receiver bandwidth has to be at least as wide as the illumination pulse itself, resulting in a noise power N of

$$N = -174\,\mathrm{dBm} + F(\mathrm{dB}) + 10\log_{10}(BW_{\mathrm{RX}})\,, \tag{4.8}$$

which needs to be compensated by the peak pulse power of the illumination signal accordingly. In non-linear radar applications, this effect is not as pronounced as in classical radar due to the $(P_{TX})^2$ proportionality of the return signal. Nevertheless, this advantage can only be used at greater slant ranges, as the tag doubler itself is easily driven into compression by such high peak powers, as shown earlier in Fig. 4.3.

An additional drawback of the magnetron based harmonic pulse radar concept is the signal source itself. Magnetrons, by their very nature, are non-coherent signal sources that do not fulfill even the most basic TI and repeatability criterion necessary for a relatively easy signal processing gain in I/Q data post-processing and coherent integration of multiple returns. In fact, most of the demonstrated harmonic pulse radar concepts do not even attempt to perform any post-processing gain, due to the sheer amount of effort necessary for magnetron sources. In modern pulse Doppler radar systems for weather and airspace observation, each and every outgoing magnetron pulse and the received signal is I/Q digitized in its full Nyquist-Shannon bandwidth to achieve processing gain by coherent integration of returns, which is also called coherent on receive or pseudo-coherent in radar terminology. This procedure results in enormous amounts of real-time data that needs to be processed by the radar signal processor to achieve post-processing gain. If a pulse bandwidth of 100 MHz and only one polarization reception channel is used for example, this results in at least $200\,\mathrm{MSPS} \cdot 16\,\mathrm{bit} \cdot 2\ \mathrm{Channels} = 800\,\mathrm{MB}/s$ of I/Q data that must be processed in real-time, which is only within reach of a custom FPGA based radar signal processor system. Due to the enormous effort required for these systems, it is understandable, that no magnetron based harmonic pulse Doppler radar system with elaborate signal processing has been presented yet.

A notable exception to this observation is the use of pseudo-random gold code spread spectrum pulse modulation in combination with a solid state pulse amplifier for harmonic radar bee tracking, presented in [61, 147], which achieves significant post-processing gain by de-spreading the wide-band harmonic radar return pulse signal in digital post-processing.

The next common radar waveform used for harmonic radar is the continuously frequency modulated CW (FMCW) radar type, which uses a swept sine wave that is continuously varied in frequency from a start to a stop frequency, either in upward or downward direction or in a combination of both. This waveform is also commonly called a chirp ([18]) and the modulation scheme is called linear frequency modulation (LFM). By mixing the received signal with a locally doubled copy of the transmitted illumination signal, the ranging can be performed by determining the beat frequency of the mixing product due to the frequency difference of the signal over time of flight and its locally generated copy.

While this could be performed for non-challenging scenarios by a simple frequency counter for the strongest return signal, the current state of the art is to use a baseband FFT analysis which also allows multi-target resolution and even radar imaging of targets when illumination under different glance angles is possible (Synthetic Aperture Radar (SAR), [18]), as shown theoretically in [14] and demonstrated in [34].

Due to the continuous presence of the frequency varied illumination carrier achieving sufficient harmonic interference suppression is much harder than in the pulse radar case. This is especially the case for the simple FMCW approach that is common in commercial short range FMCW radars which would use a locally doubled illumination signal to generate the drive-signal for the LO-Mixer. Due to finite mixer isolation and matching of components, this approach results in sub-par performance in the high dynamic range harmonic radar scenario and is therefore not followed in practice, with the exception being the purely theoretical concept in FMCW harmonic radar presented in [13], which misses actual measurement results.

All subsequently published linear modulated FMCW harmonic radar concepts ([10, 81]) forgo this classical FMCW architecture choice to increase the interference free dynamic range of the system and use a separate fixed frequency RX LO synthesizer with subsequent real-time sampling using an oscilloscope ([10]), or direct RF sampling without a mixer of both the illumination signal and the return signal with a sampling oscilloscope ([81]), instead. Reported bandwidths for the chirp signal are between 150 MHz to 200 MHz, with a corresponding range resolution of $\Delta R = 0.48\,\mathrm{m}$ ([10]). Both FMCW approaches however only demonstrate a maximum detection and ranging distance of $\approx 5.5\,\mathrm{m}$ (18 feet) using $37 \ldots 40\,\mathrm{dBm}$ of EIRP, which can be in part attributed to the inherent high noise, low resolution sampling of the return signal performed by the oscilloscopes.

An alternative to the linear frequency modulation scheme is a discrete, stepped frequency, approximation of the linear chirp waveform called *stepped frequency modulated CW (SFMCW)*. In this radar signal modulation scheme, a sweep list of individual CW frequency carriers of significant duration is sent out sequentially by the interrogator, compared to the linear modulated chirp signal used in FMCW. Due to the use of discrete stepped CW tones, this radar ranging modulation scheme is by far the slowest procedure in comparison, but allows superior noise and interference rejection because of the low

instantaneous bandwidth occupied by each interrogator illumination tone. When phase locked synthesizers are used for the generation of the illumination tones, as well as for the tracking LO signal for the receiver, coherent integration of the subsequent samples of the quasi CW return signal can be used for easy signal processing of the data to provide additional processing gain.

As SFMCW radars are generally slower than their linearly modulated FMCW counterparts, which is especially true for PLL synthesizer based design due to their lock-time required for each tone, non frequency converting SFMCW radars are only used in practice for the observation of slow moving objects (liquid level in tanks, ground penetrating radar), a sub-type of high resolution interferometric radar measurements (interferometric SAR) and remote sensing of physical properties (impedance spectroscopy), all of which either face challenging SNR or absolutely require precise phase measurements of the return signal.

All things considered, a phase evaluating SFMCW radar system is at its core essentially a (N)VNA, with similar modes of operation. While it is often erroneously stated, that SFMCW radars can only resolve one target with the strongest return, which is certainly true if only the phase component is evaluated in the frequency domain, time domain IFFT transformation of the acquired complex vector data, windowing, and additional time domain gating can be applied to the radar measurement results to resolve multiple returns and targets - which are all proven methods borrowed from common vector networks analysis techniques.

The introduction of the SFMCW radar technique into the realm of non-linear harmonic radar was mainly driven by the work of [34], which not only presented the harmonic SFMCW radar principle itself, but also non-linear SFMCW synthetic aperture radar (SAR) imaging, non-linear device classification and moving target indication (MTI) for harmonic SFMCW.

4.2 The SFMCW / Mixed Frequency S-Parameter Ranging Procedure

4.2.1 The SFMCW Waveform and Measurement Fundamentals

The formal description of the SFMCW illumination waveform is very straightforward, as it is to be expected by the time limited CW nature of the signal. If the base frequency of the sweep (or frequency list) is known as f_1, with the frequency step size Δf between frequency sampling points, the whole range of frequencies used in a sweep can be written as a time dependent frequency series f(t) in the form of

$$f(t) = \begin{cases} f_1\,, & 0 \leq t < 1 \cdot t_{\mathrm{Dwell}} \\ f_2 = f_1 + 1\Delta f\,, & 1 \cdot t_{\mathrm{Dwell}} \leq t < 2 \cdot t_{\mathrm{Dwell}} \\ f_3 = f_1 + 2\Delta f\,, & 2 \cdot t_{\mathrm{Dwell}} \leq t < 3 \cdot t_{\mathrm{Dwell}} \\ f_4 = f_1 + 3\Delta f\,, & 3 \cdot t_{\mathrm{Dwell}} \leq t < 4 \cdot t_{\mathrm{Dwell}} \\ f_5 = f_1 + 4\Delta f\,, & 4 \cdot t_{\mathrm{Dwell}} \leq t < 5 \cdot t_{\mathrm{Dwell}} \end{cases} \tag{4.9}$$

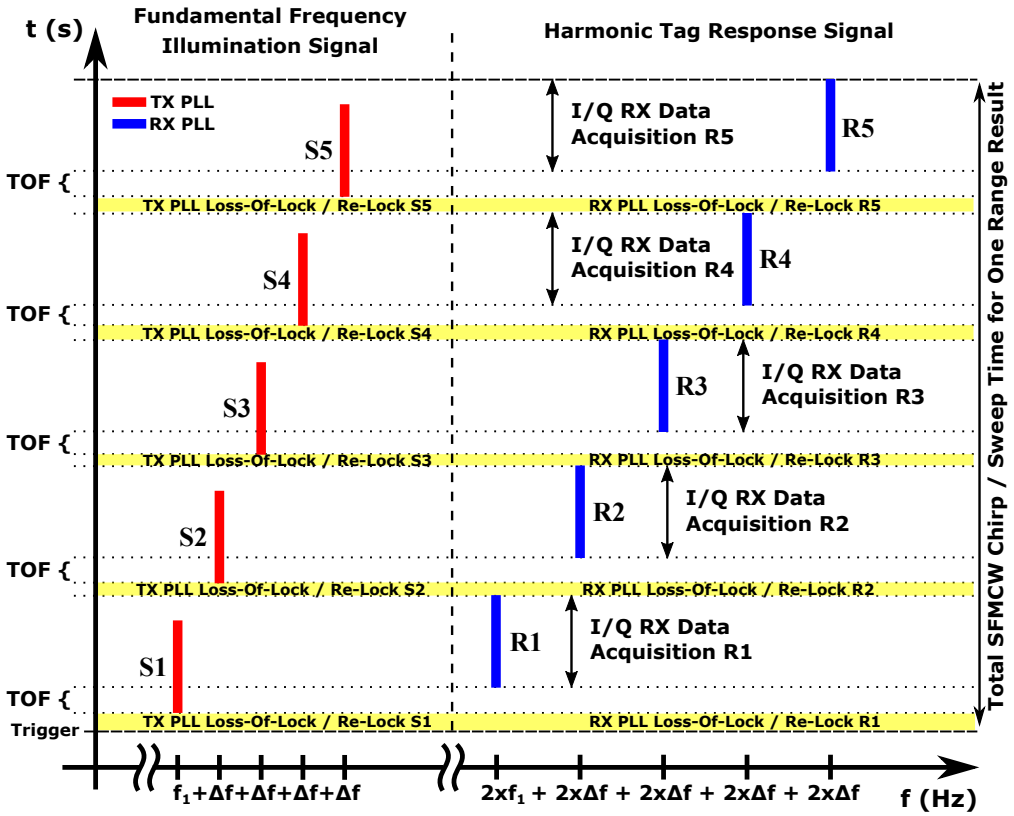

Figure 4.4: Waterfall (power over time over frequency) visualization of the stepped frequency modulated CW (SFMCW) ranging procedure for the fundamental frequency illumination and harmonic frequency response signal.

for an exemplary sweep using five equally spaced, linearly rising, frequency points, with a dwell-time of t_{Dwell} for each of the CW frequency sampling points.

The illumination signal generated by the interrogator can now be simply described by

$$E_{TX}(t) = E_0 \cdot \cos[2\pi \cdot f(t) \cdot t + \varphi_i]\,, \tag{4.10}$$

with E_0 representing the initial amplitude of the illumination signal at the antenna feed-point, and φ_i as an arbitrary, but repeatable, phase offset for each of the sampling points. By using the phase transfer properties of the memory-less harmonic power series model and abstracting all amplitude effects due to propagation, gain and losses throughout the signal path into $|E_{RX}|$, the signal received by the interrogator at the second harmonic of the illumination signal f(t) can be described as

$$E_{RX}(t) = |E_{RX}| \cdot \cos[2\pi \cdot 2f(t) \cdot (t - 2\tau) + 2\varphi_i + \varphi_j]\,, \tag{4.11}$$

with τ representing the actual one-way time of flight and φ_j as an arbitrary, but repeatable, phase offset of the frequency doubler as a product of its conversion process (extended

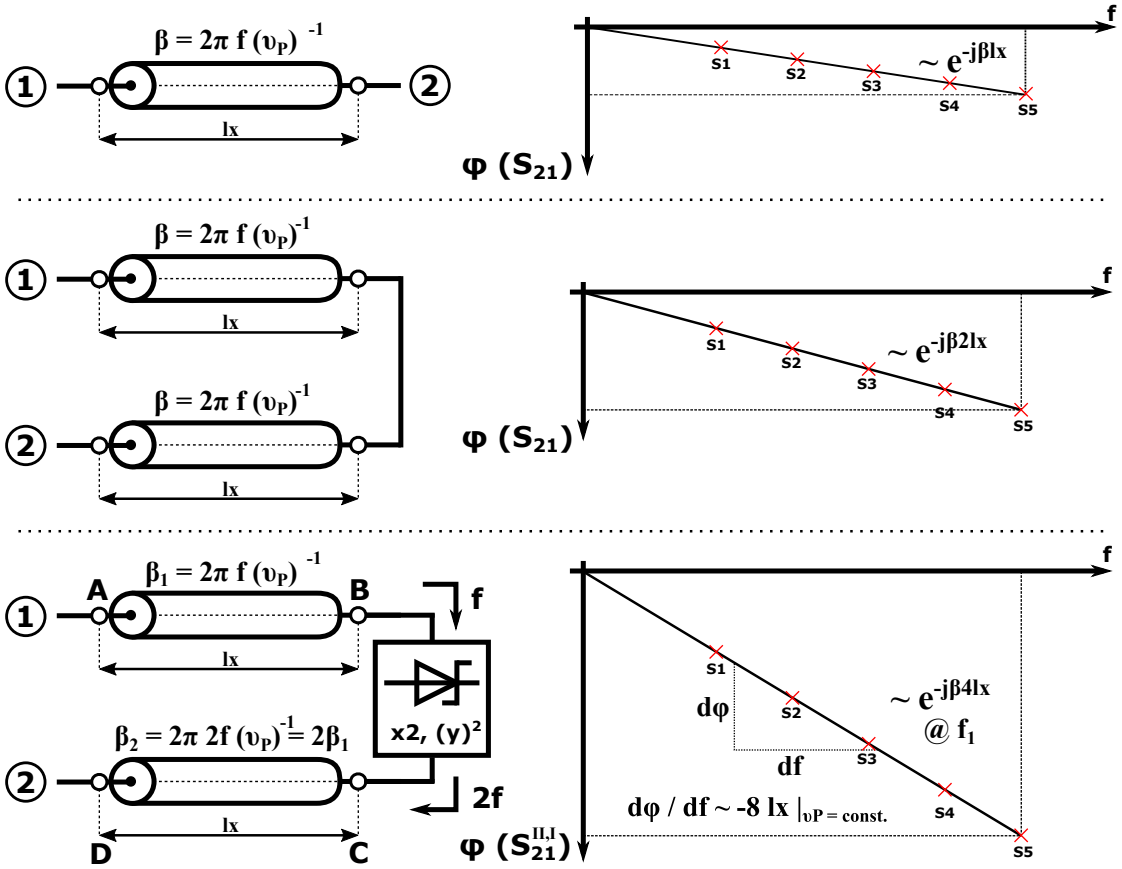

Figure 4.5: Development of the SFMCW harmonic phase progression for ranging.

from [83]). A graphical waterfall (power over time over frequency) representation of Eq. (4.10) and (4.11) is shown in Fig. 4.4, including additional highlighting of the delays involved in the process.

The ranging process itself can be theoretically achieved in two ways: By measuring the time of flight of the signals (see Fig. 4.4) and comparing the starting time of illumination with the arrival of the harmonic response, or as used in SFMCW, measuring the wave velocity and slant range dependent phase shift in the argument of Eq. (4.11) between different frequency points of the f(t) sequence to measure the slant range to the harmonic tag target.

In order to understand the phase based SFMCW ranging process, it is useful to start with the basics of transmission phase progression in the linear non-harmonic domain using normal S-parameters. When a lossless perfectly matched transmission line with the physical length l_x, using a dielectric with a relative permittivity of ε_R, resulting in the characteristic phase velocity ν_p, is considered, its forward transmission parameter S_{21}, and especially its transmission phase, can be determined by

$$S_{21} = e^{-j\beta \cdot l_x} \Leftrightarrow S_{21} = e^{-j2\pi f^I \nu_p^{-1} \cdot l_x}\,,\; S_{11} = S_{22} = 0\,,\; \nu_p = (\sqrt{\varepsilon_R \varepsilon_0 \mu_0})^{-1}\,, \tag{4.12}$$

which results in a linear phase progression over frequency $\propto e^{-j\beta l_x}$, as shown in the top of Fig. 4.5. As the slope of the phase argument progresses linearly, theoretically only two measurements at two different frequency sampling points are necessary to determine the slope $d\varphi/df$ and therefore l_x, when ν_p or ε_R is known ($\nu_p = c_0(\sqrt{\varepsilon_R})^{-1}$).

When a second perfectly matched lossless transmission line of the same length l_x with the same phase velocity ν_p is now added to the first line, simulating a signal round trip over the distance $2 \cdot l_x$, its forward transmission parameter S_{21} is calculated by concatenating both transmission parameters [47] in the form of

$$S_{21} = e^{-j\beta \cdot l_x} \cdot e^{-j\beta \cdot l_x} \Leftrightarrow S_{21} = e^{-j4\pi f^I \nu_p^{-1} \cdot l_x}\,,\; S_{11} = S_{22} = 0\,, \tag{4.13}$$

which shows that a doubling in length results in a proportional doubling of the phase argument's slope, as expected for linear phase progression.

In order to describe the harmonic phase progression from the fundamental frequency f_1 to the second harmonic f_2, when a frequency doubler is placed in between both length of transmission line after one length of l_x, as shown in the bottom part of Fig. 4.5, it is helpful to follow the progression of a rotating phasor through different points (A to D) in the schematic shown in Fig. 4.5, which is heavily extended from the basic derivation given in [34]. The initial starting phasor of the illumination signal at point A, consisting of a unit vector with its frequency f^I and time dependent argument ωt and an arbitrary, but repeatable, initial phase offset φ_0, can be described as

$$y(A) = e^{-j(\omega t + \varphi_0)} \Leftrightarrow y(A) = e^{-j(2\pi\, f^I \cdot t + \varphi_0)}\,. \tag{4.14}$$

The illumination signal now transits through the perfectly matched loss-less transmission line with its length l_x, which induces a length and phase velocity proportional phase shift on the starting signal as described earlier. Therefore, the signal at point B can be written as

$$\begin{aligned} y(B) = y(A) \cdot e^{-j\beta_1 \cdot l_x} \Leftrightarrow y(B) = e^{-j(\omega t + \varphi_0)} \cdot e^{-j2\pi f^I \nu_p^{-1} \cdot l_x}\,, \\ \Leftrightarrow y(B) = e^{-j(2\pi f^I \nu_p^{-1} \cdot l_x + \omega t + \varphi_0)}\,, \end{aligned} \tag{4.15}$$

to describe the fundamental wave reaching the input of the frequency doubler. By using the memory-less power series approximation of the frequency doubler's transfer function, the output signal of the doubler at point C is

$$y(C) = a_2 \cdot [y(B)]^2 \Leftrightarrow y(C) = a_2 \cdot e^{-2j(2\pi f^I \nu_p^{-1} \cdot l_x + \omega t + \varphi_0)}\,, \tag{4.16}$$

[47] This is only possible due to the perfect matching, i.e. $S_{11} = S_{22} = 0$ assumption, otherwise T-parameters must be used to concatenate two-ports, which was not performed here for clarity.

with a_2 being the amplitude conversion factor of the doubler to the second harmonic, which is dropped from the description for reasons of clarity, as only the progression of the phase argument is relevant for the SFMCW ranging procedure. From the argument of the phasor at point C it can be seen, that all variables of the argument are now doubled, which is obviously intended for the fundamental frequency, but also includes the initial phase offset φ_0, which is now reduced to an ambiguity free range of $[+\pi/2, -\pi/2]$. While not strictly relevant for the SFMCW ranging procedure, this could be relevant for the transmission of data to and from the the tag in a RFID like fashion for other applications.

Now that the fundamental illumination frequency is doubled at point C, the propagation constant β_2 is also different for the completion of the round trip to point D of the schematic. By using β_2 for the propagation constant of the second harmonic, the phasor at point D in can be described as

$$y(D) = y(C) \cdot e^{-j\beta_2 \cdot l_x} \,. \tag{4.17}$$

When the transmission lines are assumed to be free of dispersion, therefore $\nu_p(f^I) = \nu_p(f^{II}) = \text{const.}$ and $\varepsilon_R(f^I) = \varepsilon_R(f^{II}) = \text{const.}$, β_2 can be re-written as

$$\beta_2 = \frac{2\pi\, f^{II}}{\nu_p} \cdot l_x \,, \text{ with } f^{II} = 2 \cdot f^I \,, \text{ and } \nu_p(f) = \text{const.} \,, \tag{4.18}$$

$$\beta_2 = \frac{4\pi\, f^{I}}{\nu_p} \cdot l_x \,, \text{ and therefore}$$

$$y(D) = e^{-2j(2\pi f^I\, \nu_p^{-1} \cdot l_x + \omega t + \varphi_0)} \cdot e^{-j4\pi f^I\, \nu_p^{-1} \cdot l_x} \,, \tag{4.19}$$

which can again be re-written to the more compact form

$$y(D) = e^{-2j(\omega t + \varphi_0)} \cdot e^{-j8\pi f^I \nu_p^{-1} \cdot l_x} \,. \tag{4.20}$$

The mixed frequency S-parameter representation can now be calculated by calculating the ratio $S_{21}^{II,I} = y(D)/y(A)$, which results in

$$\angle(S_{21}^{II,I}) = -2 \cdot \varphi_0 - \frac{8\pi f^I}{\nu_p} \cdot l_x \,, \tag{4.21}$$

for the argument of the frequency converting forward transmission parameter $S_{21}^{II,I}$. In order to remove the repeatable, but unknown, initial phase offset φ_0 from Eq. (4.21), a measurement performed at a known distance l_{Ref} can be used to normalize the measurement results, resulting in

$$\angle\left(\frac{S_{21,M}^{II,I}}{S_{21,\text{Ref}}^{II,I}}\right) = -2 \cdot \varphi_0 + 2 \cdot \varphi_0 - \frac{8\pi f^I}{\nu_p} \cdot l_x + \frac{8\pi f^I}{\nu_p} \cdot l_{\text{Ref}} \,, \tag{4.22}$$

which can be simplified to the final expression

$$\angle\left(\frac{S_{21,M}^{II,I}}{S_{21,\text{Ref}}^{II,I}}\right) = \frac{-8\pi f^I}{\nu_p} \cdot (l_x - l_{\text{Ref}}) \,. \tag{4.23}$$

This approach is extremely similar to the forward transmission normalization performed on early VNAs for S_{21} measurement correction using a known thru, i.e. known length, calibration standard, except Eq. (4.23) enhances this procedure to the frequency converting measurement of the frequency doubler harmonic radar tag. In Eq. (4.23), the only unknown coefficient left is the one-way distance l_x, or slant range R to target in case of harmonic radar measurements.

While it may seem cumbersome at first to need a reference measurement at a known distance to "calibrate" the interrogator system in the harmonic radar context, it is important to remember that the free-space measurements performed with antennas ($\varepsilon_R = 1$, $\nu_p = c_0$) and the harmonic radar tag and measurement using coaxial cables of known electrical length (l_x and ν_p are known) are equal in the derivation presented here. A practical implementation could therefore use high quality coaxial relays with a sufficiently high isolation, to switch between the antennas and a doubler with attenuators internal to the system connected via a known coaxial cable length l_{Ref} to perform this calibration autonomously at power-on, similar to a simple form of a automatic calibration unit (ECAL, AutoCal) commonly used in conjunction with VNAs.

The initial phase offset φ_0 is explicitly used throughout the whole derivation of Eq. (4.23) to capture a shortcoming of the synthesizers used in the VNA module system. While TI repeatable and especially phase repeatable signals can be achieved with the ADF4356 synthesizer for arbitrary frequencies and step-sizes, this repeatability is only valid for one specific power cycle. If the device is power-cycled, a new but repeatable output phase will be generated for each frequency, resulting in a new value for φ_0. A more in-depth discussion about this matter can be found in the hardware description in chapters 2.3.3 and 3.3 in this work.

In order to measure $S_{21}^{II,I}$ with the interrogator, which is now essentially a non-linear VNA, the harmonic tag return b_2^{II} and the fundamental frequency illumination signal a_1^I must be measured to fulfill the definition of

$$S_{21}^{II,I} = \frac{b_2^{II}}{a_1^I} \,. \tag{4.24}$$

When $S_{21}^{II,I}$ is measured directly by using a standard NVNA measurement setup, as shown in Fig. 4.6, at least three vector receivers, a directional coupler, or tap, to sample the phase of the illumination signal and a harmonic phase reference for LO phase correction, is needed, which results in a fairly complex interrogator system on par with a unidirectional two-port VNA[48].

Furthermore, the addition of the illumination signal sampling and especially the incorporation of the receiver frequency tracking phase reference presents a huge potential for coherent local interference generation which can not be removed by signal processing and is hard to mitigate due to the dynamic range in excess of 140 dB required even for short range harmonic radar systems.

Fortunately the system complexity of the classical non-linear VNA shown in Fig. 4.6 can be reduced considerably for harmonic radar applications, when the TI repeatable

[48] An in-depth explanation of the NVNA concept can be found in chapter 3.1 of this work.

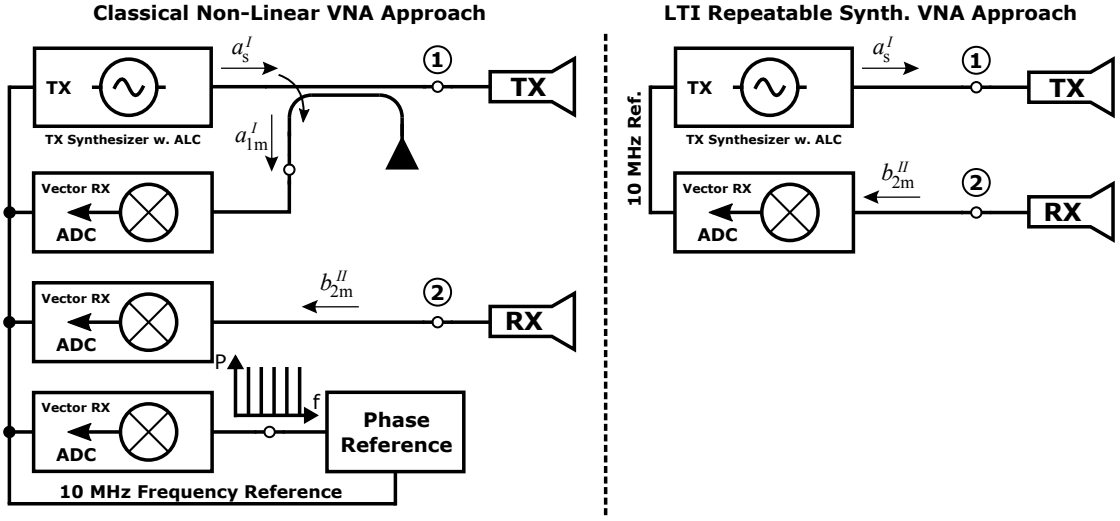

Figure 4.6: Schematic diagram comparing the harmonic radar interrogator built as a classical non-linear VNA using a phase reference for receiver LO phase correction and the new approach using TI repeatable synthesizers.

synthesizers are used for the generation of the illumination signal as well as the LO of the receiver in conjunction with the $S_{21,M}^{II,I}$ normalization, as demonstrated in Eq. (4.23).

When Eq. (4.23) is expanded with the definition of $S_{21}^{II,I}$ shown in Eq. (4.24), the measurement definition of the normalized result can be rewritten as

$$\frac{S_{21,M}^{II,I}}{S_{21,\mathrm{Ref}}^{II,I}} = \frac{b_{2,M}^{II}}{b_{2,\mathrm{Ref}}^{II}} \cdot \frac{a_{1,\mathrm{Ref}}}{a_{1,M}}\,, \text{ which simplifies to} \tag{4.25}$$

$$\frac{S_{21,M}^{II,I}}{S_{21,\mathrm{Ref}}^{II,I}} = \frac{b_{2,M}^{II}}{b_{2,\mathrm{Ref}}^{II}}\,, \text{ with } \frac{a_{1,\mathrm{Ref}}}{a_{1,M}} = 1\,, \tag{4.26}$$

when a TI repeatable stimulus signal a_1^I, and therefore a TI repeatable LO- and stimulus signal, is used for the fundamental illumination frequency generation in the interrogator.

Therefore, no actual measurement of the a_1^I must be performed at any time under these conditions. Additionally, the phase reference shown in the classical NVNA setup on the left side of Fig. 4.6 can be omitted, resulting in the lean system shown on the right side of Fig. 4.6. This reduced non-linear VNA setup is completely capable of carrying out the complete frequency converting phase based measurements required for SFMCW ranging, without any of additional components usually found in a NVNA system. As explained in the single receiver VNA chapter 2.2.1 in this work, the omission of the directional coupler, two vector receivers and an additional phase reference standard reduces the system cost of the interrogator considerably.

As the SFMCW ranging process is based on discrete frequency domain sampling and uses only the phase of the return signal, it is important to consider the maximum unambiguous range based on the frequency step-size of the sampling. The phase is

determined from the I/Q samples via the atan2 function, which is defined for results in the range of $[-\pi, +\pi]$, resulting in a total usable unambiguous phase distance of 2π. Therefore, a phase wrap-around, i.e. a phase advance of more than 2π, must be avoided over distance between two adjacent frequency sampling points in order to get an unambiguous range result.

The maximum unambiguous distance for a given frequency spacing Δf can be calculated as follows (modified and extended from [34]): When two frequency sampling points f_1 and f_2 are measured for a given slant range or distance l_x, its mixed frequency S-parameter angle results $(S_{21}^{II,I})|_{f_1}$and $(S_{21}^{II,I})|_{f_2}$ can be described using Eq. (4.23) by

$$\angle(S_{21}^{II,I})|_{f_1} = \varphi_1 = \frac{-8\pi l_x}{\nu_p} \cdot f_1^I \text{ , and } \angle(S_{21}^{II,I})|_{f_2} = \varphi_2 = \frac{-8\pi l_x}{\nu_p} \cdot f_2^I \,, \tag{4.27}$$

which must result in phase distance between frequency sampling points of

$$\varphi_2 - \varphi_1 \leq 2\pi \,, \tag{4.28}$$

to avoid range aliasing. When Eq. (4.27) is inserted into Eq. (4.28), this results in

$$\frac{-8\pi l_x}{\nu_p} \cdot f_2^I - \frac{-8\pi l_x}{\nu_p} \cdot f_1^I \leq 2\pi \,, \tag{4.29}$$

which can be rearranged in order to express the frequency step-size $\Delta f = f_2^I - f_1^I$ to

$$\frac{-8\pi}{\nu_p} \cdot l_x \cdot \underbrace{(f_2^I - f_1^I)}_{\Delta f\text{: step-size}} \leq 2\pi \,. \tag{4.30}$$

The maximum unambiguous range $l_{x,\max}$ can now be calculated from Eq. (4.30) by solving for $l_{x,\max}$ using the upper phase distance limit of 2π, yielding

$$l_{x,\max} = \frac{\nu_p}{\Delta f\ 8\pi} \cdot 2\pi \ \Leftrightarrow\ l_{x,\max} = \frac{\nu_p}{4 \cdot \Delta f} \,. \tag{4.31}$$

When classical complex inverse DFT/FFT time domain transformation radar signal processing is applied to the complex frequency domain data, the range resolution ΔR of the SFMCW radar system can be directly determined from Eq. (4.31) by dividing both sides of the equation by the amount of I/Q frequency domain sampling points N ([34]), yielding

$$\Delta R = \frac{l_{x,\max}}{N} = \frac{\nu_p}{N \cdot 4\Delta f} \ \Leftrightarrow\ \Delta R = \frac{\nu_p}{4 \cdot \mathrm{BW}} \,. \tag{4.32}$$

4.2.2 SFMCW Ranging Procedures and Harmonic Target Resolution

In order to resolve the target distance, two different methods are presented and used in this work:

- The classic but computationally intensive inverse discrete Fourier-transform (IDFT, $\mathcal{F}^{-1}$) processing of the discrete frequency domain samples $(S^{II,I}_{21,M}/S^{II,I}_{21,\mathrm{Ref}})_i = S_{R,i}$, $i = 1 \ldots N$ to obtain a time domain range profile similarly to the post-processing applied to FMCW signals ([18]), and
- A new Theil-Sen estimator ([130, 145]) based interpolated total phase slope ranging technique operating solely in the frequency domain, which uses considerably fewer resources than the IFFT approach but is only capable of ranging the strongest harmonic target return.

In case of the IFFT based SFMCW harmonic ranging, the complex valued frequency domain I/Q samples $S_{R,i} = S^{II,I}_{21,M}/S^{II,I}_{21,\mathrm{Ref}}$ obtained from Eq. (4.26) are first converted via the IDFT transformation to a complex time domain range profile $s_{R,i}$, yielding N discrete range bins, spaced ΔR apart. The scalar magnitude $|s_{R,i}|$ of the time domain range profile is then searched for one or multiple local maxima of specified prominence. The range bin index of these maxima can than be converted for a certain index j to the target range R by calculating $R = (j-1) \cdot \Delta R$.

Compared to the signal processing applied to (S)FMCW I/Q baseband data to acquire valid and reliable target range results in the form of clutter removal, coherent change detection, and moving target indication ([18], [121]), this bare-bones frequency to time domain conversion processing is usually sufficient to acquire the harmonic radar targets due to the inherent clutter and non-tagged target suppression of the harmonic radar principle when only detection and ranging are required ([102]).

A synthetic example for a harmonic range profile of a single harmonic radar tag is shown in Fig. 4.7. For this example, a tag is positioned at a slant range of R = 1.15 m away from the interrogator. The discrete fundamental frequency illumination is performed in the radar S-band from a start frequency of $f^I_{\mathrm{Start}} = 2850\,\mathrm{MHz}$ up to the upper frequency limit of $f^I_{\mathrm{Stop}} = 3000\,\mathrm{MHz}$ with a frequency step-size of $\Delta f = 7.5\,\mathrm{MHz}$, yielding $N = 21$ discrete I/Q frequency domain sampling points over a fundamental frequency bandwidth of $BW = 150\,\mathrm{MHz}$. The resulting discrete range resolution ΔR can be calculated by applying Eq. (4.32) as $\Delta R = 0.4997\,\mathrm{m}$ per IFFT range bin.

From the results shown in the upper left corner of Fig. 4.7 it can be seen, that the ranging error $R_{\mathrm{Meas}} - R = 0.151\,\mathrm{m}$ is fairly large due to the coarse range discretization of the IFFT, which in turn is caused by the low number of sampling points. Nevertheless, the actual position of the tag is still present in the range plot, although spread out over the adjacent range bins.

If this return is assumed to be the only target return present in the original range bin, which is a fair assumption with the cooperative nature of harmonic radar in contrast to primary radar, and aliasing caused by harmonic radar returns beyond $l_{x,\max}$ can be ruled out, the absolute accuracy of the ranging result can be improved by performing

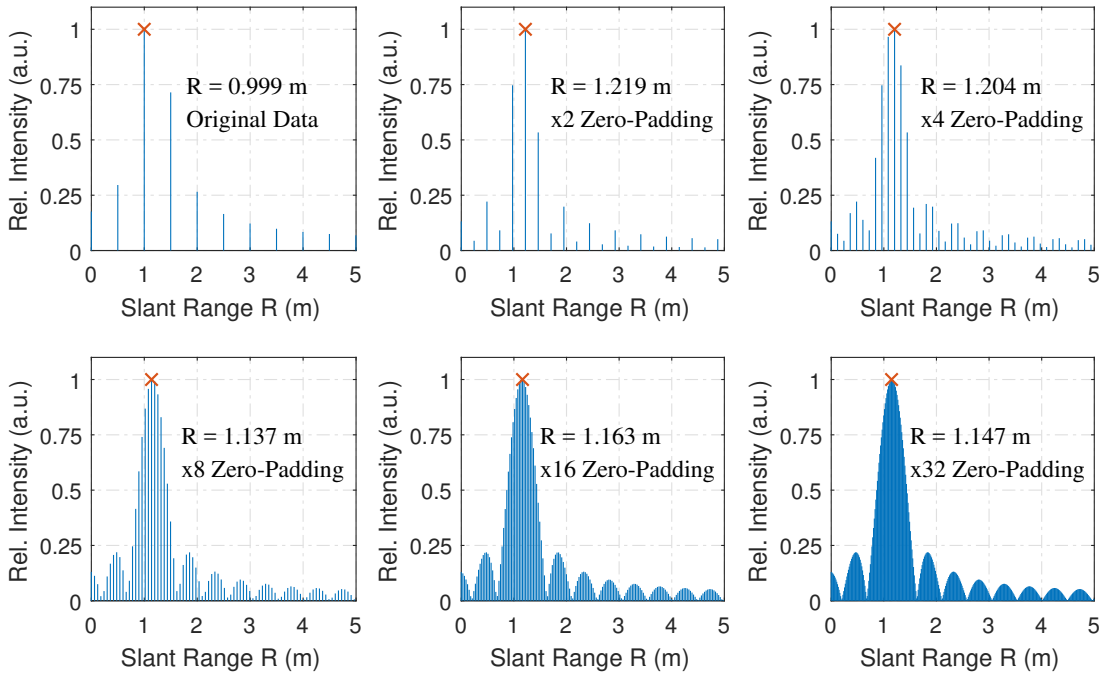

Figure 4.7: IDFT based normalized synthetic ranging results for different zero-padding factors simulated for a single harmonic radar target at $R_1 = 1.15\,\mathrm{m}$ slant range. $f^I_{\mathrm{Start}} = 2850\,\mathrm{MHz}$, $f^I_{\mathrm{Stop}} = 3000\,\mathrm{MHz}$, $N = 21$ points, $\Delta f = 7.5\,\mathrm{MHz}$, $\Delta R = 0.4997\,m$.

zero-padding at both the positive and negative frequency limits in the real and imaginary part of the frequency domain data before applying the IFFT transformation at the cost of considerably increased computing time. If the aforementioned conditions are met, this effectively results in an increased sampling rate in the frequency domain and consequently a finer discrete range resolution per bin in the time domain IFFT range plot. As the harmonic radar returns are generally not periodic frequency domain signals, the zero padding interpolated ranging results shown in Fig. 4.7 strongly exhibit the periodic ringing artifacts of the Gibbs' phenomenon around the interpolated main harmonic radar return in addition to the sinc(x) ripple caused by the rectangular window function.

Knowing this consequence of the frequency domain zero-padding, which is also sometimes called perfect interpolation or re-sampling by interpolation ([79]), is especially important in multi-tag or multi-harmonic-target scenarios which can lead to false positive target identification or ranging errors through superposition of the ripple with a weaker valid return signal in adjacent range bins.

Furthermore, it is important to realize that frequency domain zero-padding can not improve the ability to resolve individual targets beyond the original $\Delta R = 0.4997\,\mathrm{m}$ resolution for the aforementioned exemplary harmonic SFMCW system. While the harmonic radar returns for two tags, separated by a distance of $\Delta d = 1.08\,\mathrm{m} > \Delta R$,

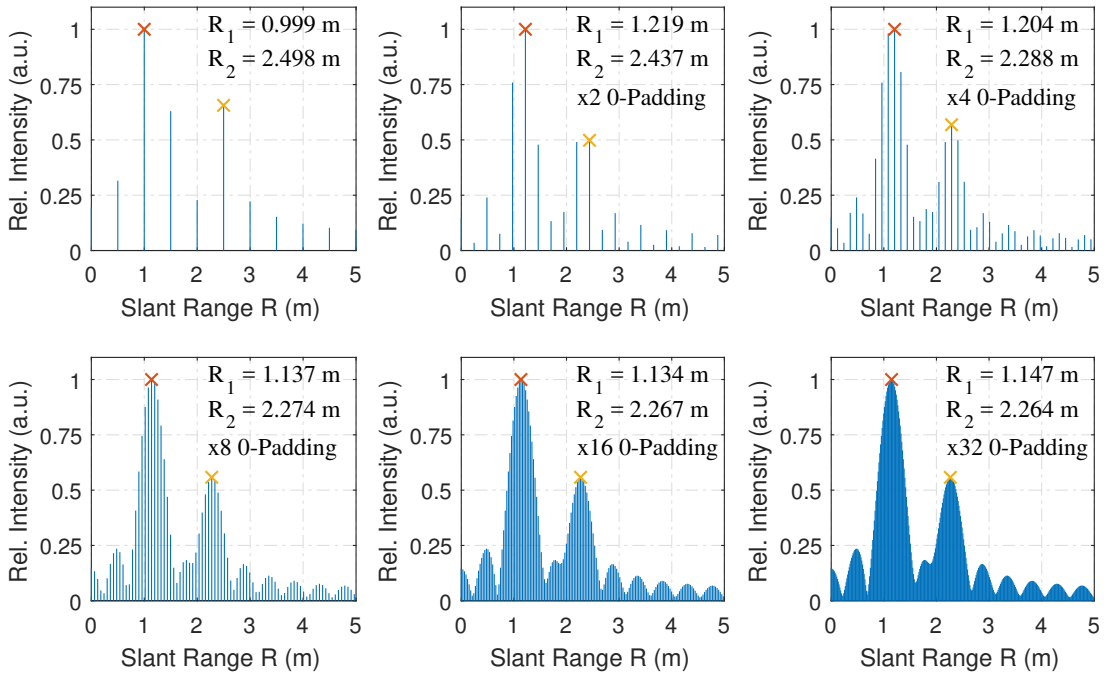

Figure 4.8: IDFT based normalized synthetic ranging results for different zero-padding factors simulated for a two harmonic radar targets. Target 1 at $R_1 = 1.15\,\mathrm{m}$ slant range, target 2 at $R_2 = 2.23\,\mathrm{m}$ slant range, -6 dB rel. amplitude. $f^I_{\mathrm{Start}} = 2850\,\mathrm{MHz}$, $f^I_{\mathrm{Stop}} = 3000\,\mathrm{MHz}$, $N = 21$ points, $\Delta f = 7.5\,\mathrm{MHz}$, $\Delta R = 0.4997\,m$.

can easily by identified, distinguished, and improved in accuracy by frequency domain zero-padding, as shown in the range plots in Fig. 4.8. In contrast, harmonic tag returns spaced closer than ΔR, as shown for a separation distance of $d = 0.23\,\mathrm{m}$ in the range plots of Fig. 4.9, can only be resolved for the mean slant range of both tags combined $((1.15\,\mathrm{m} + 1.38\,\mathrm{m})/2 = 1.265\,\mathrm{m})$.

In harmonic radar measurement scenarios, where only one single tag is present, a new, more computationally efficient, harmonic radar ranging procedure can be used: The Theil-Sen estimator phase ranging procedure that operates directly on the frequency domain $S^{II,I}_{21}$ data acquired by the NVNA interrogator system. A visual example of this procedure is shown in Fig. 4.10 for a single tag positioned at 1.15 m distance from the interrogator.

In order to perform the Theil-Sen estimator phase based ranging process, the modulo $[-\pi, +\pi]$ wrapped instantaneous phase information of $\arg(S^{II,I}_{21})$ must be converted by one-dimensional phase unwrapping (see [66]) to its unbound representation. While the phase unwrapping itself is pretty straight forward for an ideal continuous phase by performing continuous integration, additive noise in combination with discrete samples presents a challenging issue.

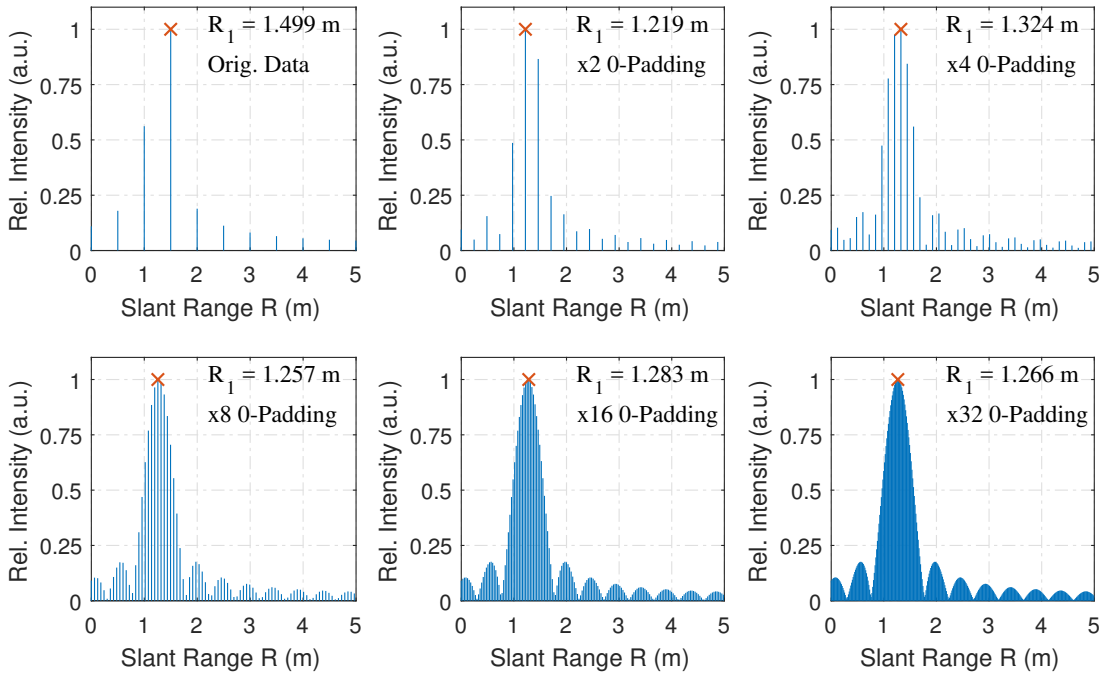

Figure 4.9: IDFT based normalized synthetic ranging results for different zero-padding factors simulated for a two harmonic radar targets. Target 1 at $R_1 = 1.15\,\mathrm{m}$ slant range, target 2 at $R_2 = 1.38\,\mathrm{m}$ slant range, -6 dB rel. amplitude. $f^I_{\mathrm{Start}} = 2850\,\mathrm{MHz}$, $f^I_{\mathrm{Stop}} = 3000\,\mathrm{MHz}$, $N = 21$ points, $\Delta f = 7.5\,\mathrm{MHz}$, $\Delta R = 0.4997\,m$.

To unwrap the discrete instantaneous phase successfully, a maximum phase advance, including noise, of $\leq \pi$ must be obeyed between sampling points to reconstruct the true unwrapped phase ([156]), which is less than the original aliasing minimal phase advance criterion used in Eq. (4.30).

In the harmonic radar context, this leads to a SNR dependent minimal frequency spacing for a given range to avoid missed or false phase wrapping points and therefore 2π steps in the unwrapped information. When a minimum SNR of 10 dB for ranging is assumed, this results in a maximum phase error of $\pm 17.5° \approx \pm 0.1\,\pi$ due to noise ([52]). This additive error reduces the maximum allowed phase advance between two frequency sampling points to $\leq \pi - 2 \cdot 0.1\,\pi = 0.8\,\pi$, for a successful unwrap. The unambiguous range of Eq. (4.30) is therefore limited to only $2/5 \cdot l_{x,\max}$ for a SNR of 10 dB due to the required unwrapping step. When the discrete unwrapped phase of $\arg(S^{II,I}_{21})$ is obtained, a linear regression of the phase slope is calculated to interpolate between the discrete sampling points and therefore discrete range results. Additionally, this reduces the effect of additive noise on the final range result. While the slope could be certainly calculated by the popular linear least-squares regression, this procedure is sensitive to data outliers. This property, coupled with the strong tendency of discontinuous $\pm 2\pi$ outliers by the

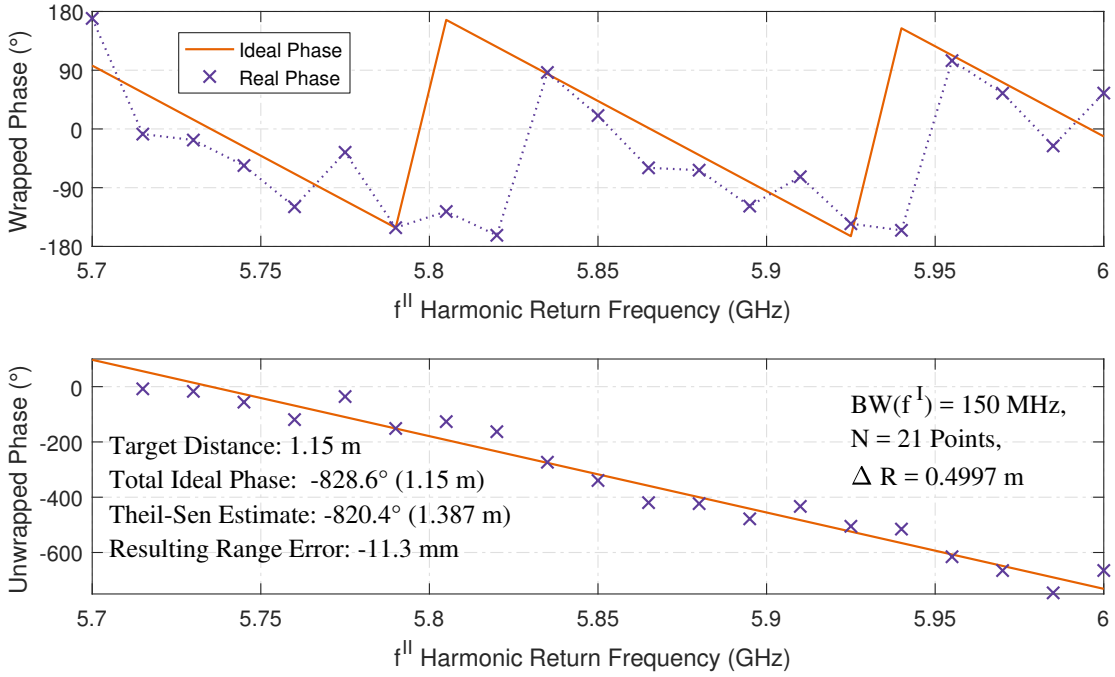

Figure 4.10: Visualization of the Theil-Sen estimator phase slope ranging process.

one-dimensional phase unwrapping in the input data to the regression, favors a far less popular but more robust and simpler linear regression estimator: The Theil-Sen (TS) slope estimator algorithm ([130, 145]), which tolerates a corruption of up to 29.3% of its input data sampling points ([117]) without significant alteration of its outcome.

The TS slope estimate is determined by calculating the phase slopes $s_{\varphi,i} = \Delta\varphi/\Delta f$ for all pairs of unwrapped phase sampling points. The median $\tilde{s_\varphi}$ of all $s_{\varphi,i}$ values represents the TS slope estimate. While the computational effort is fairly high compared to other linear regression methods, it is still lower than the effort required for calculating an IDFT with frequency-domain zero padding to achieve the same ranging accuracy, except for some cases where the IFFT algorithm can be used (TS general case: $O(n) = n^2$, IDFT: $O(n) = n^2$, IFFT $O(n) = n \cdot \log(n)$ for radix-2 n, i.e. $n = 2^m$).

With the TS phase slope estimation $\tilde{s_\varphi}$ known, the range to the target can now be obtained by calculating the derivative for the frequency f, and therefore the slope, of the argument of the mixed frequency harmonic radar S-parameter Eq. (4.23) and rearranging the result to

$$l_{\text{Target}} = -\frac{\tilde{s_\varphi}\,\nu_P}{8 \cdot \pi}\,. \tag{4.33}$$

4.3 The Experimental SFMCW Radar System and Setup

In order to verify the theoretical and numerical assumptions made in the previous sections, an experimental harmonic SFMCW radar interrogator setup with a corresponding harmonic radar tag was developed around the VNA module system, described earlier in chapters 2.3.4 to 2.3.7 in this work, with the following goals in mind:

- Demonstrating the feasibility and performance of direct narrow-band frequency domain SFMCW measurements by using a VNA vector receiver instead of the established time domain, oscilloscope based, SFMCW setup used in the publications by Gallagher, Mazzaro et al. to obtain lower receiver noise floor and higher dynamic range,
- Validating the results of harmonic power series based non-linear radar equation by precise harmonic return power measurements over tag distance,
- Validating the feasibility of the mixed-frequency S-parameter approach, including the hardware itself, for the SFMCW ranging procedure,
- Validating and comparing the Theil-Sen phase slope estimator based ranging process for both its robustness and range measurement accuracy with the results of the established IDFT ranging approach,
- Validating the power-series approximation modeling of the passive frequency doubler, which includes the illumination power independence of the phase transfer function from the fundamental to the harmonic frequency,
- Examining the impact of illumination signal and harmonic return signal polarization in a multi-path environment, as formulated in the outlook of [34],
- Performing fundamental frequency clutter receiver front-end compression tests to asses the clutter rejection ability of the system, and
- Demonstrating the clutter suppression ability and robustness of the harmonic radar principle itself.

4.3.1 The Non-Linear VNA Harmonic Radar Interrogator

The interrogator system used throughout the following sections was designed to provide an illumination signal in the lower section of the marine radar S-band from 2900 to 3000 MHz, while reception of the harmonic return occurs in parts of the 5.8 GHz ISM band, covering 5800 MHz to 6000 MHz. These frequencies are however not absolute design limits of the system, but are mandated by its intended application in the research project SEERAD[49], which aims to provide a low cost, low energy, search and rescue (SAR) assistance system as an augmentation of shipborne radar systems to aid in the cooperative

[49] SEEnotrettungssystem basierend auf einem störungsarme RADar, funded by the German Ministry of Education and Research (BMBF), Förderkennzeichen / Reference Number 13N14117.

localization of otherwise small RCS objects in sea clutter like small lifeboats, lifejackets, and immersion suits in distress at sea situations. As the interrogator is built from the components of the VNA module system presented in chapter 2.3.2 of this work, the illumination signal frequency can in principle be chosen in any suitable frequency band in the range of 275 to 3300 MHz, which is only limited by the current upper reception limit of 6600 MHz of the harmonic receiver for the return signal. Therefore, the basic system used here could also be utilized for novel SFMCW UWB harmonic radar measurements given suitable tracking filters.

One of the biggest challenges in designing and building a working harmonic (SFM)CW radar interrogator system is the adequate suppression of local coherent harmonic interference created by the system itself, as even the most linear amplifiers and components generate sufficient levels of the second harmonic to severely limit the dynamic range of the interrogator to levels far above the thermal and sampling system noise-floor. As mentioned in [83], three main sources of local harmonic interference need to be addressed:

- Sufficient suppression of the harmonic components in the illumination signal chain by employing highly linear amplifiers with output power back-off and extensive lowpass or bandpass filtering,
- Sufficient suppression of the fundamental frequency illumination signal in the receiver signal chain, in order to avoid local harmonic generation in the receiver front-end, and
- Following microwave frequency EMI/EMC best-practices and advises for the mechanical construction of the system and its enclosures to shield and absorb as much of the harmonic signal as possible, as even unrelated signal and power lines can provide a leakage path through an otherwise shielded enclosure.

In order to address the first two important points, two different filter designs were developed and realized in planar transmission line filter technology: An S-band / C-band diplexer filter, which is used as an absorptive bandpass filter in the illumination signal transmit as well as harmonic frequency reception paths, with the unwanted signal terminated in a 50 Ω SMA termination, as well as a reflective C-band bandstop filter for use in the transmit path to provide a high attenuation for the second harmonic. Both filter designs are shown in Fig. 4.11.

The use of absorptive filters is a novel approach to the harmonic radar interrogator design and tries to realize and achieve two important goals: Its usage in the harmonic reception path to suppress the fundamental illumination signal avoids the re-radiation of the illumination signal, while its use in the transmit signal chain avoids unintended load-pulling effects in the amplifiers by reflecting the second harmonic back to the linear amplifier.

The realized performance of the C-band bandstop filter is shown in Fig. 4.12, while the performance figures of the S-band / C-band diplexer filter is shown in Fig. 4.13.

The C-band bandstop filter achieves a reflective stop band attenuation of 60 dB in the band center, while attenuating the illumination signal in the S-band by merely 0.5 dB.

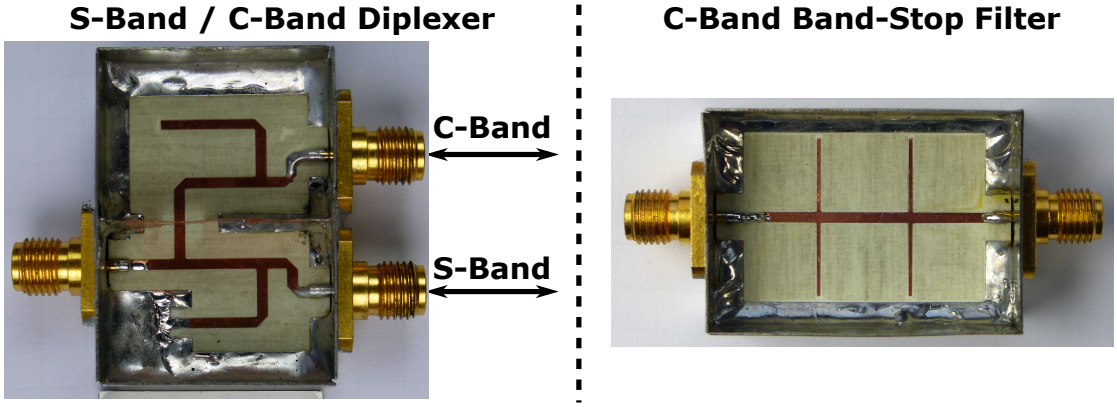

Figure 4.11: Picture of the custom planar transmission-line S-band / C-band diplexer and the C-band bandstop filters used in the experimental setup.

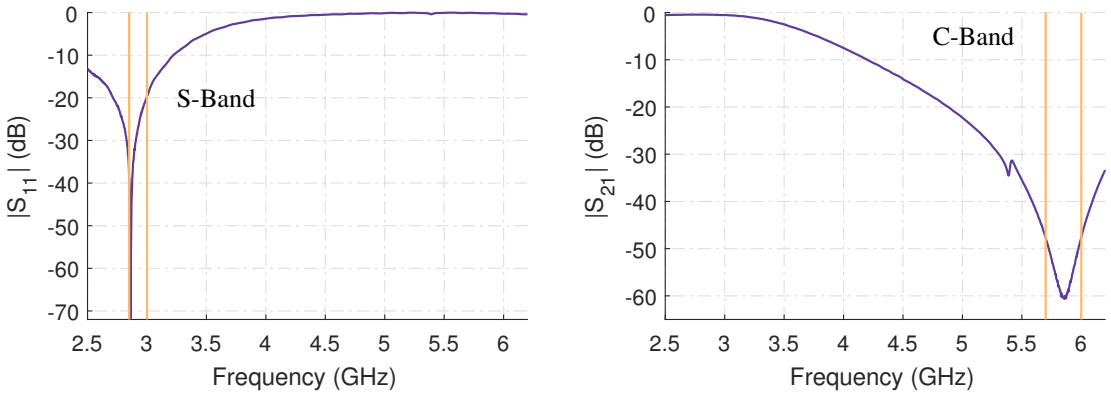

Figure 4.12: Typical measurement results of the reflective planar transmission line harmonic response bandstop filter. Intended S-band and C-band frequency limits highlighted.

The diplexer achieves a C-band attenuation of 40 dB, while displaying 0.25 dB insertion loss for the S-band path, while the C-band paths shows a maximum S-band attenuation of 35 dB, while having 0.5 dB insertion loss for the C-band signal.

In order to reduce the probability of harmonic interference by radiation coupling and RF leakage between the stimulus generator and the receiver, an effect which was already observed in the two port S-parameter measurements of the switched single receiver VNA system, both modules were housed in individual 19" rack-mountable metal enclosures.

Additional shielding measures in the form of EMI gaskets and feed-through capacitors for the power supply lines and EMI filters for signal lines were used throughout the assembly of the interrogator system. Wideband microwave polymer foam absorbers were additionally installed in each of the enclosures to de-Q the enclosures, as well as attenuating the radiated RF energy at the source. A picture of the receiver and transmitter enclosures in their opened state as used for the following measurements is

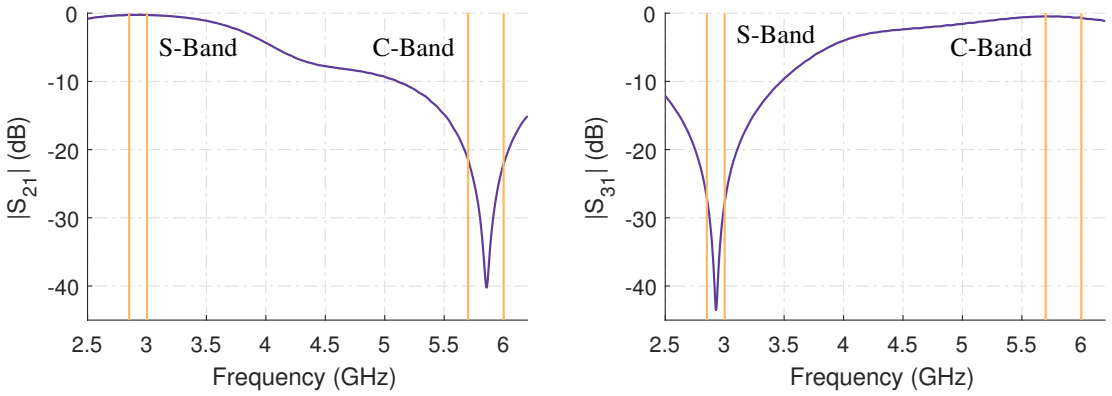

Figure 4.13: Typical measurement results of the S-band / C-band diplexer filter used as an absorptive bandpass filter. Intended S-band and C-band frequency limits highlighted. S_{21} S-band path, S_{31} C-band path.

shown in Fig. 4.14.

The author would like to thank Marc Mühmel, associated with the Institute of Microwave and Plasma technology (IMP) of the FH Aachen, for designing and building the diplexer and bandstop filters, as well as the system integration of the VNA modules and the enclosures.

An external high linearity TQP3M9028 MMIC amplifier with 14.4 dB of gain and an additional dedicated separate power supply was added to the stimulus generator assembly outside of the original enclosure and is therefore not shown in Fig. 4.14. The amplifier is followed by a S-band / C-band diplexer filter to terminate and absorb the C-band harmonics generated by the amplifier. The S-band illumination signal path is further filtered by a C-band bandstop filter for a total harmonic frequency attenuation of approximately 90 to 100 dB. Measurement results for the harmonic suppression of this setup is shown in Table 4.1 for a target fundamental frequency illumination signal output power of 10 dBm.

f (MHz)	2850	2875	2900	2925	2950	2975	3000
P(f^I) (dBm)	10.6	10.2	10.3	10.5	10.6	10.5	10.0
P(f^{II}) (dBm)	-83.9	-92.3	-97.8	-97.5	-96.8	-94.6	-91.1
ΔP (dB)	94.5	102.5	108.1	108.0	107.4	105.1	101.1

Table 4.1: Intrinsic second harmonic output power measurement results of the harmonic radar interrogator system, measured at the illumination signal S-band antenna feed-point.

In the measurements carried out in this work, the illumination transmit signal chain is finalized by an S-band WR-330 waveguide horn antenna with an integrated N-connector waveguide transition. This antenna offers approximately $G_{TX} = 10$ dBi of gain with a full-width half maximum beam opening angle of 60° in the H- and E-plane of the

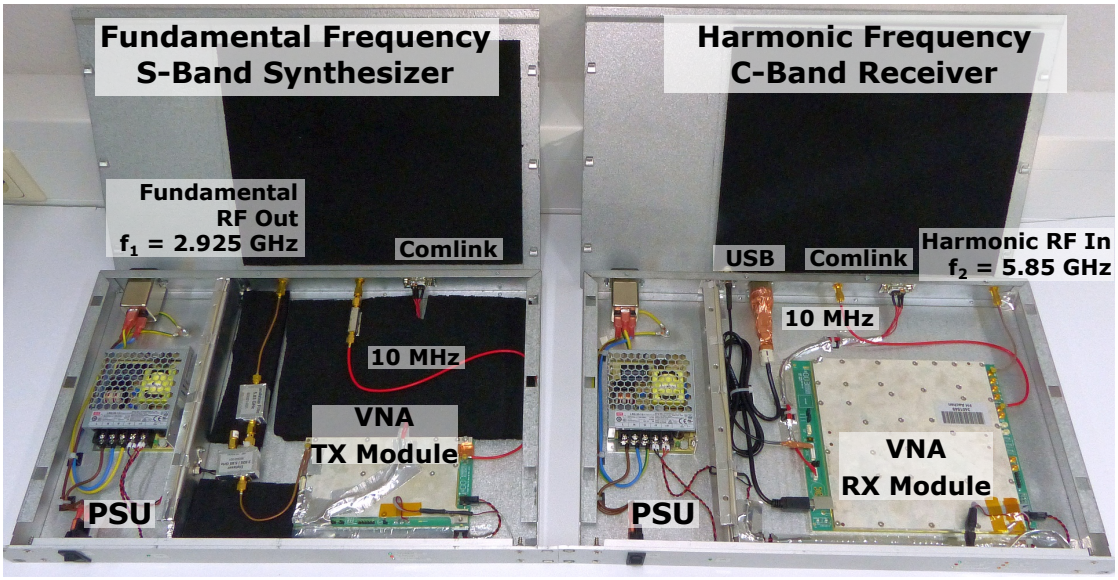

Figure 4.14: Annotated picture of the interrogator receiver and transmitter VNA modules in their rack-mount enclosures with added shielding, filtering, and support components. Frequencies denote band center frequencies.

radiation pattern. In the experiments presented later on, an antenna feed-point power of 10 dBm is used, which results in an equivalent isotropic radiated power (EIRP) of $P_{\mathrm{Illum,EIRP}} = 20\,\mathrm{dBm} \equiv 100\,\mathrm{mW}$ in combination with this antenna. By using such a low radiated power in contrast to other harmonic radar interrogator systems described in the literature (see [83] for an overview), the system presented here is fully compliant with even the most rigorous RF exposition limits. This was extremely important for the conduction of the experiments, as no dedicated and closed off outdoor measurement range or anechoic chamber was available for performing the experiments.

On the harmonic return signal reception side a C-band VT58SGAH15 WR-159 waveguide horn antenna with an integrated N-connector waveguide transition, manufactured by Vector Telecom, was used throughout the experiments. This antenna has an average gain of approximately $G_{RX} = 15\,\mathrm{dBi}$ over the frequency band of interest, with an average H- and E-plane full-width half maximum (FWHM) beam angle of 28°.

A GVA123 wideband MMIC amplifier, with a gain of approximately 16 dB and a noise figure of 4.4 dB, was installed directly at the RX antenna feed-point using a dedicated power supply and shielded power supply cables to mitigate signal leakage and interference problems. This front-end amplifier is followed by another S-band / C-band diplexer filter, with its S-band path terminated in a 50 Ω resistor in order to selectively attenuate the fundamental illumination signal, and to avoid local harmonic generation in the front-end of the VNA receiver.

All in all, these specifications presented for the transmit and receive signal path of the interrogator place this system at very low power end of the interrogator systems

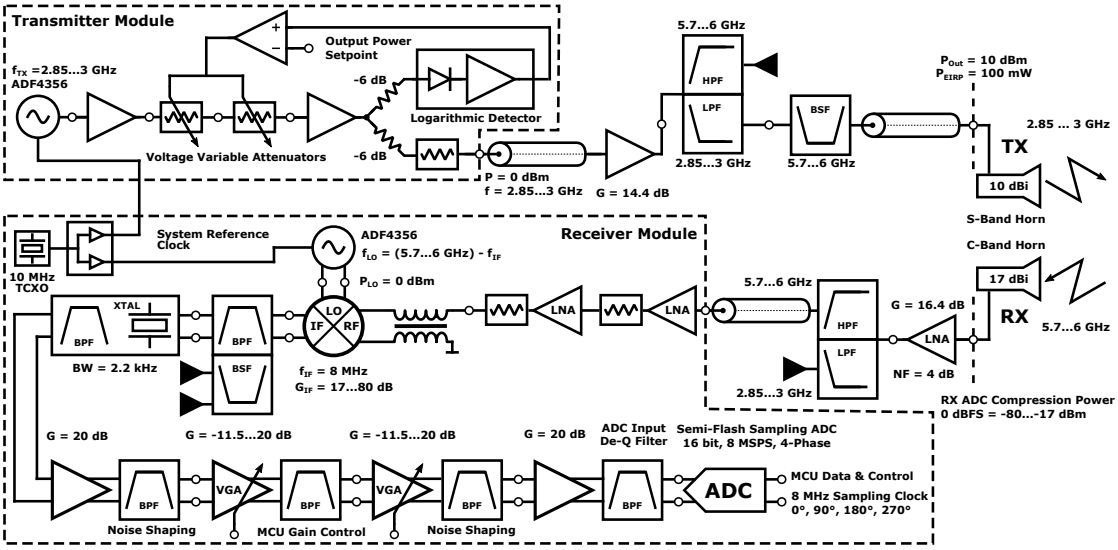

Figure 4.15: Block diagram of the complete SFMCW harmonic radar interrogator setup used in the experiments.

presented in [83], for both the RX/TX antenna gains, as well as the isotropic radiated illumination signal power. A complete block diagram of the interrogator system used in the following experiments is shown in Fig. 4.15.

As one of the main goals of the experiments is the accurate measurement of the harmonic return signal power over polarization and distance of the harmonic radar tag, a receiver power calibration ([27]) was performed. Due to the low RF input levels in harmonic radar, which are well below of the capabilities of thermal power heads, and the high amount of gain present in the receiver signal chain, which results in early compression of the front-end, a two tier receiver power calibration approach was followed.

First, the frequency doubler output of a SRS SG384 signal generator was characterized at an output power set-point of -10 dBm using a Rohde & Schwarz NRP-Z55 40 GHz precision thermal power head over the harmonic input frequency band from 5700 to 6000 MHz. Next, a combination of two 30 dB precision 18 GHz SMA attenuators and a 10 dB attenuator, for a total attenuation of 70 dB, was characterized for their precise return loss and attenuation values using a R&S ZVA67 VNA with UOSM calibration.

This 70 dB attenuator was then used to connect the 10 MHz reference linked SRS384 signal generator doubler output, still set to -10 dBm, to the RX antenna feed-point of the interrogator system. The same frequency sampling points used in the power meter calibration of the SRS384 were then remeasured using the receiver of the interrogator and recorded in dBFS values relative to the dynamic range of the ADC.

The measured S-parameters of the 70 dB attenuator combination were then used in conjunction with the measured true power look-up table of the SRS SG384 signal generator and the ADC relative measurement values of the interrogator to determine the correct offsets for converting the relative measurement results scaled in dBFS to an

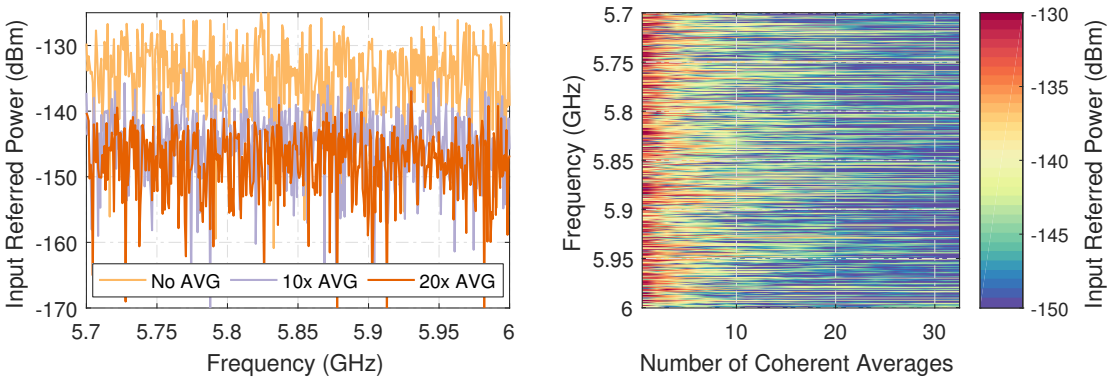

Figure 4.16: Harmonic frequency noise floor of the interrogator system with 50 Ω terminations at the antenna feed-points for different coherent averaging factors.

accurate antenna feed-point referred absolute power representation.

The system noise floor measurement results of the complete interrogator system using 50 Ω terminations instead of the antennas and with the stimulus generator running at the fundamental illumination frequency during the sweep is shown for various coherent averaging / integration factors in Fig. 4.16, using a coherent oversampling factor[50] of 1024 samples.

With an average input referenced noise power of -133 dBm with no coherent integration applied, the system presented here is slightly more sensitive than the best harmonic radar interrogator system reported in [83]. By applying 10x coherent averaging / integration to the measurements, the input referenced noise floor can be reduced even further to unprecedented average noise level of -143 dBm at the cost of prolonged measurement time.

4.3.2 The Passive Harmonic Radar Tag

The passive harmonic radar frequency doubler tag transponder used in the experiments follows a conservative design approach, in following the notion established in [103, 104]. This implicitly means, that the passive, Schottky diode based frequency doubler, and the transponder antennas are designed and tested as separate entities with $Z_L = 50\,\Omega$ interfaces. While this approach certainly does not result in a compact transponder design and also wastes a small fraction of the illumination signal in the superficial double impedance transformation necessary for matching both the antennas and the doubler to an intermediate $Z_L = 50\,\Omega$ interface, it offers the highest possible level of characterization in a scientific context, as normal coaxial transmission line measurement equipment can be used.

In contrast to this approach, a possible progressive design, which uses the antennas

[50] See description of the VNA receiver module in chapter 2.3.5 and especially chapter 2.3.7 for further explanation of the acquisition and sampling process, including the coherent oversampling and averaging procedure.

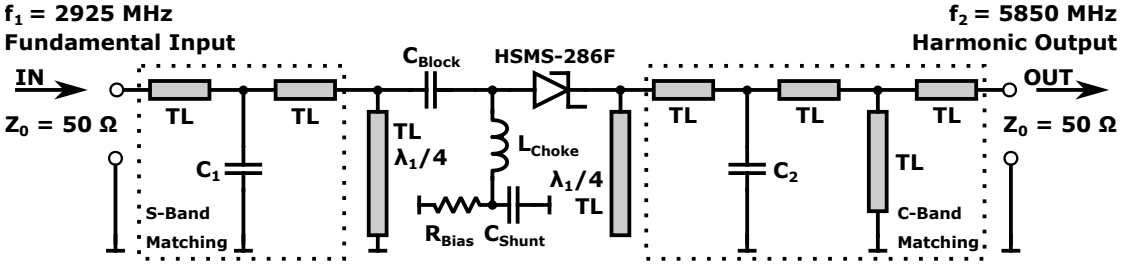

Figure 4.17: Schematic diagram of the passive Schottky diode based frequency doubler used in the harmonic radar tag.

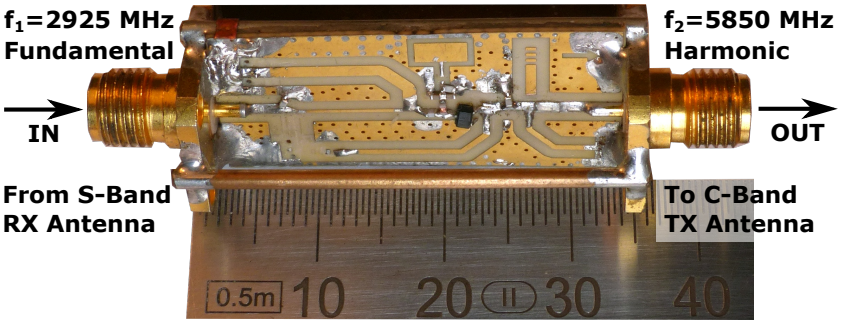

Figure 4.18: Detail picture of the passive Schottky diode based doubler circuit used in the harmonic radar tag.

themselves for the required impedance matching and filtering of the frequency doubler as shown by the various transponder examples presented in [103, 104], may offer higher overall conversion efficiency and more compact size at the cost of still unresolved tag characterization measurement procedures.

The design of the frequency doubler circuit is based around the procedures outlined in [96, 100] and was mainly carried out and incrementally optimized using the non-linear harmonic balance simulation capabilities of Keysight ADS in combination with a spice model of the, unfortunately now obsolete, HSMS-286F zero-bias Schottky detector diode by Avago / Broadcom. This diode was explicitly chosen due to its favorable transfer function characteristics, low junction capacitance without DC bias and relatively low parasitic series inductance of the package to allow for a relatively broadband matching of the doubler circuit to the $Z_L = 50\,\Omega$ interface.

Reflective transmission line bandpass filters were added in addition to the planar transmission line matching stubs at the diode itself to improve the conversion efficiency of the doubler. A DC-return path for the passive doubler circuit and parts of the impedance matching was realized with standard 0402 SMD components to allow for later optimization of the diode DC-operating point, which is caused by rectification of the RF illumination signal, and the matching itself to account for effects and parts variation not captured by the harmonic balance simulation.

A schematic of the passive frequency doubler circuits is shown in Fig. 4.17, while a

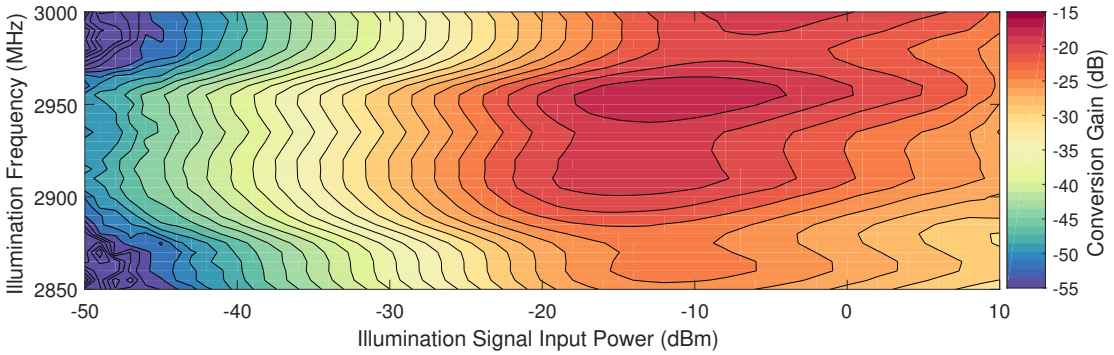

Figure 4.19: Contour plot of the tag conversion gain over illumination input power and frequency over an illumination signal bandwidth of 150 MHz centered at 2925 MHz.

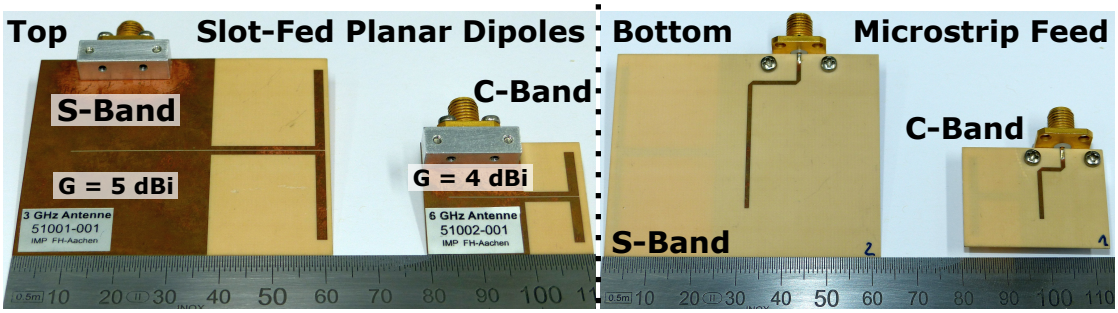

Figure 4.20: Picture of the first iteration of S-band and C-band planar dipole harmonic tag antennas used for the measurements.

picture of the actual implementation on Rogers RO4350B substrate using SMA connectors for interfacing to the transponder antennas is shown in Fig. 4.18.

The author would like to thank Marc Mühmel and Dr. Arash Sadeghfam, both associated with the Institute of Microwave and Plasma technology (IMP) of the FH Aachen, for creating and building the frequency doubler circuit design.

The conversion gain measurement results of the final frequency doubler iteration over illumination signal input power and frequency are shown in Fig. 4.19. A peak conversion gain of approximately $G_{Conv}^{\mathrm{II,I}} = -15\,\mathrm{dB}$ at an illumination signal input power of $P_{\mathrm{TRX}} = -15\,\mathrm{dBm}$ was achieved with this doubler, while still retaining good broadband frequency conversion performance for maritime radar S-band frequency range.

The planar harmonic radar transponder antennas used for the experiments were designed, characterized and provided by the Frauenhofer Institute for High Frequency Physics and Radar Techniques (FHR) in the SEERAD research program.

A picture of both transponder antennas with SMA 50 Ω interfaces is shown in Fig. 4.20. The S-band illumination signal reception and the C-band harmonic transmission antennas were designed as slot-fed planar dipole antennas using a $\lambda/4$ micro-strip transformer

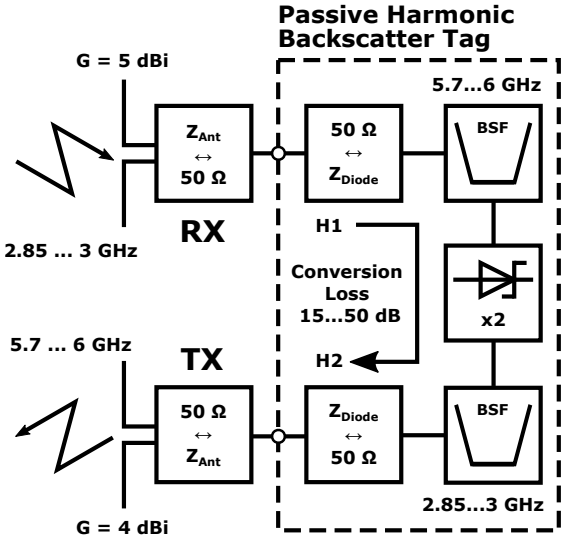

Figure 4.21: Schematic block diagram of the harmonic radar transponder tag used in the experiments.

H-field feed. A gain of $G_{RXT} = 5\,\text{dBi}$ was achieved for the S-band antenna and a gain of $G_{TXT,2} = 4\,\text{dBi}$ was realized for the C-band antenna, while still retaining an almost unidirectional radiation pattern in the E-plane antenna radiation diagram.

A complete block diagram of the harmonic radar transponder tag, as used for carrying out the following experiments, is shown in Fig. 4.21.

In order to carry out the actual experiments autonomously without manual intervention and to keep the experiments as repeatable as possible by providing repeatable RF propagation environment between experiments, a precision servo driven linear slide mechanism (LEZ9 from Isel with DC100 servo drive) with a guaranteed mechanical repeatability error of $\leq \pm 0.2\,\text{mm}$ was used to move the harmonic radar transponder over a maximum linear distance of 5.3 m.

A dielectric tag support structure made from RF-transparent wood fiber reinforced plastic construction profiles (Item KH8 profile) was fixed to the slide carriage (Isel WS11) to raise the tag 1 m above the linear slide structure. A close-up detail picture of the transponder tag fixed to the dielectric support and both planar dipole antennas mounted is shown in Fig. 4.22.

The same RF-transparent construction material was used to build a gantry structure to raise the S-band and C-band horn antennas to the same height as the tag. Standoffs were used to align both horn antennas to a common parallel aperture distance. The mounting plates were designed to allow a quick individual change of signal polarization plane for both the fundamental frequency illumination signal antenna and the harmonic return reception antenna of the interrogator.

A Sick DT35 laser-based time-of-flight distance measurement sensor with a corresponding laser reflector fixed to the transponder tag support structure was used to provide an independent ranging result and confirm the correct movement of the linear belt drive

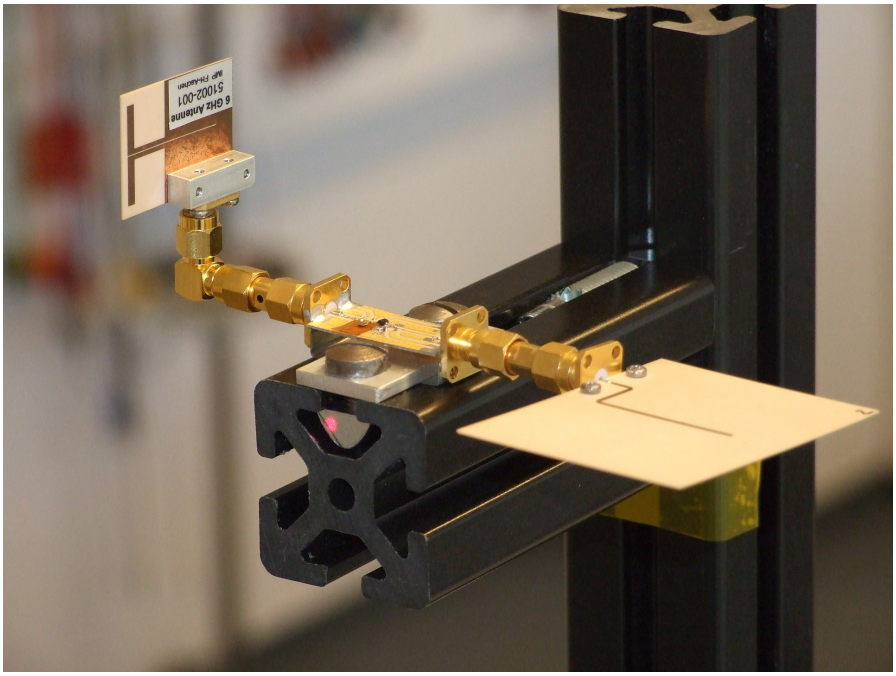

Figure 4.22: Picture of the complete harmonic radar tag mounted on the dielectric stand in the S-band horizontal, C-band vertical polarization configuration.

actuator during the autonomous measurement operations.

A schematic drawing of the complete linear actuator based measurement setup, including the position of the tag and the interrogator horn antennas, is shown in Fig. 4.23, while a picture of the measurement setup covering the key components is shown in Fig. 4.24.

The initial calibration of the interrogator is performed for all tag measurements at the $d = 1.00\,\mathrm{m}$ position of the linear actuator, which corresponds to an actual slant range $R = 1.41\,\mathrm{m}$ in the experimental setup.

This slant range was deliberately chosen, so that the spacing between the C-band and S-band antenna pairs is sufficiently large and all radiators are separated by at least the sum of their respective antenna far-field distances, resulting in a planar wavefront at the transponder for calibration purposes.

By using the approximations presented in [11], the minimum far-field distance for the $G_{\mathrm{RX}} = 10\,\mathrm{dBi}$ S-band horn antenna was calculated to be $R_{\mathrm{min,SW}} = 0.415\,\mathrm{m}$, while the higher gain $G_{\mathrm{RX}} = 15\,\mathrm{dBi}$ C-band horn antenna requires a minimum far-field distance of $R_{\mathrm{min,CW}} = 1.172\,\mathrm{m}$ to be obeyed.

The far-field distance of the low gain half-wave dipole transponder antennas can be approximated by the $R_{\mathrm{min}} \approx 2 \cdot \lambda$ rule ([11]), resulting in an additional $R_{\mathrm{min,ST}} = 0.2\,\mathrm{m}$ for the S-band antenna and $R_{\mathrm{min,CT}} = 0.1\,\mathrm{m}$ for the C-band half-wave dipole.

As these values are only mere approximations, an additional offset of $0.10\,\mathrm{m}$ was added to the more critical combined C-band far-field distance of $R_{\mathrm{min,C}} = R_{\mathrm{min,CW}} + R_{\mathrm{min,CT}} = 1.272\,\mathrm{m}$ and rounding to a convenient number was applied, resulting in the aforementioned

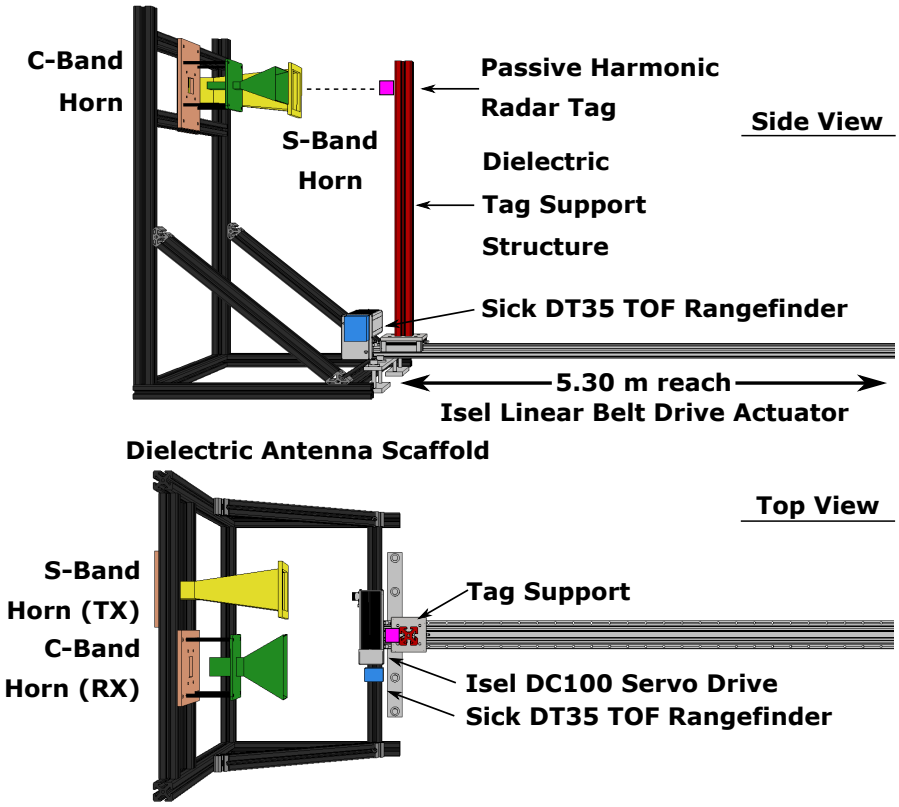

Figure 4.23: Schematic drawing of the interrogator dual-band antenna gantry, harmonic radar tag fixture and linear servo belt drive actuator.

calibration distance of $d = 1.00\,\mathrm{m}$ linear actuator travel and $R = 1.41\,\mathrm{m}$ actual slant range to the tag.

A compact system block diagram, encompassing all key system parameters as a closing resume of the harmonic radar system description, is shown in Fig. 4.25.

4.4 Low Power Short Range Measurement Results of the System

Before the verification and characterization measurements of the harmonic radar system are performed, the fundamental rejection and harmonic noise floor performance of the system with all components in place is tested. Furthermore, a characterization of the received illumination signal strength using the original transponder illumination signal reception antenna is performed over the whole test-distance of the linear actuator mechanism and horizontal and vertical polarization of the illumination signal. The results of both tests are covered below.

All measurement presented in the following sections are conducted using the following

Figure 4.24: Picture of the measurement setup showing the antenna gantry with the S-band illumination and C-band harmonic reception antenna, the harmonic radar tag fixed to the dielectric support structure, the time of flight laser distance sensor and the servo drive mechanism of the linear slide.

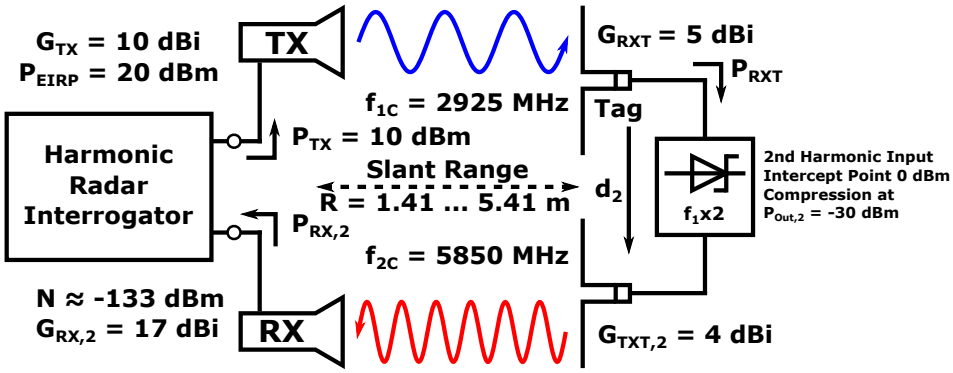

Figure 4.25: Compact schematic diagram of the harmonic radar measurement setup showing only key system parameters.

system settings, unless stated otherwise:

- Illumination signal frequency of 2850 MHz to 3000 MHz, corresponding harmonic return frequency range 5700 MHz to 6000 MHz,
- Effective isotropic radiated power of the illumination signal $P_{\mathrm{EIRP}} = 100\,\mathrm{mW}$,
- $N = 401$ frequency sampling points, illumination signal bandwidth $BW = 150\,\mathrm{MHz}$, fundamental frequency sampling point step-size $\Delta f = 375\,\mathrm{kHz}$,
- Corresponding SFMCW maximum unambiguous range of $lx_{\max} = 199.89\,\mathrm{m}$, radar range resolution $\Delta R = 499.65\,\mathrm{mm}$ per FFT bin,
- 1024x oversampling in the VNA receiver module, no internal averaging, 10 individual measurements captured per linear actuator step for optional coherent integration in post-processing of the data,
- Ranging comparison results are shown without coherent averaging applied, 10x coherent averaging applied in post-processing for the FFT range plots and power measurement plots.

4.4.1 Illumination Signal Compression Measurements

In order to assess the dynamic range of the harmonic frequency receiver and test the fundamental frequency suppression of the system, a trihedral corner reflector build from isosceles, copper cladded FR-4 substrate, triangles was fixed to the dielectric tag support structure mounted to the linear slide mechanism. The corner reflector used for this test has an isosceles triangle length of $a = 0.425\,\mathrm{m}$, which results in a radar cross section (RCS) area σ ([26]) of

$$\sigma = \frac{4\pi\, a^4}{3\,\lambda^2} = \frac{4\pi\, a^4 f^2}{3\, c_0^2} = 13.67\,\mathrm{m}^2\,, \tag{4.34}$$

Figure 4.26: Picture of the antenna bore-sight view of the experimental setup on the linear slide, the harmonic radar tag and three trihedral reflector clutter obstacles as seen from the interrogator antenna gantry used for the clutter influenced measurements in Chapter 4.4.5.

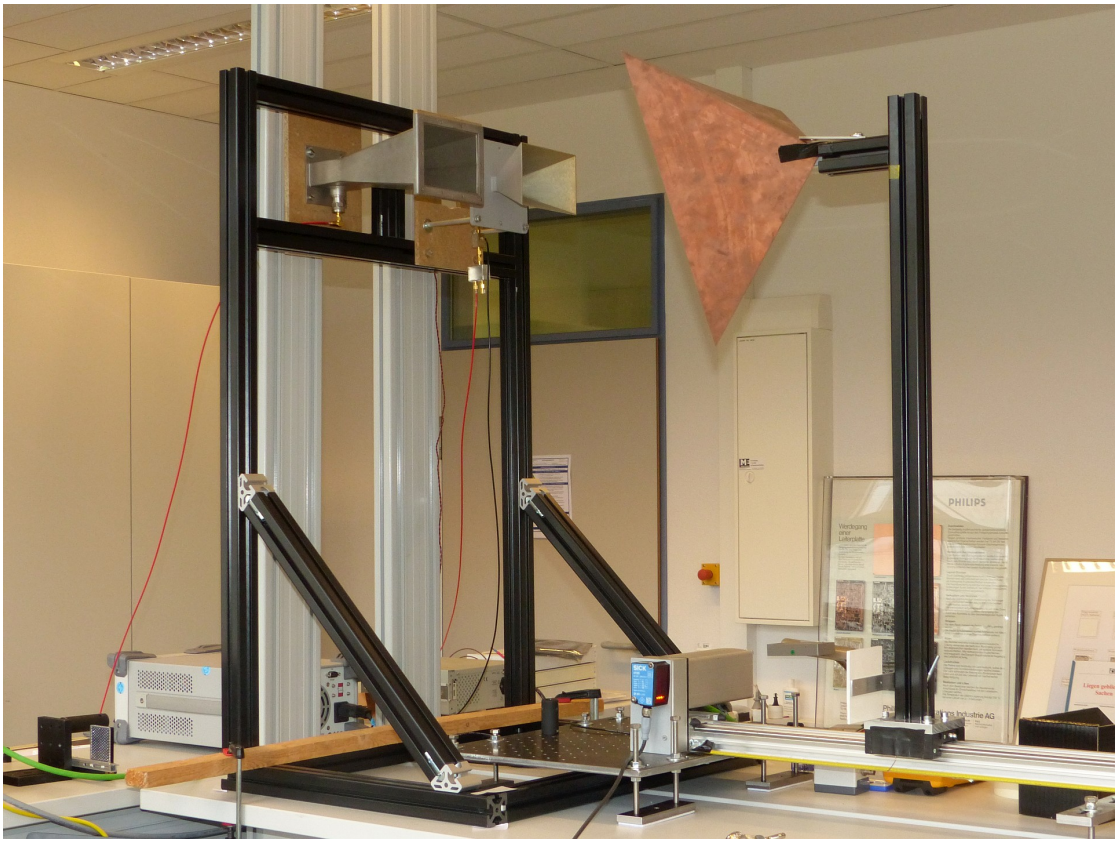

Figure 4.27: Picture of the fundamental frequency compression test and harmonic frequency dynamic range measurement setup using a trihedral reflector ($\sigma_{f=3\,\mathrm{GHz}} = 13.67\,\mathrm{m}^2$) instead of the tag on the linear rail system.

at the upper fundamental illumination frequency limit of 3 GHz, which is almost independent of the illumination angle in its frontal hemisphere due to its trihedral corner retro-reflector construction. The FWHM return angle of a trihedral corner reflector is approximately 120° ([91]). The RCS of a standing human at S-band frequencies is approximately $\sigma = 0.5\,\mathrm{m}^2$ ([89]) in comparison to the $\sigma = 13.67\,\mathrm{m}^2$ RCS of the trihedral reflector used for the compression test. A picture of the fundamental frequency compression test setup is shown in Fig. 4.27.

In contrast to the tests carried out with the harmonic radar transponder tag, the trihedral corner reflector was moved from the very beginning of the linear actuator mechanism, which corresponds to a slant range of approximately $R = 0.4\,\mathrm{m}$, measured to the root of the trihedral reflector structure, to a maximum distance of $d = 2.5\,\mathrm{m}$ in the relative coordinate system of the actuator, equivalent to a slant range of $R = 2.9\,\mathrm{m}$.

The reflector was autonomously moved in 10 mm increments via a software control routine that synchronized the linear actuator movement and the trigger mechanism of the non-linear VNA. A full harmonic radar measurement was performed by the interrogator

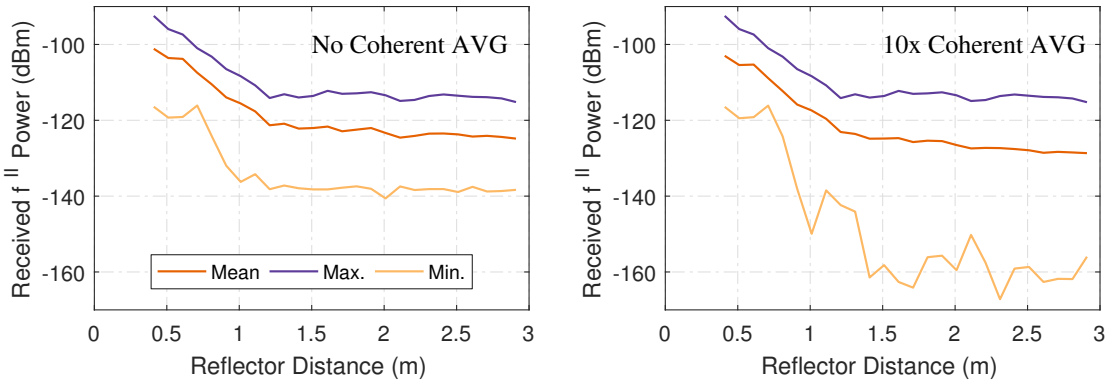

Figure 4.28: Mean, maximum and minimum received harmonic power over trihedral reflector ($\sigma_{f=3\,\mathrm{GHz}} = 13.67\,\mathrm{m}^2$) distance. Linear slide step-size $\Delta d = 0.1\,\mathrm{m}$.

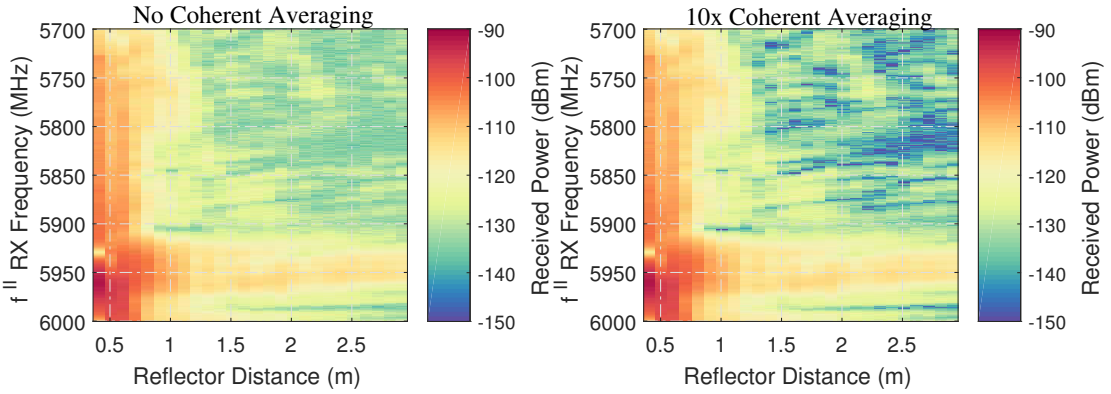

Figure 4.29: Received harmonic power over frequency and trihedral ($\sigma_{f=3\,\mathrm{GHz}} = 13.67\,\mathrm{m}^2$) reflector distance. Linear slide step-size $\Delta d = 0.1\,\mathrm{m}$.

at each position. The measurement results for this compression test are shown in Fig. 4.28 as maximum, mean and minimum received harmonic power results per linear actuator step, out of the 401 frequency sampling points measured per sweep, while Fig. 4.29 shows the raw received power over distance and frequency sampling points, as well as the effect of coherent averaging on the harmonic receiver noise-floor of the system.

While it is clearly evident from the results shown in both plots, that some fundamental to harmonic frequency conversion exists in the interrogator receiver signal chain and / or harmonic leakage in the interrogator signal component is present, a steady state is reached in the received harmonic signal power after the 1.2 m slant range position of the trihedral reflector. The mean received harmonic power values shown in Fig. 4.28 are well above the mean thermal harmonic frequency noise-floor of the interrogator (-133 dBm) using 50 Ω terminations shown earlier in Fig. 4.16.

When looking at the results of the measurements shown in Fig. 4.29 it can easily be identified, that this elevated harmonic noise floor is caused by a 50 MHz wide, radiated,

local interference, centered around 5950 MHz from the interrogator setup itself, which is fair to assume, as the received harmonic power outside of the front-end compression reflector range stays constant. Also, external interference in form of IEEE 802.11a 5.8 GHz WiFi access points or other users of this part of spectrum can be ruled out by the results for the 10-times coherently integrated data, as the results for the non-averaged and averaged data are identical in this narrow spectral band, which is only possible for correlated radiated EMI signals originating from the system itself, while external non-correlated interference would be attenuated by the coherent integration process.

Unfortunately the exact source of this interference could not be narrowed down any further during the experiments. The most likely cause is a defective EMI-gasket, which was dislocated during the assembly of the rack-mounted enclosures. Nevertheless, the system was still deemed usable for the following test, as only a small part of the overall harmonic return spectrum is affected by this minor interference.

Furthermore, it can clearly be observed, that the reference position of $R = 1.41\,\mathrm{m}$ is well outside of the compression interference distance of the interrogator system and can be successfully used as the reference and calibration point for the harmonic radar measurements, even under extremely adverse near clutter conditions as simulated by the large trihedral corner reflector.

4.4.2 Polarization Dependent Illumination Power Characterization and Scalar Channel Sounding of the Measurement Setup

After the fundamental frequency compression test, a measurement series to asses the received doubler input signal strength over transponder tag slant range distance was carried out over the full length of the experimental setup for both horizontal and vertical antenna polarizations (HH and VV) of the harmonic radar illumination signal.

This measurement was deemed necessary to measure the effect of multipath RF propagation characteristics and the associated fading effects present over the length of the linear actuator rail, to determine the best illumination signal polarization for the high-resolution verification measurements of the harmonic radar equation (4.1).

Furthermore, this measurement reassures the measurement results obtained with the actual tag, where two frequencies with their associated bandwidths are used, which results in many unknowns for propagation dependent measurements. While many harmonic radar publications assume free-space or plane-earth propagation, and therefore a quasi unlimited coherence bandwidth of the channels used for illumination and reception for their interpretation of the ranging results, this is certainly not the case with the indoor measurement carried out here.

Although directional antennas are used for the interrogator and unobstructed line-of-sight exists between the interrogator and the tag for most of the measurements, the antennas used for the transponder are omnidirectional in their E-plane and will therefore be highly susceptible to interference by multipath indoor reflections, causing frequency selective fading by destructive wave interference for both the input signal fed to the frequency doubler of the tag, as well as the harmonic power received by the interrogator.

In this context, this measurement can be seen as scalar channel sounding for the

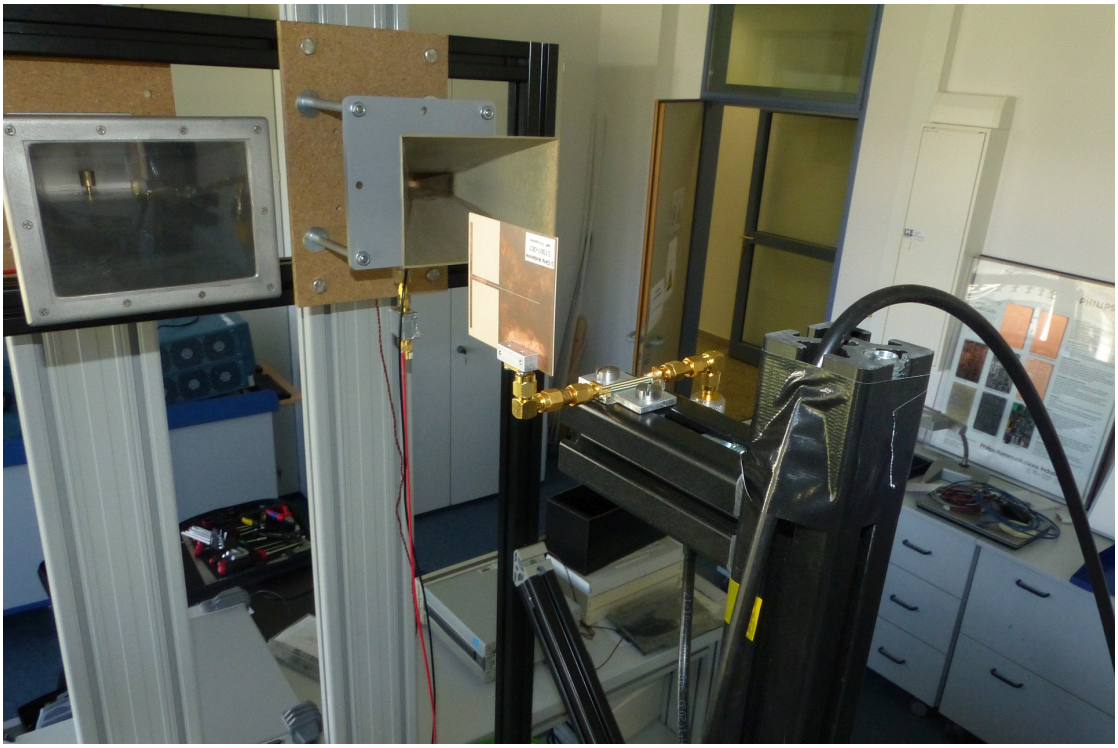

Figure 4.30: Picture of the tag doubler input power over slant range measurement setup showing the interrogator S-band and C-band horn antennas and the S-band tag antenna with dummy tag fixture and coaxial cable to the R&S FSV7 spectrum analyzer.

illumination signal of the interrogator. This is especially important for harmonic radar due to the square-law power-series, input power dependent, transfer function characteristic of the frequency doubler in the tag.

Therefore, even minor fading drop-outs of the illumination signal get amplified by input power dependent conversion gain of the doubler, which in turn causes severe pseudo-fading effects for the harmonic return signal as well, independent of the actual channel characteristics for the harmonic SFMCW return frequencies. Modeling and measuring this indoor multi-path propagation effect is still an ongoing and active research topic for the frequency bands used in this measurements, which is evident by the sheer amount of publicized additions to, and modifications of, the COST 231 multi-wall propagation and spatial attenuation model as well as the Motley-Keenan indoor model in recent years.

Due to the high amount of different indoor propagation models, which are also often empirical and therefore tailored to a specific situation, the theoretical received power over distance figures used here, and the theoretical received harmonic return power values using the non-linear harmonic radar equation Eq. (4.1), just assume free-space propagation as an arbitrary point of reference.

In order to perform an in-situ measurement of the doubler input power as accurately

as possible, a dummy transponder consisting of a 50 Ω micro-strip transmission line with the same dimensions as the actual doubler and SMA connectors on both sides was used to position the S-band tag reception antenna in exactly the same orientation and relative position to the dielectric tag support structure as in the actual transponder tag.

A SMA (m)-(m) adapter was used to connect the S-band half-wave dipole antenna for the horizontal polarization orientation. A 90° SMA (m)-(f) bend was added for the vertically polarized measurement. The polarization of the S-band interrogator antenna was changed accordingly. Instead of the C-band harmonic return antenna, a Rohde & Schwarz FSV7 signal and spectrum analyzer was connected via a 5 m flexible low-loss foamed PE dielectric coaxial cable, which was dragged along the linear actuator movement by the dielectric tag fixture.

The insertion loss of the dummy tag adapter and the coaxial cable was measured with a ZVA67 VNA beforehand and de-embedded from the measured power data. Data was captured over the whole illumination frequency range by the FSV7 in peak-hold mode for 1 minute per linear rail step size, as the frequency sweeps of both the VNA / interrogator and the FSV7 could not easily be synchronized over distance. The linear actuator was moved autonomously by a control program for both illumination signal polarizations with a step-size of 0.1 m from the tag reference position at $R = 1.41$ m to the end of the actuator movement range at $R = 5.41$ m. Data capture was performed autonomously by the control program via SCPI over Ethernet from the FSV7 spectrum analyzer. No people were present in the room during the time of the actual measurements in order to keep the disturbance in propagation pattern at a minimum and to achieve repeatable and comparable results between measurements.

A picture of the dummy tag and S-band transponder antenna setup in front of the interrogator antennas is shown in Fig. 4.30.

The measured maximum, minimum and mean doubler input power results in the frequency range of 2850 to 3000 MHz over tag slant range are shown for both illumination signal polarizations in Fig. 4.31, while the received power over frequency, distance and polarization is visualized in Fig. 4.32.

From the results of the measurements it can easily be seen, that using the vertical polarization for the illumination signal results in a much flatter frequency doubler input amplitude response over distance when compared to the measurements taken in the horizontal polarization of the antennas.

The received power over distance recorded for the S-band vertical polarization is comparatively flat and shows a close adherence to the expected power under free-space conditions. Only minor outliers from the mean are discernible in both expressions of the data set.

In contrast, the horizontal polarized measurements show deep frequency selective fading effects, which are especially pronounced around the $R = 4$ m slant range mark. Even with the coarse distance resolution of $\Delta d = 0.1\,\text{m} \approx \lambda$ used for this test, the frequency selectivity of the fading process is easily identified from the power over frequency over range plot in Fig. 4.32, where the selective fading process manifest itself in the form of bow-shaped power drop-out regions in the plot.

As the illumination signal fading depth at $R = 4$ m is in excess of 30 dB for some

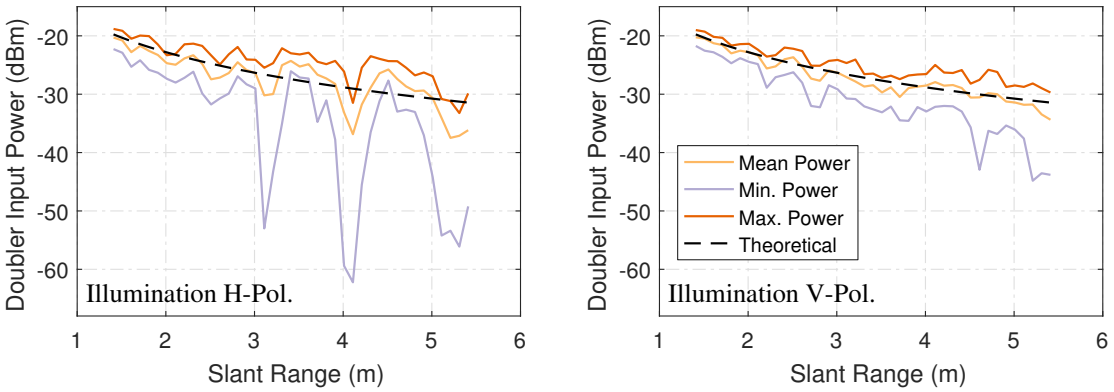

Figure 4.31: Measurement results for the received illumination signal input power at the doubler input of the tag using the tag fundamental frequency S-band antenna for horizontal and vertical polarization of the illumination signal and antenna, measurement step-size $\Delta d = 0.1\,\mathrm{m}$.

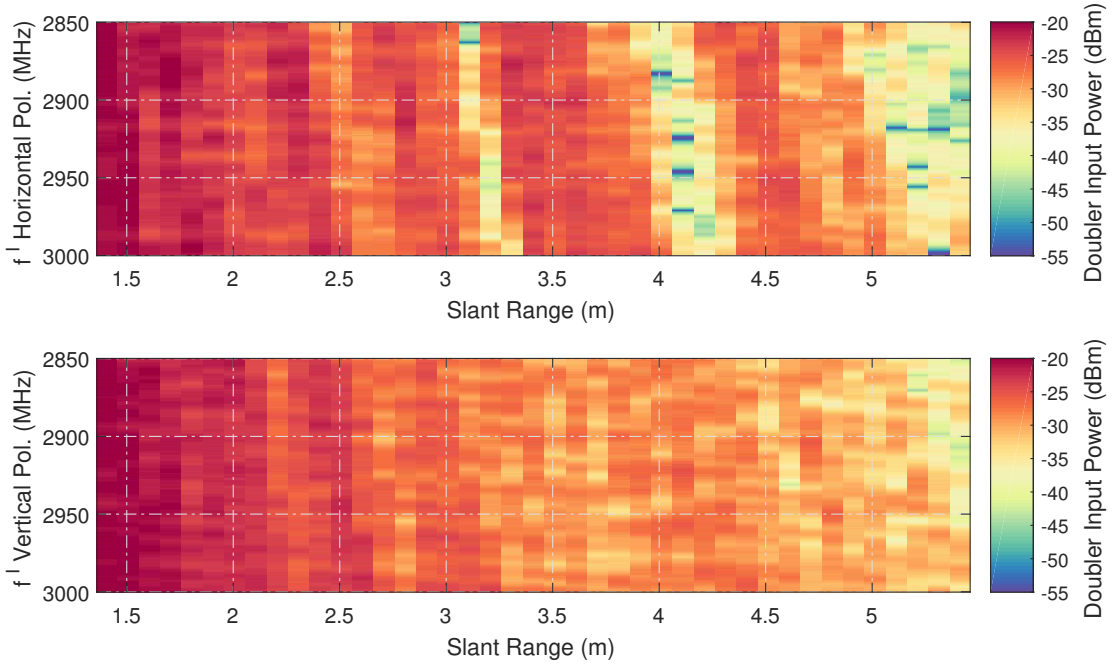

Figure 4.32: Measurement results for the received illumination signal input power at the doubler input of the tag using the tag fundamental frequency S-band antenna for horizontal and vertical polarization of the illumination signal and antenna, measurement step-size $\Delta d = 0.1\,\mathrm{m}$.

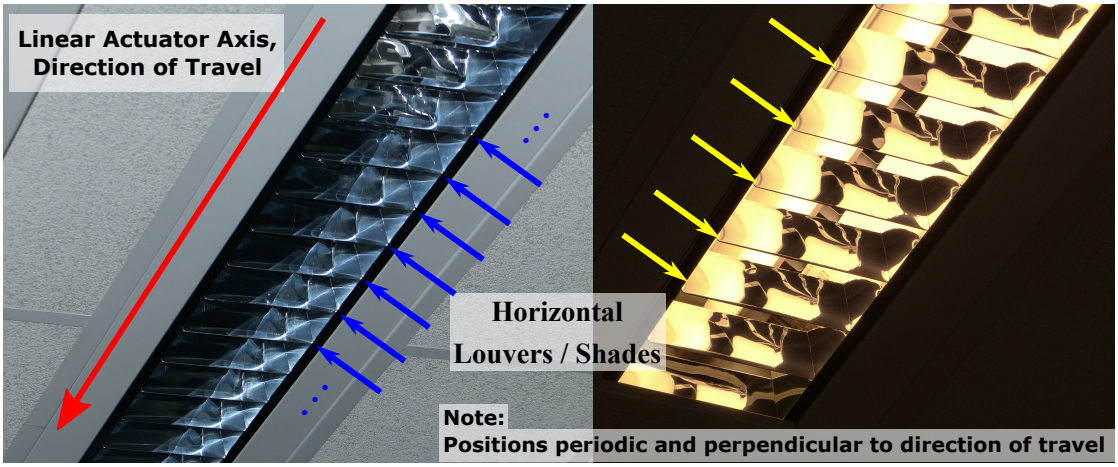

Figure 4.33: Picture of the louvers in the fluorescent lamp light fixtures, which were deemed to be the most plausible cause of frequency selective deep fading in the horizontal polarization tests.

frequencies, this will present a challenging environment and configuration for the harmonic radar and the different ranging algorithms under test, as the return signal is expected to be close to or under the harmonic noise floor of the system.

Additionally, the frequency selective fading present in the setup offers an interesting opportunity to further test the ranging robustness, as only parts of the sweep bandwidth will be affected by this phenomenon, resulting in bandpass limiting of the harmonic return signal.

While the source of this deep frequency selective fading could not be determined with absolute certainty without performing indoor ray-tracing propagation simulations, the author's best guess by applying Occam's razor to the vast list of possible back-scatterers is, that this effect is caused by knife-edge reflections from the louvers (horizontal metallized anti-glare reflectors, see Fig. 4.33) of the overhead fluorescent lighting fixtures, as the distance between fixtures approximately matches the distance pattern of the fading, when the changing grazing angle over distance is taken into account. A reflection from the linear actuator slide itself would not show up at such distinct points in the distance pattern, as its metal structure is constantly illuminated over the whole examined range.

4.4.3 Polarization Dependent Harmonic SFMCW Radar Ranging Results

Based on the results obtained from the characterization of the S-band multipath propaġation environment it was decided to perform initial low-resolution measurements using a step-size of $\Delta d = 50\,\text{mm}$ with the complete transponder tag for all feasible polarization combinations of the illumination and harmonic return signal. No in-band cross-polarization measurements (HV/VH) were performed, which results in the following polarization combinations (notation polarization interrogator, polarization tag):

- Illumination signal S-band (HH), harmonic return signal C-band (VV),

- Illumination signal S-band (HH), harmonic return signal C-band (HH),
- Illumination signal S-band (VV), harmonic return signal C-band (HH), and
- Illumination signal S-band (VV), harmonic return signal C-band (VV).

All of these measurements were again carried out completely autonomously without human intervention, in order to provide repeatable propagation and especially multipath conditions between the four different experimental setups and measurements.

The results of these four different measurements are shown as one consecutive section in order to make comparisons between results easier, starting with Fig. 4.34 to Fig. 4.49.

Four different data plots are shown for each measurement result: First an evaluation of the mean, maximum, minimum and expected theoretical harmonic signal return powers of the SFMCW sweep over distance is shown to visualize the both the power extrema, and to compare the results with the results expected from evaluating the harmonic radar equation Eq. (4.1) for the actual slant range of the transponder tag.

The second plot for each measurement shows the harmonic return power over frequency and over distance, similar to the visualization carried out for the scalar channel soundings performed for the illumination signal, in order to highlight multipath propagation effects such as frequency selective fading.

The third plot shows the actual slant range ranging results. These are obtained with the new Theil-Sen slope estimator ranging algorithm and the classical IFFT maximum search for different factors of frequency domain zero padding. The results of the different ranging algorithms are visualized in the form of a ranging error over distance, as the actual distance to the tag is known very precisely and with high confidence for each SFMCW measurement due to the closed loop servo control of the linear actuator carrying out the movement.

The fourth plot in the series visualizes the results obtained via the IFFT transformation of the complex frequency domain sampling data obtained with the SFMCW sweep for each position, the so-called range plot ([18]), over the actual tag distance. Here, the actual ranging data is oriented vertically, while the actual tag position is on the horizontal axis. The IFFT range plot results are normalized to the maximum intensity of each actual tag position, i.e. normalized vertically, to compress the huge dynamic range of the results into a more readable format. The IFFT range bins are cropped at the double of the maximum achievable slant range of the setup in order to aid the comprehensibility of the plots, as no returns are expected beyond this range even due to multipath propagation in the measurement environment. Showing the maximum unambiguous range of $lx_{\max} = 199.89\,\mathrm{m}$ in this format would simply reduce the actual tag return over distance to just a horizontal line.

The results of the harmonic return power measurements over distance and polarization configuration, shown for the (HH/VV) configuration in Fig. 4.34 and Fig. 4.35, and for (HH/HH) in Fig. 4.38 and Fig. 4.41, clearly confirm the assumptions made from evaluating the channel sounding measurements. In case of the horizontally polarized illumination signal measurements, severe deep fading can be observed in the harmonic return signal at exactly the same distances surveyed via the channel sounding measurements. While

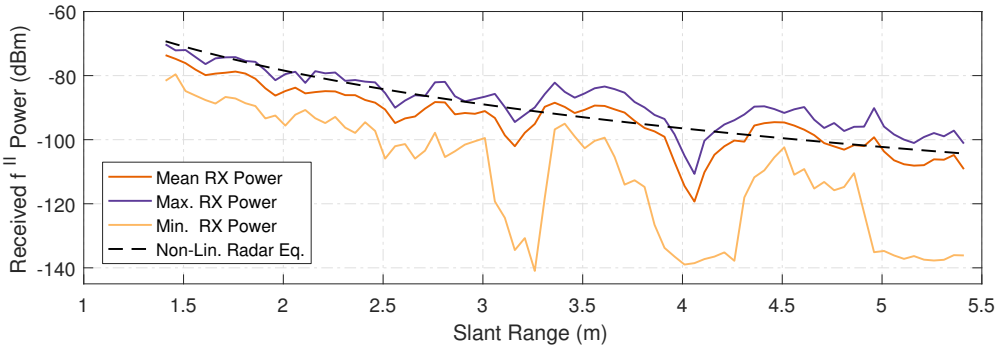

Figure 4.34: Mean, maximum and minimum f^{II} harmonic return power measurement results for the S-band horizontal, C-band vertical polarization antenna configuration over tag distance, measured with a tag distance step-size of $\Delta d = 50\,\text{mm}$.

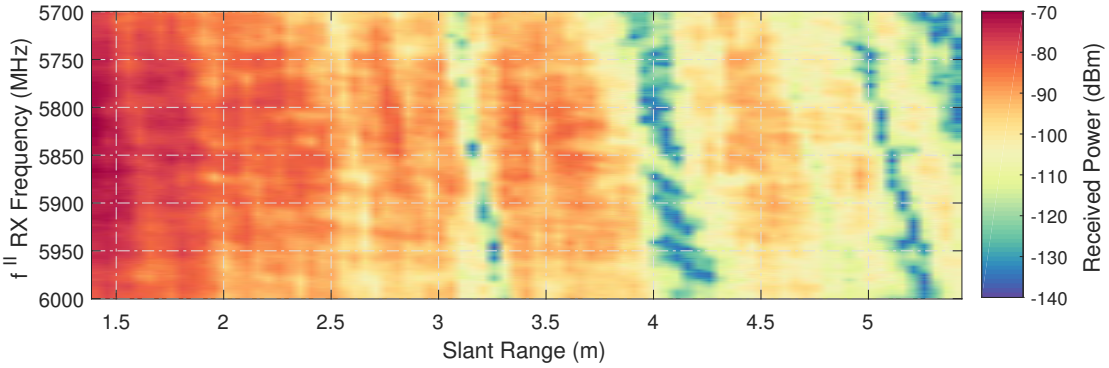

Figure 4.35: f^{II} harmonic return power measurement results for the S-band horizontal, C-band vertical polarization antenna configuration over tag distance, measured with a tag distance step-size of $\Delta d = 50\,\text{mm}$.

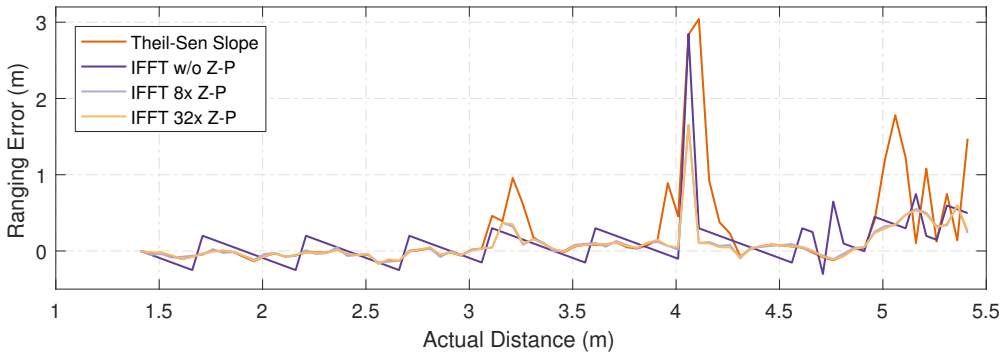

Figure 4.36: Distance ranging error for multiple ranging methods for the S-band horizontal, C-band vertical polarization antenna configuration over tag distance, measured with a tag distance step-size of $\Delta d = 50\,\text{mm}$.

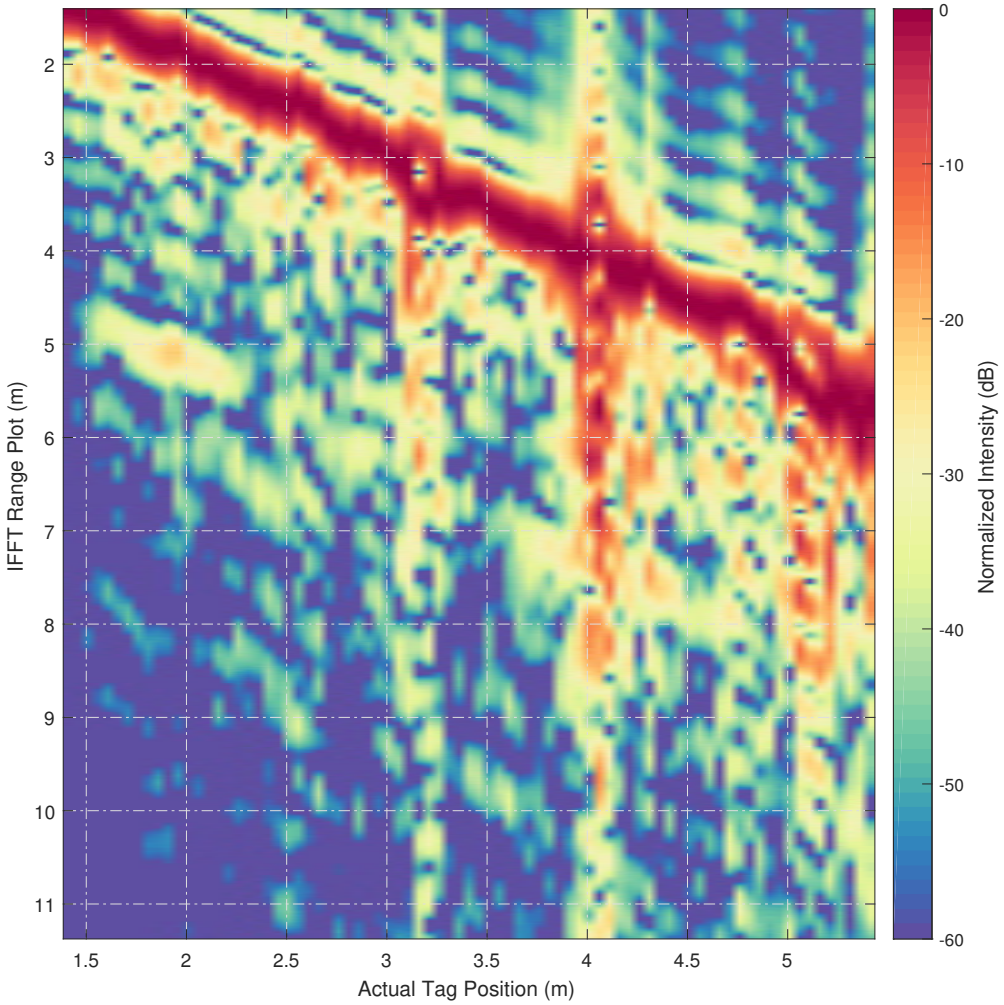

Figure 4.37: Harmonic radar IFFT range profile over tag distance, normalized on the maximum intensity for each position, for the S-band horizontal, C-band vertical polarization antenna configuration over tag distance, measured with a tag distance step-size of $\Delta d = 50\,\text{mm}$ and a frequency domain zero-padding factor of 64.

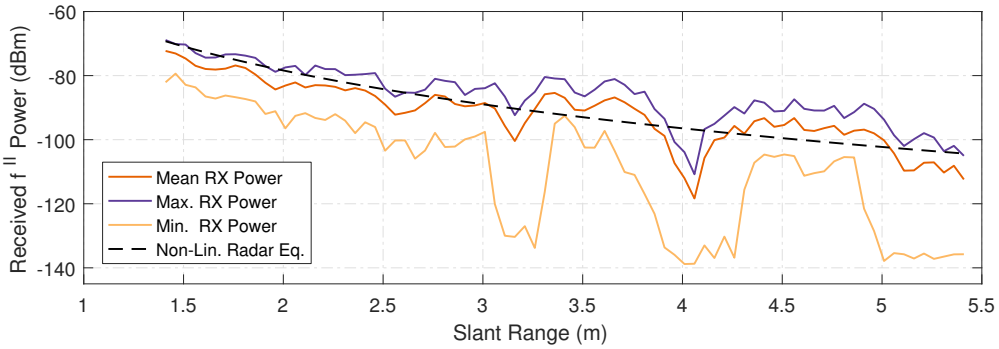

Figure 4.38: Mean, maximum and minimum f^{II} harmonic return power measurement results for the S-band horizontal, C-band horizontal polarization antenna configuration over tag distance, measured with a tag distance step-size of $\Delta d = 50\,\text{mm}$.

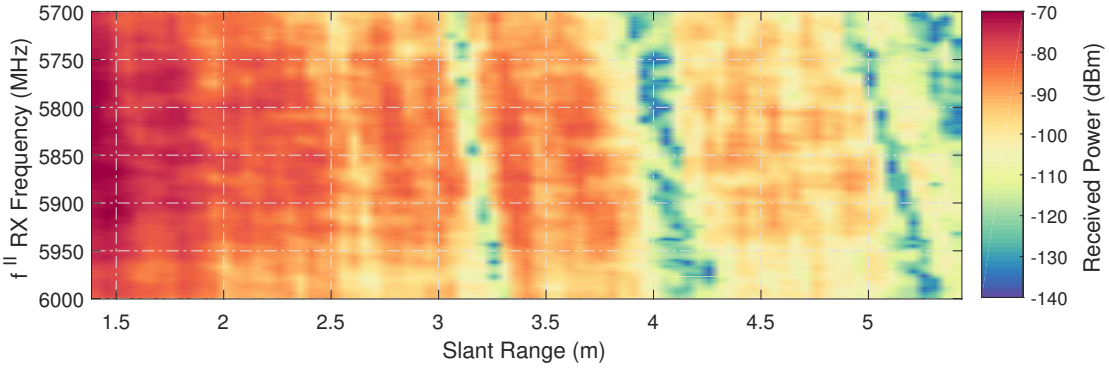

Figure 4.39: f^{II} harmonic return power measurement results for the S-band horizontal, C-band vertical horizontal antenna configuration over tag distance, measured with a tag distance step-size of $\Delta d = 50\,\text{mm}$.

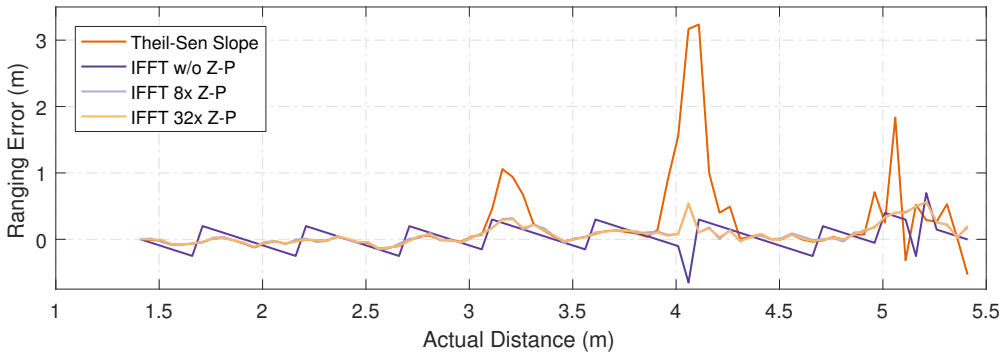

Figure 4.40: Distance ranging error for multiple ranging methods for the S-band horizontal, C-band horizontal polarization antenna configuration over tag distance, measured with a tag distance step-size of $\Delta d = 50\,\text{mm}$.

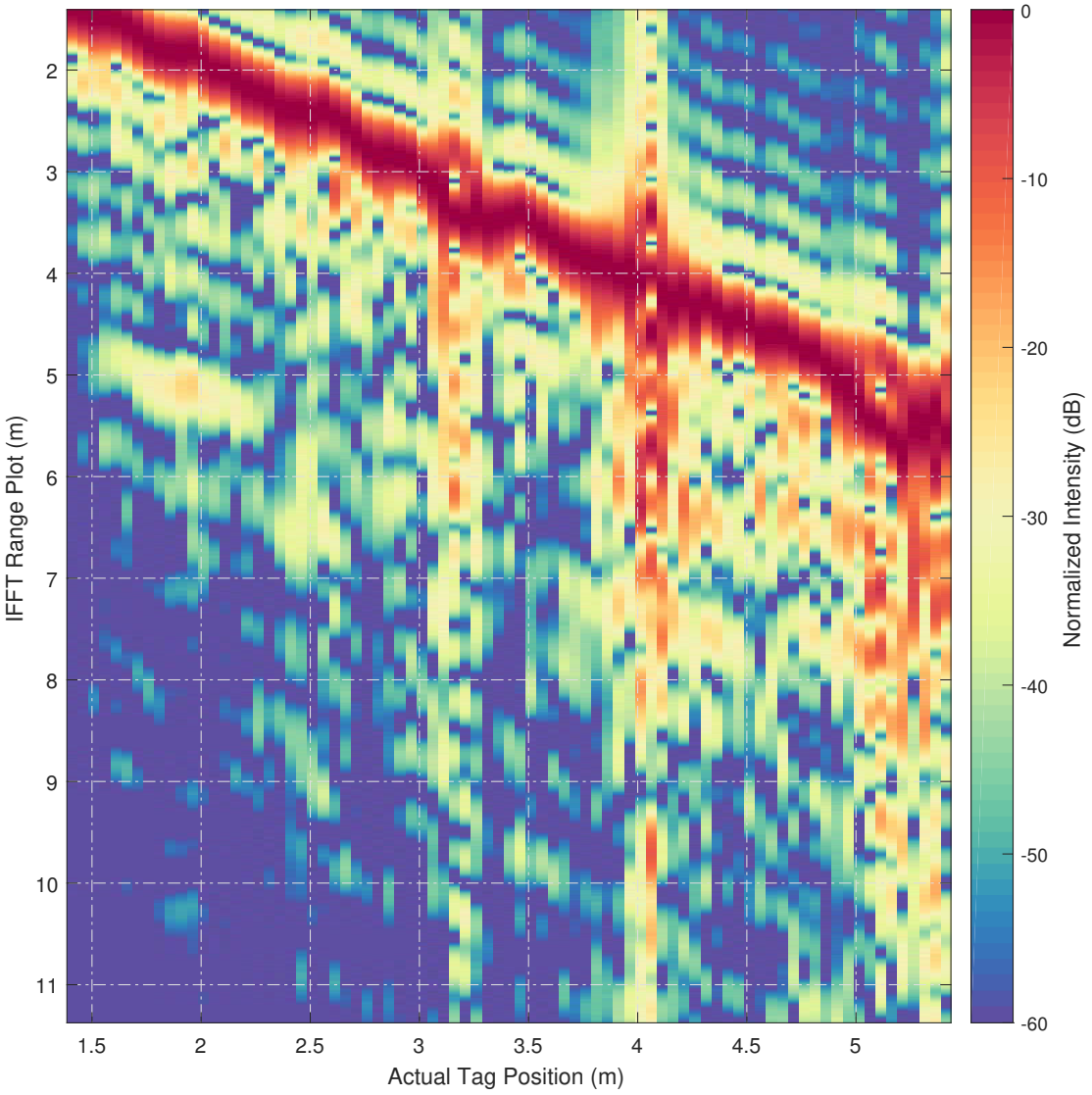

Figure 4.41: Harmonic radar IFFT range profile over tag distance, normalized on the maximum intensity for each position, for the S-band horizontal, C-band horizontal polarization antenna configuration over tag distance, measured with a tag distance step-size of $\Delta d = 50\,\text{mm}$ and a frequency domain zero-padding factor of 64.

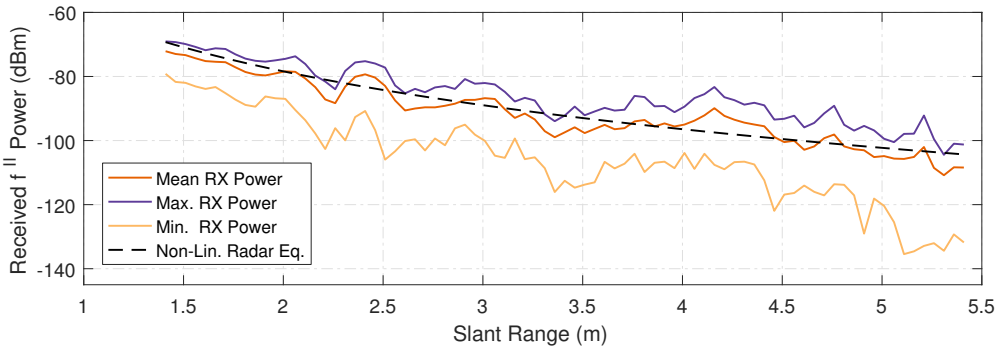

Figure 4.42: Mean, maximum and minimum f^{II} harmonic return power measurement results for the S-band vertical, C-band horizontal polarization antenna configuration over tag distance, measured with a tag distance step-size of $\Delta d = 50\,\text{mm}$.

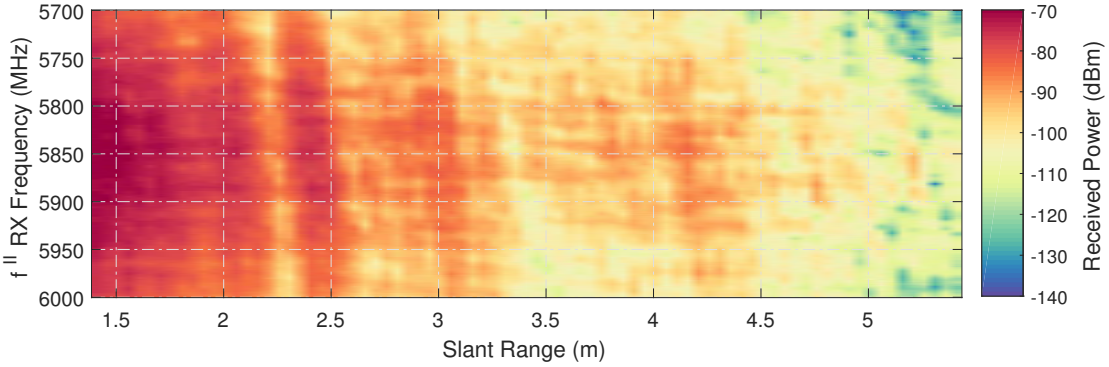

Figure 4.43: f^{II} harmonic return power measurement results for the S-band vertical, C-band horizontal antenna configuration over tag distance, measured with a tag distance step-size of $\Delta d = 50\,\text{mm}$.

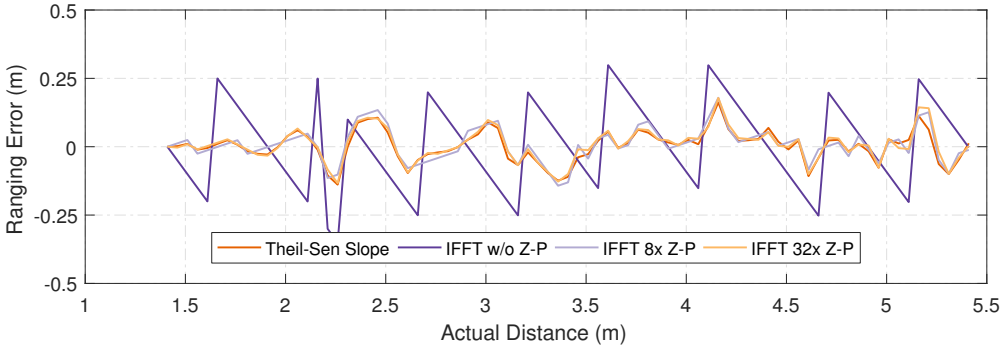

Figure 4.44: Distance ranging error for multiple ranging methods for the S-band vertical, C-band horizontal polarization antenna configuration over tag distance, measured with a tag distance step-size of $\Delta d = 50\,\text{mm}$.

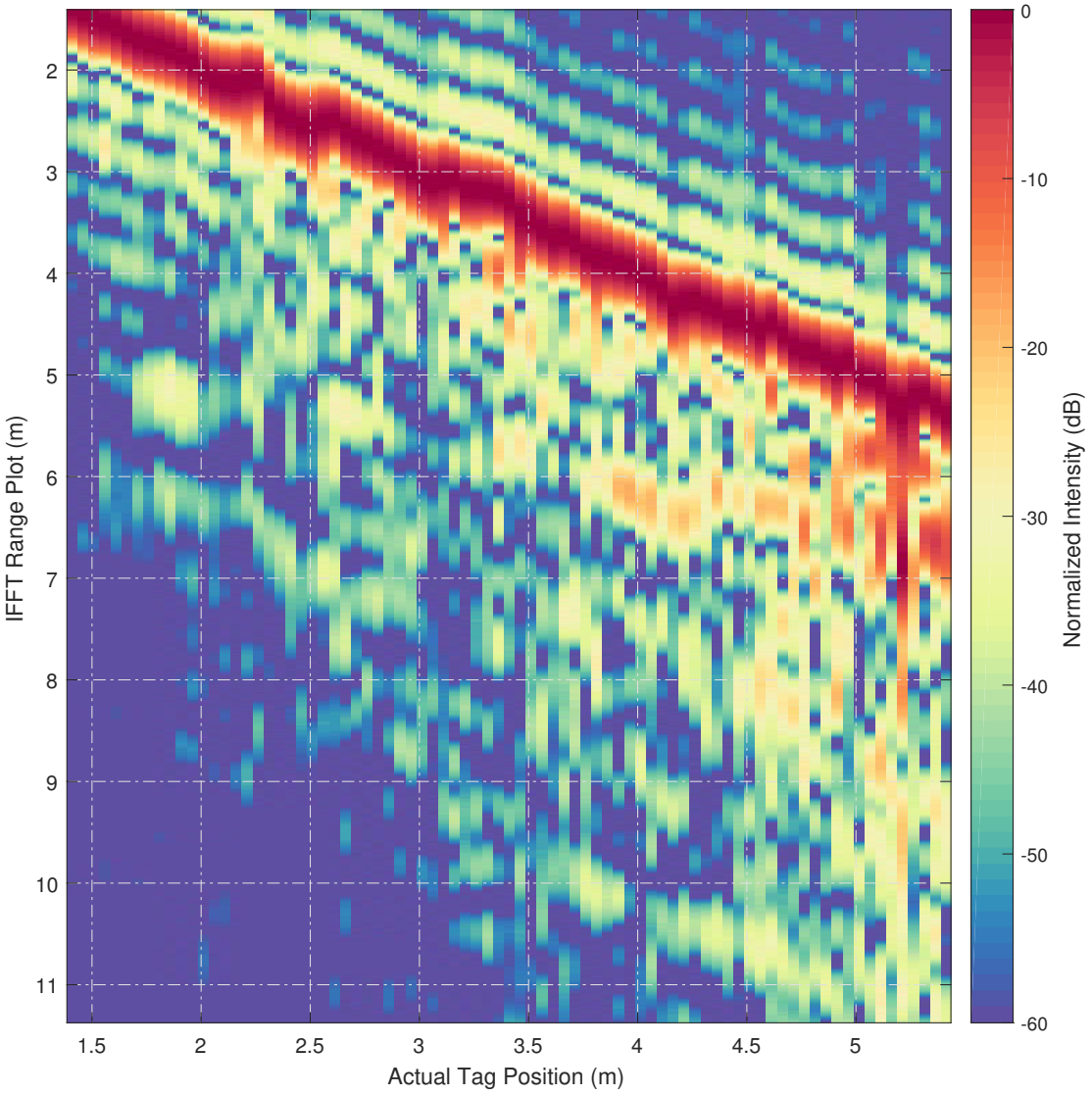

Figure 4.45: Harmonic radar IFFT range profile over tag distance, normalized on the maximum intensity for each position, for the S-band vertical, C-band horizontal polarization antenna configuration over tag distance, measured with a tag distance step-size of $\Delta d = 50\,\text{mm}$ and a frequency domain zero-padding factor of 64.

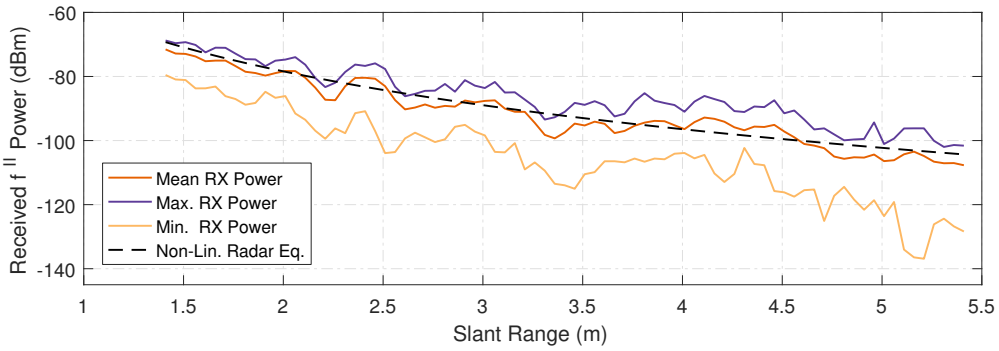

Figure 4.46: Mean, maximum and minimum f^{II} harmonic return power measurement results for the S-band vertical, C-band vertical polarization antenna configuration over tag distance, measured with a tag distance step-size of $\Delta d = 50\,\text{mm}$.

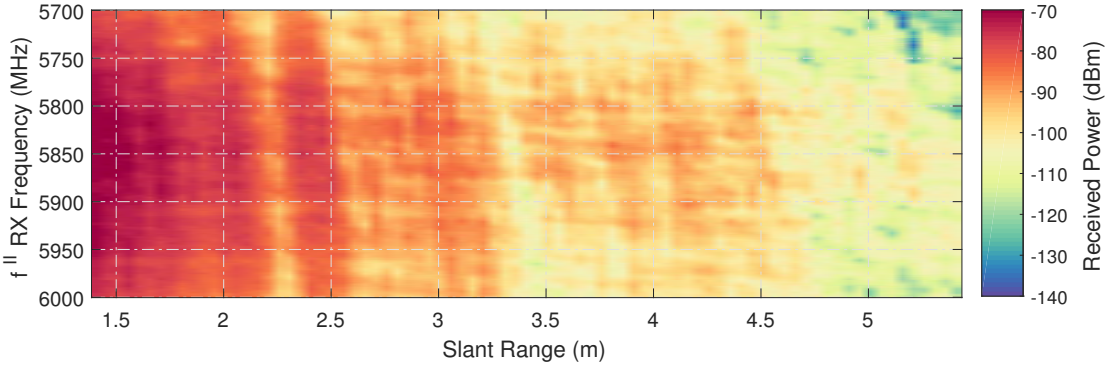

Figure 4.47: f^{II} harmonic return power measurement results for the S-band vertical, C-band vertical antenna configuration over tag distance, measured with a tag distance step-size of $\Delta d = 50\,\text{mm}$.

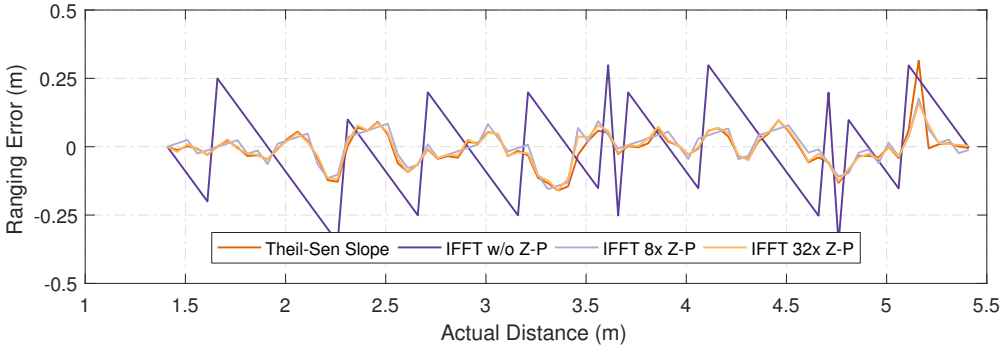

Figure 4.48: Distance ranging error for multiple ranging methods for the S-band vertical, C-band horizontal polarization antenna configuration over tag distance, measured with a tag distance step-size of $\Delta d = 50\,\text{mm}$.

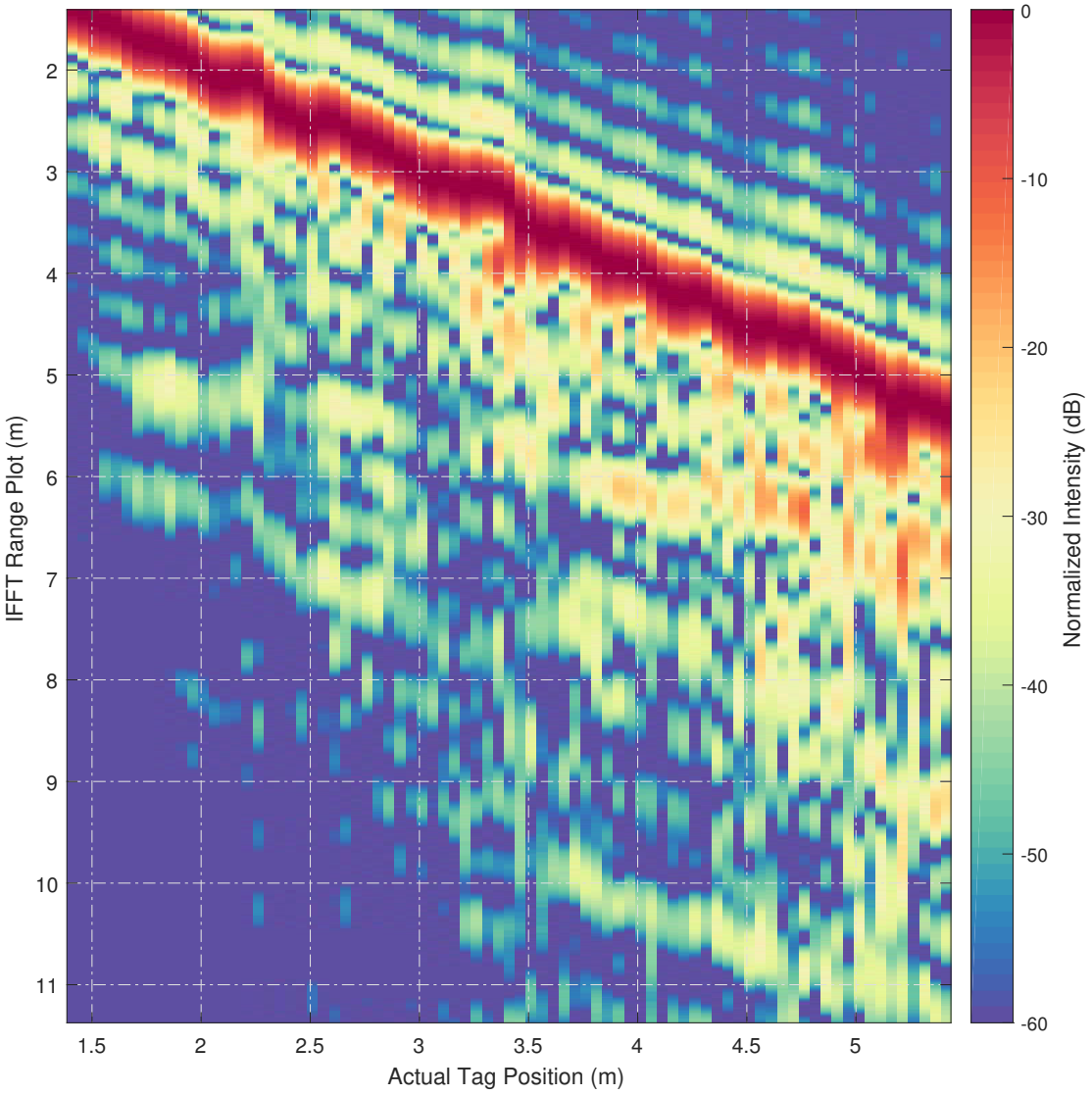

Figure 4.49: Harmonic radar IFFT range profile over tag distance, normalized on the maximum intensity for each position, for the S-band vertical, C-band horizontal polarization antenna configuration over tag distance, measured with a tag distance step-size of $\Delta d = 50\,\text{mm}$ and a frequency domain zero-padding factor of 64.

this should not be surprising, as the harmonic return signal can only be generated by the transponder from the power received via the illumination signal and with the tag conversion gain being square-law dependent on the received signal power, it is still very interesting to see such a highly dynamic fading of over 50 dB in a single sweep return over a such a relatively low relative bandwidth in this near line-of-sight scenario.

No distinct advantage for either polarization of the C-band harmonic return signal can be identified in the data shown for the (HH)-polarized illumination signal measurements. Due to the multipath interference effects, a fairly dynamic deviation from the assumed non-linear radar equation can be observed for both cases.

In contrast to the horizontal polarized illumination signal measurement results, a comparatively "flat" harmonic power over distance response can be observed for both vertically polarized illumination signal measurements, shown for the (VV/HH) configuration in Fig. 4.42 and Fig. 4.45, and for (VV/VV) in Fig. 4.46 and Fig. 4.47, as anticipated from the (VV) polarized S-band channel sounding measurement. Both the (VV/HH) and the (VV/VV) polarization configurations show mean harmonic power measurement results in very close agreement with the non-linear harmonic radar equation.

It is however interesting to note and observe, that the (VV/HH) and (VV/VV) polarized harmonic power over distance results are in such a close agreement with each other, which hints at a very flat channel response for the C-band. Unfortunately, a systematic sounding survey for the C-band to independently confirm this assumption could not be conducted in the same way as it was done for the S-band with the resources at hand, due to the extensive S-band bandpass filtering used in the interrogator stimulus synthesizer.

When the results of the ranging error are combined with the results of the measured harmonic return power over frequency and distance, it is easy to discern, that the classical IFFT is more robust against multipath frequency selective fading effects.

Nevertheless it can easily be observed, that the Theil-Sen phase slope estimator ranging algorithms generates accurate ranging results comparable to high IFFT interpolation factors (32xZP, interpolated $\Delta R_i = \Delta R/32 = 15.6\,\mathrm{mm}$), when a flat channel response and sufficient signal-to-noise ratio ($\mathrm{SNR}_{\min} \approx 20\,\mathrm{dB}$) is present.

Further analysis of the raw intermediate ranging data also revealed, that the extreme deviations observed in the Theil-Sen ranging results under multipath fading are also not caused by short-comings of the phase slope estimation process itself, but are merely a byproduct of a failed estimation in the phase unwrapping algorithm of MATLAB. This results in the insertion of erroneous 2π phase jumps into the absolute unwrapped phase, which is then used to estimate the slope. In the experiments carried out here, this generally results in a longer estimated slant range than is actually present by increasing the estimated phase slope of the harmonic return.

While different approaches to phase unwrapping, such as pre-unwrap FIR lowpass filtering of the data, and other model-less 1-D phase unwrapping algorithms, such as the approach presented in [3], were tried in post-processing of the measurement data, no significant and definitive improvement in the Theil-Sen slope estimator ranging results could be observed. Nevertheless further research in more robust, model-based, approaches that follow a predictive phase unwrap approach based on the linear progression property of the phase seems worthwhile to reduce the required computing effort and

		(HH / VV)	(HH / HH)	(VV / HH)	(VV / VV)
$\mu(\lvert\varepsilon\rvert)$	TS Slope	282.6 mm	275.3 mm	43.4 mm	45.7 mm
$\mu(\lvert\varepsilon\rvert)$	IFFT 8xZ-P	129.4 mm	106.9 mm	46.8 mm	44.9 mm
$\mu(\lvert\varepsilon\rvert)$	IFFT 32xZ-P	127.2 mm	103.0 mm	43.8 mm	44.5 mm
$\sigma(\lvert\varepsilon\rvert)$	TS Slope	559.3 mm	580.5 mm	37.0 mm	47.8 mm
$\sigma(\lvert\varepsilon\rvert)$	IFFT 8xZ-P	236.2 mm	145.5 mm	61.9 mm	58.7 mm
$\sigma(\lvert\varepsilon\rvert)$	IFFT 32xZ-P	235.5 mm	144.4 mm	59.3 mm	57.9 mm
$Q(p=0.5)(\lvert\varepsilon\rvert)$	TS Slope	72.9 mm	64.8 mm	27.3 mm	34.4 mm
$Q(p=0.5)(\lvert\varepsilon\rvert)$	IFFT 8xZ-P	66.0 mm	63.8 mm	31.2 mm	34.8 mm
$Q(p=0.5)(\lvert\varepsilon\rvert)$	IFFT 32xZ-P	65.1 mm	61.4 mm	29.3 mm	33.5 mm
$Q(p=0.8)(\lvert\varepsilon\rvert)$	TS Slope	380.8 mm	340.3 mm	71.3 mm	62.4 mm
$Q(p=0.8)(\lvert\varepsilon\rvert)$	IFFT 8xZ-P	133.5 mm	157.7 mm	84.0 mm	67.4 mm
$Q(p=0.8)(\lvert\varepsilon\rvert)$	IFFT 32xZ-P	135.0 mm	150.3 mm	79.8 mm	70.6 mm
$Q(p=0.9)(\lvert\varepsilon\rvert)$	TS Slope	936.7 mm	786.1 mm	102.6 mm	103.7 mm
$Q(p=0.9)(\lvert\varepsilon\rvert)$	IFFT 8xZ-P	330.8 mm	280.5 mm	111.2 mm	99.1 mm
$Q(p=0.9)(\lvert\varepsilon\rvert)$	IFFT 32xZ-P	350.7 mm	264.2 mm	99.9 mm	100 mm

Table 4.2: Ranging error $\varepsilon = R_{\text{Meas}} - R_{\text{Act}}$ statistics of the polarization dependent harmonic SFMCW radar measurements. Polarization: Illumination S-band, harmonic return signal C-band, n = 81 measurements, measurement distance step-size $\Delta d = 50\,\text{mm}$.

improve the outcome of the phase estimation process. While these predictive model-based unwrap procedure are well-known and actively researched for 2-D phase unwrap problems commonly encountered in SAR radar image processing and MRI data, this is not the case for the 1-D problem encountered here. When only a fraction of the interpolation capabilities demonstrated for the 2-D case could be realized for the 1-D case, this would lead to a serious overall improvement.

Despite all of these issues, it was quite a surprise that such a high range measurement accuracy was achieved with both procedures in these test-cases. A statistical evaluation of the ranging results obtained for the four polarization configuration are shown in Table 4.2. A mean deviation from the actual true distance of less $\lambda_i/2 \approx 50\,\text{mm}$ of the illumination signal was achieved, except for the multipath fading dominated measurements using the (HH) polarized illumination signal. Furthermore, half of the ranging results, regardless of the evaluation algorithm, showed a measurement error of less than 35 mm in the (VV/HH) and (VV/VV) measurements, which shows the efficacy of the interpolation process when the original SFMCW range cell size of $\Delta R = 499.65\,\text{mm}$ is considered. This is especially evident when comparing the non-interpolated IFFT ranging results with the results obtained by the other algorithms, as shown in the various plots.

The likeliest explanation for the residual, almost sinusoidal, distance measurement error, which was observed even under good SNR conditions without frequency selective fading, and is easily identified in the ranging error plots, is the presence of a second

propagation path in addition to the direct line-of-sight, with a path length of less or approximately equal to the resolution capability ΔR of the system. These two apparent targets, created by multipath and located in one range cell, lead to the situation, that only the average distance between paths can be interpolated, as shown in the introduction to the ranging procedures in chapter 4.2. Longer multipath interference path length differences of $(R_2 - R_1) \geq \Delta R$ can be ruled out, as the IFFT based target ranging algorithms would be immune to this effect and the additional propagation path could be clearly resolved in the presented IFFT over distance range plots.

In order to investigate the possible cause of this effect even further, a high resolution measurement using $\lambda_i/10 = 10\,\text{mm}$ spaced distance sampling points was carried out in the SNR stable (VV/VV) configuration to avoid possible undersampling of the propagation effects and gain more spatial resolution to interpret this effect.

4.4.4 VV-Polarized High-Resolution Measurement Results

The high distance resolution measurements were carried out in exactly the same configuration as already used for the (VV/VV) polarized measurement presented before, except with a finer position sampling grid of the transponder, which is reduced to $\lambda_i/10 = 10\,\text{mm}$.

The measurement data visualization and evaluation is carried out in exactly the same manner as presented before.

While the maximum, mean and minimum received harmonic power measurement results over tag distance shown in Fig. 4.50 just confirm the results already presented in the coarser distance sampling grid earlier (see Fig. 4.46), the results obtained by visualizing the received harmonic power over frequency and distance convey important new aspects to the effects seen before.

When the high-resolution harmonic return power measurement shown in Fig. 4.51 is analyzed closely, a tell-tale feather or wave like, high frequency power envelope ripple pattern can easily be identified in measurement results.

Closer inspection reversals a slightly slanted propagation of this pattern over illumination / harmonic return frequency with a periodicity of approximately 50 mm - which is equivalent to the free-space wavelength of the harmonic return frequency. This observation presents another hint at the close-in multipath interference and distance averaging theory as the likeliest source of the periodic ranging error observed earlier, and also here in the measurement results shown in Fig. 4.52.

In order to decide if this effect has its roots in the illumination or harmonic frequency domain, it is important to remember from the classical transmission line VSWR theory, that the observable magnitude envelope pattern, which is relevant for the detected power, shows double the frequency of the fundamental super-positioned wave. While this may seem counter-intuitive at first, the most practical example for this phenomenon is the frequency of the output ripple present on an unfiltered full-bridge rectifier fed with a sinusoidal input. This ripple also shows a periodicity of double the input frequency due to the envelope detection performed by full-quadrant rectification and magnitude detection.

With this in mind, this effect seems to be happening in the S-band illumination frequency domain and is most likely caused by the interference of the line-of-sight path

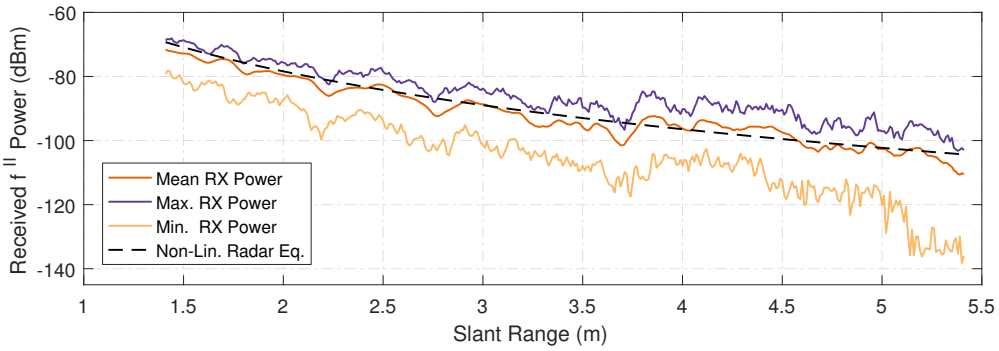

Figure 4.50: Mean, maximum and minimum f^{II} harmonic return power measurement results for the S-band vertical, C-band vertical polarization antenna configuration over tag distance, measured with a tag distance step-size of $\Delta d = 10\,\text{mm}$.

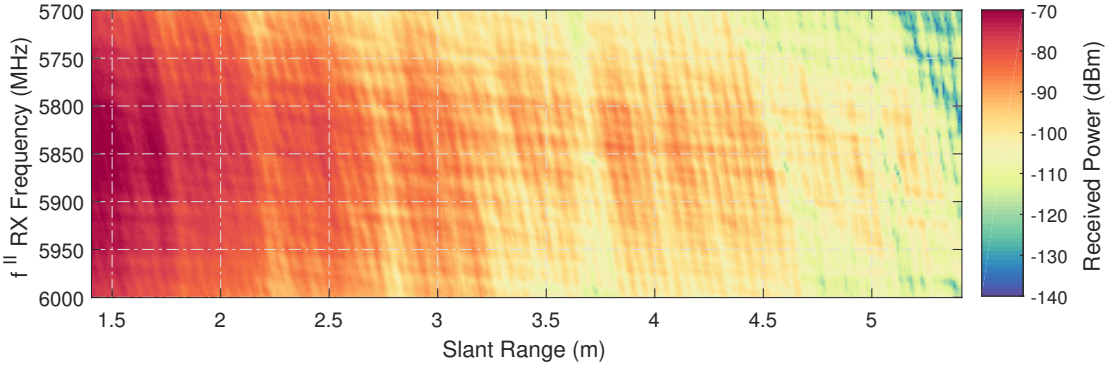

Figure 4.51: f^{II} harmonic return power measurement results for the S-band vertical, C-band vertical antenna configuration over tag distance, measured with a tag distance step-size of $\Delta d = 10\,\text{mm}$.

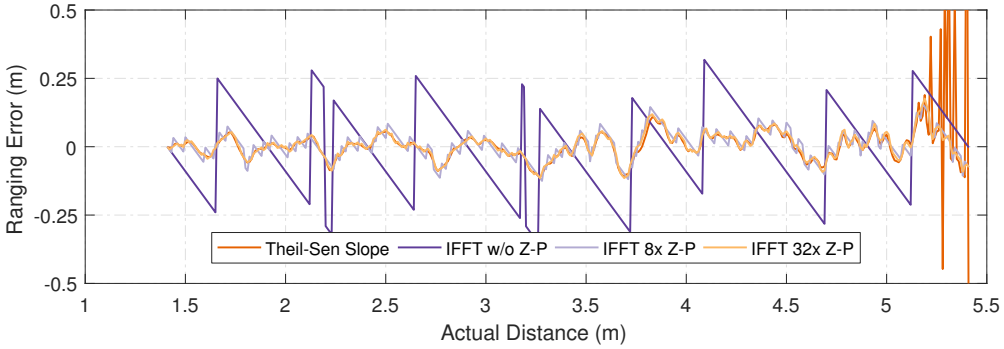

Figure 4.52: Distance ranging error for multiple ranging methods for the S-band vertical, C-band horizontal polarization antenna configuration over tag distance, measured with a tag distance step-size of $\Delta d = 10\,\text{mm}$.

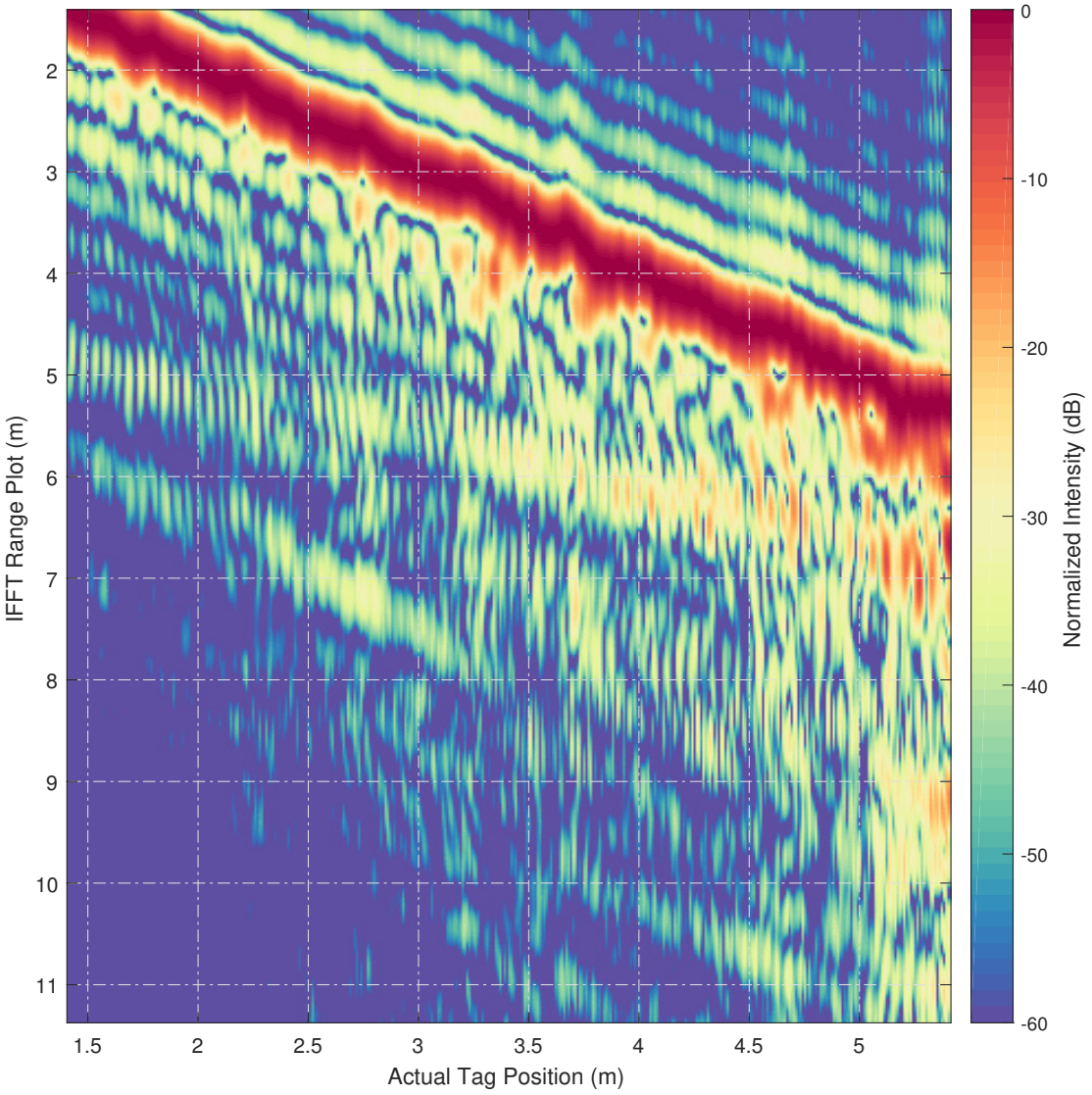

Figure 4.53: Harmonic radar IFFT range profile over tag distance, normalized on the maximum intensity for each position, for the S-band vertical, C-band horizontal polarization antenna configuration over tag distance, measured with a tag distance step-size of $\Delta d = 10\,\text{mm}$ and a frequency domain zero-padding factor of 64.

		(VV / VV) High-Resolution
$\mu(\lvert\varepsilon\rvert)$	TS Slope	47.3 mm
$\mu(\lvert\varepsilon\rvert)$	IFFT 8xZ-P	39.7 mm
$\mu(\lvert\varepsilon\rvert)$	IFFT 32xZ-P	36.1 mm
$\sigma(\lvert\varepsilon\rvert)$	TS Slope	99.3 mm
$\sigma(\lvert\varepsilon\rvert)$	IFFT 8xZ-P	50.2 mm
$\sigma(\lvert\varepsilon\rvert)$	IFFT 32xZ-P	46.9 mm
$Q(p = 0.5)(\lvert\varepsilon\rvert)$	TS Slope	28.9 mm
$Q(p = 0.5)(\lvert\varepsilon\rvert)$	IFFT 8xZ-P	33.0 mm
$Q(p = 0.5)(\lvert\varepsilon\rvert)$	IFFT 32xZ-P	28.8 mm
$Q(p = 0.8)(\lvert\varepsilon\rvert)$	TS Slope	57.8 mm
$Q(p = 0.8)(\lvert\varepsilon\rvert)$	IFFT 8xZ-P	64.2 mm
$Q(p = 0.8)(\lvert\varepsilon\rvert)$	IFFT 32xZ-P	56.9 mm
$Q(p = 0.9)(\lvert\varepsilon\rvert)$	TS Slope	83.4 mm
$Q(p = 0.9)(\lvert\varepsilon\rvert)$	IFFT 8xZ-P	84.3 mm
$Q(p = 0.9)(\lvert\varepsilon\rvert)$	IFFT 32xZ-P	77.6 mm
$Q(p = 0.95)(\lvert\varepsilon\rvert)$	TS Slope	102.4 mm
$Q(p = 0.95)(\lvert\varepsilon\rvert)$	IFFT 8xZ-P	103.6 mm
$Q(p = 0.95)(\lvert\varepsilon\rvert)$	IFFT 32xZ-P	97.0 mm

Table 4.3: Ranging error $\varepsilon = R_{\text{Meas}} - R_{\text{Act}}$ statistics of the VV / VV polarized high resolution harmonic SFMCW radar measurements. Polarization: Illumination S-band, harmonic return signal C-band, n = 401 measurements, measurement distance step-size $\Delta d = 10\,\text{mm}$.

and parts of the illumination signal being reflected at the metallic surface of the linear slide actuator mechanism.

Furthermore, a distinct far out return with a slightly different slope than the main return can now be easily identified besides the main tag harmonic return signal in the high resolution IFFT range plot results shown in Fig. 4.53. This return varies in measured path length from approximately 5 m slant range at the initial $R = 1.41\,\text{m}$ position of the transponder tag to about 7 m, when the transponder is at the maximum reach of the actuator. This return is assumed to be a valid multipath return, instead of ripples introduced by the frequency domain zero-padding process easily discernible at shorter ranges than the main return in Fig. 4.53, due to its independent slope characteristic compared to the main return of the harmonic tag.

The statistical evaluation of this high-resolution measurement run is found in Table 4.3. By comparing the values shown in this table with the results shown for the same (VV/VV) configuration at a lower distance sample count shown before, it is easy to see that the IFFT zero-padding based ranging results are slightly more consistent than the ones obtained by the Theil-Sen phase slope estimator approach, which is caused by the tendency of the phase unwrap process to create fairly large outliers. Due to the

five times higher amount of samples captured during this run, the values shown here have a significant higher statistical validity than those presented before and will also be used as the reference for the measurement performed under severe clutter, which will be presented next.

4.4.5 Severe Clutter Measurement Results

While all the previous measurements only had indoor multipath propagation and its associated detrimental effects present as a hindrance for the harmonic SFMCW radar system, one of the most important measurements to asses the system performance, and the raison d'être for harmonic radar itself, still had to be carried out: The evaluation of its clutter rejection capabilities.

In order to assess this extremely important aspect, two different clutter measurement scenarios are carried out using the following experimental setup:

First, only one large trihedral reflector with a RCS of $\sigma_{3\,\mathrm{GHz}} = 13.67\,\mathrm{m}^2$ (see Fig. 4.54 for reference), representing a single clutter scatterer, was placed besides the linear actuator track in the main lobes of the illumination and reception antenna at a distance of 2.5 m. The (VV/VV) polarized measurement was repeated using the coarse distance step-size of $\Delta d = 50\,\mathrm{mm}$, replicating the initial measurement carried out for the polarization survey.

In the second measurement scenario, two smaller trihedral reflectors with a RCS of $\sigma_{3\,\mathrm{GHz}} = 0.16\,\mathrm{m}^2$ were added to the previous scenario and placed at 1.6 m and 1.8 m distance from the interrogator antennas (see Fig. 4.26 for a picture of the setup, as seen from the bore sight of the interrogator) for a last high-resolution test with a step-size of $\Delta d = 10\,\mathrm{mm}$, in order to simulate a more realistic multi-scatterer clutter environment with superposition of different return intensities, as would be encountered in its intended application under sea clutter.

The results of the clutter test using only one large trihedral reflector will be discussed first, with the results of this measurement shown in the same format as already used in the previous measurements from Fig. 4.55 to Fig. 4.58.

It can easily be seen from the presented results, that the detection capabilities of the SFMCW harmonic radar system was not lowered by the large reflector in any way, at least at the ranges investigated with this setup. When looking at the received harmonic power results over distance (Fig. 4.55) and frequency (Fig. 4.56), the RF propagation shadowing of the large reflector can easily be identified as a sharp drop in magnitude for ranges larger than 3 m.

In direct comparison with the same measurement carried out without the reflector, the ranging results for the measurement with the reflector shown in Fig. 4.57 are very consistent up to the point, where the received harmonic amplitude approaches the harmonic signal noise-floor of the system.

All major visible deviations in ranging accuracy are directly related to low SNR events in the power plot. Out of the different investigated ranging methods, the IFFT zero-padding interpolation demonstrated extreme robustness against this interference and deviations exceeding the original range cell could only be observed towards the very end of the linear actuator setup.

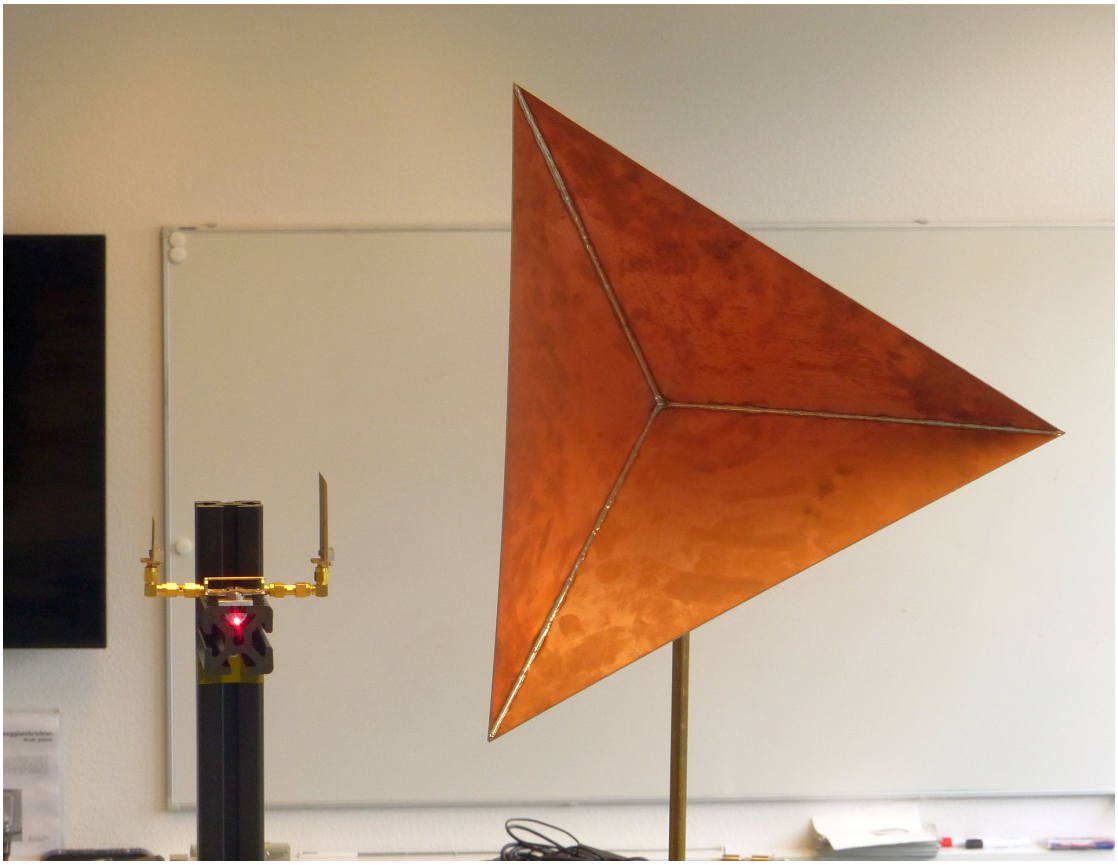

Figure 4.54: Detail picture of the harmonic radar tag in the vertical / vertical tag antenna configuration with the largest trihedral reflector ($\sigma_{f=3\,\mathrm{GHz}} = 13.67\,\mathrm{m}^2$) at approximately 0.2 m distance offset.

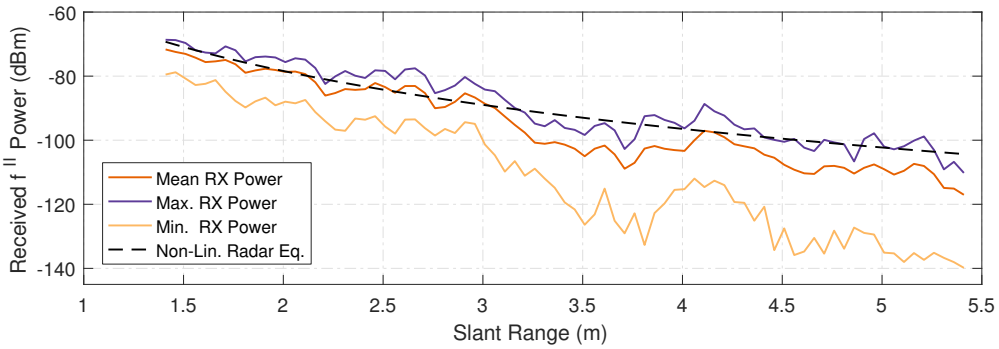

Figure 4.55: Mean, maximum and minimum f^{II} harmonic return power measurement results for the S-band vertical, C-band vertical polarization antenna configuration over tag distance, measured with a tag distance step-size of $\Delta d = 50\,\mathrm{mm}$. $\sigma_{3\,\mathrm{GHz}} = 13.67\,\mathrm{m}^2$ reflector positioned at 2.5 m distance from the interrogator antennas.

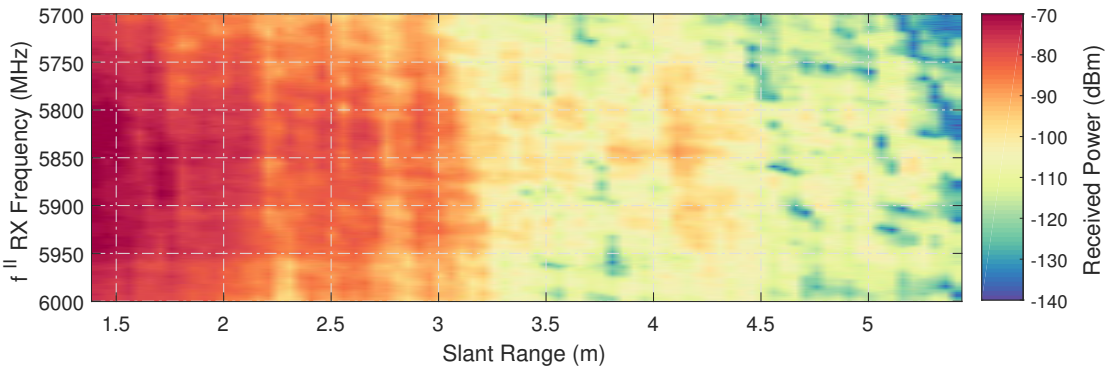

Figure 4.56: f^{II} harmonic return power measurement results for the S-band vertical, C-band vertical polarization antenna configuration over tag distance, measured with a tag distance step-size of $\Delta d = 50\,\text{mm}$ $\sigma_{3\,\text{GHz}} = 13.67\,\text{m}^2$ reflector positioned at 2.5 m distance from the interrogator antennas.

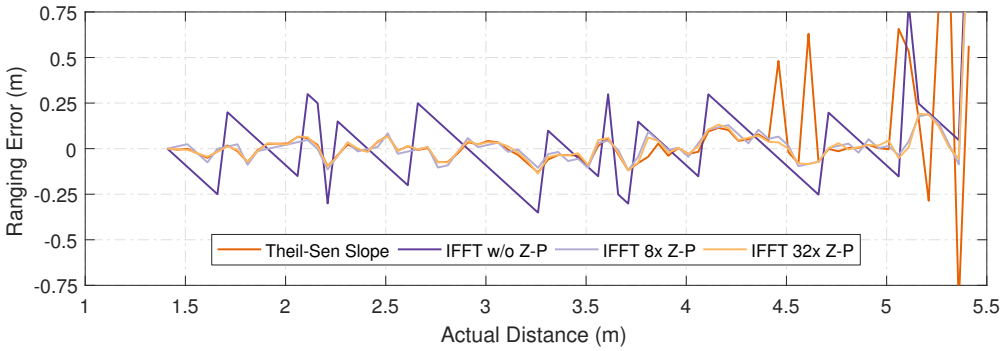

Figure 4.57: Distance ranging error for multiple ranging methods for the S-band vertical, C-band vertical polarization antenna configuration over tag distance, measured with a tag distance step-size of $\Delta d = 50\,\text{mm}$. $\sigma_{3\,\text{GHz}} = 13.67\,\text{m}^2$ reflector positioned at 2.5 m distance from the interrogator antennas.

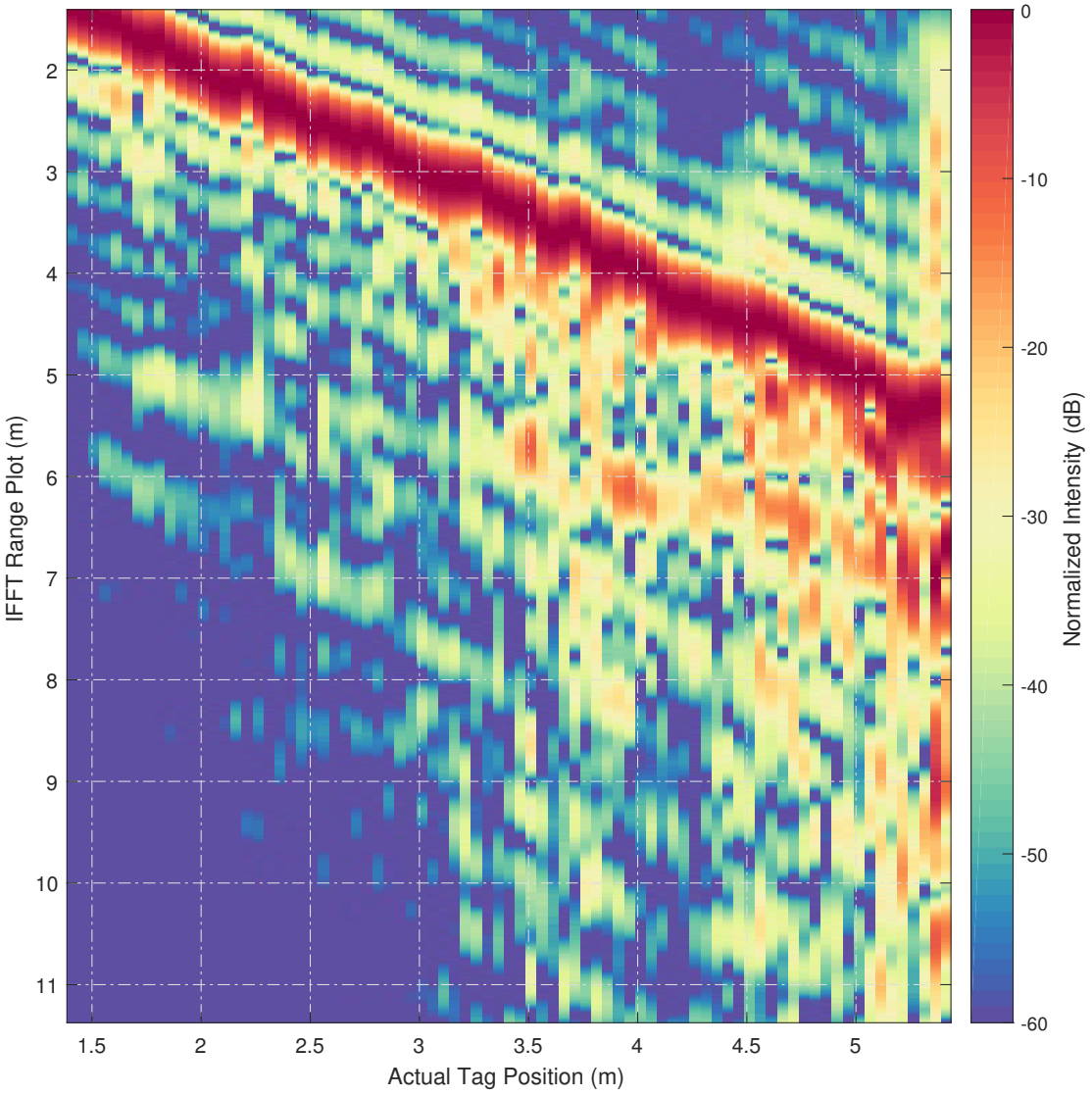

Figure 4.58: Harmonic radar IFFT range profile over tag distance, normalized on the maximum intensity for each position, for the S-band vertical, C-band vertical polarization antenna configuration over tag distance, measured with a tag distance step-size of $\Delta d = 50\,\mathrm{mm}$ and a frequency domain zero-padding factor of 64. $\sigma_{3\,\mathrm{GHz}} = 13.67\,\mathrm{m}^2$ reflector positioned at 2.5 m distance from the interrogator antennas.

		(VV / VV) w/o. Obstacle	(VV / VV) w. Large Obstacle
$\mu(\lvert\varepsilon\rvert)$	TS Slope	45.7 mm	110.2 mm
$\mu(\lvert\varepsilon\rvert)$	IFFT 8xZ-P	44.9 mm	62.8 mm
$\mu(\lvert\varepsilon\rvert)$	IFFT 32xZ-P	44.5 mm	60.6 mm
$\sigma(\lvert\varepsilon\rvert)$	TS Slope	47.8 mm	215.2 mm
$\sigma(\lvert\varepsilon\rvert)$	IFFT 8xZ-P	58.7 mm	157.1:mm
$\sigma(\lvert\varepsilon\rvert)$	IFFT 32xZ-P	57.9 mm	154.1 mm
$Q(p = 0.5)(\lvert\varepsilon\rvert)$	TS Slope	34.4 mm	35.7 mm
$Q(p = 0.5)(\lvert\varepsilon\rvert)$	IFFT 8xZ-P	34.8 mm	32.7 mm
$Q(p = 0.5)(\lvert\varepsilon\rvert)$	IFFT 32xZ-P	33.5 mm	34.6 mm
$Q(p = 0.8)(\lvert\varepsilon\rvert)$	TS Slope	62.4 mm	92.0 mm
$Q(p = 0.8)(\lvert\varepsilon\rvert)$	IFFT 8xZ-P	67.4 mm	89.3 mm
$Q(p = 0.8)(\lvert\varepsilon\rvert)$	IFFT 32xZ-P	70.6 mm	72.8 mm
$Q(p = 0.9)(\lvert\varepsilon\rvert)$	TS Slope	103.7 mm	364.0 mm
$Q(p = 0.9)(\lvert\varepsilon\rvert)$	IFFT 8xZ-P	99.1 mm	109.2 mm
$Q(p = 0.9)(\lvert\varepsilon\rvert)$	IFFT 32xZ-P	100 mm	107.4 mm

Table 4.4: Ranging error $\varepsilon = R_{\text{Meas}} - R_{\text{Act}}$ statistics of the (VV / VV) polarized harmonic SFMCW radar measurements with one $\sigma_{3\,\text{GHz}} = 13.67\,\text{m}^2$ reflector positioned at 2.5 m distance from the interrogator antennas. Polarization: Illumination S-band, harmonic return signal C-band, n = 81 measurements, measurement distance step-size $\Delta d = 50\,\text{mm}$.

This observation is supported by the direct statistical comparison shown in Table 4.4 between the measurement performed with and without the large reflector in the same configuration.

Only a minor increase in outliers can be observed in the overall measurement data for the IFFT based procedures. The Theil-Sen phase slope estimator approach suffers from the same limitations as already mentioned before and is mainly limited by its higher harmonic SNR requirement for performing a successful phase unwrap prior to phase estimation and larger outliers caused by the introduction of erroneous 2π phase jumps in the unwrapped phase result.

While the additional propagation path already discussed before seems to be more pronounced in the visualization of the IFFT range plots over distance in Fig. 4.58, this effect is caused by the drop in the main return path amplitude and the vertical, i.e. inter range plot, normalization of the results and does not necessarily imply a stronger return from this propagation path.

After obtaining these reassuring positive results, the test range was modified for a last time to conduct a simulation of a multi-clutter environment by adding two smaller trihedral reflectors between the interrogator and the larger trihedral reflector used in the previous measurement run.

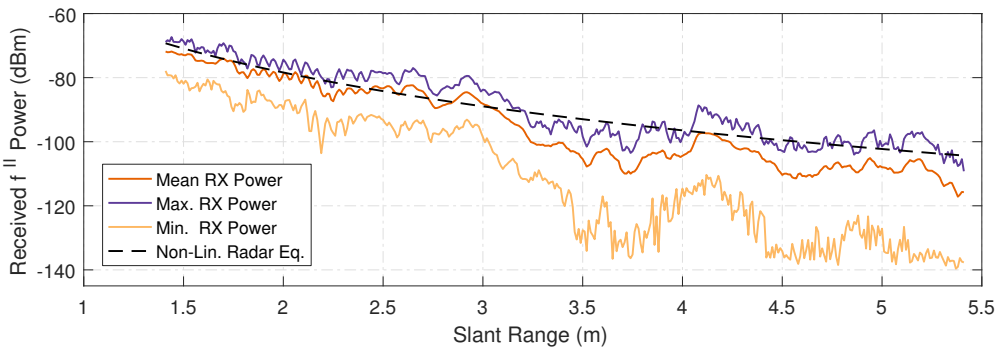

Figure 4.59: Mean, maximum and minimum f^{II} harmonic return power measurement results for the S-band vertical, C-band vertical polarization antenna configuration over tag distance, measured with a tag distance step-size of $\Delta d = 10\,\text{mm}$. $\sigma_{3\,\text{GHz}} = 13.67\,\text{m}^2$ reflector positioned at 2.5 m and two $\sigma_{3\,\text{GHz}} = 0.16\,\text{m}^2$ reflectors at 1.6 m and 1.8 m distance from the interrogator antennas.

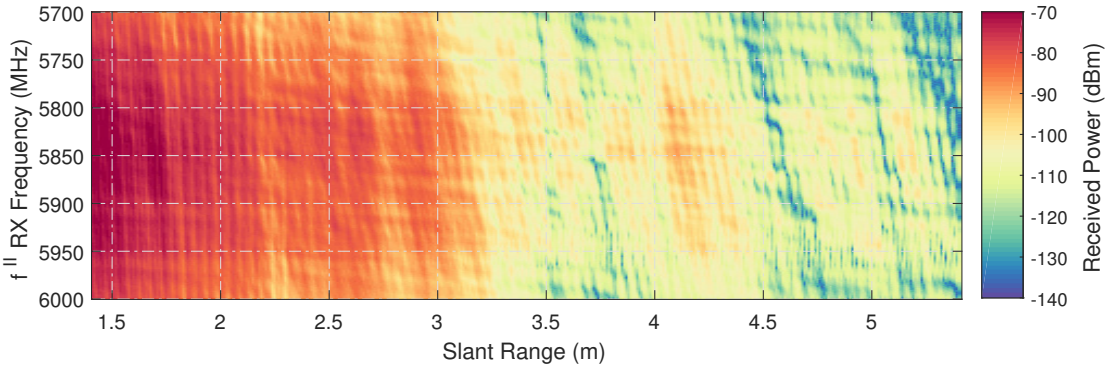

Figure 4.60: f^{II} harmonic return power measurement results for the S-band vertical, C-band vertical polarization antenna configuration over tag distance, measured with a tag distance step-size of $\Delta d = 10\,\text{mm}$. $\sigma_{3\,\text{GHz}} = 13.67\,\text{m}^2$ reflector positioned at 2.5 m and two $\sigma_{3\,\text{GHz}} = 0.16\,\text{m}^2$ reflectors at 1.6 m and 1.8 m distance from the interrogator antennas.

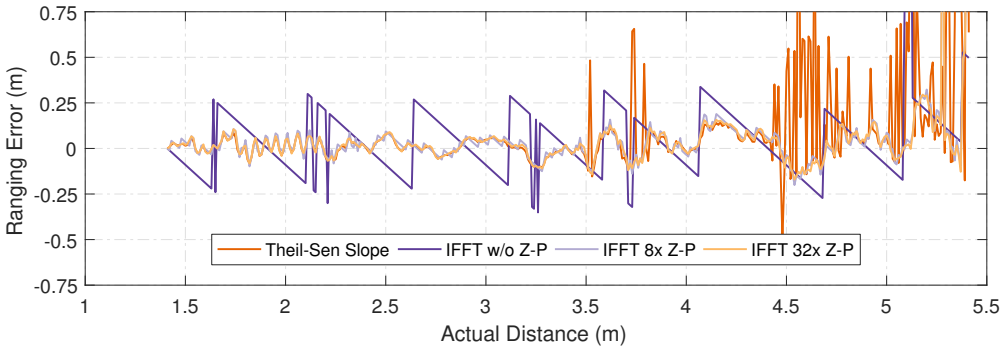

Figure 4.61: Distance ranging error for multiple ranging methods for the S-band vertical, C-band vertical polarization antenna configuration over tag distance, measured with a tag distance step-size of $\Delta d = 10\,\text{mm}$. $\sigma_{3\,\text{GHz}} = 13.67\,\text{m}^2$ reflector positioned at 2.5 m and two $\sigma_{3\,\text{GHz}} = 0.16\,\text{m}^2$ reflectors at 1.6 m and 1.8 m distance from the interrogator antennas.

For this measurement, the larger $\sigma_{3\,\text{GHz}} = 13.67\,\text{m}^2$ reflector is left at the 2.5 m distance mark from the interrogator antenna gantry reference plane and the two smaller $\sigma_{3\,\text{GHz}} = 0.16\,\text{m}^2$ reflectors are added at 1.6 m and 1.8 m distance from the interrogator antennas. This creates a complex clutter scenario right in the main lobe of both antennas and at comparatively high illumination signal field strengths, therefore generating strong clutter returns and severe downrange RF shadowing.

The results obtained in this measurement scenario, which was conducted using the high-resolution $\Delta d = 10\,\text{mm}$ distance sampling step-size, are shown in Fig. 4.59 through Fig. 4.62, with an additional statistical comparison between this multi-clutter scenario and the measurements without any artificial additional clutter found in Table 4.5.

When comparing the high-resolution multi-clutter influenced measurement results with the high-resolution data obtained without any deliberate clutter interference, it is obvious, that the results are influenced by the added reflectors, but still demonstrate the robustness of the harmonic radar concept. When comparing the ranging error over distance for both configurations, shown in Fig. 4.52 without and in Fig. 4.61 with clutter interference, it is very interesting to observe a high-frequency ripple in the measurement error, consistent with the wavelength of the illumination frequency ($\lambda_i = 10\,\text{cm}$), in the clutter influenced zone right in front of the large reflector for ranges smaller than 2.5 m. This corresponds to an illumination frequency interference pattern created by the superposition of the original illumination signal and the large reflection caused by the $\sigma_{3\,\text{GHz}} = 13.67\,\text{m}^2$ reflector.

In the high resolution received harmonic power over frequency and distance plot shown in Fig. 4.60, this effect can also be identified. Furthermore, the slant angle of the interference pattern already observed in the non-clutter interfered high resolution measurement (see Fig. 4.51 for reference) changes its slant angle between the multipath propagation zone, for ranges greater than 2.5 m, and the clutter interference zone for

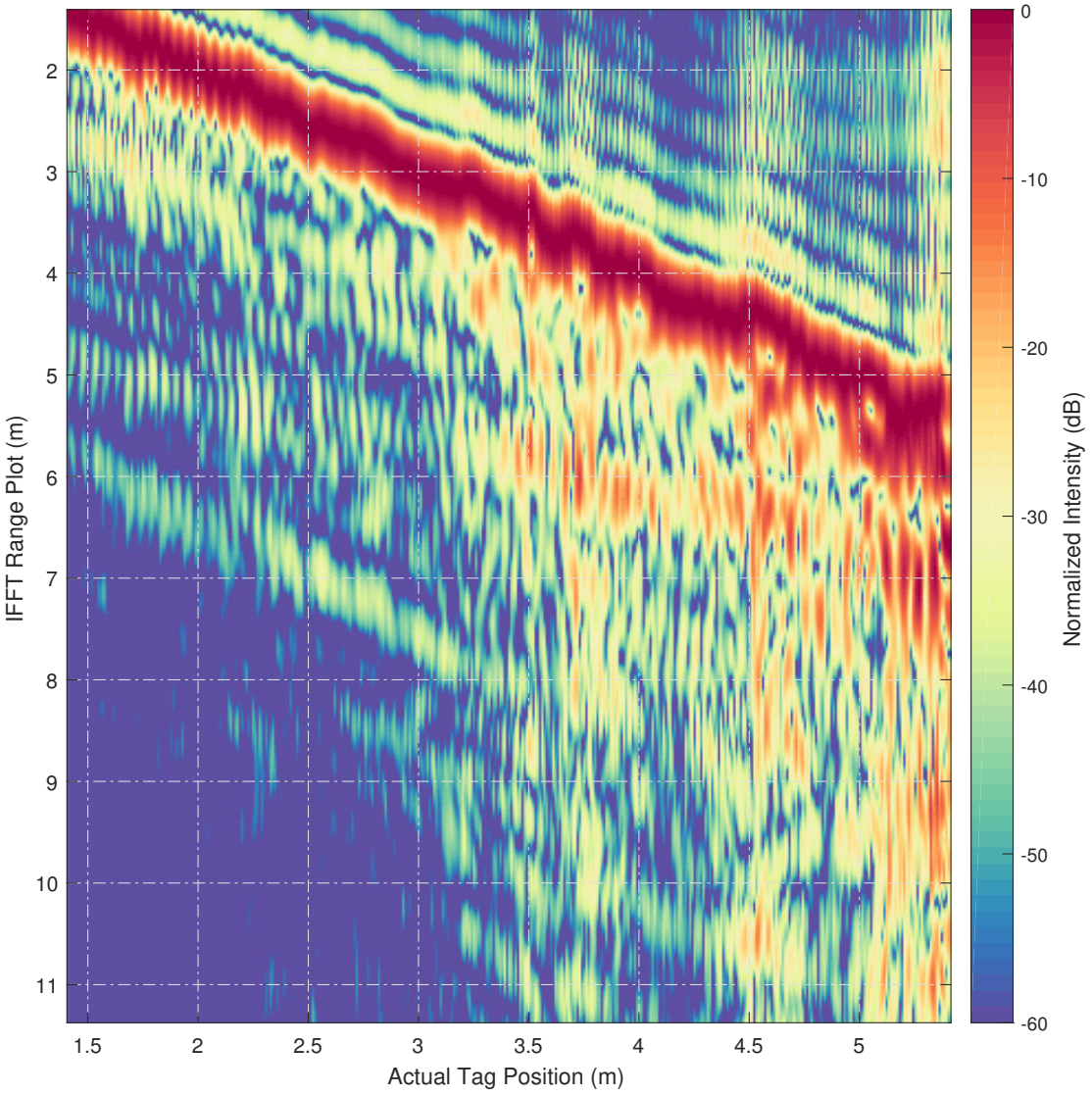

Figure 4.62: Harmonic radar IFFT range profile over tag distance, normalized on the maximum intensity for each position, for the S-band vertical, C-band vertical polarization antenna configuration over tag distance, measured with a tag distance step-size of $\Delta d = 10\,\text{mm}$. $\sigma_{3\,\text{GHz}} = 13.67\,\text{m}^2$ reflector positioned at 2.5 m and two $\sigma_{3\,\text{GHz}} = 0.16\,\text{m}^2$ reflectors at 1.6 m and 1.8 m distance from the interrogator antennas.

		w/o Clutter	3 Clutter Obstacles
$\mu(\lvert\varepsilon\rvert)$	TS Slope	47.3 mm	127.8 mm
$\mu(\lvert\varepsilon\rvert)$	IFFT 8xZ-P	39.7 mm	71.0 mm
$\mu(\lvert\varepsilon\rvert)$	IFFT 32xZ-P	36.1 mm	69.0 mm
$\sigma(\lvert\varepsilon\rvert)$	TS Slope	99.3 mm	297.3 mm
$\sigma(\lvert\varepsilon\rvert)$	IFFT 8xZ-P	50.2 mm	149.2 mm
$\sigma(\lvert\varepsilon\rvert)$	IFFT 32xZ-P	46.9 mm	147.7 mm
$Q(p = 0.5)(\lvert\varepsilon\rvert)$	TS Slope	28.9 mm	47.2 mm
$Q(p = 0.5)(\lvert\varepsilon\rvert)$	IFFT 8xZ-P	33.0 mm	45.4 mm
$Q(p = 0.5)(\lvert\varepsilon\rvert)$	IFFT 32xZ-P	28.8 mm	45.6 mm
$Q(p = 0.8)(\lvert\varepsilon\rvert)$	TS Slope	57.8 mm	103.5 mm
$Q(p = 0.8)(\lvert\varepsilon\rvert)$	IFFT 8xZ-P	64.2 mm	94.0 mm
$Q(p = 0.8)(\lvert\varepsilon\rvert)$	IFFT 32xZ-P	56.9 mm	93.5 mm
$Q(p = 0.9)(\lvert\varepsilon\rvert)$	TS Slope	83.4 mm	370.0 mm
$Q(p = 0.9)(\lvert\varepsilon\rvert)$	IFFT 8xZ-P	84.3 mm	129.4 mm
$Q(p = 0.9)(\lvert\varepsilon\rvert)$	IFFT 32xZ-P	77.6 mm	127.8 mm
$Q(p = 0.95)(\lvert\varepsilon\rvert)$	TS Slope	102.4 mm	607.0 mm
$Q(p = 0.95)(\lvert\varepsilon\rvert)$	IFFT 8xZ-P	103.6 mm	177.8 mm
$Q(p = 0.95)(\lvert\varepsilon\rvert)$	IFFT 32xZ-P	97.0 mm	150.9 mm

Table 4.5: Ranging error $\varepsilon = R_{\text{Meas}} - R_{\text{Act}}$ statistics of the (VV / VV) polarized high resolution harmonic SFMCW radar measurements without and with the three clutter obstacles. Polarization: Illumination S-band, harmonic return signal C-band, n = 401 measurements, measurement distance step-size $\Delta d = 10\,\text{mm}$.

shorter distances due to the different geometries involved between the reflection of the trihedral reflectors and the reflection and interference caused by the linear slide mechanism.

From the statistical evaluation of the measurement shown in Table 4.5, the previous findings of the coarse distance sampling size measurements are confirmed, although with higher statistical relevance due to the higher amount of samples taken during the measurement. Once again it can be observed, that the Theil-Sen estimator suffers from large outliers in the measurement results and the IFFT based ranging approaches show a higher degree of robustness against the adverse, close to system noise floor, conditions in the RF shadowed zone behind the larger trihedral reflector.

Nevertheless, the presented results easily demonstrate, that the SFMCW harmonic radar concepts holds up to its promises.

4.4.6 Conclusions Obtained from the Harmonic SFMCW Radar Measurements

In conclusion it is safe to say, that all the initial goals defined in chapter 4.3 for the harmonic SFMCW measurement were met and could be fulfilled with great success.

The feasibility of building a working high dynamic range harmonic SFMCW radar interrogator system based on the concepts of a frequency domain sampling non-linear VNA system, using the modules presented and developed in this work (see chapters 2.3.2 to 2.3.7), was successfully demonstrated by these experiments.

Furthermore, the results expected by the non-linear radar equation developed by Gallagher et al. ([34]) could be confirmed with a high degree of confidence and a high number of distance sampling points obtained via automation of the setup and measurement system. This especially includes the harmonic power series approximation model of the frequency doubler and the illumination power independence of the phase transfer function from the fundamental to the harmonic frequency. Nevertheless, a small residual uncertainty in the validity of the equation still remains, given the constraints of non ideal free-space propagation present in the indoor characterization setup.

For the VNA context of this work, the results of this experiments represent a great success, as the new concept of using TI repeatable synthesizers for the measurement of mixed-frequency S-parameters without a harmonic phase reference for LO phase correction has been proven for measurements over long timescales in these SFMCW measurements.

The TI repeatability of the whole system was found to be excellent from the results presented here. No serious drift effects could be observed even in the high distance resolution measurements, which took about 6 h each to complete.

The feasibility and accuracy of the new Theil-Sen phase slope estimator based ranging process was verified with a high degree of certainty under varying SNR and propagation conditions. This includes the assumptions made about the algorithm constraints and the increased noise susceptibility of the concept due to the 1-D phase unwrap process, as outlined in the theoretical discussion of the algorithm.

Another important contribution to the research in harmonic radar systems was made by presenting a systematic analysis of the polarization dependent ranging results and harmonic return signal properties, including the effects of multipath propagation and near-interrogator clutter on the harmonic SFMCW radar results combined with an illumination signal channel sounding of the measurement environment. An analysis for fundamental frequency illumination signal and harmonic return signal effects was provided in the realm of the constraints imposed by the experimental setup.

Finally totally new high-resolution measurement results of the clutter rejection ability of SFMCW harmonic radar and its associated propagation and ranging effects was provided in extremely fine spatial resolution of only $\lambda_i/10$, which was never carried out before to the author's knowledge, revealing harmonic radar propagation and multipath interference effects never demonstrated before in the harmonic radar context.

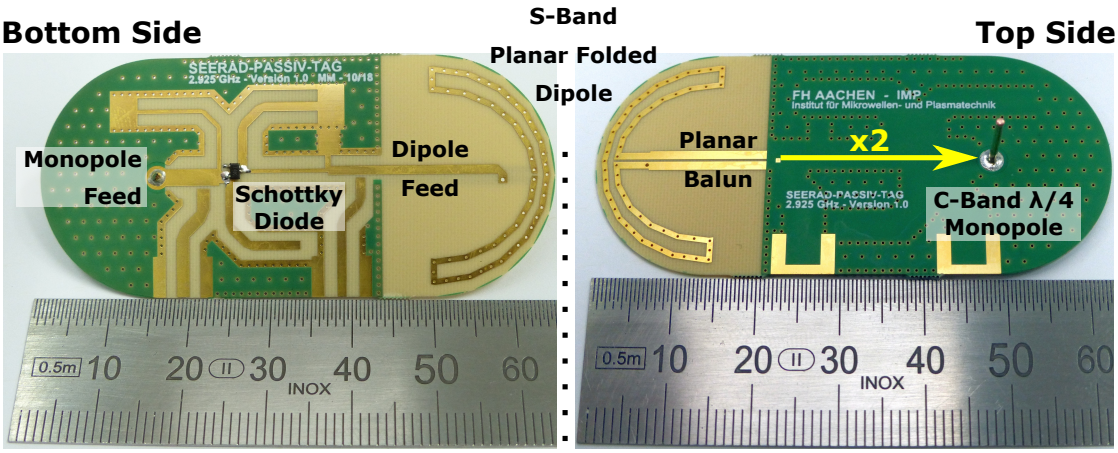

Figure 4.63: Picture of the fully integrated passive doubler harmonic radar tag.

4.5 The Ultra Low Power Active Harmonic Radar Tag and Future Developments beyond the Scope of this Work

In addition to the results already presented for the prototype SFMCW harmonic radar system, which are based on the research presented in this work, this last section presents an outlook with a broader scope more focused on the funding research project, SEERAD.

In accordance with the project goals to create a viable seaborne search and rescue (SAR) assistance system, the prototype harmonic radar transponder tag has been heavily modified for conformal integration into a life jacket or personal flotation device (PFD). Therefore, the receive and transmit antennas of the transponder tag, and the passive frequency doubler itself, were integrated into a single PCB solution by a joint cooperation of the FH Aachen and the Frauenhofer FHR. A picture of this new fully integrated passive transponder is shown in Fig. 4.63.

As a consequence of the characterization measurements and the verification of the harmonic radar equation, emphasis was placed on an efficient, compact, and sufficiently high gain illumination signal reception antenna, which was realized as a folded planar dipole structure using an integrated planar transmission line balun and an impedance matching network, instead of the half-wave dipole used for the concept verification measurements presented before.

The half-wave dipole harmonic return signal transmit antenna used in the linear actuator assisted indoor measurements was replaced by a simple $\lambda_h/4$ monopole antenna over a PCB ground-plane. While this change in antenna design slightly lowers the harmonic re-transmit antenna's gain, the loss introduced at this point is negligible in the overall harmonic radar system link budget consideration, as discussed in the introduction of this chapter.

The ability to characterize and optimize the passive frequency doubler circuit with standard coaxial measurement equipment was retained by providing direct access via

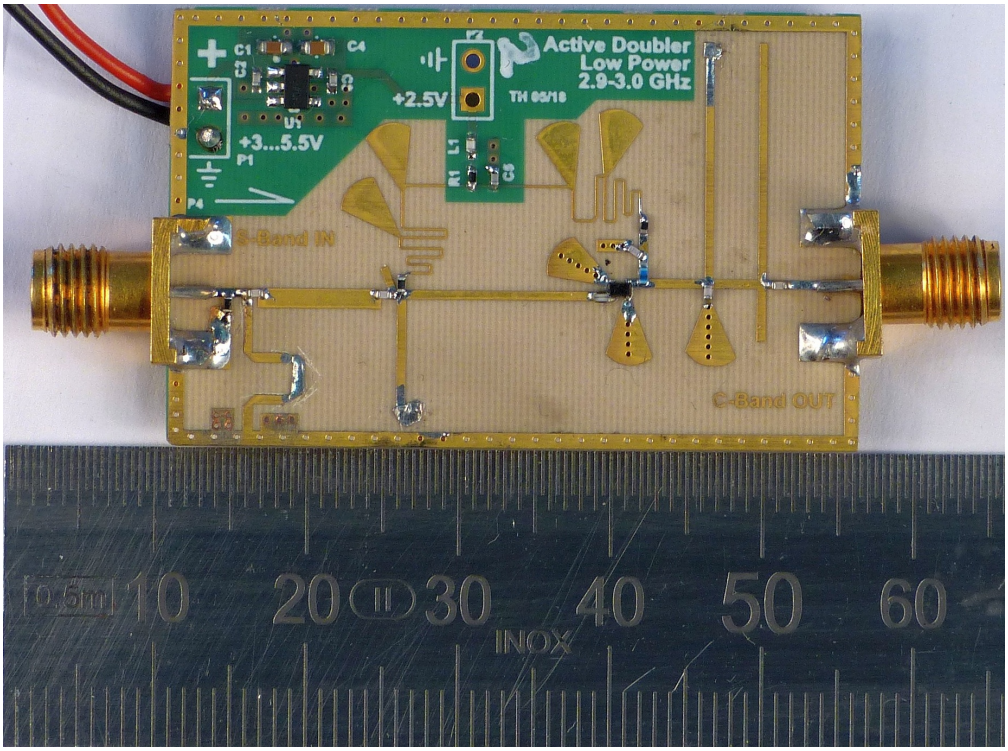

Figure 4.64: Detail picture of the novel low power active doubler based on a high f_T BJT for the harmonic radar tag.

individual micro-strip transmission lines as an option. Depending on the jumper position, these lines can also be used for antenna characterization measurement without the doubler circuitry.

Furthermore, all surface mounted components besides the Schottky diode could be eliminated through iterative optimization without loosing significant amounts of doubler conversion gain, therefore reducing the production costs of the tag to an absolute minimum.

In addition to the complete integration of the passive doubler transponder tag, a novel low-power active frequency doubler circuit based on a small signal high f_T bipolar junction transistor (BJT) was designed as an augmentation to the purely passive transponder tag using harmonic balance simulation and optimization in Keysight ADS.

A picture of this active doubler circuit with standard 50 Ω SMA interfaces, akin to the first passive doubler prototype, is shown in Fig. 4.64, while its harmonic output power over illumination signal input power and frequency as well as its corresponding conversion gain characteristics is shown in Fig. 4.65.

While this active, i.e. power consuming, approach drops one of the most attractive features of the passive transponder harmonic radar concept, it is still an extremely useful asset in the overall system concept of a marine SAR assistance system due to its extremely low power consumption of 1.8 mA at 2.5 V, which allows, when supplied with a standard

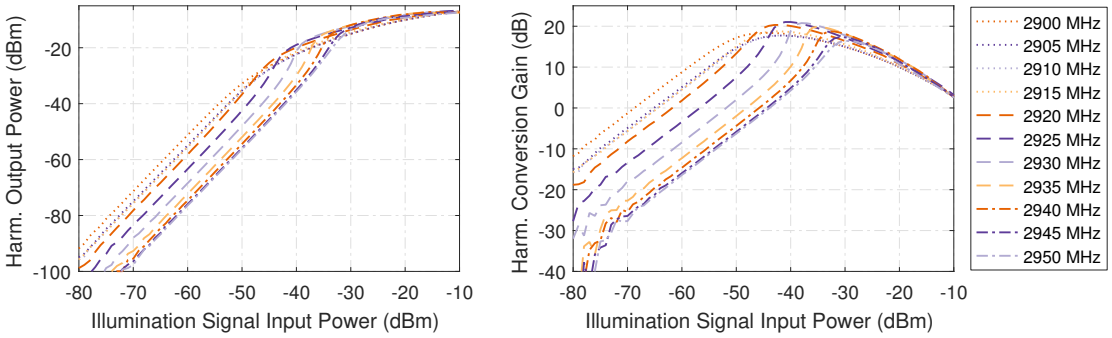

Figure 4.65: Measured output over input power and conversion gain of the active low power frequency doubler.

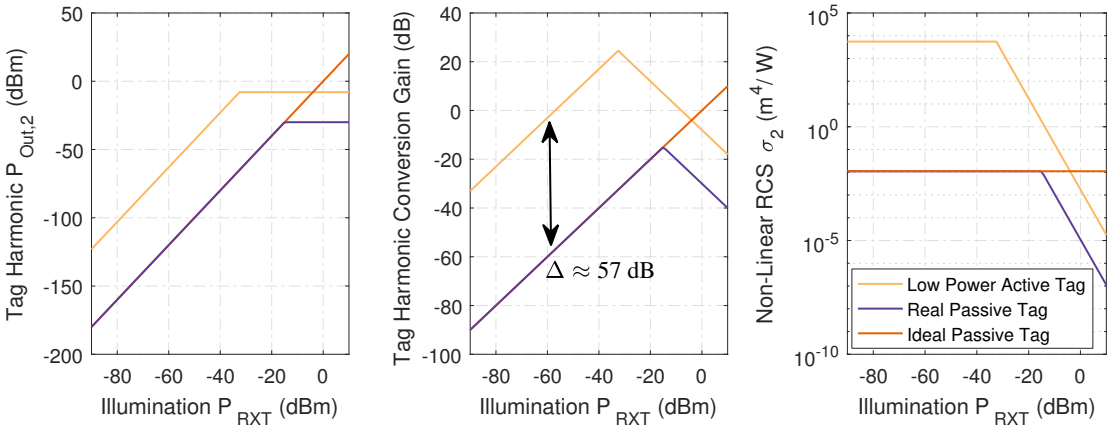

Figure 4.66: Modeled characteristic parameters of the active low power doubler based tag design in comparison with the passive doubler.

3 V CR2032 lithium coin cell, an approximate continuous operation time of 72 h.

Due to its low current draw and power requirements, this active doubler circuit could easily be integrated into existing life jackets featuring an LED based optical beacon with included batteries, while still providing longer operational availability than a GPS/Galileo/GNSS receiver and radio transmitter based solution to the original SAR distress at sea problem, as the GNSS receiver has to be continuously active after cold-start activation to acquire the required satellite almanac for 20 min or more, before a first positional fix can be made and thereby draining the overall power budget for even low active duty cycle operation.

Furthermore, this low power consumption is within the capability range provided by more unconventional power sources than primary cells. Besides a see water activated battery, which uses the water as its electrolyte and can be stored dry, resulting in extremely prolonged shelf life and doubling as the activation mechanism, the 5 mW required for operating the active frequency doubler circuit can also be obtained from

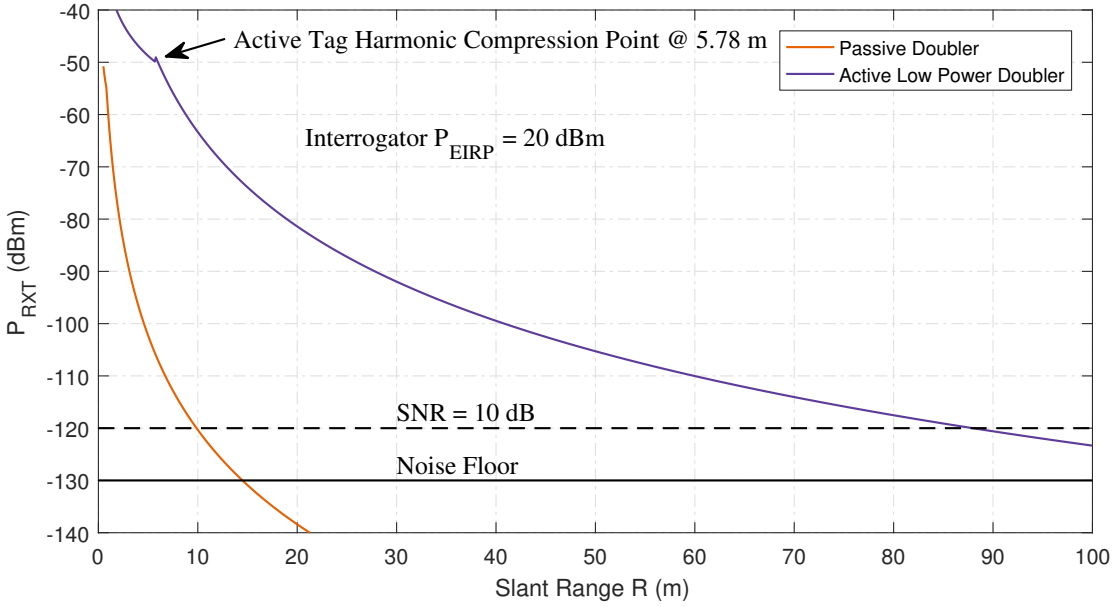

Figure 4.67: Evaluation of the harmonic radar equation for the active and passive frequency doubler circuit using the key system parameters of the characterization measurement setup. Illumination signal $P_{\mathrm{EIRP}} = 20\,\mathrm{dBm} \equiv 100\,\mathrm{mW}$.

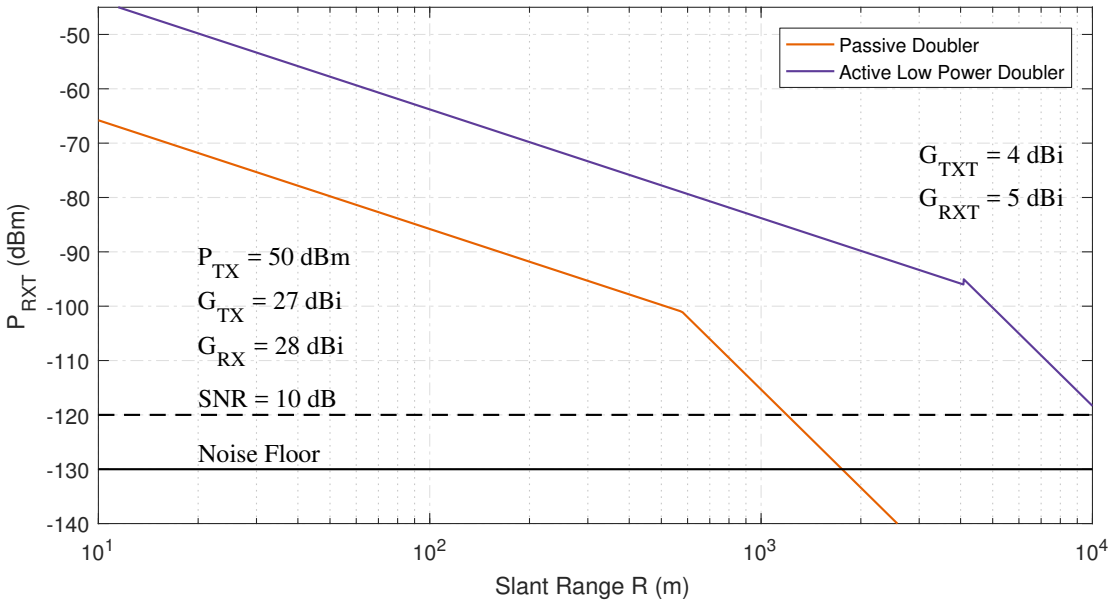

Figure 4.68: Evaluation of the harmonic radar equation for the active and passive frequency doubler circuit using a proposed high-power interrogator system.

environmental power harvesting in other applications. Examples for this would be a simple small solar cell with a super-capacitor as the storage medium or an thermoelectric generator operating on minute temperature differences.

Figure 4.69: Picture of the low power active harmonic radar tag indoor test measurement setup. Tag located at the far end of the corridor right before the door visible in the background. Distance approximately 46 m.

In a direct comparison between the passive doubler tag, the harmonic radar link budget improvements introduced by the active tag are quite dramatic, as shown in the modeled performance figures and the non-linear RCS visualized in Fig. 4.66. Compared to the passive doubler based tag presented and verified before, the effective RCS using the same illumination signal reception and harmonic re-transmission antennas is increased by 58 dB.

An exemplary comparison between the harmonic radar equation evaluation results for the harmonic reception power received at the interrogator is shown in Fig. 4.67, using the

same key system parameters, antenna gains and interrogator illumination signal output power, as used for the characterization and verification measurement presented before.

When a SNR of 10 dB is assumed to be sufficient for obtaining an approximate ranging result, it can easily be seen, that the active low power doubler tag increases the useful range of the harmonic radar system by almost a factor of nine, when compared with the same setup using the passive Schottky-diode based doubler circuit.

A harmonic SFMCW radar performance estimation of the final prototype setup for the SEERAD SAR assistance system is shown in Fig. 4.68. In this configuration, an increased antenna feed-point illumination signal CW input power of $P_{TX} = 100\,\mathrm{W} \equiv 50\,\mathrm{dBm}$ generated by a solid-state 150 W S-band power amplifier in slight output power back-off, coupled with higher antenna gains of $G_{TX} = 27\,\mathrm{dBi}$ and $G_{RX} = 28\,\mathrm{dBi}$ provided by a dual-band waveguide antenna currently under development by the Frauenhofer Institute for High Frequency Physics and Radar Techniques (FHR), are assumed.

In this final and fully equipped interrogator system configuration, passive tag ranging and detection is assumed to be possible for slant ranges up to 1200 m, while the ranging and detection range for the low power active doubler version of the transponder tag is almost extended to the LOS horizon at sea for a surface target and an interrogator height of 10 m to approximately 10 km.

Both of these maximum slant range figures would represent an enormous advancement for publicized performance figures of harmonic radar systems, as the highest currently published assumed maximum range estimate for a complete harmonic radar system consisting of the interrogator and tag for detection and ranging is 900 m under ideal conditions [147], although no experimental demonstration of this range is provided in the literature.

This system uses a solid-state pseudo random noise pulse-coded harmonic radar in the radar X-band, capable of 3 kW PEP (64.7 dBm), combined with 38 dBi illumination signal transmit and 43 dBi of harmonic signal reception antenna gain for the interrogator system. These performance figures result in an enormous EIRP of 102.7 dBm, or 18.6 MW, for the illumination signal for the system shown in [147].

In contrast, the system presented here only needs an illumination signal EIRP power of 77 dBm, or 50.1 kW to provide better results while still using a passive transponder tag, resulting in a huge power discrepancy of 25 dB between both concepts to achieve approximately the same results.

A prototype of the complete SEERAD interrogator setup, without the required automated pedestal, or azimuth rotator, for the waveguide antenna and using a prototype intermediate dual-band waveguide antenna design for S-band illumination and C-band reception, is shown in Fig. 4.72.

At the time of writing, the final characterization tests of the active doubler based transponder are still ongoing. Nevertheless, preliminary tests were already carried out, as shown in Fig. 4.69. In these tests, the active transponder tag could be detected and ranged in an indoor multipath scenario over distances of in excess of 40 m while still using the 100 mW EIRP interrogator test-setup with the low-gain waveguide horn antennas, hereby confirming the expected performance modeled by the non-linear radar equation.

Additionally, a new highly robust and linear C-band LNA was developed for the

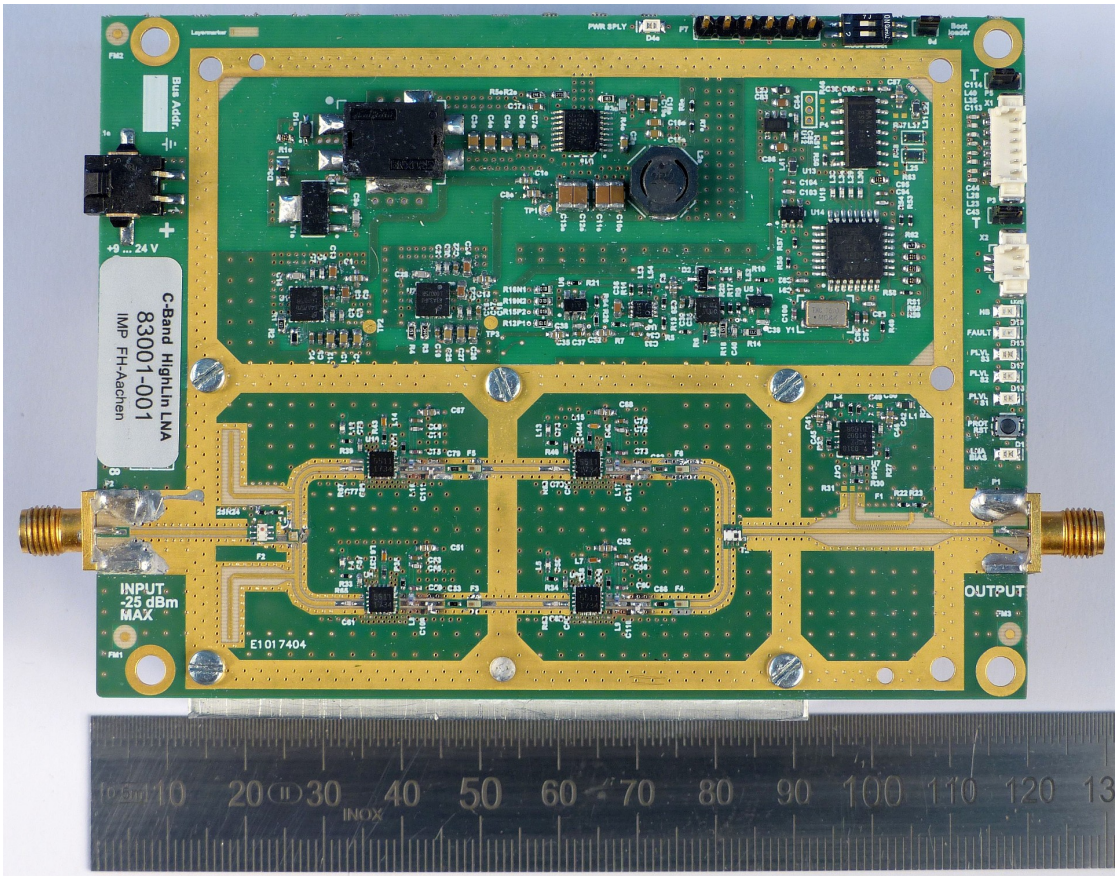

Figure 4.70: Picture of the developed high linearity, fundamental frequency suppressing, C-band LNA for the harmonic radar system with configurable output power protection.

SEERAD system to improve the fundamental frequency compression performance of the system under short distance clutter interference. This new LNA concept is based on a balanced amplifier design, which in itself provides second harmonic suppression, and integrates various stages of absorptive and reflective filtering to suppress residual remnants of the S-band illumination signal in the front-end. A picture of this new LNA is shown in Fig. 4.70, while S-parameter measurement results are provided in Fig. 4.71.

This purpose designed and build radar LNA is especially hardened against fundamental and harmonic frequency compression and, owing to the high-gain reception antenna in the final system, destruction by other high-powered signals, and especially other radars, operating in the C-band. This is accomplished by using high-output power capable high linearity LNAs, originally intended as a PA for cell phone picocells and therefore able to handle high crest factor signals, in a balanced configuration.

As these LNAs are capable of producing output powers that far exceed the tolerable input power limits of the non-linear VNA receiver, this LNA integrates a fast ($\leq 5\,\mu s$)

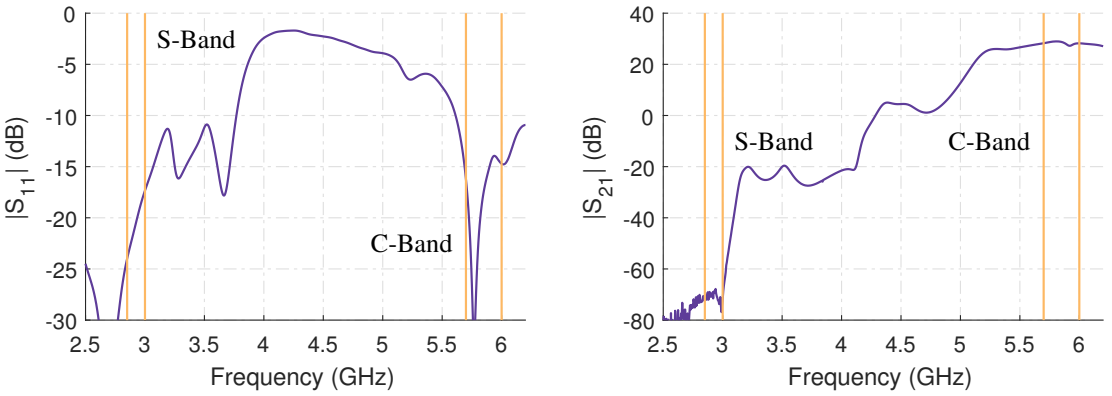

Figure 4.71: Measured S-parameters of the high linearity C-band LNA. S-band illumination signal frequency range and C-band reception frequency range highlighted.

responding peak envelope output power monitoring circuit, which immediately turns off all LNAs for input powers exceeding -25 dBm and thus protecting the VNA receiver front-end from destruction.

A gain of approximately 27.5 dB is achieved for C-band input signals while simultaneously providing more than 60 dB of selective attenuation for the S-band illumination signal. The noise figure for the LNA is expected to be around 1.5 dB.

No measurable intrinsic generation of the second harmonic can be observed with the measurement capabilities available to the author for fundamental frequency illumination signal input levels of up to +13 dBm directly applied to the input of the C-band LNA.

In conclusion, the results achieved during the SEERAD research project so far are very promising. Long range, high power interrogator using the final antenna configuration will be carried out in the near future and are hopefully able to reproduce the performance expected from the theoretical analysis of the system based on the system characterization carried out in chapter 2.3.7 of this work.

It will be interesting to see, which new applications and technologies for non-linear VNAs will emerge in the future.

Figure 4.72: Picture of the SEERAD prototype harmonic radar marine search and rescue system displayed at the International Radar Symposium (IRS) / Wachtbergforum 2018 at the Frauenhofer-Institut für Hochfrequenzphysik- und Radartechnik (FHR) in Wachtberg.

A Supplementary Synthetic Single Switched Receiver VNA Architecture Verification Measurement Results

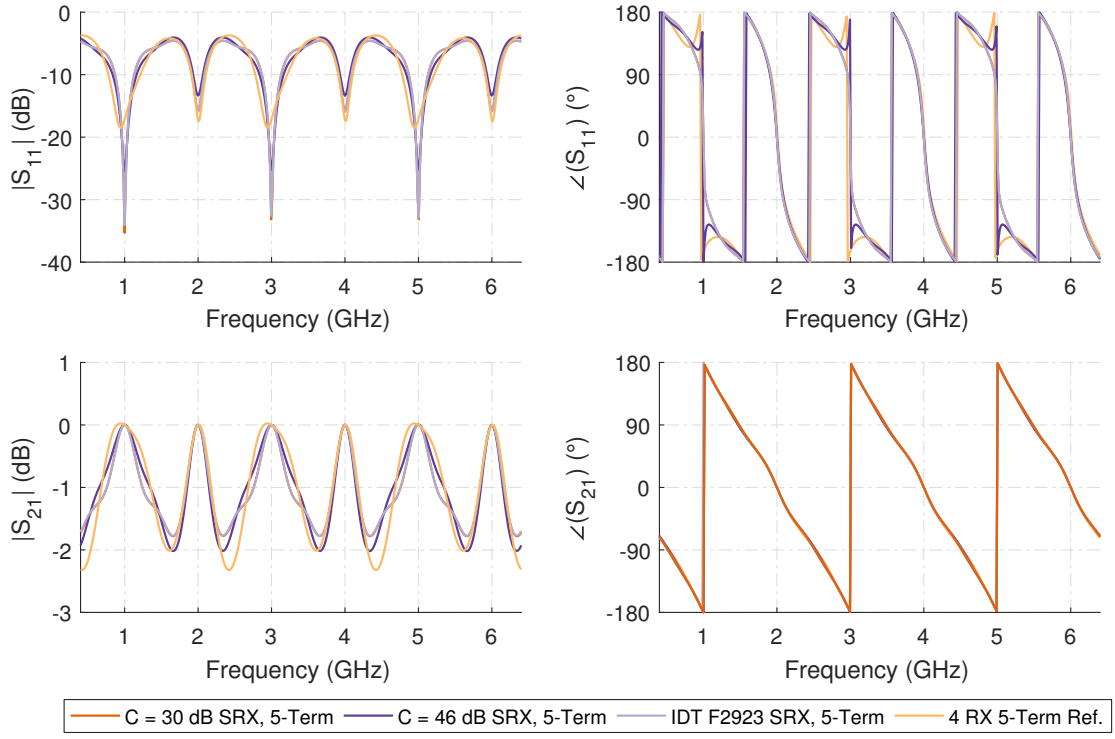

Figure A.1: Numerical 5-term error corrected results of a thru connection using a 150 mm loss-less 25 Ω transmission (or Beatty) line for the single switched receiver (SRX) test-set architecture.

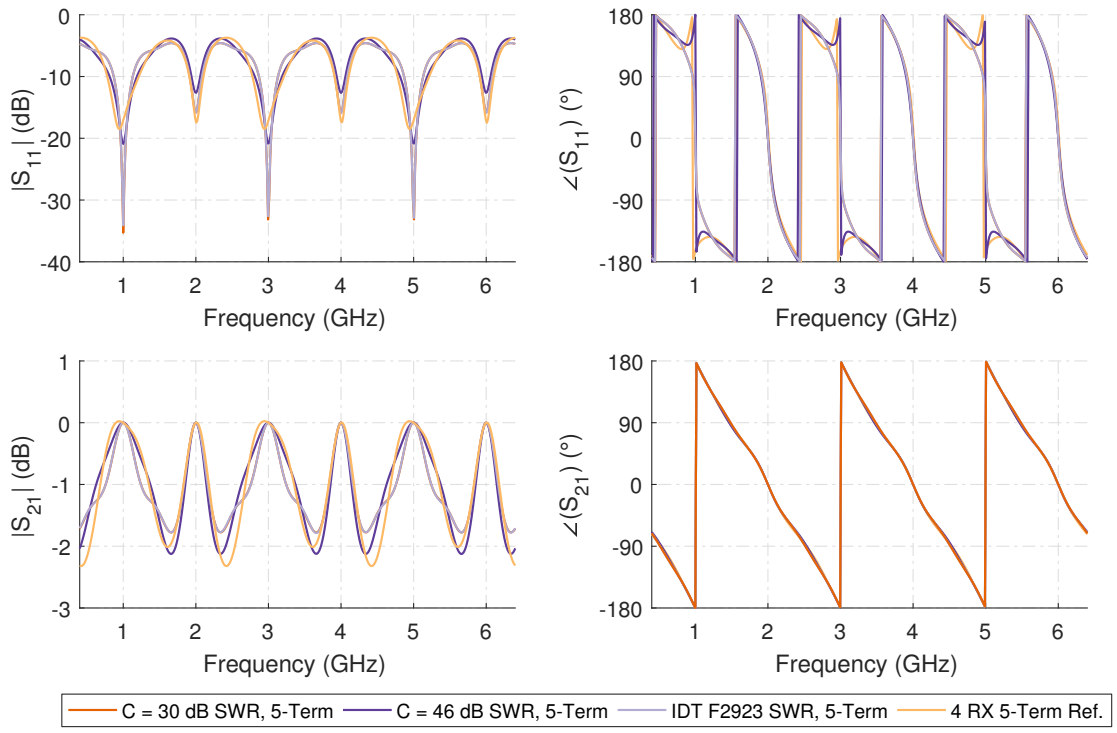

Figure A.2: Numerical 5-term error corrected results of a thru connection using a 150 mm loss-less 25 Ω transmission (or Beatty) line for the single switched receiver with reference wave switch (SWR) test-set architecture.

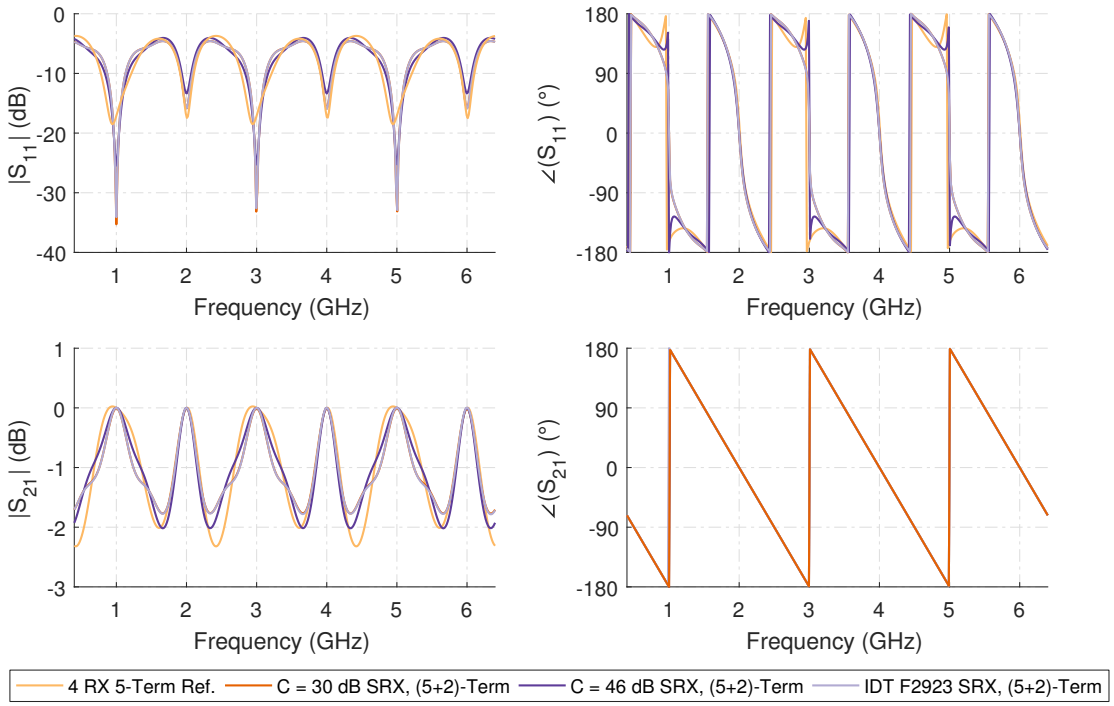

Figure A.3: Numerical (5+2)-term error corrected results of a thru connection using a 150 mm loss-less 25 Ω transmission (or Beatty) line for the single switched receiver (SRX) test-set architecture.

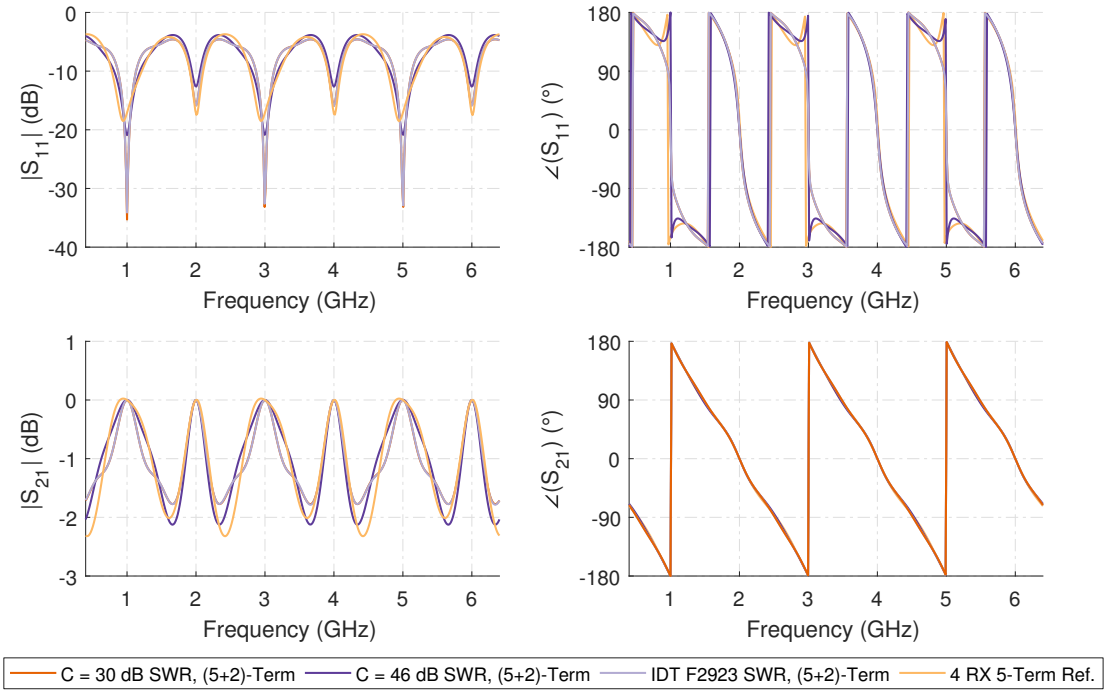

Figure A.4: Numerical (5+2)-term error corrected results of a thru connection using a 150 mm loss-less 25 Ω transmission (or Beatty) line for the single switched receiver with reference wave switch (SWR) test-set architecture.

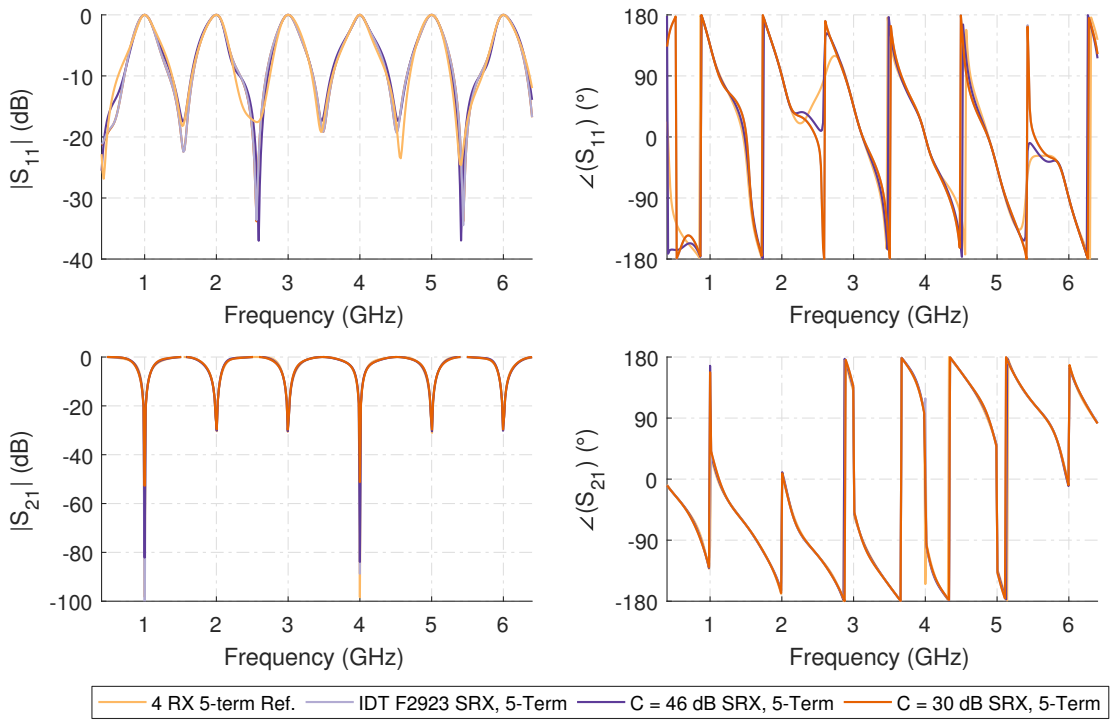

Figure A.5: Numerical 5-Term error corrected measurement results of the 150 mm symmetric reflective tee measurement for the single switched receiver (SRX) test-set architecture.

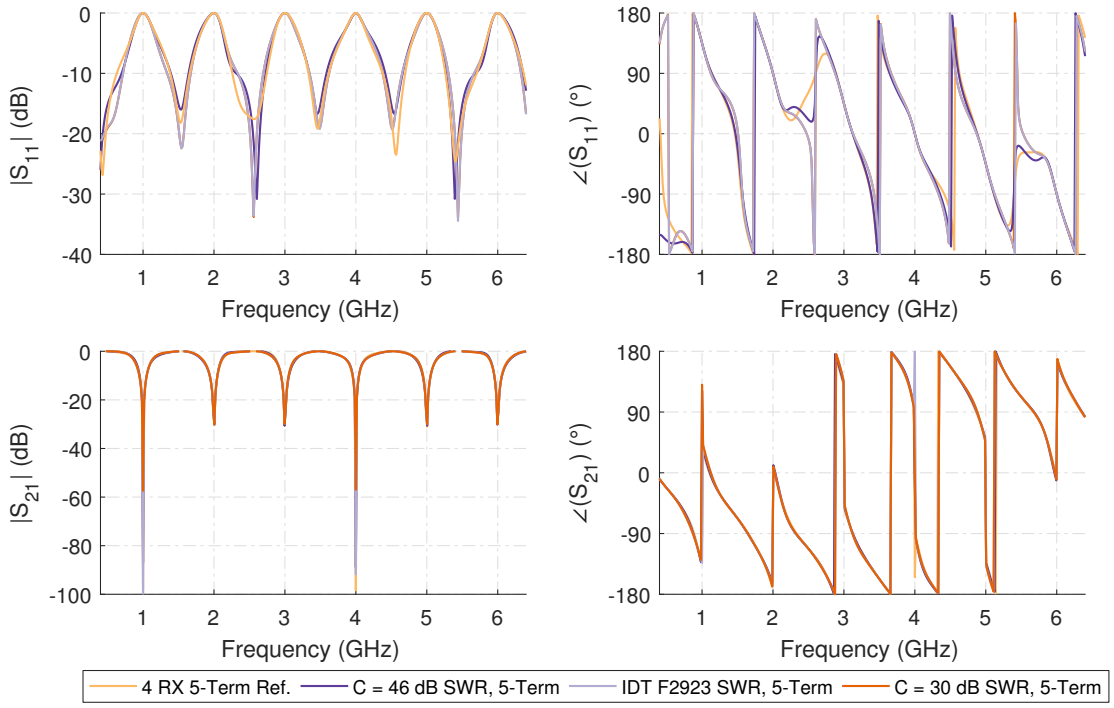

Figure A.6: Numerical 5-Term error corrected measurement results of the 150 mm symmetric reflective tee measurement for the single switched receiver with reference wave switch (SWR) test-set architecture.

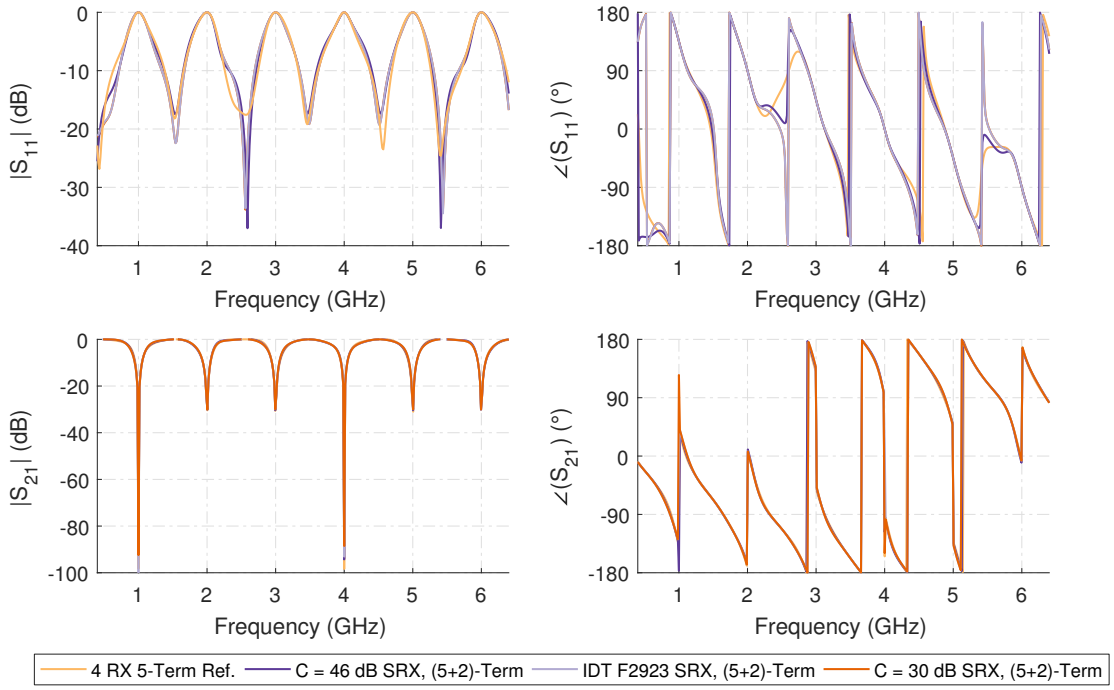

Figure A.7: Numerical (5+2)-Term error corrected measurement results of the 150 mm symmetric reflective tee measurement for the single switched receiver (SRX) test-set architecture.

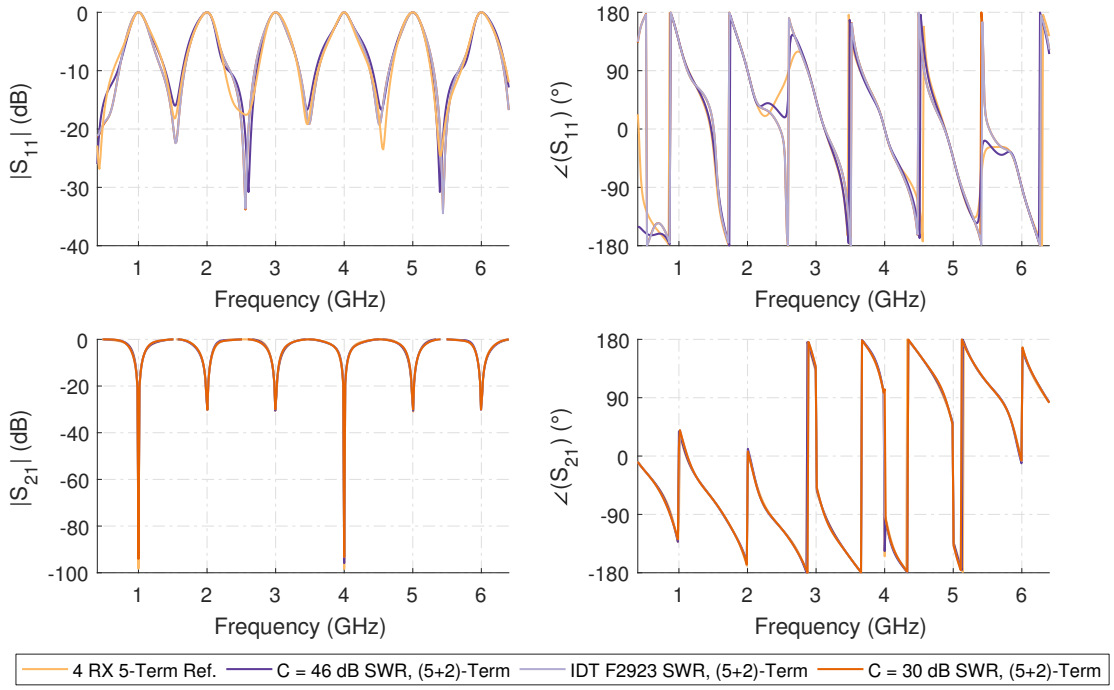

Figure A.8: Numerical 5-Term error corrected measurement results of the 150 mm symmetric reflective tee measurement for the single switched receiver with reference wave switch (SWR) test-set architecture.

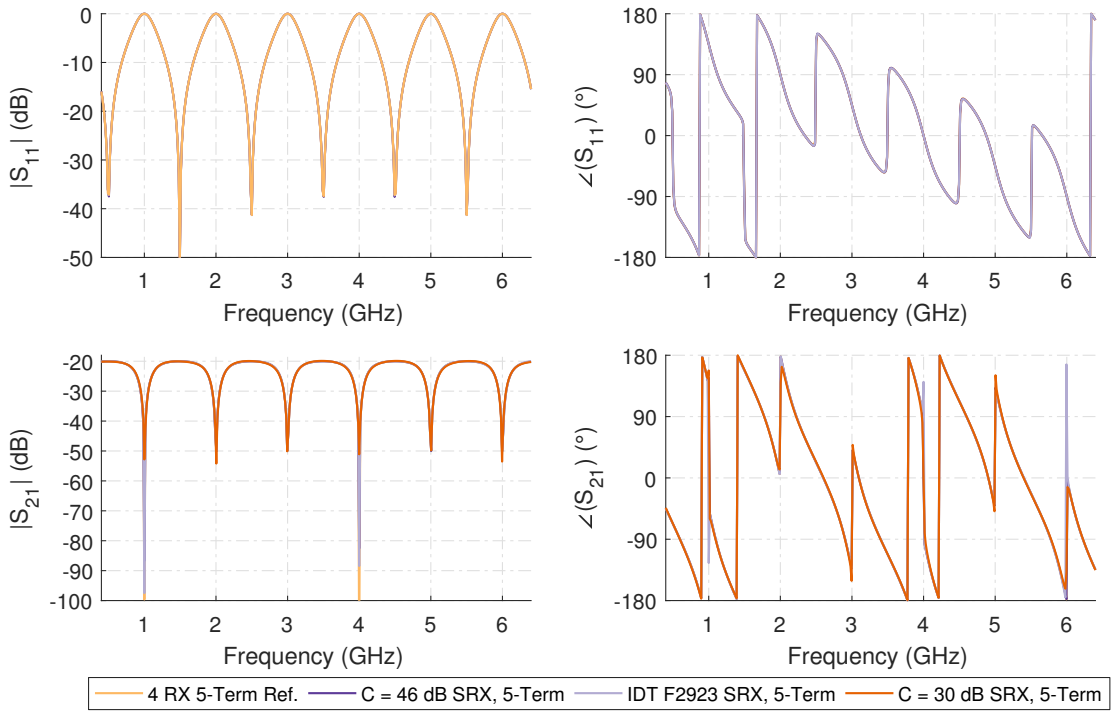

Figure A.9: Numerical 5-Term error corrected measurement results of the 150 mm asymmetric reflective lossy tee measurement using a 20 dB attenuator for the single switched receiver (SRX) test-set architecture.

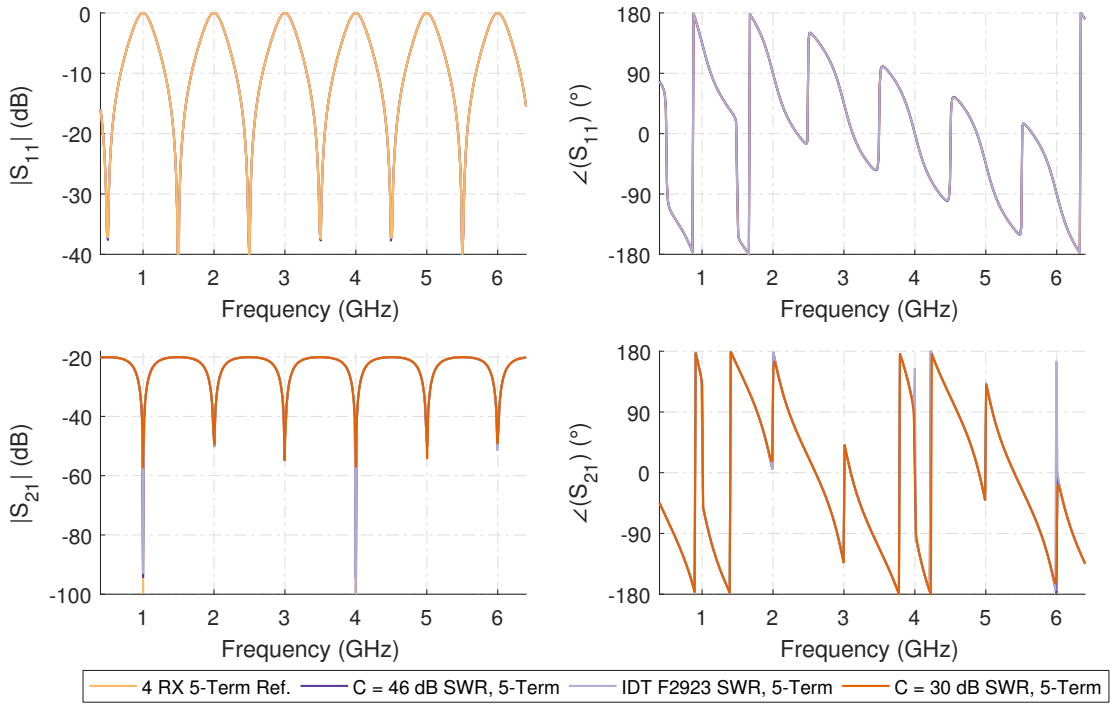

Figure A.10: Numerical 5-Term error corrected measurement results of the 150 mm asymmetric reflective lossy tee measurement using a 20 dB attenuator for the single switched receiver with reference wave switch (SWR) test-set architecture.

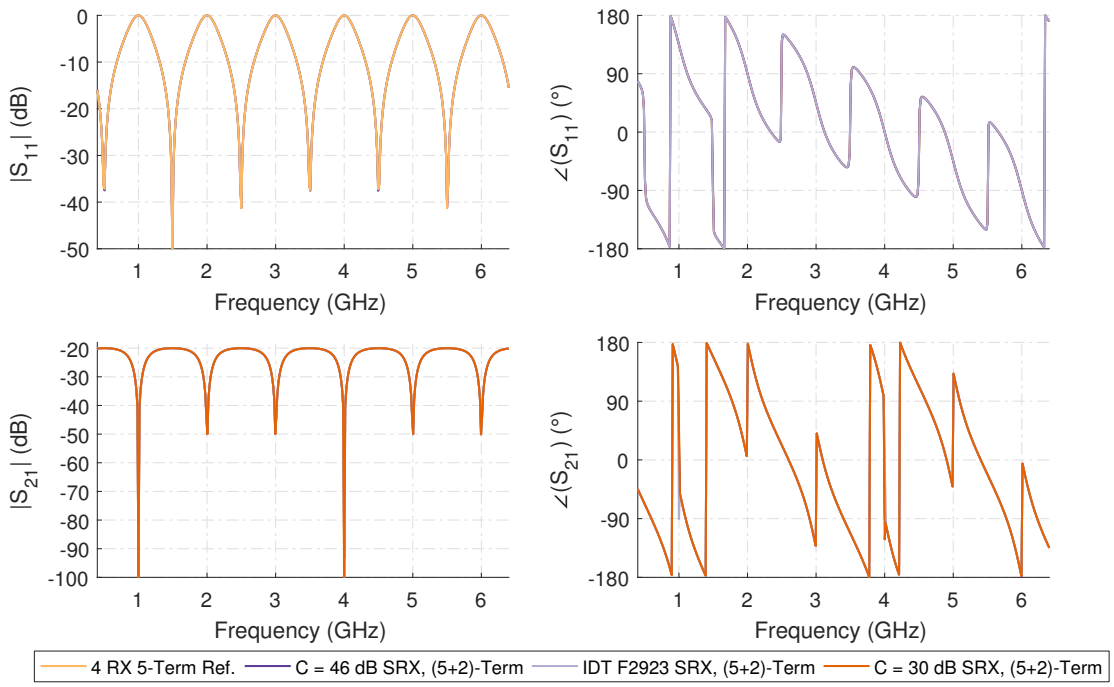

Figure A.11: Numerical (5+2)-Term error measurement corrected results of the 150 mm asymmetric reflective lossy tee measurement using a 20 dB attenuator for the single switched receiver (SRX) test-set architecture.

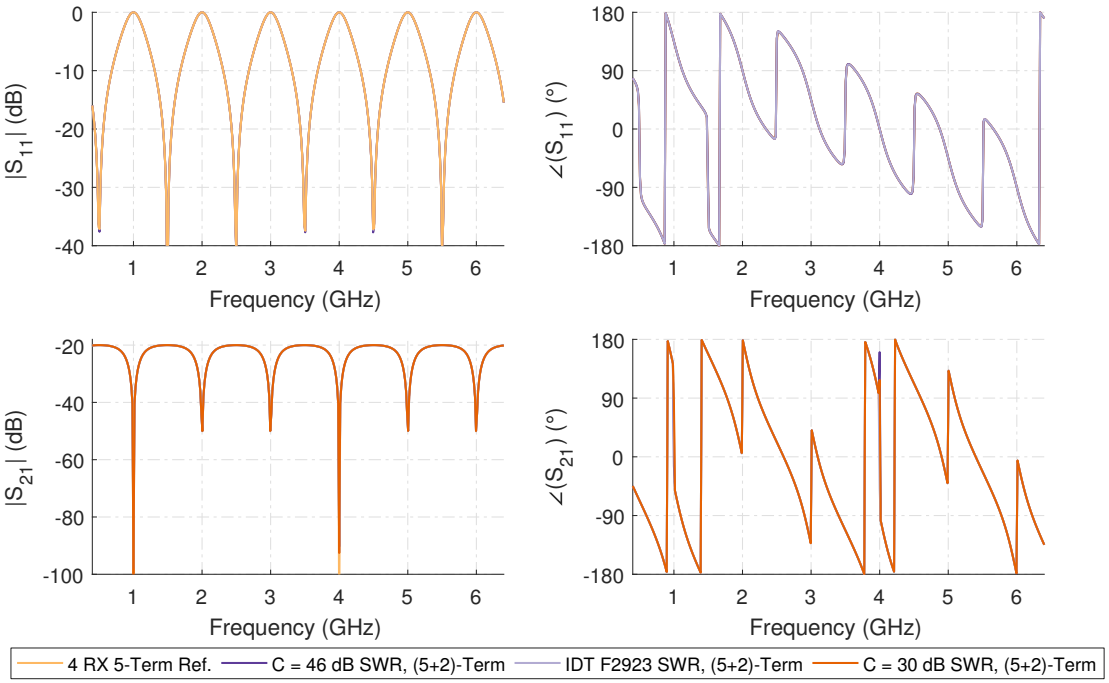

Figure A.12: Numerical (5+2)-Term error measurement corrected results of the 150 mm asymmetric reflective lossy tee measurement using a 20 dB attenuator for the single switched receiver with reference wave switch (SWR) test-set architecture.

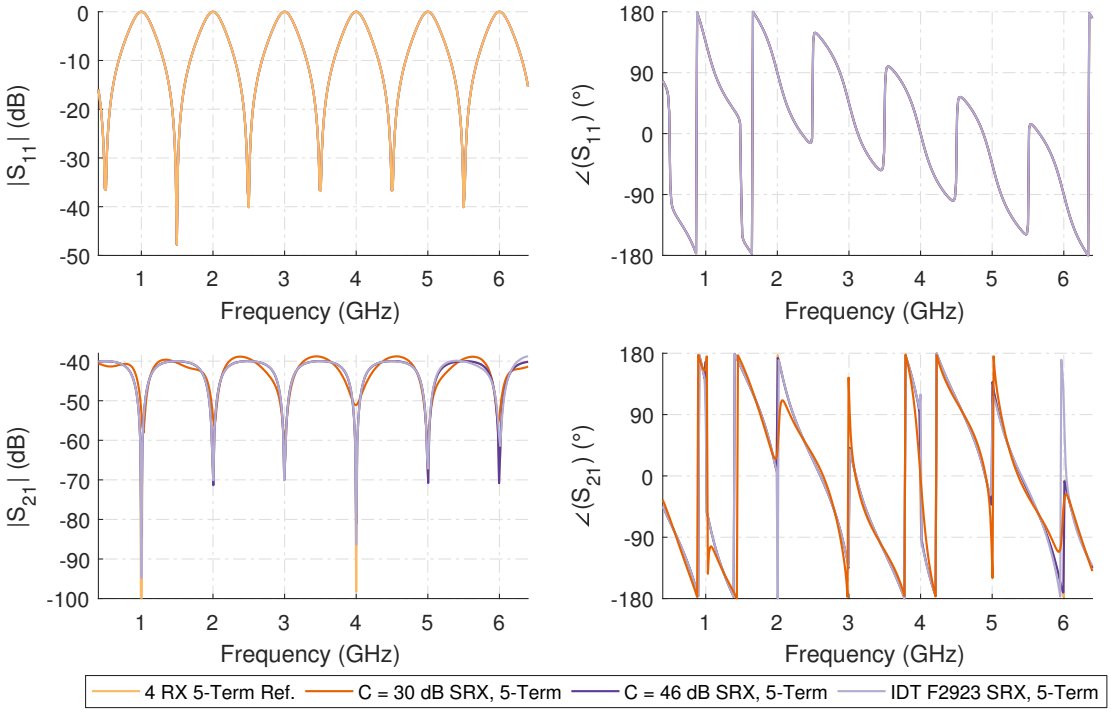

Figure A.13: Numerical 5-Term error corrected measurement results of the 150 mm asymmetric reflective lossy tee measurement using a 40 dB attenuator for the single switched receiver (SRX) test-set architecture.

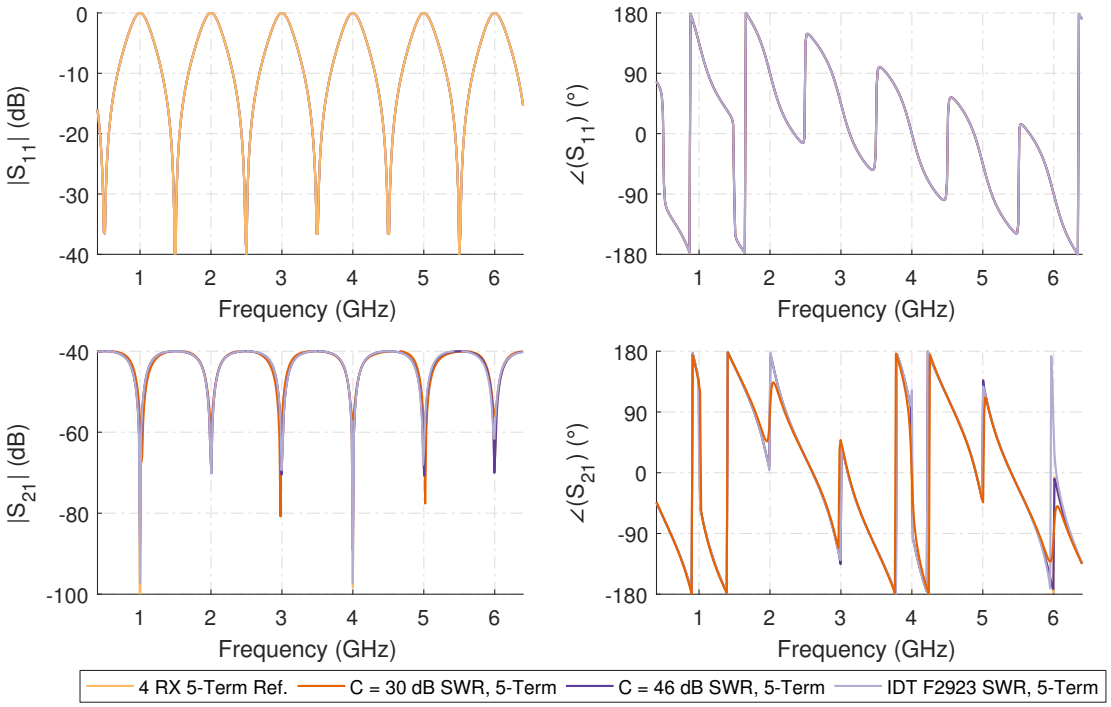

Figure A.14: Numerical 5-Term error corrected measurement results of the 150 mm asymmetric reflective lossy tee measurement using a 40 dB attenuator for the single switched receiver with reference wave switch (SWR) test-set architecture.

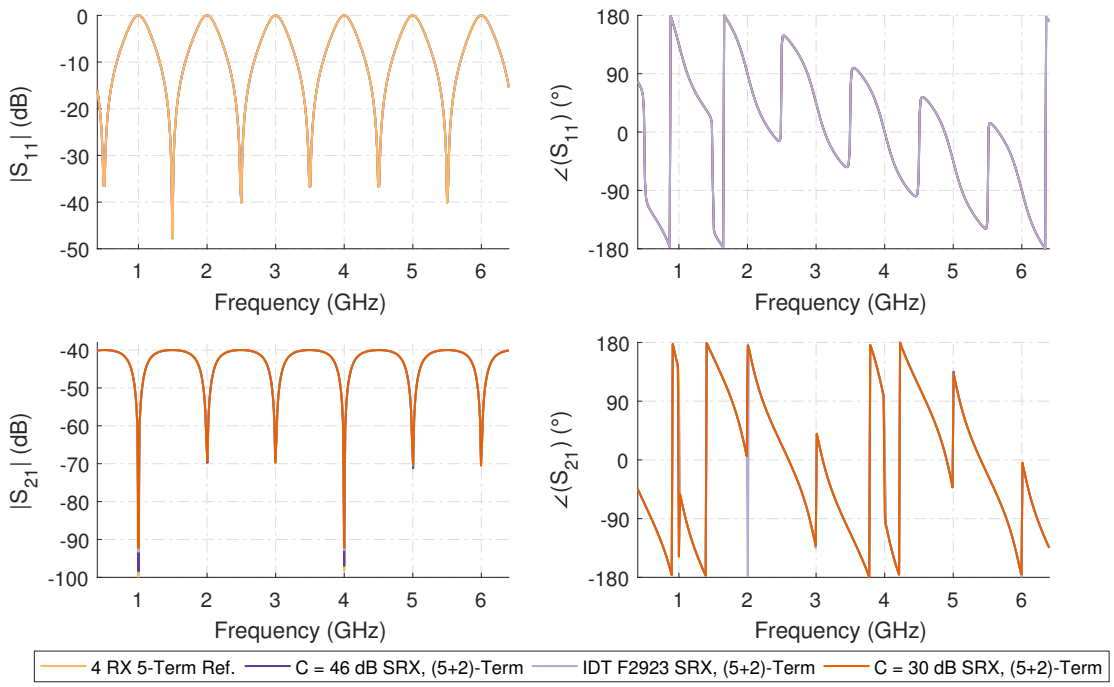

Figure A.15: Numerical (5+2)-Term error corrected measurement results of the 150 mm asymmetric reflective lossy tee measurement using a 40 dB attenuator for the single switched receiver (SRX) test-set architecture.

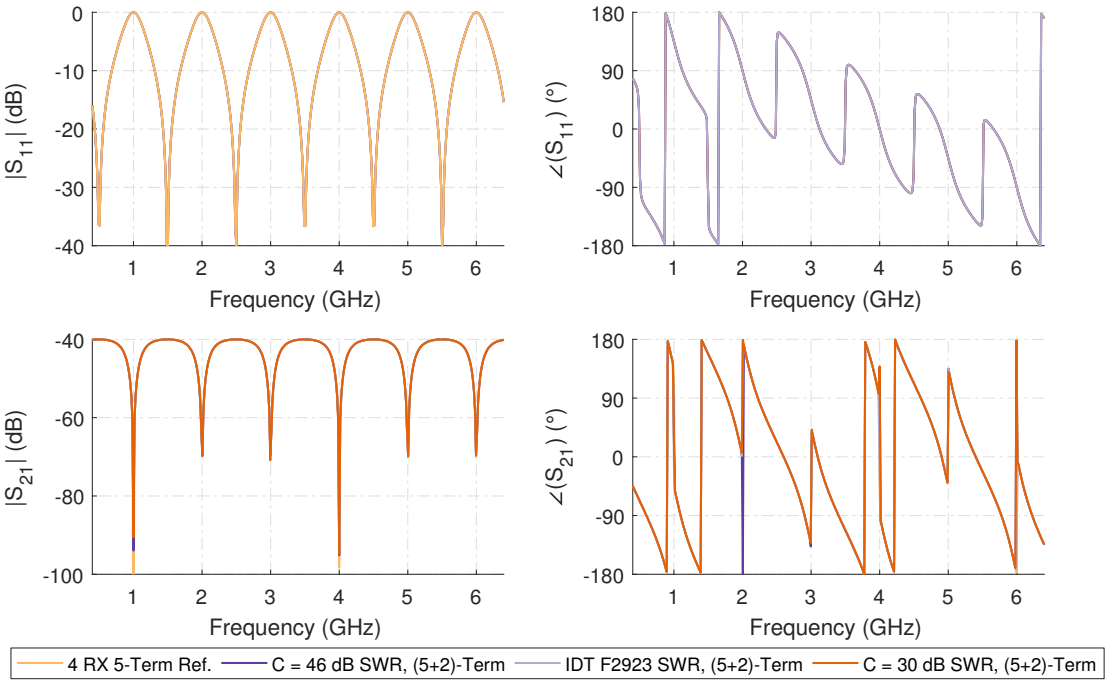

Figure A.16: Numerical 5-Term error corrected measurement results of the 150 mm asymmetric reflective lossy tee measurement using a 40 dB attenuator for the single switched receiver with reference wave switch (SWR) test-set architecture.

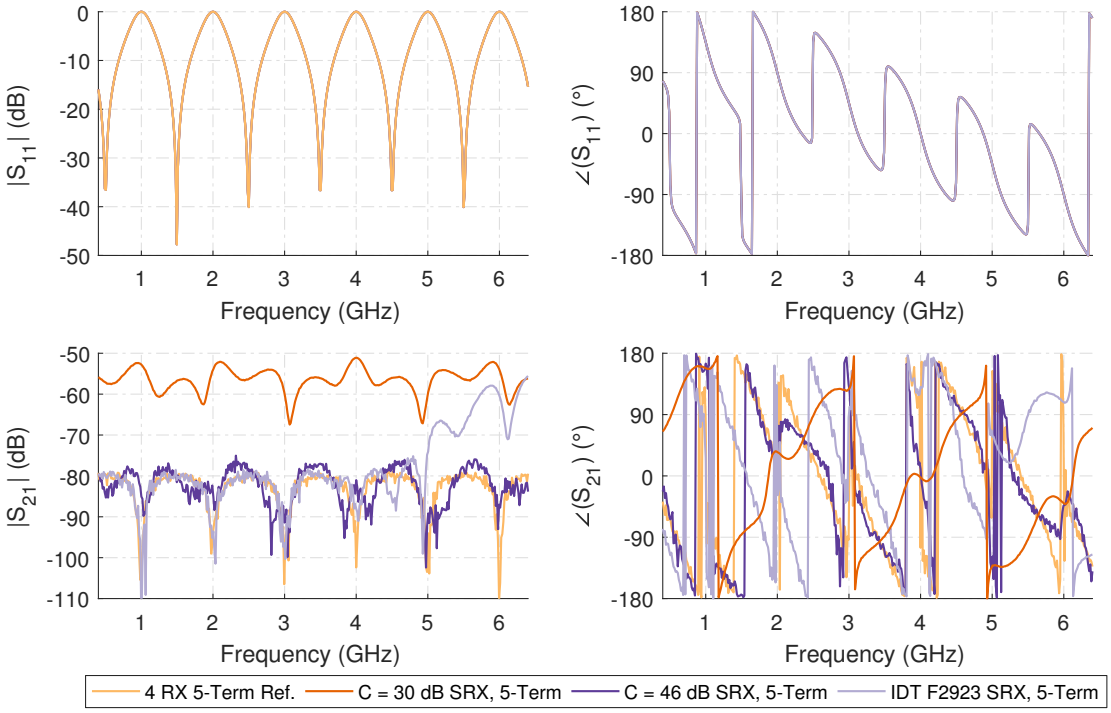

Figure A.17: Numerical 5-Term error corrected measurement results of the 150 mm asymmetric reflective lossy tee measurement using a 80 dB attenuator for the single switched receiver (SRX) test-set architecture.

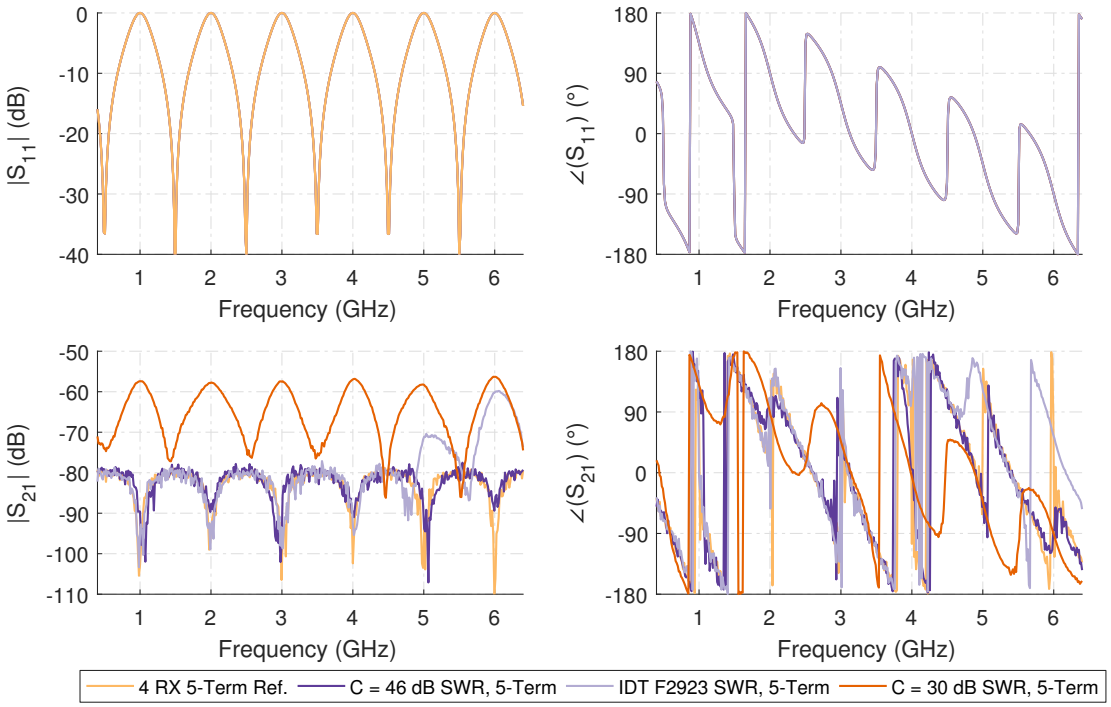

Figure A.18: Numerical 5-Term error corrected measurement results of the 150 mm asymmetric reflective lossy tee measurement using a 80 dB attenuator for the single switched receiver with reference wave switch (SWR) test-set architecture.

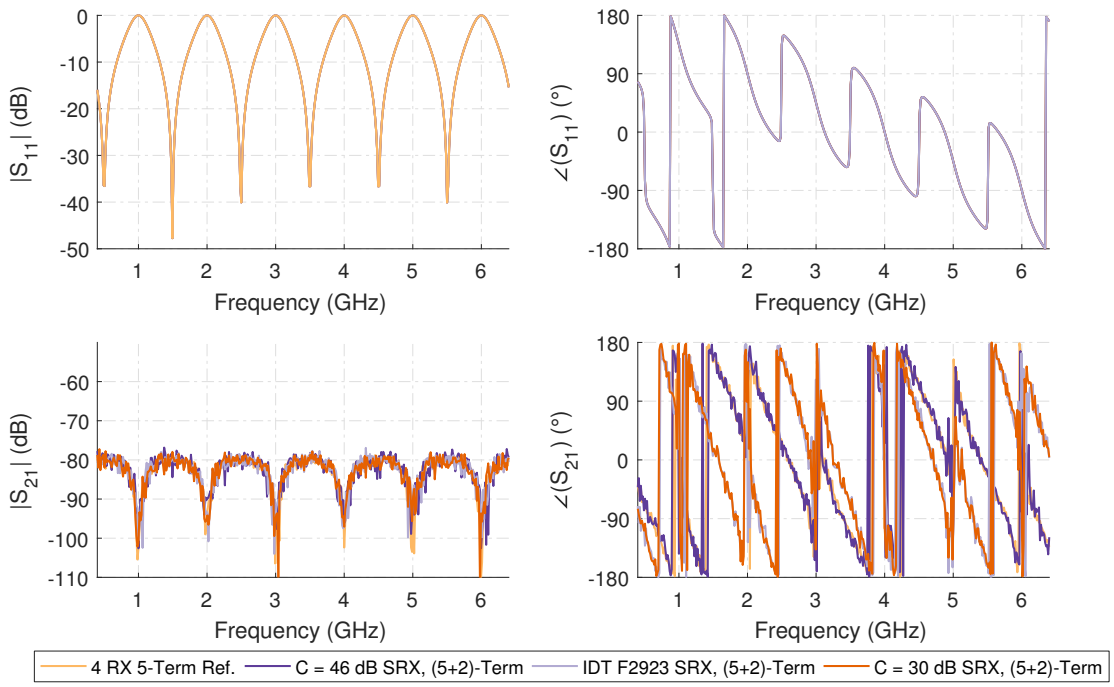

Figure A.19: Numerical (5+2)-Term error corrected measurement results of the 150 mm asymmetric reflective lossy tee measurement using a 80 dB attenuator for the single switched receiver (SRX) test-set architecture.

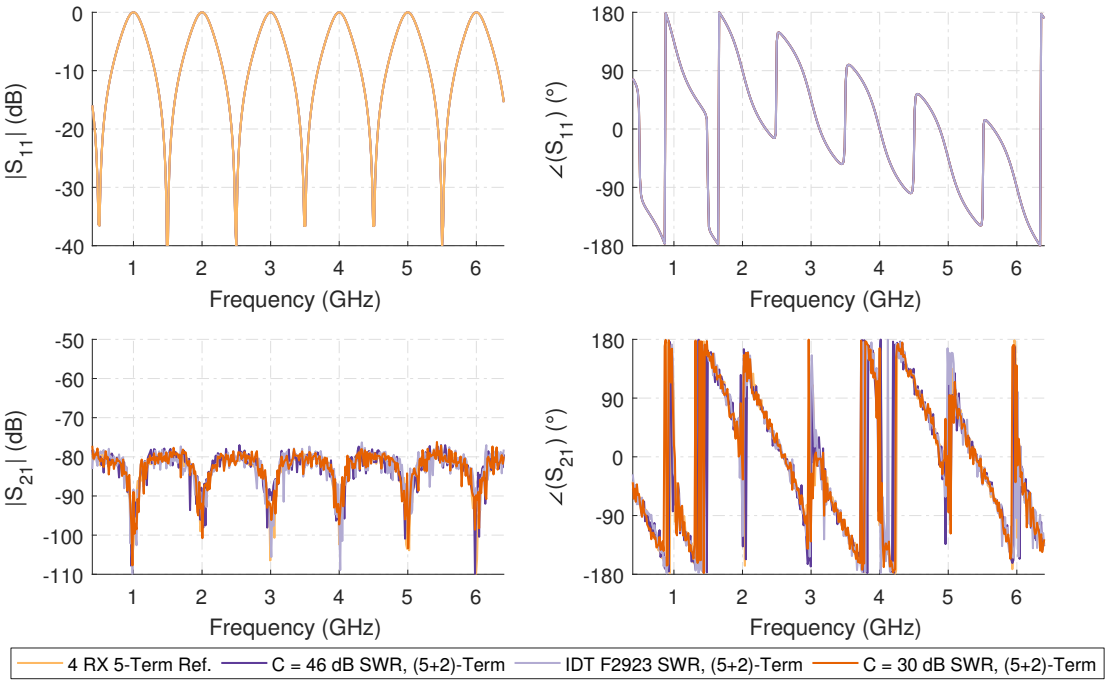

Figure A.20: Numerical (5+2)-Term error corrected measurement results of the 150 mm asymmetric reflective lossy tee measurement using a 80 dB attenuator for the single switched receiver with reference wave switch (SWR) test-set architecture.

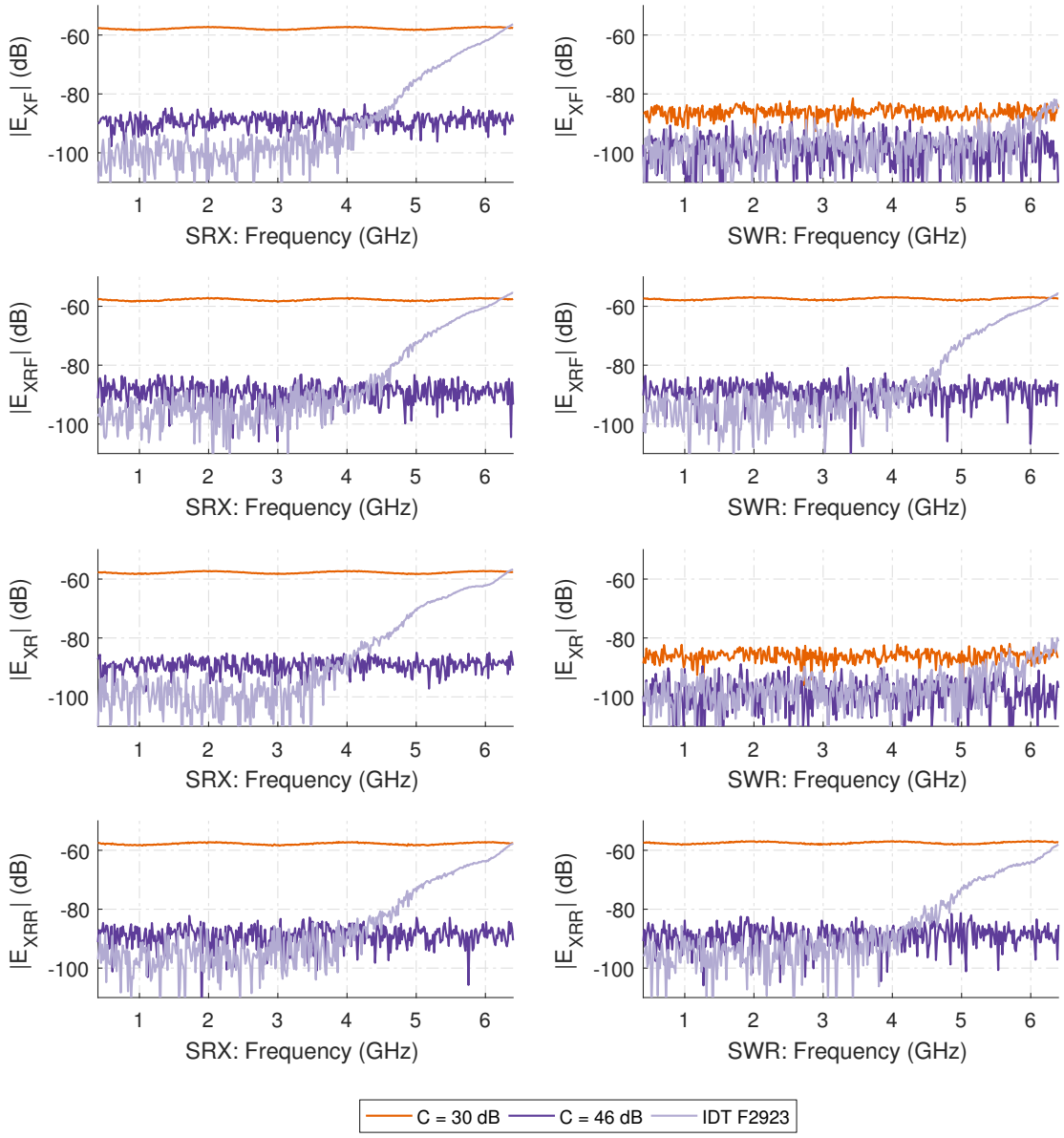

Figure A.21: Numerical results for magnitude of the forward (E_{XF}, E_{XRF}) and reverse (E_{XR}, E_{XRR}) receiver input wave selector switch crosstalk coefficients obtained by the (10+4)-term calibration for the switched single receiver (SRX) and switched single receiver with reference wave switch (SWR) architectures using the double reflectometer test-sets.

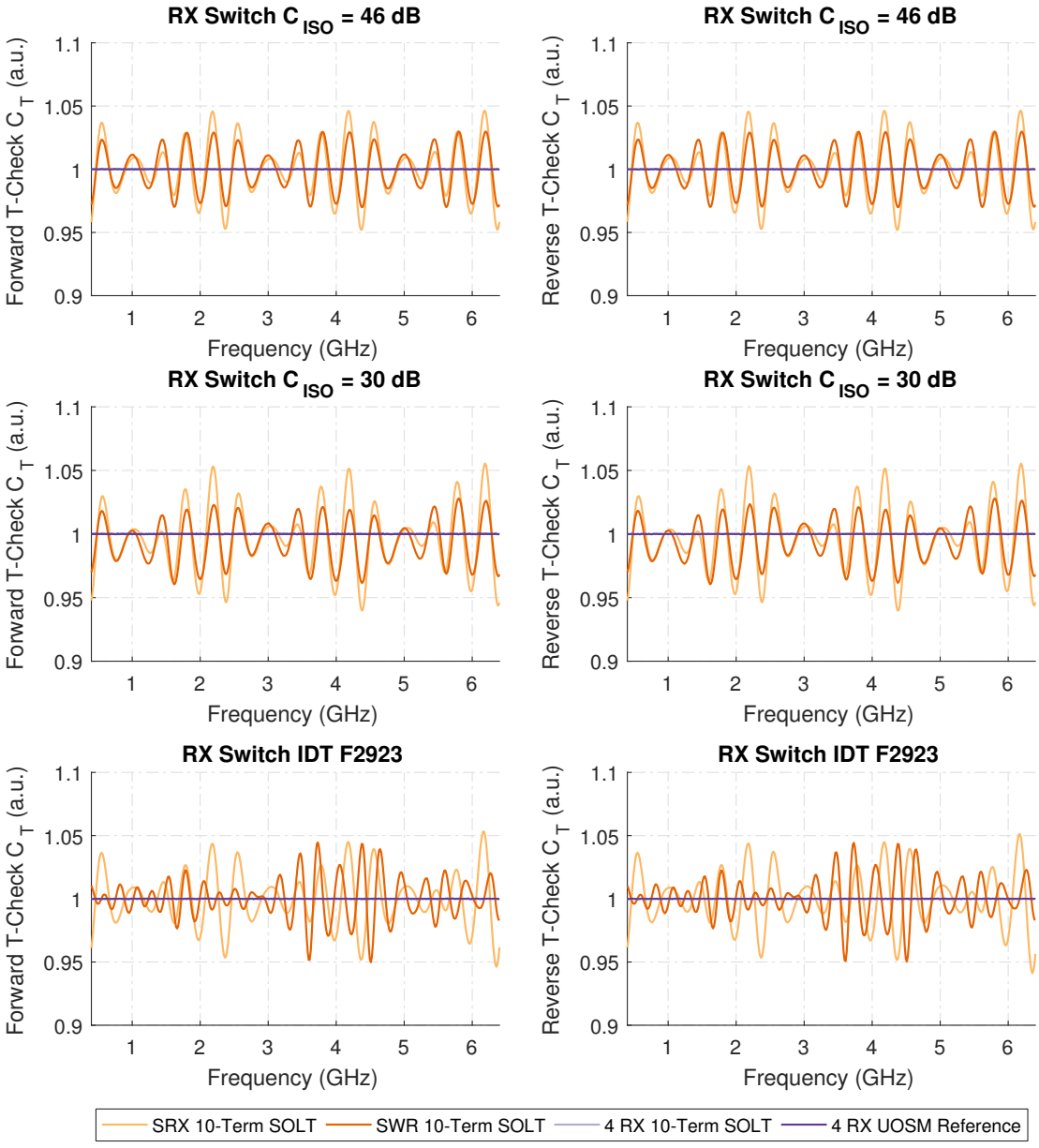

Figure A.22: Numerical results for the T-Check measurements using the 10-term correction model for all synthetic switches and for the switched single receiver (SRX) and switched single receiver with reference wave switch (SWR) architectures using the double reflectometer test-sets.

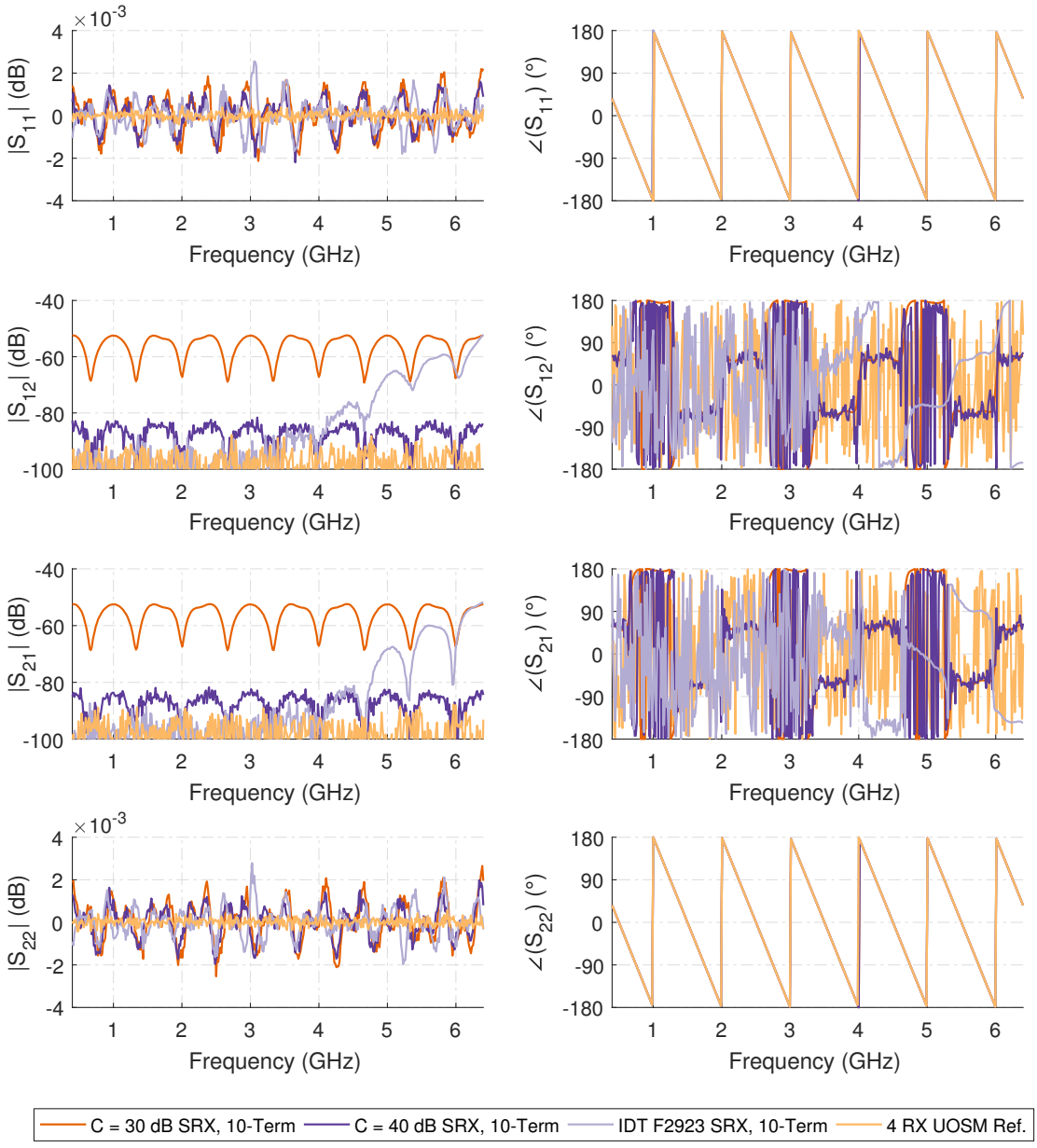

Figure A.23: Numerical results of the ripple test measurement using a 150 mm loss-less 50 Ω transmission line terminated by the calibration short using the 10-term correction model for all synthetic switches in the switched single receiver (SRX) architecture using the double reflectometer test-set.

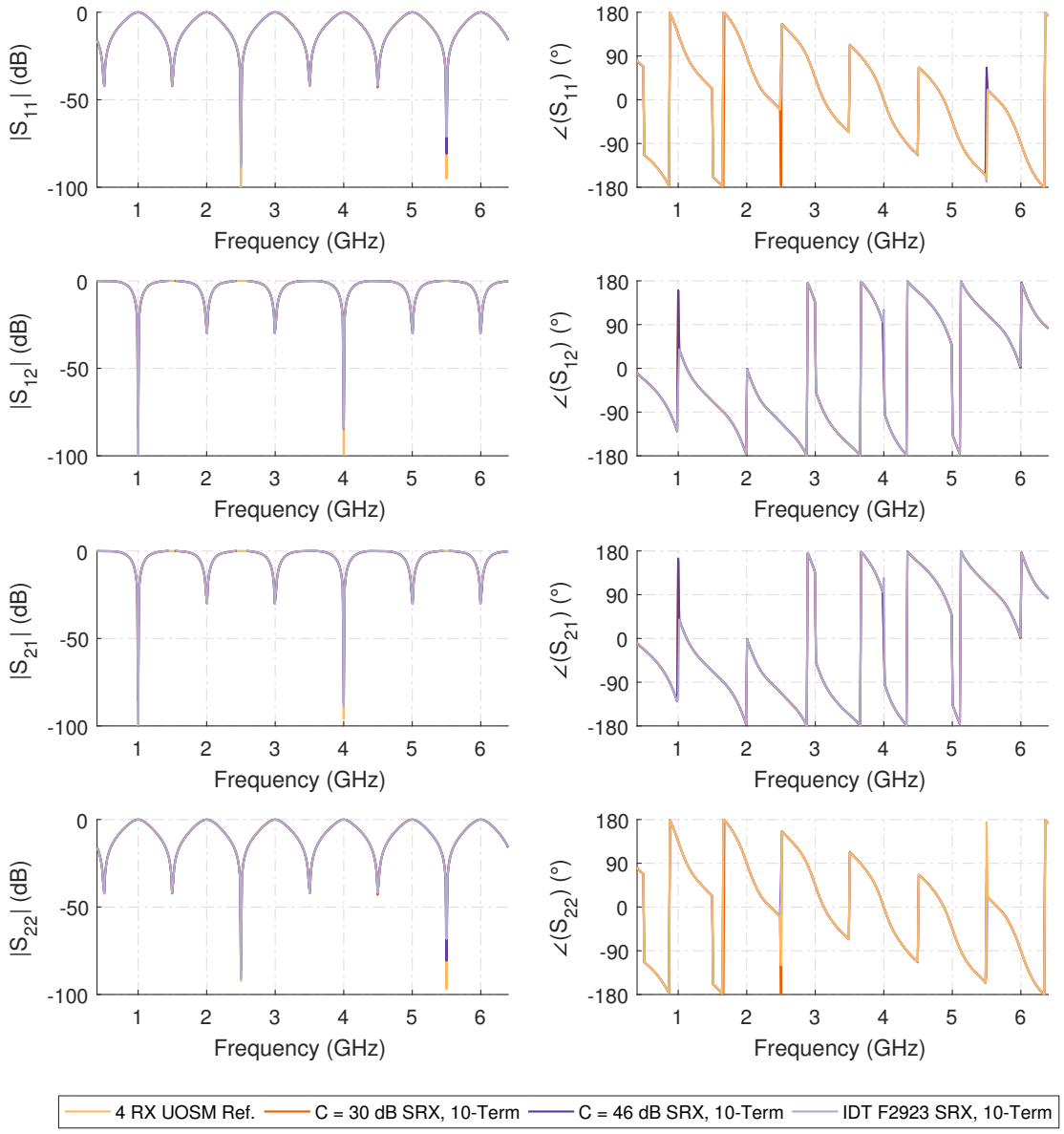

Figure A.24: Numerical 10-Term error corrected measurement results of the 150 mm asymmetric reflective lossy tee measurement using no attenuation for the single switched receiver (SRX) test-set architecture using the double reflectometer test-set.

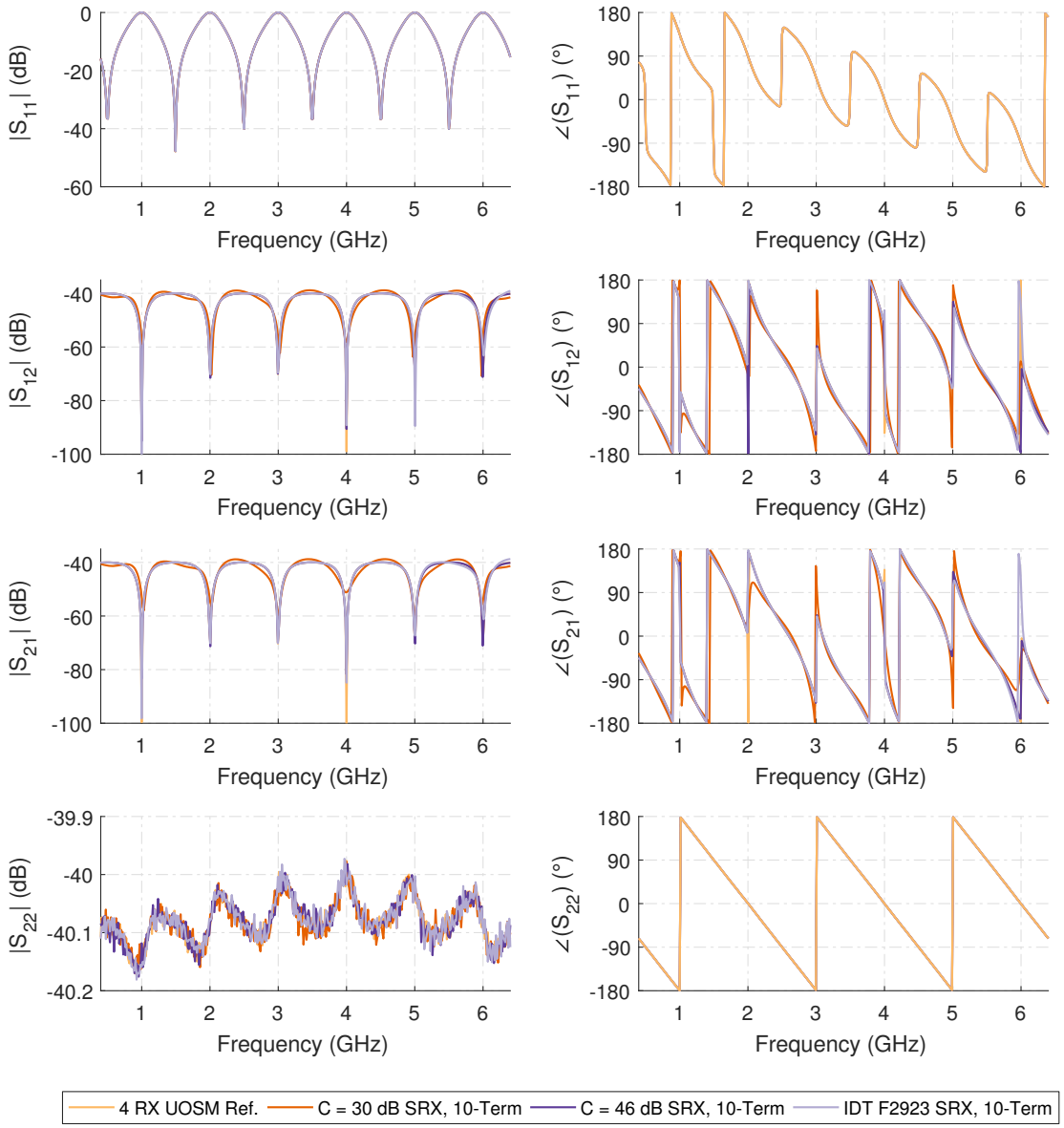

Figure A.25: Numerical 10-Term error corrected measurement results of the 150 mm asymmetric reflective lossy tee measurement using 40 dB of attenuation for the single switched receiver (SRX) test-set architecture using the double reflectometer test-set.

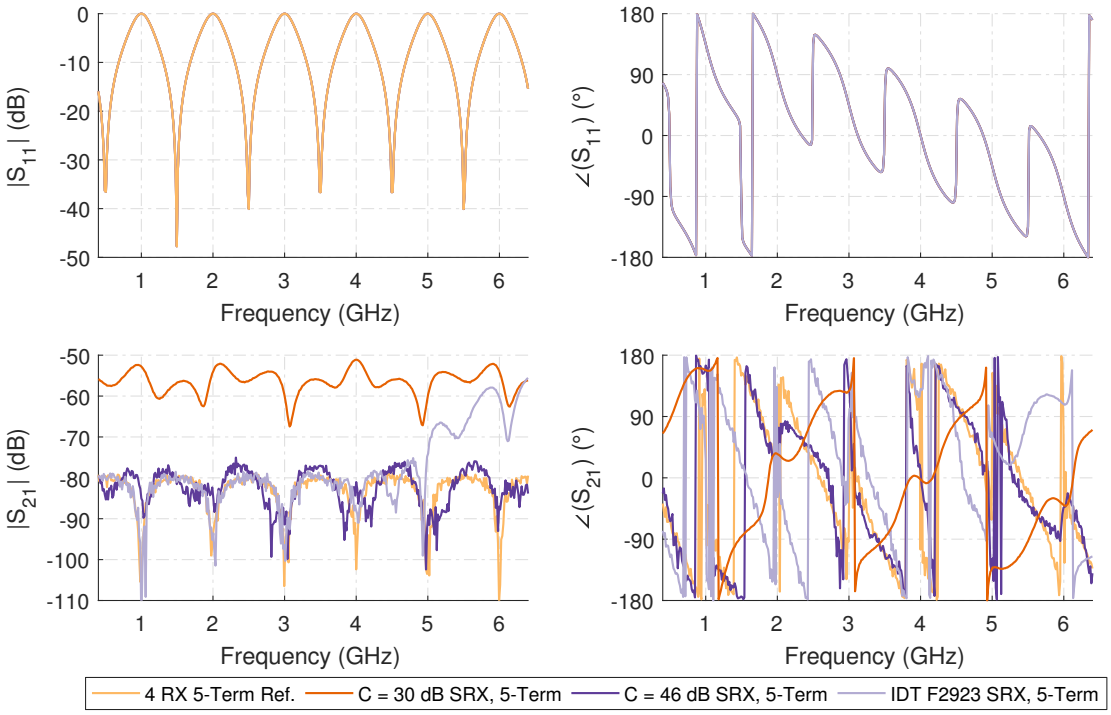

Figure A.26: Numerical 10-Term error corrected measurement results of the 150 mm asymmetric reflective lossy tee measurement using 80 dB of attenuation for the single switched receiver (SRX) test-set architecture using the double reflectometer test-set.

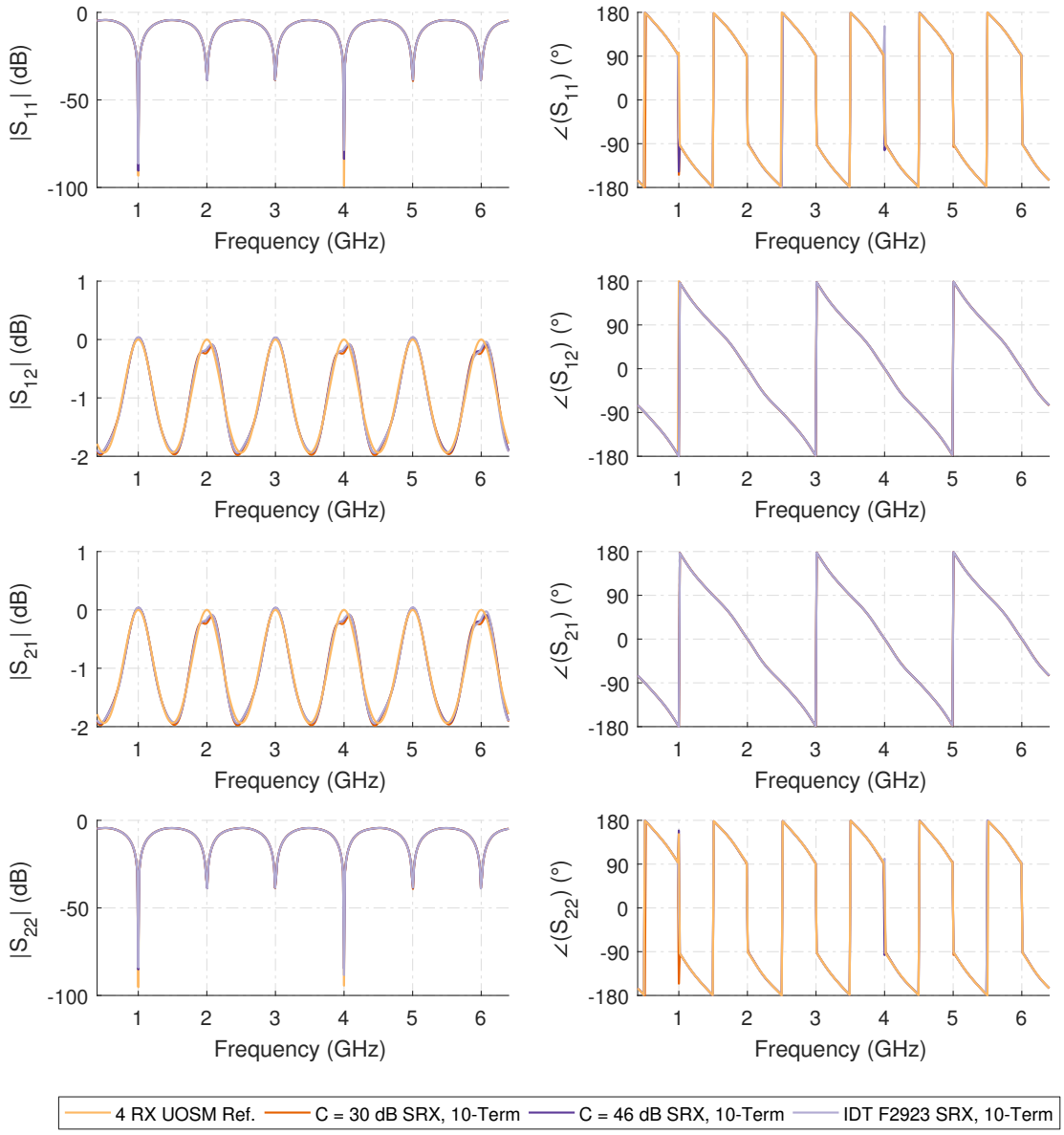

Figure A.27: Numerical 10-term error corrected results of a thru connection using a 150 mm loss-less 25 Ω transmission (or Beatty) line for the single switched receiver (SRX) test-set architecture using the double reflectometer test-set.

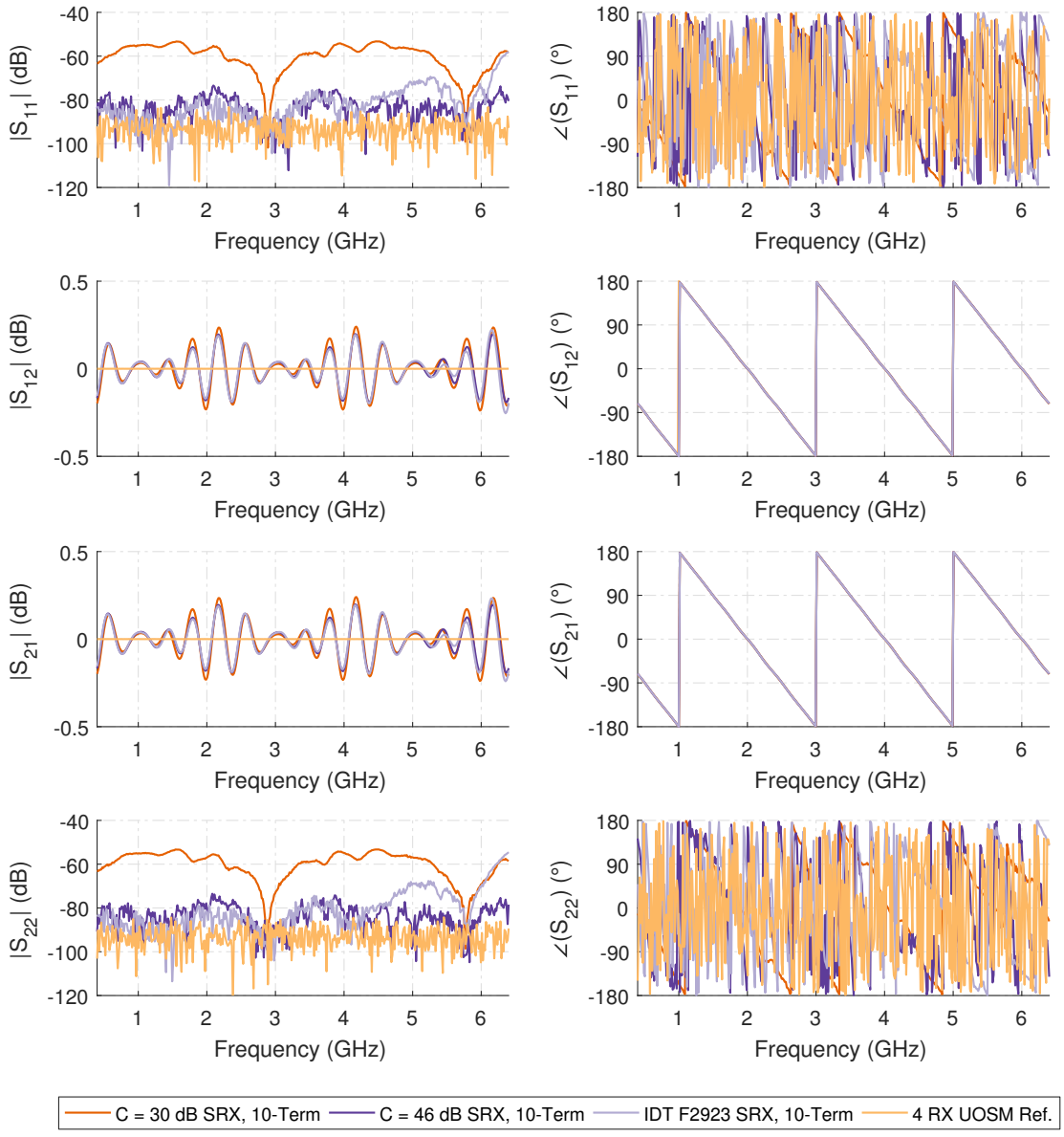

Figure A.28: Numerical 10-term error corrected results of a thru connection using a 150 mm loss-less 50 Ω transmission line for the single switched receiver (SRX) test-set architecture using the double reflectometer test-set.

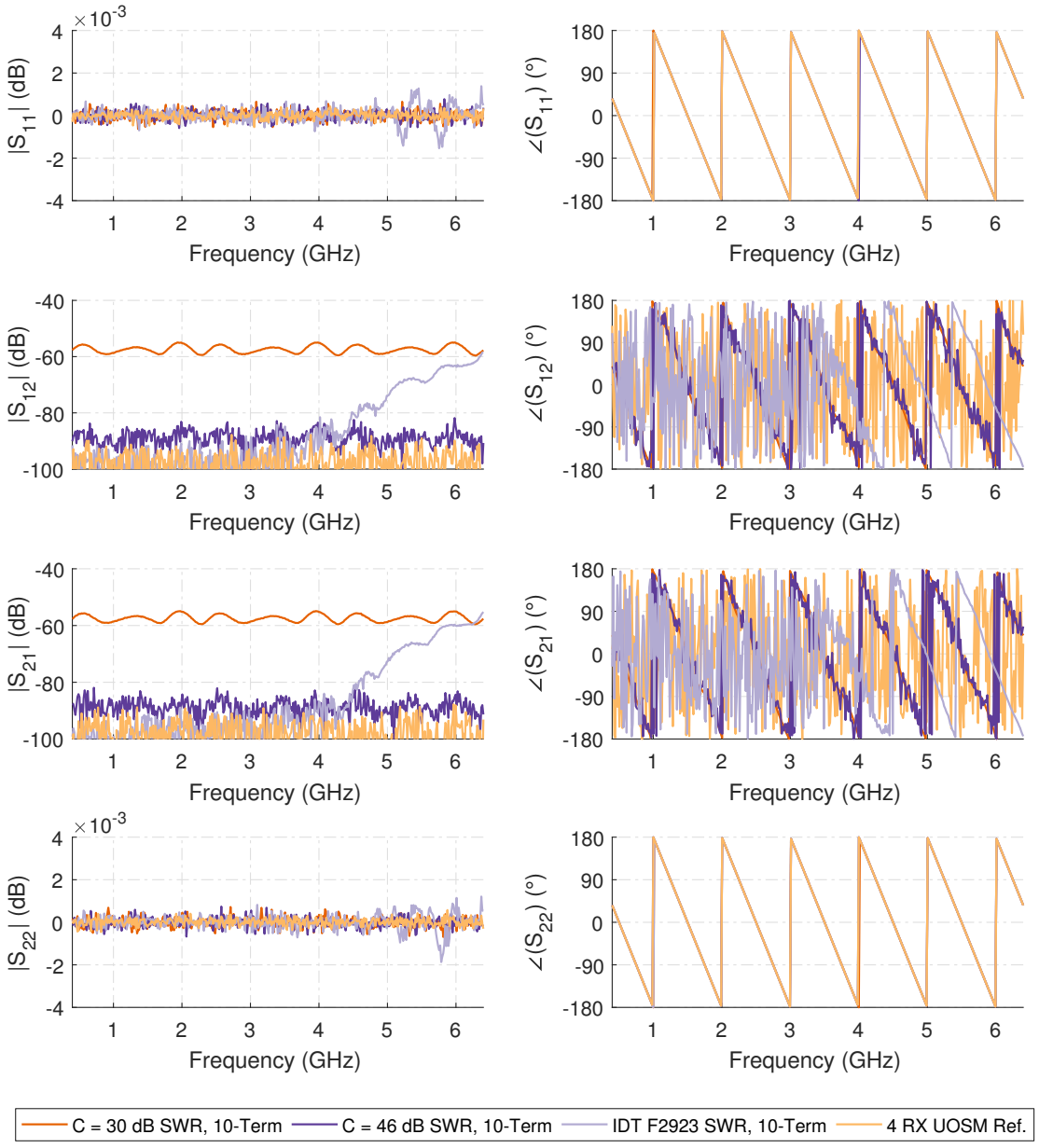

Figure A.29: Numerical results of the ripple test measurement using a 150 mm lossless 50 Ω transmission line terminated by the calibration short using the 10-term correction model for all synthetic switches in the switched single receiver with reference wave switch (SWR) architecture using the double reflectometer test-set.

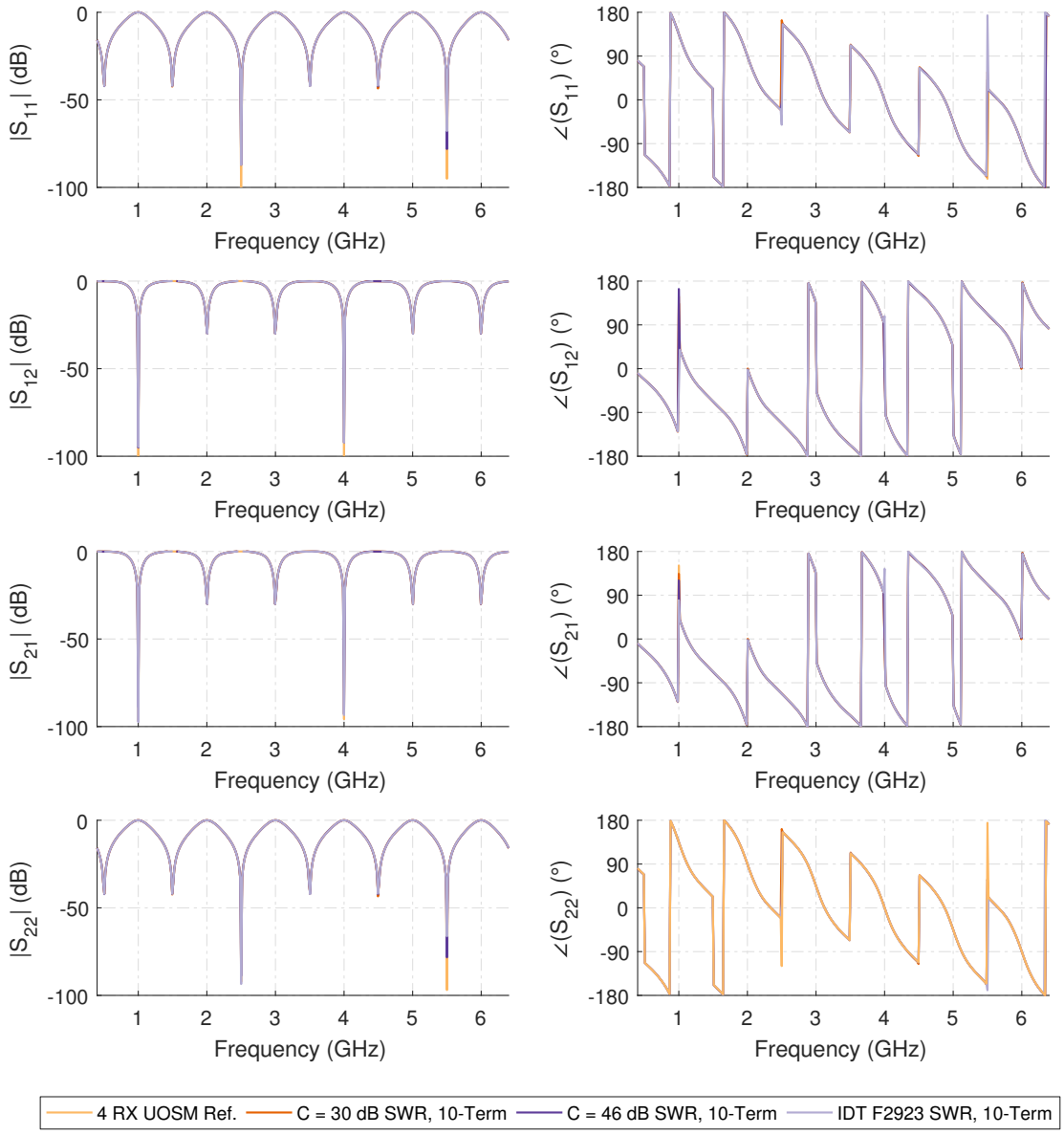

Figure A.30: Numerical 10-Term error corrected measurement results of the 150 mm asymmetric reflective lossy tee measurement using no attenuation for the switched single receiver with reference wave switch (SWR) test-set architecture using the double reflectometer test-set.

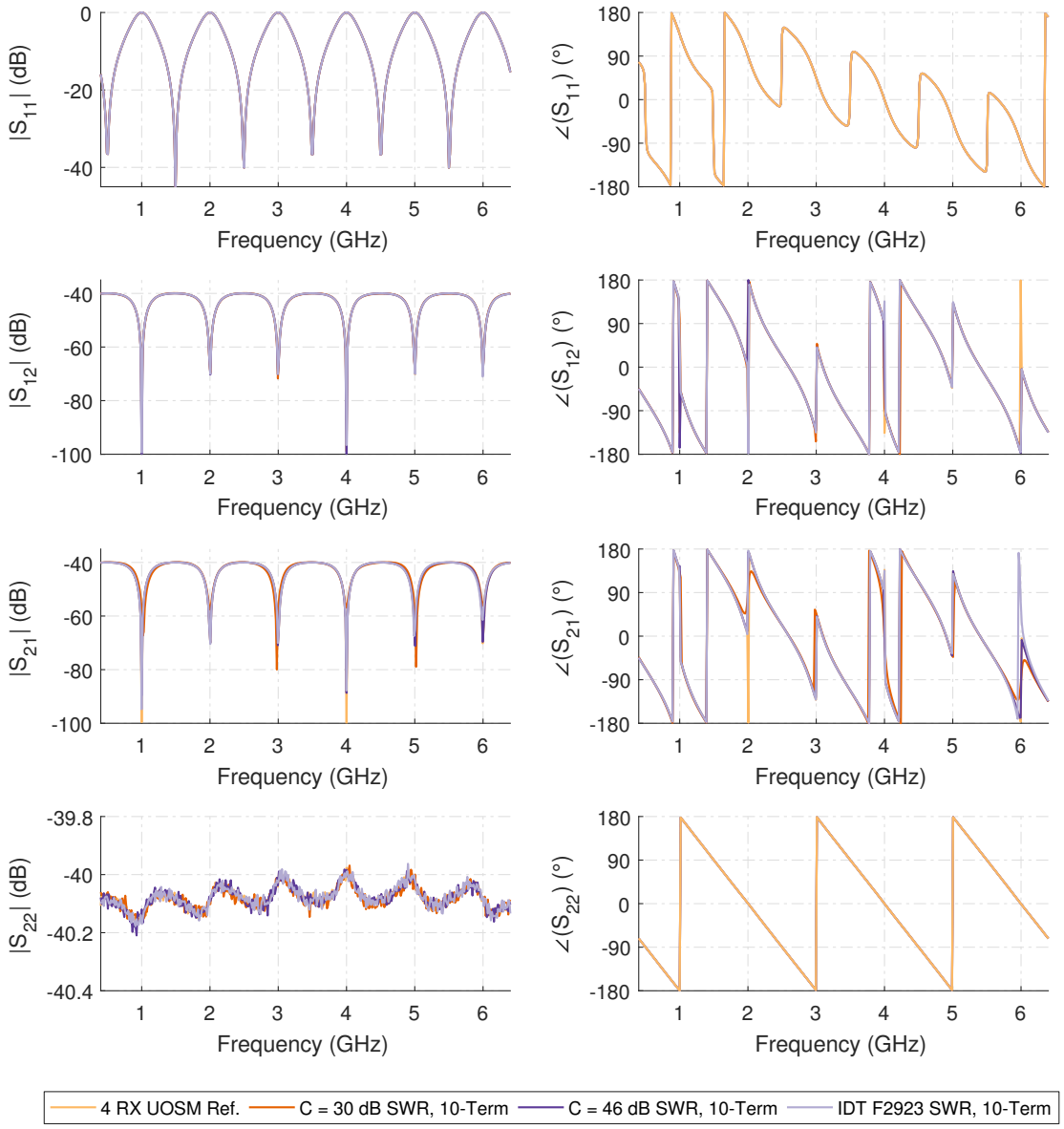

Figure A.31: Numerical 10-Term error corrected measurement results of the 150 mm asymmetric reflective lossy tee measurement using 40 dB of attenuation for the switched single receiver with reference wave switch (SWR) test-set architecture using the double reflectometer test-set.

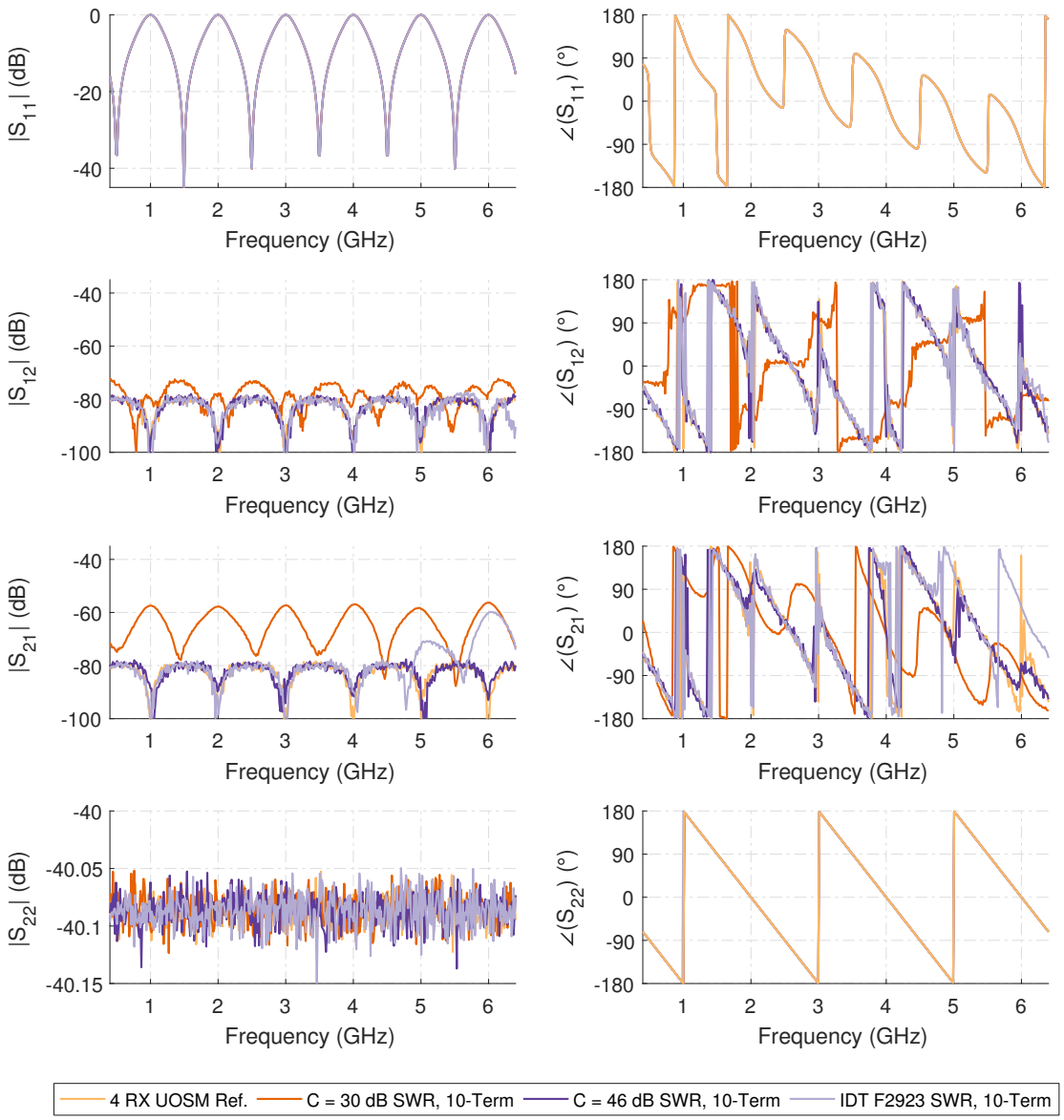

Figure A.32: Numerical 10-Term error corrected measurement results of the 150 mm asymmetric reflective lossy tee measurement using 80 dB of attenuation for the switched single receiver with reference wave switch (SWR) test-set architecture using the double reflectometer test-set.

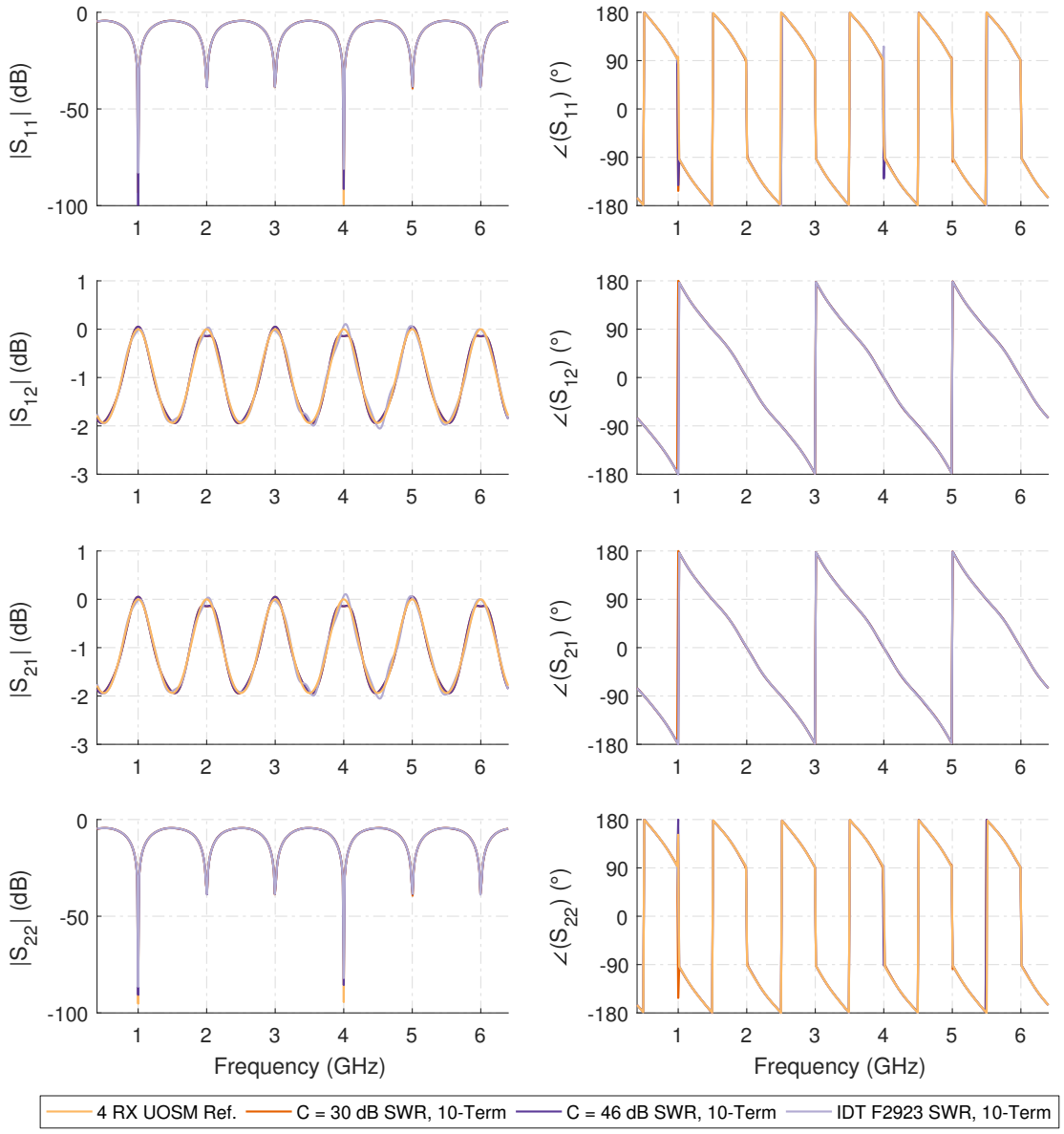

Figure A.33: Numerical 10-term error corrected results of a thru connection using a 150 mm loss-less 25 Ω transmission (or Beatty) line for the switched single receiver with reference wave switch (SWR) test-set architecture using the double reflectometer test-set.

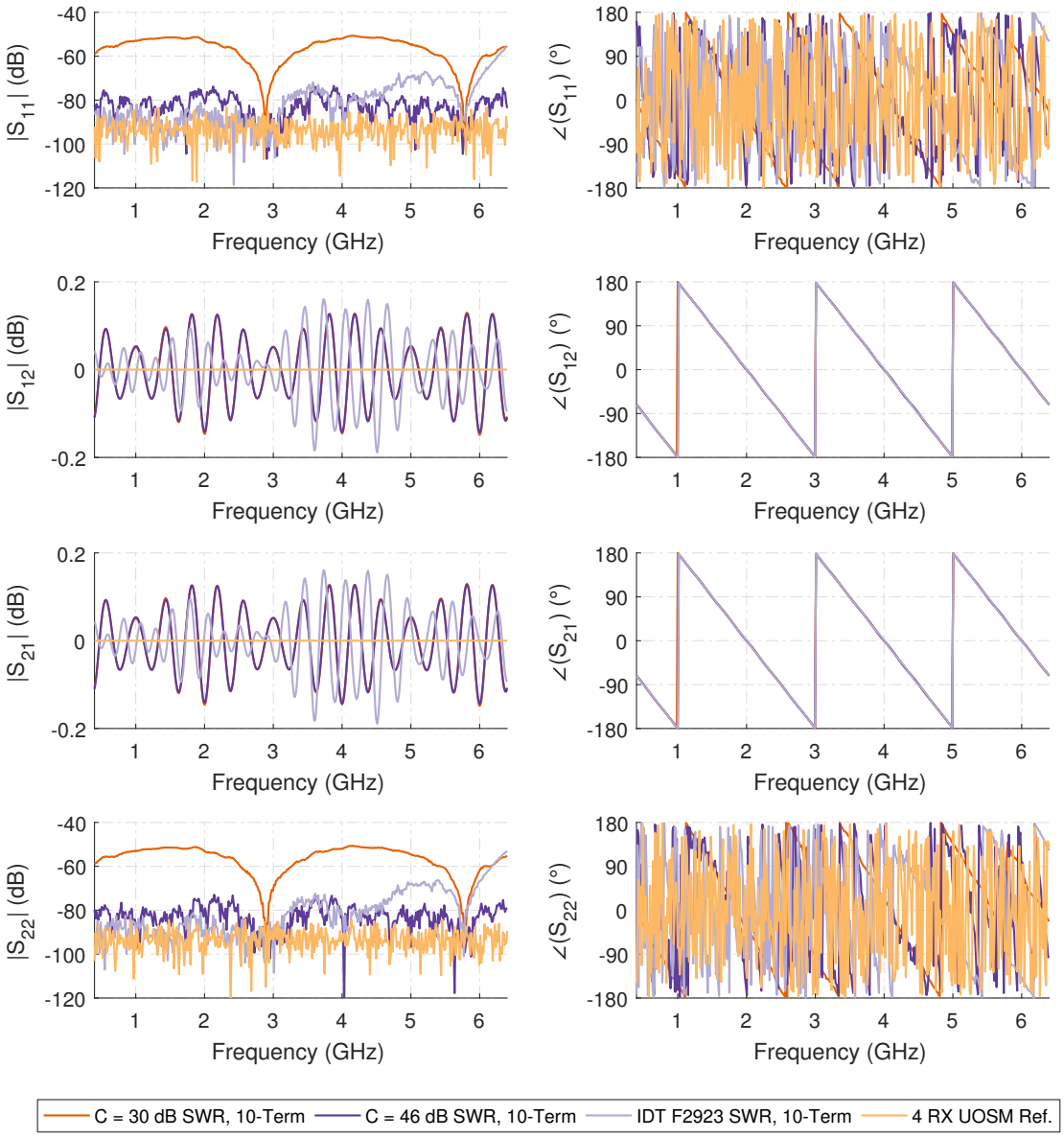

Figure A.34: Numerical 10-term error corrected results of a thru connection using a 150 mm loss-less 50 Ω transmission line for the switched single receiver with reference wave switch (SWR) test-set architecture using the double reflectometer test-set.

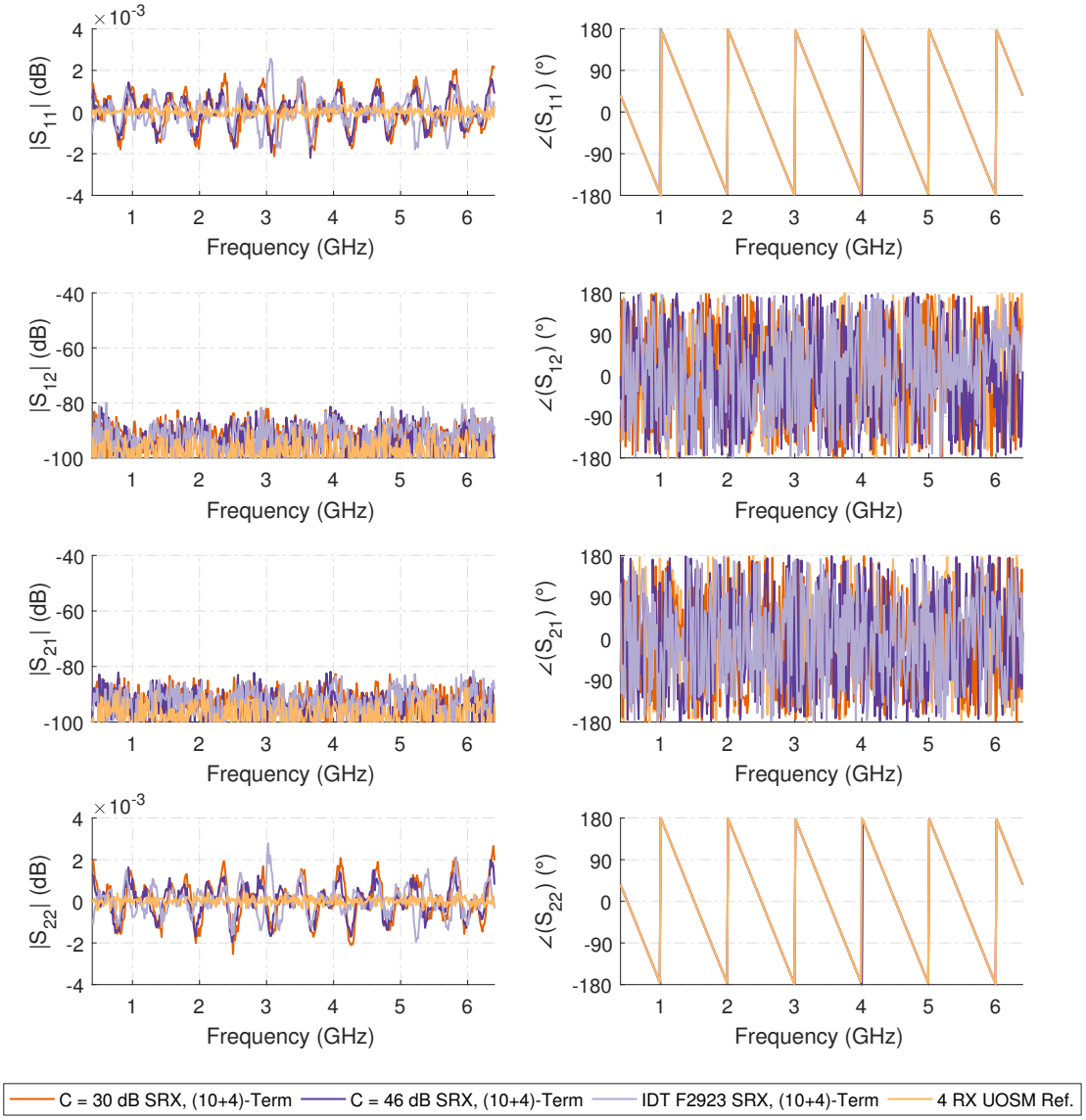

Figure A.35: Numerical results of the ripple test measurement using a 150 mm loss-less 50 Ω transmission line terminated by the calibration short using the (10+4)-term correction model for all synthetic switches in the switched single receiver (SRX) architecture using the double reflectometer test-set.

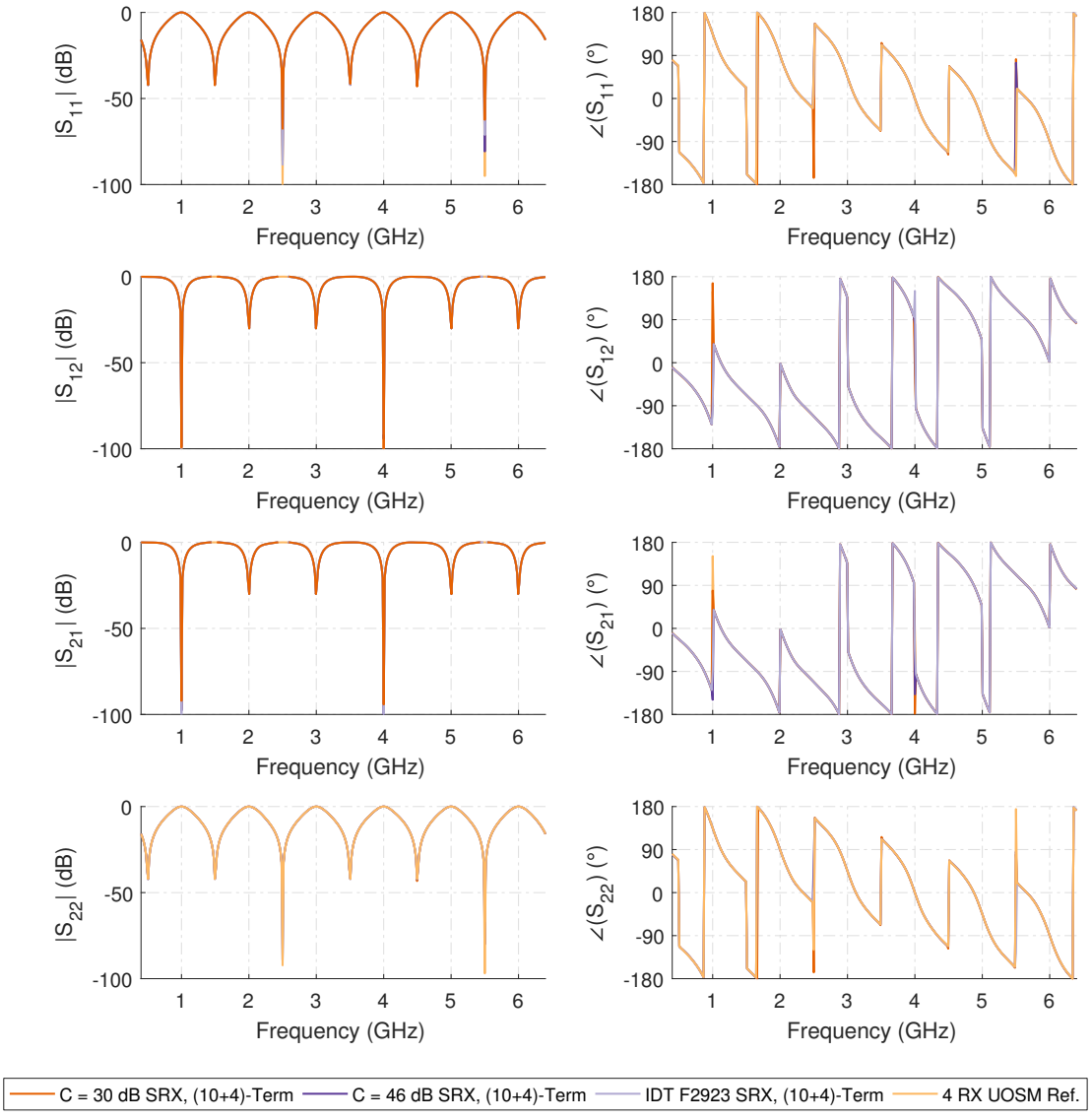

Figure A.36: Numerical (10+4)-Term error corrected measurement results of the 150 mm asymmetric reflective lossy tee measurement using no attenuation for the single switched receiver (SRX) test-set architecture using the double reflectometer test-set.

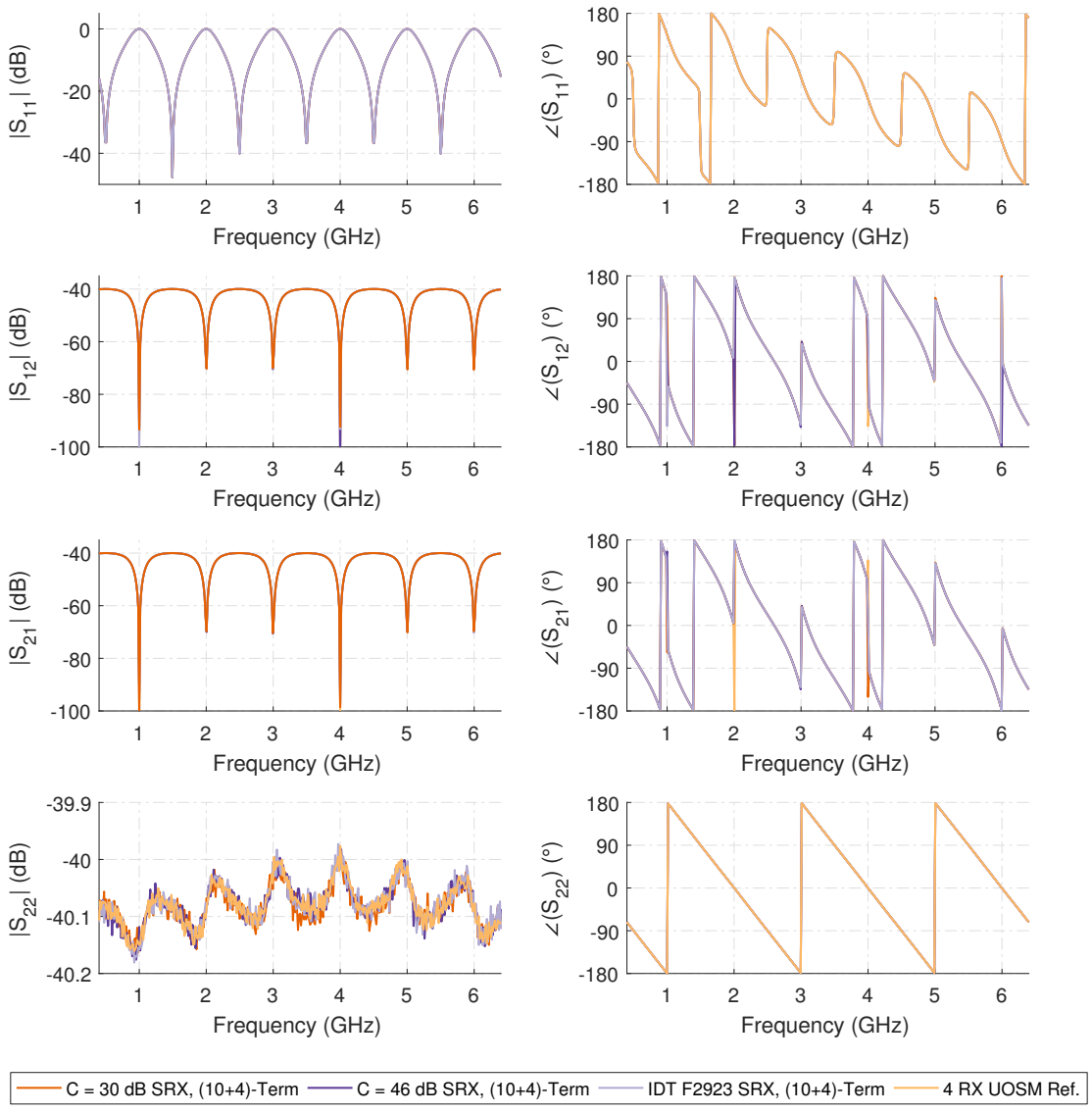

Figure A.37: Numerical (10+4)-Term error corrected measurement results of the 150 mm asymmetric reflective lossy tee measurement using 40 dB of attenuation for the single switched receiver (SRX) test-set architecture using the double reflectometer test-set.

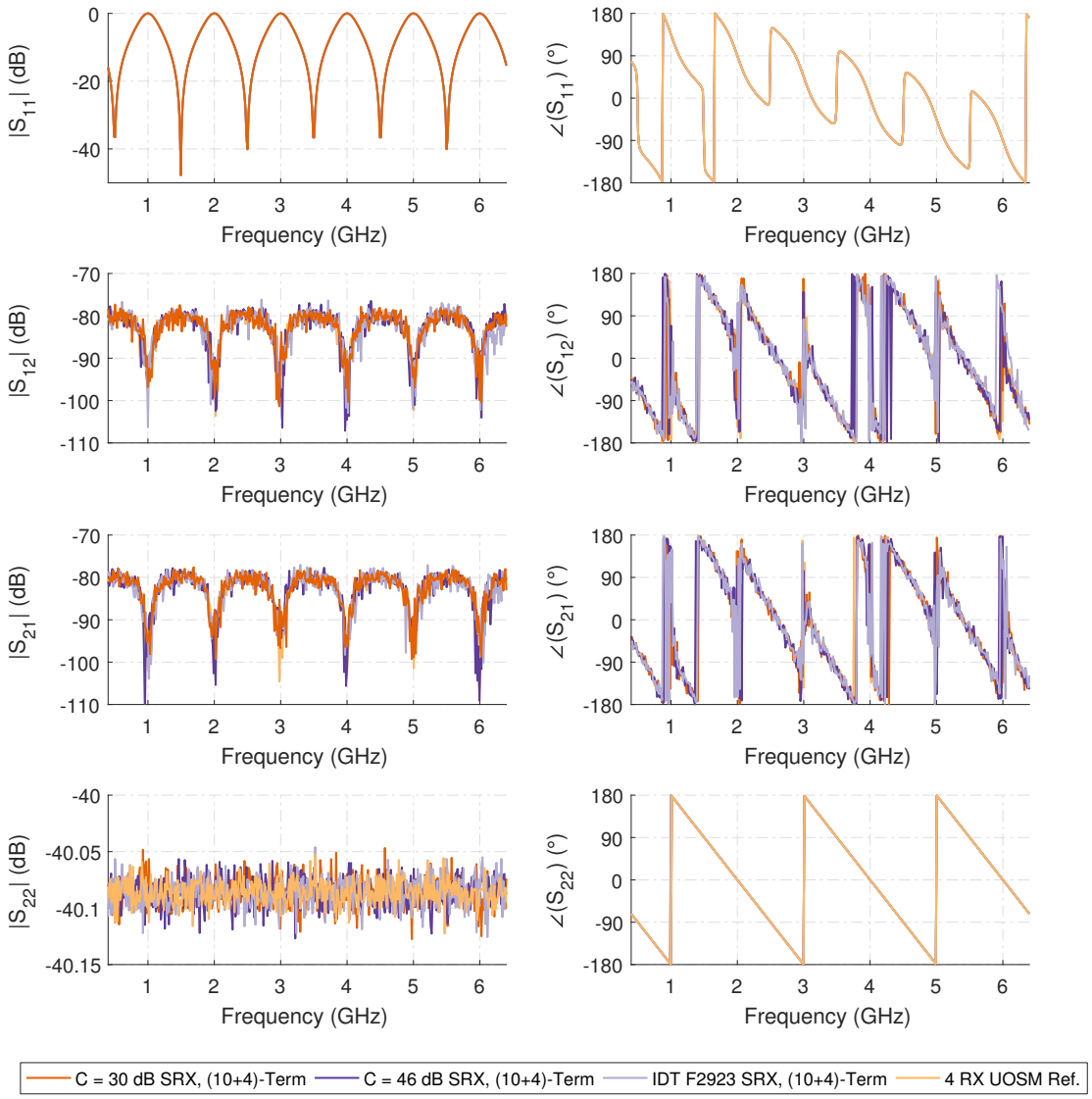

Figure A.38: Numerical (10+4)-Term error corrected measurement results of the 150 mm asymmetric reflective lossy tee measurement using 80 dB of attenuation for the single switched receiver (SRX) test-set architecture using the double reflectometer test-set.

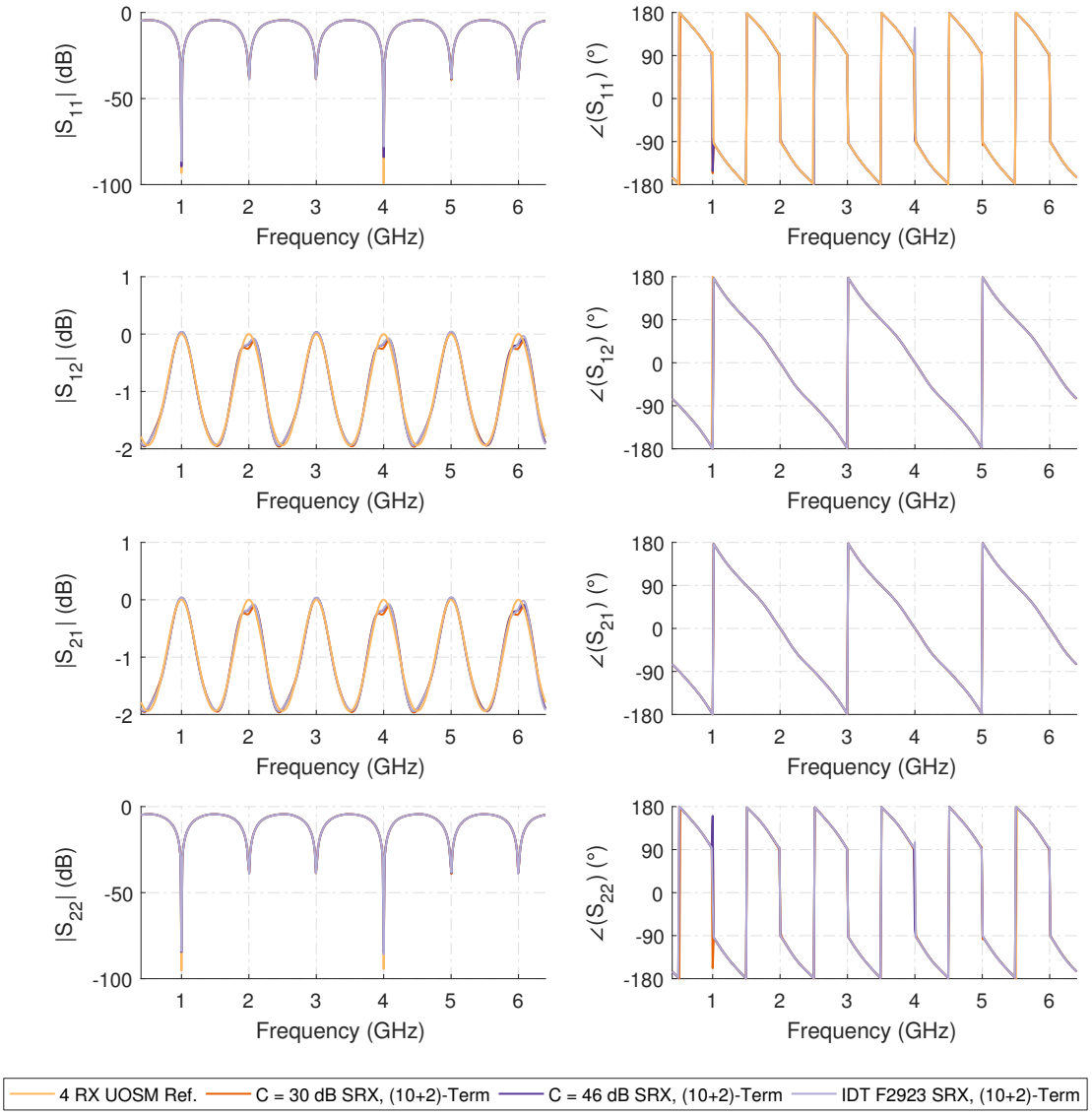

Figure A.39: Numerical (10+4)-term error corrected results of a thru connection using a 150 mm loss-less 25 Ω transmission (or Beatty) line for the single switched receiver (SRX) test-set architecture using the double reflectometer test-set.

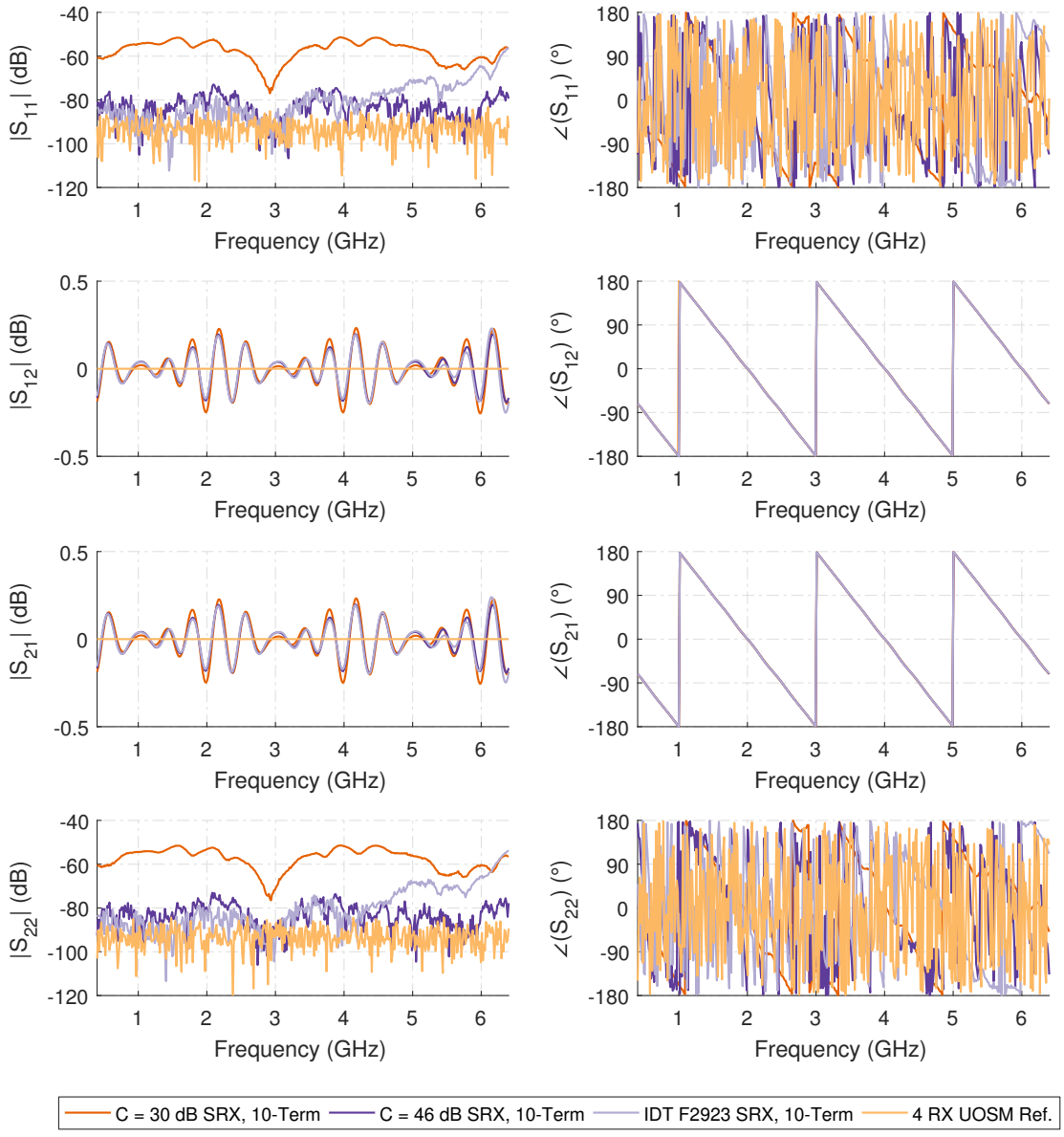

Figure A.40: Numerical (10+4)-term error corrected results of a thru connection using a 150 mm loss-less 50 Ω transmission line for the single switched receiver (SRX) test-set architecture using the double reflectometer test-set.

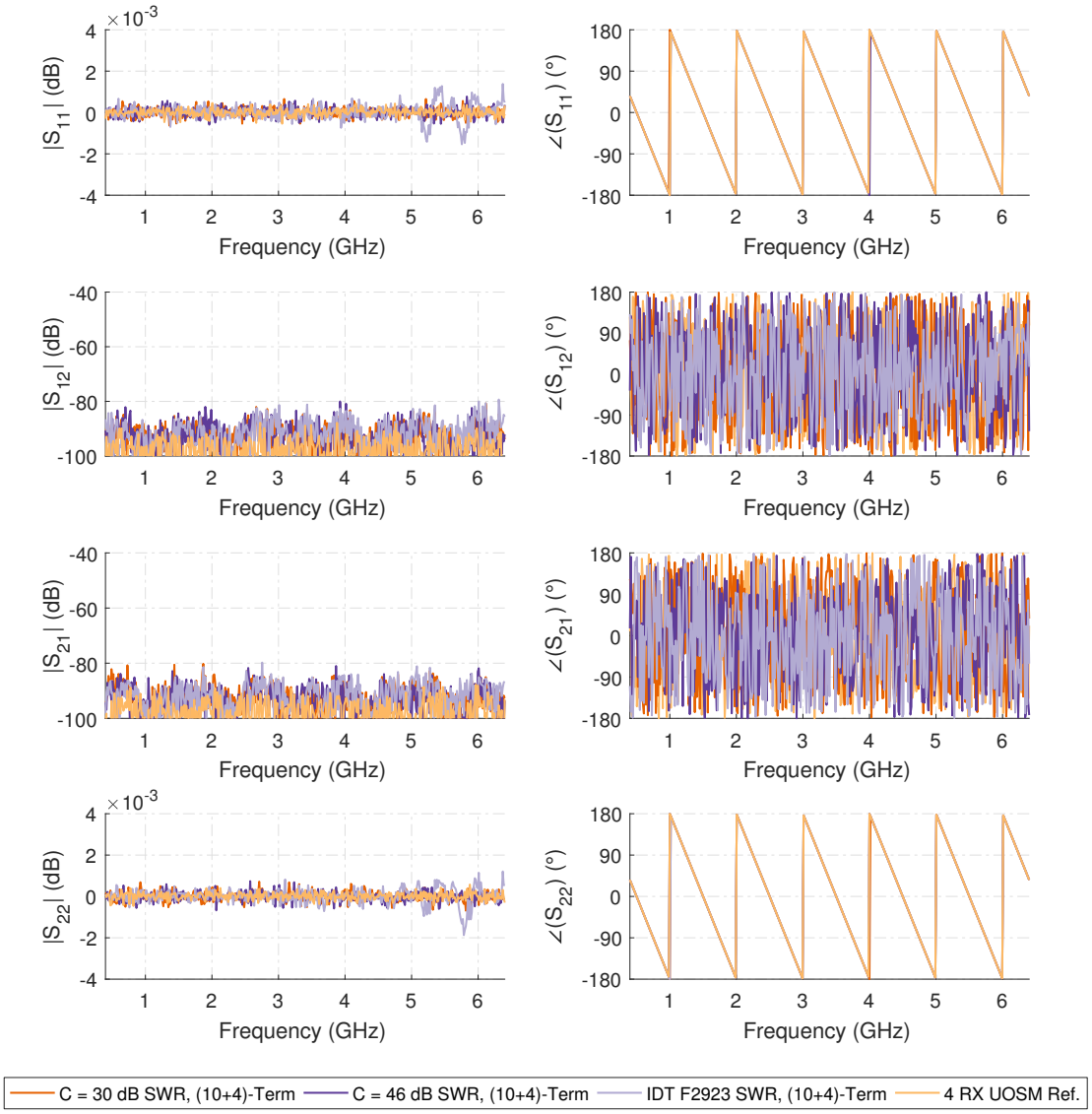

Figure A.41: Numerical results of the ripple test measurement using a 150 mm loss-less 50 Ω transmission line terminated by the calibration short using the (10+4)-term correction model for all synthetic switches in the switched single receiver with reference wave switch (SWR) architecture using the double reflectometer test-set.

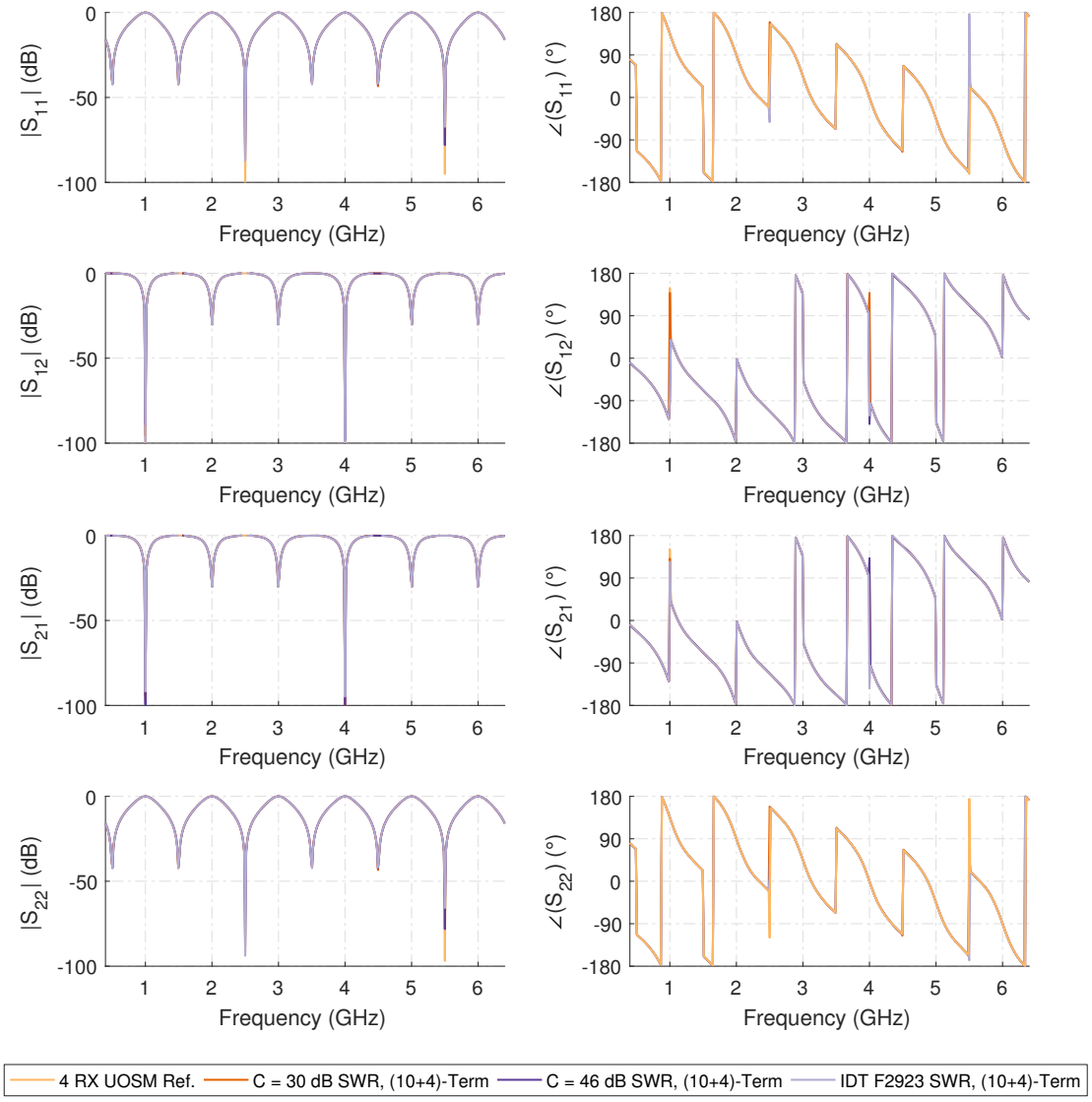

Figure A.42: Numerical (10+4)-Term error corrected measurement results of the 150 mm asymmetric reflective lossy tee measurement using no attenuation for the switched single receiver with reference wave switch (SWR) test-set architecture using the double reflectometer test-set.

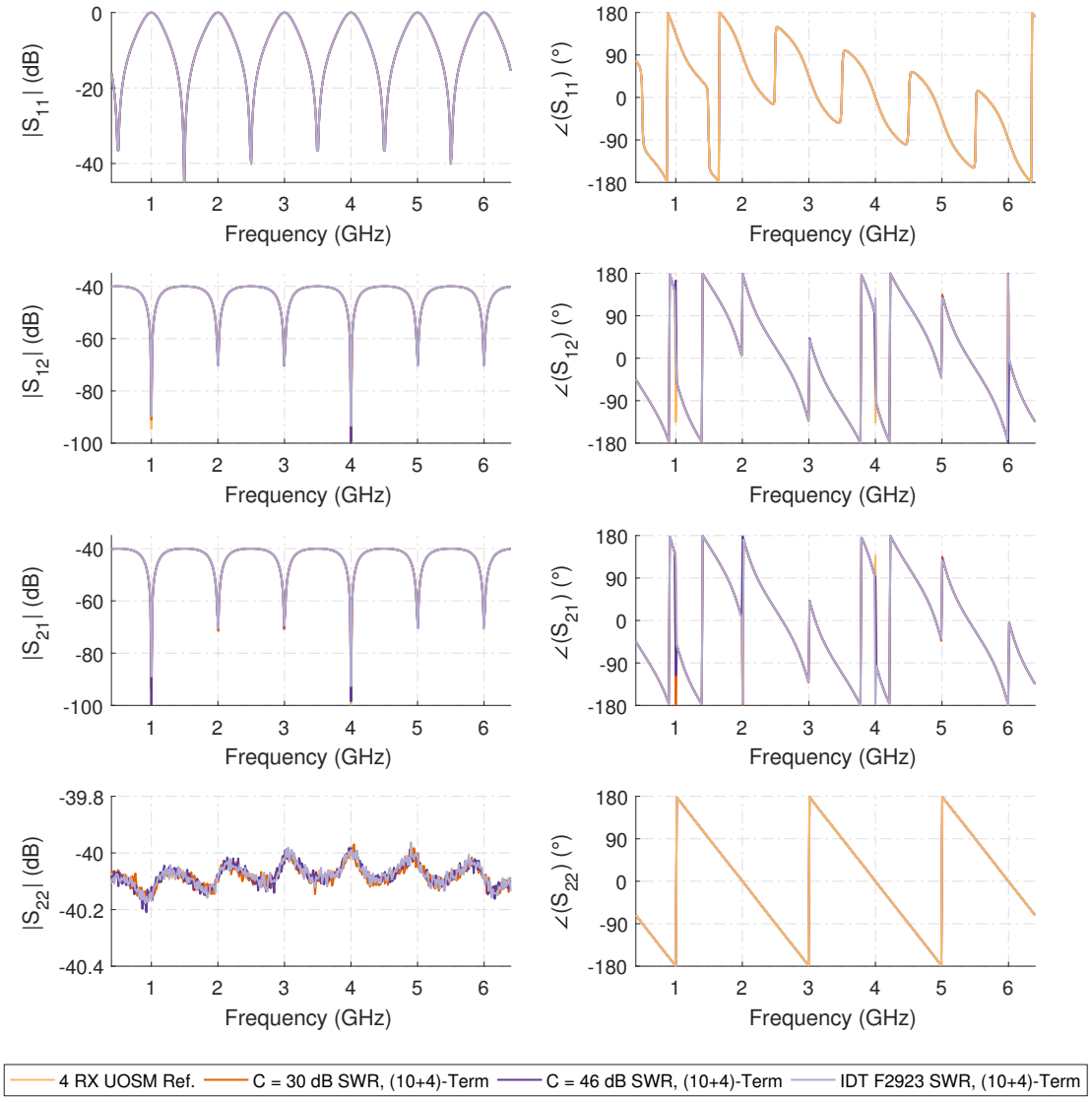

Figure A.43: Numerical (10+4)-Term error corrected measurement results of the 150 mm asymmetric reflective lossy tee measurement using 40 dB of attenuation for the switched single receiver with reference wave switch (SWR) test-set architecture using the double reflectometer test-set.

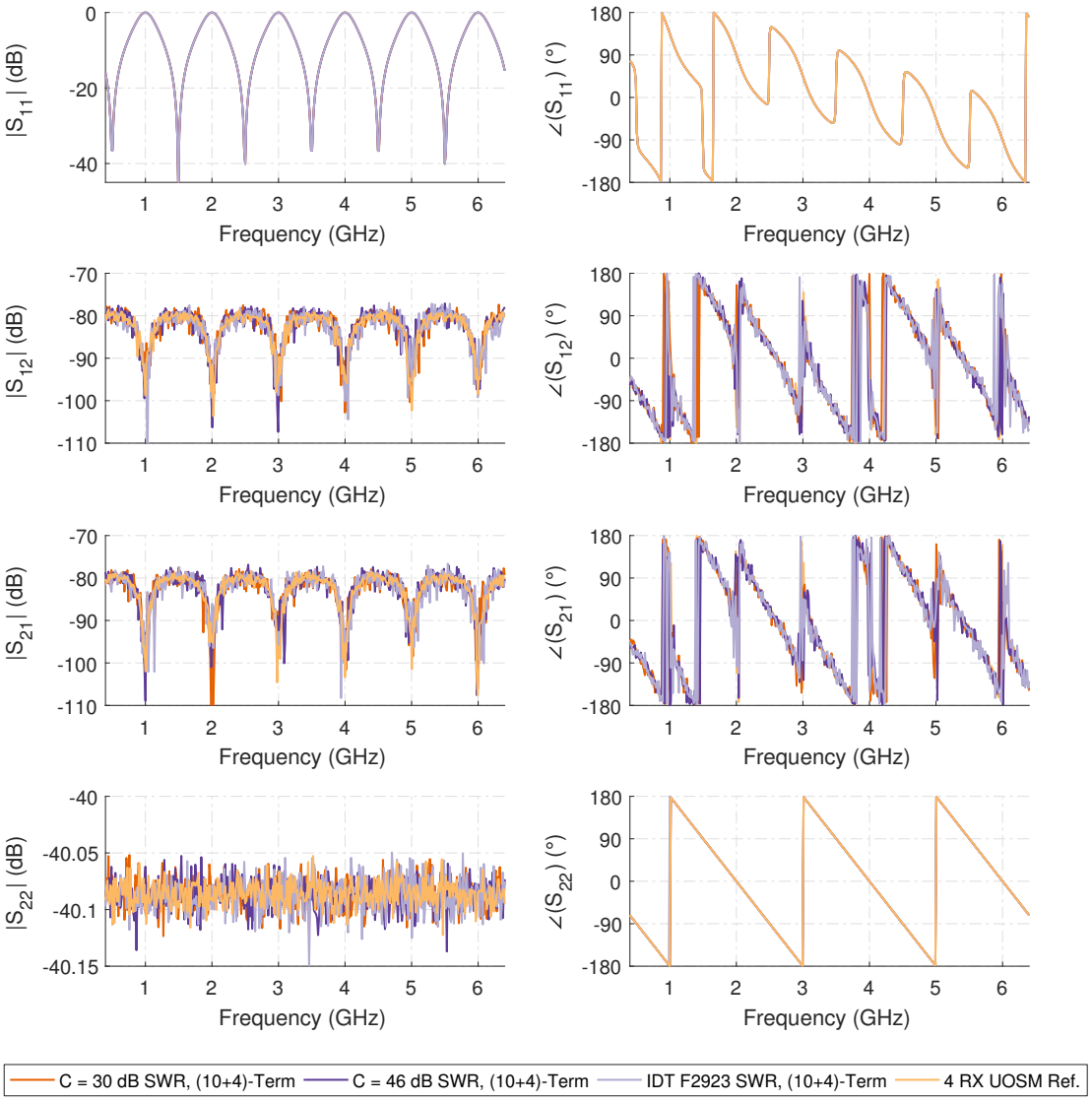

Figure A.44: Numerical 10-Term error corrected measurement results of the 150 mm asymmetric reflective lossy tee measurement using 80 dB of attenuation for the switched single receiver with reference wave switch (SWR) test-set architecture using the double reflectometer test-set.

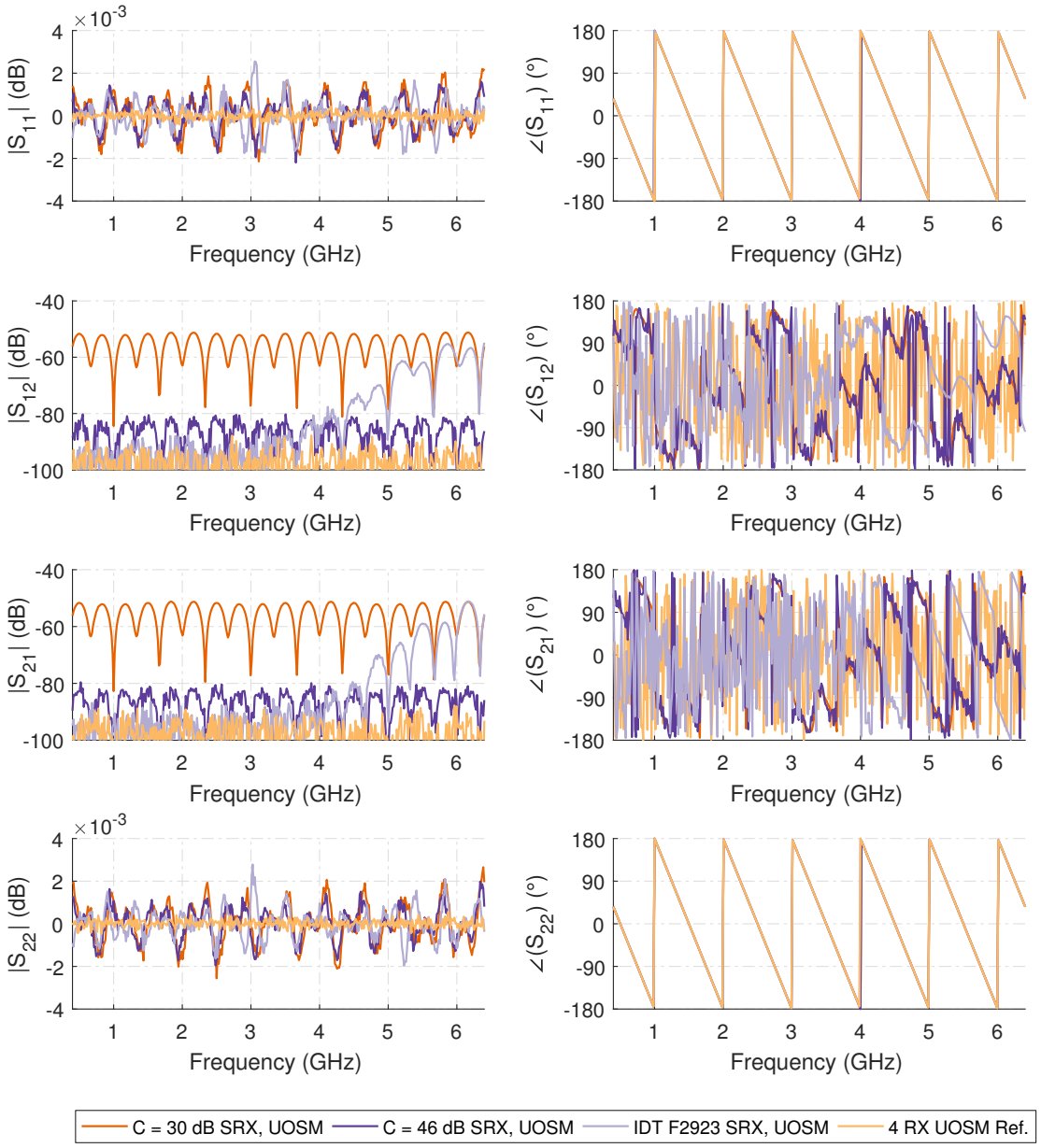

Figure A.45: Numerical results of the ripple test measurement using a 150 mm lossless 50 Ω transmission line terminated by the calibration short using the 7-term error correction model with UOSM calibration for all synthetic switches in the switched single receiver (SRX) architecture using the double reflectometer test-set.

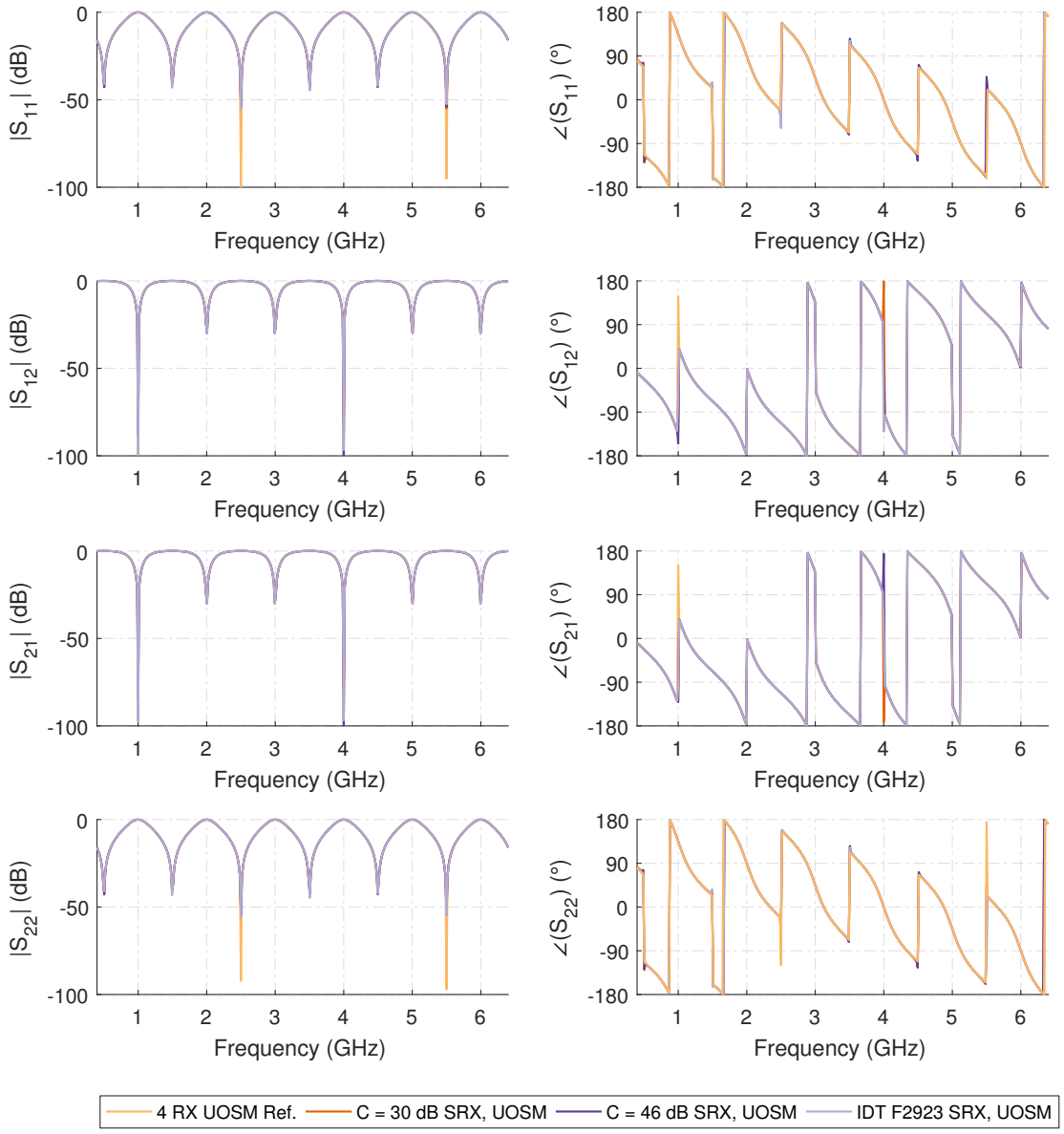

Figure A.46: Numerical 7-term error model with UOSM calibration corrected measurement results of the 150 mm asymmetric reflective lossy tee measurement using no attenuation for the single switched receiver (SRX) test-set architecture using the double reflectometer test-set.

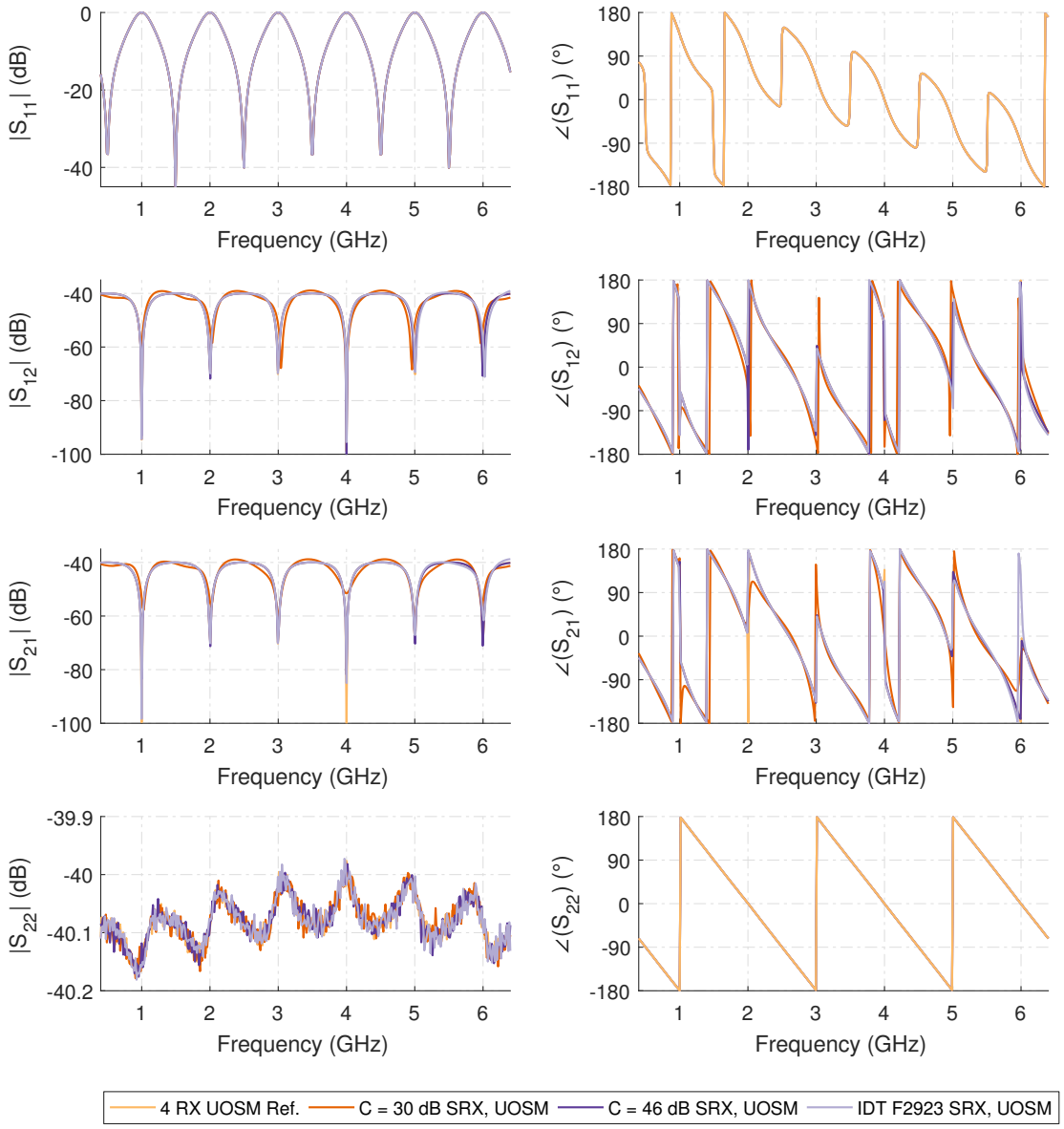

Figure A.47: Numerical 7-term error model with UOSM calibration corrected measurement results of the 150 mm asymmetric reflective lossy tee measurement using 40 dB of attenuation for the single switched receiver (SRX) test-set architecture using the double reflectometer test-set.

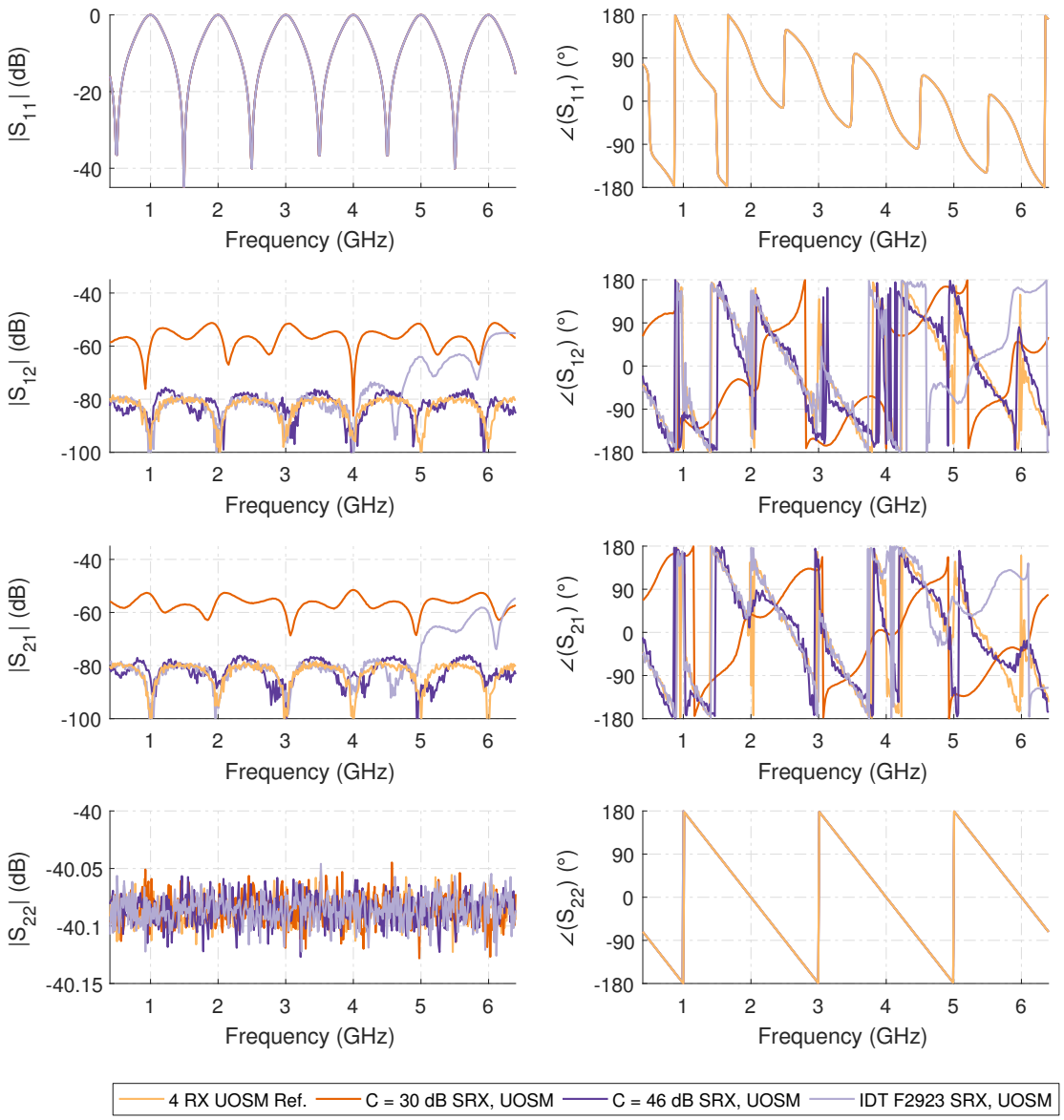

Figure A.48: Numerical 7-term error model with UOSM calibration corrected measurement results of the 150 mm asymmetric reflective lossy tee measurement using 80 dB of attenuation for the single switched receiver (SRX) test-set architecture using the double reflectometer test-set.

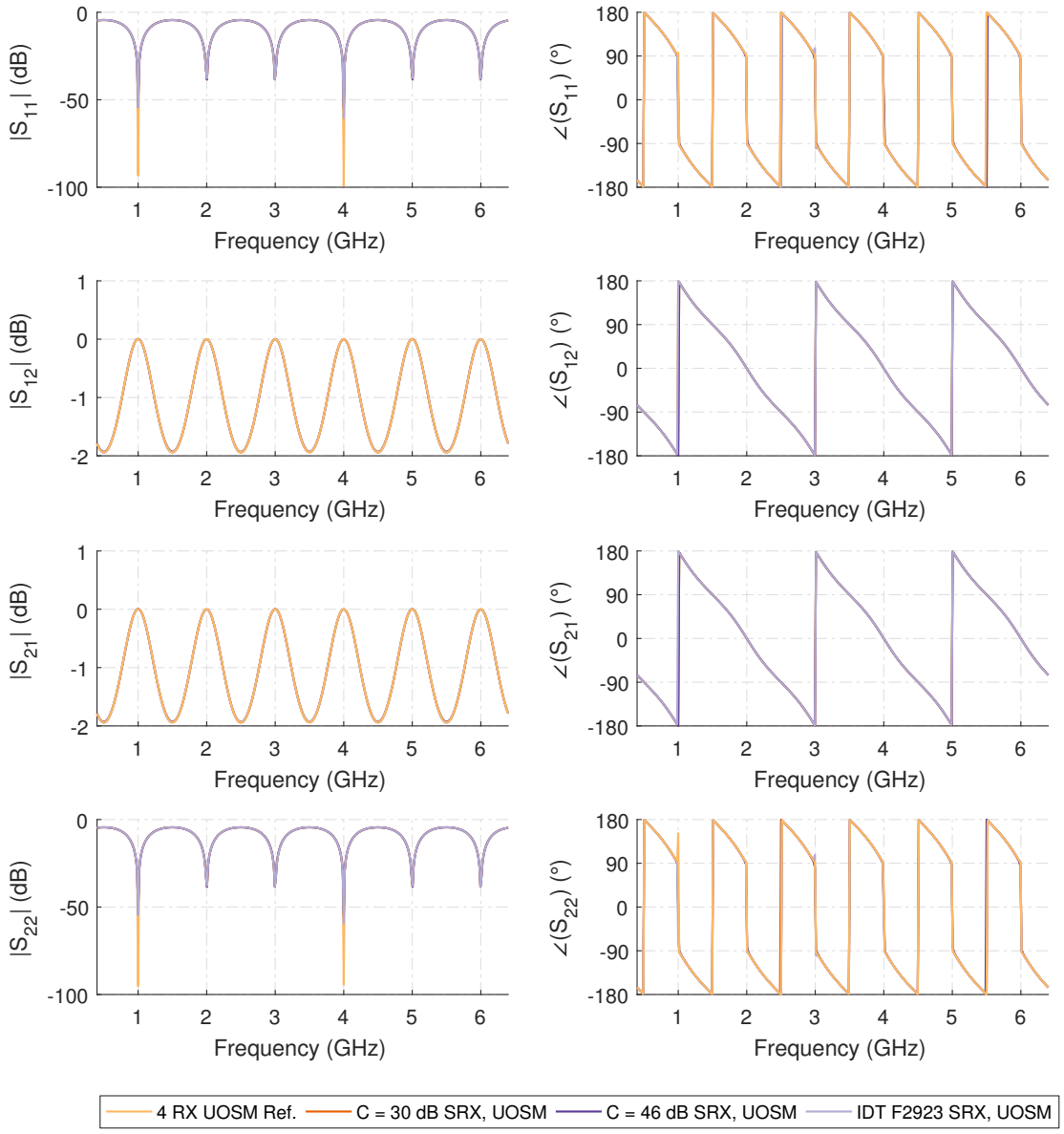

Figure A.49: Numerical 7-term error model with UOSM calibration corrected results of a thru connection using a 150 mm loss-less 25 Ω transmission (or Beatty) line for the single switched receiver (SRX) test-set architecture using the double reflectometer test-set.

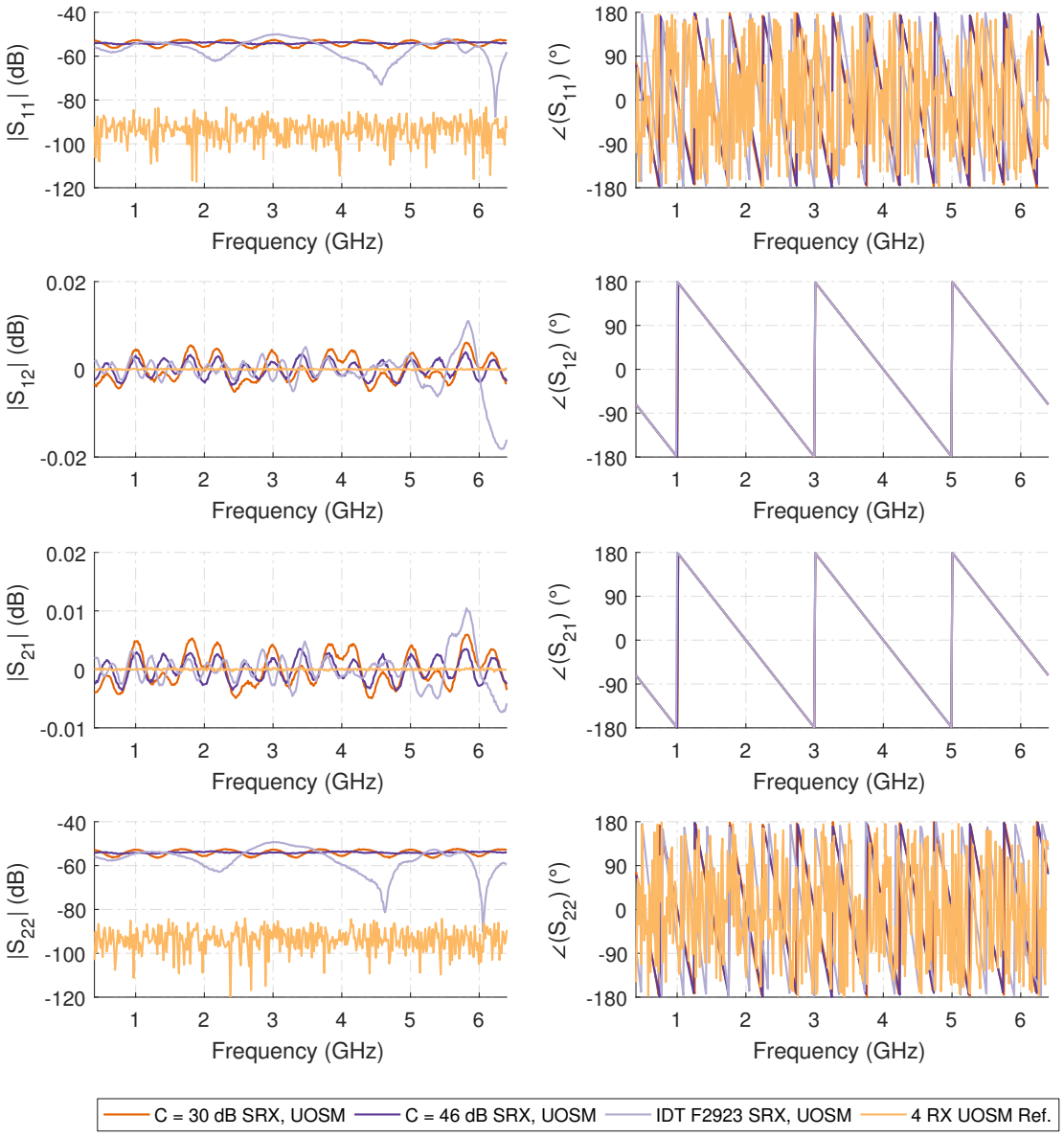

Figure A.50: Numerical 7-term error model with UOSM calibration corrected results of a thru connection using a 150 mm loss-less 50 Ω transmission line for the single switched receiver (SRX) test-set architecture using the double reflectometer test-set.

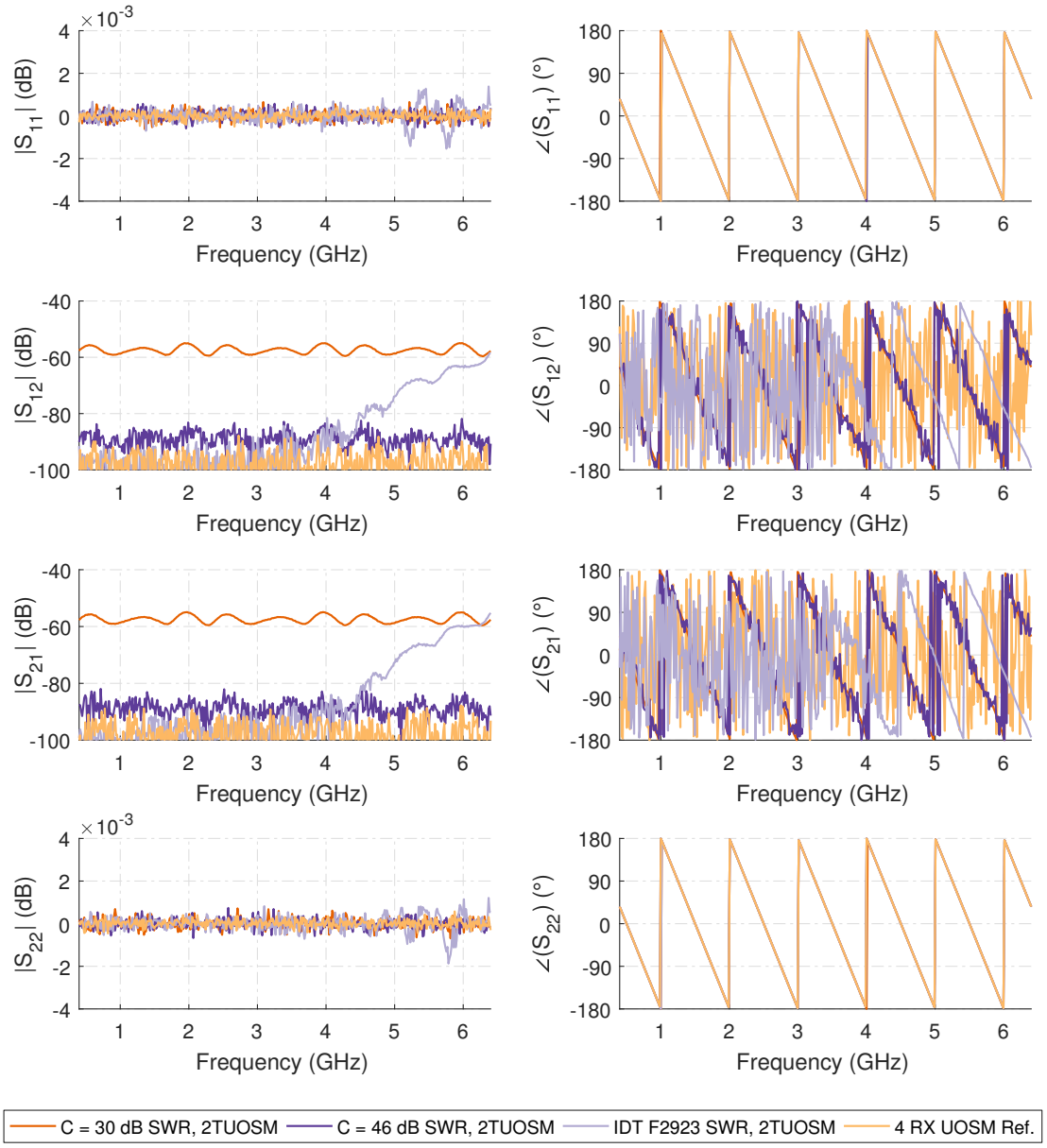

Figure A.51: Numerical results of the ripple test measurement using a 150 mm loss-less 50 Ω transmission line terminated by the calibration short using the 7-term error correction model with two-tier UOSM calibration for all synthetic switches in the switched single receiver with reference wave switch (SWR) test-set architecture using the double reflectometer test-set.

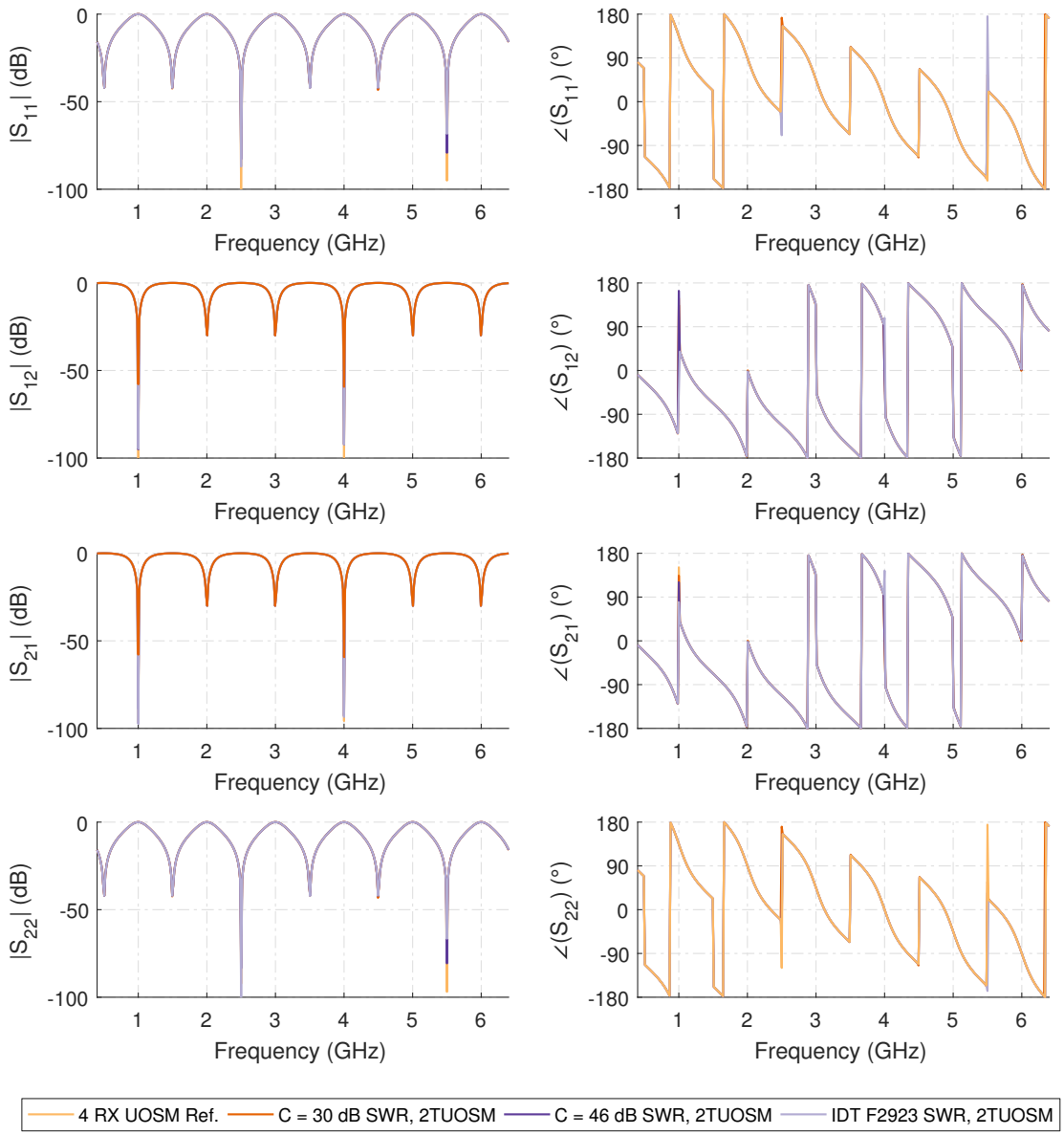

Figure A.52: Numerical 7-term error model with two-tier UOSM calibration corrected measurement results of the 150 mm asymmetric reflective lossy tee measurement using no attenuation for the switched single receiver with reference wave switch (SWR) test-set architecture using the double reflectometer test-set.

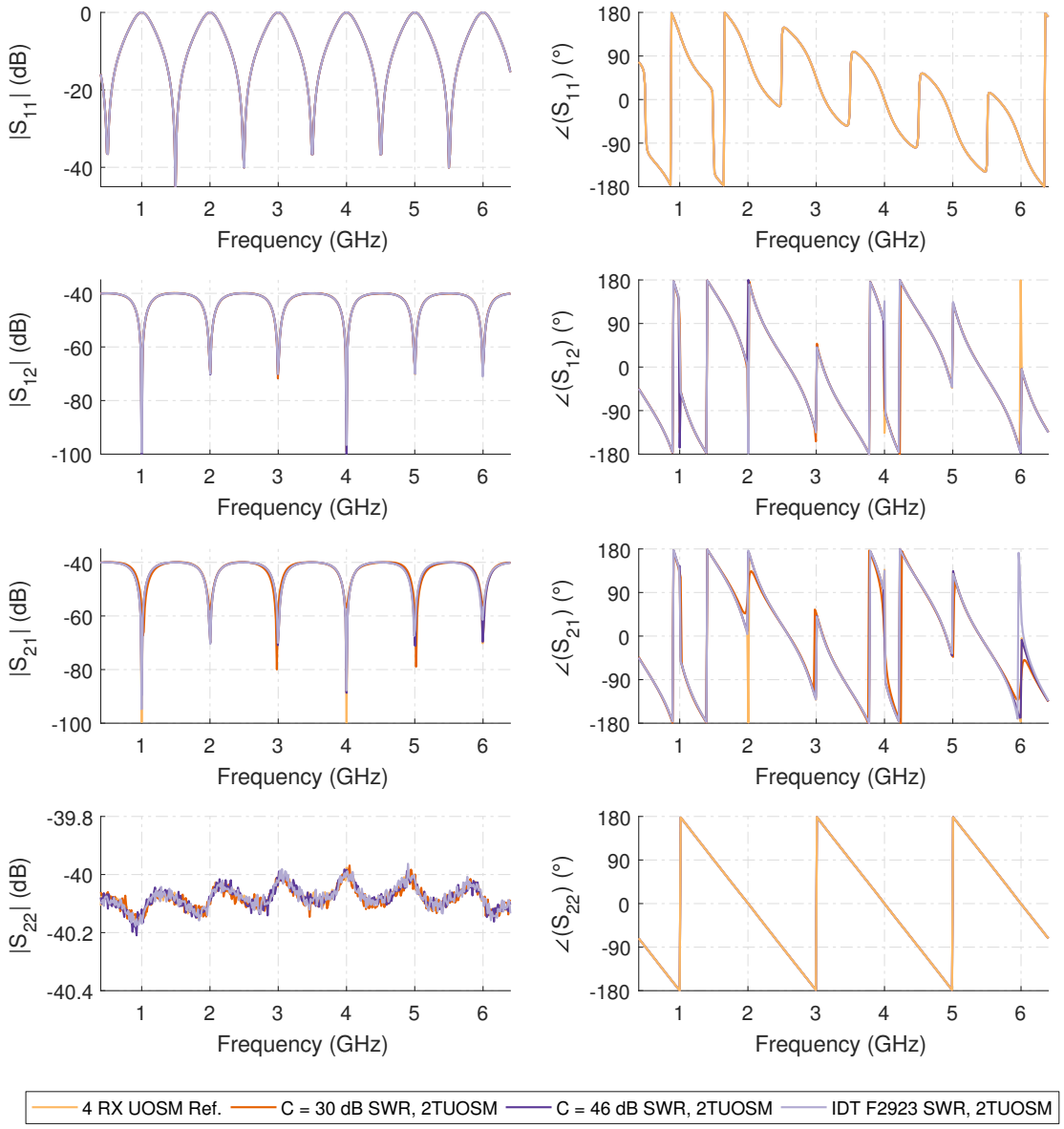

Figure A.53: Numerical 7-term error model with two-tier UOSM calibration corrected measurement results of the 150 mm asymmetric reflective lossy tee measurement using 40 dB of attenuation for the switched single receiver with reference wave switch (SWR) test-set architecture using the double reflectometer test-set.

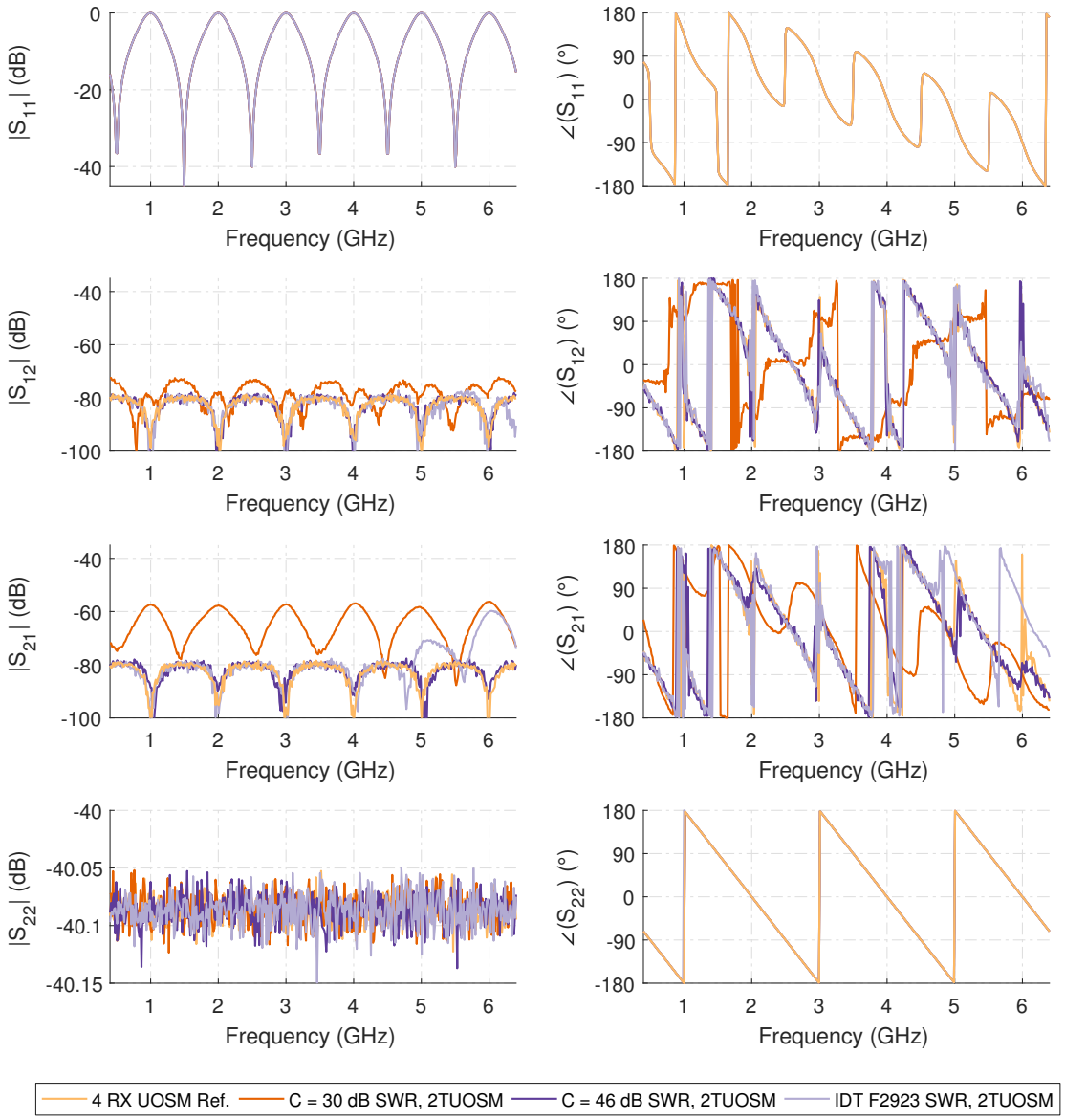

Figure A.54: Numerical 7-term error model with two-tier UOSM calibration corrected measurement results of the 150 mm asymmetric reflective lossy tee measurement using 80 dB of attenuation for the switched single receiver with reference wave switch (SWR) test-set architecture using the double reflectometer test-set.

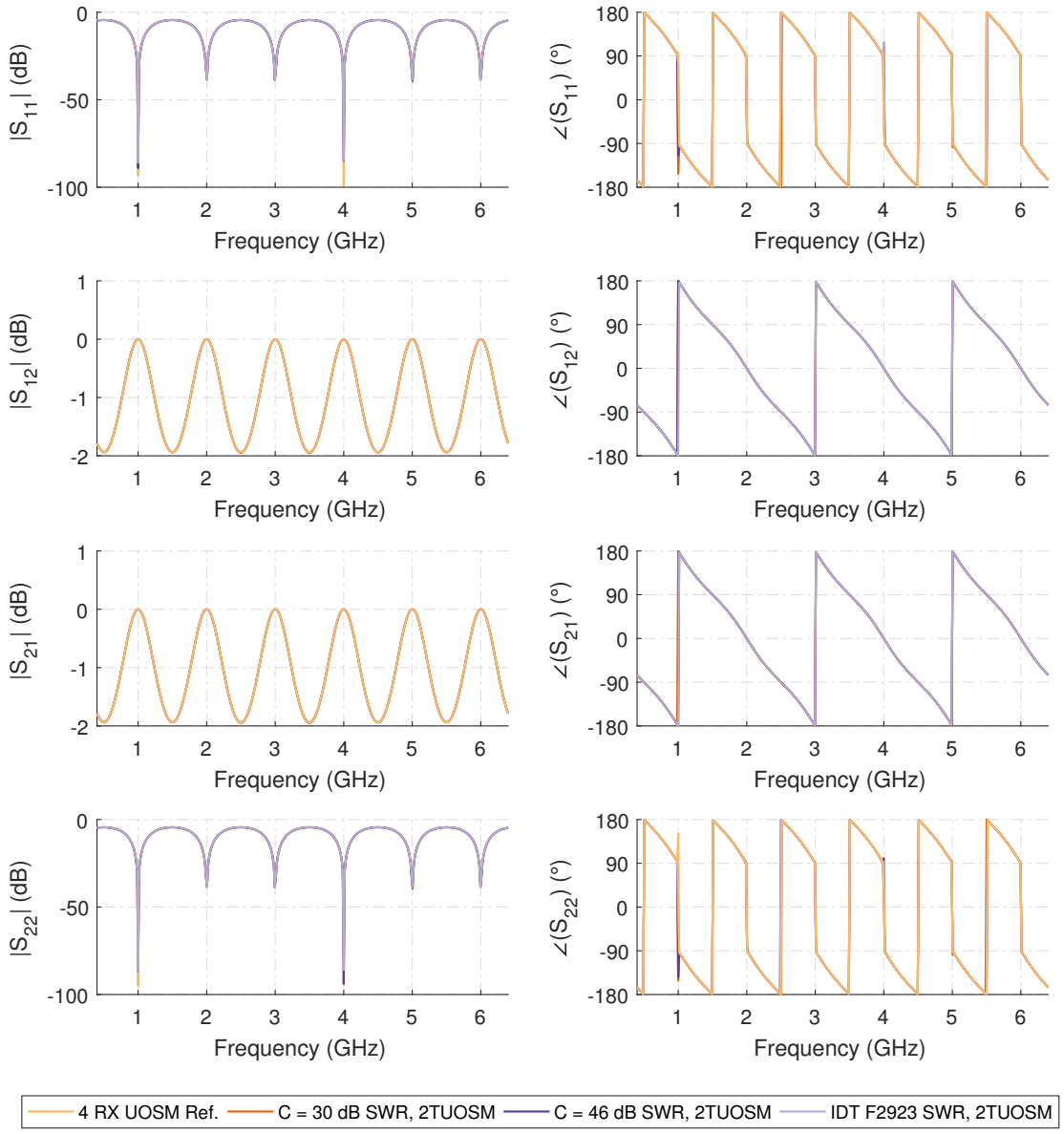

Figure A.55: Numerical 7-term error model with two-tier UOSM calibration corrected results of a thru connection using a 150 mm loss-less 25 Ω transmission (or Beatty) line for the switched single receiver with reference wave switch (SWR) test-set architecture using the double reflectometer test-set.

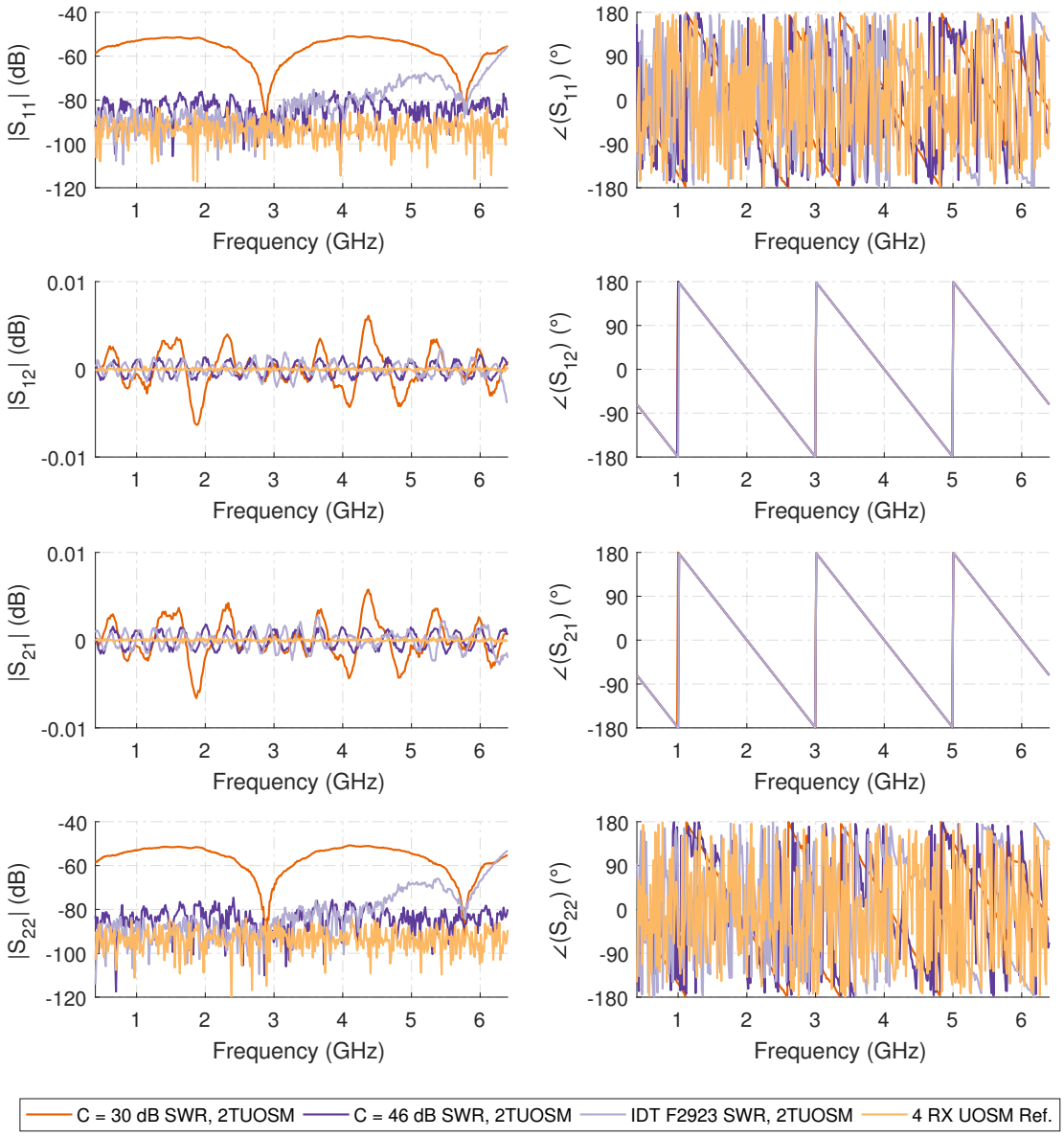

Figure A.56: Numerical 7-term error model with two-tier UOSM calibration corrected results of a thru connection using a 150 mm loss-less 50 Ω transmission line for the switched single receiver with reference wave switch (SWR) test-set architecture using the double reflectometer test-set.

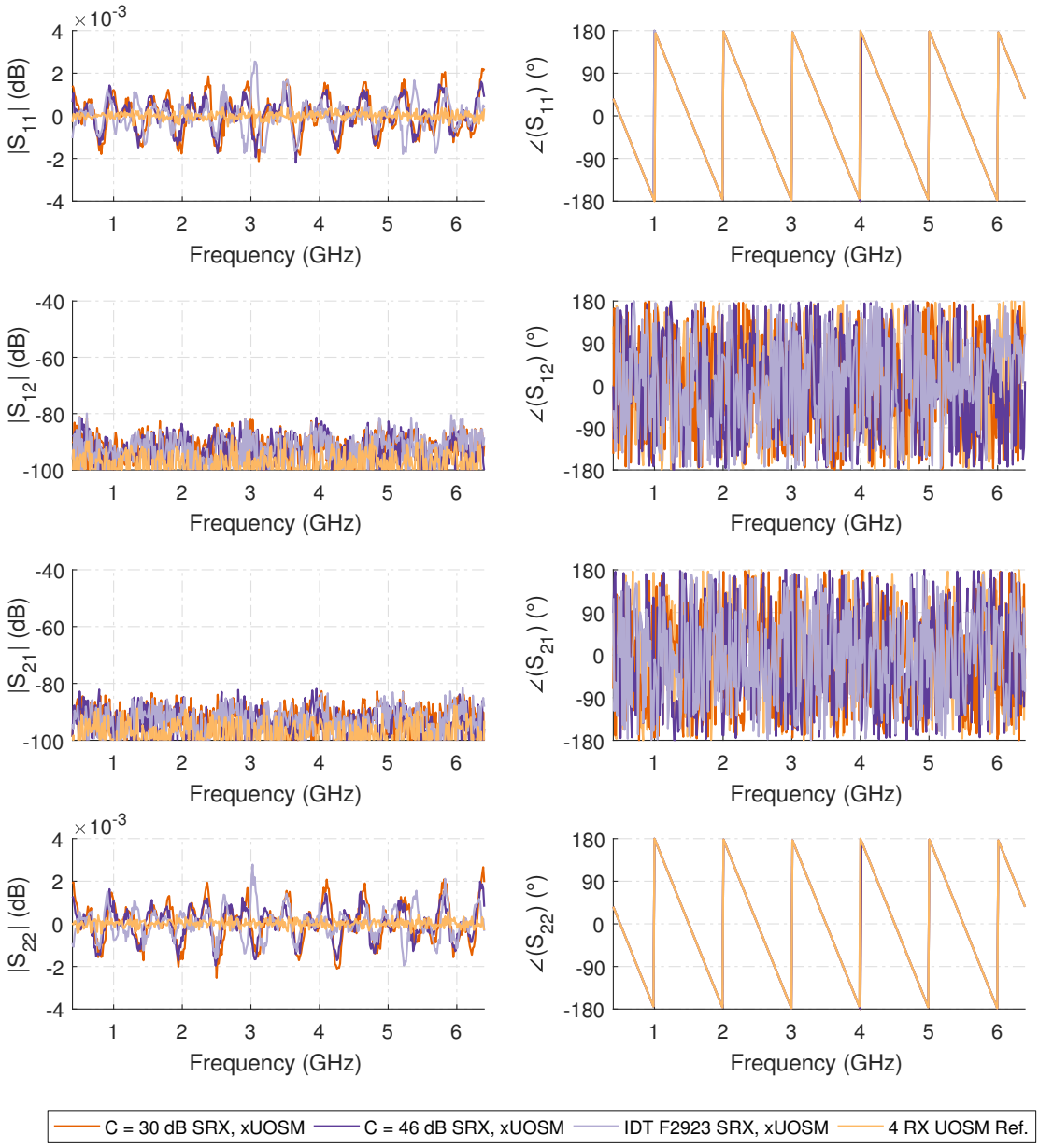

Figure A.57: Numerical 7-term error model with xUOSM calibration corrected measurement results of the 150 mm asymmetric reflective lossy tee measurement using no attenuation for the single switched receiver (SRX) test-set architecture using the double reflectometer test-set.

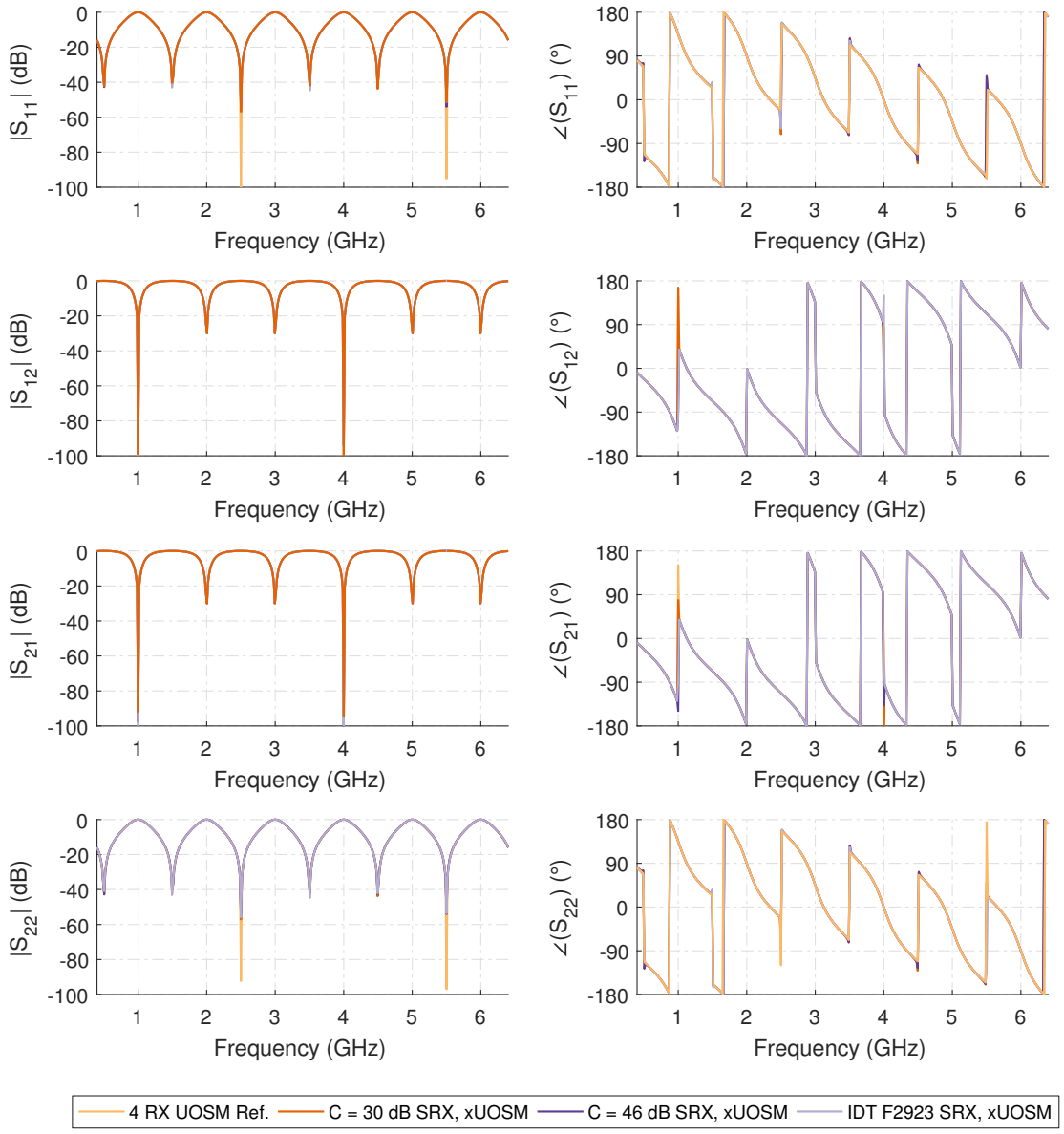

Figure A.58: Numerical 7-term error model with xUOSM calibration corrected measurement results of the 150 mm asymmetric reflective lossy tee measurement using no attenuation for the single switched receiver (SRX) test-set architecture using the double reflectometer test-set.

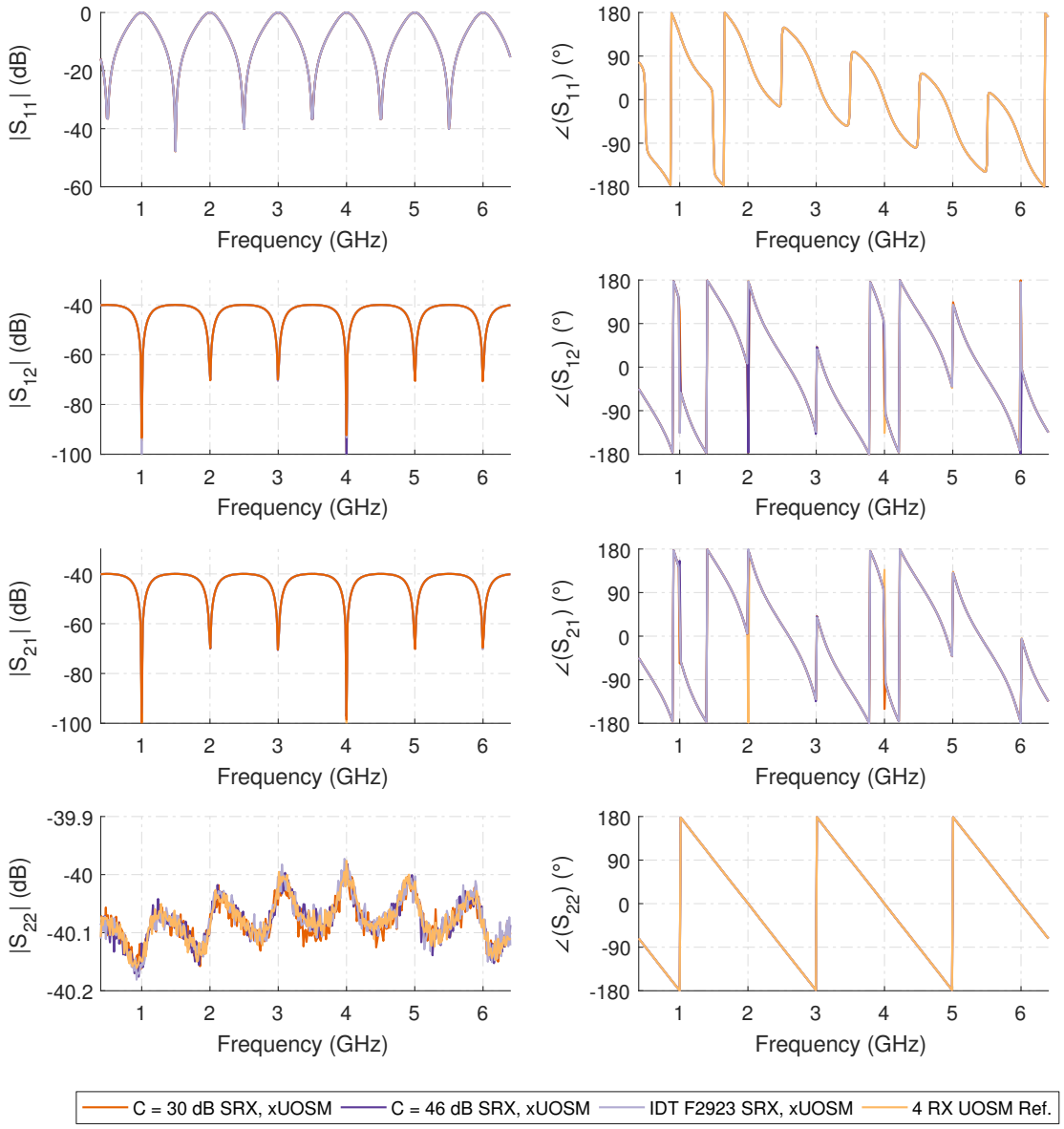

Figure A.59: Numerical 7-term error model with xUOSM calibration corrected measurement results of the 150 mm asymmetric reflective lossy tee measurement using 40 dB of attenuation for the single switched receiver (SRX) test-set architecture using the double reflectometer test-set.

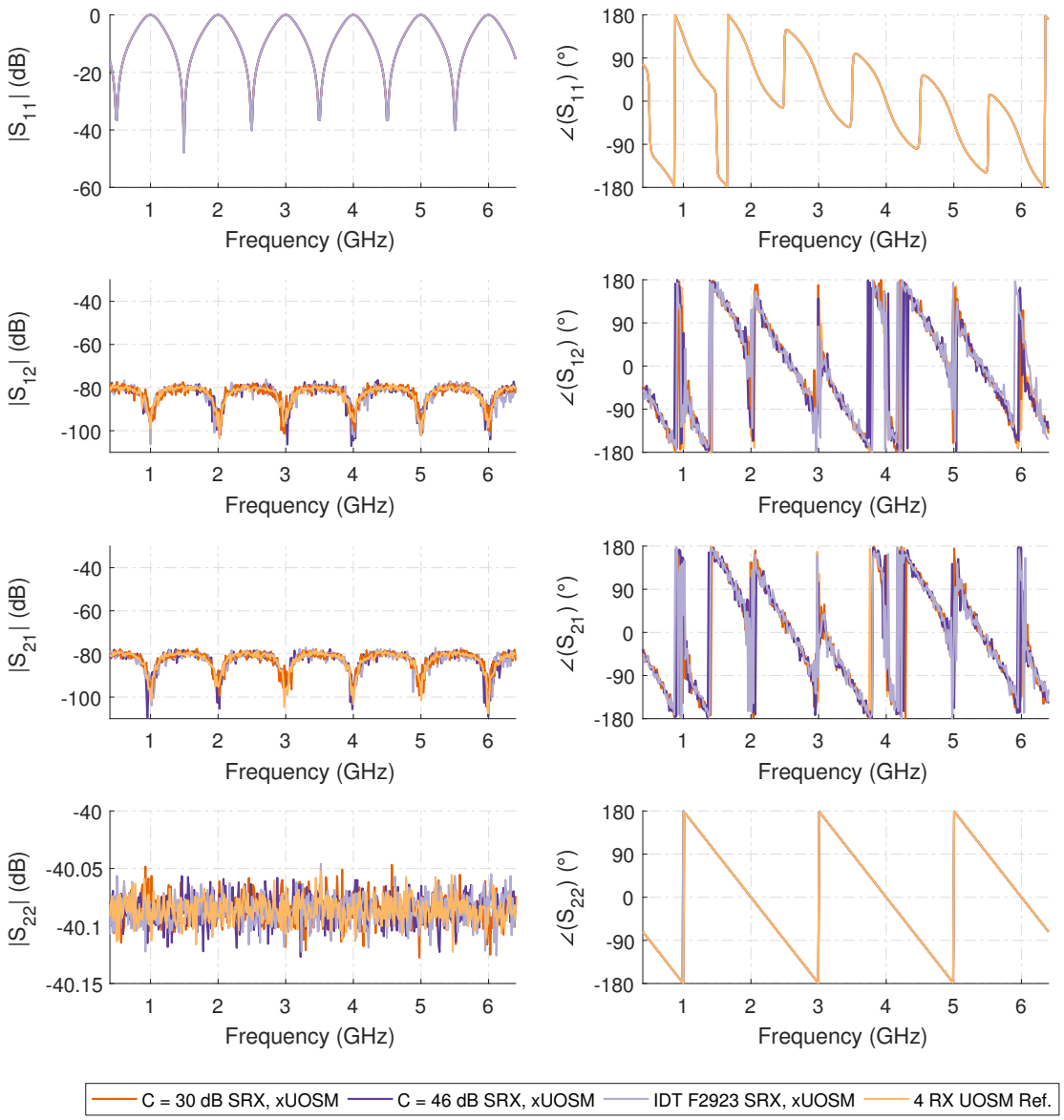

Figure A.60: Numerical 7-term error model with xUOSM calibration corrected measurement results of the 150 mm asymmetric reflective lossy tee measurement using 80 dB of attenuation for the single switched receiver (SRX) test-set architecture using the double reflectometer test-set.

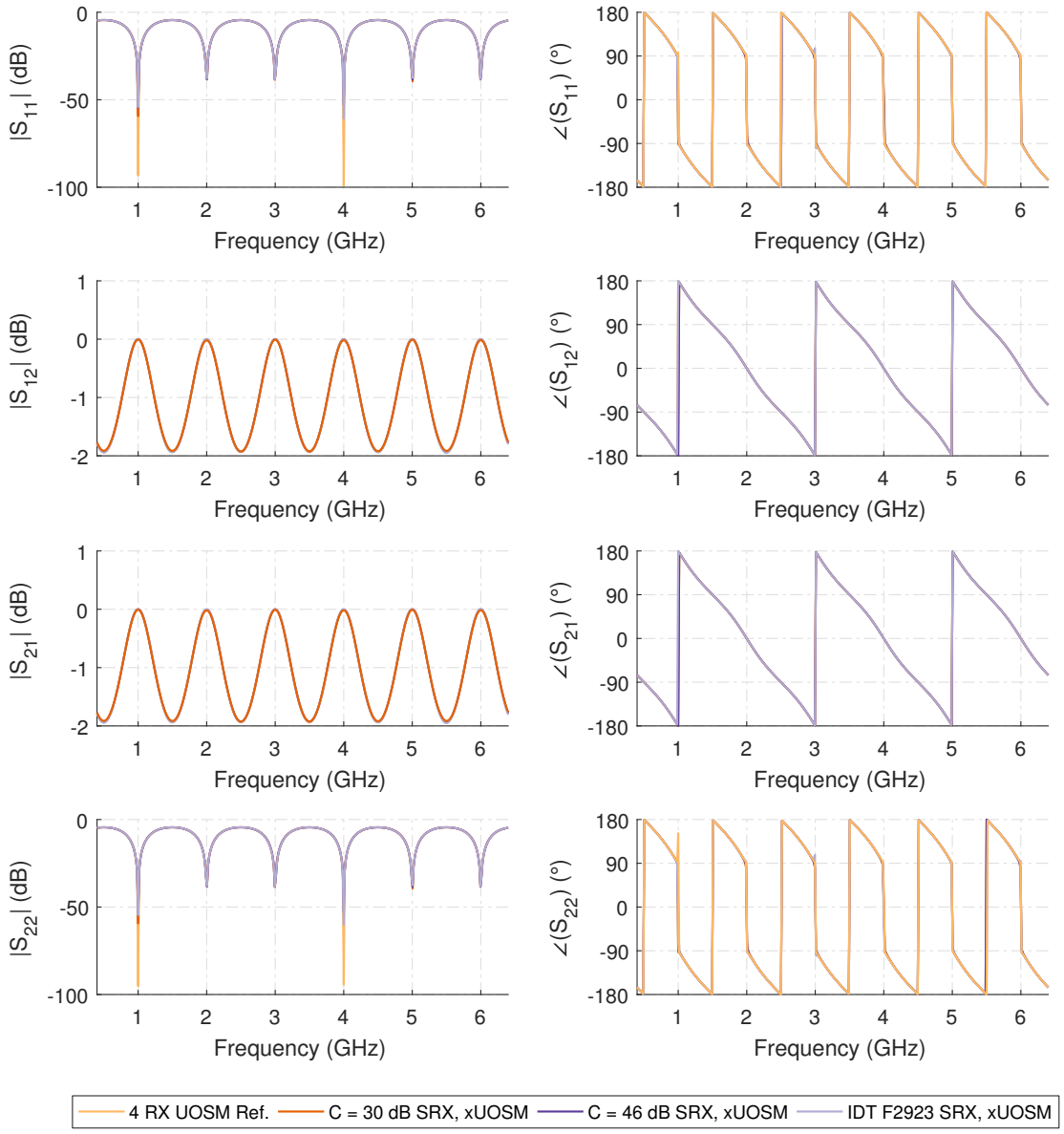

Figure A.61: Numerical 7-term error model with xUOSM calibration corrected results of a thru connection using a 150 mm loss-less 25 Ω transmission (or Beatty) line for the single switched receiver (SRX) test-set architecture using the double reflectometer test-set.

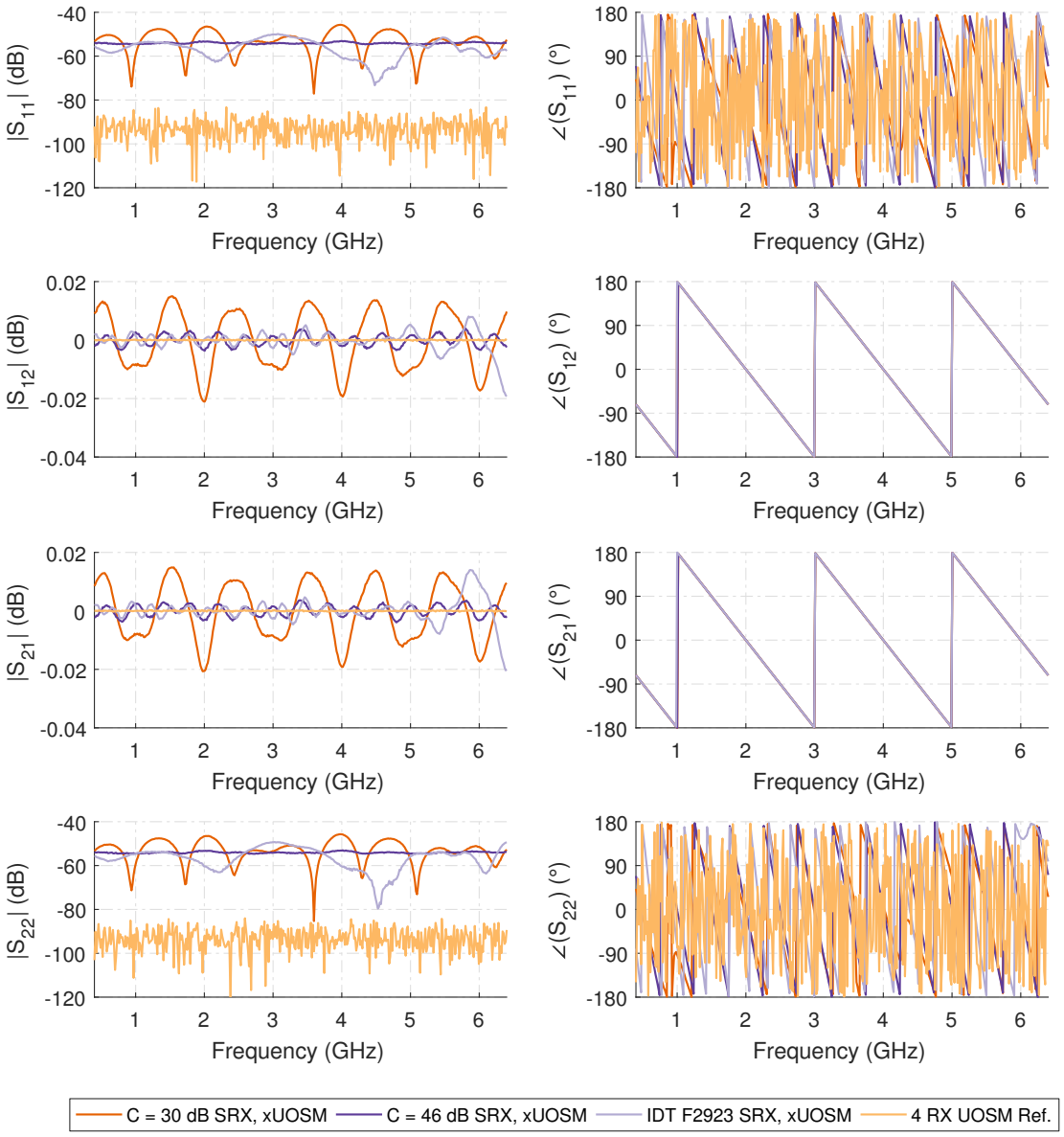

Figure A.62: Numerical 7-term error model with UOSM calibration corrected results of a thru connection using a 150 mm loss-less 50 Ω transmission line for the single switched receiver (SRX) test-set architecture using the double reflectometer test-set.

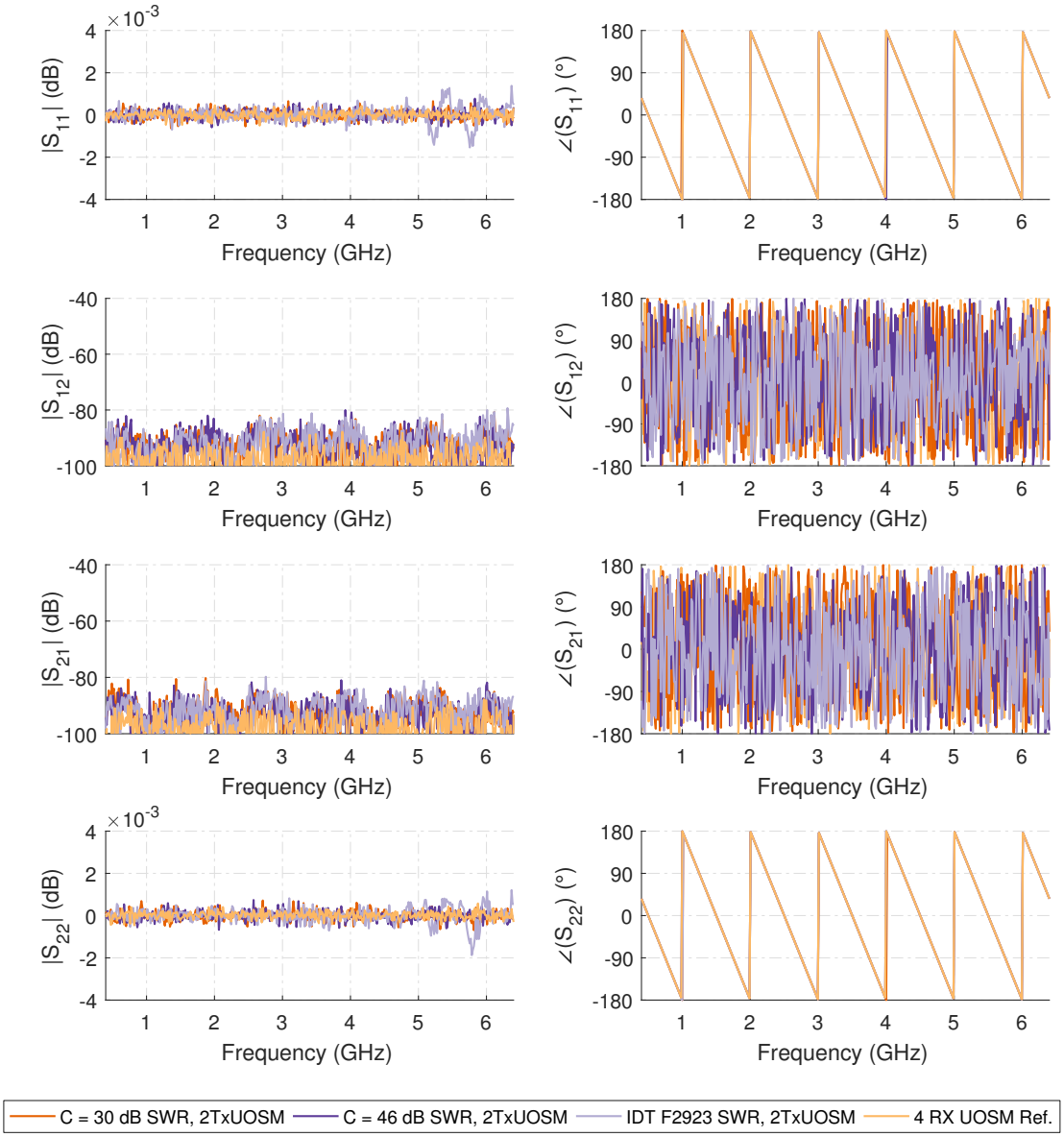

Figure A.63: Numerical results of the ripple test measurement using a 150 mm loss-less 50 Ω transmission line terminated by the calibration short using the 7-term error correction model with two-tier xUOSM calibration for all synthetic switches in the switched single receiver with reference wave switch (SWR) test-set architecture using the double reflectometer test-set.

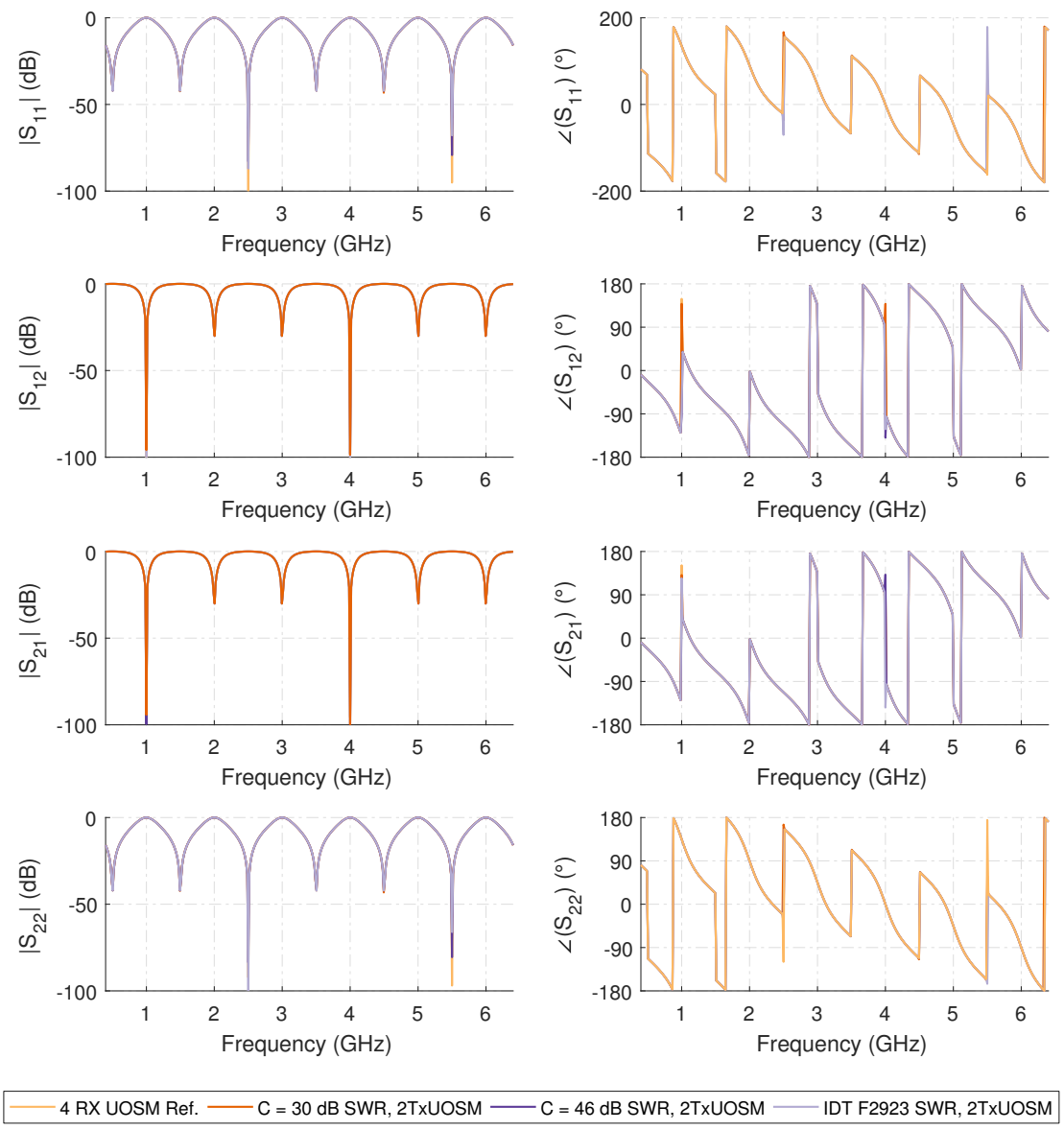

Figure A.64: Numerical 7-term error model with two-tier xUOSM calibration corrected measurement results of the 150 mm asymmetric reflective lossy tee measurement using no attenuation for the switched single receiver with reference wave switch (SWR) test-set architecture using the double reflectometer test-set.

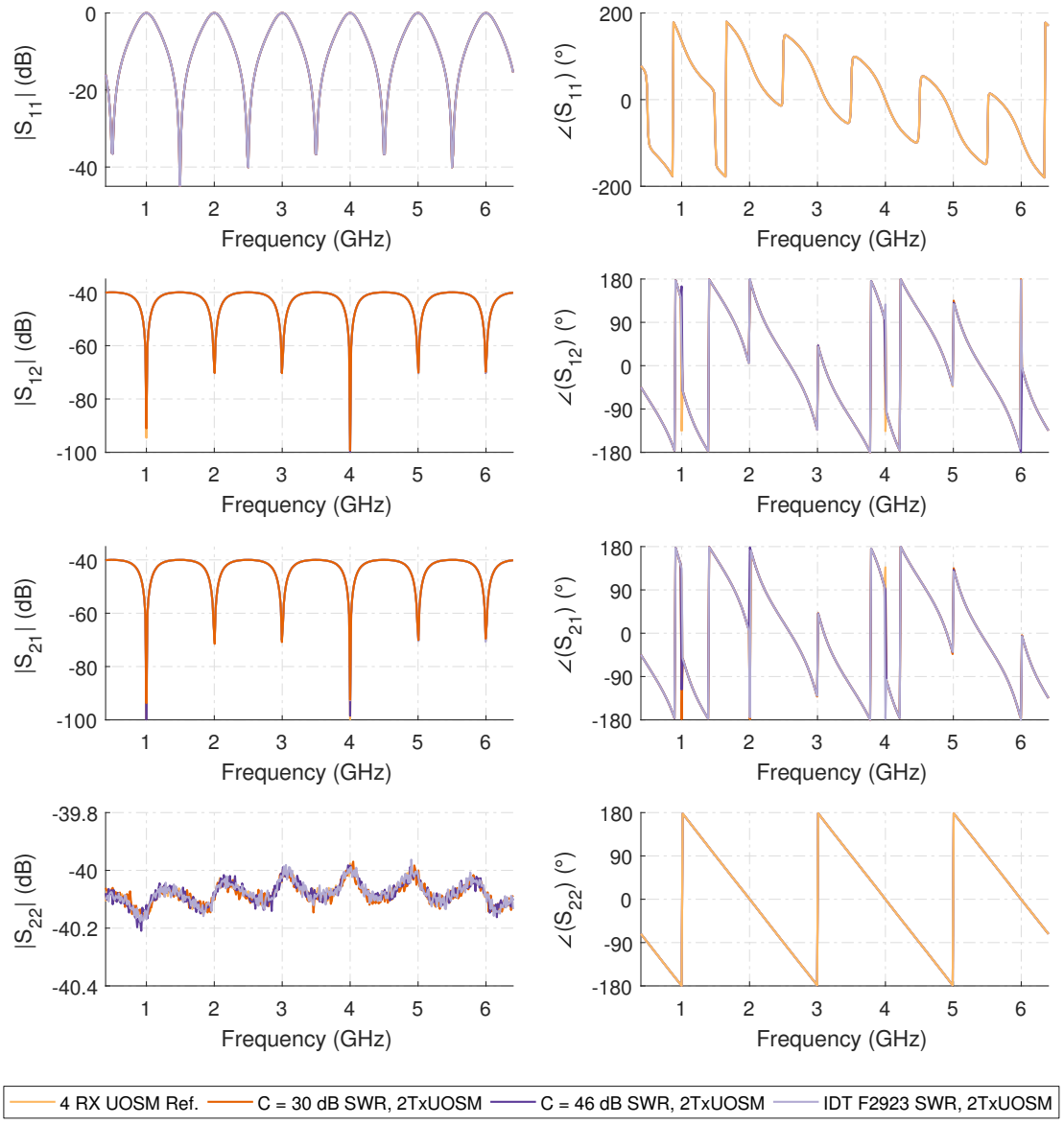

Figure A.65: Numerical 7-term error model with two-tier xUOSM calibration corrected measurement results of the 150 mm asymmetric reflective lossy tee measurement using 40 dB of attenuation for the switched single receiver with reference wave switch (SWR) test-set architecture using the double reflectometer test-set.

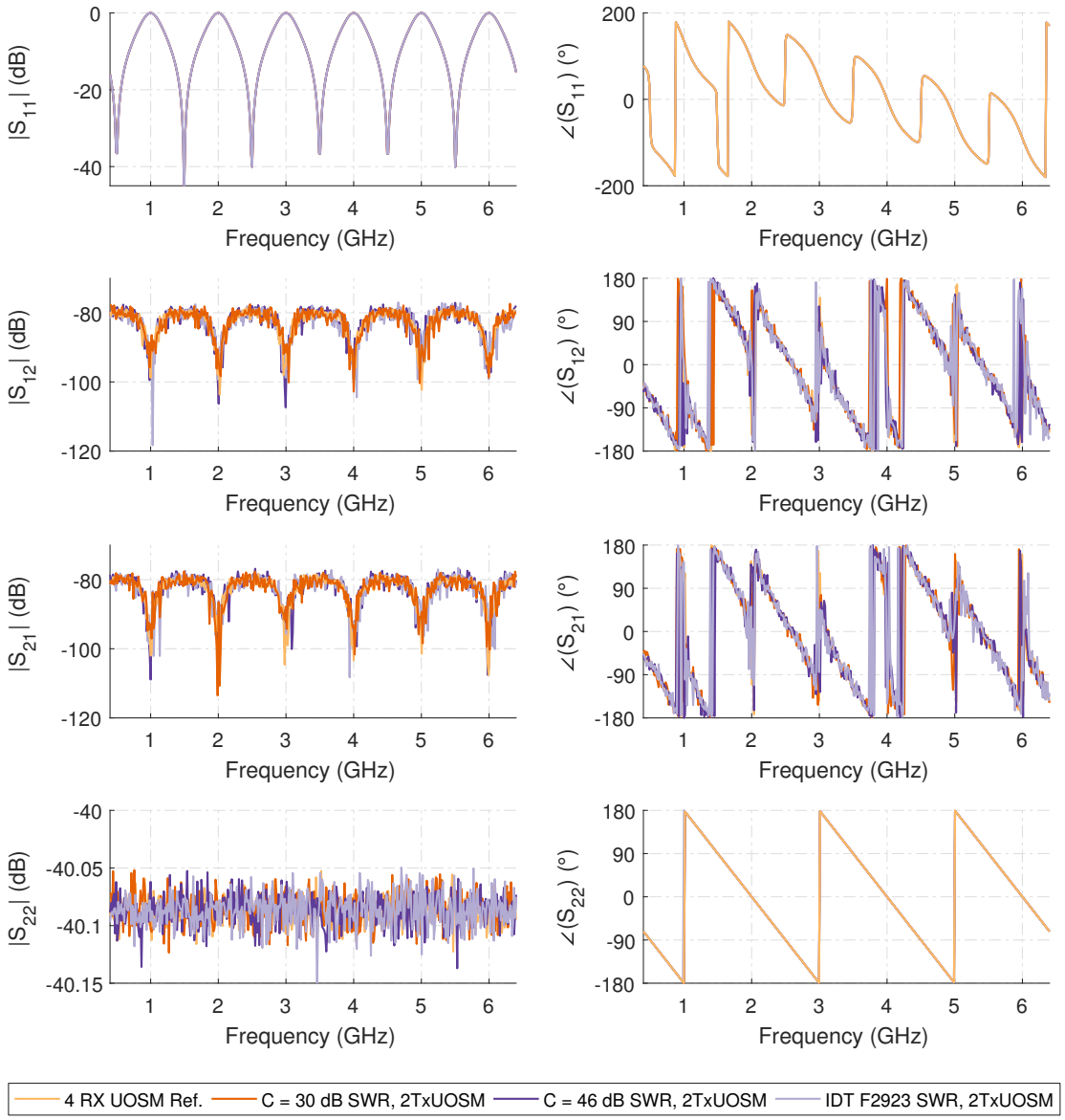

Figure A.66: Numerical 7-term error model with two-tier xUOSM calibration corrected measurement results of the 150 mm asymmetric reflective lossy tee measurement using 80 dB of attenuation for the switched single receiver with reference wave switch (SWR) test-set architecture using the double reflectometer test-set.

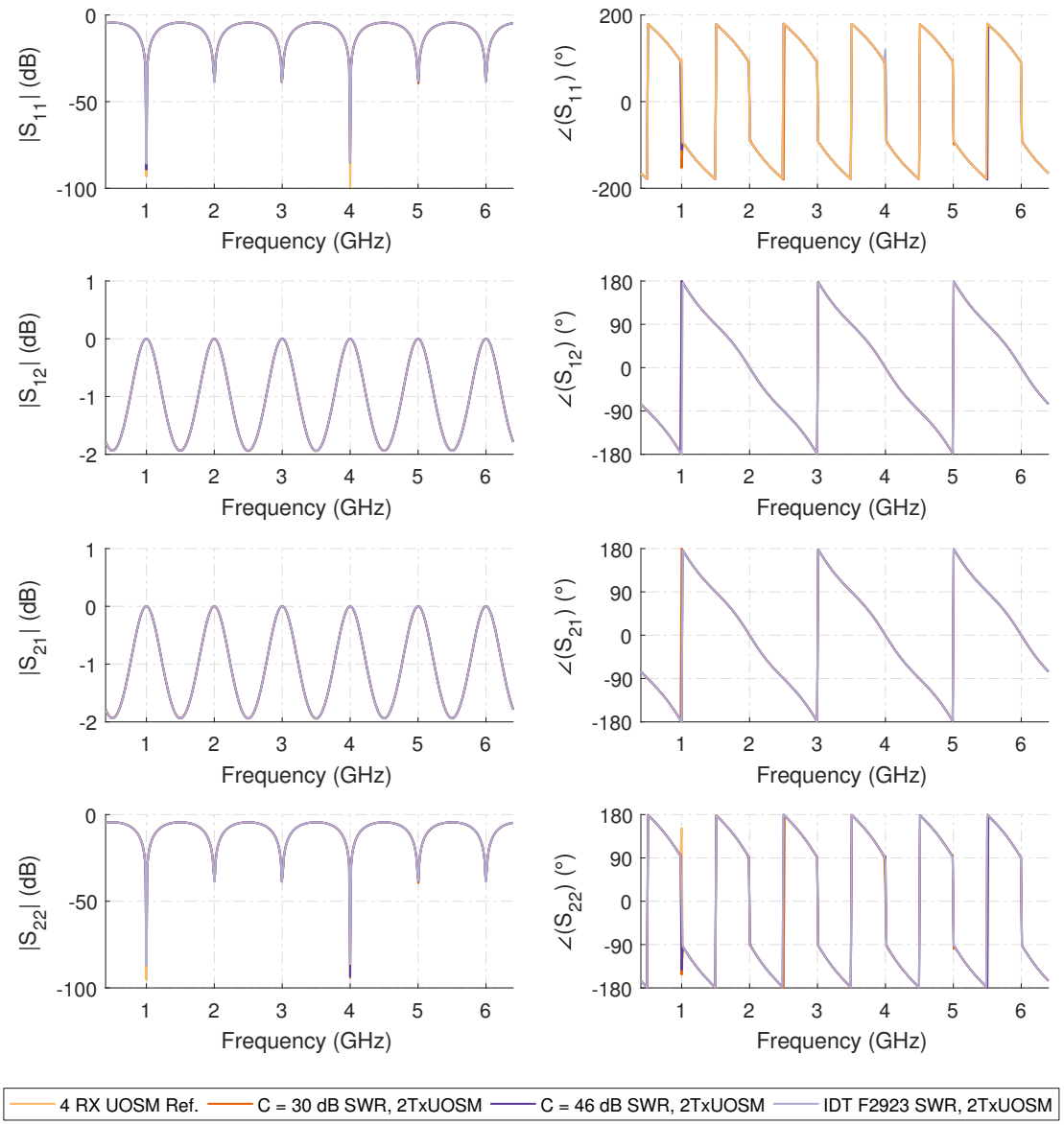

Figure A.67: Numerical 7-term error model with two-tier xUOSM calibration corrected results of a thru connection using a 150 mm loss-less 25 Ω transmission (or Beatty) line for the switched single receiver with reference wave switch (SWR) test-set architecture using the double reflectometer test-set.

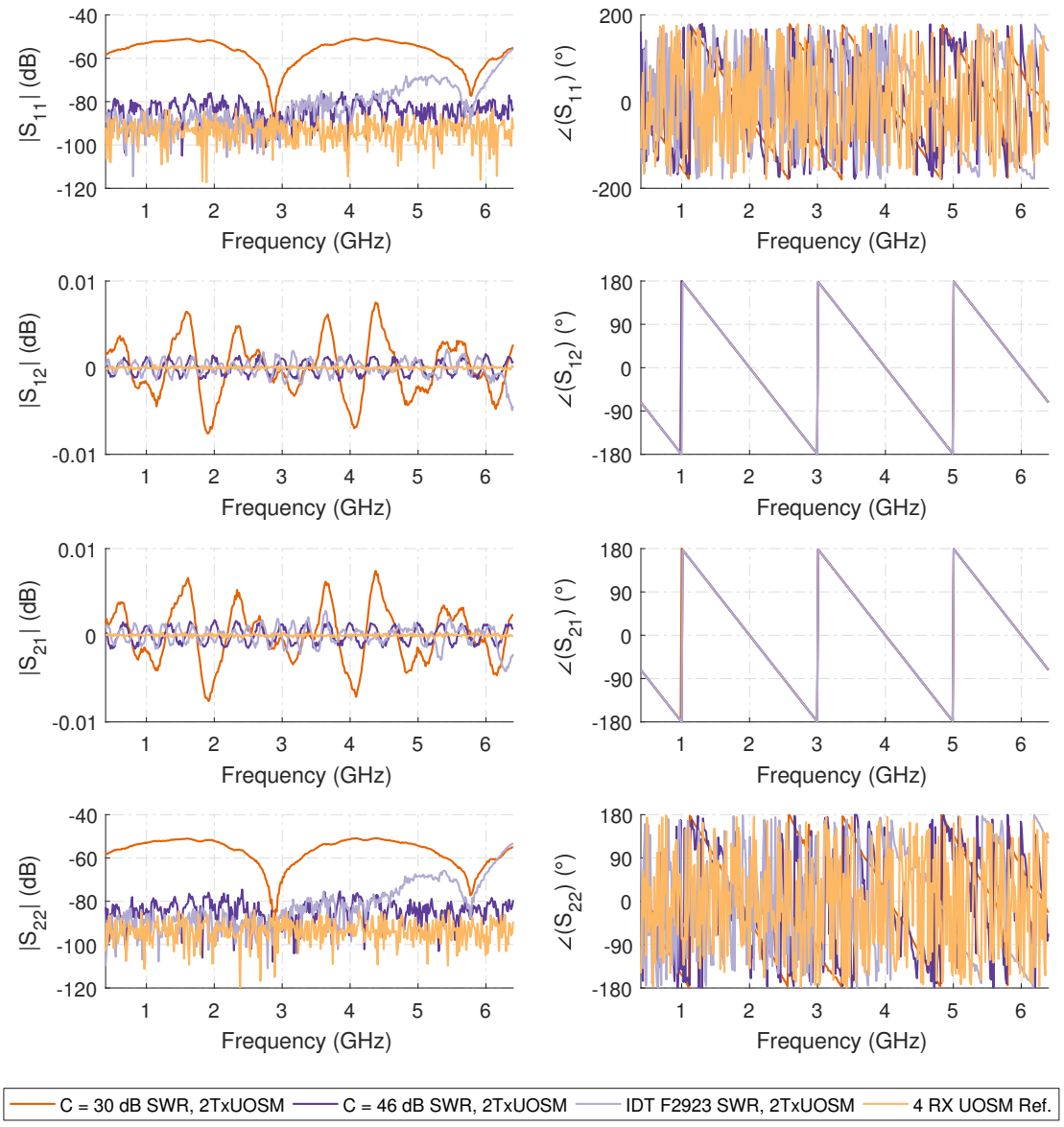

Figure A.68: Numerical 7-term error model with two-tier xUOSM calibration corrected results of a thru connection using a 150 mm loss-less 50 Ω transmission line for the switched single receiver with reference wave switch (SWR) test-set architecture using the double reflectometer test-set.

B Supplementary Single Switched Receiver VNA Hardware Architectures Measurement Results

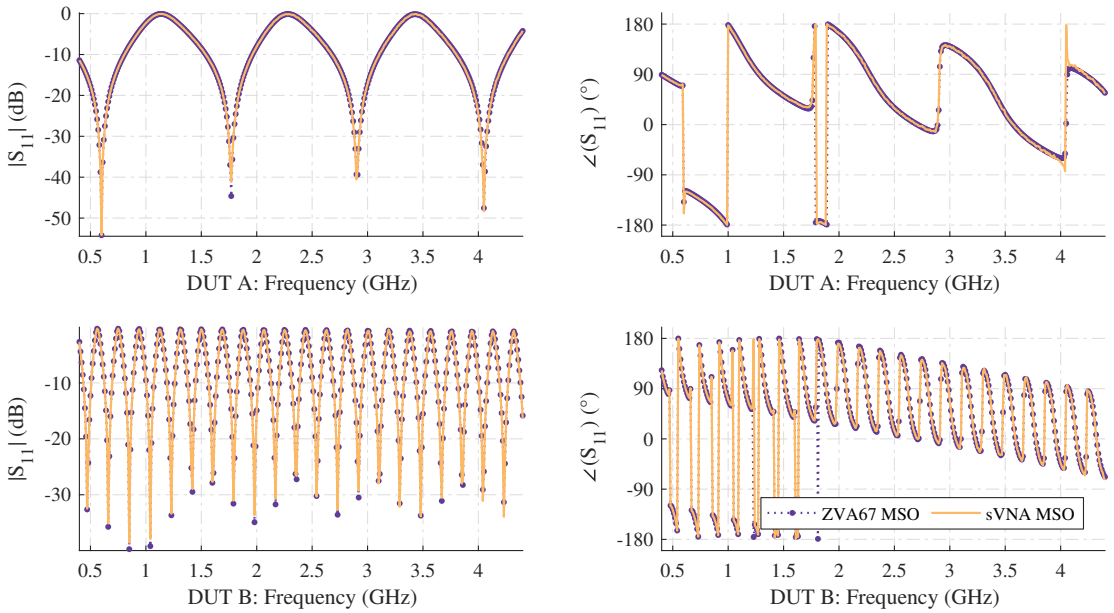

Figure B.1: Measurement results for the tee, terminated at one port by the calibration match and at the second port with different lines terminated by the calibration short, corrected with the 3-term model with the reflectometer sVNA setup. DUT A: 150 mm $Z_L = 50\,\Omega$ bead-less airline stub. DUT B: Rosenberger 600 mm RPC-N VNA test-cable stub.

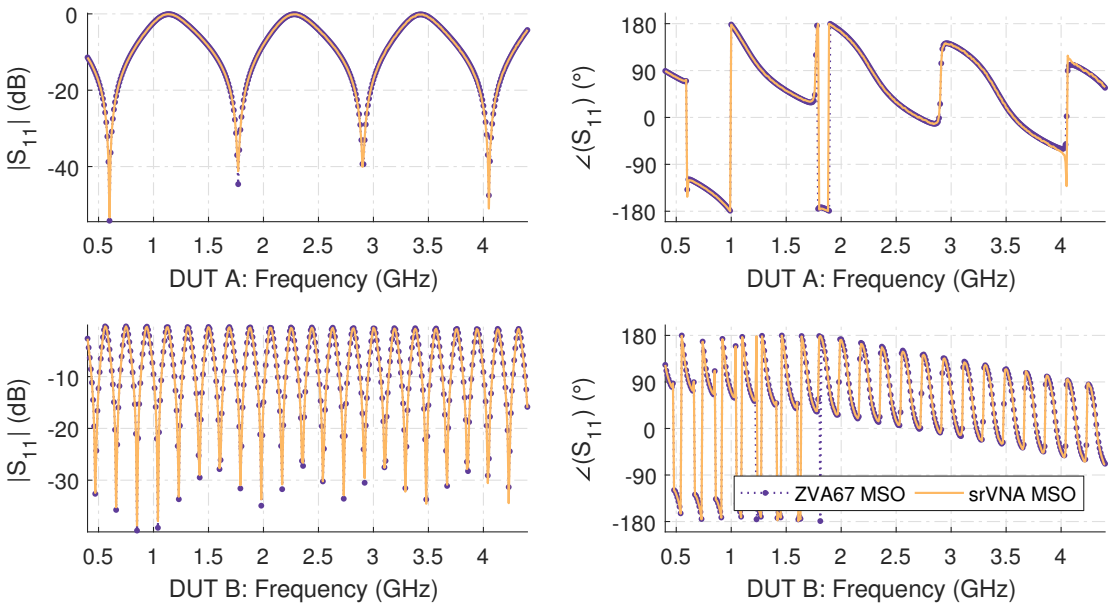

Figure B.2: Measurement results for the tee, terminated at one port by the calibration match and at the second port with different lines terminated by the calibration short, corrected with the 3-term model with the reflectometer srVNA setup. DUT A: 150 mm $Z_L = 50\,\Omega$ bead-less airline stub. DUT B: Rosenberger 600 mm RPC-N VNA test-cable stub.

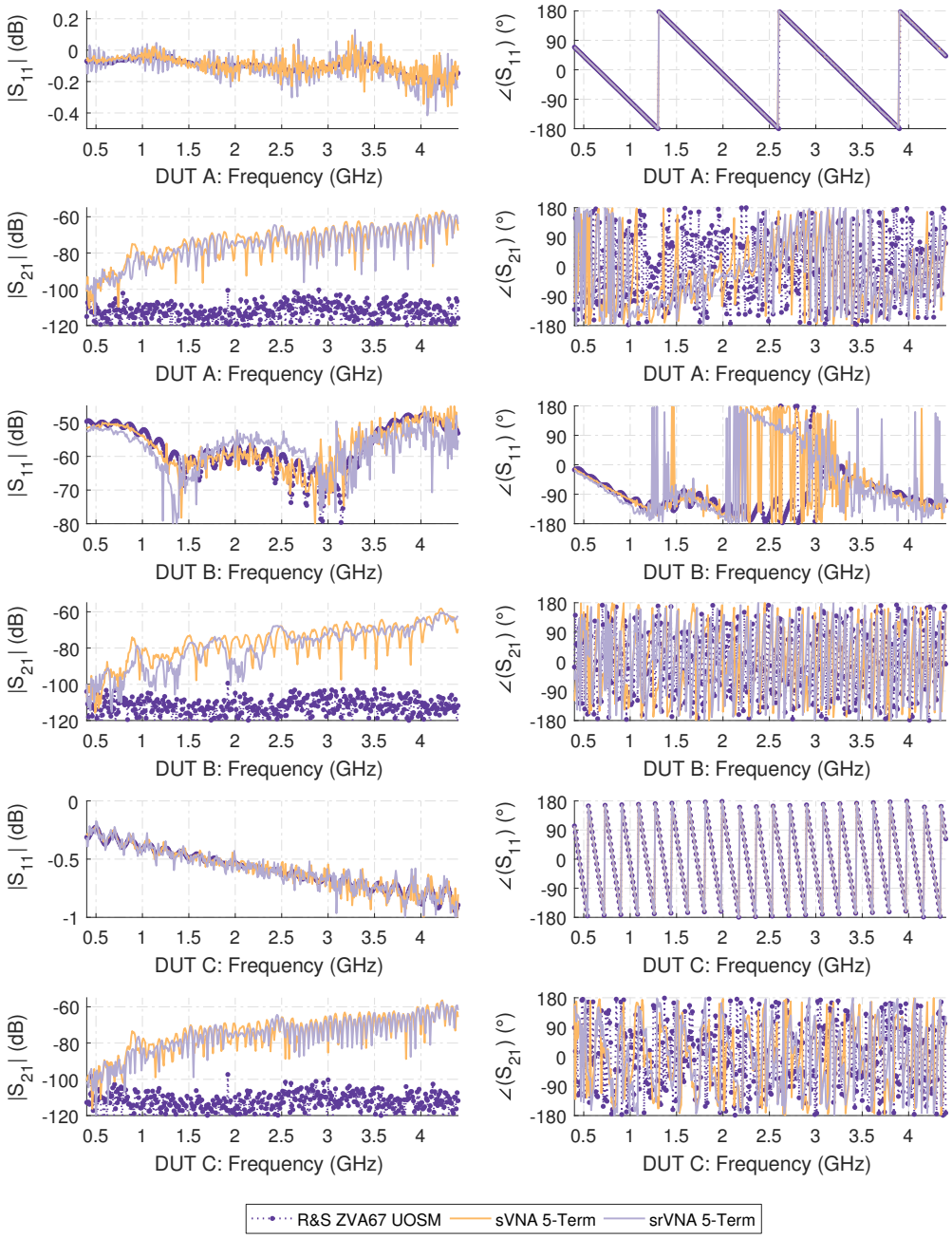

Figure B.3: Measurement results for the ripple test and residual directivity measurements corrected by the 5-term error model for both the sVNA and srVNA unidirectional test-set setup. DUT A: 150 mm $Z_L = 50\,\Omega$ bead-less airline terminated by the calibration short. DUT B: 150 mm $Z_L = 50\,\Omega$ bead-less airline terminated by the calibration match. DUT C: Rosenberger 600 mm RPC-N VNA test-cable terminated by the calibration short.

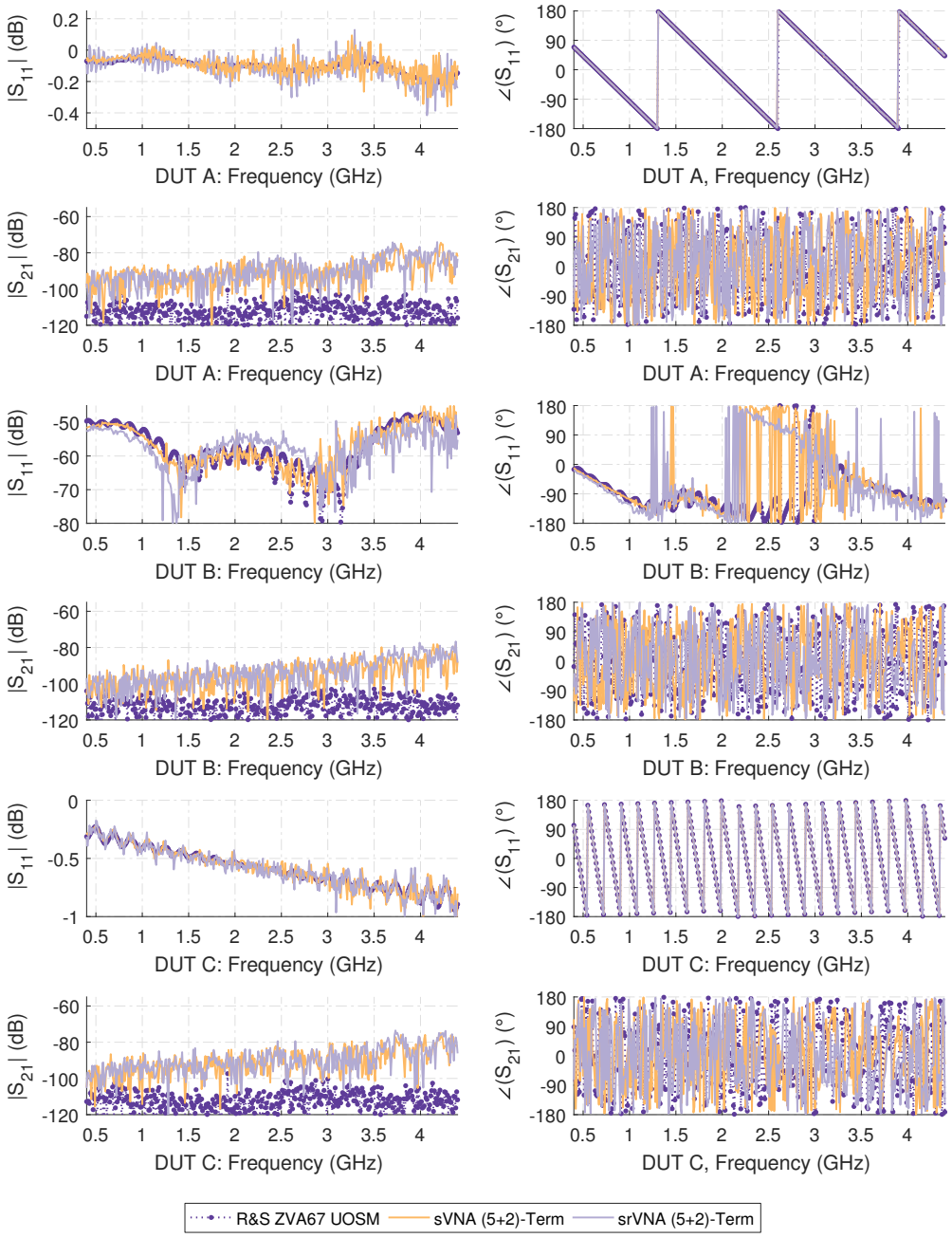

Figure B.4: Measurement results for the ripple test and residual directivity measurements corrected by the (5+2)-term error model for both the sVNA and srVNA unidirectional test-set setup. DUT A: 150 mm $Z_L = 50\,\Omega$ bead-less airline terminated by the calibration short. DUT B: 150 mm $Z_L = 50\,\Omega$ bead-less airline terminated by the calibration match. DUT C: Rosenberger 600 mm RPC-N VNA test-cable terminated by the calibration short.

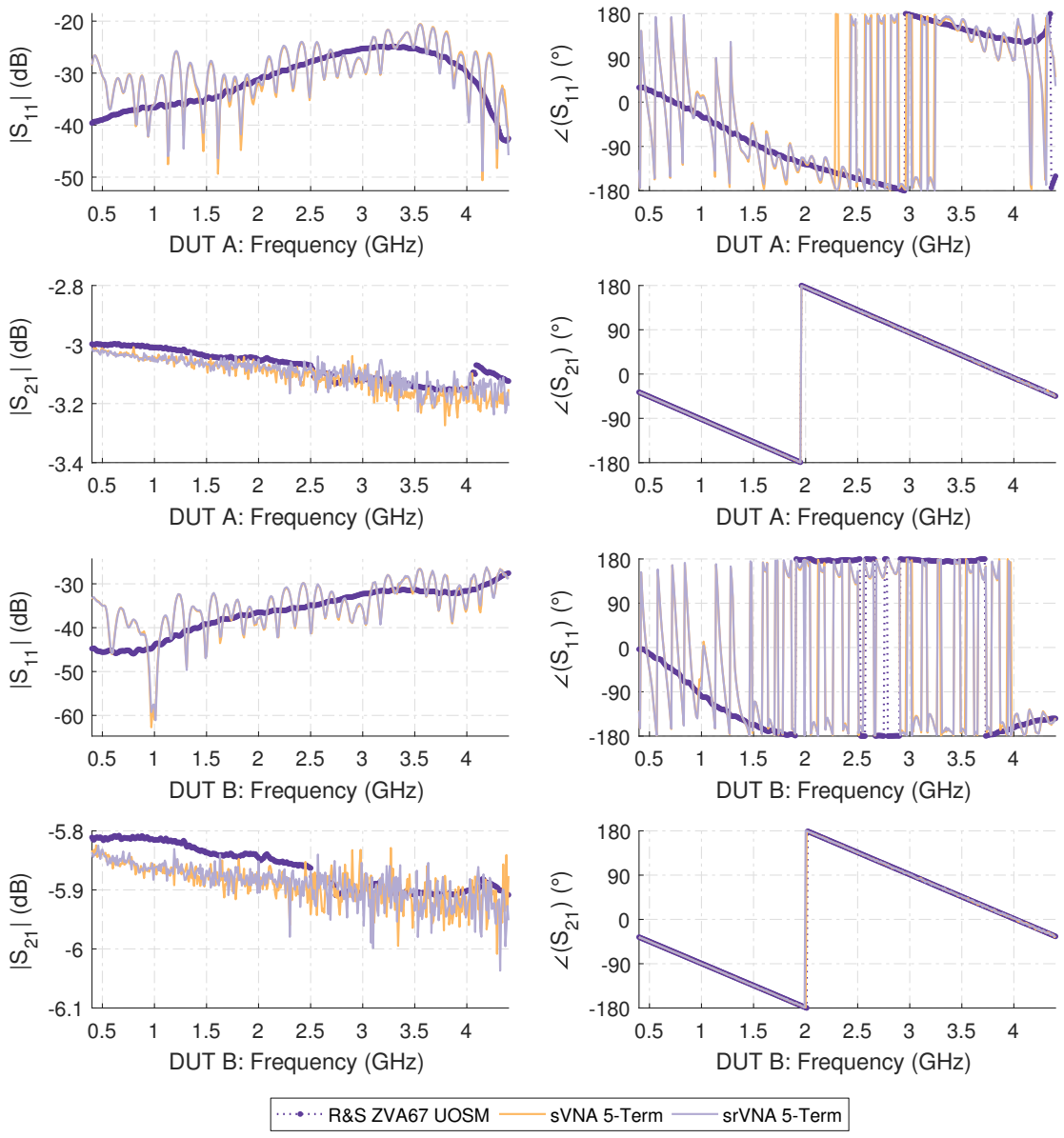

Figure B.5: Measurement results for the 3 dB and 6 dB attenuator measurements corrected by the 5-term error model for the sVNA and srVNA unidirectional test-set setup. DUT A: 3 dB SMA attenuator with RPC-N SMA adapter. DUT B: 6 dB SMA attenuator with RPC-N SMA adapter.

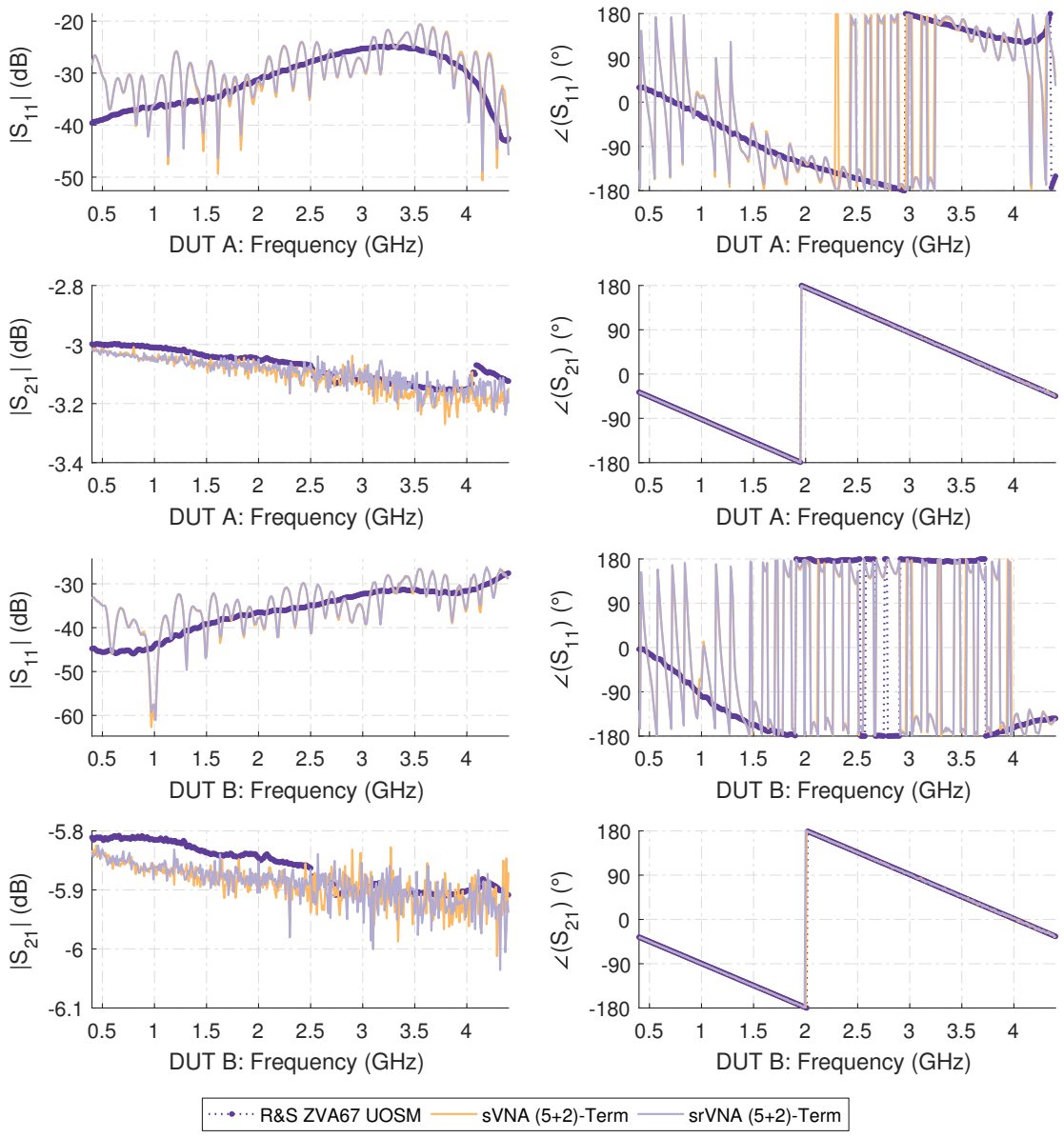

Figure B.6: Measurement results for the 3 dB and 6 dB attenuator measurements corrected by the (5+2)-term error model for the sVNA and srVNA unidirectional test-set setup. DUT A: 3 dB SMA attenuator with RPC-N SMA adapter. DUT B: 6 dB SMA attenuator with RPC-N SMA adapter.

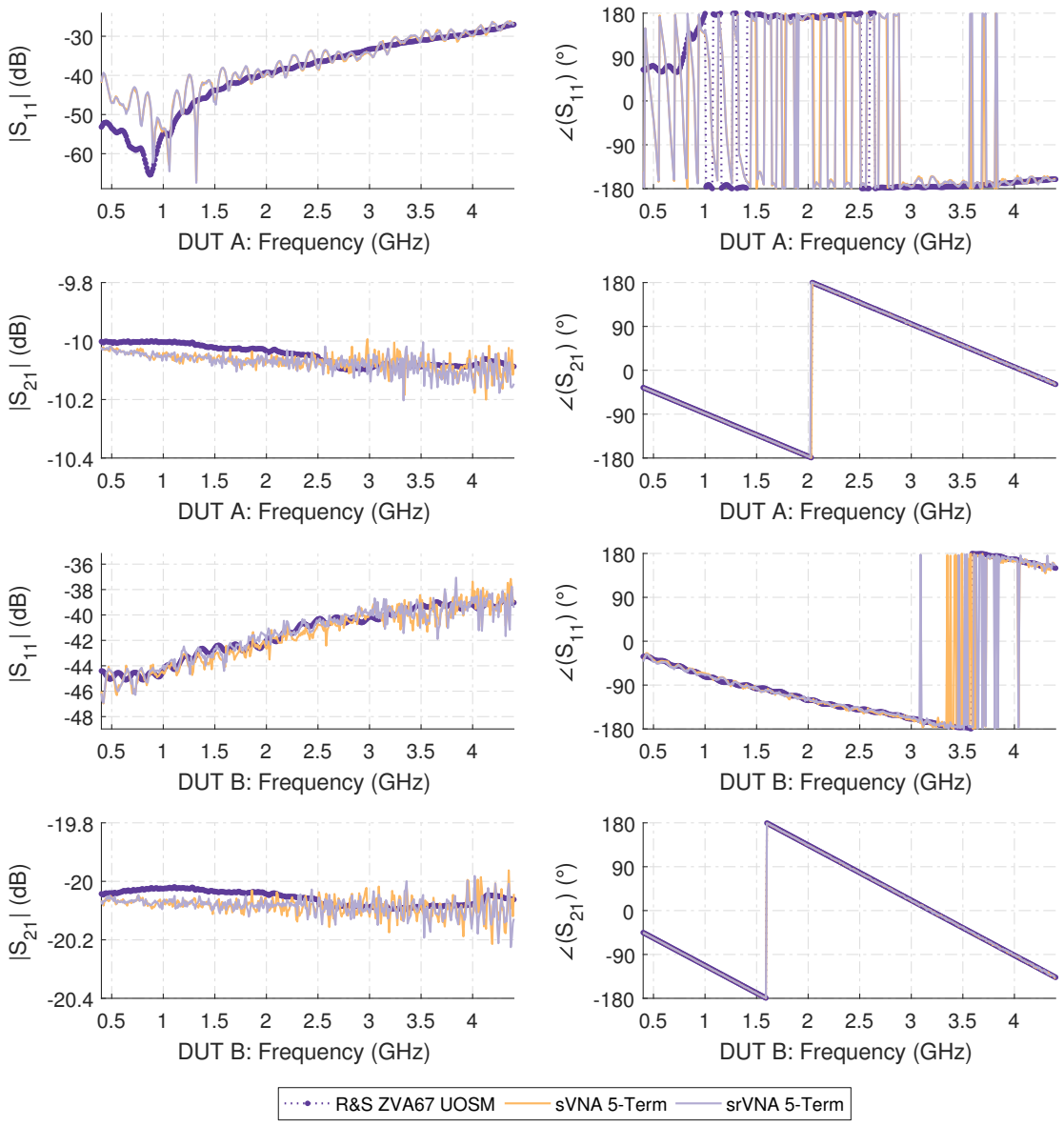

Figure B.7: Measurement results for the 10 dB SMA and 20 dB reference attenuator measurements corrected by the 5-term error model for the sVNA and srVNA unidirectional test-set setup. DUT A: 10 dB SMA attenuator with RPC-N SMA adapter. DUT B: 20 dB Rosenberger RPC-N reference attenuator with RPC-N (f)-(f) calibration thru.

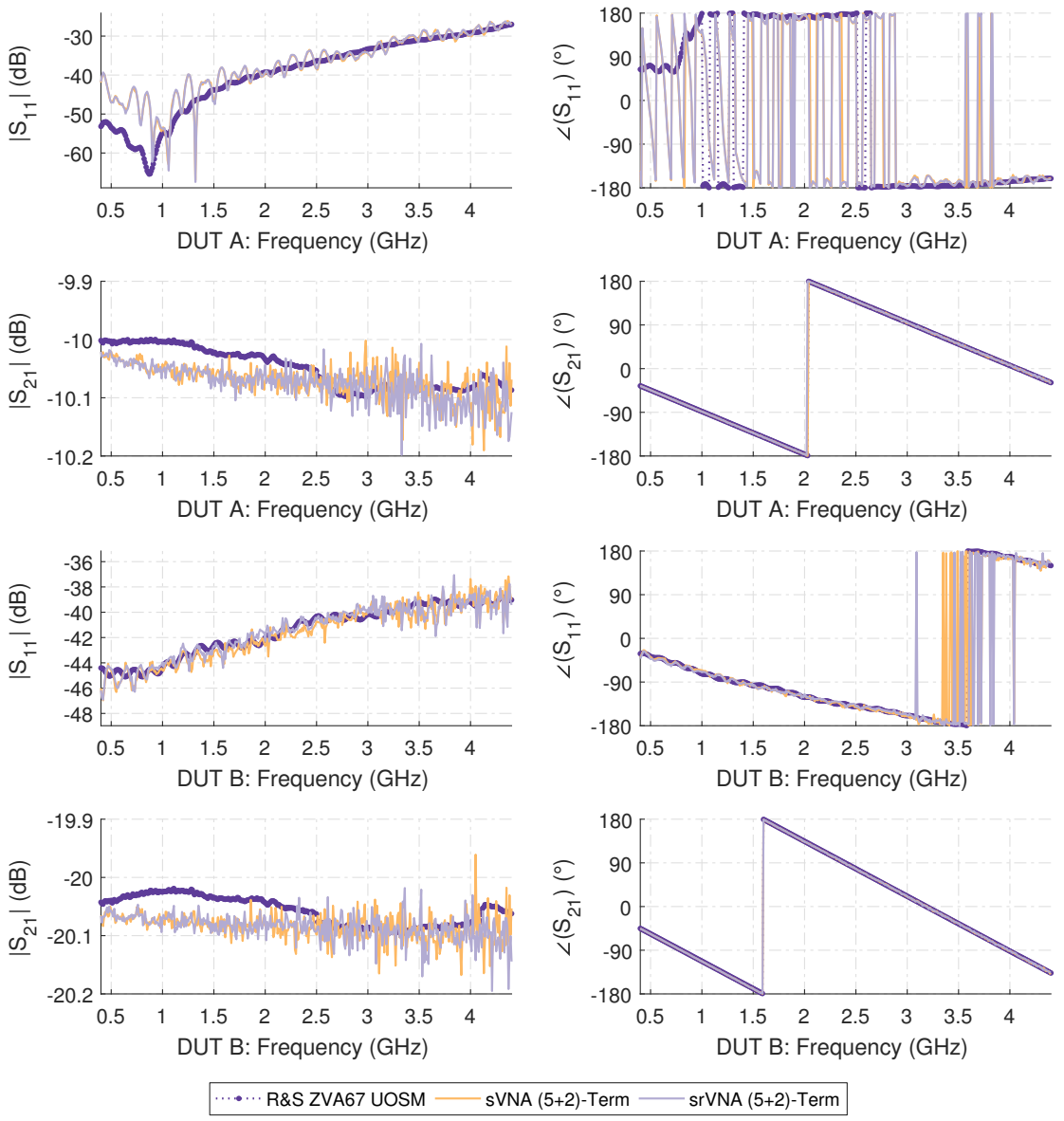

Figure B.8: Measurement results for the 10 dB SMA and 20 dB reference attenuator measurements corrected by the (5+2)-term error model for the sVNA and srVNA unidirectional test-set setup. DUT A: 10 dB SMA attenuator with RPC-N SMA adapter. DUT B: 20 dB Rosenberger RPC-N reference attenuator with RPC-N (f)-(f) calibration thru.

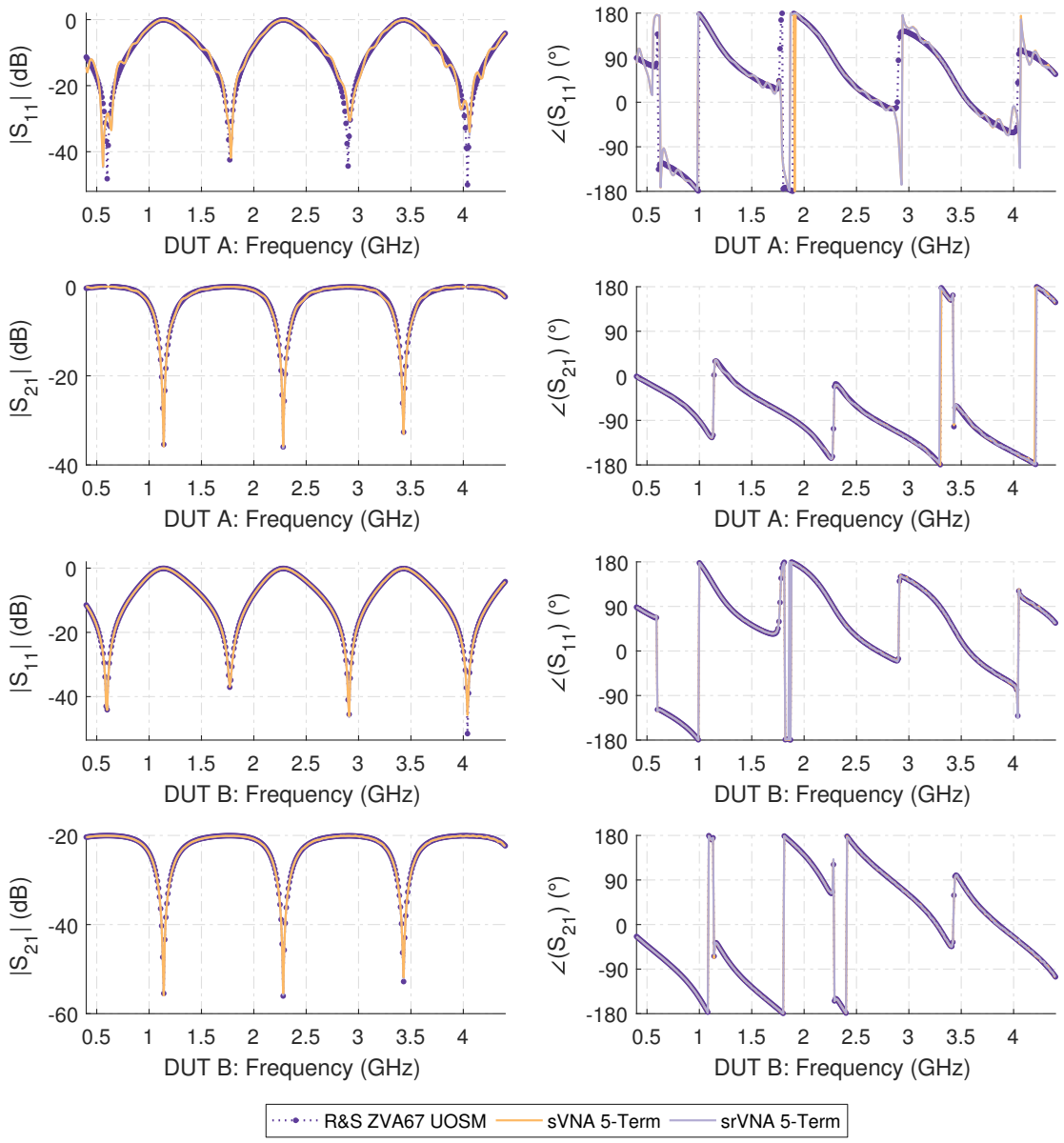

Figure B.9: Measurement results of the asymmetric reflective lossy tee (ARLT) with different attenuation values, corrected by the 5-term error model for both the sVNA and srVNA unidirectional test-set setups. DUT A: ARLT with 0 dB of attenuation. DUT B: ARLT with 20 dB of attenuation.

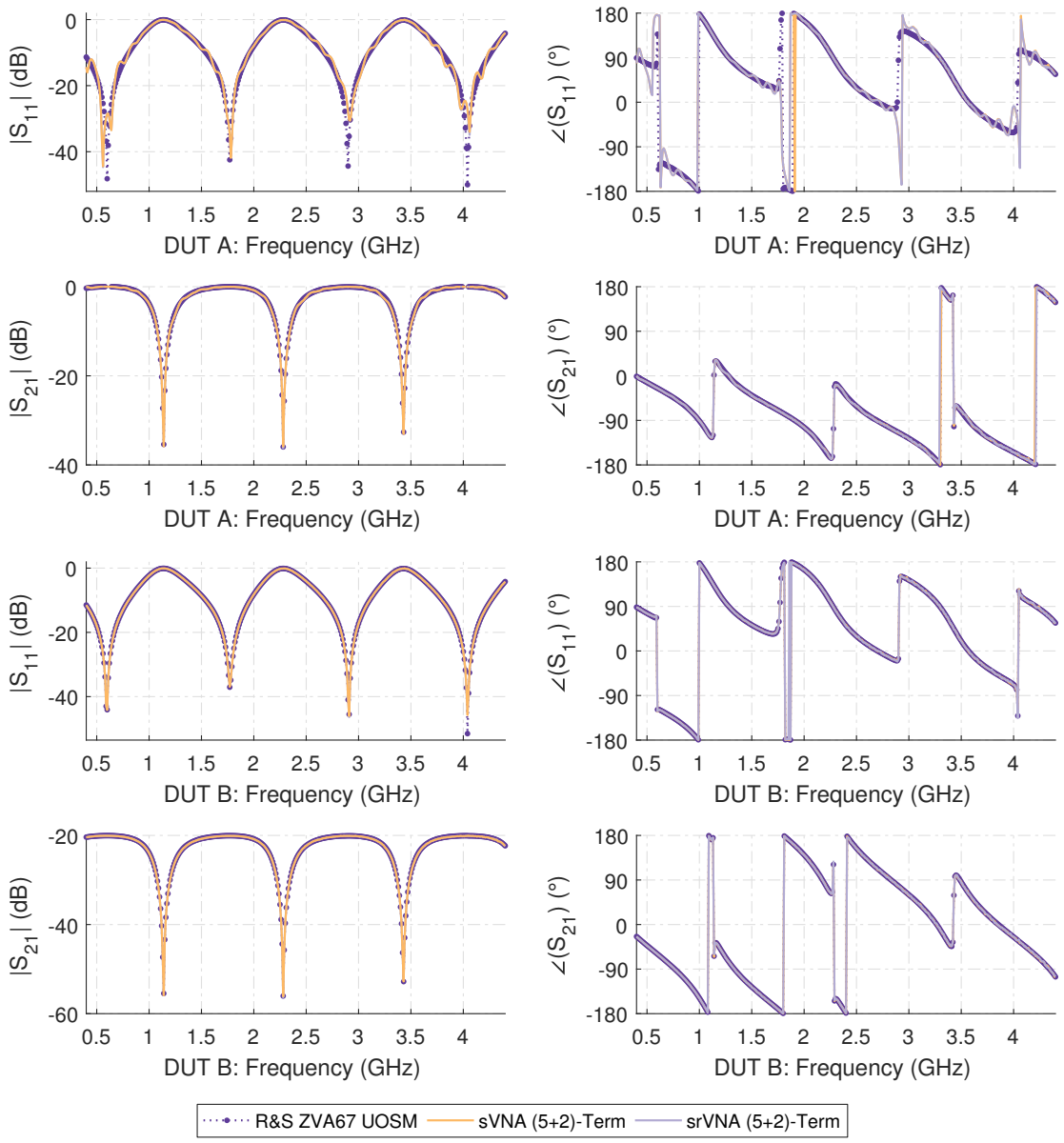

Figure B.10: Measurement results of the asymmetric reflective lossy tee (ARLT) with different attenuation values, corrected by the (5+2)-term error model for both the sVNA and srVNA unidirectional test-set setups. DUT A: ARLT with 0 dB of attenuation. DUT B: ARLT with 20 dB of attenuation.

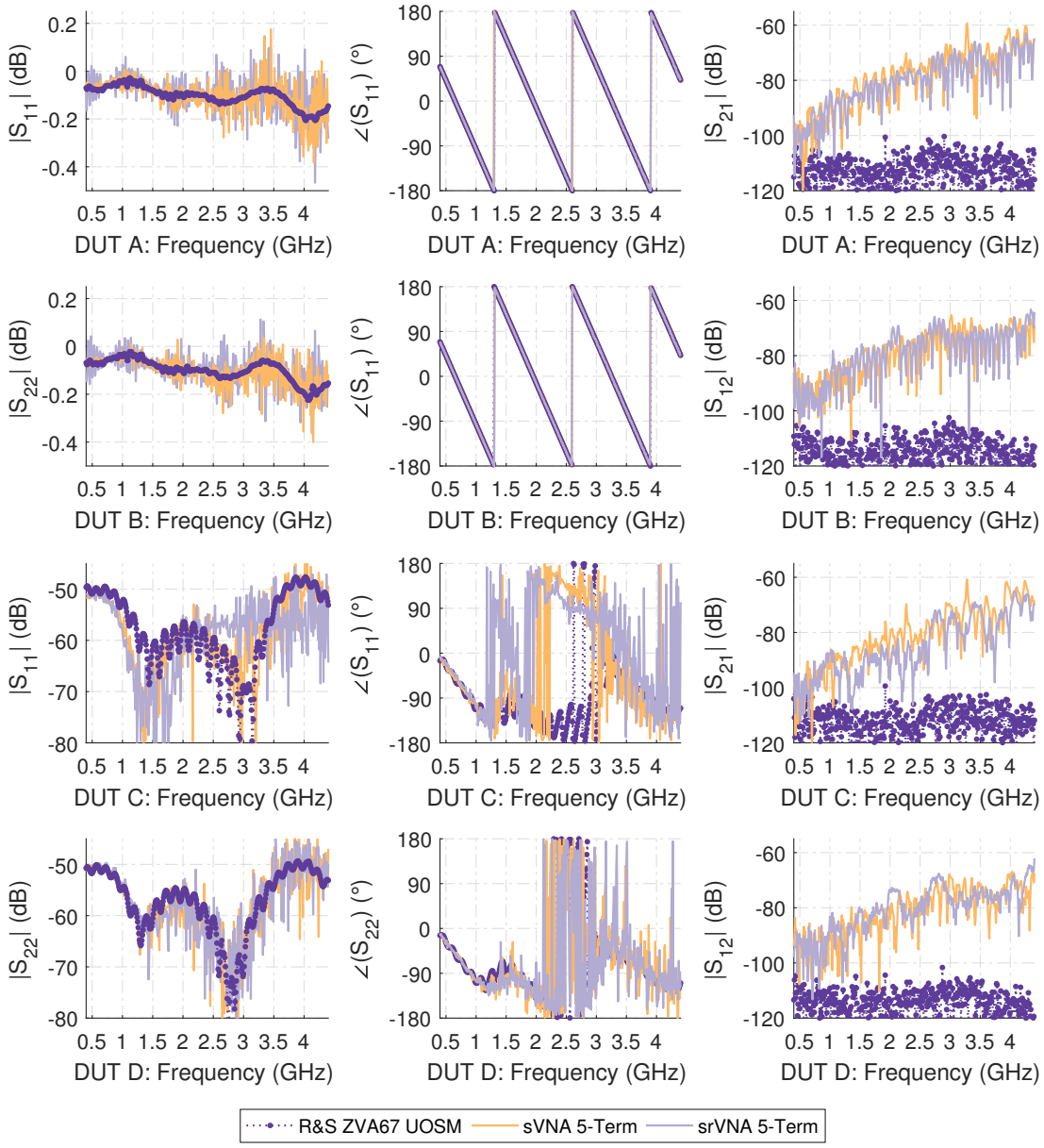

Figure B.11: Measurement results for the ripple test and residual directivity measurements corrected by the 10-term error model for both the sVNA and srVNA double reflectometer test-set setup. DUT A: Port 1, 150 mm $Z_L = 50\,\Omega$ bead-less airline terminated by the calibration short. DUT B: Port 2, 150 mm $Z_L = 50\,\Omega$ bead-less airline terminated by the calibration short. DUT C: Port 1, 150 mm $Z_L = 50\,\Omega$ bead-less airline terminated by the calibration match. DUT D: Port 2, 150 mm $Z_L = 50\,\Omega$ bead-less airline terminated by the calibration match.

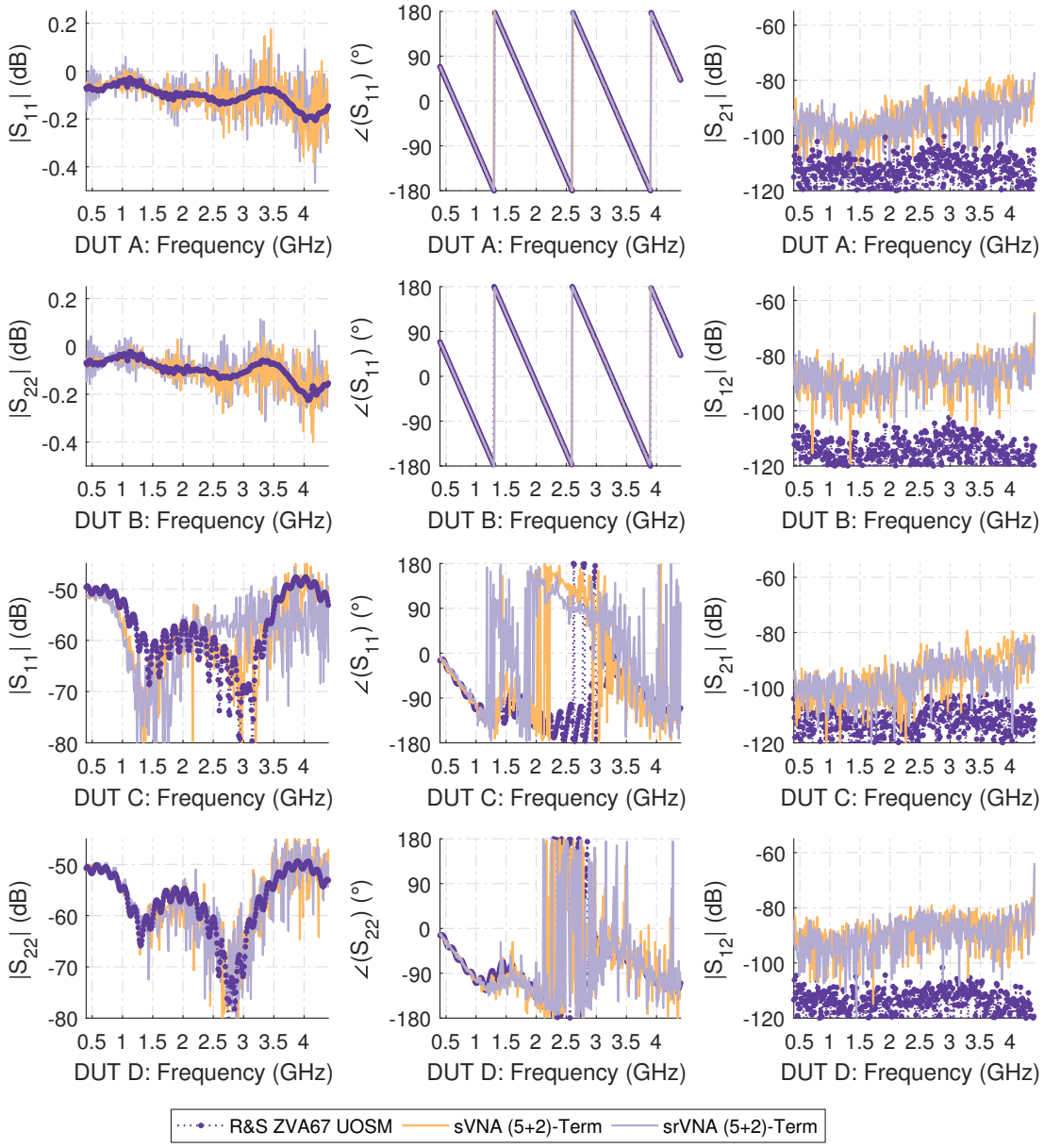

Figure B.12: Measurement results for the ripple test and residual directivity measurements corrected by the (10+4)-term error model for both the sVNA and srVNA double reflectometer test-set setup. DUT A: Port 1, 150 mm $Z_L = 50\,\Omega$ bead-less airline terminated by the calibration short. DUT B: Port 2, 150 mm $Z_L = 50\,\Omega$ bead-less airline terminated by the calibration short. DUT C: Port 1, 150 mm $Z_L = 50\,\Omega$ bead-less airline terminated by the calibration match. DUT D: Port 2, 150 mm $Z_L = 50\,\Omega$ bead-less airline terminated by the calibration match.

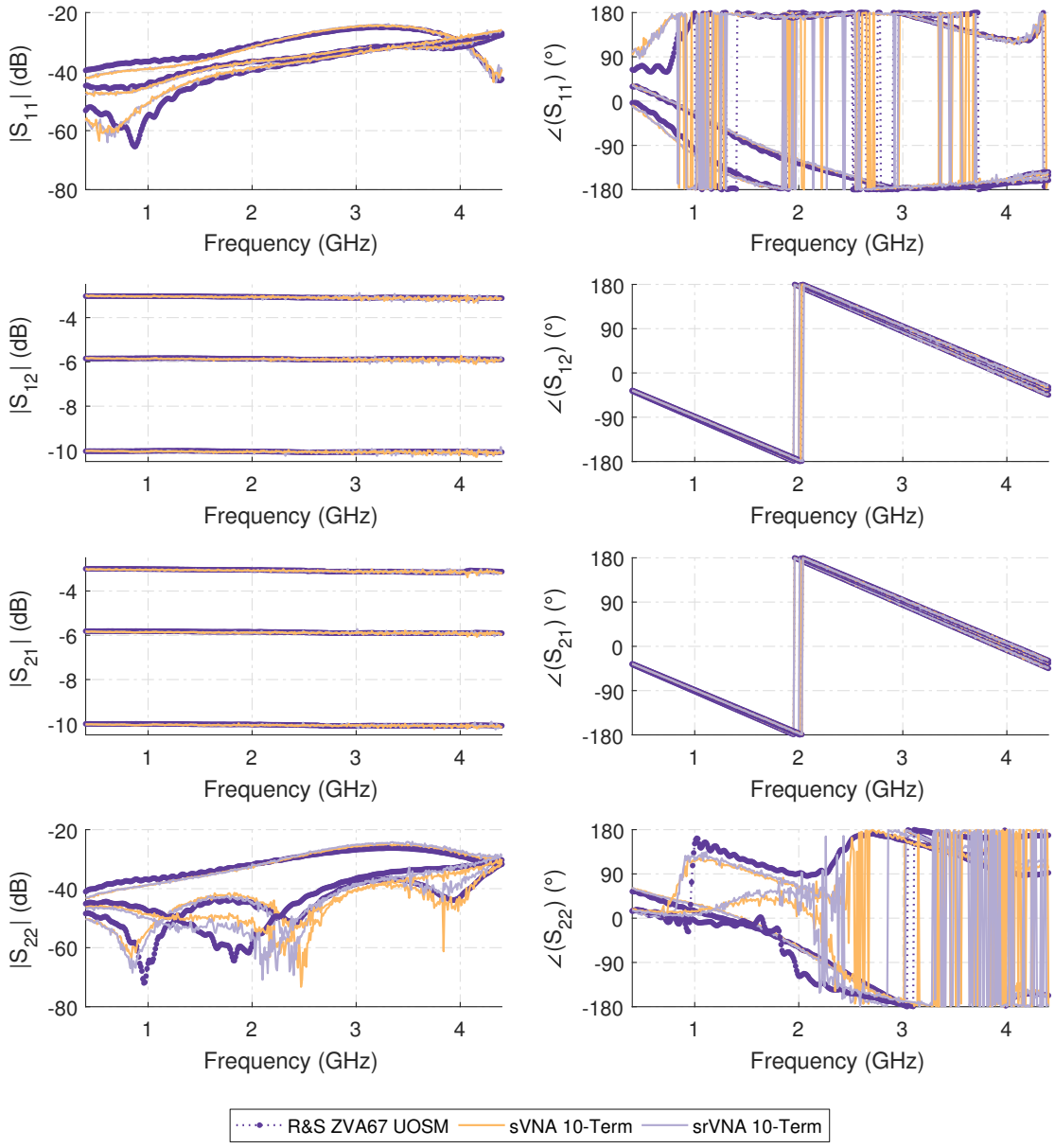

Figure B.13: Measurement results of the 3 dB, 6 dB and 10 dB attenuators with their corresponding Rosenberger RPC-N SMA adapter corrected by the 10-term procedure for both the sVNA and the srVNA double reflectometer test-sets.

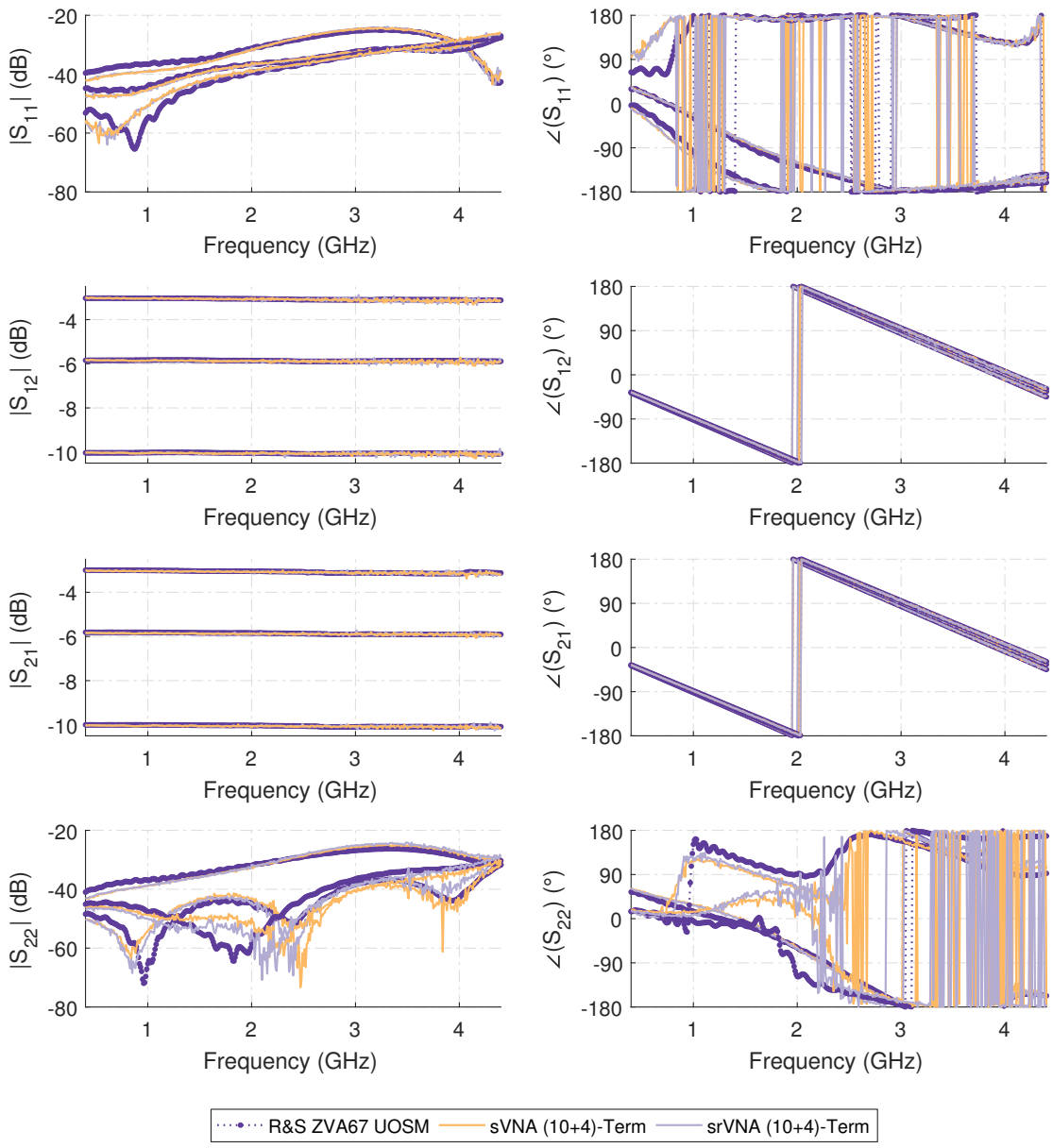

Figure B.14: Measurement results of the 3 dB, 6 dB and 10 dB attenuators with their corresponding Rosenberger RPC-N SMA adapter corrected by the (10+4)-term procedure for both the sVNA and the srVNA double reflectometer test-sets.

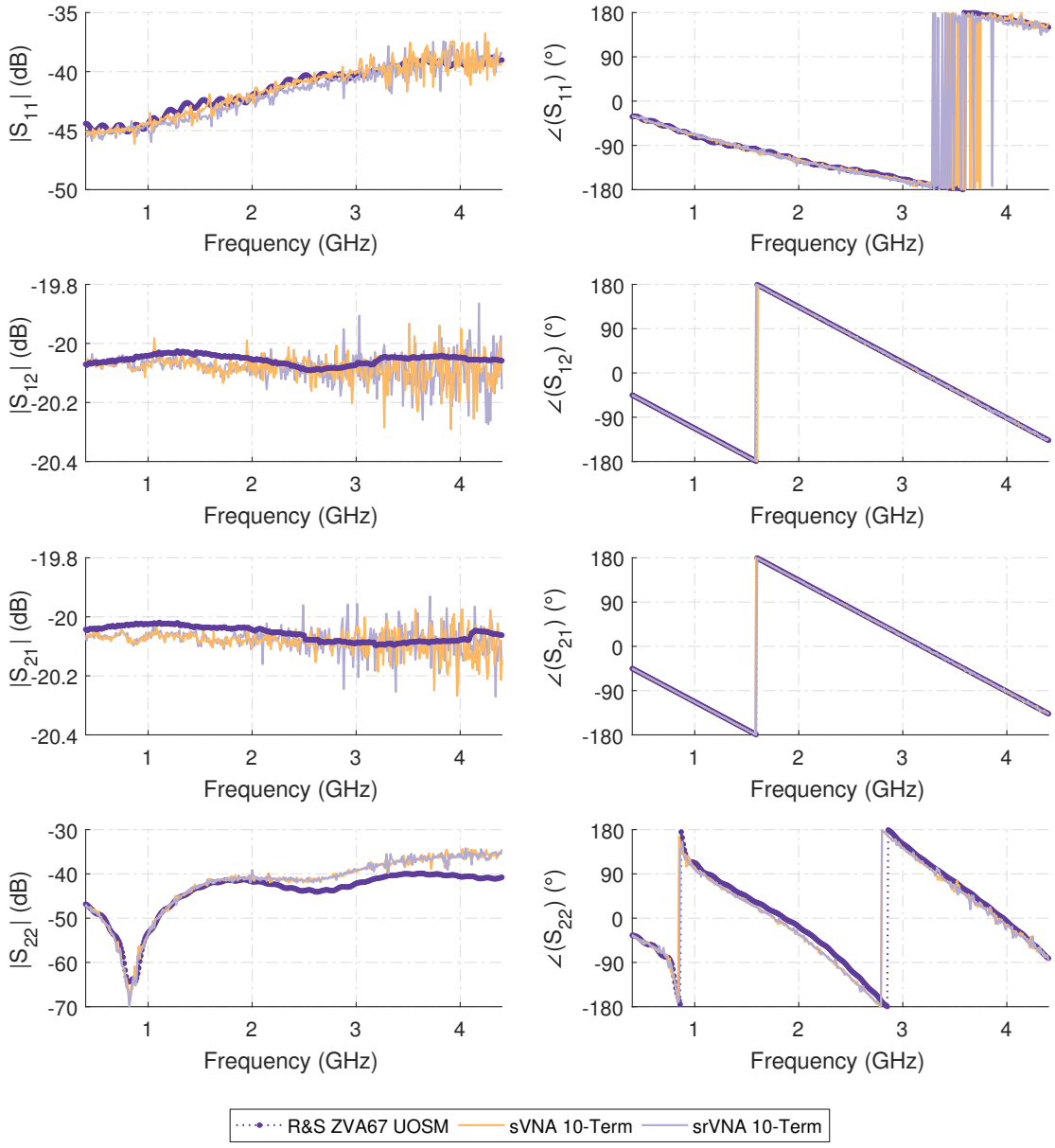

Figure B.15: Measurement results of the 20 dB reference attenuator with the additional Rosenberger RPC-N (f)-(f) calibration thru corrected by the 10-term procedure for both the sVNA and the srVNA double reflectometer test-sets.

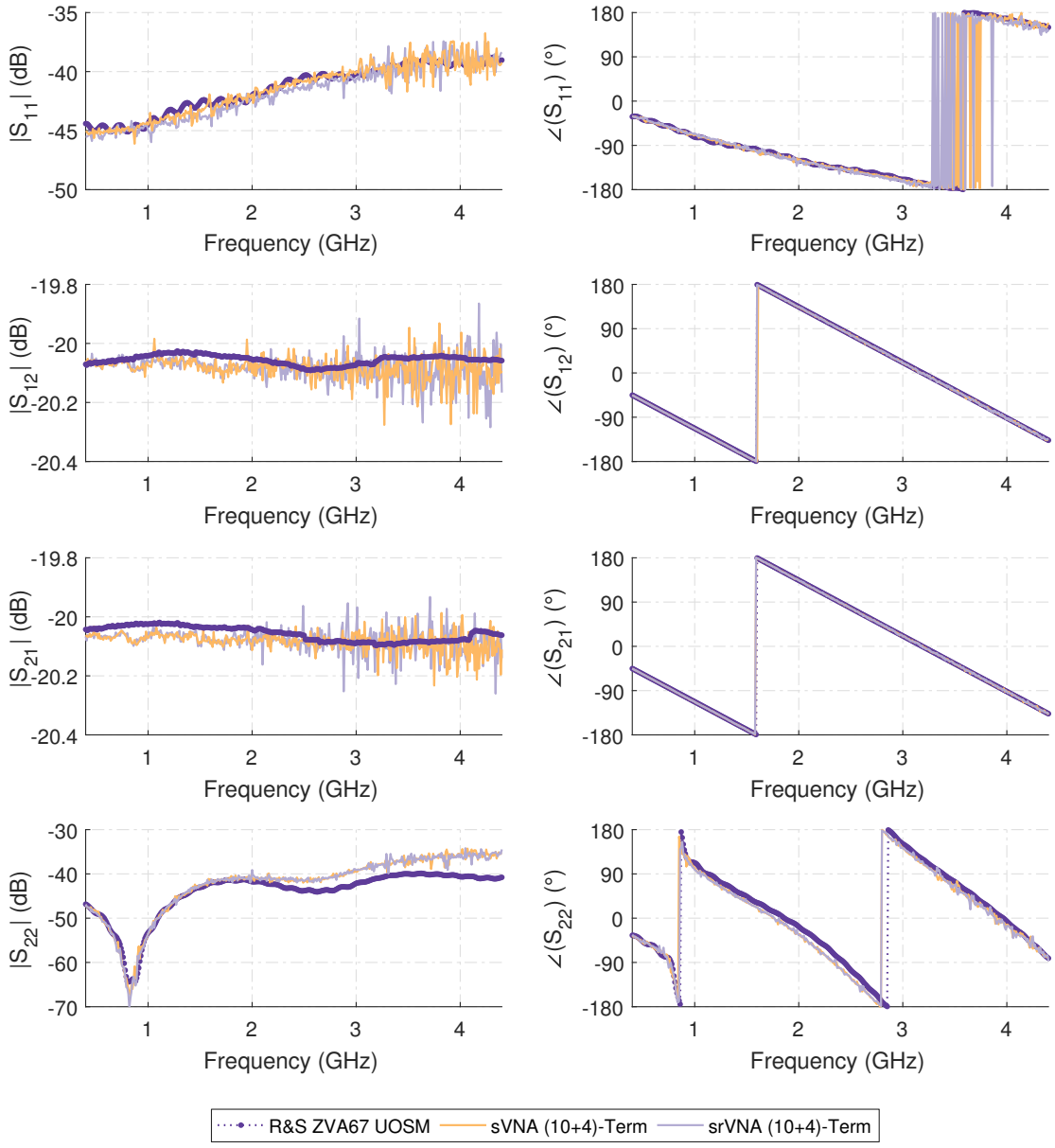

Figure B.16: Measurement results of the 20 dB reference attenuator with the additional Rosenberger RPC-N (f)-(f) calibration thru corrected by the (10+4)-term procedure for both the sVNA and the srVNA double reflectometer test-sets.

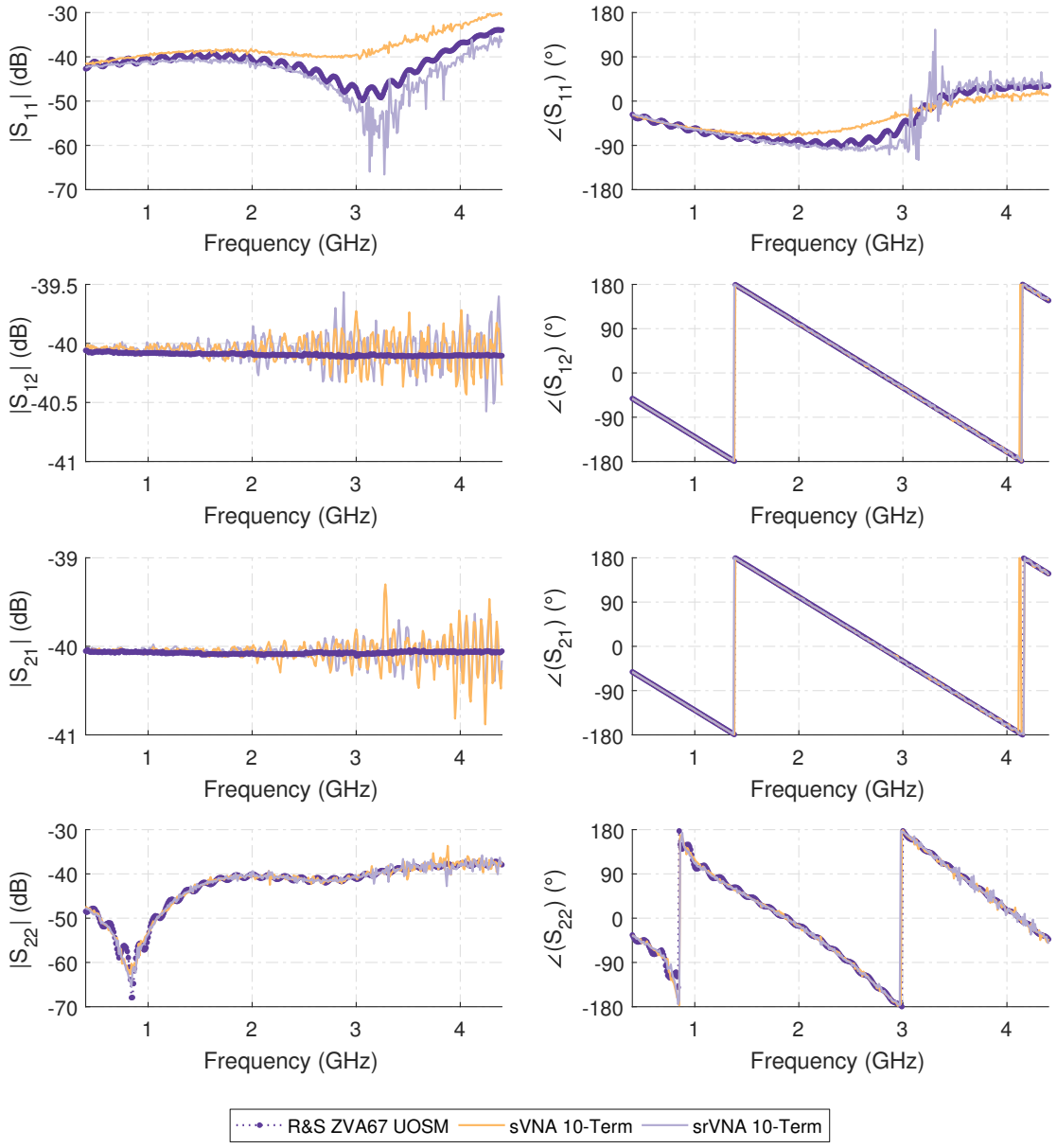

Figure B.17: Measurement results of the 40 dB reference attenuator with the additional Rosenberger RPC-N (f)-(f) calibration thru corrected by the 10-term procedure for both the sVNA and the srVNA double reflectometer test-sets.

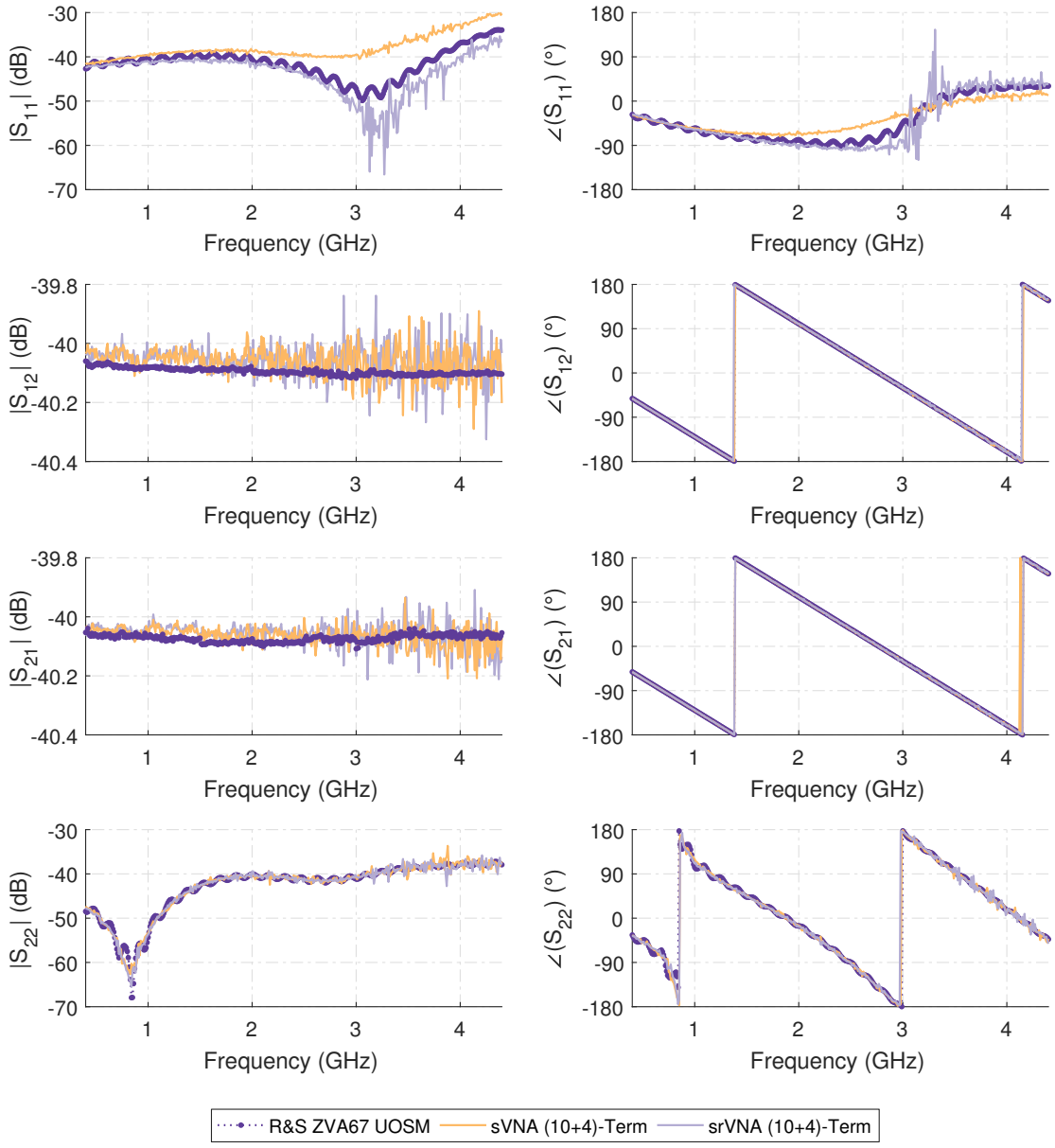

Figure B.18: Measurement results of the 40 dB reference attenuator with the additional Rosenberger RPC-N (f)-(f) calibration thru corrected by the (10+4)-term procedure for both the sVNA and the srVNA double reflectometer test-sets.

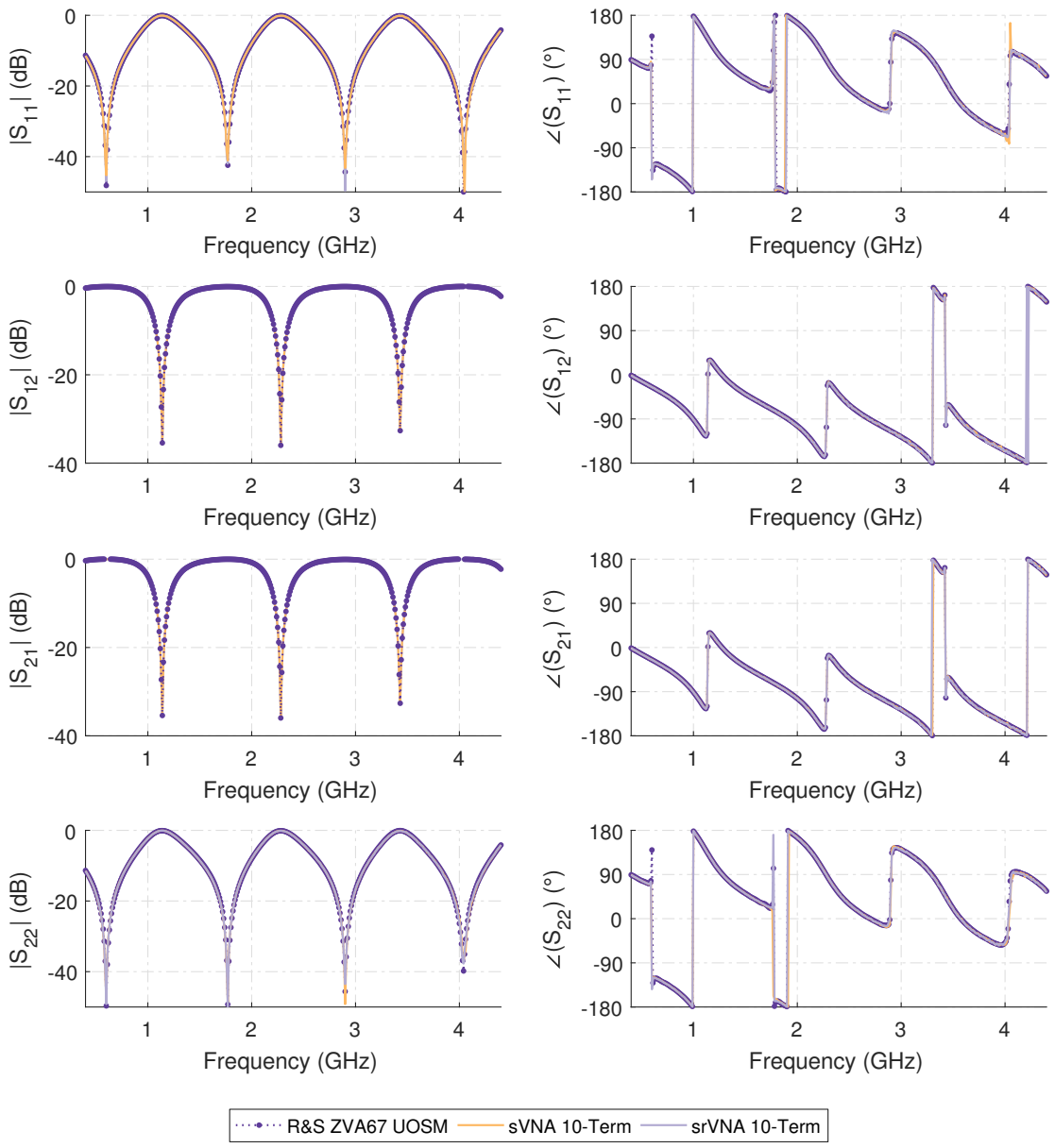

Figure B.19: Measurement results of the asymmetric reflective lossy tee using no additional attenuation with the additional Rosenberger RPC-N (f)-(f) calibration thru corrected by the 10-term procedure for both the sVNA and the srVNA double reflectometer test-sets.

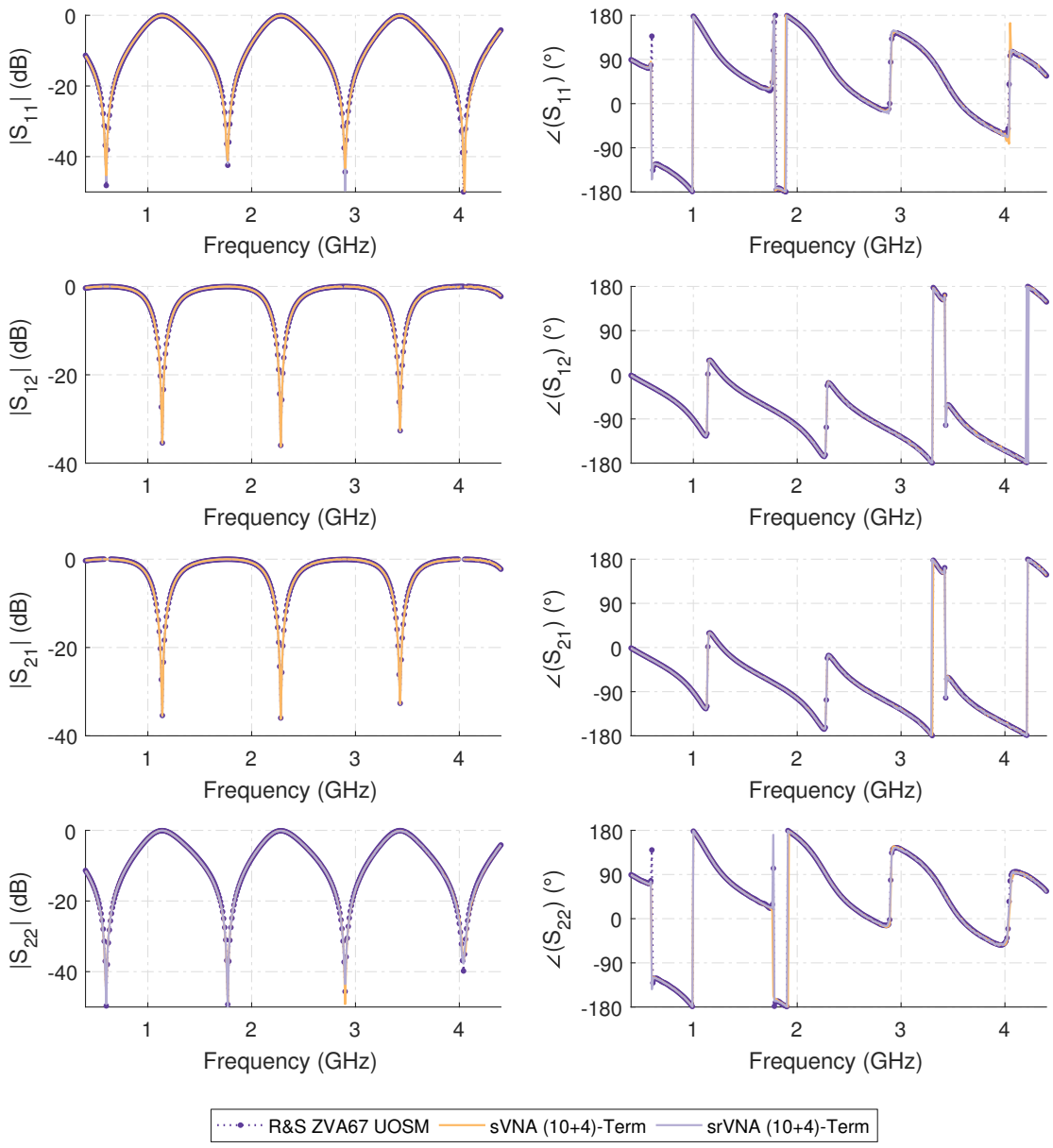

Figure B.20: Measurement results of the asymmetric reflective lossy tee using no additional attenuation with the additional Rosenberger RPC-N (f)-(f) calibration thru corrected by the (10+4)-term procedure for both the sVNA and the srVNA double reflectometer test-sets.

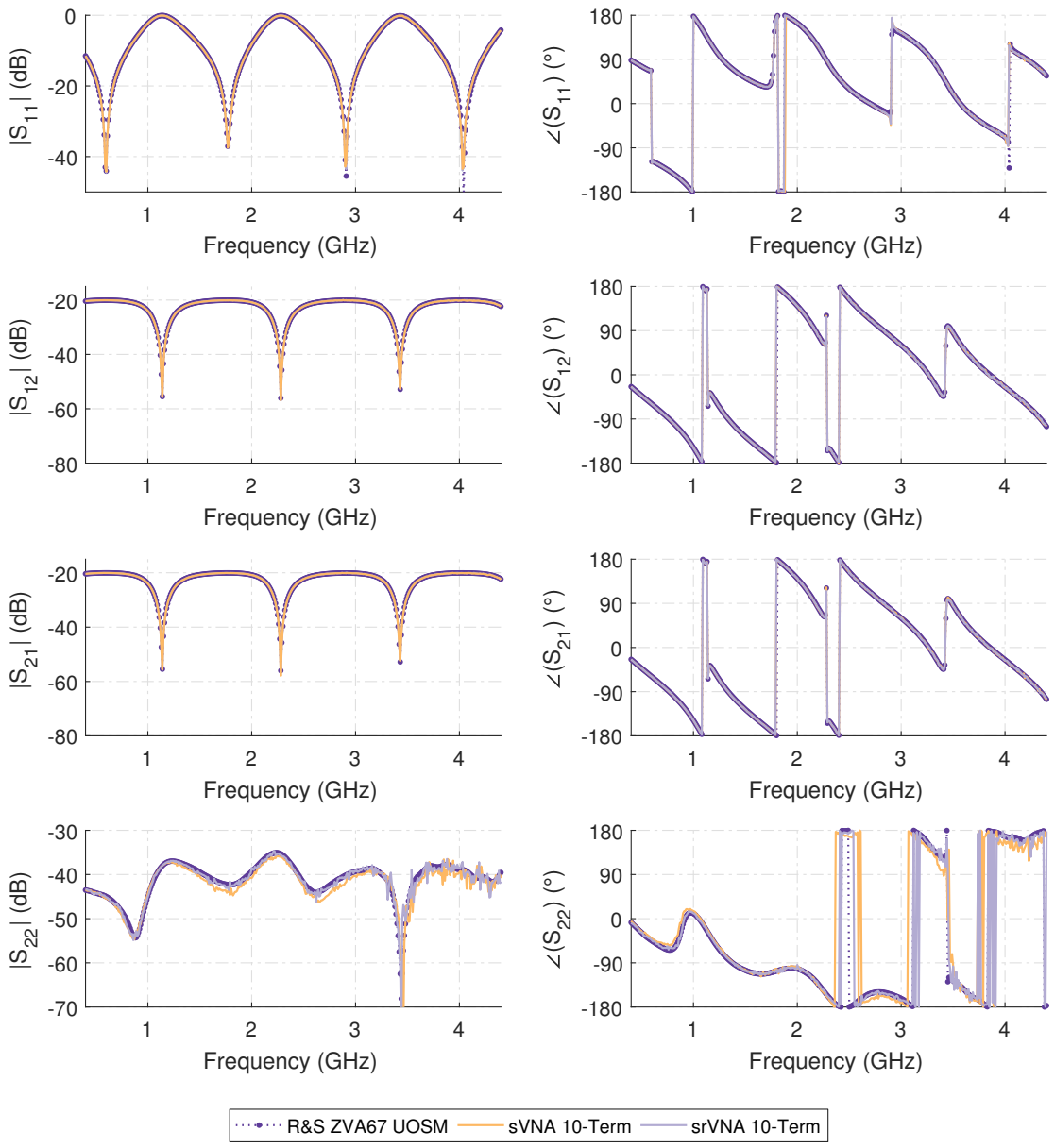

Figure B.21: Measurement results of the asymmetric reflective lossy tee using the 20 dB reference attenuator with the additional Rosenberger RPC-N (f)-(f) calibration thru corrected by the 10-term procedure for both the sVNA and the srVNA double reflectometer test-sets.

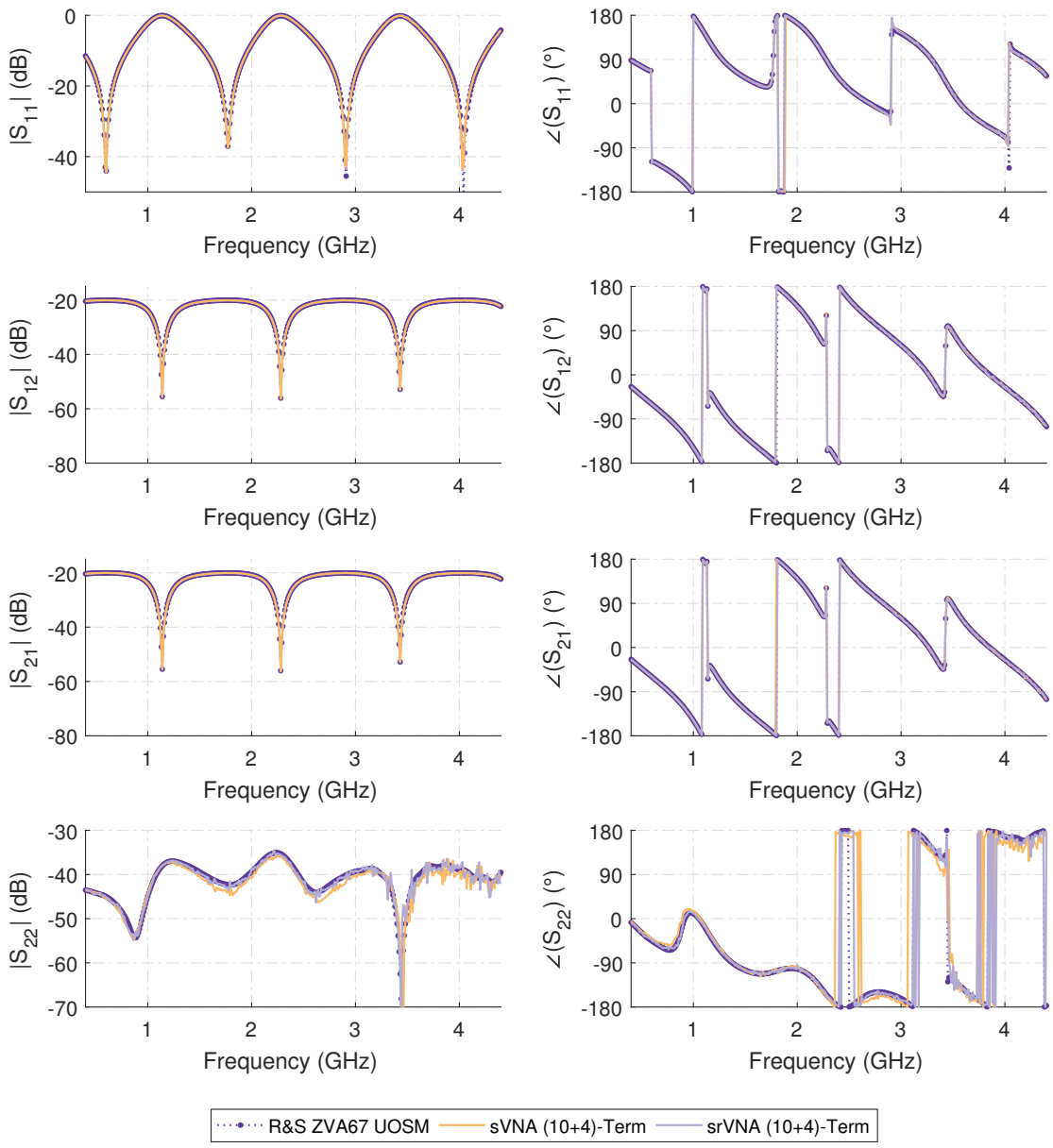

Figure B.22: Measurement results of the asymmetric reflective lossy tee using the 20 dB reference attenuator with the additional Rosenberger RPC-N (f)-(f) calibration thru corrected by the (10+4)-term procedure for both the sVNA and the srVNA double reflectometer test-sets.

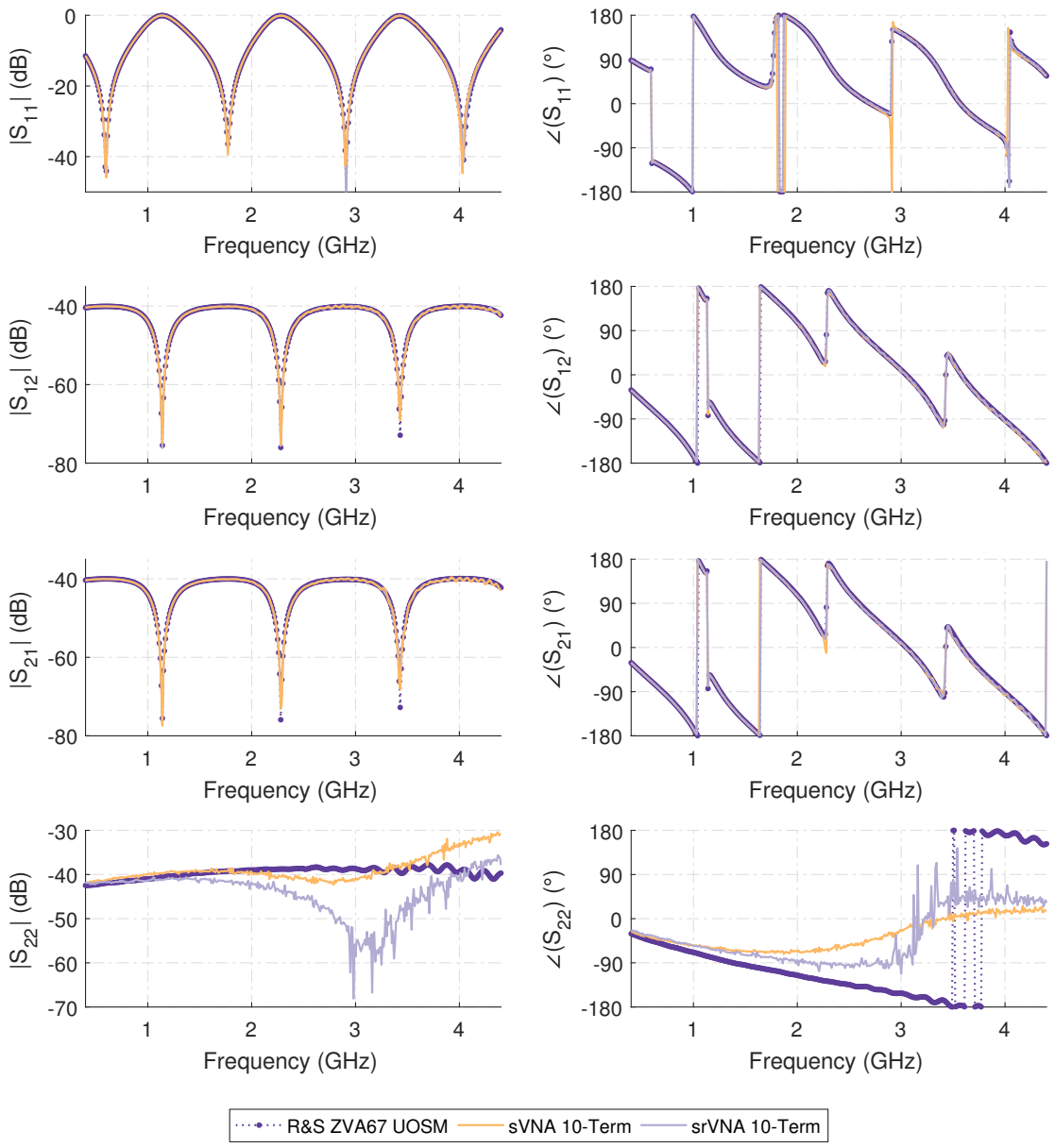

Figure B.23: Measurement results of the asymmetric reflective lossy tee using the 40 dB reference attenuator with the additional Rosenberger RPC-N (f)-(f) calibration thru corrected by the 10-term procedure for both the sVNA and the srVNA double reflectometer test-sets.

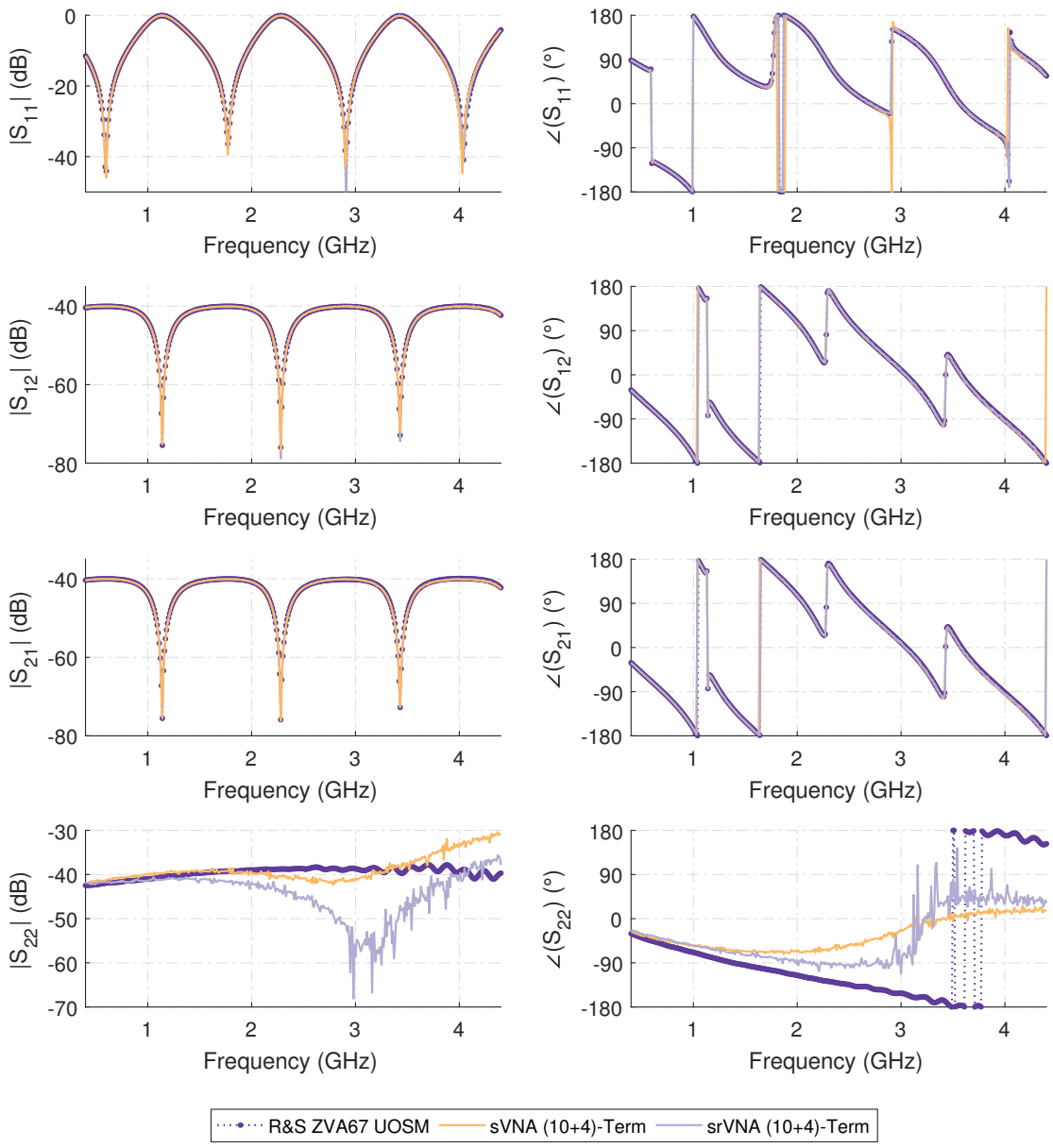

Figure B.24: Measurement results of the asymmetric reflective lossy tee using the 40 dB reference attenuator with the additional Rosenberger RPC-N (f)-(f) calibration thru corrected by the (10+4)-term procedure for both the sVNA and the srVNA double reflectometer test-sets.

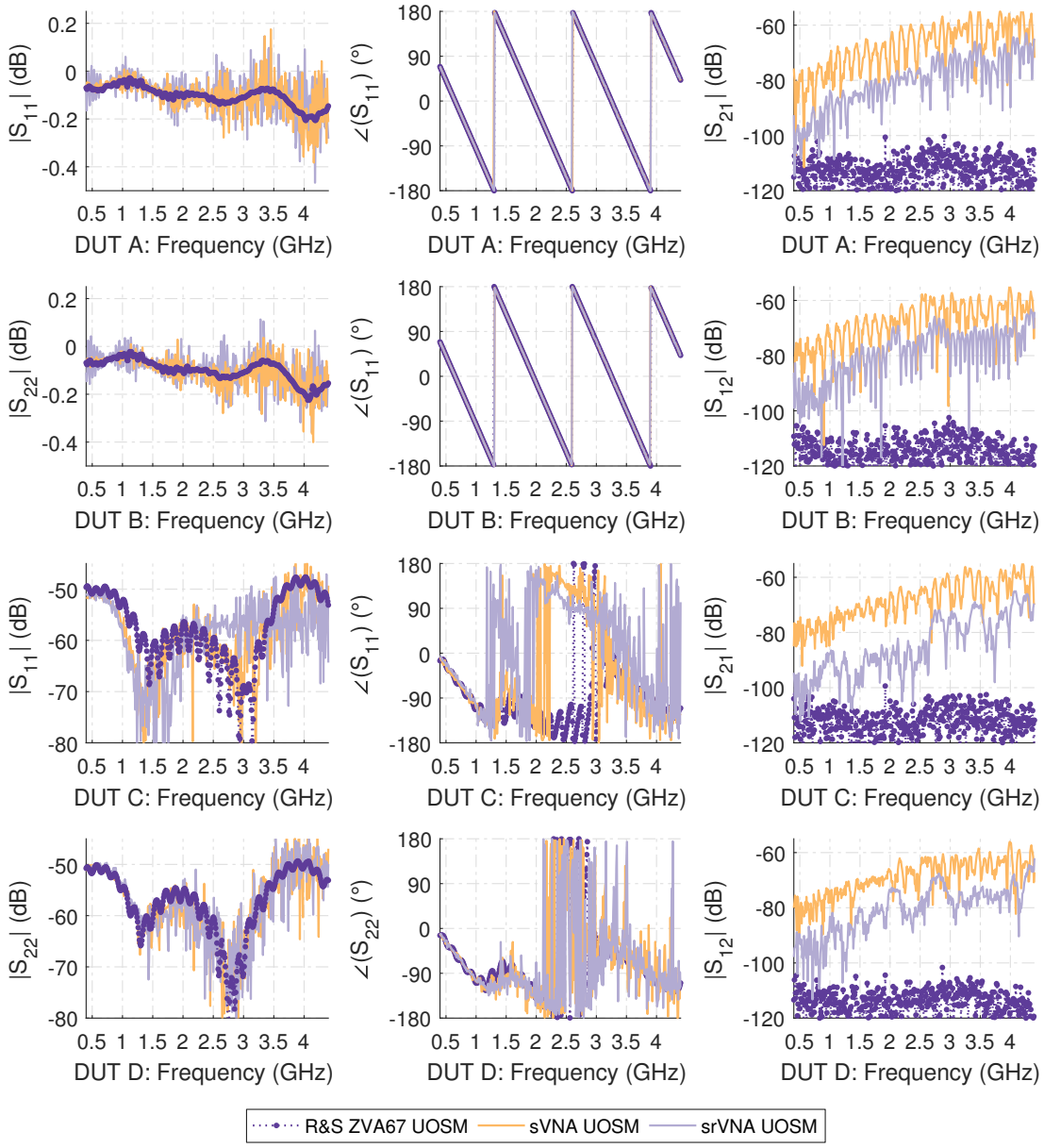

Figure B.25: Measurement results for the ripple test and residual directivity measurements corrected by the UOSM 7-term error model for both the sVNA and srVNA double reflectometer test-set setup. DUT A: Port 1, 150 mm $Z_L = 50\,\Omega$ bead-less airline terminated by the calibration short. DUT B: Port 2, 150 mm $Z_L = 50\,\Omega$ bead-less airline terminated by the calibration short. DUT C: Port 1, 150 mm $Z_L = 50\,\Omega$ bead-less airline terminated by the calibration match. DUT D: Port 2, 150 mm $Z_L = 50\,\Omega$ bead-less airline terminated by the calibration match.

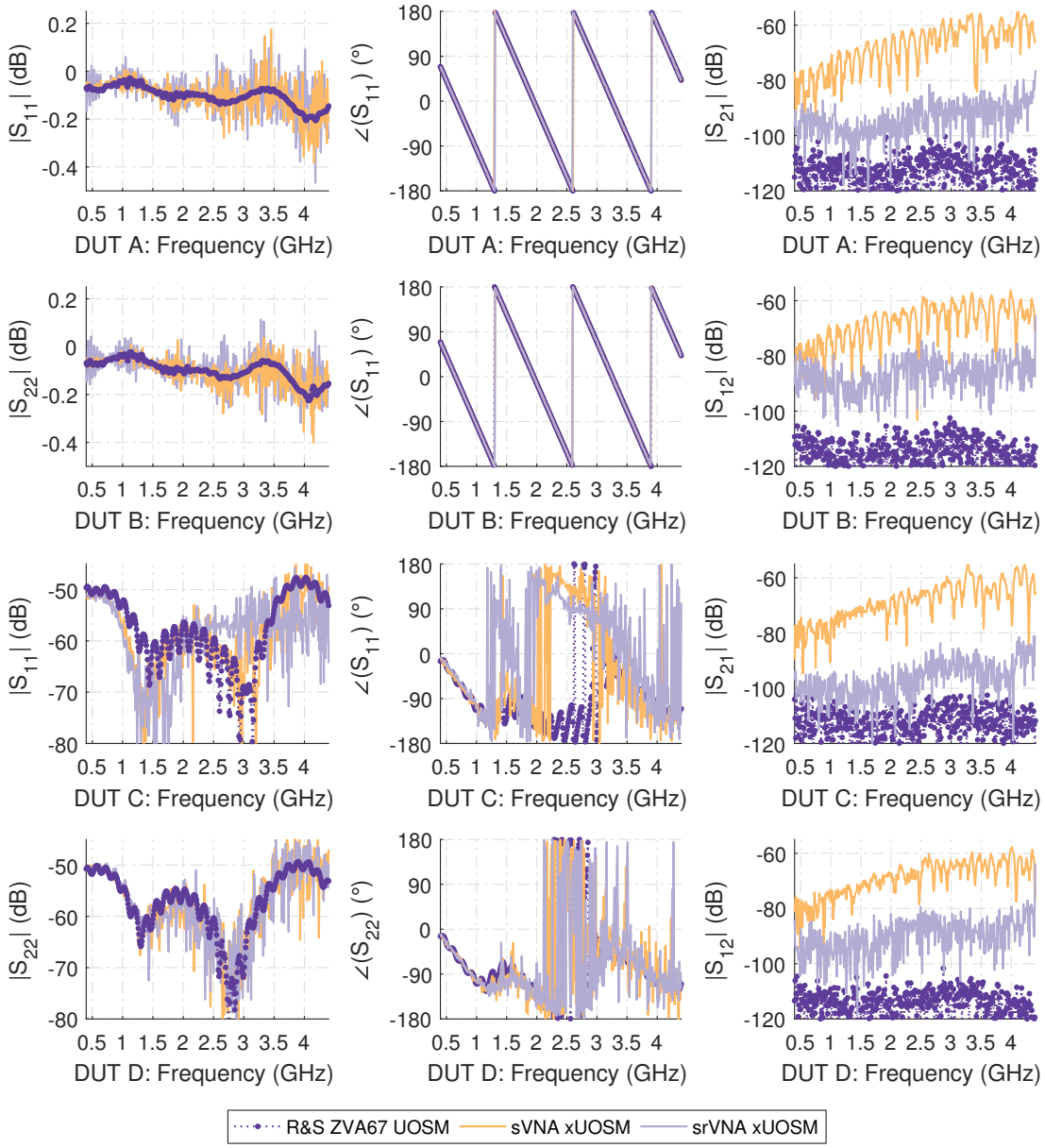

Figure B.26: Measurement results for the ripple test and residual directivity measurements corrected by the xUOSM 7-term error model for both the sVNA and srVNA double reflectometer test-set setup. DUT A: Port 1, 150 mm $Z_L = 50\,\Omega$ bead-less airline terminated by the calibration short. DUT B: Port 2, 150 mm $Z_L = 50\,\Omega$ bead-less airline terminated by the calibration short. DUT C: Port 1, 150 mm $Z_L = 50\,\Omega$ bead-less airline terminated by the calibration match. DUT D: Port 2, 150 mm $Z_L = 50\,\Omega$ bead-less airline terminated by the calibration match.

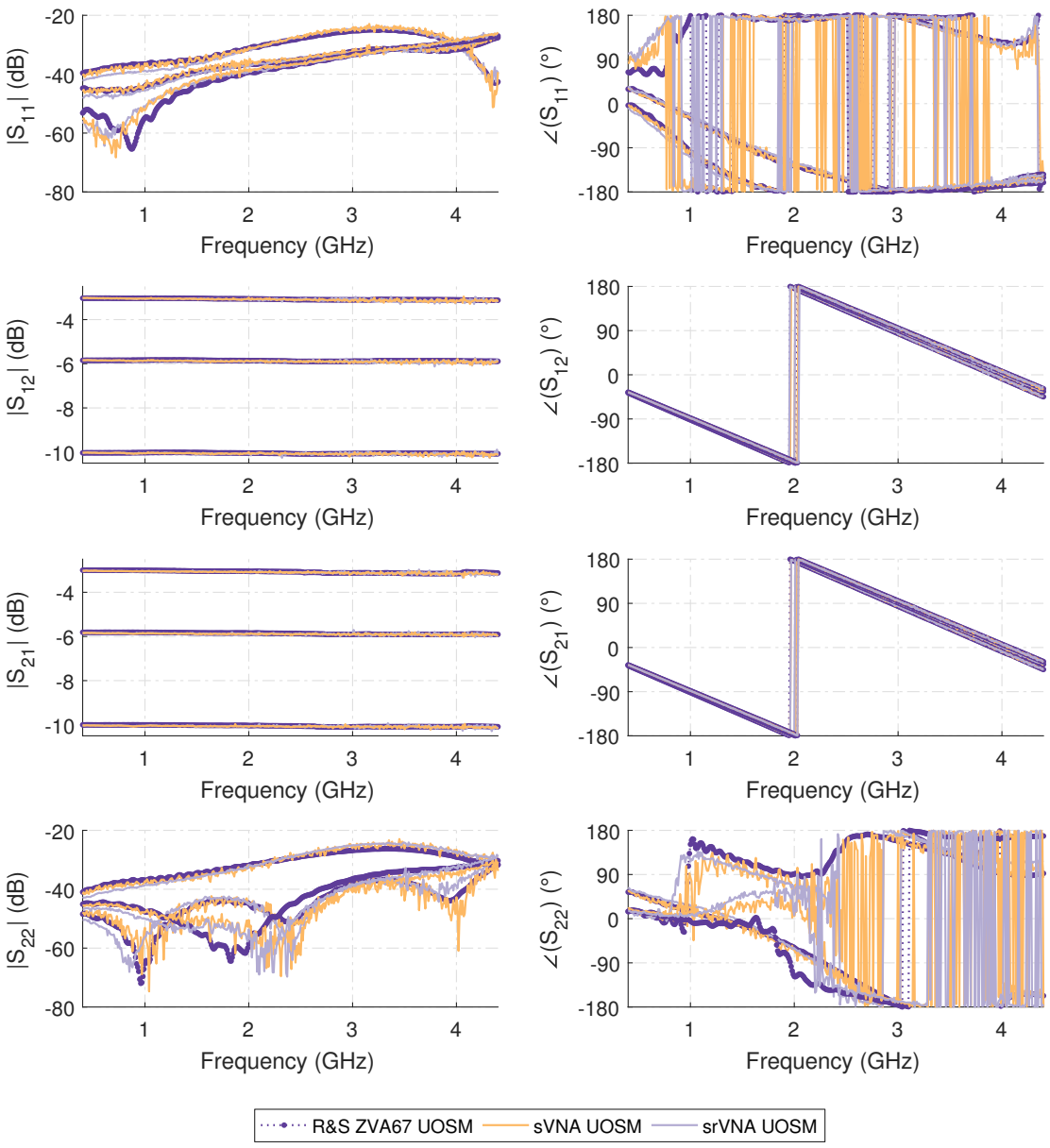

Figure B.27: Measurement results of the 3 dB, 6 dB and 10 dB attenuators with their corresponding Rosenberger RPC-N SMA adapter corrected by the UOSM 7-term procedure for both the sVNA and the srVNA double reflectometer test-sets.

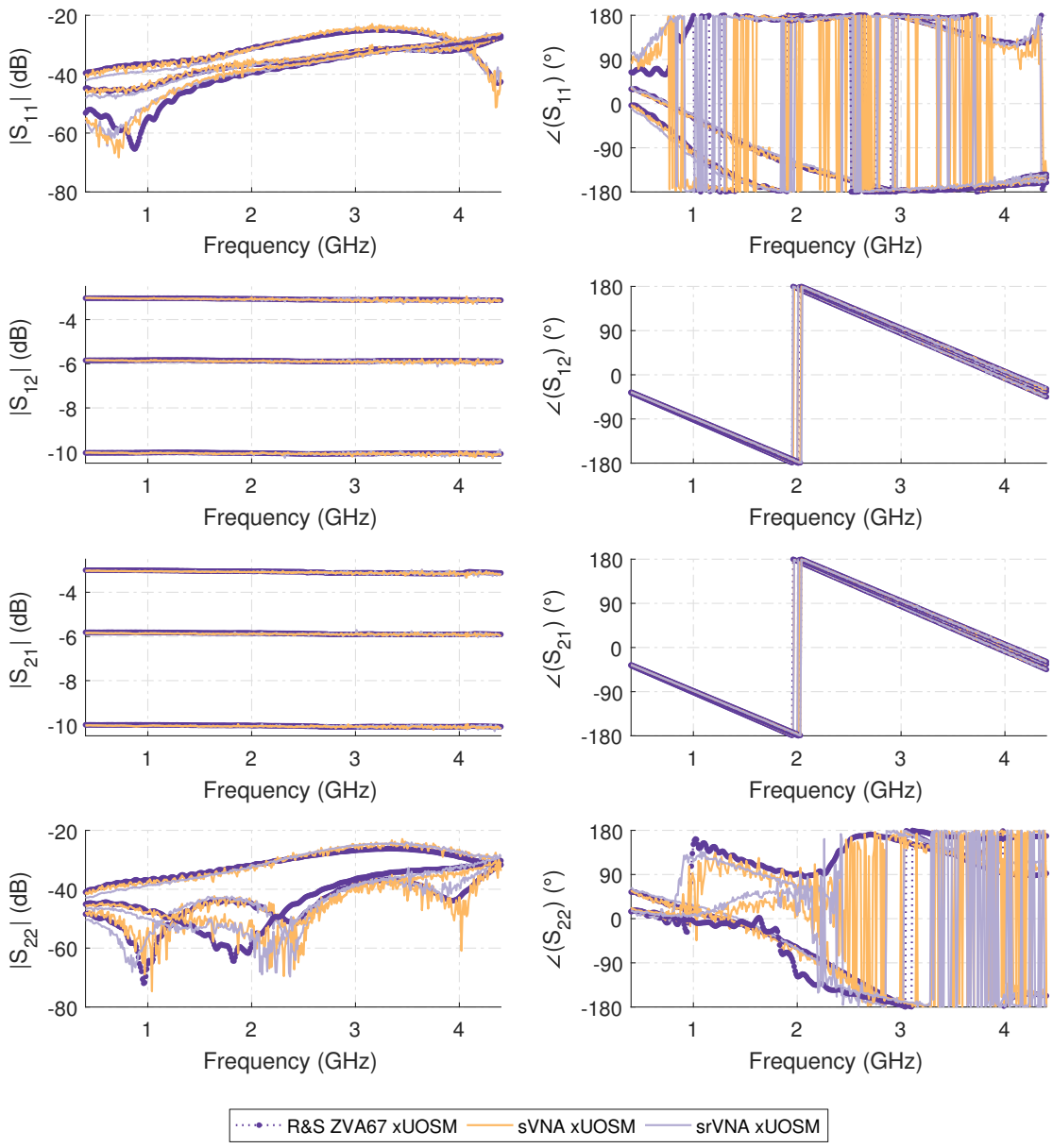

Figure B.28: Measurement results of the 3 dB, 6 dB and 10 dB attenuators with their corresponding Rosenberger RPC-N SMA adapter corrected by the xUOSM 7-term procedure for both the sVNA and the srVNA double reflectometer test-sets.

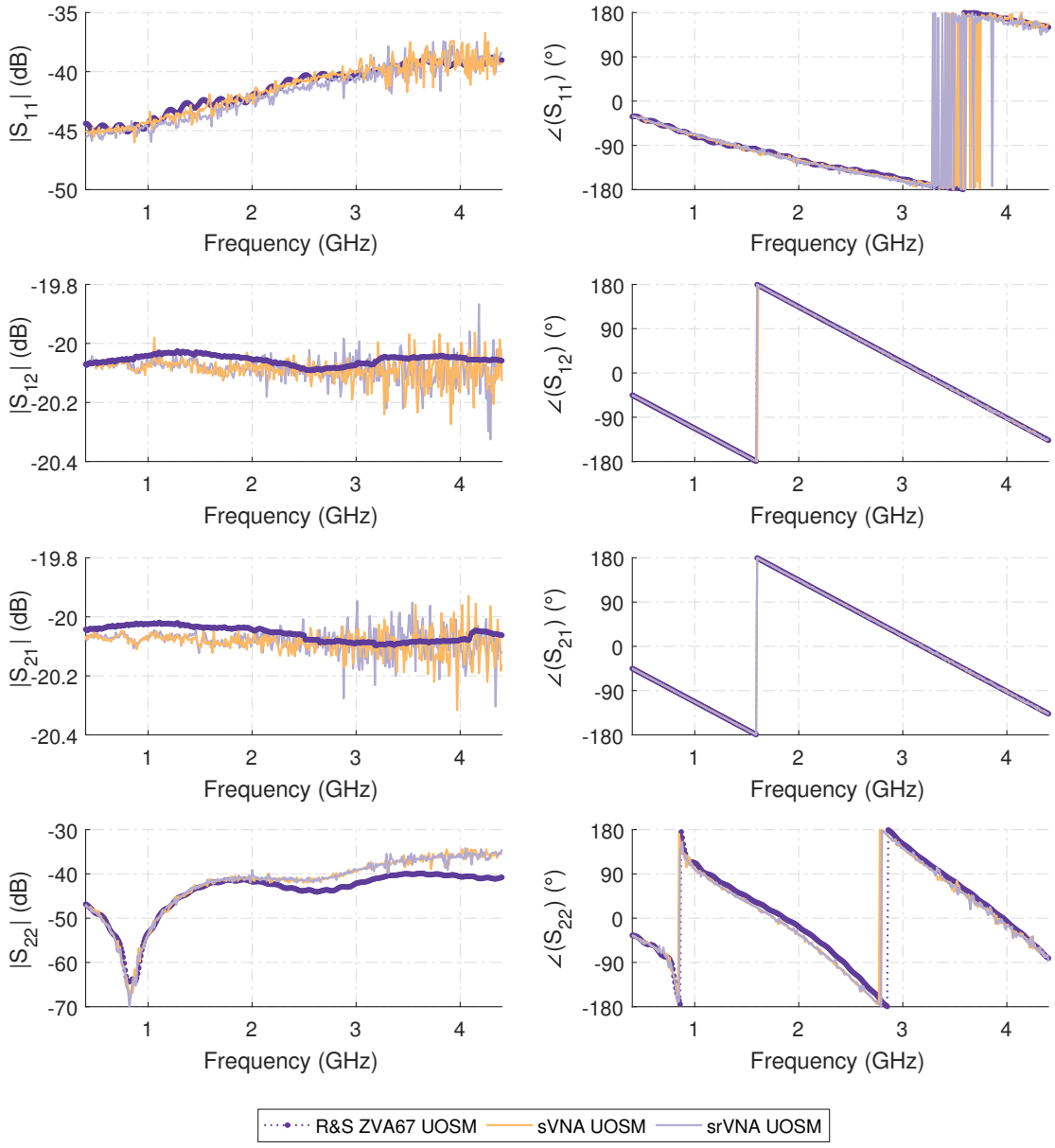

Figure B.29: Measurement results of the 20 dB reference attenuator with the additional Rosenberger RPC-N (f)-(f) calibration thru corrected by the UOSM 7-term procedure for both the sVNA and the srVNA double reflectometer test-sets.

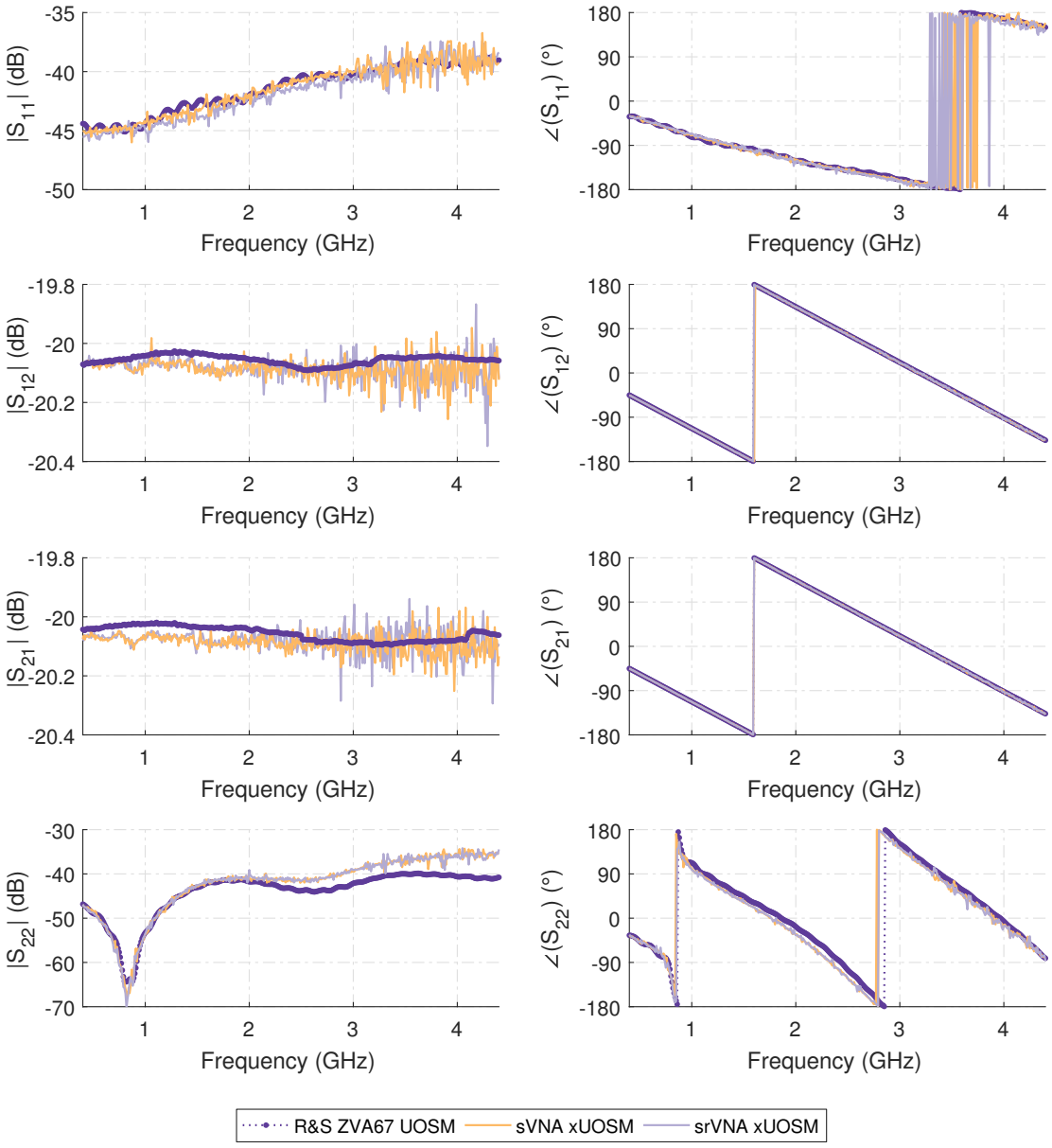

Figure B.30: Measurement results of the 20 dB reference attenuator with the additional Rosenberger RPC-N (f)-(f) calibration thru corrected by the xUOSM 7-term procedure for both the sVNA and the srVNA double reflectometer test-sets.

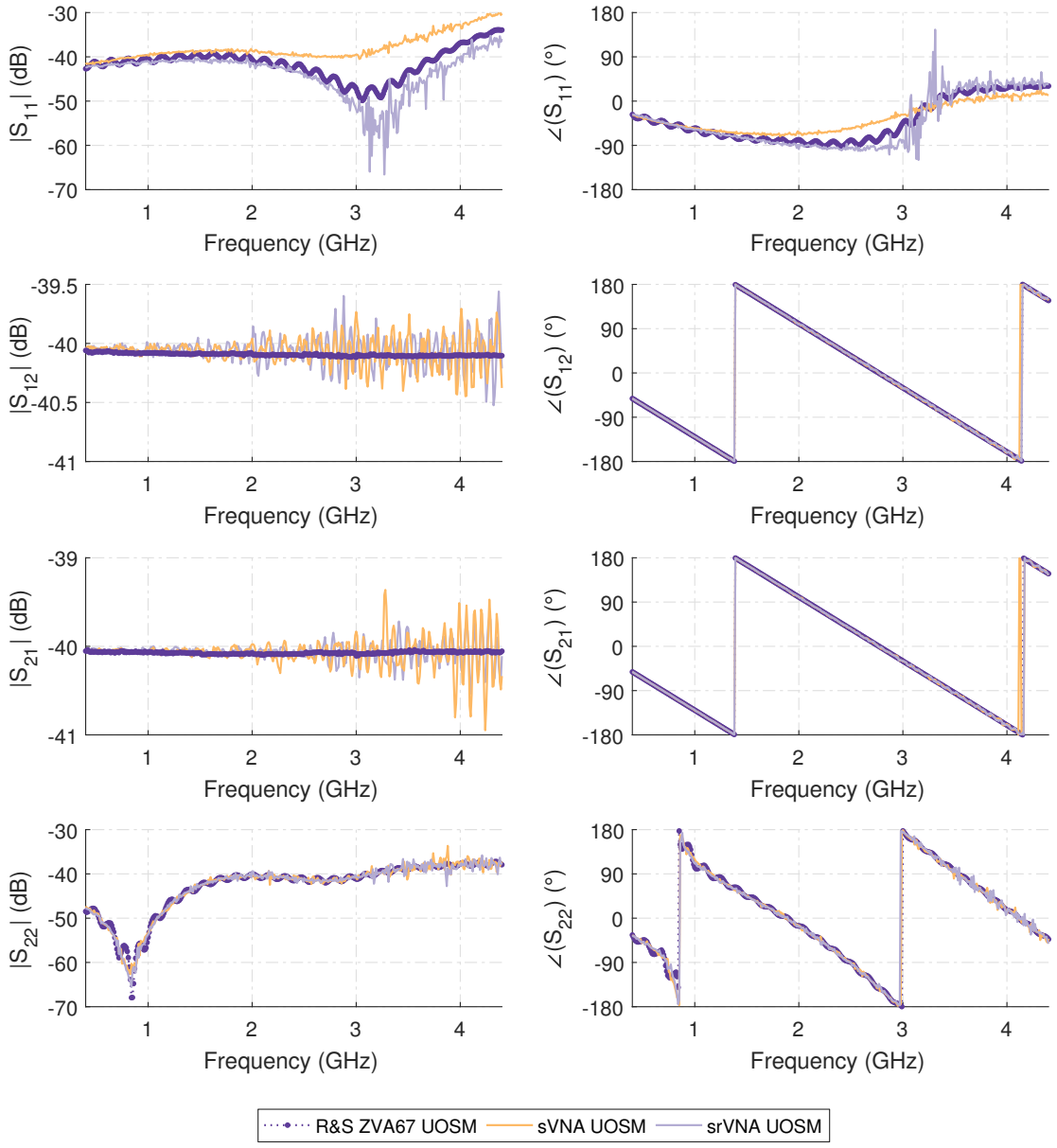

Figure B.31: Measurement results of the 40 dB reference attenuator with the additional Rosenberger RPC-N (f)-(f) calibration thru corrected by the UOSM 7-term procedure for both the sVNA and the srVNA double reflectometer test-sets.

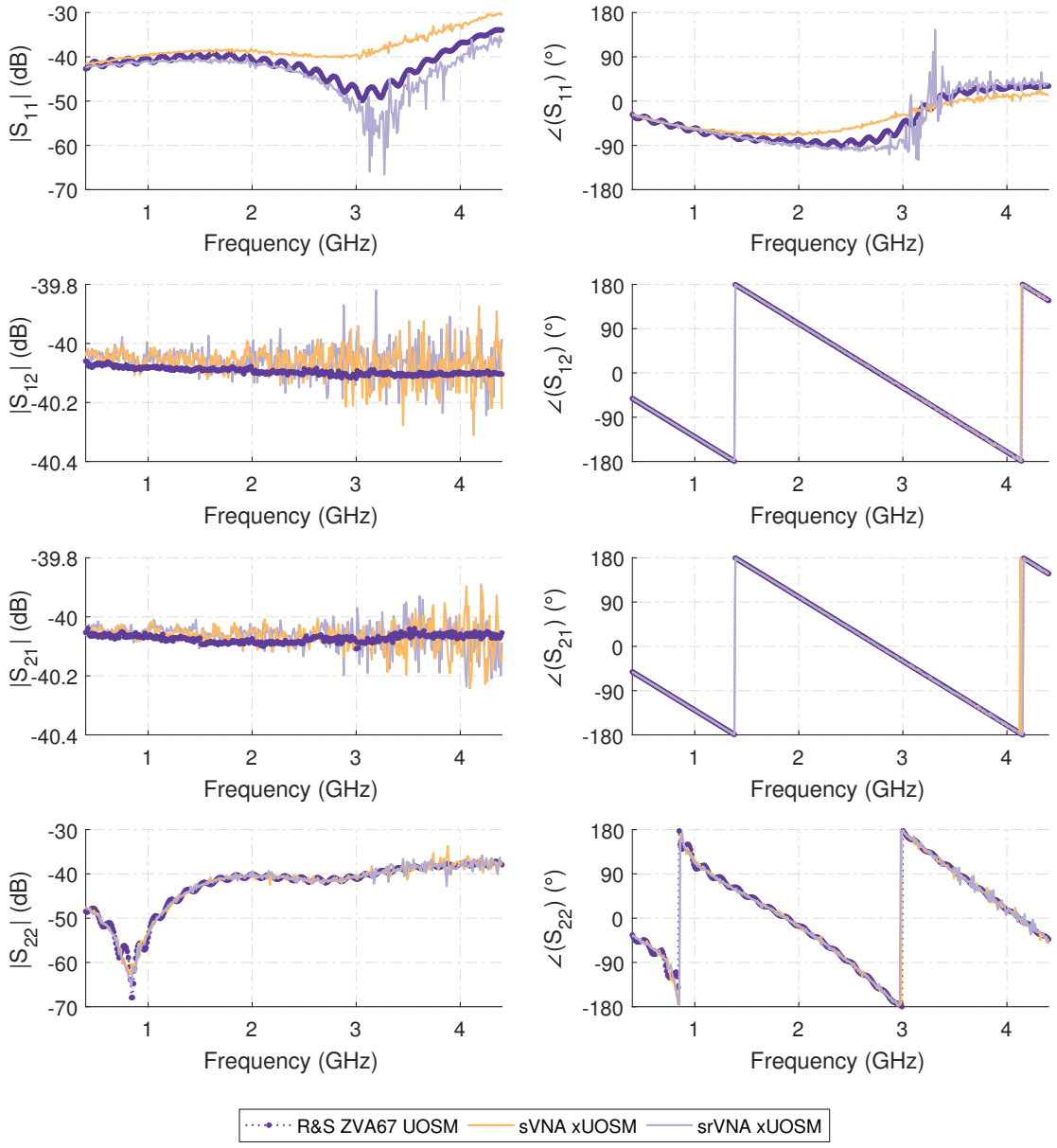

Figure B.32: Measurement results of the 40 dB reference attenuator with the additional Rosenberger RPC-N (f)-(f) calibration thru corrected by the xUOSM 7-term procedure for both the sVNA and the srVNA double reflectometer test-sets.

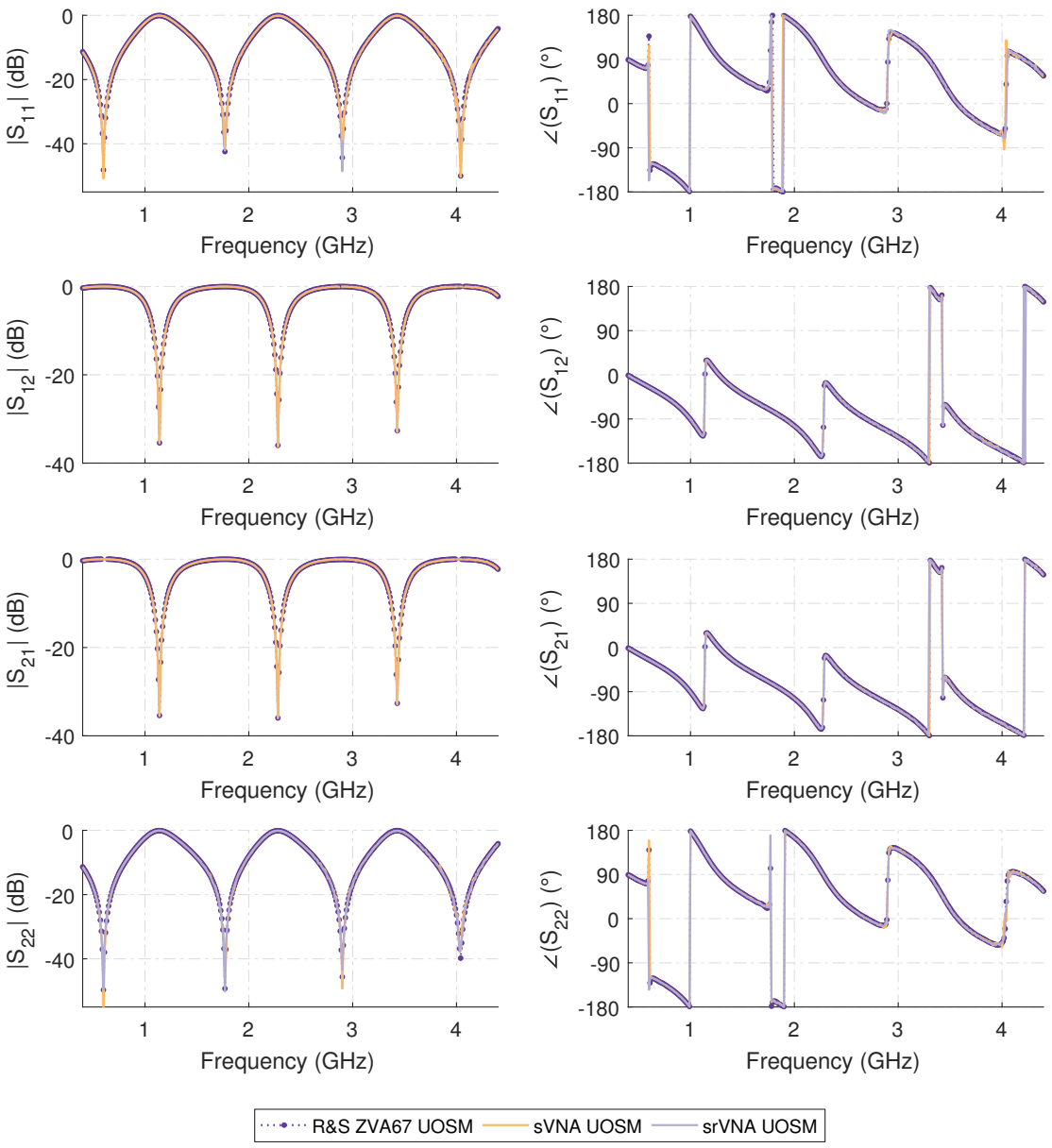

Figure B.33: Measurement results of the asymmetric reflective lossy tee using no additional attenuation with the additional Rosenberger RPC-N (f)-(f) calibration thru corrected by the UOSM 7-term procedure for both the sVNA and the srVNA double reflectometer test-sets.

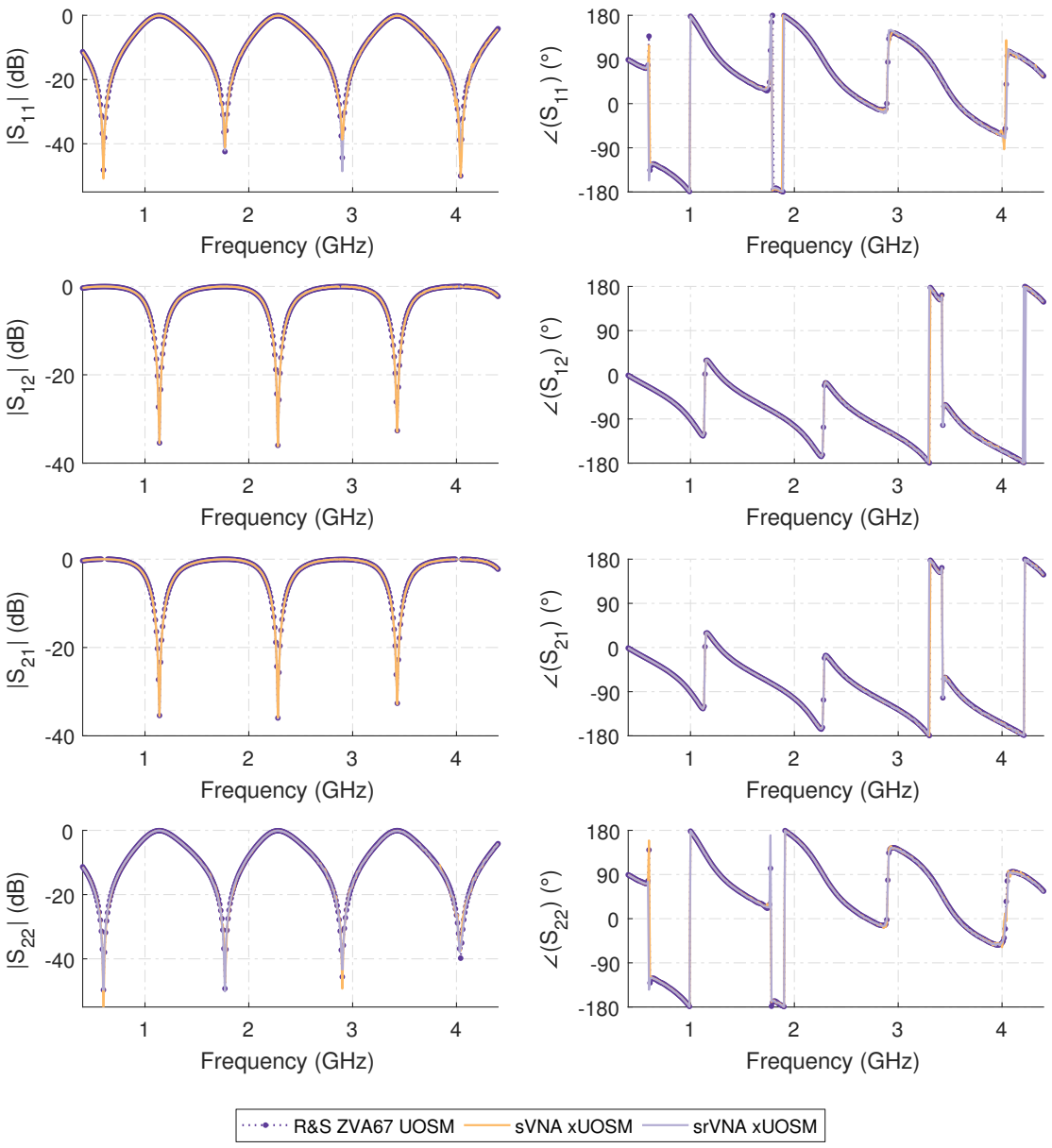

Figure B.34: Measurement results of the asymmetric reflective lossy tee using no additional attenuation with the additional Rosenberger RPC-N (f)-(f) calibration thru corrected by the xUOSM 7-term procedure for both the sVNA and the srVNA double reflectometer test-sets.

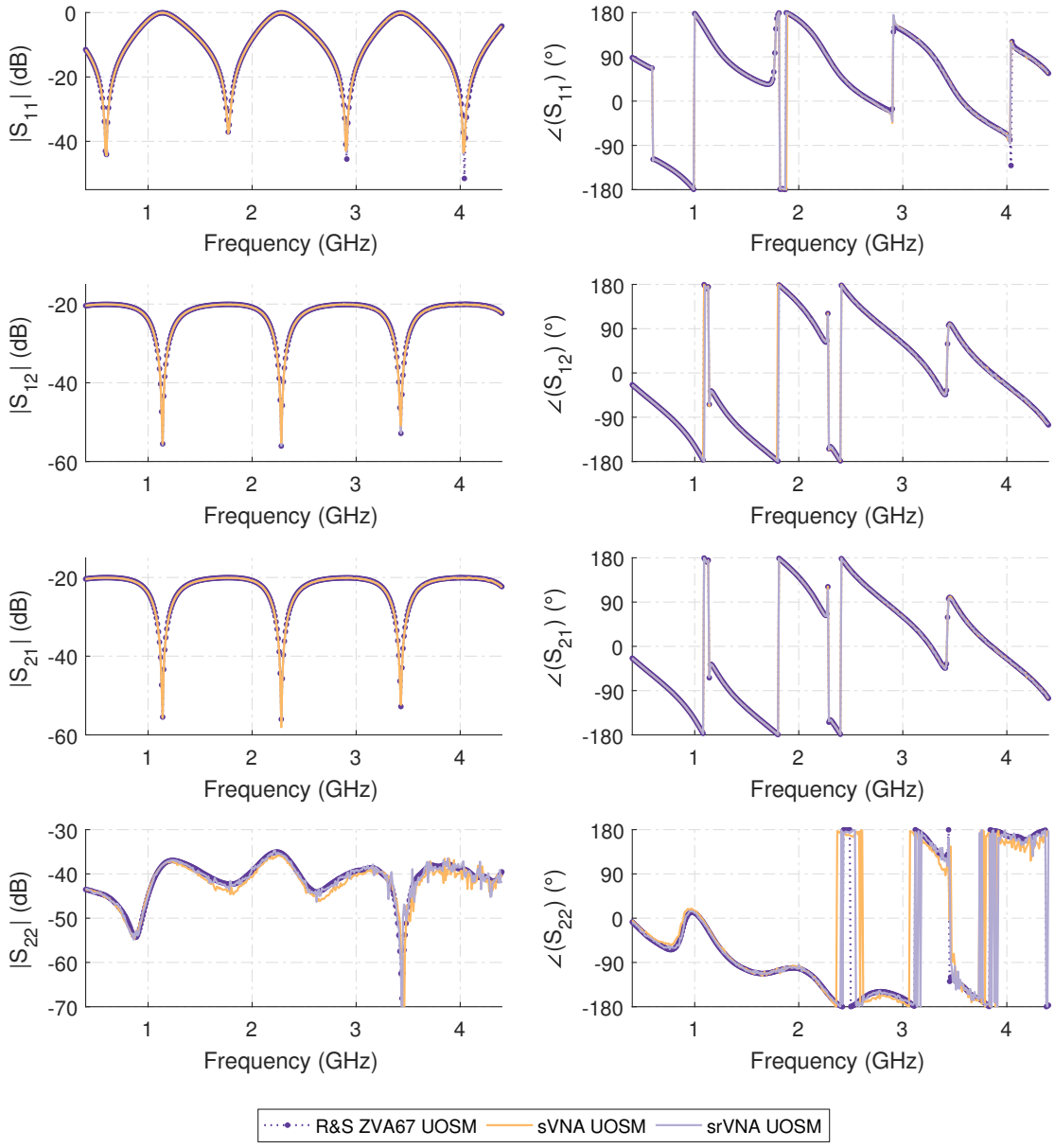

Figure B.35: Measurement results of the 20 dB reference attenuator with the additional Rosenberger RPC-N (f)-(f) calibration thru corrected by the UOSM 7-term procedure for both the sVNA and the srVNA double reflectometer test-sets.

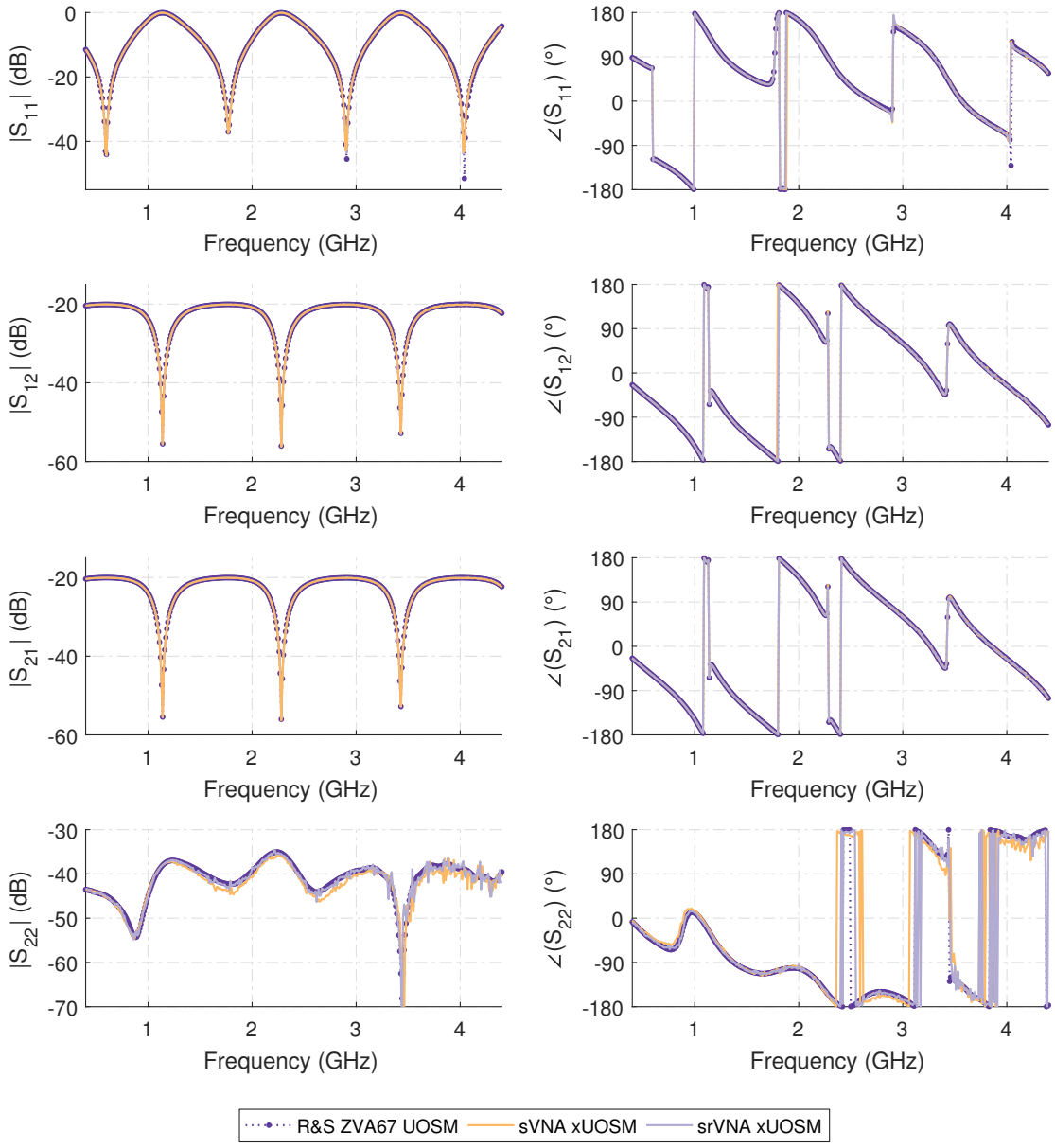

Figure B.36: Measurement results of the 20 dB reference attenuator with the additional Rosenberger RPC-N (f)-(f) calibration thru corrected by the xUOSM 7-term procedure for both the sVNA and the srVNA double reflectometer test-sets.

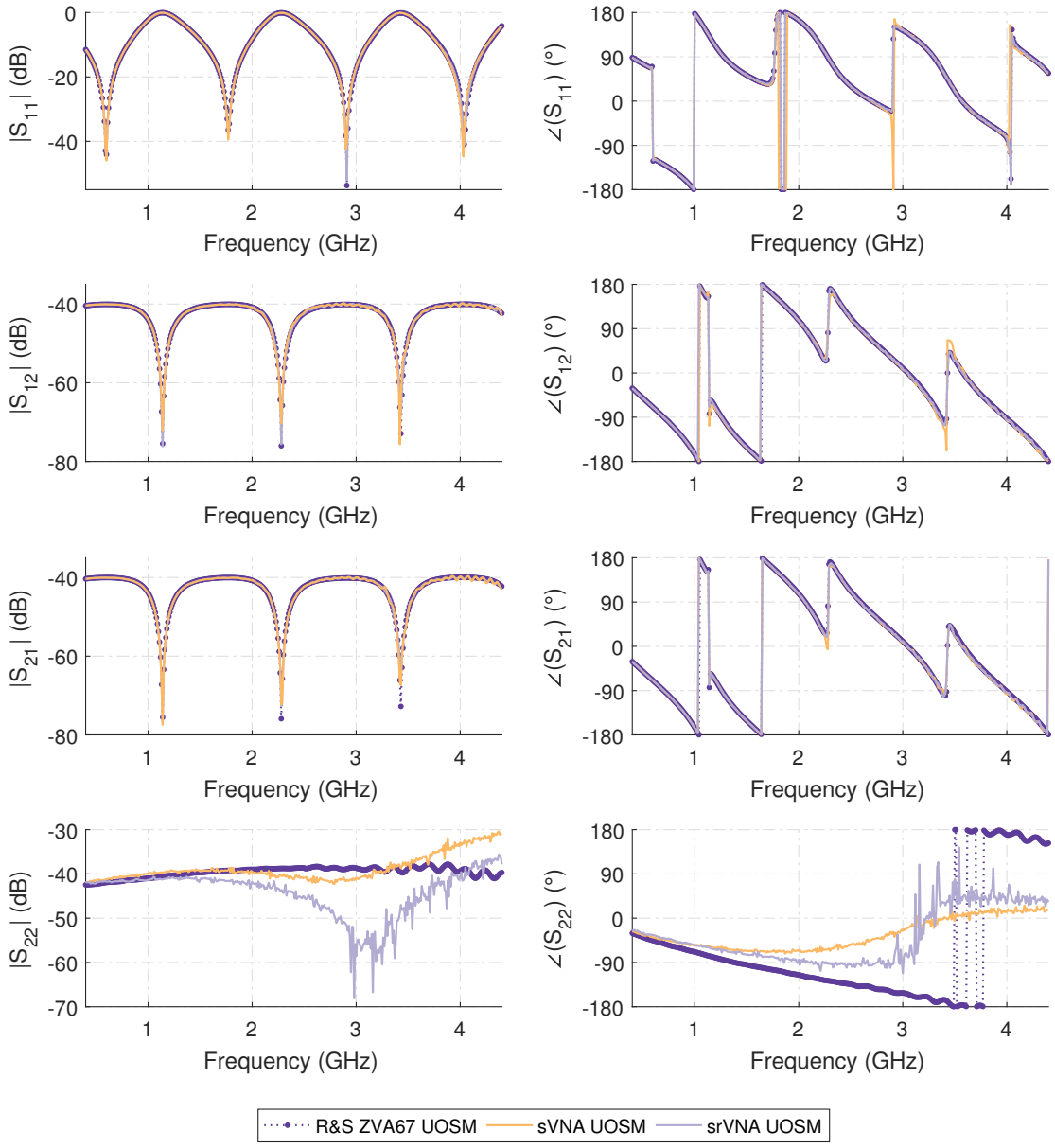

Figure B.37: Measurement results of the 20 dB reference attenuator with the additional Rosenberger RPC-N (f)-(f) calibration thru corrected by the UOSM 7-term procedure for both the sVNA and the srVNA double reflectometer test-sets.

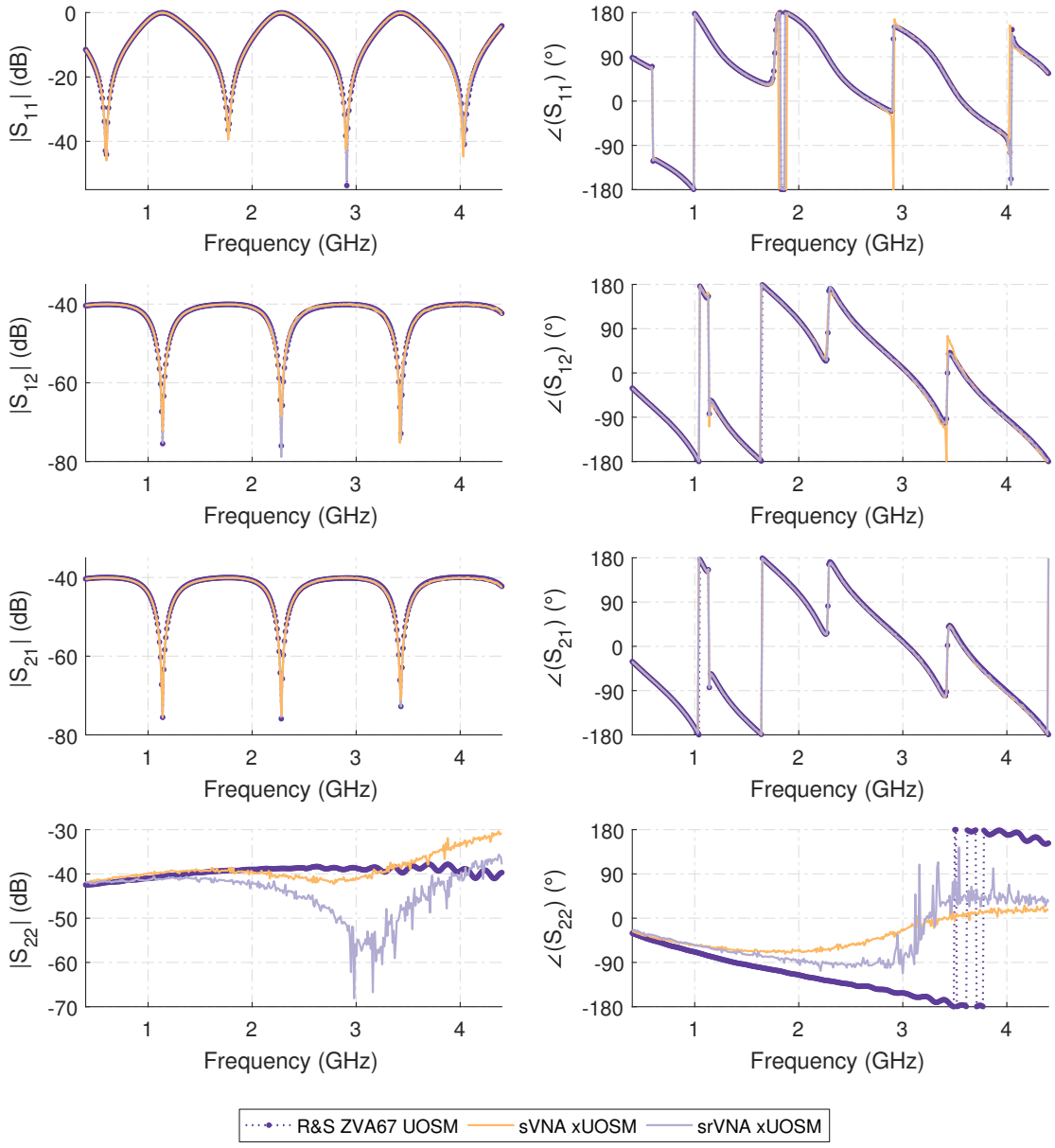

Figure B.38: Measurement results of the 20 dB reference attenuator with the additional Rosenberger RPC-N (f)-(f) calibration thru corrected by the xUOSM 7-term procedure for both the sVNA and the srVNA double reflectometer test-sets.

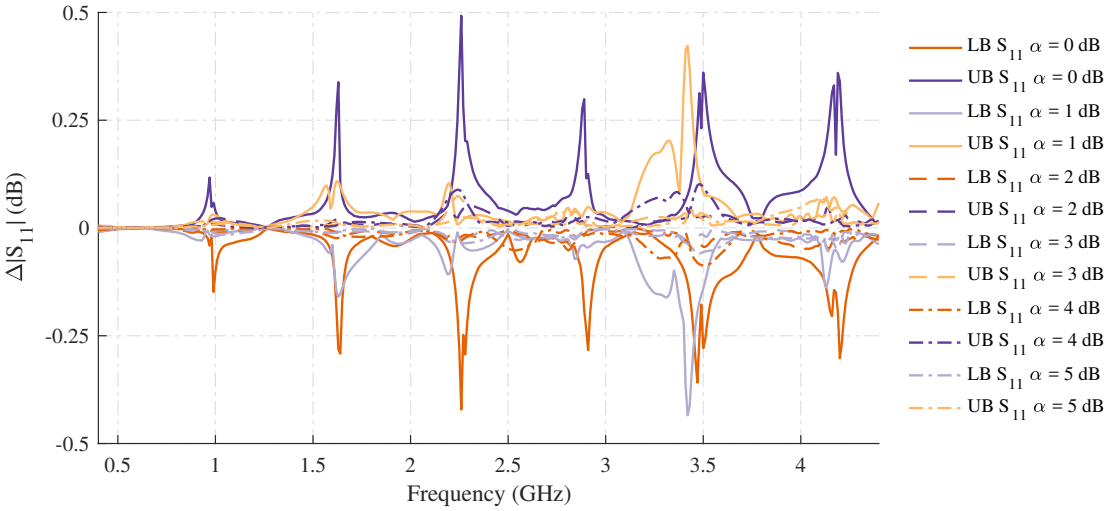

Figure B.39: $|S_{11}|$ repeatability measurement results for the 10 dB rotary 10 step attenuator in a shorted tee configuration, obtained with the ZVA67 and show for attenuation settings 0 to 5 dB. UB - upper deviation boundary from the mean of 5 full rotations, LB lower deviation boundary from the mean of 5 full rotations.

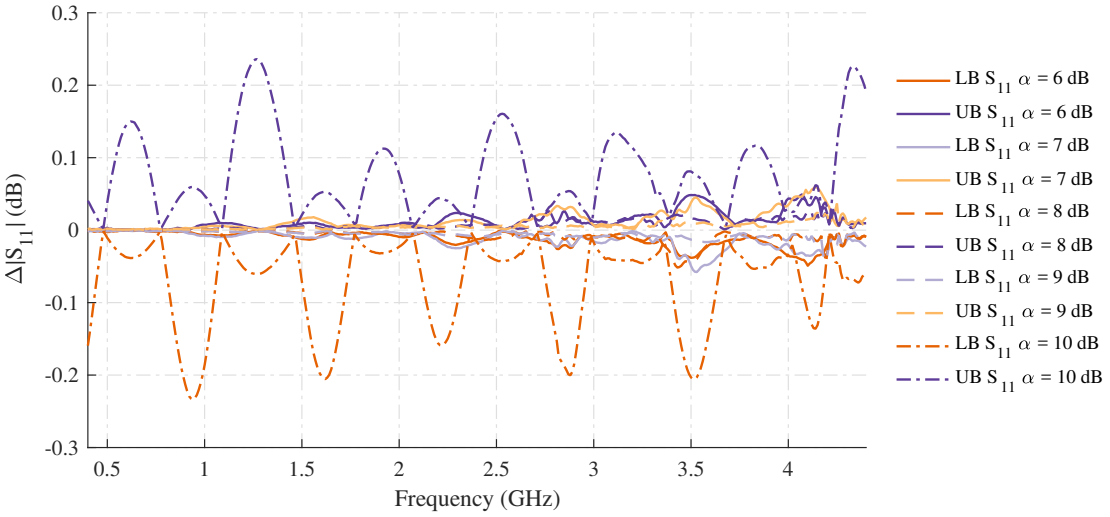

Figure B.40: $|S_{11}|$ repeatability measurement results for the 10 dB rotary 10 step attenuator in a shorted tee configuration, obtained with the ZVA67 and show for attenuation settings 6 to 10 dB. UB - upper deviation boundary from the mean of 5 full rotations, LB lower deviation boundary from the mean of 5 full rotations.

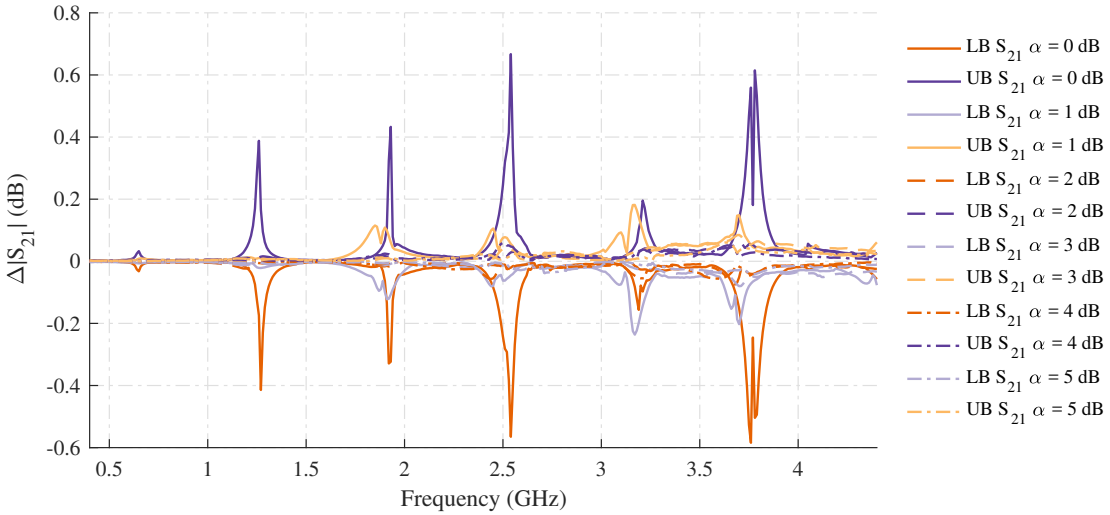

Figure B.41: $|S_{21}|$ repeatability measurement results for the 10 dB rotary 10 step attenuator in a shorted tee configuration, obtained with the ZVA67 and show for attenuation settings 0 to 5 dB. UB - upper deviation boundary from the mean of 5 full rotations, LB lower deviation boundary from the mean of 5 full rotations.

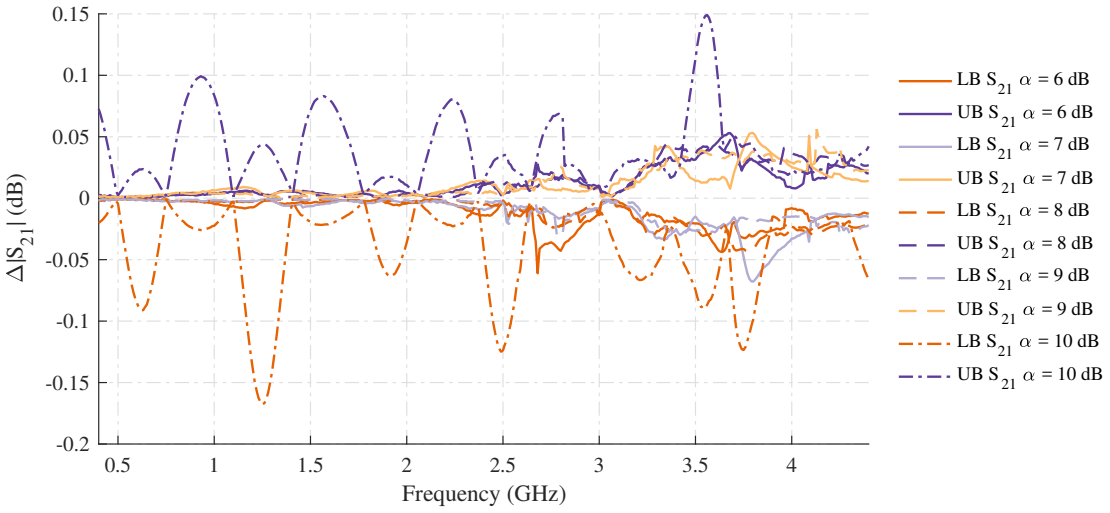

Figure B.42: $|S_{21}|$ repeatability measurement results for the 10 dB rotary 10 step attenuator in a shorted tee configuration, obtained with the ZVA67 and show for attenuation settings 6 to 10 dB. UB - upper deviation boundary from the mean of 5 full rotations, LB lower deviation boundary from the mean of 5 full rotations.

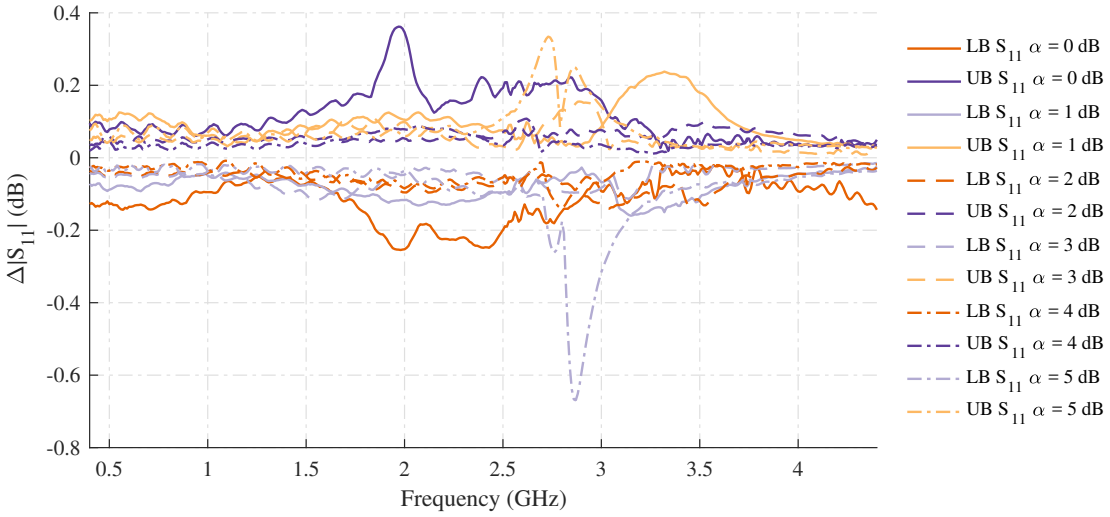

Figure B.43: $|S_{11}|$ repeatability measurement results for the 10 dB rotary 10 step attenuator in a thru configuration, obtained with the ZVA67 and show for attenuation settings 0 to 5 dB. UB - upper deviation boundary from the mean of 5 full rotations, LB lower deviation boundary from the mean of 5 full rotations.

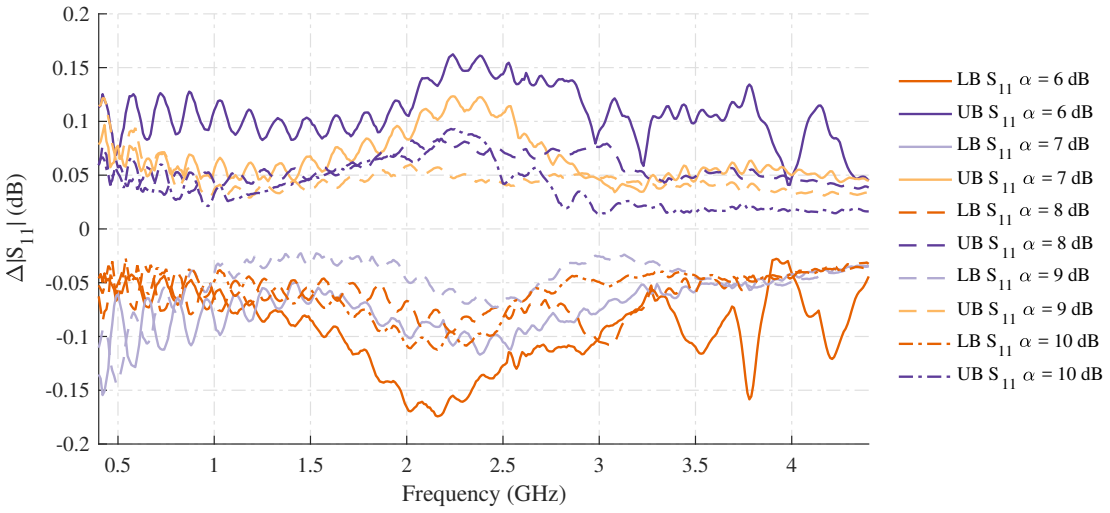

Figure B.44: $|S_{11}|$ repeatability measurement results for the 10 dB rotary 10 step attenuator in a thru configuration, obtained with the ZVA67 and show for attenuation settings 6 to 10 dB. UB - upper deviation boundary from the mean of 5 full rotations, LB lower deviation boundary from the mean of 5 full rotations.

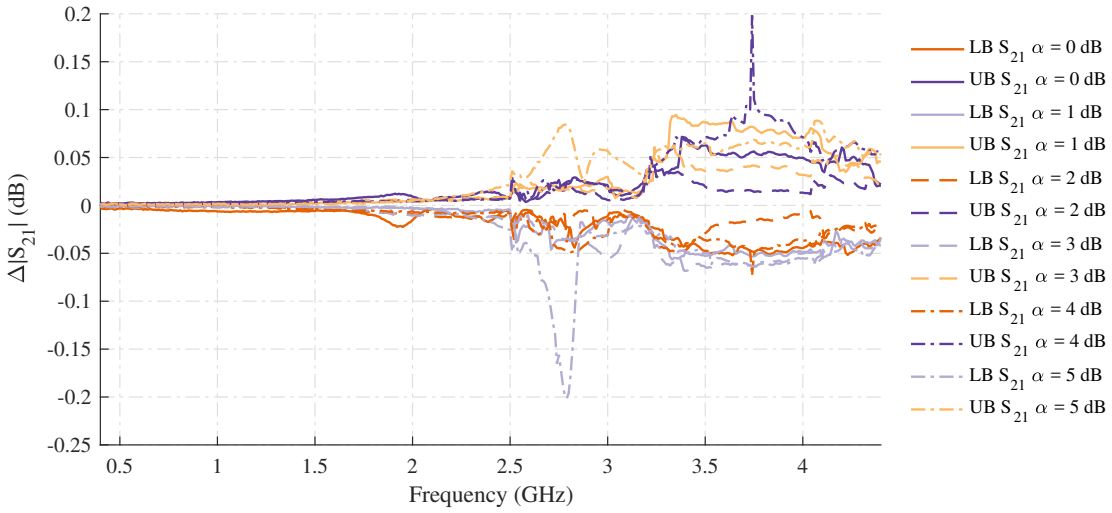

Figure B.45: $|S_{21}|$ repeatability measurement results for the 10 dB rotary 10 step attenuator in a thru configuration, obtained with the ZVA67 and show for attenuation settings 0 to 5 dB. UB - upper deviation boundary from the mean of 5 full rotations, LB lower deviation boundary from the mean of 5 full rotations.

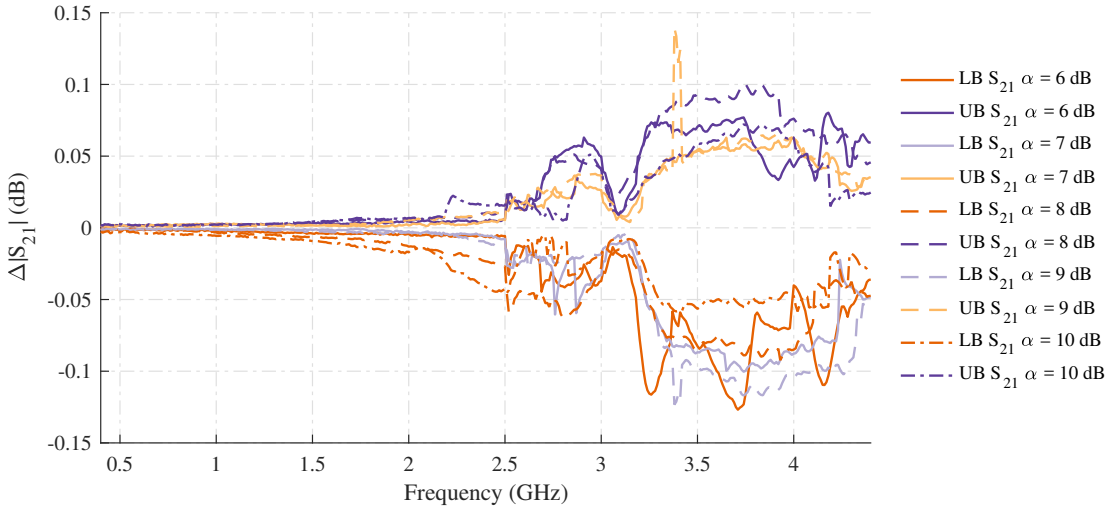

Figure B.46: $|S_{21}|$ repeatability measurement results for the 10 dB rotary 10 step attenuator in a thru configuration, obtained with the ZVA67 and show for attenuation settings 6 to 10 dB. UB - upper deviation boundary from the mean of 5 full rotations, LB lower deviation boundary from the mean of 5 full rotations.

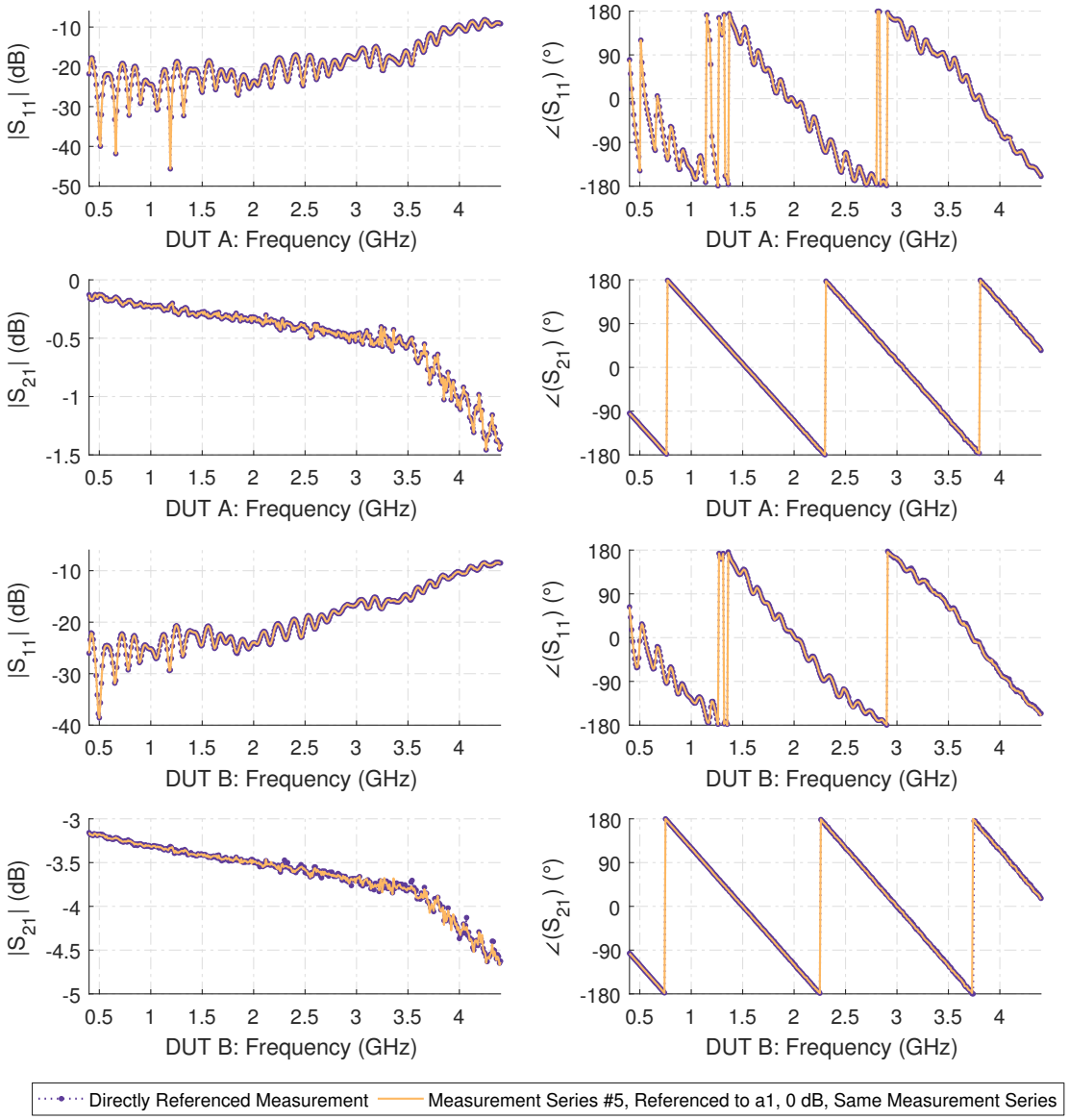

Figure B.47: S-parameter measurement results for the a-wave speed-up thru measurement DUT compared to concurrent a_1 measurement, referenced to first a_1 measurement of the cycle. DUT A - step attenuator 0 dB setting, DUT B - step attenuator 3 dB setting.

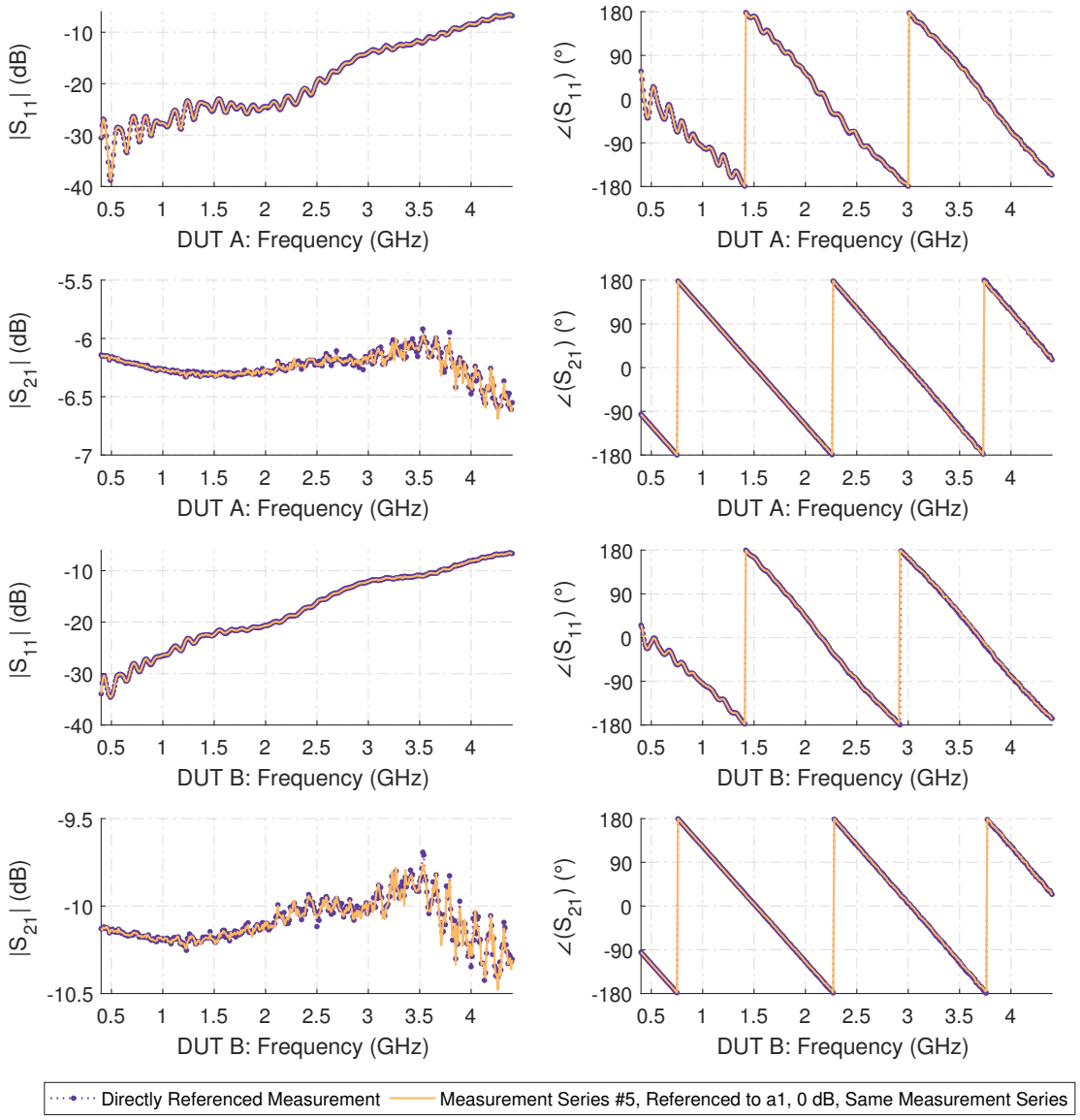

Figure B.48: S-parameter measurement results for the a-wave speed-up thru measurement DUT compared to concurrent a_1 measurement, referenced to first a_1 measurement of the cycle. DUT A - step attenuator 6 dB setting, DUT B - step attenuator 10 dB setting.

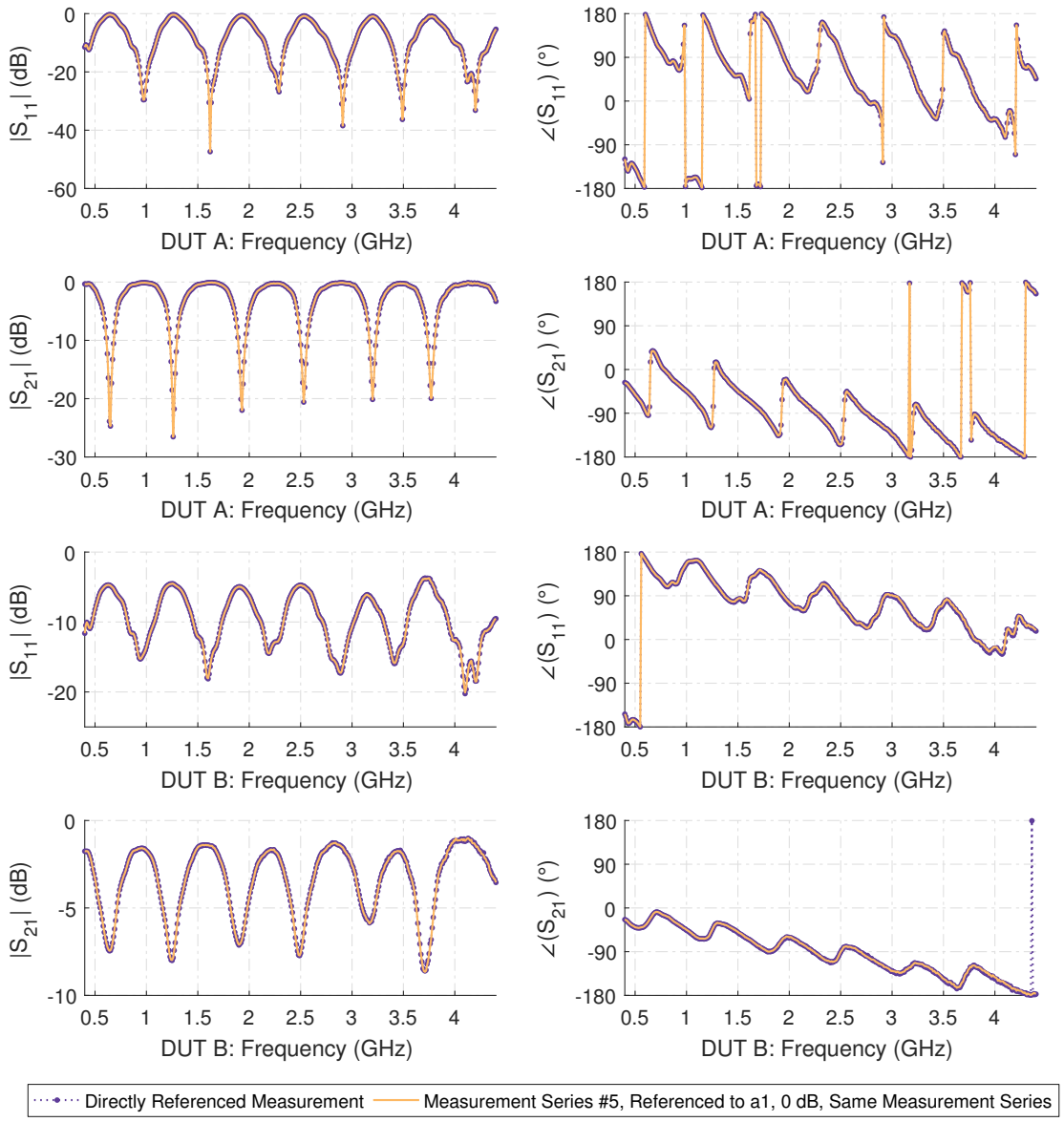

Figure B.49: S-parameter measurement results for the a-wave speed-up tee measurement DUT compared to concurrent a_1 measurement, referenced to first a_1 measurement of the cycle. DUT A - step attenuator 0 dB setting, DUT B - step attenuator 3 dB setting.

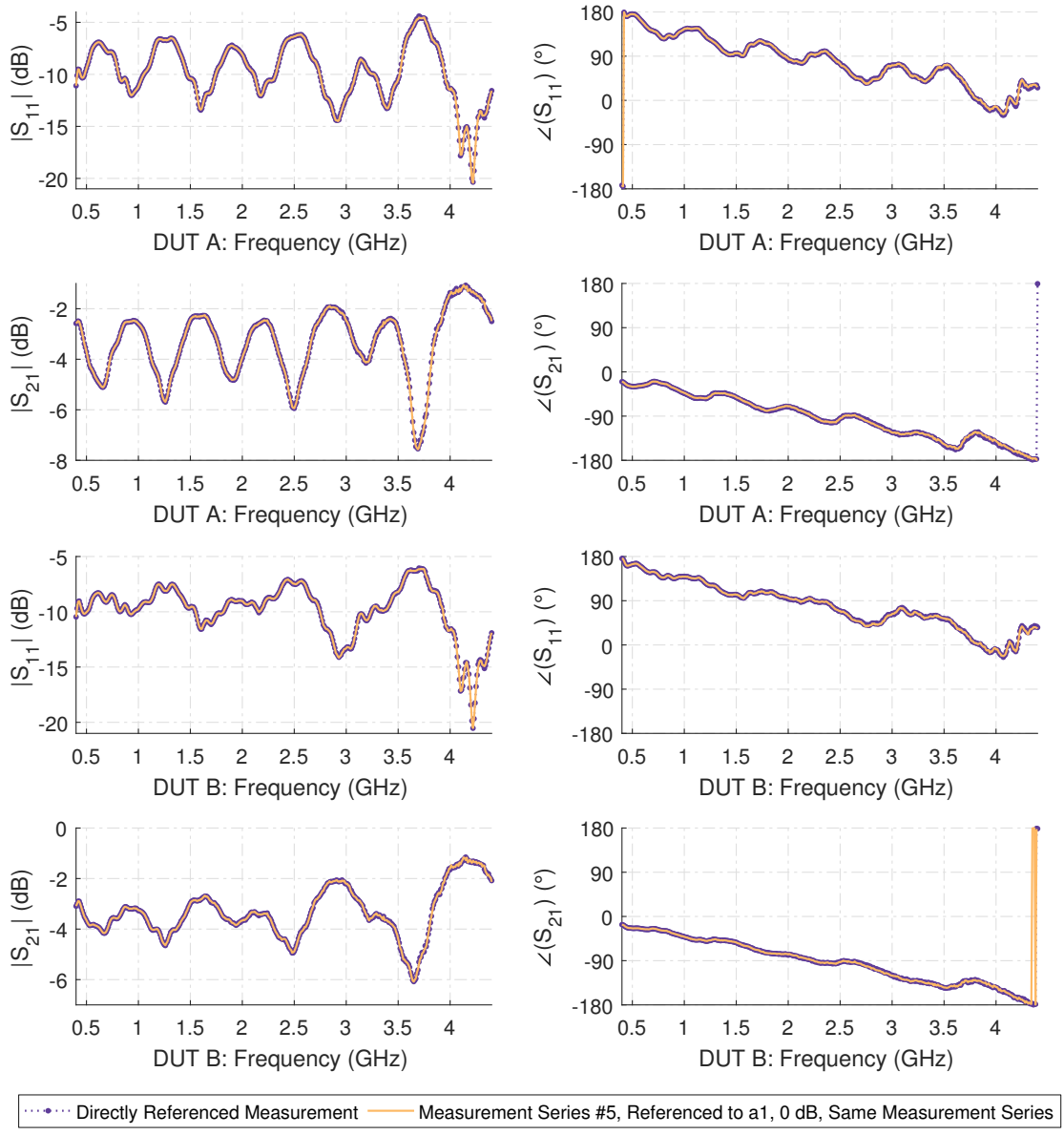

Figure B.50: S-parameter measurement results for the a-wave speed-up tee measurement DUT compared to concurrent a_1 measurement, referenced to first a_1 measurement of the cycle. DUT A - step attenuator 6 dB setting, DUT B - step attenuator 10 dB setting.

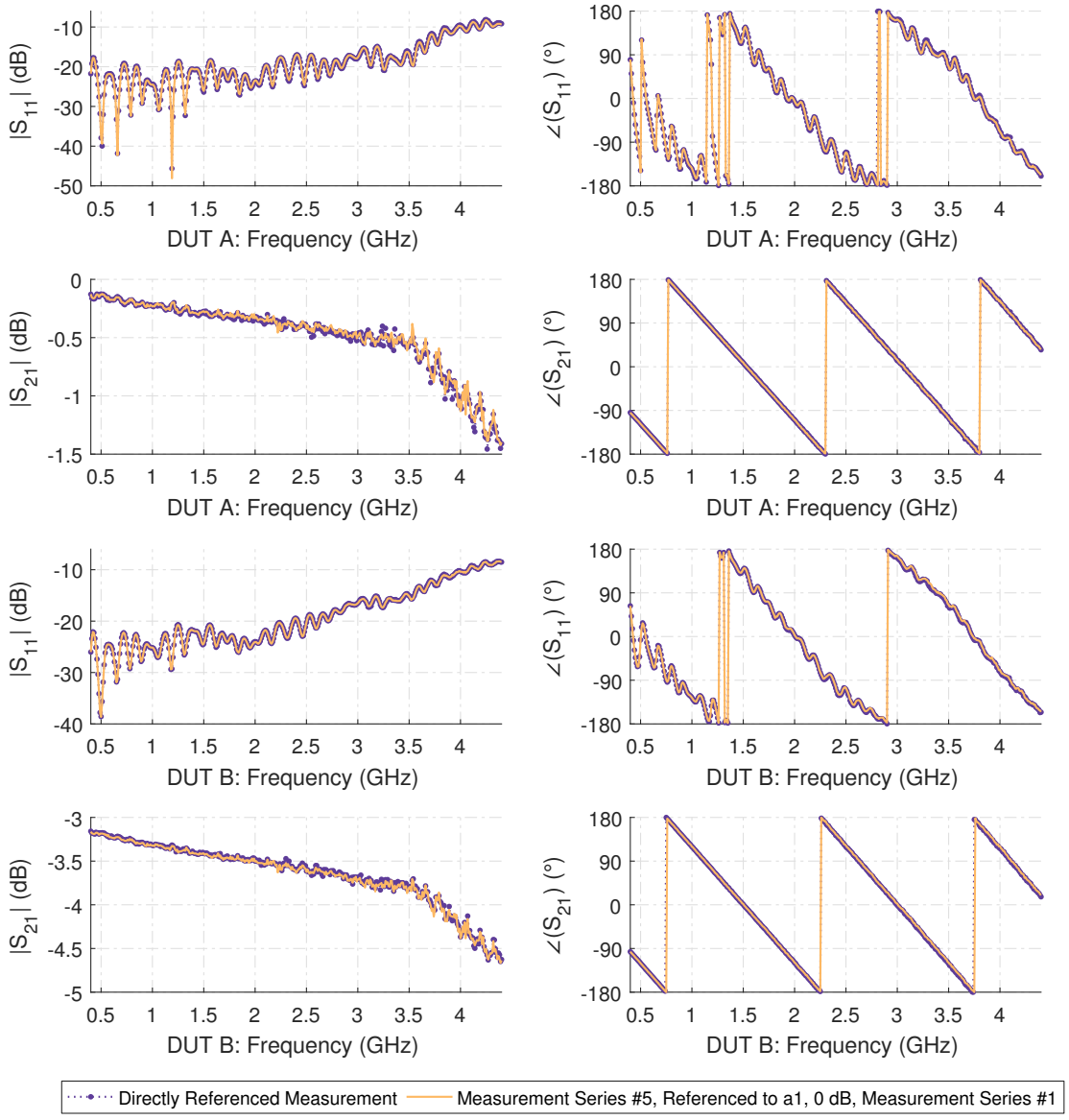

Figure B.51: S-parameter measurement results for the a-wave speed-up thru measurement DUT compared to concurrent a_1 measurement of the 5th and last tuning cycle, referenced to very first a_1 measurement. DUT A - step attenuator 0 dB setting, DUT B - step attenuator 3 dB setting.

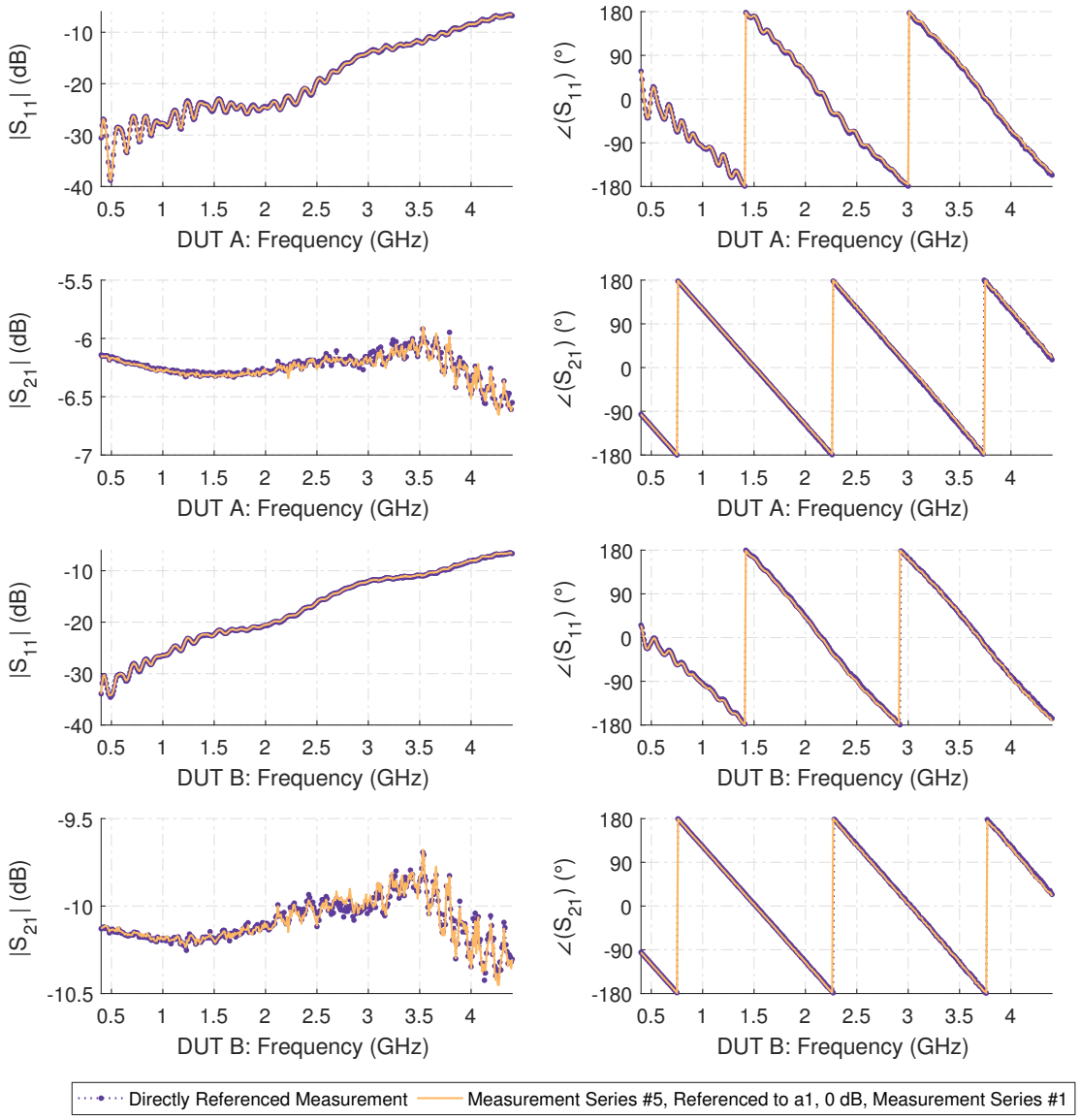

Figure B.52: S-parameter measurement results for the a-wave speed-up thru measurement DUT compared to concurrent a_1 measurement of the 5th and last tuning cycle, referenced to very first a_1 measurement. DUT A - step attenuator 6 dB setting, DUT B - step attenuator 10 dB setting.

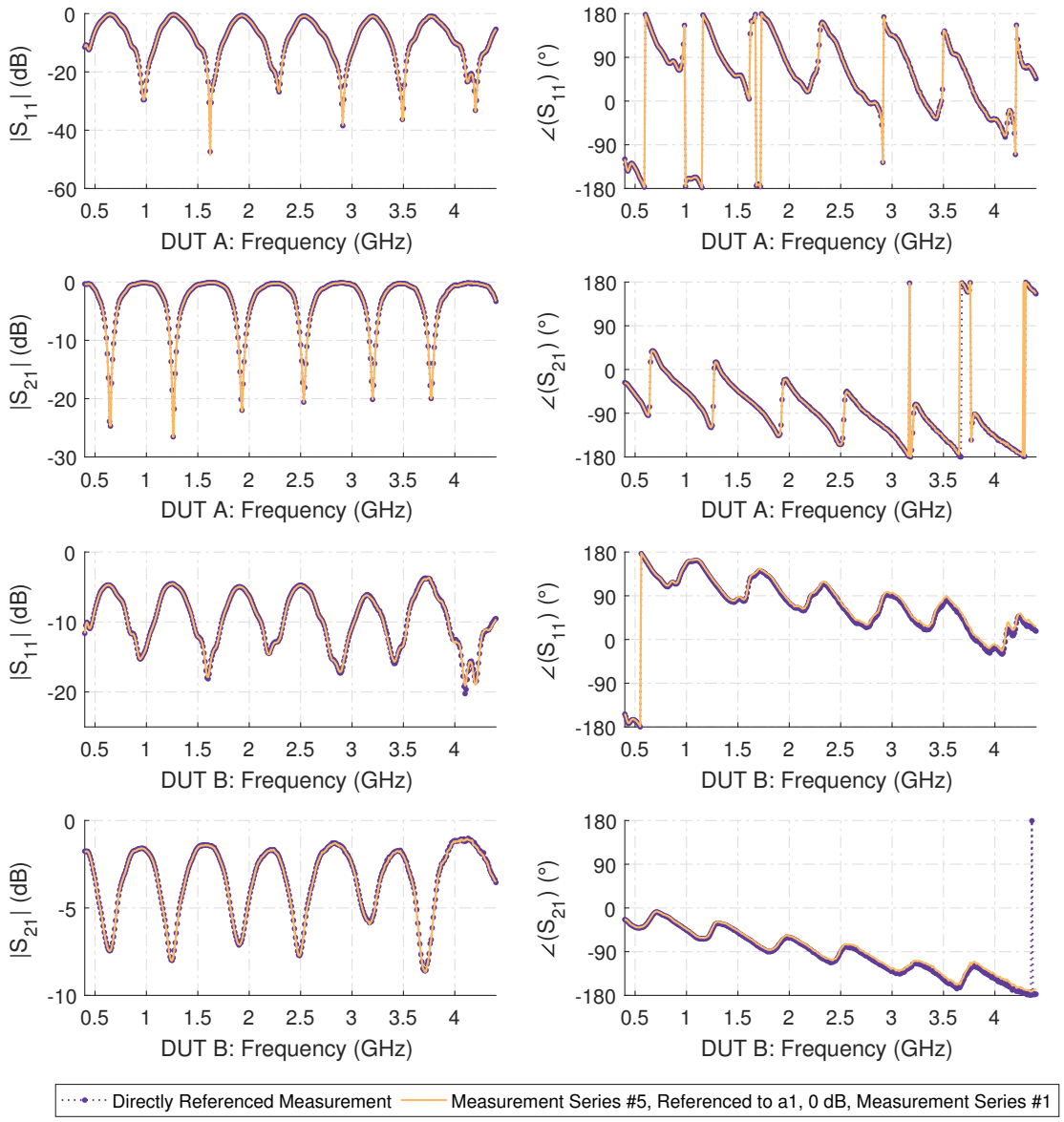

Figure B.53: S-parameter measurement results for the a-wave speed-up tee measurement DUT compared to concurrent a_1 measurement of the 5th and last tuning cycle, referenced to very first a_1 measurement. DUT A - step attenuator 0 dB setting, DUT B - step attenuator 3 dB setting.

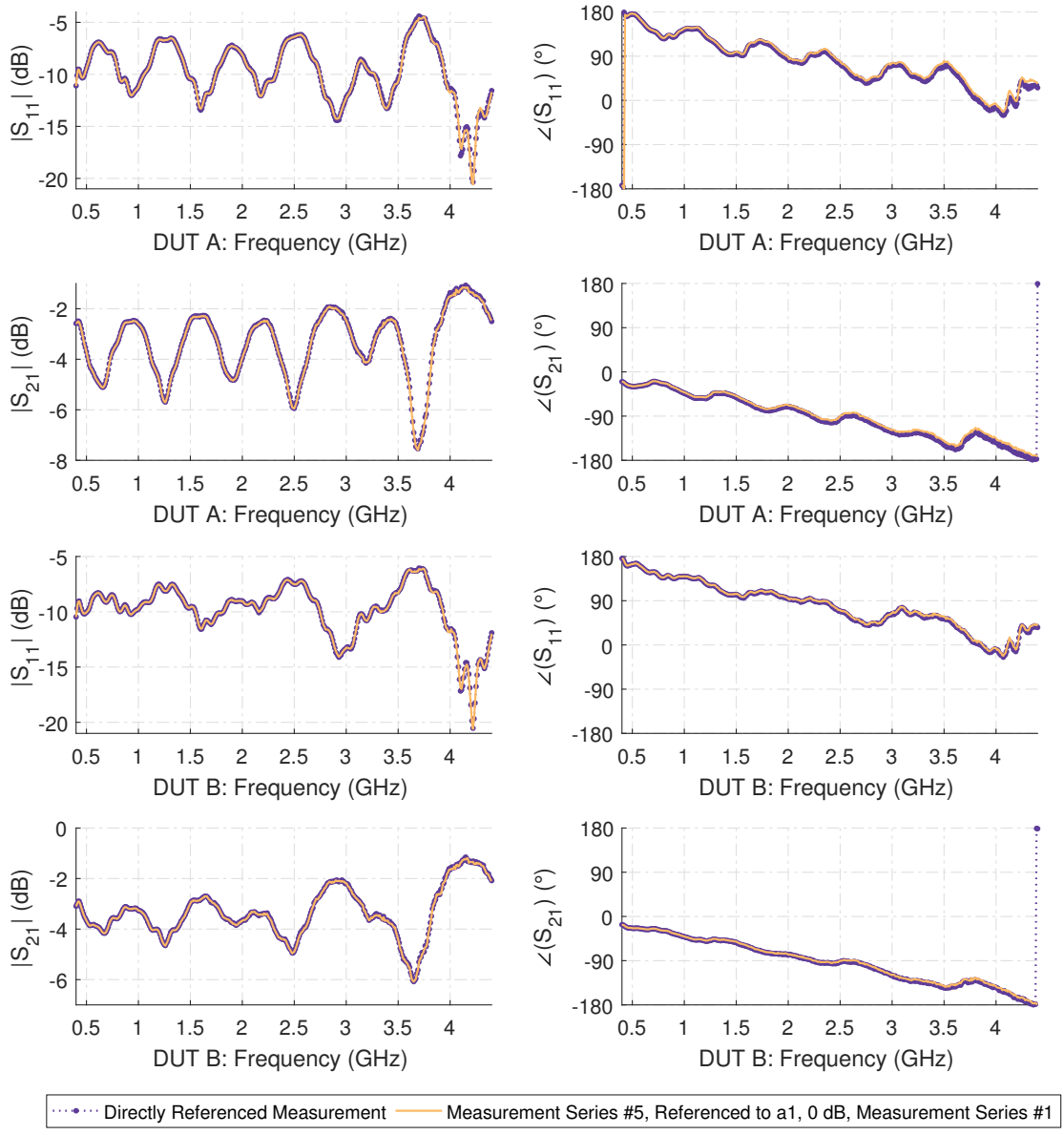

Figure B.54: S-parameter measurement results for the a-wave speed-up tee measurement DUT compared to concurrent a_1 measurement of the 5th and last tuning cycle, referenced to very first a_1 measurement. DUT A - step attenuator 6 dB setting, DUT B - step attenuator 10 dB setting.

List of Figures

Bibliography

[1] RECCO AB. Homepage. `http://www.recco.com/`.

[2] T. Aballo, L. Cabria, J. A. Garcia, T. Fernandez, and F. Marante. Taking advantage of a schottky junction nonlinear characteristic for radiofrequency temperature sensing. In *2006 European Microwave Conference*, pages 318–321, September 2006.

[3] K. Abbas. A new recurrent approach for phase unwrapping. *International Journal of Applied Science and Engineering*, 3(2):135–143, 2005.

[4] W. Akstaller, C. Musolff, R. Weigel, and A. Hagelauer. X-parameter characterization of TC SAW filters with enhanced dynamic range. *IEEE Transactions on Microwave Theory and Techniques*, 65(11):4541–4549, November 2017.

[5] A. Aldoumani, P. J. Tasker, R. S. Saini, J. W. Bell, T. Williams, and J. Lees. Operation and calibration of VNA-based large signal RF I-V waveform measurements system without using a harmonic phase reference standard. In *81st ARFTG Microwave Measurement Conference 2013*, pages 1–4, June 2013.

[6] Analog Devices. AN-1353: How to bypass VCO calibration for the ADF4355-2, ADF4355, ADF4355-3, ADF4356, ADF5355, and ADF5356. http://www.analog.com/media/en/technical-documentation/application-notes/AN-1353.pdf.

[7] Analog Devices. Homepage. `http://www.analog.com`.

[8] H. Aniktar, D. Baran, E. Karav, E. Akkaya, Y. S. Birecik, and M. Sezgin. Getting the bugs out: A portable harmonic radar system for electronic countersurveillance applications. *IEEE Microwave Magazine*, 16(10):40–52, November 2015.

[9] H. Aumann, E. Kus, B. Cline, and N. W. Emanetoglu. A 5.8 GHz harmonic RF tag for tracking amphibians. In *2012 IEEE International Conference on Wireless Information Technology and Systems (ICWITS)*, pages 1–4, November 2012.

[10] H. M. Aumann and N. W. Emanetoglu. A wideband harmonic radar for tracking small wood frogs. In *2014 IEEE Radar Conference*, pages 0108–0111, May 2014.

[11] C. A. Balanis. *Antenna Theory: Analysis and Design*. Wiley, 2015.

[12] R. W. Beatty. 2-port $\lambda/4$ waveguide standard of voltage standing-wave ratio. *Electronics Letters*, 9(2):24–26, 1973.

[13] V. V. Belyaev, A. T. Mayunov, and S. N. Razin'kov. Object detection range enhancement by means of nonlinear radar employing two signals with linear frequency modulation. *Measurement Techniques*, 46(8):802–805, 2003.

[14] T. Berger and S. Hamran. Harmonic synthetic aperture radar processing. *IEEE Geoscience and Remote Sensing Letters*, 12(10):2066–2069, October 2015.

[15] B. Brannon. Sampled systems and the effects of clock phase noise and jitter. Analog Devices Application Note 756, 2004.

[16] B. Brannon and A. Barlow. Aperture uncertainty and ADC system performance. Analog Devices Application Note 501, 2006.

[17] J. V. Butler, D. K. Rytting, M. F. Iskander, R. D. Pollard, and M. Vanden Bossche. 16-term error model and calibration procedure for on-wafer network analysis measurements. *IEEE Transactions on Microwave Theory and Techniques*, 39(12):2211–2217, December 1991.

[18] G. L. Charvat. *Small and Short-Range Radar Systems*. Modern and Practical Approaches to Electrical Engineering. CRC Press, 2015.

[19] T. S. Clement, P. D. Hale, D. F. Williams, C. M. Wang, A. Dienstfrey, and D. A. Keenan. Calibration of sampling oscilloscopes with high-speed photodiodes. *IEEE Transactions on Microwave Theory and Techniques*, 54(8):3173–3181, August 2006.

[20] Anritsu Corporation. Homepage. `http://www.anritsu.com`.

[21] S. C. Cripps. *RF power amplifiers for wireless communications*. Artech House microwave library. Artech House, 1999.

[22] B. Daly. A new approach to fractional-n PLL design yields performance breakthrough. *Microwave Product Digest*, pages 18–19, April 2003.

[23] Analog Devices. ADF4356 6.8 GHz wideband synthesizer with integrated VCO datasheet. http://www.analog.com/media/en/technical-documentation/data-sheets/ADF4356.pdf.

[24] M. Dishal. Side band crystal filters. In *13th Annual Symposium on Frequency Control*, page 404, 1959.

[25] M. Dishal. Modern network theory design of single-sideband crystal ladder filters. *Proceedings of the IEEE*, 53(9):1205 – 1216, September 1965.

[26] A. W. Doerry. Reflectors for SAR performance testing. Technical Report SAND2008-0396, Sandia National Laboratories, January 2008.

[27] J. P. Dunsmore. *Handbook of Microwave Component Measurements*. Wiley, 2012.

[28] EIA / IBIS Open Forum. *Touchstone File Format Specification Rev 1.1*, 2002. `https://ibis.org/connector/touchstone_spec11.pdf`.

[29] R. Essaadali, A. Jarndal, A. B. Kouki, and F. M. Ghannouchi. Conversion rules between X-parameters and linearized two-port network parameters for large-signal operating conditions. *IEEE Transactions on Microwave Theory and Techniques*, 66(11):4745–4756, November 2018.

[30] H.-J. Eul and B. Schiek. A generalized theory and new calibration procedures for network analyzer self-calibration. *IEEE Transactions on Microwave Theory and Techniques*, 39(4):724–731, 1991.

[31] A. Ferrero and U. Pisani. Two-port network analyzer calibration using an unknown 'thru'. *IEEE Microwave and Guided Wave Letters*, 2(12):505–507, December 1992.

[32] A. Ferrero, V. Teppati, M. Garelli, and A. Neri. A novel calibration algorithm for a special class of multiport vector network analyzers. *IEEE Transactions on Microwave Theory and Techniques*, 56(3):693–699, March 2008.

[33] H. T. Friis. Analysis of harmonic generator circuits for step recovery diodes. *Proceedings of the IEEE*, 55(7):1192–1194, July 1967.

[34] K. A. Gallagher. *Harmonic Radar: Theory and Applications to Nonlinear Target Detection, Tracking, Imaging and Classification.* PhD thesis, Pennsylvania State University, 2015.

[35] K. A. Gallagher, R. M. Narayanan, G. J. Mazzaro, and K. D. Sherbondy. Linearization of a harmonic radar transmitter by feed-forward filter reflection. In *2014 IEEE Radar Conference*, pages 1363–1368, May 2014.

[36] N. Galster, M. Frecker, E. Carroll, J. Vobecky, and P. Hazdra. Application-specific fast-recovery diode: Design and performance. *PCIM, Tokyo*, 1998.

[37] G. Goertzel. An algorithm for the evaluation of finite trigonometric series. *American Math. Monthly*, 65:34–35, 1958.

[38] A. Gronefeld and B. Schiek. Network-analyzer self-calibration with four or five standards for the 15-term error-model. In *1997 IEEE MTT-S International Microwave Symposium Digest*, volume 3, pages 1655–1658 Vol. 3, June 1997.

[39] D. Gunyan and Y.-P. Teoh. Characterization of active harmonic phase standard with improved characteristics for nonlinear vector network analyzer calibration. In *71st ARFTG Microwave Measurement Conference 2008*, pages 1–7, June 2008.

[40] P. D. Hale, A. Dienstfrey, J. C. M. Wang, D. F. Williams, A. Lewandowski, D. A. Keenan, and T. S. Clement. Traceable waveform calibration with a covariance-based uncertainty analysis. *IEEE Transactions on Instrumentation and Measurement"*, 58(10):3554–3568, October 2009.

[41] P. D. Hale, K. A. Remley, D. F. Williams, J. A. Jargon, and C. M. J. Wang. A compact millimeter-wave comb generator for calibrating broadband vector receivers. In *85th ARFTG Microwave Measurement Conference 2015*, pages 1–4, May 2015.

[42] P. D. Hale, C. M. Wang, D. F. Williams, K. A. Remley, and J. D. Wepman. Compensation of random and systematic timing errors in sampling oscilloscopes. *IEEE Transactions on Instrumentation and Measurement"*, 55(6):2146–2154, December 2006.

[43] S. Hamilton and R. Hall. Shunt-mode harmonic generation using step recovery diodes. *Microwave Journal*, 10(5):69–78, 1967.

[44] R. O. Harger. Harmonic radar systems for near-ground in-foliage nonlinear scatterers. *IEEE Transactions on Aerospace and Electronic Systems*, AES-12(2):230–245, March 1976.

[45] A. Harney and Analog Devices. Achieving phase coherence between multiple Fractional-N PLLs, ADF4350 phase resync and phase programmability. https://ez.analog.com/docs/DOC-2451.

[46] T. Harzheim and H. Heuermann. Phase repeatable synthesizers as a new harmonic phase standard for nonlinear network analysis. *IEEE Transactions on Microwave Theory and Techniques*, 66(6):2888–2895, June 2018.

[47] T. Harzheim, H. Heuermann, and M. Marso. An adaptive biasing method for SRD comb generators. In *2016 German Microwave Conference (GeMiC)*, pages 289–292, March 2016.

[48] A. Henze, N. Tempone, G. Monasterios, and H. Silva. Incomplete 2-port vector network analyzer calibration methods. In *Biennial Congress of Argentina (ARGENCON), 2014 IEEE*, pages 810–815. IEEE, 2014.

[49] H. Heuermann. *Sichere Verfahren zur Kalibrierung von Netzwerkanalysatoren für koaxiale und planare Leitungssysteme*. PhD thesis, Ruhr-Universität Bochum, 1996.

[50] H. Heuermann. Sure methods of on-wafer scattering parameter measurements with self-calibration procedures. In *47th ARFTG Conference Digest*, volume 29, pages 136–145, June 1996.

[51] H. Heuermann. GSOLT: the calibration procedure for all multi-port vector network analyzers. In *IEEE MTT-S International Microwave Symposium Digest, 2003*, volume 3, pages 1815–1818 vol.3, June 2003.

[52] H. Heuermann. Old and new accuracy estimation of s-parameter measurements with the ripple-test. In *MTT-S International Microwave Symposium Workshop TMB San Francisco*, 2006.

[53] H. Heuermann. Calibration of a network analyzer without a thru connection for nonlinear and multiport measurements. *IEEE Transactions on Microwave Theory and Techniques*, 56(11):2505–2510, November 2008.

[54] H. Heuermann. *Hochfrequenztechnik: Komponenten für High-Speed- und Hochfrequenzschaltungen*. Vieweg+Teubner Verlag, 2009.

[55] H. Heuermann and T. Harzheim. Mess- und Überwachungsvorrichtung für reifenbezogene Größen eines Fahrzeugs, July 28 2016. WO Patent App. PCT/DE2016/100,021.

[56] H. Heuermann and B. Schiek. Results of network analyzer measurements with leakage errors corrected with the TMS-15-term procedure. In *1994 IEEE MTT-S International Microwave Symposium Digest (Cat. No.94CH3389-4)*, pages 1361–1364 vol.3, May 1994.

[57] H. Heuermann and B. Schiek. 15-term self-calibration methods for the error-correction of on-wafer measurements. *IEEE Transactions on Instrumentation and Measurement*, 46(5):1105–1110, October 1997.

[58] Hewlett Packard. *Application Note 920: Harmonic generation using step recovery diodes and SRD modules*.

[59] Hewlett Packard. *HP Application Note 913: Step recovery diode multiplier design*, May 1967.

[60] M. Hiebel. *Grundlagen der vektoriellen Netzwerkanalyse*. Rohde & Schwarz, 2006.

[61] M. L. Hsu, T. H. Liu, T. C. Yang, H. C. Jhan, H. Wang, F. R. Chang, K. Y. Lin, E. C. Yang, and Z. M. Tsai. Bee searching radar with high transmit receive isolation using pulse pseudorandom code. *IEEE Transactions on Microwave Theory and Techniques*, 64(12):4324–4335, December 2016.

[62] J. Huang, Z. He, M. Nie, A. Yang, L. Wang, and Y. Zhang. Wideband NVNA phase calibration based on multisine standards and phase alignment. In *2016 IEEE International Conference on Microwave and Millimeter Wave Technology (ICMMT)*, volume 1, pages 201–203, June 2016.

[63] Indutech GmbH. Homepage. `http://www.indutech.com`.

[64] Inc. (IDT) Integrated Device Technology. Homepage. `https://www.idt.com/`.

[65] M. Isaksson and E. Zenteno. A synthetic vector network analyzing measurement system. *IEEE Transactions on Instrumentation and Measurement*, 60(6):2154–2161, June 2011.

[66] K. Itoh. Analysis of the phase unwrapping algorithm. *Applied optics*, 21(14):2470–2470, 1982.

[67] J. A. Jargon, D. C. DeGroot, and D. F. Vecchia. Repeatability study of commercial harmonic phase standards measured by a nonlinear vector network analyzer. In *62nd ARFTG Microwave Measurements Conference Fall 2003*, pages 243–258, December 2003.

[68] J. A. Jargon and R. B. Marks. Two-tier multiline TRL for calibration of low-cost network analyzers. In *46th ARFTG Conference Digest*, volume 28, pages 1–8, November 1995.

[69] J. A. Jargon, J. D. Splett, D. F. Vecchia, and D. C. DeGroot. An empirical model for the warm-up drift of a commercial harmonic phase standard. *IEEE Transactions on Instrumentation and Measurement*, 56(3):931–937, June 2007.

[70] G. Kesel, J. Hammerschmitt, and E. Lange. *Signalverarbeitende Dioden*. Halbleiter-Elektronik. Springer, 1982.

[71] W. Kester. Converting oscillator phase noise to time jitter. *Tutorial MT-008, Analog Devices*, 2009. `http://www.analog.com/media/ru/training-seminars/tutorials/MT-008.pdf`.

[72] W. A. Kester. *Data Conversion Handbook*. Elsevier Science, 2005.

[73] J. Kiriazi, J. Nakakura, K. Hall, N. Hafner, and V. Lubecke. Low profile harmonic radar transponder for tracking small endangered species. In *2007 29th Annual International Conference of the IEEE Engineering in Medicine and Biology Society*, pages 2338–2341, August 2007.

[74] H. Kobayashi, M. Morimura, K. Kobayashi, and Y. Onaya. Aperture jitter effects in wideband adc systems. In *SICE '99. Proceedings of the 38th SICE Annual Conference. International Session Papers (IEEE Cat. No.99TH8456)*, pages 1089–1094, July 1999.

[75] J. A. Kosinski, W. D. Palmer, and M. B. Steer. Unified understanding of RF remote probing. *IEEE Sensors Journal*, 11(12):3055–3063, December 2011.

[76] B. Kubina, J. Romeu, C. Mandel, M. Schüßler, and R. Jakoby. Design of a quasi-chipless harmonic radar sensor for ambient temperature sensing. In *SENSORS, 2014 IEEE*, pages 1567–1570, November 2014.

[77] Y.-T. Liu, M.-L. Hsu, H. Wang, and Z.-M. Tsai. A differential miniature transponder for 9.4/18.8 GHz harmonic bee searching radar with low gain degradation from bee's body. In *2016 IEEE MTT-S International Microwave Symposium (IMS)*, pages 1–4, May 2016.

[78] U. Lott. Measurement of magnitude and phase of harmonics generated in nonlinear microwave two-ports. *IEEE Transactions on Microwave Theory and Techniques*, 37(10):1506–1511, October 1989.

[79] R. G. Lyons. *Understanding Digital Signal Processing, Third Edition*. Pearson Education, 2010.

[80] R. B. Marks. Formulations of the basic vector network analyzer error model including switch-terms. In *50th ARFTG Conference Digest*, volume 32, pages 115–126, December 1997.

[81] G. J. Mazzaro, K. A. Gallagher, A. F. Martone, K. D. Sherbondy, and R. M. Narayanan. Short-range harmonic radar: chirp waveform, electronic targets. *Proceedings of SPIE*, 9461, 2015.

[82] G. J. Mazzaro, A. F. Martone, and D. M. McNamara. Detection of RF electronics by multitone harmonic radar. *IEEE Transactions on Aerospace and Electronic Systems*, 50(1):477–490, January 2014.

[83] G. J. Mazzaro, A. F. Martone, K. I. Ranney, and R. M. Narayanan. Nonlinear radar for finding RF electronics: System design and recent advancements. *IEEE Transactions on Microwave Theory and Techniques*, 65(5):1716–1726, May 2017.

[84] D. Milanesio, M. Saccani, R. Maggiora, D. Laurino, and M. Porporato. Design of an harmonic radar for the tracking of the asian yellow-legged hornet. *Ecology and Evolution*, 6(7):2170–2178, 2016.

[85] D. Milanesio, M. Saccani, R. Maggiora, D. Laurino, and M. Porporato. Recent upgrades of the harmonic radar for the tracking of the asian yellow-legged hornet. *Ecology and Evolution*, 7(13):4599–4606, 2017.

[86] Mini-Circuits, Inc. Homepage. `http://www.minicircuits.com/`.

[87] W. Van Moer and L. Gomme. NVNA versus LSNA: enemies or friends? *IEEE Microwave Magazine*, 11(1):97–103, February 2010.

[88] J. L. Moll and S. A. Hamilton. Physical modeling of the step recovery diode for pulse and harmonic generation circuits. *Proceedings of the IEEE*, 57(7):1250–1259, July 1969.

[89] F. E. Nathanson, J. P. Reilly, and M. N. Cohen. *Radar Design Principles: Signal Processing and the Environment*. Scitech Publishing, 1999.

[90] National Semiconductor. *Application Note 1001, An Analysis and Performance Evaluation of a Passive Filter Design Technique for Charge Pump PLLs*, July 2001.

[91] US Navy. *Electronic Warfare and Radar Systems Engineering Handbook*. Naval Air Warfare Center Weapons Division, 2013.

[92] T. S. Nielsen, C. Gillease, and V. Torres. Practical considerations for high-power X-parameter measurements for power amplifier design. In *WAMICON 2012 IEEE Wireless Microwave Technology Conference*, pages 1–9, April 2012.

[93] DRAGON Development of Resource-efficient and Advanced underground technologies. Homepage. `http://www.dragonproject.eu/`.

[94] O. Ostwald. T-check accuracy test for vector network analyzers utilizing a tee-junction, application note 1EZ43_0E. Technical report, Rohde & Schwarz, June 1998. `https://cdn.rohde-schwarz.com/pws/dl_downloads/dl_application/application_notes/1ez43/1ez43_0e.pdf`.

[95] V. Palazzi, F. Alimenti, C. Kalialakis, P. Mezzanotte, A. Georgiadis, and L. Roselli. Highly integrable paper-based harmonic transponder for low-power and long-range IoT applications. *IEEE Antennas and Wireless Propagation Letters*, 16:3196–3199, 2017.

[96] V. Palazzi, F. Alimenti, P. Mezzanotte, M. Virili, C. Mariotti, G. Orecchini, and L. Roselli. Low-power frequency doubler in cellulose-based materials for harmonic RFID applications. *IEEE Microwave and Wireless Components Letters*, 24(12):896–898, December 2014.

[97] V. Palazzi, P. Mezzanotte, and L. Roselli. Design of a novel antenna system intended for harmonic RFID tags in paper substrate. In *2015 IEEE Wireless Power Transfer Conference (WPTC)*, pages 1–4, May 2015.

[98] D. M. Pozar. *Microwave Engineering*. Wiley India, 2012.

[99] D.M. Pozar. *Microwave and RF Wireless Systems*. Wiley, 2000.

[100] S. M. Presas, T. M. Weller, S. Silverman, and M. Rakijas. High efficiency diode doubler with conjugate- matched antennas. In *2007 European Microwave Conference*, pages 250–253, October 2007.

[101] D. Psychoudakis, W. Moulder, C.-C. Chen, H. Zhu, and J. L Volakis. A portable low-power harmonic radar system and conformal tag for insect tracking. *IEEE Antennas and Wireless Propagation Letters*, 7:444–447, 2008.

[102] K. Ranney, G. Mazzaro, K. Gallagher, A. Martone, K. Sherbondy, and R. Narayanan. Instantaneous stepped-frequency, non-linear radar part 2: experimental confirmation. In *Radar Sensor Technology XX*, volume 9829, page 98291P. International Society for Optics and Photonics, 2016.

[103] K. Rasilainen, J. Ilvonen, A. Lehtovuori, J.-M. Hannula, and V. Viikari. Harmonic transponders: Performance and challenges. *Progress In Electromagnetics Research*, 41:139–147, 2015.

[104] K. Rasilainen and V. V. Viikari. Transponder designs for harmonic radar applications. *International Journal of Antennas and Propagation*, 2015, 2015.

[105] H. C. Reader, D. F. Williams, P. D. Hale, and T. S. Clement. Comb-generator characterization. *IEEE Transactions on Microwave Theory and Techniques*, 56(2):515–521, February 2008.

[106] M. Ben Rejeb, A. Raslan, and S. Boumaiza. Phase calibration for coherent multiharmonic modulated signal measurements using nonlinear vector network analyzer. In *2016 IEEE MTT-S International Microwave Symposium (IMS)*, pages 1–4, May 2016.

[107] D. C. Ribeiro, P. M. Cruz, and N. B. Carvalho. Towards a denser frequency grid in phase measurements using mixer-based receivers. In *85th ARFTG Microwave Measurement Conference 2015*, pages 1–5, May 2015.

[108] P. Roblin. *Nonlinear RF Circuits and Nonlinear Vector Network Analyzers: Interactive Measurement and Design Techniques*. The Cambridge RF and Microwave Engineering Series. Cambridge University Press, 2011.

[109] Rohde & Schwarz. ZVA Series Datasheet.

[110] Rohde & Schwarz GmbH & Co. KG. Homepage. `http://www.rohde-schwarz.de`.

[111] U. L. Rohde. *Digital PLL frequency synthesizers: Theory and design*. Prentice-Hall, 1983.

[112] O. Rompelman and H. H. Ros. Coherent averaging technique: A tutorial review part 1: Noise reduction and the equivalent filter. *Journal of Biomedical Engineering*, 8:24–9, February 1986.

[113] O. Rompelman and H.H. Ros. Coherent averaging technique: A tutorial review part 2: Trigger jitter, overlapping responses and non-periodic stimulation. *Journal of Biomedical Engineering*, 8:30–5, February 1986.

[114] D. Rönnow, S. Amin, M. Alizadeh, and E. Zenteno. Phase noise coherence of two continuous wave radio frequency signals of different frequency. *IET Science, Measurement & Technology*, 11(1):77–85, 2017.

[115] D. E. Root, J. Verspecht, J. Horn, and M. Marcu. *X-Parameters: Characterization, Modeling, and Design of Nonlinear RF and Microwave Components*. The Cambridge RF and Microwave Engineering Series. Cambridge University Press, 2013.

[116] D. E. Root, J. Verspecht, D. Sharrit, J. Wood, and A. Cognata. Broad-band poly-harmonic distortion (PHD) behavioral models from fast automated simulations and large-signal vectorial network measurements. *IEEE Transactions on Microwave Theory and Techniques*, 53(11):3656–3664, November 2005.

[117] P.J. Rousseeuw and A.M. Leroy. *Robust Regression and Outlier Detection*. Wiley Series in Probability and Statistics. Wiley, 2003.

[118] A. Rumiantsev and N. Ridler. VNA calibration. *IEEE Microwave Magazine*, 9(3):86–99, June 2008.

[119] D. Rytting. Network analyzer error models and calibration methods. *Agilent Technologies White Paper*, 1998.

[120] J. Saebboe, V. Viikari, T. Varpula, H. Seppä, S. Cheng, M. Al-Nuaimi, P. Hallbjörner, and A. Rydberg. Harmonic automotive radar for VRU classification. In *2009 International Radar Conference "Surveillance for a Safer World" (RADAR 2009)*, pages 1–5, October 2009.

[121] J.A. Scheer, M.A. Richards, W.A. Holm, and W.L. Melvin. *Principles of Modern Radar*. SCITECH PUB, 2013.

[122] B. Schiek. *Grundlagen der Hochfrequenz-Messtechnik*. Springer Berlin Heidelberg, 2013.

[123] B. Schiek, I. Rolfes, and H.J. Siweris. *Noise in High-Frequency Circuits And Oscillators*. Wiley-Interscience, 2006.

[124] T. Schilcher. RF applications in digital signal processing. *CAS 2007 - CERN Accelerator School: Course on Digital Signal Processing*, 2008. `http://cds.cern.ch/record/1100538`.

[125] M. Schramm. *Verfahren zur vektoriellen Netzwerkanalyse unter Berücksichtigung der besonderen Anforderungen beim HF-Produktionstest*. PhD thesis, Friedrich-Alexander-Universität Erlangen-Nürnberg, 2015.

[126] M. Schramm, M. Hrobak, J. Schür, L. P. Schmidt, and M. Konrad. Impact of different post-processing methods on a one-receiver 2-port synthetic VNA architecture. In *2011 41st European Microwave Conference*, pages 487–490, October 2011.

[127] M. Schramm, M. Hrobak, J. Schür, L. P. Schmidt, and M. Konrad. MOS-16: A new method for in-fixture calibration and fixture characterization. In *77th ARFTG Microwave Measurement Conference*, pages 1–7, June 2011.

[128] M. Schramm, M. Hrobak, J. Schür, L. P. Schmidt, and A. Lechner. A simplified method for measuring complex S-parameters dedicated to synthetic instrumentation. In *The 40th European Microwave Conference*, pages 264–267, September 2010.

[129] Manufacturer of the DG8SAQ VNWA3 SDR-Kits. Homepage. `http://www.sdr-kits.net/`.

[130] P. K. Sen. Estimates of the regression coefficient based on kendall's tau. *Journal of the American Statistical Association*, 63(324):1379–1389, 1968.

[131] M. Shinagawa, Y. Akazawa, and T. Wakimoto. Jitter analysis of high-speed sampling systems. *IEEE Journal of Solid-State Circuits*, 25(1):220–224, February 1990.

[132] Silicon Labs. *Application Note AN739, Estimating Clock Tree Jitter, Rev. 0.91*, 2012.

[133] Silicon Labs. *Application Note AN118, Improving ADC Resolution by Oversampling and Averaging, Rev. 1.3*, 2013.

[134] A. Singh and V. Lubecke. Body-worn passive planar harmonic tag design for use with doppler radar. In *2011 IEEE Topical Conference on Biomedical Wireless Technologies, Networks, and Sensing Systems*, pages 51–54, January 2011.

[135] A. Singh and V. M. Lubecke. Respiratory monitoring and clutter rejection using a cw doppler radar with passive RF tags. *IEEE Sensors Journal*, 12(3):558–565, March 2012.

[136] B. R. Smith. Choosing the right power splitter: Two-resistor or three-resistor. National Conference of Standards Laboratories, undatiert. [Online; Stand 29. Juli 2012] `http://www.home.agilent.com/owc_discussions/servlet/JiveServlet/download/85-18924-61584-3564/Power%20Splitter%20vs.%20Divider.pdf`.

[137] T. M. Souders, D. R. Flach, C. Hagwood, and G. L. Yang. The effects of timing jitter in sampling systems. *IEEE Transactions on Instrumentation and Measurement"*, 39(1):80–85, February 1990.

[138] J. Stenarson and K. Yhland. Automatic root selection for the unknown thru algorithm. In *2006 67th ARFTG Conference*, pages 150–155, June 2006.

[139] J. Surber and L. McHugh. Single-chip direct digital synthesis vs. the analog PLL. *Analog Dialogue*, 30(3):12–13, 1996.

[140] N. Tahir and G. Brooker. Toward the development of millimeter wave harmonic sensors for tracking small insects. *IEEE Sensors Journal*, 15(10):5669–5676, October 2015.

[141] Copper Mountain Technologies. Homepage. `http://www.coppermountaintech.com/`.

[142] Keysight Technologies. Homepage. `http://www.keysight.com`.

[143] V. Teppati, A. Ferrero, and M. Sayed. *Modern RF and Microwave Measurement Techniques*. The Cambridge RF and Microwave Engineering Series. Cambridge University Press, 2013.

[144] The Interchangeable Virtual Instruments Foundation (IVI). Standard commands for programmable instruments (SCPI) reference manual 1999. `http://www.ivifoundation.org/docs/scpi-99.pdf`.

[145] H. Theil. A rank-invariant method of linear and polynomial regression analysis. *Proceedings of the Royal Netherlands Academy of Sciences 53*, 53, 1950.

[146] Z. Tsai, F. Chang, K. Lin, E. Yang, F. Lian, and H. Wang. Application of harmonic radar on the research of bees' behavior. In *2016 International Symposium on Fundamentals of Electrical Engineering (ISFEE)*, pages 1–4, June 2016.

[147] Z. Tsai, P. Jau, N. Kuo, J. Kao, K. Lin, F. Chang, E. Yang, and H. Wang. A high-range-accuracy and high-sensitivity harmonic radar using pulse pseudorandom code for bee searching. *IEEE Transactions on Microwave Theory and Techniques*, 61(1):666–675, January 2013.

[148] Z. M. Tsai, P. H. Jau, N. C. Kuo, J. C. Kao, K. Y. Lin, F. R. Chang, E. C. Yang, and H. Wang. A high-range-accuracy and high-sensitivity harmonic radar using pulse pseudorandom code for bee searching. *IEEE Transactions on Microwave Theory and Techniques*, 61(1):666–675, January 2013.

[149] G. Vandersteen, Y. Rolain, and J. Schoukens. An identification technique for data acquisition characterization in the presence of nonlinear distortions and time base distortions. *IEEE Transactions on Instrumentation and Measurement*, 50(5):1355–1363, October 2001.

[150] J. Verspecht. *Calibration of a Measurement System for High Frequency Nonlinear Devices*. PhD thesis, Vrije Universiteit Brussel, 1995.

[151] J. Verspecht, J. Horn, L. Betts, D. Gunyan, R. Pollard, C. Gillease, and D. E. Root. Extension of X-parameters to include long-term dynamic memory effects. In *2009 IEEE MTT-S International Microwave Symposium Digest*, pages 741–744, June 2009.

[152] J. Verspecht and D. E. Root. Polyharmonic distortion modeling. *IEEE Microwave Magazine*, 7(3):44–57, June 2006.

[153] V. Viikari, H. Seppa, and D. Kim. Intermodulation read-out principle for passive wireless sensors. *IEEE Transactions on Microwave Theory and Techniques*, 59(4):1025–1031, April 2011.

[154] K. Wong. The "unknown thru" calibration advantage. In *ARFTG 63rd Conference, Spring 2004*, pages 73–81, June 2004.

[155] M. El Yaagoubi, G. Neveux, D. Barataud, T. Reveyrand, J. M. Nebus, F. Verbeyst, F. Gizard, and J. Puech. Time-domain calibrated measurements of wideband multisines using a large-signal network analyzer. *IEEE Transactions on Microwave Theory and Techniques*, 56(5):1180–1192, May 2008.

[156] L. Ying. Phase unwrapping. *Wiley Encyclopedia of Biomedical Engineering*, 6:1–11, 2006.

[157] M. Zeier, D. Allal, and R. Judaschke. Guidelines on the evaluation of vector network analysers (VNA), EURAMET calibration guide no. 12, version 3.0. Technical report, EURAMET e.V., March 2018. `https://www.euramet.org/Media/news/I-CAL-GUI-012_Calibration_Guide_No._12.web.pdf`.

[158] Y. Zhang, Z. He, H. Li, and M. Nie. Dense spectral grid NVNA phase measurements using vector signal generators. *IEEE Transactions on Instrumentation and Measurement"*, 2014.

[159] H. Zumbahlen. *Linear Circuit Design Handbook*. Elsevier Science, 2011.